AD-A046 089 ARMY ELECTRONICS COMMAND FORT MONMOUTH N J F/G 9/5
PROCEEDINGS OF THE ANNUAL SYMPOSIUM ON FREQUENCY CONTROL (30TH)--ETC(U)
1976 H K ZIEGLER

UNCLASSIFIED NL

1 OF 6
AD A046089

PROCEEDINGS OF THE 30th ANNUAL SYMPOSIUM ON FREQUENCY CONTROL

1976

held at Howard Johnsons Motor Lodge, Atlantic City, New Jersey on 2-4 June 1976

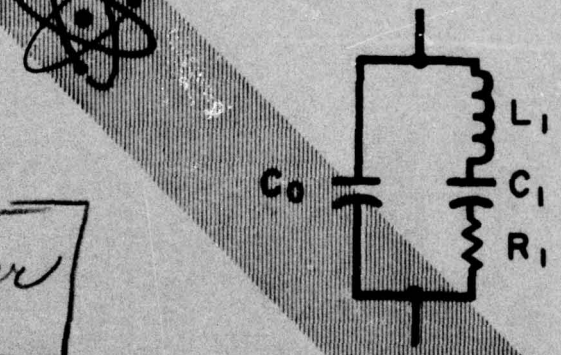

2-4 June 1976

U.S. Army Electronics Command

Fort Monmouth, New Jersey

PROCEEDINGS

of the

THIRTIETH ANNUAL FREQUENCY CONTROL SYMPOSIUM

1976

Sponsored By

U.S. ARMY ELECTRONICS COMMAND
Fort Monmouth, N.J.
Major General A. B. Crawford, Jr.
Commanding

ELECTRONICS TECHNOLOGY AND DEVICES LABORATORY
Dr. Hans K. Ziegler
Director

Copies of the Proceedings are available from:

Electronic Industries Association
2001 Eye Street, N.W.
Washington, D.C. 20006

PRICE PER COPY: $8.00

2 - 4 June 1976
Howard Johnson's Motor Lodge
Atlantic City, New Jersey

THIRTIETH ANNUAL FREQUENCY CONTROL SYMPOSIUM

Sponsored By

U.S. ARMY ELECTRONICS COMMAND

ELECTRONICS TECHNOLOGY AND DEVICES LABORATORY

Fort Monmouth, New Jersey

2 – 4 June 1976

Howard Johnson's Motor Lodge

Atlantic City, New Jersey

SYMPOSIUM EXECUTIVE COMMITTEE

Co-Chairman	Mr. Milton Tenzer
Co-Chairman	Dr. Erich Hafner
Executive Assistant	Dr. John Vig
Secretary	Mrs. Lee Hildebrandt

TECHNICAL PROGRAM COMMITTEE

Dr. Erich Hafner-Chairman
U.S. Army Electronics Command

Mr. Edward Alexander
Bell Laboratories

Dr. Art Ballato
U.S. Army Electronics Command

Mr. Andy Chi
NASA–Goddard Space Flight Center

Dr. Lewis Claiborne
Texas Instruments

Dr. Cecil Costain
National Research Council

Dr. Dick Damerow
Sandia Laboratories

Mr. Joe Giannotto
U.S. Army Electronics Command

Dr. Don Hammond
Hewlett–Packard

Dr. Helmut Hellwig
National Bureau of Standards

Mr. John Holmbeck
Northern Engineering Laboratories

Mr. Erich Kentley
C.R. Snelgrove

Mr. Art Machlin
U.S. Army Materiel Dev. & Readiness Cmd.

Mr. Pete Maresca
U.S. Army Satellite Comm. [illegible]

Mr. Dennis Reifel
Motorola

Mr. Lauren Rueger
Johns Hopkins University

Mr. Stan Schodowski
U.S. Army Electronics Command

Mr. John Sherman
General Electric

Dr. Richard Sydnor
Jet Propulsion Laboratory

Dr. Robert Vessot
Smithsonian Astrophysical Laboratory

Mr. Ted Viars
U.S. Army Electronics Command

Dr. John Vig
U.S. Army Electronics Command

Dr. Gernot Winkler
U.S. Naval Observatory

CHAIRMEN FOR TECHNICAL SESSIONS

NONLINEAR STRESS/STRAIN PHENOMENA

Dr. R. N. Thurston, Bell Laboratories

RESONATOR DESIGN AND MEASUREMENT

Mr. Edward J. Alexander, Bell Laboratories

CRYSTAL FILTERS AND MATERIAL PROPERTIES

Dr. Hans Jaffe

THEORY AND DESIGN OF RESONATORS (INCLUDING QUARTZ WATCH CRYSTALS)

Dr. Virgil E. Bottom, TYCO Crystal Products, Inc.

RESONATOR PROCESSING TECHNIQUES

Mr. John H. Sherman, Jr. General Electric

FREQUENCY GENERATION AND MEASUREMENT

Mr. Marvin E. Frerking, Collins Radio Co.

SURFACE WAVE DEVICES

Dr. Lewis Claiborne, Texas Instruments

FREQUENCY AND TIME - SYNCHRONIZATION, DISTRIBUTION AND APPLICATION

Col. William G. Huston, US Air Force

ATOMIC AND MOLECULAR FREQUENCY STANDARDS

Prof. N. F. Ramsey, Harvard University

DISCUSSION PANEL ON REMOTE SYNCHRONIZATION TECHNIQUES

Moderator - L. J. Rueger, The Johns Hopkins University

Panel: Mr. David Allan, National Bureau of Standards
Dr. Carroll Alley, University of Maryland
Dr. Thomas Clark, NASA - Goddard Space Flight Center
LCDR William Jones, US Coast Guard
Col. William G. Huston, US Air Force
Dr. Burton R. Saltzberg, Bell Laboratories
Dr. A. J. Van Dierendonck, General Dynamics
Dr. G. M. R. Winkler, US Naval Observatory

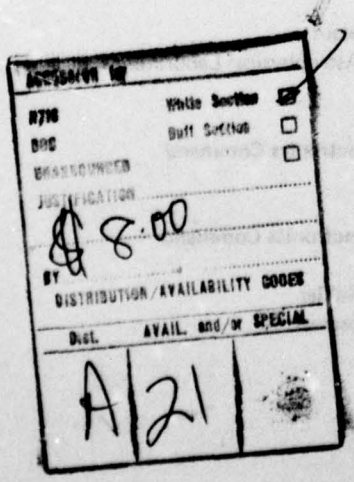

TABLE OF CONTENTS

EFFECTS OF ACCELERATION ON THE RESONNANCE FREQUENCIES OF CRYSTAL PLATES

P. C. Y. Lee and Kuang-Ming Wu
Department of Civil Engineering
Princeton University
Princeton, New Jersey

Summary

The changes in the thickness-shear resonnance frequencies of circular crystal plates subjected to steady in-plane acceleration with arbitrary direction are studied.

A closed form solution for a circular plate under acceleration with three or more points of mounting is obtained. From this solution, initial stress and strain fields are computed at each and every point of the plate as a function of plate orientation, direction of acceleration, and positions of supports. These fields are then taken into account in the coupled equations of the incremental thickness-shear and flexural vibrations through the second- and third-order elastic stiffness coefficients of the crystal.

Because of the space-dependence or non-uniformity of the initial fields and the smallness of the frequency changes ($\Delta f/f_o$ in the order of 10^{-9}) a perturbation method is used to calculate the changes in the thickness-shear resonnances. The predicted frequency changes are computed as functions of the acceleration direction and of the positions of the supports for AT cut of quartz. These are then compared with experimental values of A. W. Warner and W. L. Smith.

Introduction

This is the third in a series of studies of the frequency-sensitivity of crystal resonator plates to external forces. In the first paper of the series,[1] a system of six two-dimensional equations, accommodating the coupling of the flexure, extension, face-shear, thickness-shear and thickness-twist modes, was derived for vibrations or waves of small-amplitude superimposed on finite, elastic deformations due to static, initial stresses. In these equations, the nonlinear terms associated to the third-order elastic stiffnesses in stress-strain relations were included. Then the frequency changes of the fundamental thickness-shear modes of circular rotated Y-cuts of quarts, subjected to a pair of diametrical forces, were studied and compared with various existing experimental data.[2-5] In the second paper,[6] nonlinear effects of initial bending on the vibrations of circular quartz plates were investigated. The plate was flexed as a cantilever near the edge and stressed by a transverse, concentrated force applied at a point diametrically opposite the support. In obtaining the initial fields caused by bending, strain components were assumed to be small, but large gradients of plate deflection and large rotations of the plate element are permissible by retaining their quadratic terms in strain-displacement relations. Predicted values were compared with the measured ones by Mingins, Barcus, and Perry.[3] In both cases, explicit formulas for predicting frequency changes were obtained in terms zero- and first-order strains through the second- and third-order elastic stiffness coefficients.

In the present paper, the equations of motion for the coupled thickness-shear and flexural vibrations derived in Ref. 1 are employed in the studies of the acceleration effects on the changes in thickness-shear resonances. Experimental investigations on acceleration effects have been done by A. W. Warner,[7] W. L. Smith,[8] and by M. Valdois, J. J. Gagnepain and J. Besson.[9]

Circular Plate Under In-Plane Acceleration

A circular plate of radius R is referred to the rectangular coordinates X, Y, Z with XZ plane as the middle plane of the plate. The plate is supported by a number of metal ribbons attached to the edge of the plate. Their locations are denoted by angles α_i, $i = 1,2,\ldots n$ for n supports (See Fig. 1). The plate is subjected to a steady in-plane body force G with its orientation denoted by angle ϕ with respect to X-axis. This problem is analyzed in two stages. In this section, initial fields due to the acceleration are determined. Then the small oscillations superimposed on the initial fields are studied in the next section.

Equilibrium of Forces and Moments

Let N_i and T_i denote the normal and tangential components, respectively, of the force from the support at α_i to the plate (See Fig. 1). For the equilibrium of the plate under the body force G (force per unit volume), we require

$$\Sigma F_x = 0$$
$$G\ 2b\ \pi\ R^2 \cos\phi + \sum_{i=1}^{n} N_i \cos\alpha_i - \sum_{i=1}^{n} T_i \sin\alpha_i = 0$$
$$\Sigma F_z = 0$$
$$G\ 2b\ \pi\ R^2 \sin\phi + \sum_{i=1}^{n} N_i \sin\alpha_i + \sum_{i=1}^{n} T_i \cos\alpha_i = 0 \qquad (1)$$
$$\Sigma M_y = 0$$
$$\sum_{i=1}^{n} T_i = 0$$

Force-Displacement Relations

Let u_i and w_i denote the normal and tangential components, respectively, of the displacement of the support at α_i. Assume that the response of each metal ribbon can be represented by a cantilever beam subjected to end forces N_i and T_i. Then for a metal ribbon of length ℓ, and rectangular cross-section area $h_1 \times h_2$, the force-displacement relations are,[10]

$$N_i = -K I_1 u_i\ ,\quad T_i = -K I_2 w_i \qquad (2)$$

where $K = 3E/\ell^3$, $I_1 = h_2 h_1^3/12$, and $I_2 = h_1 h_2^3/12$. We note that

$$\gamma \equiv I_1/I_2 = h_1^2/h_2^2 << 1.$$

Compatibility of Displacements of Supports

Let u and w be the rigid body displacements in X and Z directions, respectively, and α the rigid body rotation about Y axis of the plate. Assume that relative displacements between any pair of material particles within the plate caused by the initial body force are small as compared with the rigid body translations u and w. Then the compatibility relations

among the displacements of the supports are

$$u_i = u \cos \alpha_i + w \sin \alpha_i$$
$$w_i = - u \sin \alpha_i + w \cos \alpha_i + R \alpha \tag{3}$$

We have thus obtained from eqs. (1) - (3) a system of (4 x n + 3) equations with u_i, w_i, N_i, T_i, u, w, and α as the (4 x n + 3) unknowns. It can be reduced to a system of three equations in terms of u, w, and α by substituting (3) into (2) and, in turn, into (1) as follows.

$$\begin{bmatrix} -\gamma \Sigma c_i^2 - \Sigma s_i^2 & -(1-\gamma)\Sigma s_i c_i & \Sigma s_i \\ (1-\gamma)\Sigma s_i c_i & -\gamma \Sigma s_i^2 - \Sigma c_i^2 & -\Sigma c_i \\ -\Sigma c_i & \Sigma s_i & n \end{bmatrix} \begin{bmatrix} u \\ w \\ R\alpha \end{bmatrix} = \begin{bmatrix} -\bar{G} \cos \\ -\bar{G} \sin \\ 0 \end{bmatrix} \tag{4}$$

where

$$\bar{G} = \frac{2b \pi R^2}{K I_2} G, \quad s_i = \sin \alpha_i, \quad c_i = \cos \alpha_i.$$

Once u, w, and α are obtained from (4), we can compute support displacements from (3) and support forces from (2).

Initial Stress Field

The exact solution for an isotropic circular plate which is subjected to body force G and boundary forces N_i and T_i may be obtained from Michell's solutions[11] in plane-stress theory of elasticity. The rectangular components of stress at a point $P(x,z)$ are given by

$$\sigma_x = \sum_{i=1}^{n} (\sigma_{x_i} - \frac{N_i}{4\pi bR}) - \frac{1}{2} G_x x + \frac{1}{2} G_z z$$
$$\sigma_z = \sum_{i=1}^{n} (\sigma_{z_i} - \frac{N_i}{4\pi bR}) + \frac{1}{2} G_x x - \frac{1}{2} G_z z \tag{5}$$
$$\tau_{xz} = \sum_{i=1}^{n} T_{xz_i} - \frac{1}{2} G_x z - \frac{1}{2} G_z x$$

where $G_x = \cos \phi$, $G_z = G \sin \phi$.

σ_{r_i} is the normal stress at point P(x,z) due to forces N_i and T_i applied at point $A_i(x_i,z_i)$. It is a normal stress acting in the direction $\overline{PA_i}$ or along r_i (See Fig. 2) and is given by

$$\sigma_{r_i} = \frac{1}{\pi b r_i} (N_i \cos \theta_i + T_i \sin \theta_i) \tag{6}$$

or in rectangular components

$$\sigma_{x_i} = \sigma_{r_i} \cos^2 \beta_i$$
$$\sigma_{z_i} = \sigma_{r_i} \sin^2 \beta_i \tag{6}'$$
$$\tau_{xz_i} = \sigma_{r_i} \sin \beta_i \cos \beta_i.$$

Once the locations of points A_i and P, or α_i, x_i, z_i, x, and z, are given, the other quantities in the above equations may be obtained through geometrical considerations as follows.

$$\cos \theta_i = \frac{1}{r_i R} (R^2 - z_i z - x_i x)$$
$$\sin \theta_i = \frac{1}{r_i R} (z_i x - x_i z)$$
$$r_i^2 = (x - x_i)^2 + (z - z_i)^2 \tag{7}$$
$$\beta_i = (\alpha_i + \theta_i) \pm 2 m \pi$$

where m is an integer so chosen that $0 \leq \beta_i \leq \pi$.

Initial Strain Field

Due to the symmetry of the applied forces and the plate itself with respect to XZ plane, we take $U_1^{(0)}$, $U_3^{(0)}$ and $U_2^{(1)}$ as the non-zero initial displacement components. Then by linearizing the initial strain-displacement relations, eqs. (53) of Ref. 1, we have

$$E_1^{(0)} = U_{1,1}^{(0)}, \quad E_3^{(0)} = U_{3,3}^{(0)}$$
$$E_2^{(0)} = U_2^{(1)}, \quad 2E_5^{(0)} = U_{1,3}^{(0)} + U_{3,1}^{(0)} \tag{8}$$

For the last relation of (8), it is assumed that in-plane rotation associated with initial deformation is negligible,

i.e. $(U_{1,3}^{(0)} + U_{3,1}^{(0)})/2 = 0.$

The above strain components may be computed from the initial stress-strain relations, eqs. (49) of Ref. 1,

$$T_p^{(0)} = 2b \, C_{pq} \, E_q^{(0)} \tag{9}$$

where $T_p^{(0)}$ are related to components of initial stress obtained from (5) by following relations.

$$T_1^{(0)} = 2b\sigma_x, \quad T_3^{(0)} = 2b\sigma_z$$
$$T_{13}^{(0)} = 2b \, \tau_{xz}. \tag{10}$$

The initial stress field is calculated from (5) for a circular plate with four supports. Two of the supports are along the x_1 axis and the other two along the x_3 axis. The plate is subjected to a body force G = 15 g in the $-x_1$ axis direction. The distribution of stress components along diameters oriented in x_1 direction, 45° from x_1, x_3 direction, and 9° from x_3 are shown in Figs. 3-6, respectively. Stresses due to forces which are statically equivalent to those calculated from (2), but uniformaly distributed over the supported area are also calculated and are shown in dashed lines in Figs. 5-6. The comparison shows that the differences are not significant in the electroded central area, but they are more pronounced near the edge of the plate.

Thickness-Shear and Flexural Incremental Vibrations

For rotated Y-cuts of quartz vibrating in the vicinity of the thickness-shear frequencies, the predominent component of incremental displacement is $u_1^{(1)}$ which is coupled to $u_2^{(0)}$. The coupled equations of motion of thickness-shear and flexural modes with $U_i^{(0)}$, $E_p^{(0)}$ and $T_p^{(0)}$ of (8) and (9) as unknown functions of x_1 and x_3 are obtained from eqs. (55) of Ref. 1 as follows.

$$\frac{\partial}{\partial x_1}\left[(1+U_2^{(0)})t_6^{(0)}+U_{2,1}^{(0)}t_1^{(1)}+U_{2,3}^{(1)}t_5^{(1)}+T_1^{(0)}u_{2,1}^{(0)}\right]$$

$$+\frac{\partial}{\partial x_3}\left[(1+U_2^{(1)})t_4^{(0)}+U_{2,1}^{(1)}t_5^{(1)}+U_{2,3}^{(1)}t_3^{(1)}\right.$$

$$\left.+T_5^{(0)}u_{2,1}^{(0)}\right]=2b\rho\,\ddot{u}_2^{(0)} \tag{11}$$

$$\frac{\partial}{\partial x_1}\left[(1+U_{1,1}^{(0)})t_1^{(1)}+U_{1,3}^{(0)}t_5^{(1)}\right]+\frac{\partial}{\partial x_3}\left[(1+U_{1,1}^{(0)})t_5^{(1)}\right.$$

$$\left.+U_{1,3}^{(0)}t_3^{(1)}\right]-\left[(1+U_{1,1}^{(0)})t_6^{(0)}+U_{1,3}^{(0)}t_4^{(0)}\right.$$

$$\left.+T_2^{(0)}u_1^{(1)}\right]=\frac{2}{3}\rho\,b^3\,\ddot{u}_1^{(1)}$$

where the incremental stress-strain relations, eqs. (50) of Ref. 1, are

$$t_p^{(0)}=2b\,(C_{pq}+C_{pqr}\,E_r^{(0)})\kappa_{(p)}\,\kappa_{(q)}\,\eta_q^{(0)}$$

$$t_p^{(1)}=\frac{2}{3}b^3\,(C_{pq}+C_{pqr}\,E_r^{(0)})\,\eta_q^{(1)} \tag{12}$$

and the incremental strain-displacement relations, eqs. (53) of Ref. 1, are

$$\eta_4^{(0)}=U_{1,3}^{(0)}\,u_1^{(1)}$$

$$\eta_6^{(0)}=(1+U_2^{(1)})\,u_{2,1}^{(0)}+(1+U_{1,1}^{(0)})\,u_1^{(1)}$$

$$\eta_1^{(1)}=U_{2,1}^{(1)}\,u_{2,1}^{(0)}+(1+U_{1,1}^{(0)})\,u_{1,1}^{(1)} \tag{13}$$

$$\eta_5^{(1)}=U_{2,3}^{(1)}\,u_{2,1}^{(0)}+U_{1,3}^{(0)}\,u_{1,1}^{(1)}$$

The displacement equations of motion of $u_1^{(1)}(x_1,t)$ and $u_2^{(0)}(x_1,t)$ are obtained by substituting (13) into (12) then into (11). The resulting equations in terms of dimensionless variables

$$\phi=u_1^{(1)}\quad,\quad u=u_2^{(0)}/b \tag{14}$$

are

$$\bar{T}_1\partial_{11}\phi+\bar{T}_2\partial_1\phi+\bar{T}_3\phi+\bar{T}_4\partial_{11}u+\bar{T}_5\partial_1 u=-\Omega^2\phi$$

$$\bar{F}_1\partial_{11}\phi+\bar{F}_2\partial_1\phi+\bar{F}_3\phi+\bar{F}_4\partial_{11}u+\bar{F}_5\partial_1 u=-3\Omega^2 u \tag{15}$$

where $\bar{T}_i$ and $\bar{F}_i$ are functions of initial fields and material constants C_{pq} and C_{pqr}. The space dependence of these functions through the initial fields makes the exact solutions of (15) very difficult to obtain. A careful examination of these functions reveal that each function can be separated into two parts as

$$\bar{T}_i=T_i+t_i$$

$$\bar{F}_i=F_i+f_i \tag{16}$$

where T_i, F_i are associated vibrational motion without initial stresses and dependent on material properties only, while t_i, f_i are contributed by initial fields and are space dependent. Expressions of these functions are given as follows.

$$\bar{T}_1=\frac{b^2}{3\kappa_1^2\,C_{66}}\left[(1+2U_{1,1}^{(0)})\,C_{11}^{(0)}+2U_{1,3}^{(0)}C_{15}^{(0)}\right]$$

$$\bar{T}_2=\frac{b^2}{3\kappa_1^2\,C_{66}}\left[2U_{1,11}^{(0)}\,C_{11}^{(0)}+U_{1,33}^{(0)}(C_{13}^{(0)}+C_{55}^{(0)})\right.$$

$$+4\,U_{1,13}^{(0)}C_{15}^{(0)}+(1+2U_{1,1}^{(0)})\,C_{11r}\,E_{r,1}^{(0)}$$

$$\left.+4\,U_{1,3}^{(0)}C_{15r}E_{r,1}^{(0)}+U_{1,3}^{(0)}(C_{13r}+C_{55r})E_{r,3}^{(0)}\right]$$

$$\bar{T}_3=\frac{1}{C_{66}}\left[(1+2U_{1,1}^{(0)})C_{66}^{(0)}+2U_{1,3}^{(0)}C_{64}^{(0)}\right] \tag{17}$$

$$\bar{T}_4=\frac{b^3}{3\kappa_1^2\,C_{66}}\,(U_{2,1}^{(1)}C_{11}^{(0)}+U_{2,3}^{(1)}\,C_{15}^{(0)})$$

$$\bar{T}_5=\frac{b^3}{3\kappa_1^2\,C_{66}}\left[U_{2,11}^{(1)}C_{11}^{(0)}+2U_{2,13}^{(1)}C_{15}^{(0)}+U_{2,33}^{(0)}C_{55}^{(0)}\right.$$

$$+U_{2,1}^{(1)}\,(C_{11r}E_{r,1}^{(0)}+C_{15r}E_{r,3}^{(0)})$$

$$\left.+U_{2,3}^{(1)}\,(C_{51r}E_{r,1}^{(0)}+C_{55r}E_{r,3}^{(0)})\right]$$

$$-\frac{b}{C_{66}}\left[(1+U_2^{(1)}+U_{1,1}^{(0)})\,C_{66}^{(0)}+U_{1,3}^{(0)}\,C_{64}^{(0)}\right]$$

$$\bar{F}_1=\frac{b^3}{3\kappa_1^2\,C_{66}}\,(U_{2,1}^{(1)}\,C_{11}^{(0)}+U_{2,3}^{(1)}\,C_{15}^{(0)})$$

$$\bar{F}_2=\frac{b^3}{3\kappa_1^2\,C_{66}}\left[U_{2,11}^{(1)}C_{11}^{(0)}+2U_{2,13}^{(1)}C_{15}^{(0)}+U_{2,33}^{(1)}\,C_{13}^{(0)}\right.$$

$$+U_{2,1}^{(1)}\,(C_{11r}E_{r,1}^{(0)}+C_{15r}E_{r,3}^{(0)})$$

$$\left.+U_{2,3}^{(1)}\,(C_{15r}E_{r,1}^{(0)}+C_{13r}E_{r,3}^{(0)})\right]$$

$$+\frac{b}{C_{66}}\left[(1+U_2^{(1)}+U_{1,1}^{(0)})\,C_{66}^{(0)}+U_{1,3}^{(0)}\,C_{64}^{(0)}\right] \tag{18}$$

$$\bar{F}_3=\frac{b}{C_{66}}\left[(U_{2,1}^{(1)}+U_{1,11}^{(0)})\,C_{66}^{(0)}+(U_{2,3}^{(1)}+2U_{1,13}^{(0)})C_{64}^{(0)}\right.$$

$$+U_{1,33}^{(0)}\,C_{44}^{(0)}+U_{1,3}^{(0)}\,C_{64r}E_{r,1}^{(0)}+U_2^{(1)}C_{64r}E_{r,3}^{(0)}$$

$$\left.+(1+U_2^{(1)}+U_{1,1}^{(0)})\,C_{66r}\,E_{r,1}^{(0)}\right]$$

$$\bar{F}_4=\frac{b^2}{2\kappa_1^2\,C_{66}}\left[3\kappa_1^2\,(1+2U_2^{(1)})\,C_{66}^{(0)}+3\,T_1^{(0)}/2b\right]$$

$$\bar{F}_5=\frac{b}{2\kappa_1^2\,C_{66}}\,(T_{1,1}^{(0)}+T_{5,3}^{(0)})+\frac{b^2}{C_{66}}\left[2U_{2,1}^{(1)}C_{66}^{(0)}+2U_{2,3}^{(1)}C_{64}^{(0)}\right.$$

$$\left.+(1+2U_2^{(1)})\,(C_{66r}\,E_{r,1}^{(0)}+C_{64r}\,E_{r,3}^{(0)})\right]$$

where

$$C_{pq}^{(0)}=C_{pq}+C_{pqr}\,E_r^{(0)} \tag{19}$$

By setting initial fields to zero in (17) and (18), we have

$$T_1 = \frac{b^2 C_{11}}{3\kappa_1^2 C_{66}}, \quad T_3 = -1, \quad T_5 = -b,$$
$$F_2 = b, \quad F_4 = b^2, \tag{20}$$

and $T_2 = T_4 = F_1 = F_3 = F_5 = 0$. It can be seen that (15) reduce to the coupled equations of thickness-shear and flexural vibrations when there are no initial stresses.[12] For free vibration problems, (15) may be written in the following matrix form.

$$Lv = \lambda v \tag{21}$$

where L is the linear differential operator and is separated into two parts as the following.

$$L = L_o + Q \tag{22}$$

where

$$L_o = \begin{bmatrix} T_1\partial_{11}+T_3 & T_5\partial_1 \\ \frac{1}{3}F_2\partial_1 & \frac{1}{3}F_4\partial_{11} \end{bmatrix} \tag{23}$$

$$Q_o = \begin{bmatrix} t_1\partial_{11}+t_2\partial_1+t_3 & t_4\partial_{11}+t_5\partial_1 \\ \frac{1}{3}(f_1\partial_{11}+f_2\partial_1+f_3) & \frac{1}{3}(f_4\partial_{11}+f_5\partial_1) \end{bmatrix}$$

In (21), v is the displacement in vector form and is related to the dimensionless frequency Ω as follows.

$$v = \begin{bmatrix} \phi \\ u \end{bmatrix}$$
$$\lambda = -\Omega^2 = -(\omega/\omega_1)^2 \tag{24}$$

where $\omega_1 = [3\kappa_1^2 C_{66}/\rho b^2]^{1/2}$ is the lowest thickness-shear cut-off frequency of an infinite plate without initial stresses. We note L_o is the part of the operator associated to motions without initial stresses while Q is the part of the operator which includes all the effects of initial fields. Since the values of t_i and f_i are several orders of magnitude smaller than those of T_i and F_i, respectively, it is appropriate to employ the perturbation method to obtain the frequency changes due to acceleration.

Let

$$\lambda = \lambda_o + \lambda^{(1)}$$
$$v = v_o + v^{(1)} \tag{25}$$

where v_o and λ_o satisfy

$$L_o v_o = \lambda_o v_o \tag{26}$$

(26) are the equations of motion of the thickness-shear and flexural vibrations without initial stresses. Their solution form and dispersion relation may be obtained from eqs. (20), (22), and (24) of Ref. 12. We further impose traction-free boundary conditions $t_{21}^{(0)} = t_{11}^{(1)} = 0$ (from eqs. (61) of Ref. 1), at $x_1 = \pm R$,

$$\partial_1 u + \phi = 0, \quad \partial_1 \phi = 0 \tag{27}$$

and normalization

$$\int_A v_o \cdot v_o \, dA = 1 \tag{28}$$

The changes in the resonance frequencies of the fundamental thickness-shear modes are

$$\frac{\Delta f}{f_o} = \frac{\Omega-\Omega_o}{\Omega_o} = \frac{1}{2}\frac{\int_A v_o \cdot Q \cdot v_o \, dA}{\lambda_o} = F(\theta,\phi,\alpha_1,R/b) \tag{29}$$

We see that frequency change is a function of plate orientation θ, azimuth angle of body force ϕ, locations of the supports α_i, and the ratio of the radius to thickness of the plate R/b.

Calculations for frequency changes are made for circular AT-cuts of quartz plates with diameter 2R = 15mm, thickness 2b = 1.69 mm. The plate is subjected to an acceleration with G = 15 g = 14700 cm/sec^2 and supported by four nickel ribbons of length ℓ = 6.35 mm and rectangular cross-section (h_1 = 0.076 mm and h_2 = 1.270 mm). The Young's modulus for Nickel is E = 4.82 x 10^9 dyne/cm^2. The predicted frequency changes $\Delta f/f_o$ as a function of azimuth angle ϕ for three different support configurations are made, using Bechmann's[13] values of the second-order elastic coefficients and those of Thurston, Miskimin, and Andreath[14] for the third-order coefficients. These predicted results are shown in Figs. 7-9 and compared with measured values of Warner[7] and Smith.[8] It can be seen in Figs. 7 and 8 that the agreements of $\Delta f/f_o$ between predicted and measured values are reasonable both in magnitude and variation. In Fig. 9, the measured values are quite different from the calculated values (solid lines) and also different in general character from the measured values for the two plates which have slightly different mounting configurations as shown in Figs. 7 and 8. It appears possible that, in presenting experimental values of $\Delta f/f_o$ for various orientation of accelerations, $-x_3$ axis instead of $+x_3$ axis of the plate was used as the reference. If this is the case, then all the data should be shifted by 180° in abscissa. The calculated values after shifting by 180° are plotted in dotted lines in Fig. 9 for comparison. It is seen that agreement becomes close. When looking at the results, we should keep in mind simplifications have been made in order to obtain the mathematical solutions. The plate is assumed to be uniform in thickness and vibrating at frequencies of the fundamental thickness-shear modes. The actual plates used in experiments are double-convex and excited at frequencies of the fifth overtone of the thickness-shear modes.

Once the accuracy of the analytical solutions are established, the acceleration sensitivity of resonance frequencies can be computed systematically as functions of various effecting factors, i.e. the orientation ϕ and magnitude G of acceleration, geometry of the resonator plate R/b, positions of the supports α_i, orientation of the plate θ, and the linear and nonlinear material coefficients.

References

1. P. C. Y. Lee, Y. S. Wang, and X. Markenscoff, J. Acoust. Soc. Am. 57, 95-105 (1975). Also Proc.

27th Annu. Freq. Control Symp. 1-6 (1973).

2. A. D. Ballato, Proc. 14th Annu. Freq. Control Symp. 89-114, (1960).

3. A. D. Ballato and R. Bechmann, IRE 48, 261-262 (1960).

4. C. R. Mingins, L. C. Barcus, and R. W. Perry, Repts. 1-20, Lowell Tech. Inst. Found. (1961-66).

5. J. M. Ratajski, IBM J. Res. Dev. 12, 92-99 (1968).

6. P. C. Y. Lee, Y. S. Wang, and X. Markenscoff, J. Acoust. Soc. Am. 59, 90-96 (1970). Also Proc. 28th Annu. Freq. Control Symp. 14-18 (1974).

7. A. W. Warner, Interim Reps. 10-11, Bell Telephone Lab. (1959).

8. W. L. Smith, Interim Reps. 12-13 and Final Rep., Bell Tel. Lab. (1960).

9. M. Valdois, J. J. Gapnepain, and J. Besson, Proc. 28th Annu. Freq. Control. Symp. 19-32 (1974).

10. S. Timoshenko Strength of Materials, Part I, Van Nostrand Company, Inc., N.Y.C. p. 147, (1951).

11. J. H. Michell, Proc. London Math. Soc., 32, 35-61, (1900).

12. R. D. Mindlin and P. C. Y. Lee, Int. J. Solids Structures, 2, 125-139 (1966).

13. R. Bechmann, Phys. Rev. 100, 1060-1061 (1958).

14. R. N. Thurston, H. J. McSkimin, and P. Andreatch, Jr., J. Appl. Phys. 37, 267-275 (1966).

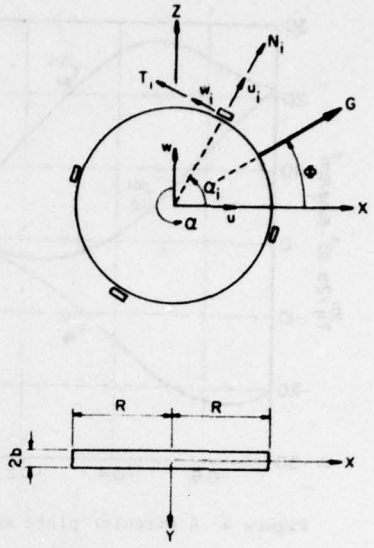

Figure 1 A circular plate under body force G.

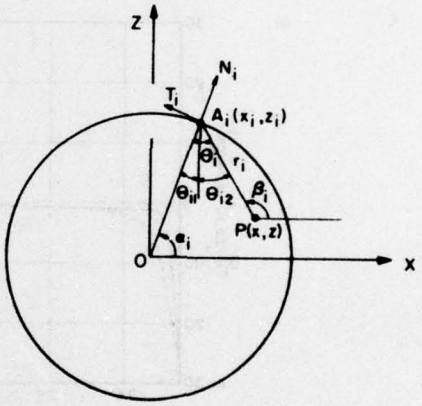

Figure 2 Geometrical relations among α_i, β_i, θ_i, and r_i.

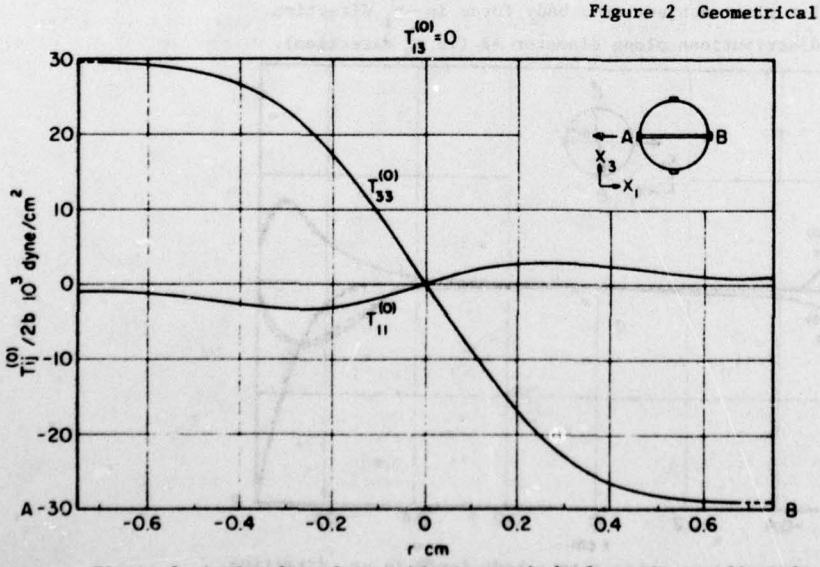

Figure 3 A circular plate subject to a body force in $-x_1$ direction. Stress distributions along diameter $\overline{AB}$ (in x_1 direction).

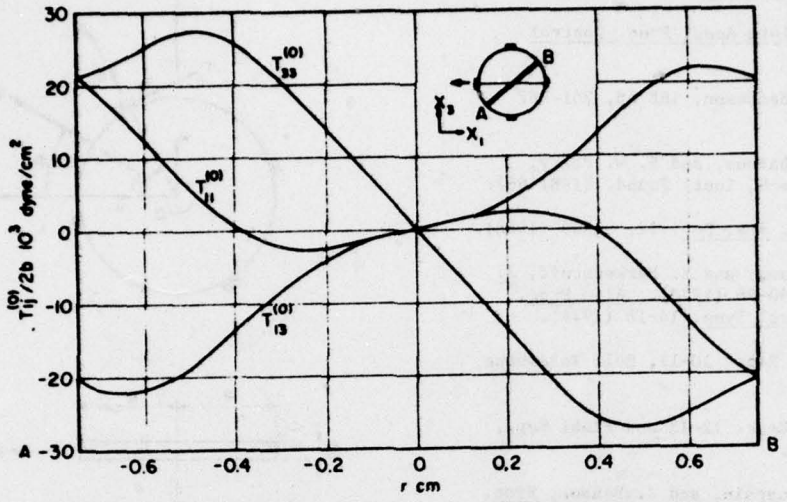

Figure 4 A circular plate subject to a body force in $-x_1$ direction. Stress distributions along diameter $\overline{AB}$ ($45°$ from x_1 axis).

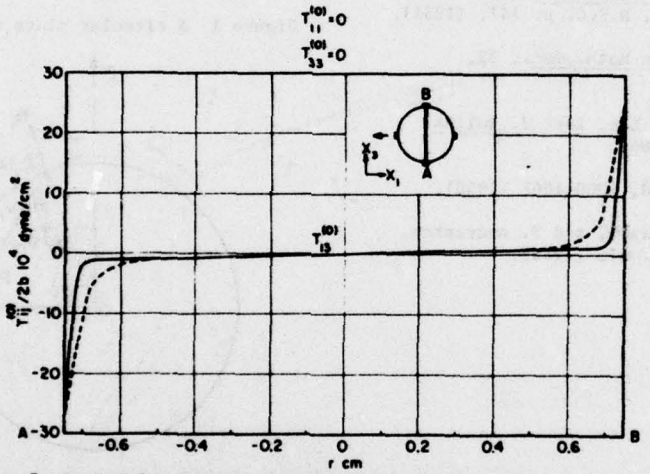

Figure 5 A circular plate subject to a body force in $-x_1$ direction. Stress distributions along diameter $\overline{AB}$ (in x_3 direction).

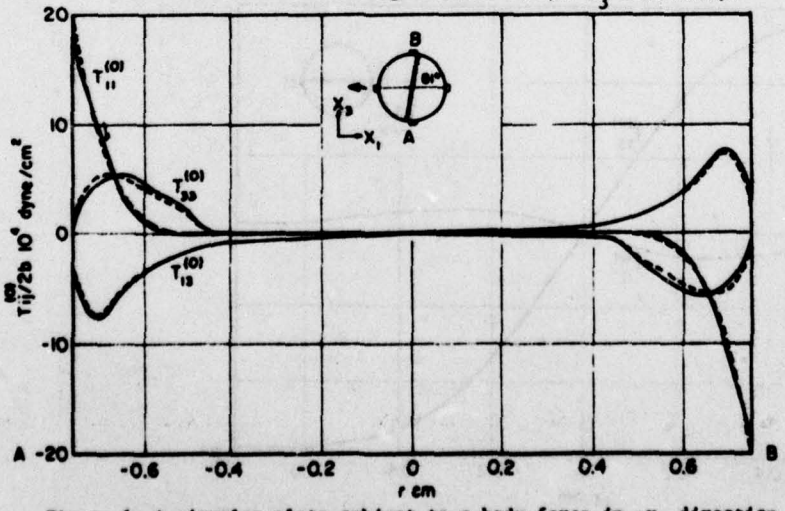

Figure 6 A circular plate subject to a body force in $-x_1$ direction. Stress distributions along diameter $\overline{AB}$ ($81°$ from x_1 axis).

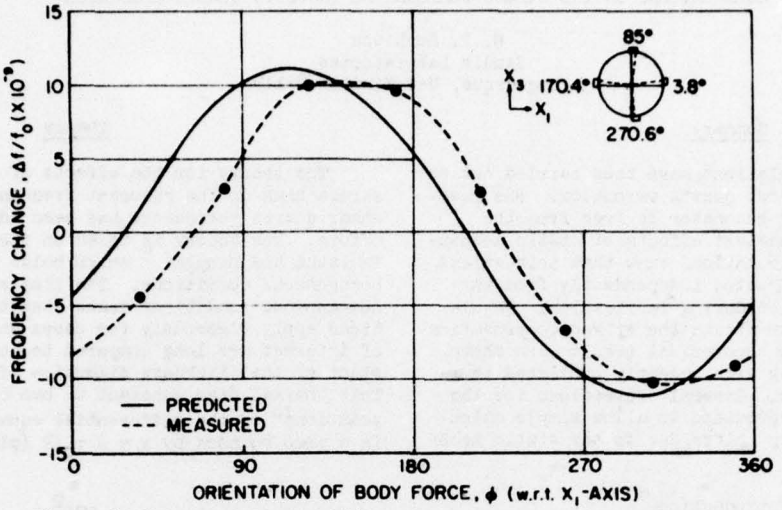

Figure 7 Frequency change $\Delta f/f_o$ as a function of azimuth angle ϕ of body force, for AT-cut plate.

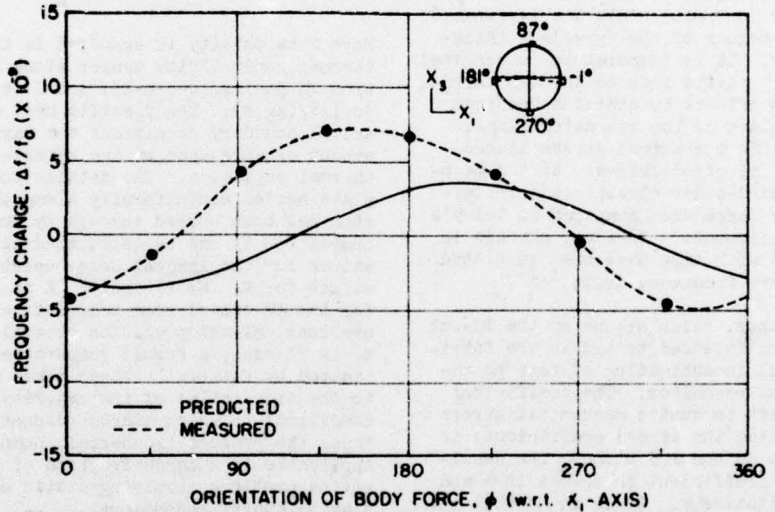

Figure 8 Frequency change $\Delta f/f_o$ as a function of azimuth angle ϕ of body force, for AT-cut plate.

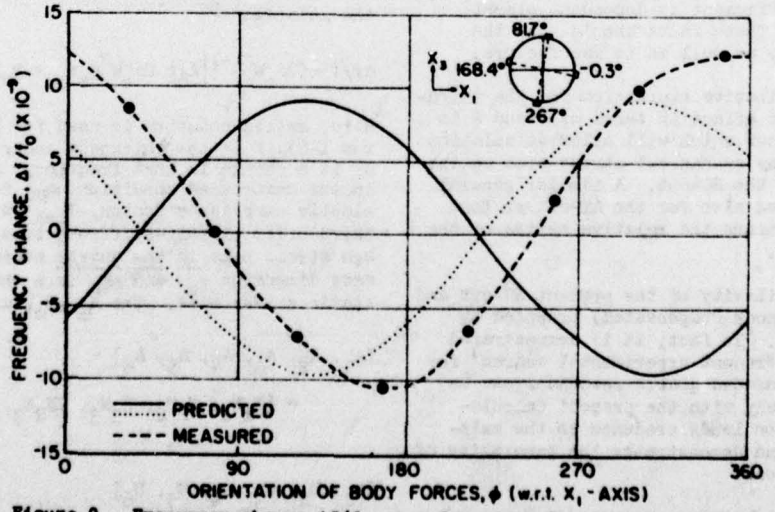

Figure 9 Frequency change $\Delta f/f_o$ as a function of azimuth angle ϕ of body force, for AT-cut plate.

CALCULATIONS ON THE STRESS COMPENSATED (SC-CUT) QUARTZ RESONATOR *

E. P. EerNisse
Sandia Laboratories
Albuquerque, New Mexico 87115

Summary

Theoretical calculations have been carried out on the doubly-rotated SC-cut quartz resonator. The resonant frequency of this resonator is free from the third-order elastic constant effects of static mechanical stress bias. Calculations show that this stress compensation can be adjusted independently from the temperature compensation during fabrication. Angular tolerances necessary to attain the stress compensation are investigated. The theoretical results are shown to agree quantitatively with recently published thermal shock measurements. General expressions for the SC-cut and AT-cut are provided to allow simple calculation of the frequency shifts due to any static mechanical stress bias.

Introduction

The SC-cut was introduced at the 29th Annual Symposium on Frequency Control.[1] This doubly-rotated, quartz resonator is a member of the $(yxwl)\phi,\theta$ thickness-shear mode family. It is temperature compensated and free from frequency shifts induced through third-order elastic constant effects by static mechanical stress biases in the plane of the resonator blank. The sources of the static mechanical stress biases could be acceleration, electrode stress, or the mechanical mounts. The third-order elastic constant effects are surprisingly large when compared to today's frequency control requirements. In fact, changes in mechanical stress bias with time have been suggested as a source of long-term frequency drift.[1,2]

In the present paper, calculations on the SC-cut are presented which are intended to aid in the fabrication and experimental investigation of this potentially important quartz resonator. The coefficient relating frequency shift to static mechanical stress in the electrodes (called the stress coefficient) is shown as contour plots on the ϕ,θ plane. The sensitivity of this stress coefficient to errors in ϕ and θ are discussed quantitatively. It is found that the stress coefficient in the vicinity of the SC-cut is dependent almost entirely on ϕ alone, while the first-order temperature coefficient is dependent almost entirely on θ alone. These facts should make the SC-cut easier to study as well as to manufacture.

A general, quantitative expression for the third-order elastic constant effect in terms of ϕ and θ is presented for the SC-cut which will allow calculation of the influence of any mechanical stress bias on the resonant frequency of the SC-cut. A similar general expression is presented also for the AT-cut so that future workers can compare the relative merits of the SC-cut vs. the AT-cut.

Finally, the similarity of the present SC-cut and the TS-cut (thermal shock compensated) proposed by Holland[3] is discussed. In fact, it is demonstrated that the results of a recent experimental search[4] for a thermal-shock compensated quartz resonator can be explained quantitatively with the present calculations. This comparison lends credence to the existence of the SC-cut and demonstrates the generality of the present calculations.

Theory

The theory for the effects of static mechanical stress bias on the resonant frequency of thickness-shear quartz resonators has been adequately presented before. The theory is based on the formulation by Thurston and Brugger,[5] which holds for isothermal, homogeneous conditions. The limitation of isothermal, homogeneous conditions means that the present calculations apply rigorously for cases where the time scales of interest are long compared to the thermal time constant of the thickness dimension of resonator plates. This thermal time constant t_τ can be estimated from solutions[6] of the differential equation for heat flow in a slab bounded by $x = \pm \tau_q/2$ (plate thickness = τ_q):

$$t_\tau = \frac{\rho C \tau_q^2}{\pi^2 K} \qquad (1)$$

Here ρ is density in kg/m^3; K is the component of the thermal conductivity tensor along the thickness direction in joules/(sec·m·K); and C is specific heat in joules/(kg K). The specific heat depends on the mechanical boundary conditions and varies according to the amount of work done by the stress-strain fields during thermal expansion. The details for the case of a plate heated nonuniformily along the thickness dimension has been worked through by Holland;[7] a typical number for t_τ can be calculated using his numerical values for the largest decay constant and handbook[8] values for K. We estimate[8] K as 8.0 joules/(sec·m·K) for the AT-cut at room temperature. For a 5 MHz, 5th overtone, AT-cut precision crystal thickness of 0.17cm, t_τ is 71 msec, a result comparable to the 65 msec estimated by Kusters.[4] These times are short relative to to the time scales of the majority of experimental conditions to which quartz resonators are subjected. Thus, the present isothermal, homogeneous theory is applicable to a large fraction of technically interesting problems involving static mechanical stress bias in quartz resonators.

The theoretical formulation can be summed up in the relation[1,5]

$$\Delta f/f = (2\rho_o W_o^2)^{-1}\left|A_\alpha + 2\rho_o W_o^2 U_\beta s_{\alpha\beta} + B_\beta B_\gamma s_{\delta\alpha} C_{\beta\gamma\delta}\right|\Delta\bar{T}_\alpha \qquad (2)$$

Here, matrix notation is used for tensors (α, β, γ, δ run 1-6), f is the thickness shear resonant frequency, Δf is a change in that frequency, ρ_o is mass density in the unstressed condition, $s_{\alpha\beta}$ is the isothermal elastic compliance tensor, $C_{\beta\gamma\delta}$ is the isothermal third-order elastic-stiffness tensor, $\bar{T}_\alpha$ is the average stress bias in the quartz averaged over the thickness dimension τ_q, and $\Delta\bar{T}_\alpha$ is a change in the average static stress bias. The A_α, B_α, and U_α are defined by

$$[A_1, A_2, A_3, A_4, A_5, A_6] = [N_1N_1, N_2N_2, N_3N_3, 2N_2N_3, 2N_1N_3, 2N_1N_2] \qquad (3)$$

$$[U_1, U_2, U_3, U_4, U_5, U_6] = \left|U_1^oU_1^o, U_2^oU_2^o, U_3^oU_3^o, U_2^oU_3^o, U_1^oU_3^o, U_1^oU_2^o\right| \qquad (4)$$

$$[B_1, B_2, B_3, B_4, B_5, B_6] = \left| N_1U_1^o,\ N_2U_2^o,\ N_3U_3^o,\ N_2U_3^o + N_3U_2^o,\ N_1U_3^o + N_3U_1^o,\ N_1U_2^o + N_2U_1^o \right| . \quad (5)$$

Here N_i is the unit vector in the direction of acoustic wave propagation (thickness of plate) and W_o^2 and U_I^o are the slow shear wave eigenvalue and eigenvector of

$$\rho_o W_o^2 U_k^o = N_r N_s c_{jrks} U_j^o \quad , \quad (6)$$

where tensor notation is used (subscripts run 1-3) and c_{jrks} is the isothermal elastic stiffness tensor. Piezoelectric effects on resonant frequency are small in quartz and are ignored here.

The values for $\Delta\bar{T}_\alpha$ are found from the specific static stress bias patterns under consideration and are usually identifiable more easily in the plate axes system. A rotation of $\Delta\bar{T}_\alpha$ to the same axes system as that used for the elastic tensors is necessary before the contractions in Eq. (2) can be carried out.

Theoretical Results

The choice of $\Delta\bar{T}_\alpha$ for Eq. (2) is unlimited and a general study is impractical. A planar isotropic stress bias is representative of many experimental situations and is chosen here for the study of stress effects as a function of ϕ and θ. The case of a planar isotropic $\bar{T}_\alpha$ which is generated by an electrode stress has been treated before.[1] Let $\tilde{T}_\alpha$ be the average static mechanical stress bias referenced to the plate axes (x_1 is length, x_2 is thickness, x_3 is width). We represent the effect of the electrode stress by the force per unit width, S, acting across the electrode-quartz interface (S is the integral through the electrode thickness of the electrode stress and is in units of dyn/cm). A change in S, ΔS, causes

$$\Delta\tilde{T}_1 = \Delta\tilde{T}_3 = -\Delta S/\tau_q$$
$$\Delta\tilde{T}_2 = \Delta\tilde{T}_4 = \Delta\tilde{T}_5 = \Delta\tilde{T}_6 = 0 \quad (7)$$

in the quartz. Here τ_q is the plate thickness and the minus sign arises because the static stress bias in the quartz is a reaction to the electrode stress (S positive is tension in the electrode). After rotation of $\Delta\tilde{T}_\alpha$ to the crystal axes to find $\Delta\bar{T}_\alpha$, $\Delta S/\tau_q$ can be factored out of $\Delta\bar{T}_\alpha$ to form

$$\frac{\Delta f}{f} = K\frac{\Delta S}{\tau_q} \quad (8)$$

where

$$K = -(2\rho_o W_o^2)^{-1}[A_\alpha + 2\rho_o W_o^2 U_\beta s_{\alpha\beta} + B_\beta B_\gamma s_{\delta\alpha} c_{\beta\gamma\delta}](\Delta T_\alpha \tau_q/\Delta S) \quad (9)$$

was called the stress coefficient in earlier works[1,9] and is a function of ϕ and θ only.

Contours of K in the (ϕ,θ) plane are shown in Fig. 1 as calculated with published values[10,11] for the various elastic constants in Eq. (9). Included in Fig. 1 is the loci of the zero first-order temperature coefficient.[12] Let us focus our attention first on the SC-cut which is the intersection of the zero contour of K and the zero first-order temperature coefficient at $\phi = 22.4°$ and $\theta = 34.3°$. The contours of K are almost horizontal there. This means that θ can be adjusted around the SC-cut with little effect on K. Likewise, the loci of the zero first-order temperature coefficient is nearly vertical there. This means that ϕ can be adjusted with little effect on the first-order temperature coefficient. This relative orthogonality of the stress effect and the temperature effect has technological impact for it suggests that one can independently adjust the stress and temperature response of the SC-cut.

The right-hand scale of Fig. 1 has been centered on the SC-cut. This was done to allow for the inevitable differences between theoretical calculations and experimental reality which arise both from inaccuracies in the values for the elastic constants and from contouring effects. Noting the right-hand side of Fig. 1, we see that fabrication with an accuracy of $\pm 1.5°$ on ϕ will reduce the stress coefficient by at least a factor of 10 relative to the AT-cut value of 0.273×10^{-11} cm^2/dyn. An accuracy of $\pm 0.2°$ on ϕ during fabrication will provide a reduction in the stress coefficient of at least 100 relative to the AT-cut.

It must be emphasized here that Eq. (9) and the definition of K are specific to the case of stress changes in the electrodes. As such, Eq. (7) leads to the minus sign in Eq. (9) which allows a direct relation between the frequency shifts (Δf) and changes in electrode stresses (ΔS). Equation (2) is the more general relation and should always be used as the starting point for studying the effects of static mechanical stress biases independent of their origin. For this reason, we present here Eq. (2) as evaluated for the SC-cut to facilitate any further work on the effects of arbitrary, static mechanical stress biases. For the SC-cut, we find ($\phi = 22.4°$, $\theta = 34.3°$ in the calculations)

$$\Delta f/f = (-0.1580\,\Delta\bar{T}_1 - 0.08914\,\Delta\bar{T}_2 + 0.1714\,\Delta\bar{T}_3 + 0.2167\,\Delta\bar{T}_4 + 0.3767\,\Delta\bar{T}_5 + 0.3694\,\Delta\bar{T}_6) \times 10^{-11} \quad (10)$$

For comparison, we find for the AT-cut ($\phi = 0°$, $\theta = 35.25°$)

$$\Delta f/f = (-0.2674\,\Delta\bar{T}_1 - 0.05161\,\Delta\bar{T}_2 + 0.2133\,\Delta\bar{T}_3 + 0.2773\,\Delta\bar{T}_4 + 0.0\,\Delta\bar{T}_5 + 0.0\,\Delta\bar{T}_6) \times 10^{-11} \quad (11)$$

In using Eqs. (10) and (11), remember that $\Delta\bar{T}_\alpha$ is referred to the crystal axes, not the resonator plate axes, and $\Delta\bar{T}_\alpha$ is in dyn/cm^2.

Alternately, most workers will find it easier to work in the resonator plate axes (x_1 = length direction x_2 = thickness direction, x_3 = width direction). See Reference 13 for the axes and $(yxwl)\phi,\theta$ conventions used here. Equations (10) and (11) have been rotated to the resonator plate axes; we find for the SC-cut

$$\Delta f/f = (-0.01786\,\Delta\tilde{T}_1 - 0.07560\,\Delta\tilde{T}_2 + 0.01772\,\Delta\tilde{T}_3 + 0.1969\,\Delta\tilde{T}_4 + 0.09044\,\Delta\tilde{T}_5 + 0.2497\,\Delta\tilde{T}_6) \times 10^{-11} \quad (12)$$

and for the AT-cut

$$\Delta f/f = (-0.2674\,\Delta\tilde{T}_1 + 0.1673\,\Delta\tilde{T}_2 - 0.005634\,\Delta\tilde{T}_3 + 0.1711\,\Delta\tilde{T}_4 + 0.0\,\Delta\tilde{T}_5 + 0.0\,\Delta\tilde{T}_6) \times 10^{-11} . \quad (13)$$

In Eqs. (12) and (13), remember that $\Delta\tilde{T}_\alpha$ is in the plate axes system and is in units of dyn/cm^2. For example, with $\Delta\tilde{T}_1 = \Delta\tilde{T}_3 = -1.0$ in Eq. (7), Eq. (12) leads to the $\Delta f/f$ of 0.273×10^{-11}, the value quoted for K of the AT-cut.

Note in Eq. (12) for the SC-cut that the coefficient of $\Delta\tilde{T}_1$ and $\Delta\tilde{T}_3$ are essentially equal in magnitude but opposite in sign (the slight difference in magnitude is representative of the numerical accuracy to which the SC-cut has been determined). For isotropic planar stress,

$$\Delta\tilde{T}_1 = \Delta\tilde{T}_3$$
$$\Delta\tilde{T}_2 = \Delta\tilde{T}_4 = \Delta\tilde{T}_5 = \Delta\tilde{T}_6 = 0 , \qquad (14)$$

and $\Delta f/f$ approaches zero according to Eq. (12).

Examination of Eq. (12) shows that for anisotropic planar stresses where $\Delta T_1 \neq \Delta T_3$ and the remainder of Eq. (14) holds, $\Delta f/f$ will still be relatively small because the magnitudes of the ΔT_1 and ΔT_3 coefficients are small. Also, the coefficient for shear in the plane of the resonator plate, $\Delta\tilde{T}_5$, is relatively small. Thus, for a large variety of planar stress patterns, $\Delta f/f$ will be small.

As seen in Eq. (13), the AT-cut is much more sensitive to stress in the $\Delta\tilde{T}_1$ direction than in the $\Delta\tilde{T}_3$ direction, so planar stress patterns such as described by Eq. (14) will cause a large $\Delta f/f$. The AT-cut will be insensitive only to the case of stress concentrated solely along the $\Delta\tilde{T}_3$ direction. Such an anisotropy is seen experimentally[14,15] in terms of the force sensitivity of a quartz resonator frequency when the plate is subjected to a one-dimensional, in-plane force. Equation (14) can be used to calculate the force sensitivity of the AT-cut similar to past theoretical works on the subject.[16] Of course, accurate determination of the static mechanical-stress bias is necessary.[15,16]

Comparison With Thermal Shock Effects

Recent numerical calculations have been carried out by Holland for the time frame in which thermal transients with temperature variations along the thickness dimension are important.[3] His results show that the stress biases set up in the plane of the resonator plate by nonuniform heating in the thickness dimension cause large frequency deviations through third-order elastic constant effects. He calculates that there is a doubly-rotated cut at $\phi = 22.8°$, $\theta = 34.3°$ which decouples from the third-order elastic constant effects, remarkably close to our isothermal calculations of $\phi = 22.4°$, $\theta = 34.3°$. Although times the order of 10's of milliseconds are involved for the thermal transient case (a regime where the present results do not apply rigorously), it might be expected that as long as third-order elastic effects predominate, the present results are useful. The small difference in the two predictions for ϕ and θ is either due to the effect of going from isothermal to adiabatic conditions in the theory or due to the planar stresses in the thermal shock case being not isotropic since the thermal expansion of quartz is anisotropic.

Recently, Kusters carried out thermal shock studies on a series of doubly-rotated resonators which were chosen to experimentally locate the ϕ and θ values for thermal shock compensation.[4] His measurements involved measuring the hysteresis in oscillator frequency vs. time plots as the temperature of an oil bath surrounding the quartz crystals was cycled between 15°C below to 15°C above the turnover temperature and back. Although the rate of change of temperature in his experiment is slow relative to the time constants for thermal equilibrium, the dynamic nature of the experiment suggests that at least small temperature gradients exist along the thickness dimension during the thermal cycling. If that is the case, frequency shifts should occur through third-order elastic constant effects which are larger than would be predicted from the static frequency-temperature characteristic. Kusters does indeed observe large frequency shifts and finds a doubly-rotated cut at $\phi = 21.93°$, $\theta = 33.93°$ which shows thermal shock effects at least two orders of magnitude smaller than his AT-cut control crystals. His results[4] are shown in columns 1 and 2 of Table I for several different doubly-rotated cuts.

If the experimental results in columns 1 and 2 of Table I are self-consistent and are due to planar stress bias in the quartz plates, they should scale with the calculated values for K shown in Fig. 1. This is indeed the case as seen in columns 3-5 of Table I where the present calculations are presented normalized to the AT-cut. The calculations are based on the right-hand scale of Fig. 1, i.e., the deviation of ϕ from the zero stress coefficient. The calculated results in column 5 of Table I compare to within 30% of the experimental results in column 2. Considering that the experiment does not exactly correspond to the present isothermal conditions assumed for the calculations, the agreement is satisfying. It should be noted, also, that the agreement seen in Table I would be attained if the stress biases in the experiments came from thermal expansion of the mounting, or some means other than thermal gradients in the thickness dimension of the resonator plate. Certainly the signs of the $\Delta f/f$ are correctly predicted by the calculations. In addition, the calculations are uniformly high in magnitude on either side of the optimum ϕ which says that the zero crossing is well-defined but that the shape of $\Delta f/f$ vs. ϕ is slightly different between the theory and experiment. Based on the agreement seen in Table I, the existence of the SC-cut *seems* assured.

Conclusions

The general applicability of the present theory has been discussed. The agreement between the present calculations and the thermal shock data of Kusters[4] lends confidence to the existence of the SC-cut. The SC-cut is general in concept in that the frequency is decoupled completely from planar stress biases and greatly decoupled from anisotropic stress biases, all of this independent of the source of the mechanical stress bias. As such, the SC-cut offers promise of better long-term frequency stability and better resistance to acceleration effects than the AT-cut. For this reason, general theoretical expressions are included for the third-order elastic constant effects in the SC-cut and the AT-cut so that any arbitrary mechanical stress bias situation can be easily treated in the future.

Acknowledgment

The author appreciates receiving the data of J. A. Kusters before its publication.

References

*Supported by the U.S. Energy Research & Development Administration under Contract AT (29-1) 789.

1. E. P. EerNisse, Proc. 29th Annual Symposium on Frequency Control, p. 1 (1975).
2. E. A. Gerber and R. A. Sykes, Proc. IEEE 55, 783 (1967).
3. R. Holland, IEEE Trans. Sonics and Ultrasonics, SU-23, p. 72 (1976).
4. J. A. Kusters, IEEE Trans. Sonics and Ultrasonics (to be published).
5. R. N. Thurston and K. Brugger, Phys. Rev. 133, A1604 (1964).

6. H. S. Carslaw and J. C. Jaeger, "Conduction of Heat in Solids," (Oxford, 1959) pp. 92-132.
7. R. Holland, IEEE Trans. Sonics and Ultrasonics, SU-21, P. 171 (1974).
8. American Institute of Physics Handbook, 3rd Edition, (McGraw-Hill, 1972).
9. E. P. EerNisse, J. Appl. Phys. 43, 1330 (1972).
10. H. J. McSkimin, P. Andreatch, Jr., and R. N. Thurston, J. Appl. Phys. [illegible] 1624 (1965).
11. R. N. Thurston, H. J. McSkimin, [illegible] P. Andreatch, Jr., J. Appl. Phys. 37, 267 (19[illegible]).
12. R. Bechman, A. D. Ballato, and [illegible] Lukaszek, Proc. IRE 50, 1812 (1962).
13. Proc. IRE 37, 1378 (1949).
14. A. D. Ballato and R. Bechman, Proc. IRE 48, p. 261 (1960).
15. J. M. Ratajski, IBM J. Res. Dev. 12, 92 (1968).
16. R. W. Keyes and F. W. Blair, Proc. IEEE 55, 565 (1967).

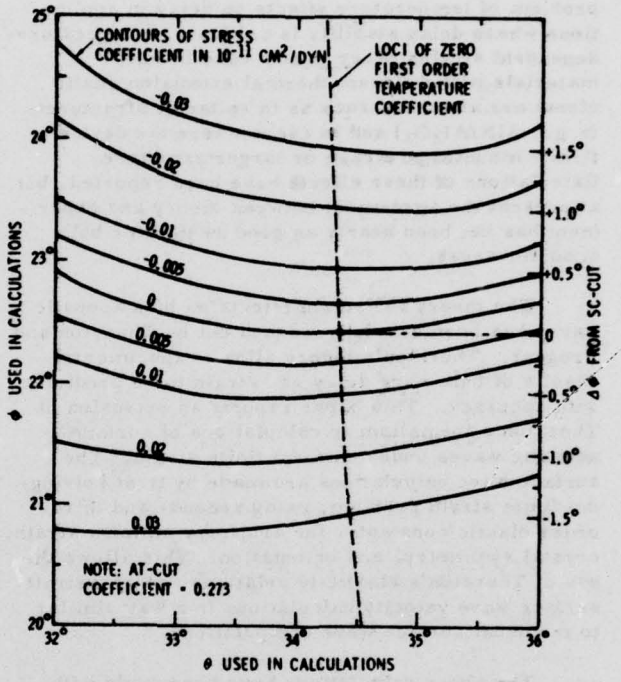

Fig. 1 Calculated contours of the stress coefficient in Eq. (9) in the ϕ,θ plane for the $(yxwl)\phi,\theta$ family of doubly-rotated quartz resonators. The loci of the calculated zero first-order temperature coefficient is included. The SC-cut is $\phi = 22.4°$, $\theta = 34.3°$. The right-hand scale is ϕ measured as a shift from the SC-cut.

TABLE I

Comparison of Thermal Shock Data and the Present Calculations

Doubly-Rotated Cut Used by Kusters (Ref. 4) (ϕ,θ)	Experimentally Observed $\Delta f/f$ (ppm) for Thermal Transients	Deviation of ϕ Angle From Optimum	Calculated Value of $K(10^{-11}$ cm^2/dyn) For ϕ in Column 3 and θ in Column 1	Calculated $\Delta f/f$ (ppm) Normalized to AT-cut
AT	-2052.5	(----)	0.273	-2052.
(21°, 34.015°)	-101.13	(-0.93°)	0.0179	-134.
(23°, 33.826°)	119.53	(1.07°)	-0.0209	157.
(25°, 33.692°)	376.4	(3.07°)	-0.0585	440.
(21.93°, 33.930°)	<-20	(0°)	0	0

STATIC STRAIN EFFECTS ON SURFACE ACOUSTIC WAVE DELAY*

R. B. Stokes and K. M. Lakin
Electronic Sciences Laboratory
University of Southern California
Los Angeles, California 90007

Summary

Strain effects on acoustic surface wave devices are of considerable interest because they add to the problem of temperature effects on delay in applications where delay stability is critical. Temperature-dependent strains occur in any case in which materials with different thermal expansion coefficients are attached, such as in epitaxial structures (e.g., AlN/Al_2O_3) and in cases where the device is firmly mounted to a case or larger structure. Calculations of these effects have been reported, but at present the agreement between theory and experiment has not been nearly as good as that for bulk acoustic waves.

The theory for strain effects on bulk acoustic waves has been carefully worked out by Thurston and Brugger. Thurston's theory allows experimental results of bulk wave delay vs. strain to be predicted with accuracy. This paper reports an extension of Thurston's formalism to calculations of surface acoustic waves under uniform finite strain. The surface wave calculations are made by first solving the finite strain problem, using second- and third-order elastic constants, for arbitrary uniform strain, crystal symmetry, and orientation. This allows the use of Thurston's elasticity relations, which permit surface wave velocity calculations in a way similar to the usual surface wave computations.

The above calculations have been made with various static boundary conditions to approximate the experimental conditions for measurements reported in the literature. Agreement with these measurements and previous calculations is discussed.

Surface wave substrates are usually thin plates, and this geometry causes a much greater sensitivity to bending forces than to pure extensional or compressional forces. Previous measurements of surface wave velocity vs. strain have all been with bending experiments. Bending strain includes several effects which do not appear in the uniform strain calculation and should be evaluated separately. These effects and their relative importance are discussed. Experiments in progress at USC which measure velocity vs. uniform strain as a check on the bending experiments are described.

Introduction

Strain effects on acoustic surface wave devices are of considerable interest because they add to the problem of temperature effects on delay in applications where delay stability is critical. Temperature-dependent strains occur whenever materials with different thermal expansion coefficients are attached, as in epitaxial structures (e.g., AlN/Al_2O_3) or in any case in which the device is firmly mounted to a larger structure. Strain effects on YZ $LiNbO_3$ have been used to temperature-compensate this material by Toda and Osaka[1], and strain effects in YX and ST-X quartz and in silicon have been used by Reeder, Cullen, and Gilden[2] to measure pressure. Strain effects on surface wave delay have been measured by Nalamwar and Epstein[3-7] (YX quartz, YZ $LiNbO_3$, ZnO on glass and fused quartz), Cullen and Reeder[8] (YX and ST-X quartz) and Toda and Osaka[1] (YZ $LiNbO_3$).

The theory for strain effects on bulk acoustic waves has been worked out carefully by Thurston and Brugger.[9-12] Thurston's theory allows experimental results of bulk wave delay vs. strain to be predicted with accuracy. Nalamwar and Epstein[4-7] have reported computations, based on another formalism, which include surface wave delay vs. strain in YX quartz and YZ $LiNbO_3$, but for these cases calculations do not agree closely with experiments.

This paper reports an extension of Thurston's formalism to calculations of surface acoustic waves under uniform finite strain. A piezoelectric correction is included as a strain-independent effect, and the importance of its strain dependence is discussed. Velocity dependences on all possible uniform surface stresses are calculated for YX quartz, ST-X quartz, and YZ $LiNbO_3$. A comparison is made with experiments reported in the literature and the possible extra effects that may result from bending experiments are discussed.

Theory

In the discussion of finite strain and wave propagation in such a strain, we attempt to stay as close as possible to the notation of Thurston.[11] The location of a particle in the medium can be described in Cartesian coordinates by its position in the unstrained crystal, a_i; its position in the initially statically strained crystal, X_i; or its position after displacement from the initial strain condition, x_i. Wave displacements are therefore $u_i = x_i - X_i$. Bars over quantities indicate values in the initially strained condition. Other quantities are:

t_{ij}	thermodynamic tensions
η_{ij}	Lagrangian strains
U	internal energy per unit mass

*This research was supported by the Joint Services Electronics Program, through the Air Force Office of Scientific Research under Contract F44620-71-C-0067.

F free energy per unit mass

ρ density

We use the convention of x_3 as the surface normal and x_1 as the direction of propagation (Fig. 1). The coordinate x_3 is zero at the surface and positive inside the medium.

A. Static Strain

Before the wave propagation problem can be described, the condition of finite static strain must be known. Strain is a measurement of deformation, and is nonlinear in the displacement gradients; for strains that cannot be considered inifinitessimal, a full definition must be used. Lagrangian strains are the most commonly used:

$$\eta_{ij} = \frac{1}{2}\left[(\partial x_s/\partial a_i)(\partial x_s/\partial a_j) - \delta_{ij}\right] \qquad (1)$$

The quantities analogous to stresses that are conjugate to the Lagrangian strains are the thermodynamic tensions:[9-12]

$$t_{pq} = \rho_o(\partial U/\partial \eta_{pq})_S = \rho_o(\partial F/\partial \eta_{pq})_T$$

(adiabatic) (isothermal)

The elasticity relation for finite static strain can be described as a power series with isothermal stiffnesses as coefficients:

$$\bar{t}_{ij} = c^{oT}_{ijkl}\,\bar{\eta}_{kl} + \frac{1}{2}c^{oT}_{ijklmn}\,\bar{\eta}_{kl}\bar{\eta}_{mn} + \cdots$$

The stiffness coefficients in the series are evaluated at zero strain, when the Lagrangian strains and thermodynamic tensions can be replaced by the usual infinitessimal strains and stresses.

The displacement gradients $\partial X_i/\partial a_j$ are needed to completely specify the state of deformation. They can be found through (1) from the static strains if they are assumed symmetric, which is analogous to the infinitessimal pure strain case of no internal rotations.

Stresses can be found from the thermodynamic tensions with the displacement gradients:

$$\bar{T}_{ij} = \frac{1}{J}\frac{\partial X_i}{\partial a_r}\frac{\partial X_j}{\partial a_s}\bar{t}_{rs}, \text{ where } J = \left\| \frac{\partial X_m}{\partial a_n} \right\| = \frac{\rho_o}{\rho}$$

(determinant).

B. Wave Equation

Acoustic waves in crystals at practical frequencies and temperatures involve elastic changes fast enough to be essentially adiabatic.[12] Under static strain, the elasticity relation for the wave is

$$\frac{\partial t_{ij}}{\partial \eta_{kl}} = c^{S}_{ijkl} = c^{oS}_{ijkl} + c^{oS,T}_{ijklmn}\,\bar{\eta}_{mn} + \cdots$$

where $c^{oS,T}_{ijklmn}$ is the third-order elastic constant of mixed isothermal and adiabatic conditions. Brugger[13] gives the conversion from this mixed coefficient to the purely adiabatic third-order constant, $c^{oS,S}_{ijklmn}$, which can be a change of several percent.

In an unstrained crystal, the wave equation is

$$\rho\ddot{u}_i = c_{ijkm}\frac{\partial^2 u_k}{\partial a_j \partial a_m} = \frac{\partial T_{ik}}{\partial a_k},$$

since we assume everywhere here that there are no body forces. Under a uniform stress, the effective elastic constants for wave propagation in general show much less symmetry than those in an unstressed crystal. This is due to the fact that the stresses themselves modify the wave propagation problem in such a way that it is not analogous to any unstressed problem.[11] The stresses in the wave depend on particle rotation in addition to strains, in contrast to the unstrained state.[11] The small-signal wave equation (displacement much less than a wavelength) valid for a uniformly strained crystal is

$$\bar{\rho}\ddot{u}_i = B_{ijkm}\frac{\partial^2 u_k}{\partial X_j \partial X_m} \qquad (2)$$

in which

$$B_{ijkm} = \delta_{ik}\bar{T}_{jm} + C_{ijkm},$$

where

$$C_{ijkm} = \frac{\bar{\rho}}{\rho_o}\frac{\partial X_i}{\partial a_p}\frac{\partial X_j}{\partial a_q}\frac{\partial X_k}{\partial a_r}\frac{\partial X_m}{\partial a_s}c_{pqrs} \qquad (3)$$

and

$$B_{ijkm} = B_{kmij}$$

but

$$B_{ijkm} \neq B_{jikm}, \quad B_{ijkm} \neq B_{ijmk}, \text{ in general.}$$

The B_{ijkm}'s cannot be reduced as the c_{ijkm}'s; there are in general forty-five elements of B_{ijkm} that must be calculated and carried.

Thurston[11] has introduced another set of constants, "wave-propagation coefficients", which acquire more useful symmetry due to a re-ordering of subscripts:

$$\hat{C}_{ijkm} = \frac{1}{2}(B_{ikjm} + B_{imjk}) = \delta_{ij}\bar{T}_{km} + \frac{1}{2}(C_{ikjm} + C_{imjk}).$$

These have the properties that

$$\hat{C}_{ijkm} = \hat{C}_{ijmk} = \hat{C}_{jikm} \text{ but } \hat{C}_{ijkm} \neq \hat{C}_{kmij}, \text{ in general,}$$

so that they can be reduced to a non-symmetric six-by-six matrix

$$\hat{C}_{\mu\nu} = \hat{C}_{ijkm} .$$

With the $\hat{C}_{ijkm}$'s, the wave equation becomes

$$\bar{\rho}\,\ddot{u}_i = \hat{C}_{ijkm}\,\frac{\partial^2 u_j}{\partial X_k\,\partial X_m} \quad .^{11} \tag{4}$$

C. Trial Solution

While Thurston[11] uses equation (4) only for bulk waves, it is just a point form of Newton's second law and is applicable to any kind of elastic wave. As is done in the usual calculations of surface waves in anisotropic substrates,[14] we use a trial solution which decays in depth

$$u_i = \beta_i\, e^{j(\omega t - kX_1 - \alpha k X_3)} .$$

Use of this trial solution leads to the eigenvalue problem (Christoffel equation):

$$(M_{ij} - \lambda\,\delta_{ij})\beta_j \qquad \text{where } \lambda = \bar{\rho}\,v^2$$

and

$$M_{ij} = (\hat{C}_{(ij)1} + 2\alpha\hat{C}_{(ij)5} + \alpha^2\,\hat{C}_{(ij)3})$$

where (ij) stands for the reduced subscript from one to six, defined in the usual way (Voigt's notation). The velocity here is in terms of real distance in the initially strained crystal, $v = dX_1/dt = d\omega/dk$.

Solution of the above eigenvalue problem leads to three modes which decay in distance from the surface:

$$u_i^{(n)} = \beta_i^{(n)}\, e^{j(\omega t - k X_1 - \alpha^{(n)} k X_3)} \text{ for modes } n = 1,2,3.$$

As in the unstrained case, the surface wave solution is a combination of these three modes which satisfies the boundary conditions for the free surface, $T_3 = T_4 = T_5 = 0$.

The general combination of modes is

$$u_i = \left[\sum_{n=1}^{3} A^{(n)}\beta_i^{(n)} e^{-j\alpha^{(n)} k X_3}\right] e^{j(\omega t - kX_1)} .$$

D. Boundary Conditions

In the unstrained case, writing equations for $T_3 = T_4 = T_5 = 0$ in terms of the $A^{(n)}$'s, $\beta_i^{(n)}$'s, and $\alpha^{(n)}$'s leads to the requirement that the determinant of the coefficients of the $A^{(n)}$'s in the three equations must be zero in order that a non-trivial solution of $A^{(n)}$'s exist. This is

$\| E_{sm} \| = 0$ where

$$E_{sm} = c_{s3kl}(\delta_{11}\beta_k^{(m)} + \delta_{13}\beta_k^{(m)}\,\alpha^{(m)}) .$$

Under static strain, the small-signal wave stresses are dependent on both strain and rotation, and can be found from the wave displacement gradients with the coefficients E_{ijkm}[11]:

$$T_{ij} - \bar{T}_{ij} = E_{ijkm}\,\frac{\partial u_k}{\partial X_m}$$

where

$$E_{ijkm} = \left[\frac{\partial T_{ij}}{\partial(\partial u_k/\partial X_m)}\right]^{X} , \tag{5}$$

evaluated at the initially strained state, and

$$E_{ijkm} = \bar{T}_{im}\delta_{jk} - \bar{T}_{ij}\delta_{km} + \bar{T}_{jm}\delta_{ik} + C_{ijkm} .$$

C_{ijkm} is reducible in subscript and symmetric just as an elastic constant in the absence of strain, forming a six-by-six symmetric matrix after reduction. E_{ijkm}, however, is reducible in the first pair of subscripts, but not the second, leaving fifty-four elements after reduction. The boundary condition for a surface wave solution is then:

$$\| F_{sm} \| = 0$$

where

$$F_{sm} = E_{s3kl}(\delta_{11}\beta_k^{(m)} + \delta_{13}\beta_k^{(m)}\,\alpha^{(m)}) .$$

It is assumed, of course, that the applied static stress is consistent with $T_3 = T_4 = T_5 = 0$, the conditions for a free surface.

E. Other Forms of the Wave Equation

The E_{ijkm} contain all the information found in the $\hat{C}_{ijkm}$; in fact,

$$\hat{C}_{ijkm} = \frac{1}{2}(E_{ikjm} + E_{imjk})$$

and the wave equation can also be written with the E_{ijkm}'s:

$$\bar{\rho}\,\ddot{u}_i = E_{jikm}\,\frac{\partial^2 u_k}{\partial X_j\,\partial X_m} . \tag{6}$$

The wave equation can also be written

$$\bar{\rho}\,\ddot{u}_i = \bar{T}_{jm}\,\frac{\partial^2 u_i}{\partial X_j\,\partial X_m} + C_{ijkm}\,\frac{\partial^2 u_k}{\partial X_j\,\partial X_m}$$

where C_{ijkm} is defined in (3). This is of the same form as Nalamwar and Epstein's wave equation in

the absence of piezoelectricity.

F. Piezoelectricity

In an unstrained crystal, piezoelectricity for small strains can be modeled with the constitutive relations:

$$T_{ij} = c^{E}_{ijkl}\,\eta_{kl} - e_{ij,k}\,E_k$$

$$D_k = \epsilon^{\eta}_{kj}\,E_j + e_{k,ij}\,\eta_{ij}$$

where $e_{ij,k} = e_{k,ij}$, and the superscripts E and η denote evaluation at constant electric field and constant strain, respectively. These relations or higher-order equivalents should ideally be used in solving the static strain problem exactly. In the strained state we can still assume general constitutive relations for small changes:

$$dT_{ij} = \left[\frac{\partial T_{ij}}{\partial(\partial u_k/\partial X_l)}\right]^{E} d(\partial u_k/\partial X_l) + \left[\frac{\partial T_{ij}}{\partial E_k}\right]^{\eta} dE_k$$

$$dD_i = \left[\frac{\partial D_i}{\partial(\partial u_k/\partial X_l)}\right]^{E} d(\partial u_k/\partial X_l) + \left[\frac{\partial D_i}{\partial E_k}\right]^{\eta} dE_k$$

The full displacement gradients are used here since the non-piezoelectric problem has shown that both strains and rotations are important.

In the absence of free charge, the waves must satisfy the equations

$$\bar{\rho}\,\ddot{u}_i = \frac{\partial T_{ik}}{\partial X_k}$$

$$\text{div } D = 0 \quad .$$

The piezoelectric wave equations are then, for small amplitudes,

$$\bar{\rho}\,\ddot{u}_i = \frac{\partial T_{ik}}{\partial(\partial u_m/\partial X_n)}\,\frac{\partial(\partial u_m/\partial X_n)}{\partial X_k} + \frac{\partial T_{ik}}{\partial E_m}\,\frac{\partial E_m}{\partial X_k}$$

$$\text{div } D = 0 = \frac{\partial D_i}{\partial E_j}\,\frac{\partial E_j}{\partial X_i} + \frac{\partial D_i}{\partial(\partial u_m/\partial X_n)}\,\frac{\partial(\partial u_m/\partial X_n)}{\partial X_i}$$

Using (5) and defining piezoelectric constants for the strained state, this is:

$$\bar{\rho}\,\ddot{u}_i = E_{jikm}\,\frac{\partial^2 u_k}{\partial X_j\,\partial X_m} + f^{X}_{ik,m}\,\frac{\partial^2 \phi}{\partial X_k\,\partial X_m} \qquad (7)$$

$$\text{div } D = 0 = \epsilon^{X}_{ij}\,\frac{\partial^2 \phi}{\partial X_j\,\partial X_i} + g^{X}_{i,mn}\,\frac{\partial^2 u_m}{\partial X_n\,\partial X_i}$$

where ϕ is the electric potential and we have used the quasi-static approximation, and

$$f^{X}_{ik,m} = \left[\frac{\partial T_{ik}}{\partial E_m}\right]^{\eta,X}, \quad g^{X}_{i,mn} = \left[\frac{\partial D_i}{\partial(\partial u_m/\partial X_n)}\right]^{E,X}$$

and

$$\epsilon_{ij} = \left[\frac{\partial D_i}{\partial E_j}\right]^{\eta,X}$$

Notice that a comparison of (7), (6), and (4) allows E_{jikm} to be replaced by the $\hat{C}_{ijkm}$, which were used in the non-piezoelectric wave equation.

Since stresses are always reducible, it can be seen that the $f_{ik,m}$'s are reducible in the first pair of subscripts. There is no simple reason, however, for assuming that the $g_{i,mn}$'s are similarly reducible, or that $g_{i,mn} = f_{mn,i}$.

The boundary conditions for surface waves at a free surface are $T_3 = T_4 = T_5 = 0$, D_3 and ϕ continuous across the surface, and the fields vanishing at a shorting plane at a specified distance from the surface.[14] If $f_{ik,m}$ and $g_{m,ik}$ are known, the Christoffel equation and boundary condition determinants similar to those of Slobodnik[14] can be written, keeping the integrity of the pair of subscripts on the $g_{m,ik}$'s.

If the assumption is made that $g_{m,ik}$ is reducible and $g_{m,ik} = f_{ik,m}$, then the piezoelectric wave problem is exactly that of Slobodnik's[14] but with the mechanical terms (those involving the stiffnesses) replaced by those in the non-piezoelectric formalism of parts C and D of this section.

Thermodynamic expressions for $f_{ik,m}$ and $g_{m,ik}$, and a proof that the dielectric constant remains symmetric even under finite strain, are given in the appendix.

Numerical Results

An existing acoustic surface wave computer program written at USC by D. Penunuri and similar to Slobodnik's[14] was modified for this problem. The second-order elastic constants used to solve the static strain problem are the same as those for the wave propagation: adiabatic and electrically free (constant E). The static strain problem is solved non-piezoelectrically with these stiffnesses, so that the result is as if the surface of the crystal were covered by an equipotential. Piezoelectricity is assumed constant since the change with strain is not available. The errors expected due to these approximations are discussed later. The computer program:

1. Rotates second- and third-order stiffness tensors (measured at zero strain) to the wave coordinate system shown in Fig. 1, using the rotation matrix a_{ij}:

$$c^{o'}_{ijkl} = a_{im}a_{jn}a_{ko}a_{lp}c^{o}_{mnop}$$ [15]

$$c^{o'}_{ijklmn} = a_{iq} a_{jr} a_{ks} a_{lt} a_{mu} a_{nv} c^{o}_{qrstuv} .$$

2. Solves the finite static strain problem, giving displacement gradients, thermodynamic tensions, stresses, etc.

3. Calculates $\hat{C}_{\mu\nu}$ and E_{ijkm} for the strained crystal.

4. Solves for a surface wave velocity using the theory from the last section and an iteration for a zero boundary condition determinant.

For a non-piezoelectric crystal, the only error in the velocity should be due to the adiabatic assumption. This error is introduced in two places:

1. in the magnitude of static stress vs. deformation.

2. in the stress used in the wave propagation problem.

Huntington[16] gives the thermodynamic conversion from adiabatic to isothermal second-order elastic constants and mentions that it is usually on the order of one percent of the constants. McSkimmon, Andreatch, Jr., and Thurston[17] measured both sets of constants in quartz. The largest absolute stiffness difference was 0.3 percent of c_{33}, *the highest stiffness*. Experience indicates that the error due to the adiabatic assumption for static strain in the γ's defined later is on the order of the fractional correction between adiabatic and isothermal stiffnesses. This correction for the diagonal stiffness in $LiNbO_3$ and quartz is less than one half percent, so correspond errors in the γ's are expected to be on the order of .005.

The electrically free case of elasticity in a piezoelectric material is not that of an isolated, insulated crystal in a typical experiment. According to Nye,[18] an isolated piezoelectric plate has the mixed electrical conditions of D normal and E tangential to the surface being zero. Nye's formula for conversion of isothermal compliances from constant E to constant D normal, E tangential indicates differences typically of less than a percent for quartz, but considerably more for $LiNbO_3$. The computed velocity shifts for YZ $LiNbO_3$ therefore can only be accurate for a device surrounded by a conductor.

In the wave propagation problem, piezoelectricity is chosen as a constant effect, since its variation with strain is not available. We use $f_{ij,k} = g_{k,ij} = e_{k,ij}$ where f and g are defined in the last section. Constant piezoelectricity is of course a very crude assumption but makes a significant difference in highly piezoelectric materials from non-piezoelectric approximations, since the added piezoelectric stiffening alters the character of the surface wave solutions.

Fractional changes in piezoelectric and dielectric constants vs. strain are probably on the order of the strain, since most physical constants (c_{ijkl}, ρ, etc.) change at that rate. These changes have much less effect on the velocity than similar fractional changes in stiffness, since the wave forces are mainly mechanical. So unless the dielectric or piezoelectric constants change surprisingly rapidly with strain, their effect on the velocity vs. strain should be small.

To investigate the effect of piezoelectric and dielectric constant changes on velocity, ordinary surface wave velocities were calculated with perturbations of each relevant $e_{k,ij}$ and ϵ_{ij}. The dielectric constant was changed symmetrically since it retains its symmetry under finite strain. To scale the perturbations for comparison with strains, they are shown as changes divided by the maximum e or ϵ for the material. These results are shown in Table I for YZ $LiNbO_3$ and ST-X quartz.

With the approximations outlined above, the shifts in SAW velocity for YZ $LiNbO_3$, YX quartz, and ST-X quartz were calculated vs. small single elements of static stress. The resulting ratios of fractional velocity change vs. stress can be used as a basis for any uniform applied stress or strain, since for small stresses the velocity shifts are additive. The results are shown in Table II, in which

$$\zeta_I = (dv/v)/dT_I .$$

At a free surface $T_3 = T_4 = T_5 = 0$, but in some static strain conditions these stresses can be nonzero immediately below the surface, where the wave forces act. For example, in the bending of a short cantilever beam by a vertical end load, T_5 is nonzero in the interior of the beam.[19] The single-element stress perturbations for T_3, T_4, and T_5 are therefore included only as indications of which of these stresses may have a heavy effect on velocity. These stresses can of course not be uniform since they vanish at the surface, while the velocity calculation assumes uniform stress.

It can be seen that the velocity shift varies widely, depending on which elements of stress are applied. For instance, YZ $LiNbO_3$ is about twelve times more sensitive to T_2 than to T_1.

Cullen and Reeder[8] have reported experimental measurements of velocity vs. strain for the cases ($\eta_1 = 0$, $\eta_2 \neq 0$) and ($\eta_1 \neq 0$, $\eta_2 = 0$). The added assumptions must be made that $T_3 = T_4 = T_5 = 0$ at the surface, and that $T_6 = 0$ by simplicity of the configuration. They define $\gamma_I = (\Delta v/v)/\eta_I$ for these cases. Converting these conditions to a uniform stress tensor allows these γ's to be assembled from the calculated values in Table II. Nalamwar and Epstein[5] assume in their theory the same strain configuration, so values of γ_I measured from their plots are also included. Table III shows the values of γ from various calculations and experiments. Conditions of single stress elements are also included, since in a very long bar the stress perpendicular to the axis vanishes, even during bending. It can be seen that our calculations resemble those of

Nalamwar and Epstein much more than any of the experiments reported. The difference from their calculations is probably due to the addition of the finite-strain formalism of wave propagation.

It can also be seen that measurements of velocity vs. strain must be done very carefully since the sensitivity of the measurements to strains or stresses other than the predominant one can drastically affect the velocity shift. For instance, YZ $LiNbO_3$ is about twelve times more sensitive to T_2 than to T_1, so unless the change in T_2 is known to a twelfth of the change in T_1, the experiment is worthless.

Experimental Considerations

Lack of agreement between theory and experiment in Table III indicates that the actual experimental conditions have not been correctly modeled. The considerable disagreement between our calculations and Cullen and Reeder's measurements for ST-X quartz are the most unsettling because quartz is only slightly piezoelectric and its third-order elastic constants are apparently well known.[20]

A. Bending Stresses

The experiments of Nalamwar and Epstein and those of Cullen and Reeder are bending experiments; this is because a thin plate requires much less force to produce a surface bending strain than to cause a uniform strain of the same magnitude. Experiments with uniform strain in thin bars are difficult to carry out, because bending must be very carefully minimized in order not to overwhelm the effect caused by the average uniform strain. However, every bending experiment involves many other effects than the obvious surface strains η_1 and η_2. The sensitivity of the bending experiments to these effects can be studied, and experiments should be designed such that these effects are either known or negligible. In this section we examine the stresses and other perturbing effects that may occur in a bending experiment.

Typical surface wave substrates used in our laboratory have dimensions of 1" or 2" x 0.5" x 0.4". These can be considered moderately short bars or rectangular plates. A cantilever beam of these dimensions can be bent easily to provide a substantial longitudinal surface strain in the center of the wide surface; several hundred times as much force is required to produce a uniform strain of the same magnitude.

Timoshenko[21] discusses the infinitessimal bending of a plate of uniform thickness with Poisson's ratio ν: For a constant bending moment M_1 (torque around the bar's center plane due to forces in the x_1 direction), the plate bends to a constant radius $R = \frac{E(2a)^3}{12 M_1}$, where E is Young's modulus and 2a is the thickness of the bar. The strain induced by this pure bending is then $\eta_1 = \frac{x_3 - x_3^o}{R}$, where x_3^o is the depth coordinate at the center of the bar's thickness. The strain η_1, however, leads to a perpendicular stress T_2 which is only relaxed when the bar also bends in the opposite direction (Fig. 2), forming a saddle shape. Considering bending moments in two perpendicular directions, M_1 and M_2 acting on x_1 or x_2 faces of any section, the bar bends with radii R_1 and R_2 (Fig. 3), and these bendings are coupled through the Poisson's ratio with the equations

$$1/R_1 = \frac{12}{E(2a)^3} (M_1 - \nu M_2)$$

$$1/R_2 = \frac{12}{E(2a)^3} (M_2 - \nu M_1) .$$

It can be seen that application of only one bending moment, such as M_1 in the ideal cantilever beam experiments, causes a bending in the plane normal to x_1 also. Similarly, if only the curvature $1/R_1$ is allowed (cylindrical bending, as in Cullen and Reeder), a second bending moment $M_2 = \nu M_1$ must be applied along with M_1. The strains at any point are simple in these two cases; in the cantilever beam $\eta_2 = -\nu \eta_1$ and in cylindrical bending $\eta_2 = 0$.

In the case of bending that is not pure, the bending moment varies along the bar's length. To avoid a net torque on any element of the bar, shear stresses must exist to balance the change in bending moment. If M_1 changes along x_1, T_5 is required; if M_2 changes along x_2, T_4 is required. Both these stresses are zero at a free surface, but are nonzero inside the bar. A nearly exact solution for the cantilever beam of rectangular cross section with width 2b and thickness 2a, and b >> a, given in Timoshenko[22] is:

$$T_1 = -\frac{P}{I} (1 - x_1) (x_3 - x_3^o) \qquad (1 - x_1) = \text{distance from load}$$

$$T_2 = T_3 = T_4 = 0$$

$$T_5 = \frac{1}{1 + \nu} \frac{P}{2I} (a^2 - (x_3 - x_3^o)^2)$$

$$T_6 = -\frac{\nu}{1 + \nu} \frac{P}{I} (x_3 - x_3^o) (x_2 - x_2^o)$$

where P is the end load, I the moment of inertia, and x_3^o and x_2^o are the coordinates of the center of the bar's cross section. It can be seen that T_5 is non-zero on the interior of the bar and that T_6 is nonzero on the surface everywhere but at the exact center of the propagation path. At a point $\epsilon = a - (x_3 - x_3^o)$ beneath the surface and $\delta = (x_2 - x_2^o)$ away from the center of the propagation path, we can see that, for small ϵ/a,

$$T_5/T_1 \simeq -\frac{\epsilon}{(1 + \nu)(1 - x_1)}$$

and

$$T_6/T_1 = \frac{\nu}{1 + \nu} \frac{\delta}{(1 - x_1)} ,$$

so that at distances far from the load in comparison with the cross-sectional dimensions, the shear

stresses T_5 and T_6 can be expected to be negligible.

An accidental load in the x_2 direction also applied to the beam would cause comparatively minor effects, due to the increased value of I for the different geometry, but stresses would be added to T_1 and T_6 (the T_5 contribution for $b >> a$ is negligible).

If the load is applied unevenly on the end so that there is a slight torsion (Fig. 4), the predominant effect is an added T_6 at the surface. For $b >> a$, Timoshenko[23] gives, for the center of the propagation path,

$$T_6 \simeq \frac{M_t}{(.3)\,(2a)^2\,(2b)^2}$$

where M_t is the end torque.

In summary, in a long cantilever beam (experiment of Nalamwar and Epstein), we have T_1 and T_5 for a properly applied load, and T_6 away from the center of the propagation path. Additional contributions to T_6 are caused weakly if the load is not purely vertical, and more strongly if a torque is accidentally applied to the end. Bending moment M_2, even if applied at the ends, will vanish at the center of the bar by St. Venant's principle as long as the bar is at least twice as long as it is wide. The strains are related to the stresses by the compliance tensor, and are in general non-zero.

For a square plate in cylindrical bending (experiment of Cullen and Reeder), two bending moments are applied by forcing the edges parallel to the axis of the cylinder to stay straight. This results in $\eta_2 \simeq 0$, since there is little distance for the straightness requirement to relax. If the cylindrical bending was actually slightly conical, the variation in M_1 and M_2 would cause slight T_4 and T_5 below the surface. If a slight torque was applied due to imprecisely positioned loading pins, T_6 would occur.

A summary of possible stresses in bending experiments is shown in Table IV.

Propagation on a Bent Surface. In the simple case of pure cylindrical bending ($R_1 = R$, $R_2 = \infty$), the wave propagates around the surface of a cylinder of constant radius. The problem of Rayleigh wave propagation around the surface of a cylinder is solved in Viktorov,[24] where a somewhat cumbersome asymptotic expression for velocity perturbation from Rayleigh waves on a plane surface is given. We have used this expression to find the velocity shift in isotropic approximations to quartz and $LiNbO_3$.

The value of $\delta = (v - v_R)/v_R$, where v_R is the plane Rayleigh wave velocity and v is the cylindrical surface Rayleigh velocity, is proportional to $1/(k_R R) = v_R/(\omega R)$ for small curvatures, so we can define a constant H for a given material such that $\delta = H/fR$. Use of Viktorov's perturbation formula with isotropic approximations to surface wave substrates allows a determination of H. The change in the velocity vs. strain coefficients γ_1 is then found by using the strain at the surface of a purely bent bar $\eta_1 = a/R_1$, where 2a is the bar's thickness:

$$\Delta\gamma_1 = \frac{\Delta v/v}{\eta_1} = \frac{\delta}{\eta_1} = \frac{H/(fR)}{a/R} = \frac{H}{fa} .$$

For convex bending, this would be a positive shift in a measurement of velocity vs. surface strain. The approximate values for H have been calculated as:

Material and orientation	H (mm - MH_z)
YX quartz	0.972
YZ $LiNbO_3$	1.131
fused quartz	1.008

It can be seen that the property is not heavily dependent on the material. This effect is usually small; for the experiment of Cullen and Reeder it would make a difference of about .05 in γ_1. For much thinner substrates, of course, it could become significant.

The cylindrical propagation correction is on the order of the reduction in path length at an average depth of the wave. An effective depth can be calculated that artificially lumps the cylindrical velocity shift into just a change in path length; for YX quartz this is $d = .289\,\lambda$. In a bar made cylindrical by bending, the change in path length with depth is accompanied by changes in density, stiffness, stress, and strain; in fact, the finite strain conditions of our uniform strain theory are all simply scaled linearly down with depth (for convex bending). It seems plausible that the extra effect due to bending can just be approximated by calculating the velocity for the strain conditions that exist at the average wave depth. If the average wave depth calculated above for the path length change alone is used, the total effect can be lumped into a new γ:

$$\gamma_{1\,(\text{bent})} = (1 - d/a)\,\gamma_{1\,(\text{plane surface})}$$

This estimate indicates that the bending causes even less than the shift due to cylindrical geometry alone, implying that the effects of increased density, etc., partly cancel it. The changes due to Viktorov's cylindrical propagation therefore should be reduced by a factor of five for the materials and orientations mentioned here.

Uniform Strain. If a long bar is under longitudinal tension or compression in such a way that no bending results, St. Venant's principle insures that in the center of the bar the stress is simply $T_1 = T$, $T_2 = \ldots = T_6 = 0$. Even if the bar is mounted nonuniformly at the ends or with restrictions on the end strain, at distances from the ends of about the width of the bar, the simple state of stress results as long as there is no bending moment or torque.

Avoiding bending moments in the longitudinal

stretching of a bar primarily consists of insuring that no net lever arm exists where this tension is applied to the bar. The similar case of a lever arm in compression of a column due to uneven end loading is analyzed in Den Hartog,[25] for a stability calculation. For loads much less than critical (a ton or so), Den Hartog's formula for rectangular beams reduces to

$$\frac{T_{1\ \text{surface}}}{T_{1\ \text{average}}} = 1 + \frac{3e}{a}$$

where e is the lever arm of the load, assuming equal lever arms at both ends, and 2a is the thickness in the direction parallel to the arms (Fig. 5). For this case, then, reduction of the bending error to ten percent of the uniform stress requires reduction of the lever arm to 2/3 mil for a 40-mil thick bar. This requires very careful design of the connections of the cables supplying the tension, and a good measurement of velocity shift requires many experiments, remounting the cables each time, to get a good statistical average.

Measurements. We are now measuring the shift in velocity for uniform stress T_1 in ST-X quartz. This material was chosen because:

1. Its properties are well known.
2. It is nearly non-piezoelectric.
3. The zero temperature coefficient should make it insensitive to adiabatic cooling caused by the stretching.
4. Bending experiments in the literature and our calculations give very different results in this case.

We have not yet done enough measurements to get a statistically reliable number for c_1.

Conclusion

Thurston's theory for bulk acoustic waves in finitely strained nonpiezoelectric crystals has been extended to surface waves. The approximation of strain-independent piezoelectricity has been added for calculations of velocity vs. all possible uniform stresses in YX quartz, ST quartz, and YZ $LiNbO_3$. Numerical results have been reported and compared with results published previously by others.

A discussion of the possible effects other than uniform strain that may enter into a bending experiment includes shear stresses, torques, and linear strain variations with depth. Uniform stress experimental difficulties are described, along with experiments presently underway at USC.

Appendix

Thermodynamics of Piezoelectricity Under Finite Strain

This formalism uses the assumption that the density is completely determined by the Lagrangian strains. This is true for infinitessimal strains, and should be nearly true for small finite strains.

Since we can write the purely mechanical energy simply in terms of the thermodynamic tensions and Lagrangian strains, we choose the Lagrangian strains η_{ij}/ρ_o, the electric field E, and the entropy S as independent variables. The finite change in volume under strain requires that we be careful about adding energy per unit mass to energy per unit volume. Mechanical strain energy is $t_{ij}\, d(\eta_{ij}/\rho_o)$[13] per unit mass; electrical energy is $D_i\, dE_i$ per unit volume. If S is the entropy per unit mass, we can write an energy function per unit mass as

$$dZ = t_{ij}\, d(\eta_{ij}/\rho_o) - \frac{D_i}{\rho}\, dE_i + T dS \ .$$

For adiabatic changes, dS is always zero. The adiabatic derivatives of Z are:

$$\left.\frac{\partial Z}{\partial(\eta_{ij}/\rho_o)}\right|_{E,S} = t_{ij}\ , \qquad \left.\frac{\partial Z}{\partial E_i}\right|_{\eta,S} = -\frac{D_i}{\rho}\ .$$

Also

$$\frac{1}{\rho_o}\frac{\partial^2 Z}{\partial(\eta_{kl}/\rho_o)\partial(\eta_{ij}/\rho_o)} = \frac{\partial t_{ij}}{\partial \eta_{kl}} = \frac{\partial t_{kl}}{\partial \eta_{ij}}$$

$$= c^{E,S}_{ijkl} = c^{E,S}_{klij}$$

and

$$\rho_o \frac{\partial^2 Z}{\partial E_j \partial E_i} = -\rho_o \left.\frac{\partial(D_i/\rho)}{\partial E_j}\right|_{\eta,S}$$

$$= -\frac{\rho_o}{\rho}\frac{\partial D_i}{\partial E_j} = -\frac{\rho_o}{\rho} e^{S,\eta}_{ij} = -\frac{\rho_o}{\rho} e^{S,\eta}_{ji}\ .$$

The piezoelectric coefficients are

$$\rho_o \frac{\partial^2 Z}{\partial E_k \partial \eta_{ij}} = \left.\frac{\partial t_{ij}}{\partial E_k}\right|_{\eta,S}$$

and

$$\rho_o \frac{\partial^2 Z}{\partial \eta_{ij} \partial E_k} = -\rho_o \frac{\partial(D_k/\rho)}{\partial \eta_{ij}} = -\left.\frac{\partial(D_k(\rho_o/\rho))}{\partial \eta_{ij}}\right|_{S,E}\ .$$

Interchanging the order of differentiation has shown us that the dielectric tensor remains symmetric, and the stiffness tensor retains the symmetry $c_{ijkl} = c_{klij}$. However, the piezoelectric constants are related by

$$-\left.\frac{\partial t_{ij}}{\partial E_k}\right|_{\eta,S} = \frac{\rho_o}{\rho}\left.\frac{\partial D_k}{\partial \eta_{ij}}\right|_{S,E} + \left.\frac{\partial(\rho_o/\rho)}{\partial \eta_{ij}}\right|_{S,E} D_k \quad (8)$$

The quantities used in the piezoelectric theory formalism, $f^X_{ik,m}$ and $g^X_{i,mn}$ can be related by the above equation by

$$f^X_{ik,m} = \left.\frac{\partial T_{ik}}{\partial E_m}\right|_{S,\eta}^{X} = \frac{\rho}{\rho_o}\frac{\partial X_i}{\partial a_r}\frac{\partial X_k}{\partial a_s}\frac{\partial t_{rs}}{\partial E_m}$$

$$g^X_{i,mn} = \left.\frac{\partial D_i}{\partial(\partial u_m/\partial X_n)}\right|_{S,E}^{X} = \frac{1}{(\partial a_k/\partial X_n)}\frac{\partial X_m}{\partial a_r}\frac{\partial D_i}{\partial \eta_{rk}} .$$

The appearance of the extra term proportional to D_k in equation (8) suggests that if strain and stress quantities conjugate to energy per unit mass are used, piezoelectric coefficients involving the usual E and D vectors are not transpose symmetric.

References

1. N. Toda and S. Osaka, IEEE Trans. SU-22, p. 39 (1975).
2. T. M. Reeder, D. E. Cullen, and M. Gilden, 1975 Ultrasonics Symposium Proceedings, IEEE Cat. #75 CHO 994-4 SU, p. 264.
3. A. L. Nalamwar and M. Epstein, 1974 Ultrasonics Symposium Proceedings, IEEE Cat. #74 CHO 896-1 SU, p. 129.
4. A. L. Nalamwar and M. Epstein, 1975 Ultrasonics Symposium Proceedings, p. 484.
5. A. L. Nalamwar and M. Epstein, J. Appl. Phys. 47, p. 43 (1976).
6. A. L. Nalamwar and M. Epstein, IEEE Trans. SU-23, p. 144 (1976).
7. A. L. Nalamwar and M. Epstein, Proc. IEEE 64, p. 613 (1976).
8. D. E. Cullen and T. M. Reeder, 1975 Ultrasonics Symposium Proceedings, p. 519.
9. R. N. Thurston and K. Brugger, Phys. Rev. 133, p. A1604 (1964).
10. R. N. Thurston, in Physical Acoustics, ed. by W. P. Mason, Academic Press, Inc. (New York, 1964), vol. 1A, p. 1.
11. R. N. Thurston, J. Acoust. Soc. Am., 37, p. 348 (1965).
12. R. N. Thurston, Proc. IEEE 53, p. 1320 (1965).
13. K. Brugger, Phys. Rev. 133, p. A1611 (1964).
14. A. J. Slobodnik, Jr., E. D. Conway, and R. T. Delmonico, Microwave Acoustics Handbook, vol. 1A, Air Force Cambridge Research Laboratories AFCRL-TR-73-0597, Bedford, Mass. (1973).
15. B. A. Auld, Acoustic Fields and Waves in Solids, vol. I, John Wiley and Sons, Inc. (New York, 1973), p. 62.
16. H. B. Huntington, in Solid State Physics vol. 7, ed. by F. Seitz and D. Turnbull, Academic Press, Inc. (New York, 1958), p. 257.
17. H. J. McSkimmon, P. Andreatch, Jr., and R. N. Thurston, J. Appl. Phys. 36, p. 1624 (1965).
18. J. F. Nye, Physical Properties of Crystals, Oxford Univ. Press (London, 1957), pp. 185-6.
19. S. Timoshenko and J. N. Goodier, Theory of Elasticity, Second Edition, McGraw-Hill (New York, 1951), p. 35.
20. R. Bechmann and R.F.S. Hearmon, "The Third-Order Elastic Constants," in Landolt-Bornstein, Numerical Data and Functional Relationships in Science and Technology, New Series, Group III, vol. 2, Springer-Verlag (Berlin, 1969), p. 112.
21. Ref. no. 19, p. 255.
22. Ref. no. 19, p. 327.
23. Ref. no. 19, p. 278.
24. I. A. Viktorov, Rayleigh and Lamb Waves, Plenum Press (New York, 1967), p. 35.
25. J. P. Den Hartog, Strength of Materials, Dover (New York, 1961), pp. 191-4 (reprinted from McGraw-Hill, 1949).
26. Y. Nakagawa, K. Yamanouchi, and K. Shibayama, J. Appl. Phys. 44, p. 3969 (1973).

TABLE I. SAW VELOCITY SENSITIVIES TO PERTURBATIONS IN DIELECTRIC AND PIEZOELECTRIC CONSTANTS

Values shown are fractional changes in velocity divided by fractional changes in the constant, where the fractional changes in the constants are vs. the largest element, E_{max} or e_{max}, for that material and orientation.

Material and Orientation	Perturbed Element	$\frac{(\Delta v/v)}{\Delta \epsilon'_{ik}/\epsilon'_{max}}$	Perturbed Element	$\frac{(\Delta v/v)}{\Delta e'_{ik}/e'_{max}}$	Perturbed Element	$\frac{(\Delta v/v)}{\Delta e'_{ik}/e'_{max}}$
YZ $LiNbO_3$	ϵ'_{11}	-.0253	e'_{11}	-.0251	e'_{11}	+.0014
$\epsilon'_{max} = \epsilon'_{33}$	$\epsilon'_{13} = \epsilon'_{31}$	+.0082	e'_{13}	+.0013	e'_{12}	-.0024
$= 1.89 \times 10^{-10}$ F/M			e'_{14}	0.	e'_{14}	0.
$e'_{max} = e'_{15}$	ϵ'_{33}	-.0081	e'_{15}	-.0222	e'_{15}	+.0575
$= 3.7$ C/M^2			e'_{16}	-.0004	e'_{16}	-.0004
(electro-mechanical coupling $\frac{\Delta v}{v} = .024$)						
ST quartz						
$\epsilon'_{max} = \epsilon'_{22}$						
$= .402 \times 10^{-10}$ F/M	ϵ'_{11}	.00062	e'_{11}	+.00091	e'_{11}	+.00002
	$\epsilon'_{13} = \epsilon'_{11}$	+.00002	e'_{13}	-.00010	e'_{12}	0.
$e'_{max} = e'_{11}$	ϵ'_{33}	-.00027	e'_{14}	-.00008	e'_{14}	0.
$= .171$ C/M^2			e'_{15}	+.00055	e'_{15}	-.00186
(electro-mechanical coupling $\frac{\Delta v}{v} = .0058$)			e'_{16}	+.00002	e'_{16}	-.00032

Primes on dielectric and piezoelectric constants denote the rotated wave coordinate system for each orientation.

TABLE II. COMPUTED VALUES OF $\zeta_1 = \frac{\Delta v/v}{T_1}$ WHEN $T_J = 0$, $J \neq 1$.

Roundoff errors are on the order of $\pm .0003 \times 10^{-10}$ M^2/N.

Material and Orientation	ζ_1 ($\times 10^{-10}$ M^2/N)					
	ζ_1	ζ_2	ζ_6	ζ_3*	ζ_4*	ζ_5*
YZ quartz	-.0494	+.1656	+.0009	-.0278	+.0295	+.0009
ST-X quartz	-.0957	+.0741	0.	+.0127	-.2030	+.0013
YZ $LiNbO_3$**	+.0046	+.0562	+.0006	-.1521	0.	+.0833

*T_3, T_4, and T_5 are zero at the surface, but T_4 and T_5 can be nonzero just below it, where the elastic energy is. The computations for ζ_3, ζ_4, and ζ_5 assume that these stresses are magically uniform up to the free surface; these are shown only as possible hints as to how important these stresses are.

**Third-order elastic constants from Ref. 26.

TABLE III. VALUES OF $\gamma_1 = \frac{\Delta v/v}{T_1}$ FROM VARIOUS CALCULATIONS AND EXPERIMENTS

Material and Orientation		EXPERIMENT: Nalamwar, Epstein (Ref. 5)	EXPERIMENT: Cullen, Reeder (Ref. 8)	THEORY: Nalamwar, Epstein (Ref. 5)	THEORY: This paper: T_1 or T_2 nonzero; other five stresses zero	THEORY: This paper: cylindrical bending (T_1 or T_2) nonzero; T_3, T_4, T_5 T_6 all zero
YX quartz	γ_1	+.10	+.439	-.45	-.386	-.225
	γ_2		+1.319		+1.713	+1.694
ST-X quartz	γ_1		-.002		-.749	-.624
	γ_2		-.164		+.620	+.425
YZ $LiNbO_3$	γ_1	-.24		+.25	+.092	+.400
Fused quartz	γ_1			+3.08	+3.00	+3.21

In addition, Toda and Osaka report the longitudinal strain dependence of YZ $LiNbO_3$ to be negligible with respect to the path elongation ($\gamma_1 \approx 0$).

TABLE IV. SUMMARY OF POSSIBLE STRESSES OCCURING AT *AND NEAR THE WAVE SURFACE DURING BENDING*

Bending Configuration	T_1	T_2	T_6	T_3	T_4	T_5
Long cantilever beam, force applied in x_3-direction	C		OC			S, B
Long cantilever beam, force applied in x_2-direction (weaker effect)	OC		C			
Cylindrically bent plate, uniform curvature	C	C				
Cylindrically bent plate, non-uniform curvature (both bending moments vary)	C	C			B	B
Torsion applied around x_1- or x_2-axis (uneven end load)			C			

Key:
- C center of propagation path
- OC off-center: found only to the sides of the propagation path center
- B below the surface only
- S expected to be small in a bar of typical dimensions

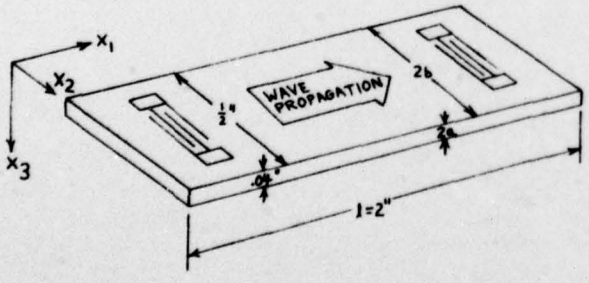

Fig. 1 Coordinate system

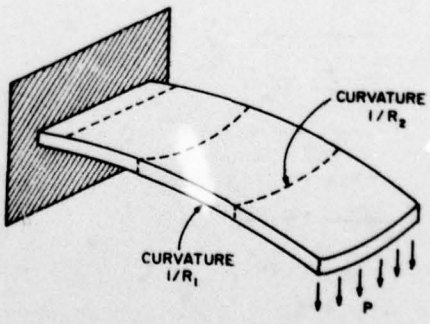

Fig. 2 Cantilever beam showing saddle-shaped bending

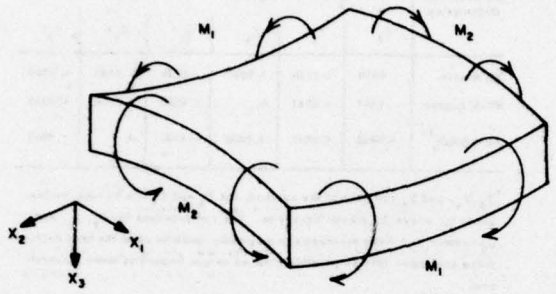

Fig. 3 Element of a plate bent in two directions

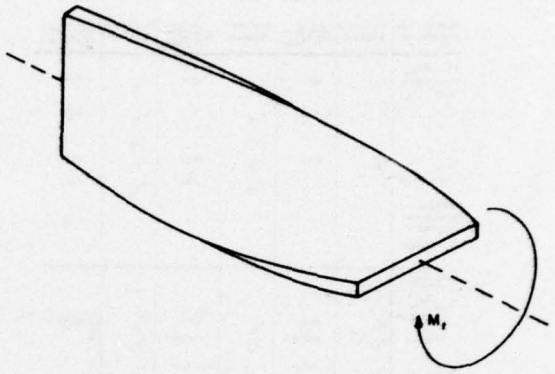

Fig. 4 Bar under torsion from ends

Fig. 5 Bending due to off-center end loads

FRACTURE RESISTANCE OF SYNTHETIC α-QUARTZ SEED PLATES

Darryl L. Brownlow
Bell Laboratories
Murray Hill, New Jersey

Summary

The fracture resistance of synthetic α-quartz as measured by spherical indenters has been investigated. Tests in an aqueous environment showed that water reduced the fracture strength 21%. Likewise, two organic solutions used in quartz cutting operations decreased the fracture strength of quartz but not to the same extent as water. Etching in hydrofluoric acid results in an initial reduction in fracture strength followed by a 20% increase after longer etching. Etching in ammonium bifluoride at room temperature results in a 20% drop in fracture strength without any eventual recovery. However the fracture behavior resulting from etching at 50°C follows a pattern similar to that of the hydrofluoric acid solution. Optical microscopic examination of the surface texture corroborates the fracture data quite well.

The fracture strength decreases with increasing temperature. However, it was found that annealing at 550°C for 24 hours caused an increase. No indenter size effect was observed. A linear relationship of fracture load versus thickness of seed plates was obtained. Tests were performed on strained and unstrained regions on both r-face and 5°X quartz; no detectable difference was found. However the 5°X quartz was found to have a higher average fracture value. A 24-hour γ-ray irradiation produced no discernible changes in fracture strength.

Key Words Quartz, Fracture of Quartz, Strength of Quartz.

Introduction

When a spherical steel ball is pressed perpendicular to the plane surface of a brittle material, such as quartz, the normal and tangental components of the force exerted by the indenter creates a surface fracture at a certain critical load. This event is immediately followed by a radial extension of the crack into the bulk of the material. The initial formation of this crack geometry displays certain Hertzian characteristics.[1] In the Hertzian experiment a circumferential surface indentation is immediately followed by a finite radial extension of the crack into the bulk of the material. The force required to initiate this type of fracture is not totally dependent on physical parameters such as Young's modulus and Poisson's ratio, but depends greatly on conditions affecting the material history of the indentation surface.

The present experiments were performed on as-received quartz seed plates in order to investigate conditions adversely affecting fracture during preparation of the seed plates. Fracture of the seed plates affects the yield of the hydrothermally grown quartz. The quartz yield is related in a complex way to the chemical, thermal and mechanical history of the seed plates. Variables relating to these conditions have been studied.

Selection of Seed Plates

All experiments were performed on synthetic α-quartz seed plates, having typical dimensions of 16.3 cm × 5 cm × .12 cm. Both minor rhombohedral seed plates, commonly referred to as r-face quartz, and seeds cut five degrees from the positive x-axis were used for experimentation.

The r-face seed plates were prepared from as-grown stones using a multi-blade wafering saw. A continuous abrasion with No. 400 SiC powder mixed in a liquid slurry is in effect during the entire cutting operation.

Seed plates of similar surface texture were chosen for experimentation. They were devoid of major blemishes, surface cracks, inclusions, and pronounced surface unevenness due to irregular cutting motion. No additional surface polishing or lapping was done prior to testing.

Polariscope

A polariscope developed by Barns[2] was used to display the strained and unstrained regions of the quartz seed plates. The essential components of the polariscope consisted of a high intensity monochromatic light, a liquid having the same refractive index as quartz, a polarizer and analyzer, a system of strategically positioned lens and filters and video-display system.

The operation of the polariscope is based on the optical phenomenon of strain induced birefringence. A detailed account of the construction of the polariscope and conditions for birefringence as related to the examination of quartz seed plates appears elsewhere.[2] Only the essential features will be presented here.

When a strained quartz seed plate is placed inside the polariscope, the polarized light entering the plate is split into components. These components are polarized in the directions of the principal stresses of the quartz plate. Due to crystalline anisotropy the components are not transmitted with a uniform velocity. Variations among the transmitted velocities result in phase differences in the emerging light. These phase differences are proportional to the differences of the principal stresses at the points of entry and the thicknesses of the plates.[3] The result is a discontinuity in light intensity between strained and unstrained regions. Figure 1 shows a typical polariscope photograph of the strain pattern of a test sample.

Indentation Fracture Test

The seed plates were mounted on a uniform steel block prior to indentation. A thin piece of paper and uniformly spaced double-coated tape was placed between the block and the quartz to facilitate specimen removal after testing. A spherical, 1.6 mm diameter ball was mounted on a shaft connected to the moving

cross-head of an Instron mechanical tester. The downward motion of the cross-head pressed the spherical ball normal to the plane surface of the seed plate until a distinctive audible fracture was induced. The force required to induce this fracture was transmitted via strain gauges to an X-Y chart recorder. A nearly static load rate was desired to avoid rate effects; hence a cross-head speed of 4.2×10^{-4} cm/sec was chosen for all indentations.

Results and Analysis

Strained vs. Unstrained Regions

Table I shows the results of indentation fracture test on both strained and unstrained areas of as-received r-face seed plates, as identified by polariscopic photographs. The mean fracture strengths are 18.2 and 17.0 kg respectively and are essentially equivalent in view of the scatter in the data. Thus the present indentation method is not sufficiently sensitive to differentiate the fracture strengths of these two types of areas, if such a difference exists.

Effect of Orientation

The mechanical properties of quartz are highly anisotropic. In order to experimentally investigate anisotropy in quartz, indentations were performed on seed plates cut 5° from the positive X-axis, as well as r-face plates. The results are also shown in Table I.

Table I shows that the fracture strength for the +5°X-cut is 50% higher than that of the r-cut. The value of Poisson's ratio is highly orientation dependent and principally accounts for the marked variation in observed fracture strength. Hartley and Wilshaw,[4] using the Hertzian test, report a larger fracture force for the basal plane than for both the prism and edge planes. The basal plane is parallel to the X-axis in quartz, therefore the +5°X-cut should be similar to the mechanical properties of the basal plane.

Effect of γ-Ray Irradiation

When electromagnetic radiation impinges upon matter, photons may become absorbed into lattice defects. Lattice defects capable of absorbing photons are known as color centers. Quartz turns dark brown after γ-ray bombardment due to these color centers. Strained areas appear as dark coloration patches in +5°X synthetic α-quartz, facilitating the immediate testing of strained and unstrained areas. The quartz seed plates received a 24-hour γ-ray bombardment prior to testing.

Gamma-ray irradiation apparently stimulates no strengthening mechanisms in the 5°X-cut quartz as noted in Table I. Also no distinction may be drawn between strained and unstrained areas in terms of mechanical strength.

Since no detectable difference in strength was found between strained and unstrained regions in the above tests, further tests described below were conducted without distinguishing these regions.

Effect of Aqueous and Organic Environments

Ordinary tap water was uniformly coated on the r-face seeds and indentations were performed to note any effect on fracture strength. The effect of two organic solutions used in the quartz cutting operations was also studied. The two solutions are Var-sol and PC. Careful attention was given to coating the samples to avoid any drying beneath the indenter at the immediate time of indentation. The results are shown in Table II.

Table II shows that water drastically reduced the fracture strength from a mean value of 17.6 kg to 13.9 kg. This result confirms the well accepted fact that water has a marked effect on strength reduction through the replacement of Si-O bonds with Si-OH bonds.

It is evident from Table II that Var-sol and PC solutions also decrease the fracture strength of quartz but not to the same extent as water.

Effect of Etching

The surface of the as-received quartz is strained and contains microflaws. Therefore one would expect an increase in fracture strength after the damaged area has been removed.[5] Initially hydrofluoric acid was used to etch the quartz prior to indentation. The seed plate was placed into a full strength solution of hydrofluoric acid for a predetermined period of time. Optical microscope photographs of the quartz surface were taken before and after etching.

Ammonium bifluoride was also used as an etching solution, at both room temperature and 50°C. A saturated solution was used as an etchant in both cases prior to indentation. Figures 2a through 2h reveal the effect of various etching times on the surface texture of quartz, using full strength hydrofluoric acid. It can be seen that the surface becomes smoother after etching for an hour or longer. Etching with ammonium bifluoride at room temperature produced no visible change in the surface texture of quartz. Raising the temperature to 50°C, however, resulted in etching behavior similar to that of hydrofluoric acid at room temperature.

Figure 3 shows the fracture strengths of quartz after etching in hydrofluoric acid and ammonium bifluoride, respectively. Etching in hydrofluoric acid results in an initial reduction in fracture strength, followed by a recovery after 60 minutes of etching and a subsequent saturation. The strength becomes higher by about 20 percent after etching for 75 minutes or longer. The initial drop in strength could be the result of enlargement of existing surface microflaws prior to their elimination at longer etching times.

Etching in ammonium bifluoride at room temperature results in a 20 percent drop in fracture strength without any eventual recovery. The fracture behavior resulting from etching at 50°C follows an etching pattern similar to that of the hydrofluoric acid solution. Thus the fracture data corroborate the surface texture observations quite well.

Effect of Temperature

The quartz seed plates were mounted on a uniform bronze test block supported by a regulated hot plate. The bronze surface was smoothly lapped to remove surface roughness and dirt. Temperature measurements were made by bonding a thermocouple directly to the quartz seed plates. Leads from the thermocouple reference junction were connected to a digital voltmeter. The temperature could readily be obtained from milli-volt temperature tables. This apparatus allowed stable temperatures to be maintained up to 332°C. Temperature stability was enhanced by a special enclosure designed to eliminate any effects due to stray air currents.

Figure 4 shows the effect of temperature on fracture strength. The values are higher than those shown in previous figures and tables due to the change in experimental setup. It is clear that the strength decreases with increasing temperature. Westbrook[6] reported a strength reduction with his hot hardness measurements on the basal and prism planes of quartz structures. The decrease, however, is less drastic than that shown in Fig. 4. No direct data comparisons may be made between the two measurements, since Westbrook's hardness numbers are measured as load divided by contact area using a Vickers indenter. Measurements presented in this paper are direct fracture values for quartz seed plates using a spherical indenter.

Effect of Indenter Size

The radius of the contact circle between indenter and sample surface varies with indenter size. This size effect increases the probability for a severe microflaw to come in contact with a large indenter. Spherical indenters of diameter 1.6, 3.2, 6.4, and 12.7 mm were used on seed plates 1.2 mm thick. The seed plates were etched in hydrofluoric acid for 105 minutes prior to indentation in order to reduce scatter in the data. The results, shown in Table III, indicate no indenter size effect. Presumably etching removed most surface flaws, resulting in a fracture strength independent of indenter size.

Effect of Annealing

Since annealing could result in healing of surface flaws and/or reduction of internal strains, an experiment was conducted to test this idea. The first set of seed plates were annealed for 24 hours at a temperature of 600°C. The plates were completely shattered, most probably due to the $\alpha \rightarrow \beta$ structural transition at 573°C. Another set of samples were annealed for 24 hours at 550°C prior to indentation, while another set were annealed for five days at 160°C.

In order to suppress thermal shock, all seed plates were initially placed into a cold oven. The heat was gradually increased until the desired temperature was obtained. After the desired annealing time had elapsed, the oven was allowed to cool overnight prior to specimen removal.

The resulting strength changes, listed in Table II, are somewhat incomplete. Annealing at 160°C for five days appears to decrease the strength somewhat, while annealing at 550°C for 24 hours tends to increase the strength. Polariscopic examinations before and after the 550°C anneal indicate no notable change in internal strain. The potential strengthening of quartz plates by high temperature anneal warrants further test.

Effect of Thickness

Seed plates of thicknesses 1.2, 1.5, 1.7, 2.0, 2.7 and 3.3 mm respectively were used to study the effect of thickness on the fracture load. The type of mounting, visual examination for defects and loading rate was the same as for the previous tests.

Figure 5 shows the results. The data indicate a linear relationship of fracture load versus thickness of seed plate. A least squares fit of the data yields 3.93×10^5 Nm^{-1} as the slope.

The experimental relationship was compared with a theory formulated by Lawn and Swain[7]. The basis of the theory involves the prediction of the ratio (P/c) where P is the fracture force and c a characteristic crack dimension for fracture beneath a point indentation. If the crack is allowed to proceed through the material, c gives a measure of the material thickness. This particular type of fracture event is characterized by a distinctive audible emission.

Lawn and Swain initiate their analysis by developing a geometrical representation of the fracture. This is attempted by first developing an expression for the stress intensity factor in terms of the ratio (P/c). The stress intensity factor, which gives a measure of the intensity of the stress field in the immediate vicinity of the crack, is combined with an expression which describes the force needed for crack extension. In order that a crack propagate under equilibrium conditions the force needed for crack extension must balance the force resisting crack extension. The resulting expression is

$$(P/c) = \frac{4\pi^4 \beta^2 \Gamma E}{(1-\nu^2)(1-2\nu)^2 \alpha p_o}$$

where

$$p_o = \frac{P_o}{\alpha \pi a^2}$$

and $\left(\frac{P_o}{a^2}\right)$ is a constant characteristic of the material and is obtained by direct measurement of the contact radius a, generated by load P_o.

α is a constant determined by indenter geometry

β is a constant determined by crack geometry

Γ is the fracture surface energy

E is Young's modulus

ν is Poisson's ratio

For the case of a spherical indenter loaded perpendicular to the plane of a flat specimen,[7] $\alpha = \beta = 1$. Therefore the relevant expression becomes

$$(P/c) = \frac{4\pi^4 \Gamma E}{(1-\nu^2)(1-2\nu)^2 \left(\frac{P_o}{\pi a^2}\right)}$$

In order to numerically evaluate this expression we use $\Gamma = 4.1 \times 10^2$ ergs cm^{-2}, which is the measured surface energy for the $(10\bar{1}1)$-face in quartz obtained by Brace and Walsh.[8] The r-face seed plate is very near this orientation. Young's modulus is calculated from the expression

$$E = [(1-\cos^2\theta)^2 S_{11} + \cos^4\theta S_{33} + \cos^2\theta(1-\cos^2\theta)(S_{44} + 2S_{13}) + 2\cos\theta \sin^3\theta S_{14}]^{-1}$$

This expression is obtained by modifying Cady's[9] general expression of Young's modulus for a quartz bar in any orientation, whose length is denoted by the direction cosines in a spherical coordinate system. The angle θ is the angle between the (0001) and $(1\bar{1}00)$ planes, and has a value of 38°13 for the r-face plate.[10] The values given as S_{ij} represent the elastic constants of quartz and are given by Cady[11] as

$$S_{11} = 1.27 \times 10^{-12} \text{ cm}^2 \text{ dyne}^{-1}$$

$$S_{33} = 0.97 \times 10^{-12} \text{ cm}^2 \text{ dyne}^{-1}$$

$$S_{13} = -0.15 \times 10^{-12} \text{ cm}^2 \text{ dyne}^{-1}$$

$$S_{44} = 2.00 \times 10^{-12} \text{ cm}^2 \text{ dyne}^{-1}$$

Poisson's ratio is estimated using the expression

$$\nu = 1/2 \left[\nu_{(0001)} + \nu_{(1\bar{1}00)}\right]$$

where $\nu_{(0001)}$ and $\nu_{(1\bar{1}00)}$ are the Poisson ratios for the basal and prism planes respectively. The values reported by Hartley and Wilshaw[12] are 0.118 for the basal plane and 0.014 for the prism plane.

Measurements of contact radii under a constant load were made in order to estimate the value of p_o. A light ink coating was placed on the quartz surface to help reveal the size of the contact area. An example is shown in Fig. 6. An average contact radius based on 10 indentations was used for each thickness study. The values of p_o corresponding to a given plate thickness are summarized in Table IV. There appears to be a general increase of p_o with plate thickness.

The numerical analysis of the data produced the theoretical fracture values recorded in Table IV. The average fracture value is $(P/c) = 3.21 \times 10^5 \text{ Nm}^{-1}$. This compares well with the experimental value of $3.93 \times 10^5 \text{ Nm}^{-1}$ from Fig. 5. Lawn and Swain[7] reported a value of $(P/c) = 4.4 \times 10^5 \text{ Nm}^{-1}$ for Vickers pyramid indentations on soda lime glass. Comparisons among data agree well, considering the uncertainties for the fracture geometry and the physical constants.

Discussion and Conclusions

The present investigation has shown that the spherical indenter may be used to obtain a measure of the fracture strength of synthetic quartz under a variety of physical conditions.

The present results support the concept that surface microflaws play a dominant role in fracture once an external force is applied. These surface microflaws are determined by the mechanical, thermal and chemical history of the quartz. It has been shown that hydrofluoric acid has a more pronounced effect on removing the surface damage, and thus increasing the fracture strength, than ammonium bifluoride. Similarly, the decrease in fracture strength due to an aqueous or organic environment was anticipated. However, the increase in fracture strength due to annealing was not anticipated, since there was no evidence of internal strain relaxation following annealing.

The agreement between experiment and the Lawn-Swain theory suggests that the theory may offer some valuable insights into the fracture nature of quartz. There may exist a means of predicting the depth of fracture damage in terms of a given applied external force.

With regard to processsing of quartz plates, the present results indicate that the

A. Strength of quartz is decreased by
   1. Changing from basal plane to r-face,
   2. Processing in aqueous and organic environments, particularly the former,
   3. Increasing the temperature above 110°C,
   4. Decreasing the plate thickness.

B. Strength is increased by etching in hydrofluoric acid at room temperature and ammonium bifluoride at elevated temperature. There is also an indication of a strength increase with a 24 h anneal at 550°C. Further work, however, is needed.

C. Gamma-ray irradiation has no detectable effect on fracture strength.

Acknowledgments

The author wishes to express his sincere appreciation to G. Y. Chin for suggesting this investigation and for his most helpful guidance and encouragement throughout the course of this work. The author also wishes to thank K. Kroupa and E. Simpson for supplying the quartz seed plates, R. L. Barns for the polariscopic photographs and general discussions related to quartz, E. D. Kolb for clarifying details concerning the manufacture of synthetic quartz and R. R. Hart for use of the Instron Mechanical Tester.

References

1. H. Hertz, J. Reine Angew. Math. 92, 156 (1881); Verhandlungen des Vereins zur Beförderung des Gewerbe Fleisses 61, 449 (1882).
2. R. L. Barns, E. D. Kolb, P. L. Key, R. A. Laudise, E. E. Simpson and K. M. Kroupa, Proceedings of the 29th Annual Symposium on Frequency Control (1975).
3. A. W. Hendry, "An Introduction to Photo-Elastic Analysis" (Blackie & Son, London, 1948).
4. N. E. W. Hartley and T. R. Wilshaw, J. Mater. Sci., 8 (1973) 265.
5. A. J. Miller, Proc. 24th Annual Sym. Frequency Control (1970).
6. J. H. Westbrook, J. Am. Ceram. Soc. 41[8] 433 (1958).
7. B. R. Lawn and M. V. Swain, J. Mater. Sci., 10 (1975) 113.
8. W. F. Brace and J. B. Walsh, Am. Mineral 10 (1962) 1111.
9. W. G. Cady, "Piezoelectricity" (Dover, New York, 1964) p. 72.
10. A. J. Miller, Bell Laboratories, Allentown, Pa., Unpublished work.
11. W. G. Cady, "Piezoelectricity" (Dover, New York, 1964) p. 137.
12. N. E. W. Hartley and T. R. Wilshaw, J. Mater. Sci., 8 (1973) 271.

Table I. Strained vs. Unstrained Regions

Sample Description	Number of Test Points		Fracture Load (kg)	
	Strained	Unstrained	Strained	Unstrained
r-face, as received	90	119	18.2±3.4	17.0±3.4
5°X, as received	89	88	26.8±6.6	25.6±6.5
5°X, γ-ray irradiated	88	73	24.4±4.5	24.4±4.0

Table II. Effect of Aqueous and Organic Environments and Annealing

Sample Description	Number of Test Points	Fracture Load (kg)
Surface coated with H_2O	88	13.9±2.5
Surface coated with var-sol solution	90	15.4±2.9
Surface coated with pc solution	99	15.5±2.6
Annealed 24 h, 550°C	90	20.8±5.2
Annealed 5d, 160°C	47	15.1±3.3

Table III. Fracture Load of r-face Quartz as a Function of Indenter Size

Indenter Diameter (in)	Number of Test Points	Fracture Load (kg)
$\frac{1}{16}$	51	18.5±3.1
$\frac{1}{8}$	61	19.8±3.9
$\frac{1}{4}$	53	19.0±4.3
$\frac{1}{2}$	42	18.1±3.0

Table IV. Experimental Values of p_o and Calculated Values of P/c as a Function of Thickness for r-face Quartz

Plate Thickness (mm)	Value of p_o $Nm^{-2} \times 10^8$	Theoretical Value of (P/c) $Nm^{-1} \times 10^5$
1.2	7.24	3.7
1.5	5.03	5.3
1.7	6.92	3.86
1.9	10.7	2.5
2.7	11.0	2.46
3.3	18.4	1.44

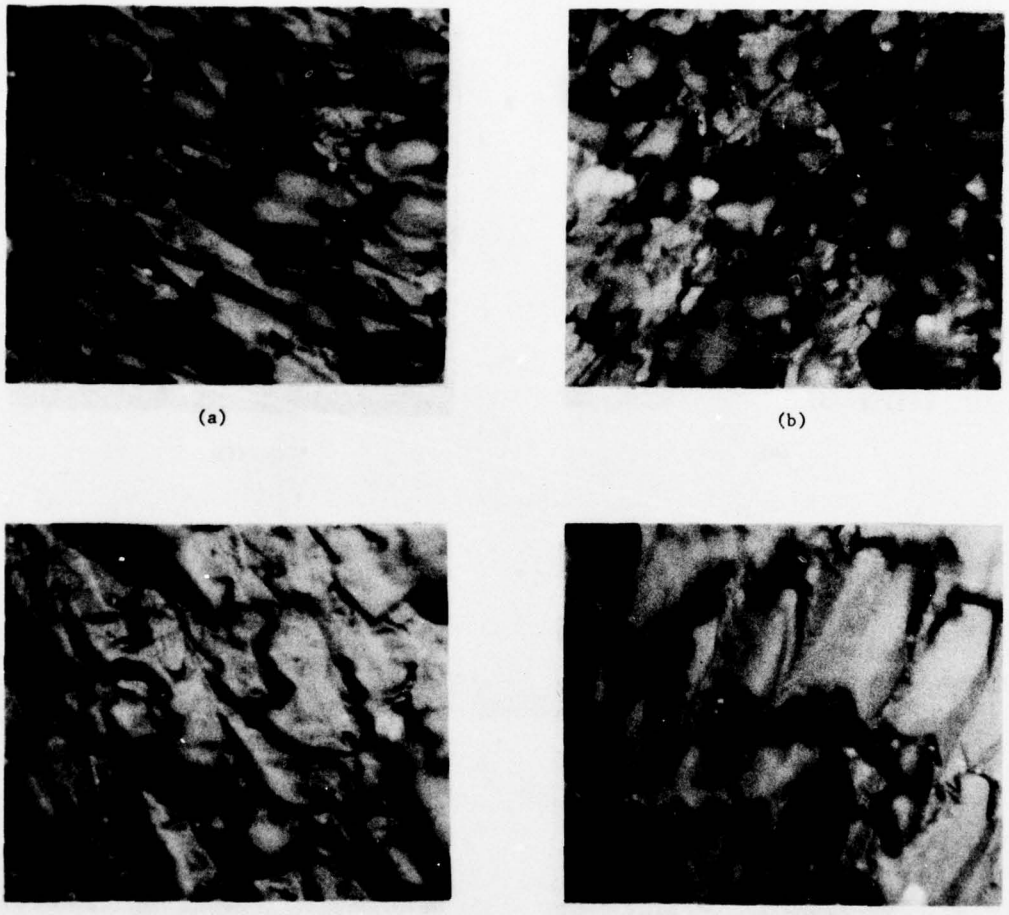

(a) (b)

(c) (d)

FIGURE 2

(e)

(f)

(g)

(h)

FIGURE 2

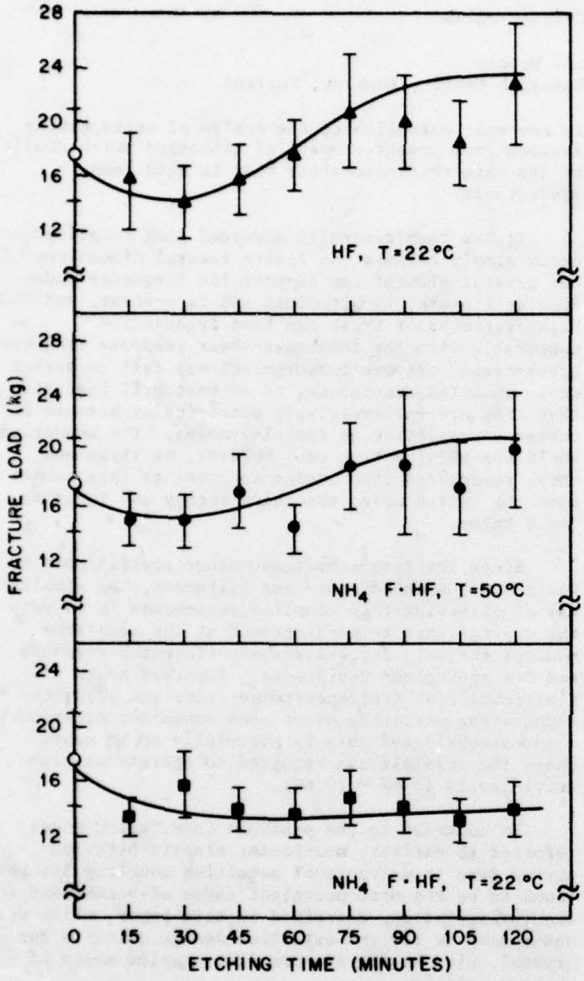

FIGURE 3

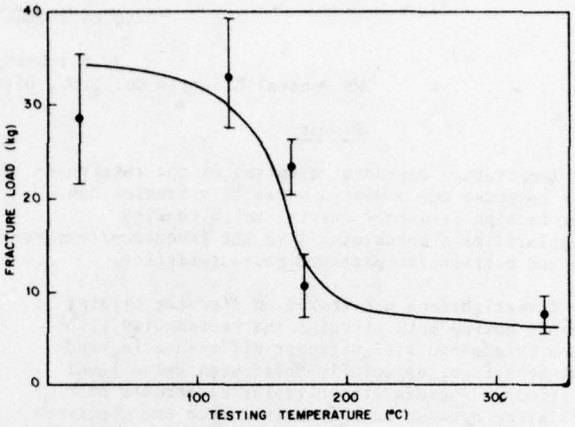

FIGURE 4

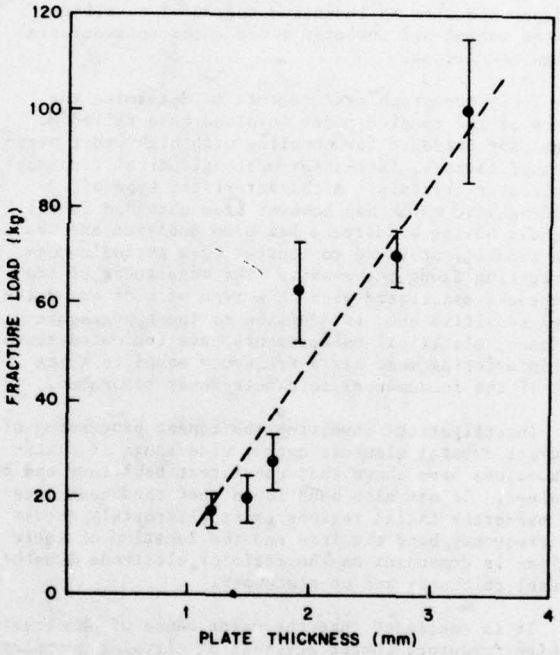

FIGURE 5

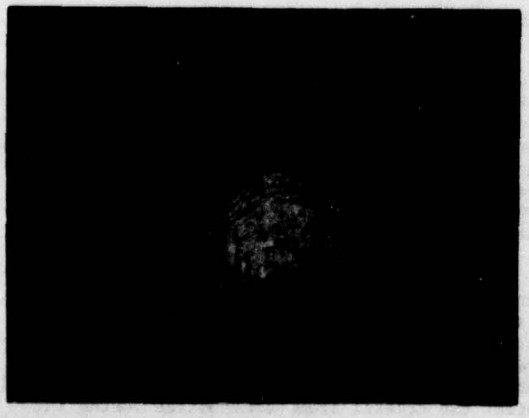

FIGURE 6

FREQUENCY/TEMPERATURE, ACTIVITY/TEMPERATURE ANOMALIES IN HIGH FREQUENCY QUARTZ CRYSTAL UNITS

J. Birch and D.A. Weston
The General Electric Co. Ltd., Hirst Research Centre, Wembley, England

Summary

Temperature dependent coupling of the thickness-shear response and unwanted modes of vibration can occur in high frequency crystal units causing irregularities ('bandbreaks') in the frequency/temperature and activity/temperature characteristics.

Investigations undertaken on circular crystal elements having both circular and rectangular electrodes have shown a significant difference in bandbreak behaviour, especially under high drive level conditions. Whereas with circular electrodes no correlation between bandbreak incidence and electrode diameter could be found over the frequency range from 9 MHz to 15 MHz, the use of accurately oriented rectangular electrodes has revealed a systematic dependence and also an increased degree of coupling between wanted and unwanted modes under unfavourable design conditions.

X-ray topograph measurements to determine the nature of the coupled modes involved have failed to reveal any evidence for coupling with high order overtones of flexure, face-shear or longitudinal responses in circular crystals. A characteristic type of standing wave which has however been observed in all crystals having bandbreaks has been analysed and the main constituent found to consist of a periodic mode propagating along the x-axis. The magnitudes of the bandbreaks associated with this type of mode are drive level sensitive and, in addition to the topographic evidence, electrical measurements have indicated that the interfering mode has a frequency equal to twice that of the fundamental thickness-shear resonance.

Investigations involving the repeat processing of numerous crystal elements over a wide range of plateback values have shown that consistent behaviour can be obtained. It has also been found that bandbreak free and bandbreak fouled regions exist alternately across the frequency band examined and the location of these regions is dependent on the ratio of electrode length/crystal thickness and on plateback.

It is concluded that the major cause of bandbreaks in high frequency quartz crystals of circular geometry can be explained by coupling via non-linear elastic properties to one particular type of mode excited at twice the frequency of the fundamental mode. Coupling to this mode, which to the best of knowledge has not been previously identified, occurs when the electrode length approximates to an integral number of half-wavelengths and terminates at antinodes of the interfering response. The implication of the results is that by careful choice of electrode size, orientation and plateback, it is possible to produce crystal units which are free of bandbreaks over a wide temperature range at any frequency.

Introduction

The problem of unwanted resonances in thickness-shear vibrating AT-cut quartz crystals has occupied the attention of numerous workers engaged in the development of h.f. and v.h.f. crystal units over a number of years. Whilst the design theory for crystal elements having good freedom from anharmonic thickness-shear resonances is now well established, the design of units having freedom from unwanted modes of vibration which couple to the main thickness-shear mode is much less predictable.

It has been generally accepted that coupling can occur simply because the finite lateral dimensions of the crystal element can support low frequency modes such as flexure, longitudinal and face-shear, and that high overtones of these can have frequencies comparable with the thickness-shear response frequency[1]. Transmission network measurements may fail to detect these unwanted resonances, or at best will indicate that they are extremely weak electrically because of charge cancellation at the electrodes. The mechanical amplitude of vibration can, however, be large and these resonances then become apparent as they couple into the wanted mode, absorbing energy and lowering the Q value.

Since the frequency/temperature coefficients of wanted and unwanted modes are different, the simplest way of observing this coupling phenomenon is to vary the crystal unit temperature and at the same time monitor the main thickness-shear frequency response and its equivalent resistance. Recorded plots ('bandruns') of frequency/temperature and activity/temperature variation often show anomalous behaviour ('bandbreaks') and this is especially so in cases where the crystals are required to operate at high drive-levels (5 mW - 10 mW).

In contrast to the possible interfering modes referred to earlier, non-linear elastic behaviour giving rise to drive-level sensitive coupling has been found to be the most prevalent cause of bandbreaks in the investigations described in this paper, which were undertaken to try and establish design criteria for crystal units having freedom from coupled modes of whatever origin.

Initial Investigations of Electrical Performance

Electrode Diameter

The major work undertaken during the initial stage of the investigations was to examine the incidence of bandbreaks in crystal units in the frequency range 9 MHz to 15 MHz as dependent on electrode diameter. Crystal blanks of 8 mm diameter with a small edge bevel of 60 mm radius were used and gold electrodes were deposited by sputtering to give electrode diameters ranging from 3.4 mm to 5.8 mm at a nominal plateback of $\Delta f/f_B^2 = 1.53$ kHz/MHz^2.

It was desired to reprocess the same crystal blank when studying the effects of changing electrode size. To satisfy this requirement, and at the same time facilitate bandrunning from -20°C to +70°C, the crystals were left uncanned and placed in a small electrically heated enclosure which could be hermetically sealed to protect the crystal from condensation during the temperature test. A typical enclosure is shown in Figure 1. The hermetic seal was made using an O-ring, and dry nitrogen was flushed through the enclosure before pinching off the rubber hoses to ensure that the crystal was in a dry and inert atmosphere for testing. With this arrangement it was practicable to cool the

crystal to -20°C, plug the container into the test oscillator preset to the required room temperature drive-level (usually 7.5 mW) and heat the crystal to +70°C in a controlled time of 2 minutes, 20 seconds.

A frequency synthesizer was used to produce a beat frequency in conjunction with the test oscillator output. The synthesizer frequency was set below the crystal frequency at room temperature so as to produce an inverted frequency/temperature characteristic compared to the normal viewing of the AT-cut cubic curve. This arrangement has the advantage that a large positive frequency swing occurring at a bandbreak will produce a maximum pen deflection without any possible ambiguity such as can exist with deflection through the zero-beat condition when the reference frequency is set higher than the crystal frequency. A double trace chart recorder was used to display the deviations in activity (equivalent parallel resistance) and frequency occurring during bandrun testing. Examples of bandrun plots are reproduced in Figure 2.

Typical results from the first investigations are given in the form of a scatter diagram in Figure 3 and show no correlation between bandbreak incidence and electrode diameter. The plotted points indicate crystals having large bandbreaks, whilst the circles and slashed-circles represent bandbreak-free and minor bandbreak incidence respectively.

Electrode Thickness

The effect of electrode thickness was first studied on 30 units by evaporating a circular gold spot on to one of the electrodes of previously base coated and mounted crystal elements. The crystals were driven continuously by an oscillator during the deposition and the activity deviation was plotted using an XY recorder. A typical 'smoothed' plot obtained during the course of this frequency trimming is shown in Figure 4. The test crystals were, with one or two exceptions, base plated between 40 kHz and 70 kHz below the blank frequency f_B (c. 10 MHz) before mounting and starting the adjustment.

Figure 5 compares the behaviour of four crystals and in each case a shaded portion represents the initial stages of adjustment (c. 100 kHz) which usually revealed a number of minor activity dips. As the plateback was increased, very large dips in activity were observed and these are represented in Figure 5 by the large vertical arrows. Figure 4 would be represented by four such arrows, one of these being shown in the shaded region.

During the course of the above tests, bandruns were sometimes made to see if there was correlation between the activity dips observed and bandbreaks. In Figure 5 the results of such bandrun tests are indicated and show good correlation. For nominally identical blank frequencies and base plating conditions, such as for units P4, P10 and P14 there was some semblance of a pattern in the location of the activity dips but, considering all the results, the behaviour was most complex. Since normal frequency adjustment would occur within the shaded region the prospect of eliminating the minor anomalies by overall electrolytic plating, i.e. over base electrode and lead-off, was tried but improved results were not obtained.

In view of the significant effect of plateback, which the foregoing experiments had illustrated, and the results of X-ray topography studies proceeding in parallel, the investigations were extended to look in more detail at the relationship between electrode geometry and bandbreak incidence. The results of these studies are described in a later section.

X-Ray Topography

A study of the mechanical vibrations of AT-cut crystals was undertaken as part of the general bandbreak investigations, by colleagues working on X-ray topographic analysis in the Materials Characterisation Department at the Hirst Research Centre[2,3].

Figure 6 shows topographs obtained on circular and rectangular crystals mounted in slotted nickel tapes and driven at similar power levels as used in the electrical study. In the case of the rectangular crystals the nickel tapes were 'kinked' to contact the electrode lead-off plating.

The light area in the topograph of Figure 6(a) shows the antinodal region of thickness-shear vibration obtained by X-ray diffraction from the $(\bar{1}011)$ Bragg plane; in this bandbreak-reject crystal the active area extends beyond the central portion covered by the overlapping electrodes because of coupling to an unwanted mode. Using the $(0\bar{4}\bar{4}3)$ Bragg plane, which is almost parallel to the crystal surface and thus virtually insensitive to thickness-shear vibrations, the interfering mode can be seen in greater detail {Figure 6(b)} and extends to the bevelled edge of the blank along the x-axis. This reflection is highly sensitive to strain and saturates at a relatively low level so that a vibration pattern can usually be seen at a temperature far removed from the temperature of maximum coupling especially if a high crystal drive-level is used. For the majority of topographs the drive-level was set at 7.5 mW and the crystals were heated to locate the bandbreak temperature when this was above ambient.

The most symmetrical patterns were obtained using overlapping electrode strips to form accurately oriented rectangular electrodes of sufficient mass to 'energy-trap' the unwanted mode. Figure 6(c) shows 'scrambling' of the pattern caused when the lead-off plating was oriented 10° away from the z'-axis, and Figure 6(d) shows the restricted active area, or energy trapped region, of an unwanted mode obtained by the use of relatively heavy plating. With 3.4 mm square electrodes and $\Delta f/f_B^2 = 1.4$ kHz/MHz^2 the active area extends just beyond the electrode area in the latter crystal and, in a similar fashion to Figure 6(b), the wavelength of the mode appears to double in the outer region. An interpretation of this effect is given in Reference 1 where it is shown that the observed patterns can be accounted for by the superimposition of two modes of vibration having twice the resonant frequency of the main thickness-shear mode. The modes combining to produce the pattern in Figure 6(d) can be represented by Figure 7(a) which shows the variation in lattice strain gradient q (curvature) due to a periodic mode p(x) of short wavelength along the x-axis which is superimposed on a modulating mode m(x). Combining these two modes in the manner of the X-ray topograph measurement, which is insensitive to reversals in the strain gradient, gives the integrated X-ray topograph intensity I(x) pattern in Figure 7(b). Since the modulating mode is shown with a large amplitude (strain gradient) in the region outside the electrodes, only alternate antinodes of the periodic mode, where the two modes are in phase, correspond to intensity maxima, the intervening antinodes becoming minima. An apparent doubling of wavelength thus occurs in the outer regions of the crystal. A similar effect is seen in Figure 6(e) which shows a transmission topograph and the modulation of a length/thickness flexural mode by the large amplitude thickness-shear mode which is energy trapped in one half of the crystal. In the latter example the electrodes extended to the edge of the crystal in the x-direction

and overlapped by approximately 5 mm in the z'-direction. This rectangular crystal operated at a frequency of 9.49 MHz, consistent with the mode being the 71st overtone of flexure[3] as indicated in the topograph.

Figures 6(f), (g) and (h) show selected topographs taken on a 10 mm square blank, having an uncoated frequency f_B = 11.315 MHz, which was subsequently plated with electrodes of 4 mm × 4 mm in area to reduce its frequency in eight steps finishing at 10.800 MHz. Figure 6(f) shows the unwanted mode extending over the whole area of the blank at a plateback Δf = 85 kHz; for Δf between 180 kHz and 240 kHz this mode was absent in the unplated portion of the crystal but the area under the electrode lead-off plating revealed the mode extending out to the mounting tapes; Figure 6(g) illustrates this behaviour at a plateback of 240 kHz. For Δf exceeding 330 kHz the unwanted mode was energy trapped under the overlapping electrodes in the same manner as the thickness-shear mode; Figure 6(h) shows the behaviour at a plateback of 380 kHz.

A flexural mode extending to the edge of the blank is seen in Figure 6(g) to be energy trapped in the z'-direction by the overlapping electrodes. There are an estimated 83 antinodes in this mode which is consistent with the measured frequency being 11.074 MHz.

Other examples of flexural and thickness-shear mode coupling, but without the characteristic unwanted mode dealt with in this paper, have been observed in rectangular crystals but never in circular crystals.

From measurements on topographs of crystals in the frequency range 9 MHz to 15 MHz Goodall and Wallace[2] found that the product of crystal blank frequency and wavelength of the periodic plane wave pattern seen at a bandbreak was approximately constant, giving $\lambda_x f_B$ = 4.53 ± 0.08 mm MHz.

In a similar manner to that predicted theoretically by Mindlin and Lee[4], and confirmed experimentally by Sasaki and Jumonji subsequent to our findings[5], for coupling between thickness-shear, flexure and face-shear, it appeared probable that the conditions for excitation and coupling to the unwanted mode should be fulfilled when the product of electrode length (ℓx) and frequency is a multiple of $\lambda_x f_B$. Experimental results, some of which are considered below, have been obtained to confirm that the incidence of bandbreaks attributable to the particular type of unwanted mode in question does vary in a systematic way dependent on electrode length, mass loading and crystal frequency.

Detailed Investigation of Bandbreak Incidence as Dependent on Electrode Geometry

In view of the simplified plane wave patterns seen in topographs of crystals having well oriented rectangular electrodes, a detailed investigation was undertaken on such units covering the frequency range 9 MHz to 13 MHz with plateback values ranging from $\Delta f/f_B^2$ = 1.5 to 5.0 kHz/MHz^2. Analysis of the bandrun results obtained at 7.5 mW crystal drive-level showed that many frequency/temperature and activity/temperature anomalies were characterised by pronounced deviations, as illustrated in Figure 2, and plotting the incidence of these gross bandbreaks gave the results shown in Figure 8, in which two regions are clearly definable as producing unsatisfactory units.

To investigate the behaviour in greater detail further crystal units were prepared with rectangular electrodes measuring 3.42 mm × 3.42 mm. After bandrun testing the crystals, these were removed from their mounting tapes and, without damaging the existing electrodes, were further plated, remounted and bandrun. In this manner a number of units were plated from about $\Delta f/f_B^2$ = 1.8 to 5.0 kHz/MHz^2, then stripped of plating in aqua regia and processed once again in a similar way to test the repeatability of processing to obtain the same bandrun characteristics.

Figure 9 shows plots of crystal frequency versus plateback which include the above repeatability tests (crystals A-F). The experimental points for the same crystal are enclosed within a rectangle and contacting rectangles correspond to repeat runs. The results confirmed that with strict control of the processing it was indeed possible to obtain good repeatability and bandbreak characteristics of closely similar appearance were obtained.

Further experiments produced additional results enabling Figure 9 to be completed and indicating that for a given crystal plateback certain frequencies would constitute bandbreak free regions whilst others would be bandbreak fouled. A number of the experiments are summarised in the figure by giving the numbers and percentages of results conforming to the expected pattern, e.g. 23 out of 24 units (96%) at approximately 11.4 MHz with $\Delta f/f_B^2$ c. 1.8 kHz/MHz^2 were clear of bandbreaks as expected in a bandbreak clear zone.

Observation of topograph patterns for crystals in the various regions of Figure 9, and the translation of the activity dips towards higher temperatures as the plateback was increased, confirmed that the same interfering mode with a negative frequency/temperature coefficient was responsible for the broad fouled regions and that coupling was to higher order modes at the higher frequencies, i.e. $13^{\lambda}/2$, $15^{\lambda}/2$ and $17^{\lambda}/2$ in the three fouled regions. From the wavelength frequency constant and the topograph patterns it is evident that the electrodes overlap the central energy trapped region and terminate on antinodes of the unwanted mode.

Investigation of the Coupled Mode

Examination of typical crystal responses in the vicinity of the coupling temperature revealed characteristics similar to those shown in Figure 10(a) which illustrates results obtained on a sweep measuring set at four different values of drive-level applied to a pi-network containing the crystal. Furthermore, by driving the crystal in an oscillator and obtaining an audio beat frequency it was possible to detect a frequency jump between the two coupled modes as the temperature was varied through the bandbreak. This behaviour is similar to that expected for modes coupling at nominally the same frequency but having different temperature coefficients of frequency {Figure 10(b)}. X-ray topographs of crystals exhibiting this behaviour have, however, shown the characteristic pattern attributable to a coupled mode at twice the fundamental frequency, and a crystal driven at a resonance corresponding to twice the frequency of the fundamental thickness-shear mode has given a topograph pattern of similar character to that found at the fundamental response. Two $\bar{1}011$ transmission topographs illustrating the latter point are reproduced in Figure 11.

Wood and Seed[6] have reported on non-linear

elastic coupling between thickness-shear modes at f_r and modes at $2f_r$, and Franx[7] have shown that unwanted modes at $3f_r$ may cause activity dips. An equivalent electrical circuit[8] which takes account of the coupled mode is shown in Figure 12 which includes the possibility of both mechanical and electrical coupling. Non-linear mechanical coupling is represented by the capacitor C_c which is considered to vary depending on the charge on the crystal. Ignoring the crystal static capacitance C_o and electrical coupling ($\phi = 0$), the analysis by Wood and Seed shows that first order non-linearity with

$$C_c = \frac{C_{co}}{q}$$

best describes the behaviour observed at a bandbreak as regards the change in crystal equivalent series resistance which should increase as the square of the crystal current. An experiment described in the paper by Wood and Seed showed that in the expression

$$\Delta R = KI^n$$

the value of the index n was 1.75 approximately rather than 2 as predicted theoretically, but difficulties in the experimental verification were reported.

Our attempts at this measurement showed that a pi-network arrangement, using a vector-voltmeter to determine the zero phase frequency, equivalent series resistance and crystal current by calculation, gave the most repeatable results. Values for the index n obtained from measurements on five crystals ranged from 2.0 to 2.3. Figure 13 shows a characteristic typical of the five crystals.

Investigation of the resonance spectra in the vicinity of $2f_r$ and $3f_r$ has revealed that there are resonances which may or may not couple to produce the bandbreak behaviour observed at the fundamental response. Figure 14 shows part of the spectra measured in the vicinity of $2f_r$ and $3f_r$, at room temperature and also at a higher temperature, on a crystal which was free of bandbreaks. Three points may be noted:

(i) Since there is a weak response which moves through $2f_r$ it is evident that not all responses detectable at $2f_r$ cause bandbreaks.

(ii) Considered from the point of view of third-overtone operation, the crystal orientation has a negative angle with respect to the UTC zero angle; this leads to a positive temperature coefficient for the third-overtone anharmonic series of resonances. Since the frequency/temperature behaviour observed at a bandbreak is only consistent with coupling to a mode having a negative temperature coefficient, there should be no interference from the third-anharmonic series.

(iii) With changing temperature an even order anharmonic response is seen to move through $3f_r$ without causing a bandbreak.

Conclusions

The major cause of bandbreaks in high frequency quartz crystals of circular geometry can be explained by coupling via non-linear elastic properties to one particular type of mode excited at twice the frequency of the fundamental mode. To the best of knowledge no previous identification of this mode has been reported.

By means of X-ray topographs obtained on numerous crystals exhibiting gross bandbreaks the interfering mode has been analysed as comprising two strain wave components, the principal one being a periodic plane wave propagating along the x-axis.

Using rectangular electrodes of a particular size, bandbreak clear or bandbreak fouled regions become evident over a range of frequencies. The bandbreak fouled regions occur when an odd number of half wavelengths of the periodic mode are covered by the electrodes which terminate at antinodes. Bandbreak clear regions, on the other hand, are to be expected when the electrodes span a whole number of wavelengths and terminate at nodes. The use of circular electrodes is clearly incompatible with this criterion for the suppression of coupling.

The high degree of repeatability obtained during the experiments has required close control of the crystal processing conditions, but given the necessary control it is evident that units capable of operation at high drive levels can be systematically designed to be free of bandbreaks.

Acknowledgement

This work was initiated by Salford Electrical Instruments Ltd., part of GEC Electrical Components Ltd.

References

1. W.J. Spencer, "Observation of Resonant Vibrations and Defect Structure in Single Crystals by X-ray Diffraction Topography", Physical Acoustics, Vol.V, Chapter 3, Ed. W.P. Mason, Academic Press, 1968

2. B.J. Isherwood and C.A. Wallace, "The Analysis of Unwanted-Mode Vibration Patterns in AT-cut Quartz Oscillator Crystals Revealed by X-ray Diffraction Topography: I. Interpretation of the X-ray Diffraction Topographs", J. Phys. D., Appl. Phys., Vol. 8, 1975, pp. 1827 - 1842

3. F.M. Goodall and C.A. Wallace, "The Analysis of Unwanted-Mode Vibration Patterns in AT-cut Quartz Oscillator Crystals Revealed by X-ray Diffraction Topography: II. A Partial Theoretical Description of the Unwanted Mode", Ibid. pp. 1843 - 1850

4. R.D. Mindlin and P.C.Y. Lee, "Thickness-Shear and Flexural Vibrations of Partially Plated Crystal Plates", Int. Jnl. of Solids Structures, 2, 1966, pp. 125 - 139

5. E. Sasaki and H. Jumonji, "Effects of Electrode Dimensions on Resonant Q of Energy-Trapped AT-cut Quartz Resonators", Electronics and Communications in Japan, 56-A, 10, 1973, pp. 69 - 76

6. A.F.B. Wood and A. Seed, "Activity Dips in AT-cut Crystals", Proc. 21st Annual Symposium on Frequency Control, US Army Electronics Command, Fort Monmouth, NJ, pp. 420 - 435, (1967), NTSI Accession No.AD659792

7. C. Franx, "On Activity Dips of AT Crystals at High Levels of Drive", Proc. 21st Annual Symposium on Frequency Control, Ibid, pp.436-454

8. M. Onoe, "Analysis and Detection of Unwanted Modes in Quartz Crystal Units for Oscillators", Jnl. Elect. Comm. Eng., Japan, 47, 1, 1964, pp.82 - 93.

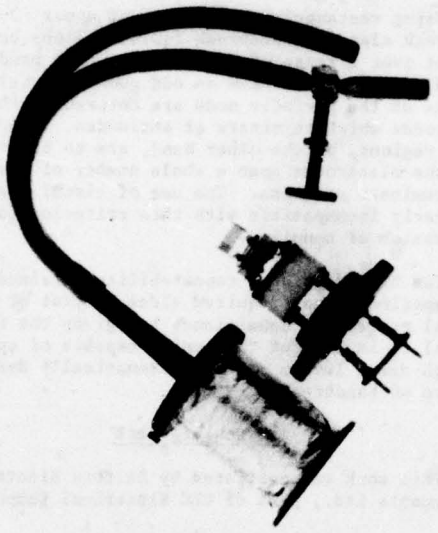

Figure 1 Oven used for experimental bandruns

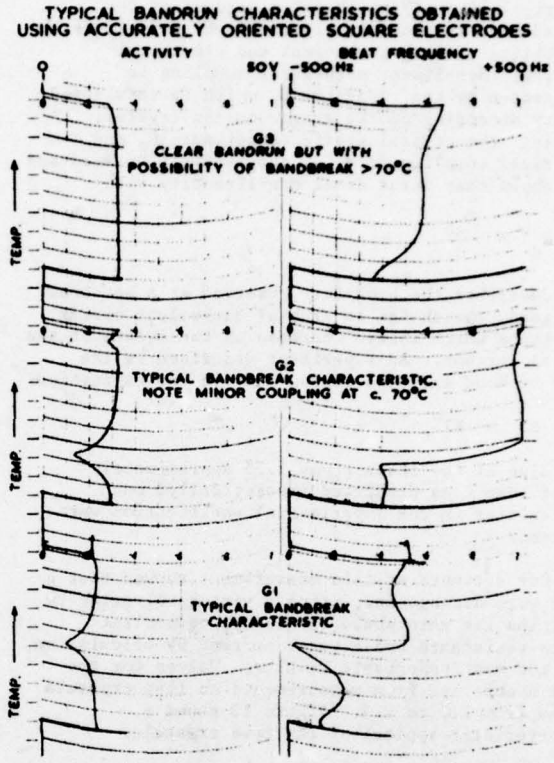

Fig 2 Typical bandrun characteristics obtained using accurately oriented square electrodes

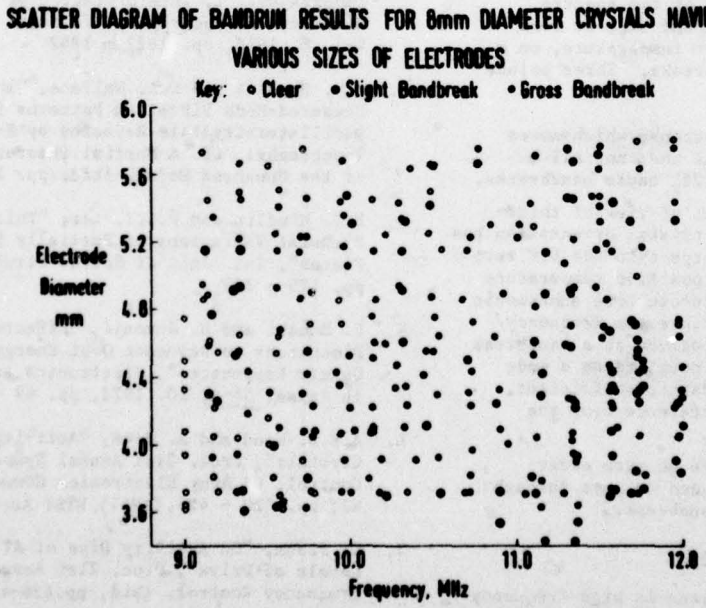

Fig 3 Scatter diagram of bandrun results for 8 mm diameter crystals having various sizes of electrodes

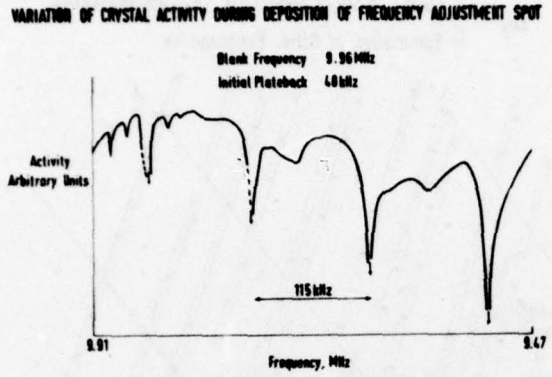

Fig 4 Variation of crystal activity during deposition of a frequency adjustment spot

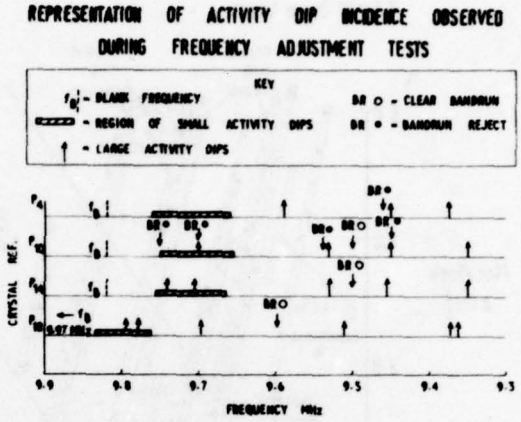

Fig 5 Representation of activity dip incidence observed during frequency adjustment tests

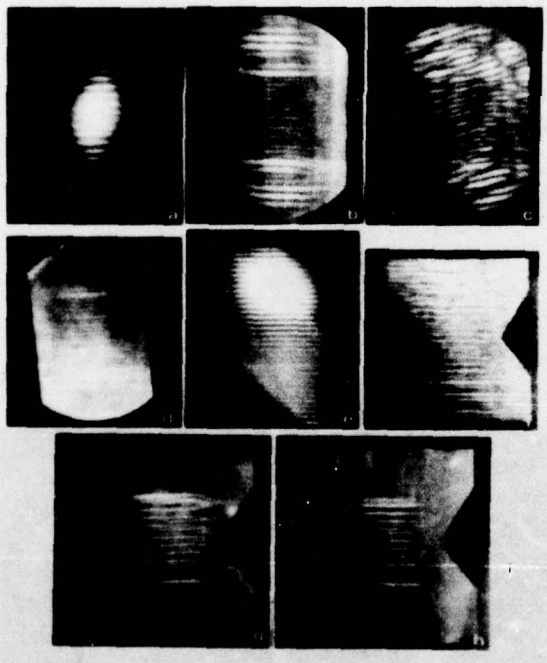

Fig 6 X-ray topographs

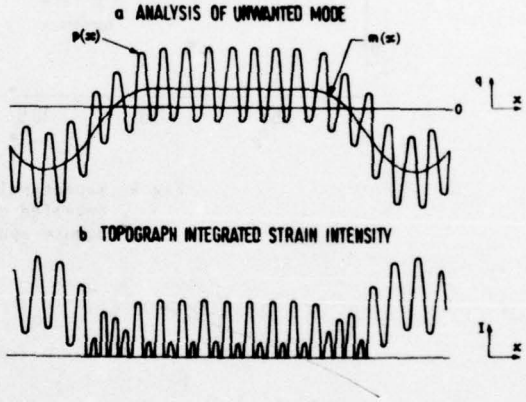

Fig 7 Interpretation of topograph pattern as a superimposition of a periodic mode p(x) and a modulating mode m(x)

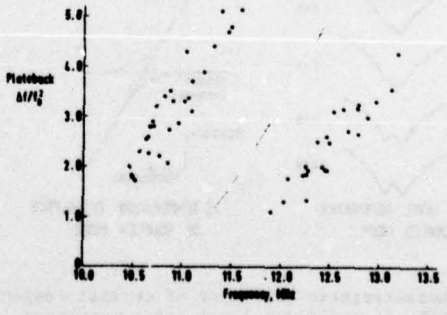

Fig 8 Incidence of gross bandbreak rejects for crystals having accurately oriented square electrodes

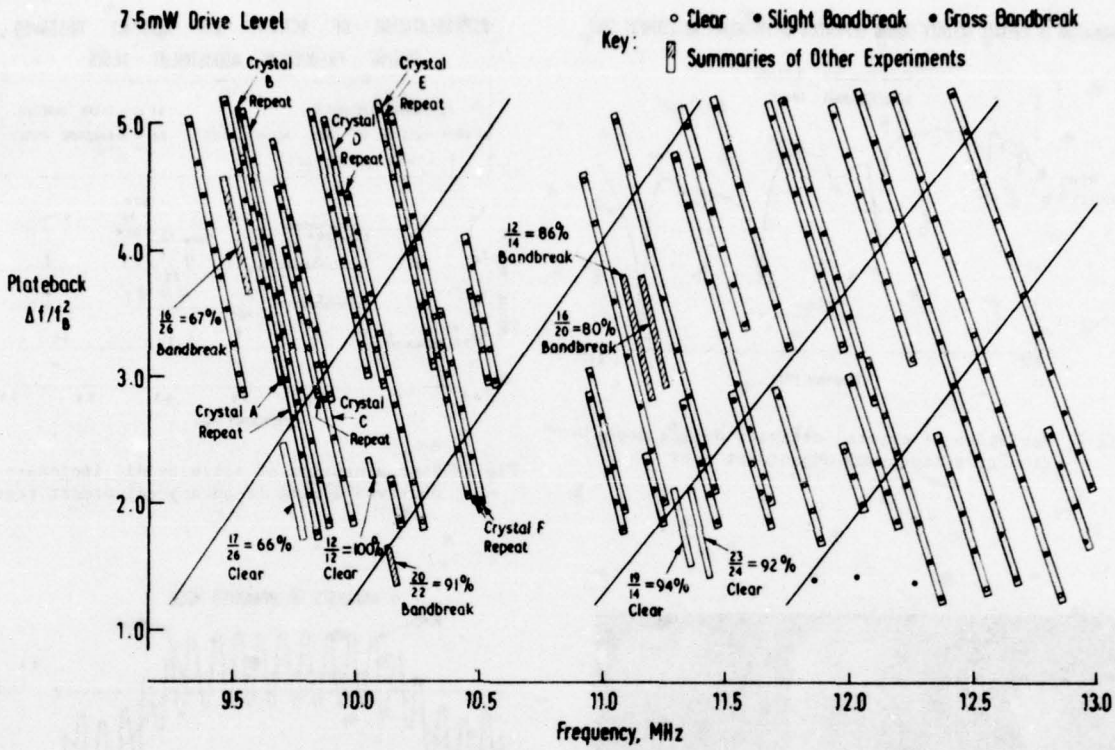

Fig 9 Repeatability tests on 8 mm diameter, bevelled crystal blanks having 3.42 mm square sputtered electrodes

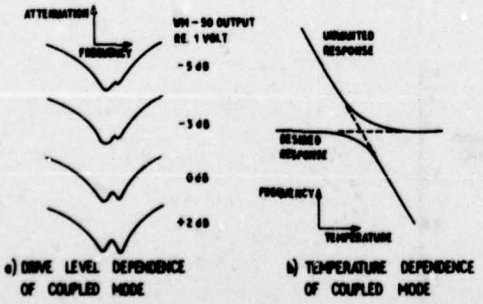

Fig 10 Characteristic behaviour of crystal response with varying drive level and temperature

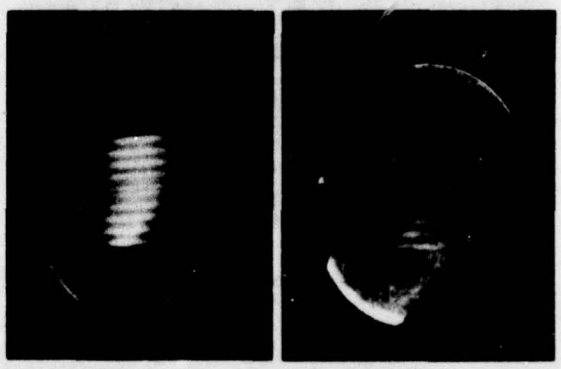

Fig 11 Transmission topographs showing similarity of strain distribution for resonances at $1f_r$ and $2f_r$

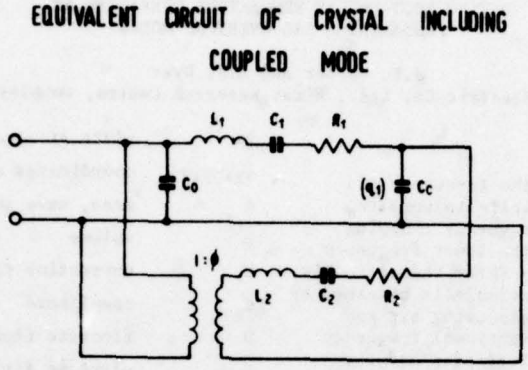

Fig 12 Equivalent circuit of crystal including coupled mode

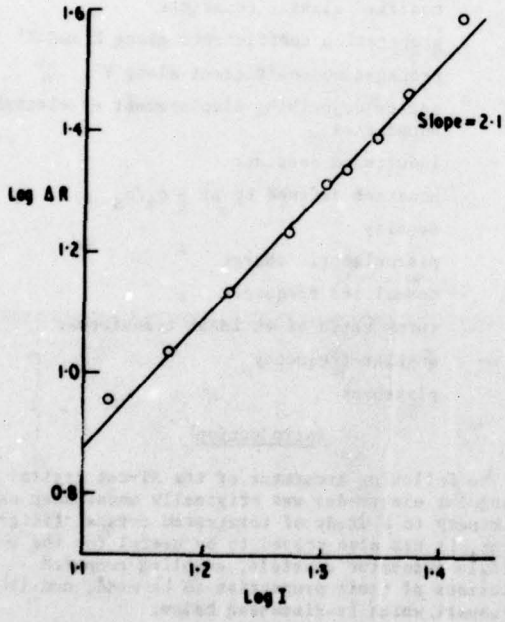

Fig 13 Typical relationship between crystal current and equivalent series resistance measured in the neighbourhood of a bandbreak

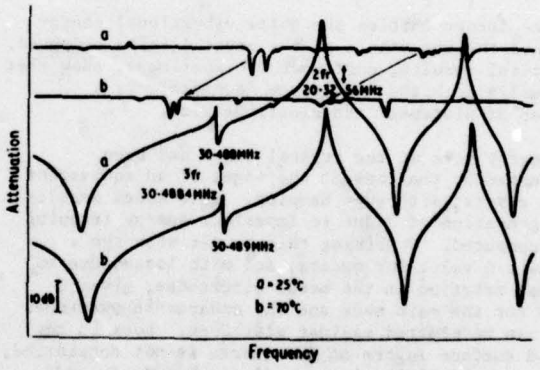

Fig 14 Temperature dependence of $2f_r$ and $3f_r$ frequency spectra typical of the experimental crystals

THE RELATIONSHIP BETWEEN PLATEBACK, MASS LOADING AND ELECTRODE DIMENSIONS FOR AT-CUT QUARTZ CRYSTALS HAVING RECTANGULAR RESONATORS OPERATING AT FUNDAMENTAL AND OVERTONE MODES

J.F. Werner and A.J. Dyer
The General Electric Co. Ltd., Hirst Research Centre, Wembley, England

Summary

Blank frequency, defined as the frequency of thickness-shear vibration for an infinite unplated blank, is an important quantity in energy trapping theory and is closely related to the lower frequency limit for wave propagation. It is shown theoretically and experimentally that a close estimate is obtained by measurements at high overtone orders using air gap electrodes. 'Plateback' is the fractional frequency lowering due to the mass of the electrodes and the reduction of piezoelectric stiffness caused by connecting the resonator in a low impedance circuit. The equations relating resonator frequency, mass loading and electrode geometry are given, and the computational method for rectangular electrodes with edges parallel to the X and Z' crystallographic axes is explained.

Using a simple edge correction enables good agreement with experiment to be obtained for crystals with square electrodes at the fundamental and overtone modes. An interesting result is that a crystal with small electrodes ($\ell/t \doteq 7$) at fairly low mass loadings can have virtually zero plateback and therefore a very low Q at the fundamental mode while operating well at third overtone. It can thus control an untuned oscillator at the crystal third overtone frequency.

The theory enables the total vibrational energy and hence the inductance of the crystal to be computed. Theoretical results, confirmed by experiment, show that the usually accepted inductance 'constant' is a function of plateback and electrode size.

Energy loss at the crystal edges has been represented by the loss at the edges of an equivalent square crystal with edge damping. This model enables the degradation of Q due to imperfect energy trapping to be computed. Combining this result with the intrinsic Q value for quartz, and with losses due to internal friction in the metal electrodes, gives Q values for the main mode and the anharmonic overtones which can be plotted against plateback. Loss in the damaged surface layers of the quartz is not considered, so that practical Q values are less than predicted. However, this computational procedure, which takes blank size into account, has proved useful in designing single response crystals.

List of Symbols

$2a$	length of electrode along Z'
$2b$	thickness of plate (= t)
c_{ik}	elastic constants
h_{26}	piezoelectric constant
k	constants
ℓ	length of electrode (= 2a or 2w)
m	thickness-shear overtone order
n_i	unit normal to a surface
t	thickness of plate (= 2b)
u	particle displacement
$2w$	width of electrode along X
x_1, x_2, x_3	coordinates along the X, Y', Z' axes
A	area, wave amplitude
B	volume
C	correction factor
C_m	compliance
D	electric flux density
E	electric field strength
L_m	motional mass of crystals
L_1	inductance of crystals
M	mass/unit area
Q	Q factor
R, S, P_X, P_Z	denote regions of the crystal plate
T	stress
V	potential difference
α_x, α_z	coefficients of exponential decay along X and Z'
$1/\beta$	permittivity
γ_{ik}	modified elastic constants
ζ_x, ζ_z	propagation coefficients along X and Z'
η	propagation coefficient along Y'
θ_x, θ_z	angles describing displacement at electrode boundaries
λ	inductance constant
μ	constant defined by $\mu^2 = \rho_R/\rho_S$
ρ	density
σ	piezoelectric charge
ϕ	normalised frequency
ψ	turns ratio of an ideal transformer
ω	angular frequency
Δ	plateback

Introduction

The following treatment of the AT-cut crystal with rectangular electrodes was originally undertaken as a preliminary to a study of integrated crystal filters. However, it has also proved to be useful for the design of single resonator crystals, enabling computed predictions of their properties to be made, and it is this aspect which is discussed below.

The wave propagation analysis is based on that outlined for integrated filters by Reilly and Redwood[1] and discussed more fully by Reilly in a doctorate thesis[2]. Similar simplifying assumptions are made, but the theory is extended to deal with rectangular electrodes of finite dimensions, rather than strip electrodes having infinite width.

Outline of the Theory

Simplifying Assumptions

(i) It is assumed that the wave propagation in the crystal is substantially the same as for a non-piezoelectric body with boundary conditions modified by the piezoelectric effect. This approximation is justified for quartz, which has low piezoelectric coupling, and means that difficult electrical terms in the wave equations can be neglected.

(ii) Traction free crystal boundaries, i.e. $T_{ij}n_j = 0$, where n_j is the unit vector normal to the crystal surface.

(iii) Continuity of stress T and displacement u at all internal boundaries between regions.

(iv) The voltage on all electrodes is zero and the charge density on the remaining surface is zero. Since the external field is neglected this last condition reduces to $D_i n_i = 0$, where D_i is the component of electric flux density.

(v) It is assumed u_1 (parallel to the X axis) is the only significant particle displacement and E_2 and D_2 (normal to the plate) are the only significant components of electric field and flux.

(vi) The extreme edges of the plate are ignored. It is assumed that either 'trapping' prevents appreciable energy reaching the edges or that what does reach them is absorbed.

Simplified Equation of Motion

Using these assumptions a simplified equation of motion of the form

$$\gamma_{11}\frac{\partial^2 u_1}{\partial x_1^2} + c_{66}\frac{\partial^2 u_1}{\partial x_2^2} + \gamma_{55}\frac{\partial^2 u_1}{\partial x_3^2} + \rho\omega^2 u_1 = 0 \qquad (1)$$

can be shown to apply, where we are dealing with a purely elastic solution, the piezoelectric properties of the quartz simply modifying the boundary conditions. ρ is the density of quartz, ω the angular frequency of the vibration, and

$$\gamma_{55} = c_{55} - \frac{c_{56}^2}{c_{66}}$$

is Voigt's face shear constant, where the c constants are the appropriate rotated elastic constants for the AT-cut (see Table 1).

The modulus γ_{11} has the form

$$\gamma_{11} = c_{11} - \frac{c_{12}^2}{c_{22}} + kc_{66}$$

A value for k of $\pi^2/12$ has been quoted in the literature, the derivation being attributed to Tiersten and Mindlin. However, the value of γ_{11} used in our computations has been determined empirically and will be discussed later.

Piezoelectric Effect on the Boundary Conditions

Simplified forms of the piezoelectric relations are used as follows:-

$$E_2 = \beta_{22}^S D_2 - h_{26}\frac{\partial u_1^{(o)}}{\partial x_2} \qquad (2)$$

$$T_6^{(o)} = T_6 + h_{26}D_2 \qquad (3)$$

where the superscript (o) denotes quantities used in the purely elastic solution, β_{22} is reciprocal permittivity and h_{26} is a piezoelectric constant (see Table 1). In equation (2) a term in $h_{25}(\partial u_1/\partial x_3)$ has been neglected, which is justified because the electrodes are usually much larger in the x_3 direction than the plate thickness. Differentiating with respect to x_3 thus gives a term much less than that arising from differentiation with respect to x_2. In equation (3) a term in $h_{36}D_3$ has been neglected in consequence of assumption (v).

Provided that variation in the x_1 and x_3 directions is not so great as to invalidate the simplifications, equations (2) and (3) can be used to determine the boundary conditions which apply when seeking the solutions of the elastic equations. There are two cases, i.e. for unplated and plated crystals, for which the values of propagation coefficient, η_S and η_R respectively, can now be determined.

Unplated Crystals

In the general case, a solution to equation (1) is $u_1 = A\sin\eta_S x_2 . f_1(x_1) . f_3(x_3)$. From assumptions (ii) and (iv), $T_6 = 0$ at $x_2 = \pm b$ and $D_2 = 0$ at $x_2 = \pm b$. Hence from equation (3) $T_6^{(o)} = 0$ at $x_2 = \pm b$ is the appropriate boundary condition. Applying this gives

$$T_6^{(o)} = c_{66}\frac{\partial u_1}{\partial x_2} = A\eta_S\cos\eta_S(\pm b) . f_1(x_1) . f_3(x_3) = 0$$

if the term in $c_{56}(\partial u_1/\partial x_3)$ is neglected. Thus $\eta_S = m\pi/2b$, where $m = 1,3,5\ldots$ is the overtone order.

In the special case of a uniformly excited plate, the terms in x_1 and x_3 disappear from equation (1), and the frequency

$$\omega_B = \eta_S\sqrt{\frac{c_{66}}{\rho_S}} = \frac{m}{2b}\sqrt{\frac{c_{66}}{\rho_S}}$$

is obtained by substituting back. This frequency ($\omega_B = 2\pi f_B$) is the 'blank frequency' which is of importance in the theory.

Plated Crystals

From assumption (iv) the voltage V on the electrodes is zero, so that the boundary conditions at $x_2 = \pm b$ are

$$V = -\int_{-b}^{b} E_2 dx_2 = 0 \qquad (4)$$

and $T_6 = 0$. Thus from equation (3) we obtain $T_6^{(o)} = h_{26}D_2$ at $x_2 = \pm b$ as the boundary condition for the elastic solution. Since div D = 0 we can say $\partial D_2/\partial x_2 = 0$ and D_2 is therefore uniform in x_2. Therefore from equations (2) and (4)

$$\int_{-b}^{b} E_2 dx_2 = \beta_{22}^S D_2 . 2b - h_{26}[u_1]_{-b}^{b} = 0$$

$$\text{i.e.} \qquad D_2 = \frac{h_{26}}{2b\beta_{22}^S}[u_1]_{-b}^{b} \qquad (5)$$

This shows that the piezoelectric excitation is only significant for modes antisymmetrical in x_2 as would be

expected.

A solution of equation (1) is

$$u_1 = A\sin n_R x_2 . f_1(x_1) . f_2(x_2)$$

so that

$$T_6^{(o)} = c_{66}\frac{\partial u_1}{\partial x_2} = Ac_{66}n_R \cos n_R(\pm b) . f_1(x_1) . f_3(x_3)$$

$$= h_{26}D_2$$

again neglected the term in $c_{56}(\partial u_1/\partial x_3)$. Substituting for D_2 from equation (5) leads to

$$\frac{\tan n_R b}{n_R b} = \frac{\beta_{22}c_{66}}{h_{26}^2}$$

the solutions to which give the propagation coefficients n_R to use for plated areas of the crystal. Normalising to unit half thickness b, i.e. $\bar{n}_R = n_R b$ gives

$$\frac{\tan\bar{n}_R}{\bar{n}_R} = \frac{\beta_{22}^S c_{66}}{h_{26}^2} \qquad (6)$$

In this equation β_{22}^S, c_{66} and h_{26} are the appropriate rotated constants for the AT-cut (see Table 1). The equation has been solved computationally and solutions for the antisymmetric modes m = 1,3,5,7 and 9 are given in Table 2, together with values of the quantity $4\bar{n}_R/m^2\pi^2$. It will be noted that as the overtone order increases this latter quantity approaches unity, i.e. $\bar{n}_R$ approaches $m\pi/2$. This is because the higher overtones have less piezoelectric coupling to modify the surface boundary condition.

In the hypothetical case of uniform excitation by large area massless short circuited conducting electrodes the solutions of equation (6) give the plateback directly. Since in this case $\omega_r = n_R\sqrt{c_{66}/\rho_R}$ and $\rho_R = \rho_S$ we have

$$\text{plateback } \Delta = \frac{f_B - f_R}{f_B} = \frac{\bar{n}_S - \bar{n}_R}{\bar{n}_S} = 1 - \frac{2\bar{n}_{R(m)}}{m\pi}$$

These values are given in Table 2.

Rectangular Electrodes of Finite Size

Referring to Figure 1, the electrodes have length 2a along the Z'(x_3) axis, width 2w along the X(x_1) axis, and the crystal thickness is 2b. The plated area is designated the R region, the unplated area being divided into P_X, P_Z and S regions as indicated.

The effective density in the R region is ρ_R and a constant μ is defined by $\rho_R = \mu^2\rho_S$, where ρ_S is the density of quartz in the unplated region. The equation of motion (1) applies, a purely elastic solution being considered. In this equation, ρ is either ρ_R or ρ_S according to the region being analysed. The method of solution by considering one mode alone and treating the regions as if they are of the same thickness but different densities was first proposed by Shockley et al[3], and greatly simplifies the treatment.

An energy trapped mode of vibration can be supported when the frequency lowering due to the electrodes is such that real propagation coefficients ζ_x and ζ_z exist in the R region, but the wave in the surrounding quartz is evanescent having coefficients of exponential decay α_x and α_z. The process of setting up and solving the equations to find symmetrical solutions for such modes will now be described.

In the R region a solution is of the form

$$u_1 = A_1\sin n_{R(m)} x_2 . \cos\zeta_z x_3 . \cos\zeta_x x_1$$

i.e. antisymmetrical in x_1 and symmetrical in x_2 and x_3. $n_{R(m)}$ is the appropriate value of propagation coefficient for the overtone mode m. Inserting this solution in equation (1) and normalising to unit half thickness b, i.e. $\bar{\zeta}_{x,z} = b\zeta_{x,z}$ and $\bar{n}_{R(m)} = bn_{R(m)}$ gives

$$\gamma_{11}\bar{\zeta}_x^2 + c_{66}\bar{n}_{R(m)}^2 + \gamma_{55}\bar{\zeta}^2 - b^2\rho_R\omega^2 = 0 \qquad (7)$$

Putting $\phi = \omega/\omega_B$ and using $\omega_B = m\pi/2b\sqrt{c_{66}/\rho_S}$ in equation (7) gives

$$\gamma_{11}\bar{\zeta}_x^2 + \gamma_{55}\bar{\zeta}_z^2 + c_{66}\bar{n}_{R(m)}^2 - \mu^2\phi^2\left(\frac{m\pi}{2}\right)^2 c_{66} = 0 \qquad (8)$$

In region P_Z using a solution of the form $u_1 = A_2\sin n_S x_2 . \cos\zeta_x x_1 . \exp\{-\alpha_z c_3\}$ leads in a similar manner, remembering that $n_S = m\pi/2$, to an equation

$$\gamma_{11}\bar{\zeta}_x^2 - \gamma_{55}\bar{\alpha}_z^2 + \left(\frac{m\pi}{2}\right)^2 c_{66}(1-\phi^2) = 0 \qquad (9)$$

Similarly for region P_X

$$\gamma_{55}\bar{\zeta}_z^2 - \gamma_{11}\bar{\alpha}_x^2 + \left(\frac{m\pi}{2}\right)^2 c_{6b}(1-\phi^2) = 0 \qquad (10)$$

Applying the conditions of assumption (iii) at the boundary $x_3 = a$ gives

$$A_1\sin n_{R(m)} x_2 . \cos\zeta_x x_1 . \cos\zeta_z a = A_2\sin n_S x_2 . \cos\zeta_x x_1 \exp\{-\alpha_z a\} \qquad (11)$$

for continuity of displacement; for continuity of stress the quantity $T_5^{(o)}$ must be considered. Now

$$T_5^{(o)} = c_{56}\frac{\partial u_1}{\partial x_2} + c_{55}\frac{\partial u_1}{\partial x_3}$$

but it may be shown that the effect of the term $c_{56}\frac{\partial u_1}{\partial x_2}$ can be neglected, basically because c_{56} is small compared with c_{55} (see Table 1) and the quantity $n_R\cot n_R x_2 - n_S\cot n_S x_2$ is always small. Thus we can equate the values of $\partial u_1/\partial x_3$ at the boundary

$$-A_1\zeta_z\sin n_{R(m)} x_2 . \cos\zeta_x x_1 \sin\zeta_z a = -A_2\alpha_z\sin n_S x_2 . \cos\zeta_x x_1 \exp\{-\alpha_z a\} \qquad (12)$$

Dividing equation (12) by equation (11) and normalising to unit half thickness b gives

$$\tan\bar{\zeta}_z\bar{a} = \bar{\alpha}_z/\bar{\zeta}_z \qquad (13)$$

and this equation also holds for the boundary at $x_3 = -a$.

For the boundaries at $x_1 = \pm w$ the procedure is similar, but the values of $T_{11} = c_{11}(\partial u_1/\partial x_1)$ are

equated. The resulting equation is

$$\tan\bar{\zeta}_x\bar{w} = \bar{\alpha}_x/\bar{\zeta}_x \qquad (14)$$

Equations (8), (9), (10), (13) and (14) describe the particle motion for the resonator. Introducing normalised elastic parameters $\bar{\gamma}_{11} = (2/m\pi)^2\,\gamma_{11}/c_{66}$ and $\gamma_{55} = (2/m\pi)^2\,\gamma_{55}/c_{66}$ gives the following set of five simultaneous equations in the six quantities $\bar{\zeta}_x$, $\bar{\zeta}_z$, $\bar{\alpha}_x$, $\bar{\alpha}_z$, ϕ and μ

$$\left.\begin{aligned}
&\bar{\gamma}_{11}\bar{\zeta}_x^2 + \bar{\gamma}_{55}\bar{\zeta}_z^2 + \left(\frac{2}{m\pi}\right)^2 \bar{\eta}_{R(m)}^2 - \mu^2\phi^2 = 0\\
&\bar{\gamma}_{11}\bar{\zeta}_x^2 - \bar{\gamma}_{55}\bar{\alpha}_z^2 + 1 - \phi^2 = 0\\
&\bar{\gamma}_{55}\bar{\zeta}_z^2 - \bar{\gamma}_{11}\bar{\alpha}_x^2 + 1 - \phi^2 = 0\\
&\bar{\alpha}_z = \bar{\zeta}_z\tan\bar{\zeta}_z\bar{a}\\
&\bar{\alpha}_x = \bar{\zeta}_x\tan\bar{\zeta}_x\bar{w}
\end{aligned}\right\} \qquad (15)$$

Solution of the equations

If a value is inserted for either ϕ (the normalised frequency) or μ (representing the mass loading due to the electrodes) the equations can be solved. In practice it is generally desired to design the device for a given frequency, so ϕ is therefore chosen as a known quantity and μ as one of the unknown quantities to be found.

The term $\left(\frac{2}{m\pi}\right)^2 \bar{\eta}_{R(m)}^2$ in the first of equations (15) is tabulated in Table 2. Since the unknown μ only appears in the first of equations (15) the other four equations can be solved. Substituting from the fourth and fifth into the second and third respectively, and rearranging gives a form suitable for computation:-

$$\left.\begin{aligned}
&B_x - \bar{\gamma}_{55}\bar{\zeta}_z^2 + (B_x + \bar{\gamma}_{55}\bar{\zeta}_z^2)\cos 2\bar{\zeta}_z\bar{a} = 0\\
&B_z - \bar{\gamma}_{11}\bar{\zeta}_x^2 + (B_z + \bar{\gamma}_{11}\bar{\zeta}_z^2)\cos 2\bar{\zeta}_x\bar{w} = 0
\end{aligned}\right\} \qquad (16)$$

where $B_x = \bar{\gamma}_{11}\bar{\zeta}_x^2 + 1 - \phi^2$

and $B_z = \bar{\gamma}_{55}\bar{\zeta}_z^2 + 1 - \phi^2$

Equations (16) can be solved computationally for $\bar{\zeta}_x$ and $\bar{\zeta}_z$ by a process of successive substitution, which, if carried out in the correct order, gives a rapid convergence. Thus, starting with $\bar{\zeta}_z = 0$ substituted in the second of equations (16), a root-hunting procedure solves the equation for $\bar{\zeta}_x$. This value is then substituted in the first equation (16) and the same procedure finds a closer approximation to $\bar{\zeta}_z$. Repetition of the cycle from 2 to 5 times is usually enough to obtain values of sufficient accuracy. Having solved equations (16) for $\bar{\zeta}_x$ and $\bar{\zeta}_z$, the remaining unknown quantities μ, $\bar{\alpha}_x$ and $\bar{\alpha}_z$ can be found by direct substitution into the first of equations (15) for μ and into either the second and third, or the fourth and fifth to obtain $\bar{\alpha}_x$ and $\bar{\alpha}_z$.

It is worth commenting that equations (15) lead to values of the 'cut-off' frequencies below which energy trapping occurs. For the thickness-shear wave propagating along x_1 putting $\bar{\alpha}_x = 0$ in the third of equations (15) gives $\phi_{cox} = \sqrt{(1 + \bar{\gamma}_{55}\bar{\zeta}_z^2)}$ and similarly for the thickness twist wave we find $\phi_{coz} = \sqrt{(1 + \bar{\gamma}_{11}\bar{\zeta}_x^2)}$. These frequencies are higher than the blank frequency ($\phi = 1$) as a consequence of the finite size of the electrodes.

Calculation of Inductance

In the equivalent circuit of Figure 2(a) the quantities to the right of the ideal transformer of 1:ψ turns ratio are mechanical. Thus L_m is the motional mass of the crystal and the current in this part of the circuit represents velocity at some reference point. If $\dot{u}$ is the velocity, $\dot{u}_o$ that at the reference point, e.g. the position of maximum velocity, L_m is found by equating kinetic energies, i.e.

$$\tfrac{1}{2}L_m\dot{u}_o^2 = \tfrac{1}{2}\int_B \rho\dot{u}^2\,dB$$

where B is the volume of the vibrating body. Since sinusoidal motion is considered, $\dot{u} = j\omega u$ and $\dot{u}_o = j\omega u_o$. Thus

$$L_m = \frac{1}{u_o^2}\int \rho u^2\,dB \qquad (17)$$

ψ represents the piezoelectric coupling between the electrical circuit on the left and the mechanical circuit on the right. If i is the electrical current, therefore, $i = \psi\dot{u}_o$. Current is rate of transfer of charge, so $i = j\omega\sigma = j\psi\omega u_o$, where σ represents the total instantaneous piezoelectric charge.

$$\text{Thus } \psi = \sigma/u_o \qquad (18)$$

The circuit of Figure 2(a) simplifies to that of Figure 2(b) where L_1 is the crystal inductance in electrical units. $L_1 = L_m/\psi^2$ so from equations (17) and (18)

$$L_1 = \frac{\int_B \rho u^2 dB}{\sigma^2} = \frac{\int_B \rho u^2 dB}{\left(\int_A D_2 dA\right)^2} \qquad (19)$$

since in the MKS system surface charge density is equivalent to electric flux density.

From equation (5), $D_2 = (h_{26}/b\beta_{22})u(x_1,b,x_3)$ so that

$$L_1 = \frac{b^2\beta_{22}^2}{h_{26}^2}\,\frac{\int_B \rho u^2 dB}{\left(\int_A u dA\right)^2} \qquad (20)$$

where B is the volume of the whole crystal and A the area of the electroded region.

Carrying out first the integration in the denominator, remembering that at the surface $x_2 = b$ the term $\sin\eta_R b$ is negligibly different from unity

$$\int_A u dA = \int_{-a}^{a}\int_{-w}^{w} A_1\cos\zeta_x x_1.\cos\zeta_z x_3 dx_1 dx_3 = \frac{4A_1 aw\sin\theta_x\sin\theta_z}{\theta_x\theta_z} \qquad (21)$$

where $\theta_x = \zeta_x w$ and $\theta_z = \zeta_z a$.

The integration in the numerator must be carried out in separate parts for the different regions of Figure 1. Thus in the region R

$$u_1 = A_1 \sin n_{R(m)} x_2 . \cos\zeta_z x_3 . \cos\zeta_x x_1$$

and the required integral is

$$I_R = \rho_S A_1^2 \left\{ \frac{\mu^2 awb}{\theta_x \theta_z} \cdot \frac{2\bar{n}_{R(m)}}{m\pi} (\theta_x + \sin\theta_x \cos\theta_x) . (\theta_z + \sin\theta_z \cos\theta_z) \right\}$$

In region P_Z

$$u_1 = A_2 \sin n_S x_2 . \cos\zeta_x x_1 . \exp\{-\alpha_z x_3\}$$

and applying the boundary conditions with region R at $x_3 = a$ gives

$$A_2 = \frac{A_1 \cos\zeta_z a}{\exp\{-\alpha_z a\}}$$

neglecting the difference between $\sin n_{R(m)} b$ and $\sin n_S b$. The required integral is

$$I_{P_Z} = \rho_S A_1^2 \frac{awb}{2\theta_x \theta_z} (\theta_x + \sin\theta_x \cos\theta_x) \frac{\cos^3\theta_z}{\sin\theta_z}$$

in which the fourth of equations (15) has been used to make the substitution $\alpha_z = (\theta_z/a) \tan\theta_z$.

In a similar manner we find

$$I_{P_X} = \rho_S A_1^2 \frac{awb}{2\theta_z \theta_x} (\theta_z + \sin\theta_z \cos\theta_z) \frac{\cos^3\theta_x}{\sin\theta_x}$$

and for region S, where $u = A_3 \sin n_S x_2 . \exp\{-\alpha_x x_1\} \exp\{-\alpha_z x_3\}$ we obtain

$$I_S = \frac{\rho_S A_1^2 awb \cos^3\theta_x \cos^3\theta_z}{4\theta_x \theta_z \sin\theta_x \sin\theta_z}$$

Combining these results, with equation (21), into equation (20) gives

$$L_1 = \frac{b^2 \beta_{22}^2}{h_{26}^2} \cdot \frac{\theta_x^2 \theta_z^2 (I_R + 2I_{P_Z} + 2I_{P_X} + 4I_S)}{16 A_1^2 a^2 w^2 \sin^2\theta_x \sin^2\theta_z}$$

Making the approximation of replacing the term $2\bar{n}_{R(m)}/m\pi$ by 1 (the difference being less than 4 parts in 10^3 at worst), using a value of frequency constant of 1660 kHz mm and the values of β_{22} and h_{26} from Table 1 give

$$L_1 \text{ (henries)} = \frac{0.39848}{A_{cm^2} \left(f_{B\,MHz}\right)^3} \cdot \frac{m^3}{} \cdot \frac{\theta_x \theta_z}{\sin^2\theta_x \sin^2\theta_z} \left\{ (\theta_x + \cot\theta_x)(\theta_z + \cot\theta_z) + (\mu^2 - 1) \left(\theta_x + \frac{\sin 2\theta_x}{2} \right) \left(\theta_z + \frac{\sin 2\theta_z}{2} \right) \right\} \quad (22)$$

where A_{cm^2} is the area of the electrodes in square centimetres and $f_{B\,MHz}$ is the blank frequency in megahertz at the appropriate overtone.

Results and Comparison with Experiment

In order to obtain experimental confirmation of the theory it has been necessary, firstly to improve the method of determining blank frequency, a knowledge of which is essential in finding the plateback, and secondly to use an experimental method in which electrodes can be deposited on the crystals with known values of mass loading.

Determination of Blank Frequency

Referring to the first of equations (15), in the case of large electrode size there is little variation with x_1 or x_3 so that the coefficients ζ_x and ζ_z are small. Also at high overtone orders $4\bar{n}_{R(m)}^2/m^2\pi^2$ approaches unity and $\bar{\gamma}_{11}$ and $\bar{\gamma}_{55}$ become small. The equation thus reduces to $\phi^2 = 1/\mu^2$ and since $\phi = 1 - \Delta$ this gives $\Delta = (\mu-1)/\mu$ as the limiting case. The blank frequency ($\phi = 1, \Delta = 0$) is thus given by the frequencies of the crystal at a high overtone with large electrodes of various mass loadings when extrapolated back to zero mass loading ($\mu = 1$). Since the piezoelectric effect is small at high overtones, the effect upon frequency of an air gap is small. Consequently, the frequency obtained by using large area air gap electrodes on the unplated blank at a high overtone should agree with the blank frequency as defined above.

In Figure 3 the lowering of frequency at ninth overtone is plotted against mass loading (represented by the total amount of gold evaporated in each plating operation) for some 60.3 MHz crystals. The crystal blank frequencies were measured at ninth overtone using 6.5 mm diameter air gap electrodes. Extrapolating the results to zero mass loading, gives a discrepancy of about 10 kHz only, representing an uncertainty in the fundamental blank frequency of only about 1 kHz.

Table 3 shows some measurements of blank frequency carried out on one of these crystals (a 12 mm diameter blank) using various types of jig, both at fundamental frequency and at ninth overtone, the latter measurements being given as f/9. Whereas the spread of the measurements at fundamental is about 13 kHz, the values obtained by measurement at the ninth overtone spread by less than 1 kHz and are also significantly lower. Experience also shows that at higher frequencies correspondingly larger discrepancies are found between measurements of fundamental blank frequency made with various jigs.

It can be concluded that the best way to estimate blank frequency for the purposes of using energy trapping theory and determining coupling in integrated filters is to use a measurement at high overtone. It should not be necessary to make more than two or three such measurements at the frequency of interest to determine a correction to apply to the fundamental blank frequency measurements made with the preferred type of jig.

In the experiments described in this paper, 12 mm diameter polished crystals have been used and their blank frequencies have been measured in a low impedance π-network at ninth overtone using the 6.5 mm diameter jig listed in Table 3.

Calibration of Mass Loading

Crystals used in the experiments were mounted in metal shim masks to define the electrode pattern. Gold was deposited by vacuum evaporation from a set of four V-loop filaments held in a stationary relationship with the crystal. The filaments were loaded each time with measured lengths of 0.2 mm diameter gold wire, and the gold was completely evaporated in each operation.

The mass loading produced was determined by

weighing test pieces held in place of the crystals and a value of 0.114 mg/cm^2 was found per cm of gold wire loaded on each filament. For the 6.695 MHz blanks used in the experiments this corresponds to a fractional mass loading $\Delta M/M$ of 0.00173 per cm of gold wire per loop. In a typical case a total length of gold wire of 20 cm (divided between the four filaments) could be 0.5 mm in error at worst. The assumed fractional mass loading of 0.00865 would thus have an error attributed to this cause of ±0.00002.

For a uniformly excited plate, if M is the mass of quartz per unit area, the motional mass per unit area is $L_{m_S} = M/2 = \rho_S b$. If a surface loading ΔM/unit area (total of both sides) is applied the motional mass becomes $L_{m_R} = L_{m_S} + \delta L_m = M/2 + \Delta M = \rho_R b$ where ρ_R is the effective density for the electroded area. Note that ρ_R is not simply given by adding the total mass of quartz and electrode.

$$\text{Thus } \mu^2 = \frac{\rho_R}{\rho_S} = 1 + \frac{2\Delta M}{M}$$

and the fractional mass loading $\Delta M/M = (\mu-1).(\mu+1)/2$. Direct comparison between theory and experiment is therefore possible. Since μ is always close to unity, there is little error in equating the fractional mass loading $\Delta M/M$ to the quantity $\mu-1$ found in the computations.

Relationship between Plateback, Mass Loading and Electrode Dimensions

A series of crystals were plated with electrodes 1.75 and 3.0 mm square. After mounting, the resonance frequencies at various overtones were used to find the plateback $\Delta = (f_B - f_R)/f_B$. Experimental points relating Δ with fractional mass loading $\Delta M/M$ were then plotted to compare with computed curves of Δ versus $\mu-1$. The first trials showed a systematic divergence from the computed curves in that plateback was found to be higher than that predicted for a given mass loading. The discrepancy was large for the fundamental mode, becoming progressively smaller as the overtone order increased and becoming negligible as the seventh overtone. The discrepancy also reduced as the electrode size increased. An example of this behaviour is shown in Figure 4 for crystals with 1.75 mm square electrodes.

These discrepancies were all within the range which could be covered by a simple edge correction to the electrode dimensions of less than a crystal thickness. Trial computations showed that a correction placing the effective edge of the electrode a distance 0.8t/m further into the unplated region greatly improved the fit. This correction is in some respects analogous to the end correction for organ pipes and has the effect of increasing the effective t/t and w/t ratios for an electrode by 1.6/m. The largest effect is on the calculations for small electrodes operating in the fundamental mode and there is negligible effect at high overtones.

There is, of course, no reason to suppose that this correction is a true constant. It may well be expected to vary slightly with the value of the propagation constants ζ_x and ζ_z, so that it could be a function of electrode size and plateback and could have different values for the anharmonic overtones. However, there is insufficient data available to define it more precisely and the factor 0.8 which has been chosen may be regarded as a satisfactory mean value.

Figure 5 shows how the application of this correction improves the agreement between the computed curves and experimental results for the 1.75 mm square electrodes. Results for 3 mm square electrodes are shown in Figure 6, together with computed curves. The agreement between theory and experiment appears reasonable, particularly when it is considered that blank contour may begin to have an effect on the results at this electrode size.

Inductance Measurements

The inductances of the experimental crystals were measured using a bridge method and compared with computed values. The edge corrections mentioned above make a few modifications to the computations. These corrections should be used in summing the kinetic energy of the motion, but not in summing the charge. Applying these conditions equation (22) becomes modified to

$$L_1 = \frac{0.39848 \text{ m}^3}{\frac{A}{\text{cm}^3}\,\frac{f_B^3}{\text{MHz}}} \cdot \frac{\theta_x\theta_z}{\sin^2\theta_x \sin^2\theta_z} \times \left\{ (\theta'_x + \cot\theta'_x)(\theta'_z + \cot\theta'_z) + (\mu^2 - 1)\left(\theta'_x + \frac{\sin 2\theta'_x}{2}\right)\left(\theta'_z + \frac{\sin 2\theta'_z}{2}\right) \right\} \quad (23)$$

where the primed symbols indicate those quantities computed for the modified boundaries.

Values of inductance calculated from equation (23) are found to diverge systematically from the experimental points and it is reasonable to assume that an edge correction, due to a 'fringing' effect, should be used in computing the total charge collected by the electrodes.

Assume charge is collected from additional strips of width kt around the electrode, and let $u_{a_{eff}}$ and $u_{w_{eff}}$ be the effective displacements in these regions. Then equation (21) is modified to

$$\int_A u\,dA = \frac{4A_1 aw}{\theta_x\theta_z}\sin\theta_x\sin\theta_z + 2u_{a_{eff}}.kt.2w + 2u_{w_{eff}}.kt.2a \quad (24)$$

Taking $u_a = A_1\cos\zeta_z a$ we can assume that

$$\left.\begin{aligned} u_{a_{eff}} &= u_a + \left(\frac{\partial u}{\partial z}\right)_a \cdot \frac{kt}{2} = A_1\left(\cos\theta_z - \frac{kt\theta_z}{2a}\sin\theta_z\right) \\ \text{similarly} \\ u_{w_{eff}} &= A_1\left(\cos\theta_x - \frac{kt\theta_x}{2w}\sin\theta_x\right) \end{aligned}\right\} \quad (25)$$

Applying equations (25) to equation (24) we obtain a correction factor C for the computation of charge defined by

$$\int_A u\,dA = \frac{4A_1 aw}{\theta_x\theta_z}\sin\theta_x\sin\theta_z.C$$

where

$$C = 1 + \frac{2k\bar{\zeta}_x\bar{\zeta}_z}{\sin\theta_x \sin\theta_z}\{\bar{w}\cos\theta_z + \bar{a}\cos\theta_x$$

$$- k\bar{\bar{w}}\bar{\zeta}_z \sin\theta_z - k\bar{\bar{a}}\bar{\zeta}_x \sin\theta_x\}$$

The corrected value of inductance is therefore found from the equation (23) by dividing by C^2.

Trial computations have shown a reasonable fit between theory and experiment if a value of k = 0.3 is used. It is to be expected that the fringing correction should be independent of the overtone order, and this value has therefore been chosen for the best overall fit with the available experimental results.

Figures 7 and 8 show comparison of experimental and computed inductance values at various overtones for crystals with 1.75 mm and 3.0 mm square electrodes.

Notes on the Empirical Edge Corrections and the γ_{11} Constant

As described above, the following empirical modifications have been made to the theory:-

(i) A mechanical edge correction is applied to electrode dimensions in order to obtain agreement with experiment for plateback Δ plotted against fractional mass loading (μ-1).

(ii) An electrical fringing correction is used to obtain agreement with experiment for inductance L_1 plotted against plateback Δ.

As mentioned earlier, the theory has been extended to the computation of coupling between neighbouring electrodes. In these investigations, not reported here, discrepancies have been obtained in experimental values of coupling along the X-axis (thickness-shear wave), which vary with overtone order, and may be partly attributable to neglect of coupling to flexural modes. However, by choosing empirical values of γ_{11} depending on overtone order (see Table 4) improved agreement has been obtained, and the values given in Table 4 have been used in the computations reported in this paper. Trial computations have shown that within the range examined the value of γ_{11} has very little or negligible effect on the computed results for fractional mass loading (μ-1) and inductance L at given values of plateback Δ. Any uncertainty as to the correct value of γ_{11}, therefore, does not invalidate the conclusions about the magnitude of the edge corrections needed to reconcile the theoretical computations with practical determinations of Δ and L_1.

Universal Curves for Square Electrodes

Since the theory is completely expressed in quantities normalised to the half plate thickness b, the results are universally true as functions of electrode length/crystal thickness. Computed curves of plateback Δ plotted against fractional mass loading (μ-1) for square resonators of various electrode length/thickness ratios are given in Figures 9 and 10 for the fundamental and third overtone modes respectively.

To obtain corresponding curves for inductance L_1 an inductance 'constant' λ is defined by

$$L_1 = \frac{\lambda m^3}{A\ f_B^3} \text{ henries}$$

$\frac{}{cm^2\ MHz}$

The computed curves in Figures 11 and 12 show that λ is in fact a function of both plateback and electrode size. The usually accepted value of 1.8 is, however, seen to be near the centre of the range for the most frequently used electrode sizes.

In using the curves of Figures 9 - 12 it should be remembered that the plateback Δ is based on the values of blank frequency which would be indicated by measurements at high overtone orders.

Third Overtone Oscillator Crystals

Examination of the curves shown in Figures 9 and 10 shows that the effect of restricted electrode size on plateback is much greater for the fundamental mode than for overtone modes. Whereas for ℓ/t = 15 the plateback is roughly proportional to fractional mass loading for both the fundamental and third overtone modes, a marked difference between these modes is shown for smaller electrode sizes, e.g. ℓ/t = 7. In this case a fractional mass loading of 0.004 produces no significant plateback at the fundamental mode but a plateback of about 0.002 at the third overtone. Also see Figure 5 (for ℓ/t = 7.03) where fundamental responses are shown with negative plateback. These were all very low Q responses; their behaviour depends upon the whole crystal and its mounting and, being untrapped modes, they do not enter into the scope of the theory described in this paper.

Crystals having electrodes of around this size and mass loading, therefore, display little or no energy trapping for the fundamental mode which is consequently of very low Q, but have third overtone modes which are energy trapped and active. Such a crystal can be used to control an untuned oscillator at the third overtone frequency, thus saving the complication of a tuned circuit in the oscillator. This type of crystal design has been described elsewhere in a patent application[4].

Further Applications of the Theory to Crystal Design

The use of Bechmann's constant to determine the plateback limit for the design of single response crystals in which the anharmonic overtones are to be untrapped is well known. However, by applying the theory described in this paper, a more quantitative approach can be made to the problem, with account being taken of the crystal size.

The solutions of equations (15), as described above, lead to a mathematical description of the distribution of particle displacement in the electroded and surrounding regions, and it has been seen that the kinetic energy of vibration can be computed. The energy loss at the crystal edges can be represented by the loss at the edges of an equivalent square crystal with edge damping, and estimated by integrating the energy in the tails of the exponential distribution. Estimates of the degradation of Q due to imperfect energy trapping can therefore be made for the wanted mode. Similar estimates can be found for the symmetric anharmonic overtones by seeking the next higher order solutions if they exist (for untrapped modes no such solutions will be found and in this simplified model are presumed not to exist). A simple modification of equation (15) allows the same process to be carried out for the antisymmetric anharmonic overtones.

Combining these results with the intrinsic Q value for quartz, and with estimates of losses due to internal friction in the metal electrodes and, if applicable, losses due to the viscosity of the surrounding

atmosphere (see Reference 5 on the subject of gas damping) enables curves of Q versus Δ to be plotted for the main mode and the anharmonic overtones. Electrical loss due to resistance of the electrode films is another factor of importance in many cases, and can also be estimated. An example of these curves, with some experimental results for crystals at 6.7 MHz fundamental and 20.1 MHz third overtone is shown in Figure 13.

Loss in the damaged surface layers of quartz is not considered in this model, so that, as is seen for the third overtone results in Figure 13, practical Q values fall short of those predicted. Another source of energy loss not considered in this simple theory is that due to coupling to flexural modes cf. Mindlin and Lee[6]. The measured Q values for the fundamental mode in Figure 13 are significantly higher than predicted. As mentioned earlier, these are untrapped modes involving the whole crystal plate, and would be suppressed by adding damping at the crystal edges.

The crystal performance shown in Figure 13 illustrates the behaviour of the third overtone oscillator crystal described in the previous section. It will be seen that within the fractional mass loading range 0.004 to 0.01 (corresponding in this case to a plateback range for the third overtone of 0.0025 to 0.007) the third overtone response has a Q of up to thirty times that of the fundamental. In other experiments much greater ratios than this have been obtained.

The main benefit of the Q calculations, however, is in the design of single response filter crystals to indicate the range of usable plateback values, and the procedure has been used by us in the development of miniature filter crystals. The calculations show that at low plateback there is loss of Q due to imperfect energy trapping, while at higher platebacks the symmetric overtones become trapped. By computing the inductance, as well as Q, for these overtones their relative activity at any plateback value can be estimated. On the other hand, the antisymmetric overtone modes cannot usually be untrapped without degrading the wanted mode, so that freedom from this type of overtone can only be achieved by maintaining good symmetry of the blank and plating thicknesses so as to obtain precise charge cancellation.

These points are illustrated by Figures 14 and 15, which show computed curves of Q versus Δ for 1.5 mm square electrodes with a blank frequency of 18.5 MHz. Figure 14 is for an 8 × 8 mm blank while Figure 15 is for a 4 × 4 mm blank. The Bechmann limit to avoid trapping the symmetric overtones would be the same in both cases and, if the formula $\Delta < [2.4/(\ell/t)]^2$ was used, would give a maximum plateback of 0.0206. As the figures show, however, the size of crystal blank has a very marked effect on the activity of the various modes. For the large plate (Figure 14) a plateback of less than 0.01 would probably be chosen for the best operation, but in the case of the small plate (Figure 15) such a low plateback would lead to excessive Q degradation of the wanted mode. $\Delta = 0.015$ would seem a good compromise to both maintain Q and avoid excessive activity of the symmetric modes. Experimental values of Q found at platebacks of 0.015 and 0.016 are shown on Figure 15, and in Figure 16 a frequency response spectrum is given for an experimental miniature crystal on a 4.5 mm diameter blank with plateback of 0.0151. As is seen, this is a substantially single response crystal.

Conclusions

It has been shown that a simplified theory of wave propagation for the AT-cut crystal, which neglects coupling to other modes (such as flexural modes), and replaces piezoelectric effects by modified boundary conditions, is adequate to predict the principal measurable properties of crystals with rectangular electrodes. Using the theory, modified only by applying simple edge corrections to the electrode dimensions, the values of plateback and inductance for any particular electrode geometry and mass loading can be readily computed, and are shown to agree well with experiment.

The investigation has already led to the development of third overtone oscillator crystals with virtually zero activity at the fundamental frequency, and the computational techniques are being applied in the design of miniature single response filter crystals, where the effect of restricted blank size on the crystal performance can be predicted.

Further extensions of the theory to the study of integrated filters are being made and it is hoped will lead to better predictions of coupling and unwanted mode incidence in these devices.

Acknowledgement

This work was initiated by Salford Electrical Instruments Ltd., part of GEC Electrical Components Ltd.

References

1. N.H.C. Reilly and M. Redwood, "Wave Propagation Analysis of the Monolithic Crystal Filter", Proc. IEE, Vol. 116, No. 5, May 1969, p. 653 - 660

2. N.H.C. Reilly, "Wave Propagation Analysis of the Evanescent Mode Piezoelectric Filter", Doctorate Thesis, 1969, University of London

3. W. Schockley, D.R. Curran and D.J. Koneval, "Energy Trapping and Related Studies of Multiple Electrode Filter Crystals", Proc. 17th Annual Frequency Control Symposium, 1963, p. 88 - 126

4. J. Birch, A.J. Dyer and J.F. Werner, "Improvements in or Relating to Piezoelectric Resonators", UK Patent Application No. 28133/74

5. A. Seed, "Microminiature Cold Weld Crystal Units", Proc. 20th Annual Frequency Control Symposium, 1966, p. 234 - 251

6. R.D. Mindlin and P.C.Y. Lee, "Thickness-Shear and Flexural Vibrations of Partially Plated Crystal Plates", Int. J. Solid Structures, 1966, 2, p. 125 - 139.

TABLE 1

Constants for the quartz AT-cut (MKS units)

Density	$\rho = 2.65 \times 10^3$	kg/m^3
Reciprocal permittivity	$\beta_{22} = 2.480 \times 10^{10}$	m/F
Piezoelectric constant	$h_{26} = 2.418 \times 10^9$	N/C
Elastic constants	$c_{11} = 87.49 \times 10^9$	N/m^2
	$c_{12} = -8.92 \times 10^9$	N/m^2
	$c_{22} = 130.7 \times 10^9$	N/m^2
	$c_{55} = 69.50 \times 10^9$	N/m^2
	$c_{56} = -2.32 \times 10^9$	N/m^2
	$c_{66} = 29.48 \times 10^9$	N/m^2

These rotated constants were computed by Reilly[2] from Bechmann's values for the principal constants of quartz.

TABLE 2

Solutions of the equation

$$\tan\bar{\eta}_R = \bar{\eta}_R(\beta_{22}c_{66}/h_{26}^2)$$

m	$\bar{\eta}_R$	$4\bar{\eta}_R^2/m^2\pi^2$	Δ
1	1.56568837	0.9935075	0.00326
3	4.71069050	0.9992796	0.00037
5	7.85296249	0.9997408	0.00013
7	10.99484444	0.9998679	0.00007
9	14,13660049	0.9999201	0.00004

Δ is the effective plateback created by short-circuited massless conducting electrodes on an infinite blank.

TABLE 3

Blank frequency measurements at fundamental and 9th overtone

Type of air gap jig used	Fundamental frequency measurement MHz	9th o/t frequency 9 MHz
1 mm diameter	6.704	6.695
3 mm diameter	6.701	6.695
6.5 mm diameter	6.698	6.695
2 mm × 2 mm square, surrounding crystal clamped	6.709	6.695

TABLE 4

Empirical values of γ_{11} (MKS units)

$$c_{11} = 87.49 \times 10^9 \text{ N/m}^2$$

$$\gamma_{11} = c_{11} - \frac{c_{12}^2}{c_{22}} + \frac{\pi^2 c_{66}}{12} = 111.13 \text{ N/m}^2$$

Overtone order m	Empirical value of γ_{11} N/m^2
1	100.0
3	75.0
5	90.0
7	80.0
9	87.5

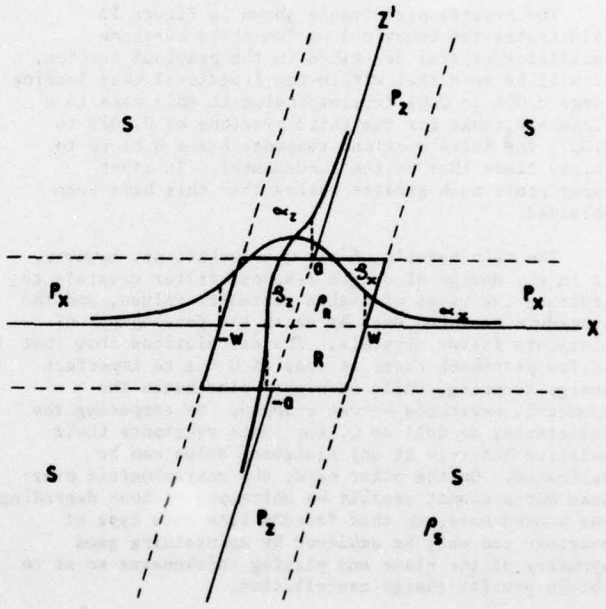

Figure 1. Particle displacement for a rectangular resonator.

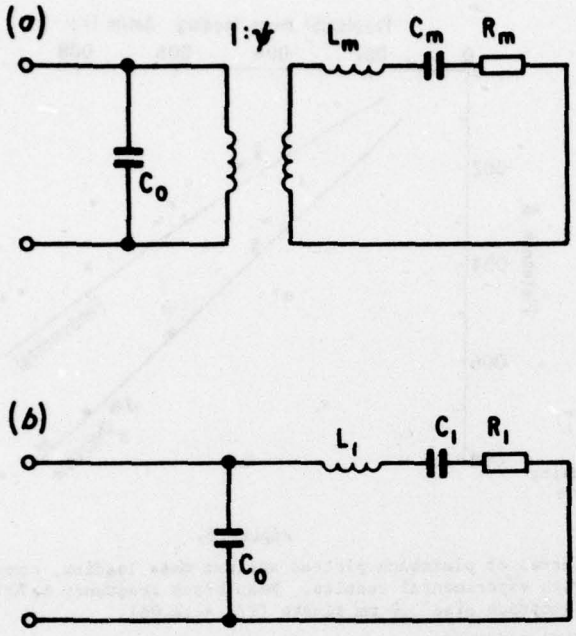

Figure 2. Equivalent circuits of a quartz crystal.

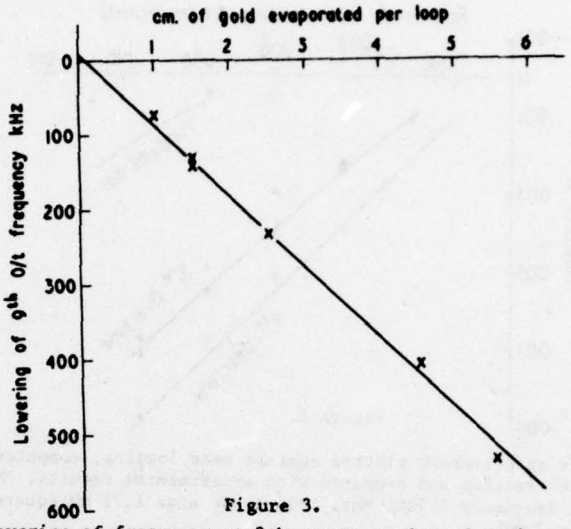

Figure 3.
Lowering of frequency at 9th overtone plotted against mass loading. Electrode size 1.75 mm square.
Evaporation was from a system of 4 loop filaments.
Zero on frequency scale is that measured on the blank using a 6.5 mm diameter air gap electrode at 9th overtone.
Mean value 60.3013 MHz.

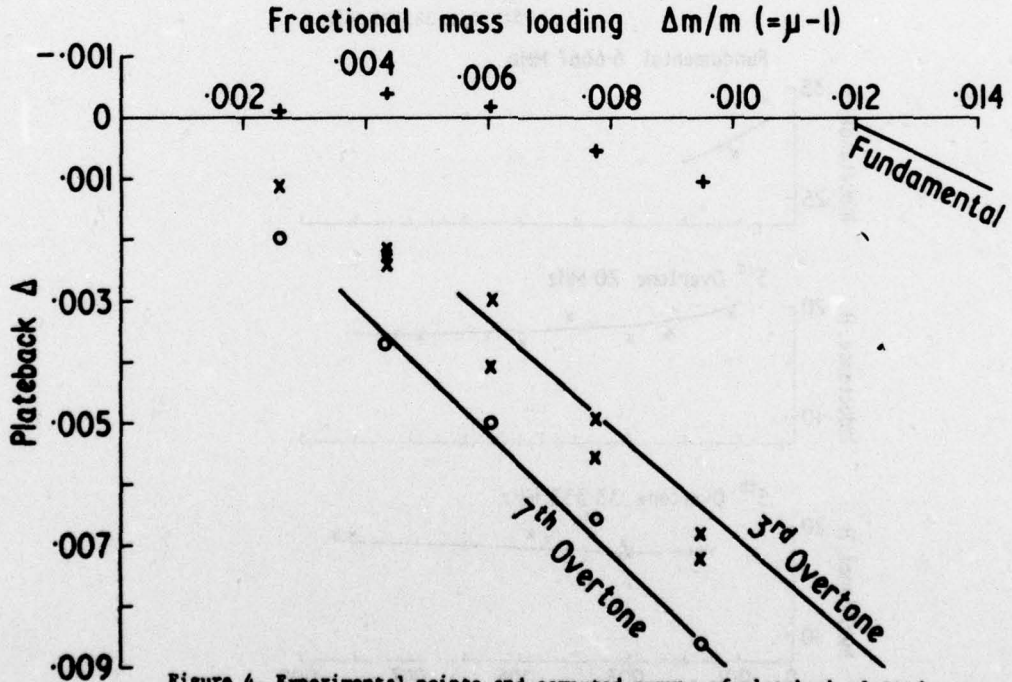

Figure 4. Experimental points and computed curves of plateback plotted against mass loading. Mean blank frequency 6.7001 MHz.
Electrode size 1.75 mm square (t/t = 7.03).

Computed curves ——————
Fundamental 6.6667 MHz +
3rd O/t 20.0 MHz X
7th O/t 46.6667 MHz ⊙

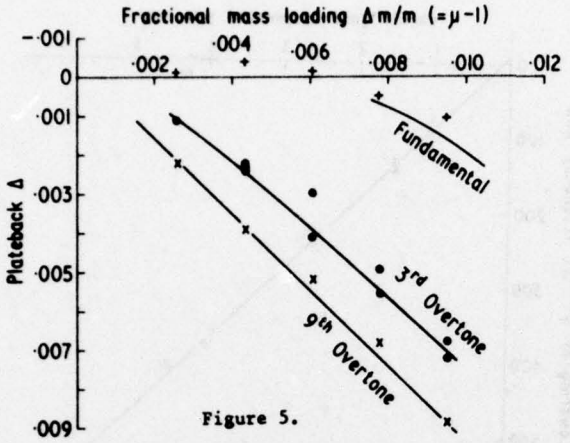

Figure 5.

Curves of plateback plotted against mass loading, computed using edge correction and compared with experimental results. Mean blank frequency 6.7001 MHz. Electrode size 1.75 mm square (ℓ/t = 7.03).

Computed curves	———
Fundamental 6.6667 MHz	+
3rd O/t 20.0 MHz	•
9th O/t 60.0 MHz	X

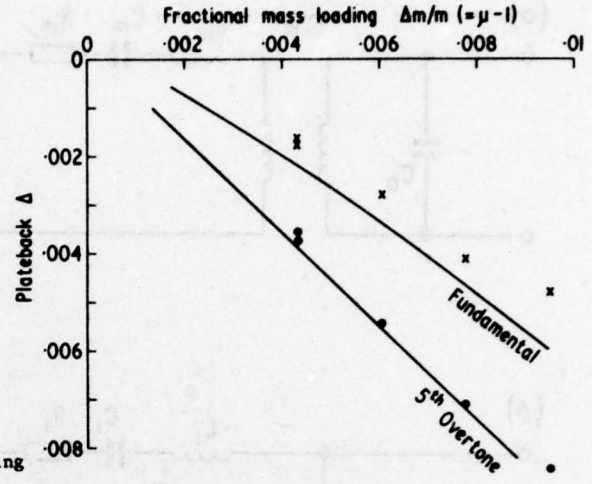

Figure 6.

Curves of plateback plotted against mass loading, compared with experimental results. Mean blank frequency 6.7001 MHz Electrode size 3.0 mm square (ℓ/t = 12.06).

Computed curves	———
Fundamental 6.6667 MHz	X
5th O/t 33.333 MHz	•

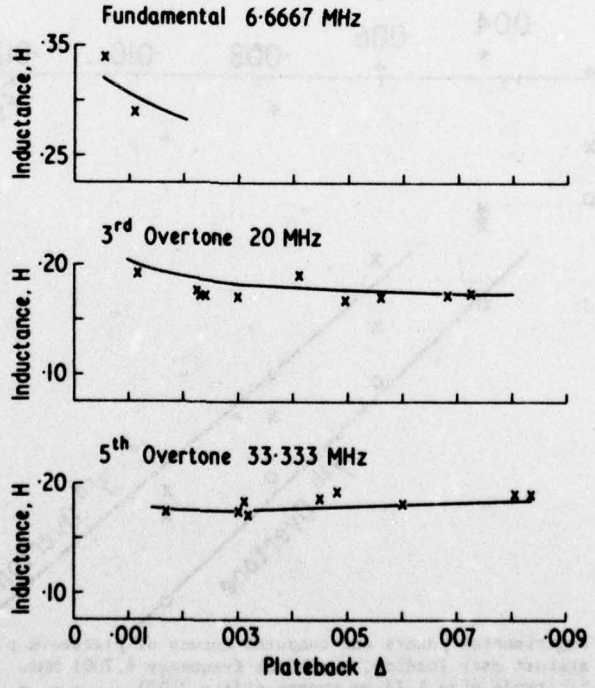

Figure 7. Inductance values computed using edge corrections plotted against plateback and compared with experimental results. Electrode size 1.75 mm square.

Computed curves	———
Experimental points	X

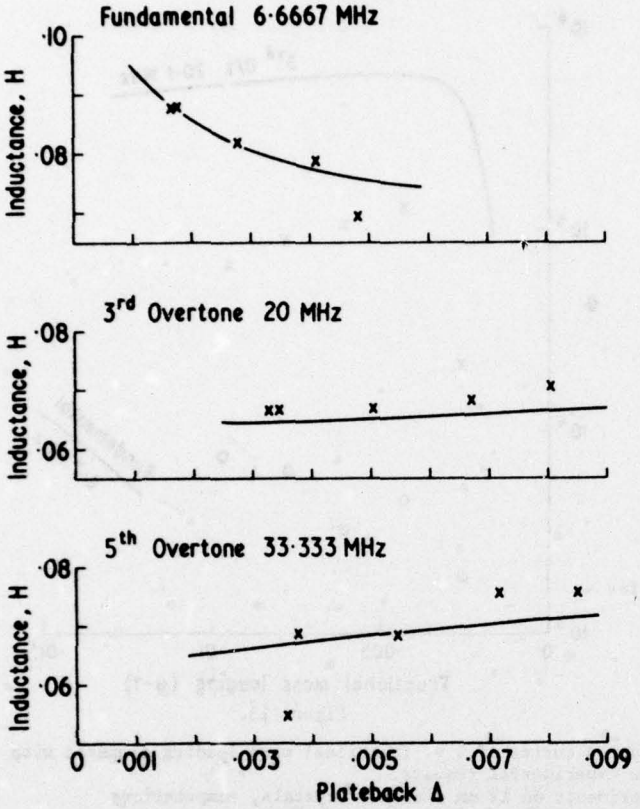

Figure 8.

Inductance values computed using edge corrections plotted against plateback and compared with experimental results. Electrode size 3.0 mm square.

Computed curves ——

Experimental points X

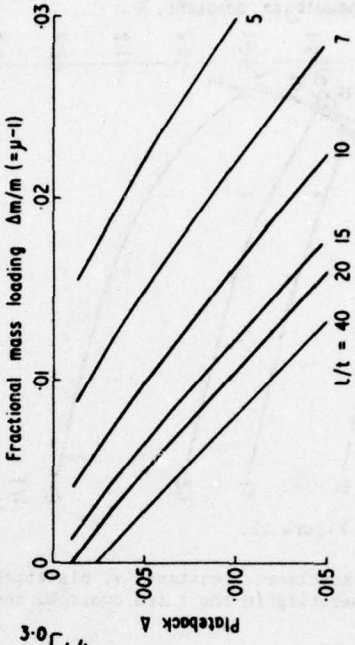

Figure 9.

Computed curves of plateback Δ versus fractional mass loading (μ-1) for square resonators operating in the fundamental mode, for various values of electrode length/crystal thickness.

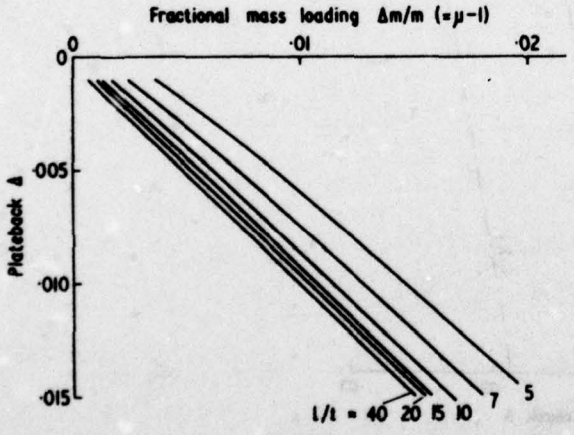

Figure 10.

Computed curves of plateback Δ v. fractional mass loading (μ-1) for square resonators operating in the third overtone mode, for various values of electrode length/crystal thickness.

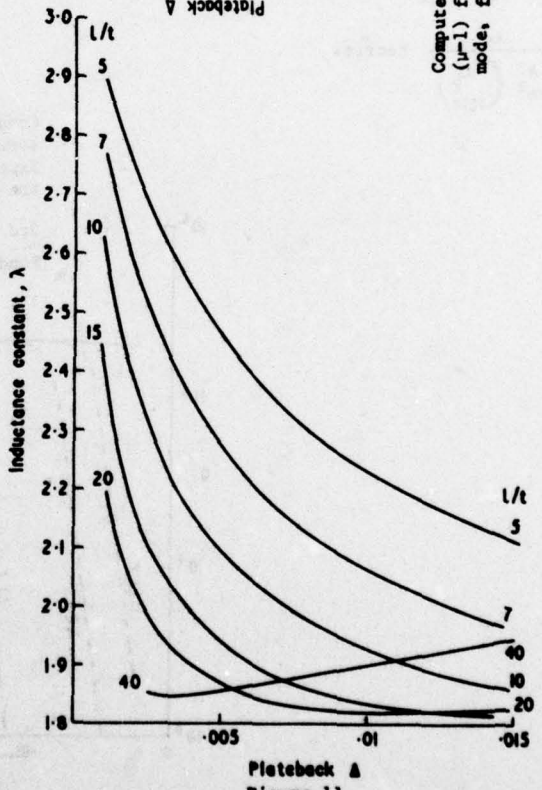

Figure 11.

Computed curves of inductance 'constant' versus plateback for square resonators operating in the fundamental mode

$$L = \frac{\lambda}{\frac{A}{cm^2}\left(\frac{f_B}{MHz}\right)^3} \text{ henries}$$

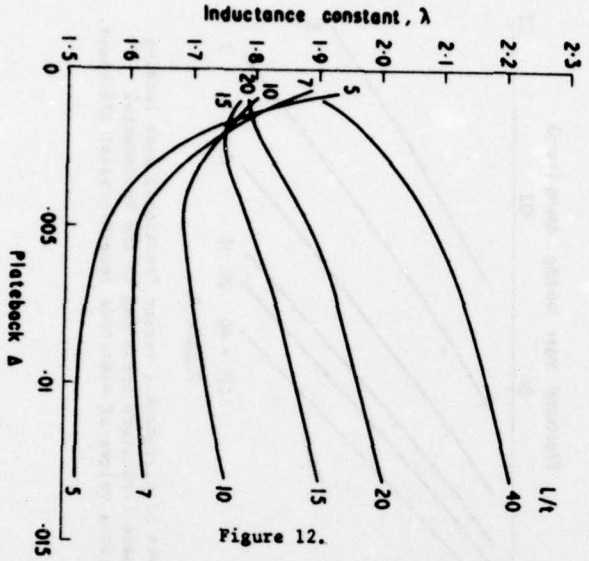

Figure 12.

Computed curves of inductance 'constant' v. plateback for square resonators operating in the third overtone mode

$$L = \frac{\lambda_m^3}{\frac{A}{cm^2}\left(\frac{f_B}{MHz}\right)^3} \text{ henries}$$

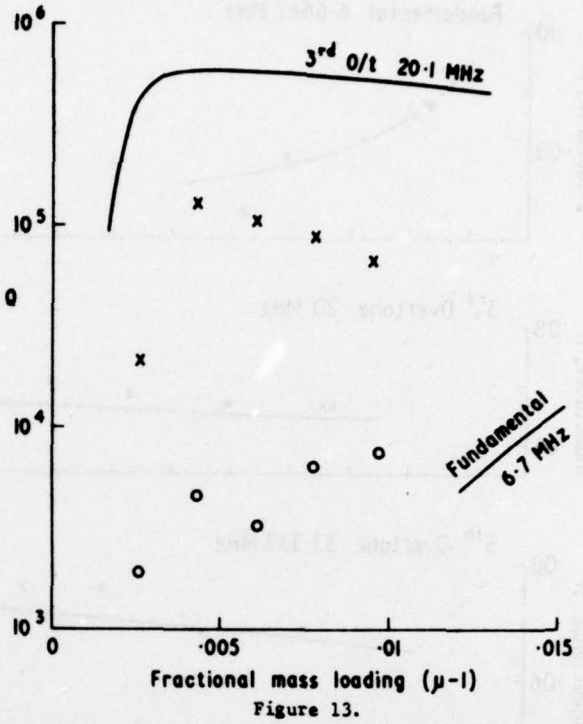

Figure 13.

Computed curves of Q v. fractional mass loading compared with some experimental results.
Experiments on 12 mm diameter crystals, computations are for 10 mm square crystals.

3rd O/t X

Fundamental ⊙

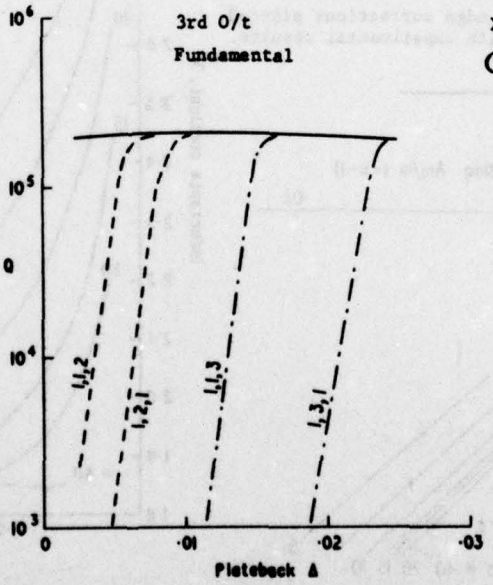

Figure 14. Computed curves of Q_{AIR} v. Δ for 1.5 mm square electrodes on an 8 mm square plate at 18.5 MHz fundamental frequency.

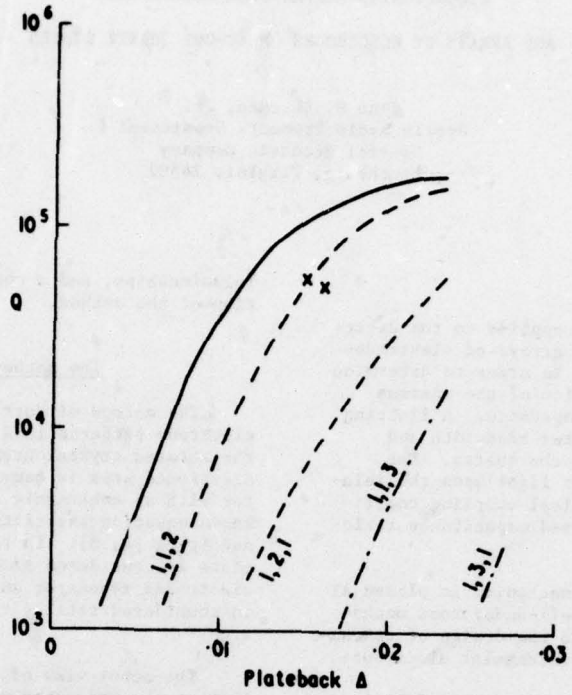

Figure 15. Computed curves of Q_{AIR} v. Δ for 1.5 mm square electrodes on a 4 mm square plate at 18.5 MHz fundamental frequency.

Experimental points using 4.5 mm diameter crystal blanks X

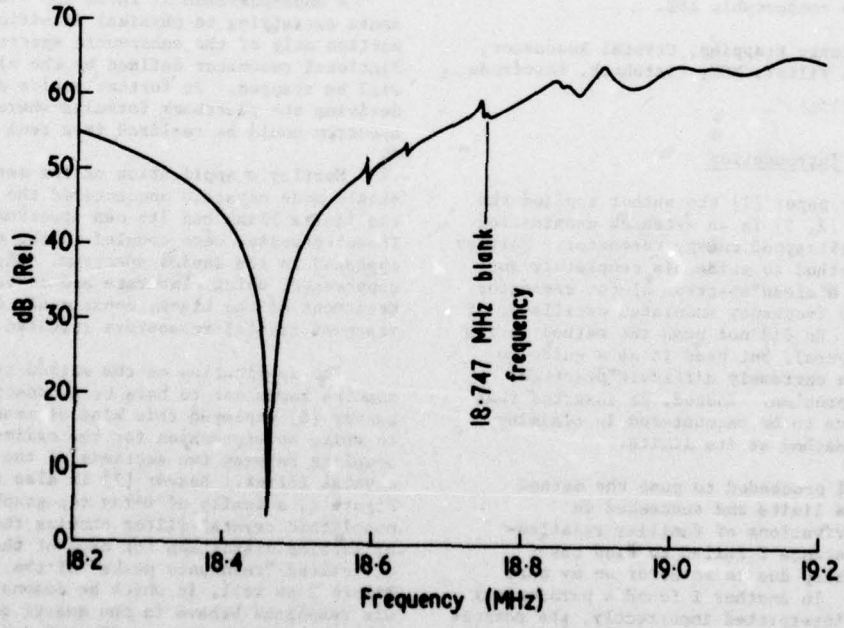

Figure 16. Response spectrum for an 18.5 MHz fundamental crystal with 1.5 mm square electrodes on a 4.5 mm diameter blank with Δ = 0.0151.

DIMENSIONING RECTANGULAR ELECTRODES

AND ARRAYS OF ELECTRODES ON AT-CUT QUARTZ BODIES

John H. Sherman, Jr.
Mobile Radio Products Department
General Electric Company
Lynchburg, Virginia 24502

Summary

The method of Mortley is applied to the determination of the dimensions of arrays of electrodes of monolithic crystal filters in order to determine those configurations which allow of the maximum plateback or of the minimum impedance. A limiting relation is found between filter bandwidth and impedance which is imposed by the quartz. The method is also applied to cast light upon the relationship of the electromechanical coupling coefficient of quartz and the observed capacitance ratio of crystals.

Flexure as a Q limiting mechanism in plated AT resonators is shown to be a well-understood mechanism readily incorporated into the design of resonators and filter arrays with rectangular electrodes.

The validity of the method is examined by examining the amplitude of the standing wave through the entire extended blank. The errors of the method are shown to be conservative. The dimensional ratios calculated are correct and the correct maximum of plateback is shown to exceed the maximum indicated in the method by a comfortable 18%.

Keywords: Energy trapping, Crystal Resonator, Monolithic Crystal Filter, MCF, Plateback, Electrode design.

Introduction

In an earlier paper [1] the author applied the method of Mortley [2, 3] in an extended examination of the single-mode trapped energy resonator. Mortley had created the method to guide his completely successful design of a clean spectrum AT-cut resonator used in a directly frequency modulated oscillator of high performance. He did not push the method to its limits (in his papers), but used it as a guide to the solution of an extremely difficult practical resonator design problem. Indeed, he asserted that there were problems to be encountered in claiming validity for the method at its limits.

In my paper I proceeded to push the method further toward its limits and succeeded in extracting new derivations of familiar relationships. In one instance I failed to find the familiar relationship due to an error on my part corrected herein. In another I found a paradoxical relation which I interpreted incorrectly, the correct interpretation of which leads to a demonstration of the kind and high degree of validity which can be ascribed to the method.

The present paper contains further useful results obtained by pushing the method -- rules for dimensioning arrays, more new derivation of familiar relationships, and a contribution toward the validation of the method.

The Method of Mortley

The method of Mortley presupposes rectangular electrode patterns laid out with edges parallel to the rotated crystalographic axes. Initially the electroded area is considered as an isolated resonator with an enharmonic spectrum given by the well-known equation associated with the names of McSkimin, and Sykes [4, 5]. In this view the remainder of the plate is considered simply as a support for the electroded resonator and the energy of the resonator is considered totally trapped within the electroded area.

The other view of the remainder of the plate is that at the frequency of the unelectroded plate the plate would act as an energy sink for the electroded area. At the plate frequency and above, the energy would be "un-trapped" and no electrode-associated resonance could occur.

A superposition of these two views yields a sense satisfying to physical intuition of how a portion only of the enharmonic spectrum of the fictional resonator defined by the electrode pattern will be trapped. It further yields an approach to deriving the plateback formulas whereby that limited spectrum could be realized in a real device.

Mortley's application of the method to generate single mode crystals encountered the problem that the finite blank had its own spectrum of responses. These responses were coupled to the electrodes and appeared in the device spectrum. When they were suppressed, using elaborate and ingenious edge treatment of the blank, consciously designed single response crystal resonators resulted.

The application of the method to more complex spectra seems not to have been consciously made. Beaver [6] employed this kind of reasoning in order to write an expression for the maximum value of the coupling between two sections of the monolithic crystal filter. Beaver [7] is also the source of Figure 1, a family of x-ray topographs of a 6-section monolithic crystal filter showing the standing wave of lattice distortion for each of the six short circulated "resonance peaks" of the crystal, and of Figure 2 as well, in which he demonstrated that these six responses behave in the quartz as six enharmonic responses of a resonator dimensioned essentially as the overall array.

To me this says the method of Mortley may offer further understanding of the properties of the array. Earlier I had found optimization formulas for single-response rectangular electroded resonators. This

clue should lead to similar optimization formulas for the arrays of monolithic crystal filters.

Application of the Method

The search for optimization criteria requires that a well-behaved array be clearly defined. Reference again to Figure 1 will illustrate behavior along the length and width of the array of a well-designed array.

The first thing to notice is that this array of 6 electrodes has 6 and not 7 enharmonic modes associated with the length of the array and has 1 and not 3 associated with the width. These 6 enharmonic modes result in six resonances which are identified with the six response peaks of the shorted filter. Note that this is really a reverse identification. Actually Beaver excited the six response peaks of the shorted filter and the x-ray topographs permit us to make the identification that they are the six enharmonic modes of the extended resonator.

These responses are all trapped by the extended resonator. The topographs illustrate the location of the trapping sites. The bandwidth of the filter is very well defined by these responses. In a sense the bandwidth of the filter itself can be said to be the separation of the lowest and highest of these response peaks. When the filter is inserted into a circuit which faces it with finite impedances the overall response will be slightly wider and much smoother, but this is an interactive effect.

Thus the entire bandwidth of the filter lies across the frequency range of the trapped responses. It follows that the frequency lowering of the entire array in phase, which is the lowest response peak of the filter, must exceed the bandwidth of the filter.

It is equally true that the array must not have 7 responses associated with its length nor 3 with its width or there would be at least one more trapped response and at least one more shorted response peak for the filter. Whatever the resulting filter would turn out to be, it certainly would not be the filter intended to be designed.

Thus a well-designed array of E electrode segments will have E and not E+1 enharmonic modes trapped along its length and 1 and not 3 associated with its width.* When this condition obtains then the plateback of the entire extended array with all electrodes in phase, the "main response" of the extended electrode, will equal or exceed the bandwidth of the filter.

This latter conclusion is necessary from another viewpoint as well. If any portion of the desired passband lies at such a frequency that it is not in the range trapped by the electrode array there is no propagation path through the quartz from the input to the output terminals. Under such circumstances that portion of the signal would not propagate through the filter and the realized passband would not be as wide as the desired one.

We now proceed to write the equation for the resonant frequencies of the electroded region, treating the entire array as a single developed electrode:

$$f_{mnp} = \frac{1}{2\sqrt{\rho}} \sqrt{\frac{m^2\bar{C}'_{66}}{t^2} + \frac{n^2\bar{C}'_{11}}{X^2} + \frac{p^2\bar{C}'_{55}}{Z^2}} \qquad (1)$$

$$= \frac{m}{2t}\sqrt{\frac{\bar{C}'_{66}}{\rho}}\sqrt{1 + \frac{t^2}{m^2\bar{C}'_{66}}\left(\frac{n^2\bar{C}'_{11}}{X^2} + \frac{p^2\bar{C}'_{55}}{Z^2}\right)}$$

$$= f_{moo}\sqrt{1 + \frac{t^2}{m^2\bar{C}'_{66}}\left(\frac{n^2\bar{C}'_{11}}{X^2} + \frac{p^2\bar{C}'_{55}}{Z^2}\right)} \qquad (2)$$

where X and Z are the array dimensions in the x and z' directions respectively and t = Y is the equivalent thickness of the resonator (in the y'direction). This thickness is of the fictional unelectroded resonator of the same extension as the electrodes which has the same gravest response. The indices m, n and p count the number of half waves in the standing wave of the resonance in the appropriate dimension of the resonator, m being the conventional overtone order. The elastic module $\bar{C}'$ ij are barred to remind me to use the piezoelectrically stiffened values when the time comes for numerical computation.

As noted, an array of E electrodes must have E and not E+1 enharmonic resonances along its length and 1 and not 3 resonances along its width. It is argued per the method that increasing plateback generally causes an enharmonic response in one direction before the other resulting in either less than the maximum plateback for a given inductance or more than the minimum inductance for a given bandwidth. Equating the expressions for the frequency of the two unwanted modes provides the formula for the proportions of the array which simultaneously optimizes this pair of parameters.

Long along Z:

$$f_{m1(E+1)} = f_{m31} \qquad (3z)$$

$$\frac{\bar{C}'_{11}}{X^2} + \frac{(E+1)^2\bar{C}'_{55}}{Z^2} = \frac{9\bar{C}'_{1}}{X^2}\ \frac{\bar{C}'_{55}}{Z^2} \qquad (4z)$$

$$\frac{Z^2}{X^2} = \frac{(E+1)^2-1}{8}\frac{\bar{C}'_{55}}{\bar{C}'_{11}} \qquad (5z)$$

* The reasoning for ignoring the even enharmonics across the width of the array is that these should not occur. The field should be exactly shorted out by the electrodes. If a second enharmonic is detected in the response of any unit, it is treated as evidence of defective processing either of the blank or of the electrode -- the defective unit is simply rejected. This may be considered differently in other establishments. If, the second must be suppressed by design then the "numbers", which can be derived by the same principles, will be much more restrictive.

similarly, "Long along X":

$$f_{m(E+1)1} = f_{m13} \qquad (3x)$$

generates

$$\frac{X^2}{Z^2} = \frac{(E+1)^2-1}{8}\,\frac{\bar{C}'_{66}}{\bar{C}'_{11}} \qquad (5x)$$

These relationships give the ratio of array length to width which permits the greatest plateback, since neither the length nor the width will trap the first unwanted response before the other. For the same argument these relationships give the ratio which yields the largest area of array.

In the frequency equation f_{moo} is what is known as a "characteristic frequency". From the equation it is seen that a resonance at this frequency would require either an electrode of infinite extent or zero variation in the amplitude of the disturbance across the electrode. Since neither of these conditions can be achieved, f_{moo} is not accessable for measurement. In the literature of energy trapping f_{moo} is called f_e, the characteristic frequency of the electroded area. The lowest observable frequency of the electrodes is f_{m11}.

Another characteristic frequency pertains to the unelectroded quartz surrounding the electroded area. This frequency called f_s in the energy trapping literature is also, strictly speaking, not measurable. For a rectangular blank it can be calculated from the blank frequency and the blank dimensions. If the blank is to have edge treatment to suppress total system resonances f_s must be known. If total system resonances will be allowed to occur then the measured blank frequency should be used for f_s anyway. This is the frequency at which energy spreads from the electroded area into the entire blank.

The maximum electrode (thickness or area) is that at which the first unwanted response just escapes into the whole blank.

Again considering "Long along Z" define, following Beaver,

$$\Delta f = f_s - f_{m11} \geq BW$$

and $$\Delta = \Delta f / f_{m11}$$

and recalling Equation 3

$$f_s = f_{m11} + \Delta f \leq f_{m31} = f_{m1}\,(E+1)$$

$$1 + \Delta \leq f_{m31}/f_{m11} = f_{m1}(E+1)/f_{m11} \qquad (6)$$

$$1+\Delta \leq \sqrt{\frac{1+\frac{\bar{C}'_{11}\,t^2}{m^2\bar{C}'_{66}X^2}\left(\frac{8}{(E+1)^2-1}\right)^{+9}}{1+\frac{\bar{C}'_{11}\,t^2}{m^2\bar{C}'_{66}X^2}\left(\frac{8}{(E+1)^2-1}\right)^{+1}}} \qquad (7)$$

$$= \sqrt{1+\frac{8\bar{C}'_{11}\,t^2}{m^2\bar{C}'_{66}X^2} + \text{other terms}}$$

similarly "Long along X" generates

$$1+\Delta \leq \sqrt{1+\frac{8\bar{C}'_{55}\,t^2}{m^2\bar{C}'_{66}Z^2} + + \text{other terms}} \qquad (8x)$$

Whence by the standard approximation

$$1+\Delta \leq 1+\frac{4\bar{C}'_{11}\,t^2}{m^2\bar{C}'_{66}X^2} \qquad 1+\Delta \leq 1+\frac{4\bar{C}'_{55}t^2}{m^2\bar{C}'_{66}Z^2} \qquad (9)$$

and

$$\Delta \leq \frac{4\,\bar{C}'_{11}t^2}{m^2\bar{C}'_{66}X^2} \qquad \Delta \leq \frac{4\bar{C}'_{55}t^2}{m^2\bar{C}'_{66}Z^2} \qquad (10)$$

Equations 10 and 5 are cast into the conventional form of design equations by inserting numerical values* and rearranging:

$$\frac{X}{t}\Delta^{1/2} \leq \frac{3.88}{m} \qquad \frac{Z}{t}\Delta^{1/2} \leq \frac{3.07}{m} \qquad (11)$$

$$\frac{Z}{X} = 0.794\sqrt{\frac{(E+1)^2-1}{8}} \qquad \frac{X}{Z} = 1.26\sqrt{\frac{(E+1)^2-1}{8}} \qquad (12)$$

$$\Delta \geq \frac{(BW)}{f_{m11}} \qquad \Delta \geq \frac{(BW)}{f_{m11}}$$

Limitations on MCF Realization

The foregoing derivations reflect upon the possible relationships between bandwidth and terminating impedance which can be realized in a monolithic crystal filter. Taking frequencies in Hz, dimensions in mm, inductance in henries and impedances in ohms, we may write, per electrode segment [6]

$$L \quad \frac{1.8E\,(10)^{20}m^3}{f^3\,A}$$

$$= \frac{1.8E\,(10)^{20}m^3}{f^3\,X\,Z}$$

$$= \frac{1.8E\,(10)^{20}m^3}{f^3\,X^2}$$

*In this paper three elastic constants keep recurring C'_{11}, C'_{55} and C'_{66}. These have different values for static deformations and for waves. For waves the symbol is written with a bar, viz, $\bar{C}'_{11}$

$C'_{11} = 86.740\text{X}10^9$ $\qquad$ $\bar{C}'_{11} = 110.602\text{X}10^9$

$C'_{55} = 68.807\text{X}10^9$ $\qquad$ $\bar{C}'_{55} = 69.241\text{X}10^9$

$C'_{66} = 29.013\text{X}10^9$ $\qquad$ $\bar{C}'_{66} = 29.350\text{X}10^9$

and since

$$f \simeq mk_f/t$$

$$L \geq \frac{1.8\ E\ (10)^{20}\ m^3}{FK^2_f m^2 \frac{X^2}{t^2}\sqrt{\frac{\bar{C}'_{55}}{\bar{C}'_{11}}}\sqrt{\frac{(E+1)^2-1}{8}}}$$

Furthermore

$$\frac{X^2}{t^2} \leq \frac{4\bar{C}'_{11}}{m^2\ \bar{C}'_{66}}$$

and

$$\Delta \geq (BW)/f$$

and substituting for $K_f = 1.66 \times 10^6$

$$L \geq 4.62\ (10)^7\ m^3\ \frac{\bar{C}'_{66}}{\sqrt{\bar{C}'_{11}\ \bar{C}'_{55}}}\ \frac{E}{\sqrt{(E+1)^2-1}}\ \frac{(BW)}{f^2}$$

$$L \geq 1.55\ (10)^7\ m^3\ \frac{E}{\sqrt{(E+1)^2-1}}\ \frac{(BW)}{f^2} \qquad (14)$$

When designing a filter by recent methods a designer has access to the properties of tabulated normalized filters [9]. He either uses one of those already tabulated or has the problem of calculating a new normalized filter, then by well known principles "denormalizing" it to get actual component values for the filter.

The element inductance of the monolithic crystal filter is given by:

$$L = \frac{R\ N_1}{2\ \pi\ (BW)}$$

where N_1 is the first normalized element value and R is the resistive source or load terminating the filter.

Writing this for L in the preceding inequality yields:

$$R > \frac{2.9(10)^8 m^3}{N_1}\ \frac{\bar{C}'_{66}}{\sqrt{\bar{C}'_{11}\ \bar{C}'_{55}}}\ \frac{E}{\sqrt{(E+1)^2-1}}\ \frac{(BW)^2}{f^2}$$

$$> \frac{9.73(10)^8 m^3}{N_1}\ \frac{E}{\sqrt{(E+1)^2-1}}\ \frac{(BW)^2}{f^2} \qquad (15)$$

This limitation imposed by the medium is not normally the first encountered. In most instances bandwidth limitations due to the electrical properties of C_0 are encountered, requiring the use of external coils for C_0 cancellation. This relationship describes the kind of limitation which the quartz substrate imposes over and beyond the effects of circuit elements.

Single Mode Resonators

Because in a symmetrical singly electroded configuration the electrode will short out the field of an antisymmetric distribution of lattice distortion the equations written here have allowed across the width 1, not 3, half waves instead of 1, not two. In the case of singly electroded resonator, then one can plateback as if 2, not 3 is allowed. When this is done in this derivation the radical

$$\sqrt{\frac{(E+1)^2-1}{8}}$$

becomes unity and equations 5 and 10 reduce to

$$\frac{Z}{X}\sqrt{\frac{\bar{C}'_{55}}{\bar{C}'_{11}}} = .794 \qquad \frac{X}{Z}\sqrt{\frac{\bar{C}'_{11}}{\bar{C}'_{55}}} = 1.26 \qquad (16)$$

$$\frac{X}{t}\Delta^{1/2} \leq \frac{3.88}{m} \qquad \frac{Z}{t}\Delta^{1/2} \leq \frac{3.07}{m} \qquad (17)$$

This 1.26 is the correct ratio of the dimensions for the optimum electrode on AT quartz, a correction of the erroneous value derived in [1]. The error in [1] is the consequence of using "static" constants to evaluate the derived expressions numerically [10].

Capacitance Ratio

The electrode has another effect on the nature of the resonances discussed. Without an electrode all of the resonances are of the nature of anti-resonances, but with the electrode a series resonance can occur as well, and as at least an intellectual exercise we can discuss the behavior of a massless electrode on a quartz plate. Whatever happens due to the massless electrode happens in an ideological sense "first", and to its consequence is added the consequence of the mass of the electrode material.

To do this we recall Equation 2

$$f_{mnp} = f_{moo}\sqrt{1 + \frac{t^2}{m^2\bar{C}'_{66}}\left(\frac{n^2\bar{C}'_{11}}{X^2} + \frac{p^2\bar{C}'_{55}}{Z^2}\right)} \qquad (2)$$

and require, as always, that

$$\frac{X^2}{Z^2} = \frac{\bar{C}'_{11}}{\bar{C}'_{55}}$$

so

$$f_{mnp} = f_{moo}\sqrt{1 + \frac{t^2\bar{C}'_{11}}{X^2\bar{C}'_{66}}\left(\frac{n^2 + p^2}{m^2}\right)}$$

which we will write as

$$\frac{f^2_{mnp}}{f^2_{moo}} = 1 + \frac{t^2\bar{C}'_{11}}{X^2\bar{C}'_{66}}\left(\frac{n^2 + p^2}{m^2}\right) \qquad (18)$$

This is similar in form to the equation relating the resonances of a practical crystal unit:

$$\frac{f_a^2}{f_s^2} = 1 + \frac{1}{r_c}$$

which basically describes a matter equally independent of the mass of the electrodes.

The capacitance ratio gives an expression for the partition of energy between the electrode capacitance and the motional capacitance; the electromechanical coupling coefficient gives an expression for the partition of the electrical and mechanical energy. They are both measures of the same thing and are related by the well-known formula

$$\frac{C_e}{C} = \frac{\pi^2}{8K^2}$$

Substituting for K its value for AT quartz 0.0880,

$$\frac{C_e}{C} = 159.3$$

The massless electrode hasn't affected the antiresonant frequency of the quartz which still is f_s, while it has established another characteristic frequency for the series resonant frequency which is related as:

$$\frac{f_a^2}{f_o^2} = \frac{f_s^2}{f_{100}^2} = 1 + \frac{1}{159.3}$$

We can consider the spectrum as the area of the massless electrode is allowed to grow and recognize that at some electrode area another mode will be trapped, then another. f_{111} will continue to decrease, approaching f_{100} and the antiresonant frequency will remain f_s. If we look at the condition at which this system is marginally a single mode system, that is when $f_{113} = f_{131} = f_s$, we can write

$$\frac{f_{113}}{f_{100}^2} = \frac{f_{131}}{f_{100}^2} = 1 + \frac{1}{159.3} = 1 + 10\,\frac{t^2\,\bar{C}'_{11}}{X^2\,\bar{C}'_{66}}$$

Whence

$$\frac{X}{t} = \sqrt{1593\,\frac{\bar{C}'_{11}}{\bar{C}'_{66}}} = 77.5\,, \quad \frac{Z}{t} = .794\,\frac{X}{t} = 61.5$$

which is a large electrode, but this is not surprising as this is a very small plateback, the theoretical minimum.

Though we cannot measure f_{100}, ever, in this case we know it surely and can calculate from it f_{111}.

$$\frac{f_{111}^2}{f_{100}^2} = 1 + 2\,\frac{t^2}{X^2}\left(\frac{\bar{C}'_{11}}{\bar{C}'_{66}}\right)$$

and

$$\frac{f_a^2}{f_o^2} = \frac{f_s^2}{f_{111}} = \frac{1 + 10\,\dfrac{t^2\,\bar{C}'_{11}}{X^2\,\bar{C}'_{66}}}{1 + 2\,\dfrac{t^2\,\bar{C}'_{11}}{X^2\,\bar{C}'_{66}}}$$

$$= \frac{1 + \dfrac{1}{159.3}}{1 + \dfrac{1}{5(159.3)}} = 1.005015674$$

$$= 1 + \frac{1}{r_c}$$

From this

$$r_c = 199.4 \qquad (20)$$

If an expression is extracted for just the capacitance ratio associated with f_{m11} in, this limiting case it is, to a very good approximation (see Equation 8):

$$r_c \simeq \frac{m^2\,X^2\,\bar{C}'_{66}}{8\,t^2\,\bar{C}'_{11}} \simeq 200\,m^2$$

which asserts that the capacitance ratio varies with the square of the overtone order. This, of course, is not a newly discovered relationship, but it is reassuring, again, that the method yields the right result.

Anticipating a result generated in the last section of the paper which shows that the accurate frequency lowering is greater than that calculated by the method, this coefficient is adjusted from approximately 200 to 172. This is a very credible number for the ratio of capacitance of crystals which is often measured in the practical case right around 180.

This is what happens first, due to the conductivity of the electrode. The mass of the electrode depresses both of these frequencies, but a crystal maintains essentially this capacitance ratio, which is solely the consequence of the conductivity of the electrode.

Flexure

Sykes [11] presents an empirical formula for the flexure resonances of an AT-cut rectangular blank. His expression expresses the condition for a flexure overtone frequency to coincide with the thickness mode frequency. He writes:

$$f_{xf} = \frac{1338.4}{X}\,n_{xf}$$

and notes that even values of n represent resonances which are coupled, hence interefere, with the xy shear mode. The odd values are not coupled to the shear, hence provide a method for the optimum dimensioning of the blank. If $2\underline{K}$ be written for n and the resulting frequency expression equated to the xy shear frequency there results

$$\frac{1338.4}{X}(2\underline{K}) = \frac{1660}{t}$$

or

$$\frac{X}{t} = 1.613\underline{K}$$

One way of viewing the generation of xy shear in a crystal is as the consequence of pairs of couples with axes along Z' applied at the two x-ends of the electrode. This is equivalent to a number of other presentations, but has the advantage that it focuses attention on the generation of flexure.

Each couple, in addition to generating a shear which is trapped by the electrode, generates a flexure wave which can propagate through the entire blank. An the couples occur in pairs. The phase of each flexure wave passing the axis of the other couple depends upon the velocity of the flexure wave and upon the separation of the couples along x. At certain separations the two flexure waves are exactly out of phase and the flexure amplitude is everywhere zero. When this condition occurs the flexure extracts zero energy from the electroded area and the resonator Q is maximized. Half way between the flexure amplitude is maximum, the maximum energy is transported from the electrode and Q is minimums.

Mindlin and Lee [12] addressed this situation and generated the curve of Figure 3 relating the Q of a trapped energy resonator with rectangular electrodes to the X/t ratio of the electrode. The periodicity of the Q maxima is 1.608 thicknesses, or

$$\frac{X}{t} = 1.608\ K$$

This is certainly the same periodicity Sykes discussed, but with the difference that this is an optimum electrode dimension formula, not a blank dimension formula to be avoided. Also half way between these ratios are the minimum Q electrode ratios, not the optimum blank dimensions. It is easy to recognize the source of the difference in the reflection which the flexure wave suffers at the boundary of the blank. There is no reflection at the boundary of the electrode. This causes the significance of the even and odd multipliers of the basic periodicity of 0.8 X/t to be interchanged.

This result interacts with the results earlier for the X/t ratio. If is is necessary to design for the maximum Q then this relationship, which applies to each individual electrode and not to the overall array, must be observed along with the plateback limitation. When combined with the inductance specification which sets the electrode area the Q requirement may cause the entire array proportion to deviate slightly from optimum. When this occurs the maximum plateback must again be reduced, though only slightly.

If the array is laid out along Z' it becomes quite easy to design for maximum Q, as the x-dimension of the resonators is simply the width of the array. If the array is laid out along x then adjusting the length of each resonator for Q will affect the overall length of the array, hence the resonator separation, making necessary an iterative calculation of the final array dimensions and plateback.

Amplitude Distribution

Central to the understanding of the limitations of the method is the recognition of how the model is oversimplified. The method posits an "all or nothing at all" condition of reflection of energy at the boundary of the electrode. Trapped energy is not held this way, in fact.

The introduction of a finite region of characteristic frequency f_e into the extended region of characteristic frequency f_s creates a situation exactly analogous to the finite rectangular potential well employed so extensively in basic Quantum Mechanics courses [13] to teach Schroedinger [1 [13, 14, 15] methods. The normalized acoustic amplitude is the accurate analogue of the Schroedinger amplitude and the trapped energy in any region of the Born expectation for that region. The indication, then, is that the method of Mortley is related to the complete description of a resonator as classical particle physics is to the wave mechanics of potential wells and boxes.* In this sense it is an example of the complementarity proclaimed by Bohr.

To study the fringing of the trapped energy of an AT resonator at the boundaries of the electrode, propagation constants are written in the form:**

$$\xi_x = \frac{\pi}{t}\sqrt{\frac{\bar{c}'_{66}}{\bar{c}'_{11}}}\sqrt{\frac{w_x^2 - w^2}{w_x^2}}$$

$$\xi_z = \frac{\pi}{t}\sqrt{\frac{\bar{c}'_{66}}{\bar{c}'_{55}}}\sqrt{\frac{w_x^2 - w^2}{w_x^2}}$$

*Actually of the original DeBroglic formulation to Schroedinger's. Slater in [13] disposes of the problem of a particle in a potential well in a condensed mathematical treatment and describes, almost in passing the case of two wells. He illustrates the amplitude distribution of four modes in a single well and two modes in a pair of wells, thus outlining the solution of the single resonator and the coupled dual. Rojansky, [14] in 1941, discussed both a particle in a box and a particle in a well. On the other hand the University of Pittsburg staff [15] in 1936 only discussed the particle in a box. (This method of Mortley finds solutions like those of a particle in a box.) Apparently the quantum physicists learned to handle the penetrable wall just before 1940.

**In the material to follow, lower case w is typed for the frequency variable omega. Although initially shocking, the expressions are readily followed.

where the frequency w_x is the characteristic frequency associated with the region of interest, either the electrode (w_e) or the surrounding extended blank (w_s). The domain of w is the range $w_e < w \leq w_s$. The elastic constants will be written singly or doubly primed depending upon whether they apply to the electroded or non-electroded regions.

Since the two directions have their propagation functions formulated similarly except that $\bar{C}'_{11}$ is written for the x-direction and $\bar{C}'_{55}$ for the z-direction, only one will be followed in detail in derivation and the other written when necessary by symmetry.

Since $w_e < w$, $\dfrac{w_e^2 - w^2}{w_e^2}$ is imaginary,

giving rise to a sinusoidal amplitude distribution of the standing wave under the electrode. The distribution outside the electrode is, by the same token, exponential.

The electroded domain and the surrounding domain will be examined in the right half plane, in parallel:

Electroded Domain	Surrounding domain
$0 \leq x \leq X/2$	$X/2 \leq x < \infty$
Sinusoidal envelope	Exponential envelope

Case 1; Even functions:

$$U = A \cos\frac{\pi x}{t}\sqrt{\frac{\bar{C}'_{66}}{\bar{C}'_{11}}}\sqrt{\frac{w^2 - w_e^2}{w_e^2}} \qquad U = B \exp\frac{\pi x}{t}\sqrt{\frac{\bar{C}''_{66}}{\bar{C}''_{11}}}\sqrt{\frac{w_s^2 - w^2}{w_s^2}} \tag{24}$$

Since both the amplitude and the derivative of the amplitude must be continuous across the electrode boundary, the logarithmic derivative must also be continuous across the boundary.

$$\frac{1}{U}\frac{dU}{dx} = \frac{-\pi}{t}\sqrt{\frac{\bar{C}'_{66}}{\bar{C}'_{11}}}\sqrt{\frac{w^2 - w_e^2}{w_e^2}}\tan\frac{\pi x}{t}\sqrt{\frac{\bar{C}'_{66}}{\bar{C}'_{11}}}\sqrt{\frac{w^2 - w_e^2}{w_e^2}} \cdot \qquad \frac{1}{U}\frac{dU}{dx} = \frac{-\pi}{t}\sqrt{\frac{\bar{C}''_{66}}{\bar{C}''_{11}}}\sqrt{\frac{w_s^2 - w^2}{w_s^2}}$$

which expressions are to be equated at x = X/2, resulting in:

$$\tan\frac{\pi X}{2t}\sqrt{\frac{\bar{C}'_{66}}{\bar{C}'_{11}}}\sqrt{\frac{w^2 - w_e^2}{w_e^2}} = \sqrt{\frac{\bar{C}'_{11}\bar{C}''_{66}}{\bar{C}''_{11}\bar{C}'_{66}}}\sqrt{\frac{w_e^2(w_s^2 - w^2)}{w_s^2(w^2 - w_e^2)}} \tag{25}$$

The radical containing all four $\bar{C}$ coefficients will be called Q. Using the identity $\cos x = 1/\sqrt{1 + \tan^2 x}$ equation (24) can be evaluated at X/2, allowing the amplitude continuity to be made explicit:

$$B = \pm A\sqrt{\frac{w_s^2(w^2 - w_e^2)}{(Q-1)w_e^2 w_s^2 + w^2(w_s^2 - Qw_e^2)}} \tag{26}$$

while equation (25) will yield to iterative numerical solution to supply frequencies.

Case 2; Odd functions:

$$U = A \sin\frac{x}{t}\sqrt{\frac{\bar{C}'_{66}}{\bar{C}'_{11}}}\sqrt{\frac{w^2 - w_e^2}{w_e^2}} \qquad U = B \exp\frac{x}{t}\sqrt{\frac{\bar{C}''_{66}}{\bar{C}''_{11}}}\sqrt{\frac{w_s^2 - w^2}{w_s^2}} \tag{27}$$

When this pair of equations are treated as above, the result is to replace tan with cot in the equation which corresponds to (25) and everything else is identical. We will, therefore no longer make anything of the difference between even and odd amplitude functions, but will lump them together.

With this condensation (25) becomes:

$$\tan\frac{\pi X}{2t}\sqrt{\frac{\bar{C}'_{66}}{\bar{C}'_{11}}}\sqrt{\frac{w^2-w_e^2}{w_e^2}}=\sqrt{\frac{\bar{C}'_{11}\bar{C}''_{66}}{\bar{C}''_{11}\bar{C}'_{66}}}\sqrt{\frac{w_e^2(w_s^2-w^2)}{w_s^2(w^2-w_e^2)}}$$

In order to examine the untrapping of energy we let w equal w_s. Since we are considering only variations in the x' direction we are dealing with the frequency in our old nomenclature, f_{1n0}. Now $w-w_e = 0$, and:

$$\tan\frac{\pi X}{2t}\sqrt{\frac{\bar{C}'_{66}}{\bar{C}'_{11}}}\sqrt{\frac{w_s^2-w_e^2}{w_e^2}}=0 \qquad (28)$$

which is satisfied by the condition:

$$\frac{\pi X}{2t}\sqrt{\frac{\bar{C}'_{66}}{\bar{C}'_{11}}}\sqrt{\frac{w_s^2-w_e^2}{w_e^2}}=\frac{n\pi}{2}, \quad n \text{ an integer} \qquad (29)$$

Solving this for w_s/w_e yields:

$$\frac{w_s}{w_e}=\frac{f_{1n0}}{f_{100}}=\sqrt{1+\frac{n^2t^2\bar{C}'_{11}}{X^2\bar{C}'_{66}}} \qquad (30)$$

A similar derivation based upon propagation along z' would develop the parallel expression:

$$\frac{w_s}{w_c}=\frac{f_{10p}}{f_{100}}=\sqrt{1+\frac{p^2t^2\bar{C}'_{55}}{Z^2\bar{C}'_{66}}} \qquad (31)$$

These are recognized to be the relationships postulated according to the method and constitute a substantial validation of the method. We write with substantial confidence:

$$\frac{f_{1np}}{f_{100}}=\sqrt{1+\frac{n^2t^2\bar{C}'_{11}}{X^2\bar{C}'_{66}}+\frac{p^2t^2\bar{C}'_{55}}{Z^2\bar{C}'_{66}}} \qquad (32)$$

A suspicion that a term in $\bar{C}'_{15}$ might properly appear is purely of academic interest, since $\bar{C}'_{15}$ is zero.

This development applies to the marginal untrapping of the frequency f_{1np}, that is at the condition:

$$f_{1np} = f_s$$

and is a necessary relation for the method to be valid. From this relation all the dimension ratios were derived, so the dimension ratios are also shown to be valid.

What remains for validation of the method is to examine the frequency f_{111}. The amplitude distribution of f_{111} is even so the equation to be studied is Equation 25. Solutions of this equation must satisfy Equation 24:

$$\tan\frac{\pi X}{2t}\sqrt{\frac{\bar{C}'_{66}}{\bar{C}'_{11}}}\sqrt{\frac{w^2-w_e^2}{w_e^2}}=\sqrt{\frac{\bar{C}'_{11}}{\bar{C}''_{11}}\frac{\bar{C}''_{66}}{\bar{C}'_{66}}}\sqrt{\frac{w_e^2(w_s^2-w^2)}{w_s^2(w^2-w_e^2)}} \qquad (25)$$

which is capable of numerical solution.

The first thing to note is that this equation always has at least one solution. Naive application of the method leads to the conclusion that there is a certain minimum of plateback required before energy can be trapped. The wave mechanical analogue of this error is the presumption that the walls of a potential well of finite depth are impenetrable. Impenetrable walls are of infinite height -- these are the bounds of the real crystal blank. The bounds of the electrode are finite walls of quite moderate height, of only a few percent and are penetrable.

A substantial amount of discussion of this minimum is to be found in [1]. This was misguided effort. A real minimum requirement of plateback can occur if the electrode is designed to come too close to the edge of the wafer, but no otherwise well designed crystal will fail to trap at least one mode because the frequency lowering due to the electrode is too small. On the other hand too heavy a freq. plate spot can trap a mode of its own inside the electrode region below the first response of the main electrode deposit. (The wave mechanical analogue of a freq. plate spot is a depression in the bottom of a finite recess, just as the analogue of the electrode on a real wafer is of a finite recess in the bottom of an infinitely deep well.) On this basis, and because there really is a minimum here to trap an unwanted additional mode, the freq. plate frequency lowering must be kept less than that minimum.

Numerical Calculations of Resonant Frequency

According to the frequency equations used in the method of Mortley the resonant frequency is related to the electrode characteristic frequency at the optimum X: Z ratio by

$$\frac{f_{111}}{f_{100}}=\sqrt{1+\frac{2\bar{C}'_{11}t^2}{\bar{C}'_{66}X^2}}$$

while the untrapping frequency, identified with f_{113} or f_{131} is given by

$$\frac{f_{113}}{f_{100}}=\sqrt{1+\frac{10\bar{C}'_{11}t^2}{\bar{C}'_{66}X^2}}$$

This latter equation is the point of intersection of the two computational approaches discussed in this paper. The comparison of the two approaches is made by computing f_{113}/f_{111} by both for the same value of f_{113}/f_{100}. For ease of computation a convenient value of f_{113}/f_{111} is chosen and f_{113}/f_{100} computed by the method. This makes both of these rational numbers and allows the easy comparison of the computed number with the chosen one.

Let:

$$\frac{f_{113}}{f_{111}} = 1 + \Delta$$

$$\frac{f_{113}^2}{f_{111}^2} = (1+\Delta)^2 = \frac{1+\dfrac{10\bar{C}'_{11}}{\bar{C}'_{66}}\dfrac{t^2}{X^2}}{1+\dfrac{2\bar{C}'_{11}}{\bar{C}'_{66}}\dfrac{t^2}{X^2}} \qquad (33)$$

so

$$\frac{2\bar{C}'_{11}}{\bar{C}'_{66}}\frac{t^2}{X^2} = \frac{(1+\Delta)^2-1}{5-(1+\Delta)^2} \qquad (34)$$

whence

$$\frac{f_{113}^2}{f_{100}^2} = \frac{w_s^2}{w_e^2} = 1 + 5\left[\frac{(1+\Delta)^2-1}{5-(1+\Delta)^2}\right] \qquad (35)$$

and

$$\frac{X}{t} = \sqrt{\frac{\bar{C}'_{66}}{\bar{C}'_{11}}}\sqrt{\frac{2\,[5-(1+\Delta)^2]}{(1+\Delta)^2-1}} \qquad (36)$$

So if we let

$$\frac{X}{t} = \rho\sqrt{\frac{\bar{C}'_{66}}{\bar{C}'_{11}}},\quad \frac{w_s^2}{w_e^2} = K^2 \text{ and } \frac{w_s^2}{w^2} = \phi^2$$

equation 25 transforms into

$$\tan\rho\frac{\pi}{2}\sqrt{\frac{K^2-\phi^2}{\phi^2}} = \sqrt{\frac{\bar{C}'_{11}}{\bar{C}''_{11}}\frac{\bar{C}''_{66}}{\bar{C}'_{66}}}\sqrt{\frac{\phi^2-1}{K^2-\phi^2}}$$

which is to be solved for ϕ

The coefficient $\sqrt{\dfrac{\bar{C}'_{11}}{\bar{C}''_{11}}\dfrac{\bar{C}''_{66}}{\bar{C}'_{66}}}$ requires evaluation. It is evaluated at identically unity for the reason that the amplitude of the standing wave is continuous across the boundary of the electrode. Piezoelectric stiffening is the consequence of the wave itself and not of the electrode. While a problem of interpretation exists beyond the boundary, at the boundary of the electrode the elastic constants are continuous.

The equation to be solved numerically, then is:

$$\tan\rho\frac{\pi}{2}\sqrt{\frac{K^2-\phi^2}{\phi^2}} = \sqrt{\frac{\phi^2-1}{K^2-\phi^2}} \qquad (37)$$

The solution and various other relationships of interest are plotted in Figure 4, plotted as functions of Δ in the range of 1 to 7 percent.

Curve 1 is the value of X/t corresponding to Δ on a scale range of 0 to 100. The value of Z/t corresponding is found by dividing by 1.26.

Curve 2 is a curve of K-1, the fractional value $(w_s - w_e)/w_e$, the scale is read in percent.

Curve 3 is a curve of ϕ-1, the fractional value $(w_s-w)/w$, the scale is read in percent. This is the result of the solution of the equation, and is the primary objective of this part of the study. The point to be noted is that this lies above Curve 4, which is Δ plotted vs Δ by some 18%. This indicates that the method of Mortley contains a safety factor of 18%, and that the values of plateback given as limits of inequalities may often actually be used, treating the inequalities as equations.

Curve 4 is simply Δ plotted against Δ to facilitate the interpretation of curves 2 and 3.

Curve 5 is a plot of $\rho\sqrt{\dfrac{K^2-\phi^2}{\phi^2}}$ and is the fraction of a half wave in the sinusoidal part of the standing wave lying under the electrode, the range of the scale is from 0 to 1. This fraction ranges from 82.9% at 1% to 81.9% at 7% plateback, an average of 82.4%. This implies an interpretation of the fringe (there may well be more than one interpretation) as totaling 17.6% of the x and z' extension of the electrode, 8.8% on a side. The fringe can thus be found by combining curves 1 and 5 appropriately.

Conclusions

The method of Mortley provides a convenient method of determining useful design equations for the electrodes of both resonators and monolithic crystal filters. Detailed examination of the amplitude distribution in an electroded resonator has disclosed that the approximation involved is conservative and the design principles derived may be used with confidence.

Acknowledgements

Figures 1 and 2 are reprinted from W. D. Beaver, "Theory and Design of the Monolithic Crystal Filter," 21st Annual Frequency Control Symposium, 1967 by permission of Dr. Beaver.

Figure 3 which appears in Mindlin and Lee "Thickness - Shear and Flexural Vibrations of Partially Plated, Crystal Plates," Int. J. Solids Structures, 1966 Vol. 2 and also in Mindlin "Studies in the Mathematical Theory of Vibrations of Crystal Plates," 20th Annual Frequency Control Symposium, 1966 is reprinted by permission of Dr. Mindlin.

Particular acknowledgement is due to Dr. Arthur Ballato of USAEL, Fort Monmouth whose criticism of this paper in draft was of greatest assistance.

References

1 Sherman, J. H., "A Novel Algorithm for the Design of the Electrodes of Single-Mode AT-Cut Resonators," Proc. 23rd Annual Frequency Control Symposium, 1969.

2 Mortley, W. S., "Circuit Giving Linear Frequency Modulation of a Quartz Crystal Oscillator," Wireless World 57, October 1951.

3 Mortley, W. S., "Frequency-Modulated Quartz Oscillators for Broadcasting Equipment," Proc. IEE, Vol. 104B, May 1957.

4 Sykes, R. A., "Modes of Motion in Quartz Crystals, the Effects of Coupling and Methods of Design," BSTJ Vol. XXII, No. 1 reprinted as Heising "Quartz Crystals for Electrical Circuits," Van Nostrand, Chapter 6.

5 McSkimin, H. J., "Theoretical Analysis of Modes of Vibration for Isotropic Rectangular Plates Having All Surfaces Free," BSTJ Vol. XXIII, No. 2, reprinted as Heising Chapter 7 (see [4]).

6 Beaver, W. D., "Theory and Design Principles of the Monolithic Crystal Filter," Doctoral Dissertation, Lehigh University, 1967; University Microfilm, 1967.

7 Beaver, W. D., "Theory and Design of the Monolithic Crystal Filter," Proc. 21st Annual Frequency Control Symposium, 1967.

8 Sykes, R. A., Smith, W. L., and Spencer, W. J., "Monolithic Crystal Filters," 1967 IEEE International Convention Record, pt. 11, pp 78-93, p 84 eq. (22)

9 Weinberg L., "Network Analysis and Synthesis" McGraw-Hill, 1962.

10 Sheahan, D. F., "An Improved Resonance Equation for AT-Cut Quartz Crystals," Proc. IEEE, Vol. 58, No. 2, February 1960, pp 260-261.

11 Ref. [4] Equation 6.19.

12 Mindlin, R. D. and Lee, P. C. Y., "Thickness-Shear and Flexural Vibrations of Partially Plated, Crystal Plates," Int. J. Solids Structures, 1966, Vol. 2.

13 Slater, J. C., "Quantum Theory of Atomic Structure," Vol. 1, Chapter 3, McGraw-Hill 1960.

14 Rojansky V., "Introductory Quantum Mechanics," Chapter 4, Pientice Hall 1942.

15 Pitt. U. Physics Staff, "Atomic Physics," 2nd Ed., Chapter 8, Wiley, 1937.

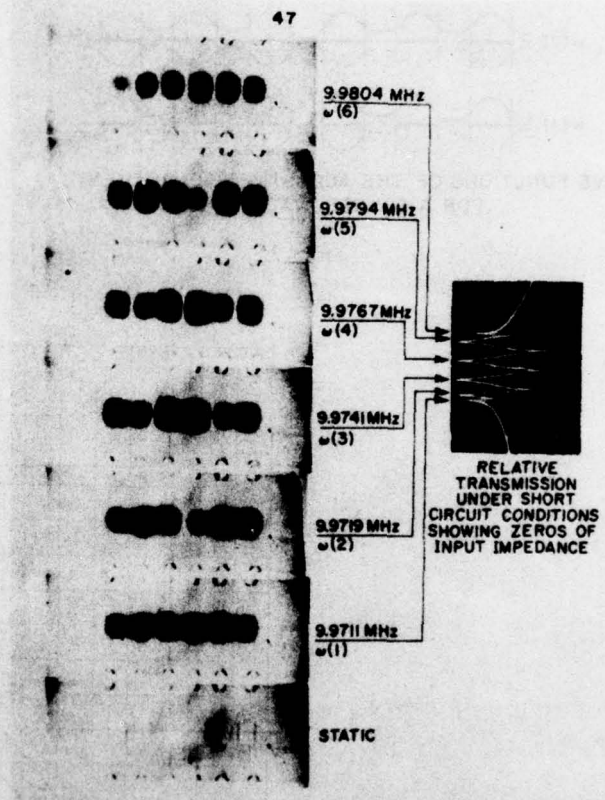

MAXIMUM DARKENING IN THE TOPOGRAPHS CORRESPONDS TO THE MAXIMUM AMPLITUDE OF THE ACOUSTICAL DISPLACEMENT. THE LIGHT AREAS ARE QUIESCENT OR NODAL REGIONS. THE DARK LINES IN THESE LIGHT REGIONS ARE DEFECTS IN THE QUARTZ.

FIGURE 2.18

FIGURE 1

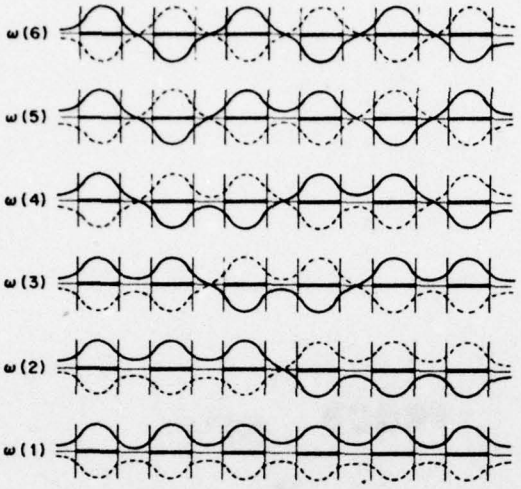

WAVE FUNCTIONS OF THE ACOUSTIC DISPLACEMENT FOR A SIX RESONATOR MCF

FIGURE 2

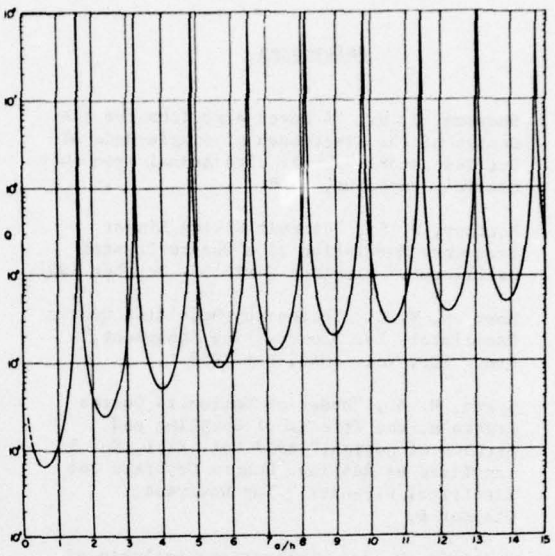

FIGURE 3

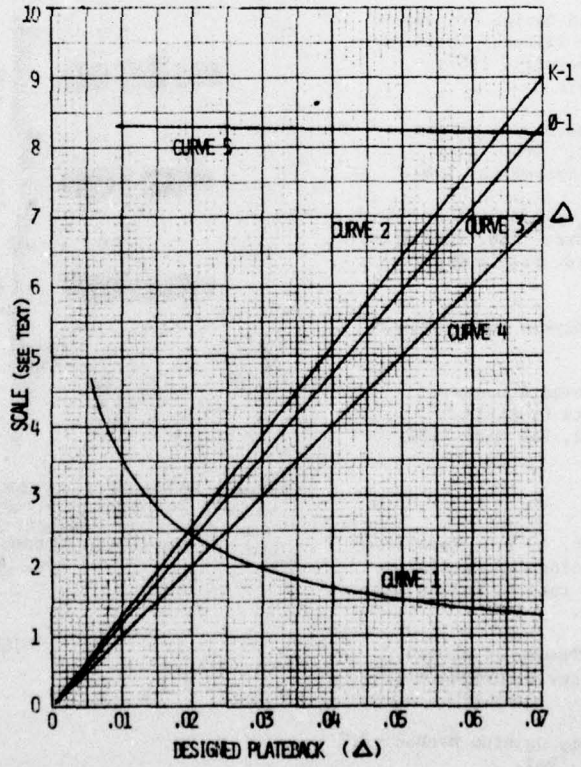

FIGURE 4

LASER INTERFEROMETRIC MEASUREMENT OF THE VIBRATION DISPLACEMENTS OF A PLANO-CONVEX AT-CUT QUARTZ CRYSTAL RESONATOR

K. Iijima, Y. Tsuzuki, Y. Hirose, and M. Akiyama
Yokohama National University
Yokohama, Japan 233

Summary

Detailed vibrational displacement distributions of the thickness-shear modes of a plano-convex AT-cut quartz plate have been measured for the first time utilizing a laser interferometric technique. The technique is unique in that simple introduction of a low-frequency phase modulation into one of the laser beams makes measurements essentially free from environmental mechanical disturbances, and hence, relatively simple optical setups may be used for measuring in-plane vibration displacements down to the order of several angstroms.

Introduction

The circular plano-convex AT-cut quartz crystal resonators[1] have been in wide use as high-stability oscillator elements in the frequency range from 1 MHz to 10 MHz. In spite of their great practical importance, it has been very difficult to make a satisfactory analysis of their thickness-shear vibrations. This is primarily because of the special geometries of these resonators as well as the crystal anisotropy itself. It would therefore be of great help if the detailed distributions of the vibration displacements over the entire crystal surface were experimentally known beforehand.

We have previously reported a holographic technique[2], and have proved it to be a powerful means for measuring displacements of contour vibrations of quartz resonators and mechanical vibrators having relatively large vibration amplitudes of the order of several thousand angstroms. It can not be applied, however, to the thickness-shear vibrations, since their maximum vibration amplitudes are estimated to be not more than several hundred angstroms. Instead, use of laser interferometric techniques would seem to be a reasonable procedure for them. When using such techniques, however, special care is needed to isolate the optical setup from low-frequency environmental mechanical disturbances.

We have developed a new laser interferometric technique in which simply introducing a low-frequency phase modulation into one of the illuminating beams makes measurements essentially free from these disturbances[3]. Employing this technique, detailed displacement distributions of the thickness-shear modes of a plano-convex AT-cut resonator have been obtained.

Measurement Method

Fig. 1 shows the standard system arrangement for measuring in-plane thickness-shear vibration displacements. The laser beams A and B, one of which is phase modulated at a low-frequency by the PZT-driven mirror, are focused onto one point on the resonator surface of diffuse surface finish. The lights scattered into the normal direction of the resonator surface are then collected by a condenser lens to the p-i-n photo-diode optical detector. In the presence of a vibration displacement $U\cos\omega t$ to be studied, the beam A undergoes a phase modulation of $(2\pi U/\sqrt{2}\lambda)\cos\omega t$ and the beam B, of $-(2\pi U/\sqrt{2}\lambda)\cos\omega t$, where λ is the wavelength of the laser light. If we further take into consideration the low-frequency phase modulation $\theta(t)$, which is the sum of the phase modulations $\Phi\cos\Omega t$ introduced to the beam A and $\phi_n(t)$ caused by the environmental mechanical disturbances, then the phase difference $\Delta\Phi(t)$ between the two beams can be expressed as

$$\Delta\Phi(t) = \theta(t) + 2(2\pi U/\sqrt{2}\lambda)\cos\omega t. \quad (1)$$

The light intensity incident upon the optical detector is

$$I = E_a^2 + E_b^2 + 2E_aE_b \times \cos[\theta(t) + (4\pi U/\sqrt{2}\lambda)\cos\omega t] \quad (2)$$

where E_a and E_b are the amplitudes of the beams A and B, respectively. Equation (2) can be expanded, using Bessel functions, into a series with a number of different frequency components.

The displacement amplitude U is then obtained from two of the components in the following manner. The lowest frequency component, the J_0 component, is

$$I_0 = 2E_aE_b\cos\theta(t)J_0(4\pi U/\sqrt{2}\lambda). \quad (3)$$

The component with the center frequency of ω, the J_1 component, is

$$I_1 = -4E_aE_b\sin\theta(t)J_1(4\pi U/\sqrt{2}\lambda)\cos\omega t. \quad (4)$$

If the maximum phase deviation Φ of the employed low-frequency phase modulation is chosen by adjusting the supply voltage of the PZT-driven mirror phase modulator in such a manner that $\cos\theta(t)$ and $\sin\theta(t)$ reach the peak values ± 1 at several instants of time, then the peak-to-peak values of the J_0 and J_1 components are given by

$$I_{pp0} = 4E_aE_bJ_0(4\pi U/\sqrt{2}\lambda) \quad (5)$$

$$I_{pp1} = 8E_aE_bJ_1(4\pi U/\sqrt{2}\lambda). \quad (6)$$

Since the range of U of our interest is not more than several hundred angstroms, the approximations $J_0(x) \approx 1$ and $J_1(x) \approx x/2$ can be used, and from Equations (5) and (6), U is obtained as

$$U = (I_{pp1}/I_{pp0})\sqrt{2}\lambda/4\pi. \quad (7)$$

It should be noted here that U, which is determined from the ratio I_{pp1}/I_{pp0}, is not affected by the environmental mechanical disturbances, since both I_{pp0} and I_{pp1} can be made independent of the waveform of $\theta(t)$ by proper adjustment of Φ as seen in Equations (5) and (6). It should also be noticed that the vibration displacement component in any direction within the object surface can be measured separately since the phase difference $\Delta\Phi(t)$ of Equation (1) is sensitive only to the vibration in the direction shown in Fig. 1.

In actual measurements, the ratio I_{pp1}/I_{pp0} can easily be determined by displaying on an oscilloscope the output voltages of the selective amplifier, with known gains $G(\omega)$ and $G(0)$ for the J_1 and J_0 components, respectively. Fig. 2 shows typical waveforms of the J_1 and J_0 components. In these waveforms, one takes its maximum or minimum when the other becomes zero, and vice versa, since they are proportional to $\cos\theta(t)$ and $\sin\theta(t)$. The appearance of several peaks of the same magnitude ensures the existence of instants of time when $|\cos\theta(t)|$ and $|\sin\theta(t)|$ are at their maximum, as discussed above.

Results of Measurements

Employing the technique outlined above, measurements were made on the circular plano-convex AT-cut resonator depicted in Fig. 3. The resonator has gold-evaporated electrodes on its surfaces of diffuse finish (#2000). The flat surface is fully coated so as to maintain high optical reflectivity, and hence, to make measurements over the entire surface possible. The convex surface is partially coated, with a cut along the x (crystallographic) axis, as shown in the figure. This cut was made in order to enable excitations of the fundamental and an inharmonic thickness-shear vibrations using the same resonator.

Fig. 4 gives the results for the fundamental thickness-shear vibration along with the method of its excitation. Figs. 4 (C) and (D) are the distributions of the displacement components U_x and U_z in the x and z directions, respectively. Measurements were made along the lines $\overline{AA'}$—$\overline{DD'}$ shown in Fig. 4 (B). The U_x distributions in Fig. 4 (C) indicate that they are concentrated to the center region of the resonator plate and have similar shapes with slightly narrower width in the z direction than in the x direction. It should be pointed out that this vibration mode does have finite z displacement components, although their maximum value is only 1/16 of that of the x components.

Fig. 4 (E) shows the vibration pattern with equal displacement lines of the x and z components. This was drawn based on the results of Figs. 4 (C) and (D), and additional vibrational components measured at a number of points on the top-right quadrant of the resonator, since the displacement distributions were found to be symmetrical with respect to the x and z axes. Fig. 4 (F) gives the loci of equal displacement amplitude and the directions of vibration, obtained by combining the x and z components. The phase relations between these two components, which are related to the directions of vibration, were determined by rotating the resonator about its axis and finding the direction where the displacement amplitude became maximum. It is seen from Fig. 4 (F) that the directions of vibration are crooked toward outside because of the existence of finite z displacement components. They are, however, almost parallel to the x axis in the center region of the plate where vibration displacements are large, and hence, the equal displacement lines of this vibration in this region are nearly the same as those of the x displacement components.

Using the same resonator, one of the inharmonic thickness-shear modes was also studied. The results are shown in Fig. 5. In order to excite this mode, the half portion of the electrode on the convex surface devided along the x axis was used as shown in Fig. 5 (A).

It is noticed that the vibration displacement distributions over the upper or lower half surface are essentially similar to those of Fig. 4. The entire vibration pattern is, however, more extended toward outside and the maximum vibrational amplitude of the z component, which is about 1/5 of that of the x component, is relatively large in comparison with the fundamental mode. It appears from these results that thickness-shear motion is predominant compared to thickness-twist motion in this mode, although it is sometimes called the thickness-twist mode.

Conclusions

We have developed a new laser interferometric technique which is, in principle, free from the environmental mechanical disturbances and is capable of measuring small in-plane vibrations down to the order of several angstroms. Employing this technique, detailed and quantitative displacement distribution patterns of the fundamental and an inharmonic thickness-shear vibrations of a plano-convex AT-cut quartz resonator were obtained for the first time.

It is concluded that these distribution patterns can provide important and detailed information on such practically important modes, and the technique described in this paper can be a powerful means for the study of the vibrations of the AT-cut resonators and other small in-plane vibrations.

Acknowledgements

The authors wish to thank The Kokusai Denshin Denwa Co. (Japanese Overseas Radio and Cable System) for its support to this work.

References

[1] A. W. Warner, "Design and performance of ultraprecise 2.5 MHz crystal units", Bell Syst. Tech. J., vol. 39, pp. 1193-1218, 1960.

[2] Y. Tsuzuki, Y. Hirose, and K. Iijima, "Measurement of vibration modes of piezoelectric resonators by means of holography", Proc. of the 25th Annual Freq. Cont. Symp., pp. 113-117, April 26-28, 1971.

[3] K. Iijima, Y. Tsuzuki, Y. Hirose, and M. Akiyama, "Laser interferometric measurement of the vibration displacements of a plano-convex AT-cut quartz crystal resonator", Proc. IEEE Lett., vol. 64, no. 3, pp. 386-387, March 1976.

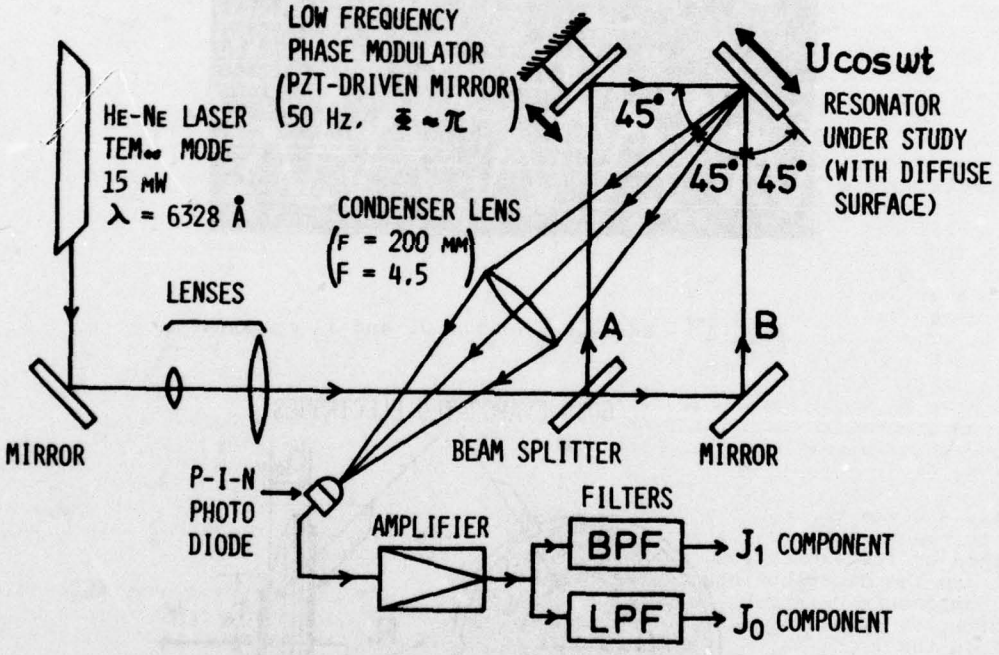

FIG. 1 SYSTEM ARRANGEMENT FOR MEASURING SMALL IN-PLANE VIBRATION DISPLACEMENTS.

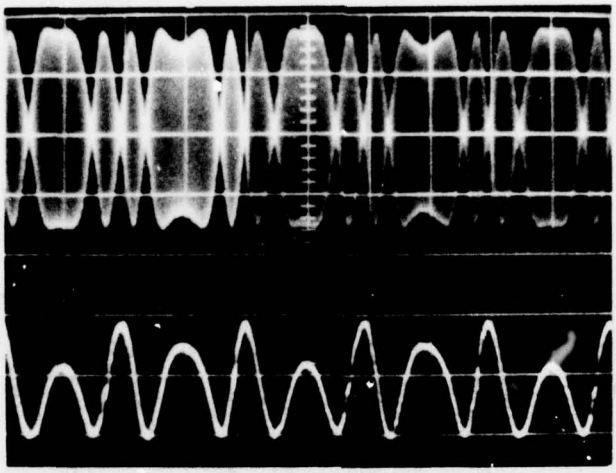

Fig. 2 Waveforms of the J_1 and J_0 components.

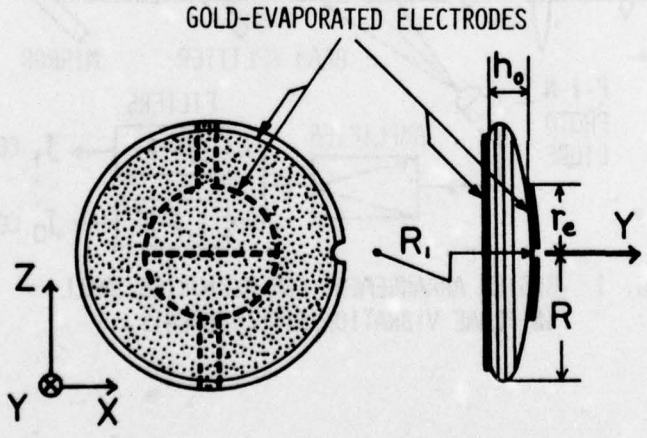

FIG.3 TOP AND SIDE VIEWS OF THE AT-CUT QUARTZ RESONATOR (DIFFUSE SURFACE FINISH)
(CUT ANGLE : 35° 3', FUNDAMENTAL RESONANCE FREQUENCY : 1.286 MHz, R = 11.0 mm, r_e = 6.0 mm, h_o = 1.38 mm, R_1 = 95 mm.)

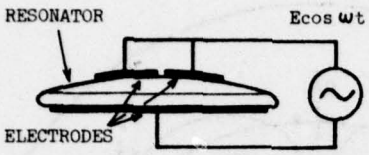

(A) METHOD OF EXCITATION.

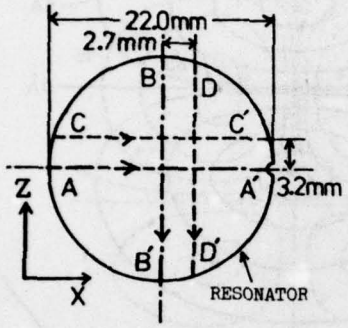

(B) LINES ON WHICH MEASUREMENTS WERE MADE.

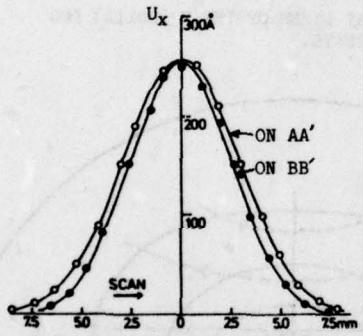

(C) MEASURED X DISPLACEMENT COMPONENTS, U_X.

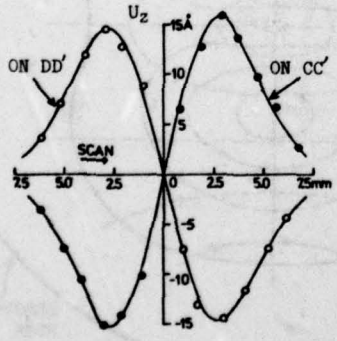

(D) MEASURED Z DISPLACEMENT COMPONENTS, U_Z (U_Z = 0 ON X AND Z AXES).

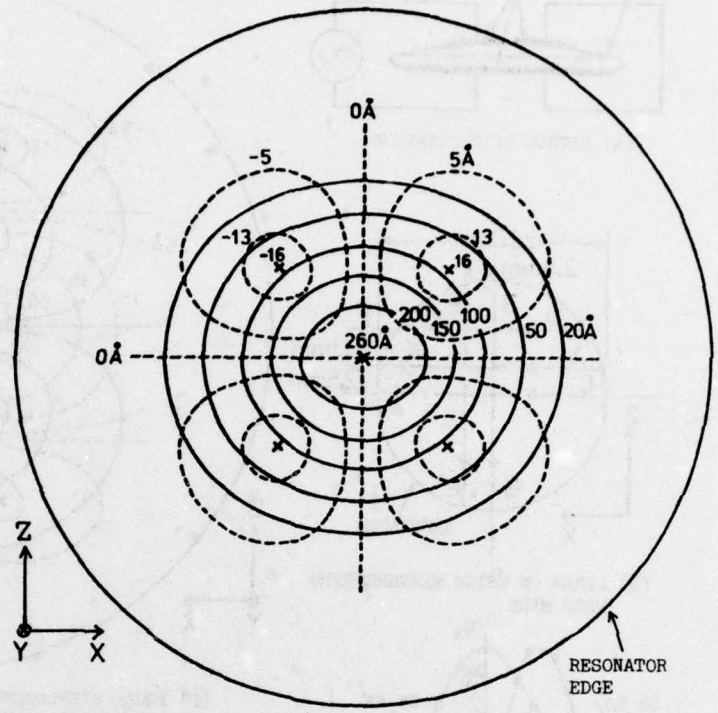

(E) EQUAL DISPLACEMENT LINES OF THE X (SOLID) AND Z (DOTTED) COMPONENTS.

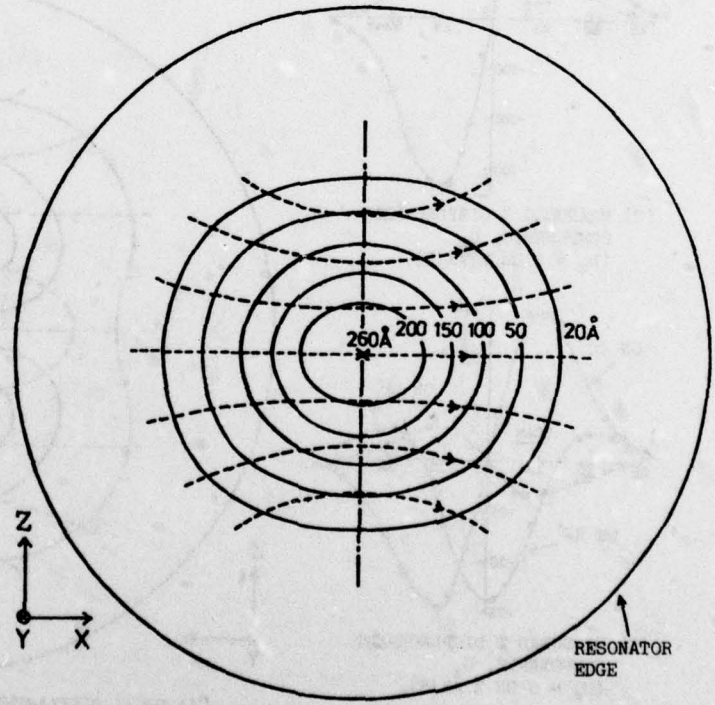

(F) EQUAL DISPLACEMENT LINES (SOLID) AND DIRECTIONS OF VIBRATION (DOTTED).

FIG. 4 FUNDAMENTAL THICKNESS-SHEAR VIBRATION OF PLANO-CONVEX AT-CUT QUARTZ RESONATOR (RESONANCE FREQUENCY 1.286 MHz, DRIVE CURRENT 1.0 mA)

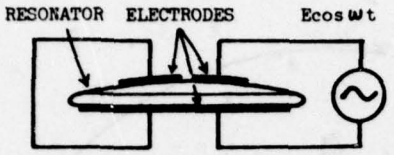

(A) METHOD OF EXCITATION.

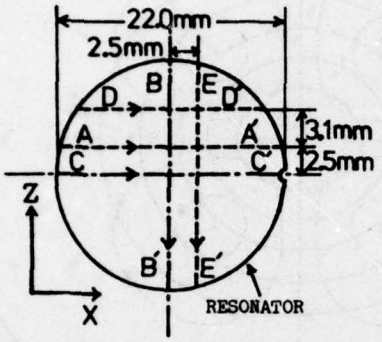

(B) LINES ON WHICH MEASUREMENTS WERE MADE.

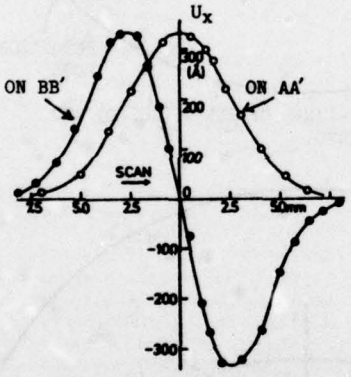

(C) MEASURED X DISPLACEMENT COMPONENTS, U_x (U_x = 0 ON X AXIS).

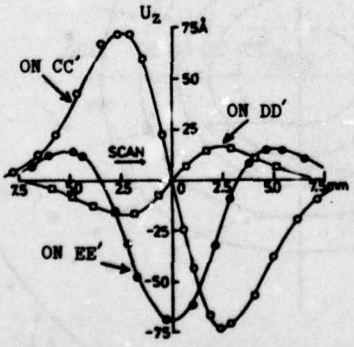

(D) MEASURED Z DISPLACEMENT COMPONENTS, U_z (U_z = 0 ON Z AXIS).

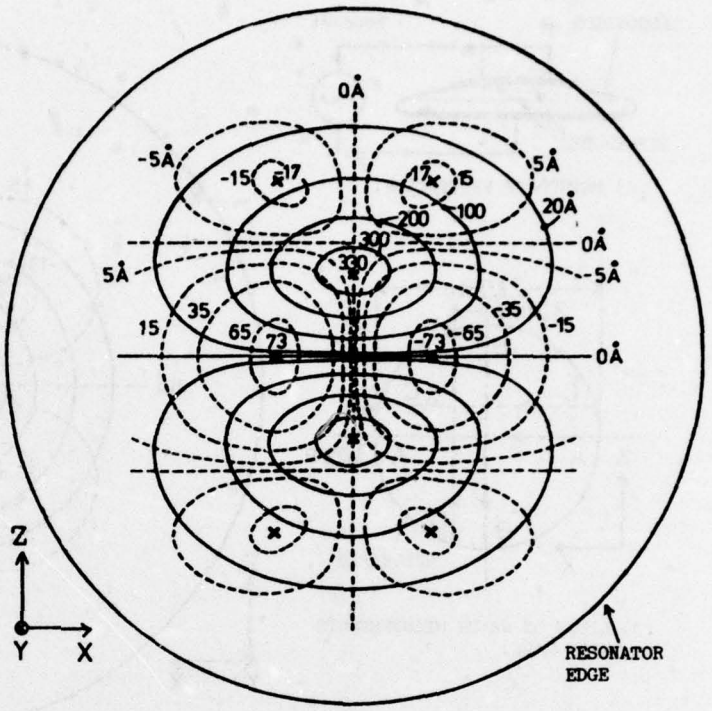

(E) EQUAL DISPLACEMENT LINES OF THE X (SOLID) AND Z (DOTTED) COMPONENTS.

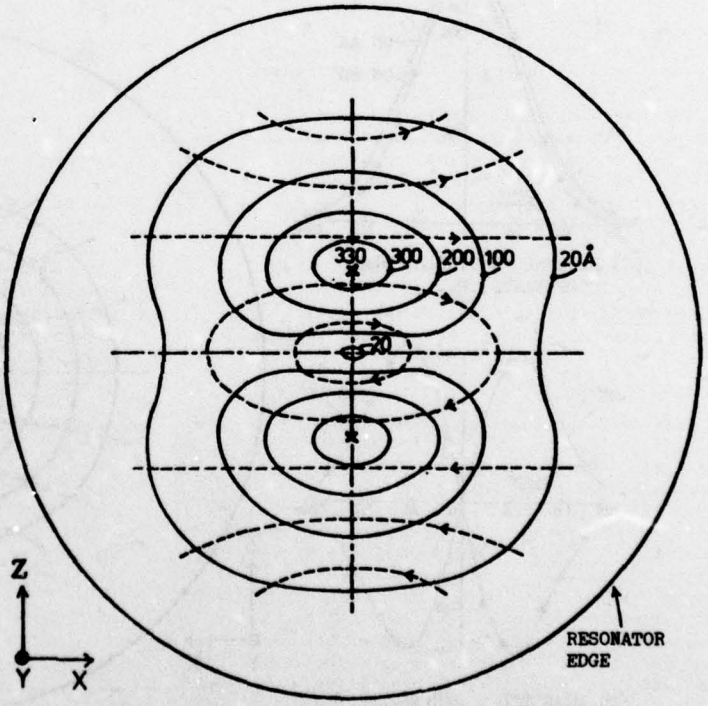

(F) EQUAL DISPLACEMENT LINES (SOLID) AND DIRECTIONS OF VIBRATION (DOTTED).

FIG.5 INHARMONIC THICKNESS-SHEAR VIBRATION OF PLANO-CONVEX AT-CUT QUARTZ RESONATOR (RESONANCE FREQUENCY 1.349 MHz. DRIVE CURRENT 0.75 mA)

TAILORED DOMAINS IN QUARTZ AND OTHER PIEZOELECTRICS

R. E. Newnham and L. E. Cross
Materials Research Laboratory
Pennsylvania State University
University Park, Pennsylvania

Summary

Ferroic crystals contain domain states which can be switched by suitably chosen external forces. The domains in a primary ferroic differ in spontaneous polarization (ferroelectricity) spontaneous magnetization (ferromagnetism), or spontaneous strain (ferroelasticity), while those in a secondary ferroic differ in induced strain, induced magnetization, or induced polarization. Examples of ferrobielastics, ferroelastoelectrics and other secondary ferroics are discussed, together with their applications as multidomain piezoelectric resonators. Twinning is usually considered a nuisance in piezoelectric applications, but it can be used to enhance certain modes of motion, or to eliminate others, but making use of differences in the piezoelectric coefficients. Multi-domain crystals and ceramics can also be used to produce "forbidden" harmonics, or as high-frequency resonators, and as focused acoustic transducers.

The concepts of secondary ferroic switching and domain-divided piezoelectric will be illustrated with laser-induced twinning in α-quartz. Dauphine twinning in quartz is characterized by reversal in polarity of the <100> axes. Structurally the change is slight, but twin wall motion is accompanied by reversal in sign of piezoelectric coefficient d_{111}, making tailored-domain configurations possible. Quartz is ferrobielastic, so that Dauphine twins can be induced by mechanical stress. During World War II, electrical twins were partially eliminated from natural quartz by applying mechanical torque to heated crystals. But twinning can be controlled more conveniently using lasers or other high-intensity light beams. Differential thermal expansion caused by localized heating generates the required stresses to induce twinning. Tailored domain patterns have been incorporated in X-, AT- and DT-cut plates using a CO_2 laser and simple irradiation patterns. The characteristics of multidomain quartz resonators are described.

Key Words (for information retrieval)
Twinning, quartz, piezoelectric, laser heating.

Introduction

This paper provides a review of our recent work on secondary ferroics[1,2], domain-divided piezoelectrics[3,4], laser-induced twinning in quartz.[5] The ultimate goal of this line of research is to optimize the performance of solid state devices through the manipulation of ferroic twin patterns, a type of domain engineering. To achieve this goal we are searching for ways to control twinning on a very fine scale by applying localized fields and stresses. Most of our efforts have been devoted to electrical and mechanical control since magnetic domain devices are already well developed. In the applications described here, the twins differ in piezoelectric properties, but one can also imagine applications for twin patterns in which the twins differ in elastic constants, refractive indices, or other material parameters. Such domain-divided devices can be operated in a fixed twin pattern, as in the twinned piezoelectric resonators discussed later, or with movable twins, such as magnetic bubble domains.

Ferroic Crystals

The term "ferroic" has been suggested[6,7] to describe all types of mimetically twinned crystals in which the orientation of one or more of the twin components may be effected by the application of suitably chosen external driving forces. Ferroics may be broadly classified from the nature of the property tensors which differ between orientation states (twins) in the crystal, since these differences will determine the nature and orientation of driving fields which are required to accomplish reorientation between states. A very simple classification on this basis is given in Table I.

The first section in Table I lists the well known primary ferroics[6], primary being used here in the sense that the domain or twin states are distinct in the orientation of the lowest rank response tensor, i.e., electric polarization, elastic strain, or magnetization. It must be recognized that in many primary ferroic species more than one type of response may occur. For example, in ferroelectric species derived from non-centric prototypic structures, the twin states are frequently distinct in both the orientation of spontaneous electric polarization and of spontaneous elastic strain, and may be driven between states either by electric fields or elastic stresses.

Even the most elementary consideration, however, shows that there are many crystals with mimetic twin systems in which the different twin components do not differ in the orientation of the primary quantities electric polarization, elastic strain or magnetization. It is perhaps surprising that the possibility of ferroic responses driven by the differences of orientation in higher rank tensor properties has only very recently been suggested[7], and the systematization given in the second part of Table I proposed.[1]

Consider for example a system in which the twin domains differ in the orientation of the piezoelectric tensor d_{ijk}. To effect a difference in free energy between domains both an electric field E_i and an elastic stress σ_{jk} must be applied at the same time, since either field alone will leave the energy changes identical. Thus the ferroelastoelectric is neither ferroelectric nor ferroelastic, but is in fact a completely new and interesting species.

Table I gives examples of crystals in each category. In several cases, though the appropriate response of the twinning has been observed, the terminology used here has not been specifically applied to the system concerned.

Although at present there are only a few well documented examples, secondary ferroic phenomena may prove to be rather common, since the symmetry requirements are not especially stringent. Symmetry restrictions for ferrobielectricity, ferrobielasticity, ferrobimagnetism, ferroelastoelectricity, ferromagnetoelasticity and ferromagnetoelectricity were described in a recent paper.[2] Ferrobielectricity can be expected in antiferroelectric ferroelastic species with substantial dielectric anisotropy. Low-temperature $SrTiO_3$ may be an example.[8] Nickel oxide[9,10] and other antiferromagnetic ferroelastics with anisotropic magnetic

TABLE I

Primary and Secondary Ferroics

Ferroic Class	Orientation States Differ in	Switching Force	Example
Primary			
Ferroelectric	Spontaneous polarization	Electric field	$BaTiO_3$
Ferroelastic	Spontaneous strain	Mechanical stress	$Pb_3(PO_4)_2$
Ferromagnetic	Spontaneous magnetization	Magnetic field	Fe_3O_4
Secondary			
Ferrobielectric	Dielectric susceptibility	Electric field	$SrTiO_3$(?)
Ferrobimagnetic	Magnetic susceptibility	Magnetic field	NiO
Ferrobielastic	Elastic compliance	Mechanical stress	SiO_2
Ferroelastoelectric	Piezoelectric coefficients	Electric field and mechanical stress	NH_4Cl
Ferromagnetoelastic	Piezomagnetic coefficients	Magnetic field and mechanical stress	CoF_2
Ferromagnetoelectric	Magnetoelectric coefficients	Magnetic field and electric field	Cr_2O_3

susceptibility show ferrobimagnetism. Evidence for ferromagnetoelastic domains is found in CoF_2[11] and $FeCO_3$[12], while Cr_2O_3[13] shows ferromagnetoelectric switching. Of the 90 magnetic point groups, 35 are potentially ferromagnetoelastic and 40 potentially ferromagnetoelectric.

Regarding ferrobielasticity and ferroelastoelectricity, it can be shown that there are five pure ferrobielastic species, fifteen pure ferroelastoelectric species, and ten which show both phenomena. Ammonium chloride[14] is a pure ferroelastoelectric while α-quartz[15] is ferrobielastic and potentially ferroelastoelectric. Quartz will be considered in more detail in the following sections together with its application as a domain-divided piezoelectric.

Domain-Divided Piezoelectrics

An alternating voltage applied to a piezoelectric crystal causes the crystal to vibrate, and if the frequency corresponds to one of the mechanical resonances, the amplitude of vibration may be very large. Every crystal has a number of such resonant frequencies that depend on the crystal dimensions, the orientation of the plate with respect to the crystal axes, and the type of mechanical oscillation involved. The most important vibration modes are longitudinal, flexural, face-shear and thickness-shear.[16] Each type of vibration can exist in a fundamental and in higher order or harmonic modes. To make matters still more complicated, the modes are often mechanically-coupled to one another, giving rise to additional combination modes.

The difficulties caused by secondary resonances are especially severe for the high-frequency modes of a thin plate. Under these conditions, harmonics of the numerous resonances associated with the lateral dimensions of the plate may approximate the fundamental thickness mode in frequency. As a result of the coupling, the frequency spectrum may consist of a large number of resonances rather than the desired single-mode of the thickness vibration. Such undesirable behavior can be partly eliminated by orienting and proportioning the plate so that the resonant frequencies of the interfering modes differ appreciably from that of the desired mode. Additional improvement can be achieved by contouring the plates and by mounting the crystal in such a way that the undesired modes are suppressed by clamping. In recent years, modern evaporation and photo-etch techniques have been used to produce carefully-designed electrode patterns which further enhance the resonance characteristics. Monolithic crystal filters[17] are an outgrowth of this work.

Partial-electroding and the other techniques help suppress spurious modes, but they also reduce the amplitude of the desired mode. Much of the crystal is not properly coupled in phase with the field when electrodes cover only part of the surface, or when the plate is contoured, or when supports clamp the crystal. This results in lowered power levels and smaller electronic signals.

There is another way of enhancing piezoelectric vibration modes which has not been explored in the past. Many piezoelectric crystals are also ferroic, and therefore exist in more than one orientation state or domain. When referred to a common set of axes, piezoelectric coefficients often differ in the two domain states. Under suitably chosen driving forces, domain walls can be moved to a desired configuration. Making use of the differences in piezoelectric coefficients, the domains can be arranged to drive only the desired vibration modes.

A possible objection to the tailored domain concept is that domains might switch during use, especially when driven at high power levels. This is certainly true for many ferroelectric crystals, but not for all ferroic crystals. Quartz is ferrobielastic, but not ferroelectric, and cannot be switched by electric fields. The same is true of certain primary ferroics such as lithium niobate and other frozen ferroelectrics with high Curie points. In general, it is possible to build in domain structures which are immovable at room temperature.

Selective Excitation of Harmonic Modes

Some examples of piezoelectric crystals with tailored domain configurations will now be considered to illustrate the utility of the idea. The motion of a plate in a low-frequency face shear mode is illustrated in Figure 1. CT and DT quartz plates used as filters and oscillators operate in low-frequency face-shear modes.[16]

Figure 1a shows the plate at rest. The fundamental face-shear vibration and one of its harmonics are shown in 1b and 1c, respectively. The fundamental consists of expansion and compression in opposite phase along the two diagonals of the plate. Shear motion may break up into higher frequency modes similar to its

fundamental. The harmonic shown in 1c consists of two segments vibrating in opposite phase. To generate other harmonics, the motion may be reversed in phase any number of times along either length or width.

Modes of motion are excited by alternating electric fields, making use of the piezoelectric effect. To excite the face shear fundamental, the major faces are electroded and a field is applied normal to the plate. If X_1 is the direction normal to the plate, then E_1 is the field in this direction. Let X_2 and X_3 be the directions parallel to the length and width of the plate, then ε_{23} is a shear strain about X_1. The face shear fundamental consists of alternating strains of $\pm\varepsilon_{23} = d_{123}E_1$. Resonance motion results when the frequency of the applied field E_1 corresponds to the natural resonant frequency of the plate determined by its dimensions and elastic constants.

The harmonic shown in 1c cannot be excited when the plate is fully electroded because the two halves of the plate are out of phase. To excite such a motion, a partially electroded sample could be used. A twinned crystal could also be used, with a simpler electrode pattern, less field distortion, and superior electromechanical energy conversion. Consider a crystal plate twinned through the center Figure 2. Suppose, for example, the twins are of a simple type in which the orientations are related by reflection across crystal plane (100).

Ammonium chloride has mirror twins of this type. NH_4Cl belongs ferroic symmetry species m3mF43m and is ferroelastoelectric below -30°C.[14] The twins differ in the sign of piezoelectric coefficient d_{123}, so that an electric field directed along X_1 produces shearing strains of opposite signs in the two domains.

Suppose the domain structure shown in Figure 2a were incorporated in a crystal of ammonium chloride, and the plate was electroded on its major faces perpendicular to X_1. An alternating field E_1 would generate the mode shown in Figure 2b because of the difference in piezoelectric coefficient. Comparing Figure 2b and Figure 1c, it is obvious that the fundamental vibration of a twinned crystal may correspond to a harmonic vibration of an untwinned crystal.

Ordinarily it is difficult to excite an even harmonic in a single crystal vibrator where most of the energy goes into the fundamental and lesser amounts into the odd harmonics. Vibration patterns for the various harmonics and combination modes are well known. When the domain pattern corresponds to one of these vibration patterns, selective excitation results so that any mode can be excited with a suitably chosen domain structure. In this way, it is possible to convert any harmonic to a fundamental, resulting in more efficient electromechanical energy conversion, and greater vibration amplitude at the desired frequency. Closely-spaced domain patterns may give very high frequencies.

The feasibility of the tailored-domain concept has been tested with piezoelectric gadolinium molybdate by comparing the impedance spectrum before and after twinning.[3] $Gd_2(MoO_4)_3$ is both ferroelectric and ferroelastic at room temperature and belongs to ferroic species 42mF2mm. Thin rectangular bars were cut and polished with the length of the bar parallel to the orthorhombic [110] direction. Dimensions along [110], [$1\bar{1}0$], and [001] were approximately (13 x 2 x 1) mm^3. With the crystal poled to a single-domain state, the (001) faces were fully electroded and the resonant frequency spectrum measured from 10 kHz to 5 MHz (Figure 3a). The prominent peak at 10 kHz is the fundamental extensional mode along the length of the bar. This mode is being driven by piezoelectric coefficient d_{333} which excites a thickness vibration along [001]. The thickness vibration is coupled through Poisson's ratio to expansions and contractions in the [110] direction. Third, fifth, and seventh harmonics of the length extension were also observed but even order harmonics are absent as expected.

One-half of the crystal was then poled in the opposite direction giving a two-domain bar (Figure 3b). The frequency spectrum was then remeasured, using full c-face electrodes as before. Second and sixth-order harmonics of the length extension mode were observed as prominent resonances while the fundamental and odd harmonics were greatly attenuated. Resonant frequencies are therefore effectively doubled in the two-domain bar. In addition to raising the frequency, the experiment also demonstrates the feasibility of exciting vibration modes forbidden to the single-domain crystal.

Ferrobielasticity in Quartz

Quartz is a crystal of very considerable technological importance, combining elastic, dielectric and piezoelectric properties which are highly desirable for many electromechanical filter, transducer and frequency control operations. Early devices used natural Brazilian quartz, and at that time twinning in such crystals was studied extensively.[16]

However, with the advent of large scale production of synthetic quartz, twin properties have been largely ignored. Synthetic crystals are generally twin-free since they are grown on untwinned seed plates below the α-β inversion at 573°C.

In natural quartz, two types of interpenetrant twinning occur: optical or Brazil twins and electric or Dauphine twins. The optical twins are essentially growth twins, involving the handedness of the arrangement of silicon oxygen tetrahedra in the structure. To convert right-handed quartz to left-handed quartz, strong silicon oxygen bonds must be broken and the twinning is <u>not</u> ferroic.

Electric twinning involves much more subtle distortions of the structure, associated with the loss of symmetry which occurs at the β → α transition (from point groups 622 to 32). These symmetries are consistent with ferroic species 622F32 which is both ferrobielastic and potentially ferroelastoelectric. The inequivalence in free energy between two electric twin states of quartz induced by an electric field and an elastic stress applied in general orientations is given by:

$$\Delta G = 4S_{1123}(\sigma_{11}\sigma_{23} - \sigma_{22}\sigma_{33} + 2\sigma_{12}\sigma_{13})$$

$$+ 2d_{111}(E_1\sigma_{11} - E_1\sigma_{22} - 2E_2\sigma_{12})$$

Ferrobielastic switching via S_{1123} has been demonstrated[15] but ferroelastoelectric switching through d_{111} has not.

The phenomena of stress-induced twinning and detwinning of the electric twins in quartz has been known for considerable time.[18] With the shortage of high quality natural quartz which occurred during World War II, efforts were made to detwin samples for resonator applications[19,20], however, the studies at that time appeared to have had no clear theoretical basis for understanding the phenomena and used both temperature gradients and torsional stresses (piezocrescence) to modify the electric twin structure in quartz cuts of

interest in transducer applications.

Much more recently Aizu[15] demonstrated controlled twin motion in quartz, using uniaxial stress applied normal to [100] and at 45° to [001]. When viewed along [100] in polarized light domains were visible because of differences in photoelastic coefficients.

Using a rather simple stress generator, Aizu measured values for the coercive stress of 5×10^8 N/m^2 at 25°C and 3.5×10^8 N/m^2 at 150°C. In quartz, the $\beta \rightarrow \alpha$ transition which introduces electric twinning is close to second order, and the phonon mode softening which drives the transition is rather similar to that in the ferroelastic $LaAlO_3$ and the improper ferroelectric-ferroelastic $Gd_2(MoO_4)_3$. One might then expect that the coercive stress for ferrobielastic switching drop to near zero at the transition point (573°C). This is not inconsistent with the present sparse experimental data.

Laser-Induced Twinning in Quartz

The mechanical stress technique is rather cumbersome, however, and a better method is needed to produce textured domains in quartz. We have recently demonstrated[3] that domain patterns can be created optically using lasers or other high-intensity light beams. Large thermal stresses can be induced by localized heating since the surrounding cooler regions tend to restrain thermal expansion. X-, AT-, and DT-cut quartz crystals have been twinned with a 10.6 μm CO_2 laser employing a simple mask to generate localized heating and thermal stresses. Small quartz platelets having dimensions of approximately 0.08 x 0.6 x 0.6 cm were cut from untwinned synthetic crystals. The plates were covered with a graphite mask in which a slit measuring 0.4 x 0.015 cm was machined. The orientation of the slit with respect to the crystal axes was carefully controlled.

In order to lower the coercive stress for ferrobielastic switching, the apparatus was placed in a small furnace and heated to approximately 500°C, as monitored by a thermocouple. The crystal was then irradiated and allowed to cool gradually to room temperature. After etching in hydrofluoric acid, the crystals were examined for twinning in reflected light. Two of the twin patterns produced in AT-cut plates are shown in Figure 4. X- and DT-cut patterns are somewhat different and have been described elsewhere.[5]

At low laser power and for certain slit orientations, the twins in AT-cut plates resemble the slit in size and orientation (Figure 4a), while at medium power levels a characteristic four-leaf clover pattern (Figure 4b) developed regardless of irradiation pattern. Under high level irradiation, the plates fracture. Similar tendencies were noted in X- and DT-cut twin patterns.

To explain the observed domain patterns in quartz we examine the free energy function for twinned crystals, for which the stress combination required to produce ferrobielastic switching is $\sigma_{11}\sigma_{23} - \sigma_{22}\sigma_{23} + 2\sigma_{12}\sigma_{13}$. Whenever this combination is large, twin wall motion may result. This expression has been evaluated for X-, AT-, and DT-cut plates, assuming that the laser beam generates stresses within the plane of the plate.

The coordinate system chosen to illustrate the switching stresses for AT-cuts is shown in Figure 5a. The principal directions within the plane of the plate are X_1 and X_3'. X_1 is the crystallographic [100] direction, and X_3' is obtained by rotating X_3 (=[001]) through an angle θ toward X_2 (=[120]). θ is 35°15' for an AT-cut.

Let σ be a tensile stress along X_3'', an arbitrary direction within the plane of the AT-cut. X_3'' is obtained by rotating X_3' through an angle ϕ toward X_1. We now evaluate the switching stress product $\sigma_{11}\sigma_{23} - \sigma_{22}\sigma_{23} + 2\sigma_{12}\sigma_{13}$ in terms of an applied stress σ along X_3''. Performing the appropriate transformations leads to the result $\sigma^2(3\sin^2\phi - \cos^2\phi \sin^2\theta)\cos^2\phi \sin\theta \cos\theta$ for the switching stress product. This function is plotted for an AT-cut crystal in Figure 5b by substituting 35°15' for θ. The result is a six-lobe figure with four large positive lobes and two narrow negative lobes of smaller size. The positive lobes of the theoretical curve reach a maximum at an angle ϕ slightly larger than 45°. The analytic expression is $\tan^2\phi_{max} = 1 + \frac{2}{3}\sin^2\theta$, which gives ϕ_{max} of 47.9° for AT-cuts and 49.9° for DT-cuts. It is obvious from Figure 5b that tensile stresses directed along $X_3(\theta = 0°)$ or perpendicular to $X_3(\theta = 90°)$ are useless in switching Dauphine twins.

The positive lobes of the switching stress function in Figure 5b bear a strong resemblance to the observed twin patterns in AT-cut plates (Figure 4b). The four-leaf clover patterns are similar both in shape and orientation. We interpret this similarity to mean that under laser irradiation, thermal stresses are being induced nearly radially around the central heated region, and that domain walls move out from the center most rapidly in the effective switching directions. This seems to be the case at medium power levels where different illumination patterns give substantially the same domain structure, but at lower power levels the twin pattern more closely resembles the illumination pattern (Figure 4a). Slit-shaped illumination in the $\phi = 45°$ orientation gives stresses at 135° along one of the positive lobe directions causing the illuminated area to switch.

Additional details concerning the experimental techniques and the theoretical description of the twin patterns are given in an earlier paper.[5] In searching for the best conditions to generate reproducible domain patterns, there are an enormous number of variables which remain to be optimized. The fact that rather similar patterns can be produced over a wide range of conditions makes us feel optimistic about the possibilities of controlling Dauphine twins in quartz. Quantitative analysis of the energy and stress distributions is presently being undertaken to aid in the optimization of experimental parameters which control domain size and shape. These parameters include aperture size, shape, and orientation, plate shape and thickness, ambient temperature, irradiation time and power, and laser wavelength. Control and understanding of the effect of these variables is a necessary prelude to incorporating tailored domains in quartz.

Acknowledgements

This work was sponsored by the Army (DAA 29-76-G-0145), Navy (N00014-76-C-0515), and National Science Foundation (ENG 75-02398). We also wish to thank our colleagues at Penn State for their advice and assistance. Crystals were supplied by Western Electric, Bell Laboratories, Motorola, and DuPont.

References

1. R. E. Newnham, Amer. Min. 59, 906 (1974).
2. R. E. Newnham and L. E. Cross, Mat. Res. Bull. 9, 927 (1974); 9, 1021 (1974).
3. R. E. Newnham, C. S. Miller, L. E. Cross and T. W. Cline, Phys. Stat. Solidi (a) 32, 69 (1975).
4. R. E. Newnham and L. E. Cross, Ferroelectrics (in press).
5. T. L. Anderson, R. E. Newnham, L. E. Cross and J. W. Laughner, Phys. Stat. Solidi (submitted).

6. K. Aizu, J. Phys. Soc. Japan 37, 387 (1971).
7. K. Aizu and T. Hirai, Reports on Autumn 1969 Meeting of Phys. Soc. Japan 4, 37 (1969).
8. M. A. Saifi and L. E. Cross, Phys. Rev. B2, 677 (1970).
9. W. L. Roth, Appl. Phys. 31, 2000 (1960).
10. G. A. Slack, J. Appl. Phys. 31, 1571 (1960).
11. A. S. Borovik-Romanov, J. Exp. Theor. Phys. U.S.S.R. 38, 1088 (1960).
12. A. S. Borovik-Romanov, G. G. Aleksanjan and E. G. Rudashevskij, Intl. Conf. on Magnetism and Crystallography, Kyoto, Japan, Pap 155 (1962).
13. S. Shtrikman and D. Treves (1963), Phys. Rev. 130, 968 (1963).
14. E. Mohler and R. Pitka, Solid State Comm. 14, 791 (1974).
15. K. Aizu, J. Phys. Soc. Japan 34, 121 (1973).
16. R. A. Heising, Quartz Crystals for Electrical Circuits (D. Van Nostrand Co., New York, 1946).
17. R. A. Sykes and W. L. Smith, Bell Lab. Report 46, 52 (1968).
18. E. V. Zinserling and A. Shubnikov, Zeit. f. Krist. 35, 454 (1933).
19. C. Frondel, Amer. Min. 30, 447 (1945).
20. W. A. Wooster, N. Wooster, J. L. Rycroft and L. A. Thomas, Trans. I.E.E. (G.B.) 94, 927 (1947).

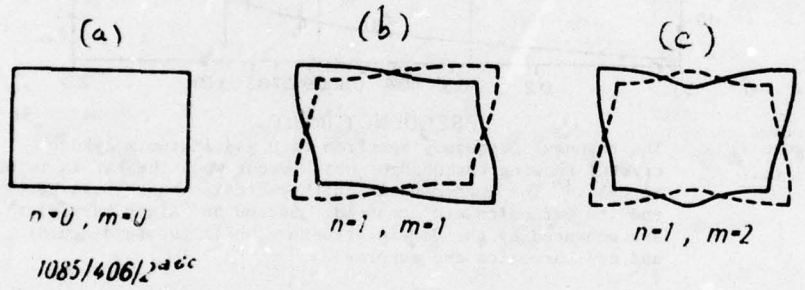

Figure 1. Motion of a plate in low frequency shear.[16] The crystal is at rest in (a), and in motion in (b) and (c) where two phases are shown; one a solid curve and the other a dashed curve to illustrate the distortion with respect to the original shape.

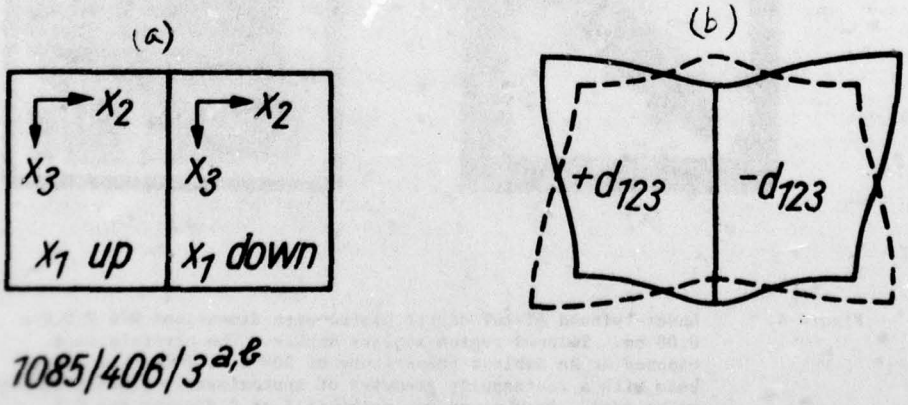

Figure 2. (a) Twinned piezoelectric with vertical domain wall dividing the crystal in half. Under uniform alternating field E_1 the crystal vibrates in pattern (b) because the piezoelectric coefficient d_{123} is of opposite sign in the two twins, thereby inducing opposite shears.

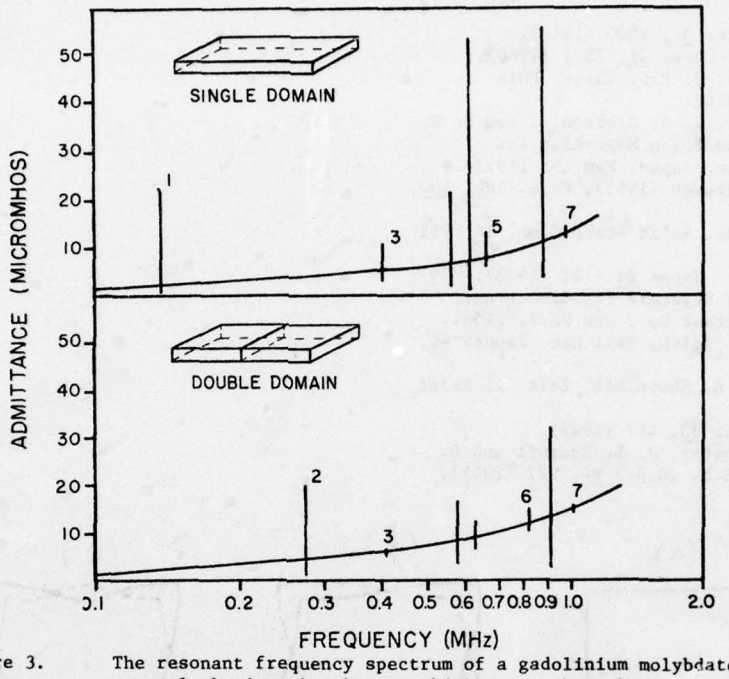

Figure 3. The resonant frequency spectrum of a gadolinium molybdate crystal showing the changes which occur when the bar is twinned in half.[3] The fundamental length-extension mode (0.14 MHz) and its harmonics are numbered. Second and sixth harmonics are enhanced by the domain structure while the fundamental and odd harmonics are suppressed.

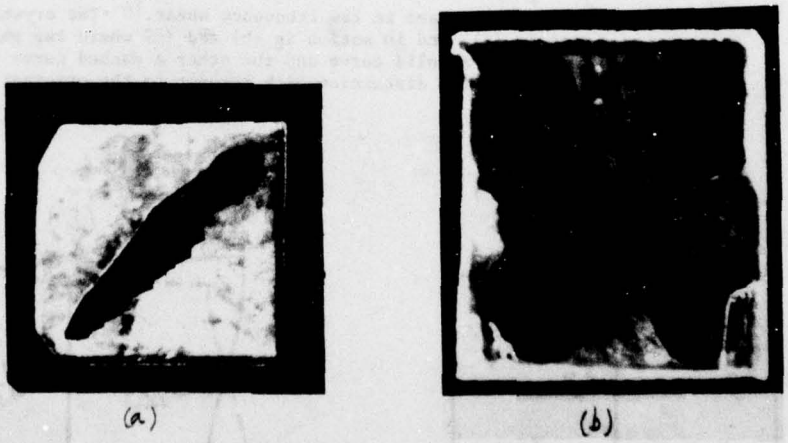

Figure 4. Laser-twinned AT-cut quartz plates with dimensions 0.6 x 0.6 x 0.08 cm. Twinned region appears darker. The crystals were exposed at an ambient temperature of 500°C to a 10.6 μm laser beam with a rectangular geometry of approximately 0.015 x 0.4 cm on an edge. Beam power was maintained at 0.9 watts for 0.5 sec (a) and 3 sec (b). With reference to the crystal axes in Figure 5a, X_1 is vertical and X_3' is horizontal. The slit was oriented at 45° to X_1 and X_3'.

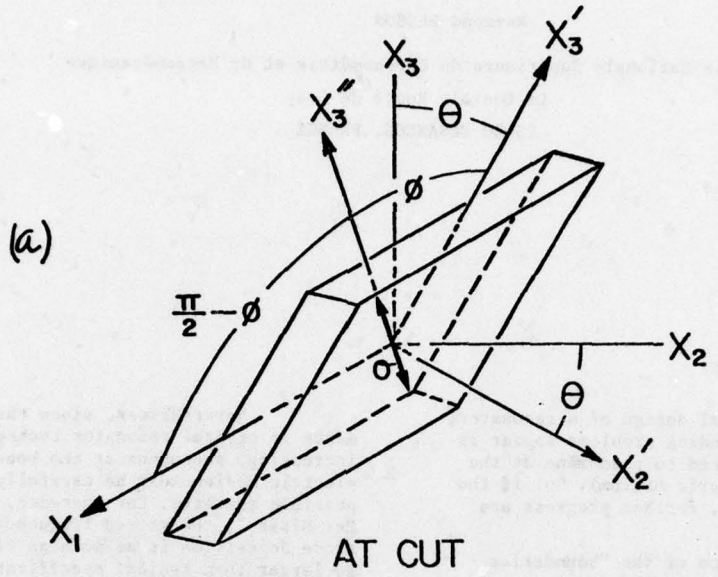

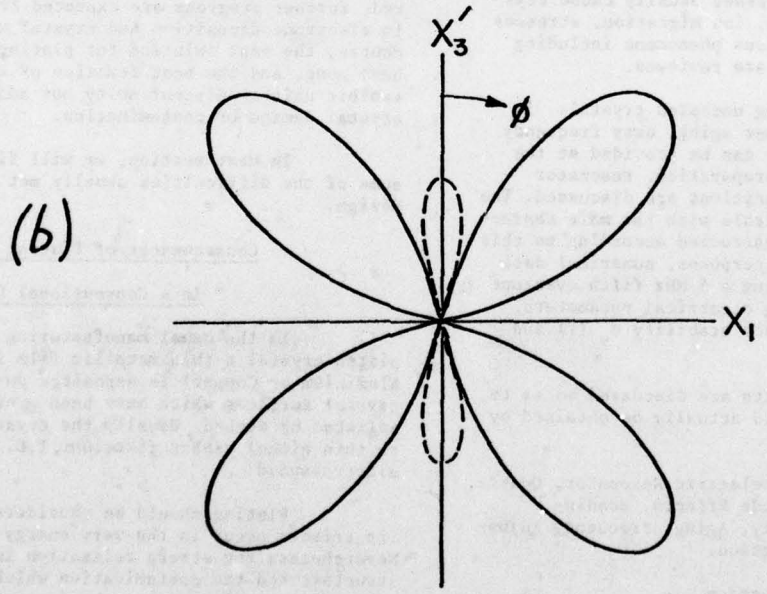

Figure 5. The coordinate system used to derive the switching stress combination for an AT-cut quartz plate is shown in (a). X_3'' denotes the thermal stress (σ) direction in the crystal plate. X_3' is obtained by rotating X_3 about the X_1 axis through an angle θ in the $X_2 - X_3$ plane; θ is 35°15' for an AT-cut plate. ϕ represents the angle between X_3' and X_3''. In (b) the thermal stress combination $\sigma^2(3\sin^2\phi - \cos^2\phi \sin^2\theta)\cos^2\theta \sin\theta \cos\theta$ is plotted as a function of ϕ. The solid lines indicate directions stabilizing one Dauphine twin state while the dashed lines indicate directions stabilizing the other twin state. The angle of maximum stabilization for the solid line lobes is 47.9°.

A NEW PIEZOELECTRIC RESONATOR DESIGN †

Raymond BESSON

Ecole Nationale Supérieure de Chronométrie et de Micromécanique

La Bouloie Route de Gray

25030 BESANCON, FRANCE

Summary

In the conventional design of a resonator, electrode deposition and bonding problems appear as important limitations (related to phenomena at the boundaries of the piezoelectric medium). So, if the enclosure is not considered, further progress are mainly expected from :

- a better solution of the "boundaries problems" including electrode deposition.
- improvements of crystals mounting.

First, it is quickly shown that electrode deposition and bonding processes usually cause crystals damages, contamination, ion migration, stresses and, as a consequence, various phenomena including aging. Different solutions are reviewed.

A new design using uncoated crystals is proposed and described. Lower aging, easy frequency adjusting and high Q factor can be provided at the same time. Sample surface preparation, resonator mounting and excitation conditions are discussed. The second part of this paper deals with the main characteristics of resonators constructed according to this new design. For comparison purposes, numerical data and typical curves concerning a 5 MHz fifth overtone design are given (including electrical parameters, frequency spectrum, frequency stability $\sigma_y(\tau)$ and long-term drift).

The various results are discussed so as to see which improvements could actually be obtained by use of this new technique.

Key Words : Piezoelectric Resonator, Quartz, Unplated Resonator, Electrode Effects, Bonding Effects, Frequency Stability, Aging, Frequency Adjusting, Crystal's Noise Reduction.

Introduction

The conventional design of a resonator using plated crystals is almost the only design available nowadays. The universal use of coated units has been introduced by Roger A Sykes in the Years 1948. Since Warner's design achievement [1] in 1952, various improvements have been added but no major change has appeared. The conventional design actually reaches the top of the state of the art.

Nevertheless, since the today's requirements in crystal resonator technology are constantly increasing, phenomena at the boundaries of the piezoelectric medium must be carefully checked and if possible mastered. For instance, as pointed out by Eer Nisse [2], the stored frequency shift due to electrode deposition is as much as five order of magnitude larger than typical specifications for long term drift (5 MHz fifth overtone units). But, mastering the boundary phenomena could reduce the aging and crystal's noise contribution as well. Then if the difficult problem of the enclosure [3] is not considered, further progress are expected from improvements in electrode deposition and crystal mounting. Of course, the best solution for plating should be to have none, and the best fixation of a crystal should exhibit neither discontinuity nor additionnal stress, crystal damage or contamination.

In Next section, we will first point out some of the difficulties usually met in a conventional design.

Consequences of Plating and Bonding In a Conventional Design

In the usual manufacturing process of a plated crystal a thin metallic film (gold, silver, Aluminium or Copper) is deposited on-to contoured crystal surfaces which have been previously either polished or etched. Usually the crystal is cemented to thin nickel ribbon fixations, T.C. bonded or electrobonded.

Plating should be considered first since its effects occur in the very energy trapping zone. Nevertheless the stress relaxation in the mounting structure and the contamination which is caused by the bonding process cannot be ignored.

Plating is always a very rough process for the crystal surface neighbourhood. The crystalline arrangement is partly upset, piezoelectric properties are locally modified, metallic ions penetrate inside the crystal thereby generating further ion migration. The surface of the crystal is drastically perturbed and the perturbation will not be constant versus time so giving rise to further frequency drift. At the same time, thin film stresses cause a non negligible frequency shift, which is not stable with time. Several fundamental phenomena beeing involved it is difficult to predict the exact noise contribution of

† This work is supported by the "Direction des Recherches et Moyens d'Essais", DRME.

the plating and the exact frequency drift contribution as well. Nevertheless, it has been possible to prove that small intrinsic stresses correspond to improved aging [4] and that probably the intrinsic aging of quartz material is orders of magnitude lower than aging exhibited by plated units.

At the same time, the Q factor, mainly determined by the internal friction in quartz, is reduced by the damping due to the metal deposited on the surface. But this effect should not be exaggerated, since the Q factor obtained with plated units according to the Warner's design is close to the intrinsic Q factor of the material. Moreover excitation by reduced electrodes, annular electrodes or parallel field technique have been widely used and can be considered as a first attempt to suppress plating [5]. At last, it must also be pointed out that, recently, A. G. Smagin [6] obtained very high Q factor with an experimental device using an unplated artificial crystal.

Let us consider now the frequency adjustement of plated units. It is a very important problem. Various techniques operating by additionnal deposition of metal are used, in situ environment or not.
First, the stability of the frequency adjustement, especially in situ environment, is a matter of discussion.
Second, it is generally difficult to adjust the frequency of a given unit to better than one p.p.m of the nominal frequency. (Of course, this does not include the laser machining technique which is only available for glass enclosure type units). Nevertheless a more accurate frequency adjustement is needed for some applications ; so further progress is also desirable in this domain.

New Design Using Unplated Crystals

Starting from a conventional design we tried to obtain :

- a preparation of the crystal surface avoiding acoustic absorption in the first few surface layers of the quartz plate. This preparation included a correct decontamination of the surface.
- electrical excitation by electrodes deposited close to the crystal surface on insulators mechanically stable with respect to the crystal.
- improved fixation (more precision and less contamination, additionnal stresses and discontinuities).

For facility, the new design will be called B.V.A design (B.V.A stands for the French "inside a Box with Lower Aging"). The very first trials, were achieved in 1972. More systematic investigations have recently lead to several designs named $B.V.A_n$, all using uncoated crystals. If n is odd a rather conventional bonding and a special fixation are used.
If n is even the design uses improved bonding and mounting. This denomination indicates two successive steps of our attempt to reduce the crystal's noise and frequency drift contribution.

As an example we shall completely describe the basic design of one type of the first serie.

$B.V.A_1$ Design (A.T. cut)

1) General description :

The resonator is represented in Fig. 1 and Fig. 4 and includes :

- a crystal, ref. 1, the surface of which has been very carefully prepared. This crystal is enclosed between two silica condenser plates ref. 3, 4, while a silica ring ref. 2 keeps the tickness of the condenser constant. Electrodes are deposited on the disks ref. 3, 4
- a crystal fixation
- a metallic experimental soldered enclosure which is sealed by a pinch off process.

2) Sample surface preparation :

The crystal is very carefully lapped and sometimes polished. Especially, at the end of the manufacturing, we used two processes matching together. The first process P_1 gives a correct geometrical contour, the second P_2 cleans or etches the surface. The resonant frequency f_r of the crystal is used as a test. P_1 is used, then P_2, then P_1 and so on, so as to obtain an asymptotic increasing of f_r. And the end P_2 is always used to obtain correct cleaning and avoid layers destroyed by P_1.

As far as possible, we try to operate in a clean atmosphere i.e. free from dust particles and chemically controlled. Of course the quartz wafer is very carefully rinced, dried and cleaned (including U.V cleaning) using the results of recent investigations [7].

3) Resonator mounting and excitation conditions :

Let us suppose for instance a 5 MHz, fifth overtone, plano-convex wafer. The crystal is T.C. bonded fellowing the usual process and fixation is made by means of two, or even more, thin nickel ribbons. (The crystal may, of course, be cemented too, but T.C. bonding is prefered to avoid, later on, vacuum modifications in the sealed enclosure). The lower silica disk insures the crystal fixation. Holes, approximately 3 mm in diameter, have been drilled in the disk. They are slightly conical (approximately 1°) little nickel cylinders ref. 5 are given the same external conical shape and inserted into the holes. The nickel ribbons are soldered to the nickel cylinders so that an air gap ranging from some microns to a few tens of microns is left between the disk and the crystal.
The upper disk may be contoured (using the some contour used for the crystal), or it may be flat. It is located very close to the crystal (between some microns and a few tens of microns) by means of a ring which can be made out of fused silica but which can also be piezoelectric and variable in thickness for instance. This ring provides a very accurate frequency adjustement since a variation of 1 micron of its thickness corresponds approximately to a variation of 1 Hz of the resonant frequency. Actually, rings are not lapped individually to the correct thickness but choosen among a lot having slightly different thicknesses.
The main advantage of this ring is to allow very accurate frequency adjustements (better than 1 Hz for a 5 MHz fifth overtone) and to introduce more parameters on which the resonator properties depend. Especially it must be pointed out that the resonant frequency may be easily modulated.

For accurate frequency adjustement, the following procedure is used :

- first obtain a plot of the frequency versus temperature curve of the wafer mounted in a test device
- second mount the resonator at a well known temperature and take into account the frequency variations from various origins (temperature, enclosure under vacuum, ...).

Main Characteristics of B.V.A$_1$ Resonators

B.V.A resonators can be achieved at any usual frequency but they are given more interest in the high frequency range since the electrode phenomena are relatively more important at high frequencies for thin crystals. Nevertheless, for comparison purposes, we choose to study first the 5 MHz, fifth overtone, classical AT cut, resonator.
The comparison will then be performed in good conditions since :

- in the usual design the electrode problem is less important for thick crystals.
- the 5 MHz, fifth overtone, classical resonator represents a well known top of the state of the art.

Electrical parameters :

The equivalent linear circuit is given fig. 2, and the ordinary plated units correspond to the scheme of fig. 3. The two equivalent circuits are connected by :

$$L_1 = \left(\frac{Cg + Ce}{Cg}\right)^2 L$$

$$C_1 = \frac{Cg^2}{(Cg+Ce)\ (C+Ce+Cg)}\ C$$

$$R_1 = \left(\frac{Cg + Ce}{Cg}\right)^2 R$$

$$Co = \frac{Cg\ Ce}{Cg + Ce}$$

Numerical values clearly indicate that L_1 C_1 R_1 are very close to L, C, R respectively if the air gap is in the micron range. Also, the frequency of the unit can be easily pulled by means of a serie capacitor.
The following results have been currently obtained using natural quartz :

$$R_1 \simeq 85\ \Omega \qquad Q \simeq 2.45\,10^6$$

The gaps were about 20 microns each, the electrodes were golden circular electrodes 10 mm in diameter. We obtained some improved results by using artificial quartz and certainly it would be useful to select the blanks (this has not been done yet).

Frequency spectrum and non linear effects :

Frequency spectra very similar to those obtained with coated units, are found, resonance peaks are exhibited at the same frequencies (identical to better than 2×10^{-4}). No additionnal resonances appear and it seems that the elimination of unwanted modes is at least as good with the B.V.A design.

The amplitude frequency effect was investigated and was found to be two times more important than observed with usual design (a crystal driven with 2 m A exhibited a relative frequency change of $1.5\,10^{-6}$).

Thermal properties :

The B.V.A resonator exhibits longer time constants but the frequency temperature curve is similar to those usually obtained. In addition some gradient effects appear. Of course, the heat transfer process between the crystal and the medium outside the enclosure is very different from usual since the crystal is not connected to the outside through metallic conductors.

Frequency stabilities and frequency drift :

Direct measurements of the fluctuations of the resonant frequency, in a passive circuit, have been performed [8].
The crystal beeing driven at 5µw, the flicker level was found to correspond to :

$$\sigma_y(\tau) = 4.2\,10^{-12}$$

The results could later be related to the mechanisms contributing to the frequency instabilities in crystals [9-10].
The relative frequency stability has also been measured [11] using an ordinary test oscillator with gain automatic control but without special environment conditions. The fellowing results have been obtained for a drive level of 2.5 µw :

$\tau = .36$ s $\qquad \sigma_y(\tau) = 1.2\,10^{-11}$
$\tau = 3.6$ s $\qquad \sigma_y(\tau) = 1.7\,10^{-11}$
$\tau = 36$ s $\qquad \sigma_y(\tau) = 2.7\,10^{-11}$

Long term drift experiments have not been completely carried out yet. Nevertheless oscillators have been tested [12] after 3 days continuous operation in an excellent laboratory environment.
The temperature stability in one point of the oven beeing within 10^{-3}°C and the oscillator level less than 1µw, the frequency drift was lower than 3×10^{-10} per day

Systematic investigations concerning tests with respect to vibrations and shocks have not been carried out yet.

Other B.V.A. Types

Resonators using designs slightly different or different from the basic B.V.A$_1$ design are now constructed and tested [11-12]. It is certainly too soon to give complete description and results since we are just beginning the tests which are devoted to design improvements. Nevertheless we can point out that some encouraging data have been obtained.

For instance the very first resonators of the B.V.A$_2$ type (neither major discontinuity nor major local stress caused by the bonding process) evaluated from ordinary natural quartz exhibited the following results :

$$Q \simeq 2.8\,10^6 \qquad R_1 \simeq 60\ \Omega$$

The crystal beeing driven at 5 µw the flicker noise level was found to correspond to [8]

$$\sigma_y(\tau) = 3.7\,10^{-13}$$

The relative frequency stability using exactly the same oscillator [11] used for the B.V.A$_1$ type is better than :

$\tau = 0,1$ s $\quad \sigma_y(\tau) = 210^{-12}$

$\tau = 1$ s $\quad \sigma_y(\tau) = 10^{-12}$

$\tau = 10$ s $\quad \sigma_y(\tau) = 10^{-12}$

The results are just indicative since the experiments are still carried on.

Comments and Provisional Conclusions

The results of our first attempts are rather encouraging since many features of the resonators can be improved. Particularly it must be pointed out that the enclosure problem has not been solved at all (at least, cold welded type enclosure should be used). When some evident improvements of the technique are effective the results should be much better.

The new resonators are interesting for fundamental studies. Some of their properties are different from usual, especially the properties related to heat transfer processes, to the crystal's noise contribution and to the frequency drift of oscillators.

It must also be pointed out that some additionnal construction parameters appear, because the properties of the resonator do not depend only on the crystal.

The frequency stabilities obtained are also interesting since the very first results are involved.

Much work is to be done before more definitive conclusions are given but, nevertheless, this first attempt indicates that this technique could be very promissive.

References

1 - A.W. Warner Proc I.R.E. p.p. 1030-1033 Sept. 1952

2 - E.P. Eer Nisse A.F.C.S. p.p. 1-4 1975

3 - P.D. Wilcox G.S. Snow E. Hafner J.R. Vig A.F.C.S. p.p. 202-210 1975

4 - E. Hafner and R.S. Blewer, Proc. I.E.E.E. 56, 336 (1968)

5 - R. Bechmann A.F.C.S. 1953
W. Ianouchevsky A.F.C.S. p.p. 233-247 1963

6 - A.G. Smagin Pribory i Teckhnika Eksperimenta N°6, p.p. 143-145 Nov. Dec. 1974

7 - J.R. Vig J.W. Lebus Proc 29th A.F.C.S. p.p. 220-229 1975

8 - Measurements performed in the National Bureau of Standards by J.J. Gagnepain

9 - F.L. Walls I.E.E.E. Trans. Instr. and Meas. vol I M 24 N°1 March 1975

10 - J.J."Gagnepain Fundamental Noise Studies of quartz resonators" elsewhere in this Proceedings volume.

11 - Measurements performed in the Laboratoire de Physique et Métrologie des Oscillateurs C.N.R.S. by G. Marianneau

12 - Measurements performed in our Laboratory.

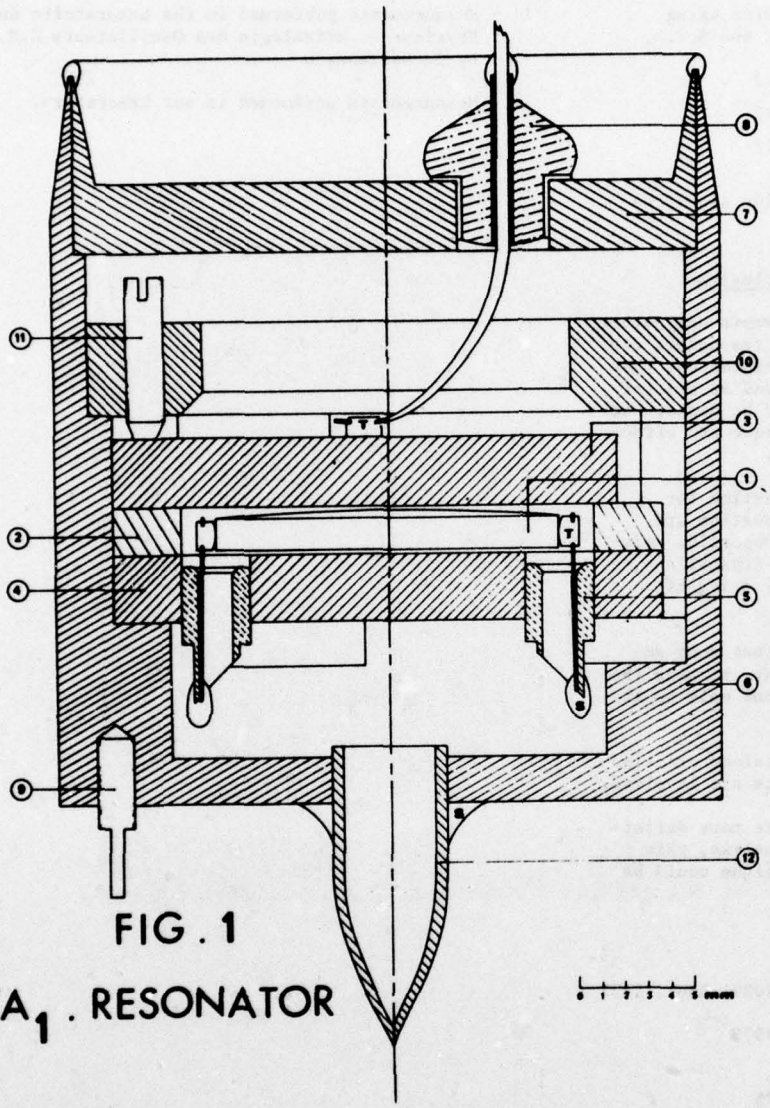

(1)	Crystal
(2)	Silica ring
(3) (4)	Silica disks
(5)	Mount
(6) (7)	Enclosure
(8)	Isolator
(9)	Grounding
(10)	Metallic ring
(11)	Screw or spring
(12)	Pinch-off
S	Solder
T	T.C.bond

FIG . 1

B.V.A$_1$. RESONATOR

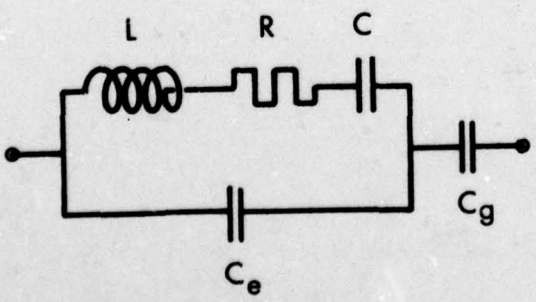

FIG - 2

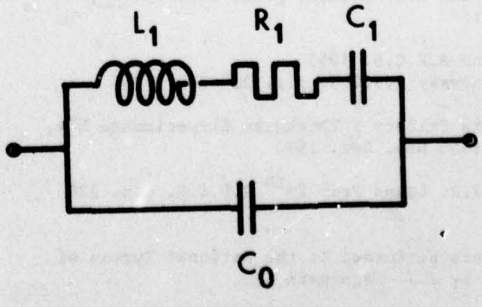

FIG - 3

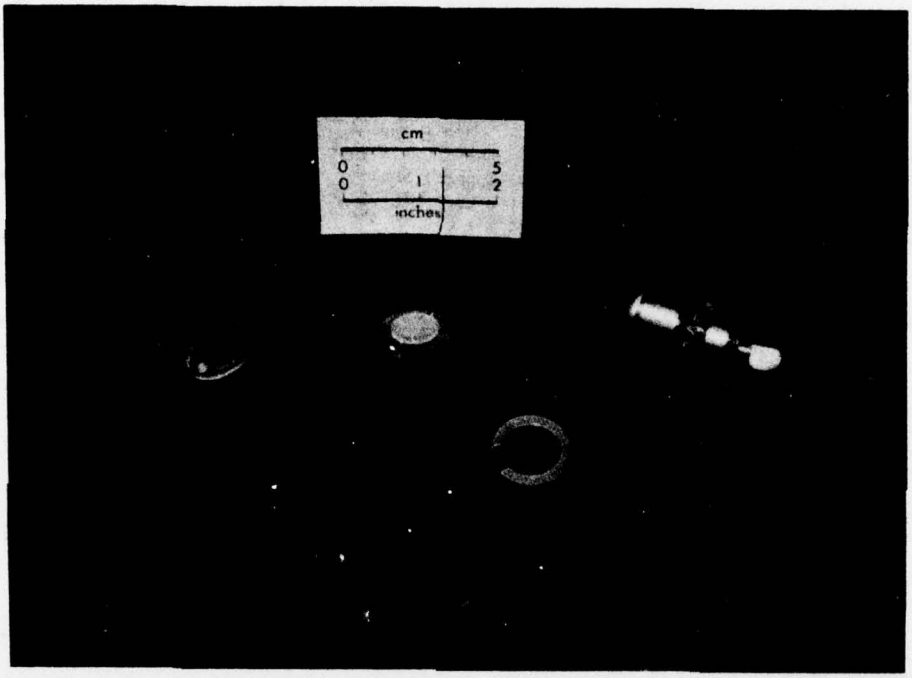

FIG - 4

FUNDAMENTAL NOISE STUDIES OF QUARTZ CRYSTAL RESONATORS

J.J. Gagnepain

Ecole Nationale Superieure de Chronometrie et Micromecanique*
Besancon, France

Summary

The studies of quartz crystal oscillator frequency instabilities show they are not entirely due to electronics noise but the quartz resonator itself must be considered as a noise source. The previous investigations of resonator frequency noises (given by F. Walls) gave an important indication about their levels. This work presents the results of measurements of frequency fluctuations of quartz resonators used as passive fourports. The noise is characterized in the frequency domain.

Several noise sources contribute to the frequency fluctuations. Correlation with external perturbations as vibrations and temperature fluctuations are studied. In the power density spectra the noise at the lowest Fourier frequencies is related with thermal effects and mainly with thermal stresses. The flicker noise level is partially related with the resonator design. Different kinds of resonators at different frequencies are used with particular plating types and shapes.

Introduction

To improve the quartz crystal oscillator stability it is important to be able to separate in the noise the part due to the resonator from the part due to the electronics. Measurements of resonator resonance frequency noise have been performed by F. Walls [1] at 5 MHz and 10 MHz. The present work is a continuation of these previous measurements.

The short-term stability is mostly limited by the additive thermal noise and therefore could be improved by increasing the driving voltage. But relatively high powers cannot be achieved because they increase the flicker noise level, and the amplitude to frequency noise conversion. On the other hand this can have an influence on the long-term stability, as the power drifts will be converted to frequency drifts.

The long-term stability is affected by the electronic components and, principally, by a change of resonator parameters with age. These phenomena are related to the technology and some mechanisms like impurity migrations inside the crystal lattice, surface transformations, and leaks in the enclosure. There is also stress relaxation in the electrodes [2]. One interesting solution is the actual development of electrodeless resonators [3].

The stability in the region from about 1 s to 100 s is limited by the flicker noise and the random walk frequency noise. These noises are direct modifications of the resonator resonance frequency. Their physical mechanisms are not understood yet and the best way to study them appears to be the use of resonators as passive devices.

Measurement System

The measurement system which has been used is similar to the one presented by F. Walls [1] but features some modifications. This system is schematically shown in Fig. 1.

Two resonators Q_1 and Q_2, identical or made identical by means of the resistors r_1, r_2 and of tuning capacitors Γ_1 and Γ_2, are driven in transmission by the source S and their phases are compared with the double balanced mixer M_1. An adjustable phase shifter permits one to operate the mixer at the quadrature point. The phase noise at the mixer output is proportional to the resonator's frequency fluctuations. Using the integrator I_1 and the varactor diode D_1 it is possible to lock the frequencies of both resonators together with an appropriate attack time. The second device using the mixer M_2 is used to calibrate the sensitivities (in fact to control the factor Q/w, where Q is the quality factor and w the resonance frequency) for each resonator. This is very important when any parameter in the measurement system is changed. It is also useful to lock the quartz Q_2 with the source using the integrator I_2 and the varactor diode D_2. Special care must be taken in the adjustment of the frequency tuning and Q factors balancing in order to remove the influence of both frequency and amplitude noises from the source. The equivalent circuit is shown in Fig. 2.

Let's introduce the angular resonance frequencies ω_1 and ω_2

$$(1) \qquad \omega_1^2 = 1/L_1C_1, \quad \omega_2^2 = 1/L_2C_2$$

the Q factors Q_1 and Q_2

$$(2) \qquad Q_1 = L_1\omega_1/R_1, \quad Q_2 = L_2\omega_2/R_2$$

The capacitors Γ_1 and Γ_2 will tune the angular frequencies to the values ω'_1 and ω'_2.

$$(3) \quad \omega'^2_1 = \omega_1^2\left(1 + \frac{\Gamma_1}{\Gamma_1+C_0}\right), \quad \omega'^2_2 = \omega_2^2\left(1 + \frac{C_2}{\Gamma_2+\gamma_0}\right).$$

The resonator tuning will force $\omega'_1 = \omega'_2$. Let's introduce the driving signal angular frequency $\omega = \omega_1 + \Delta\omega$ where $\Delta\omega$ is the difference between ω and the resonator resonance angular frequency ω_1. After several approximations (high Q factors, $\Delta\omega$ small and $Q_1/\omega_1 = Q_2/\omega_2$) the phase difference Φ at the mixer output is given by the relation:

$$(4) \quad \Phi \simeq 2\,\Delta\omega\left(\frac{Q_1}{\omega_1} - \frac{Q_2}{\omega_2}\right) + 4\,\Delta\omega^2\,Q_1\left(\frac{1}{k_1\omega_1^2} - \frac{1}{k_2\omega_2^2}\right) + \frac{\omega_1^2}{Q_1}\left(\frac{1}{k_2\omega_2^2} - \frac{1}{k_1\omega_1^2}\right)$$

with

$$(5) \quad k_1 = \frac{C_1\Gamma_1}{C_0(C_0+\Gamma_1)} \quad \text{and} \quad k_2 = \frac{C_2\Gamma_2}{\gamma_0(\gamma_0+\Gamma_2)}.$$

The first term in the relation (4) can be cancelled out, balancing the Q/ω factors. The third term is frequency independent and can be removed, adjusting the DC output amplitude offset. In the case of $C_0 = \gamma_0$ and C_0, $\gamma_0 \leq \Gamma_1$, Γ_2 the relation becomes:

*This work is being performed at the Frequency & Time Standards Section, National Bureau of Standards, Boulder, Colorado 80302.

$$(6) \quad \Phi = 2\,\Delta\omega\left(\frac{Q_1}{\omega_1} - \frac{Q_2}{\omega_2}\right) + 4\,Q_1\,C_0\Delta\omega^2\,(L_2-L_1) + \frac{\omega_1^2 C_0}{Q}\,(L_2-L_1).$$

The source frequency fluctuations influence will be minimum for the particular value $\Delta\omega_0$ of $\Delta\omega$:

$$(7) \quad \Delta\omega_0 = -\frac{(Q_1/\omega_1 - Q_2/\omega_2)}{4\,Q_1\,C_0(L_2-L_1)}.$$

If the source frequency adjustment is achieved with a small error ε_0 and if the source fractional frequency fluctuations y_s are introduced, the phase noise $\delta\Phi_s$ due to these source fluctuations is given by the relation:

$$(8) \quad \delta\Phi_s \simeq 8\,Q_1 C_0\,(L_2-L_1)\,\varepsilon_0\,\omega_1 y_s.$$

Introducing the fractional frequency fluctuations of the resonator, y_q, we find for the corresponding phase noise $\delta\Phi_q$ for the pair:

$$(9) \quad \delta\Phi_q = -2\sqrt{2}\,Q_1 y_q.$$

For 5 MHz, 5th overtone, resonators with , for instance, $C_0 = 10 \times 10^{-12}$ F, $L_2-L_1 = 2$H, $\varepsilon_0 = 5$ rad/s we will obtain the following ratio between both noises

$$(10) \quad \frac{\delta\Phi_q}{\delta\Phi_s} = 2\times10^3\,\frac{y_q}{y_s}$$

which shows that the source noise influence can be removed with the appropriate adjustment. The curves shown in Fig. 3 represent the mixer output voltage as a function of the source frequency and the Q factor balancing. A residual noise is unbalanced because of time delay differences in the cables and circuitry. It is included in the measurement system noise and it is measured substituting resistors in place of the resonators.

The previous calculation is valid for frequencies within the resonator linewidth. For frequencies outside the linewidth it is necessary to take into account the resonator's filtering effect. If $S_y(f)$ is the power spectrum of fractional frequency fluctuations and $S_\phi(f)$, the corresponding phase spectrum, they are related by the following relation where f is the Fourier frequency:

$$(11) \quad S_\phi(f) = S_y(f)\,\frac{\omega_1^2}{(2\pi f) + \frac{\omega_1^2}{4Q_1^2}}.$$

Moreover, the source amplitude noise is transformed into frequency noise by the resonator amplitude-frequency effect. This depends on the driving level, but there is compensation between the two resonators if they are identical. With the source* used in these studies, and a power of 1 μw, the equivalent $S_y(f)$ (in 1 Hz bandwidth) at 1 Hz from the carrier, due to this effect is equal to 10^{-28} for regular 5 MHz, 5th overtone, resonators. The second effect of amplitude modulation will be to introduce noise at the mixer output because of the nonlinearities of the mixer. With voltage amplitude of 1V p.t.p. the corresponding noise is of the order of 1 nv (at 2 Hz). It is lower than the measurement system noise and, in fact it is always possible to adjust the driving levels on both the mixer inputs to minimize this noise.

*The source was a high quality frequency synthesizer

Most important is the load impedance, particularly the reactive part, because any variation in this will change the resonator frequency following the relation:

$$(12) \quad \left|\frac{d\omega'_1}{\omega'_1}\right| = \frac{C_1}{2\Gamma_1}\,\frac{d\Gamma_1}{\Gamma_1}$$

where Γ_1 includes the tuning capacitor and the first stage amplifier input capacitor (with the assumption $\Gamma_1 > C_0$). For a 5 MHz, 5th overtone, resonator $C_1 = 4\times10^{-4}$ pF and, for example, with $\Gamma_1 = 100$ pF we obtain $d\omega'_1/\omega'_1 = 2\times10^{-6}\,d\Gamma_1/\Gamma_1$. It is therefore necessary to choose tuning capacitors with quality such as $d\Gamma_1/\Gamma_1 \leq 10^{-8}$.

In fact, in most oscillators the medium term stability can be limited by the fluctuations of the reactive part of the impedance, if enough care is not taken. The choice of the vibration mode of the resonator is important too, because the value of the motional capacitor C_1 is approximately inversely proportional to n^3, where n is the overtone rank. The electrodes' size also defines the C_1 value. Therefore the higher the overtone rank and the smaller the electrode surface, the lower will be C_1.

The noise obtained at the measurement system output is applied to a spectrum analyzer with a 1 Hz bandwidth and a 2 - 1000 Hz frequency range. At the same time this noise is filtered using a constant Q filter, in the range 0.01 - 10 Hz. The filtered voltage is converted into frequency and its mean square value measured and calculated with a computing counter. These two parts of this frequency domain phase noise measurement system thus have overlapping ranges and allow the direct measurement of $S_\phi(f)$ over a total range of f = 0.01 Hz to f = 1000 Hz.

Experimental Results

The fractional frequency fluctuation's density power spectrum $S_y(f)$ is calculated from the relation (11) where $S_\phi(f)$ is obtained as described above, taking into account the mixer sensitivity (3.7 mV/degree) and the amplifier gain (10^4).

Frequency and Plating Influence

Fig. 4 depicts the spectra of resonators at 1 MHz, 5 MHz, 10 MHz and 25 MHz. The lowest noise level is obtained with the 5 MHz crystals. In the spectra the slope of f^{-1} corresponds to flicker noise. The dotted part is the directly measured result, corrected using relation (11). At low Fourier frequencies, the spectra present slopes of f^{-2} (random walk of frequency) and f^{-3}. With the 10 MHz resonators, important differences in the flicker noise levels have been found between resonators of the same type. A resonator with a flicker noise of 4×10^{-19} (at f = 1 Hz) at room temperature, heated up to 90° C presented a decrease of its noise level to 1×10^{-22}, which remained unchanged after coming back to room temperature. This phenomenon may be related to stress relaxation in the electrodes [2].

Several 5 MHz resonators vibrating in the fundamental mode have been studied with circular platings and Z shaped platings, but with the same mounting. The noise

level is decreasing with the electrodes surface, but without significant proportionality. The same study performed with 5 MHz, 5th overtone, resonators using circular and rectangular platings of different surface area presents also a noise increasing with the plating area. Among this series of resonators made with the same technology, the lowest noise levels obtained at f = 1 Hz, using a power of 10 μw during these measurements are shown in Table I.

resonator type	sample size	S_y(1 Hz)
5 MHz fund. circular plating	2	5×10^{-22}
5 MHz fund. Z plating	4	1×10^{-22}
5 MHz 5th overtone circular plating	6	1×10^{-24}
5 MHz 5th overtone rectangular plating	2	1.5×10^{-23}
5 MHz 5th overtone electrodeless	2	2×10^{-25}

TABLE I.

Vibrations

The external vibrations can be "naturally" present in the room, or experimentally applied accelerations. These acceleration experiments were carried out using a loudspeaker and a power amplifier. The accelerations were measured by an piezoelectric ceramic-type accelerometer mounted close to the tested resonator.

With one 5 MHz fundamental mode resonator, a direct influence of the vibrations have been found, shown in Fig. 5a. The spectrum presents a floor and a peak in the range 8 - 20 Hz, directly related with the vibration spectrum (Fig. 5b). In fact this sensitivity was entirely due to induced vibrations of the mounting and resonator output leads and it can be easily removed using stronger leads and fixation. Similar experiments with other resonators of Table I show no direct correlation between noise spectrum and low level external vibrations.

Temperature

More significant are the temperature effects. Noise measurements have been done at different temperatures. If there was a direct correlation between the resonator temperature coefficient and the noise level, this last one should be minimum at the temperature turnover point. Experimentally this was found not to be the case (except for very high temperature sensitivity). Under thermal perturbation the quadratic thermal properties of the crystal are not valid anymore and it becomes necessary to take into account the thermal gradients. Applying very fast temperature variations with a laser beam (power 1 mw) at different points on the crystal surface, thermal gradients and therefore thermal stresses were induced. The resulting frequency variations were measured with the previously discussed phase bridge. The frequency response of the 10 MHz resonators is shown in Fig. 6. The most sensitive points are those close to the fixation points. It is possible to calculate from these curves an equivalent temperature coefficient to compare it with the regular quadratic one. For instance, for the 10 MHz resonator, at room temperature the quasistatic temperature coefficient is 5.4 Hz/°C. For the curves of Fig. 6 with a slope (df/dt) at the origin, with m the crystal mass, C its specific heat, and P the beam power, the apparent temperature coefficient a is given by the relation:

$$(13) \qquad a = \left(\frac{df}{dt}\right) \frac{mC}{P} .$$

a is found equal to 50 Hz/°C for the worst case. The frequency variation due to thermal stresses is ten times greater than the variation due to thermal expansion and elastic coefficient changes.

For resonators with very high temperature coefficients an important noise level increase can be observed. Fig. 7 shows the noise spectrum of a double rotated cut resonator which is used as temperature sensor. Its temperature coefficient is equal to 360 Hz/°C. If, at 1 Hz, the frequency fluctuations are totally due to thermal fluctuations, this corresponds to temperature fluctuations of 8 μ°C.

The correlation between 10 MHz resonators frequency noise and the temperature fluctuations inside the oven has been studied using the previous temperature sensor, the frequency noise of which was measured using also a phase bridge. The resolution of this phase bridge corresponds in this case to a temperature resolution, at 1 Hz, equal to 0.2 μ°C. Both noise voltages $e_1(\tau)$ from the 10 MHz resonators and $e_2(\tau)$ from the sensor are filtered at a given common frequency, thus converted into frequencies using voltage to frequency converters. The cross correlations function $Re_1e_2(\tau)$ and the autocorrelation functions $Re_1e_1(\tau)$ and $Re_2e_2(\tau)$ are calculated with the computing counter. The cross-correlation coefficient $K(\tau)$ is defined by the relation:

$$(14) \qquad K(\tau) = \frac{Re_1e_2(\tau)}{\sqrt{Re_1e_1(0) \cdot Re_2e_2(0)}} .$$

Its maxima, at different Fourier frequencies, are shown in Table II.

Frequency	0.01 Hz	0.1 HZ	1 Hz
$K_{max}(\tau)$	60%	30%	6%

Table II.

There is a direct correlation for low frequencies corresponding in the spectra to the frequency random walk noise. This correlation decreases quickly at frequencies where the flicker noise becomes predominant. The measurements have been done using resonators in the differential method of Fig. 1. In fact, there must be some compensation between the temperature fluctuations of the two resonators, reducing the measured correlation. At this time, a quantitative assessment of this effect appears difficult. For an individual resonator the correlation will be stronger. The correlation depends also on the sensor position with respect to the resonators and certainly the best way would be to combine resonator and sensor in the same enclosure.

Remarks

The driving power level has an influence on the flicker noise level. This has been already observed in hard driven oscillators. But these is no precise

*Prototype resonators made by R. Besson, ENSCM, Besancon, France.

law as has been found for excess noise in resistors [4], where the noise power density is directly proportional to the dissipated power. In quartz crystal resonators this is true for high excitation powers ($\geq$ 10 µw), but for lower values it depends more on the crystal type and the technology used. A floor can be observed or even a noise increase. It is difficult to give interpretations of these phenomena, but they could be explained by surface effects due to impurities and vibrationally dead zones on the crystal.

The noise level is also a function of life time especially if the resonator is oscillating for the first time. Fig. 8a shows the noise level variation (at 1 Hz) versus time for 5 MHz, 5th overtone, resonators. Any perturbation of the oscillation gives also a temporary noise increase, but with different time constant, which could mean that both of these phenomena do not have the same physical origin. In Fig. 8b is shown the noise level evolution versus the time after the driving voltage has been turned off for one minute.

The thermal noise in quartz crystal resonators has never been measured. A theoretical evaluation of its value can be performed knowing the losses inside the crystal. The simplest way is to consider it as an additive noise, inducing phase fluctuations. An equivalant resonator frequency noise, giving the same phase noise, can be calculated and its power spectrum is given by the relation:

$$(15) \qquad S_y(f)_{thermal} = \frac{kT}{2Q^2P}$$

where k is the Boltzmann constant, T the absolute temperature, P the dissipated power, Q the Q factor and w_o the resonance angular frequency. For a power of 1 µw, a Q factor of 2×10^6 and at 300K $S_y(f)$ is equal to 1×10^{-27}(inside the resonator line width) and it is much lower than the measured noises.

Conclusion

Several noise sources contributing to quartz crystal resonator frequency fluctuations have been found. Among them, two main noises are to be distinguished: one related to temperature fluctuations at low Fourier frequencies, the other one causing flicker noise spectral behavior. This flicker noise could be related to several relaxation phenomena inside the crystal lattice but with some influence of environmental and surface effects which can be sometimes important.

It follows that it may be impossible to achieve in a single oscillator state-of-the-art short- and long-term stabilities at the same time. The solution could be the use of two resonators, as active and/or passive devices, driven respectively with high and low power to realize the possible stability over all Fourier frequencies. One other application is the possibility of using a passive resonator in a discriminator mode for the measurement of frequency instabilities of not so stable oscillators (or synthesizers).

From all available published material it appears that stabilities like aging of 10^{-12} per day and flicker floors in the high range of 10^{-14} could be achieved with quartz crystal devices in the near future.

Acknowledgements

This work has been carried out in the Frequency and Time Standards Section of the National Bureau of Standards. The author wishes to thank H. Hellwig for giving the opportunity to perform this study and for helpful discussions. He is deeply grateful too to F. Walls for his help and suggestions, and to R. Besson for providing the electrodeless resonators.

References

[1] F.L. Walls, A.E. Wainwright, "Measurement of the Short-Term Stability of Quartz Crystal Resonators and the Implications for Crystal Oscillator Design and Applications," IEEE Trans. on Instrumentation and Measurement, Vol. IM-24. no. 1, March 1975.

[2] E.P. Eer Nisse, "Quartz Resonator Frequency Shifts Arising from Electrode Stress," Proc. 29th SFC, Ft. Monmouth, NJ, 1975.

[3] R. Besson, A New Piezoelectric Resonator Design," Proc. 30th SFC, Ft. Monmouth, NJ, 1976.

[4] C.S. Bull, S.M. Bozic, "Excess Noise in Semi-Conducting Devices due to Fluctuations in their Characteristics when Signals are Applied," Brit. J. of Appl. Phys, Vol. 18, 1967.

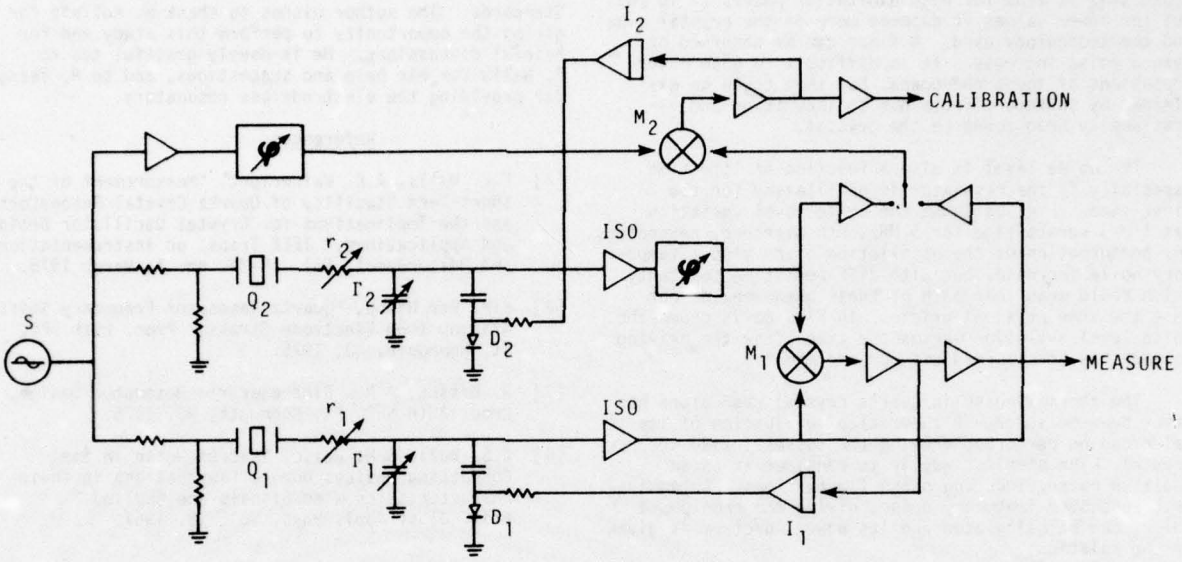

Fig. 1 Measurement system

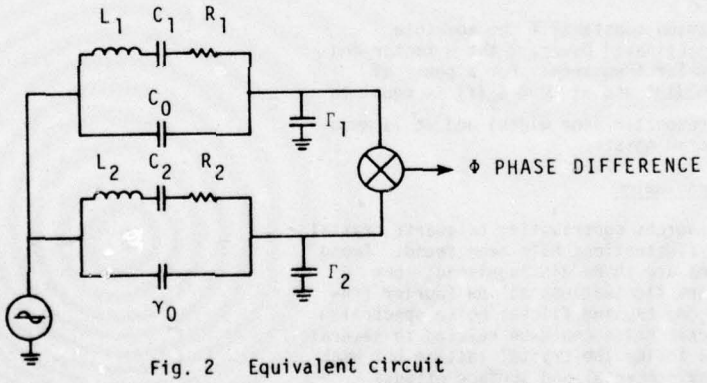

Fig. 2 Equivalent circuit

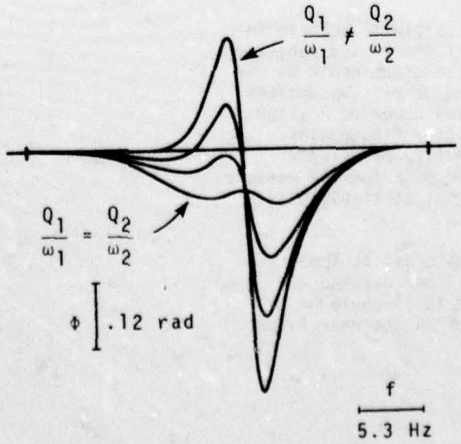

Fig. 3 Phase response of the measurement system as a function of the Q/ω factor balancing

AD-A046 089 ARMY ELECTRONICS COMMAND FORT MONMOUTH N J F/G 9/5
PROCEEDINGS OF THE ANNUAL SYMPOSIUM ON FREQUENCY CONTROL (30TH)--ETC(U)
1976 H K ZIEGLER

UNCLASSIFIED NL

2 OF 6
AD A046089

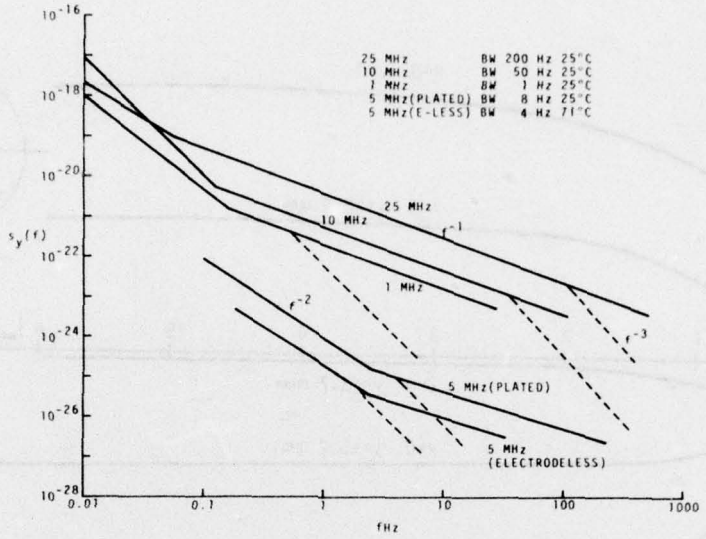

Fig. 4 Fractional frequency fluctuation's density power spectra of quartz crystal resonators at different frequencies

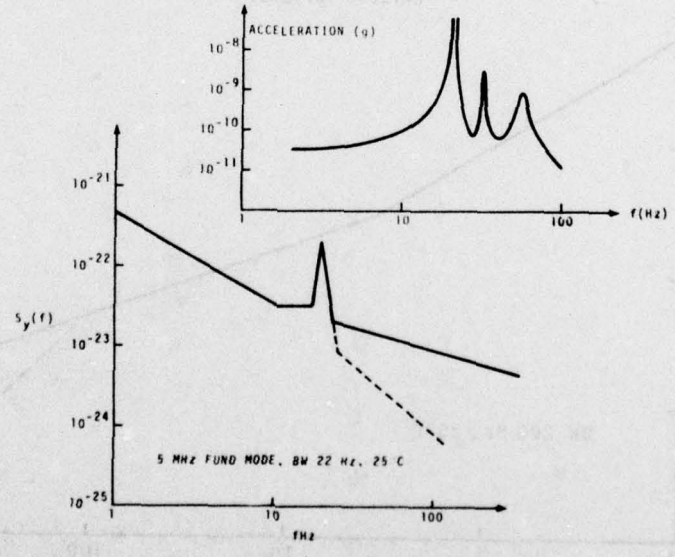

Fig. 5a Density power spectrum correlated with external vibrations

Fig. 5b External vibration amplitude spectrum

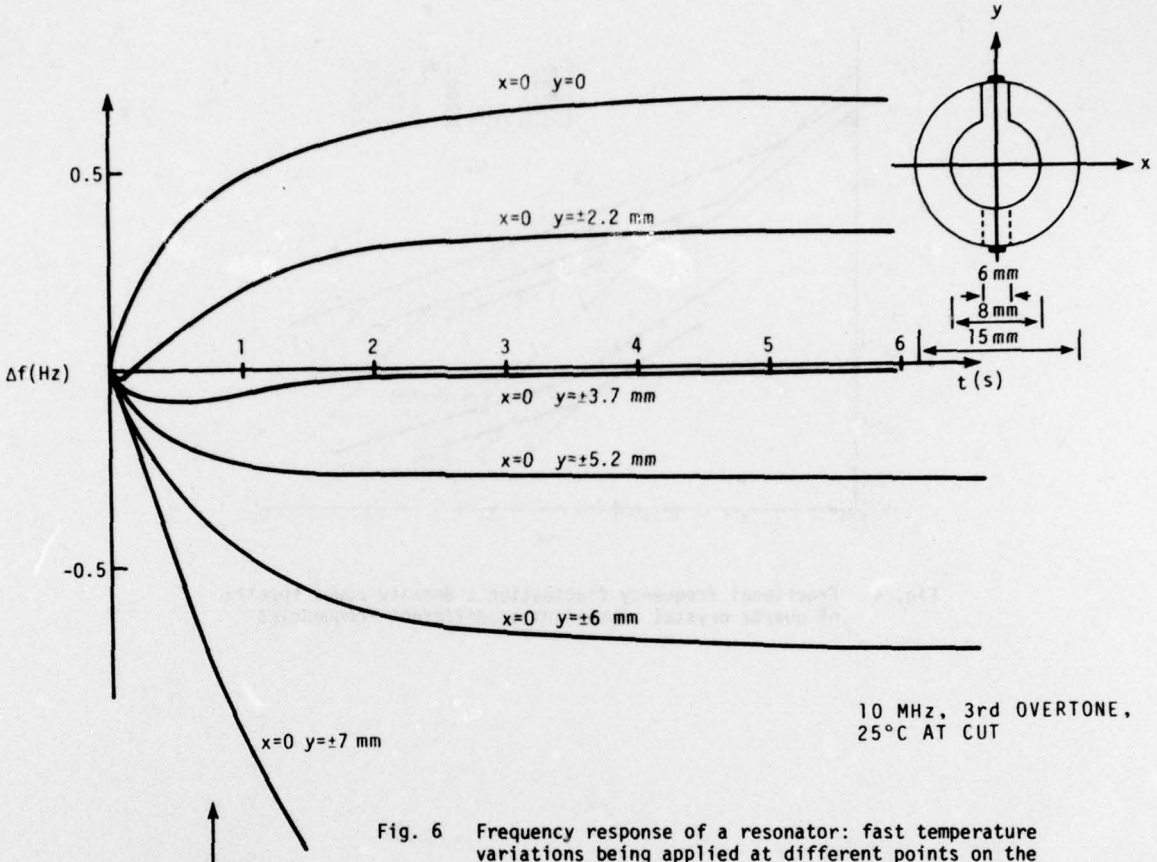

Fig. 6 Frequency response of a resonator: fast temperature variations being applied at different points on the crystal surface.

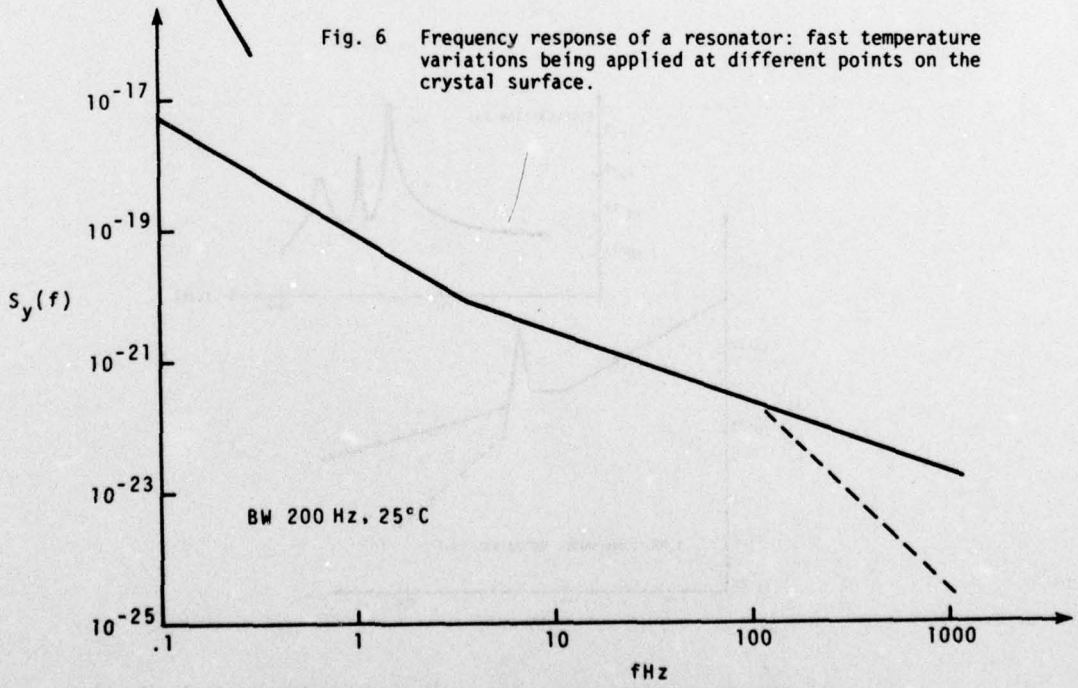

Fig. 7 Fractional frequency fluctuation's density power spectrum of a resonator with a high temperature coefficient (360 Hz/°C)

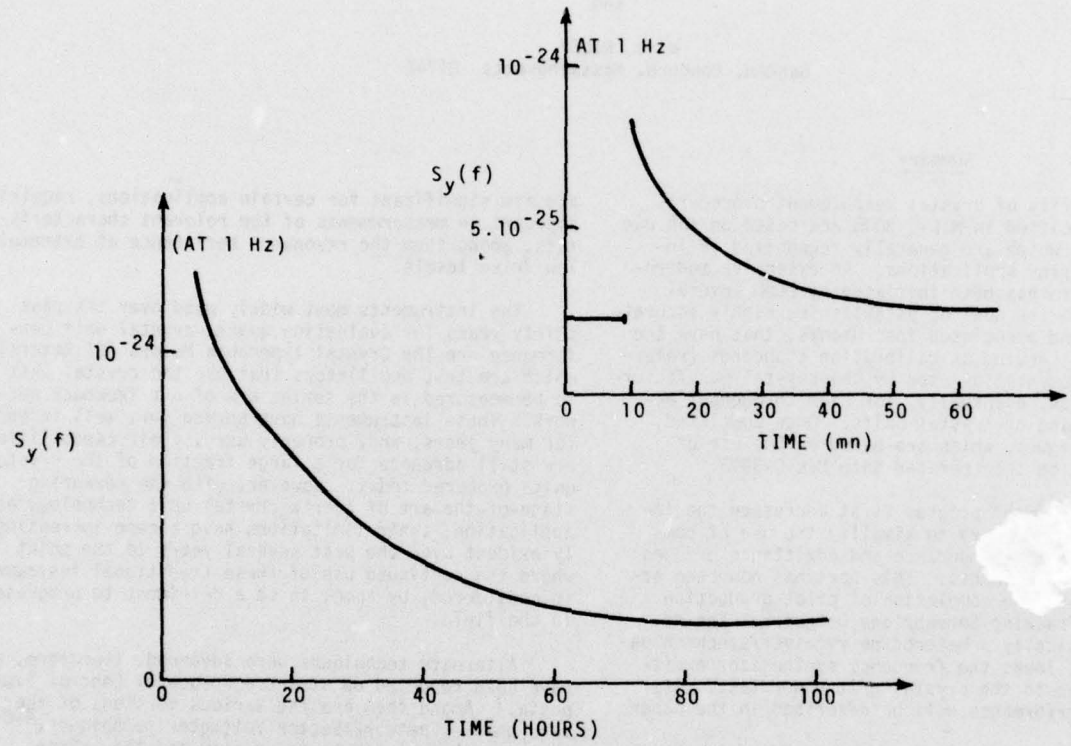

Fig. 8a Density power spectrum at 1 Hz variation versus time, the crystal being oscillating for the first time

Fig. 8b Density power spectrum variations at 1 Hz after a perturbation.

IMPLEMENTATION OF BRIDGE MEASUREMENT TECHNIQUES FOR QUARTZ CRYSTAL PARAMETERS

E. HAFNER
US Army Electronics Technology & Devices Laboratory (ECOM)
Fort Monmouth, New Jersey 07703

and

W. J. RILEY
GenRad, Concord, Massachusetts 01742

Summary

The majority of crystal measurement procedures currently specified in MIL-C-3098 are based on the use of CI Meters, which are generally recognized as inadequate for many applications. An extensive modernization program has been initiated by ECOM several years ago with the goal of establishing highly accurate techniques, and associated instruments, that have the capability of serving as calibration standards (referee) for instrumentation used by the crystal manufacturers, as well as, eventually, for high throughput acceptance testing of crystal units. Once completed, the new techniques, which are based on the use of bridges, will be incorporated into MIL-C-3098.

The development program first addressed the instrumentation necessary to simplify the use of commercially available impedance and admittance bridges for crystal measurements. This part has now been accomplished with the completion of pilot production models of a Tracking Servobridge Detector. The detector is basically a heterodyne receiver/synchronous detector that locks the frequency synthesizer exciting the bridge to the crystal unit under test. Its design and performance will be described in the paper.

The second phase of the program addresses the replacement of currently available mechanically operated bridges with a microcircuit admittance bridge that is electronically tuneable and capable of performing optionally manual, semi-automatic or fully automatic crystal measurements. The design of this bridge and its current state of development will be discussed.

Key Words
Measuring-Devices (Electrical-Electronic), Impedance-Bridges, Admittance-Bridges, Schering-Bridge, Microcircuit-Bridge, Crystal-Measurements, Crystal-Impedance-Meter, Detectors, Synchronous-Detection, Servo-Bridge-Detector, Quartz-Resonators, Piezoelectric-Resonators, Frequency-Standards, Heterodyne-Receiver.

Introduction

The complete characterization of the properties of quartz crystal units as electrical circuit elements requires evaluation of a large number of different performance aspects. The most basic of these are the resonance frequency and resistance, and their behavior with temperature and time. Frequently of comparable importance, but always of interest are, additionally, the motional arm inductance or capacitance, the static capacitance and the spurious mode spectrum, whereby at least the resistance of the strongest spurious modes must be determined. Many other aspects exist[1] and are significant for certain applications, requiring appropriate measurements of the relevant characteristics, among them the resonance resistance at extremely low drive levels.

The instruments most widely used over the past thirty years for evaluating quartz crystal unit performance are the Crystal Impedance Meters (CI Meters)[2], which are test oscillators that use the crystal unit to be measured in the series arm of a π feedback network. These instruments have served very well indeed for many years, and, properly used, their capabilities are still adequate for a large fraction of the crystal units procured today. However, with the advancing state-of-the-art of quartz crystal unit technology and application, their limitations have become increasingly evident over the past several years to the point where the continued use of these traditional instruments is considered, by some, to be a detriment to progress in the field.

Alternate techniques were advanced, therefore, and have been reported on at these Frequency Control Symposia.[3] Among them are the various versions of the zero phase π network/Vector Voltmeter techniques,[4-6] the network analyzer techniques[7,8] and the bridge technique.[9-11] All of them represent improvements to varying degrees, and at varying cost, over the instrumentation currently specified in MIL-C-3098. A particular version of the zero phase π network/Vector Voltmeter technique has already been selected as the recommended[12] basic technique for crystal measurements by the International Electrotechnical Committee (IEC). The maximum and minimum transmission use of the π network is recommended[13] by IEEE Standard 177.

It is apparent to most, familiar with the field, that the measurement aspects of MIL-C-3098, the basic procurement document for crystal units purchased by and for the US Government Services, are in urgent need of revision. It should be apparent also, based on past history, that the techniques that are selected now for this purpose will not easily be changed again in the near future, quite possibly not for another twenty years. In order not to be constrained soon again with an inadequate measuring system, the techniques to be introduced now should, at least, be capable of handling, with confortable margin and as economically as possible, all measuring tasks on crystal units now in production, as well as on those currently in the R&D phase. The most advanced unit in the latter category, expected to be used in relatively large quantities by the early 1980's has an anticipated frequency tolerance of 1×10^{-7} and $<2 \times 10^{-10}$/week aging.

The candidate technique with the best promise of meeting these requirements is based on the use of admittance bridges, and a concerted program is being pursued at and by the US Army Electronics Command to realize this promise in a practical manner. The purpose of this paper is to relate the progress being made on this program.

Bridge Measurements - General

Impedance and admittance bridges are designed to measure the resistive and reactive components of an "unknown" impedance by adjusting, in a calibrated manner, two electrically orthogonal internal elements until the output of the bridge is zero, i.e., the bridge is balanced. The values of the adjustable elements at balance are related to the "unknown" resistance and reactance respectively. The calibration of these values is checked by reference to "standard" elements inserted into the "unknown" terminals of the bridge.

Depending upon the design of the bridge, and depending on the magnitude of the parasitic circuit elements and leakage signals within the bridge, the density of calibration check points required to assure a desired level of accuracy will vary, with respect to the number of different "standard" values to be used and the number of different frequencies at which the calibration is to be performed. Thus, one might gain the impression that the accuracy of any particular bridge measurement is totally dependent upon the accuracy of the "standard" elements, which, certainly at high frequencies, are themselves rather difficult to evaluate. More specifically, one might be led to suspect, that bridge measurements on crystal units are fundamentally similar to alternate techniques which rely on the use of substitution elements.

There is a significant difference, however. Each substitution measurement stands on its own, with no link to any other measurement before or after, and hence without a means to detect the presence of extraneous factors affecting the measurement. A bridge, on the other hand, when used to measure broadband passive components, such as resistors or capacitors over a wide range of frequencies, should produce a self-consistent set of resistance and reactance readings which define, with arbitrary redundancy, the equivalent circuit of any particular component. This circuit should consist of only a small number of constant, i.e., frequency independent, elements to be plausible. The self-consistency requirement provides a very rigid check on the validity of the bridge calibration, in fact, it imposes a most unforgiving constraint on the proper design of the bridge.

Commercially available rf bridges can be expected to meet the self-consistency tests over their primary impedance and frequency ranges. The use of these instruments for crystal measurements, however, presents a number of practical difficulties. Being manually operated, their use carries a degree of tedium which is not easily eliminated by automation. The bridges are designed for use at room temperature and hence, crystal units in a temperature chamber can be connected to it only by means of comparatively long lines or cables. In fact, the electrical length between the plane of measurement within the bridge and the reference plane, where the crystal unit is located, is significant, and must be corrected or compensated for, even when the crystal unit is connected directly to the "unknown" terminals of these bridges.[14]

In an effort to circumvent these difficulties, ECOM has been exploring the feasibility of constructing an electronically tuneable microcircuit admittance bridge. The current status of this work will be described below.

Regardless of what type bridge is used for crystal measurements, a stable signal generator and a sensitive heterodyne receiver are required. If this receiver is equipped with a means to lock the generator frequency to the minimum of the bridge output signal, a very significant simplication of the measuring process results.[15] ECOM has pursued the development of an advanced receiver with suitable generator control functions through various stages [10, 16] of a program that has now resulted[17] in the completion of a pilot production line, at GenRad, for the "Tracking Servobridge Detector", to be described below. Incorporated in this device are already all features necessary to permit automating the operation of the elctronically tuneable microcircuit bridge. An interface unit between the bridge and the Tracking Servobridge Detector will be required, however. Both, the bridge and the interface unit are the subject of an ECOM R&D contract just awarded to GenRad.

Electronically Tuneable Microcircuit Admittance Bridge

Currently available commercial HF and VHF bridges were designed at a time when solid state devices, whose parameter values are electronically variable, were either not yet invented or in their infancy, and microelectronic technology in general was unknown. Application of these comparatively new components and techniques in the construction of bridges appeared to offer obvious advantages over the older designs; however, the degree to which the performance goals for bridges suitable for piezoelectric crystal resonator evaluation could be approached remained to be demonstrated. A number of breadboard models were constructed, therefore, with successively improved performance. The behavior of the two models completed most recently confirmed the feasibility of the basic approach.

The physical size of the recent breadboard models is illustrated in Figure 1. The entire bridge is contained in the round block in front of a Tracking Servobridge Detector (TSBD). The solid coax lines connecting the bridge to the TSBD are feedlines only, and not part of the measuring circuit. The bridge can thus be used quite remotely from the TSBD, such as in a multiple crystal oven. The two ten turn potentiometers in the box on top of the TSBD are used here for manual adjustment of the DC control voltages applied to the bridge. Crystal units can be clamped to the bridge terminals by means of the two spring loaded piano keys visible on top of the bridge block.

Figure 2 shows another configuration of the bridge body, mounted in a shell that can be used to form an oven around the bridge for single crystal measurements at elevated temperatures.

The circuit diagram of the bridge is shown in Figure 3. The configuration is that of a traditional Schering bridge, with additional elements as required for biasing the varactors C_1 and C_4, which serve as the variable bridge elements. The element values used are listed in Figure 3, except for R_5 and R_6, which are 450 kΩ and 850 kΩ respectively. All resistors are thick film elements, the fixed capacitors porcellain chips. The largest "unknown" conductance for which balance can still be achieved is G_x = 300 mmho, i.e., all crystal units with resistances greater than about 3.5 Ω can be measured. The "unknown" capacitance range is about ±45 pF.

Of crucial importance in the physical construction of the bridge is the elimination of residual rf leakage,

and the common mode rejection of the output transformer. The former is aided by the use of subminiature semi-rigid coax cables between the bridge network and the transformers, and by shielding between elements, the latter by the use of three transformers in tandem. The first of these is a 1:1 unit, specially wound, using 8 turns of two tightly twisted two strand acetate insulated wires, with the two strands in each wire connected serially to form the center tapped primary and secondary windings respectively. It, as well as the following two transformers T_2 and T_3 are housed in TO-5 cans. The bridge input transformer and the latter two are commercial, off the shelf items (Watkins and Johnson BT8C).

An exploded view of one form of the bridge is shown in Figure 4. The gold plated 7.62 cm diameter brass block has cavities machined into it to receive the transformers, the bridge proper and the DC and rf leads. In the second row of components in Figure 4, below the TO-5 transformers, is a top view of the platform which carries essentially all of the bridge components. It fits into the rectangular cavity in the block. To the left of it is the cavity cover for hermetic sealing, below it the bridge terminal block which also carries three chip capacitors that can be selected as series load capacitors when needed.

The equations governing the behavior of an ideal Schering bridge are frequency independent. Frequency dependent terms are caused primarily by the residual inductance associated with the finite dimensions of the bridge elements and the length of the interconnecting conductors. The significance of these terms increases with the square of the operating frequency, and with the inverse square of the bridge resistance values. The low impedance level and the wide frequency range of the bridge discussed here thus imposes particularly severe constraints on size, which, even in microcircuit form, are difficult to meet. Figures 5 and 6 show the results of measurements taken on the latest breadboard model which was completed only quite recently. In Figure 5 are the values of the capacitances C_1 and C_4 required to establish "initial balance", i.e., when the "unknown" terminals are open-circuited. The values at the highest frequency used (240 MHz) are seen to differ from those at low frequencies by about 8% due to the combined effects of the residual reactive elements present in the bridge. The behavior of C_{40} at frequencies below about 4 MHz is increasingly sensitive to residual leakage, i.e., construction details, as well as to the magnitude of the resistive elements which appear, actually or effectively, in the C_2 branch of the bridge.

The consequences of the residual inductances in the bridge model are even more apparent in Figure 6, where the solid curves represent the uncorrected data obtained when thick film resistors of various DC values and capacitor chips, respectively, were clamped into the bridge "unknown" terminals. Preliminary analysis of these results indicates that the dominant residual inductances are associated with well defined bridge elements, namely C_2 and C_6 (i.e., the C_4 branch) in Figure 3, and with the lead to the "unknown" terminal. If the values of these three residual inductances are assumed to be L_{c2} = 0.8 nH, L_{c4} = 1.0 nH and L_x = 1.5 nH, a self consistent set of corrected values can be calculated, with the result indicated by the dashed lines in Figure 6. These are seen to be easily within 5% of the low frequency values at all frequencies, except for the low frequency anomaly in the capacitance values similar to that discussed above for C_{40}.

The calculations required to effect these corrections are simple, and can be carried out along with those required to convert the DC bias voltage readings for C_1 and C_4 into resistance and capacitance values for the "unknown", on a hand held calculator if desired. Thus, even if the residual inductances can be further reduced by modification of the current design of the bridges - some modifications will be required in any case to reduce the low frequency anomaly -, their presence in the circuit is not intolerable. Their effect could, of course, be reduced also, possibly to the point where no corrections are required even at 220 MHz, by raising the impedance level of the bridge elements, i.e., by accepting, for example, 10 ohms as the lowest resistance for which the bridge can still be balanced. A separate bridge model would then be required to evaluate lower resistance crystals, such as are encountered frequently in the 5-25 MHz range. The current goal is to use only one model.

Of greater importance for the use of the bridge for crystal unit measurement, then the residual inductances still present, is the orthogonality of the resistive and reactive balance controls. Referring to Figure 3, it will be observed that, when a purely reactive "unknown" is inserted into an ideal bridge, only the value of C_4 needs to be adjusted to reestablish balance; when the "unknown" is purely resistive, only C_1 has to be changed, i.e., the adjustments in C_1 and C_4 are orthogonal.

If these two controls are perfectly orthogonal in a bridge, it will be capable of measuring the resonance frequency of a crystal unit with perfect accuracy, regardless of any other imperfections it might have. It is only necessary to leave C_4 at C_{40}, the value established during initial balance, and, with the crystal unit inserted, reestablish balance by adjusting C_1 and the generator frequency. The frequency found in this manner is, obviously, the resonance frequency, i.e., that frequency at which the crystal impedance is purely resistive. Alternatively, if cross terms exist between C_4 and C_1, due to some spurious bridge elements and/or rf leakage, the value of C_4 at balance, when a pure resistor is inserted in the "unknown" terminals, will differ from C_{40}, and the crystal frequency found at $C_4 = C_{40}$, will deviate from f_r.

The magnitude of the cross terms between the resistance and reactance balance controls of a particular bridge can be evaluated by analyzing data obtained on a sufficiently large number of resistors and capacitors. This has not yet been done for the microcircuit bridges constructed under the present program, hence no statements can be made about the probable accuracy of resonance frequency measurements. However, using the Tracking Servobridge Detector, it is possible to observe that any lack of orthogonality between the C_1 and C_4 controls of these bridges does not exceed 2 degrees at 240 MHz. None is observable below 100 MHz.

The repeatability of a measuring instrument can be determined only by an adequate number of tests extending over a period of time. The data accumulated on the microcircuit bridge system to date is insufficient to assess it. The resolution of the system, however, has been evaluated and is depicted in Figure 7, expressed as the smallest susceptance and largest resistance, respectively, which, when placed across the "unknown" terminals, can still be measured with 1% resolution. The curves shown apply to a bridge null of 140 dB, which is readily and smoothly attainable with the microcircuit bridge and Tracking Servobridge Detector. The latter has a useable sensitivity of about -150 dBm. As a matter of interest, when the input signal into the bridge is 0 dBm, the rf voltage across the open circuited "unknown" terminals is about 35 mV, providing a drive level of 30 μW for a 40 ohm crystal unit.

The bridge resolution in terms of susceptance, as shown in Figure 7, can be translated into attainable frequency resolution, when measuring crystal units, with the aid of Figure 8. The lower curve in Figure 7 shows that a susceptance change of 10^{-1} mmho can be resolved to better than 1% at all frequencies of interest here. Figure 8 then shows that, for example, on a crystal unit with R_r = 20 Ω and Q = 50,000, i.e., $\zeta = 10^6$, a frequency change of 3×10^{-8} can be observed with comparable resolution, that is to better than 3×10^{-10}. Thus, the resolution of the microcircuit bridge system appears to be adequate for precision performance evaluation, including aging, on all crystal units currently envisioned.

Tracking Servobridge Detector

The Tracking Servobridge Detector[17] is designed for use in conjunction with rf bridges and frequency synthesizers, or other suitable signal generators, to measure quartz crystals with high reproducibility and accuracy. The unit serves as a very sensitive detector for the bridge unbalance signal, permitting measurements at power levels ranging from several milliwatts to well below a nanowatt. High detectivity (-155 dBm) is achieved by super-heterodyne conversion, low-noise IF amplification and synchronous detection. The latter not only provides independent reactive and resistive unbalance detection but also permits the use of a control loop to lock the synthesizer frequency to the crystal under test, automatically maintaining reactive bridge balance. This key feature makes practical the widespread use of bridge measurements of crystals.

Other features of the Tracking Servobridge Detector include a X10 Frequency Multiplier (45-220 MHz) to extend the utility of synthesizers of limited frequency range, a broadband power amplifier with attenuator (+30 to -70 dBm) for control of the measurement power level, linear and log detector response modes, adjustment of synchronous detector phase, a wide range of swept frequency displays for initial setup and inspection of spurious modes, and a versatile servo amplifier for locked operation with automatic lock acquisition. The frequency lock servo system not only permits fast, automatic determination of a certain characteristic frequency of the resonator (series resonance, for example) but also can follow the impedance circle to determine crystal inductance or track frequency variations versus temperature.

A frequency range of 0.8 to 220 MHz is covered. The instrument (with companion Offset LO unit) provides all needed functions for crystal measurements with a rf bridge, other than a signal source, counter and oscilloscope.

The Tracking Servobridge Detector conforms to all essential requirements of MIL-D-55361 (EL). A condensed list of those specifications is shown in Table I.

The single most difficult requirement is an internal rf leakage level which is below the noise level over most of the frequency range and represents a shielding factor of over 180 dB between the RF Output and Receiver Input ports. This requirement has a profound influence on the design from the block diagram through circuit design, component selection and packaging. Isolation amplifiers and balanced mixers are critical to reducing the level of generator signal which appears at the receiver input through internal leakage paths. Extensive power supply filtering, rf tight module shield enclosures and the use of solid jacketed coaxial cable interconnections are all vital.

Table I

Condensed Specifications for Tracking Servobridge Detector*

Frequency Range: 0.8 to 220 MHz for the basic instrument and 45 to 220 MHz for the X10 frequency multiplier.

Generator, LO and Multiplier Inputs: +10 dBm nominal.

Rf Output: +30 to -70 dBm nominal, 0.8 to 20 MHz; +24 to -76 dBm nominal, 20 to 220 MHz; (continuously adjustable).

Receiver Sensitivity: -155 dBm typical equivalent input noise level in bandwidth of synchronous detector meters.

Internal Leakage: <-145 dBm equivalent input. Typically <-155 dBm below 150 MHz.

IF Modes: Linear and log.

RF Modes: Direct and X10 frequency multiplier.

Servo Modes: Sweep, center, lock and automatic modes are provided.

Synthesizer Compatibility: GenRad 1060 and 1160 series; Hewlett-Packard 5100 series.

Detectors: Magnitude and quadrature synchronous detector meters with continuously adjustable reference phase.

RF Monitor Output: 0 dBm nominal

LO Compatability: Generator output and control/power interface compatable with Offset LO unit.

Temperature Range: +15°C to +40°C.

Power: 99 to 121 V, 198 to 242 V, 50 to 60 Hz, 60 W nominal (with external Offset LO).

Mechanical: DIMENSIONS (wxhxd), Bench 435 x 180 x 445 mm (17 x 7 x 17.5 in.); Rack 483 x 180 x 445 mm (19 x 7 x 17.5 in.). Depth includes handles.

*See MIL-D-55361 (EL) for complete specifications.

Other important requirements are a low distortion broadband rf power amplifier, a low noise and wide dynamic range receiver, synchronous detectors with excellent quadrature rejection and low dc offset and a servo integrator with exceptionally low drift.

Environmental requirements are all in the general context of laboratory operation.

The instrument is packaged in a 180 mm (7") high rack/bench enclosure as seen in Figure 1.

A block diagram of the Tracking Servobridge Detector is shown in Figure 9. The diagram shows the major functional modules (except for the power supplies) and the main signal paths between them.

Generator Section

An external rf source, e.g., a frequency synthesizer, is connected either to the Generator Input or to the Multiplier Input (in which case the Multiplier Output is connected to the Generator Input). These are 50 Ω interface at a power level of +10 dBm. The

frequency range of 0.8 - 220 MHz is covered by the basic unit with associated offset LO unit in 12 overlapping bands. The X10 Frequency Multiplier has an output range of 45 to 220 MHz so that the synthesizer needs an upper frequency of only 22 MHz for complete coverage. An auxiliary function of the Multiplier is to increase the resolution of frequency measurements between 4.5 and 22 MHz.

The Generator Isolation Amplifier splits the generator signal into three isolated paths, a +7 dBm level to drive the RF Power Amplifier, a -15 dBm signal which is applied to the Reference Mixer via a 20 dB pad and 0 dBm output for the external Offset LO unit.

The RF Power Amplifier produces a low distortion, leveled output to drive the rf bridge. A step attenuator and variable level control are provided to adjust the rf output over a 101 dB range. The maximum power output is +30 dBm up to 20 MHz and +24 dBm to 220 MHz. A panel meter indicates both proper generator drive signal and the rf output level ahead of the step attenuator. An auxiliary 0 dBm output is provided to drive external frequency measuring equipment.

Detector Section

The detector section consists of a superheterodyne receiver and synchronous detector system which requires a local oscillator signal offset from the generator by the IF frequency of 80 kHz.

The LO Input signal is applied to the LO Isolation Amplifier which supplies isolated +7 dBm drive to both the Receiver and Reference Mixers. The Receiver Mixer converts the Receiver Input signal into one at the 80 kHz IF frequency. The Reference Mixer does the same thing to an internal generator signal to produce a phase coherent IF reference.

The receiver IF signal is amplified by the IF Amplifier which has both linear and log response modes. In the linear mode the IF gain is continuously adjustable over a 120 dB range. The log mode dynamic range is over 70 dB. The IF amplifier output level is displayed on a panel meter and is available as a dc signal at an output connector.

The reference IF signal is applied to the IF Reference and Phase Shifter which supplies phase adjustable reference signals for the synchronous detectors. A complete 360^{0} range is covered by a continuously adjustable control and a 0 - 180^{0} reversal switch is also provided. The IF phase is remote programmable for automatic system applications.

The Synchronous Detectors accept the IF Amplifier output and display the magnitude of the in-phase and quadrature components on panel meters and as dc outputs.

Sweep/Servo Section

The Sweep and Servo Amplifier has a variety of control and display functions. It produces a control output signal which is connected to the frequency control input of the synthesizer and can cause the synthesizer frequency to follow a manual panel control, to be swept at adjustable deviations and rates or to lock to the null point of one synchronous detector. Auxiliary outputs provide oscilloscope horizontal and vertial signals for swept displays. Provision is made for automatic lock acquisition by sweeping until a crystal response is found. An integrating amplifier can be used to increase the dc gain of the frequency lock loop. Servo gain is adjustable by two step attenuator controls. Another feature is a Δ FM function which, by modulating the generator frequency, can produce an oscilloscope display to aid in adjustment of the IF phase.

Offset LO Unit

The local oscillator signal for the receiver is produced by an external Offset LO unit which is powered and controlled by the main Tracking Servobridge Detector. The LO signal, offset from the generator frequency by +80 kHz, must be free of any generator frequency component by 100 - 110 dB if the resulting leakage signal is not to limit the receiver detectivity. The Offset LO unit achieves this level of performance by producing the offset at half-frequency by phasing-type SSB techniques and then filtering by means of a phase-locked VCO at the LO frequency. This is shown in the block diagram of Figure 10. One of twelve overlapping frequency ranges is selected by a band switch on the Tracking Servobridge Detector. A view of the LO chasis is shown in Figure 11.

Basic Operation

The functions and capabilities of the hardware described above for bridge-type quartz crystal parameter measurements may be illustrated by describing its basic operation.

A typical equipment setup using a manually operated bridge is shown in Figure 12 and the major interconnections are shown in Figure 13. Preliminary adjustments are made to set the approximate synthesizer frequency, LO frequency range and measurement power level.

First an initial bridge balance is made (with the crystal replaced by an open or short as appropriate). The synchronous detectors are then bought into phase alignment with the bridge arms by adjusting the IF phase to a minimum response of one detector to changes in the orthogonal bridge arm.

The crystal under test is then connected to the bridge and the bridge is rebalanced. If the reactive component is nulled by changing the synthesizer frequency and the resistive component nulled with the corresponding bridge control, the result will be a determination of the zero reactance frequency and resistance for the resonator (f_r and R_r).[14] Other characteristics of the crystal can be determined by similar measurements at difference bridge settings and frequencies.

Locked Operation

The servo system may be used to automatically vary the synthesizer frequency so as to maintain reactive bridge balance. Analog control of the synthesizer is used for high resolution. Once initial adjustments are made for servo range, phasing and gain, multiple crystals of the same type may be measured by simply pressing the "auto" button and nulling the resistive bridge arm. The servo may also be used to track variations versus temperature.

Swept Operation

The crystal under test may be examined for spurious modes by sweeping the generator frequency and observing an oscilloscope display of the detector output. Controls are provided for sweep rate and width. Triangular or sawtooth sweep waveforms is selectable.

System Operation

Provisions are made for completely automatic system operation of the Tracking Servobridge Detector when used with a voltage controlled rf bridge. An autobalancing system can be designed to make (after initial setup for a particular crystal type) completely automatic bridge measurements of a selected crystal parameter. This would make this type of measurement practical for production line use.

Conclusions

With the feasibility of the electronically tuneable microcircuit bridge established and the development of the Tracking Servobridge Detector now completed, a new generation measuring system for piezoelectric crystal units is nearing the point of practical application. The capabilities of this system in terms of accuracy, resolution, and throughput, will be adequate for the system to serve as Government Reference Standard for the forseeable future. Its automatic operation features may make it a desirable choice for general quality control and inspection purposes by crystal unit manufacturers and users.

Acknowledgements

One of us takes pleasure in acknowledging the competent [illegible]lastic support received in the construction [illegible]readboard models of the microcircuit bridge from personnel of the ECOM R&D Technical Support Activity, the Hybrid Microcircuit laboratory and from Mr. John Wenzel of the Frequency Control Devices Team. Work on the Tracking Servobridge Detector at GenRad was supported by the US Army Electronics Command under Contract DAAB05-73-C-0609.

References

Note: The Proceedings of the Annual Frequency Control Symposium are cited in the following as "Proc. AFCS, Symposium Number, pages, date. AD document number and availability information are provided on inside back cover of Proc. AFCS, 30 June 1976.

1. Hafner, E., "Crystal Resonators" IEEE Trans. on Sonics and Ultrasonics, SU-21, pp 220-237, Oct 1974.
2. Prichard, A.C. and Bernstein, M., "Crystal Impedance Meter Replaces Test Sets" Electronics, 26, pp 176-180, May 1953.
3. see Index to Proceedings, Annual Frequency Control Symposia Vol 10-30, Category 11, Measurements and Specifications, to be published in Proc. AFCS, Vol 30.
4. Flicker, H., "Measuring Instruments for Determination of Electrical Characteristics of Quartz over the Range from 0 to 300 MHz". Proc. AFCS, 13, pp 354-370, May 1959.
5. Frerking, M. E., "Vector Voltmeter Crystal Measurement System", Proc. AFCS, 23, pp 93-101, May 1969.
6. Metcalf, W.S., "Practical Crystal Measurements and Standardization". Proc. AFCS, 27, pp 55-62, June 1973.
7. Nelson, G.E., "Calculator Controlled Testing of Crystals and Crystal Filters". Proc. AFCS, 26, pp 79-83, June 1962.
8. Pustarfi, H.S. and Smith, W.L., "An Automatic Crystal Measurement System". Proc. AFCS, 27, pp 63-72, June 1973.
9. Gerber, E.A., "A review of Methods for Measuring the Constants of Piezoelectric Vibrators". Proc. IRE. 41, pp 1103-1112, Sept 1953.
10. Horton, W.H. and Boor, S.B., "Comparison of Crystal Measuring Equipment". Proc. AFCS, 19, pp 436-467, April 1965.
11. Hafner, E., Ballato, A., and Blomster, P., "Quartz Crystal Measurements". Proc. AFCS, 24, pp 177-190, April 1970.
12. IEC Publication 444 (1973) "Basic Method for the Measurement of Resonance Frequency and Equivalent Series Resistance of Quartz Crystal Units by Zero Phase Technique in a π Network".
13. IEEE Standard No. 177 (1966) "Piezoelectric Vibrators, Definitions and Methods of Measurement". (ANSI. C83.17 - 1970).
14. Hafner, E., "The Piezoelectric Crystal Unit - Definitions and Methods of Measurement". Proc. IEEE 57, pp 179-201, Feb 1969.
15. Hafner, E., "A New Method to Simplify Bridge Type Measurements on Quartz Crystal Units". USASEL, Report E1220A, Nov 1957 and 1958, National Convention Record, Vol 6, Part 5, pp 243-250, Mar 1958.
16. Layden, O.P., Ballato, A., and Shibla, C., " Newly Developed Crystal Measurement Instruments". Proc. AFCS, 22, pp 282-297, April 1968.
17. Riley, W.J., and Stràtemeyer, H.P., "Tracking Servobridge Detector". Final Report on Contract DAAB05-73-C-0609, USAECOM, Fort Monmouth, NJ, June 1973 - June 1976, by GenRad, Inc., Concord, Massachusetts.

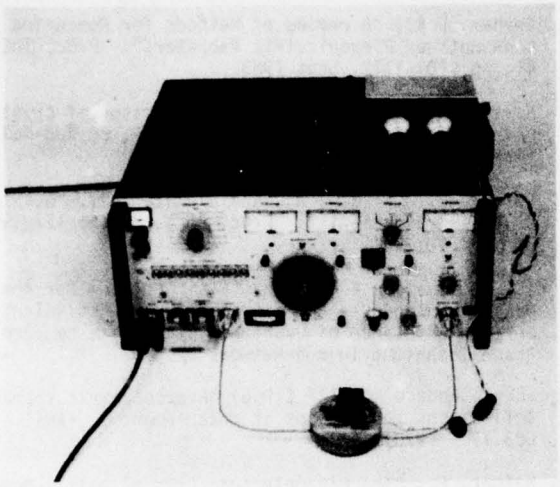

Figure 1.

Breadboard Model of Electronically Tuneable Microcircuit Bridge (front) with Tracking Servobridge Detector.

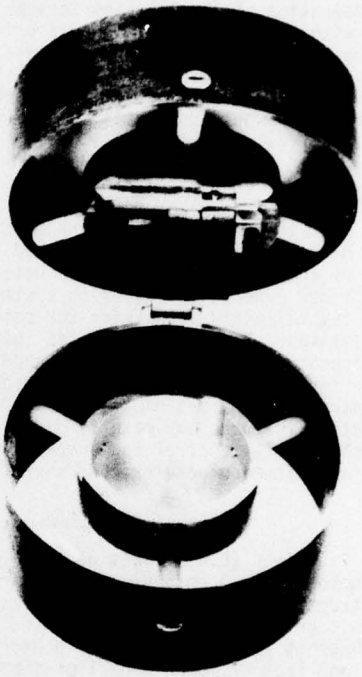

Figure 2. Microcircuit Bridge in Oven Shell.

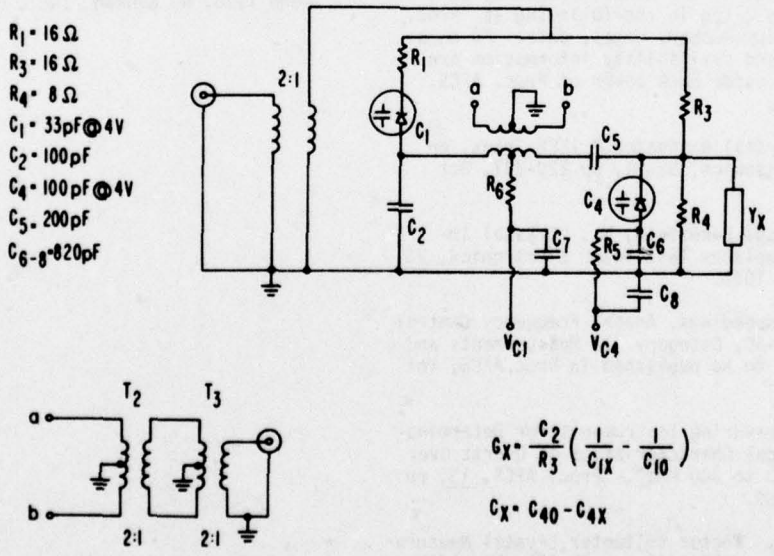

Figure 3. Circuit Diagram of Microcircuit Bridge. Ranges: $0.8 \leq f \leq 220$ MHz $R_X = 1/G_X \geq 3.5\ \Omega$; $-45 \leq C_X \leq +45$ pF.

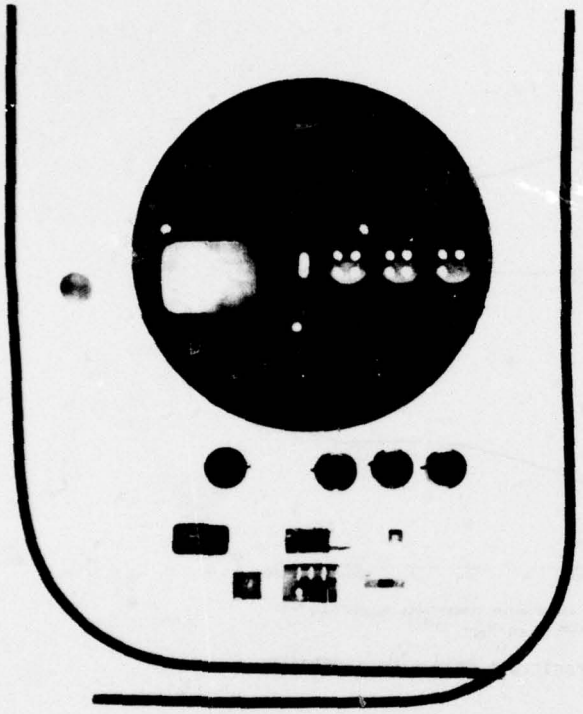

Figure 4. Components of Microcircuit Bridge.

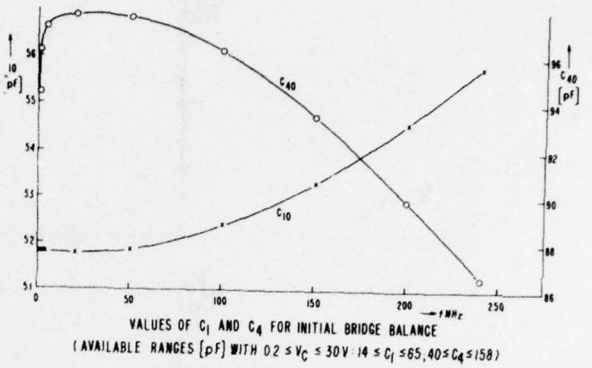

Figure 5.

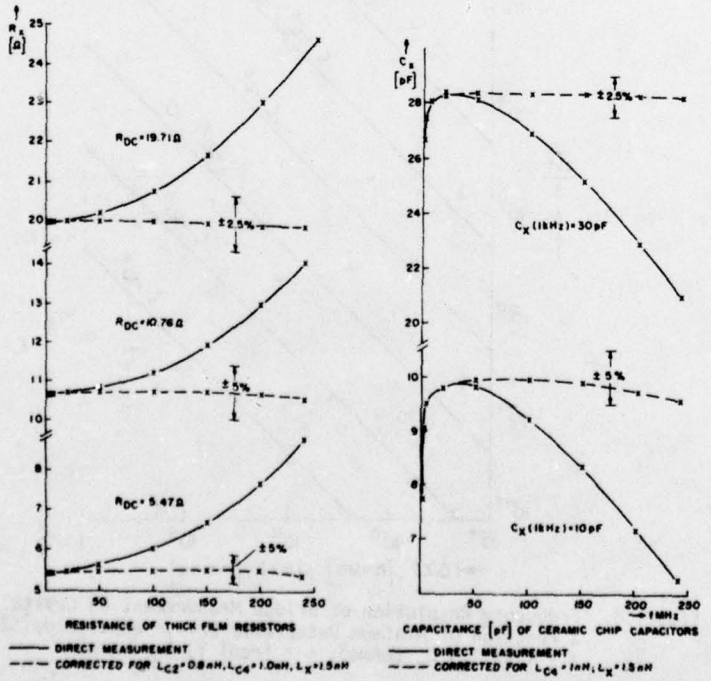

Figure 6. Microcircuit Bridge Measurements on Resistors and Capacitors.

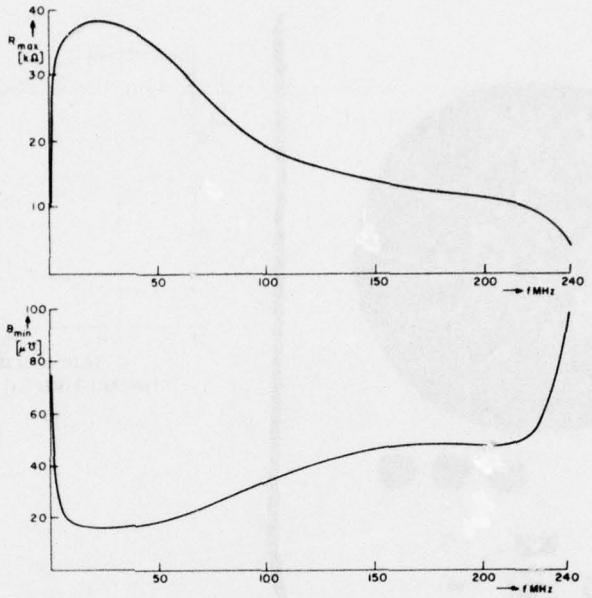

Figure 7. Resolution of Microcircuit Bridge Measurements.

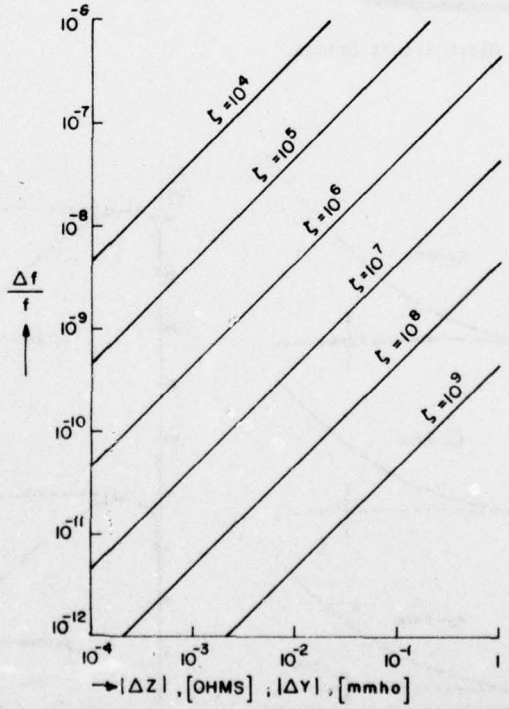

Figure 8. Frequency Resolution of Bridge Measurement on Crystal Units as a Function of Minimum Detectable Bridge Unbalance $|\Delta Z|$ or $|\Delta Y|$. ζ = (real Z) Q_0 (ohms); ζ = (real Y) Q_0 (mmho).

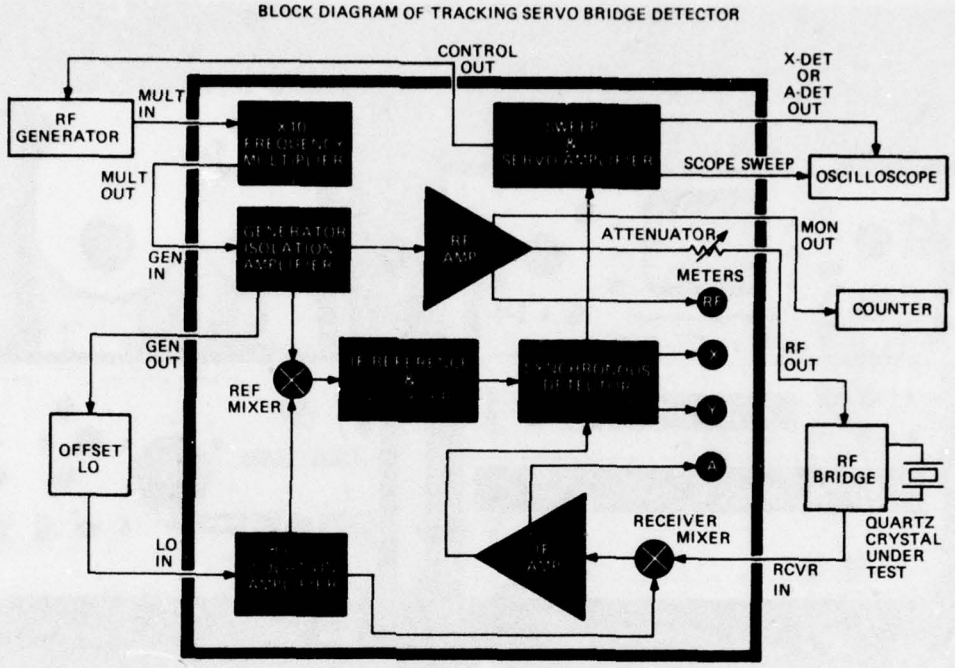

Figure 9. Block Diagram of Tracking Servobridge Detector.

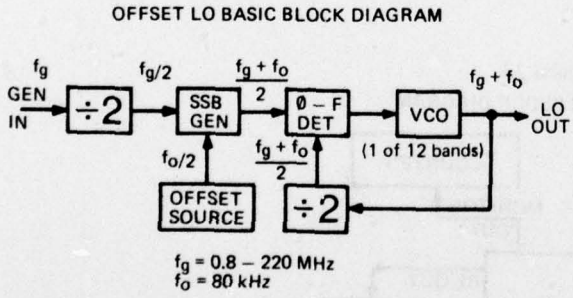

Figure 10. Offset LO Basic Block Diagram.

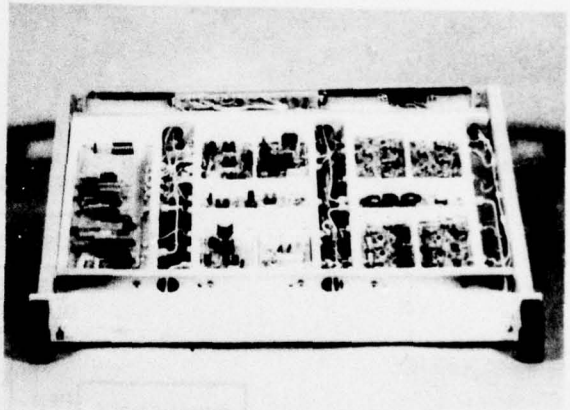

Figure 11. Top view of Offset LO chasis.

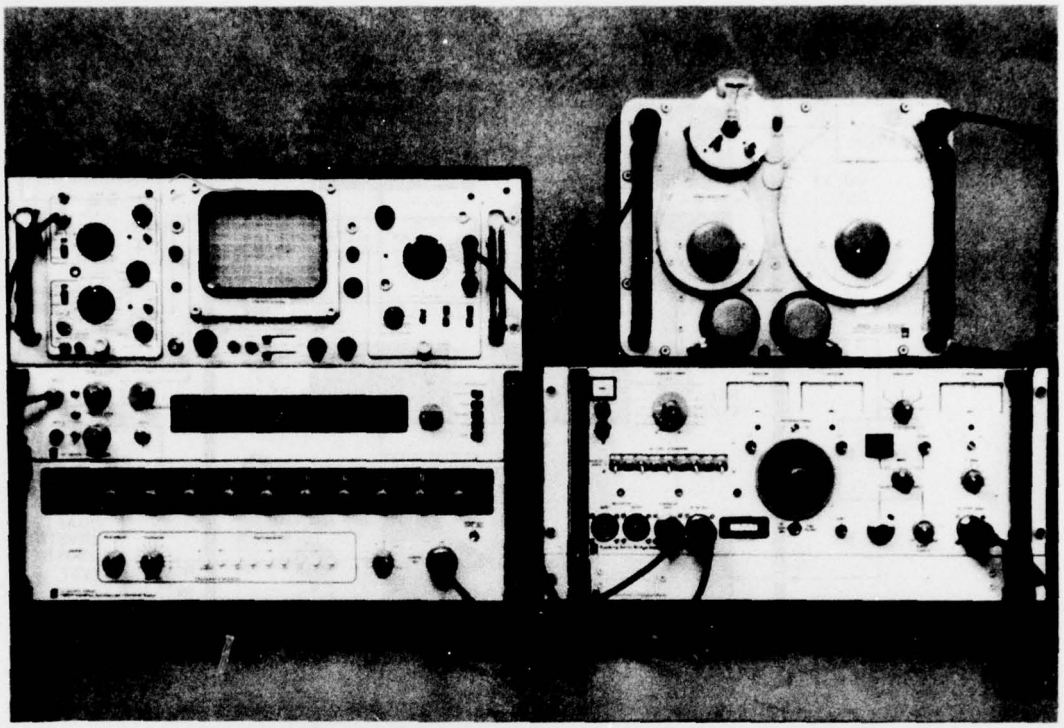

Figure 12. Equipment Setup using Manually Operated Bridge.

Figure 13

BASIC SYSTEM BLOCK DIAGRAM

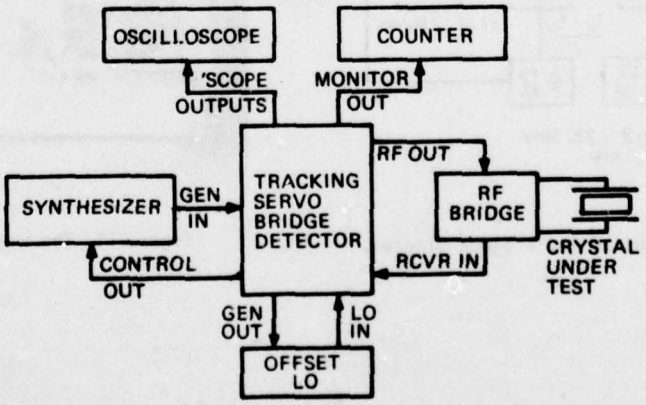

AN ANALYSIS OF OVERTONE MODES IN MONOLITHIC CRYSTAL FILTERS

H.F. Tiersten
Department of Mechanical Engineering,
Aeronautical Engineering & Mechanics
Rensselaer Polytechnic Institute
Troy, New York 12181

Abstract

A previous treatment of overtone modes in trapped energy resonators is extended to the case of two pole monolithic crystal filters. The asymptotic dispersion relations for the fundamental and odd overtone coupled thickness-shear and thickness-twist waves near cutoff along with the simple approximate edge conditions at junctions, which were employed in the earlier treatment of resonators, are applied in the analysis of two-pole monolithic crystal filters. Both thickness-shear and thickness-twist coupling directions are considered. The influence of piezoelectric stiffening, electrode mass loading and electrical shorting is included in the analysis. A lumped parameter representation of the admittance matrix for the two-port device is obtained. Numerical results are presented for a few geometrical configurations.

1. Introduction

In a recent investigation[1,2] the three-dimensional equations of linear piezoelectricity, with the aid of certain simplifying assumptions, were applied in the analysis of rotated Y-cut quartz trapped energy resonators with rectangular electrodes operating in overtones of coupled thickness-shear and thickness-twist vibrations. To this writer's knowledge the only other treatment of trapped energy resonators operating in coupled thickness-shear and thickness-twist vibrations is due to Meeker[3], who used equations[4] obtained from Mindlin's[5] plate equations, which hold for the fundamental thickness mode only. With the aid of the aforementioned simplifying assumptions[1,2], asymptotic expressions for the fundamental and odd overtone coupled thickness-shear and thickness-twist dispersion equations valid in the vicinity of the cutoff frequencies were determined for both the electroded and unelectroded regions of the plate. In addition, simple approximate boundary conditions at each junction between an electroded and unelectroded region were established. Moreover, in an unelectroded region adjacent to an electroded region the wavenumbers in the direction of the junction line were taken to be the same in order that the simple approximate continuity conditions at the junction be satisfied.

In this paper the previous analysis is extended to the case of two element monolithic crystal filters operating in overtone modes. The asymptotic dispersion relations and simple approximate edge conditions at junctions, which were employed in the earlier treatment[1] of resonators are employed in the present analysis of two-pole monolithic crystal filters. Although all the equations associated with the electroded and adjacent unelectroded regions are satisfied to second order in the small wave and decay numbers along the plate, the equations associated with the relatively unimportant corner type regions are satisfied pointwise only to first order in the same small quantities. The influence of piezoelectric stiffening, electrode mass loading and electrical shorting is included in the analysis and a lumped parameter representation of the admittance matrix for the two port device is obtained. Some numerical results obtained from the analysis are presented.

2. Preliminary Considerations

A schematic diagram of a cross-section of a two-element monolithic crystal filter is shown in Fig.1 along with the associated Cartesian coordinate system. On the basis of the simplifying assumptions of small piezoelectric coupling, the neglect of certain relatively small unimportant elastic constants and the fact that in the essentially thickness-shear modes of interest, the wave, or decay, numbers in both the x_1- and x_3-directions are much smaller than the thickness wavenumbers, it has been shown[2] that to second order in small quantities the differential equations that remain to be satisfied take the form given in Eqs.(2.3) and (2.1) of Ref.1, hereafter referred to as I. To the same order of approximation the pertinent constitutive equations take the form given in Eqs.(2.4) of Ref.1, where it was shown that T_{23} and T_{33} are negligible to the order of approximation being obtained, and the boundary conditions that remain to be satisfied on the major surfaces of the plate take the form given in (2.5) of I for the unelectroded plate and the form given in (2.6) of I for the fully electroded plate. Clearly, the notation employed here is defined in I.

It has been shown[2] that a typical asymptotic solution to second order in ξ and ν for plate waves in an unelectroded region can be written in the form given in Eqs.(2.7), with (2.8) - (2.11), all of I. Similarly, it has been shown[2] that a typical asymptotic solution to second order in $\bar{\xi}$ and $\bar{\nu}$ for plate waves in an electroded region with shorted electrodes can be written in the form given in (2.12), with (2.13) - (2.15), of I. It has also been shown[2] that for purposes of analysis of a trapped energy resonator or monolithic crystal filter operating in the vicinity of the cutoff frequencies of overtones of coupled thickness-shear and thickness-twist vibrations, the solutions in the unelectroded and electroded regions, respectively, can be represented in the form

$$u_1 = B_1^{(1)} \sin \eta_1 x_2 e^{-\xi x_1} \cos \nu x_3 e^{i\omega t},$$
$$u_1 = \bar{B}_1^{(1)} \sin \bar{\eta}_1 x_2 \cos \bar{\xi} x_1 \cos \bar{\nu} x_3 e^{i\omega t}, \qquad (2.1)$$

where it is understood that (2.9), (2.11) and (2.14), $(2.15)_{1,2}$, all of I, respectively, are satisfied.

It has been shown[2] that at an x_1-junction between an electroded and unelectroded region of the plate, the four existing continuity conditions can be satisfied, approximately, by requiring the continuity of only the two quantities

$$u_1 , \quad u_{1,1} , \qquad (2.2)$$

while at an x_3-junction it has been shown[2] that the continuity of only the two quantities

$$u_1 , \quad u_{1,3} , \qquad (2.3)$$

is required as in I. As noted in the Introduction, it has been shown[6] that, since ξ and ν are small compared with η, it is more appropriate to satisfy all equations associated with a corner type region to first order in ξ and ν pointwise than to satisfy (2.9) of I, which contains terms of zero and second order in ξ and ν, pointwise and the continuity conditions at junctions (2.2)

and (2.3), which have conditions of zero and first order in ξ or ν, respectively, as integral conditions only. Consequently, in the interior of a corner type region we do not satisfy (2.9) of I, but at the junctions between corner type regions and adjacent regions we do satisfy the continuity conditions consisting of either (2.2) or (2.3) pointwise. This means that in the interior of a corner type region we satisfy the conditions to first order in ξ and ν, since first order terms do not exist in (2.9) of I, and at junctions between corner type regions and adjacent regions we satisfy the continuity conditions pointwise to first order in ξ and ν. Thus, all equations associated with the relatively unimportant corner type regions are satisfied to first order in ξ and ν, while all equations associated with all other regions are satisfied to second order in ξ and ν.

3. Monolithic Crystal Filter

The cross-section and plan view of the monolithic crystal filter are shown in Figs.1 and 2, respectively. In the vicinity of two extremely close resonances, the lower one, say the N$\tau$$\epsilon$th or NSth, being the fundamental symmetric (in x_1) mode and the upper one, the N$(\tau+1)\epsilon$th or NAth, being the next higher, i.e., the fundamental antisymmetric (in x_1) mode, the two terms in the series solution[7] corresponding to these two modes dominate the others and the solution can very accurately be written in the form

$$\bar{u}_1^{(p)} = [H^{NS}\hat{u}_{1N}^{(p)S} + H^{NA}\hat{u}_{1N}^{(p)A}]e^{i\omega t} - (e_{26}V^{(p)}/c_{66}2h)e^{i\omega t},$$

$$\bar{\varphi}^{(p)} = (V^{(p)}x_2/2h)e^{i\omega t} + (e_{26}/\epsilon_{22})[H^{NS}(\hat{u}_{1N}^{(p)S} - \hat{u}_{1N}^{(p)S}(h)x_2/h) + H^{NA}(\hat{u}_{1N}^{(p)A} - \hat{u}_{1N}^{(p)A}(h)x_2/h)]e^{i\omega t}, \quad (3.1)$$

$$u_1^{(\alpha)} = [H^{NS}u_{1N}^{(\alpha)S} + H^{NA}u_{1N}^{(\alpha)A}]e^{i\omega t}, \quad \varphi^{(\alpha)} = (e_{26}/\epsilon_{22})u_1^{(\alpha)}, \quad (3.2)$$

where p = 1,3 represents the two electroded regions, α represents the remaining unelectroded regions and the expressions for $\hat{u}_{1N}^{(p)S}$, $\hat{u}_{1N}^{(p)A}$, $u_{1N}^{(\alpha)S}$ and $u_{1N}^{(\alpha)A}$ are given by

$$u_{1N}^{(0)S} = \sin\frac{N\pi}{2h}x_2A_{1N}^{(4)S}e^{\bar{\xi}_{NS}[x_1+(\ell_2+2\ell_3)]}\cos\bar{\nu}_{NS}x_3e^{i\omega t}, \quad N = 1,3,5, \ldots.$$

$$\hat{u}_{1N}^{(1)S} = \sin\frac{N\pi}{2h}x_2[\bar{A}_{1N}^{(3)S}\cos\bar{\xi}_{NS}(x_1+\ell_2) - \bar{B}_{1N}^{(3)S}\sin\bar{\xi}_{NS}(x_1+\ell_2)]\cos\bar{\nu}_{NS}x_3e^{i\omega t},$$

$$u_{1N}^{(2)S} = \sin\frac{N\pi}{2h}x_2A_{1N}^{(2)S}\cosh\xi_{NS}x_1\cos\bar{\nu}_{NS}x_3e^{i\omega t},$$

$$\hat{u}_{1N}^{(3)S} = \sin\frac{N\pi}{2h}x_2[\bar{A}_{1N}^{(3)S}\cos\bar{\xi}_{NS}(x_1-\ell_2) + \bar{B}_{1N}^{(3)S}\sin\bar{\xi}_{NS}(x_1-\ell_2)]\cos\bar{\nu}_{NS}x_3e^{i\omega t},$$

$$u_{1N}^{(4)S} = \sin\frac{N\pi}{2h}x_2A_{1N}^{(4)S}e^{-\bar{\xi}_{NS}[x_1-(\ell_2+2\ell_3)]}\cos\bar{\nu}_{NS}x_3e^{i\omega t},$$

$$u_{1N}^{(0)FS} = \Gamma_N^S u_{1N}^{(0)S}\frac{e^{-\nu_{NS}(x_3-w)}}{\cos\bar{\nu}_{NS}x_3},$$

$$\hat{u}_{1N}^{(1)FS} = \Gamma_N^S\hat{u}_{1N}^{(1)S}\frac{e^{-\nu_{NS}(x_3-w)}}{\cos\bar{\nu}_{NS}x_3},$$

$$u_{1N}^{(2)FS} = \Gamma_N^S u_{1N}^{(2)S}\frac{e^{-\nu_{NS}(x_3-w)}}{\cos\bar{\nu}_{NS}x_3},$$

$$\hat{u}_{1N}^{(3)FS} = \Gamma_N^S\hat{u}_{1N}^{(3)S}\frac{e^{-\nu_{NS}(x_3-w)}}{\cos\bar{\nu}_{NS}x_3},$$

$$u_{1N}^{(4)FS} = \Gamma_N^S u_{1N}^{(4)S}\frac{e^{-\nu_{NS}(x_3-w)}}{\cos\bar{\nu}_{NS}x_3},$$

$$u_{1N}^{(0)RS} = \Gamma_N^S u_{1N}^{(0)S}\frac{e^{\nu_{NS}(x_3+w)}}{\cos\bar{\nu}_{NS}x_3},$$

$$\hat{u}_{1N}^{(1)RS} = \Gamma_N^S\hat{u}_{1N}^{(1)S}\frac{e^{\nu_{NS}(x_3+w)}}{\cos\bar{\nu}_{NS}x_3},$$

$$u_{1N}^{(2)RS} = \Gamma_N^S u_{1N}^{(2)S}\frac{e^{\nu_{NS}(x_3+w)}}{\cos\bar{\nu}_{NS}x_3},$$

$$\hat{u}_{1N}^{(3)RS} = \Gamma_N^S\hat{u}_{1N}^{(3)S}\frac{e^{\nu_{NS}(x_3+w)}}{\cos\bar{\nu}_{NS}x_3},$$

$$u_{1N}^{(4)RS} = \Gamma_N^S u_{1N}^{(4)S}\frac{e^{\nu_{NS}(x_3+w)}}{\cos\bar{\nu}_{NS}x_3}, \quad (3.3)$$

for the symmetric modes, while for the antisymmetric modes $(3.3)_{1-3}$ are replaced by

$$u_{1N}^{(0)A} = -\sin\frac{N\pi}{2h}x_2A_{1N}^{(4)A}e^{\bar{\xi}_{NA}[x_1+(\ell_2+2\ell_3)]}\cos\bar{\nu}_{NA}x_3e^{i\omega t},$$

$$\hat{u}_{1N}^{(1)A} = \sin\frac{N\pi}{2h}x_2[-\bar{A}_{1N}^{(3)A}\cos\bar{\xi}_{NA}(x_1+\ell_2) + \bar{B}_{1N}^{(3)A}\sin\bar{\xi}_{NA}(x_1+\ell_2)]\cos\bar{\nu}_{NA}x_3e^{i\omega t},$$

$$u_{1N}^{(2)A} = \sin\frac{N\pi}{2h}x_2A_{1N}^{(2)A}\sinh\xi_{NA}x_1\cos\bar{\nu}_{NA}x_3e^{i\omega t}, \quad (3.4)$$

and in the remaining equations in (3.3) all scripts S are replaced by scripts A. The solutions presented in (3.1) - (3.4) satisfy the differential equations and boundary conditions on the respective major surfaces of the electroded and unelectroded regions of the plate provided

$$M_N\bar{\xi}^2 + c_{55}\bar{\nu}^2 - k_N\bar{\epsilon} = 0, \quad M_N\xi^2 - c_{55}\bar{\nu}^2 + k_N\epsilon = 0,$$

$$-M_N\bar{\xi}^2 + c_{55}\nu^2 + k_N\epsilon = 0, \quad M_N\xi^2 + c_{55}\nu^2 + k_N\epsilon = 0, \quad (3.5)$$

where as in I, and repeated here for completeness,

$$M_N = \left[c_{11} + (c_{12}+c_{66})r + \frac{4(r\bar{c}_{66} - c_{66})(c_{22}r + c_{12})\cot\varkappa N\pi/2}{c_{22}N\pi\varkappa}\right], \quad (3.6)$$

$$r = (c_{12}+c_{66})/(\bar{c}_{66} - c_{22}), \quad \bar{c}_{66} = c_{66} + e_{26}^2/\epsilon_{22}, \quad (3.7)$$

$$\omega = \omega_N + \epsilon, \quad \omega = \bar{\omega}_N + \bar{\epsilon}, \quad \omega_N = (N\pi/2h)(\bar{c}_{66}/\rho)^{\frac{1}{2}}, \quad (3.8)$$

$$\bar{\omega}_N = (N\pi/2h)(\bar{c}_{66}/\rho)^{\frac{1}{2}}[1 - (4k_{26}^2/N^2\pi^2) - R], \quad (3.9)$$

$$k_{26}^2 = e_{26}^2/\bar{c}_{66}\epsilon_{22}, \quad k_N = (\bar{c}_{66}\rho)^{\frac{1}{2}}N\pi/h, \quad R = 2\rho'h'/\rho h, \quad (3.10)$$

$(3.5)_1$ is for the electroded region, $(3.5)_2$ is for regions 0,2 and 4, $(3.5)_3$ is for regions 1^F, 3^F, 1^R and 3^R and $(3.5)_4$ is for the corner type regions 0^F, 2^F, 4^F, 0^R, 2^R and 4^R. However, as noted earlier the solutions in the corner type regions do not satisfy the dispersion relation $(3.5)_4$, which contains quadratic, but not linear, terms in the small decay numbers ξ and ν.

The solutions presented in (3.1) - (3.4) satisfy the respective edge conditions in (2.2) and (2.3) provided

$$\tan 2\bar{\xi}\ell_3 = \frac{\xi\bar{\xi}(\cosh\xi\ell_2 + \sinh\xi\ell_2)}{(\bar{\xi}^2\cosh\xi\ell_2 - \xi^2\sinh\xi\ell_2)}, \quad \tan\bar{\nu}w = \frac{\nu}{\bar{\nu}}, \quad (3.11)$$

for the symmetric modes and

$$\tan 2\bar{\xi}_S \ell_3 = \frac{\xi_S \bar{\xi}_S (\cosh \xi_S \ell_2 + \sinh \xi_S \ell_2)}{(\bar{\xi}_S^2 \sinh \xi_S \ell_2 - \xi_S^2 \cosh \xi_S \ell_2)}, \quad \tan \bar{\nu}_S w = \frac{\nu}{\bar{\nu}}, \tag{3.12}$$

for the antisymmetric modes. The amplitude ratios for the symmetric modes are given by

$$\bar{A}_1^{(3)S}/A_1^{(2)S} = \cosh \xi_S \ell_2, \quad \bar{B}_1^{(3)S}/A_1^{(2)S} = (\xi_S/\bar{\xi}_S) \sinh \xi_S \ell_2, \quad \Gamma^S = \cos \bar{\nu}_S w,$$
$$A_1^{(4)S}/A_1^{(2)S} = \cosh \xi_S \ell_2 \cos 2\bar{\xi}_S \ell_3 + (\xi_S/\bar{\xi}_S) \sinh \xi_S \ell_2 \sin 2\bar{\xi}_S \ell_3, \tag{3.13}$$

and for the antisymmetric modes are given by

$$\bar{A}_1^{(3)A}/A_1^{(2)A} = \sinh \xi_A \ell_2, \quad \bar{B}_1^{(3)A}/A_1^{(2)A} = (\xi_A/\bar{\xi}_A) \cosh \xi_A \ell_2, \quad \Gamma^A = \cos \bar{\nu}_A w,$$
$$A_1^{(4)A}/A_1^{(2)A} = \sinh \xi_A \ell_2 \cos 2\bar{\xi}_A \ell_3 + (\xi_A/\bar{\xi}_A) \cosh \xi_A \ell_2 \sin 2\bar{\xi}_A \ell_3. \tag{3.14}$$

As in Ref.2, we now note that from $(3.5)_{1-3}$, (3.8) and (3.9), we may write

$$\xi = [(k_N/M_N)\Delta_N - \bar{\xi}^2]^{\frac{1}{2}}, \quad \nu = [(k_N/c_{66})\Delta_N - \bar{\nu}^2]^{\frac{1}{2}}, \tag{3.15}$$

where

$$\Delta_N = (N\pi/2h)(\bar{c}_{66}/\rho)^{\frac{1}{2}}[(4k_{26}^2/N^2\pi^2) + R]. \tag{3.16}$$

Clearly, Eqs.(3.15) hold for symmetric and antisymmetric modes. Equation $(3.11)_1$, with $(3.15)_1$, and $(3.11)_2$, with $(3.15)_2$, constitute two independent transcendental equations for $\bar{\xi}_S$ and $\bar{\nu}_S$ for a given ℓ_2, ℓ_3 and w, which may readily be solved for all the symmetric modes with respect to x_1 and x_3. The eigenfrequency for any one of those modes may then be determined from $(3.5)_1$, $(3.8)_2$ and (3.9). Similarly, Eq.$(3.12)_1$, with $(3.15)_1$, and $(3.12)_2$, with $(3.15)_2$, constitute two independent transcendental equations for $\bar{\xi}_A$ and $\bar{\nu}_A$ for a given ℓ_2, ℓ_3 and w, which may readily be solved for all the modes antisymmetric with respect to x_1 and symmetric with respect to x_3. Again, the eigenfrequency for any one of those modes may then be determined from $(3.5)_1$, $(3.8)_2$ and (3.9). The foregoing analysis is for interresonator coupling in the thickness-shear or x_1-direction. The analysis may be made applicable to the case of interresonator coupling in the thickness-twist or x_3-direction simply by interchanging M_N and c_{66} in (3.5) and (3.15). Some calculated results for fundamental and overtone modes are given in Table I.

The amplitude factor H^{NS} for the symmetric (in x_1) mode appearing in (3.1) - (3.2) is given by

$$H^{NS} = \frac{(-1)^{(N-1)/2} 4e_{26} F^{NS} (V^{(1)} + V^{(3)})}{c_{66}(1 - \omega_{NS}^2/\omega^2) N^2\pi^2 L_{NS}}, \tag{3.17}$$

where

$$F^{NS} = \frac{2 \sin \bar{\nu}_{NS} w}{\bar{\nu}_{NS} \bar{\xi}_{NS}} \left[\bar{A}_{1N}^{(3)S} \sin 2\bar{\xi}_{NS} \ell_3 + \bar{B}_{1N}^{(3)S}(1 - \cos 2\bar{\xi}_{NS} \ell)\right], \tag{3.18}$$

$$L_{NS} = \left[w + \frac{\sin 2\bar{\nu}_{NS} w}{2\bar{\nu}_{NS}} + \frac{\cos^2 \bar{\nu}_{NS} w}{\nu_{NS}}\right]\left[\frac{(\bar{A}_{1N}^{(4)S})^2}{\bar{\xi}_{NS}} + (\bar{A}_{1N}^{(3)S})^2\left(2\ell_3 + \frac{\sin 4\bar{\xi}_{NS}\ell_3}{2\bar{\xi}_{NS}}\right) + \frac{\bar{A}_{1N}^{(3)S}\bar{B}_{1N}^{(3)S}}{\bar{\xi}_{NS}}(1 - \cos 4\bar{\xi}_{NS}\ell_3) + (\bar{B}_{1N}^{(3)S})^2\left(2\ell_3 - \frac{\sin 4\bar{\xi}_{NS}\ell_3}{2\bar{\xi}_{NS}}\right) + (A_{1N}^{(2)S})^2\left(\frac{\sinh 2\xi_{NS}\ell_2}{2\xi_{NS}} + \ell_2\right)\right] \tag{3.19}$$

and, of course, in performing a calculation we set $A_{1N}^{(2)S} = 1$. For the antisymmetric (in x_1) modes, we have

$$H^{NA} = \frac{(-1)^{(N-1)/2} 4e_{26} F^{NA} (V^{(3)} - V^{(1)})}{c_{66}(1 - \omega_{NA}^2/\omega^2) N^2\pi^2 L_{NA}}, \tag{3.20}$$

where

$$F^{NA} = \frac{2 \sin \bar{\nu}_{NA} w}{\bar{\nu}_{NA} \bar{\xi}_{NA}}\left[\bar{A}_{1N}^{(3)A} \sin 2\bar{\xi}_{NA}\ell_3 + \bar{B}_{1N}^{(3)A}(1 - \cos 2\bar{\xi}_{NA}\ell_3)\right], \tag{3.21}$$

$$L_{NA} = \left[w + \frac{\sin 2\bar{\nu}_{NA} w}{2\bar{\nu}_{NA}} + \frac{\cos^2 \bar{\nu}_{NA} w}{\nu_{NA}}\right]\left[\frac{(A_{1N}^{(4)A})^2}{\xi_{NA}} + (\bar{A}_{1N}^{(3)A})^2\left(2\ell_3 + \frac{\sin 4\bar{\xi}_{NA}\ell_3}{2\bar{\xi}_{NA}}\right) + \frac{\bar{A}_{1N}^{(3)A}\bar{B}_{1N}^{(3)A}}{\bar{\xi}_{NA}}(1 - \cos 4\bar{\xi}_{NA}\ell_3) + (\bar{B}_{1N}^{(3)A})^2\left(2\ell_3 - \frac{\sin 4\bar{\xi}_{NA}\ell_3}{2\bar{\xi}_{NA}}\right) + (A_{1N}^{(2)A})^2\left(\frac{\sinh 2\xi_{NA}\ell_2}{2\xi_{NA}} - \ell_2\right)\right], \tag{3.22}$$

where, of course, $A_{1N}^{(2)A} = 1$. As usual, the ω_{NS} and ω_{NA} in Eqs.(3.17) and (3.20) are to be replaced by

$$\hat{\omega}_{NS} = \omega_{NS} + i\omega_{NS}/2Q_N, \quad \hat{\omega}_{NA} = \omega_{NA} + i\omega_{NA}/2Q_N, \tag{3.23}$$

in which Q_N is the unloaded quality factor of the plate in the Nth thickness mode.

The current through the pth electrode is obtained by substituting from (3.1), with (3.3), (3.4), (3.17) and (3.20), into (2.2) of I, which is then substituted into

$$I^{(p)} = -\int_{-w}^{w}\left(\int_{-(\ell_2+2\ell_3)}^{-\ell_2} + \int_{\ell_2}^{(\ell_2+2\ell_3)}\right) \dot{D}_2^{(p)}\, dx_1 dx_3, \tag{3.24}$$

where the negative limits on the second integral are for p = 1 and the positive limits are for p = 3. From (3.24) we obtain

$$I^{(1)} = Y_{11}V^{(1)} + Y_{13}V^{(3)}, \quad I^{(3)} = Y_{31}V^{(1)} + Y_{33}V^{(3)}, \tag{3.25}$$

where

$$Y_{11} = Y_{33} = \frac{i\omega e_{22}}{2h}\left[4w\ell_3(1 + \hat{k}_{26}^2) + \frac{8\hat{k}_{26}^2}{N^2\pi^2}\left(\frac{(F^{NS})^2}{[(\omega_{NS}^2/\omega^2) - 1]L_{NS}} + \frac{(F^{NA})^2}{[(\omega_{NA}^2/\omega^2) - 1]L_{NA}}\right]\right.$$
$$Y_{13} = Y_{31} = \frac{i\omega e_{22}}{2h}\left[\frac{(F^{NS})^2}{[(\omega_{NS}^2/\omega^2) - 1]L_{NS}} - \frac{(F^{NA})^2}{[(\omega_{NA}^2/\omega^2) - 1]L_{NA}}\right]. \tag{3.26}$$

The quantities C_0, C_{NS} and C_{NA} defined by

$$C_0 = 4w\ell\epsilon_{22}(1+\hat{k}_{26}^2)/2h\,, \tag{3.27}$$

$$C_{NS} = 2\epsilon_{22}8\hat{k}_{26}^2(F^{NS})^2/N^2\pi^2 2hL_{NS}\,, \tag{3.28}$$

$$C_{NA} = 2\epsilon_{22}8\hat{k}_{26}^2(F^{NA})^2/N^2\pi^2 2hL_{NA}\,, \tag{3.29}$$

are called the static capacitance and symmetric and antisymmetric motional capacitances, respectively, and have been calculated for a range of cases from tightly coupled to weakly coupled and are tabulated in Table I.

Acknowledgement

The author wishes to thank R.C. Smythe of Piezo Technology, Inc. for many stimulating discussions and for calculating and providing the results presented in Table I.

This work was supported in part by the Office of Naval Research under Contract No.N00014-76-C-0368.

References

1. H.F. Tiersten, "Analysis of Trapped Energy Resonators Operating in Overtones of Coupled Thickness-Shear and Thickness-Twist," Proceedings of the 29th Symposium on Frequency Control (U.S. Army Electronics Command, Fort Monmouth, N.J., 1975) p.71.

2. H.F. Tiersten, "Analysis of Trapped-Energy Resonators Operating in Overtones of Coupled Thickness-Shear and Thickness-Twist," J. Acoust. Soc. Am., 59, 879 (1976).

3. T.R. Meeker, "Plate Constants and Dispersion Relations for Width-Length Effects in Rotated Y-Cut Quartz Plates," Proceedings of the 29th Symposium on Frequency Control (U.S. Army Electronics Command, Fort Monmouth, N.J., 1975) p.54.

4. H.F. Tiersten, Linear Piezoelectric Plate Vibrations (Plenum, New York, 1969), Chap.16, Secs.2-5.

5. R.D. Mindlin, "High Frequency Vibrations of Crystal Plates," Q. Appl. Math., 19, 51 (1961).

6. In the Appendix of Ref.2 it is stated that in the solution discussed only the large continuity conditions are satisfied on the minor surfaces at the junctions between the corner regions and the adjacent regions and that, consequently, the conditions associated with a corner region are satisfied to zero order in the small decay numbers along the plate. However, since in actuality the solution satisfies the small continuity conditions at the junctions as well as the large and the condition in the corner region contains terms of zero and second order, and no term of first order, in the decay numbers along the plate, the solution discussed in the Appendix of Ref.2 actually satisfies all conditions associated with a corner region to first order in the small decay numbers along the plate.

7. H.F. Tiersten, "An Analysis of Overtone Modes in Monolithic Crystal Filters," issued as Technical Report No.18 under ONR Contract No. N00014-76-C-0368.

TABLE I

N	$2\ell_2$	R	$\frac{1}{2}(\omega_3 + \omega_A)/2\pi$	$(\omega_A - \omega_3)/2\pi$	C_{1S}	C_{1A}	C_{1S}/C_{1A}
	in		kHz	kHz	fF	fF	
1	.002	.01	9925.90	34.68	7.90	7.01	1.127
1	.002	.02	9834.65	37.74	7.97	7.47	1.068
1	.01	.01	9927.29	26.28	7.72	7.30	1.057
1	.01	.02	9837.65	25.04	7.94	7.73	1.027
1	.02	.01	9928.12	18.68	7.59	7.55	1.006
1	.02	.02	9839.16	15.32	7.92	7.92	1.000
1	.05	.01	9928.65	6.69	7.52	7.79	0.966
1	.05	.02	9839.95	3.60	7.95	8.05	0.987
1	.100	.01	9928.66	1.20	7.60	7.73	0.983
1	.100	.02	9839.99	0.32	8.00	8.02	0.997
3	.002	.00333	29947.54	29.27	.212	.189	1.120
3	.002	.00667	29859.56	31.21	.220	.208	1.056
3	.005	.00333	29948.29	24.08	.208	.195	1.066
3	.005	.00667	29861.39	23.05	.219	.213	1.028
3	.010	.00333	29948.95	17.44	.204	.202	1.010
3	.010	.00667	29862.76	14.14	.219	.219	1.000
3	.020	.00333	29949.33	9.14	.201	.208	0.967
3	.020	.00667	29863.43	5.41	.219	.222	0.986

Unelectroded thickness frequency: $\omega_1/2\pi$ = 10 MHz

Coupling: thickness-shear

N = 1, $2\ell_3$ = 2w = .1 in., C_0 = 1.558 pF

N = 3, $2\ell_3$ = 2w = .05 in., C_0 = 0.390 pF.

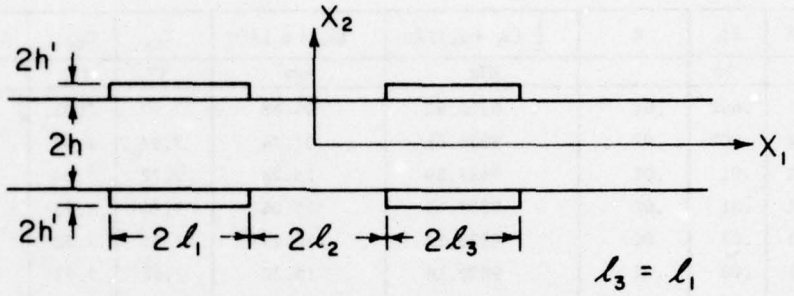

Figure 1 Schematic Diagram of the Monolithic Crystal Filter

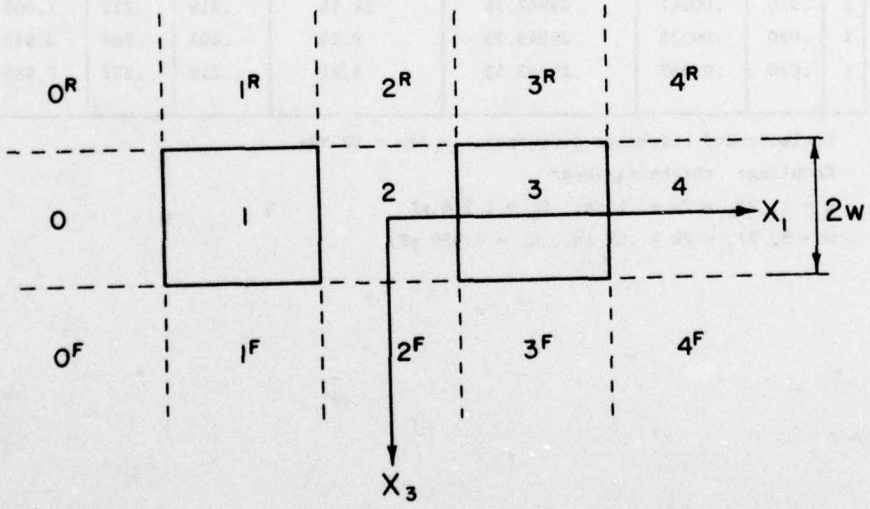

Figure 2 Plan View of the Monolithic Crystal Filter

A HYBRID INTEGRATED MONOLITHIC CRYSTAL FILTER

Kazuo Okuno and Takaya Watanabe
Nippon Electric Company Ltd.
Kawasaki City, Kanagawa 211 Japan

Summary

Progress in various communication system equipments is reflected in the filters becoming smaller in size, having higher stability and higher reliability. To meet these requirements, a new device, hybrid integrated monolithic crystal filter (HIMF), was developed. This HIMF consists of thin film lumped element circuit and energy trapped resonator in integrated structure on a substrate. In this paper a general discussion of a HIMF and its problem on the design and fabrication is described.

Key words (for information retrieval)

Hybrid integrated monolithic crystal filter, Energy trapped resonator, Thin film lumped element circuit, Spiral inductor, Microstrip line, Substrate, Fused quartz, Nd:YAG laser, Spiral resonator, 100Mb/s PCM timing pick-up filter.

List of symbols

do,di,ho	:	Outside diameter, inside diameter and thickness of spiral inductor, distances
w'	:	Spiral width, distances
s'	:	Distance between edges of two adjacent spirals, distances
n	:	Number of turns
Rs	:	Sheet resistance of strip conductor, ohms/sq
R	:	Resistance of spiral inductor, ohms
lo	:	Total length of rectangular strip, distances
r,d	:	Radius and length of cross over wire, distances
L	:	Inductance value of spiral inductor, henry
Q	:	Quarlity factor of spiral inductor
fr	:	Self-resonant frequency of spiral inductor, hertz
Cd	:	Distributed capacitance of spiral inductor, farad
μ	:	Permeability, henry/m
σ	:	Conductivity, mho/m
ε_r	:	Dielectric constant
ε_o	:	Permittivity of free space, farad/m
v_o	:	Velocity of light, m/s
f	:	Frequency, hertz
w	:	Angular frequency
K	:	Correction facter as a function w'/h_o
K'	:	Correction facter as a function s'/w'
a,b,c	:	Width, length and height of rectangular shield wall, distances
Ca,Cb	:	Shunt-gap capacitance and series capacitance
Cte,Ctm	:	Capacitance correspond to the electric and magnetic wall, farad
w	:	Width of microstrip line, distances
s	:	Gap spacing between microstrip lines, distances
α	:	Coefficient factor is to be determind so as to maximize the capacitance Cte or Ctm.
h	:	Thickness of substrate, distances

Introduction

Filters used in VHF range are classified into those employing distributed components, such as spiral or helical resonators, and those employing piezoelectric components, such as energy trapped resonators or surface acoustic wave devices. There are some disadvantages inherent in filters belonging to the first category. The size of filter is large for use in VHF range. It is also difficult to fabricate them with marrow bandwidth and high stability.

On the other hand, advantages for the latter are component miniaturization because of shorter wavelength than that of electromagnetic wave by a factor of approximately 10^{-5}, very high Q being independent of physical size, better temperature frequency characteristics, and stable aging characteristics.

To obtain these advantages, it is important to combine piezoelectric components with conventional electric circuits for the filter. A new device, hybrid integrated monolithic crystal filter (HIMF), was developed for this combination. The HIMF is compatible with present microwave integrated circuits and ultrasonic technology. The HIMF consists of thin film lumped elements and energy trapped resonators in integrated structures on a single substrate (fused quartz or ceramic). In particular there are two different configurations of integrated structure:

(1) Thin film lumped elements + energy trapped resonators.

(2) Thin film lumped elements + surface acoustic wave devices.

The filter discussed here, illustrated in Figure 1, is for a configuration of type (1).

This paper describes the factors involved in the design and construction of thin film lumped elements, such as the spiral inductor and gap capacitance in microstrip lines, the energy trapped resonator, the considerations involved in design and construction of a HIMF for trial use in a 100Mb/s PCM system as timing pick-up filter.

Lumped elements

(A) Spiral inductors

Figure 2 schematically depicts a simple, planar, spiral inductor on a substrate. The L, Q, fr and Cd of this spiral inductor can be calculated from

$$L = A\frac{a_o^2 n^2}{8a_o+11_o} + 0.2d\left(\ln\frac{2d}{r}-1\right) + 5.08\times10^{-3} l_o A\left(\ln\frac{l_o}{w+h_o} + 1.193 + 0.2235\frac{w'+h_o}{l_o}\right) \quad (1)$$

$$Q = \frac{\omega L}{R} = \frac{\omega L}{KK'R_s f \ell / 2w'} = \frac{4\pi L}{KK'\ell}\sqrt{\frac{f}{\pi\mu\sigma}} \quad (2)$$

$$f_r = \frac{v_o}{2\pi n(d_o+d_i)} \quad (3)$$

$$C_0 = \frac{1}{(2\pi f_r)^2 L} \quad (4)$$

where ℓ, c_o, a_o and A are as follows:

$\ell = 2\pi n a_o$
$c_o = (do - di)/2$
$a_o = (do + di)/4$
$A = 39.37007874$ [nH/mm]

In order for above expression to hold, do should be >1.2di, n should be 1 or greater. First term in (1) is given by physical dimensions of spiral inductor. Second and third terms in (1) are correction ones for

cross over. The correction factor K takes into account the crowding of the current from the corner of the spiral inductor. Figure 3 is a plot of K versus w'/h_o taken from Terman.

Figure 4 is Q of spiral inductor as a function of di/do, with the inductance L and length of spiral as constants. It has been shown that di/do = 7/15 will optimize Q. In order to easily design, Figure 5 gives the design chart of spiral inductor.

Table 1 shows the measured and calculated L's for a number of different size spiral inductors. As for this experiment, conductors of the spiral inductor are deposited a metal sandwich an a fused quartz substrate by vacuum evaporation using electron beam heating. The bottom metal (NiCr) of layer is about 350Å-thick. The top metal (Au) of layer is about 7.5μm-thick. It is noted that the measured values are close to the theoretical ones, within 3 % deviation.

(B) Gap capacitance in microstrip lines

Since gap capacitance in microstrip lines can have enough distributed capacity to influence on transmission characteristics of HIMFs in VHF range, it is primarily important to design the discontinuity structures precisely.

The analytical configulation of the gap is illustrated in Figure 6. It is preferable to represent the gap structure with the equivalent π circuit as shown in Figure 6 (c), because the parameters of equivalent π circuit show the physical meanings well. The shunt-gap capacitance Ca can be inferred from the effect of the disorder of the electrostatic field distribution at the edge of the strip conductor. The series capacitance Cb arises from the coupling effect of the adjacent strip conductors.

Hence, the shunt-gap capacitance Ca and the series capacitance Cb for the new equivalent-circuit parameter Cte, Ctm and Co are given by

$$C_a = \frac{C_{tm} - C_o}{2} \qquad (5)$$

$$C_b = \frac{C_{te} - C_{tm}}{4} \qquad (6)$$

where C_o is the line capacitance of the uniform microstrip line with its length of b-s.

The capacitance C_{te} and C_{tm} are given by the variational expression which is stationary with respect to arbitrary first-order variations in the charge distribution on the strip conductor pi(x,y,z):

$$\frac{1}{Cti} = \frac{\iint pi(x,y,z)\,Gi(x,y,z|x',y',z')\,pi(x',y',z')\,dv\,dv'}{\left(\int pi(x,y,z)\,dv\right)^2}, \quad i=e,m \qquad (7)$$

where the three dimensional potential Green's function Gi(x,y,z|x',y',z'), satisfying the boundary conditions with the electrode walls (i=e) or the magnetic walls (i=m) at y=0, and b, is the solution of following poisson's equation

$$Gi(x,y,z|x',y',z') = -\frac{1}{\varepsilon_o \varepsilon_r}\,\delta(x-x')\,\delta(y-y')\,\delta(z-z') \qquad (8)$$

where $\delta(x - x')$ is a Dirac's delta function.

For the thin microstrip line case, the charge distribution way has taken the form

$$pi(x,y,z) = pi'(x,y)\,\delta(z-h) \qquad (9)$$

Then the capacitance Cte, Ctm and C_o can be obtained as follows.

$$Cte = \frac{25}{64}\,\varepsilon_o \cdot a \cdot b \left(\frac{b}{s}\right)^2 \left(1 - \frac{s}{b} + \alpha \cdot \frac{h}{b}\right)^2 \sum_{m=1,3,\cdots}^{\infty} \sum_{n=1,3,\cdots}^{\infty} \frac{\gamma_{mn}}{P_m^2\, R_n^2} \cdot \left\{\varepsilon_r \cdot \coth(\gamma_{mn} \cdot c) + \coth(\gamma_{mn}(c-h))\right\} \qquad (10)$$

$$Ctm = \frac{\frac{25}{32}\, a \cdot b \cdot \varepsilon_o}{\frac{2}{\left(1 - \frac{s}{b} + \alpha \cdot \frac{h}{b}\right)^2} \sum_{m=1,3,\cdots}^{\infty} \sum_{n=2,4,\cdots}^{\infty} \frac{P_m^2\, Q_n^2}{\gamma_{mn}\left\{\varepsilon_r \cdot \coth(\gamma_{mn} \cdot h) + \coth(\gamma_{mn}(c-h))\right\}} * + \sum_{m=1,3,\cdots}^{\infty} \frac{P_m^2}{\gamma_{mo}\left\{\varepsilon_r \cdot \coth(\gamma_{mo} \cdot h) + \coth(\gamma_{mo}(c-h))\right\}}} \qquad (11)$$

$$Co = \frac{25}{32}\,\varepsilon_o \cdot a \cdot (b-s) \sum_{m=1,3,\cdots}^{\infty} \frac{\gamma_{mo}}{P_m^2}\left\{\varepsilon_r \cdot \coth(\gamma_{mo} \cdot h) + \coth(\gamma_{mo}(c-h))\right\} \qquad (12)$$

where

$$\gamma_{mn} = \sqrt{\left(\frac{m\pi}{a}\right)^2 + \left(\frac{n\pi}{b}\right)^2} \qquad (13)$$

$$P_m = 2 \cdot \left(\frac{2a}{m\pi w}\right) \cdot \sin\left(\frac{m\pi w}{2a}\right) + 8\left(\frac{2a}{m\pi w}\right) \cdot \cos\left(\frac{m\pi w}{2a}\right) - 6\left(\frac{2a}{m\pi w}\right)^4 \cos\left(\frac{m\pi w}{2a}\right) - 6\left(\frac{2a}{m\pi w}\right)^3 \cdot \sin\left(\frac{m\pi w}{2a}\right) + 6\left(\frac{2a}{m\pi w}\right)^4 \qquad (14)$$

$$Q_n = \frac{2b}{n\pi s} \cdot \sin\left(\frac{n\pi s}{2b}\right) + \alpha \cdot \left[\frac{2b}{n\pi s} \sin\left(\frac{n\pi s}{2b}\right) + \frac{2b}{n\pi h} \cdot \frac{2b}{n\pi s} \sin\left(\frac{n\pi h}{2b}\right) \cdot \sin\left\{\frac{n\pi h}{2b} + \frac{n\pi s}{2b}\right\}\right] \qquad (15)$$

$$R_n = \frac{2b}{n\pi s} \cdot \cos\left(\frac{n\pi s}{2b}\right) + \alpha \cdot \left[\frac{2b}{n\pi s} \cos\left(\frac{n\pi s}{2b}\right) - \frac{2b}{n\pi h} \cdot \frac{2b}{n\pi s} \cdot \sin\left(\frac{n\pi h}{2b}\right) \cdot \cos\left\{\frac{n\pi h}{2b} + \frac{n\pi s}{2b}\right\}\right] \qquad (16)$$

Numerical data for the equivalent circuit parameters of the gap can be readily obtained by computing the above formulas with the aid of a digital computer and using (5), (6). The calculated gap capacitances for parameters are shown in Figure 7.

Energy trapped resonators and substrates

From the system requirements the desired filter characteristic is determined a 2-pole chebyshev design with a center frequency at 97.728 MHz, and an 1 dB ripple and a 3 dB bandwidth of 22.5 kHz. On the basis of this result, the plate dimensions and electrode size of the energy trapped resonator are selected. The resonator spacings are determined using an analysis of the piezo-electric equations and interactive computer (Figure 8). Table 2 shows the measured and calculated parameters values.

The resonator frequencies are adjusted by mass removal. Nd:YAG laser machining facility to perform this operation is in use. The resonators are left slightly low in frequency so that after this operation the filter characteristic has the proper center frequency and bandwidth, but is located 1 - 5 kHz low in frequency. The accuracy of resonant frequency is adjusted within $\pm 1 \times 10^{-6}$.

Table 3 describes the properties of two popular substrate. The thermal expansion coefficient of substrate for HIMF is an important factor for the temperature stability. Figure 9 shows frequency deviation versus temperature for energy trapped resonator mounted on a fused quartz and ceramic substrate. It is noticed that fused quartz substrate is the more suitable.

Design procedure for HIMFs and its construction

The general HIMF design process is illustrated in

Figure 10, which is based on the theoretical principle prebiously presented.

An example of hybridization is the HIMF shown in Figure 11. Although the lumped capacitor can be formed by the fringing field between an interdigital gap or a metal-silicon dioxide-metal sandwich, the trial thin film lumped element circuit consists of spiral inductors and chip capacitors ($1.4 \times 1.4 \times 1.4$ mm^3). Hybrid techniques use a polished fused quartz substrate with the energy trapped resonator and chip capacitors mounted and bonded in place. In particular the energy trapped resonator is mounted on the concave surface of substrate by the ultrasonic machining. Nd:YAG laser is also used to connect thin film lumped element circuit and energy trapped resonator on this substrate.

Experimental results

Table 4 shows design perameters of thin film lumped element circuit. Attenuation characteristic of the thin film lumped element circuit obtained experimentally in the 10 to 200 MHz range closely fit theoretical calculation as shown in Figure 12.

Figure 13 also shows influence of proximity effect ($k' = 1.5$) between spirals.

The measured attenuation characteristic of the HIMF is shown in Figure 14. Figure 15 shows passband characteristic of the HIMF. It is realized with an 1.5 dB ripple and a 3 dB bandwidth of 23.5 kHz. Figure 16 shows the phase-temperature characteristic of the HIMF. Figure 17 is a photograph of the HIMF which is proposed for trial use as a new 100Mb/s PCM timing pick-up filter. Its dimensions are as follows:

Length	34 mm
Width	21 mm
Thickness	7 mm

The proposed HIMF volume represents a 10 : 1 reduction the present spiral resonator volume.

Conclusions

It has been shown that a hybrid integrated monolithic crystal filter (HIMF) can be used in a 100 Mb/s PCM system as timing pick-up filter. This HIMF consists of a thin film lumped element circuit and an energy trapped resonator in integrated structure on a fused quartz substrate. Distinct HIMF features are as follows:

(1) Considerable size reduction in VHF use, 1/10 in volume compared to spiral resonators, make it possible to construct remarkably small VHF filters for communication systems.

(2) High stability and high reliability are obtained because of energy trapped resonators and integrated structures.

For these reasons, the HIMF has become a very important factor in the VHF filter field.

Acknowledgement

The authors gratefully acknowledge Dr. M. Onoe of Institute of Industrial Science, the University of Tokyo for his helpful discussions and criticisms. They are also indebted to a great many members of Transmission Division of NEC, in particular: to Dr. M. Takahashi for his gratitude for the guidance and encouragement, and to Mr. T. Yuki for his many valuable suggestions.

References

(1) M. Onoe, H. Jumonji and N. Kobori, "High Frequency Crystal Filters Employing Multiple Mode Resonators Vibrating in Trapped Energy Modes," Proc. 20th Annual FCS, April 1966, pp.266-287.

(2) M. Caulton, S.P. Knight, and D.A. Daly, "Hybrid integrated lumped-element microwave amplifiers," IEEE Trans. Electron Devices, vol. ED-15, July 1968, pp.459-466.

(3) H. Engan, "Excitation of Elastic Surface Waves by Spatial Harmonics of Interdigital Transducers," IEEE Trans. Electron Device, vol. ED-16, December 1969, pp.1014-1017.

(4) E. Yamashita and K. Atsuki, "Analysis of Thick-Strip Transmission Lines," IEEE Trans. MTT-19, January 1971, pp.120-122.

(5) M. Maeda, "An Analysis of Gap in Microstrip Transmission Lines," IEEE Trans. MTT-20, June 1972, pp.390-396.

(6) J.L. Hokanson, "Laser-Machining Thin-Film Electrode Arrays on Quartz Crystal Substrates," J. Appl. Phys., vol. 40, No. 8, July 1969, pp.3157-3160.

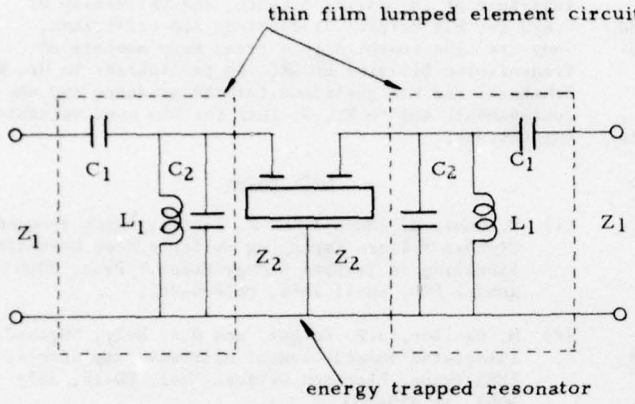

Figure 1. Equivalent circuit of the trial hybrid integrated monolithic crystal filter

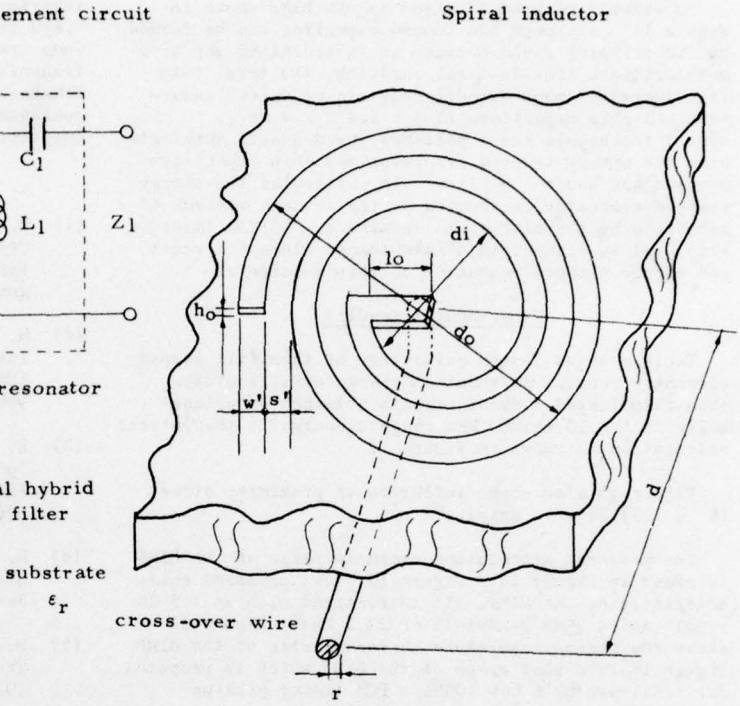

Figure 2. Spiral inductor on substrate

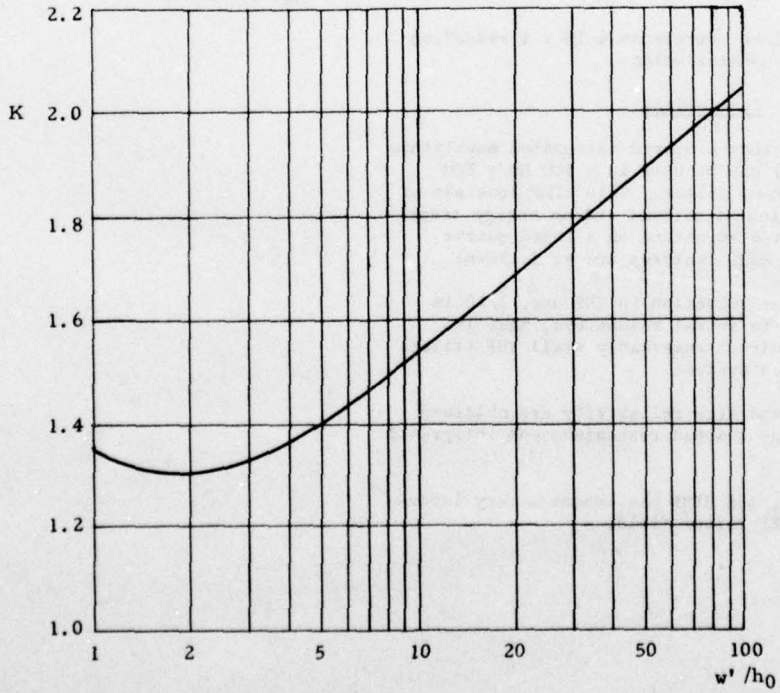

Figure 3. Correction factor K as a function of w'/h_0 (taken from Terman)

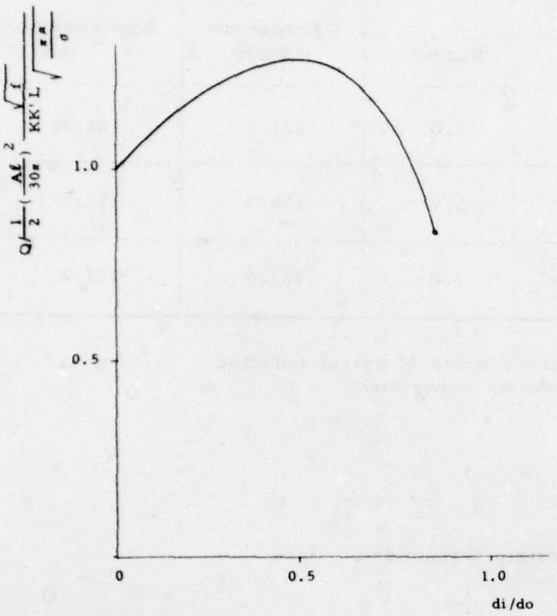

Figure 4. Q of spiral inductor as a function of di/do, with the inductance L and length of spiral l as constants.

Figure 5. Frequency f as a function of inductance L, with the Q and metal layer on the substrate as parameters. The assumed dielectric constant of the substrate $\varepsilon_r = 3.6$.

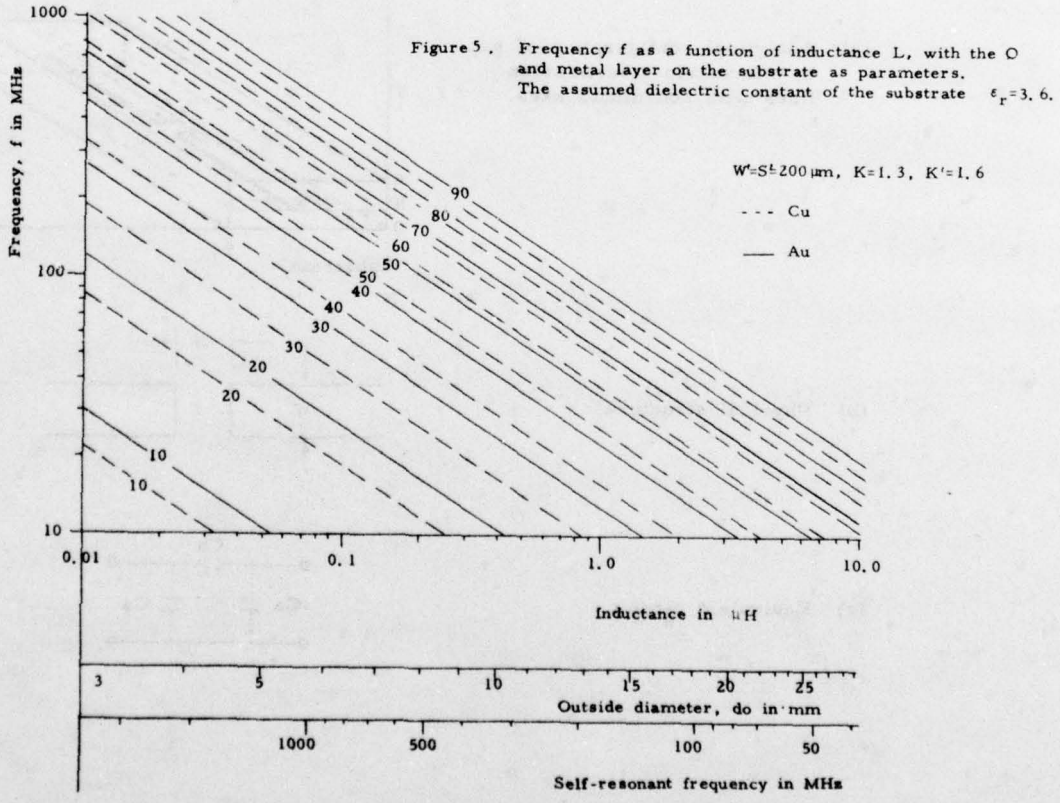

	Dimensions				Calculations (n H)	Experiments (nH)
	n(turns)	w=s(μ m)	do(mm)	di(mm)		
Sample 1	4	400	9.9	3.8	121.2	121.4
Sample 2	3.75	300	9.9	5.7	155.1	151.3
Sample 3	4	200	6.9	3.8	127.4	131.2

Table 1. Comparison of inductance values of spiral inductor obtained by a theory and an experiment.

Figure 6. Gap in microstrip transmission lines

(a) Analytical configuration of gap in microstrip transmission lines with coordinate axes.

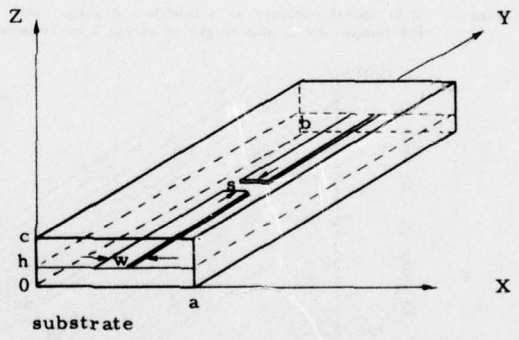

(b) Physical structure

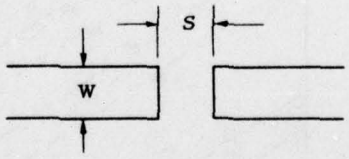

(c) Equivalent circuit

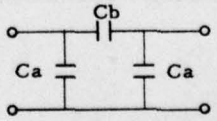

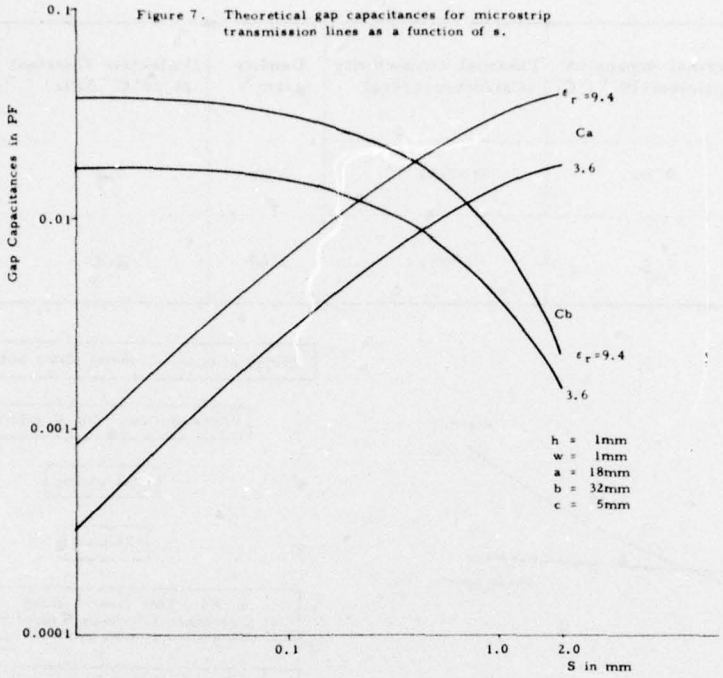

Figure 7. Theoretical gap capacitances for microstrip transmission lines as a function of s.

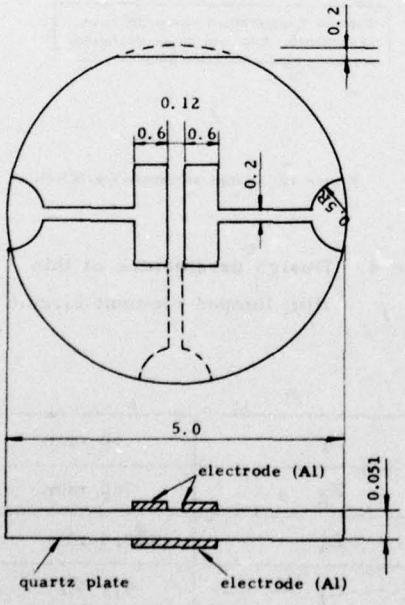

Figure 8. The quartz plate dimension and electrode size of the trial energy trapped resonator (in mm)

Table 2. Parameters of energy trapped resonator

Parameters	Design	Experiment
Quartz plate cut-angle	35°19'±1'	
Ething frequency	98.1 MHz	
Plateback	0.424%(1370Å-thick)	
Plated material	Al	
Mode of operation	3rd overtone TT-mode	
Equivalent inductance	5.24 mH	5.62 mH*
Bandwidth	22.5 KHz	23.5 KHz
Q		20,000

* at symmetric mode (measured by IEC method)

Table 3. Properties of substrate materials

Property / Substrate material	Thermal-expansion coefficient (10^{-6}/°C)	Thermal conductivity (Cal/cm/sec/deg)	Density (g/cm^3)	Dielectric Constant at 25°C, MHz	Power factor (loss tangent) at 25°C, MHz
Fused quartz	0.56	0.0034	2.20	3.6	0.00002
Ceramic (99.5% Al_2O_3)	7.1	0.088	3.67	9.4	0.0009

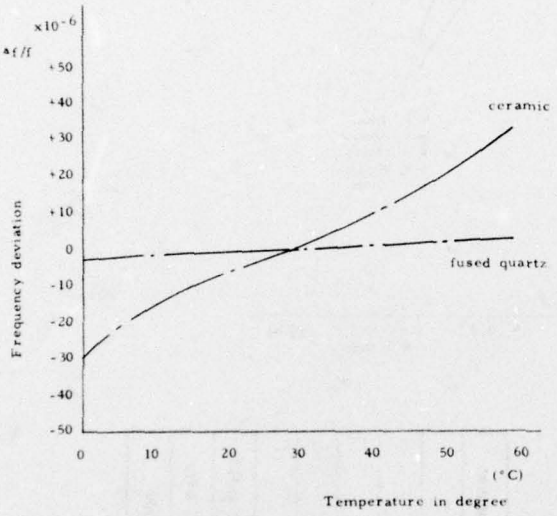

Figure 9. Frequency deviation versus temperature for energy trapped resonator on fused quartz and ceramic substrate.

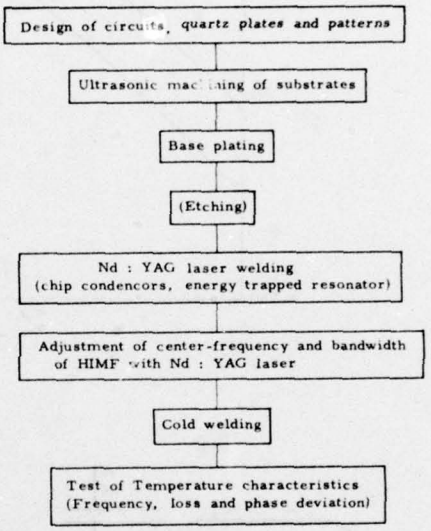

Figure 10. Design procedure for HIMFs

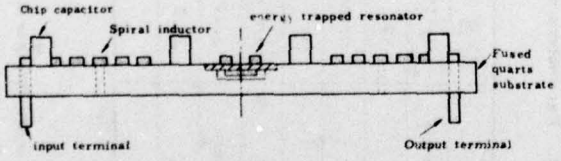

Figure 11. Cross-sectional view of the trial hybrid integrated monolithic crystal filter

Table 4. Design parameters of thin film lumped element circuit

Z_1	50 ohm
Z_2	700 ohm
L_1	127.4 nH
C_1	9.1 PF
C_2	11.6 PF
3 dB bandwidth	21.8 MHz

Figure 12. Typical characteristic of thim film lumped element circuit

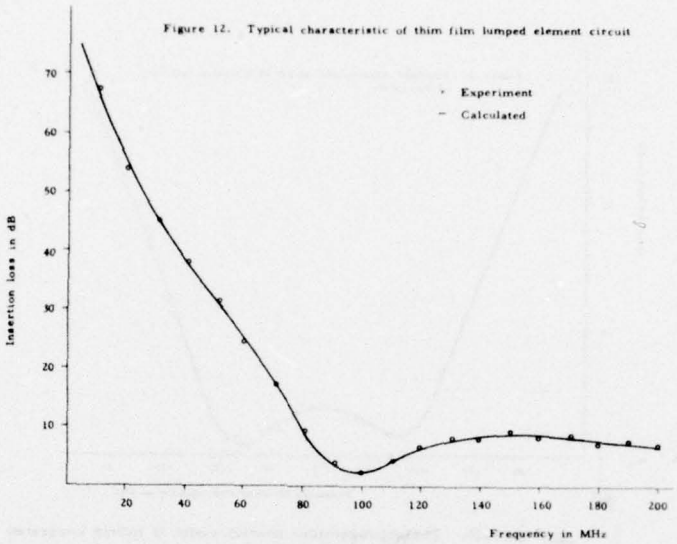

Figure 13. Effect of correction facter K' on attenuation characteristic of thim film lumped element circuit.

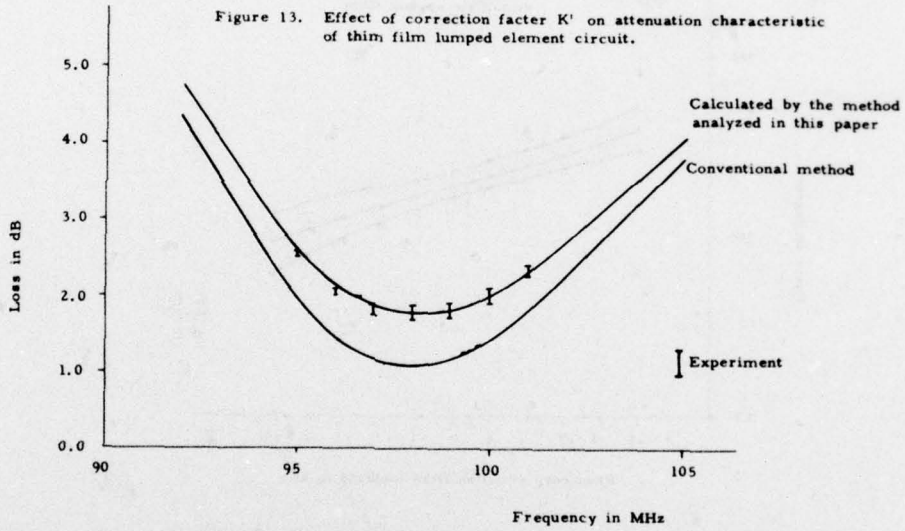

Figure 14. Attenuation characteristic of hybrid integrated monolithic crystal filter

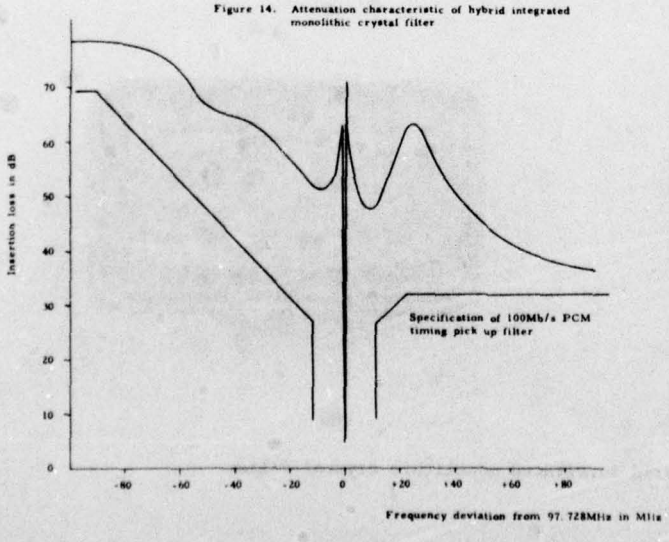

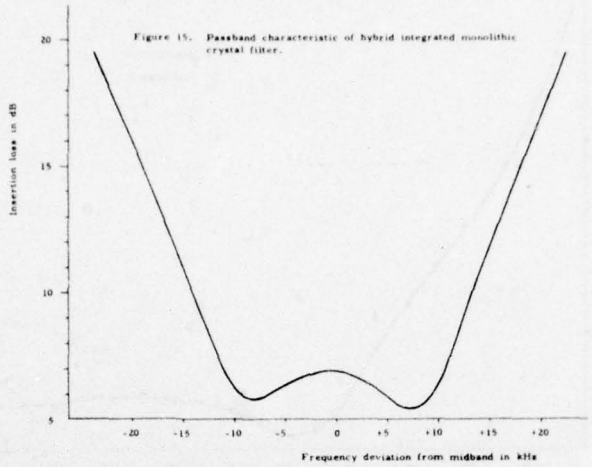

Figure 15. Passband characteristic of hybrid integrated monolithic crystal filter.

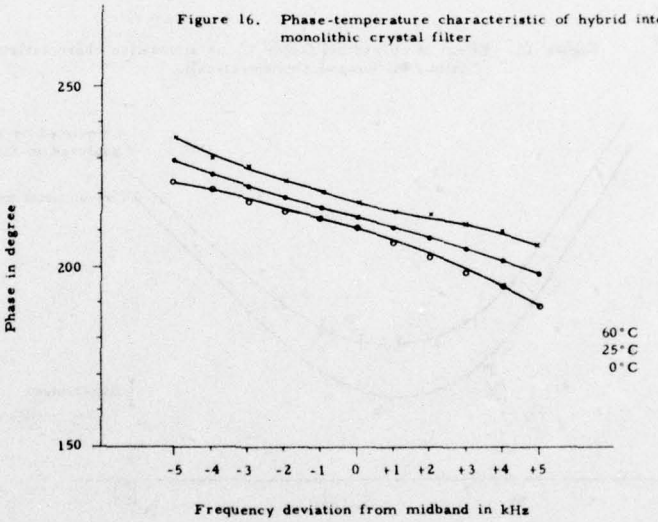

Figure 16. Phase-temperature characteristic of hybrid integrated monolithic crystal filter

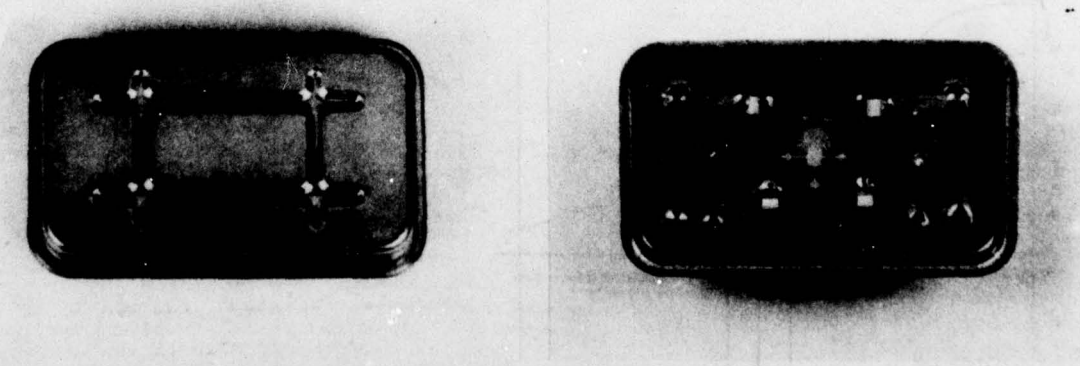

Figure 17. Proposed hybrid integrated monolithic crystal filter

Surface Acoustic Wave VIF Filters for TV Using ZnO Sputtered Film

Satoru Fujishima, Hideki Ishiyama, Atushi Inoue, Hideharu Ieki

Murata Mfg. Co., Ltd.

Summary

Surface acoustic wave VIF filters for TV have been researched and developed in the world because they have many merits such as small size, non-alignments and uniform frequency or phase characteristics. We have succeeded to make the surface acoustic wave filters using ZnO-sputtered films. Here, the method to make the ZnO thin films and the characteristics of the SAW filters are reported compared with other materials like $LiNbO_3$ single crystals and PZT ceramics.

Introduction

Surface acoustic wave filters for TV Video IF have been recently researched and developed in the United States, Europe and also in Japan. Materials for these filters are mainly single crystals like $LiNbO_3$, $LiTaO_3$ and $Bi_{12}GeO_{20}$ or piezoelectric ceramics like PZT. However, the cost of single crystals like $LiNbO_3$ is very high at present compared with ordinary LC IFT in TV VIF module and it is difficult to expect to reduce this price even in the mass production. And for another point, the temperature coefficient of frequency for $LiNbO_3$ is more than 70 ppm/ °C. This means we have some limitation to use $LiNbO_3$.

Piezoelectric ceramics like PZT have many merits which electro-mechanical coupling coefficient Ksaw is big enough, size and shape is free, and the cost is comparatively low because of ease to mass production. However to use piezoelectric ceramics for SAW filters for TV VIF, we must make quite non-porous ceramics of at least less than 2 - 3 μm grain size. At present, hot press technique is the most suitable to make such fine grain ceramics, but this technique is also the reason of cost-up.

ZnO thin film materials have been studied as a thin film transducer to exite bulk wave in micro wave range since 1960, and recently studied to use SAW filter since White and others have pronounced to make interdigital electrode in 1965.

ZnO is a low price material, especialy ZnO thin film sputtered from sintered ZnO target is cheeper than $LiNbO_3$ or hot pressed PZT ceramics. As we found it is very easy to make good oriented ZnO thin films and very stable materials having good performance, we would introduce here the results.

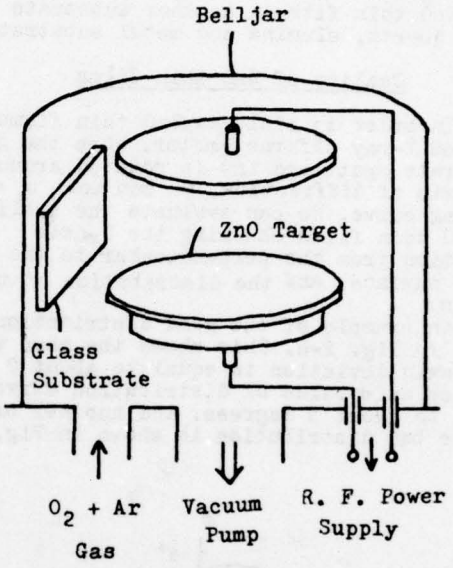

Fig.1 Outline of Sputtering Equipment and Substrate Position

ZnO thin film fablication

We used an ordinary diode RF sputtering equipment. The outline of electrodes and substrates position in the bell jar is shown in Fig. 1.

We used the ZnO powder which purity is better than 99 % to make the ZnO target. After this powder is mixed with binder and dried, the powder is pressed by the pressure of about 1 ton/cm2 to make the disc of 100 mm diameter and 5 mm thichness. This disc is shintered to the 85 mm diameter and 4 mm thickness after the firing of about 1200 °C in 2 hours. It was effective to add 1 to 3 wt % of Li_2CO_3 in this target to increase the insulation resistance of sputtered ZnO thin film. According to the ordinary sputtering method, substrates should be fixed in parallel to the ZnO target. But in this case, it was difficult to make good ZnO thin films because of the heating up of substrate by direct heat radiation from plasma and target. So, we found it is better to fix the substrate in perpendicular to the side of the ZnO target as shown in Fig. 1 to protect the heating up of substrate.

We used argon 50 % mixed oxigen 50 % gas in pressure of 7×10^{-2} Torr and the anode voltage of RF power oscillator was 1,8 to 2,0 kV. In this case, the growth speed of ZnO

thin film was about 0,2 to 0,4 μm/hr and the temperature of substrate was from 150 to 200 °C. We needed about 50 to 100 hours to make the 20 μm thickness. This seems a little slow to the practical production, but we expect to speed up this time in two or three times by controlling the temperature of substrate. Used substrates were standard alkaline free glasses for thin film resistors which size was 50 × 50 mm and 0,5 mm thickness. And the flatness of these glasses was good enough to make fine pattern on the surfaces. It was also easy to make this ZnO thin film on another substrate like fused quartz, alumina and metal substrate.

Quality of ZnO thin films

In order to evaluate ZnO thin films, we used X-ray diffractometer. When the glass substrate sputtered ZnO is rotated around the axis of diffraction, we can make a locking curve. We can evaluate the quality of ZnO thin films checking the C-axis deviation from the perpendicular to the glass surface, and the distribution of this C-axis.

An example of the good distridution is shown in Fig. 2-a. This shows the mean value of C-axis deviation is equal to about 2 degrees and σ value of distribution curve is equal to about 3 degrees. And another example of the bad distribution is shown in Fig. 2-b.

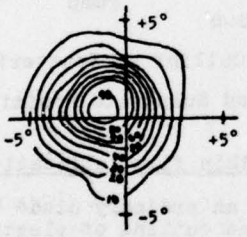

Fig. 2-a Good Orientation of C-axis

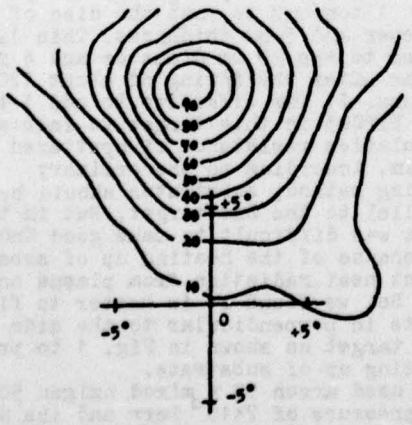

Fig. 2-b Bad Orientation of C-axis

The electro-mechanical coupling coefficient Ksaw was about 10 %. This value was measured from the difference between the maximum and minimum impedance of an interdigital electrode. The dielectric constant of ZnO thin films was 8,5 and the resistivity was $10^{10}\,\Omega$-cm. Table 1 shows each constant of ZnO thin films comparing with LiNbO3 single crystals and PZT ceramics.

Material	LiNbO3	ZnO	PZT
Effective Permittivity	50	8,5	300
$Ksaw^2/2$	0,024	0,005	0,012
Propagation Loss (dB/cm)	<0,1	4~5	6~7
Temperature Coefficient (ppm/°C)	-80	-30	-45
Pore Size (μm)	-	<1	4

Table 1 Material Constants

Structure of SAW filter

Fig. 3 shows the structure of SAW filters we made this time. Interdigital electrodes of Cr + Au are made by photo-etching directly on the glass substrate of 0,5 mm thickness. ZnO thin films are sputtered on this electrodes to make 20 μm thickness.

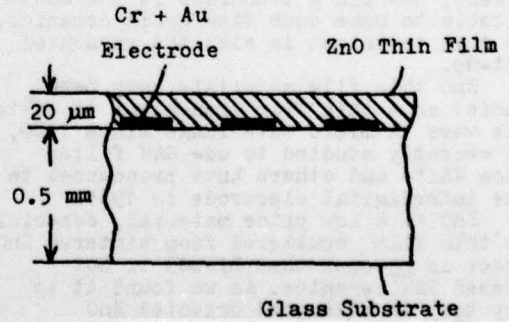

Fig.3 Stracture of SAW Filter

Input is a nomal interdigital electrode with 15 finger pairs and output is an apodized one with 24 finger pairs which finger and space width are 10 μm for 58 MHz Japan TV. Photo 1 shows this structure. To improve the spurious response excited by bulk wave, it is useful to etch the back side of the glass substrate by sand blast and to coat silicone rubber on both outer side of input and output electrodes.

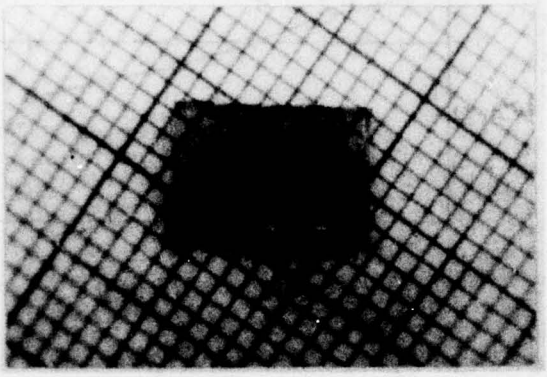

Photo. 1 Transducer Structure

Characteristics of SAW filter

Fig. 4 shows a block diagram of color TV which includes a SAW filter with a input series inductor. Output of a SAW filter is terminated with a 330 ohm resistor.

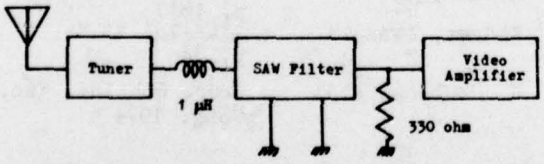

Fig. 4 Block Diagram

Fig. 5 shows an example of the frequency response and group delay time curve for Japan TV measured by Fig. 4 diagram. In Fig. 5, dotted line shows the calculated response. Both calculated and measured line coincide good enough in main pass band. Fig. 6 shows the spurious response until 100 MHz frequency range.

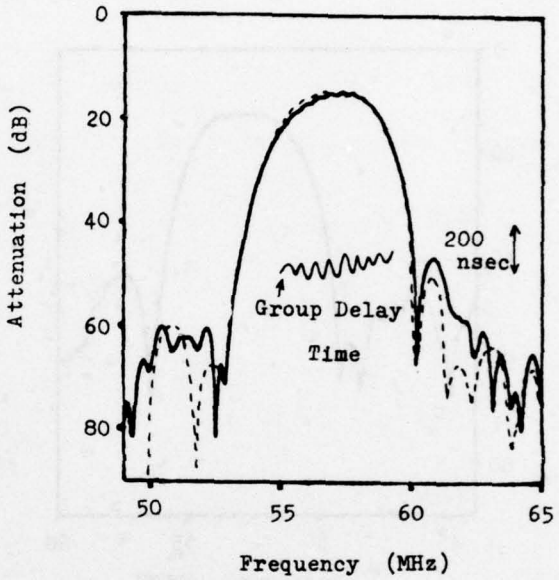

Fig. 5 Frequency Characteristic of ZnO SAW Filter

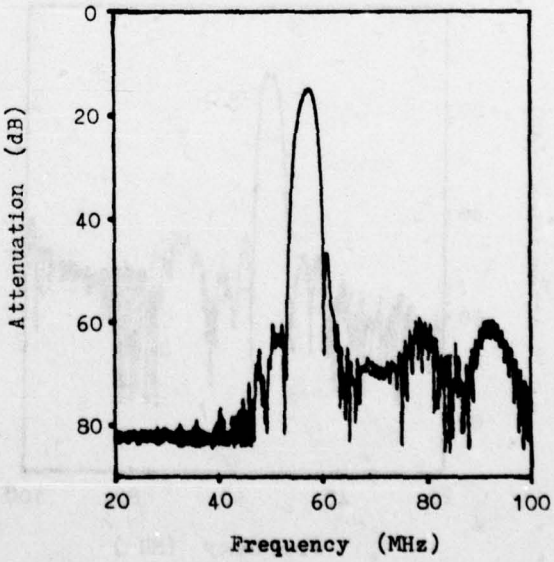

Fig. 6 Spurious Response of ZnO SAW Filter

For reference, we show in Fig. 7 and Fig. 8 for PZT materials by same electrode pattern. From these figures, we find that the bottom level response by PZT is worse than ZnO because of the electro-magnetic and static coupling between input and output electrodes.

Fig. 9 shows an example of the temperature characteristics of center frequency. From this curve, we can calculate N 30 ppm/ °C for the temperature coefficient which means quite enough for practical use. The aging characteristics have been measured for 400 days in room temperature to give less than 0,1 %.

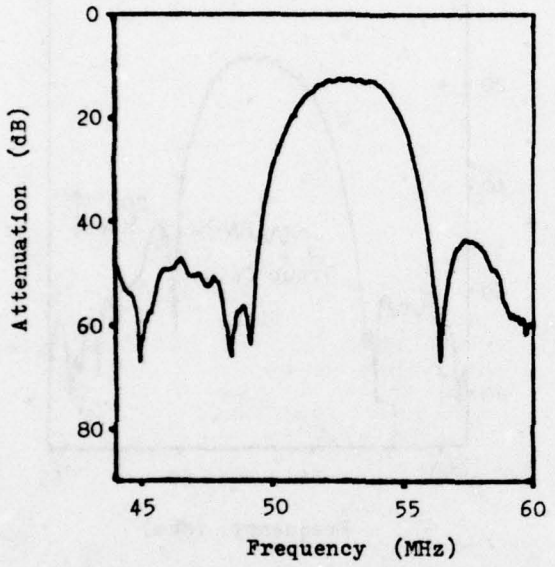

Fig. 7 Frequency Characteristic of PZT SAW Filter

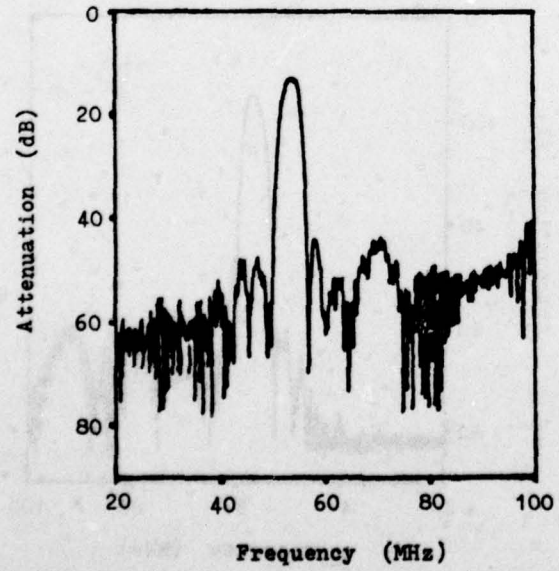

Fig. 8 Spurious Response of PZT SAW Filter

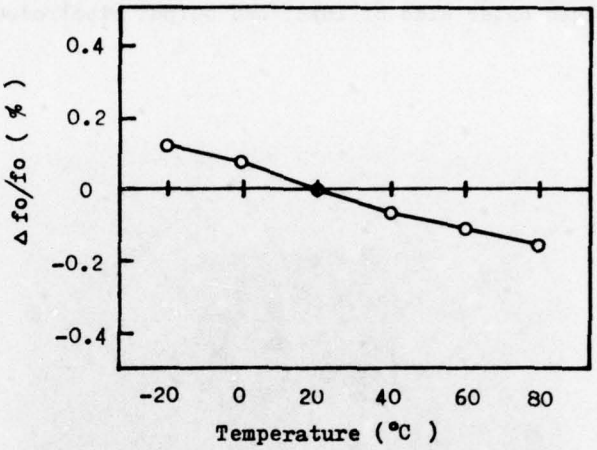

Fig. 9 Temperature Characteristic of Center Frequency

Conclusion

We found it is possible to make surface wave VIF filter for TV using ZnO-sputtered film on glass substrate. The low cost and low temperature coefficient of the frequency will be the big merits of this filter.

The authors wish to thank Dr. A. Kawabata and Dr. T. Shiosaki of Kyoto University for many advices.

References

1) A. J. DeVries etal : IEEE Trans. BTR (1971) p. 16
2) A. J. DeVries etal : IEEE Ultrasonic Symp. Proc. 1974 p. 147
3) Kodama, Egami : JJAP Vol 14 No. 11 p. 1847
4) Kodama, Iwasaki : JJAP Vol 13 No. 1 p. 34
5) N. Chubachi etal : Proc. 6th Int. Vac. Cong. 1974

FILTERING WITH ANALOG CCD'S AND SWD'S

C. R. Hewes, L. T. Claiborne, C. S. Hartmann and D. D. Buss
Texas Instruments Incorporated
Dallas, Texas

Introduction

Charge-coupled devices (CCDs) and surface acoustic wave devices (SWDs) are currently emerging as two very important technologies for implementing filtering functions. Both CCDs and SWDs are very efficient in performing the transversal filter operations which are illustrated in the prototype block diagram of Figure 1. This efficiency is a result of the fact that both CCDs and SWDs perform the time delay, accurate analog multiplication and addition operations.

Although the two device types can perform similar filtering functions they are complementary rather than competative. CCDs are essentially low frequency ($f < 10$ MHz) and long time delay ($T < 1$ sec) devices while SWDs are IF and RF devices ($f > 10$ MHz) with moderate time delays ($T < 100$ µsec). Time bandwidth products are on the order of $T \times BW < 10^3$ for CCDs and $T \times BW < 10^4$ for SWDs.

CCDs are sampled data filters with a discrete time base (i.e. clock signal) which can be controlled by crystal oscillator for very accurate and precise filtering. CCDs can also be tuned by means of the external clock frequency. SWDs on the other hand operate with a continuous time base and a delay time which is fixed once the device is fabricated.

Below we briefly describe the CCD filter and the SWD filter and give examples and more detailed references for each.

CCD Transversal Filters

The block diagram of a CCD transversal filter is given in Figure 1. It consists of delay stages D together with circuitry for performing the weighted summation of node voltages v_n. Each delay stage consists of p transfer electrodes in a p-phase CCD. The filter is sampled and clocked at clock frequency f_c, and the z-transform characteristic H(z) is given by

$$H(z) = \sum_{n=0}^{N-1} h_n z^{-n} \qquad (1)$$

where h_n, n=0, N-1, are the weighting coefficients, and z is related to frequency f through the relation

$$z = \exp\left[i2\pi f/f_c\right] . \qquad (2)$$

The CCD transversal filter is an important component primarily because the weighting and summing circuitry is quite simple. Using the split electrode weighting technique[1], a CCD delay line can be made into a transversal filter by splitting one of the electrodes in each delay stage and putting a differential current integrator (DCI) in the clock line as shown schematically in Figure 2.

In Figure 2, the signal charges are sampled on the ϕ_3 clock electrodes. As charge transfers from the kth ϕ_2 electrode to the kth ϕ_3 electrode, the current flowing to the kth ϕ_3 electrode line consists of current which would flow if no signal charge were present plus a signal current. Therefore, the signal charge can be determined by integrating the current flowing to the ϕ_3 electrode during charge transfer. Weighting is performed by splitting the ϕ_3 electrode and integrating the current flowing to the ϕ_3 electrode during charge transfer. Weighting is performed by splitting the ϕ_3 electrode and integrating separately the current flowing to each portion. A weighting coefficient of zero corresponds to a split in the center of the electrode, and positive and negative h_k are achieved by appropriately proportioning the charge between ϕ_3^+ and ϕ_3^-. The summation is achieved by connecting together the ϕ_3^+ electrode and the ϕ_3^- electrode as shown in Figure 2b, and the filter output is obtained by integrating and differencing the ϕ_3^+ and ϕ_3^- clock line currents in the output (DCI) as shown.

The split electrode technique was first developed for use with bucket-brigade devices (BBDs)[2] and has been widely used for both CCD and BBD filters.[3-8] The design techniques are further described in Reference 1 and 8.

CCD Examples

The frequency response of an 800-stage CCD bandpass filter is shown in Figure 3.[9] The filter was designed with optimum weighting to have uniform sidelobes at -40 dB. The highest measured sidelobe is degraded to -37 dB by a weighting coefficient error as discussed in Reference 8. It has a 0.7 percent fractional bandwidth at -3 dB and a 1.0 percent fractional bandwidth at -40 dB.

The chirp z-transform (CZT) is an algorithm for performing the discrete Fourier transform (DFT) in which the bulk of the computation is performed in a chirp transversal filter and, for this reason, it is particularly attractive for CCD implementation.[10-12] Beginning with the definition of the DFT

$$F_k = \sum_{n=0}^{N-1} f_n e^{-i2\pi nk/N} \qquad (3)$$

and using the substitution

$$2nk = n^2 + k^2 - (n - k)^2 \qquad (4)$$

the following equation results

$$F_k = e^{-i\pi k^2/N} \left[\sum_{n=0}^{N-1} \left(f_n e^{-i\pi n^2/N} \right) e^{i\pi (k-n)^2/N} \right] . \qquad (5)$$

This equation has been factored to emphasize the three operations which make up the CZT algorithm: premultiplication by a chirp, filtering in a chirp transversal filter, and postmultiplication by a chirp. When only the power density spectrum is required, the postmulti-

plication by $\exp(-i\,k^2/N)$ can be eliminated, and a block diagram of the circuit implementation is given in Figure 4.

Five hundred-stage CCD filters have been used to implement the block diagram of Figure 4; the result is shown in Figure 5. The CCD CZT is discussed further in Reference 8 and 13.

SWD Bandpass Filters

In many respects, SAW bandpass filters have been pushed closer to ultimate levels of achievable performance than most other SAW devices.[14] Table I summarizes several important performance characteristics of surface-wave bandpass filters and, simultaneously, suggests general limitations of the surface-wave technology itself. Many outstanding achievements have been demonstrated with SAW filters, as shown in the first column. The second column lists values that can currently be obtained in a high-yield moderate-production environment. The third column represents estimates of anticipated improvements due to refinements in transducer weighting and better second-order design, including diffraction and electrical loading effects.

Some of the parameters in Table I are interrelated in ways such that the limiting values of parameters cannot all be realized in a single filter. For example, minimum achievable insertion loss depends on fractional bandwidth,[15] as will be discussed shortly. In addition, although nominally linear phase response is usually obtained unless a desired dispersion is specified, triple-transit echoes produce a periodic ripple in phase and amplitude in the passband of some SAW filters. This ripple diminishes with increasing insertion loss in conventional filter geometries but, notably, is nearly eliminated with unidirectional design.[16]

An example of a high performance SWD bandpass filter is shown in Figure 6. This filter was developed for space application and had a 287 MHz center frequency with a 6 MHz bandwidth. The most notable feature of this filter is the out of band rejection which is not less than 70 dB and often near 100 dB from dc to 1.2 GHz. This device and others are discussed more fully in Reference 14.

SWD Chirp Z-Transform

Chirp z-transform units employing SWD chirp devices have recently been used to implement a continuously variable bandpass/bandstop filtering capability.[14,17] The basic algorithm is similar to the CCD chirp transform discussed above with two major differences. First, the SWD chirp z-transform is continuous in time whereas the CCD version is time sampled. Second, the SWD transform works at a carrier frequency which allows both real and imaginary (in-phase and quadrature) components to be processed in a single channel whereas the CCD unit requires multiple channels to process real and imaginary components of the signals. The chirp transform orders the frequency components on an input signal serially in time, i.e., the output time response is proportional to the Fourier transform (or frequency spectrum) of the input time signal. The chirp transform is realized by a chirp filter, two chirp generators, and two mixers as shown in Figure 7. This unit was built using SAW chirp filters with the time lengths and bandwidths shown. Figure 8 shows the actual chirp transform output for a succession of 7 CW input signals from 120 to 180 MHz in 10 MHz steps. The frequency content of the input signal is clearly displaced in time proportional to the chirp rate of the SAW chirp filter, as one might expect.

The availability of accurate spectral information in real time permits important new signal processing applications, such as the programmable matched filtering and prewhitening.[17] In another configuration, the transform adaptable processing system (TAPS) provides continuously variable SAW bandpass and bandstop filtering.

Since the chirp transform converts the input signal piecewise into a time signal that is proportional to the Fourier transform of each signal block, adaptable filtering can be effected by simply multiplying each of the frequency components, which are now separated in time, by an appropriate amplitude- and phase-weighting coefficient using an RF mixer. This "modulated" chirp transform signal can then be inverse transformed with a second chirp transform to reconstruct the "filtered" time signal. By varying the modulation function, the portion of the input spectrum that is passed or stopped can be arbitrarily selected, in any combination of bandpass and/or bandstop responses, simply by changing the width and position of a gating pulse or pulses.

The results of the prototype are more completely discussed and demonstrated in Reference 17, but Figures 9 and 10 demonstrate bandpass and bandstop operation, respectively. In both cases, two sets of pulses are used for the input signal: the first pulse train has 0.8 μs width at 134 MHz and the second 0.2 μs width at 168 MHz. This input signal is shown in the top trace of both figures. The second trace is the chirp transform of the input signal repeated every 1.9 μs with the transform of each successive interval of the input. To implement a bandpass filter, the modulation function, or gate, is simply turned off except when the desired frequency components of the transform are present in time. The third trace of Figure 9 shows the modulated transform data for the case in which the 0.8 μs pulse train at 134 MHz is passed and all other frequencies are rejected. Since the transform repeats each 1.9 μs, the gate must also be activated every 1.9 μs to remove the shorter pulses from every interval of the signal. The final trace of Figure 9 is the output of the prototype following the inverse transform of the modulated transform trace. The short pulses are clearly rejected and the desired longer pulses are correctly passed and reconstructed.

Alternatively, one might wish to reject the longer pulses at 134 MHz and pass all other frequencies. This would be implemented by turning off the gate only during the time corresponding to the frequency components of the 134 MHz pulses, as shown in the third trace of Figure 10. The inverse transform shown in the last trace shows that only the narrow pulses are passed and properly reconstructed by the inverse transform. More than 40 dB of rejection was obtained at the stopband frequencies.

The prototype system has clearly demonstrated its capability to perform adaptable bandpass/bandstop filtering. All the components required are conventional and easy to build, in contrast to the fabrication difficulties associated with the conventional switched tapped delay line programmable approach. Development of this approach has begun for a communications system application for programmable matched filtering and prewhitening although realization of the potential of real time transform processing is still in its early stages.

Conclusion

Analog CCD and SWD technology can provide many important filtering and signal processing functions. The functions performed by these devices are similar but have differing frequency ranges. Both technologies will have an important place in future communications systems.

References

1. D. D. Buss, D. R. Collins, W. H. Bailey, and C. R. Reeves, "Transversal filtering using charge transfer devices," IEEE J. Solid-State Circuits, vol. SC-8, pp 134-146, April 1973.

2. F. L. J. Sangster, "The bucket-brigade delay line, a shift register for analogue signals," Philips Tech. Rev., vo. 31, pp 97-110, 1970.

3. R. D. Baertsch, W. E. Engeler, H. S. Goldberg, C. M. Puckette, and J. J. Tiemann, "Two classes of charge transfer devices for signal processing," in Proc. Int. Conf. Technology and Appiication of CCD's, Edinburgh, Scotland, September 1974, pp. 229-236.

4. D. D. Buss and W. H. Bailey, "Application of charge transfer devices to communication," in Proc. CCD Applications Conf., San Diego, CA, September 1973, pp 83-93.

5. A. Ibrahim and L. Sellars, "CCDs for transversal filters applications," in IEEE Int. Electron Devices Meeting, Tech. Digest, Washington, December 1974, pp 240-243.

6. J. A. Sekula, P. R. Prince, and C. S. Wang, "Non-recursive matched filters using charge-coupled devices," in IEEE Electron Devices Meeting, Tech. Digest, Washington, December 1974, pp 244-247.

7. M. F. Tompsett, A. M. Mohsen, D. A. Sealer, and C. H. Sequin, "Design and characterization of CCDs for analog signal processing," in IEEE Advanced Solid-State Components for Signal Processing (IEEE Int. Symp. Circuits and Systems, Newton, MA, April 1975), pp 83-89.

8. R. W. Brodersen, C. R. Hewes, and D. D. Buss, "A 500-stage CCD transversal filter for spectral analysis," to be published in a joint issue of IEEE J. Solid State Circuits and IEEE Trans. Electron Devices.

9. C. R. Hewes, "A self contained 800-stage CCD transversal filter," Proc. Int. Conf. Application of Charge Coupled Devices, San Diego, CA, October 1975, p 309.

10. L. R. Rabiner, R. W. Schafer and C. M. Rader, "The chirp z-transform algorithm," IEEE Trans. Audio Electroacoust., vol. AU 17, pp 86-92, June 1969.

11. H. J. Whitehouse, J. M. Speiser, and R. W. Means, "High speed serial access linear transform implementations," presented at the All Applications Digital Computer Symp., Orlando, FL, January 1973, paper NUC TN 1026.

12. R. W. Brodersen, H. S. Fu, R. C. Frye, and D. D. Buss, "A 500-stage fourier transform using charge-coupled devices," in 1975 Int. Solid-State Circuits Conf. Digest of Technical Papers, Phila., PA, February 1975, pp 144-145.

13. D. D. Buss, R. L. Veenkant, R. W. Brodersen, and C. R. Hewes, "Comparison between the CCD CZT and the digital FFT," in Proc. Int. Conf. Application of Charge-Coupled Devices, San Diego, CA, October 1975, pp 267-281.

14. R. M. Hays and C. S. Hartmann, "Surface-acoustic-wave devices for communications," Proceedings of the IEEE, vol. 64, No. 5, May 1976, pp 652-671.

15. C. S. Hartmann, D. T. Bell, Jr., and R. C. Rosenfeld, "Impulse model design of acoustic surface-wave filters," IEEE Trans. Microwave Theory Tech., vol. MTT-21, April 1973, pp 162,175.

16. C. S. Hartmann, W. S. Jones, and H. Vollers, "Wide-band unidirectional interdigital surface wave transducers," IEEE Trans. Sonics Ultrason., vol. SU-19, July 1972, pp 378-370.

17. R. M. Hays, W. R. Shreve, D. T. Bell, Jr., L. T. Claiborne, and C. S. Hartmann, "Surface wave transform adaptable processor system," in 1975 Ultrasonics Symp. Proc., IEEE Pub. No. 75 CHO 994-4SU, September 1975, pp 363-370.

TABLE I
SURFACE WAVE BANDPASS FILTER CAPABILITIES

	Demonstrated	Production	Projected Practical Limits
Center Frequency	1.0 MHz -2.75 GHz	10 MHz - 1.5 GHz	10 MHz - 2.0 GHz
Minimum Insertion Loss	0.65 dB	1.0 dB	0.5 dB
Maximum Fractional Bandwidth	100%	50%	100%
Sidelobe Rejection	70 dB	60 dB	90 dB
Minimum Bandwidth*	100 kHz	100 kHz	50 kHz
Minimum Transition Bandwidth*	100 kHz	100 kHz	50 kHz
Minimum Shape Factor	1.15	1.2	1.1
Triple Transit Suppression	55 dB	45 dB	60 dB
Amplitude Ripple	± 0.02 dB	± 0.05 dB	± 0.01 dB
Phase Deviation from Linear**	$\pm 0.1^{\circ}$	$\pm 2^{\circ}$	$\pm 0.1^{\circ}$

* Excludes performance achievable with SAW resonators

** Excludes Electrical Loading Effects (Ref. 15) which can be compensated by proper design

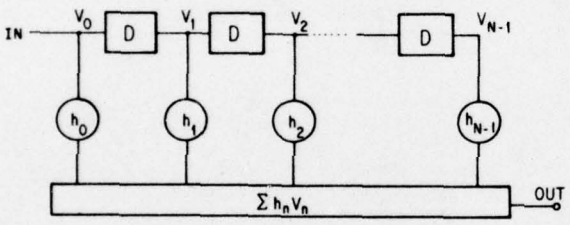

Figure 1. Block diagram of a transversal filter showing delay stages D and weighting coefficients h_n where n=0, N-1.

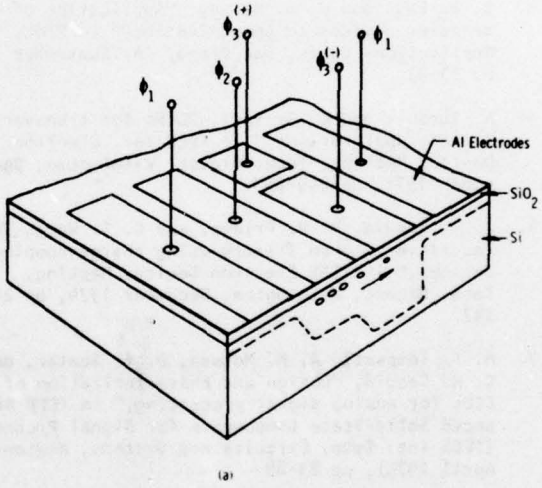

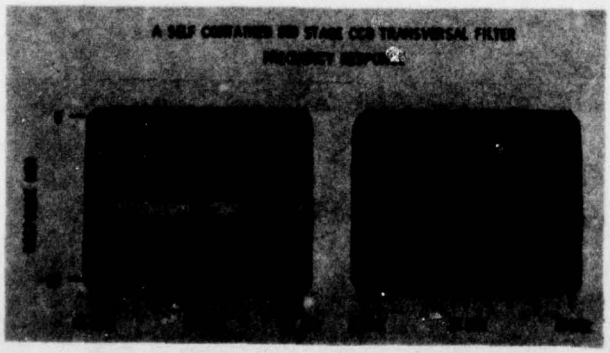

Figure 3. Measured frequency response of an 800-stage CCD bandpass filter. The filter was designed using optimum weighting to have -40 dB sidelobes, and a passband at one-quarter of the clock frequency.

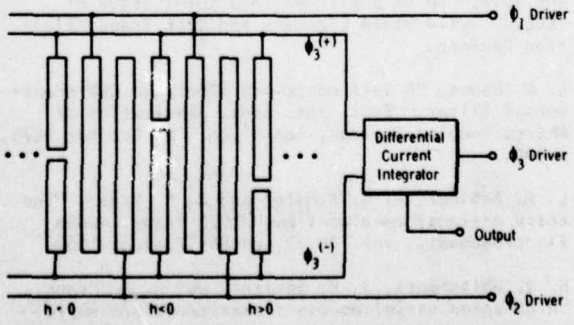

Figure 2. Schematic of the split electrode technique for realizing the weighting coefficients of a transversal filter.

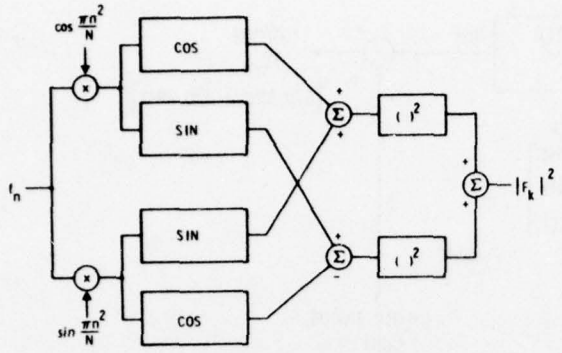

Figure 4. Implementation of the CZT algorithm to achieve the power density spectrum.

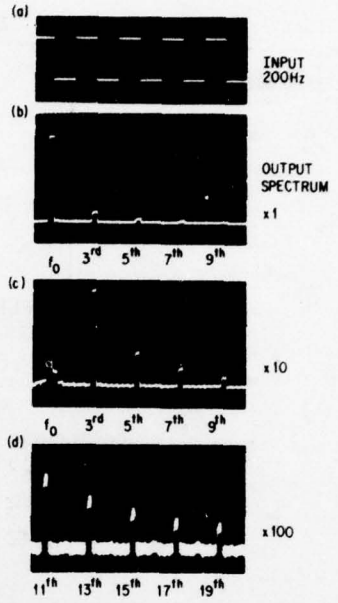

Figure 5. Spectrum of a 200 Hz square wave obtained using the system of Figure 5. (a) Input signal. (b) Output spectrum showing odd harmonics through the 9th. (c) Output spectrum on a 10X expanded scale. The fundamental is off scale and the arrow indicates the trailing pulse which results from imperfect transfer efficiency. (d) Output on a 100X expanded scale.

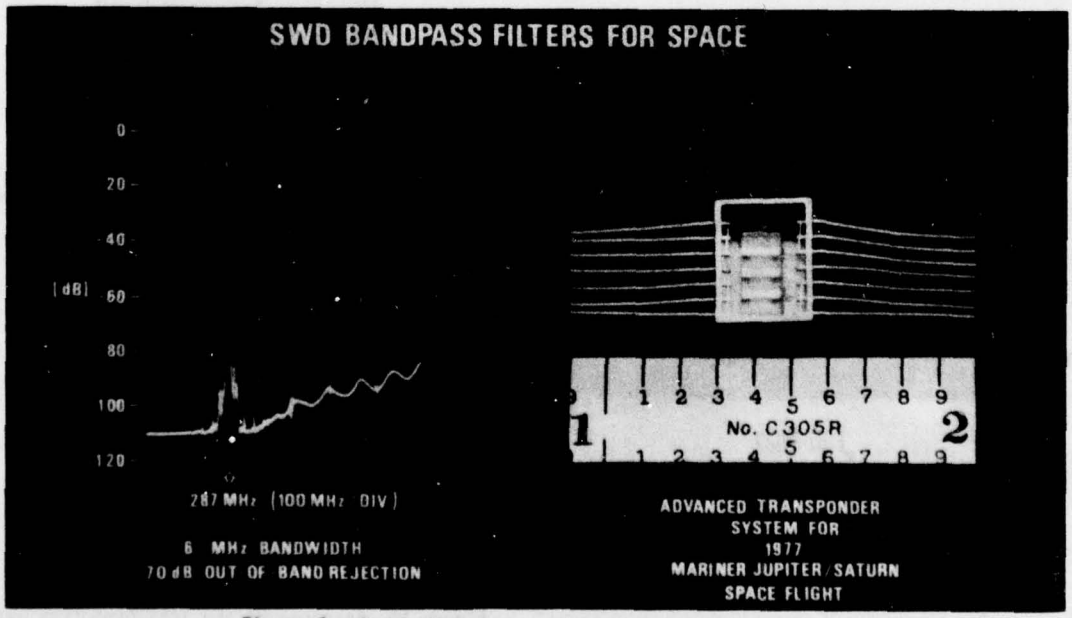

Figure 6. Rejection greater than 70 dB, from dc to 1.0 GHz, in a 287 MHz quartz filter for a communications application in space.

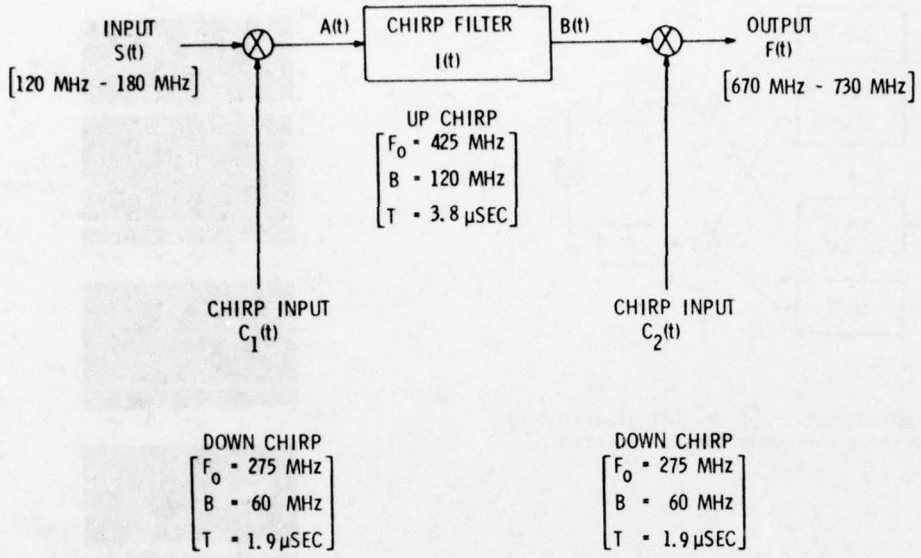

Figure 7. Implementation of a prototype chirp transform system.

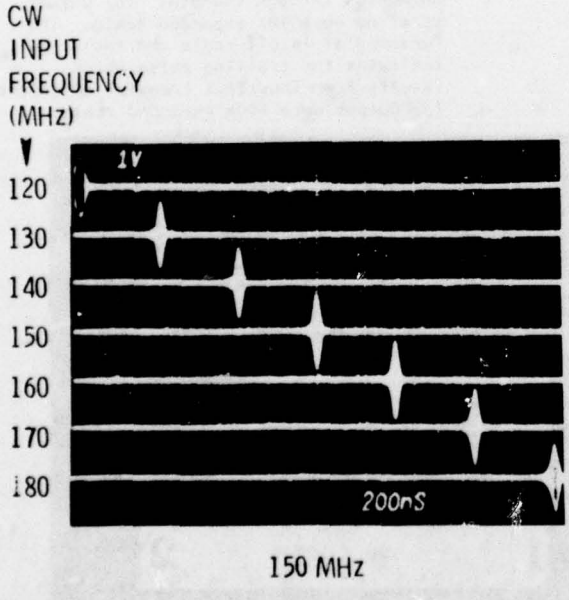

Figure 8. Prototype chirp transform of seven successive CW input signals.

800 nSEC PULSES AT 134 MHz and
200 nSEC PULSES AT 168 MHz

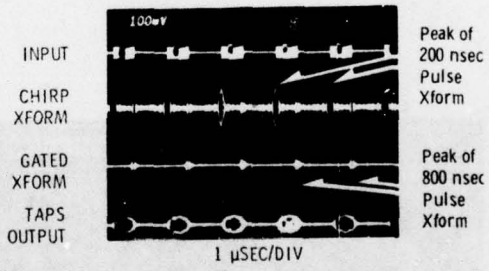

Figure 9. Response of the TAPS prototype system implementing a bandpass filter to pass the 0.8 µs pulses at 134 MHz.

800 nSEC PULSES AT 134 MHz and
200 nSEC PULSES AT 168 MHz

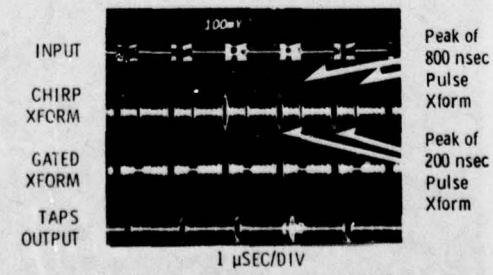

Figure 10. Response of the TAPS prototype system performing bandstop filtering to reject the 0.8 µs pulses at 134 MHz.

NEW TEMPERATURE COMPENSATED MATERIALS WITH HIGH PIEZOELECTRIC COUPLING

Paul H. Carr and 1Lt Robert M. O'Connell
Deputy for Electronic Technology (RADC/AFSC)
Hanscom AFB, Massachusetts 01731

Summary

The development of new materials with piezoelectric coupling greater than that of quartz will be discussed. A major milestone towards this goal has been the discovery of a physical model for explaining why known materials are temperature compensated. This model has been used to predict new temperature compensated materials. For bulk waves berlinite, $AlPO_4$, has been found to have temperature compensated cuts similar in orientation to the AT and BT cuts of quartz, but with electromechanical coupling coefficients 2.5 times as large. For surface waves, temperature compensated orientations have been calculated to have up to 4 times the electromechanical coupling of ST-cut quartz. Nepheline, $(KAlSiO_4)(NaAlSi_4)_3$, has positive temperature coefficients for c_{11} and c_{66}, which indicates that it should have temperature compensated orientations for both bulk and surface acoustic wave applications. Other promising materials will be identified.

Introduction

This paper will review the state-of-the-art of materials available for surface acoustic wave (SAW) devices. Large-bandwidth SAW devices are in general not small, lightweight, and energy conserving. This is due to the ovens or other energy consuming schemes which are required to compensate for the large temperature coefficient of lithium niobate. Narrow-band SAW devices have, on the other hand, achieved their potential for being small, lightweight, and passive devices due to the temperature-compensated ST-cut of quartz.

A major milestone towards discovering temperature compensated materials with piezoelectric coupling greater than that of quartz is a phenomenological model which explains why known materials are temperature compensated.[1] Temperature compensated solids have either one of the two anamolous properties: (1) a negative coefficient of thermal expansion or (2) a positive temperature coefficient of velocity or elastic constant. Quartz is temperature compensated because the temperature coefficient of c_{66} for shear propagation along the Z-axis is positive. The structures of alpha- and beta-quartz provide an understanding of this behavior. The alpha-quartz structure is a partially collapsed derivative of beta-quartz. Above room temperature, the SiO_2 tetrahedra rotate and distort towards the straighter beta-structure. The phenomenological model gives the following qualities of temperature compensated crystals: (1) an open lattice structure with associated bending moments, (2) the existence of structural phase transitions, and (3) low coordination number of major constituents.[1]

Berlinite

As expected on the basis of the theory, berlinite, $AlPO_4$, has been found to have temperature compensated cuts for bulk waves similar in orientation to the AT and BT cuts of quartz, but with electromechanical coupling coefficients 2.5 times as large.[2,3] Better quality crystals must be grown to determine if the acoustic Q of this material is comparable to that of quartz.[4] Both materials have a similar frequency per unit thickness.

In order to investigate the presence of temperature compensated cuts for surface acoustic waves in berlinite, a theoretical computer model[5] was used in conjunction with the data of refs 2,3 to calculate the surface acoustic wave velocity, electromechanical coupling coefficient ($\Delta V/V$), electromechanical power flow angle, and temperature coefficient of time delay (TCD) for several standard crystallographic cuts. The variation of these quantities, as the direction of propagation changes in the YZ plane, is shown for X-cut Berlinite in Figure 1, for example. The shapes of the curves are similar to those of X-cut quartz,[6] which is to be expected since the materials are so much alike. Note that for this cut there are two orientations which are temperature compensated. The corresponding values of surface wave velocity, electromechanical coupling, and power flow angle and its rate of change are shown for these and several other promising orientations in Table I. For comparison, the data for ST cut quartz is shown also. The most significant feature to be gleaned from Table I is that the electromechanical coupling of the temperature compensated cuts of berlinite is as much as 4 times as large as that of ST cut quartz.

Another noteworthy feature of Table I is provided by the Z-axis cylinder data. From this data and Figure 2 it is seen that as the Euler angle λ is varied from 0.0° to 11.2°, a trade-off is provided between an orientation having 1 PPM/$^\circ$C TCD with 0.0° power flow angle and a temperature compensated orientation having a 4.1° power flow angle.

Other Promising Substrates

As can be seen in Fig. 3 and Table II, lithium iodate has the highest piezoelectric coupling of any known substrate available for SAW[7]. The temperature coefficient of time delay for the Z-cut is only 7 parts per million. Other orientations are temperature compensated, but the piezoelectric coupling is much smaller. Lithium iodate has the disadvantage of being hygroscopic, which makes this material difficult to process for surface acoustic wave devices.

Weinert and Isaacs[8] have reported a temperature compensated orientation of Tl_3VS_4 with an electromechanical coupling factor, $k^2 = 3\%$. The velocity of this material was very slow, of the order of 900 m/sec, which is a disadvantage for high frequency filter applications but an advantage for long delay lines. The power flow or beam steering angle of about - 17 degrees is another disadvantage of this orientation. However, it may be possible to find orientations of this material with no beam steering, as was the case for Tl_3TaSe_4.[9]

By sputtering a silicon dioxide film on Y-cut, Z-propagating lithium tantalate, Parker and Schulz[10] have produced a temperature compensated composite. The temperature compensation is produced by the fact that the temperature coefficient of the silicon dioxide is opposite to that of the lithium tantalate. The thin film produces dispersion and loss, the former limiting the bandwidth of coded devices and the latter the time delay. The most exciting property of this composite is that the parabolic temperature coefficient of time delay is an order of magnitude less than it is for ST-quartz. This material should be important for SAW oscillator applications. It has the highest velocity of the materials in Table II, an advantage for producing high frequency devices when limited by the photolithographic resolution required to make the transducers. Nepheline, $(KAlSiO_4)(NaAlSiO_4)_3$, has positive tempera-

ture coefficients for c_{11} and c_{66}, which indicates that it should have temperature compensated orientations for both bulk and surface wave applications.[11]

Beta-eucryptite, $LiAlSiO_4$, is a promising silicate that has been grown at Pennsylvania State University.[2,12] This material is interesting because of its large negative thermal expansion in the direction of the hexagonal c-axis. This may give rise to temperature compensation even with negative values of the temperature coefficients of the elastic constants. $Pb_2KNb_5O_{15}$ has been found to have large electromechanical coupling factors of the order 0.7 and opposite signs for the temperature coefficients of the bulk wave resonance frequency for different vibrational modes. It therefore gives promise of being temperature compensated. However, it is difficult to grow large samples due to its tendency to crack upon cooling.[13]

Conclusions

Several years ago, the only temperature compensated material available for SAW devices was ST-cut quartz. In Table II are summarized four new temperature compensated materials which have become available with higher piezoelectric coupling than quartz. No one substrate is perfect for all devices, but these and other materials under development, such as $Pb_2KNb_5O_{15}$, increase the variety of choices for the device designer. They remove the requirement of an oven for broad-band, low insertion loss devices, for which ST-quartz is not adequate.

Needed now is a readily available supply of these materials to the device manufacturer. Berlinite is currently not available, but if it can be grown with suitable quality by the method already demonstrated by Stanley,[4] it may replace many quartz devices because of its higher piezoelectric coupling.

References

1. R.E. Newnham, "Elastic Properties of Oxides and the Search for Temperature Compensated Materials," AFCRL Report No. TR-73-0220, Contract No. F19628-73-C-0108 (March 1973).

2. G.R. Barsch and R.E. Newnham, "Piezoelectric Materials with Positive Elastic Constant Temperature Coefficients," AFCRL-TR-75-0163, Final Report, Contract No.F19628-73-C-0108 (April 1975).

3. Z.P. Chang and G.R. Barsch, IEEE Trans.Sonics & Ultrasonics SU-23, 127 (1976)

4. J.M. Stanley, Industrial and Engineering Chemistry, vol. 46, pp 1684-1689, (August 1954).

5. J.J. Campbell and W.R. Jones, IEEE Trans. Sonics & Ultrasonics SU-15, 209 (1968)

6. A.J. Slobodnik,Jr., "The Temperature Coefficients of Acoustic Surface Wave Velocity and Delay on Lithium Niobate, Lithium Tantalate, Quartz and Tellurium Oxide," USAF Cambridge Res.Labs.,Bedford, Mass., Rep. AFCRL-72-0092, 1971 (unpublished)

7. V.B. Jipson, J.F. Vetelino, A. Jhunjhunwala and J.C. Field, Proc. IEEE 64, 568 (1976)

8. R.W. Weinert and T.J. Isaacs, "Proceedings of the 29th Annual Symposium on Frequency Control, 1975," pp 139-142, (May 1975).

9. T.J. Isaacs and R.W. Weinert, Journal of Electronic Materials 5, 13 (1976).

10. T.E. Parker and M.B. Schulz, "Proceedings 1975 Ultrasonics Symposium," 261 (Sept 1975).

11. L.E. Bouczar and G.R. Barsch, J.Appl.Phys., 46, 4339 (1975).

12. L.E. Bouczar and G.R. Barsch, to be published.

13. W.B. Regnault, G.R. Barsch, and K.E. Spear, to be published.

TABLE I

TEMPERATURE COMPENSATED CUTS OF BERLINITE

MATERIAL	ORIENTATION	EULER ANGLES	$\frac{1}{f}\frac{\partial f}{\partial T}$ (PPM/°C)	$\Delta V/V_{SD}$	POWER FLOW ANGLE ϕ (DEGREES)	$\partial\phi/\partial\alpha^{\circ}$	SAW VELOCITY (M/SEC)
BERLINITE ($AlPO_4$)	X CUT $\theta = 22.6^{\circ}$ a)	90.0, 90.0, 22.6	0	0.00211	- 0.68	+ 0.366	2750
	X CUT $\theta = 168.7^{\circ}$	90.0, 90.0, 168.7	0	0.00222	- 11.3	+ 0.309	2926
	Y CUT $\theta = 0.0^{\circ}$ b)	0.0, 90.0, 0.0	0	0.00218	+ 5.6	+ 0.511	2761
	Z AXIS CYL. $\lambda = 11.2^{\circ}$ c)	11.2, 90.0, 0.0	0	0.00236	+ 4.1	+ 0.335	2739
	Z AXIS CYL. $\lambda = 0.0^{\circ}$	0.0, 90.0, 0.0	1	0.00225	0.0	+ 0.365	2736
QUARTZ (SiO_2)	ST CUT $\theta = 0.0^{\circ}$	0.0, 132.75, 0.0	0	0.00000	0.0	+ 0.378	3158

- $\frac{\partial\phi}{\partial\alpha}$ = RATE OF CHANGE OF POWER FLOW ANGLE WITH RESPECT TO VARIABLE EULER ANGLE
- a) θ = ANGLE BETWEEN Y AXIS AND DIRECTION OF PROPAGATION
- b) θ = ANGLE BETWEEN X AXIS AND DIRECTION OF PROPAGATION
- c) λ = DIRECTION OF PLATE NORMAL

TABLE II

COMPARISON OF VARIOUS TEMPERATURE COMPENSATED MATERIALS

MATERIAL	ORIENTATION	$\frac{1}{f}\frac{\partial f}{\partial T}$ (PPM/°C)	$\Delta V/V_{SD}$	POWER FLOW ANGLE ϕ (DEGREES)	$\partial\phi/\partial\alpha$	SAW VELOCITY (M/SEC)
$LiIO_3$	Z CUT	7	0.0434	0.0	0.0	2250
Ti_2VS_4	(110) CUT 70° PROP	0	~0.01	~ -17	-	~900
SiO_2 on $LiTaO_3$	Y CUT Z PROP	0	~0.007	0.0	-	3455
BERLINITE ($AlPO_4$)	X CUT 22.6° PROP	0	0.00211	- 0.68	+ 0.366	2750
QUARTZ (SiO_2)	ST CUT X PROP	0	0.00000	0.0	+ 0.378	3158

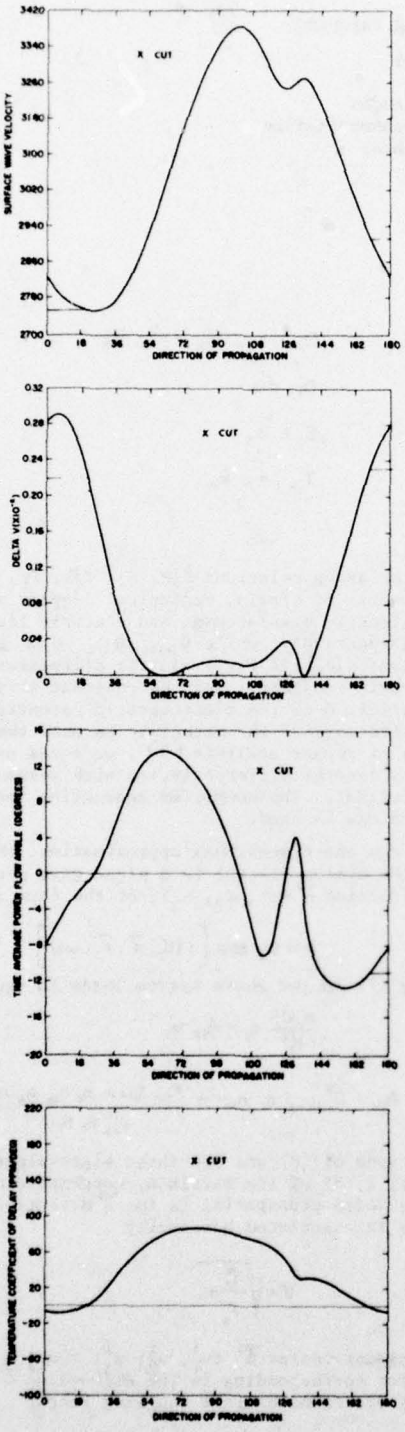

Figure 1. The variation of SAW velocity, piezoelectric coupling, power flow angle, and temperature coefficient of time delay for X-cut Berlinite as a function of the angle between the Y axis and the direction of propagation.

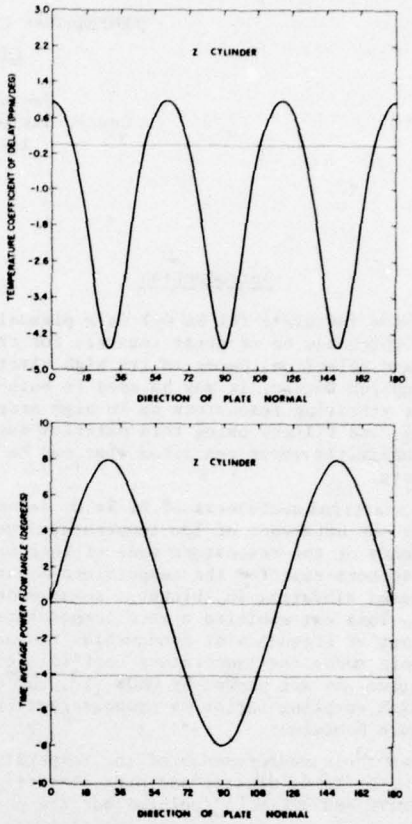

Figure 2. The variation of temperature coefficient of time delay and power flow angle for Z-axis cylinder Berlinite as a function of the direction of the plate normal.

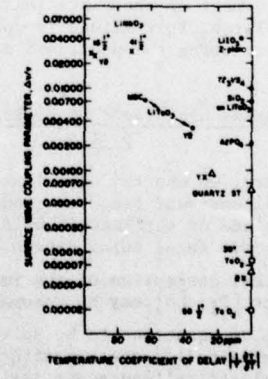

Figure 3. Temperature coefficient of time delay versus piezoelectric coupling for various SAW materials.

TEMPERATURE CHARACTERISTICS OF HIGH FREQUENCY LITHIUM TANTALATE PLATES

Jacques Détaint and René Lançon
Centre National d'Etudes des Télécommunications
Issy-les-Moulineaux (France)

Introduction

Lithium tantalate (Li Ta O_3) is a piezoelectric material which may be of great interest for frequency control and selection. Owing to its high electromechanical coupling factor, it may be used in bulk-wave thickness vibrating resonators up to high order of overtones, and filters using this material may have maximum bandwiths about ten times what can be reached with quartz.

The practical usefulness of Li Ta O_3 depends widely on the existence of low temperature-coefficient of frequency of the resonators made of this material. Several authors reported the temperature behaviour of X-cut plates vibrating in thickness shear modes [1], [2], [3]. This cut exhibits a zero temperature coefficient of frequency at fondamental resonance, but at harmonic modes the temperature coefficient is large and negative. As was shown by ONOE [4], the effect of the high coupling factor is preponderant in this temperature behaviour.

After their measurements of the temperature coefficientsof Li Ta O_3 elastic and piezoelectric constants, SMITH and WELSH [5] pointed out the possibility of existence of zero temperature coefficients cuts. WELSH also reported temperature coefficients of antiresonance frequencies of thickness shear modes in rotated Y-cuts [6].

In contrast with what is done for quartz where the study of antiresonance is sufficient, in highly piezoelectric materials, resonances and antiresonances exhibit quite different behaviours.

We present a method of calculation of the first order temperature coefficients of resonance and antiresonance frequencies at any harmonic, which uses the general treatment of the vibrations of thin piezoelectric plates. This method is applied to lithium tantalate using the published data for this material [5].

Thickness vibrations of piezoelectric plates

In this work, we use the classical model of infinite, one-dimensional resonator consisting in a piezoelectric plate of thickness h with unweighty electrodes, the two faces being stress free.

The classical derivation of the impedance formula *of the resonator* [7], [8] may be resumed as follows :

The system of equations to be solved includes the definition of strain (1), the constitutive equations (2), (3), the electrical equations (4), (5) and the stress equation of motion (6).

$$S_{jk} = \frac{1}{2}(u_{j,k} + u_{k,j}) \tag{1}$$

$$T_{jk} = C^E_{jklm}\, S_{lm} - e_{ijk}\, E_i \tag{2}$$

$$D_i = e_{ijk}\, S_{jk} + \epsilon^S_{im}\, E_m \tag{3}$$

$$D_{i,i} = 0 \tag{4}$$

$$E_i = -\phi_{,i} \tag{5}$$

$$T_{jk,j} = \rho\, \ddot{u}_k \tag{6}$$

In the above relations Sjk, Uj, Tjk, D_1, E_1 are the components of strain, mechanical displacement, stress, electric displacement and electric field tensors respectively, while C_{jklm}, e_{ijk}, ϵ_{lm} are the constant electric field elastic stifnesses, the piezoelectric constants, and the constant strain permitivities. ϕ is the electrostatic potential and ρ the specific mass of the material. We used the usual notations of tensor analysis [9] : an index preceded by a comma denotes differentiation with respect to the space coordinate. The summation convention for repeated tensor indices is used.

For the one-dimensional approximation, the solution of the system (1)-(6) is a plane wave propagating in the direction $\vec{n}$ (n_1, n_2, n_3), of the form :

$$\Psi = \Psi_o \exp\left[i\,(K\,.\,\vec{n}\,.\,\vec{r} - \omega t)\right] \tag{7}$$

Reporting (7) in the above system leads to equation :

$$\frac{\rho\,\omega^2}{K^2}\, u_j = A_{jk}\, u_k \tag{8}$$

where :

$$A_{jk} = C^E_{jlkm}\, n_l\, n_m + \frac{e_{pjl}\, e_{qkm}\, n_l\, n_m\, n_p\, n_q}{\epsilon^S_{rs}\, n_r\, n_s} \tag{9}$$

The solutions of (8) are the three eigenvalues $\bar{C}^i$ (i = 1, 2, 3) of the matrix A, corresponding to the three modes propagating in the $\vec{n}$ direction. To each mode is associated a velocity

$$V^i = \sqrt{\frac{\bar{C}^i}{\rho}} \tag{10}$$

a displacement vector $\vec{u}^i$ (u^i_1, u^i_2, u^i_3) which is the eigenvector corresponding to the eigenvalue $\bar{C}^i$, and an effective electromechanical coupling factor

$$k^i = \sqrt{\frac{(e_{jkl}\, n_j\, n_k\, u^i_l)^2}{\bar{C}^i\, \epsilon^S_{pq}\, n_p\, n_q}} \tag{11}$$

With electrical and mechanical boundary conditions on the two faces, one obtains the impedance formula of the resonator :

$$Z(\omega) = \frac{1}{i C_o \omega}\left[1 - \sum_{i=1}^{3} k^{i2}\,\frac{tg\,\theta^i}{\theta^i}\right] \qquad (12)$$

where : $\theta^i = \frac{\omega h}{2V^i}$ $(\omega = 2\pi f)$. $C_o = \frac{\varepsilon S}{h}$ (13), (14)

is the static capacitance of an area S of plate,

$$\varepsilon = \varepsilon^s_{kl}\, n_k n_l \qquad (15)$$

is the dielectric permittivity in the $\vec{n}$ direction. The poles of $Z(\omega)$ give the antiresonance frequencies associated with each mode :

$$F^i_{An} = \frac{n V^i}{2h} \qquad (n \text{ odd}) \qquad (16)$$

while the resonance frequencies are the roots F_r of :

$$1 - \sum_{i=1}^{3} k^{i2}\,\frac{tg\,\theta^i}{\theta^i} = 0 \qquad (17)$$

Classification of the modes :

The modes propagating in the direction $\vec{n}$ may be separated in three groups A, B, C according to their velocities so as to have :

$$V_A > V_B > V_C \qquad (18)$$

Mode A is the thickness-quasi-extension and modes B and C are thickness-quasi-shear. The antiresonance frequencies at a given harmonic follow the same order :

$$f_{aA} > f_{aB} > f_{aC} \qquad (19)$$

By convention the resonance frequencies are also separated in three groups in such a way that a resonance frequency of a group is the root of (17) immediately lower than the antiresonance of the same group. Such a classification is the easiest to use in computer programs but will produce some discontinuities in the following curves when the velocities of two modes become equal. For instance, a classification based on the continuity of displacement vector $\vec{u}$ gives much more complexity in computation.

Derivation of the temperature coefficients

The dependence of a function X which temperature T may be expressed by a polynomial expansion :

$$X(T) = X(T_o)\left[1 + \sum_{1}^{\infty} T_X^{(n)}\,(T - T_o)^n\right] \qquad (20)$$

where

$$T_X^{(n)} = \frac{1}{n!\,X(T_o)}\left(\frac{\partial^n X}{\partial T^n}\right) \qquad (21)$$

is the n^{th} order temperature coefficient. In the present work we limit the expansion to the first order, the temperature coefficient being, when ΔT is small :

$$T_X = \frac{1}{X(T_o)}\,\frac{X(T_o + \Delta T) - X(T_o)}{\Delta T} \qquad (22)$$

If the material constants and their first order temperature coefficients are known, the above derivation of $\bar{c}^i$, k^i, F_a and F_r may be performed for a reference temperature T_o and for a temperature $T_o + \Delta T$. The temperature coefficients of frequency are then deduced in the following manner.

Antiresonance frequencies temperature coefficients (A.F.T.C.)

From relations (10) and (16) the A.F.T.C. of a mode i is :

$$T_{F^i_a} = \frac{1}{2}\,T_{\bar{c}^i} - \frac{1}{2}\,T_\rho - T_h \qquad (23)$$

This coefficient is independant of the order n of the harmonic. $T_{\bar{c}^i}$ is computed from definition (22). The other terms of relation (23) are calculated from the coefficients of thermal expansion α_{ij} :

$$T_\rho = -\alpha_{ii} \qquad (24)$$

$$T_h = n_i n_j \alpha_{ij} \qquad (25)$$

Resonance frequencies temperature coefficients (RFTC)

An explicit formula for RFTC was given by ONOE in the single mode approximation [4] :

$$T_{Fr} = T_{Fa} - T_k\left(\frac{2k^2}{\theta_r^2 + k^2(k^2-1)}\right) \qquad (26)$$

where T_{Fr} , T_{Fa} , T_k , are the temperature coefficients of resonance, antiresonance and coupling factor, and θr the solution of the single mode equation :

$$1 - k^2\,\frac{tg(\theta)}{\theta} = 0 \qquad (27)$$

This approximation is valid for the resonances of the longitudinal mode and when only one transverse mode is excited, as in the rotated Y-cuts of Li Ta O_3, but in an arbitrary direction, specially when the velocities of the transverse modes are nearly equal, this approximation no more holds.

The method used here permits a rigourous calculation of RFTC. The resonance frequencies are computed from equation (17) for T_o and $T_o + \Delta T$ up to a given harmonic and the RFTC are deduced from :

$$T_{F_r} = \frac{1}{F_r(T_o)}\,\frac{F_r(T_o + \Delta T) - F_r(T_o)}{\Delta T} \qquad (28)$$

Calculated results

The method descriebed above was applied to lithium tantalate. We used the material constants and their first order temperature coefficients published by SMITH and WELSH [5], except for the value of e_{33} that we set equal to 1.9 C/m^2, value published by WARNER et al. [10] and closer from our experimental measurements.

The direction of the normal to the plate is defined by two angles φ and θ as shown in fig. 1. The results are presented in two forms : (1) plots in rectangular diagrams with θ as abscissa and φ as parameter, (2) altitude charts in polar diagrams. Electromechanical coupling factors for the three modes are represented in fig. 2 to 6, antiresonance frequencies temperature coefficients in fig. 7 to 11, and resonance frequencies temperature coefficients for the fundamental modes in fig. 12 to 16. Similar curves of RFTC may be obtained for harmonic modes but above the third harmonic they become practicaly the same as the AFTC.Fig. 17 shows the AFTC of the non piezoelectric transverse mode and the AFTC and RFTC of the piezoelectric transverse mode of rotated Y-cuts. Curves of AFTC are similar to that published by WELSH [6].

Fig. 18, where coupling factor, AFTC and RFTC for fundamental, third and fifth harmonic for plate rotated around the Y axis, shows clearly the influence of piezoelectric effect on the temperature behaviour.

Fig. 13 shows that the mode B exhibits two lines with zero temperature coefficient of resonance frequency. The first is the well-known X-cut family. The X-cut has a parabolic frequency temperature curve

with a minimum at ~ 10° C [1]. By lightly rotating the plate one can obtain a zero temperature coefficient at 20° C. The other line runs near the Y axis ($\varphi \simeq 90°$) with negative θ angles. This zero temperature line also exists for antiresonance frequency as was shown in fig. 8 .

Experimental results

To verify our calculations, we choose a cut on the second zero coefficient line of mode B. To facilitate the orientation process, the cut was chosen in the vicinity of the lattice plane $[0\,1.\,\bar{2}]$ which is a Y-cut rotated of an angle - 32°56' around X axis. The zero temperature cut is obtained by performing a second rotation around Z' axis of a little angle α (fig. 19). The fig. 20 shows for these YX lw/- 32° 56'/ α cuts (the orientation of the plates are given according to the IRE standards [11]), the coupling factor and the temperature coefficients of antiresonance and resonance of fundamental, 3rd and 5th overtones. The first experimental cut corresponds to an angle α of about 5°, which on the polar diagram of fig. 15, corresponds to $\varphi = 84°$, $\theta = -32° 47'$.

The resonator was a circular plate of diameter 7 mm and thickness 0.3 mm with gold electrodes of diameter 1.2 mm. This resonator exhibits strong resonances on modes A and C which, as expected, have large and negative temperature coefficient of frequency. The mode B is lightly excited with a measured coupling factor of 5 %, while the calculated k for plane waves is 15 %. Nevertheless this mode has good temperature behaviour on harmonic resonances, as shown in fig. 21 where the 5th and 7th overtone frequency temperature curves are reported. They have both zero temperature coefficients, with a turn-over point at 20° C for the 5th overtone and - 5° C for the 7th overtone. The second order temperature coefficient of frequency is about 60 10^{-9} / $(°\,C)^2$.

The second experimental cut (YX lw /-32°56'/8°) has an angle α lighly higher. The resonator prepared from this cut has a coupling factor of 17 % and exhibits strong resonances on the mode B even at high order overtones. For instance, fig. 22 shows the response curve of a mode B, 7th overtone (43,9 MHz) resonance. The measured Q is 40000. In fig. 23 we reported the temperature characteristics of 5th, 7th and 11th overtones. The curves have turn-over points at about 110° C and the second order coefficient is 85. 10^{-9} / $(°\,C)^2$.

We have not explored all the possible orientations for zero temperature coefficient cuts but from our results one can say that cuts chosen in the vicinity of our experimental cuts would exhibit good characteristics, both in coupling factor and temperature coefficient on overtones.

Some light discrepancies between calculated and measured results was observed. One probable reason is that our theoretical model uses plane waves while the experimental resonators uses trapped energy modes which have different behaviours in piezoelectric efficiency and in temperature characteristics. An other reason comes from the fact that crystals may have different characteristics according to their growing conditions. For instance, during a systematical investigation, made in collaboration with the crystal growth laboratory of C.N.E.T., of lithium tantalate crystals of various relative compositions in lithium and tantalum, we observed some variations in elastic and piezoelectric properties [12]. As an example, fig. 24 shows the variation of elastic stiffness C_{33} of plates cut from ingots whose compositions were determined from Curie temperature measurements.

Conclusion

We have discriebed a method of calculation of the first order temperature coefficient of frequency of infinite thin plates of piezoelectric crystals with arbitrary coupling factor, for any orientation and at any harmonic. This method, applied to lithium tantalate shows that some cuts vibrating in thickness mode exhibit zero temperature coefficients even at high order overtone where the resonators have still good quality factors. Experimental results confirm our calculations, and a good compromise between the value of the coupling factor and the location of the minimum of frequency temperature curve may be found. This method may be easily extended to higher order temperature coefficients. Nevertheless the theoretical results must be used carefully because the model does not account for energy trapping and because crystals of different sources may exhibit different behaviours.

Acknowledgments : We thank M. PASSARET, R. COQUILLE and N. NOLF of crystal growth laboratory, C.N.E.T., Lannion, for supplying crystals and R. DUMONT, R. CHENEBAULT and D. SERVAJEAN of our laboratory for the preparation of the samples.

References

1. A.W. WARNER, A.A. BALLMAN, Low temperature coefficient of frequency in a lithium tantalate plate. Proc. IEEE, 55, 450 (1967).

2. T.R. SLIKER, D.J. KONEVAL, Frequency temperature behavior of X-cut lithium tantalate resonators, Proc. IEEE, 56, 1402 (1968)

3. M. ONOE, T. ASHIDA, K. SAWAMOTO, Zero temperature coefficient of resonant frequency in a X-cut lithium tantalate at room temperature, Proc. IEEE, 57, 1446 (1969).

4. M. ONOE, Relationship between temperature behavior of resonant frequencies and electromechanical coupling factors of piezoelectric resonators, Proc. IEEE, 57, 702 (1969).

5. R.T. SMITH, F. S. WELSH, Temperature dependance of the elastic, piezoelectric, and dielectric constants of lithium tantalate and lithium niobate, J. Appl. Phys., 42, 2219 (1971).

6. F.S. WELSH, Surface wave temperature coefficients on lithium tantalate, IEEE Trans. Sonics Ultras., SU-18, 108 (1971).

7. H.F. TIERSTEN, Thickness vibrations of piezoelectric plates, J. Acoust. Soc. Am., 35, 53 (1963).

8. A. GLOWINSKI, Vibrations d'épaisseur des lames piézoélectriques, Annales Télécomm., 27, 147 (1972).

9. J.F. NYE, Physical properties of crystals, Clarendon Press, Oxford (1957).

10. A.W. WARNER, M. ONOE, G.A. COQUIN, Determination of elastic and piezoelectric constants for crystals in class (3m), J. Acoust. Soc. Am., 42, 1223 (1967).

11. IRE Standards on piezoelectric crystals, 1949, Proc. IRE, 37, 1378 (1949).

12. To be published.

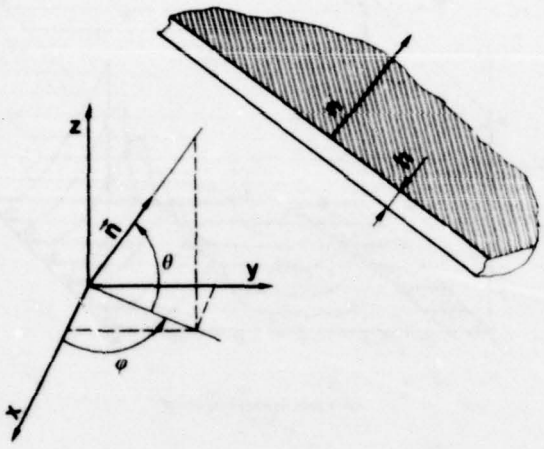

Figure 1

PLATE ORIENTATION

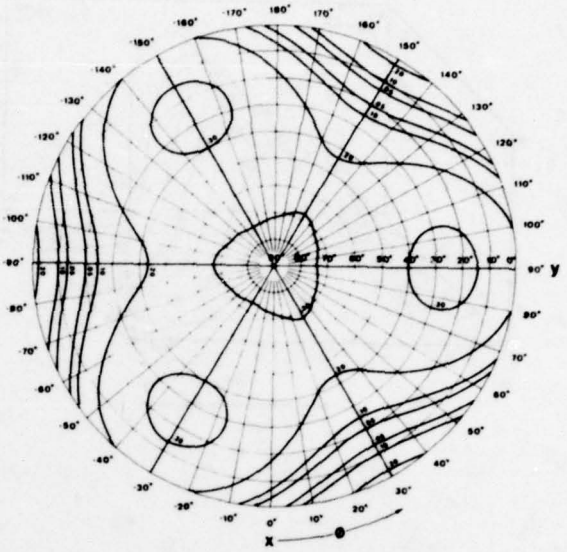

Figure 2

COUPLING COEFFICIENT
(Mode A)

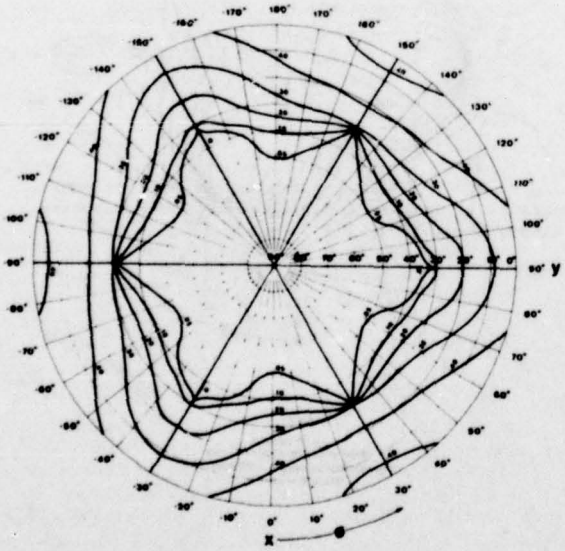

Figure 3

COUPLING COEFFICIENT
(Mode S)

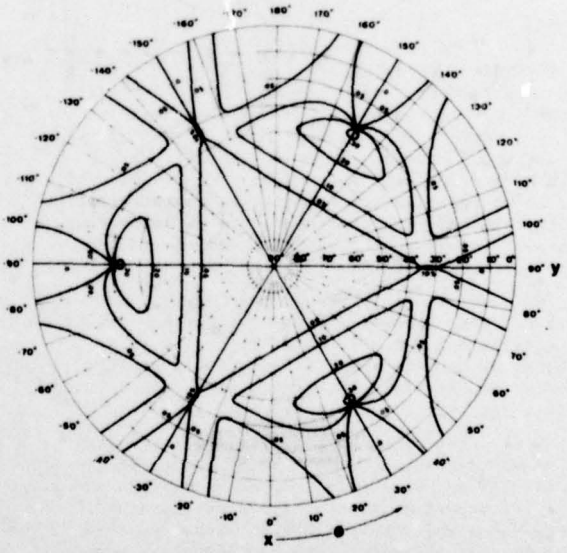

Figure 4

COUPLING COEFFICIENT
(Mode C)

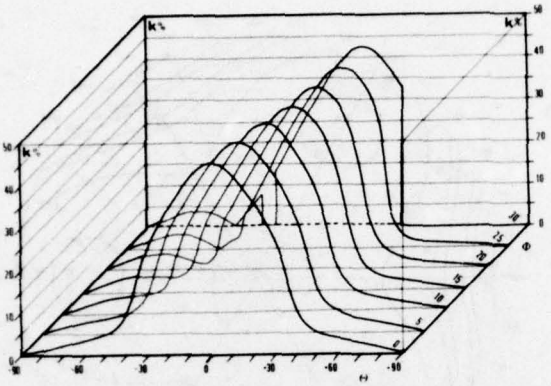

Figure 5. COUPLING COEFFICIENT (Mode B)

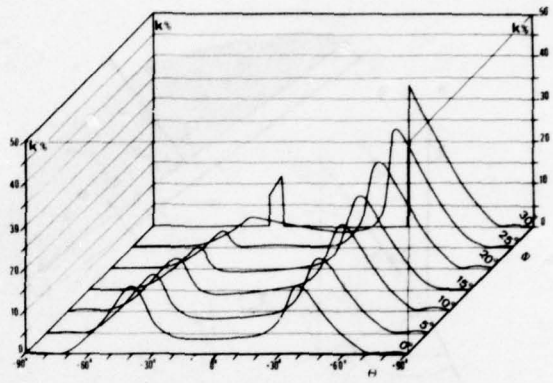

Figure 6. COUPLING COEFFICIENT (Mode C)

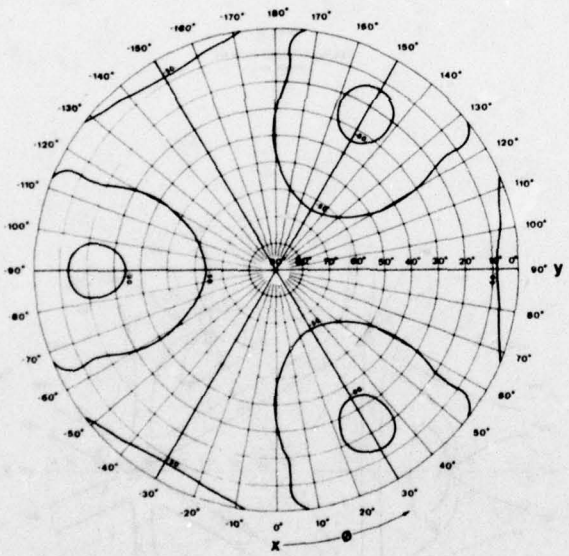

Figure 7

FIRST ORDER
TEMPERATURE COEFFICIENT
OF ANTIRESONANCE FREQUENCY
(Mode A – ppm $^{\circ}C^{-1}$)

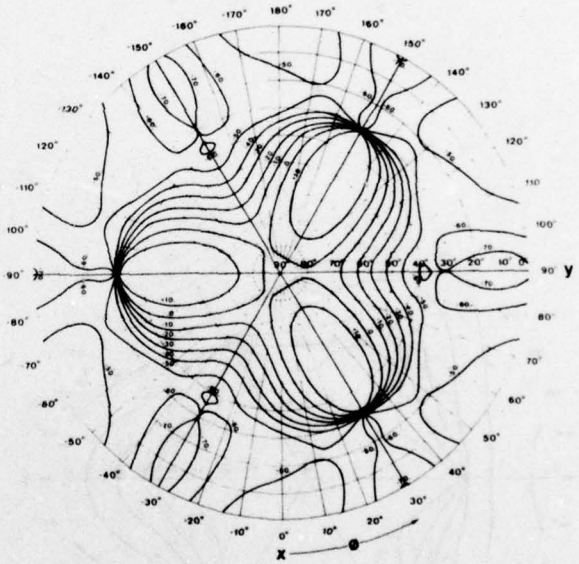

Figure 8

FIRST ORDER
TEMPERATURE COEFFICIENT
OF ANTIRESONANCE FREQUENCY
(Mode B – ppm $^{\circ}C^{-1}$)

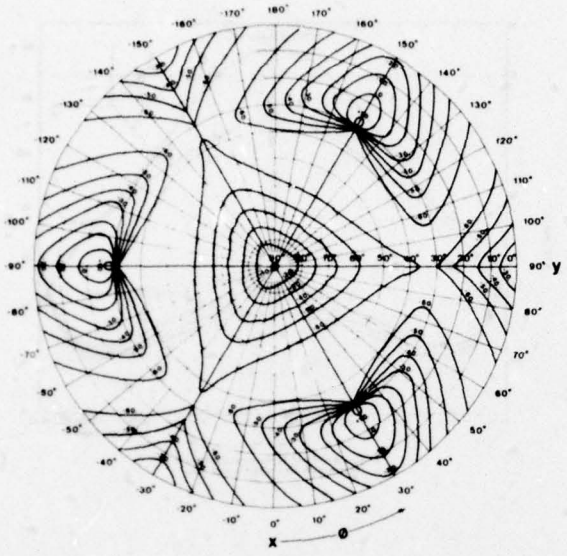

Figure 9

FIRST ORDER
TEMPERATURE COEFFICIENT
OF ANTIRESONANCE FREQUENCY
(Mode C – ppm.°C⁻¹)

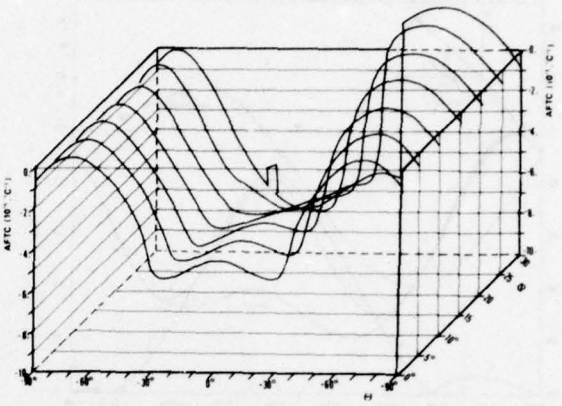

Figure 10. A.F.T.C. Mode B.

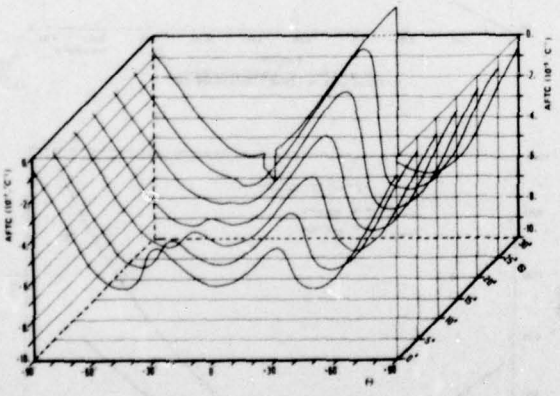

Figure 11. A.F.T.C. Mode C

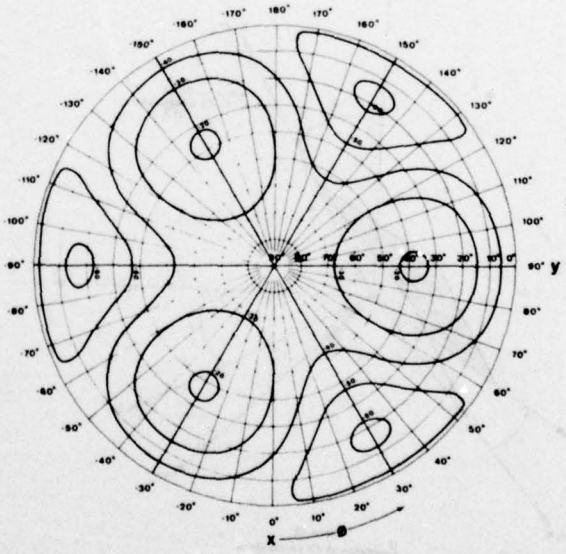

Figure 12

FIRST ORDER
TEMPERATURE COEFFICIENT
OF RESONANCE FREQUENCY
(mode A – ppm.°C⁻¹)

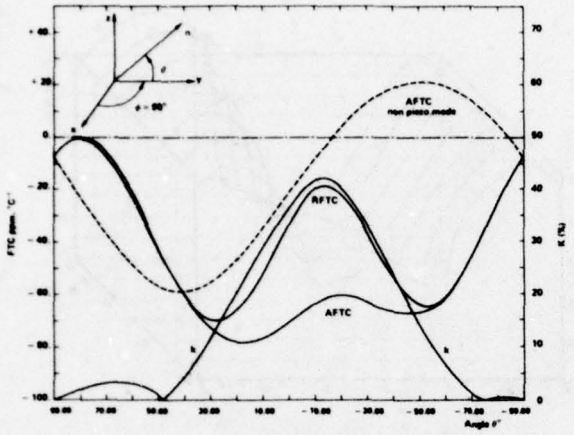

Figure 17
RFTC of the transverse piezo-mode and AFTC of both transverse modes of the γ rotated cuts. (no account was taken of previous mode conversion)

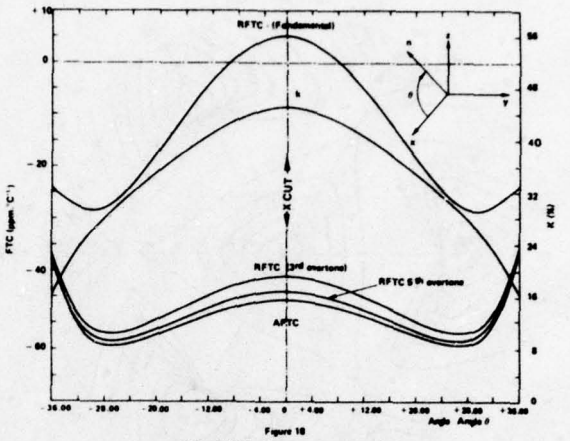

Figure 18
AFTC and RFTC of Fundamental and harmonics of B mode in plate rotated around Y axis

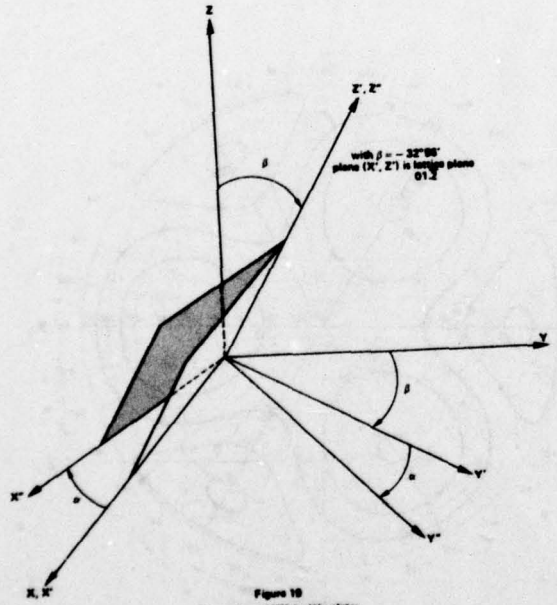

Figure 19
Orientation of YX t(α/β/α plates

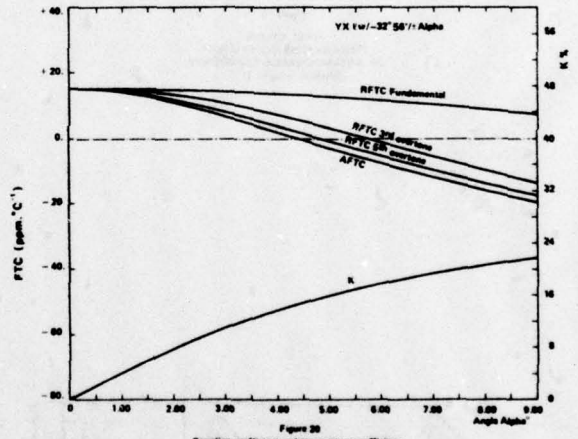

Figure 20
Coupling coefficient and temperature coefficient of B mode on YX t(α/−32°56'/+ Alpha rotated cuts

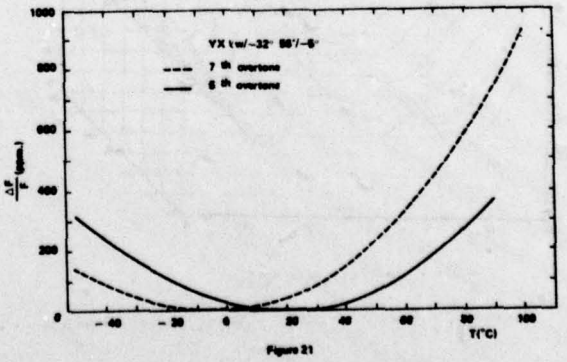

Figure 21
Experimental temperature behaviour of the resonance Frequency (5 th and 7 th overtone) of YX t(α/−32°56'/−6° plates

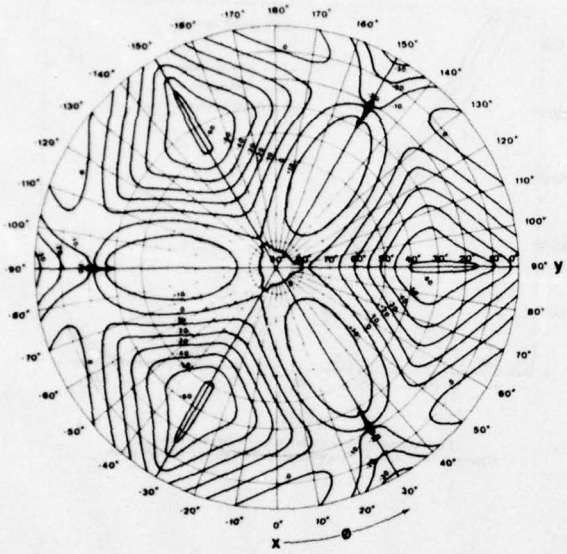

Figure 13

FIRST ORDER
TEMPERATURE COEFFICIENT
OF RESONANCE FREQUENCY
(Mode B – ppm.°C⁻¹)

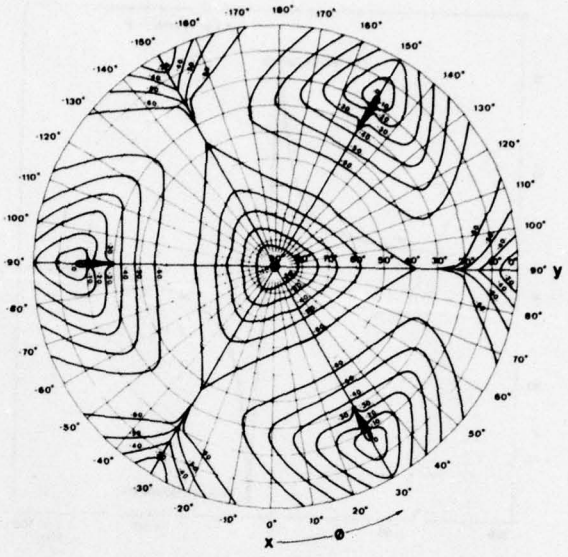

Figure 14

FIRST ORDER
TEMPERATURE COEFFICIENT
OF RESONANCE FREQUENCY
(Mode C – ppm.°C⁻¹)

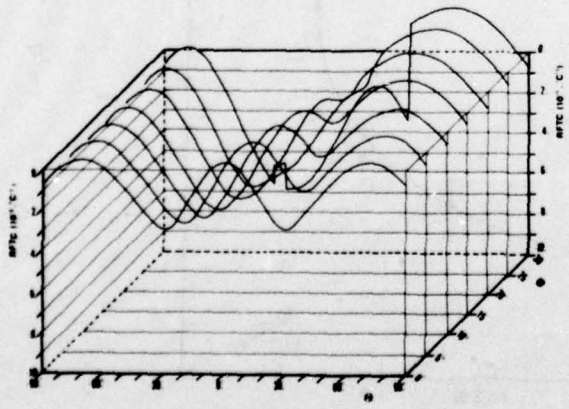

Figure 15. R.F.T.C. Mode B

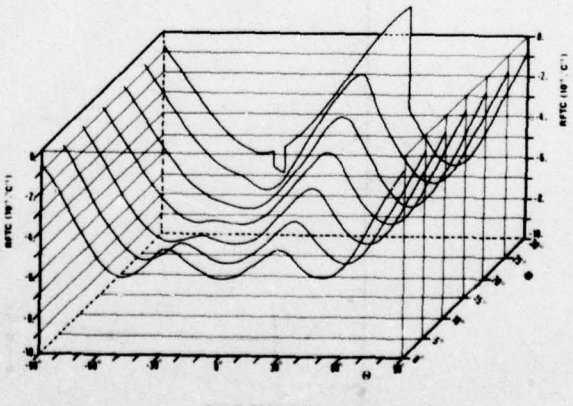

Figure 16. R.F.T.C. Mode C

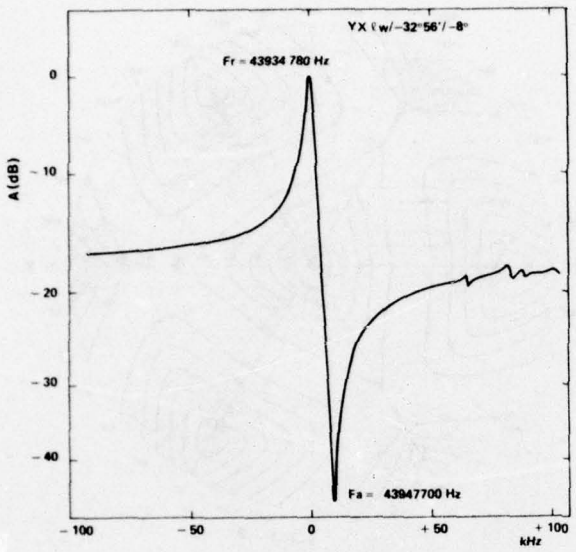

Figure 22
7th overtone of B mode
(YX l w/−32°56'/−8° cut, plate thickness 300 μm)

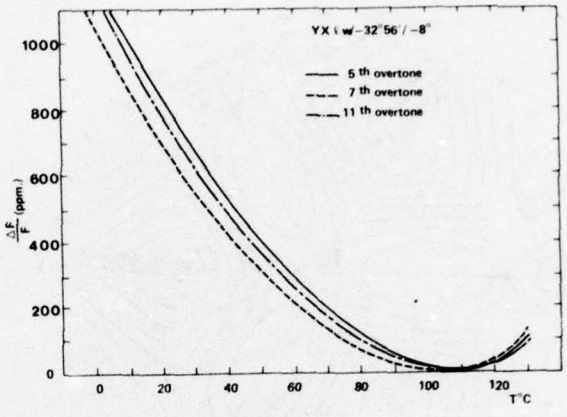

Figure 23
Expérimental temperature behaviour of the resonance
Frequency (5 th, 7 th, 11 th overtones) of YX l w/−32°56'/−8° plates

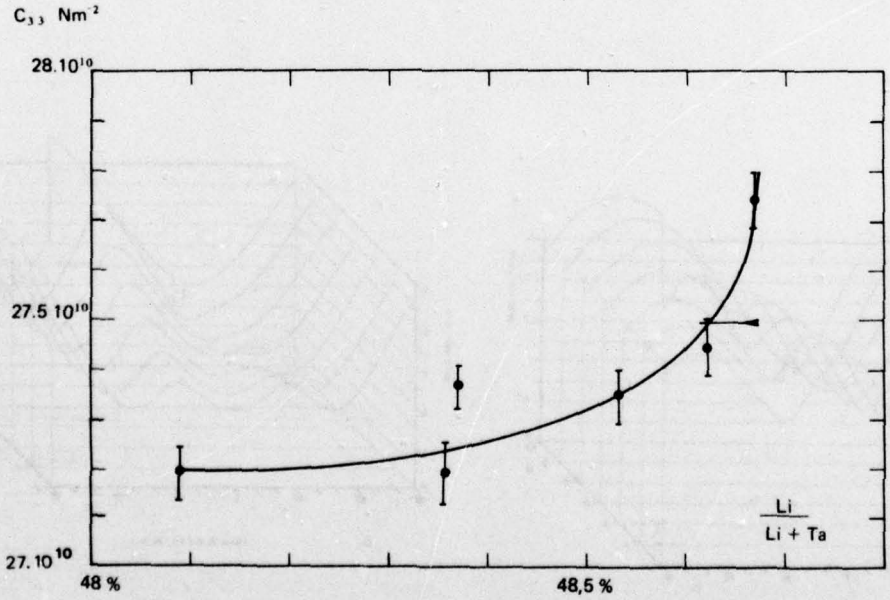

Figure 24
Variations of C_{33} according to the stoichiometry of lithium tantalate

THE ANGULAR DEPENDENCE OF PIEZOELECTRIC PLATE FREQUENCIES AND THEIR TEMPERATURE COEFFICIENTS

A. Ballato and G. J. Iafrate
US Army Electronics Technology & Devices Laboratory (ECOM)
Fort Monmouth, New Jersey 07703

Summary

Doubly rotated plate vibrators of quartz are known to possess a locus of zero first order temperature coefficient of frequency for all values of the azimuthal angle. Along this locus a number of cuts (V, FC, IT, SC/TS, RT) have been used for particular purposes but, by and large, past applications have been relatively few. Consequently, little in the way of detailed information has been published regarding the general properties of arbitrary cuts on the locus.

In this paper we consider the problem of plane wave propagation in doubly rotated piezoelectric crystals and compute the quantities of importance, such as frequency, coupling factor and their temperature coefficients, as function of orientation for plates along the zero temperature coefficient locus in quartz. Included are graphs of the angle gradients of these quantities from which the orientation sensitivities may be obtained.

The results are applied to misorientation corrections also. For example, it is shown that rotated-Y-cuts are unaffected to first order by misorientations in azimuth angle, and the second-order corrections are determined.

Although we concentrate on quartz applications because of their immediate interest, the methods we use are valid in general and may be applied to any crystal for which the material constants are known, such as aluminum phosphate and lithium tantalate. A series of graphs present typical frequency constant, coupling and temperature coefficient calculations for aluminum phosphate.

Introduction

Precision frequency control requirements for digital communication and position location systems, currently undergoing development, make it imperative that crystal resonator performance be improved in a number of aspects. These include both static and transient frequency-temperature behavior, as well as shock and acceleration insensitivity.[1-4]

It appears certain that singly rotated quartz resonators of the AT- and BT-cut variety are intrinsically incapable of achieving the necessary tolerances, while a strong possibility exists that several of the effects requiring improvement may be brought well within tolerance simultaneously by the expedient of using more general quartz cuts.

Both singly and doubly rotated plates are shown in Figure 1 in relation to the crystallographic axes X, Y, Z. The singly rotated cut is described in IEEE notation[5] as $(YX\ell)\theta$, the doubly rotated as $(YX\omega\ell)\varphi/\theta$. Also shown in Figure 1 is the bulk wave zero temperature coefficient locus for quartz. The most promising region is that branch of the locus for $\theta > 0$, and this is where we will concentrate our attention in this paper.

Work on doubly rotated quartz cuts began shortly after the discovery of the AT- and BT-cuts, with the work of Bokovoy and Baldwin on V-cuts.[6-9] In 1951 the IT-cut was introduced;[10-11] the entire locus was then explored by Bechmann, et al.,[12-14] in the early 1960's.

Additional cuts have been described in the intervening years up to the present,[15-24] and in view of this and because of the stringent resonator requirements mentioned,[1-4] it is particularly appropriate at this time to tie together a number of these past results and to examine more closely some of the physical and electrical properties of doubly rotated cuts along the zero temperature coefficient locus for thickness modes. Included are graphs of the derivatives with respect to φ and to θ of most of the quantities of interest.

Our considerations here will be confined to the upper branch of the locus, but it would be a mistake to assume that interest in doubly rotated cuts is limited to the thickness mode zero temperature coefficient locus or that it is limited to quartz. The LC-cut[16-18] is a doubly rotated thickness mode quartz cut having extremely linear frequency-temperature behavior rather than a zero temperature coefficient.

For surface acoustic wave (SAW) applications, the ST-cut of quartz[25-27] (a singly rotated cut, $(YX\ell) + 42.5^{\circ}$) is the quasi-Rayleigh wave counterpart of the AT-cut ($(YX\ell) + 35.25^{\circ}$). Both have wave propagation along the X-axis; the AT-cut has particle motion along X exclusively, while the SAW motion is compounded of X and Y^1 displacements. In doubly rotated cuts the analogous SAW mode propagates along X^1, and the locus of zero temperature coefficient of delay may be traced in angle space, starting from the ST-cut at $\varphi = 0^{\circ}$, along a path approximating the bulk wave locus. Thus the bulk wave locus suggests angular regions for future SAW research. Of course, SAW's have an additional degree of freedom, viz., the angle ψ that describes the direction of propagation in the plane of the plate with respect to the X^1 axis, so that the zero coefficient locus consists of a surface in φ, θ, ψ space. Other considerations, such as coupling factor and power flow angle, will determine the relative importance of these more general cuts. Insensitivity to certain nonlinear effects (to be discussed below for bulk waves) appears a tempting possibility, for quartz and for other substances such as aluminum phosphate.

In a fashion similar to the SAW situation, it happens that contour modes of plates and discs exhibit temperature behavior closely akin to thickness modes. The DT-cut is the counterpart of the AT-cut, as the CT-cut is of the BT-cut. For doubly rotated contour mode vibrators[8,9] the locus of Figure 1 is again close to the locus of zero temperature coefficient and may be used as a first approximation.

In succeeding sections we give brief discussions of plane wave propagation in piezoelectric crystals, piezoelectric plate frequencies, static temperature behavior, angle sensitivities, symmetry axes, and applications to quartz and berlinite.

Plane Wave Propagation

The plate problem may be solved in either of two ways. One either transforms the elastic, piezoelectric, and dielectric constants to a coordinate system one of whose axes is along the plate thickness, or one works in the crystallographic system, describing the plate normal by direction cosines α_{xi}.

In this latter method, which we adopt, one forms

$$\Gamma_{ik}^{E} = c_{ijkl}^{E}\, \alpha_{2l}\, \alpha_{2j} \quad , \tag{1}$$

$$\Xi_i = e_{ij}\, \alpha_{2n}\, \alpha_{2j} \quad , \text{ and} \tag{2}$$

$$\epsilon_{22}^{S'} = \epsilon_{jn}^{S}\, \alpha_{2n}\, \alpha_{2j} \quad . \tag{3}$$

Then, using the piezoelectrically stiffened values

$$\bar{\Gamma}_{ik} = \Gamma_{ik}^{E} + \Xi_i\, \Xi_k / \epsilon_{22}^{S'} , \tag{4}$$

the eigenvalue equation

$$0 = \left(\bar{\Gamma}_{ik} - \bar{c}\, \delta_{ik} \right) \bar{\gamma}_k \tag{5}$$

is solved. This results in three roots $\bar{c}_m$ and corresponding eigenvectors $\bar{\gamma}_{mk}$. The roots are ordered according to the relations

$$\bar{c}_a > \bar{c}_b > \bar{c}_c \tag{6}$$

The effective piezoelectric constant for mode m is

$$e_m = \Xi_i\, \bar{\gamma}_{mi} \quad , \tag{7}$$

and the corresponding coupling factor is

$$k_m = e_m / \sqrt{\epsilon_{22}^{S'} \bar{c}_m} \quad . \tag{8}$$

One may include the phenomenological effects of small loss by incorporating the effects of viscosity, considering it as the imaginary part of the elastic stiffness:[28,29]

$$c_{ijkl}^{*} = c_{ijkl}^{E} + j\omega \eta_{ijkl} . \tag{9}$$

This leads to a complex eigenvalue equation, which can be avoided by realizing that for quartz at room temperature $\eta / \bar{c}$ is typically 10^{-14} seconds, so that to an excellent approximation one may simply form

$$H_{ik} = \eta_{ijkl}\, \alpha_{2l}\, \alpha_{2j} \quad , \tag{10}$$

and compute the effective viscosity for mode m using the lossless eigenvectors:

$$\eta_m = H_{ik}\, \bar{\gamma}_{mi}\, \bar{\gamma}_{mk} \quad . \tag{11}$$

Piezoelectric Plate Frequencies

The traction-free piezoelectric plate problem was solved exactly for thickness modes by Tiersten.[30] When the electrodes are open-circuited, the three thickness modes are uncoupled. The resulting antiresonance frequencies form three harmonically-related sequences.

$$f_A^{(m)} \text{ (mode } m) = M \cdot \sqrt{\bar{c}_m / \rho} / 4h \quad . \tag{12}$$

Corresponding to these frequencies are the three frequency constants

$$N_m = 2h \cdot f_A^{(1)} \text{ (mode } m) = \tfrac{1}{2} \cdot \sqrt{\bar{c}_m / \rho} \quad . \tag{13}$$

The short circuit resonance frequencies, $f_R^{(m)}$ (mode m), are found from

$$\sum_m k_m^2 \, \tan x_m / x_m = 1 , \tag{14}$$

where

$$x_m = h\omega / 2 N_m = \frac{\pi}{2} \left(f_R^{(m)} / f_A^{(1)} \right) , \tag{15}$$

and where k_m is given by (8). It is important to note that the proper coupling factor driving each mode, k_m, could only be known after the plate problem had been correctly solved.[30] That it turned out to be easily calculable from quantities that appear when only the infinite medium is considered is a fortunate after-the-fact happenstance.

For the AT-cut, two of the k_m vanish, and the piezoelectric coupling between the modes, seen in (14), disappears; with doubly rotated plates all three k_m will generally be present. However, if the k_m are not large, and the frequency constants N_m are sufficiently well separated, then the resonance frequencies may be approximated by applying the uncoupled equation

$$\tan x = x / k^2 \tag{16}$$

to each mode separately.

Shifting the position of the immittance circle operating point by the introduction of a load capacitor C_L in series with the crystal is treated by modifying the three k_m values:

$$(k_m^2)' = k_m^2 / \left(1 + C_o / C_L \right) , \tag{17}$$

where

$$C_o = \epsilon_{22}^{S'} A_e / 2h , \tag{18}$$

and A_e is the effective electrode area.

Static Frequency-Temperature Behavior

The first order temperature coefficient of any quantity is defined as the logarithmic derivative of that quantity with respect to temperature. Applying this definition to (12) gives

$$T_{f_{A(m)}} = -T_h - \tfrac{1}{2} T_\rho + \tfrac{1}{2} T_{\bar{c}_m} . \tag{19}$$

The temperature coefficients of density and of plate thickness are expressible in terms of the thermal expansion constants,[31] while $T_{\bar{c}_m}$ is obtained by differentiating the cubic resulting from (5):

$$\bar{c}^3 - A\bar{c}^2 + B\bar{c} - C = 0 . \tag{20}$$

In (20),

$$A = (\bar{\Gamma}_{11} + \bar{\Gamma}_{22} + \bar{\Gamma}_{33}) , \tag{21}$$

$$B = (\bar{\Gamma}_{22}\bar{\Gamma}_{33} + \bar{\Gamma}_{33}\bar{\Gamma}_{11} + \bar{\Gamma}_{11}\bar{\Gamma}_{22} - \bar{\Gamma}_{23}^2 - \bar{\Gamma}_{13}^2 - \bar{\Gamma}_{12}^2) , \tag{22}$$

$$C = (\bar{\Gamma}_{11}\bar{\Gamma}_{22}\bar{\Gamma}_{33} + 2\bar{\Gamma}_{23}\bar{\Gamma}_{13}\bar{\Gamma}_{12} - \bar{\Gamma}_{11}\bar{\Gamma}_{23}^2 - \bar{\Gamma}_{22}\bar{\Gamma}_{13}^2 - \bar{\Gamma}_{33}\bar{\Gamma}_{12}^2) . \tag{23}$$

The differentation yields $T_{\bar{\kappa}_m}$ as

$$T_{\bar{\kappa}_m} = \frac{(\bar{\kappa}_m^2 \frac{dA}{dT} - \bar{\kappa}_m \frac{dB}{dT} + \frac{dC}{dT})}{\bar{\kappa}_m (3\bar{\kappa}_m^2 - 2A\bar{\kappa}_m + B)} \quad , (24)$$

where

$$\frac{dA}{dT} = \left(\frac{d\bar{\Gamma}_{11}}{dT} + \frac{d\bar{\Gamma}_{22}}{dT} + \frac{d\bar{\Gamma}_{33}}{dT} \right) \quad , (25)$$

$$\frac{dB}{dT} = \left((\bar{\Gamma}_{22}+\bar{\Gamma}_{33}) \frac{d\bar{\Gamma}_{11}}{dT} + (\bar{\Gamma}_{33}+\bar{\Gamma}_{11}) \frac{d\bar{\Gamma}_{22}}{dT} + (\bar{\Gamma}_{11}+\bar{\Gamma}_{22}) \frac{d\bar{\Gamma}_{33}}{dT} \right.$$
$$\left. - 2\bar{\Gamma}_{23} \frac{d\bar{\Gamma}_{23}}{dT} - 2\bar{\Gamma}_{13} \frac{d\bar{\Gamma}_{13}}{dT} - 2\bar{\Gamma}_{12} \frac{d\bar{\Gamma}_{12}}{dT} \right) \quad , (26)$$

$$\frac{dC}{dT} = \left((\bar{\Gamma}_{22}\bar{\Gamma}_{33} - \bar{\Gamma}_{23}^2) \frac{d\bar{\Gamma}_{11}}{dT} + (\bar{\Gamma}_{33}\bar{\Gamma}_{11} - \bar{\Gamma}_{13}^2) \frac{d\bar{\Gamma}_{22}}{dT} \right.$$
$$+ (\bar{\Gamma}_{11}\bar{\Gamma}_{22} - \bar{\Gamma}_{12}^2) \frac{d\bar{\Gamma}_{33}}{dT} - 2(\bar{\Gamma}_{11}\bar{\Gamma}_{23} - \bar{\Gamma}_{13}\bar{\Gamma}_{12}) \frac{d\bar{\Gamma}_{23}}{dT}$$
$$\left. - 2(\bar{\Gamma}_{22}\bar{\Gamma}_{13} - \bar{\Gamma}_{23}\bar{\Gamma}_{12}) \frac{d\bar{\Gamma}_{13}}{dT} - 2(\bar{\Gamma}_{33}\bar{\Gamma}_{12} - \bar{\Gamma}_{23}\bar{\Gamma}_{13}) \frac{d\bar{\Gamma}_{12}}{dT} \right) . \quad (27)$$

In order to determine the temperature coefficient of the resonance frequency, $T_{f_{R(m)}}$, the differentiation must be applied to (14), or it may be determined by numerical methods.[32] For low coupling materials, where the frequency constants are adequately separated almost everywhere, as with quartz, it is sufficient to make the single mode approximation. It was shown by Onoe[33] that the difference between T_{f_R} and T_{f_A} is proportional to the temperature coefficient of the coupling when only a single mode is considered:

$$T_{f_R} - T_{f_A} = T_k = -G_o \cdot T_k \quad . (28)$$

It has also been shown that the presence of electrode mass-loading is an additional influence on the temperature coefficient difference.[31,34]

A series load capacitance C_L shifts the point of zero reactance from the resonance frequency f_R to a load frequency f_L; C_L also alters the temperature coefficient of the crystal:

$$T_{f_R} - T_{f_L} \cong -\alpha \cdot G_o \cdot T_k \quad , (29)$$

where $\alpha = C_o / (C_o + C_L)$. The capacitance ratio

$$n = C_o / C_1 \quad (30)$$

is proportional to k^{-2}, and G_o in first approximation is

$$G_o \cong 1/n \quad , (31)$$

so (29) may be written as

$$T_{f_R} - T_{f_L} \cong \frac{\alpha}{2n} \cdot T_n \quad . (32)$$

A more accurate expression, including the effects of mass loading[31] is

$$T_{f_R} - T_{f_L} \cong \frac{\alpha}{2n} \left\{ (1+2\mu) \left(T_n \right. \right.$$
$$\left. \left. + (1-\alpha)(T_{C_L} - T_{C_o}) \right) + 2\mu \cdot T_\mu \right\} \quad . (33)$$

The presence of C_L in series with the crystal is equivalent to operation of the crystal at a place on its immittance circle between f_R and f_A.

Angle Gradients

Resonator frequency-temperature behavior is usually expressed as a Taylor series in temperature difference from a reference temperature,[35] and variations in orientation angle θ are treated in like manner. While frequency-temperature behavior for quartz is rather well known, at least near the zero coefficient locus, the angle gradients are not very well known. With anticipated demand for doubly rotated cuts on the zero coefficient locus, it is important to know the values of the angle gradients of the quantities of interest such as N_m, k_m, and $T_{f(m)}$, since these will determine the angle specifications necessary for holding the pertinent quantities in tolerance.

We will present graphs below showing the behavior of the angle derivatives of interest along the zero temperature coefficient locus. In the next section we discuss the case of what happens near $\varphi = 0°$.

Symmetry Axis

In quartz, X_1 is a digonal axis of symmetry. For $\phi = 0°$, X_1 passes through the plane of the plate. As a consequence of this

$$c_{25}^E,\ c_{26}^E,\ c_{35}^E,\ c_{36}^E,\ c_{45}^E, \text{ and } c_{46}^E$$

vanish; also vanishing are

$$e_{22},\ e_{23},\ e_{24},\ e_{32},\ e_{33}, \text{ and } e_{34},$$

with the consequent results that the desired mode (the slow shear mode) is a pure mode and that most of the important quantities have a zero ϕ derivative, so that departures in ϕ are manifested only in second order.

For the doubly rotated plate of Figure 1 the α_{2m} are

$$\alpha_{21} = -\sin\phi \cos\theta \quad (34)$$

$$\alpha_{22} = +\cos\phi \cos\theta \quad (35)$$

$$\alpha_{23} = +\sin\theta \quad (36)$$

For $\phi = 0°$, the Γ^E are

$$\Gamma_{11}^E = c_{66}^E \cos^2\theta + c_{55}^E \sin^2\theta + 2c_{56}^E \cos\theta \sin\theta \quad (37)$$

$$\Gamma_{22}^E = c_{22}^E \cos^2\theta + c_{44}^E \sin^2\theta + 2c_{24}^E \cos\theta \sin\theta \quad (38)$$

$$\Gamma_{33}^E = c_{44}^E \cos^2\theta + c_{33}^E \sin^2\theta + 2c_{34}^E \cos\theta \sin\theta \quad (39)$$

$$\Gamma_{23}^E = c_{24}^E \cos^2\theta + c_{34}^E \sin^2\theta + (c_{23}^E + c_{44}^E) \cos\theta \sin\theta \quad (40)$$

$$\Gamma_{13}^E = c_{46}^E \cos^2\theta + c_{35}^E \sin^2\theta + (c_{45}^E + c_{36}^E) \cos\theta \sin\theta \quad (41)$$

$$\Gamma_{12}^E = c_{26}^E \cos^2\theta + c_{45}^E \sin^2\theta + (c_{46}^E + c_{25}^E) \cos\theta \sin\theta \quad (42)$$

For $\phi = 0^\circ$, the Ξ are

$$\Xi_1 = e_{26}\cos^2\theta + e_{35}\sin^2\theta + (e_{25}+e_{36})\cos\theta\sin\theta \quad (43)$$

$$\Xi_2 = e_{22}\cos^2\theta + e_{34}\sin^2\theta + (e_{24}+e_{32})\cos\theta\sin\theta \quad (44)$$

$$\Xi_3 = e_{24}\cos^2\theta + e_{33}\sin^2\theta + (e_{23}+e_{34})\cos\theta\sin\theta. \quad (45)$$

For $\phi = 0^\circ$, ϵ is

$$\epsilon'_{22} = \epsilon'_{22}\cos^2\theta + \epsilon'_{33}\sin^2\theta + 2\epsilon'_{23}\cos\theta\sin\theta. \quad (46)$$

The derivatives $d/d\phi$, for $\phi = 0^\circ$, are

$$\frac{d\Gamma''_{11}}{d\phi} = -\mathcal{C}^E_{15}\sin 2\theta - 2\mathcal{C}^E_{14}\cos^2\theta \quad (47)$$

$$\frac{d\Gamma^E_{22}}{d\phi} = -\mathcal{C}^E_{46}\sin 2\theta - 2\mathcal{C}^E_{26}\cos^2\theta \quad (48)$$

$$\frac{d\Gamma^E_{33}}{d\phi} = -\mathcal{C}^E_{35}\sin 2\theta - 2\mathcal{C}^E_{45}\cos^2\theta \quad (49)$$

$$\frac{d\Gamma^E_{23}}{d\phi} = -\tfrac{1}{2}(\mathcal{C}^E_{45}+\mathcal{C}^E_{36})\sin 2\theta - (\mathcal{C}^E_{46}+\mathcal{C}^E_{25})\cos^2\theta \quad (50)$$

$$\frac{d\Gamma^E_{13}}{d\phi} = -\tfrac{1}{2}(\mathcal{C}^E_{13}+\mathcal{C}^E_{55})\sin 2\theta - (\mathcal{C}^E_{56}+\mathcal{C}^E_{14})\cos^2\theta \quad (51)$$

$$\frac{d\Gamma^E_{12}}{d\phi} = -\tfrac{1}{2}(\mathcal{C}^E_{56}+\mathcal{C}^E_{14})\sin 2\theta - (\mathcal{C}^E_{12}+\mathcal{C}^E_{66})\cos^2\theta \quad (52)$$

$$\frac{d\Xi_1}{d\phi} = -\tfrac{1}{2}(e_{31}+e_{15})\sin 2\theta - (e_{16}+e_{21})\cos^2\theta \quad (53)$$

$$\frac{d\Xi_2}{d\phi} = -\tfrac{1}{2}(e_{36}+e_{14})\sin 2\theta - (e_{12}+e_{26})\cos^2\theta \quad (54)$$

$$\frac{d\Xi_3}{d\phi} = -\tfrac{1}{2}(e_{35}+e_{13})\sin 2\theta - (e_{14}+e_{25})\cos^2\theta \quad (55)$$

$$\frac{d\epsilon'_{22}}{d\phi} = -\epsilon'_{13}\sin 2\theta - 2\epsilon'_{12}\cos^2\theta. \quad (56)$$

The second derivatives $d^2/d\phi^2$ are, for $\phi = 0^\circ$

$$\frac{d^2\Gamma''_{11}}{d\phi^2} = 2(\mathcal{C}^E_{11}-\mathcal{C}^E_{66})\cos^2\theta - \mathcal{C}^E_{61}\sin 2\theta \quad (57)$$

$$\frac{d^2\Gamma^E_{22}}{d\phi^2} = 2(\mathcal{C}^E_{44}-\mathcal{C}^E_{22})\cos^2\theta - \mathcal{C}^E_{24}\sin 2\theta \quad (58)$$

$$\frac{d^2\Gamma^E_{33}}{d\phi^2} = 2(\mathcal{C}^E_{55}-\mathcal{C}^E_{44})\cos^2\theta - \mathcal{C}^E_{34}\sin 2\theta \quad (59)$$

$$\frac{d^2\Gamma^E_{23}}{d\phi^2} = 2(\mathcal{C}^E_{56}-\mathcal{C}^E_{24})\cos^2\theta - \tfrac{1}{2}(\mathcal{C}^E_{23}+\mathcal{C}^E_{44})\sin 2\theta \quad (60)$$

$$\frac{d^2\Gamma^E_{13}}{d\phi^2} = 2(\mathcal{C}^E_{15}-\mathcal{C}^E_{46})\cos^2\theta - \tfrac{1}{2}(\mathcal{C}^E_{45}+\mathcal{C}^E_{36})\sin 2\theta \quad (61)$$

$$\frac{d^2\Gamma^E_{12}}{d\phi^2} = 2(\mathcal{C}^E_{16}-\mathcal{C}^E_{26})\cos^2\theta - \tfrac{1}{2}(\mathcal{C}^E_{46}+\mathcal{C}^E_{25})\sin 2\theta \quad (62)$$

$$\frac{d^2\Xi_1}{d\phi^2} = 2(e_{11}-e_{26})\cos^2\theta - \tfrac{1}{2}(e_{25}+e_{36})\sin 2\theta \quad (63)$$

$$\frac{d^2\Xi_2}{d\phi^2} = 2(e_{16}-e_{22})\cos^2\theta - \tfrac{1}{2}(e_{24}+e_{32})\sin 2\theta \quad (64)$$

$$\frac{d^2\Xi_3}{d\phi^2} = 2(e_{15}-e_{24})\cos^2\theta - \tfrac{1}{2}(e_{23}+e_{34})\sin 2\theta \quad (65)$$

$$\frac{d^2\epsilon'_{22}}{d\phi^2} = 2(\epsilon'_{11}-\epsilon'_{22})\cos^2\theta - \epsilon'_{23}\sin 2\theta. \quad (66)$$

For class 32 (quartz), these reduce to

$$\Gamma''_{11} = \mathcal{C}^E_{66}\cos^2\theta + \mathcal{C}^E_{44}\sin^2\theta + 2\mathcal{C}^E_{14}\cos\theta\sin\theta \quad (67)$$

$$\Gamma^E_{22} = \mathcal{C}^E_{11}\cos^2\theta + \mathcal{C}^E_{44}\sin^2\theta - 2\mathcal{C}^E_{14}\cos\theta\sin\theta \quad (68)$$

$$\Gamma^E_{33} = \mathcal{C}^E_{44}\cos^2\theta + \mathcal{C}^E_{33}\sin^2\theta \quad (69)$$

$$\Gamma^E_{23} = -\mathcal{C}^E_{14}\cos^2\theta + (\mathcal{C}^E_{13}+\mathcal{C}^E_{44})\cos\theta\sin\theta \quad (70)$$

$$\Gamma^E_{13} = 0 \quad (71)$$

$$\Gamma^E_{12} = 0 \quad (72)$$

$$\Xi_1 = -e_{11}\cos^2\theta - e_{14}\cos\theta\sin\theta \quad (73)$$

$$\Xi_2 = 0 \quad (74)$$

$$\Xi_3 = 0 \quad (75)$$

$$\epsilon'_{22} = \epsilon'_{11}\cos^2\theta + \epsilon'_{33}\sin^2\theta \quad (76)$$

$$\frac{d\Gamma''_{11}}{d\phi} = 0 \quad (77)$$

$$\frac{d\Gamma^E_{22}}{d\phi} = 0 \quad (78)$$

$$\frac{d\Gamma^E_{23}}{d\phi} = 0 \quad (79)$$

$$\frac{d\Gamma_{23}^E}{d\phi} = 0 \tag{80}$$

$$\frac{d\Gamma_{13}^E}{d\phi} = -\tfrac{1}{2}(c_{13}^E + c_{44}^E)\sin 2\theta - (2c_{14}^E)\cos^2\theta \tag{81}$$

$$\frac{d\Gamma_{12}^E}{d\phi} = -\tfrac{1}{2}(2c_{14}^E)\sin 2\theta - (c_{12}^E + c_{66}^E)\cos^2\theta \tag{82}$$

$$\frac{d\Xi_1}{d\phi} = 0 \tag{83}$$

$$\frac{d\Xi_2}{d\phi} = -\tfrac{1}{2} e_{14}\sin 2\theta + 2e_{11}\cos^2\theta \tag{84}$$

$$\frac{d\Xi_3}{d\phi} = 0 \tag{85}$$

$$\frac{d\epsilon_{22}^S}{d\phi} = 0 \tag{86}$$

$$\frac{d^2\Gamma_{11}^E}{d\phi^2} = 2(c_{11}^E - c_{66}^E)\cos^2\theta - c_{14}^E \sin 2\theta \tag{87}$$

$$\frac{d^2\Gamma_{22}^E}{d\phi^2} = 2(c_{66}^E - c_{11}^E)\cos^2\theta + c_{14}^E \sin 2\theta \tag{88}$$

$$\frac{d^2\Gamma_{33}^E}{d\phi^2} = 0 \tag{89}$$

$$\frac{d^2\Gamma_{23}^E}{d\phi^2} = 4c_{14}^E\cos^2\theta - \tfrac{1}{2}(c_{13}^E + c_{44}^E)\sin 2\theta \tag{90}$$

$$\frac{d^2\Gamma_{13}^E}{d\phi^2} = 0 \tag{91}$$

$$\frac{d^2\Gamma_{12}^E}{d\phi^2} = 0 \tag{92}$$

$$\frac{d^2\Xi_1}{d\phi^2} = 4e_{11}\cos^2\theta + \tfrac{1}{2} e_{14}\sin 2\theta \tag{93}$$

$$\frac{d^2\Xi_2}{d\phi^2} = 0 \tag{94}$$

$$\frac{d^2\Xi_3}{d\phi^2} = 0 \tag{95}$$

$$\frac{d^2\epsilon_{22}^S}{d\phi^2} = 0 \,. \tag{96}$$

Starting from (20) and differentiating twice with respect to ϕ leads to the required relations for the ϕ gradients in terms of Γ^E, Ξ and ϵ^S plus their derivatives. In like manner the θ gradients are obtained. These are quite lengthy but straightforward to obtain and are omitted here.

Power Series in Two Variables

Small variations in both φ and θ are treated by using a Taylor series in two variables. Using the temperature coefficient of frequency as an example:

$$T_f(\varphi+\Delta\varphi, \theta+\Delta\theta) = T_f(\varphi,\theta) + (\Delta\varphi\cdot\partial/\partial\varphi + \Delta\theta\cdot\partial/\partial\theta)\cdot T_f(\varphi,\theta) + \ldots + (\Delta\varphi\cdot\partial/\partial\varphi + \Delta\theta\cdot\partial/\partial\theta)^n\cdot T_f(\varphi,\theta)/n! + \cdots \,. \tag{97}$$

Retaining terms up to second order in angular differences gives

$$T_f(\varphi+\Delta\varphi, \theta+\Delta\theta) - T_f(\varphi,\theta) = \Delta T_f = (\partial T_f/\partial\varphi)\cdot\Delta\varphi + (\partial T_f/\partial\theta)\cdot\Delta\theta + \tfrac{1}{2}(\partial^2 T_f/\partial\varphi^2)\cdot\Delta\varphi^2 + \tfrac{1}{2}(\partial^2 T_f/\partial\theta^2)\cdot\Delta\theta^2 + (\partial^2 T_f/\partial\varphi\partial\theta)\cdot\Delta\varphi\Delta\theta \,. \tag{98}$$

The rotated-Y-cuts of quartz, containing the digonal axis X_1, have

$$\partial T_f/\partial\varphi = \partial^2 T_f/\partial\varphi\partial\theta \equiv 0 \,. \tag{99}$$

When the angular derivatives of (19) are evaluated, using (67) to (96) and the temperature derivatives of (67) to (96), the following values are found for the AT-cut with $\theta = +35.25^\circ$:

$$\partial T_f/\partial\theta = -5.08 \times 10^{-6}/K,{}^\circ\theta \tag{100}$$

$$\partial^2 T_f/\partial\theta^2 = +0.96 \times 10^{-9}/K,(^\circ\theta)^2 \tag{101}$$

$$\partial^2 T_f/\partial\varphi^2 = -17.99 \times 10^{-9}/K,(^\circ\varphi)^2 \,. \tag{102}$$

The magnitudes in (99) - (102) permit (98) to be approximated by the simple expression

$$\Delta T_f \simeq (-5.1\times10^{-6}/K,{}^\circ\theta)\cdot\Delta\theta + (-9.0\times10^{-9}/K,(^\circ\varphi)^2)\cdot\Delta\varphi^2 \,, \tag{103}$$

so that, for constant ΔT_f, a parabola describes the resulting curve. Setting ΔT_f equal to zero yields the curve of Figure 2, which describes the locus of constant first order temperature coefficient. For any other constant value of ΔT_f, the parabola is simply shifted up or down along the $\Delta\theta$ axis. This figure permits determination of the tradeoff between φ and θ necessary to preserve a required value of T_f.

Calculations on the Quartz Locus

The loci shown in Figure 1 trace the paths of zero temperature coefficient for the two quasi-shear modes in quartz. Our attention is directed in this paper to the upper ($\theta > 0$) branch of the c-mode locus, but it is instructive to see the overall structures of the temperature coefficient surfaces in angle space. Figures 3 and 4 are provided for this purpose. Figure 3 shows the c-mode locus, including the position of the AT-cut at $\phi = 0^\circ$, and the IT-cut at $\phi = 19.1^\circ$, both on the upper branch. Figure 4 shows the b-mode branch, with the position of the BT-cut at $\phi = 0^\circ$ indicated.

The upper c-mode locus is adequately described by a straight line with equation

$$\theta^\circ = +35.25^\circ - 11\cdot\varphi^\circ/180. \tag{104}$$

We use the elastic, piezoelectric and dielectric constants of Bechmann,[36] and the temperature coefficients of these quantities given in Bechmann, et al.;[14] use of more recent values[37] does not change the results perceptibly.

In the following series of graphs for quartz, the relation (104) has been used to define θ corresponding to the ϕ values appearing on the abscissas.

A. Frequency Constant.

Figure 5 shows the quasi-extensional a-mode frequency constant Na; Nb and Nc are given in Figure 6. Modes b and c are separated by 11% at $\phi = 0^\circ$; the separation decreases with increasing ϕ, becoming 10% at $\phi = 21.9^\circ$ (the SC-cut), and 7% at $\phi = 30^\circ$.

For all three modes the angle gradients $\partial\mathcal{N}/\partial\varphi$ are given in Figure 7; all three vanish for $\phi = 0^{\circ}$. Figure 8 shows the gradients $\partial\mathcal{N}/\partial\theta$. In the vicinity of the SC-cut the value of $\partial\mathcal{N}/\partial\varphi$ is about six times the AT-cut value of $\partial\mathcal{N}/\partial\theta$.

B. Piezoelectric Coupling.

Piezoelectric coupling factor $|k|$ is given in Figure 9; near the SC-cut both thickness quasi-shear modes have nearly equal coupling. The derivative $\partial|k|/\partial\phi$ is given in Figure 10. For the AT-cut $\partial|k|/\partial\phi$ vanishes for the c-mode, whereas near the SC-cut it is an extreme and a one degree error in φ results in about a 5% change in $|k|$. Figure 11 shows $\partial k/\partial\theta$, which vanishes near the FC-cut; at the SC-cut it is slightly less sensitive than at the AT-cut.

C. Time Constant.

The motional time constant[38] τ_1 is defined as

$$\tau_{1\,(mode\,m)} = \eta_m \,/\, \bar{c}_m \quad . \tag{105}$$

With the quartz viscosity values of Lamb & Richter,[29] the τ_1 values along the locus are given in Figure 12. The units are femtoseconds (10^{-15} seconds). From (105), τ_1 may be re-expressed in a number of ways, such as

$$\tau_1 = R_1 C_1 = 1/\omega_0 Q. \tag{106}$$

In (106), R_1 and C_1 are the motional resistance and capacitance of the equivalent electrical circuit, ω_0 is the nominal resonance frequency of the mode considered, and Q is its quality factor. From Figure 12 it is seen that, for ω_0 constant, the Q of the desired c-mode increases slightly with increasing φ. Figures 13 and 14 show $\partial\tau_1/\partial\varphi$ and $\partial\tau_1/\partial\theta$, respectively.

D. Particle Displacement.

Figures 15 - 17 show the angles made by the particle displacements for the three modes. Mode a is predominantly extensional, that is, the motion is largely along the x_2'' (thickness) axis. For this mode φd and θd are defined as follows: φd is the angle of the first rotation, about x_3, from x_2 to x_2', and θd is the angle of the second rotation, about x_1', from x_2' to x_2''. This definition is similar to the plate rotation, shown in Figure 1, where φ is the measure of the rotation about x_3, and θ the measure of the rotation about x_1'.

In like fashion, for the b-mode with particle displacement mostly along x_3'', φd is defined as the angle of first rotation, about x_1, from x_3 to x_3', and θd is the second rotation angle, about x_2', from x_3' to x_3''.

For the c-mode, we continue the permutation and take φd as the angle between x_1 and x_1' for the rotation about x_2, and θd as the rotation angle between x_1' and x_1'' for the rotation about x_3'. From Figure 17 we see that the AT-cut ($\varphi = 0^{\circ}$) is a pure mode cut, with φd and θd equal to zero. As φ increases, so do φd and θd. This has the practical consequence that unless some technique such as bevelling is used,[24] it would be expected that doubly rotated plates would suffer from Q degradation due to mounting losses when compared to the AT-cut, even though their intrinsic Q's are slightly higher.

E. Capacitance Ratio.

The ratio of static to dynamic, or motional, capacitance appearing in the equivalent circuit representation of the plate vibrator is shown in Figure 18. It is seen that the SC-cut value is approximately three times that of the AT-cut, which is a disadvantage in monolithic filters and TCXO's, but the value is quite acceptable for precision oscillator use. The ratio has been calculated from the relation

$$\pi_m = \pi^2/8k_m^2 \quad . \tag{107}$$

Figures 19 and 20 give the angle derivatives of π.

F. Motional Capacitance.

Motional capacitance is proportional to electrode area $\bar{A}e$ and to resonator frequency. Considering $\bar{A}e$ and frequency fixed, motional capacitance normalized to the equivalent AT-cut plate is

$$C_{1(mode\,m)}/C_{1\,(AT\text{-}cut)} = (\epsilon_{22}'/\pi_m N_m)/(\epsilon_{22}'/\pi_c N_c)_{AT\text{-}cut}; \tag{108}$$

This ratio is shown in Figure 21.

G. Motional Resistance.

Since

$$\tau_1 = R_1 C_1 \quad , \tag{106}$$

and τ_1 is given in Figure 12, one may calculate the motional resistance ratio of a plate with respect to an AT-plate with identical electrode area and frequency. The result is given in Figure 22.

H. Mode Spectrograph.

The plate vibrator input admittance is

$$Y_{in} = j\omega C_o \Big/ \Big\{1 - \sum_m k_m^2 \tan X_m/X_m\Big\}. \tag{109}$$

From this, one obtains the mode spectrograph, which is a plot of the plate susceptance versus frequency. Usually measured in practice[39] is a quantity proportional to the susceptance of the plate when the shunt capacitance Co has been balanced out. We have computed spectrographs of this quantity, B_R, normalized to the susceptance, Bo, of the shunt capacitance. These are shown for various cuts in the following figures. All curves have been plotted for the lossless case, but each resonance has been marked with a figure in percent to indicate the level of the response when losses are present. The levels have been normalized to that of the c-mode AT-cut at the fundamental resonance.

The relative levels are given by

$$\left(\pi_c^{(n)} \cdot \tau_{1\,(mode\,c)}\right)_{AT\text{-}cut} \Big/ \left(\pi_m^{(m)} \cdot \tau_{1\,(mode\,m)}\right). \tag{110}$$

Figure 23 is for the AT-cut; the c-mode has capacitance ratio 159 and motional time constant of 11.8 femtoseconds. Fourteen percent above the c-mode is the frequency of the b-mode, but it is not piezoelectrically driven.

Figures 24 and 25 are for $\phi = 13.9^{\circ}$ and for the FC-cut at $\phi = 15^{\circ}$, respectively. A strong X-ray plane exists for the 13.9° cut, making it easy to orient accurately.

The IT-cut spectrograph is given in Figure 26. Mode c has become somewhat weaker than mode b which is 10% above it. Figure 27 shows the spectrograph plot for the SC-cut. The capacitance ratios are nearly equal, but the c-mode loss is nearly double that of the b-mode, which is 10% higher. A wider frequency plot with ordinate in dB is shown in Figure 28 for the SC-cut. The levels are relative to that of the b-mode fundamental, labeled $b^{(1)}$. One sees here the cluttering of the spectrum produced by the three series of harmonics. These are only the thickness modes; in practice each

will have associated with it anharmonic overtones due to the lateral phase reversals across the plate, further crowding the spectrum. Contouring can reduce these effects very much. More important in many respects is the strength and proximity of the b-mode fundamental to the c-mode fundamental resonance.

Figure 29 is the graph for the rotated-x-cut, with $\phi = 30^\circ$.

I. Temperature Coefficient of Frequency.

The temperature coefficient of antiresonance frequency, T_{fa}, is plotted in Figure 30. If, instead of computing T_{fa} at a reference temperature T_o of 25°C, one transforms T_{fa} to the inflection temperature T_i, the curve for mode c is found to increase with increasing ϕ as shown on the graph. T_i increases from 26.4°C for the AT-cut to 95.4°C for the SC-cut, to 157°C for the rotated-X-cut. The gradients $\partial T_{fa}/\partial \phi$ and $\partial T_{fa}/\partial \theta$ are shown in Figures 31 and 32, respectively.

J. Temperature Coefficient of Coupling.

T_k, the temperature coefficient of piezoelectric coupling, is plotted in Figure 33; Figures 34 and 35 contain plots of the derivatives of T_k. Using the curves in Figure 33 and the relation (28), T_x may be obtained; the plots are shown in Figure 36, from which it is seen that T_x for mode c is not sensitive to changes in ϕ.

K. Frequency-Temperature Behavior.

Figure 37 contains plots of frequency versus temperature for the SC-cut. Values of $\partial T_{fa}/\partial \theta$ from Figure 32 have been used to obtain the curves at various θ-offsets; the second- and third-order coefficients were taken from Bechmann, et al.[12-14] From the graph it is seen that the SC-cut should be excellent for oven-controlled applications due to its high inflection temperature (95.4°C); comparison with the corresponding AT-cut set (Figure 12 of Reference 31) discloses that the SC-cut is flatter than the AT-cut and is less sensitive to changes in θ.

Conclusions - Quartz

Doubly rotated quartz plates on the upper zero temperature coefficient locus appear to have a very promising future for applications where various nonlinear effects have to be minimized. A short list of advantages and disadvantages follows. Comparisons are with respect to an AT-cut with identical frequency and electrode size.

A. Advantages.

- Improved static frequency-temperature behavior.
- Greatly improved transient frequency-temperature behavior.[24]
- Lessened edge-force sensitivity.[40-41]
- Greatly improved planar stress behavior.[23]
- Reduced acceleration sensitivity.
- Improved amplitude-frequency behavior.
- Lessened intermodulation effects.
- Fewer activity dips.
- Slightly improved quality factors.
- Thicker, less fragile plates.
- Mode separations and couplings adjustable for stacked-crystal filter use.

B. Disadvantages.

- X-raying and orienting more difficult.
- Tighter tolerances required on angle because of finite gradients.
- Higher r and R_1 for filter and TCXO applications; smaller C_1.
- Out-of-plane displacements-increased mounting losses.
- Proximity of b mode with moderate strength.
- Mode spectra more complicated.

Berlinite

Berlinite ($A\ell PO_4$) is a material very like quartz in structure and material properties. It occurs naturally only as tiny crystals, but may be grown to large size relatively easily.[42] An evaluation of the elastic, piezoelectric, and dielectric constants has recently been completed;[43] these are used here to calculate some of the properties of doubly rotated cuts of this interesting material.

Aluminum phosphate has coupling coefficients roughly three times those of quartz. A sample of what is obtainable is shown in Figure 38, showing the k_m for cuts of the orientation $(YX\omega)\varphi$.

For cuts $(YX\omega\ell)12^\circ/\theta$, Figure 39 presents N_m versus θ. It is very similar to the corresponding set for quartz, but the values are slightly lower. Figure 40 gives the k_m for $\varphi = 12^\circ$; again the similarity to quartz is to be noted, but the magnitudes are about three times larger. In Figure 41 are the T_{fa} (mode m) for $\varphi = 12^\circ$. As may be seen from a glance at Figure 3, the c-mode quartz curve becomes much more positive in the region $|\theta| < 30^\circ$ than the berlinite curve. Small changes in the berlinite temperature coefficient values could have the effect of shifting the zero temperature locations significantly.

In Figure 42 the loci of $T_{fa} = 0$ are shown for berlinite; the similarity to quartz is again apparent. Because the material coefficients are not as well known for $A\ell PO_4$ as for quartz, and firm applications are not yet established, it is not advisable to pursue calculations of gradients at this time. However, the magnitudes of the coupling factors and the presence of zero temperature coefficients in a material structurally similar to quartz justifies further efforts to grow, measure, and apply this material. In particular, paralleling what we have said about the temperature behavior of bulk and surface waves on quartz, the surface wave properties of $A\ell PO_4$ appear very appealing, with a zero temperature coefficient locus all but a certainty.

Acknowledgment

The authors take this opportunity to thank Mr. Robert Broadbelt and Mrs. Caroline Harris for their careful drafting and Mrs. Anita Earle for her expert typing.

References*

1. F. E. Butterfield; "Frequency Control and Time Information in the NAVSTAR/Global Positioning System," these Proceedings.

2. A. J. Van Dierendonck; "Time Requirements in the NAVSTAR/Global Positioning System (GPS)," these Proceedings.

3. R. A. Maher/ "Oscillator and Frequency Management Requirements for GPS User Equipments," these Proceedings.

---

* AFCS: Annual Frequency Control Symposium, US Army Electronics Command, Fort Monmouth, NJ 07703.

4. J. Moses; "NAVSTAR/Global Positioning System Oscillator Requirements for the GPS Manpack," these Proceedings.

5. "Standards on Piezoelectric Crystals, 1949." Proc. IRE, Vol. 37, No. 12, Dec. 1949, pp. 1378-1395. (IEEE Standard No. 176.)

6. C. F. Baldwin and S. A. Bokovoy; "Piezoelectric Quartz Element," US Patent 2,212,139, filed 18 Mar. 1936, awarded 20 Aug. 1940.

7. C. F. Baldwin and S. A. Bokovoy; "Improvements in or Relating to Piezo-Electric Crystals," Australian Patent 21,957, filed 27 Mar. 1935, awarded 27 Mar. 1936.

8. S. A. Bokovoy and C. F. Baldwin; "Improvements in or Relating to Piezo-Electric Crystals," UK Patent 457,342, filed 31 May 1935, awarded 26 Nov. 1936.

9. C. F. Baldwin and S. A. Bokovoy; "Piezoelectric Crystal Element," US Patent 2,254,866, filed 28 Mar. 1936, awarded 2 Sept. 1941.

10. V. E. Bottom and W. R. Ives; "Zero Temperature Coefficient Piezoelectric Crystal," US Patent 2,743,144, filed 7 Apr. 1951, awarded 24 Apn 1956.

11. W. R. Ives and D. L. Hammond; "Present Performance Limitations of Crystal Filters," IRE Westcon Convention Record, Vol. 1, Pt. 6, 1957, pp. 113-119.

12. R. Bechmann, A. D. Ballato, and T. J. Lukaszek; "Frequency-Temperature Behavior of Thickness Modes of Double-Rotated Quartz Plates," Proc. 15th AFCS, May-June 1961, pp. 22-48.

13. R. Bechmann, A. D. Ballato, and T. J. Lukaszek; "Frequency-Temperature Characteristics of Quartz Resonators Derived from the Temperature Behavior of the Elastic Constants," Proc. 16th AFCS, April 1962, pp. 77-109.

14. R. Bechmann, A. D. Ballato, and T. J. Lukaszek; "Higher-order Temperature Coefficients of the Elastic Stiffnesses and Compliances of Alpha-Quartz," Proc. IRE, Vol. 50, No. 8, August 1962, pp. 1812-1822, and Vol. 50, No. 12, Dec. 1962, p. 2451.

15. R. Bechmann; "Thickness-Shear Mode Quartz Cut with Small Second- and Third-Order Temperature Coefficients of Frequency (RT-Cut)," Proc. IRE, Vol. 49, No. 9, Sept. 1961, p. 1454.

16. D. L. Hammond and A. Benjaminson; "The Linear Quartz Thermometer - a New Tool for Measuring Absolute and Difference Temperatures," Hewlett-Packard Jour., Vol. 16, No. 7, March 1965, pp. 1-7.

17. D. L. Hammond, C. A. Adams, and P. Schmidt; "A Linear, Quartz-Crystal, Temperature-Sensing Element," ISA Transactions, Vol. 4, No. 4, Oct. 1965, pp. 349-354.

18. D. L. Hammond and A. Benjaminson; "The Crystal Resonator--A Digital Transducer," IEEE Spectrum, Vol. 6, No. 4, Apr. 1969, pp. 53-58.

19. G. Lagasse, J. Ho, and M. Bloch; "Research and Development of a New Type of Crystal - The FC-Cut," Proc. 26th AFCS, June 1972, pp. 148-151.

20. R. Holland; "Nonuniformly Heated Anisotropic Plates: II. Frequency Transients in AT and BT Quartz Plates," 1974 Ultrasonic Symposium Proceedings, IEEE Cat. No. 74 CHO 896-1SU, pp. 592-598.

21. R. Holland; "Temperature Coefficients of Stiffness in Quartz," IEEE Trans. Sonics Ultrason., Vol. SU-23, No. 1, Jan. 1976, pp. 72-75.

23. E. P. EerNisse; "Calculations on the Stress-Compensated (SC-cut) Quartz Resonator," these Proceedings.

24. J. A. Kusters; "Transient Thermal Compensation for Quartz Resonators," IEEE Trans. Sonics Ultrason., Vol. SU-23, No. 4, July 1976, pp. 273-276.

25. M. B. Schulz, B. J. Matsinger, and M. G. Holland; "Temperature Dependence of Surface Wave Velocity on α Quartz," J. Appl. Phys., Vol. 41, June 1970, pp. 2755-2765.

26. M. B. Schulz and M. G. Holland; "Surface Acoustic Wave Delay Lines with Small Temperature Coefficient," Proc. IEEE, Vol. 58, No. 9, Sept. 1970, pp. 1361-1362.

27. M. F. Lewis, G. Bell, and E. Patterson; "Temperature Dependence of Surface Elastic Wave Delay Lines," J. Appl. Phys., Vol. 42, No. 1, Jan. 1971, pp. 476-477.

28. W. Voigt; Lehrbuch der Kristallphysik, Teubner, Leipzig, 1928, Section IX, pp. 792-796.

29. J. Lamb and J. Richter; "Anisotropic Acoustic Attenuation with New Measurements for Quartz at Room Temperatures," Proc. Roy. Soc., A, Vol. 293, 1966, pp. 479-492.

30. H. F. Tiersten; "Thickness Vibrations of Piezoelectric Plates," J. Acoust. Soc. Am., Vol. 35, No. 1, Jan. 1963, pp. 53-58.

31. A. Ballato and T. Lukaszek; "Higher-Order Temperature Coefficients of Frequency of Mass-Loaded Piezoelectric Crystal Plates," Proc. 29th AFCS, May 1975, pp. 10-25.

32. J. Détaint and R. Lançon; "Temperature Characteristics of High Frequency Lithium Tantalate Plates," these Proceedings.

33. M. Onoe; "Relationship Between Temperature Behavior of Resonant and Antiresonant Frequencies and Electromechanical Coupling Factors of Piezoelectric Resonators," Proc. IEEE, Vol. 57, No. 4, Apr. 1969, pp. 702-703.

34. A. Ballato; "Apparent Orientation Shifts of Mass-Loaded Plate Vibrators," Proc. IEEE, Vol. 64, No. 9, Sept. 1976, in press.

35. R. Bechmann; "Frequency-Temperature-Angle Characteristics of AT-Type Resonators Made of Natural and Synthetic Quartz," Proc. IRE, Vol. 44, No. 11, Nov. 1956, pp. 1600-1607.

36. R. Bechmann; "Elastic and Piezoelectric Constants of Alpha-Quartz," Phys. Rev., Vol. 110, No. 5, Jun. 1958, pp. 1060-1061.

37. J. Zelenka and P. C. Y. Lee; "On the Temperature Coefficients of the Elastic Stiffnesses and Compliances of Alpha-Quartz," IEEE Trans. Sonics Ultrason, Vol. SU-18, No. 2, Apr. 1971, pp. 79-80.

38. G. K. Guttwein, T. J. Lukaszek, and A. D. Ballato; "Practical Consequences of Modal Parameter Control in Crystal Resonators," Proc. 21st AFCS, Apr. 1967, pp. 115-137.

39. F. K. Priebe and A. D. Ballato; "Measurement of Mode Parameters by Sweep Frequency Methods in the Frequency Range from 20 to 250 MHz," Proc. 20th AFCS, April 1966, pp. 465-499.

40. A. Ballato; "Effects of Initial Stress on Quartz Plates Vibrating in Thickness Modes," Proc. 14th AFCS, May-Jun. 1960, pp. 89-114.

41. R. L. Filler and J. R. Vig; "The Effect of Bonding on the Frequency vs. Temperature Characteristics of AT-Cut Resonators," these Proceedings.

42. J. M. Stanley; "Hydrothermal Synthesis of Large Aluminum Phosphate Crystals," Industrial and Engineering Chem., Vol. 32, Aug. 1954, pp. 1684-1689.

43. Z. -P. Chang and G. R. Barsch; "Elastic Constants and Thermal Expansion of Berlinite," IEEE Trans. Sonics Ultrason., Vol. SU-23, No. 2, Mar. 1976, pp. 127-135.

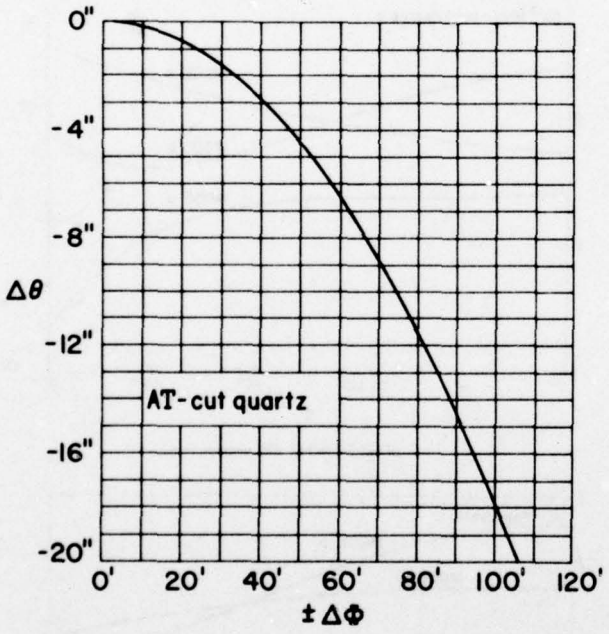

2. Locus of constant temperature coefficient as function of $\Delta\theta$ and $\Delta\phi$ about the AT-cut.

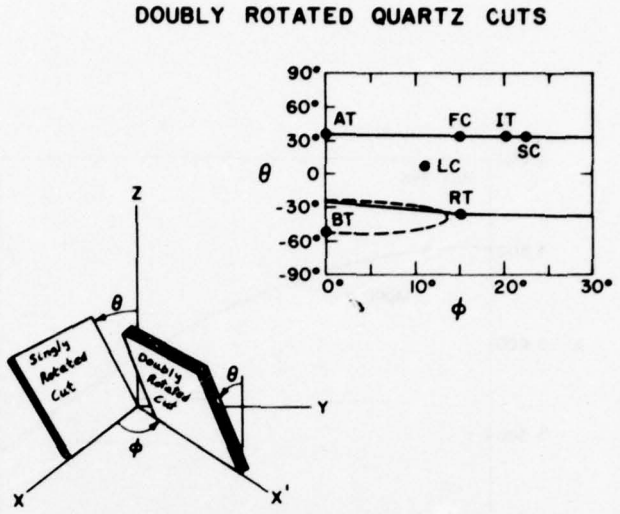

1. Crystal cut orientations (left); locus of zero temperature coefficient (ZTC) in quartz (right).

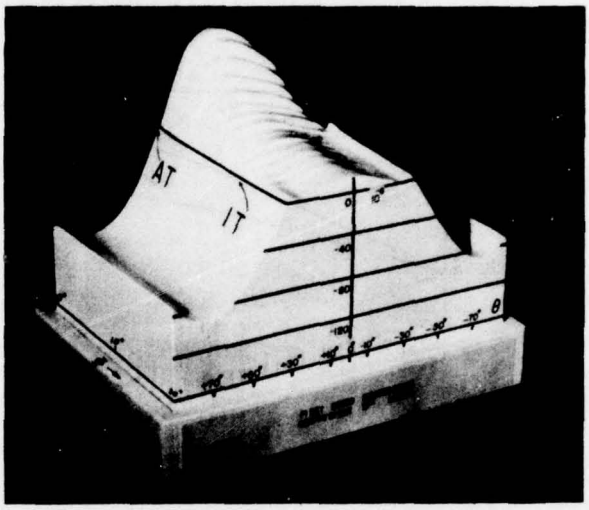

3. Temperature coefficient surface for the c mode in quartz.

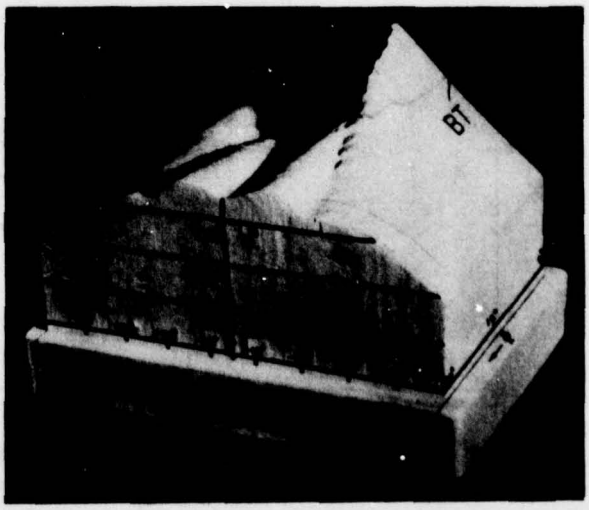

4. Temperature coefficient surface for the b mode in quartz.

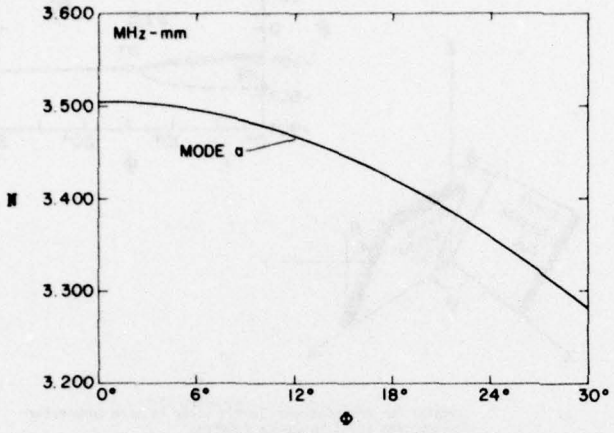

5. Frequency constant for the a mode along ZTC quartz locus.

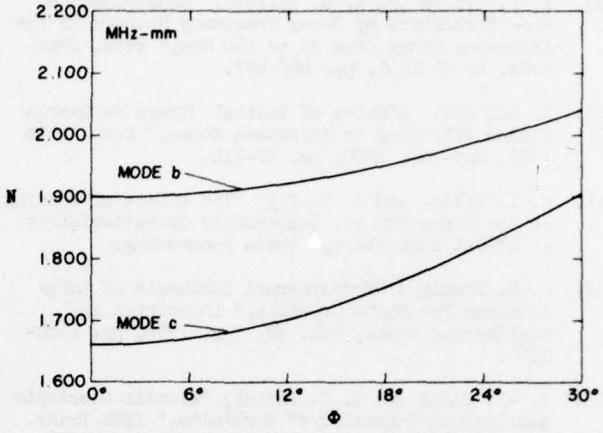

6. Frequency constants for the b and c modes along ZTC quartz locus.

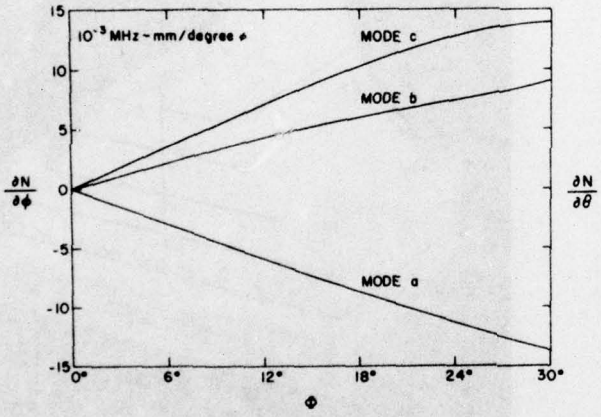

7. $\partial N_m / \partial \phi$ along ZTC quartz locus.

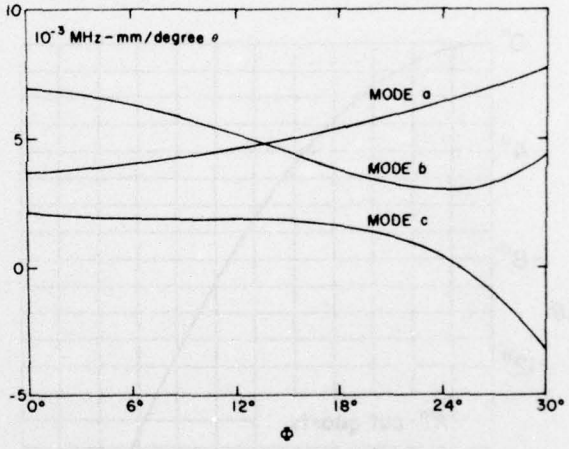

8. $\partial N_m / \partial \theta$ along ZTC quartz locus.

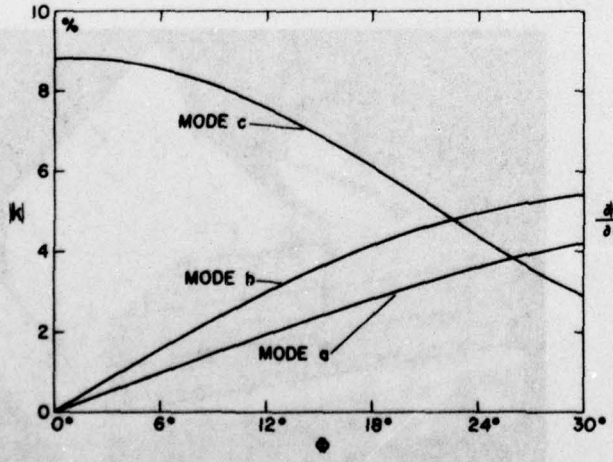

9. Piezoelectric coupling factors along ZTC quartz locus.

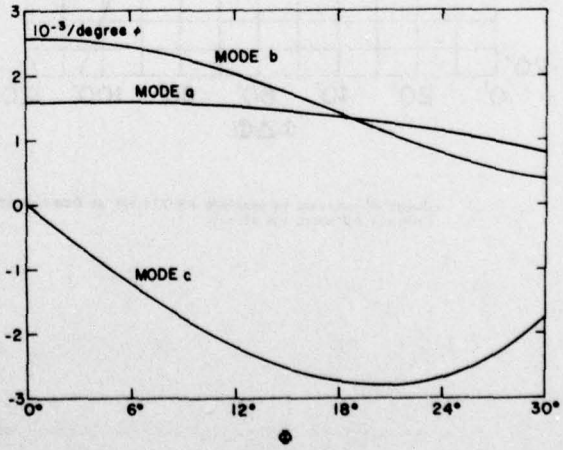

10. $\partial |k_m| / \partial \phi$ along ZTC quartz locus.

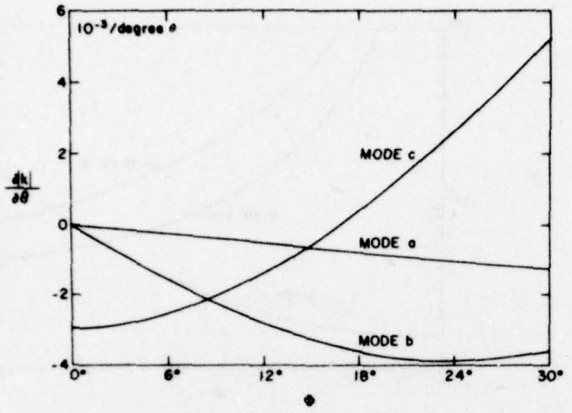

11. $\partial|k_m|/\partial\theta$ along ZTC quartz locus.

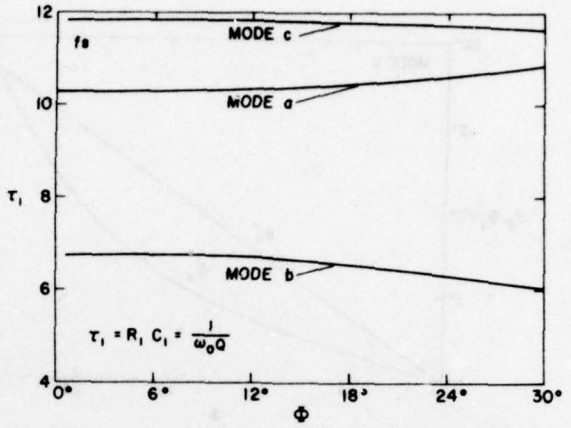

12. Motional time constants along ZTC quartz locus.

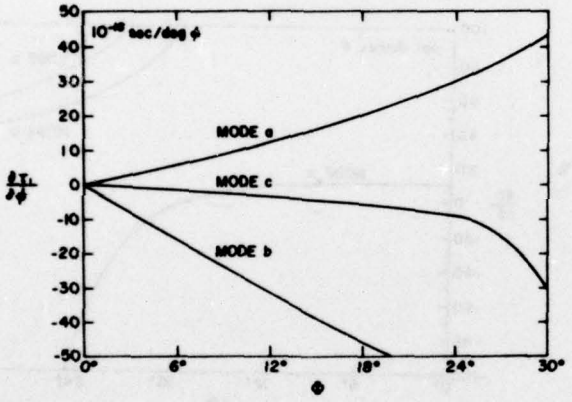

13. $\partial\tau_1/\partial\phi$ along ZTC quartz locus.

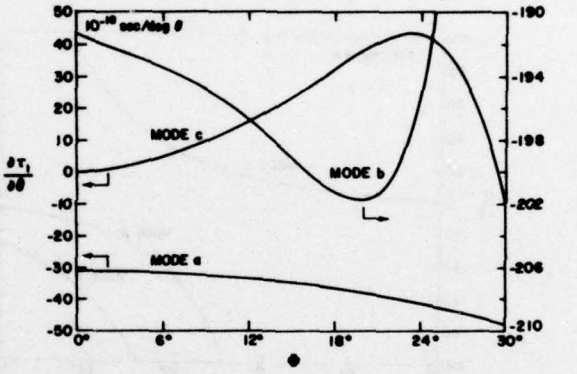

14. $\partial\tau_1/\partial\theta$ along ZTC quartz locus.

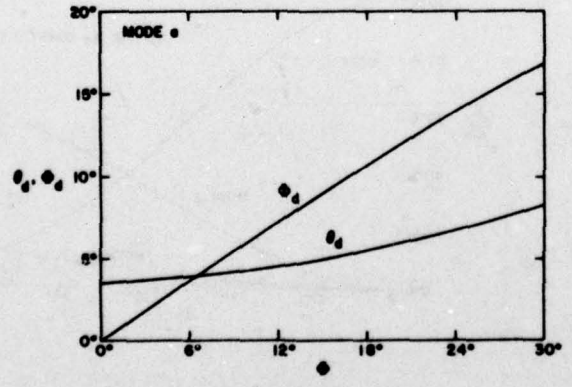

15. Mode a particle displacement angles along ZTC quartz locus.

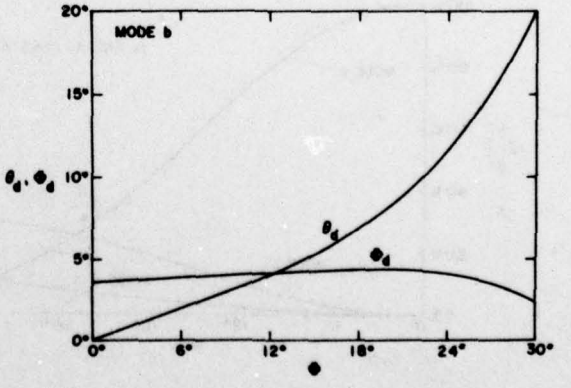

16. Mode b particle displacement angles along ZTC quartz locus.

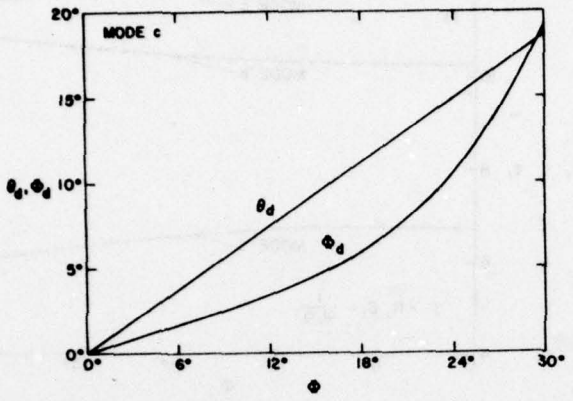

17. Mode c particle displacement angles along ZTC quartz locus.

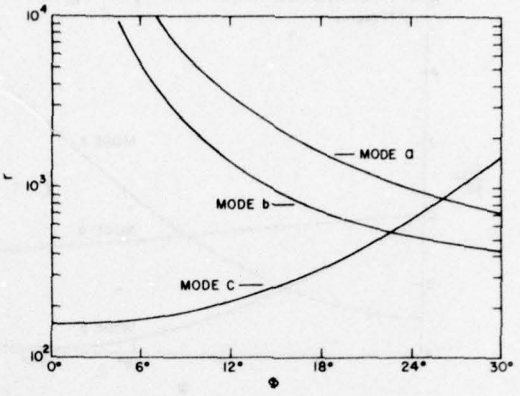

18. Capacitance ratios along ZTC quartz locus.

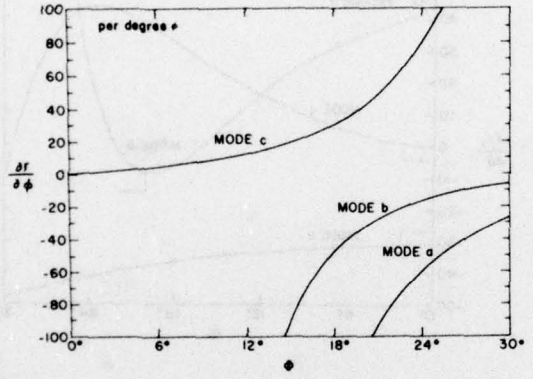

19. $\partial r / \partial \phi$ along ZTC quartz locus.

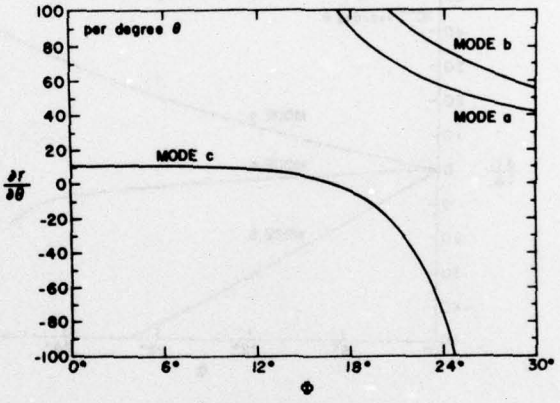

20. $\partial r / \partial \theta$ along ZTC quartz locus.

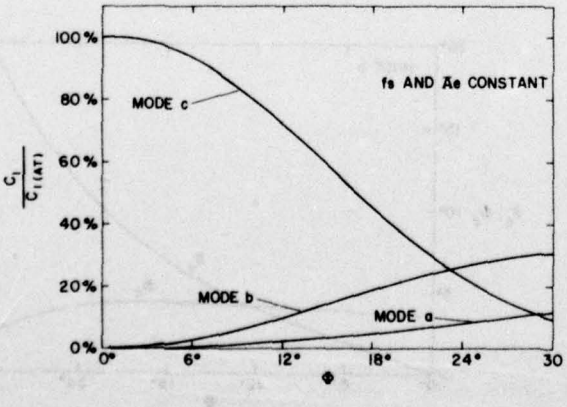

21. Motional capacitance, normalized to that of an AT-cut having equal frequency and electrode area, along ZTC quartz locus.

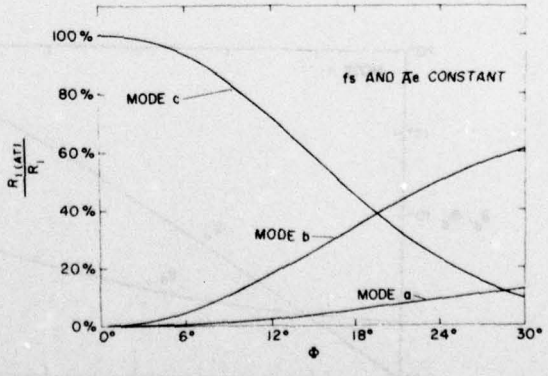

22. Motional resistance, normalized to that of an AT-cut having equal frequency and electrode area, along ZTC quartz locus.

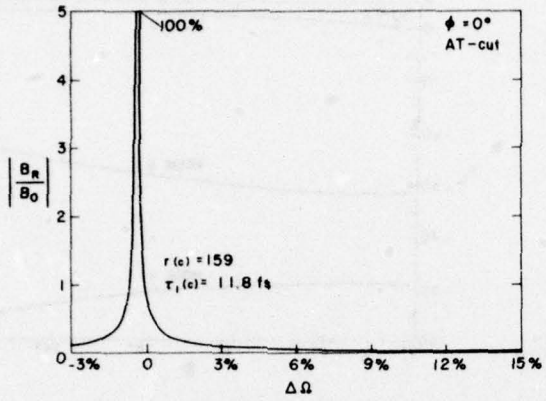

23. Mode spectrograph of quartz plate (YXωℓ)0°/θ, θ = 35.25°. (AT-cut).

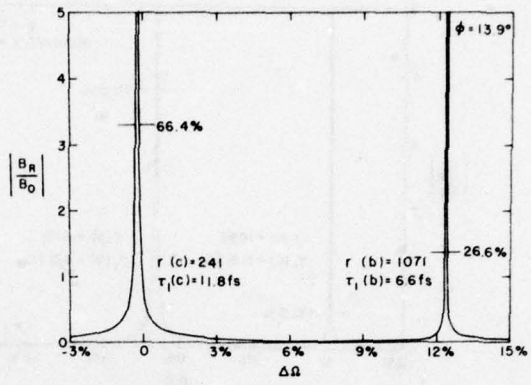

24. Mode spectrograph of quartz plate (YXωℓ)13.9°/θ, θ = 34.40°.

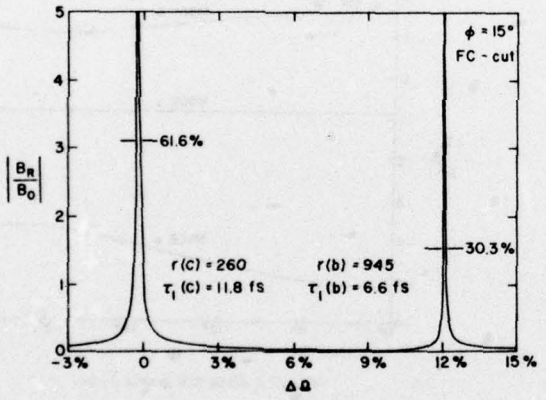

25. Mode spectrograph of quartz plate (YXωℓ)15°/θ, θ = 34.33°. (FC-cut).

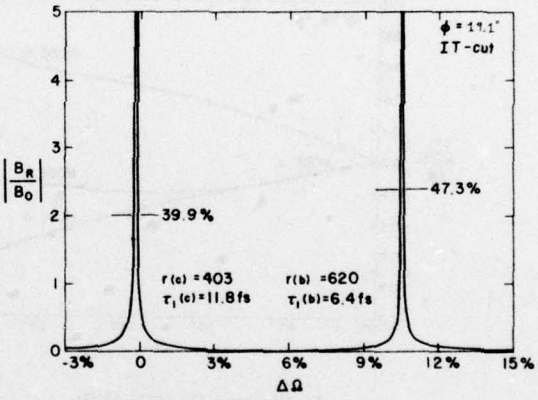

26. Mode spectrograph of quartz plate (YXωℓ)19.1°/θ, θ = 34.08°. (IT-cut).

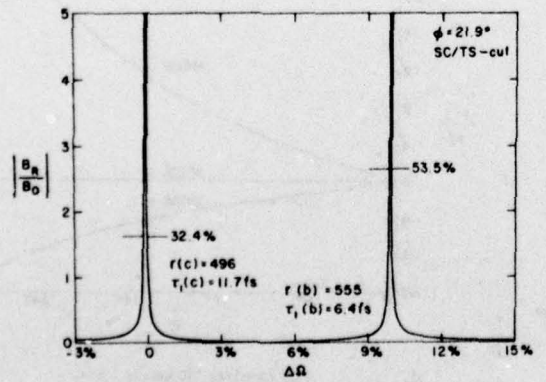

27. Mode spectrograph of quartz plate (YXωℓ)21.9°/θ, θ = 33.91°. (SC-cut).

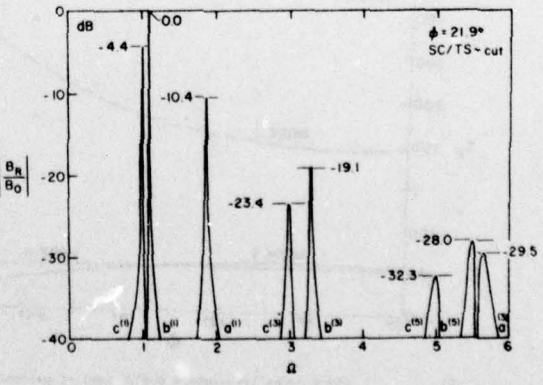

28. Mode spectrograph of SC-cut on dB scale over extended frequency range.

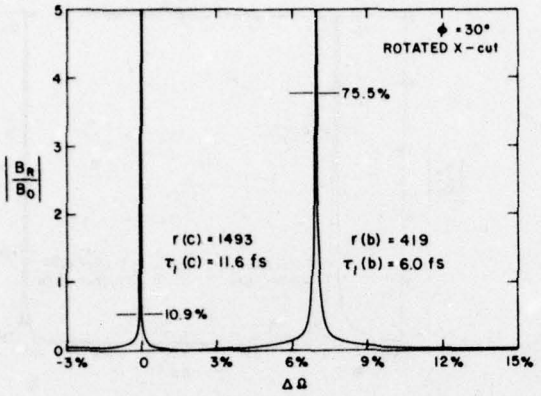

29. Mode spectrograph of quartz plate (YXωℓ)30°/θ, θ = 33.42°. Rotated-X-cut.

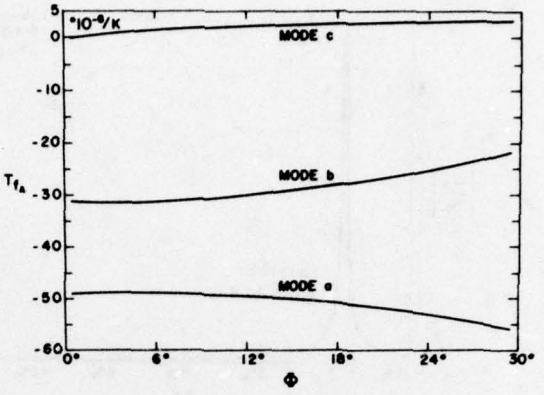

30. First order temperature coefficient of antiresonance frequency, T_{fA} along ZTC quartz locus.

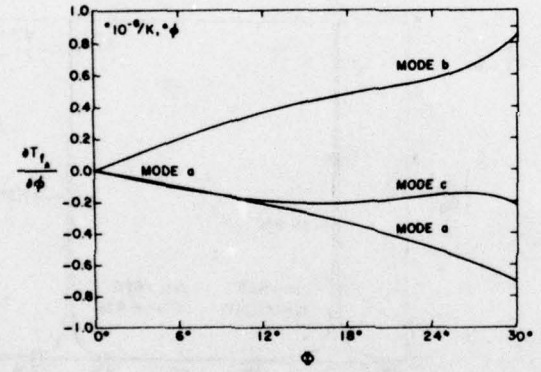

31. $\partial T_{fa}/\partial \phi$ along ZTC quartz locus.

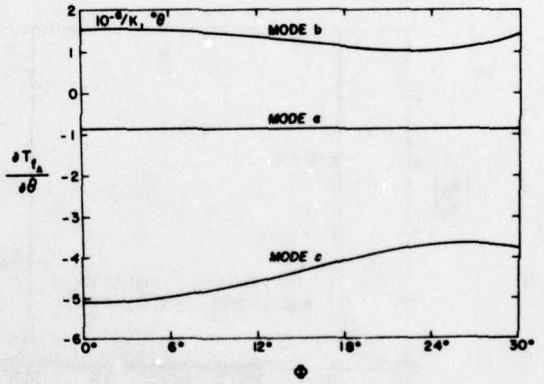

32. $\partial T_{fa}/\partial \theta$ along ZTC quartz locus.

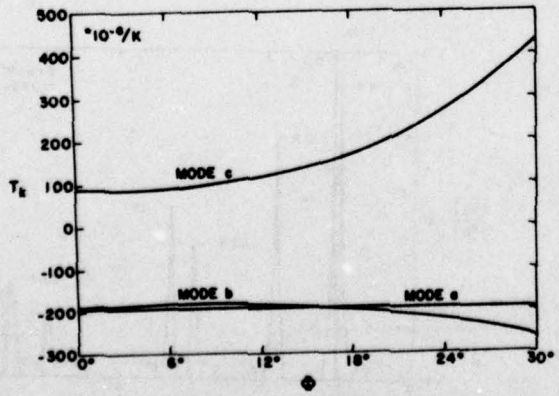

33. First order temperature coefficient of piezoelectric coupling, T_k, along ZTC quartz locus.

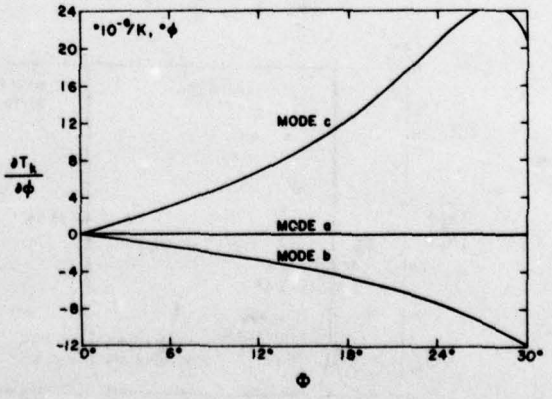

34. $\partial T_k/\partial \phi$ along ZTC quartz locus.

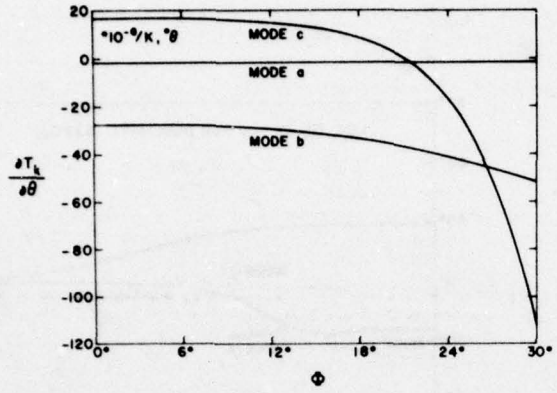

35. $\partial T_k / \partial \theta$ along ZTC quartz locus.

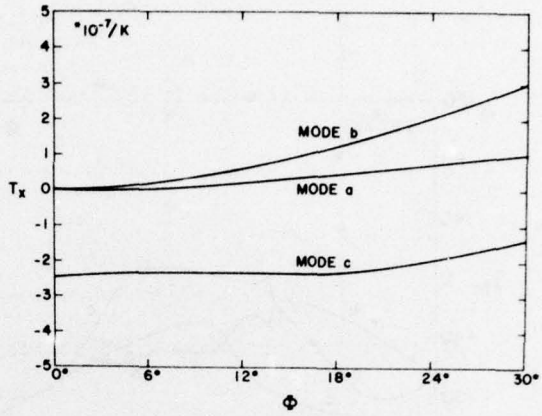

36. Difference between first order temperature coefficients of resonance and antiresonance frequencies, T_x, along ZTC quartz locus.

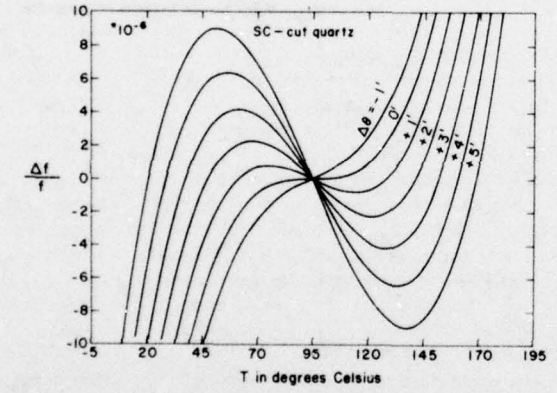

37. Frequency-temperature-angle behavior of SC-cut quartz resonators.

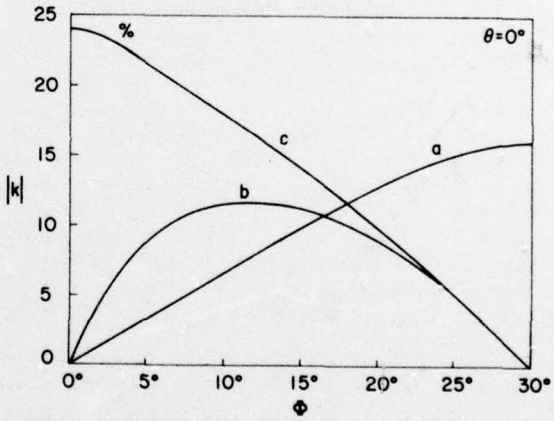

38. Piezoelectric coupling factors $|k_{ms}|$ for (YXω-ϕ)ϕ cuts of berlinite. ($AlPO_4$).

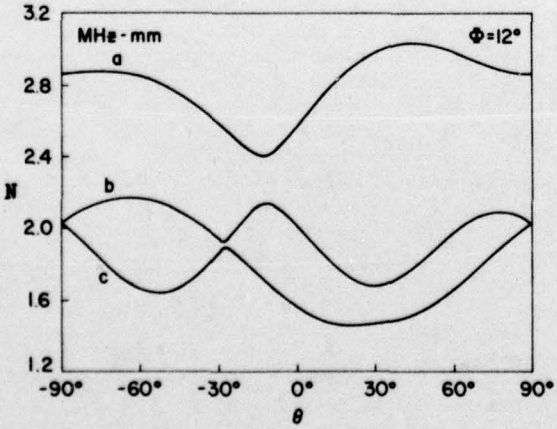

39. Frequency constants N_m for (YXω-ϕ)12°/θ cuts of berlinite. ($AlPO_4$).

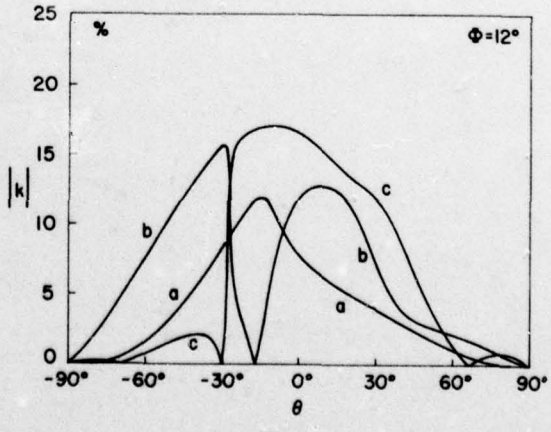

40. Piezoelectric coupling factors $|k_{ms}|$ for (YXω-ϕ)12°/θ cuts of berlinite. ($AlPO_4$).

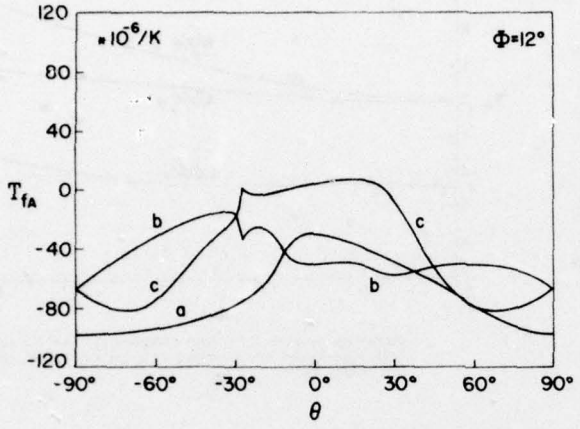

41. Temperature coefficients of antiresonance frequency T_{fA} for (YX ωℓ)12°/θ cuts of berlinite. ($AlPO_4$).

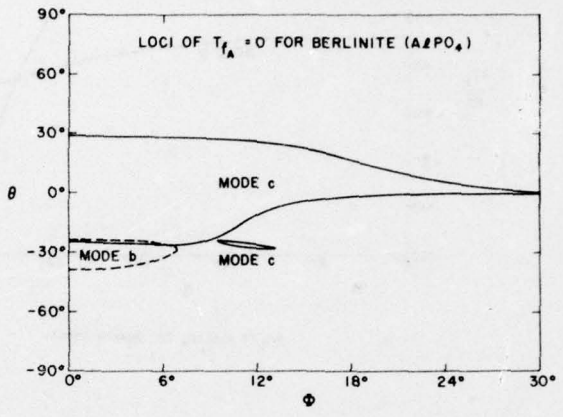

42. Loci of T_{fA} = 0 for b- and c-modes of berlinite. ($AlPO_4$).

PROGRESS REPORT ON SURFACE ACOUSTIC WAVE DEVICE MMT

Alan R. Janus
Hughes Aircraft Company
Fullerton, California

Summary

In July 1975, Hughes began a two-year, USAECOM sponsored Manufacturing Methods program on surface acoustic wave devices. A status report is presented which identifies the extent to which program objectives have been met in terms of design, fabrication, packaging and test considerations.

The object of the program is the establishment of a production capability for SAW devices of varied design and material. Specifically, the contract identifies six test vehicles with rigid electrical and environmental specifications. These are bandpass filters, tapped delay lines and pulse compression filters with center frequencies of 100 to 200 MHz on both lithium niobate and ST-quartz. The program is divided into four phases. During the first, design phase, the six devices were designed, fabricated and tested to specification. The second phase was directed at the redesign or design modification required by the failure of first phase samples to meet specification. The program is currently entering the third phase. This phase calls for testing of the devices to an environmental specification. The final phase calls for the establishment of a pilot line and the production of one hundred fifty of each of the devices.

Introduction

This paper deals with the preliminary results of an effort to satisfy the requirements of a Manufacturing Methods and Technology (MMT) program based on a broad range of surface acoustic wave device designs. It encompasses both the initial and redesign efforts on six differing SAW designs as well as a discussion of the accompanying fabrication effort.

Program Requirements

The overall objective of the MMT program is the establishment of a production capability for SAW device functions that are representative of a proven technology. Table I summarizes the six device designs chosen by ECOM for the program. They are broadly classified into bandpass, phase coded tapped delay line, and pulse compression filters. Substrate materials specified are lithium niobate and ST-quartz.

In order to address the design, electrical test, environmental and volume fabrication requirements of the program in an orderly fashion, the program is broken into four phases as shown in Table II. During the first phase, the six devices were designed, fabricated and tested to specification. Ten devices of each of the six designs were delivered to ECOM at the end of this phase. In order to meet the program requirements for auto correlation (phase coded tapped delay line filters) and pulse compression line test, the appropriate reverse coded tapped delay lines and pulse expansion lines were included in this shipment.

During the second phase of the program, testing and analysis of those devices that failed to meet full specification was performed. This redesign effort resulted in a finalization of electrical specification for the balance of the program. Ten devices of each of the six designs, fully adherent to the finalized specification, were delivered at the end of this phase.

The third phase calls for the testing of devices to a MIL-STD 883B type of environmental specification and will result in the delivery of fifty each of the six device types. During the final phase of the program, a pilot line will be established for the production and delivery of one hundred fifty of each of the devices, fully adherent to electrical and environmental requirements of the program. An important element of this phase calls for the development of realistic manufacturing cost data on each of the device designs.

Program Accomplishments

Phase I

Design - A detailed discussion of each of the designs is beyond the scope of this paper[1] and will be addressed here only to clarify certain test data. In general, each design approach chosen was verified to be consistent with specification requirements by computer simulation prior to commitment to maskmaking. Maskmaking utilized an Electromask step and repeat apparatus for both pattern generation (10 X-emulsion reticle) and working plate fabrication (1 X-anti-reflection chromium). This approach allowed for rapid turnaround as well as a lowered recurring cost during anticipated redesign efforts. A typical mask layout is shown in Figure 1.

Appropriate series inductive tuning and series padding resistors required to meet the VSWR specification are indicated. Due to the uncertainty in the final series resistance level at the prototype stage, three levels of aluminum film resistance have been incorporated into the device. The final mask has a die array that exceeds the area capacity of the substrate in order to provide redundancy for patterns damaged in processing.

Fabrication - Substrate materials were obtained from Valpey-Fisher Corp.[2] (3 x 0.75 x 0.025 inch ST-quartz, ± 15' orientation to x axis) and Crystal Technology, Inc.[3] (2 (dia) x 0.020 inch lithium niobate, ± 6' orientation to z axis).

Both materials were cleaned with an acetone soak and scrub and a detergent scrub. Intermediate steps involved a deionized water rinse. The substrates were dried under a dry nitrogen stream. These substrates were then metallized with aluminum to a thickness appropriate to the design requirement (2000 Å ± 10% except TDL, 1250 ± 10%). The metallized substrates were spun at 5000 rpm in order to achieve a positive resist thickness (Shipley AZ-1350B) of 3000 Å ± 10% a prebake schedule of 10 min. at 90°C was utilized.

Transducer patterns were exposed at from 3-6 sec. using a Kasper Alligner, Model 1800. Development of the resist involved a 50% dilution of commercial developer. Exposure and development times were adjusted to give the proper line-to-space ratios for a given filter pattern. The patterns were then defined in the aluminum using a nitric acid, phosphoric acid, water (2:40:9) etchant. The photoresist was stripped in acetone prior to visual inspection at 200X magnification. In the majority of cases to date, the predice yield has exceeded fifty percent. The criterion for this yield is based on the number of good die vs. the number of die printed. A good dice is defined as having no shorts and less than 5 opens.

Prior to dicing, the substrates were recoated with photoresist for protective purposes. They were then pitch mounted and diced using a 6 mil. OD diamond blade. Dice were then individually recleaned prior to packaging. Die mounting utilized Dow Corning 3140 RTV, cured for 24 hours in air. Thermocompression gold wire bonding (2 mil dia.) completed the packaging operation.

Due to the complexity of this dicing procedure as well as the lack of proper sawing equipment, device yields have been significantly lower than that indicated by the predice inspection during this phase of the program.

During this initial phase, the requirement for confirming the device design, independent of feedthrough and tuning losses, has dictated the use of machined chassis employing SMA connectors.

Initial results on quartz substrates indicated that supposedly identical plates from the same shipment were capable of producing devices at zero and plus four percent of the design frequency in approximately a 1 to 1 ratio. With reference to Figure 2, this frequency difference can be accounted for by an equivalent acoustic velocity difference. This acoustic velocity difference can be related to the polarity of the y-axis rotation relative to the z axis. Here, for the proper acoustic velocity of 3158 m/sec, the rotation angle is a +42.75° rotated y-cut (ST-quartz). For an acoustic velocity of 3290 m/sec the notation angle is a -42.75° rotated y-cut (not ST-quartz). It has been confirmed through the vendor that all the plates received under the original order were cut from the same stone. Given that the stone must be bisected in order to remove the seed crystal, it is hypothesized that the stone halves could have been misaligned relative to one another in regard to x-polarity prior to slicing. The vendor has now implemented an x-ray screening procedure to correct this problem.

Test Results - Tables III through VIII compare specification requirements to the tested results of the first design effort. With the bandpass filters, the insertion loss specification was only nominally achieved on BP-Q. On BP-LN, both insertion loss and VSWR specifications were exceeded. The two tapped delay lines failed to meet specification in a number of areas; insertion loss, sidelobe and spurious suppression, and VSWR. The pulse compression filters were deficient only in sidelobe suppression and VSWR.

Phase II

Design - The redesign effort during the 2nd Engineering Phase involved in-depth analysis and testing of the devices in order to improve the degree to which the designs meet the specifications imposed by the program. It was also determined that specification relief, primarily in the area of VSWR, was required in order to (1) prevent a substantial reduction in device yield, and (2) negate substantial device cost increases projected for additional matching components. In view of the relatively insignificant impact of VSWR on system performance at IF, this relief was granted by the program office. Tables IX through XIV reflect these specification modifications as well as changes in test data that resulted from the redesign effort.

The insertion loss achieved on prototype BP-Q (Table IX) devices was marginally at 22 dB, potentially lowering device yield. In order to lower this value to an acceptable 20 dB, the series resistance on both input and output transducers was appropriately reduced. This, however, raised the VSWR level in excess of the specification.

In the BP-LN design (Table X), Hughes learned that the multistrip coupler specified for

this device was incurring additional insertion loss. An agreement was reached with ECOM to proceed with a new design eliminating the coupler. A thorough theoretical evaluation of a number of designs was then performed. Of the best of these, it was found that the inherent Q of the transducers caused the theoretical insertion loss (15 dB) and spurious echo suppression (35 dB) to be barely met. Adaption of this design would require a relaxed echo suppression of 30 dB. A more serious problem is that the new design requires addition of six lumped matching network components, including two broadband impedance transformers. Furthermore, it should be noted that this design has not been evaluated experimentally, and that the actual performance data could conceivably be further modified by deviations from the assumed ideal transformer performance behavior. It was therefore deemed desirable to adopt the original design with appropriate specification modification in insertion loss and VSWR.

For both tapped delay lines (Tables XI, XII), it was determined that a VSWR of 1.5:1 could not be achieved with an insertion loss of 30 dB under any circumstances. A somewhat reduced VSWR could be obtained with the addition of two additional components on the input transducer and one on the output tap array. This approach was not considered desirable from a cost standpoint, and appropriate VSWR specification modifications were implemented. Due to the lower fractional bandwidth of the TDL-200 design, the proposed VSWR level is lower. Indeed, the relaxed VSWR specification contributed to an improved insertion loss in both designs.

The specified metallization thickness (1000-2000 Å) caused the spurious echo suppression specification to be exceeded. A reduction in thickness to 400 Å allowed this specification to be met. The specified time-sidelobe level, influenced by a complex inter-relationship of orientation, metallization thickness, and die mounting procedure, was only marginally achievable on engineering samples. A 2 dB reduction in this level was implemented into the specification.

As with the TDL designs, the PC-Q VSWR insertion loss trade-off was resolved in favor of the latter parameter. In PC-LN, component cost dictated VSWR specification relief. Finally, in the PC-LN design, the time sidelobe limit has been attributed to an anomalous interaction between the surface acoustic wave and the transducer metallization. The identification and resolution of this anomally were felt to be beyond the scope of the program and a 5 dB specification relief was implemented for the first leading and trailing sidelobes only.

On both pulse compression filters, changes in shunt and series resistance were required at the mask level in order to otherwise meet specification parameters.

The net result of the Phase II effort has been the finalization of the electrical specification for the balance of the MMT program.

Fabrication - In order to more effectively utilize substrate material from both a cost and throughput standpoint, substrate sizes were revised during the 2nd Engineering Phase. ST-quartz (2 x 2 x 0.025 inch) from Valpey-Fisher Corp. and y-z lithium niobate (2 x 1.75 x 0.020 inch) from Union Carbide Corp.[5] are now used for the balance of the program.

The dicing problem identified during the 1st Engineering Phase was resolved by receipt and implementation of an Electroglas[6] dicing saw, Model 106. Initially, the new saw met all expectations on lithium niobate in terms of yield, kerf loss and speed. However, a blade life problem was encountered in the dicing of quartz. This problem was resolved by the implementation of an improved saw blade at reduced spindle speed.

During the 2nd Engineering Phase, commercially available semiconductor pin packages[7] were successfully substituted for machined chasis (Figure 3). A ten fold packaging cost reduction was achieved by this implementation. While the new packages do not show as good a feedthrough suppression as the machined units, (Tables IX through XIV), specification is still met. The key element in meeting this specification lies in the intimate grounding of the package base.

Conclusions

Design and test efforts during the initial phases of a surface acoustic wave MMT program have resulted in six bandpass, biphase coded tapped delay line and pulse compression filter designs that, in general, meet electrical specification. The major exception to specification adherence has been with the VSWR parameter. During the course of this effort, a number of fabrication problems in orientation, dicing and packaging have been resolved. Work is now proceeding into the environmental and pilot line phases of the program.

Acknowledgments

The author wishes to express his appriciation to T. W. Bristol, W. R. Smith, and G. W. Judd for their efforts in design and test, and to L. Dyal for device fabrication. This work was performed under USAECOM contract No. DAAB07-75C-0044.

References

1. Contract #DAAB07-75C-0044 (Quarterly Report #1), USAECOM, Fort Monmouth, N.J.

2. Valpey-Fisher Corp., 75 South Street, Hopkington, MA 01748

3. Crystal Technology, Inc., 2510 Old Middlefield Way, Mountain View, California 94040

4. Slobodnik, A. J.; Conway, E. D.; and Delmonico, R. T., AFCRL - TR-73-0597, (1973)

5. Union Carbide Corp., 8888 Balboa Avenue, San Diego, California 92123

6. Electroglas Co., 2901 Coronado Drive, Santa Clara, California 95050

7. Tekform Co., 2770 Coronado Street, Anaheim, California 92806

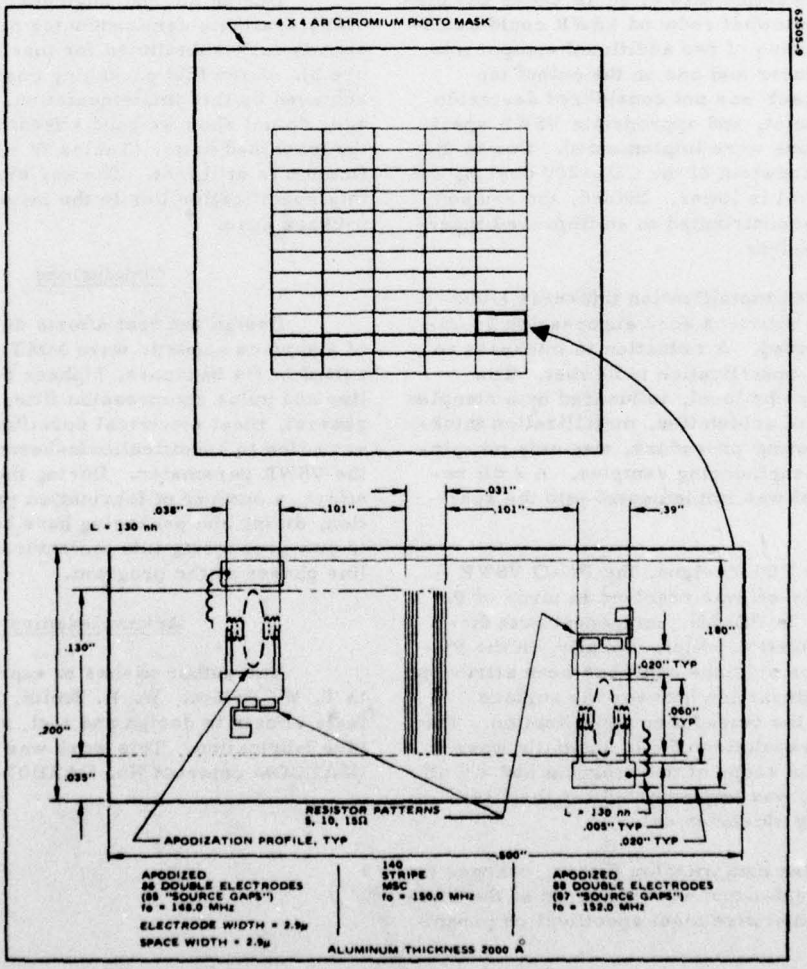

Figure 1 Typical Mask Layout

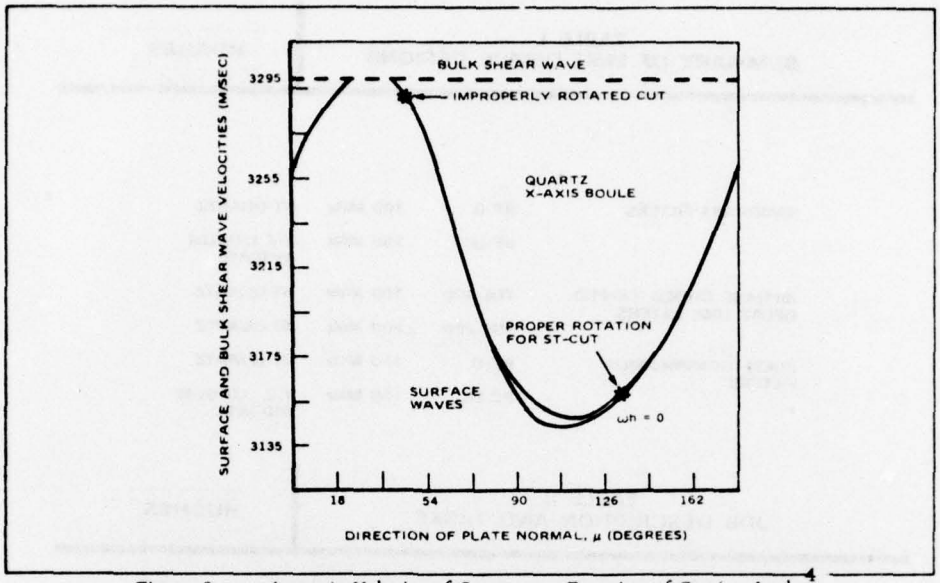

Figure 2. Acoustic Velocity of Quartz as a Function of Cutting Angle[4]

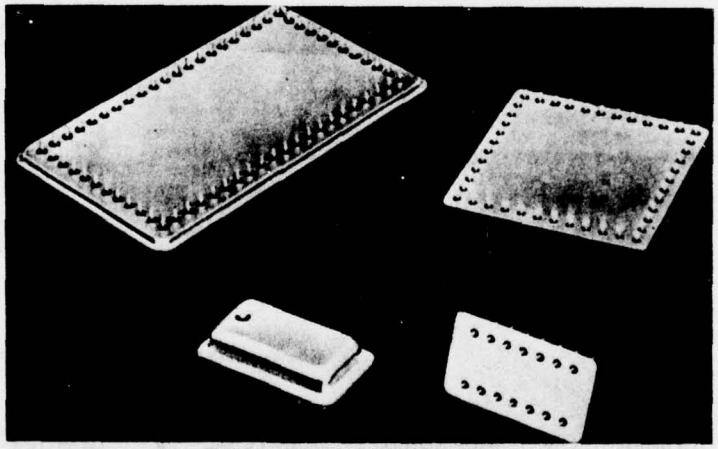

(a) TYPICAL SEMICONDUCTOR PIN PACKAGES

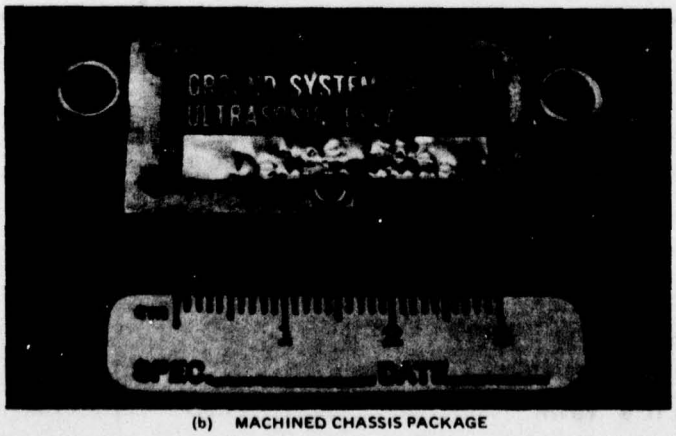

(b) MACHINED CHASSIS PACKAGE

Figure 3 Comparison of First and Second Engineering Phase Packaging

TABLE I
SUMMARY OF MMT DEVICE DESIGNS

HUGHES

BANDPASS FILTERS	BP-Q	100 MHz	ST-QUARTZ
	BP-LN	150 MHz	Y-Z LITHIUM NIOBATE
BIPHASE CODED TAPPED DELAY LINE FILTERS	TDL-100	100 MHz	ST-QUARTZ
	TDL-200	200 MHz	ST-QUARTZ
PULSE COMPRESSION FILTERS	PC-Q	150 MHz	ST-QUARTZ
	PC-LN	150 MHz	Y-Z LITHIUM NIOBATE

TABLE II
JOB DESCRIPTION AND TASKS

HUGHES

STEP I – PHASE I – FIRST ENGINEERING SAMPLES

- DESIGN SIX SAW DEVICES TO SPECIFICATION
- FAB, PACKAGE AND TEST DEVICE DESIGN
- DELIVER TEN EACH

PHASE II – SECOND ENGINEERING SAMPLES

- REDESIGN DEVICES AS NECESSARY
- FINALIZE ELECTRICAL SPECIFICATION
- DELIVER TEN EACH

PHASE III – CONFORMAL SAMPLES

- TEST DEVICES TO ENVIRONMENTAL SPECIFICATION
- FINALIZE ENVIRONMENTAL SPECIFICATION
- DELIVER FIFTY EACH

PHASE IV – PILOT RUN SAMPLES

- FINALIZE LINE
- ESTABLISH DEVICE COST
- DELIVER 150 EACH

STEP II

- DEVELOP PLAN FOR 500/MO. PRODUCTION RATE

COMPARISON OF MEASURED PARAMETERS AND SPECIFICATIONS FOR BP-Q FILTERS

HUGHES

	SCS-476	MEASURED
3.10.1 fo (MHz)	100 ± 2	100.2
3.10.2 β @ -3 dB (MHz)	2 ± 0.04	2.04
3.10.3 τ (μ SEC)	2 ± 0.01	1.995
3.10.4 $\tau \times \beta$	4	4
3.10.5 INSERTION LOSS (dB)	20 ± 2	22 ✓
3.10.6 SIDELOBE SUPP. (dB)	35	40
3.10.7 FEEDTHROUGH SUPP. (dB)	50	58
3.10.8 SPURIOUS SUPP. (dB)	35	43
3.10.9 VSWR	< 1.5:1	< 1.2:1

Table III

COMPARISON OF MEASURED PARAMETERS AND SPECIFICATIONS FOR BP-LN FILTER — HUGHES

	SCS-476	MEASURED
3.10.1 fo (MHz)	150 ± 3	150.0
3.10.2 β @ -3 dB (MHz)	30 ± 0.6	30.0
3.10.3 τ (μ SEC)	2 ± 0.01	2.00
3.10.4 τ X β	60	60
3.10.5 INSERTION LOSS (dB)	15 ± 1.5	21 ✓
3.10.6 SIDELOBE SUPP. (dB)	35	40
3.10.7 FEEDTHROUGH SUPP. (dB)	50	53
3.10.8 SPURIOUS SUPP. (dB)	35	39
3.10.9 VSWR	<1.5:1	<2.3:1 ✓

Table IV

COMPARISON OF MEASURED PARAMETERS AND SPECIFICATIONS FOR TDL-100 FILTER — HUGHES

	SCS-476	MEASURED
3.10.1 fo (MHz)	100 ± 2	100.0
3.10.2 β @ -3 dB (MHz)	10 ± 0.2	10.0
3.10.3 τ (μ SEC)	12.7	12.7
3.10.4 τ X β	127	127
3.10.5 INSERTION LOSS (dB)	30 ± 3	40 ✓
3.10.6 SIDELOBE SUPP. (dB)	19	15 TO 18 ✓
3.10.7 FEEDTHROUGH SUPP. (dB)	50	60
3.10.8 SPURIOUS SUPP. (dB)	35	28 ✓
3.10.9 VSWR	< 1.5:1	< 6:1 ✓

Table V

COMPARISON OF MEASURED PARAMETERS WITH SPECIFICATIONS FOR TDL-200 FILTER — HUGHES

	SCS-476	MEASURED
3.10.1 fo (MHz)	200 ± 4	200.1
3.10.2 β @ -3 dB (MHz)	10 ± 0.2	10.0
3.10.3 τ (μ SEC)	12.7	12.7
3.10.4 τ X β	127	127
3.10.5 INSERTION LOSS (dB)	30 ± 3	38 ✓
3.10.6 SIDELOBE SUPP. (dB)	18	16 TO 19 ✓
3.10.7 FEEDTHROUGH SUPP. (dB)	50	50
3.10.8 SPURIOUS SUPP. (dB)	35	34 ✓
3.10.9 VSWR	< 1.5:1	< 3.5:1 ✓

Table VI

COMPARISON OF MEASURED PARAMETERS TO SPECIFICATIONS FOR PC-Q FILTER — HUGHES

	SCS-476	MEASURED
3.10.1 fo (MHz)	150 ± 3	149.5
3.10.2 β (MHz)	50 ± 1	50.0
3.10.3 τ X (μ SEC)	2 ± 0.01	2
3.10.4 τ X β	100	100
3.10.5 INSERTION LOSS (dB)	55 ± 5	39 TO 48
3.10.6 SIDELOBE SUPP. (dB)	25	19 TO 28 ✓
3.10.7 FEEDTHROUGH SUPP. (dB)	50	70
3.10.8 SPURIOUS SUPP. (dB)	35	49
3.10.9 VSWR	< 1.5:1	< 2:1 ✓

Table VII

COMPARISON OF MEASURED PARAMETERS WITH SPECIFICATION FOR PC-LN FILTER — HUGHES

	SCS-476	MEASURED
3.10.1 fo (MHz)	150 ± 3	150
3.10.2 β (MHz)	50 ± 1	50
3.10.3 τ X (μ SEC)	2 ± 0.01	2
3.10.4 τ X β	100	100
3.10.5 INSERTION LOSS (dB)	30 ± 3	24 TO 28
3.10.6 SIDELOBE SUPP. (dB)	25	19 TO 28 ✓
3.10.7 FEEDTHROUGH SUPP. (dB)	50	65
3.10.8 SPURIOUS SUPP. (dB)	35	45
3.10.9 VSWR	< 1.5:1	< 10:1 ✓

Table VIII

COMPARISON OF MEASURED PARAMETERS AND SPECIFICATIONS FOR BP-Q FILTERS — PHASE II — HUGHES

	SCS-476	MEASURED
3.10.1 fo (MHz)	100 ± 2	100.2
3.10.2 β @ -3 dB (MHz)	2 ± 0.04	2.04
3.10.3 τ (μ SEC)	2 ± 0.01	1.995
3.10.4 τ X β	4	4
3.10.5 INSERTION LOSS (dB)	20 ± 2	~~22~~ 20
3.10.6 SIDELOBE SUPP. (dB)	35	40
3.10.7 FEEDTHROUGH SUPP. (dB)	50	~~58~~ 63
3.10.8 SPURIOUS SUPP. (dB)	35	43
3.10.9 VSWR	~~< 1.5:1~~ < 2:1	~~< 1.2:1~~ < 1.5:1

Table IX

COMPARISON OF MEASURED PARAMETERS AND SPECIFICATIONS FOR BP-LN FILTER — PHASE II

HUGHES

	SCS-476	MEASURED
3.10.1 fo (MHz)	150 ± 3	150.0
3.10.2 β @ -3 dB (MHz)	30 ± 0.6	30.0
3.10.3 τ (μ SEC)	2 ± 0.01	2.00
3.10.4 τ X β	60	60
3.10.5 INSERTION LOSS (dB)	~~15 ± 1.5~~ 20 ± 1.5	~~21~~ 20
3.10.6 SIDELOBE SUPP. (dB)	35	40
3.10.7 FEEDTHROUGH SUPP. (dB)	50	~~53~~ 60
3.10.8 SPURIOUS SUPP. (dB)	35	39
3.10.9 VSWR	~~< 1.5:1~~ < 3:1	< 2.3:1

Table X

COMPARISON OF MEASURED PARAMETERS AND SPECIFICATIONS FOR TDL-100 FILTER — PHASE II

HUGHES

3.10.1 fo (MHz)	100 ± 2	~~100.0~~ 100.1
3.10.2 β @ -3 dB (MHz)	10 ± 0.2	10.0
3.10.3 τ (μ SEC)	12.7	12.7
3.10.4 τ X β	127	127
3.10.5 INSERTION LOSS (dB)	~~30 ± 3~~ 27 ± 3	~~40~~ 27
3.10.6 SIDELOBE SUPP. (dB)	~~19~~ 17	~~15 TO 18~~ 20
3.10.7 FEEDTHROUGH SUPP. (dB)	50	~~60~~ 52
3.10.8 SPURIOUS SUPP. (dB)	35	~~28~~ 40
3.10.9 VSWR	~~< 1.5:1~~ < 4:1	~~< 6:1~~ < 3:1

Table XI

COMPARISON OF MEASURED PARAMETERS WITH SPECIFICATIONS FOR TDL-200 FILTER — PHASE II

HUGHES

	SCS-476	MEASURED
3.10.1 fo (MHz)	200 ± 4	200.1
3.10.2 β @ -3 dB (MHz)	10 ± 0.2	10.0
3.10.3 τ (μ SEC)	12.7	12.7
3.10.4 τ X β	127	127
3.10.5 INSERTION LOSS (dB)	~~30 ± 3~~ 26 ± 3	~~38~~ 26
3.10.6 SIDELOBE SUPP. (dB)	~~19~~ 17	~~16 TO 19~~ 20
3.10.7 FEEDTHROUGH SUPP. (dB)	50	50
3.10.8 SPURIOUS SUPP. (dB)	35	~~34~~ 40
3.10.9 VSWR	~~< 1.5:1~~ < 3:1	~~< 3.5:1~~ < 2.3:1

Table XII

COMPARISON OF MEASURED PARAMETERS TO SPECIFICATIONS FOR PC-Q FILTER — PHASE II

HUGHES

	SCS-476	MEASURED
3.10.1 fo (MHz)	150 ± 3	149.5
3.10.2 β (MHz)	50 ± 1	50.0
3.10.3 τ (μ SEC)	2 ± 0.01	2
3.10.4 τ X β	100	100
3.10.5 INSERTION LOSS (dB)	~~55 ± 5~~ 50 ± 5	~~39 TO 48~~ 50
3.10.6 SIDELOBE SUPP. (dB)	25	~~19 TO 28~~ 30
3.10.7 FEEDTHROUGH SUPP. (dB)	50	~~70~~ 52
3.10.8 SPURIOUS SUPP. (dB)	35	49
3.10.9 VSWR	~~< 1.5:1~~ < 2.5:1	< 2:1

Table XIII

COMPARISON OF MEASURED PARAMETERS WITH SPECIFICATION FOR PC-LN FILTER — PHASE II

HUGHES

	SCS-476	MEASURED
3.10.1 fo (MHz)	150 ± 3	150
3.10.2 β (MHz)	50 ± 1	50
3.10.3 τ (μ SEC)	2 ± 0.01	2
3.10.4 τ X β	100	100
3.10.5 INSERTION LOSS (dB)	30 ± 3	~~24 TO 28~~ 30
3.10.6 SIDELOBE SUPP. (dB)	25*	~~19 TO 28~~ 25*
3.10.7 FEEDTHROUGH SUPP. (dB)	50	~~65~~ 52
3.10.8 SPURIOUS SUPP. (dB)	35	45
3.10.9 VSWR	~~< 1.5:1~~ < 3.5:1	~~< 10:1~~ < 2.5:1

*20 dB FOR 1ST LEADING AND TRAILING SIDELOBES ONLY

Table XIV

ANALYSIS OF TUNING FORK CRYSTAL UNITS AND APPLICATION INTO ELECTRONIC WRIST WATCHES

S. Kanbayashi, S. Okano, K. Hirama & T. Kudama
Toyo Communication Equipment Co., Ltd.
Kawasaki-city, Kanagawa Pref. Japan

and

M. Konno & Y. Tomikawa
Faculty of Engineering, Yamagata University
Yonezawa-city, Yamagata Pref. Japan

Summary

In order to standardize the design method of tuning fork crystal unit, the resonance frequencies, displacement and stress distribution are analized by finite element method. From the results of these analysis, further investigation was executed, and an ultraminiature tuning fork crystal unit (32.768 kHz) has been manufactured. Statistical data of the crystal unit in actual production line are introduced here.

Introduction

Most electronic wrist watches manufactured worldwide at present employ crystal units vibrating at 32.768 kHz (2^{15}). The crystal units are designed in two different types; free free bar and tuning fork, both in flexure vibration mode. At the preceding symposium on frequency control, unique reports [1]~[6] were presented concerning electrical performances and manufacturing technologies of these two types. We aimed to manufacture XY flexure tuning fork crystal units excelling in shock and vibration-resistivity and other performance characteristics. At that time, however, we could hardly find results of theoretical analysis published for this mode of vibration. Therefore, we decided to use the finite element method of simulation. This paper presents results of our analysis, and the statistical data of tuning fork crystal units manufactured on the basis of the analytical results.

Finite element simulation of tuning fork crystal units

Conventionally, the tuning fork crystal unit has been regarded as a kind of cantilever vibrating in flexure vibration mode and been analized only in a simple way. In the actual design, however, detail information is necessary about dimensional varieties of crystal blanks, electrical influences of supporting and other actual manufacturing considerations. First, for obtaining the design guidelines, we have calculated resonance frequencies and displacement and stress distributions by the finite element method.

Method of analysis

Crystal blanks to be analized were prepared from a Z-plate at the cut angle +2° about the x-axis. The size of the specimen is shown in Fig. 1. Electrodes were arranged to induce electrical fields at arm portions which have opposite phases and excite vibrations in the xy plane (Fig. 2). For the analysis by the finite element method, the crystal blank was devided into 64 rectangular elements in the arm portion and 80 rectagular elements in the base portion as shown in Fig. 3. The calculation was executed by a computer CDC-6600 employing a program of QDMEM1 (MSC/NASTRAN)[7]. The piezoelectricity of the specimen was ignored and the elastic constants shown in Table 1 were used.

Definition

Length of base : Represented by "h"

Symmetrical crystal blank : A crystal blank having arms of equal lengths (ℓo) and equal widths (do)

Unsymmetrical crystal blank : A crystal blank having arms of different lengths and/or widths. The lengths are identified by $\ell 1$ and $\ell 2$, and the widths by d1 and d2.

Free vibration : Vibration of the crystal blank not supported

Clamped vibration : *Vibration of the crystal blank clamped at bottom*

Fof : Resonance frequency of free vibration

Foc : Resonance frequency of clamped vibration

$\Delta Fcf : \dfrac{Foc-Fof}{Foc}$

Symmetrical Crystal Blanks

In order to evaluate the influences of supporting, we calculated resonance frequencies and displacement and stress distributions under extreme conditions, free vibration and clamped vibration. Resonance frequencies were calculated for h/do = 1, 2, 3, 4, 5, 6, 7 with the results as shown in Table 2 and Fig. 4. It is seen from Fig. 4 that for $h/do < 3$ the difference between Fof and Foc is large, that is, this range of dimensions has large influences of supporting. For $h/do \geq 3$ Fcf is smaller than 10ppm indicating that, when the arrangement of arms is sufficiently symmetrical, there is little influence of supporting. As to displacement distributions, the base displacement for h/do = 1, 2, 3, 4, 5, 6 only was calculated with the results as shown in Fig. 5. For this figure, it is assumed that the displacement at the upper-end of the arm is 1. In the shaded area, the x-direction and/or y-direction displacement are larger than $|2.5 \times 10^{-3}|$ and in the other areas, both displacements are smaller than $|2.5 \times 10^{-3}|$.
It is seen from Fig. 5 that for $h/do \geq 4$ there is little displacement of the base portion in the case of free vibration. Moreover, there is no significant difference in displacement distribution between free and clamped vibration. In short, for $h/do \geq 4$, the influence of clamping is negligible.
Stress distributions for h/do = 1 and h/do = 4 are shown in Fig. 6. Arrows in this figure represent the magnitude and distribution of principal stresses (Because of symmetrical patterns, arrows in the other half are omitted.)

It follows roughly from this figure that for h/do = 1 a difference in stress distribution is seen between free vibration and clamped vibration, but for h/do = 4, this difference is practically negligible. Moreover, it is seen that the stress concentration is not limited to the arm of the tuning fork but extends to the base.

Unsymmetrical Crystal Blanks

In practice, crystal blanks have necessarily unsymmetrical dimensions by the influence of fabricating precision, and therefore, we have to examine the characteristics of the unsymmetrical crystal blanks as well. Noting the findings with symmetrical crystal blanks that for h/do ≧ 4 there is little influence of support, we selected the case of h/do = 4 for calculating the behavior of the unsymmetrical crystal blanks. Resonance frequencies were calculated for h/do = 4, and 1) (d1-d2)/do = 3%, 2) (d1-d2)/do = 6% and 3) $(f_1-f_2)/f_o$ = 1.3% with the results as shown in Table 3. The ratio difference in resonance frequency between free vibration and clamped vibration, ΔFcf, is shown in Fig. 7. It is seen from this figure that by the influence of unsymmetrical arms the difference in resonance frequency is large indicating that these dimensions bring about large influences of support. Displacement distributions also were calculated under the same dimmensional conditions as above with the results as shown in the same manner as in the case of symmetrical crystal blanks. (Fig. 8). As the symmetricity of arms is lost, displacements at the bottom in free vibration become large, increasing significantly in the difference from those in the case of the clamped bottom.
From these results and those of the calculation of the rate of frequency change mentioned above, it is found that the unsymmetricity of arms should be minimized as far as possible.

Consideration

Shock-resistivity and aging

The free free bar has nodal points and usually, it is supported at these points. Each nodal point is a single point which is stressed to a considerable degree. (Fig. 9). In practice, however, supporting requires some area which extend to the portions of large displacements and thereby interfares with vibration of a crystal blank. This means that rigid supporting can not be done and the shock-resistivity is low; or rigid soldering, if done, resulting in small Q and large variation of temperature characteristic. The tuning fork crystal blank has little displacement and stress at the base of this crystal blank as shown by the analysis. This means that rigid soldering can be done and the shock-resistivity is high. Especially in the case of a symmetrical tuning fork, the difference in the resonance frequency between free vibration and clamped vibration is less than 10ppm and this is a strong support to the statement given above. The tuning fork crystal unit is advantageous even in respect of the aging-performance over the free free bar crystal unit, because the former can be clamped at the bottom which is little stressed.

Second harmonics

The free free bar has different nodal points for the fundamental mode and the higher modes, and if the crystal unit is clamped at the nodal point in the fundamental mode, higher modes are suppressed automatically. In the tuning fork crystal unit, higher harmonics are quite free and are easily excited.

Especially, in the 32.768 kHz tuning fork crystal unit, about six times the fundamental frequency, that is, 190 kHz (second harmonics) is easily excited if the load capacitance CL is small. Therefore, referring to the stress distribution of the cantilever shown in Fig. 9, we experimentally investigated the relation between electrode arrangement in the arm portion and the resonance resistance of the second harmonics, for designing the electrode arrangement which is free from excitation of the second harmonics.

Electrical characteristics

A 32.768 kHz tuning fork crystal unit was manufactured referring to the theoretical analysis explained above. An outline of this crystal unit is as follows:

Holder size (Fig. 10) : 3φ x 8 mm (I.E.C. Recommendation No. 49)

Blank size : Width = 1.37 mm
Thickness = 0.5 mm
Length = 6.2 mm
h/do = 4.2

Cut angle : +2°

Support (Fig. 11) : Direct clamping at the bottom by high temperature solder

Electrical equivalent circuit parameters

An electrical equivalent circuit of the 32.768 kHz tuning fork crystal unit is shown in Fig. 12. The measurement was made at room temperature at all times. Distributions of R1 and Q of 500 specimens are shown in Fig. 13 and Fig. 14. The typical value of R1 is so small as 11kΩ that the power consumption of the crystal unit can be small. The typical values of Co and Co/C1 are 1.7pF and 540, respectively, both being almost equal to those of the XY free free bar. Fig. 15 shows the load capacitance characteristics of typical crystal units. It follows from this figure that the frequency change rate at the load capacitance of 12pF (in the most common use for wrist watches) is -8.2ppm/pF.

Spurious response of second harmonics

As seen in Fig. 16, the series resonance resistance in the second mode is higher than about four times that in the fundamental mode. It has been confirmed that under these conditions second harmonics oscillations can be suppressed adequately.

Frequency temperature characteristics

The temperature characteristic of the XY tuning fork crystal unit can be approximated by a parabolic curve which can be determined completely by the turnover temperature and parabolic constant.
Fig. 17 and Fig. 18 show histograms of turnover temperature and parabolic constant distributions. The spreads of these distributions are smaller in general than XY free free bars probably because the supporting method employed in the tuning fork crystal unit is superior to that in the free free bar crystal unit.

Shock and vibration-resistivity

For the shock-resistivity test, crystal units were dropped three times from the height of 750mm onto a hard wooden board of thickness 25mm; and frequency shifts measured before and after the drops are shown in Fig. 19. There is a tendency that the frequency is changed to the minus side by the drop test, but its shift is less than 3ppm.

For the vibration-resistivity test, crystal units were subjected to continuous vibration within the frequency range of 10 ~ 55 Hz continuously varied and having a double amplitude of 0.7mm in cycle of two minutes for 40 minutes in each of x, y and z directions. The frequency shifts by this test are shown in Fig. 20.

Aging characteristic

Fig. 21 shows a typical aging curve, together with a histogram of frequency change distributions of 30 specimens measured at the room temperature for one year. It is seen from this figure that all the specimens fall within the range of ±3 ppm/year. Moreover, frequency changes with storage at -30°C and +85°C for 500 hours were measured. As shown in Fig. 22, the frequency change with the -30°C storage is almost linear and is small, while the frequency change with the +85°C storage is initially negative but becomes positive with the lapse of time. The probable causes for the phenomenon in the high temperature storage test are the relief of strains developed in the blank and the sorption or desorption of gases at high temperatures, the reaction will be rapid resulting in large frequency changes.

Heat cycle

Ten heat cycles of -30°C (30 minutes) → +25°C (15 minutes) → +85°C (30 minutes) → +25°C (15 minutes) → -30°C (30 minutes) each were repeated. The frequency differences before and after this test are shown in Fig. 23. All specimen fall within the range of ±2 ppm.

Heat shock by soldering

Fig. 24 shows frequency and series resonance resistance changes of 20 specimens subjected to 5 second immersion in a soldering bath at 280°C. It is seen in this figure that the crystal unit is little affected by the soldering.

Conclusions

(1) In the manufacturing of tuning fork crystal units for wrist watches, the finite element method was used for the analysis of tuning fork vibration. By this analysis, information about bottom dimensions, influences of supporting, electrode arrangement, and the importance of arm symmetricity was obtained.

(2) Based on the results of the analysis mentioned above, it was made possible to manufacture those tuning fork crystal units having excellent charactristics such as series resonance resistance, capacitance ratio, temperature characteristics, shock and vibration-resistivity, aging, etc.

(3) The use of these crystal units in wrist watches is advantageous in respect of current consumption, frequency adjustment, shock and vibration-resistivity, suppression of second mode vibration, etc.

References

(1) Max P. Forrer
"A Flexure-Mode Quartz for an Electronic Wrist Watch"
The 23rd Frequency Control Symposium ('69)

(2) F.H. Musa and R.G. Daniels
"The Crystal Controlled Electronic Watch System"
The 25th Frequency Control Symposium ('71)

(3) Hiroshi Yoda, Hiroo Ikeda and Yasuyuki Yamabe
"Low Power Crystal Oscillation for Electric Wrist Watch"
The 26th Frequency Control Symposium ('72)

(4) M. Onoe, T. Shinada, K. Itoh and S. Miyazaki
"Low Frequency Resonators of Lithium Tantalate"
The 27th Frequency Control Symposium ('73)

(5) Juergen H. Staudte
"Subminiature Quartz Tuning Fork Resonator"
The 27th Frequency Control Symposium ('73)

(6) Jean Engdahl and Hubert Matthey
"32 kHz Quartz Crystal Unit for High Precision Wrist Watch"
The 29th Frequency Control Symposium ('75)

(7) R.H. Mac Neal
"The NASTRAN Theoretical Manual" Level 15.5, Suppliment, NASA, SP-221(01), P5.8-33, National Aeronautics and Space Administration, (1972-121)

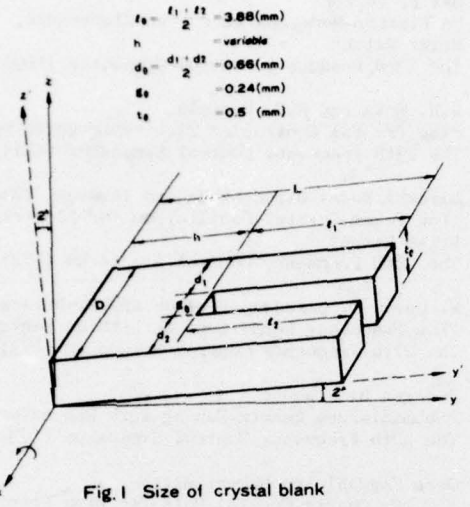

Fig. 1 Size of crystal blank

Young's modulus	$E(=C'_{22})$	$=8.9453\times10^{11}(g\cdot mm/sec^2\cdot mm^2)$
density	ρ	$=2.6487\times10^{-3}(g/mm^3)$
Poisson's ratio	$\sigma\left(=\frac{S'_{12}}{S'_{11}}\right)$	$=0.122894$

Table 1. Module table

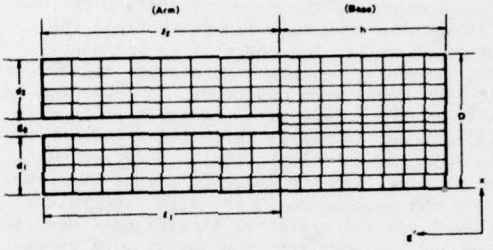

Fig.3 Element partition

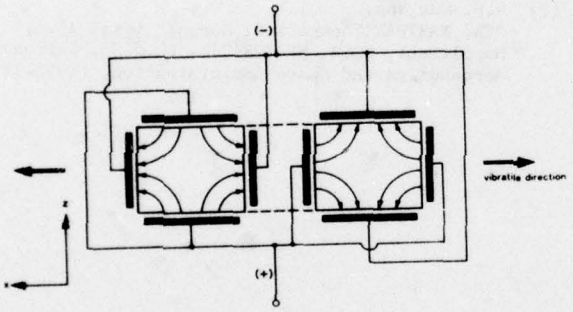

Fig.2 Connection of electrodes

h d_0	h(mm)	F_{of}(kHz)	F_{oc}(kHz)	$\Delta F_{cf} = \frac{F_{oc} - F_{of}}{F_{oc}}$ (PPM)
1	0.66	31.33814	34.24045	+84763.5
2	1.32	33.69518	33.74751	+ 1550.6
3	1.98	33.82417	33.82446	+ 8.6
4	2.64	33.92837	33.92818	− 5.6
5	3.30	34.03714	34.03693	− 6.2
6	3.96	34.14698	34.14688	− 2.9
7	4.62	34.25530	34.25546	+ 4.7

Table 2. Resonacs frequency of symmetrical crystal blank

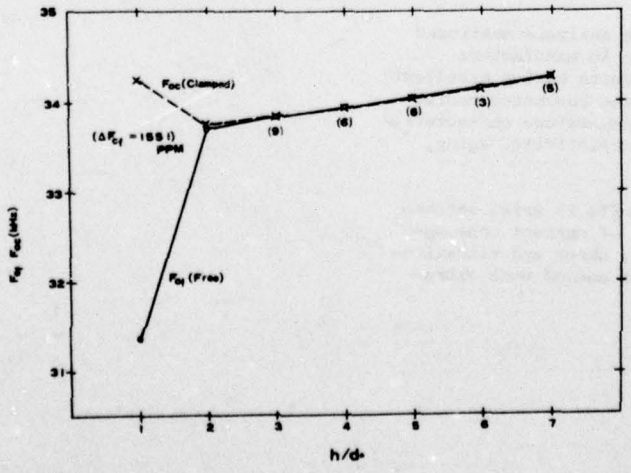

Fig.4 Resonace frequeney vs base length

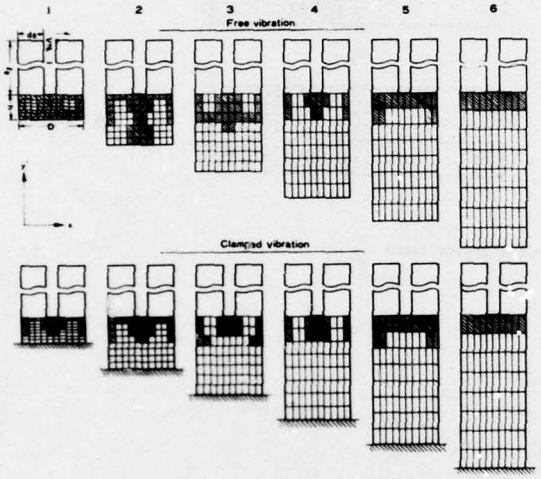

Fig.5 Displacement distribution of symmetrical crystal blank

h/d₀	$\frac{d_1-d_2}{d_0}$ (%)	$\frac{\ell_1-\ell_2}{\ell_0}$ (%)	F_{of}(kHz)	F_{oc}(kHz)	$\Delta F_{cf}=\frac{F_{oc}-F_{of}}{F_{oc}}$ (PPM)
4	0	0	33.92837	33.92818	− 6
	3.0	0	33.95616	33.97882	+ 668
	6.0	0	33.86158	33.93535	+2174
	0	1.3	33.92961	33.94531	+ 463

Table 3. Resonance frequency of unsymmetrical crystal blanks

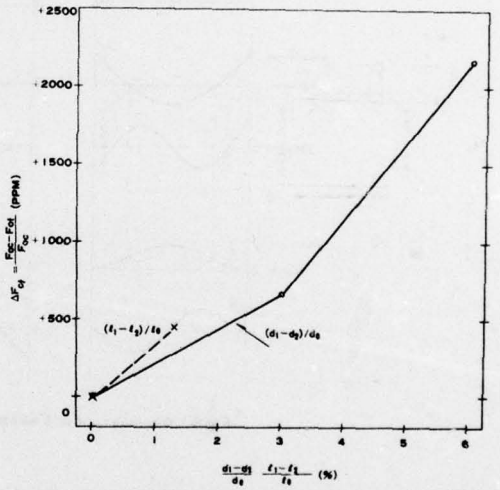

Fig.7 Frequency difference ratio vs unsymmetricity

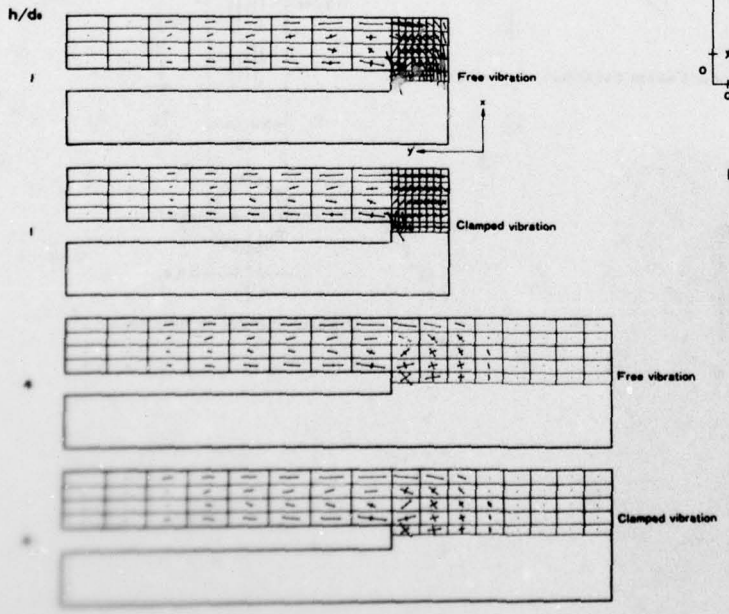

Fig.8 Stress distribution of symmetrical crystal blanks

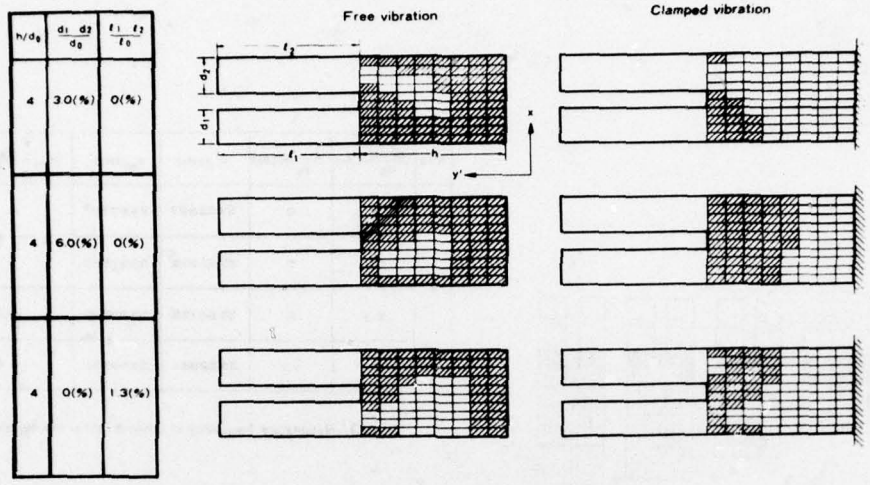

Fig.8 Displacement distribution of unsymmetrical crystal blank

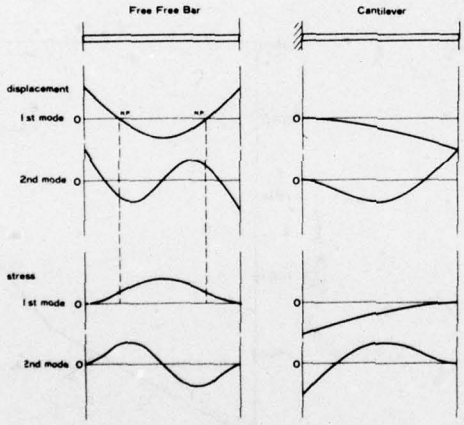

Fig.9 Displacement and stress distribution

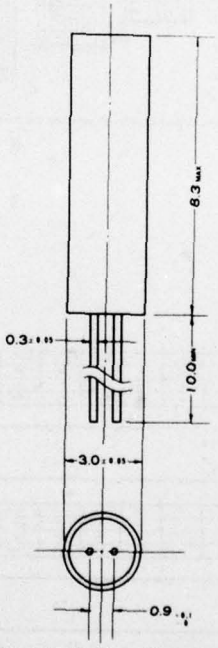

Fig.10 Holder dimension

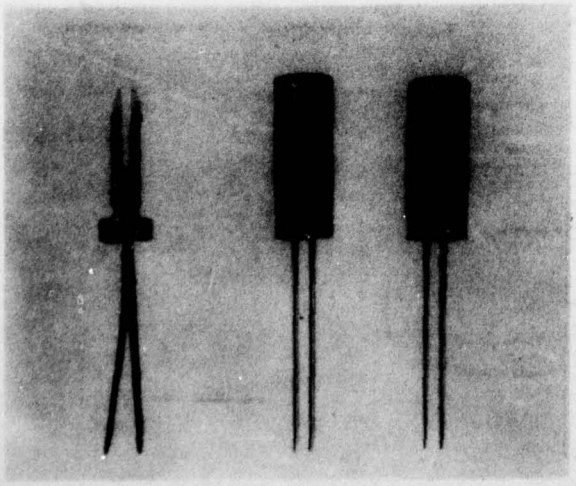

Fig. 11 Inner and outer view of tuning fork resonator

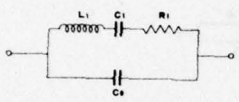

Fig.12 Electrical equivalent circuit

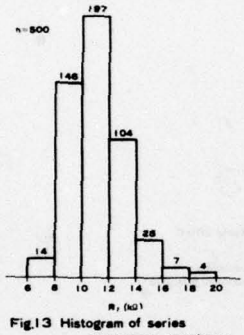

Fig.13 Histogram of series resonance resistance

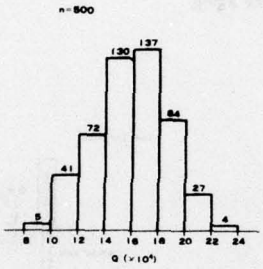

Fig.14 Histogram of quality factor

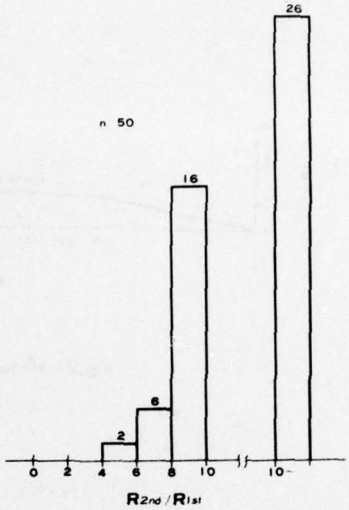

Fig.16 Histogram of spurious response ratio

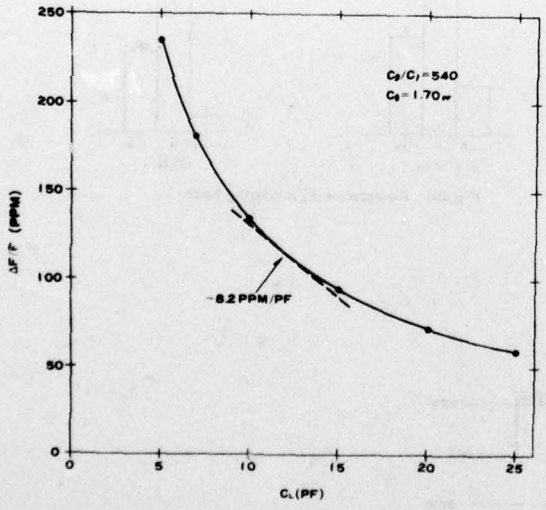

Fig.15 Load capacitance characteristics

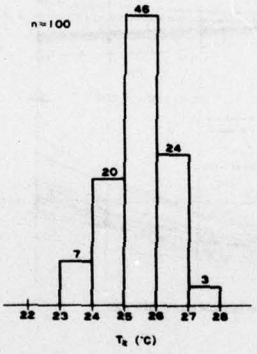

Fig.17 Histogram of turnover temperature

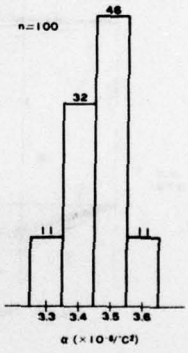

Fig.18 Histogram of paraboric constant

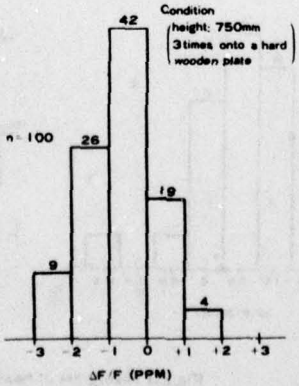

Fig.19 Schok resistivity

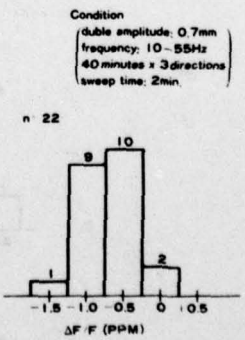

Fig.20 Vibration resistivity

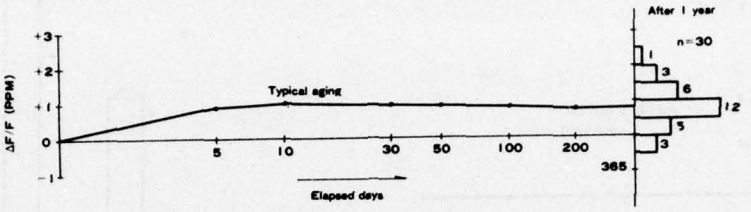

Fig.21 Histogram of frequency aging

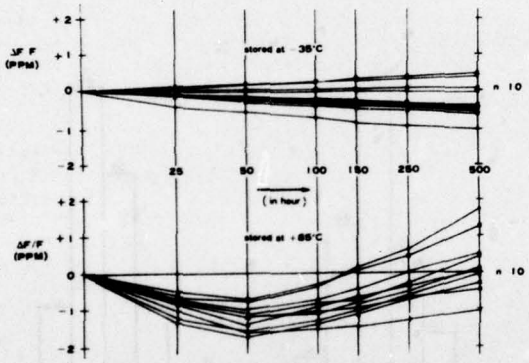

Fig.22 High and low temperature storage

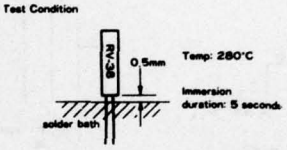

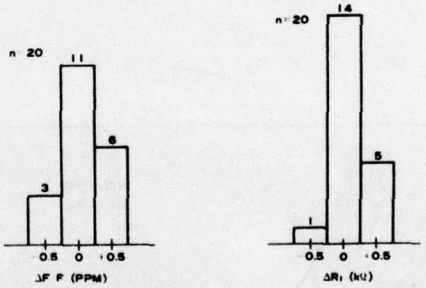

Fig.24 Resistance to soldering heat

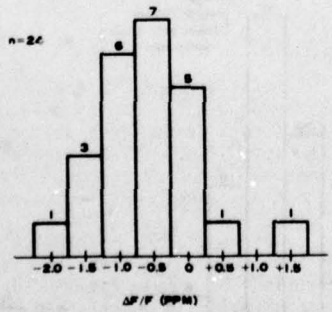

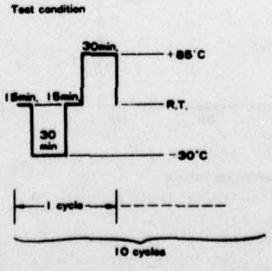

Fig.23 Histogram of heat cycle

ANALYTICAL AND EXPERIMENTAL INVESTIGATIONS OF 32KHz QUARTZ TUNING FORKS

J. A. Kusters, C. A. Adams & H. E. Karrer
Hewlett-Packard Labs
Palo Alto, California

and

R. W. Ward
Litronix Corporation
Santa Clara, California

Summary

The quartz tuning fork, operating at 32,768 Hz, and fabricated using planar integrated circuit technology, has been shown by Staudte[1] to be a precise time base for quartz crystal watches. The tuning fork configuration typically has better long-term stability, less susceptibility to shock and vibration, and occupies less volume than a comparable flexure bar.

Recent work at HP has concentrated on theoretical analysis of tuning fork behavior, and mounting, etch techniques, and orientational dependence of fork parameters.

Initial theoretical analysis concentrated on predicting the frequency and temperature performance of simple flexure bars such as +5° X-cut and NT cuts. Following excellent theoretical agreement with the flexure bars, an attempt was made to synthesize a tuning fork model using sections of such simple bars. Correlation between predicted and observed frequency was satisfactory. Agreement with observed temperature behavior was generally poor.

Concurrent with the theoretical work, experiments were run on a magnetically driven steel model of a tuning fork to gain insight on possible mounting techniques and dependence of Q on mount location.

Many 1.5 mil thick quartz wafers were fabricated at various orientations. After pattern definition and exposure, the wafers were etched using a variety of techniques including ammonium biflouride chemical etching, and plasma etching. After mounting, vacuum baking, sealing, and backfilling to 50 μ of He, the temperature performance and equivalent circuit parameters of all units were measured.

Typically, the plasma-etched units exhibit more consistent behavior and generally higher Q than chemical-etched units at the same orientation.

All units show a strong orientational dependence on drive level, with certain orientations showing an anomalous drive-level dependence similar to that of a highly over-driven AT resonator, but with a drive level less than 0.2 μ watt.

Introduction

Tuning forks were first made of crystalline quartz by Koga[2] in 1928. This was a 1000 Hz device and had proportions similar to classical metal tuning forks. Later, Mason[3] described a planar tuning fork where the tines are very thin compared to the tine width. This design operated up to 10 kHz and had the advantage that the frequency depended primarily on the tine width and length.

All quartz tuning forks rely on a piezoelectrically excited extentional motion to drive a flexure motion in a bar (i.e., the tine). Yoda[4] has described the tuning fork as a traditional linear free-free flexure bar which has been bent in-half. The two nodes of the flexure bar then move down to the base of the resulting tuning fork.

One critical problem has been the fabrication of tuning forks to operate at high frequency. This was solved by Staudte[1] who used planar integrated circuit technology and photolithographic techniques to etch the forks from 1 mil thick quartz wafers. He described tuning forks operating at 32.768 kHz with Q's of 70,000, equivalent series resistance of 300 kΩ, and a second-order frequency/temperature coefficient of 40 x $10^{-9}/°C^2$.

As part of our continuing interest in quartz resonators, we investigated the properties of the quartz tuning fork as a possible time base for small, hand-held instruments. The program involved a theoretical study of tuning fork behavior concurrently with experimental work on mounting, etching, and crystal parameter measurements.

Theoretical

Background

Initial attempts in analyzing tuning fork behavior centered on simple, empirically derived expressions[5] of the fork's frequency dependence on the geometry of the fork tine. It was apparent that due to the anisotropy of quartz and the complex acoustic activity of the tine, these models were not adequate.

As a result, the theoretical study was divided into two areas. The first involved deriving suitable expressions of simple flexure bar behavior useful for any orientation in quartz, and for any geometry. From this, using simple flexure bar sections and matching boundary conditions, an attempt was made to synthesize a tuning fork model which would have utility in predicting fork behavior.

Simple Bar Analysis

The analysis of a simple free-free flexure bar is an extension of the work of Mindlin[6] and Lee[7]. The full details are given in the Appendix. The key point in the analysis is that instead of choosing bar orientations for which the set of 5 coupled differential equations separate into sets where closed form solutions exist, we allowed computer generated solutions to be sought for any orientation. As a result, each solution generally involved to some degree, contributions from each of the five acoustic modes allowed, flexure, length-extension, face-shear, thickness-shear, and thickness-twist.

To test the validity of the model, a comparison was made between the theoretical solutions found and the data presented by Mason and Sykes[8] on the +5° X-cut operating in the flexure mode, and a 0° X, 50° Y' NT flexure bar. Solutions were found as a function of the width-to-length ratio. In each case, no difference is observed in the frequency vs. width-length ratio plots between the model and the Mason data. As a further check, the first-order temperature coefficient for the two cases was also calculated. The comparisons are shown in Figure 1. In each case, the sign and magnitude agree quite closely. The remaining small discrepancy is most probably due to truncation of the model to displacements through 2nd order, and strain through 1st order, and not allowing coupling to elastic modes of higher order.

The model was also checked against experimental data obtained from other NT-type flexure bars. In every case, frequency agreement was excellent, and first-order temperature coefficient agreement was quite good.

Tuning Fork Synthesis

Once a satisfactory flexure bar model had been derived, a natural step was to use this model to synthesize a model of the tuning fork. An analysis by Schwarz[9] of the eigenfrequencies of isotropic tuning forks was used as a starting point. In this model, the tuning fork is viewed as a composite of straight bar sections as shown in Figure 2. Each section is assumed to operate only in flexure and length-extensional modes. As a result, the differential equations governing the individual section can be written as:

$$w''''(x) - \lambda^4 w(x) = 0 \tag{1}$$

$$v''(x) + \mu^2 v(x) = 0 \tag{2}$$

where λ and μ are the wave numbers derived from the simple bar model of the flexure and extensional modes respectively, and higher order effects such as rotary inertia are ignored.

By making the substitutions shown, Equations (1) and (2) can be written in matrix form as:

$$\begin{bmatrix} w_1 \\ w_1' \\ w_1'' \\ w_1''' \\ v_1 \\ v_1' \end{bmatrix} = \begin{bmatrix} C & S & c & s & 0 & 0 \\ \lambda^4 s & C & S & c & 0 & 0 \\ \lambda^4 c & \lambda^4 s & C & S & 0 & 0 \\ \lambda^4 S & \lambda^4 c & \lambda^4 s & C & 0 & 0 \\ 0 & 0 & 0 & 0 & CU & SU/\mu \\ 0 & 0 & 0 & 0 & -\mu SU & CU \end{bmatrix} \begin{bmatrix} w_0 \\ w_0' \\ w_0'' \\ w_0''' \\ v_0 \\ v_0' \end{bmatrix} \tag{3}$$

where:

$$\begin{aligned} C = C(\lambda x) &= [\cosh(\lambda x) + \cos(\lambda x)]/2 \\ S = S(\lambda x) &= [\sinh(\lambda x) + \sin(\lambda x)]/2\lambda \\ c = c(\lambda x) &= [\cosh(\lambda x) - \cos(\lambda x)]/2\lambda^2 \\ s = s(\lambda x) &= [\sinh(\lambda x) - \sin(\lambda x)]/2\lambda^3 \\ CU = CU(\mu x) &= \cos(\mu x) \end{aligned} \tag{4}$$

and $SU = SU(\mu x) = \sin(\mu x)$.

The derivatives w' ', w''', and v' in (3) can be replaced by their mechanical equivalents of the bending moment M, the shear force Q and the normal force N by taking into account the following relationships:

$$M(x) = -\frac{\beta}{\lambda_4} w''(x)$$

$$Q(x) = -\frac{\beta}{\lambda_4} w'''(x) \tag{5}$$

and

$$N(x) = \frac{\beta}{\mu} v'(x)$$

where $\beta = \omega^2 \rho A$, and where ω, ρ, and A are the circular frequency, the density, and the cross-sectional area respectively. By making the appropriate substitution and introducing state vectors Z_0 and Z_1 and the transfer matrix F, we obtain:

$$Z_1 = F Z_0 \tag{6}$$

where $Z = (w, w', M, Q, v, N)^t$. The importance of this notation is that at a free end, M, Q, and N vanish, whereas, at a clamped end, w, w', and v vanish.

In the corners of Figure 2, each bar section connects to its nearest neighbor at a small angle θ. Under the assumption of a rigid connection of the two bars, it is evident that the displacements w and v, and the shear forces Q and normal forces N are transformed by an orthogonal substitution, whereas the derivative w' and the bending moment M must remain unchanged. Therefore, we can define a transformation between the Z_i state vector and the Z_{i+1} state vector as:

$$Z_{i+1} = K Z_i \tag{7}$$

where K is a nodal matrix and is given by:

$$\begin{bmatrix} \cos\theta & 0 & 0 & 0 & -\sin\theta & 0 \\ 0 & 1 & 0 & 0 & 0 & 0 \\ 0 & 0 & 1 & 0 & 0 & 0 \\ 0 & 0 & 0 & \cos\theta & 0 & -\sin\theta \\ \sin\theta & 0 & 0 & 0 & \cos\theta & 0 \\ 0 & 0 & 0 & \sin\theta & 0 & \cos\theta \end{bmatrix} \tag{8}$$

By means of the transfer and nodal matrices, it is now possible to state the following linear relationship between the state vector Z_n at the end of the last bar section, and the state vector Z_0 at the beginning of the first section:

$$Z_n = F_n K_{n-1} F_{n-1} \cdots F_2 K_1 F_1 Z_0 \tag{9}$$

Formally, we have the linear transformation:

$$Z_n = P Z_0 \tag{10}$$

where the matrix P depends on the geometry of the synthesized tuning fork and can be computed numerically for any value of the circular frequency (ω).

The resonant frequency of the composite fork may now be determined by taking into account the boundary conditions at the free ends of the tines. Therefore, (10) becomes:

$$\begin{bmatrix} w_n \\ w'_n \\ 0 \\ 0 \\ v_n \\ 0 \end{bmatrix} = P \begin{bmatrix} w_0 \\ w'_0 \\ 0 \\ 0 \\ v_0 \\ 0 \end{bmatrix} \qquad (11)$$

Hence, there exists a subset of (11) for which:

$$\begin{bmatrix} 0 \\ 0 \\ 0 \end{bmatrix} = P_s \begin{bmatrix} w_o \\ w'_o \\ v_o \end{bmatrix} \qquad (12)$$

A necessary condition that a non-trivial solution exists for (12) requires that det $P_s = 0$. The frequencies for which this condition is fulfilled are the resonant frequencies of the composite fork structure.

During the experimental work to be reported later, this model was checked against measurements made on a variety of quartz tuning forks with differing geometry and crystallographic orientation. The resonant frequency predicted by the model was invariably five per cent low when compared to the experimental data. More importantly, the frequency derivatives, with respect to the various fork parameters proved to be quite accurate and useful in determining new designs and orientations. The value of derivative information becomes apparent when one realizes that there are seven degrees of freedom available in the tuning fork design, the three orientational angles, the tine length, width, and thickness, and the tine gap width. With the exception of the tine thickness, a change in any of these can significantly affect the tuning fork performance.

The original goal for the development of the model was to use the computer as a tool for seeking orientations which had a zero first-order and minimum second-order temperature coefficients of frequency at 25°C. Thus the model was used to predict expected temperature coefficients as a function of geometry and orientation. As will be shown later, the results are generally quite poor. As a result , the utility of the model was substantially diminished.

The failure of the composite fork model is most probably due to several simplistic assumptions made in the analysis. The effect of the tuning fork stem on its acoustic behavior was ignored. Mass loading due to the electrode patterns was neglected. In addition, all higher order corrections, such as rotary inertia, were not included in the differential equations for the individual sections.

At this stage in our investigation, it was apparent from the experimental data that suitable orientations existed, if at all, only in a rather small region about that described by Staudte[10]. As a result, except for the derivative data mentioned previously, further work on a theoretical model of a tuning fork was stopped.

Mounting

As part of the experimental program, the influence of the mounting structure and its location on the resonator Q and frequency was studied.

When a tuning fork is vibrating in its fundamental acoustic mode, characterized by the tines moving in opposition in the plane of the fork, the region around the bottom of the fork gap, or crotch, experiences a large local particle motion. As one moves further from the crotch, the amount of elastic energy present in the fork stem decreases. A long stem can be rigidly clamped at its base with little effect on the Q or vibrational frequency. However, if the fork is rigidly clamped near the crotch, the Q of the fork will drop due to elastic losses in the base, and the frequency of the fork will be altered due to changes in effective elastic constants near the crotch.

Ideally, a tuning fork is mounted rigidly in such a way that Q is not degraded and no frequency effects are noted. However, if the base is clamped too far from the crotch, the effective cantilever becomes too long and shock and vibration vulnerability increases.

Steel Model

In evaluating mount location, a moveable mount is desirable. Because of the rather small size of the 32 kHz quartz tuning fork, a stainless steel model resonant at 1460 Hz was constructed. The steel unit had the same dimensional ratios as a standard quartz tuning fork. The model was placed in a mount whose location could be easily varied. The assembly was then placed in a vacuum chamber to reduce the influence of air damping on the fork performance. The steel fork was driven magnetically with driving coils on either side of the fork. A light emitting diode and photo detector pair were positioned at a tine edge to determine the relative magnitude of the tine displacement. The experimental device is shown in Figure 3.

For each position of the mount, the fork was driven magnetically and the frequency varied until the detector indicated that a steady-state resonance had been achieved. The drive was then turned off, and the resonator Q determined by the decrement method. The resultant data, plotted as a function of the length-to-width ratio, is shown in Figure 4. The data shows a significant drop in Q and an abrupt shift in the resonant frequency at certain discrete, repeatable mount locations. Further investigation showed the existance of an unwanted transverse longitudinal mode in addition to the flexure mode at these mount locations. If the fork is mounted at locations for which ℓ/d is approximately 2, 3, etc., then the coupling to this transverse mode can be minimized. Practically, ℓ/d ratios greater than 3 are not feasible due to increased shock and vibration susceptability.

Quartz Tuning Fork Mount

The quartz tuning fork is rigidly mounted by using a brazed mount as shown in Figure 5. A nickel pad is brazed to a standard TO-5 header using germanium-gold alloy. The fork has a chrome-gold ground plane on the backside of the unit. A tin-gold eutectic alloy is then used to braze the fork to the nickel pad. The all metal mount is used to insure

cleanliness and good aging of the final unit. No evaluation of epoxy mounts was done during the program.

Although the steel model indicated that preferred mount locations existed at $\ell/d \simeq 2, 3$, etc., the exact values for the quartz tuning fork are a complex function of the fork geometry and its elastic properties. To examine this, several units were constructed with an ℓ/d ratio of 2.5. The measured Q was significantly lower than those mounted at ratios of 2 or 3. Thus, although the steel model is at best an analog of the quartz fork, the data obtained is adequate to optimize the quartz fork mounting location.

Fabrication

Wafers

Oriented wafers, 1" square, .1" thick, are cut from cultured quartz. After angle correction with a double-crystal X-ray diffractometer, the wafers are lapped to .030" thick. Laue' techniques are used to adjust the rotation angle of the wafer to the proper orientation. The wafers are then cut and lapped to a final finished dimension of 0.8" in the direction of the major axis of the tuning fork and 0.75" orthogonal to this.

The dimensioned wafers are waxed onto lapping carriers using filtered Tizon II wax. After lapping with 5 micron Al_2O_3 abrasive to 10 mils and polishing with a zirconium oxide suspension (Lustrox 1000) to 8 mils, the wafers are removed, flipped over, and rewaxed to the lapping plate. The second side is then lapped to 3.5 mils, then polished to a final thickness of 1.5 miles. With crystal blanks this thin, it becomes essential that all wax used be filtered thoroughly, and that both sides are polished an equal amount to prevent unequal surface stresses and resultant curling.

Cleaning

The polished wafers are cleaned with acetone, aqua regia, NH_4OH and formic acid, methanol, bubble rinsed in de-ionized water, then placed in an ultrasonically agitated Freon TF bath, and dried in Freon TF vapor. The cleaned wafers are stored in a UV box[11] until ready for use.

Photolithographic Processing

A multi-step process is used to define the various electrode patterns and the quartz etch resist patterns. The electrodes are formed by vacuum deposition of 300Å of chrome and 1000Å of gold on both sides of the wafer. Then, Kodak 747 photoresist is spun onto the wafer, baked, exposed, developed, and unwanted metallization removed from both sides of the wafer. A photograph of the top electrode pattern is shown in Figure 6.

After thorough cleaning to remove the remaining photoresist, a further vacuum deposition of metallic films is applied to both sides of the wafer. If the wafer is destined for chemical etching, this consists of 2000Å of chrome followed by 4000Å of silver. If plasma etching is to be used, the silver layer is replaced by 4 microns of aluminum. Again, photoresist is applied and a second set of photomasks used to define the tuning fork outline. After processing and etching the unwanted metal film, and thorough cleaning, the wafers are ready for quartz etching. At this time, each wafer contains the necessary etch patterns and complete electrode patterns for 45 finished tuning forks.

Etching

The remaining process necessary to produce tuning forks ready for mounting is to etch out the unwanted quartz material around the tuning forks. The process used must etch through 1.5 mils of quartz in a reasonable time leaving walls that are near vertical and uniform. Although a number of different technqiues were used initially, the majority of the forks made were etched using chemical etching and plasma etching.

The chemical etching consists of immersion of the entire wafer in concentrated ammonium biflouride at 40°C for approximately 4 hours. This is a two-sided etching process. Its advantages are that it is inexpensive, and relatively fast.

Plasma etching is done in a proprietary system developed by Hewlett-Packard for the rapid removal of crystalline material. This is a single-sided etching process which is capable of removing 1.5 mils of crystalline quartz in about two hours. At this rate, however, the removal of the aluminum etch resist is also quite high. A typical run takes 14 hours to etch through the quartz wafer. The primary advantage of the plasma etching technique is that no selective etching or faceting occurs.

Figure 7 shows SEM photographs of tuning fork cross-sections made using the two processes. The faceting and undercutting are quite evident on the chemically-etched unit, whereas, the plasma-etched unit exhibits smooth, uniform walls.

Final Processing

After etching, the metallic etch resist masks are carefully stripped off, leaving 45 tuning forks, complete with electrode patterns, suspended in a quartz frame. After mounting on the header in the manner discussed previously, thermocompression bonded flyleads are attached to the top electrodes, the header and cap are cold-welded, and the units are installed in a vacuum bake-out head. After a 4 hour bakeout at 200°C, the units are backfilled with 50 microns of helium and sealed. After preliminary aging, the finished tuning forks are ready for test. No attempt was made to produce tuning forks that resonated exactly at 32,768 Hz. Techniques for tuning these devices have already been demonstrated by Staudte[12].

Experimental Results

Procedure

Resonant frequency, Q, motional resistance, and the frequency temperature response were measured for each tuning fork. For each orientation checked, a number of tuning forks were used. Data contained in this paper reflects the mean value for all units of the same orientation and method of etching. In each group, all tuning forks were obtained from the same wafer, insuring uniformity of crystallographic orientation and processing.

All measurements were made using the equipment setup shown in Figure 8. This is a low frequency version of the measurement system described previously[13]. All time bases were slaved off of an internal house frequency standard allowing frequency measurements to be made to an accuracy of better than 5 parts

in 10^9. Temperature measurements were made using a quartz thermometer calibrated to 0.01°C.

Temperature coefficients were determined by taking frequency data as a function of temperature at roughly 15°C steps in the range from -75° to 80°C. This data was then computer-fitted to a polynomial yielding the necessary temperature coefficients for each units.

Resistance and resonant frequency were determined directly from the test setup used. Crystal Q was determined by offsetting the phase tracking angle ±45° in the frequency control amplifier, and measuring the resultant frequency.

Results

From initial computer predictions and results from several preliminary attempts to make quartz tuning forks, we decided to restrict the major part of our effort to a region where the normal to the major surface of the fork (the thickness direction) was within 35° of the + Z-axis. A number of wafers were fabricated at orientations spaced 10° apart about the Z-axis. These are shown in Figure 9. Initially, the intention was to have the major surface inclined 20° with respect to the Z-axis, but for other reasons, the final inclination angle was 20.568°. Preliminary results indicated that a smaller inclination angle on the -Y-rotated cut would yield better turnover results. The data reported here is for a -Y-rotated cut with an inclination angle of 17.33° from the Z-axis.

The rotational orientation about the thickness direction was chosen to obtain the largest electromechanical coupling factor for each orientation. For the data shown, $\psi = 0°$ is defined as the length direction parallel to the X-Y plane.

Table I gives the final results for the six orientations examined in depth. Shown are the measured and predicted first-order temperature coefficients. The second-order coefficients for all orientations measured were essentially identical, $-40 \pm 5 \times 10^{-9}/°C^2$. Also shown are data for two orientations where both plasma and chemical etching were used.

The measured motional resistance, Q, and effective inductance are shown in Table II as a function of orientation for the six cases.

Data for two orientations for which both plasma and chemical etching were used is also given. Typically the plasma etched units exhibit higher Q and greater unit-to-unit repeatability. Most probably, this is due to the more uniform tine edges obtained in this process as shown in Figure 7.

Drive Level Dependence

Measurement procedures were complicated by an anomolous drive level dependence noted in a number of the test units. Tuning forks at certain orientations and drive levels have resonant frequencies significantly lower than the frequencies measured at the ±45° phase points. Data taken on a crystal not exhibiting a strong drive level dependence is shown in Figure 10. As a comparison, an identical unit at a different orientation has a dependence as shown in Figure 11. Drive level effects such as this were noted in all units for which ϕ was less than 40°. This effect is similar to that noted in AT-cut resonators[14,15]. The significant difference is that this effect occurs in 1 MHz AT's at a drive level of 250 μ watts, and in tuning forks at drive levels less than 0.1 μ watt.

Even though the tuning fork has a Q an order of magnitude lower than the AT-cut, the onset of the effect occurs at drive levels more than three orders of magnitude lower. No effort was made to eliminate the drive level effect, except to note its existance and to take proper precautions in making all measurements.

Conclusion

The purpose of this project was to investigate the technologies and problem areas associated with the quartz tuning fork. Effort was concentrated on mounting, etching, and crystallographic orientational dependence of parameters. During the program, the anomolous drive level effect was discovered and its effects on performance explored. No attempts were made to directly duplicate the work of Staudte reported previously.[1]

Nevertheless, the results obtained indicate that the only usable orientations for quartz tuning forks most likely lie within a few degress of the preferable orientation disclosed by Staudte[10]. Without exception, every orientation examined outside of this region has high drive level effect, poor turnover temperature, or high motional resistance, and in most cases, a combination of all three.

References

1) J.H. Staudte, "Subminiature Quartz Tuning Fork Resonator," Proc. of 27th Annual Symp. on Frequency Control, pp. 50-54, 1973.

2) I. Koga, "Tuning Fork Made of Quartz Crystal", J. Inst. of Elec. Engrs.,(Japan), Vol 48, pp 100-101, 1928.

3) W.P. Mason, Physical Acoustics, D.Van Nostrand Co., New York, pg. 54, 1958.

4) H. Yoda, H. Ikeda, and Y. Yamabe, "Low Power Crystal Oscillator for Electronic Wrist Watch," Proc. of 26th Annual Symp. on Frequency Control, pp. 140-147, 1972.

5) K. Tanno, M. Konno, and M. Ono, "Resonant Frequency and Vibration Mode of Plate Tuning Fork," J. Acous. Society of Japan, Vol. 30, No. 6, pp. 336-343, June 1974.

6) R.D. Mindlin, "High Frequency Vibrations of Crystal Plates," Quart. Appl. Math., Vol. 19, pp. 51-61, 1961.

7) P.C.Y. Lee, "Extensional, Flexural, and Width-Shear Vibrations of Thin Rectangular Crystal Plates," J. Appl. Phys., Vol. 42, No. 11, pp. 4139-4144, Oct. 1971.

8) W.P. Mason and R.A. Sykes, "Low-Frequency Quartz-Crystal Cuts Having Low Temperature Coefficients," Proc. I.R.E., Vol. 32, pp. 208-215, April 1944.

9) H.R. Schwarz,"Eigenfrequencies of Tuning-Forks," Computer Methods in Appl. Mech. and Engineering, Vol. 1, pp. 159-172, 1972.

10) U.S. Patent 3,766,616, issued Oct. 23, 1973.

11) J.R. Vig, C. Cook, Jr., K. Schwidtal, J. Lebus, and E. Hafner, "Surface Studies for Quartz Resonators," Proc. of 28th Annual Symp. of Fre-

quency Control, pp. 96-108, 1974.

12) J. H. Staudte, "Quartz Crystals for Electronic Wrist Watches," Ultrasonics Symposium Proceedings, pp. 583-588, 1974.

13) C. Adams, J. Kusters, and A. Benjaminson, "Measurement Techniques for Quartz Crystals", Proc. of 22nd Annual Symp. on Frequency Control, pp. 248-258, 1968.

14) D. Hammond, C. Adams, and L. Cutler, "Precision Crystal Units," Proc. of 17th Annual Symp. on Frequency Control, pp. 215-232, 1963.

15) A.W. Warner, "Design and Performance of Ultra-precise 2.5 mc Quartz Crystal Units," Bell Syst. Tech. Jr., Vol 39 pp. 1193-1218, Sept. 1960.

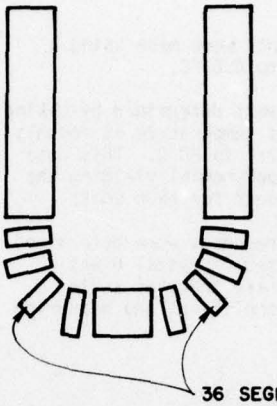

Figure 2 - Composite Tuning Fork Model

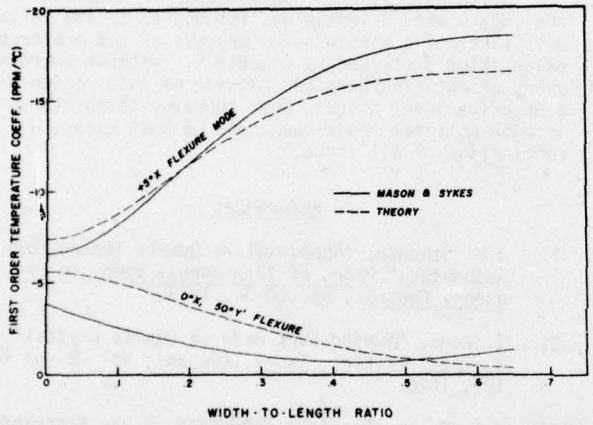

Figure 1 - First-Order Temperature Coefficients vs. Width-Length Ratio for Simple Bar Model

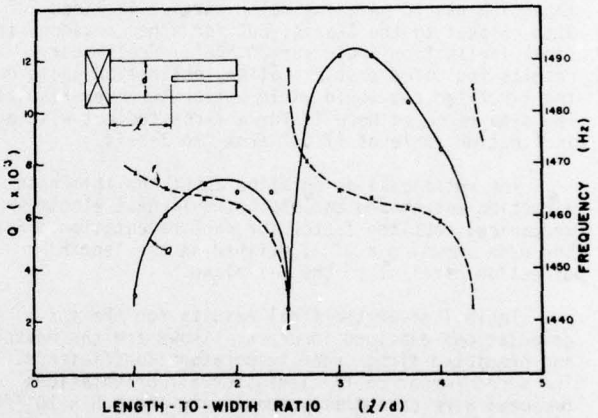

Figure 4 - Experimental Frequency and Q Data for Adjustable Tuning Fork Mount

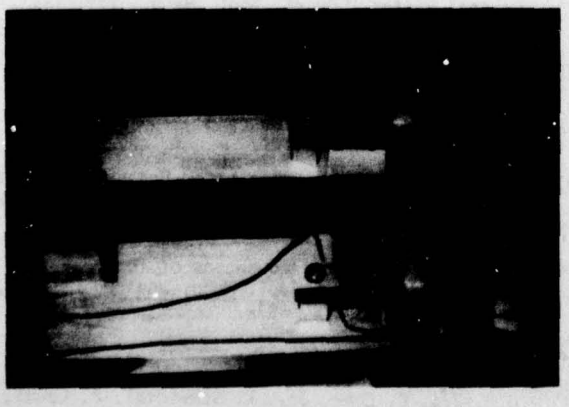

Figure 3 - Experimental Steel Tuning Fork in Adjustable Mount

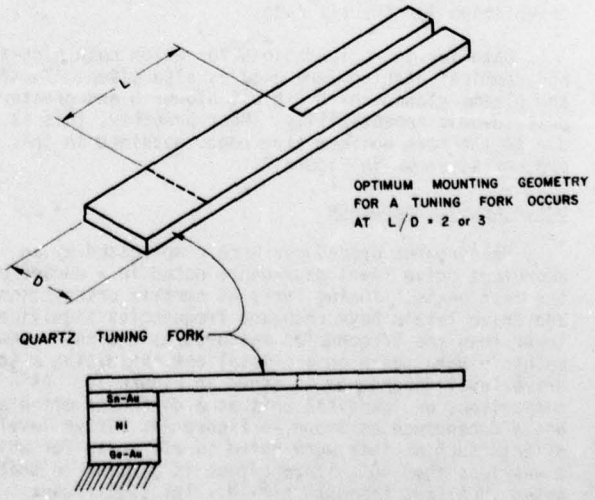

Figure 5 - Quartz Tuning Fork Brazed Mount

Appendix

The analysis of simple flexure bar behavior is primarily an extension of the previous work of Mindlin[6] and Lee[7].

Consider a rectangular plate with length 2a in the '1' direction, width 2b in the '2' direction, and thickness 2c in the '3' direction. In this case, the proper two-dimensional, first-order stress equations of motion for a body with stress-free surfaces are:

$$T_{ij,i}^{(0)} = 2b\rho\ddot{u}_j^{(0)} \qquad i,j = 1,2,3$$

$$T_{ab,a}^{(1)} - T_{2b}^{(0)} = \frac{2b^3}{3}\rho\ddot{u}_b^{(1)} \qquad a,b=1,3 \tag{A1}$$

where $u_i^{(0)}$ are the components of displacement and $u_i^{(1)}$ are the components of rotation in the x_i direction of a plate element, $T_{ij}^{(0)}$ are the resultant stresses and $T_{ij}^{(1)}$ are the stress couples, and only terms through first order in stress and strain, and second order in displacement are retained.

The stress-strain relationship for a generalized crystal can be written as:

$$T_{ij}^{(0)} = 2b\, c_{ijk\ell}S_{k\ell}^{(0)}$$

$$T_{ij}^{(1)} = \frac{2b^3}{3}\, c_{ijk\ell}S_{k\ell}^{(1)} \tag{A2}$$

where $i,j,k,\ell = 1,2,3$, and $c_{ijk\ell}$ is the appropriate (rotated) elastic constant. The strains, $S_{ij}^{(m)}$ can be defined as:

$$S_{ij}^{(0)} = \frac{1}{2}\left(u_{i,j}^{(0)} + u_{j,i}^{(0)} + \delta_{2j}u_i^{(1)} + \delta_{2i}u_j^{(1)}\right) \tag{A3}$$

$$S_{ab}^{(1)} + \frac{1}{2}\left(u_{a,b}^{(1)} + u_{b,a}^{(1)}\right)$$

where δ_{ij} is the Kronecker Delta function.

Under the assumptions of traction-free surfaces, and thickness 2c small when compared with the acoustic wavelengths and other plate dimensions, the components of displacement, stress, etc., can be approximated by their integrated average across the thickness as:

$$v_j^{(m)}(x_1,t) \equiv \frac{1}{2c}\int_{-c}^{c} u_j^{(m)}(x_1,x_3,t)\, dx_3$$

$$\sigma_{ij}^{(m)}(s_1,t) \equiv \frac{1}{2c}\int_{c}^{c} T_{ij}^{(m)}(x_1,x_3,t)\, dx_3 \tag{A4}$$

Further, extensional and flexure motion in the x_1 direction is assumed symmetrical so that:

$$\int_{-c}^{c} [u_1^{(0)}, u_1^{(1)}, u_2^{(0)}]_{,3}\, dx_3 \equiv 0 \tag{A5}$$

Finally, a system of solutions to (A1) is assumed to be of the form:

$$v_j^{(0)} = b\sum_{i=1}^{5} A_i\,\alpha_{ji}\exp j(\xi_i x_1 - \omega t) \qquad j = 1,2,3$$

$$v_1^{(1)} = \sum_{i=1}^{5} A_i\,\alpha_{4i}\exp j(\xi_i x_1 - \omega t) \tag{A6}$$

$$v_3^{(1)} = \sum_{i=1}^{5} A_i \exp j(\xi_i x_1 - \omega t)$$

where ω is the circular frequency, ξ_i are the wavenumbers of the five allowed modes, A_i is the amplitude for the i^{th} component of $v_3^{(1)}$ and α_{ji} are the amplitude ratios.

In the process of deducing the final form of the equation which results from substituting all of the above (Equations A2 through A6) into Eqn. A1, the following substitutions are used:

$$\bar{C}_{ij} = C_{ij} - \frac{C_{i2}\,C_{2j}}{C_{22}} \quad ; \quad \bar{\gamma}_{ij} = C_{ij} - \frac{C_{i4}\,C_{4j}}{C_{44}}$$

$$C_{ij}^{*} = \bar{C}_{ij} - \frac{\bar{C}_{i3}\,\bar{C}_{3j}}{C_{33}} \quad ; \quad \gamma_{ij}^{*} = \bar{\gamma}_{ij} - \frac{\bar{\gamma}_{i3}\,\bar{\gamma}_{3j}}{\gamma_{33}}$$

$$\hat{C}_{ij} = \frac{C_{ij}^{**}}{C_{66}^{**}} \quad ; \quad \hat{\gamma}_{ij} = \frac{\gamma_{ij}^{*}}{3C_{66}^{**}} \tag{A7}$$

where reduced notation is used for C.

Dimensionless frequencies and wavenumbers can be defined as:

$$\Omega^2 = \frac{\rho\omega^2 b^2}{3C_{66}^{**}} \quad ; \quad \xi = \xi_i b \tag{A8}$$

and they are related by the dispersion relationship

$$F(\Omega,\xi) = |a_{ij}| = 0 \quad ; \quad (a_{ij} = a_{ji}) \tag{A9}$$

where:

$$a_{11} = \hat{C}_{11}\xi^2 - 3\Omega^2,\ a_{12} = \hat{C}_{16}\xi^2,\ a_{13} = \hat{C}_{15}\xi^2,$$

$$a_{14} = -\hat{C}_{16}\xi,\ a_{15} = -\hat{C}_{14}\xi,\ a_{22} = \xi^2 - 3\Omega^2,$$

$$a_{23} = \hat{C}_{56}\xi^2,\ a_{24} = -\xi,\ a_{25} = -\hat{C}_{46}\xi,$$

$$a_{33} = \hat{C}_{55}\xi^2 - 3\Omega^2,\ a_{34} = -\hat{C}_{56}\xi,\ a_{35} = -\hat{C}_{45}\xi,$$

$$a_{44} = \hat{\gamma}_{11}\xi^2 + 1 - \Omega^2,\ a_{45} = \hat{\gamma}_{15}\xi^2 + \hat{C}_{46},$$

and $a_{55} = \hat{\gamma}_{55}\xi^2 + \hat{C}_{44} - \Omega^2$ (A10)

The solution of (A9) yields five values of ξ^2 where ξ is the wave number of the desired solution.

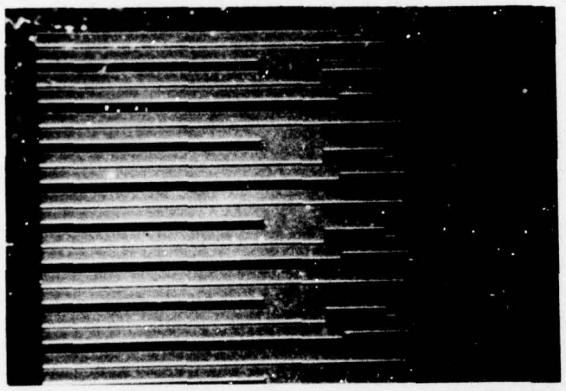

Figure 6 - Top Electrode Patterns

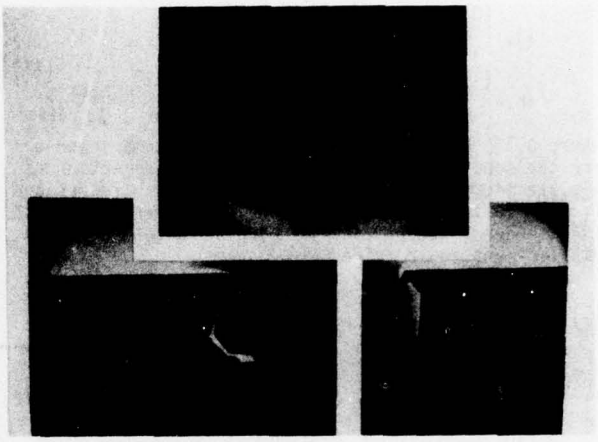

Figure 7 - SEM Photographs of Etched Tuning Forks
Top View - Plasma Etched
Bottom Views - Chemical Etched

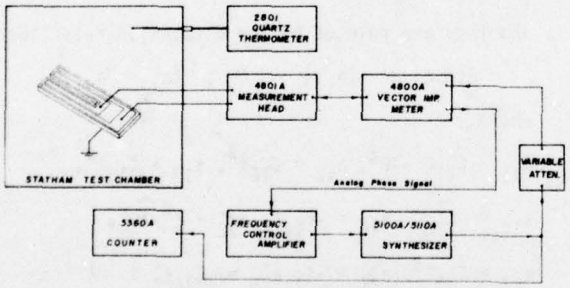

Figure 8 - Experimental Equipment Setup

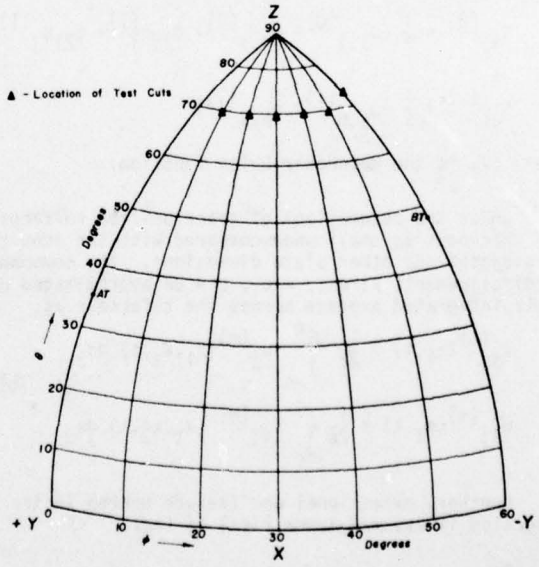

Figure 9 - Crystallographic Location of Experimental Tuning Forks

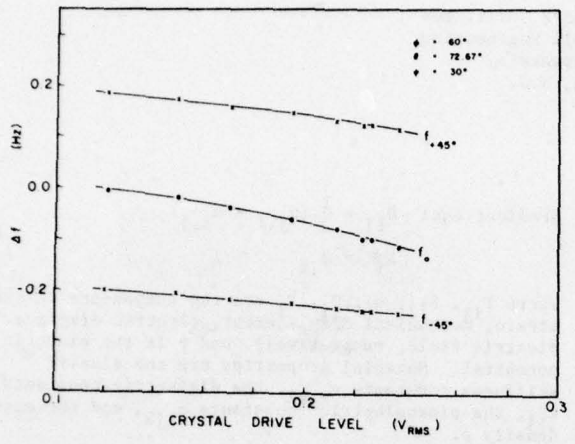

Figure 10- Drive Level Effect on Frequency "Good" Unit

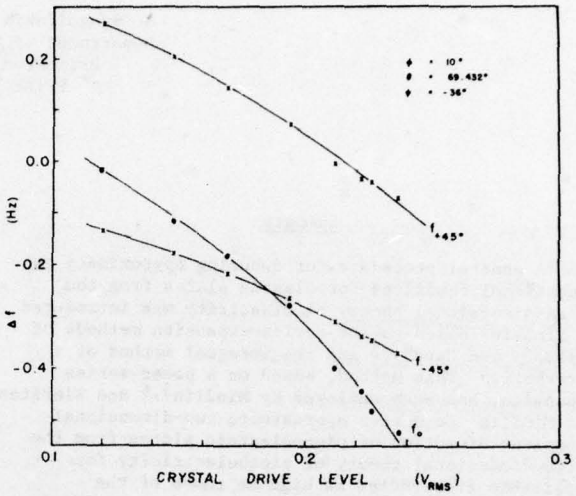

Figure 11- Drive Level Effect on Frequency "Poor" Unit

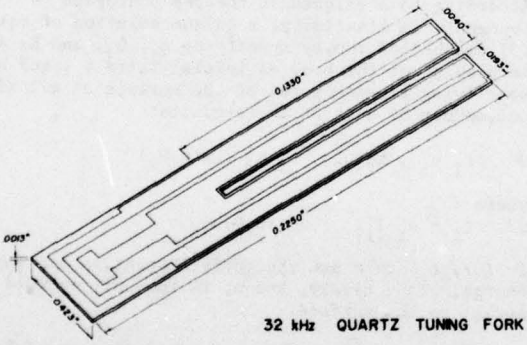

32 kHz QUARTZ TUNING FORK

Figure 12- Finished Tuning Fork Dimensions

PHI	THETA	PSI	FIRST-ORDER TEMP. COEFF. THEORY	FIRST-ORDER TEMP. COEFF. EXPERIMENTAL	TURNOVER TEMPERATURE	NUMBER OF UNITS
10°	69.432°	-36°	-18.8×10^{-8}	-8.86×10^{-8}	-80.4°C	6 (PLASMA)
20	69.432	-22	-13.2	-7.25	-73.3	6 (PLASMA)
30	69.432	0	-6.16	-4.18	-53.2	14 (PLASMA)
40	69.432	25	-8.20	-19.4	(-185)[1]	7 (PLASMA)
				-21.4	(-222)	10 (CHEM.)
50	69.432	37	-12.4	-17.4	(-194)	7 (PLASMA)
60	72.67	30	-7.04	-1.20	9.15	6 (PLASMA)
				-1.52	3.85	6 (CHEM.)

[1] COMPUTED - NOT MEASURED

Table I - Measured and Predicted First-Order Temperature Coefficients for Experimental Units (Averaged Values)

PHI	THETA	PSI	RESISTANCE	Q	INDUCTANCE	METHOD [1]
10°	69.432°	-36°	697 kΩ	15.4×10^6	49 kH	P
20	69.432	-22	462	36.1	79	P
30	69.432	0	335	46.2	76	P
40	69.432	25	600	56.9	160	P
			444	39.0	89	C
50	69.432	37	518	26.0	76	P
60	72.67	30	386	136	255	P
			258	133	150	C

[1] P - PLASMA ETCHED
C - CHEMICAL ETCHED

Table II - Measured Equivalent Circuit Parameters for Experimental Units (Averaged Values)

AN APPROXIMATE THEORY FOR THE HIGH-FREQUENCY VIBRATIONS OF PIEZOELECTRIC CRYSTAL PLATES

S. Syngellakis and P. C. Y. Lee
Department of Civil Engineering
Princeton University
Princeton, N.J.

Summary

A general procedure for deducing approximate two-dimensional equations for elastic plates from the three-dimensional theory of elasticity was introduced by Mindlin[1] based on the series-expansion methods of Poisson[2] and Cauchy,[3] and the integral method of Kirchhoff.[4] This method, based on a power-series expansion, has been employed by Mindlin[5,6] and Tiersten and Mindlin[7] to derive approximate two-dimensional equations of motion of piezoelectric plates from the three-dimensional theory of piezoelectricity for applicable frequencies as high as those of the fundamental thickness-shear modes. In references 5 and 6, the mechanical displacement and electric potential are expanded in the power series, while in the reference 7 the mechanical displacement and electric displacement are expanded in the same series.

By employing the same general procedure but using a trigonometric-series expansion, Lee and Nikodem[8,9] have deduced approximate two-dimensional equations of motion for both the isotropic and anisotropic elastic plates. The main advantage of this approach is that the generation of higher-order approximate equations to accommodate any harmonic overtones in plates can be made in a simple and systematic manner.

In the present paper, two-dimensional equations of successively higher orders of approximation for piezoelectric crystal plates have been deduced from a three-dimensional variational principle of piezoelectricity by expanding the mechanical displacement and electric potential in a trigonometric series. By a truncation procedure established in the previous studies,[8,9] equations of various order of approximation are extracted from the infinite set. Then for the truncated system of order N, the kinetic energy and electric enthalpy density are formulated; a theorem for the uniqueness of solutions is proved and the orthogonality of modes of free vibrations is established. In order to examine the accuracy of these equations of motion, from zeroth upto fourth order approximation, the dispersion curves for real and imaginary wave numbers of an infinite plate are explored in detail and are compared with the corresponding solutions of the exact frequency equation of the three-dimensional theory of piezoelectricity.[10]

Three-Dimensional Equations

The three-dimensional piezoelectricity may be summarized by the following twenty-two equations

Divergence eqs:
$$T_{ij,i} = \rho \ddot{u}_j \qquad D_{i,i} = 0 \tag{1}$$

Algebraic eqs:
$$T_{ij} = c_{ijk\ell} S_{k\ell} - e_{kij} E_k \qquad D_i = e_{ijk} S_{jk} + \epsilon_{ij} E_j \tag{2}$$

Gradient eqs:
$$S_{ij} = \frac{1}{2}(u_{j,i} + u_{i,j}) \qquad E_i = \phi_{,i} \tag{3}$$

where T_{ij}, S_{ij}, u_i, D_i, E_i are the components of stress, strain, mechanical displacement, electric displace, electric field, respectively, and ϕ is the electric potential. Material properties are the elastic stiffness constants $c_{ijk\ell}$, the dielectric constants ϵ_{ij}, the piezoelectric constants e_{ijk}, and the mass density ρ.

Equations (1) - (3) may be reduced to four-equations in four unknowns:

$$c_{ijk\ell} u_{k,\ell i} + e_{kij} \phi_{,ki} = \rho \ddot{u}_j \qquad e_{kij} u_{i,jk} - \epsilon_{ij} \phi_{,ij} = 0 \tag{4}$$

According to a uniqueness theorem analogous to Neumann's in elasticity, a unique solution of eqs. (1)-(3) can be insured by specifying u_j, $\dot{u}_j$, and E_i at each point of the body of initial time t_o, and by specifying at each point of the surface at all times one member of each of the products

$$t_1 u_1 \ , \ t_2 u_2 \ , \ t_3 u_3 \ , \ \phi(n_i D_i) \tag{5}$$

where

$$t_i = n_i T_{ij} \ , \ \sigma = n_i D_i \tag{6}$$

In (6), t_i and σ are the surface traction and surface charge, respectively, and n_i is the unit outward normal to the surface.

These equations may be derived from the following variational principle: in a region V bounded by a surface S,[6]

$$\delta \int_{t_o}^{t_1} dt \int_V (K-H)\, dV + \int_{t_o}^{t_1} dt \int_S (t_j \delta u_j + \sigma \delta \phi) dS = 0 \tag{7}$$

where K is the kinetic energy density

$$K = \frac{1}{2} \rho \dot{u}_j \dot{u}_j \tag{8}$$

and H is the electric enthalpy density

$$H = \frac{1}{2} c_{ijk\ell} S_{ij} S_{k\ell} - \frac{1}{2} \epsilon_{ij} E_i E_j - e_{ijk} E_i S_{jk} \tag{9}$$

so that

$$T_{ij} = \partial H / \partial S_{ij} \qquad D_i = -\partial H / \partial E_i . \tag{10}$$

AD-A046 089 ARMY ELECTRONICS COMMAND FORT MONMOUTH N J F/G 9/5
PROCEEDINGS OF THE ANNUAL SYMPOSIUM ON FREQUENCY CONTROL (30TH)--ETC(U)
1976 H K ZIEGLER

UNCLASSIFIED NL

3 OF 6
AD
A046089

Two-Dimensional Equations

The plate is referred to rectangular coordinates x_i with the face, of area A, at $x_2 = \pm b$ and with x_1 and x_3 the coordinates of the middle plane which intersects the right cylindrical boundary of the plate in a curve C (Shown in Fig. 1). The components of mechanical displacement and electric potential are expanded in an infinite series with their thickness-dependence expressed by the trigonometric functions as follows.

$$u_j = \sum_{n=0}^{\infty} \cos \frac{n\pi}{2}(1-\psi)\, u_j^{(n)}(x_1,x_3,t)$$
$$\phi = \sum_{n=0}^{\infty} \cos \frac{n\pi}{2}(1-\psi)\, \phi^{(n)}(x_1,x_3,t) \qquad (11)$$

where $\psi = x_2/b$ and $u_j^{(n)}$, $\phi^{(n)}$ are functions of x_1, x_3 and time t only.

By inserting (11) into (7), and requiring independent variations of each $\delta u_j^{(n)}$ and $\delta\phi^{(n)}$, and employing the relations (2), a system of two-dimensional equations are obtained and summarized as follows.

Divergence Equations (2D)

$$T_{ij,i}^{(n)} - \frac{n\pi}{2b}\bar{T}_{2j}^{(n)} + \frac{1}{b}F_j^{(n)} = (1+\delta_{no})\,\rho\ddot{u}_j^{(n)}$$
$$D_{i,i}^{(n)} - \frac{n}{2b}\bar{D}_2^{(n)} + \frac{1}{b}D^{(n)} = 0 \qquad (12)$$

where the nth-order components of stress, electric displacement, face-traction and face-charge are defined, respectively, by

$$T_{ij}^{(n)} = \int_{-1}^{1} T_{ij}\cos\frac{n\pi}{2}(1-\psi)\,d\psi$$
$$\bar{T}_{ij}^{(n)} = \int_{-1}^{1} T_{ij}\sin\frac{n\pi}{2}(1-\psi)\,d\psi$$
$$D_i^{(n)} = \int_{-1}^{1} D_i\cos\frac{n\pi}{2}(1-\psi)\,d\psi \qquad (13)$$
$$\bar{D}_i^{(n)} = \int_{-1}^{1} D_i\sin\frac{n\pi}{2}(1-\psi)\,d\psi$$
$$F_j^{(n)} = {}^{2}t_j(b) + (-1)^n\, {}^{-2}t_j(-b)$$
$$D^{(n)} = \sigma(b) - (-1)^n\,\sigma(-b)$$

and

$$\delta_{no} = \begin{cases} 1 & n=0 \\ 0 & n\neq 0 \end{cases}$$

Natural Boundary Conditions on C

$$t_j^{(n)} = n_a\, T_{aj}^{(n)}$$
$$\sigma^{(n)} = n_a\, D_a^{(n)} \qquad (a = 1,3) \qquad (14)$$

where edge-traction and edge-charge are defined, respectively, by

$$t_j^{(n)} = \int_{-1}^{1} (t_j^{\nu})_c \cos\frac{n\pi}{2}(1-\psi)\,d\psi$$
$$\sigma^{(n)} = \int_{-1}^{1} (\sigma)_c \cos\frac{n\pi}{2}(1-\psi)\,d\psi \qquad (15)$$

and ν indicates the normal direction to C (See Fig. 1).

Gradient Equations (2D)

The nth-order components of strain and electric field are defined

$$S_{ij}^{(n)} = \frac{1}{2}(u_{j,i}^{(n)} + u_{i,j}^{(n)})$$
$$\bar{S}_{ij} = \frac{n\pi}{4b}(\delta_{2i}\, u_j^{(n)} + \delta_{2j}\, u_i^{(n)}) \qquad (16)$$
$$E_i^{(n)} = -\phi_{,i}^{(n)}$$
$$\bar{E}_i^{(n)} = -\frac{n\pi}{2b}\delta_{2i}\,\phi^{(n)}$$

such that

$$S_{ij} = \sum_{n=o}^{\infty}[S_{ij}^{(n)}\cos\frac{n\pi}{2}(1-\psi) + \bar{S}_{ij}^{(n)}\sin\frac{n\pi}{2}(1-\psi)]$$
$$E_i = \sum_{n=o}^{\infty}[E_i^{(n)}\cos\frac{n\pi}{2}(1-\psi) + \bar{E}_i^{(n)}\sin\frac{n\pi}{2}(1-\psi)] \qquad (17)$$

Constitutive Equations (2D)

$$T_{ij}^{(n)} = (1+\delta_{no})(c_{ijk\ell}\, S_{k\ell}^{(n)} - e_{kij}\, E_k^{(n)}) + \sum_{m=1}^{\infty} A_{mn}(c_{ijk\ell}\,\bar{S}_{k\ell}^{(m)} - e_{kij}\,\bar{E}_k^{(m)})$$
$$D_i^{(n)} = (1+\delta_{no})(e_{ijk}\, S_{jk}^{(n)} + \varepsilon_{ij}\, E_j^{(n)}) + \sum_{m=1}^{\infty} A_{mn}(e_{ijk}\,\bar{S}_{jk}^{(m)} + \varepsilon_{ij}\,\bar{E}_j^{(m)}) \qquad (18)$$
$$\bar{T}_{ij}^{(n)} = \sum_{m=0}^{\infty} A_{nm}(c_{ijk\ell}\, S_{k\ell}^{(m)} - e_{kij}\, E_k^{(m)}) + c_{ijk\ell}\,\bar{S}_{k\ell}^{(n)} - e_{kij}\,\bar{E}_k^{(n)}$$
$$\bar{D}_i^{(n)} = \sum_{m=0}^{\infty} A_{nm}(e_{ijk}\, S_{jk}^{(m)} + \varepsilon_{ij}\, E_j^{(m)}) + e_{ijk}\,\bar{S}_{jk}^{(n)} + \varepsilon_{ij}\,\bar{E}_j^{(n)}$$

where

$$A_{mn} = \begin{cases} \dfrac{4m}{(m^2-n^2)\pi} & m+n = \text{odd} \\ 0 & m+n = \text{even} \end{cases}$$

Define plate kinetic energy density and plate electric enthalpy density, respectively, by

$$\bar{K} = \int_{-1}^{1} K\, d\psi \quad , \quad \bar{H} = \int_{-1}^{1} H\, d\psi \tag{19}$$

It can be verified that the following relations are satisfied.

$$\begin{aligned} T_{ij}^{(n)} &= \partial\bar{H}/\partial S_{ij}^{(n)} \quad , \qquad \bar{T}_{ij}^{(n)} = \partial\bar{H}/\partial\bar{S}_{ij}^{(n)} \quad , \\ D_k^{(n)} &= \partial\bar{H}/\partial E_k^{(n)} \quad , \qquad \bar{D}_k^{(n)} = \partial\bar{H}/\partial\bar{E}_k^{(n)} \quad . \end{aligned} \tag{20}$$

At this point, it may be noted that all mechanical variables of the present formulation were introduced earlier in reference 9. Also, an illustration of the components of displacement $u_j^{(n)}$, and strains $S_{ij}^{(n)}$ and $\bar{S}_{ij}^{(n)}$, can be found in reference 8.

Truncation of Series and Adjustment

The process of series truncation for obtaining a system of two-dimensional equations of approximation of order N (N > 0, it can be considered as the number of harmonic overtones accommodated in the theory) is to let

$$u_j^{(n)} = 0 \ , \quad \phi^{(n)} = 0 \quad \text{for} \quad n > N$$

and also to discard $S_{ij}^{(n)}$, $\bar{S}_{ij}^{(n)}$, $E_j^{(n)}$, $\bar{E}_j^{(n)}$ for $n > N$.

Two correction factors α_1 and α_2 are introduced into the kinetic and electric enthalpy energy densities for the truncated finite system of equations. The positions of these factors are indicated in the following expanded forms of $\bar{K}$ and $\bar{H}$:

$$2\bar{K} = \rho(2\alpha_2^{-2\mu_{jj}}\, \dot{u}_j^{(0)}\, \dot{u}_j^{(0)} + \dot{u}_j^{(1)}\, \dot{u}_j^{(1)} + \ldots) \tag{21}$$

and

$$\begin{aligned}
2\bar{H} = {} & c_{ijk\ell}[2S_{ij}^{(0)}S_{k\ell}^{(0)} + \alpha_2^{\mu_{ij}+\mu_{k\ell}} S_{ij}^{(1)}S_{k\ell}^{(1)} + S_{ij}^{(2)}S_{k\ell}^{(2)} + \ldots\ldots + \bar{S}_{ij}^{(1)}\bar{S}_{k\ell}^{(1)} + \bar{S}_{ij}^{(2)}\bar{S}_{k\ell}^{(2)} + \\
& + 2S_{ij}^{(0)}(\alpha_1 A_{10}\bar{S}_{k\ell}^{(1)} + A_{30}\bar{S}_{k\ell}^{(3)} + \ldots\ldots) \\
& + 2S_{ij}^{(1)}(A_{21}\bar{S}_{k\ell}^{(2)} + A_{41}\bar{S}_{k\ell}^{(4)} + \ldots\ldots) \\
& + 2S_{ij}^{(2)}(A_{12}\bar{S}_{k\ell}^{(1)} + A_{32}\bar{S}_{k\ell}^{(3)} + \ldots\ldots) + \ldots\ldots\ldots] \\
& - e_{ijk}[4S_{ij}^{(0)}E_k^{(0)} + 2\alpha_2^{\mu_{ij}} S_{ij}^{(1)}E_k^{(1)} + 2S_{ij}^{(2)}E_k^{(2)} + \ldots\ldots\ldots + 2\bar{S}_{ij}^{(1)}\bar{E}_k^{(1)} + 2\bar{S}_{ij}^{(2)}\bar{E}_k^{(2)} + \ldots\ldots \\
& + 2S_{ij}^{(0)}(\alpha_1 A_{10}\bar{E}_k^{(1)} + A_{31}\bar{E}_k^{(3)} + \ldots\ldots) + 2E_k^{(0)}(\alpha_1 A_{10}\bar{S}_{ij}^{(1)} + A_{30}\bar{S}_{ij}^{(3)} + \ldots\ldots) \\
& + 2S_{ij}^{(1)}(A_{21}\bar{E}_k^{(2)} + A_{41}\bar{E}_k^{(4)} + \ldots\ldots) + 2E_k^{(1)}(A_{21}\bar{S}_{ij}^{(2)} + A_{41}\bar{S}_{ij}^{(4)} + \ldots\ldots) \\
& + 2S_{ij}^{(2)}(A_{12}\bar{E}_k^{(1)} + A_{32}\bar{E}_k^{(3)} + \ldots\ldots) + 2E_k^{(2)}(A_{12}\bar{S}_{ij}^{(1)} + A_{32}\bar{S}_{ij}^{(3)} + \ldots\ldots) + \ldots\ldots\ldots] \\
& - \epsilon_{k\ell}[2E_k^{(0)}E_\ell^{(0)} + E_k^{(1)}E_\ell^{(1)} + E_k^{(2)}E_\ell^{(2)} + \ldots\ldots\ldots + \bar{E}_k^{(1)}\bar{E}_\ell^{(1)} + \bar{E}_k^{(2)}\bar{E}_\ell^{(2)} + \ldots\ldots \\
& + 2E_k^{(0)}(\alpha_1 A_{10}\bar{E}_\ell^{(1)} + A_{30}\bar{E}_\ell^{(3)} + \ldots\ldots) \\
& + 2E_k^{(1)}(A_{21}\bar{E}_\ell^{(2)} + A_{41}\bar{E}_\ell^{(4)} + \ldots\ldots) \\
& + 2E_k^{(2)}(A_{12}\bar{E}_\ell^{(1)} + A_{32}\bar{E}_\ell^{(3)} + \ldots\ldots) + \ldots\ldots\ldots]
\end{aligned} \tag{22}$$

where

$$\mu_{ij} = \cos^2\left(\frac{ij\pi}{2}\right)$$

Governing Equations on $u_j^{(n)}$ and $\phi^{(n)}$

The governing equations on $u_j^{(n)}$ and $\phi^{(n)}$ can be obtained by inserting eqs. (16) into (18) then, in turn, into (12). The resulting equations for plates with m-monoclinic symmetry are given as follows.

$$
\begin{aligned}
&c_{11}u_{1,11}^{(n)}+c_{55}u_{1,33}^{(n)}-\left(\tfrac{n\pi}{2b}\right)^2 c_{66}u_1^{(n)}+(c_{14}+c_{56})u_{2,13}^{(n)}+(c_{13}+c_{55})u_{3,13}^{(n)}+(e_{31}+e_{15})\phi_{,13}^{(n)}\\
&\quad+\frac{\pi}{2b}\sum_{m=0}^{N}\{a_{mn11}u_{1,3}^{(m)}+a_{mn12}u_{2,1}^{(m)}+a_{mn13}u_{3,1}^{(m)}+a_{mn14}\phi_{,1}^{(m)}\}+\frac{1}{b}F_1^{(n)}=\rho\ddot{u}_1^{(n)}\\
&(c_{56}+c_{14})u_{1,13}^{(n)}+c_{66}u_{2,11}^{(n)}+c_{44}u_{2,33}^{(n)}-\left(\tfrac{n\pi}{2b}\right)^2 c_{22}u_2^{(n)}+c_{56}u_{3,11}^{(n)}+c_{34}u_{3,33}^{(n)}-\left(\tfrac{n\pi}{2b}\right)^2 c_{24}u_3^{(n)}\\
&\quad+e_{16}\phi_{,11}^{(n)}+e_{34}\phi_{,33}^{(n)}-\left(\tfrac{n\pi}{2b}\right)^2 e_{22}\phi^{(n)}+\frac{\pi}{2b}\sum_{m=0}^{N}\{a_{mn21}u_{1,1}^{(m)}+a_{mn22}u_{2,3}^{(m)}+a_{mn23}u_{3,3}^{(m)}+a_{mn24}\phi_{,3}^{(m)}\}\\
&\quad+\frac{1}{b}F_2^{(n)}=\rho\ddot{u}_2^{(n)}\\
&(c_{55}+c_{13})u_{1,13}^{(n)}+c_{56}u_{2,11}^{(n)}+c_{34}u_{2,33}^{(n)}-\left(\tfrac{n\pi}{2b}\right)^2 c_{24}u_2^{(n)}+c_{55}u_{3,11}^{(n)}+c_{55}u_{3,33}^{(n)}-\left(\tfrac{n\pi}{2b}\right)^2 c_{44}u_3^{(n)}\\
&\quad+e_{15}\phi_{,11}^{(n)}+e_{33}\phi_{,33}^{(n)}-\left(\tfrac{n\pi}{2b}\right)^2 e_{24}\phi^{(n)}+\frac{\pi}{2b}\sum_{m=0}^{N}\{a_{mn31}u_{1,1}^{(m)}+a_{mn32}u_{2,3}^{(m)}+a_{mn33}u_{3,3}^{(m)}+a_{mn34}\phi_{,3}^{(m)}\}\\
&\quad+\frac{1}{b}F_3^{(n)}=\rho\ddot{u}_3^{(n)}\\
&(e_{15}+e_{31})u_{1,13}^{(n)}+e_{16}u_{2,11}^{(n)}+e_{34}u_{2,33}^{(n)}-\left(\tfrac{n\pi}{2b}\right)^2 e_{22}u_2^{(n)}+e_{15}u_{3,11}^{(n)}+e_{33}u_{3,33}^{(n)}-\left(\tfrac{n\pi}{2b}\right)^2 e_{23}u_3^{(n)}\\
&\quad-\varepsilon_{11}\phi_{,11}^{(n)}-\varepsilon_{33}\phi_{,33}^{(n)}+\left(\tfrac{n\pi}{2b}\right)^2\varepsilon_{22}\phi^{(n)}+\frac{\pi}{2b}\sum_{m=0}^{N}\{a_{mn41}u_{1,1}^{(m)}+a_{mn42}u_{2,3}^{(m)}+a_{mn43}u_{3,3}^{(m)}-a_{mn44}\phi_{,3}^{(m)}\}\\
&\quad+\frac{1}{b}D^{(n)}=0
\end{aligned}
\tag{23}
$$

where

$$
a_{mnij}=\frac{4}{(m^2-n^2)\pi}\begin{bmatrix}
(m^2+n^2)c_{56} & m^2c_{12}+n^2c_{66} & m^2c_{14}+n^2c_{56} & m^2e_{21}+n^2e_{16}\\
m^2c_{66}+n^2c_{12} & (m^2+n^2)c_{24} & m^2c_{44}+n^2c_{23} & m^2e_{24}+n^2e_{32}\\
m^2c_{56}+n^2c_{14} & m^2c_{23}+n^2c_{44} & (m^2+n^2)c_{34} & m^2e_{23}+n^2e_{34}\\
m^2e_{16}+n^2e_{21} & m^2e_{32}+n^2e_{24} & m^2e_{34}+n^2e_{23} & (m^2+n^2)\varepsilon_{23}
\end{bmatrix} \quad \text{if } m+n=\text{odd} \tag{24}
$$

$$
a_{mnij}=0 \quad \text{if } m+n=\text{even}
$$

It is noted that

$$
a_{mnij}=-a_{nmji}
$$

General Nth-Order Dispersion Relation

Considering plane harmonic waves propagating in an infinite plate which has faces free of traction and open to the vacuum, we let

$$F_j^{(n)} = 0 \quad , \quad D^{(n)} = 0$$

and

$$\begin{aligned} u_i^{(2k)} &= A_i^{(2k)} \cos(\xi_1 x_1 + \xi_3 x_3 - \omega t); \\ u_i^{(2k+1)} &= A_i^{(2k+1)} \sin(\xi_1 x_1 + \xi_3 x_3 - \omega t); \\ \phi^{(2k)} &= A_4^{(2k)} \cos(\xi_1 x_1 + \xi_3 x_3 - \omega t); \\ \phi^{(2k+1)} &= A_4^{(2k+1)} \sin(\xi_1 x_1 + \xi_3 x_3 - \omega t) \end{aligned} \tag{25}$$

Substitution of (25) into (23) yields:

$$\begin{aligned} \underset{\sim}{C}_{2k}/A^{(2k)} - \sum_{\ell=0}^{R} \underset{\sim}{D}_{(2\ell+1)2k}/A^{(2\ell+1)} &= 0 \; ; \; k=0,1,\ldots,S \\ \underset{\sim}{C}_{2k+1}/A^{(2k+1)} + \sum_{\ell=0}^{S} \underset{\sim}{D}_{2\ell(2k+1)}A^{(2\ell)} &= 0 \; ; \; k=0,1,\ldots,R \end{aligned} \tag{26}$$

where

$$R = \frac{N}{2} - 1 \quad ; \quad S = \frac{N}{2} \text{ for } N = \text{even}$$

and

$$R = S = \frac{N-1}{2} \text{ for } N = \text{odd}$$

In eqs. (26) the matrices $\underset{\sim}{C}_m$ and $\underset{\sim}{D}_{mn}$ are given by

$$\underset{\sim}{C}_m = \begin{bmatrix} \bar{c}_{11}z_1^2+\bar{c}_{55}z_3^2+m^2-\bar{c}_{66}-\Omega^2 & (\bar{c}_{14}+\bar{c}_{56})z_1z_3 & (\bar{c}_{13}+\bar{c}_{55})z_1z_3 & (\bar{e}_{31}+\bar{e}_{15})z_1z_3 \\ (\bar{c}_{14}+\bar{c}_{56})z_1z_3 & \bar{c}_{66}z_1^2+\bar{c}_{44}z_3^2+m^2-\bar{c}_{22}-\Omega^2 & \bar{c}_{56}z_1^2+\bar{c}_{34}z_3^2+m^2-\bar{c}_{24} & \bar{e}_{16}z_1^2+\bar{e}_{34}z_3^2+m^2-\bar{e}_{22} \\ (\bar{c}_{13}+\bar{c}_{55})z_1z_3 & \bar{c}_{56}z_1^2+\bar{c}_{34}z_3^2+m^2-\bar{c}_{24} & \bar{c}_{55}z_1^2+\bar{c}_{33}z_3^2+m^2-\bar{c}_{44}-\Omega^2 & \bar{e}_{15}z_1^2+\bar{e}_{33}z_3^2+m^2-\bar{e}_{24} \\ (\bar{e}_{31}+\bar{e}_{15})z_1z_3 & \bar{e}_{16}z_1^2+\bar{e}_{34}z_3^2+m^2-\bar{e}_{22} & \bar{e}_{15}z_1^2+\bar{e}_{33}z_3^2+m^2-\bar{e}_{24} & -\bar{\varepsilon}_{11}z_1^2-\bar{\varepsilon}_{33}z_3^2-m^2 \end{bmatrix} \tag{27}$$

$$\underset{\sim}{D}_{mn} = \begin{bmatrix} \bar{a}_{mn11}z_3 & \bar{a}_{mn12}z_1 & \bar{a}_{mn13}z_1 & \bar{a}_{mn14}z_1 \\ \bar{a}_{mn21}z_1 & \bar{a}_{mn22}z_3 & \bar{a}_{mn23}z_3 & \bar{a}_{mn24}z_3 \\ \bar{a}_{mn31}z_1 & \bar{a}_{mn32}z_3 & \bar{a}_{mn33}z_3 & \bar{a}_{mn34}z_3 \\ \bar{a}_{mn41}z_1 & \bar{a}_{mn42}z_3 & \bar{a}_{mn43}z_3 & \bar{a}_{mn44}z_3 \end{bmatrix} \tag{28}$$

where

$$z_1 = \frac{2b\xi_1}{\pi}, \; z_3 = \frac{2b\xi_3}{\pi}, \; \Omega = \omega/\frac{\pi}{2b}\left(\frac{\hat{c}_3}{\rho}\right)^{1/2}$$

$$\bar{c}_{pq}=c_{pq}/\hat{c}_3, \; \bar{e}_{iq}=e_{iq}/(\hat{c}_3\varepsilon_{22})^{1/2}, \; \bar{\varepsilon}_{ij}=\varepsilon_{ij}/\varepsilon_{22}$$

$$\hat{c}_3 = \frac{\hat{c}_{22}+\hat{c}_{44}}{2} - \left(\frac{\hat{c}_{22}-\hat{c}_{44}}{2}\right)^2 + \hat{c}_{24}^2$$

and

$$\hat{c}_{pq} = c_{pq} + e_{2p}\, e_{2q}/\varepsilon_{22}.$$

The condition for the existence of nontrivial solutions of (25) leads to the dispersion relation for the Nth-order approximate theory:

$$\begin{vmatrix} 2\underset{\sim}{C}_0 & -\alpha_1\underset{\sim}{D}_{10} & 0 & -\underset{\sim}{D}_{30} & 0 & \cdots & \\ \alpha_1\underset{\sim}{D}_{01} & \underset{\sim}{C}_1 & \underset{\sim}{D}_{21} & 0 & \underset{\sim}{D}_{41} & \cdots & \\ 0 & -\underset{\sim}{D}_{12} & \underset{\sim}{C}_2 & -\underset{\sim}{D}_{32} & 0 & \cdots & \\ \underset{\sim}{D}_{03} & 0 & \underset{\sim}{D}_{23} & \underset{\sim}{C}_3 & \underset{\sim}{D}_{43} & \cdots & \\ 0 & -\underset{\sim}{D}_{14} & 0 & -\underset{\sim}{D}_{34} & \underset{\sim}{C}_4 & \cdots & \\ \cdots & & & & & & \\ \cdots & & & & & & (-1)^N\underset{\sim}{D}_{N,N-1} \\ \cdots & & & & & (-1)^{N-1}\underset{\sim}{D}_{N-1,N} & \underset{\sim}{C}_N \end{vmatrix} = 0 \tag{29}$$

In the case of straight-crested waves propagating along x_3 direction, components $u_2^{(n)}$, $u_3^{(n)}$ and $\phi^{(n)}$ are uncoupled from $u_1^{(n)}$. It can be seen by setting $z_1 = 0$ and $z_3 = z$ in eqs (27) and (28). The dispersion relation for the coupled modes is, of course, still given by (29), however with the simplification that the first rows and first columns in all C_m and D_{mn} have been eliminated. For example, the dispersion relation for the first-order approximate theory is reduced to

$$\begin{vmatrix}
2(\bar{c}_{44}z^2 - \frac{\Omega^2}{\alpha_2^2}) & 2\bar{c}_{34}z^2 & 2\bar{e}_{34}z^2 & -\alpha_1\frac{4}{\pi}\bar{c}_{24}z & -\alpha_1\frac{4}{\pi}\bar{c}_{44}z & -\alpha_1\frac{4}{\pi}\bar{e}_{24}z \\
2\bar{c}_{34}z^2 & 2(\bar{c}_{33}z^2 - \Omega^2) & 2\bar{e}_{33}z^2 & -\alpha_1\frac{4}{\pi}\bar{c}_{23}z & -\alpha_1\frac{4}{\pi}\bar{c}_{34}z & -\alpha_1\frac{4}{\pi}\bar{e}_{23}z \\
2\bar{e}_{34}z^2 & 2\bar{e}_{33}z^2 & -2\bar{\varepsilon}_{33}z^2 & -\alpha_1\frac{4}{\pi}\bar{e}_{32}z & -\alpha_1\frac{4}{\pi}\bar{e}_{34}z & \alpha_1\frac{4}{\pi}\bar{\varepsilon}_{23}z \\
-\alpha_1\frac{4}{\pi}\bar{c}_{24}z & -\alpha_1\frac{4}{\pi}\bar{c}_{23}z & -\alpha_1\frac{4}{\pi}\bar{e}_{32}z & \alpha_2^2\bar{c}_{44}z^2 + \bar{c}_{22} - \Omega^2 & \alpha_2\bar{c}_{34}z^2 + \bar{c}_{24} & \alpha_2\bar{e}_{34}z^2 + \bar{e}_{22} \\
-\alpha_1\frac{4}{\pi}\bar{c}_{44}z & -\alpha_1\frac{4}{\pi}\bar{c}_{34}z & -\alpha_1\frac{4}{\pi}\bar{e}_{34}z & \alpha_2\bar{c}_{34}z^2 + \bar{c}_{24} & \bar{c}_{33}z^2 + \bar{c}_{44} - \Omega^2 & \bar{e}_{33}z^2 + \bar{e}_{24} \\
-\alpha_1\frac{4}{\pi}\bar{e}_{24}z & -\alpha_1\frac{4}{\pi}\bar{e}_{23}z & \alpha_1\frac{4}{\pi}\bar{\varepsilon}_{23}z & \alpha_2\bar{e}_{34}z^2 + \bar{e}_{22} & \bar{e}_{33}z^2 + \bar{e}_{24} & -\bar{\varepsilon}_{33}z^2 - 1
\end{vmatrix} = 0 \qquad (30)$$

In order to correct the slope of the lower flexural branch at $z = 0$, we set

$$\alpha_1 = \frac{\pi}{2\sqrt{2}} \qquad (31)$$

and to correct the slopes of the lower flexural and extensional branches as $z \to \infty$, we set

$$\alpha_2 = V_s[\tilde{c}_{44} - \tilde{c}_{34}^2/(\tilde{c}_{33} - V_s^2)]^{-1/2} \qquad (32)$$

where V_s is the dimensionless surface wave velocity and

$$\tilde{c}_{pq} = \tilde{c}_{pq}/\hat{c}_3$$

For the Nth order theory:

$$\alpha_1^2 = 1 + \frac{\pi^2}{8} - \left(1 + \frac{1}{3^2} + \frac{1}{5^2} + \ldots + \frac{1}{N'^2}\right) \qquad (33)$$

where $N' = \begin{cases} N & \text{if N is odd} \\ N-1 & \text{if N is even} \end{cases}$

The roots of (30) have been computed for a 45° rotated Y-cut of Lithium Tantalate and are shown by the solid lines in Fig. 2. The values of the material constants used are those by Smith and Welsh.[11] In the same figure, the roots of the exact frequency equation obtained in a previous paper[10] are shown in dashed lines for comparison. In the similar manner, roots of (29) are computed for N = 2,3 and 4. These are the dispersion curves of the second- third- and fourth-order approximate theory, respectively, and they are shown in Figs. 3-5. The close agreement between the approximate and exact solutions indicates that the applicable range of frequency for each Nth-order theory is $0 \leq \Omega < N + 1/2$.

References

1. R. D. Mindlin, An introduction to the mathematical theory of vibrations of elastic plates, U.S. Army Signal Corps Engineering Laboratories, Fort Monmouth, New Jersey (1955), chap. 3.
2. S. D. Poisson, Memoire sur l'equilibre et le mouvement des corps e'lastiques, Mem. Acad. Sci., Paris, Ser. 2, 8, 357-570 (1829).
3. A. L. Cauchy, Sur l'equilibre et le mouvement d' une plaque elastique n'est pas la meme dans tous les sens; Exercises de Mathematiquec, 4, 1-14 (1829).
4. G. Kirchhoff, Uber das Gleichgewicht und die Bewegung einer elastischen Scheibe, Crelles J. 40, 51-88 (1850).
5. R. D. Mindlin, Forced thickness-shear and flexural vibrations of piezoelectric crystal plates, J. Appl. Phys. 23, 83-88 (1952).
6. R. D. Mindlin, High frequency vibrations of piezoelectric crystal plates, Int. J. Solids Structures, 8, 895-906, (1972).
7. H. F. Tiersten and R. D. Mindlin, Forced vibrations of piezoelectric crystal plates. Q. Appl. Math. 22, 107-119 (1962).
8. P. C. Y. Lee and Z. Nikodem, An approximation theory for high-frequency vibrations of elastic plates, Int. J. Solids Structures, 8, 581-612(1972).
9. Z. Nikodem and P. C. Y. Lee, Approximate theory of vibration of crystal plates at high frequencies, Int. J. Solids Structures, 10, 177-196 (1974).
10. P. C. Y. Lee and S. Syngellakis, Waves and vibrations in an infinite piezoelectric plate, Proc. 29th Annual Symp. on Frequency Control, 65-70, U.S. Army Electronics Command, Fort Monmouth, New Jersey, (1975).

11. R. T. Smith and F. S. Welsh, Temperature dependence of the elastic, piezoelectric, and dielectric constants of lithium tantalate and lithium niobate. J. Appl. Phys. 42, 2219-2230 (1971).

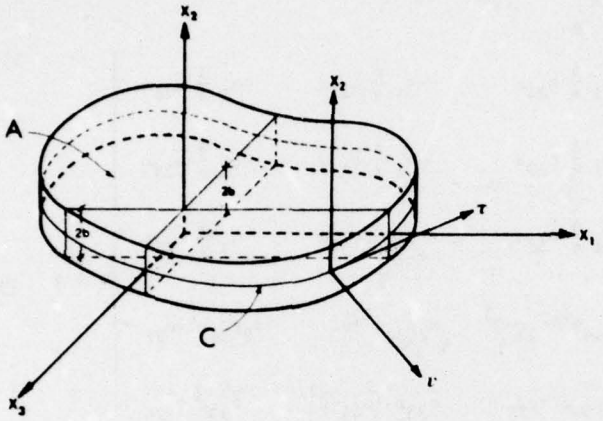

Figure 1: Plate coordinates and boundaries

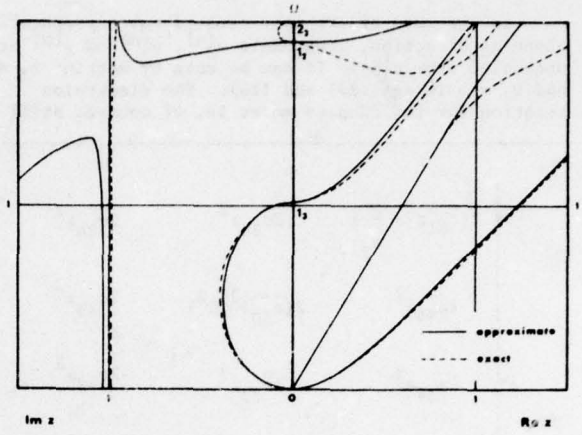

Figure 2: Dispersion curves for the first-order approximate theory. Waves in x_3 direction. 45° rotated Y-cut of $LiTaO_3$.

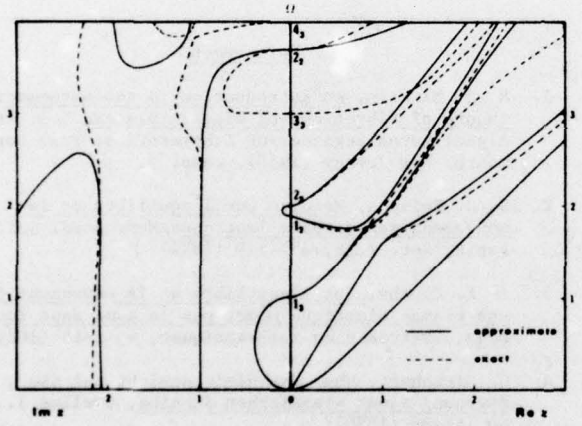

Figure 3: Dispersion curves for the second-order approximate theory. Waves in x_3 direction. 45° rotated Y-cut of $LiTaO_3$.

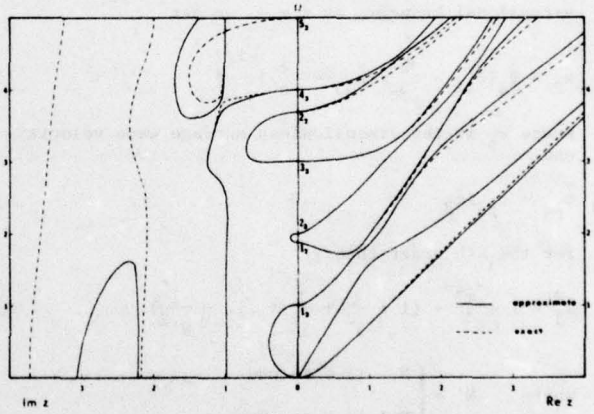

Figure 5: Dispersion curves for the fourth-order approximate theory. Waves in x_3 direction. 45° rotated Y-cut of $LiTaO_3$.

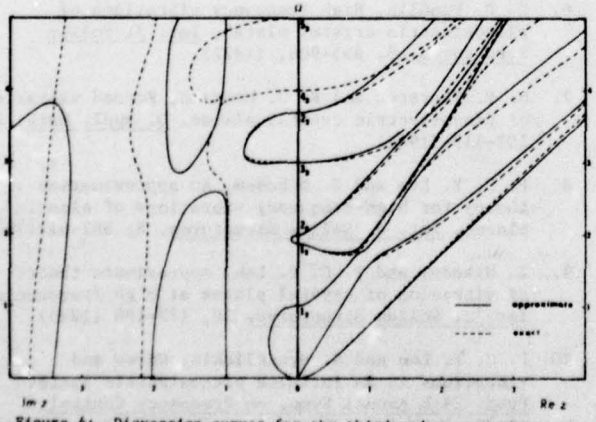

Figure 4: Dispersion curves for the third-order approximate theory. Waves in x_3 direction. 45° rotated Y-cut of $LiTaO_3$.

THE VIBRATION OF A BICONVEX CIRCULAR AT-CUT PLATE

Nobunori Oura, Hitohiro Fukuyo
Tokyo Institute of Technology
4259 Nagatsuta, Midoriku, Yokohama 227, Japan

and

Akira Yokoyama
Kumamoto University
Kurokamicho, Kumamoto 860, Japan

Summary

The thickness-shear fundamental vibration mode of a biconvex circular AT-cut plate is analyzed. As an analytical approach, the mode chart and electric polarization patterns of the biconvex circular AT-cut plate are compared in detail with those of the circular flat AT-cut plate of which vibration modes are well known.[1] As a result, it is found that the dominant displacement is u along the electrical axis as is the case for the circular flat AT-cut plate. Therefore, the equation of motion for the circular flat plate is employed in describing the vibration of the biconvex circular AT-cut plate. From the facts that the biconvex plate has a geometry similar to an oblate spheroid and that the electric polarizations are concentrated near the center of the plate, the biconvex plate is approximated by an oblate ellipsoid in carrying out the mode analysis.

1. Introduction

Planoconvex and biconvex circular AT-cut quartz plates have recently been used widely for highly stable quartz oscillators. The circular plates can be lapped very easily compared with rectangular and bevelled AT-cut plates because the cutting direction of the contour does not have to be aligned during the lapping process. However, convex AT-cut quartz plates must be lapped so as to coincide its axis as a lens with angle of cut of the plate. In spite of such difficulties in manufacturing the AT-cut plate is currently used extensively partly because the unwanted responses can be suppressed very effectively, and a high Q-value can be realized without fine adjustments of the support. However, the three-dimensional vibration analysis of biconvex circular AT-cut plates has not been done. We previously analyzed the thickness-shear vibration modes of the circular flat AT-cut plate, and in this paper, we apply the same technique to the vibration mode analysis of the biconvex circular AT-cut plate.

We measured frequency spectra and electric polarization patterns produced by the thickness-shear vibrations of the biconvex circular AT-cut plate. Thus it is found that the thickness-shear vibration characteristics of the biconvex plate are essentially the same as those of the circular flat AT-cut plate. As regards the thickness-shear vibration, the biconvex circular AT-cut plate is approximated by an equivalent ellipsoidal plate which is inscribed at the center of the plate.

2. Vibration Modes of Biconvex Circular AT-Cut Plate

The vibration modes have been analyzed in the following processes:

(1) The relationship between the plate size and resonance frequencies of the fundamental and spurious vibration modes is observed and the result is plotted in the mode chart. The mode chart is drawn every time the radius of curvature is modified by lapping while thickness must be kept invariant. The two spherical surfaces of the plate are ground with a curve generator having a No. 300 diamond wheel which is used for optical lens cutting until they acquire the same radius of curvature. The identical plate must be ground down at about a 5-mm step of radius of curvature. A silver film is evaporated on almost the whole area of each surface of the plate except the periphery. For the measurement of resonance frequencies, the plate is placed on a copper ring with a thin lead wire for ease of vibration and furthermore the same ring is put on the plate. An exciting voltage at the resonance frequency is applied to two copper rings. The resonance frequency spectrum is measured automatically and recorded on a strip chart. The mode spectrum thus obtained is shown in Fig. 1.

(2) A test sample having almost no spurious resonance is fabricated. The geometry of this sample is represented by points A, B and C in Fig. 1. The electric polarization patterns generated by the vibration are observed by means of the conventional electric probe method. Since the sample plate has two convex surfaces, a concave glass which has the same radius of curvature as the sample plate and on which a silver film is deposited is used as a lower electrode; after mounting a probe in it it is plated with copper and polished. The plate sits in an epoxy resin frame; a small motor drives the frame and the crystal slides along the lower electrode. The upper electrode is a silver film evaporated on the upper convex surface of the test sample. A thin lead wire is fixed to the periphery of this film with a conductive adhesive. Electric polarization intensities produced by the thickness-shear vibration thus measured are shown in Fig. 2. In Fig. 2(B), the central peak showed have the opposite polarity to the side peaks, and in Fig. 2(C) the two peaks should also have the opposite polarity to the other three which sandwich the two.

3. Vibration Modes of a Biconvex Circular AT-Cut Plate and Those of a Circular Flat AT-Cut Plate

The thickness-shear vibration modes are not strongly affected by the geometry of the plate, circular or square; the features of vibrational modes with the two different AT-cut plates are as follows:

(1) The thickness-shear vibration comprises not only the fundamental mode but also many inharmonic modes. The resonance frequencies of the biconvex AT-cut plate slightly increase as the radius of curvature is decreased while the thickness is kept constant. Similarly, those of the flat AT-cut plate increase as the radius of the plate decreases. As a whole, the electric polarization pattern is invariant substantially although the plate is biconvex.

(2) The intensity of electric polarization decreases more rapidly toward the periphery in the z direction than in the x direction, but (a) the electric polarization patterns of the biconvex circular AT-cut plate

are smoother than that of the circular flat AT-cut plate because of the weak coupling of the thickness-shear mode to the other modes; and (b) the electric polarization of the biconvex circular AT-cut plate is concentrated more strongly in the central area of the plate than that of the circular flat AT-cut plate.

From these similarities it may be concluded that the vibrational displacements of the thickness-shear mode with the biconvex circular plate are mainly along the electrical axis.

4. Theory for Thickness-Shear Vibrations of a Biconvex Circular AT-cut Plate

4.1 Equivalent Ellipsoidal Plate and its Equation of Motion

The thickness-shear vibration of the biconvex circular AT-cut plate produces displacement u along the electrical axis and we have the same equation of motion as for the circular flat AT-cut plate and the rectangular AT-cut plate[2]

$$c_{11}\frac{\partial^2 u}{\partial x^2} + c_{66}\frac{\partial^2 u}{\partial y^2} + c_{55}\frac{\partial^2 u}{\partial z^2} + \rho\omega^2 u = 0 \qquad (1)$$

where c_{11}, c_{66} and c_{55} are elastic constants referring to the x, y and z-axis, respectively, shown in Fig. 3, ρ is the mass density of quartz, and ω ($=2\pi f$) is the resonance angular frequency.

In terms of the replacements

$$\frac{c_{66}}{c_{11}} = \nu^2 \ , \quad \frac{c_{55}}{c_{11}} = \mu^2 \ , \quad \frac{\rho\omega^2}{c_{11}} = k_1^2 \qquad (2)$$

$$x = X \ , \quad y = \nu Y \ , \quad z = \mu Z \qquad (3)$$

Eq. (1) can be transformed into the Helmholtz equation

$$\frac{\partial^2 u}{\partial X^2} + \frac{\partial^2 u}{\partial Y^2} + \frac{\partial^2 u}{\partial Z^2} + k_1^2 u = 0 \qquad (4)$$

The resonance frequencies can be obtained from the values of k_1 which satisfy the given boundary condition. As mentioned already, however, it is difficult to solve Eq. (4) under the required boundary condition because there is no orthogonal coordinates which represent the geometry of the plate. Since the electric polarization is already found to be concentrated in the central area of the plate and the shape of the biconvex plate is similar to that of an ellipsoidal plate, the biconvex circular plate is replaced by an equivalent ellipsoidal plate which inscribes the given biconvex plate at the center of the plate surface and has the radius of curvature as the biconvex plate (see Fig. 3).

The radius of major axis of the equivalent ellipsoid represented by ellipsoidal coordinates is given by

$$e = \sqrt{tR/2} \qquad (5)$$

Therefore the ellipsoid is represented by

$$\frac{x^2}{\left(\sqrt{\frac{tR}{2}}\right)^2} + \frac{y^2}{\left(\frac{t}{2}\right)^2} + \frac{z^2}{\left(\sqrt{\frac{tR}{2}}\right)^2} = 1 \qquad (6)$$

which is rewritten as

$$\frac{X^2}{\frac{tR}{2}} + \frac{Y^2}{\left(\frac{1}{2}\frac{1}{\nu}\right)^2} + \frac{Z^2}{\frac{tR}{2}\frac{1}{\mu^2}} = 1 \qquad (7)$$

On the other hand, the rectangular coordinates are related to the ellipsoidal coordinates as follows:

$$Y^2 = \frac{(\xi_1^2-a^2)(\xi_2^2-a^2)(\xi_3^2-a^2)}{(a^2-b^2)\,a^2} \ , \quad X^2 = \frac{(\xi_1^2-b^2)(\xi_2^2-b^2)(\xi_3^2-b^2)}{(b^2-a^2)\,b^2}$$

$$Z^2 = \frac{\xi_1^2\xi_2^2\xi_3^2}{a^2b^2} \qquad (8)$$

where ξ_1, ξ_2 and ξ_3 are parameters and a and b are constants. These parameters and constants are related as

$$\frac{X^2}{\xi^2-b^2} + \frac{Y^2}{\xi^2-a^2} + \frac{Z^2}{\xi^2} = 1 \qquad (9)$$

and

$$\xi_1 > a > \xi_2 > b > \xi_3 > 0 \qquad (10)$$

As shown in Fig. 4, Eq. (9) represents an ellipsoid if ξ_1 is constant, a hyperboloid of one sheet if ξ_2 is constant, and a hyperboloid of two sheets if ξ_3 is constant. For the equivalent ellipsoidal plate, parameter should be replaced by ξ_f on the surface of the equivalent ellipsoidal plate.

$$\xi_f = \frac{Rt}{2\mu^2} \qquad a^2 = \frac{t}{2}\left(\frac{R}{\mu^2} - \frac{t}{2\nu^2}\right)$$

$$b^2 = \frac{Rt}{2}\left(\frac{1}{\mu^2} - 1\right) \qquad (11)$$

If u is expressed by $u = F_1(\xi_1)F_2(\xi_2)F_3(\xi_3)$[3], Eq. (4) may be rewritten as

$$\sum_{1\cdot2\cdot3} \frac{1}{(\xi_2^2-\xi_1^2)(\xi_3^2-\xi_1^2)}\sqrt{\frac{(\xi_1^2-a^2)(\xi_1^2-b^2)}{F_1}}\frac{\partial}{\partial\xi_1}\left\{\sqrt{(\xi_1^2-a^2)(\xi_1^2-b^2)}\cdot\frac{\partial F_1}{\partial\xi_1}\right\} + k_1^2F_1 = 0 \qquad (12)$$

which is further rewritten by separation of variables

$$\frac{1}{\sqrt{(\xi_n^2-a^2)(\xi_n^2-b^2)}}\frac{d}{d\xi_n}\left\{(\xi_n^2-a^2)(\xi_n^2-b^2)\right\}\frac{dF_n}{d\xi_n} + \left\{k_1^2 + \frac{k_2^2}{\xi_n^2-a^2} + \frac{k_3^2}{(\xi_n^2-b^2)(a^2-b^2)}\right\}F_n = 0 \qquad (13)$$

where n = 1, 2, 3 and k_2, k_3 are the separation constants. In Eq. (13) we must find values of k_1, k_2 and k_3 which satisfy the given boundary conditions.

4.2 Approximate Analysis of Thickness-Shear Fundamental Vibration

A long computing time is required to determine the values of k_1, k_2 and k_3 by solving the eigenvalue problem. μ in Eq. (3) for the AT-cut plate is approximately equal to unity, and the electric polarization is concentrated in the central area of the plate, and the plate has a shape similar to an oblate spheroid; consequently the equivalent ellipsoid in Fig. 3 may be replaced by an oblate spheroid which is represented by the oblate spheroidal coordinates, which takes the Y-axis as the axis of revolution. Here the parameters are set as $\xi_1 = \xi$, $\xi_2 = \eta$ and $\xi_3 = \sin\phi$ for the oblate spheroidal coordinates. Then, the following relations are obtained.

$$Y^2 = a^2\xi^2\eta^2 \ , \quad X^2 = a^2(1+\xi^2)(1-\eta^2)\cos^2\phi \ ,$$

$$Z^2 = a^2 \quad (1-\eta^2)\sin\phi \ , \quad 0 \le \xi \le \infty \ , \quad -1 \le \eta \le 1 \qquad (14)$$

Equation (4) is transformed by Eq. (14) as follows;

$$\frac{1}{a^2(\xi^2+\eta^2)}\left\{\frac{d}{d\xi}\left\{(1+\xi^2)\frac{du}{d\xi}\right\}+\frac{d}{d\eta}\left\{(1-\eta^2)\frac{du}{d\eta}\right\}\right\}+ \frac{\xi^2+\eta^2}{(1+\xi^2)(1-\eta^2)}\frac{d^2u}{d\phi^2}+k_1^2u=0 \qquad (15)$$

By assuming that u is separable in variables as

$$u = \Phi(\phi)\,S(\eta)\,J(\xi) \qquad (16)$$

the following equations are obtained from Eq. (15)

$$\frac{d^2\Phi}{d\phi^2}+m\Phi=0$$

$$\frac{d}{d\xi}\left\{(1+\xi^2)\frac{dJ}{d\xi}\right\}-\left(A-g^2\xi^2-\frac{m^2}{1+\xi^2}\right)J=0 \qquad (17)$$

$$\frac{d}{d\eta}\left\{(1-\eta^2)\frac{dS}{d\eta}\right\}+\left(A+g^2\eta^2-\frac{m^2}{1-\eta^2}\right)S=0$$

$$g \equiv k_1 a$$

where m and A are separation constants.[4] Since we find $\Phi(\phi) = \Phi(\phi + 2\pi)$ from its physical meaning, we put

$$\Phi(\phi) = \cos m\phi \qquad (19)$$

where m = 0, 1, 2, 3, ...

Since S must take a finite value, A becomes discontinuous and S in Eq. (16) is given by an associated Legendre function when $g \to 0$. Then, the separation constant is given by $l(l+1)$, l being equal to m, m+1, ... Therefore

$$A = A_{ml}(g) \qquad (19)$$

where m = 0, 1, 2, ... and l = m, m+1, m+2, ... Consequently, $S(\eta)$ and $J(\xi)$ are expressed as[4]

$$S(\eta) = S_{ml}(ig|\eta) = \sum{}' d_n(ig|ml)\,P^n_{m+n}(\eta) \qquad (20)$$

$$J(\xi) = je_{ml}(ig|-i\xi) = \left(\frac{\xi^2+1}{\xi^2}\right)^{m/2}\sum{}' a_n(ig|ml)\,j_{m+n}(g\xi) \qquad (21)$$

where $P^n_{m+n}(\eta)$ is the associated Legendre function and $j_{m+n}(g\xi)$ is the spherical Bessel function; a_n and d_n are constants and the prime indicates that n takes only even or odd numbers.

The X-Y cross section of the equivalent spheroid is given by

$$\frac{X^2}{a^2(1+\xi^2)}+\frac{Y^2}{a^2\xi^2}=1 \qquad (22)$$

The value of ξ_f on the plate surface is given by

$$\xi_f = \sqrt{\frac{C_{11}}{C_{66}}}\,t \Big/ 2e\sqrt{1-\frac{C_{11}t}{4C_{66}e^2}} \qquad (23)$$

where t is the thickness of the plate. Then the boundary condition is represented as follows by taking into account the thickness-shear mode.

$$\left(\partial u/\partial\xi\right)_{\xi_f} = 0 \qquad (24)$$

Equation (24) indicates that $\partial u/\partial\xi_f$ should vanish on the plate surface, where n is the normal to the surface. Equation (24) does not hold rigorously for the actual biconvex circular AT-cut plate except the center of the plate. However, the boundary condition represented by Eq. (24) is valid because the electric polarization is concentrated in the central area of the plate. In order to obtain the resonance frequency f, we must first determine the value of ξ_f and then obtain the value of g satisfying Eq. (24). According to Eq. (24), u is regarded as a function only of ξ and the following equation is obtained from Eqs. (21) and (24).

$$\sum_n \frac{g}{2(m+n)+1}a_n\left\{(m+n)j_{m+n-1}(g\xi_f)-(m+n+1)j_{m+n+1}(g\xi_f)\right\} - \frac{m}{\xi_f(\xi_f+1)}\sum_n a_n j_{m+n}(g\xi_f)=0 \qquad (25)$$

The electric polarization produced by the thickness-shear fundamental vibrational mode is distributed uniformly toward the periphery. Therefore m takes zero. The resonance frequency f is given by

$$f = \frac{1}{2t}\sqrt{\frac{C_{66}}{\rho}}\left(\frac{2}{\pi} g \xi_f\right) \qquad (26)$$

by using Eqs.(2), (11), (17) and (23).

The calculated resonance frequency is compared with the measured one in Fig. 5. The vibrational mode is given only by $S(\eta)$, because $J(\xi)$ is constant on the plate surface. Since $m = l = 0$, it is possible to calculate Eq. (20). Further, according to Eq. (14), the distance from the origin is given by

$$r = \sqrt{a(1+\xi_f^2)(1-\eta^2)} \qquad (27)$$

Since a and ξ_f are constant, the normalized radius of the plate is given by

$$r/r_0 = \sqrt{1-\eta^2} \qquad (28)$$

The calculated and observed thickness-shear fundamental vibrational modes are shown in Fig. 6.

5. Conclusions

In this paper, we have experimentally obtained the mode chart of a biconvex circular AT-cut quartz plate. With the aid of this mode chart we can find the relation between resonance frequency and plate size,and design resonators. We have observed the vibrational modes by measuring the electric polarization patterns and compared these with those of the circular flat and rectangular AT-cut plate. As a result, it has been confirmed that the plate vibrates dominantly in the direction parallel to the electrical axis, that is, the dominant displacement is u. For ease of the analysis of vibration of the biconvex circular plate, we have replaced the plate by an equivalent ellipsoid in view of the experimental facts that the electric polarization concentrates in the central area of the plate. The oblate spheroid model has been adopted to analyze the vibrational modes. The results obtained from this analysis indicate that the numerical solution is sufficiently useful so far as the thickness-shear fundamental vibration is concerned.

References

1. Fukuyo, Yokoyama and Oura, Trans. I.E.E., Japan, Vol.93-A, p.355, Aug. 1973.
2. Koga and Fukuyo, Jour. I.E.C.E., Japan, Vol.36, p.59, Feb. 1953.
3. P.M. Morse and H. Feshbach, Method of Theoretical Physics, Vol.1, p.511, 1953.
4. J.A. Stratton, et al., Spheroidal Wave Functions Including Tables of Separation Constants and Coefficients, 1956.

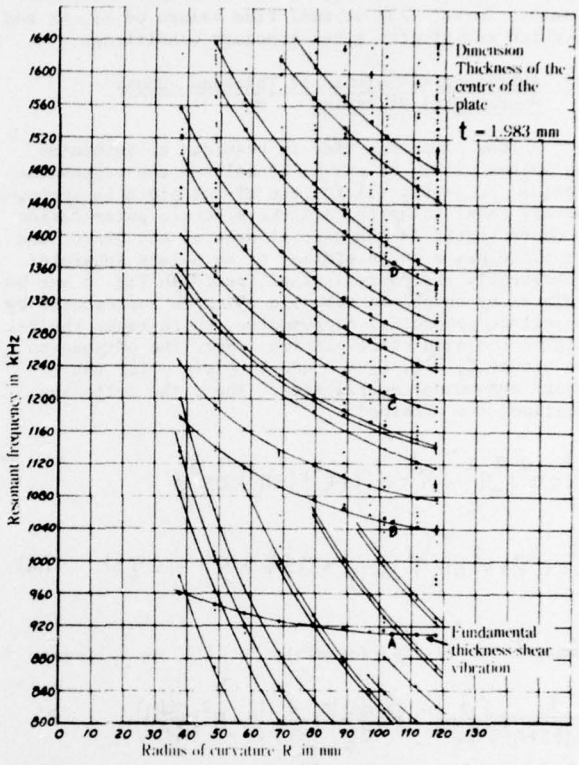

Fig.1 Mode chart of biconvex circular AT-cut plate.

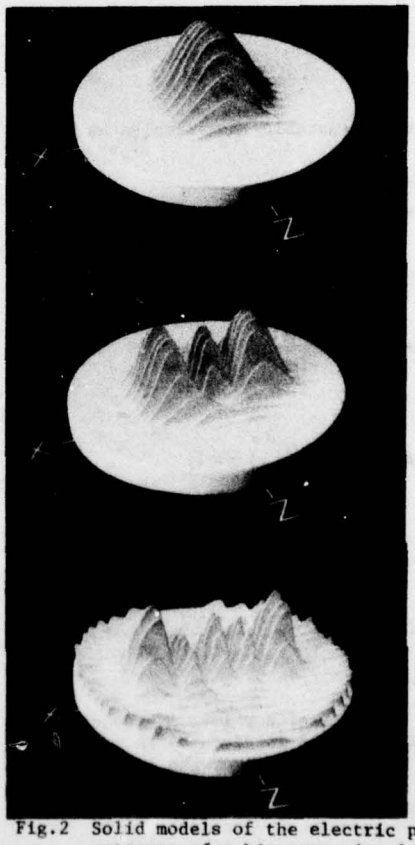

Fig.2 Solid models of the electric polarization patterns of a biconvex circular AT-cut plate.

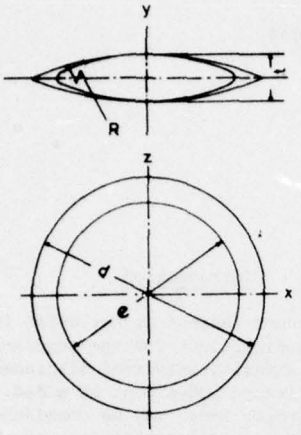

Fig.3 A biconvex circular AT-cut plate and its equivalent ellipsoidal plate.

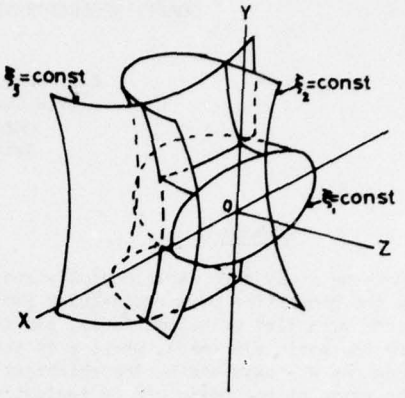

Fig.4 Ellipsoidal coordinates.

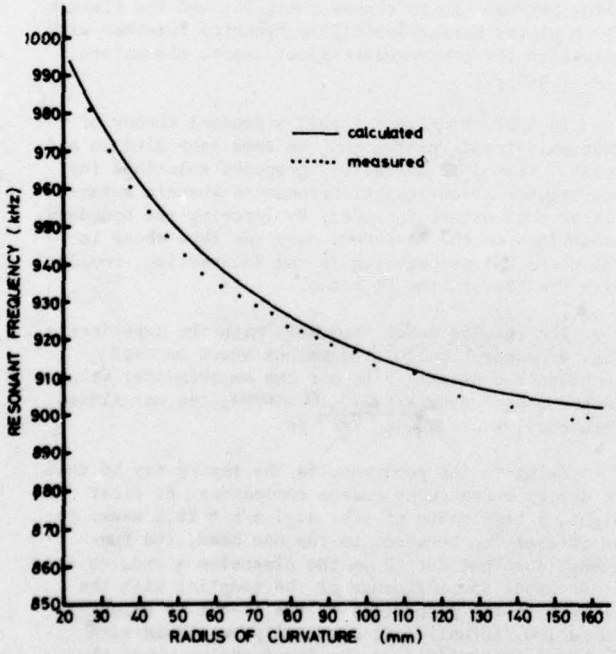

Fig.5 Resonance frequencies of the thickness-shear fundamental vibration of a biconvex circular AT-cut plate.

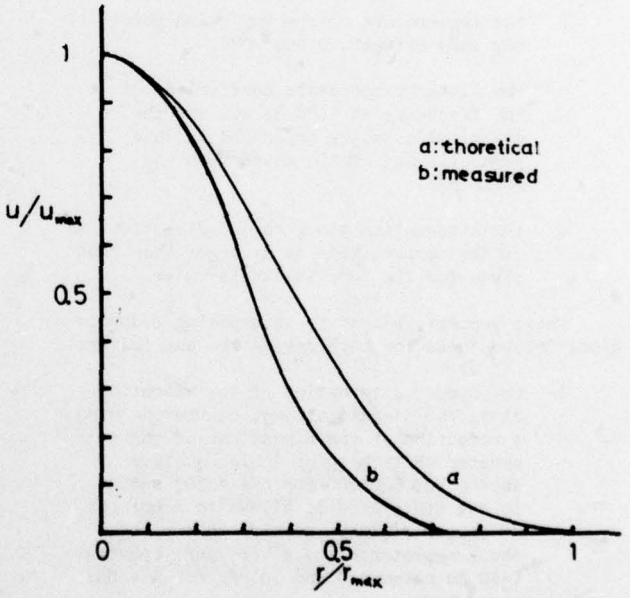

Fig.6 The vibrational mode of the thickness-shear fundamental vibration of a biconvex circular AT-cut plate.

PROPERTIES OF A 4 MHZ MINIATURE FLAT RECTANGULAR QUARTZ RESONATOR VIBRATING IN A COUPLED MODE

A.E. Zumsteg and P. Suda
SSIH-QUARTZ Division
OMEGA, Bienne
Switzerland

Summary

In this work we study both experimentally and theoretically the properties of a rectangular AT-cut quartz resonator with flat principal faces, particularly for very low ratio a/b ($\sim$3), where a is the dimension along the X - axis and b, the thickness of the plate. The value of the ratio c/b is typically 25 where c is the dimension along the Z'-axis. For such low values of a/b, the coupling between the thickness shear and the flexure is very important; the transversal displacement due to the flexion amounts to 50% of the tangential displacement at the surface of the plate due to the thickness shear. This coupling modifies many of the well-known properties of the usual AT-cut.

a the frequency vs temperature curve is asymmetric of "third order" and more open than usual AT curves.

b the temperature of the inflexion point may vary between 50 and 90°C.

c the linear temperature coefficient of the frequency at 25°C as well as the dynamical capacity depend both, in a parabolic and cyclic manner, on the ratio a/b.

d the attenuation along the Z'-direction of the coupled mode is stronger than that given for the pure thickness-twist.

These properties lead to interesting technological consequences for both resonators and filters.

i the strong attenuation of the vibration along the Z'-axis allows, on the one hand a reduction of the dimensions of the resonator while keeping a high quality factor (Q > 500'000 for c/a = 20) and, on the other hand it allows to mount the resonator rigidly, getting thus a high shock resistance and a very pure spectrum (-60 db between 0 and 10 MHz for a 4 MHz resonator).

ii possibility to use a high-frequency resonator with an inversion point at room temperature and with a parabolic temperature coefficient of -1.10^{-8} /(°C)^2 instead of -4.10^{-8} /(°C)^2 for the BT cut.

iii easy fabrication since all faces are plane, all sections are rectangular and only two faces need to be partially metallized.

Its utilization seems most suitable for high-quality wrist-watches (1 sec./month)

Introduction

A pure thickness shear does not exist in a free plate with finite dimensions for the angular momentum would not be conserved. Transversal displacements which result in flexure modes must be added. The coupling between these modes may be considered as fundamental for it exists independently of the crystalline symmetry. Other couplings may be considered as accidental for they depend e.g. on the value of an elastic or piezo-electric constant; these constants may cancel for some symetries or may be cancelled by a judicious rotation.

The mathematics of the fundamental couplings is complicated because a perturbation methode can only be locally applied. So, we have to wait until 1951, year when a theory due to R.D. Mindlin[1] (named I hereafter) started discussing in a quantitative manner the coupling between the thickness shear TS_1 and the flexure F_1 in plates having monoclinic symmetry together with solutions for rectangular AT-cut quartz resonators. Fig. 1 and 2.

In 1961, Mindlin [2] issued a general theory of thin anisotropic plates and the same year Mindlin and Gazis [3] (named II hereafter) proposed solutions for rectangular AT-cut quartz resonators wherein extentional motions are included. By ignoring the boundary conditions on the Z'-faces, only the face shear in the plane XZ' propagating in the X-direction, couples with the TS_1 and the F_1 modes.

The results match very well with the experiments[3]. Fig. 3 compares calculated values where we used Bechmann's constants [4] to our own experimental values in the range $2{,}8 \leq a/b \leq 10$, $\Omega = \omega/\omega_s$ the normalised frequency, $\omega_s = \pi\sqrt{c'_{66}/\rho}\,/a$.

Owing to the good results the theory may be used to design rectangular quartz resonators. At first sight, a high value of a/b, e.g. a/b = 29,5 seems to be interesting because, on the one hand, the frequency does not depend on the dimension a and, on the other hand, the influence of the coupling with the flexure on the properties of the AT-cut is expected to be low. Actually, it can easily be proved with I that in the middle of the first shelve above the axis $\Omega = 1$ the ratio of the vibration amplitude of both modes TS_1 and F_1 is inversely proportional to n-1, where n is the order (even) of the flexure harmonic. This leads to resonators which are elongated along the x-axis[5] as depicted in fig. 4a.

However these resonators present a disadvantage for they only offer a middle quality factor which is moreover affected with a great dispersion. This is due to the flexure mode F_1 which is propagating in the X-direction and which undergoes no attenuation

outside the metallized region (Fig. 4b). So there exists an energy flow absorbed or partially reflected by the mounting structure. Mindlin and Lee[6] have calculated the quality factor of such resonators,* the losses due to the flexure must be suppressed i.e. the X-faces must be kept free. A resonator elongated along the Z', with a narrow dimension a as depicted in fig. 5a and b, gives good results.[7,8]
As the flexure mode arises from coupling with the thickness shear mode, an attenuation of the latter along the Z'-direction (which is stronger than along the X-direction) also leads to an attenuation of the F_1 mode along the Z'-direction, resulting in a perfect energy trapping. The reduction of the dimension causes an important coupling between both TS_1 and F_1 modes modifying substantially the properties of the usual AT-cut[8]. Some of these modifications are studied hereafter.

*in the case of infinite plate. In order to improve the quality

Coupling

According to II, the terminology of which is used here, the displacements are given by:

$$\bar{u}_2 = h(\bar{A}_1 \alpha_{21} \sin \xi_1 x_1 + \bar{A}_2 \alpha_{22} \sin \xi_2 x_1 + \bar{A}_3 \alpha_{23} \sin \xi_3 x_1)$$

$$\bar{u}_3 = h(\bar{A}_1 \alpha_{31} \sin \xi_1 x_1 + \bar{A}_2 \alpha_{32} \sin \xi_2 x_1 + \bar{A}_3 \alpha_{33} \sin \xi_3 x_1)$$

$$\Psi_1 = \bar{A}_1 \cos \xi_1 x_1 + \bar{A}_2 \cos \xi_2 x_1 + \bar{A}_3 \cos \xi_3 x_1$$

where $\bar{u}_2$ and $\bar{u}_3$ are the displacements directed along Y' and Z', Ψ_1 is the rotation about Z', ξ_1, ξ_2, ξ_3 the wave numbers associated respectively to the flexure, the face shear and the thickness shear mode. h $\bar{A}_1 \alpha_{21}$ represents the vibration amplitude perpendicular to the plate due to the flexure mode and h $\bar{A}_3$ the tangential vibration amplitude on the surface of the plate due to the thickness shear mode. We characterize the coupling by the ratio $\bar{A}_1 \alpha_{21} / \bar{A}_3$ which is depicted on fig. 6 for the vibrations coupled to the 4th and 8th flexure harmonic. For a/b ~ 3 the ratio $\bar{A} \alpha_{21} / \bar{A}_3$ amounts to nearly 0,5 which also means that the kinetic energies of the tangential and transversal displacements are nearly equal. Consequently, it is not possible to discribe the vibration of such a resonator simply by a pure thickness shear. The coupling rate may be adjusted by varying the ratio a/b modifying thus the properties of the resonator and, as is shown hereafter, the smallest coupling does not yield the most interesting properties.

Thermal properties

The resonance frequencies vs temperature have been calculated within the frame of both theories I and II on the basis of the temperature coefficient of Bechmann et al[4] as well as those of Adams et al[9]. The calculations are quite long specially in the frame of II where the IBM computer 360/135 of the OMEGA-watch firm was used.

The differences due to both sets of temperature coefficients are an order of magnitude smaller than that between I and II. The results published here are calculated with Bechmann's set. Fig. 7 shows the influence of the dimension on the frequency vs temperature curve calculated according to I and fig. 8 according to II. Fig. 9 shows the same measurements obtained on energy trapped resonators. There is a qualitative agreement between the theory and the experiments as far as the shape of the curves is concerned, but the rotation angles are fairly different. The curves are asymmetric with inflexion point lying between 40 and 90°C. The radius of curvature is small in the upper inversion point* Pi at 25°C with parabolic temperature coefficient of the order of -1.10^{-8} / $(°C)^2$ and one at 55° with $-2.10^{-9}/(°C)^2$.

Fig. 11 gives a comprehensive view of the linear temperature coefficient of the frequency $T_f^{(1)}$ at 25°C. The most interesting point is the parabolic and cyclic behaviour of $T_f^{(I)}$ as a function of a/b. It is forecasted by I, particularly for the values of a/b corresponding to the top of each parabola. Theory II does not report a parabolic behaviour of $T_f^{(I)}$, although its absolute value is closer to the measured one than that yielded by I. The discrepancy between II and the measurements may be due to the energy trapping which induces a partial inhibition of the extentional motion; this is not accounted for by II whereas it is indirectly reported in I where no extentional motions are allowed. We found experimentally that $T_f^{(I)}$ diminishes with increasing electrode thickness in the order of magnitude calculated by Zelenka[10].

* and big in the lower one. Fig. 10 shows an inversion point

Dynamical capacity

A dynamical capacity as high as possible is often required for resonators as well as for filters. Fig. 12 shows the measurements on 4 MHz resonators. The electrodes are 3 mm long and a/b = 2,96. As for $T_f^{(I)}$, the dynamical capacity C_1 bears a parabolic and cyclic behaviour as function of a/b. The maxima of $T_f^{(I)}$ and C_1 amount to the same values of a/b which differ from those corresponding to the minima of the coupling (cf. fig. 11, 12 and 6). The choice of a maximum dynamical capacity of the main mode provides simultaneously a minimum dynamical capacity of the other modes of the same kind, thus contributing to the spectral purity.

Quality factor

The optimization of the quality factor has been achieved by incremental metalization in ultra high vacuum followed by measurements in situ. Fig. 13 shows the quality factor Q vs gold electrode thickness t per side. The maximum is very sharp and depends on the value of a/b. By metalizing at once the optimal thickness, the Q values are higher, thus showing that some losses are due to the electrodes. These losses probably account only for a part of the strong decrease of Q value beyond the maximum. There may exist a mechanism owing to the distribution of the vibration amplitude as function of the electrode thickness which can explain a maximum of the Q value. This is suggested by the dependance of the optimal electrode thickness on the ratio a/b. The high value of Q reveals that the attenuation of vibration amplitude along the Z'-direction is much stronger than that given by the well-known formula for a pure thickness twist

$$e = 2.94 \sqrt{\Delta} \; d/b$$

where d is the distance from the electrode edge. Theoretical work and interferometric vibration amplitude measurements are in progress.

Spectrum

Fig. 14 shows a spectrum between 0,01 and 10 MHz of a resonator presenting the following characteristics:

frequency 4.2 MHz, a/b = 2,96, Q = 265'000, R_{serie} = 98Ω

The ordinate is the current response, the applied voltage being 100 mV. This spectrum is very pure, the most important unwanted mode lying 60 db below the fundamental one. The reasons are:

a. the good energy trapping allows a rigid mounting that damps down all modes which are not trapped.

b. the coupled modes TS_1 and F_1 immediately above and below the fundamental are on the one hand far away in frequency while having, on the other hand, a very low dynamical capacity.

c. the a dimension being small, the frequencies of all modes depending thereon are high and scarce in the considered frequency range.

Aging

Since the aging is mainly due to the mounting and the encapsulation, a compromise must be chosen between a high shock resistance and a low aging. Measurements on encapsulated resonators suffering shocks of 5000 g on three axis show an aging of the order of 1 to 2.10^{-9} per day after 60 days in stock.

Conclusion

A rectangular AT-cut resonator elongated in the Z'-direction offers interesting thermal and electrical properties, a high quality factor and an aging low enough to be used advantageously everywhere, where very small dimensions are required. The most promising application is to be found in the high quality wrist-watches (1 sec. per month) because the following resonator may be produces economically in large quantities.

Frequency	$f = 4{,}194304$ Hz $= 2^{22}$
Resistance	$R = 50\Omega$
Dyn. Capacity C_1	$C_1 = 1{,}6.10^{-15}$ F
Qual. Factor	Q = 500'000
Static Capacity	$C_o = 1{,}0$ pF
Inversion Temperature	$T_o = 25^oC$
Thermal coefficient	$\beta = -1{,}1.10^{-8}\ /(^oC)^2$
Case dimensions	13,4 x 3,4 x 2,8 mm (0.530 x 0.134 x 0.110")

References

1. R.D. Mindlin, J Appl. Phys. 22, 316, (1951)
2. R.D. Mindlin, Quart. Appl. Math. 19, 51 (1961)
3. R.D. Mindlin and D.C. Gazis Proc. 4th Natl. Congr. Appl. Mech. US, 305 (1961)
4. R. Bechmann et al., Proc. IRE 50, 1812, (1962)
5. J.J. Royer, Proc. 27th AFCS, 30,(1973)
6. R.D. Mindlin and P.C.Y. Lee, Int. J. Solids Strut. 2, 125, (1966)
7. Patent pending US SN 364266 and SN 528 829
8. Patent pending US SN 650 643
9. C.A. Adams et al. Proc. 24th AFCS, 55, (1970)
10. J. Zelenka, Int. J. Solid Strut, 11, 871, (1975).

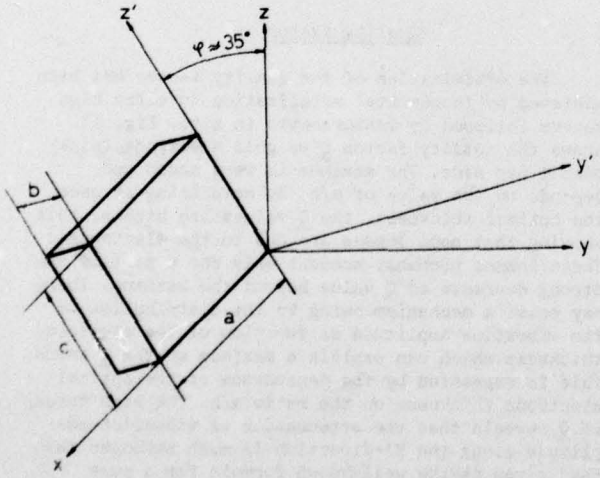

Fig. 1 Orientation of the quartz plate

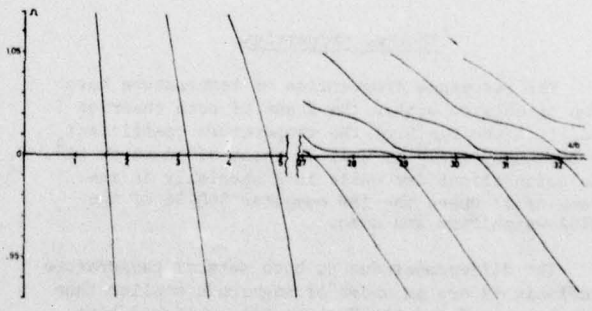

Fig. 2 Frequency spectrum after I

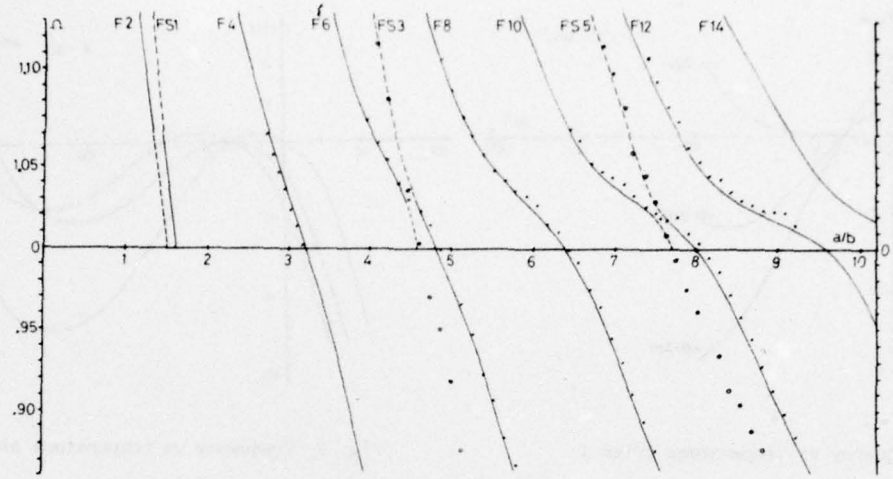

Fig. 3 Comparison of the theory with experimental values
x measurements thickness shear o measurements face shear
Curves are calculated after II

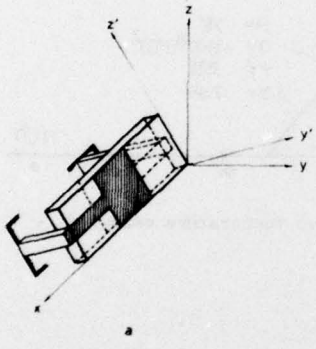

Fig. 4 Rectangular quartz resonator elongated along X

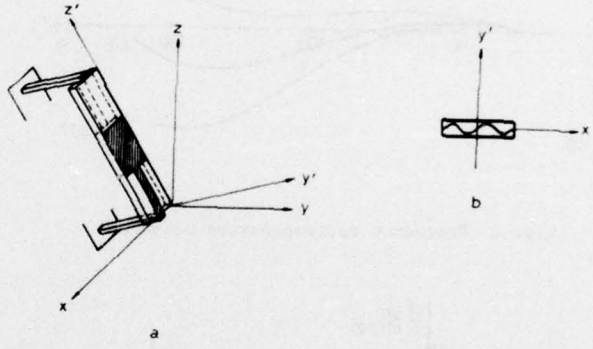

Fig. 5 Rectangular quartz resonator elongated along Z'

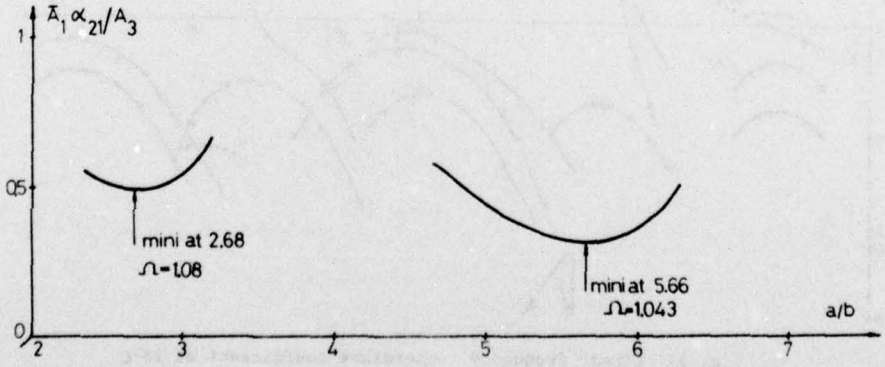

Fig. 6 Amplitude ratio of flexure to thickness shear displacement

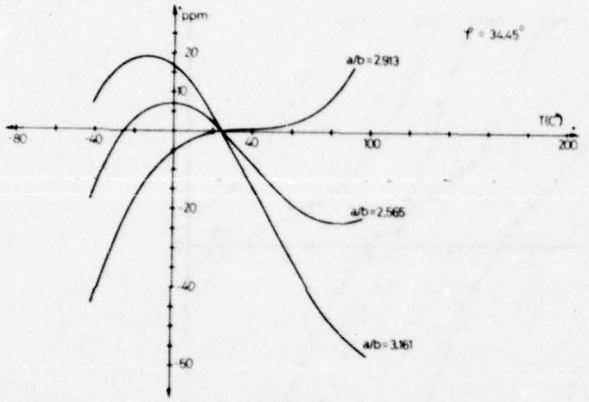

Fig. 7 Frequency vs temperature after I

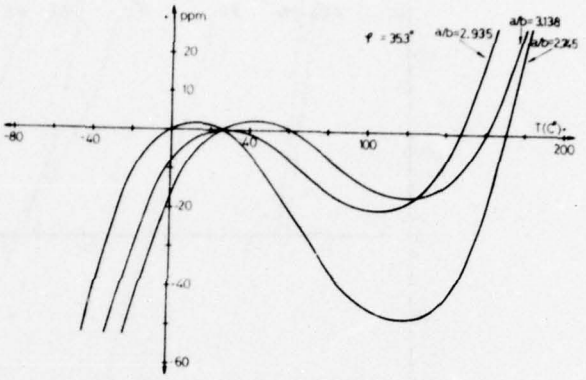

Fig. 8 Frequency vs temperature after II

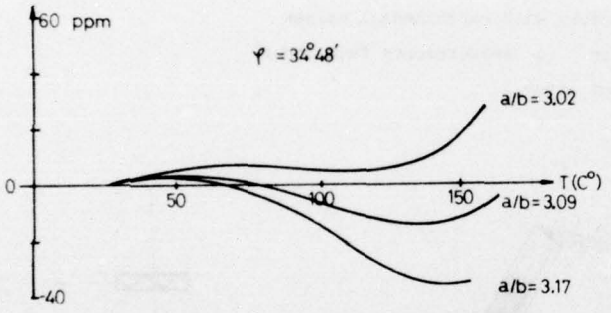

Fig. 9 Frequency vs temperature measured

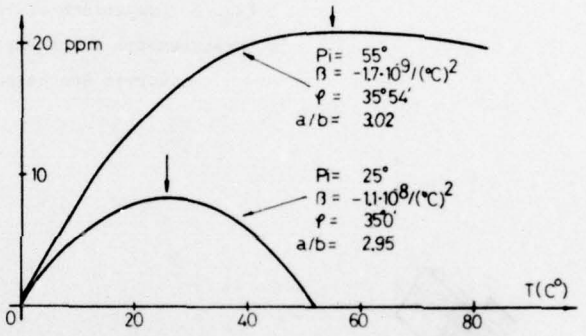

Fig. 10 Frequency vs temperature measured

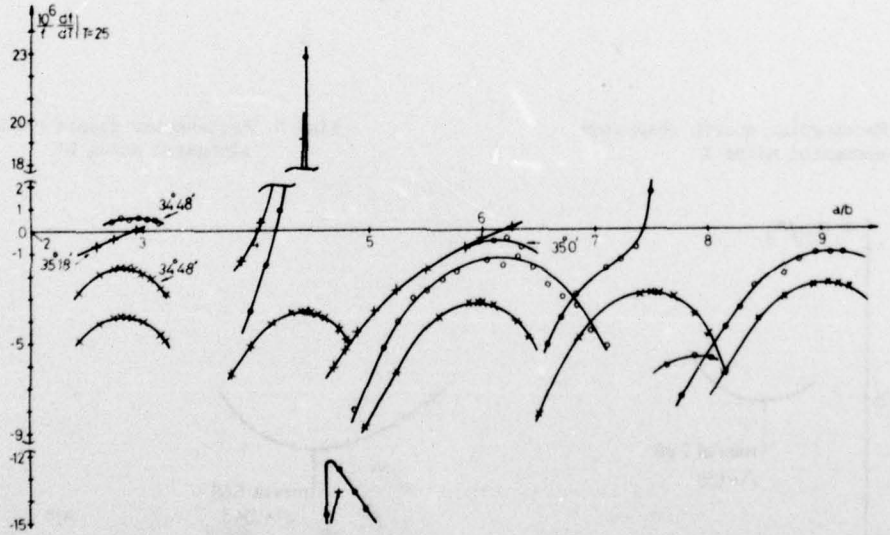

Fig. 11 Linear frequency temperature coefficient at 25°C
x calculated after I, + calculated after II, o measured
All curves without angle value are for 35°15'

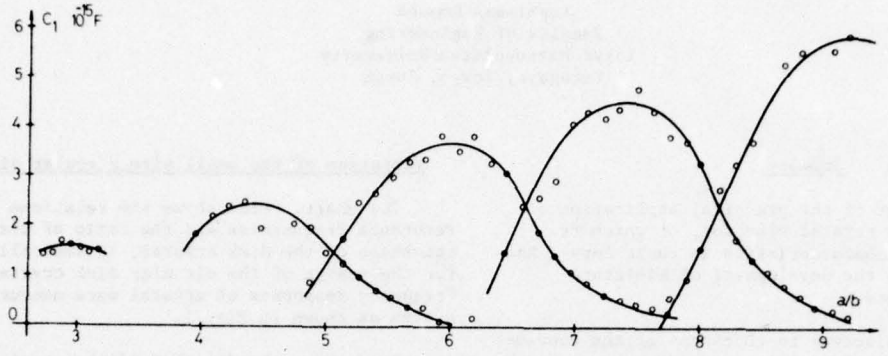

Fig. 12 Dynamical capacity

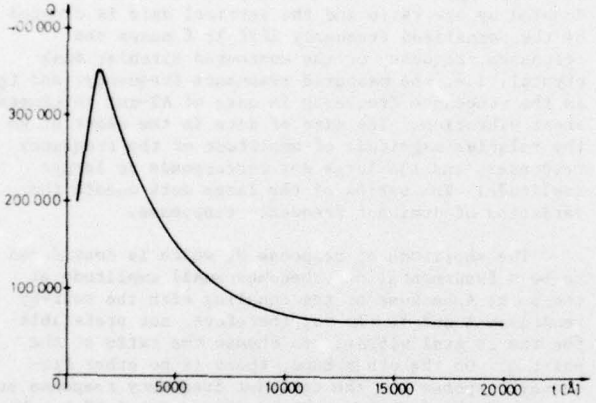

Fig. 13 Quality factor vs electrode thickness

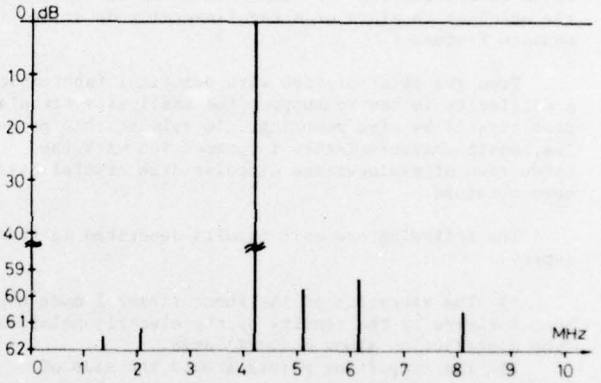

Fig. 14 Spectrum

MINIATURIZED CIRCULAR DISK AT-CUT CRYSTAL VIBRATOR

Yoshimasa Oomura
Faculty of Engineering
Tokyo Metropolitan University
Setagaya, Tokyo, Japan

Summary

The requirement of the practical application of miniaturized AT-cut crystal vibrator, of which frequency temperature characteristics is cubic curve, has been increased with the development of miniature electronic components.

The ratio of diameter to thickness of the conventional circular disk AT-cut plate that has been used for thickness shear mode is usually more than 15, but the ratio of miniaturized one described in this paper is 4.68 (diameter: 6.824 mm, thickness: 1.459 mm, Frequency: about 1.2 MHz). This ratio is determined from a chart which expresses the variation of frequency responses versus the ratio of diameter to thickness. It is understood from the chart that the vibration of the specimen consists of shear flexural mode at resonance frequency.

From the point of view with practical fabrication, a difficulty is how to support the small size circular disk crystal by wire mounting. In solving this problem, basic characteristics in connection with the production of miniaturized circular disk crystal have been obtained.

The following are main results described in this paper.

1) The vibration of the shear flexural mode has been analyzed by the results of the electric polarization distribution along X and Z' axis.
2) The supporting points around the side of specimen are examined by the mechanical probing method, and a pair of supporting positions at the center of thickness on Z' axis are found best. A pair of supporting wires are adhered to these points.
3) The reproducibility of the frequency temperature characteristics has been considered to be satisfactorily good.
4) The flexural mode of the side wire mounted circular disk crystal is observed by Michelson's interferometer, and the results on the supporting points show good agreement with the results obtained from the mechanical probing method.

Introduction

The miniaturized crystal vibrator, of which shapes are the tuning fork type and the bar type, have been put into practice in the industry of wrist watches in compliance with the development of miniature electronic components. Owing to the electrical behaviors of those crystals, the temperature compensating circuits are necessary in accordance with the requirement of accuracy.

Recent development of application of IC and LSI in the frequency range of MHz urges miniaturization of AT-cut crystal vibrator.

The present paper concerns with the convenient manufacturing process on the miniaturization of the circular disk AT-cut crystal and their electrical characteristics.

Vibration of the small size circular disk crystal

The chart, which shows the relations between the resonance frequencies and the ratio of diameter to thickness of the disk crystal, is basically necessary for the design of the circular disk crystal vibrator. Frequency responses of crystal were measured by the system as shown in Fig. 1.

Decreasing the diameter of the specimen by polishing, frequency responses on the specimen at different diameter (6.5 mm - 25 mm) were measured. An air gap holder was used in the measurements. A part of the above mentioned chart obtained from the experiments is shown in Fig. 2. In this chart, the abscissa is denoted by the ratio and the vertical axis is denoted by the normalized frequency (f/f_0); f means the resonance frequency of the contoured circular disk crystal, i.e. the measured resonance frequency; and f_0 is the resonance frequency in case of AT-cut thickness shear vibration. The size of dots in the chart shows the relative magnitude of amplitude of the frequency responses, and the large dot corresponds to larger amplitude. The series of the large dots denote the variation of dominant frequency responses.

The amplitude of response 2, which is considered to be a fundamental one, becomes small amplitude at the point A because of the coupling with the near-by responses 1 and 3. It is, therefore, not preferable for the crystal vibrator to choose the ratio at the point A. On the other hand, there is no other frequency response but the dominant frequency response at the point B. So, the ratio at this point 4.68 has been decided for the specimen of crystal vibrator and its frequency responses is shown in Fig. 3.

Fig. 4 shows the electrical probing method to measure the distribution of polarization[1], and obtained distributions are shown in Fig. 5. As shown in Fig. 5, the piezo electric changes are in accordance with the strain excited by the resonance frequency.

R. Stark applied the optical interferometer to the study of the vibrational mode of the AT-cut circular disk crystal[2]. Calculation on the electric polarization distribution along X axis was made by using formulae obtained by him, and the result showed good agreement with the measured one. These calculated formulae are referred to Appendix. It is understood from the above mentioned results that the vibration of the miniaturized circular disk crystal is consisted of the shear flexural vibration.

Supporting Method

Supporting positions

The conventional supporting method is not applicable to the small size crystal treated in this paper. Previous to the establishment of supporting method, the mechanical probing method was used to find a pair of positions on the crystal.

Fig. 6 shows the apparatus of the mechanical probing method. Silver electrodes were applied to surfaces and side of the disk crystal specimen. The belt electrodes (width: about 1 mm) were arranged for

the connection between the surface electrodes (diameter: 6 mm) and the side one. The thickness of these electrodes was 1,000 Å.

The experimental procedure is as follows. The specimen is held by the upper and the lower rods at the center of thickness. With the change of holding position by 30 degree, the resonance frequency and the crystal impedance (CI) are measured by the π network. These measurements are also carried out by changing the weights on the upper rod to examine the external force effects. The experimental results are shown in Fig. 7 and Fig. 8. It is clarified from these results that a pair of centers of thickness on Z' axis are very good for the supporting positions.

Side wire mounting

An air gap holder shall not be used for the miniaturization of the crystal vibrator because of its large construction and of the instability in the resonance frequency which might be caused by the portable usage. Therefore, the side wire mounting has been adopted. Fig. 9 shows the appearance of the side wire mounting on Z' axis. The wires used for this mounting are the bronzephospher headed wires coated by gold. After mounting, silver electrodes were formed by evaporation in vacuum of 2×10^{-5} Torr. The specimen is connected to the lead wires of the HC-25/U socket as shown in Fig. 10. Fig. 11 shows the photograph of the specimen.

Characteristics of the side wire mounted crystal

Electrical characteristics of the miniaturized circular disk crystal vibrator were measured by the π network.

Reproducibility of the side wire mounting

Reproducibility of the side wire mounting was taken into consideration from the point of the frequency temperature characteristics and relations between the CI values and temperature. The experiments with regard to the reproducibility were carried out by the following procedures. After completion of the first measurements of the above mentioned characteristics, all of the supporting wires and electrodes were taken off from the crystal. Consequently the specimen was made return to the initial state of crystal. This crustal was again subjected to attach the wires and electrodes in accordance with the previously mentioned processes, and was served to the second measurements. These processes--preparation of the specimen for measurements, and elimination of the wires and electrodes--were repeated three times. The results obtained in this experiment are shown in Fig. 12 and Fig. 13.

In these figures the results measured by air gap holder are plotted for comparison. It is seen from Fig. 12 that the change in frequency with the temperature change is less than 3×10^{-6}, and this shows that the reproducibility of mounting is fairly good.

The measured values of the crystal impedance change from about 500Ω to 900Ω as shown in Fig. 13. The curve (1) in Fig. 13 shows the result obtained by air gap holder, and the curves (2), (3), and (4) are the results by the side wire mounting. These numbers attached to the curves correspond to the order of measurements, and then the curve (5) means the results measured by air gap holder after the side wire mounting had been done. Comparing the curves between (1) and (5), the increments of crystal impedance are nearly 120Ω to 250Ω. The above mentioned increment of CI may be caused by the defects and the scratches which are seemed to exist in the crystal under the manufacturing treatment.

Length of the supporting wires

It is more advantageous for miniaturization of crystal vibrator to make the supporting wire length shorter. Fig. 14 shows variations of CI and changes in frequency with the change of the length of supporting wire. If the supporting wires are adhered to the center of thickness on Z' axis, the length of wire exerts little influence on the characteristics within 1.5 mm.

Cubic curve

Frequency temperature characteristics for crystal of various cut angles from Z-minor face were measured at the previously decided ratio of diameter to thickness. Zero temperature coefficient has been obtained in the range of 45°C to 55°C at the cut angle 4°15'. Fig. 15 shows the typical cubic curve of the frequency temperature characteristics in the range of -10°C to 145°C. The CI value is comparatively small and its Q value is about 340,000.

Observation of flexural vibration

The flexural vibration mode was observed by Michelson's interferometer[3]. Fig. 16 shows the observed interference fringes for the crystals of different supporting axis. The crystal current in these experiments was kept at constant of 1 mA. Black stripes in the photographs are considered to be unmoved regions in the flexural vibration.

Fig. 17 shows the calculated displacement along X axis according to the reference (2), and the displacement corresponds to the observed interference fringes in the photograph of Fig. 16. It is, therefore, considered that both ends of the crystal diameter on X axis move as like as the calculated displacement.

Fig. 18 shows the calculated electric polarization distribution along X axis. The distribution consists of of the sum of both components of polarization due to the shear vibration and the flexural one. The measured electric polarization distribution as shown in Fig. 5 is in good agreement with the calculated one in Fig. 18.

Conclusion

The miniaturized circular disk AT-cut crystal vibrator, of which ratio of diameter to thickness is below 5, is still not utilized, but the possibility of their practical use has been proved experimentally, provided that the suitable supporting positions and methods have been found.

Appendix I

From the results of reference (2) concerning on the vibrational mode of the circular disk AT-cut crystal with the ratio 20 and 40, the components of displacement are expressed by the following formulae according to the polar coordinates.

$$U_x = \bar{U}_r \cos^2\theta - \bar{U}_\theta \sin^2\theta$$

$$U_{z'} = (\bar{U}_r + \bar{U}_\theta) \sin\theta \cos\theta$$

$$\eta = \bar{\eta} \cos\theta$$

where U_X, $U_{Z'}$ are the displacement components of X and Z' axis, and η is the thickness direction displacement. The symbols expressed in the above mentioned formulae are the same definitions as those in the reference (2).

The displacement of the flexural mode on X axis is obtained in case that the angular θ becomes zero. The calculated flexural displacement is shown in Fig. 17.

The electric polarization distribution on X axis is expressed by the next formula.

$$\left|\frac{P\ (r,0)}{\bar{P}\ (r,0)}\right| \propto U_x\ (r,0) + \frac{\partial \eta(r,0)}{\partial r}$$

where $\bar{P}\ (r,0)$ is the maximum value.

References

1. H. Fukuyo, "Researches in Modes of Vibrations of Quartz Crystal Resonators by Means of the Probe Method". Tokyo Institute of Tech. Bulletin No. 1 (1955)

2. R. Stark, "Die Kopplungen zwichen Dickenscher und Biegeschwingungen runder AT-geschnittener Quarzscheiben". Telefunken Ztg. 31, pp. 179-185, September (1958)

3. Born and Wolf, "Principles of Optics". pp. 300-302, Pergamon Press, 3rd Edition (1965)

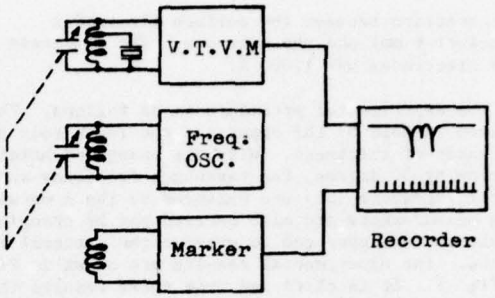

Fig. 1 - Measuring System for Frequency Response.

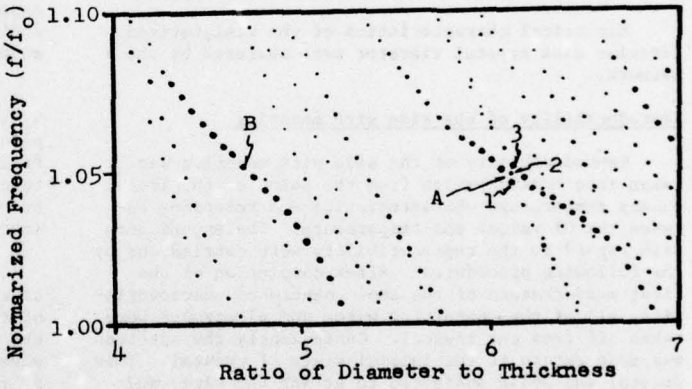

Fig. 2 - Chart of Resonance Frequencies versus Ratio of Diameter to Thickness.

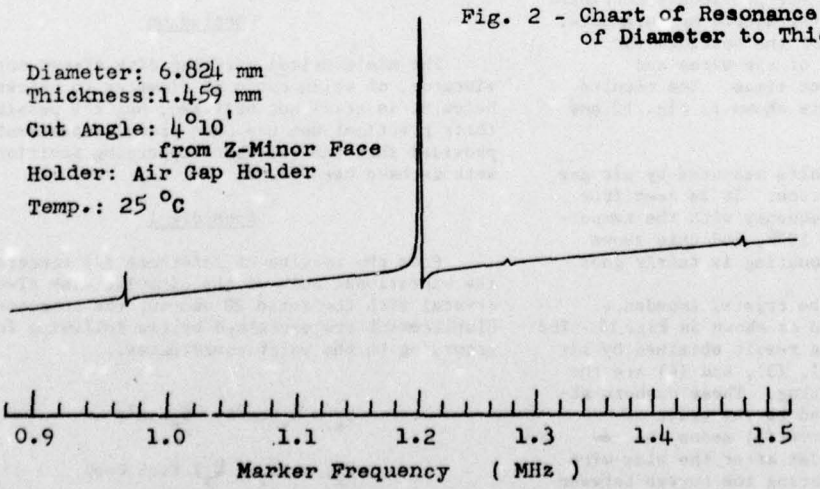

Fig. 3 - Measured Frequency Response of AT-Cut Circular Disk Crystal Vibrator.

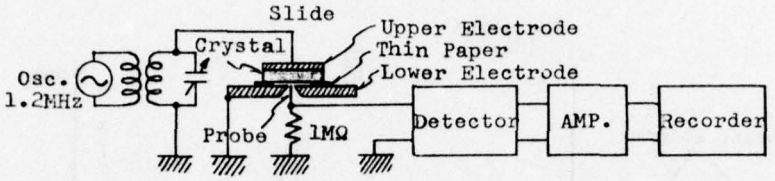

Fig. 4 - Measuring System for Electric Polarization Distribution. (Electric Probing Method).

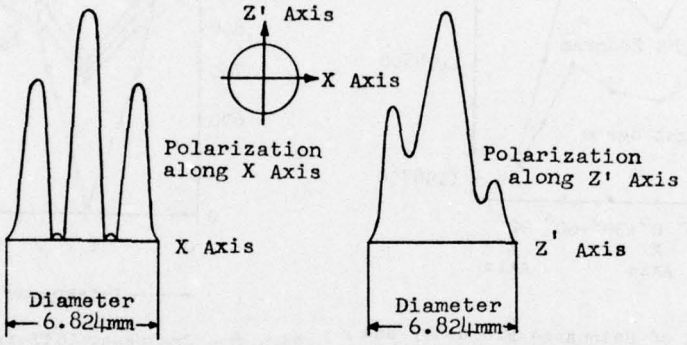

Fig. 5 - Measured Electric Polarization Distributions.

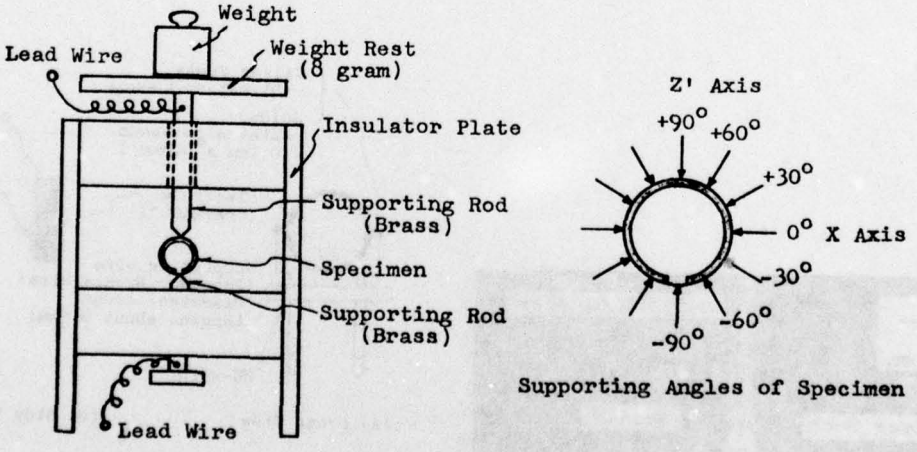

Fig. 6 - Apparatus of Mechanical Probing Method and Supporting Angles of Specimen.

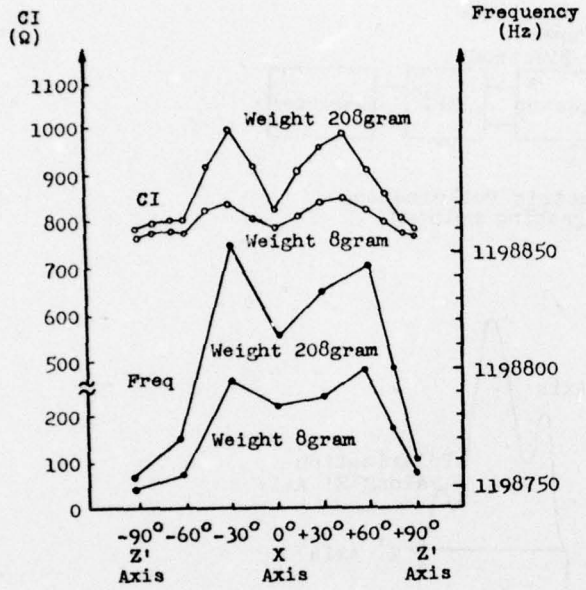

Fig. 7 - Variations of Resonance Frequency and CI with Supporting Angles and Weights. Crystal Current : 0.2mA.

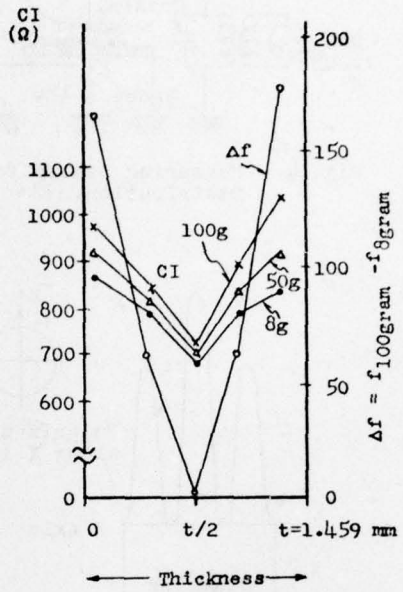

Fig. 8 - Frequency Differencies $\Delta f = f_{100g} - f_{8g}$ and *CI Distributions for Weights and* Supporting Points along Thickness of Crystal at Z' Axis.
Crystal Current : 0.2mA.

Fig. 9: Appearance of Side Wire Mounting.

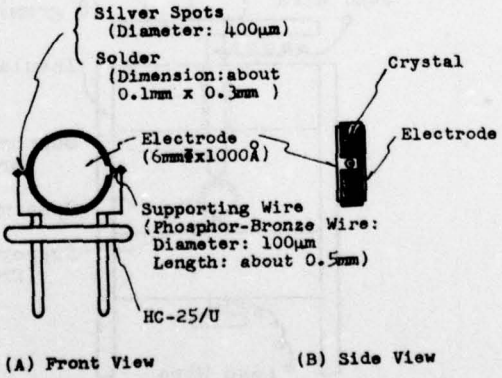

Fig. 10- Miniaturized Circular Disk AT-Cut Crystal.

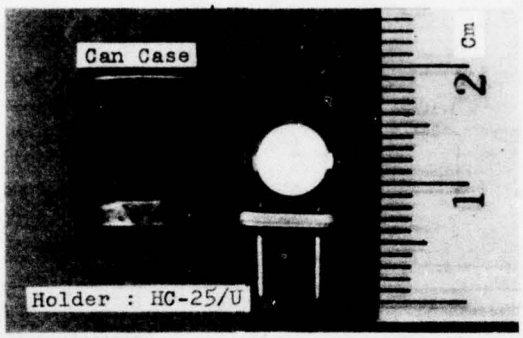

Fig. 11: Miniaturized AT-Cut Circular Disk Crystal Vibrator.
Holder: HC-25/U. Diameter: 6.824 mm, Thickness: 1.459 mm,
Frequency: 1.2 MHz.

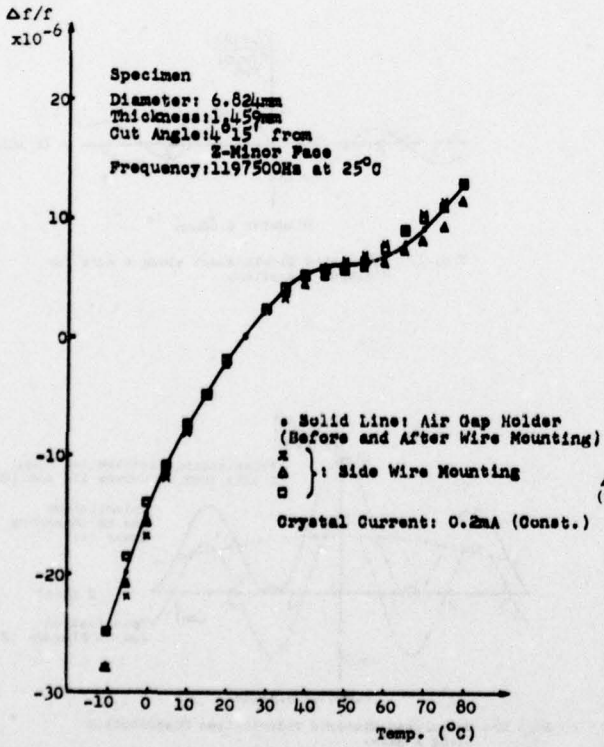

Fig. 12- Frequency Temperature Characteristics.

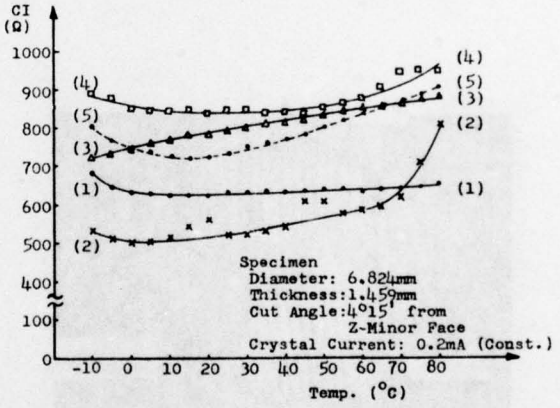

Fig. 13- Crystal Impedance - Temperature Characteristics of Side Wire Mounted Crystal (2),(3),(4) and Air Gap Holder (1),(5).

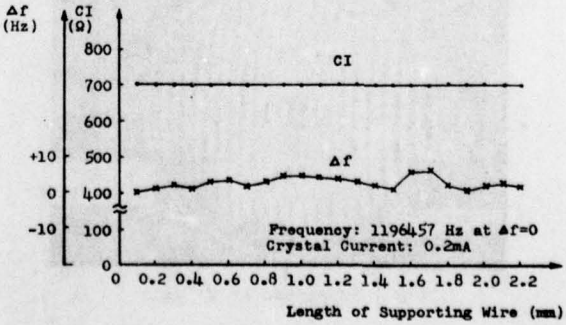

Fig. 14- Length of Supporting Wire versus CI., Frequency Variations Δf.

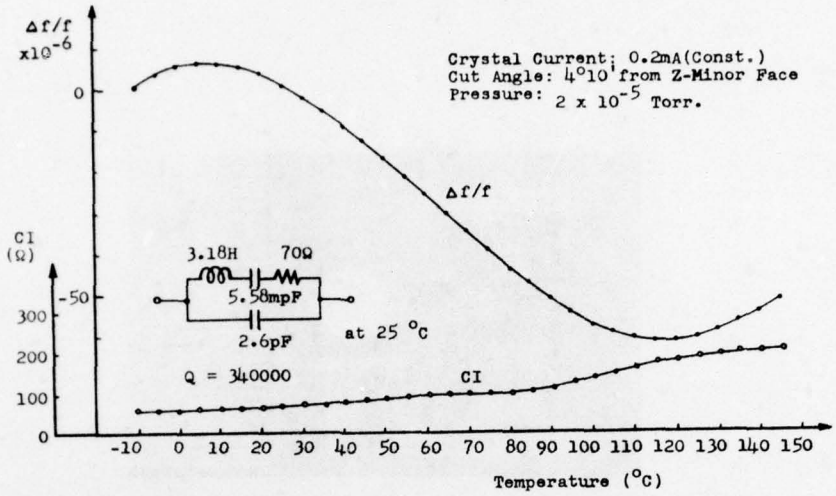

Fig. 15- Frequency and CI Temperature Characteristic in Case of Side Wire Supporting.

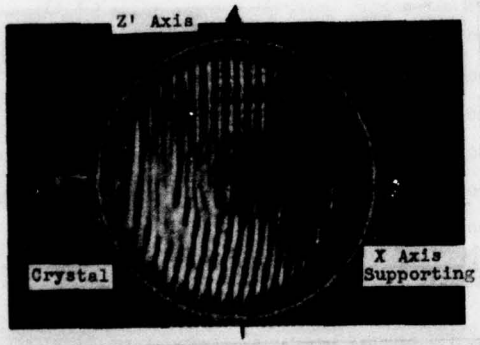

(A) Supported at X Axis

(B) Supported at Z' Axis

Fig. 16: Interference Fringes of Side Wire Mounted Crystal experimented in This Paper. (A): Supported at X Axis. (B): Supported at Z' Axis. Crystal Current: 1 mA.

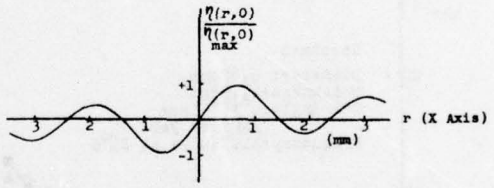

Diameter 6.824mm

Fig. 17- Calculated Displacement along X Axis for Flexural Vibration.

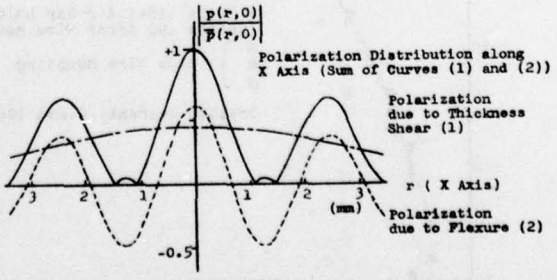

Diameter 6.824mm

Fig. 18 - Calculated Electric Polarization Distribution along X Axis.

DIRECT PLATING TO FREQUENCY - A POWERFUL FABRICATION METHOD FOR CRYSTALS WITH CLOSELY CONTROLLED PARAMETERS

R. Fischer, L. Schulzke
KVG - Germany

Summary

Besides for low aging rates crystal specifications of today call more and more for closely controlled motional parameters and defined spurious attenuation. The conventional method of base plating the electrode configuration and overplating it with a spot for final adjustment of frequency raises problems especially in the higher frequency ranges, where the spot dimensions are becoming the governing factor for the motional parameters. Direct plating to frequency, i.e. simultaneously plating both sides of the carefully masked resonator is a way to obtain a uniform and reproducible electrode configuration.

The plating equipment is described with some details of the vacuum system, the evaporation sources, the masking technique of the crystal and the control circuit basing on the transmission-line method covering the frequency range from 3 to 200 MHz.

Experimental data cover the relation between motional parameters of the crystal and the relative mass loading, both for the conventional spot plating and the single-step plating procedure. Figures on the frequency drift after the plating process due to gas absorption are given taking into account the deposition rate and the surface structure of the resonator. Typical aging records of single-step plated crystals sealed in resistance-welded enclosures are given at the end of the paper.

Introduction

This paper will deal specifically with the fabrication method of plating high-frequency crystals in a single-step procedure to their final frequency.

This procedure and its associated equipment was evaluated at KVG under the objective to achieve a highly flexible and economic fabrication facility for commercial and military crystals. Although the subject is still to be improved in many respects, it is used in current high volume production now for more than 3 years.

Frequency Adjustment Methods

A quartz crystal must be considered as a composite resonator consisting mainly of the crystal plate and its electrode configuration. The mechanical properties of this composite resonator in conjunction with the piezoelectric effect of energy conversion results in a device with one or several pronounced resonance frequencies, for each of which an equivalent 2 -port electrical network can be used in approximation. We will restrict here the problem to the high-frequency thickness-shear vibrator and will thus neglect the influence of the supporting system.

Despite of the technology of today it is not possible to manufacture the composite resonator within those close mechanical tolerances required by most applications, an individual calibration must be performed with each crystal. According to the equivalent network where the motional inductance is equivalent to the mass of the active region, mass loading or removal is the most economic way for calibrating the individual resonator.

A survey of the practically used calibration methods is shown in Fig. 1, a classification is made whether the crystal can be kept oscillating whilst being calibrated and thus giving a good control of the amount of loading or not.

Electroplating

Electrolytic deposition from a nickel bath is a cheap method but is difficult to be controlled because the deposition rate changes considerably if the process is performed repeatedly. When done in a single-step procedure with the aid of a constant-current source and a precision timer, results are by far better but close tolerances in the order of some ppm are still difficult to achieve. When properly applied nickel plating gives very uniform layers with only a small detoriation of the motional parameters, its disadvantage is poor control and the necessity of a thermal treating to obtain stable resonators.

Mass Removal by Etching

It is usable only with Aluminium-plated resonators and also very difficult to be controlled, it requires thermal treating for stability reasons too.

Dielectric Mass Loading

Overplating the resonator and its electrode with a dielectric layer of Silicon-monoxyde keeps its mesa-structure nearly unchanged and therefore permits large tuning ranges without significant changes of the energy-trapping conditions with filter resonators. The still unsolved problem seems to be the long-time stability of the dielectric layer, which remains chemically active and thus causes drift effects due to gas absorption and/or oxydation. Until now this method has only a limited range of application to filter resonators.

Laser Trimming

Although not fully evaluated regarding its influence on the crystal parameters in general, laser trimming is the only method to remove electrode material selectively with respect to its location and is therefore especially attractive for the adjustment of multiresonator arrays in the filter field.

Chemical Reaction from Gas Atmosphere

When iodine is brought onto an Ag-electrode to form AgJ, stable layers are achieved only up to a limited temperature and if only very small amounts were applied. Careful thermal treating is required.

Sputtering

Sputtering is not widely used because of the low deposition rate of this process and the difficulty to measure the resonator whilst being exposed to the glow discharge. New sputtering sources and the advantages of RF-sputtering may become attractive in the fabrication of crystals , for final calibration other methods are superior.

Metal Deposition by Spot Plating

This method is obviously the one most widely used because its efficiency and its excellent control of deposition. Its disadvantage is the 2-layer system of electrode material with possible interactions between them, and the fact, that with increasing plateback the properties of the deposited spot are governing the resonator's behavior.

An oscillator or filter crystal is normally designed according to the required motional inductance or capacitance by selecting the proper electrode diameter, the total plateback is then defined either for minimum resistance or for optimum suppression of spurious modes by application of the energy trapping principle.

The diameter of the spot is chosen somewhat smaller than that of the base electrode to prevent an increase of the effective electrode area due to shadowing and alignment tolerances. To expand the effect for experimental investigation crystals with fundamental frequencies of 10, 15, and 20 MHz were base plated with K = 0.4 kHz/MHz^2 and then spotted with about half of their base electrode diameter. All motional parameters were measured as a function of spotting plate back on the fundamental, 3rd and 5th harmonic and scaled to the corresponding parameter of the base plated crystal.

It can be clearly seen on Fig. 2, 3, and 4 that a sharp decrease of the motional capacitance occurs with increasing plate back due to spotting, the exponential decay for large platebacks moves exactly to the figure, which corresponds to the diameter of the spot. As expected this exponential decay is much more pronounced with the overtone modes than with the fundamental and thus seriously affects the calibration of overtone crystals with close motional parameters.

The motional resistance increases with the spotting plateback except for the fundamental mode, where the basic plateback obviously was too low. The corresponding relation of the effective Q of the resonators in Fig. 5, 6, and 7 shows a flat maximum of Q versus the spotting plateback, except the 10 MHz-crystal because of the above mentioned reason. If the effective Q of the resonators remains relatively stable, an increase of the motional resistance is the consequence of decreasing motional capacitance due to the spotting plateback, it seems that this effect was quite often misinterpreted to originate from excessive mass loading.

Spotting causes a pronounced change of the boundary conditions of the resonator because the active region of the resonator decreases. This can be measured with the inharmony of the main modes, i.e. by calculating the difference of the actual overtone frequency to n-times the actual fundamental frequency, this behavior can be seen from the graphs 5, 6, and 7.

Summing up these results it can be stated, that any fine-calibration method must change, by deposition or removal, the designed base electrode uniformly if the motional parameters should not be affected too much. This shifts, for close-tolerance crystals, the problem towards an extreme control of the base plating procedure: an E-gun evaporation source in conjunction with an elaborate masking or moving system for the substrates and control of thickness and rate of deposition is a must to keep the spread of the base-electrode plateback to less than one percent. These problems can be overcome with a plating procedure, which individually deposits the electrode onto the crystal under permanent control of the resonators frequency.

Fabrication and Equipment for Single-Step Plating

Preparation of Blanks

Multiblade cutting of wafers from angle-corrected lumbered Y-bars is the first step, followed by rough-lapping to a standard thickness and semi-automatic X-ray sorting into groups of ± 15 minutes of arc. The so far rectangular wafers are then brought to their circular shape by an automatic 2-gang diamond-wheel grinder which optionally can leave a small reference segment at the circumference for easier electrode alignment. The crystals then undergo 3 consecutive lapping steps, are re-X-rayed if necessary, and finally polished or semi-polished. Flatness control by interferometry is followed by a thoroughful cleaning and etching procedure. The crystals come out with a normal tolerance of ± .075 kHz/MHz^2 , selective etching is added if the specification calls for closer limits.

Masking of the Crystals

The blanks are mounted onto the holder in a precise fixture, which exactly positions the plate with respect to the holder base-plate. After applying the conductive cement by a dispenser, the fixtures with the crystals are transferred to stainless steel ovens for curing (see Fig.8).

The mask for single-step plating is a precision tool and different designs are used for each crystal holder family. The mask is constructed from two phenolic parts with imbedded guidance shafts and compressed by springs and air gap between the mask and the crystal plate is in the order of .3 mm. The mask is referenced to the base plate (see Fig.9), misalignment of the crystal can result only in a slight excentricity of the electrode and not in a displacement of both electrodes to each other.

The set of electrode diameters is dimensioned for a 5 %-increase of the motional capacitance, the exact electrode diameter is milled-out with the mask already assembled. Overplating of the mask in continuous operation can be removed by etching in sulphuric acid. As the basic components and the alignment of the masks are relatively inexpensive, regular replacements raise no cost problems. Fig. 10 gives an impression of the different steps of production.

Vacuum System and Evaporation Chamber

The general layout of the plating station is shown in Fig.11: The evaporation chamber is located in an optimum position for the operator with the high-speed pumping system below the table. Either a 1800 l/sec diffusion pump with a liquid-nitrogen-cooled baffle or a turbomolecular pump is used, to achieve a start vacuum of 5.10^{-3} torr within less than 20 seconds. This relative low figure is sufficient because the mean free path of gas molecules must be seen in relation to the distance between evaporation source and substrate, which length is only about 30 mm in this configuration. The chamber is designed for minimum volume with the main valve mounted to it as close as possible.

The evaporation chamber contains the exchangeable evaporation source units and the shutter system. The chamber is closed alternatingly by the 2 cover plates, which hold the masked crystals precisely positioned by the knife-edge contacts of the build-in Pi-networks. Closing the chamber activates the control circuits for pumping-down and RF-switching. As long as the evaporation vacuum is not achieved, the operator checks frequency and resistance of the crystal of the prior cycle and masks a new one for reloading.

The principal arrangement of the evaporation chamber is shown in Fig. 13: If sufficiently low pressure has been reached, the control circuit opens both shutters and energizes the evaporation heaters. The operator controls the rate of deposition by panel meters. When the crystal frequency crosses a preset offset, the control circuit reduces the deposition rate by a factor of 10 with the fine shutter and interrupts evaporation at zero offset. Deposition control by a shutter system has proven to be superior than controlling the current of the heaters.

The evaporation sources are easily exchangeable units with a horizontal beam output (see Fig.14). A thin molybdenium sheet metal with a tilted area of minimum cross-section is used, thus giving a defined area of maximum temperature. The hole on the top of the evaporation unit is for recharging it with hooked Ag-wires and is closed by a spring supported plate from the cover.

Control Circuit Applying the Transmission-Line Method

The transmission-line method has proven the most versatile me thod in fabrication, it gives corresponding readings within better than 1 ppm of frequency and 5 % of resistance throughout our facilities. By measuring the frequencies at 2 defined phase-offsets the motional parameters of the crystal can be easily calculated.

The general layout of the control circuit is given in Fig.15: Pi-networks of 3 different designs are used at KVG depending on the frequency range:

1 to 30 MHz: A network with an adjustable symmetric load capacitance for fundamental mode crystals.

20 to 100 MHz: The conventional network. Crystals designed to work into load capacitances are adjusted to a calculated offset frequency, the error resulting from parameter variations of the crystal is acceptably small in most cases.

80 to 200 MHz: A special version is used, which compensates the static capacitance C_0 by an electronically tuned wideband resonance circuit.

The system consists basically of the Pi-networks, which are switched-in alternatingly by PIN-diods coaxial relays, a programmable decade generator as a somewhat luxurious VCO, the HP-8405A vector-voltmeter and a fast search-and lock circuit. Calibration to zero-phase is accomplished by inserting a compensated resistor and the drive level is set to the corresponding B-channel voltage reading of the vector-voltmeter.

As long as there is no conductive layer onto the crystal plate, the B-channel voltage is small. The voltage step-up, which occurs when the electrodes are becoming conductive, is sensed by a level detector and starts the search-and-lock circuit. The loop then remains locked to the crystal's zero-phase frequency, which moves downward until the end of plating, thus giving a continuous information of frequency and resistance.

A computing counter with auxiliary outputs monitors and controls the plating process: Manual input keys are provided for crystal frequency, harmonic order and the offset for fine-shutter activation. The counter presets the coarse figures of the decade generator, interlocks the heater current module and controls the shutter system. Analog outputs for display of the deposition rate are provided, although the evaporation sources are now running with a preset deposition rate, a closed-loop rate control system is a subject of further investigations.

Closing of the final shutter ends the plating procedure, the chamber is then vented with dry nitrogen to keep water contamination of the chamber walls to a minimum. The crystals finally undergo a stabilization period of one hour at +150°C in stainless steel ovens before being sealed in a capacitor-discharge welding station.

Experimental Results

To get comparative figures to spot plating, crystals with fundamental frequencies of 10, 15, and 20 MHz were directly plated, and the motional parameters of the fundamental and overtone modes were measured as a function of mass loading.

There still can be observed an exponential decay of the motional capacitance with increasing plateback, but the rate of decay is much smaller than that observed with spot plating (when comparing Fig.2,3, and 4 with Fig.16,17, and 18 the abscissa compression by the factor of 2 should be noticed with the directly plated crystals). When taking the derivative of both slopes at the base plate amount of $K = .4\ kHz/MHz^2$ of the first investigation and calculating the plateback range for a 5 % - tolerance of the motional capacitance, direct plating allows for a 30times larger calibration range with fundamental and at least a 10times larger range with overtone crystals. These figures are of course valid only for the cited 1:2 ratio of overlayed electrodes from spot plating and will approach unity for a perfect overlay, but as the electrode diameters of overtone crystals are getting smaller because of increasing demands of spurious suppression, the investigated ratio of 1:2 is not too far from reality.

The Q vs. mass-loading characteristic is not significantly affected by the method of plating: As the motional capacitance C_1 changes less with direct plating, this consequently allows for a much larger plating range with respect to changes of motional resistance. This statement, experimentally verified by Fig. 16 through 21, is a further advantage of the direct plating method.

It would be beyond the scope of this paper, to discuss the relations of the mass-loaded resonator from acoustic theory, yet a simplified electromechanical analogon will show the main relations: The plated crystal is a composite resonator, where the mass of the active region (equivalent to the motional inductance) and its compliance (equivalent to the motional capaci-

tance) are determining the frequency. Plating the active region increases the mass, but simultaneously decreases its compliance to a lesser extent, so the resulting frequency goes negative. As mass and stiffness, the reverse of compliance, are acting upon the frequency with opposite sign, their electrical equivalents, if considered separately, show changes orders of magnitude larger than it would be expected from the frequency change. Designing a crystal for a defined motional inductance or capacitance now means nothing else then designing it for a specific ratio of mass to compliance with the product of both being responsible for the resultant frequency. When disregarding the static capacitance C_o, this gives a certain range of choice, to obtain the specified parameter either by the size of the electrode or by the amount of plateback. This adjustment by 2 variables can be used practically, but of course it is easier, to make the design in accordance with a theoretically derived or experimentally verified standard plateback and then calculate the electrode diameter.

Two further details should be covered here because of general interest and their special importance for the direct plating procedure: A freshly plated crystal exhibits an exponentially decaying frequency drift downwards in the order of several ppm, which definitely not originates from thermal effects. The stabilization time is proportional to the inverse of pressure and the total amount of drift is related to the effective surface of the plated region. Adsorption of gas molecules at the newly generated and therefore chemically very active surface is a reasonable explanation of this effect, which is practically used with getter pumps. The effective surface of the electrode is mainly governed by the surface finish of the blank, a crystal with a 2 micron finish exhibits a drift about 2.5 times larger than a semi-polished crystal with a polishing time of 5 minutes (see Fig.22). But even with identical surfaces of the blanks, the rate of electrode deposition has an influence onto the effective surface of the electrode: Doubling the deposition rate results in an increase of drift by about 50 %. The amount of drift for a given blank surface is sufficiently predictable and therefore raises no problems in fabrication.

The aging behavior of directly plated crystals seems in no way to differ from conventionally plated units, provided the fabrication process is within good control. Aging records from samples of both plating procedures were taken in logarithmic time increments up to 210 days, with the crystals exposed to +85°C. 45 MHz-resonators in 3rd overtone exhibited, with no exception, positive frequency shifts between .2 and .9 ppm over the total period of observation. An interesting result further was, that no significant difference in aging was observed between crystal s sealed by a capacitor-discharge welder with 3 ms pulse duration and coldwelded units in the HC-42/U crystal holder.

Conclusion

The method of directly plating crystals to their final frequency has proven in practice as an efficient and economic fabrication process, as it eliminates completely the step of base plating and its associated tolerance problems. Direct plating renders fabrication of crystals with close motional tolerances or, in reverse, allows for larger blank tolerances for moderate tolerance crystals.

Gas adsorption after plating is the main subject of further investigations, as until now the use of polished or semi-polished blanks is imperative for crystals with very narrow adjustment tolerances. The achievement of higher uniformity of the electrode structure by a controlled rate of deposition is under evaluation now.

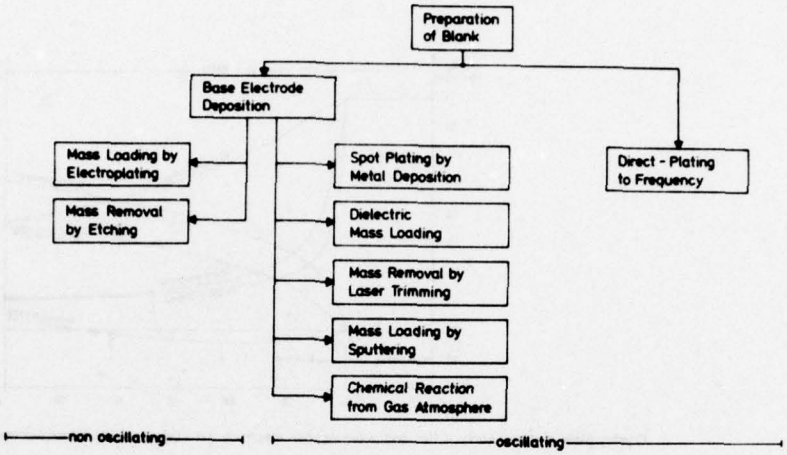

Fig. 1: Survey of the frequency adjustment procedures of quartz crystals.

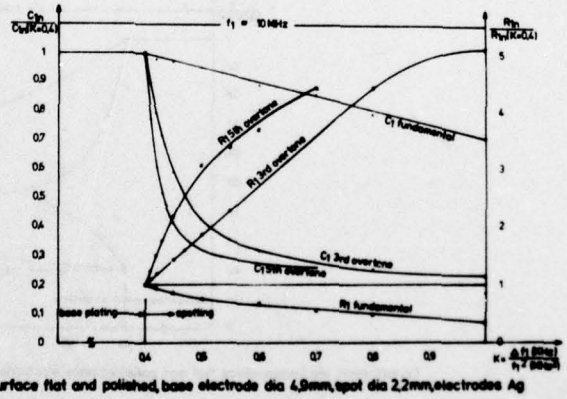

Crystal: plate dia 9mm, surface flat and polished, base electrode dia 4,9mm, spot dia 2,2mm, electrodes Ag

Fig.2: Effect of spotting on the motional capacitances C_{1n} and resistances R_{1n} related to the values of the base plated crystal (K = 0,4)

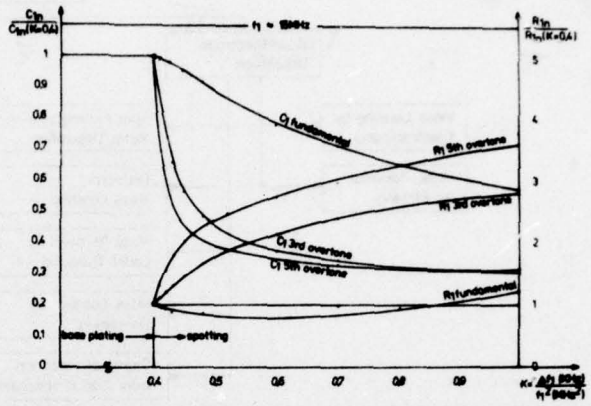

Crystal: plate dia 9mm, surface flat and polished, base electrode dia 4,0mm, spot dia 2,2mm, electrodes Ag

Fig.3: Effect of spotting on the motional capacitances C_{1n} and resistances R_{1n} related to the values of the base plated crystal (K=0,4)

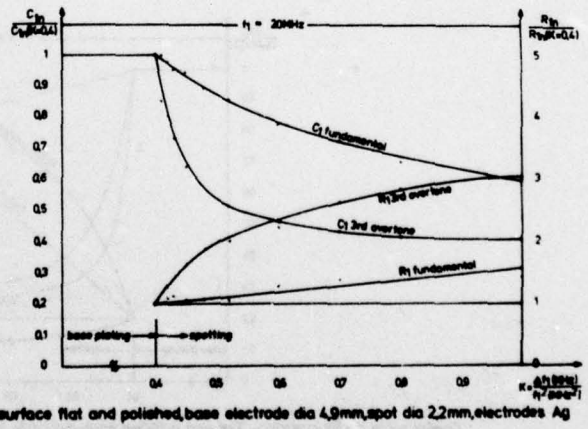

Crystal: plate dia 9mm, surface flat and polished, base electrode dia 4,9mm, spot dia 2,2mm, electrodes Ag

Fig.4: Effect of spotting on the motional capacitances C_{1n} and resistances R_{1n} related to the values of the base plated crystal (K=0,4)

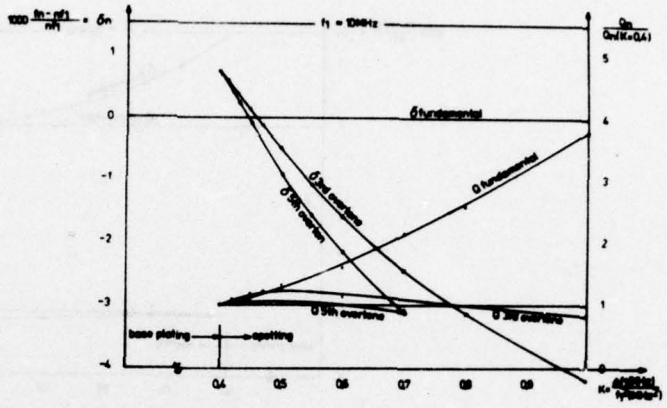

Crystal: plate dia 9mm, surface flat and polished, base electrode dia 4,9mm, spot dia 2,2mm, electrodes Ag

Fig.5: Effect of spotting on frequencies δ_n and quality factors Q_n.

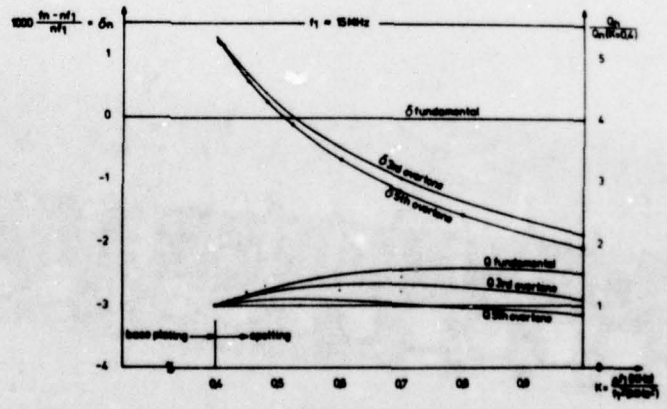

Crystal: plate dia 9mm, surface flat and polished, base electrode dia 3,5mm, spot dia 2,2mm, electrodes Ag

Fig.6: Effect of spotting on frequencies δ_n and quality factors Q_n

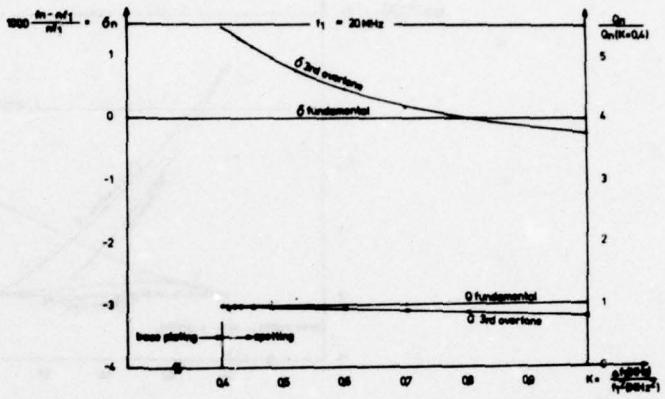

Crystal: plate dia 9 mm, surface flat and polished, base electrode dia 3,5 mm, spot dia 2,2 mm, electrodes Ag

Fig. 7: Effect of spotting on frequencies δ_n and quality factors Q_n.

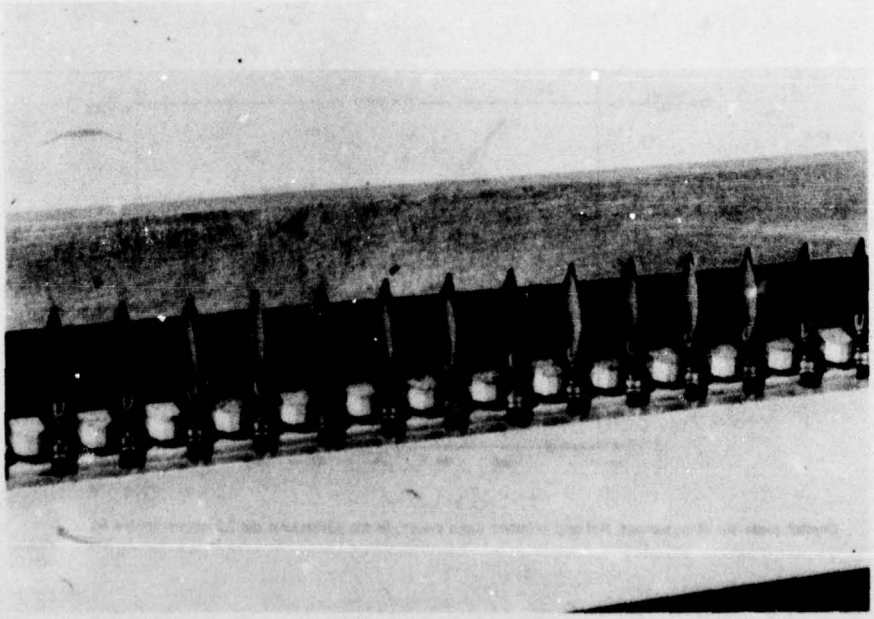

Fig. 8: Mounting and transfer fixture for directly plated crystals.

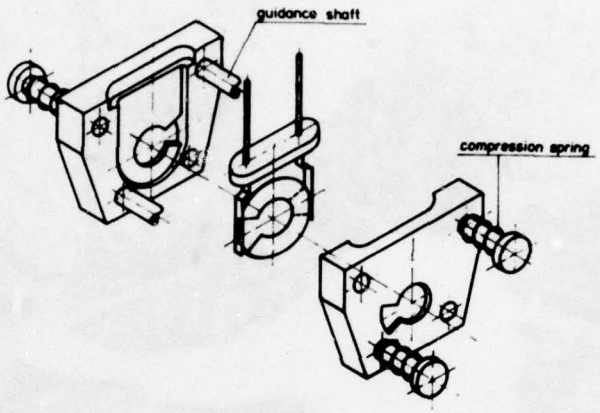

Fig.9: Principle of masking arrangement for single-step plating

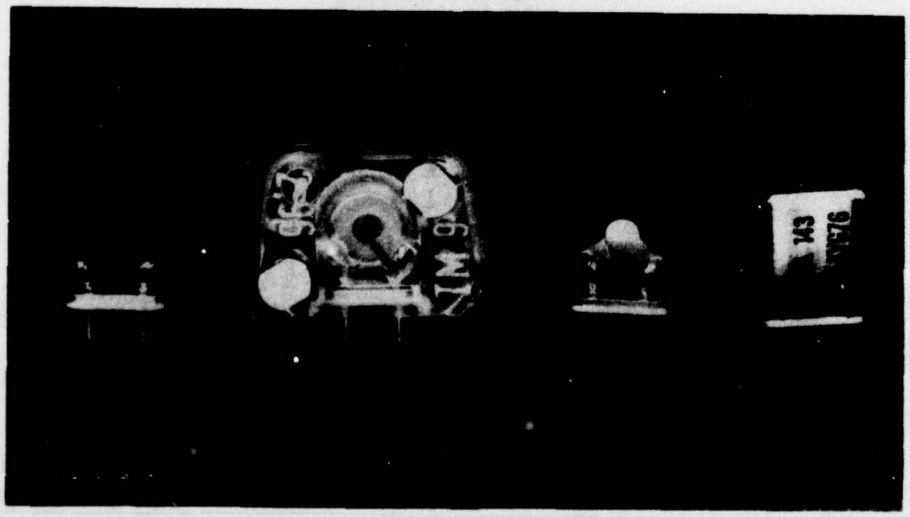

Fig. 10: Line-up of the succeeding steps of direct plating.

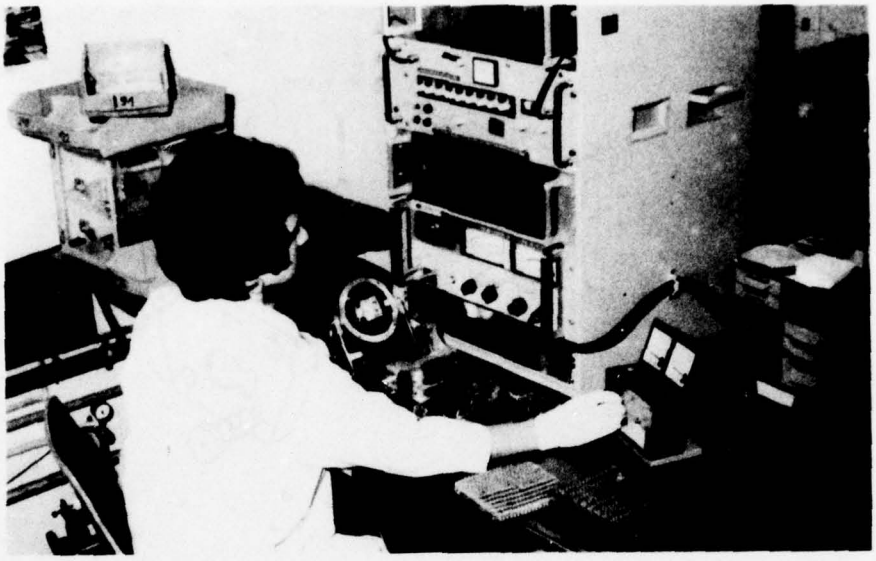

Fig. 11: Operating position of the direct plating station.

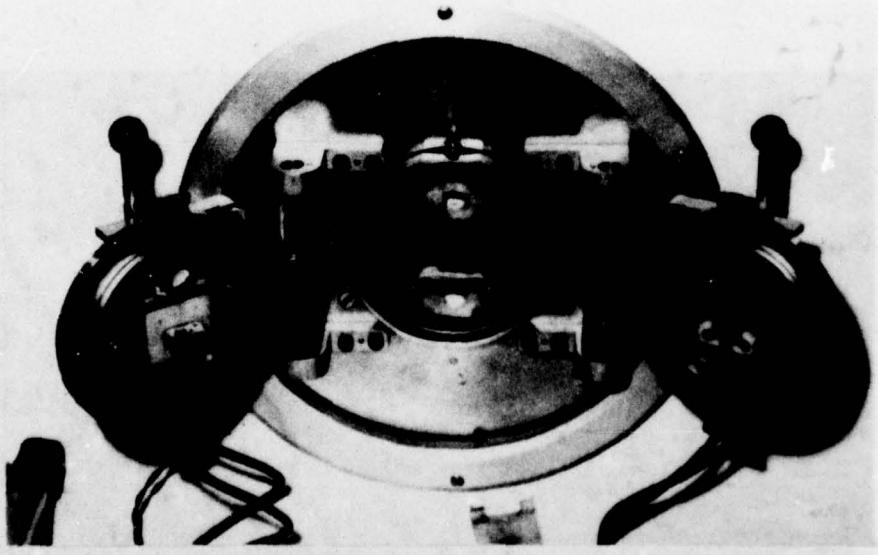

Fig. 12: Vacuum chamber with shutter system, evaporation sources and Pi-network arrangement.

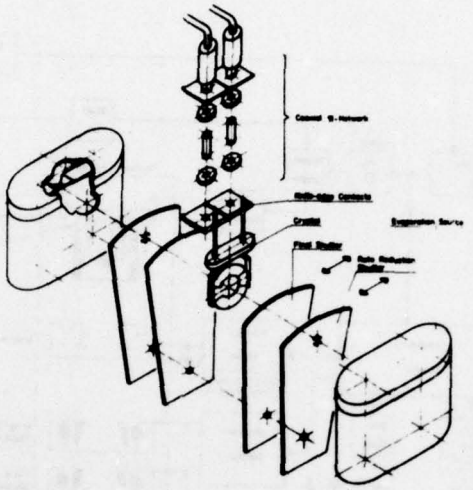

Fig.13: Arrangement of main components inside the vacuum chamber.

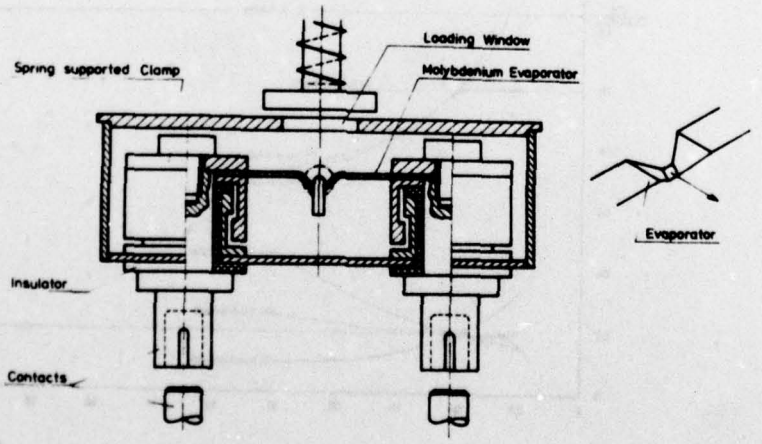

Fig.14: Evaporation source for single-step plating.

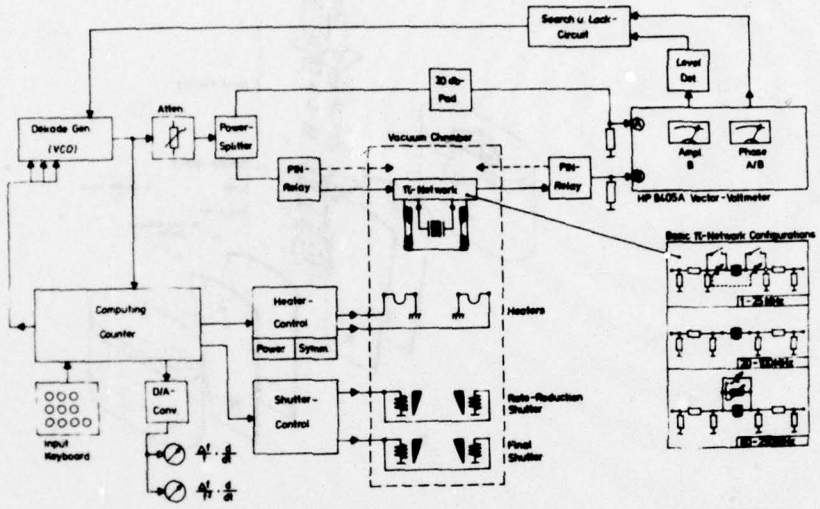

Fig.15: Evaporation control and associated transmission-line circuit.

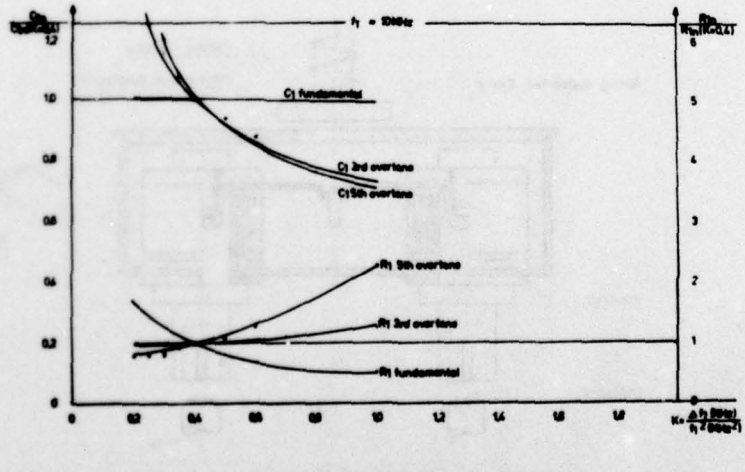

Crystal: plate diameter 8mm, surface flat and polished, electrodes Ag dia 4,9mm

Fig.16: Effect of direct plating on motional capacitances C_{1n} and resistances R_{1n}

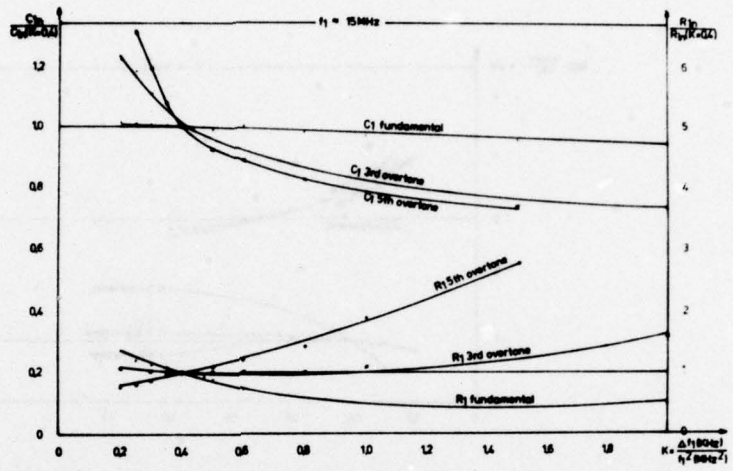

Crystal: plate diameter 9mm, surface flat and polished, electrodes Ag dia 4,0mm

Fig.17: Effect of direct plating on motional capacitances C_{1n} and resistances R_{1n}

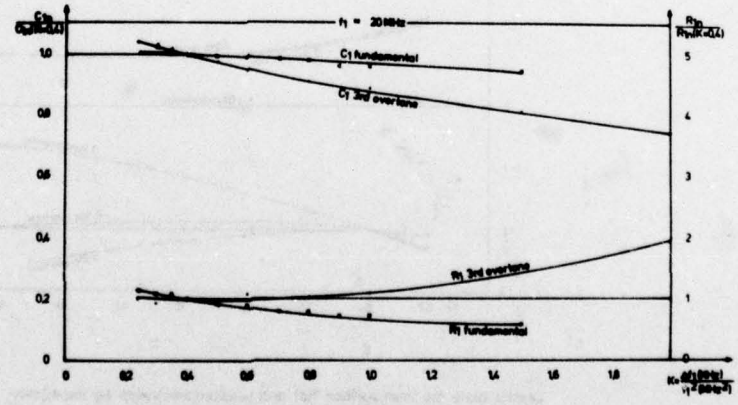

Crystal: plate diameter 9mm, surface flat and polished, electrodes Ag dia 3,5mm

Fig.18: Effect of direct plating on motional capacitances C_{1n} and resistances R_{1n}

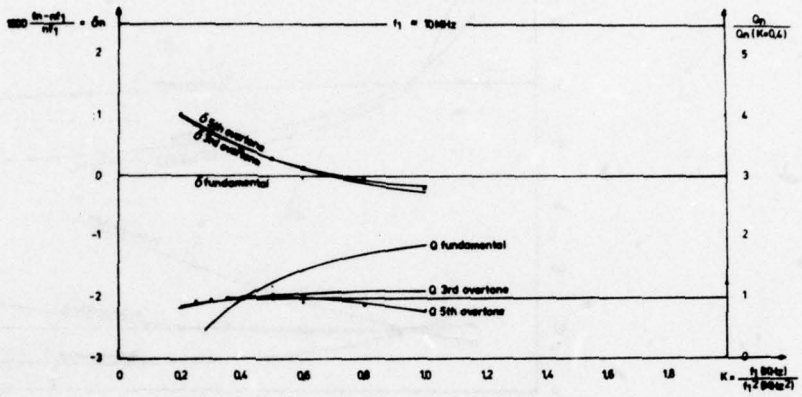

Crystal: plate diameter 9mm, surface flat and polished, electrodes Ag dia 4,9mm

Fig.19: Effect of direct plating on frequencies δ_n and quality factors Q_n

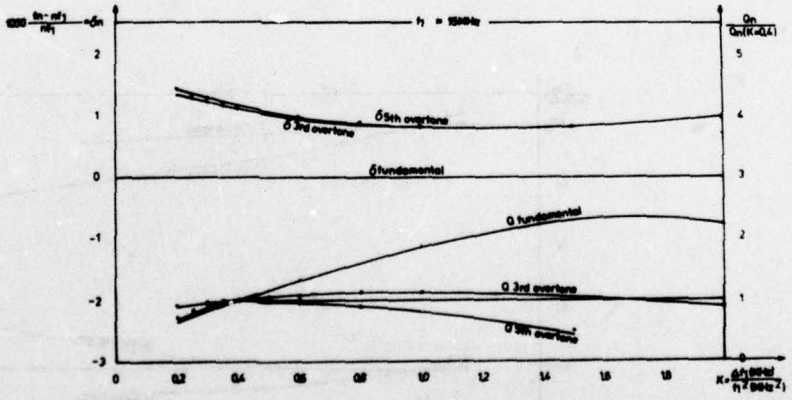

Crystal: plate dia 9mm, surface flat and polished, electrodes Ag dia 4,0mm

Fig.20: Effect of direct plating on frequencies δ_n and quality factors Q_n

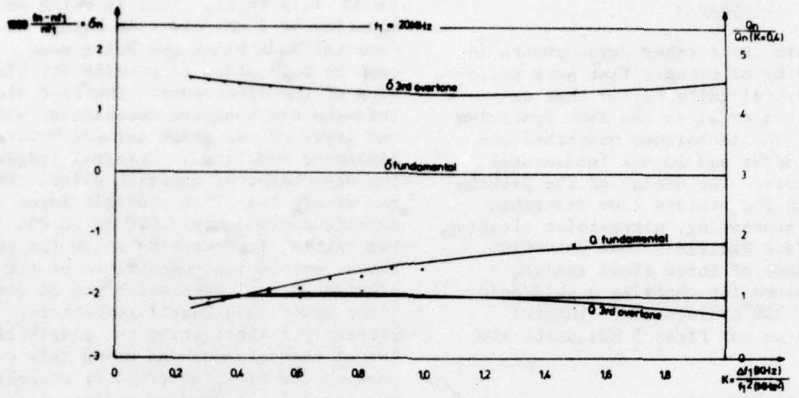

Crystal: plate dia 9mm, surface flat and polished, electrodes Ag dia 3,5mm

Fig. 21: Effect of direct plating on frequencies δ_n and quality factors Q_n.

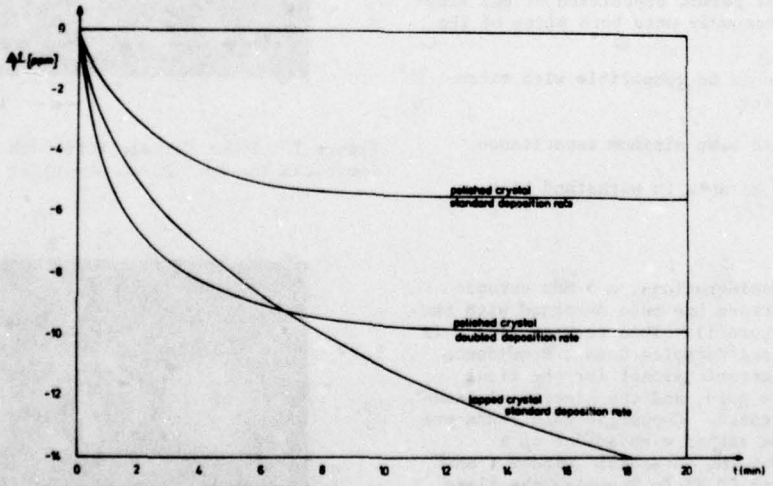

Crystal: 90MHz, 3rd overtone plate dia 9,0mm, electrodes Ag 4,0mm, plateback K = 0,4

Fig. 22: Frequency drift in high vacuum after direct plating.

CERAMIC FLAT PACK ENCLOSURES FOR PRECISION QUARTZ CRYSTAL UNITS*

R. Donald Peters
General Electric Company
Neutron Devices Department
St. Petersburg, Florida

Summary

This paper will discuss further developments in the design and processing of ceramic flat pack enclosures for precision crystal units beyond that described by Hafner, Wilcox et al at the 29th Symposium on Frequency Control. The techniques described are being applied to both 5 MHz and 20 MHz fundamental mode precision resonators. The design of the package will be illustrated and the process flow described including high vacuum processing, ultraviolet cleaning, nickel electrobonding and Radiflo** leak detection. A comparison will be made of three final sealing techniques and the reasons for choosing a gold/gold diffusion bond made at 300°C discussed. Initial accelerated aging data on our first 5 MHz units are also included.

Introduction

The requirements for a precision package have been described by Hafner and Vig[1] and further discussed by Hafner, Wilcox et al.[2] Briefly stated these requirements are:

1. Materials must have low gas permeation and solubility.
2. Materials must withstand vacuum bakeout temperatures of up to 800°C.
3. The final seal must be made in a vacuum or inert atmosphere.
4. The design must permit deposition of the electrodes simultaneously onto both sides of the resonator.
5. The design should be compatible with microcircuit mounting.
6. The unit should have minimum capacitance.
7. The unit must be able to withstand high shock.

5-MHz Package Design

Based on these considerations, a 5 MHz ceramic flat pack resonator package has been designed with the assistance of ECOM (Figure 1). This package, which is manufactured by Metalized Ceramics Corp., Providence, R. I., is 95% alumina ceramic except for the final closure seals which are gold, and the electrical feedthroughs which are tungsten. Copper or gold leads are attached to the outside either with solder or a thermocompression bond. The octagonal "window frame" body (Figure 2) is 19 mm (0.75 in.) across the flats and is made of laminated alumina approximately 3 mm (0.12 in.) thick. This is thick enough to allow mounting of 5 MHz overtone blanks as well as the fundamental mode blank now being used. This frame is open on both sides to provide for simultaneous deposition of the electrodes. The four electrical feedthroughs are tungsten metallizing which is painted on one layer of the green ceramic before the frames are laminated and fired. Internal ledges are provided for the attachment of mounting clips. The top and bottom covers are made from a single layer of "doctor bladed" ceramic approximately 0.9 mm (0.035 in.) thick. The two "extra" feedthroughs allow for redundant connections, enable instrumentation of the package, and also provide an enclosure which can be used for applications other than quartz resonators. In fact, we are presently investigating the possibility of combining two of these frames and using this configuration to package the oscillator/heater assembly to be used with the precision 5 MHz resonator.

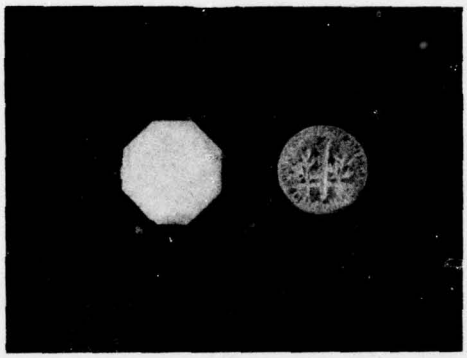

Figure 1. 5 MHz Ceramic Flat Pack
(American Ten-Cent Piece Shown for Size Comparison)

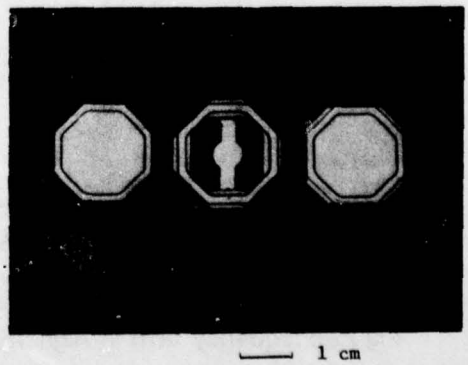

Figure 2. 5 MHz Ceramic Flat Pack Covers and Frame/Resonator Assembly Prior to Final Assembly

*This work funded and directed by U.S. Army Electronics Command (ECOM), Fort Monmouth, N.J.

**Trademark, Consolidated Electrodynamics Corp.

20 MHz Package Design

The 20 MHz ceramic flat pack (Figure 3) has been previously described by Hafner and Wilcox. It is 10-mm (0.4 in.) square and made using the same processes described for the 5 MHz package. The frame (Figure 4) is approximately 1.5 mm (0.060 in.) thick and covers are 0.5 mm (0.020 in.) thick. The only changes we have made in this design are in the clip area, where we have reduced the surface area in contact with the blank to eliminate void formation during nickel electrobonding, and in the final bond, where we have substituted a gold/gold diffusion bond for the aluminum to alumina bond previously reported.

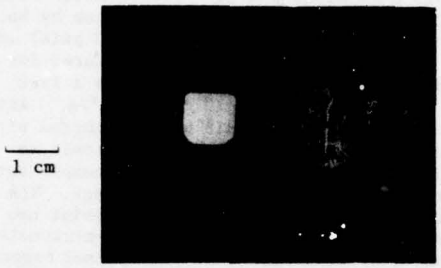

Figure 3. 20 MHz Ceramic Flat Pack
(American Ten-Cent Piece Shown for Size Comparison)

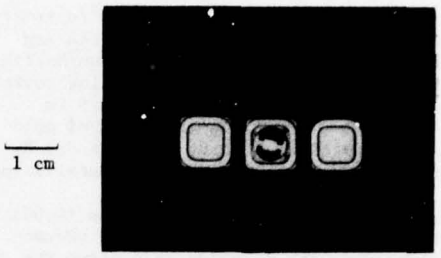

Figure 4. 20 MHz Ceramic Flat Pack Covers and Frame/Resonator Assembly Prior to Final Assembly

Processing

A generalized process flow for our fabrication of both the 5 and 20 MHz ceramic flat pack resonator units is given in Figure 5. After receipt from the vendor, the sealing surface of the ceramic parts are ground flat and parallel to within ± 0.0127 mm (±0.0005 in.) and then the frames are helium leak checked. Some problems were encountered with interlaminar leaks in the 5 MHz frames in the first batch received from the vendor. This problem resulted from improper pressing of the "green" ceramic prior to final sintering and was soon corrected. No leak problems have been encountered with the 20 MHz frames.

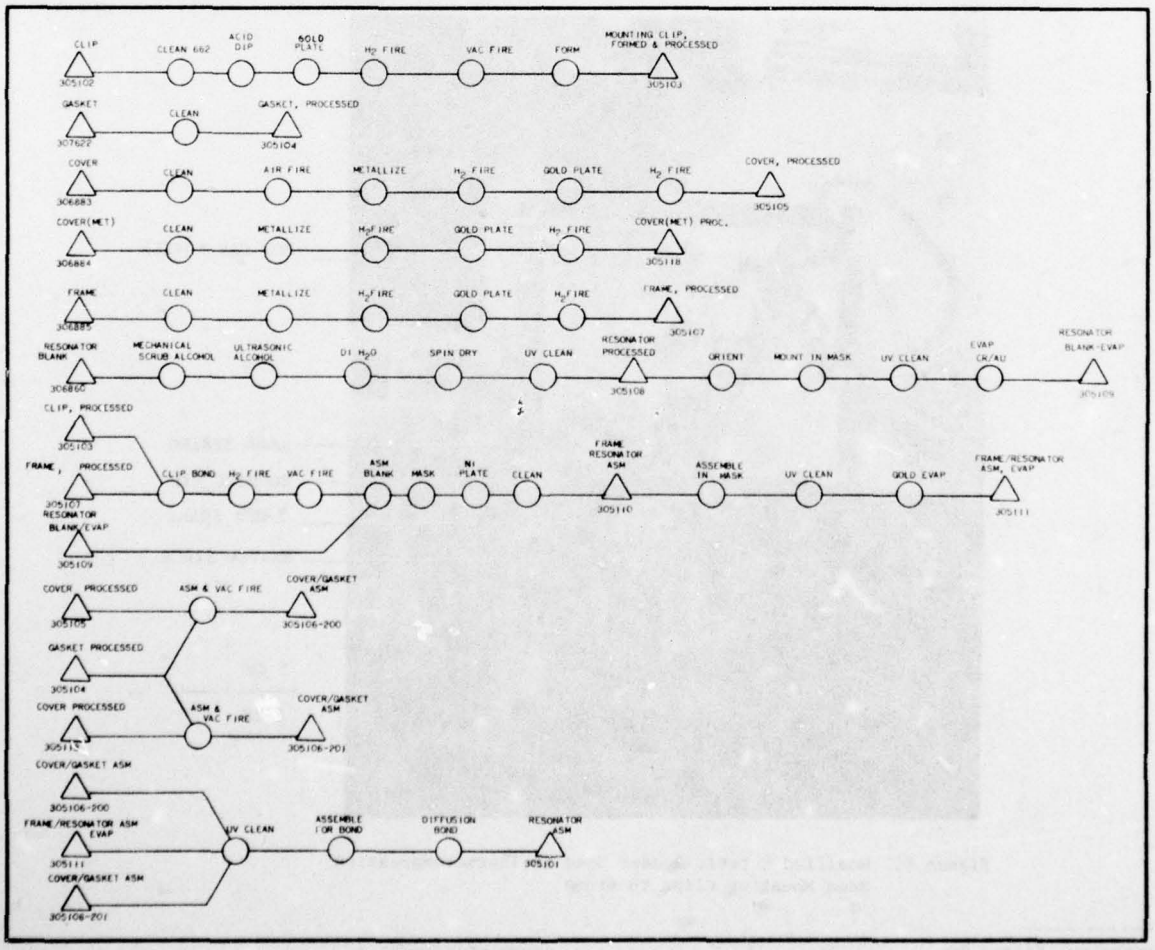

Figure 5. 5 MHz Resonator Flow Chart

After helium leak check (~1 x 10^{-10} std cm^3/s sensitivity), the ceramics are cleaned and the sealing surfaces are screen print metallized with Mo/Mn/TiH_2[3] and hydrogen sintered at 1475°C. The sealing surfaces and clip bonding pads are plated with 0.0025 to 0.0075 mm (0.0001 to 0.0003 in.) thickness of gold using Selrex BDT510* plating bath, and then dry H_2 fired at 900°C to sinter the gold to the metallizing.

The mounting clips, which are 0.025 mm (0.001 in.) nickel and have gold plated tabs, are next thermocompression bonded to the mounting pads using the fixture shown in Figure 6. This bond is made at approximately 400°C. Heating is from three sources; Calrod** units in the base, a directed hot helium gas jet, and the heated bonding tip. The bonding force is applied with a spring. Extensively pretested resonator blanks which already have Cr/Au pads evaporated at the edges are then mounted in the clips. Nail polish is used to mask off areas from the nickel plating to avoid discontinuities at the electrode/Ni interface[4] and to provide a hinge in the nickel plate on the Ni mounting clip to reduce mounting induced stress. The resonators are then nickel electrobonded to the clips using a sulfamate nickel bath with the temperature carefully controlled to minimize plating stress.[5] After plating the nail polish is removed and the parts are degreased and ultraviolet cleaned. The gold electrodes are then evaporated onto the blank on both sides at the same time in an all-metal vacuum system. The parts are plated to frequency in two steps; first, the rough evaporation is made at a blank temperature of approximately 200°C, and then the parts are cooled and the turning point frequency determined. They are then final tuned with the blank temperature near the turning point. The assemblies are removed from the vacuum system and ultraviolet cleaned again prior to final assembly and bonding.

The final closure is made with a gold/gold diffusion bond in high vacuum. Bonds are made at 300°C and approximately 225-kg (500 lb) load. System pressure at the time of bonding after 1-hour minimum system bakeout at 325°C is about 1 x 10^{-8} Torr. After bonding the units are leak checked. This is done by holding the resonators 64 hours at 0.42 MPa (60 psia) in krypton 85. They are then cleaned and measured for residual radioactivity. This technique has a leak sensitivity of better than 1 x 10^{-10} std cm^3/s.[6] After leak check the bottom of the unit will be coated with RTM* electroless nickel directly on the ceramic so that the flat pack can be soldered to the temperature controller to provide optimum thermal contact. The tensile strength of the RTM nickel solder joint has been measured using ASTM buttons with a 0.81-micrometer (32-microinch) surface finish that were joined together using 60/40 solder. The average strength was found to be approximately 46 MPa (6600 psi). (See Table 1.)

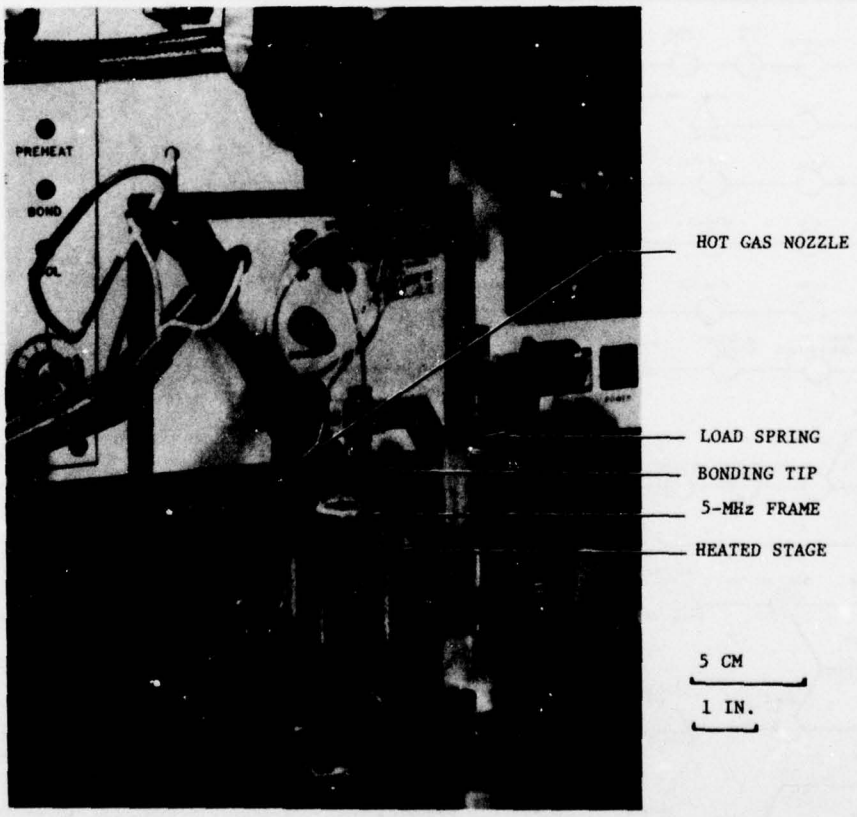

Figure 6. Modified Eutetic Bonder Used to Thermocompression Bond Mounting Clips to Frame

*Trademark, Selrex Co.
**Trademark, General Electric Co.

*Trademark, Transene Co., Inc.

Table 1. Electroless Nickel Metallizing Solder Joint Strength

Sample No.	Tensile Strength MPa	(psi)
0	52	(7397)
1	44	(6325)
2	42	(6050)
3	62	(8855)
4	42	(5995)
5	33	(4675)
Average	46	(6600)

Sealing

Before a final closure sealing technique was chosen, three methods were evaluated: direct bonding of Al_2O_3 to aluminum[2] tin soldering to gold plated and metallized Al_2O_3; and gold diffusion bonding of gold plated metallized Al_2O_3. ASTM tensile test buttons which were fabricated from 95% Al_2O_3 manufactured by Diamonite Products Mfg. Co. were ground flat and parallel and used for these tests. ASTM samples were used for our purposes since they could be readily leak checked using a helium leak detector and standard fixtures were available for tensile testing of the specimens. (See Table 2.)

Table 2. Bond Results Summary

Bond System	Sample Size	Strength Range MPa	(psi)	Leak Tight
Al/Al_2O_3	30	0-112	(0-16 000)	3%
Sn/Au	5	105	(15 000)	60%
Au/Au	20	56-245	(8 000-35 000)	90%

Our results with the Al_2O_3/Al bond described in reference 2 were variable, indicating that this technique is probably very sensitive to processing. Ultraviolet cleaning the parts before bonding did, however, increase bond strengths. The tin-gold system was investigated only as a backup. It capitalizes on the fact that, when tin and gold alloy, the melting point of the alloy increases.[7] Therefore, a bond can be made by melting tin at 232°C, and because of the alloy formation, this bond will remain intact to considerably higher temperatures. A major drawback to this type of seal is that the presealing bakeout must be below the final sealing temperature. Another drawback is that the tin actually melts and can run onto areas where it is not wanted, possibly causing shorts.

The gold/gold diffusion bond is made in the fixture shown in Figure 7. This consists of a 900-kg (1-ton) hydraulic ram mounted on a 6-in. diameter vacuum flange. The load is applied via a metal

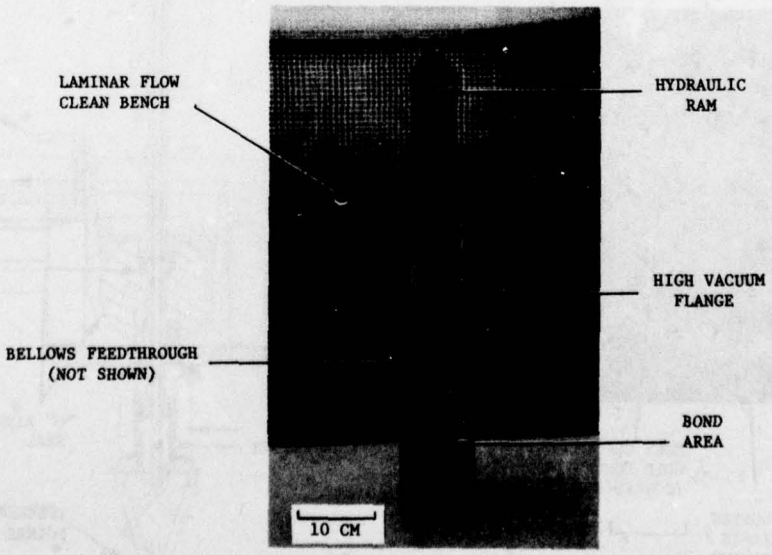

Figure 7. Diffusion Bond Fixture

bellows against the bottom of a stainless steel cylinder welded to the inside of the same flange. An advantage of this design is that the load is applied against the welds and bolts that hold the cylinder and ram to the flange, but no load is applied against the bolts holding the vacuum seal together. This design allows the entire bonding fixture to be removed from the system to aid in the assembly of the parts to be bonded. This assembly can also be aligned or replaced as a unit to avoid taking the vacuum system out of service should a problem develop.

The gold/gold diffusion bond used for the final closure of the flat pac has several advantages over other sealing techniques evaluated:

1. Strong, vacuum tight joint (to 245 MPa [35 000 psi]).
2. Low gas permeation.[8]
3. Ability to withstand bakeout at temperatures above final bond temperature.
4. Nonoxidizing surface for ultraviolet cleaning.
5. Proven technology.

Evaporation

Because of the long cycle time of an all-metal high vacuum system, approximately one run per shift, especially if it is baked out to remove adsorbed gas, it is necessary to process more than one resonator per pumpdown of the system. The first step to accomplish this is a simple "brute strength" approach, where nine filaments are mounted in the system such that any one of six resonators can be evaporated individually (Figure 8). Evaporation rate control is provided by resistance monitors. These monitors are simply sapphire discs on which a serpentine pattern of evaporant is deposited and its resistance monitored. These devices work well at high temperatures and can be monitored with simple equipment. They are used to adjust the two filament evaporation sources to equal evaporation rates. Shutters allow for premelting of the gold and evaporation rate adjustment before resonator evaporation. The long-term solution to increasing the production rate is felt to be the fabrication of a directional evaporation source which will recycle the evaporant, such as that which is described by Dr. Andres elsewhere in these proceedings, and a vacuum manipulator which can insert and then remove the resonator assemblies from the evaporation or bonding fixturing so that a large quantity of resonators can be put into the system and then processed sequentially without opening the vacuum system. The manipulator shown here has been suggested by Dr. Hafner and a prototype is being built at present (Figure 9). The unique feature of this design is the use of a rough vacuum on the inside of the bellows to reduce the pressure differential that an operator must work against and thus improve his ability to handle small parts.

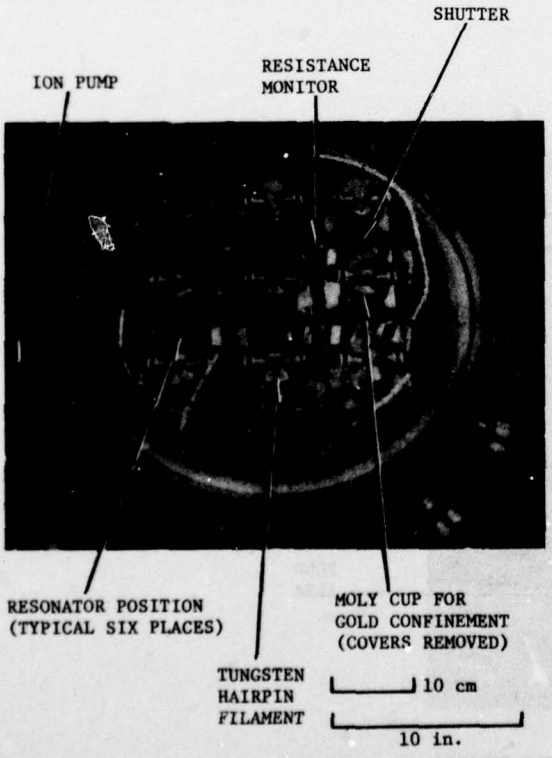

Figure 8. All-Metal Vacuum System With Multiple Filament Evaporation Sources

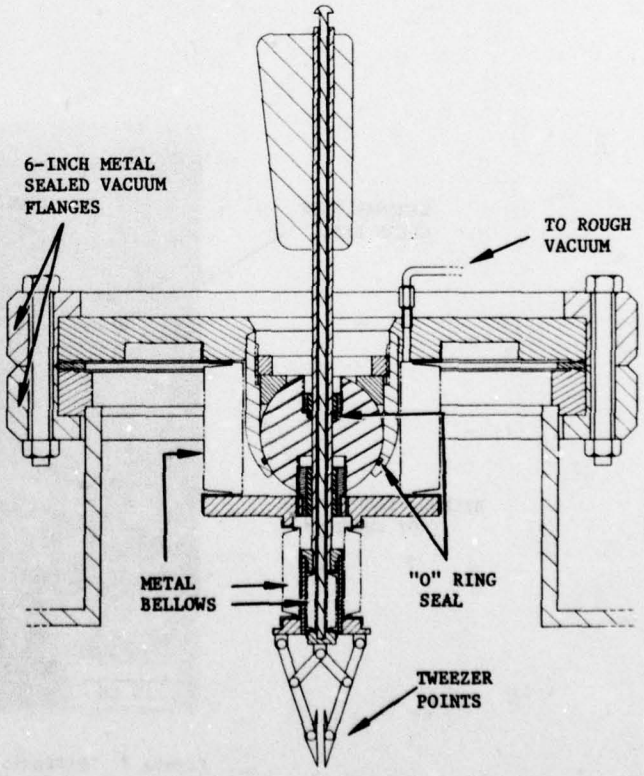

Figure 9. Vacuum Manipulator

Auger Studies

Our Auger electron spectrometer was used to investigate the ultraviolet cleaning process. Two pieces of quartz having gold deposits on their surface were cleaned by our normal solvent cleaning process. One was put directly in the Auger equipment; the other was ultraviolet cleaned for 15 minutes and then put in the Auger chamber. Scans showed that there was considerably less than a monolayer of carbon-type contamination on the ultraviolet cleaned specimen, while there was significantly more carbon on the one not ultraviolet cleaned (Figure 10). After the gold surface was characterized, it was removed by ion sputtering until the carbon peak disappeared. The buildup of the carbon peak was then monitored for 1000 minutes, during which time considerably less than a monolayer of carbon accumulated on the surface (Figure 11). This amount of carbon could cause a considerable frequency shift in a sealed-off unit, but is probably not sufficient to cause an adherence problem between subsequent layers of gold when evaporating to frequency in a two-step process such as that previously described.

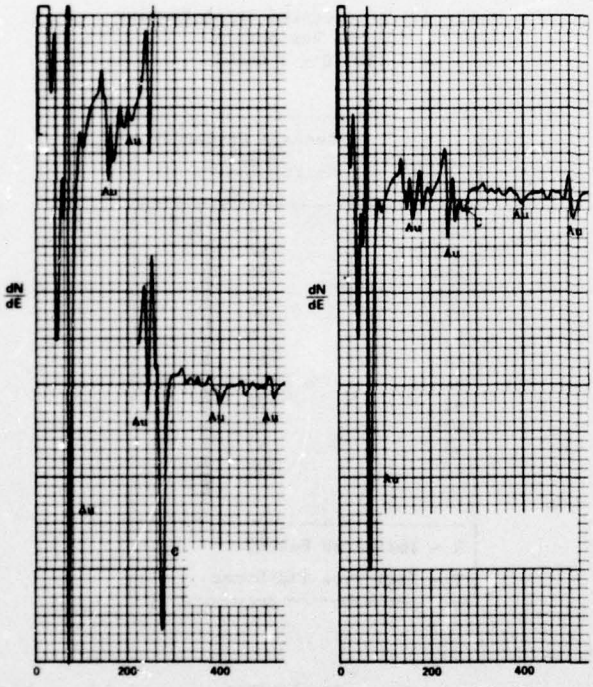

Figure 10. Au Specimen Not UV Cleaned (Left) and Au Specimen After UV Cleaning (Right)

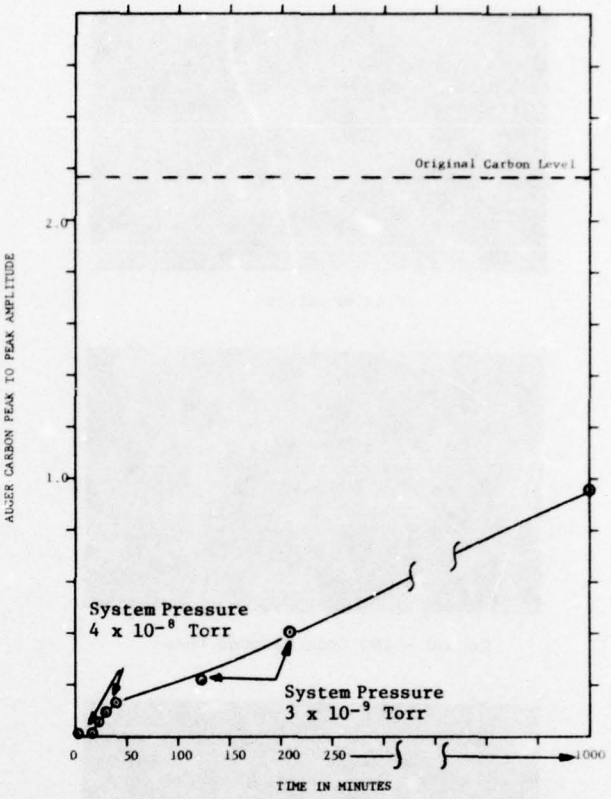

Figure 11. Carbon Regrowth on Clean Gold Surfaces

Surface Finish (SEM)

The diffusion bond final closure requires the ceramic parts to be very flat and parallel, or else they are cracked by the high force used. To accomplish this, all parts used to date have been ground on a surface grinder using a 180-grit bonded diamond wheel after final firing. SEM photos of this surface (Figure 12) show a very rough high surface area topography. This can be considerably improved by lapping with fine diamond dust. The effect of the ceramic surface finish on long-term aging has not been evaluated as yet; we do not know whether the surface acts as a source or sink for contaminants. The effect of the surface area of the inside of the ceramic enclosure will be evaluated in the near future. If properly cleaned and baked, however, we hope the surface finish will have little effect on aging.

As Received

Ground - 180 Grit Diamond Wheel

Polished - 15 Micron Diamond Compound

Polished - 1 Micron Diamond Compound

Figure 12. Ceramic Surface Topography
SEM-3000X Magnification

Aging Results

Some aging data has been obtained by ECOM on our first group of 12 prototype 5 MHz ceramic flat packs built using these techniques. Table 3 shows the results of one week storage at 105°C. The frequency measurements were made before and after the storage period at 40°C and the accuracy of the $\Delta F/F$ measurement is felt to be $\pm$ 7 x 10^{-8}. These units showed a maximum frequency shift ($\Delta F/F$) of 26 x 10^{-8}. This is up to an order of magnitude better than the best quality military units usually encountered. This same group of resonators was then aged for 30 days at 85°C. The average of the absolute values of the aging rate ($\Delta F/F$) was 6 x 10^{-10} per day. The range was from + 13 x 10^{-10} to - 14 x 10^{-10} per day. It should be stressed that these results are from our first prototype assemblies. With improved technique and batch processing, considerably improved results can reasonably be expected. These units were made by personnel who had extensive experience in high vacuum thin film technology, but who had never made resonators before.

Table 3. Accelerated Aging Results
5 MHz Resonators
(105°C - 1 week)

Resonator Number	Average Frequency Shift $\left(\frac{\Delta F}{F}\right)$
33	-2 x 10^{-8}
34T	+7
35R	-26
36R	-6
37	-6
39	0
40	+13
41	+13
42	+22
43	+8
45	+2
47	+20

R - Indicates Rebond

T - Indicates Tin Braze

Conclusions

Ceramic flat pack enclosures are now available for both 5 and 20 MHz crystal units. Resonators built using these enclosures in conjunction with nickel electrobonding, ultraviolet cleaning and high vacuum processing are showing very encouraging accelerated aging results. Many of the techniques being developed, such as the gold diffusion bond, the modular bonding unit, and the precision manipulator will be applicable to a system in which the resonator can be cleaned, electroded and sealed all without exposure to atmosphere.

Acknowledgments

The guidance and support of Dr. Erich Hafner and Dr. John Vig of ECOM are gratefully acknowledged. Thanks are also due to Mike Holloway, General Electric Neutron Devices Department (GEND), for AES analysis, Jim Spinks (GEND) for SEM photos, and Les Shilba (ECOM) for aging measurements.[9] The implementation of the processes described is the result of Jim Frank's (GEND) tireless efforts.

References

1. John R. Vig and Erich Hafner, "Packaging Precision Quartz Crystal Resonators," Technical Report ECOM-4134, U. S. Army Electronics Command, Fort Monmouth, N. J., July 1973.

2. P. D. Wilcox, G. S. Snow, Erich Hafner and John R. Vig, "A New Ceramic Flat Pack for Quartz Resonators," Proceedings of the 29th Annual Symposium on Frequency Control, U. S. Army Electronics Command, Fort Monmouth, N. J., pp 202-210 (1975), copies available from Electronics Industries Association, 2001 Eye Street N. W., Washington, D. C. 20006.

3. H. P. LaBuff, W. G. Schmidt, "Some Effects of Thermal Cycles on Ceramic-to-Metal Seal Strength," Technical Paper AD75-870, Society of Manufacturing Engineers, Dearborn, Michigan, 1975.

4. J. R. Vig, J. W. LeBus, and R. L. Filler, "Further Results on Ultraviolet Cleaning and Ni Electrobonding," Proceedings of the 29th Annual Symposium on Frequency Control, U. S. Army Electronics Command, Fort Monmouth, N. J., pp 220-229 (1975).

5. Jack L. Marti, "The Effects of Some Variables Upon Internal Stress of Nickel as Deposited from Sulfamate Electrolytes," Plating, January 1966, pp 2-12, reprints available from Allied-Kelite Div., The Richardson Co., Des Plaines, Illinois 60018.

6. V. H. Troutner, "Resume of Radiflo Leak Detection," Technical Report No. R63XF22, General Electric Co. X-Ray Dept., St. Petersburg, Florida, 1963.

7. Max Hansen, "Constitution of Binary Alloys," pp 232-233, McGraw-Hill Book Co., Inc., New York, 1958.

8. William Ierna, "Hydrogen Permeation Through Pure Gold," Technical Report TDE 73-18, General Electric Company, Neutron Devices Dept., St. Petersburg, Florida.

9. Les Shilba, ECOM, private communication.

DESIGN OF A NOZZLE BEAM TYPE METAL VAPOR SOURCE[1]

Ronald P. Andres
Beam Kinetics Laboratory
Department of Chemical Engineering
Princeton University
Princeton, New Jersey 08540

Summary

A prototype design of a directional high flux source for use in vapor deposition of electrode materials during fabrication of precision quartz crystal resonators is presented. The design is based on the theory and technology of nozzle beams. This nozzle beam type source is conceived: (1) to permit large deposition rates with minimum wastage of electrode material, (2) to operate in high vacuum, (3) to emit vapor in a horizontal direction, thereby permitting the use of a pair of sources to plate both sides of a substrate simultaneously, and (4) to operate for extended periods without requiring frequent breaking of the vacuum in order to replenish the source. It is estimated that this design can operate at a deposition rate equal or above that of a conventional evaporation type source with less than one percent of the wastage of electrode material experienced with a conventional source.

Introduction

A critical step in the fabrication of ultra high precision quartz crystal resonators is the vacuum deposition of the electrode material. In order to minimize stresses that could cause aging, both sides of the resonator are plated simultaneously and at equal rates so that the final thicknesses of the electrodes are approximately equal. In order to minimize aging due to mass transfer, the electrode material is of high purity and is deposited rapidly under high vacuum conditions so as to minimize sorption of contaminants.

These requirements place rather stringent performance requirements on the metal vapor source used in the vacuum plating operation. Ideally it should minimize wastage of expensive electrode material (such as gold), should be capable of operation over a wide range of controlled deposition rates, should be compatible with high vacuum operation, should not require frequent maintenance, and should permit simultaneous plating of both sides of a substrate.

These requirements led Drs. E. Hafner and J. Vig of the U.S. Army Electronics Command, Fort Monmouth, New Jersey, to investigate the possibility of using molecular beam techniques to develop a new highly directional vapor deposition source [1]. Their concept was a source such as is shown schematically in Figure 1. This source is divided into two chambers interconnected by means of an aperture. The first of these chambers (source chamber) is held at a high temperature so as to maintain the vapor pressure of the evaporant at a high value. The second chamber (collimation chamber) is maintained at the melting point of the evaporant thereby maintaining a relatively low vapor pressure. Because of the pressure differential between the two chambers, a vapor flow is established through the source aperture. A portion of this flow passes through a collimation aperture and plates the substrate. By far the largest fraction of the flow, however, strikes the walls of the collimation chamber, condenses, and is recycled to the source chamber by means of a liquid transfer line. The great advantage of such a design over conventional evaporation sources is that the major part of the evaporant flow not needed to plate the substrate is recycled and not wasted. The need for high deposition rates leads to the requirement that the flow from the source chamber be at a relatively high density. Such unconstrained expansion of a vapor from a high pressure source through an orifice into a vacuum is termed a nozzle or free jet flow.

This paper sets forth general design considerations for such a nozzle beam type source and a theoretical model for its operation. Experiments run with several source configurations are reported. Finally a prototype design is presented and discussed.

General Design Considerations

The flow distribution from a circular orifice into a region of vacuum can be theoretically predicted both in the limit of vanishing source density (i.e., large mean free path in the source relative to the diameter of the source aperture) and in the limit of high source density (i.e., small mean free path relative to aperture diameter).

In the first case we have the classical expressions for effusive flow:

$$f_o = (0.282)n_o\left(\frac{2kT_o}{m}\right)^{1/2}\left(\frac{\pi d_o^2}{4}\right) \tag{1}$$

and

$$I(\theta=0,\ell) = f_o\left(\frac{1}{\pi\ell^2}\right) \tag{2}$$

where

- f_o = total source flow (molecules/sec)
- n_o = source density (molecules/cc)
- T_o = source temperature (°K)
- k = Boltzmann's constant (erg/°K)
- m = molecular weight of vapor molecule (gm/molecule)
- d_o = source aperture diameter (cm)
- $I(\theta=0,\ell)$ = centerline flux intensity (molecules/cm sec)
- ℓ = distance from source aperture (cm).

In this effusive limit the flux intensity, $I(\theta,\ell)$, varies as the cosine squared of the angle, θ, measured with respect to the centerline of the flow. Thus, in the region

about $\theta = 0$ the flux of molecules is: (1) practically constant with θ, (2) proportional to the total source flow, f_o, and (3) inversely proportional to the distance, ℓ, squared.

Sherman and Ashkenas [2] have analyzed the structure of the supersonic free jet flow that exists in the limit of high source density. Making use of their results yields simple expressions for total source flow and centerline intensity which have the form:

$$f_o = (0.513)n_o\left(\frac{2kT_o}{m}\right)^{1/2}\left(\frac{\pi d_o^2}{4}\right) \tag{3}$$

$$I(\theta=0,\ell) = (1.85)f_o\left(\frac{1}{\pi\ell^2}\right) \tag{4}$$

The numerical constants in Eqns. (3) and (4) are for the case of a monatomic vapor. The flux intensity, $I(\theta,\ell)$, varies in this high density limit as

$$I(\theta,\ell) \simeq I(\theta=0,\ell)\cos^2\left(\frac{\pi\theta}{2\phi}\right) \tag{5}$$

where $\phi = 1.36$ radians for the case of a monatomic vapor. Thus, in the region about $\theta = 0$ the flux of molecules is again: (1) practically constant with θ, (2) proportional to the total source flow, f_o, and (3) inversely proportional to the distance, ℓ, squared. In the high density or nozzle flow limit, however, the centerline flux intensity for a given source flow is nearly twice what it would be if effusive conditions obtained. Furthermore, the source flow and thereby the centerline intensity of a nozzle type source can be orders of magnitude greater than the effusive values for a given size aperture thereby permitting much higher vapor deposition rates.

In most plating operations the distance, ℓ, is taken to be fairly large so as to minimize the effects of thermal radiation from the source. The actual solid angle about $\theta = 0$ that is subtended by the substrate is a small fraction of the total solid angle of the flow. Thus, only a small fraction of the total vapor passing through the source aperture is deposited on the substrate. The remainder of the source flow deposits onto various collimators or masks used to define the actual area on the substrate that is to be plated and onto the walls of the vacuum system. While this material can in principle be recovered for eventual reuse, such recovery involves breaking open the vacuum system and substantial repurification. Ideally one would like to continuously recycle the material that is not deposited on the substrate. It is this concept that forms the basis of a nozzle beam type source.

The elements of such a source are schematically pictured in Figure 1. A directed beam of vapor molecules is collimated from the total flow passing through the source aperture and this collimated beam is used to plate the substrate. The remaining portion of the vapor condenses on the walls of the chamber containing the collimation aperture. This collimation chamber is then either maintained at a temperature above the melting point of the material being used so that the material continuously flows back into the source chamber or it is periodically heated to melt and recycle the condensate.

As long as n_1 is kept low enough so that the vapor molecules flowing through the source aperture are not appreciably scattered by the background density in the collimation chamber, the source flow will become free molecular at some point and the intensity distribution in the collimated beam will be roughly that from a virtual free molecular source situated at the position of the source aperture [3]. In the case of effusive flow the diameter of this virtual source, d_o^*, equals the actual aperture diameter, d_o. In the nozzle or high density limit the diameter of the virtual source is a multiple, α, of the actual aperture diameter, where α depends on the product $n_o d_o$ (increasing slowly as $n_o d_o$ increases). The parameter, α, is always greater than unity but is typically less than four for flows in which nucleation and condensation of the vapor do not take place [3].

The intensity distribution from such a collimated free molecular source is shown schematically in Figure 1. The intensity profile consists of two regions: (1) a central portion characterized by a diameter, a, in which the intensity is that of the uncollimated flow and (2) an annular region characterized by an outer diameber, b, in which the intensity falls to essentially zero. Straightforward geometrical considerations yield the following expressions for a and b:

$$a = d_1\frac{\ell}{\ell_1} + d_o^*\left(1 - \frac{\ell}{\ell_1}\right) \tag{6}$$

$$b = d_1\frac{\ell}{\ell_1} + d_o^*\left(\frac{\ell}{\ell_1} - 1\right) \tag{7}$$

The only part of such a collimated beam that is useful for uniform plating of a substrate is the central portion. The diameter of this constant flux region can be designed, however, to be equal to or slightly greater than the diameter of the substrate area that is to be plated. The essential feature of such a collimated beam source is that only that fraction of the vapor flowing through the collimation aperture that is directed into the annular region with inner diameter a and outer diameter b need be wasted in contrast to the usual case of an uncollimated source when everything passing through the source aperture that is not directed onto the substrate is wasted. Even the small fraction of the flow that is wasted can be minimized by keeping d_o^*/d_1 small and/or by keeping ℓ/ℓ_1 close to unity.

Gold Vapor Source

It is possible, using relevant physical data [4] and Eq. (3), to evaluate f_o for a nozzle type gold vapor source. The results of such a calculation are plotted in Figure 2 as a function of source temperature, T_o. A standard aperture diameter, d_o, of 1 mm was arbitrarily assumed in these calculations. The flow through any other aperture can be found by multiplying f_o from Figure 2 by the square of the actual diameter in mm. Two sets of units in which to express f_o are used. The left hand scale reads in molecules/second while the right hand scale reads in milliliters liquid gold/second.

The ideal centerline intensity of a nozzle beam type gold vapor source can now be obtained through use of Eq. (4) and values of f_o obtained from Figure 2. As an example of the order of magnitude of this flux, assume a standard arrangement in which $d_o = 1$ mm and $\ell = 10$ cm. Expressing the flux of gold vapor as an equivalent deposition rate, the deposition rate for this configuration in Å/sec equals 10^{-17} times f_o expressed in mol/sec.

A rate of 0.01 Å/sec is achieved when $T_o \simeq 1300°C$. A deposition rate of 10 Å/sec requires a source chamber temperature of 1900°C. High deposition rates, therefore, restrict the material of construction for a gold vapor source to one of the refractory metals.

The temperature of the collimation chamber for the case of a gold vapor source is set by the melting point of gold, 1063°C. At this temperature there are a number of oxide ceramics that can be used as materials of construction. In particular, high purity Al_2O_3 seems

attractive. It exhibits negligible chemical interaction with Au, is an electrical insulator, is easily fabricated into practically any shape, is tolerant of thermal shock, and is inexpensive[2].

Experimental Considerations

The primary difficulties in achieving a practical source based on the foregoing ideas arise from: (1) the high temperatures required and (2) the need to move the liquid evaporant against a pressure differential from the collimation chamber to the source chamber. A number of experiments were carried out to determine a suitable solution to these problems. In all of these experiments Cu was used as the evaporant. The material of choice for the collimation chamber (crucible) was high purity Al_2O_3 and for the source chamber was tungsten, although in some of the experiments lava was substituted for Al_2O_3 and tantalum was substituted for tungsten because their availability and lower cost permitted a larger range of experiments to be performed.

The easiest way to heat a refractory metal object to a high temperature is by electrical resistance heating. In this case the best geometry for the object is that of a cylinder with a small O.D. Thus, in all of the experiments the configuration of the source chamber was that of a long thin cylindrical tube, closed at one end and communicating with the fluid reservoir via the opposite open end. The source aperture was drilled into the side of the tube.

The only feasible way to transfer the liquid evaporant appears to be by means of capillary forces or by means of a differential liquid head. The contact angle of liquid gold on a clean tungsten surface in vacuum is less than 90° and decreases with increasing temperature [5]. Thus, it is expected that for this system surface tension forces will tend to draw liquid evaporant into the source tube. In all of the experiments with Cu, however, the opposite phenomenon was observed, i.e. there was a decided capillary lowering of the liquid level in the tube. A contact angle greater than 90° was also observed at the Cu-Al_2O_3 interface.

The first experimental configuration studied is shown schematically in Figure 3. The collimation chamber had a helical groove machined on the outside. Tungsten wire (0.015" diam.) was wound in this groove and was used to electrically heat the crucible. This technique proved very successful and was improved in later models by transforming the groove into one with a flat cross section in which 1/16" wide by 0.005" thick tantalum ribbon could be wound and by increasing the thickness of the crucible's bottom to assure a more uniform inside temperature. The source chamber was a 1/8" O.D. tantalum tube with a wall thickness of 0.010". Electrical current to heat the tube was supplied by means of a stainless steel clamp at the closed upper end and by means of a 1/8" O.D. tungsten rod immersed into the pool of liquid metal at the bottom of the crucible.

Several attempts were made to test the performance of this design. None of these runs were successful in producing a copper beam. They served to point out a number of serious flaws in the design. First, copper exhibited a relatively large contact angle with the Al_2O_3 so that liquid Cu was excluded from the region around the bottom of the Ta tube. This could of course be remedied by increasing the dimensions of the entire crucible. A more serious flaw, however, involved the joint between the Ta tube and the Al_2O_3 crucible. After several runs the tube became embrittled at this joint and failed. The joint was a force fit at room temperature. Due to the difference in thermal expansion of Ta and Al_2O_3, the tube was constricted at its operating temperature and this may have caused the failure. Whatever the reason, it was decided to modify the source to that shown in Figure 4.

This configuration eliminates the need for metal-ceramic joints and has the decided advantage of a greatly simplified collimation chamber design. The interior of the crucible is machined with a slight taper so that its I.D. at the top is larger than at the bottom. This permits extraction of the metal charge as a solid block should the need arise. The prototype source chamber shown in Figure 4, i.e., a small O.D. tungsten tube inside a larger tungsten sheath, is based on the experiments described below but has not actually been tested in our laboratory due to the lack of facilities for its fabrication.

Two experiments were run to simulate the source design shown in Figure 4. Both of these experiments were run with inner tubes of tantalum encased in an alumina outer tube. The first experiment involved a 1/8" O.D. tantalum tube with a wall thickness of 0.010" encased in a 10 mm O.D., 6 mm I.D., alumina tube. The alumina tube was originally closed at one end, and a hole was drilled through this end to permit passage of the tantalum tube. The joint was a force fit at room temperature.

This source produced an intense copper beam. The temperature of the tantalum tube, however, did not rise much above that of the crucible and the spatial distribution of the beam, while directed, did not agree with the predictions of Eqns. (6) and (7). Although the temperature of the liquid copper pool in the collimation chamber wasn't monitored, it is felt that this temperature became high enough so that effusive flow from the collimation chamber itself formed a major part of the beam.

The second experiment involved a 1/16" O.D. tantalum tube with a wall thickness of 0.005" encased in a 4 mm O.D., 2 mm I.D., alumina tube. This time the tantalum tube reached a temperature of 2,000°C and produced a sharply defined beam. For the conditions of the experiment (d_o = 0.5 mm, ℓ_1 = 5 cm, d_1 = 6 mm, and ℓ = 15 cm) the beam should theoretically have been ≃ 18 mm in diameter and this is what was observed experimentally. Unfortunately, as was the case with the source shown in Figure 3, the source tube eventually cracked where it passed through the alumina sheath. It is perhaps worthwhile mentioning that initially the copper would not flow into this tantalum tube even under a differential head of 4 cm. This problem was solved by placing a small amount of Cu wire inside the tube.

Finally, a third source configuration was explored. This source consisted of a 0.195" O.D. tungsten tube with a wall thickness of 0.005". Inside this tube was supported a filament of 0.015" diameter tungsten wire, which had been wound on a mandril into the form of a spring. The bottom 1/4" of this spring had an O.D. just smaller than the I.D. of the tube so as to center the filament in the source tube while the remaining portion of the spring had an O.D. approximately 1/3 of the tube's I.D. Electrical current to heat the source passed down through this filament and then back via the tube. It was possible to control the source chamber temperature at above 2000°C with this arrangement. Unfortunately, the portion of the tube submerged in the copper pool remained at a relatively low temperature and no measureable copper beam was produced.

As was the case with the other experiments, the dimensions of the components used in this source where dictated primarily by their availability in our laboratory. The liquid level inside the source tube for this configuration will in general lie below that of the liquid surrounding the tube. Thus, the tube wall in the region of the liquid-vapor interface will be near that of the surrounding liquid (i.e. approximately the melting

temperature of evaporant). The temperature of the liquid near the filament will on the other hand be much higher, approaching that of the filament itself. Accurate modeling of this situation is quite difficult but it seems that there should be situations in which an appreciable net flux of evaporant into the tube exists. Because of its relatively simple construction, this configuration should be studied further.

Proposed Design

A suggested prototype nozzle beam type source for use in vapor deposition is shown schematically in Figure 4. This design makes use of the theoretical and experimental considerations described in the previous sections. The dimensions of the collimation chamber in Figure 4 were arrived at by assuming the substrate is located at a distance of 20 cm from the source orifice with a diameter of about 2.5 cm. Under different situations the size of the collimation aperture can be altered following Eqns. (6) and (7) and the earlier discussion.

The Al_2O_3 collimation chamber employed in this design has proved simple to operate and quite reliable. Because of its large size and relatively high operating temperature, it is necessary to provide radiation shielding around this chamber so as to not raise the temperature of the substrate. It may prove in practice that the best way to operate is to actually have the collimation chamber near room temperature during substrate plating and to heat this chamber to recycle evaporant only after the plating operation is over. Whatever turns out to be the case, a thermocouple should be placed inside a closed end alumina tube and immersed in the metal pool in this chamber to monitor its temperature.

The source chamber in Figure 4 has been shown to be feasible in concept but has not been constructed or operated. Probably further experiments with a tantalum source having this configuration should be carried out before constructing one from tungsten. Certainly more work has to be done before the design of this critical part of the source is finalized (see discussion in section on experimental considerations).

This source should exhibit only a very small fraction of the wastage of electrode material experienced with conventional sources. It is estimated that such a nozzle beam type source can operate with deposition rates equal or above that of conventional evaporation sources. At the same time this source is capable of very low, controlled rates of deposition. A source containing two separate source chambers with different size apertures would yield an even larger range of controlled plating rates.

Acknowledgments

I want to thank Drs. E. Hafner and J. Vig for numerous helpful discussions and suggestions throughout this work. Finally, I want to acknowledge the aid of J. Bittner who built the experimental models and of Y. Wong who ran many of the experiments.

Footnotes

1 This work was supported through the U.S. Army Research Office by the U.S. Army Electronics Command, Fort Monmouth, New Jersey.

2 Fabrication with alumina is achieved by starting with green material, which is easily machined, and then firing. Shrinkage of about a factor of 1.25 occurs on firing. The Al_2O_3 collimation chambers used in the present work were fabricated by Western Gold and Platinum Co., 205 Oraton Street, Newark, New Jersey, 07104.

References

1. Hafner, E., Vig, J. and Andres, R.P., Invention Disclosure - "A Highly Directional Source for Vacuum Evaporation", U.S. Army Electronics Command

2. Ashkenas, H. and Sherman, F.S., "The Structure and Utilization of Supersonic Free Jets in Low Density Wind Tunnels", Rarefied Gas Dynamics, (ed. de Leeuw), Vol. 2, p.84, Academic Press, New York (1965).

3. Sikora, G.S., "Analysis of Asymptotic Behavior of Free Free Jets: Prediction of Molecular Beam Intensity and Velocity Distributions", Ph.D. Dissertation, Princeton University (1973).

4. Handbook of Chemistry and Physics (ed. Weast) Chemical Rubber Co., Cleveland (1967).

5. Sugita, T., Ebisaka, S., Kawasaki, K., "Contact Angles of Gold and Silver on a Clean Tungsten Substrate", Surface Sci. 20, p.417 (1970).

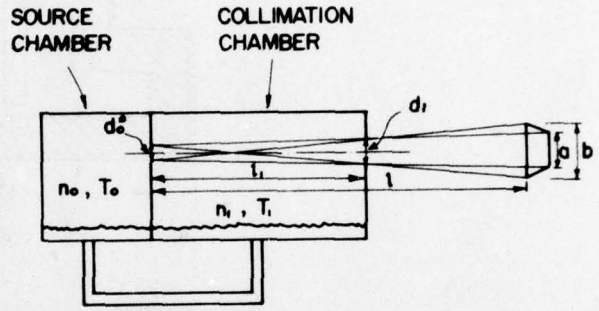

Figure 1. Schematic of Nozzle Beam Type Source

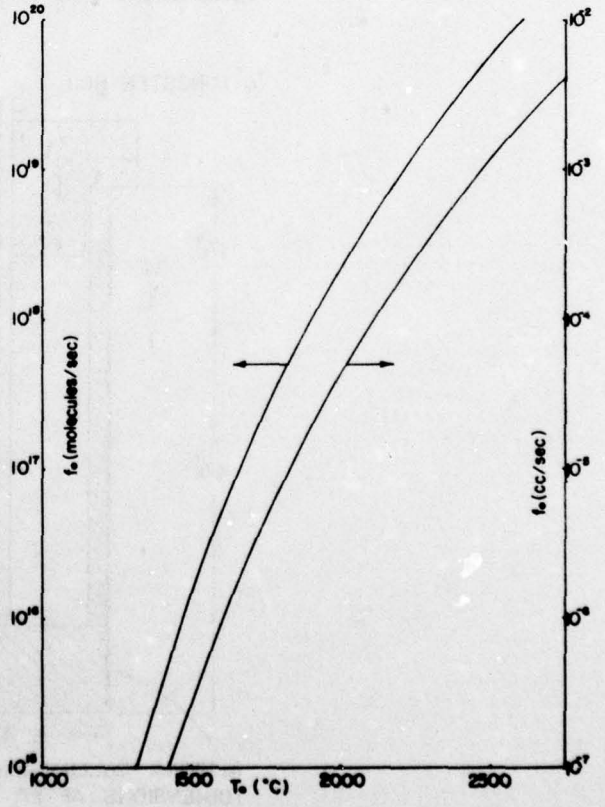

Figure 2. Gold Flow Through One Millimeter Diameter Aperture

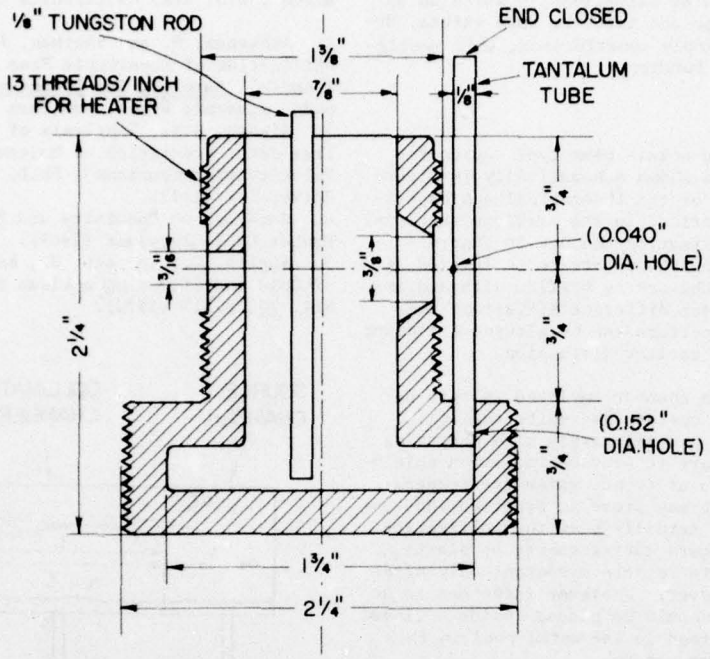

Figure 3. Experimental Nozzle Beam Type Source

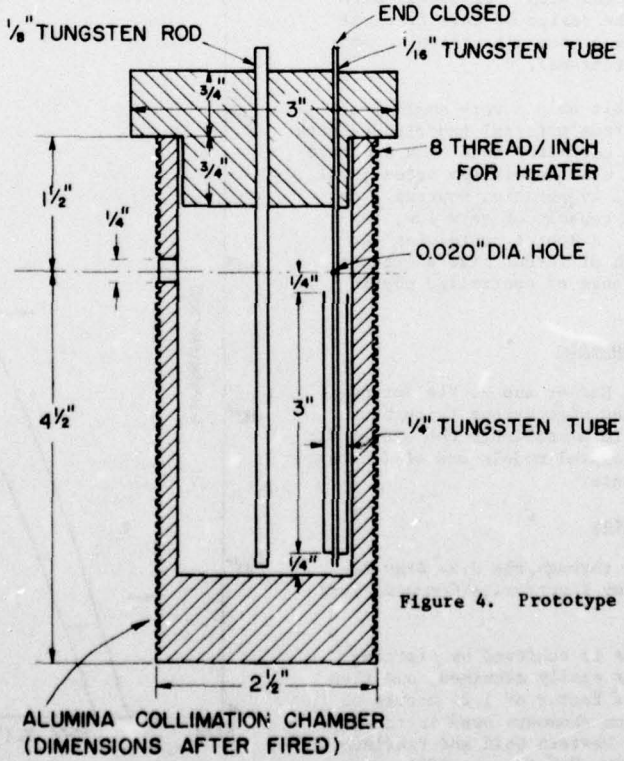

Figure 4. Prototype Nozzle Beam Type Source

AN EVALUATION OF LEAK TEST METHODS FOR HERMETICALLY SEALED DEVICES

Ralph E. McCullough
Texas Instruments Incorporated
Dallas, Texas

Summary

Test methods which are available for leak testing hermetically sealed packages are discussed in this report. Emphasis is given to helium and radioisotope tracer gas methods because of the stringent hermeticity requirements for frequency control devices.

The different results which are obtained using the various military specification methods on the same device are discussed and the reasons for these different results examined. The effect of changes in the various parameters which affect the measurement of leak rates is explained. This discussion includes the effects of changes in internal free volume of the device being tested, changes in pressurization, changes in pressurization time and changes in wait time from out of pressure to read out.

The problem of correlation between the helium and the radioisotope methods is discussed in terms of why there is a problem and what must be done to overcome it. The range over which correlation can exist and the reasons why it cannot exist beyond that point are also examined.

Gross leak methods which will test the leak rate range not tested by normal helium or radioisotope methods will be examined. The advantages and disadvantages of each of the commonly used techniques are included.

Proper sequence of testing is examined and techniques discussed which will assure that the fine leak test method utilized will overlap the gross leak test method used.

The test methods of MIL-STD-202, MIL-STD-750 and MIL-STD-883 for hermetic seal testing are the most commonly used to determine the hermeticity of device packages. Helium or krypton 85 with appropriate equipment is used for the fine leak range of less than 10^{-5} atmospheric cubic centimeters per second. Fluorocarbon bubble or weight gain condition is then used to test the gross range greater than 10^{-5} atm cc/sec.

The fine leak conditions and limits specified in these documents are shown in Tables I-A and I-B.

TABLE I-A - HELIUM

MIL-STD	Pressure Time (hours)	Pressure PSIG	Reject Point Indicated	Reject Point Calculated	Package Volume
202	Per equip. mfg's manual		1×10^{-8}		All
750	4	60	5×10^{-8}	NA	All
883	1	75	5×10^{-8}	5×10^{-7}*	<0.1cc
883	1	75	5×10^{-7}	5×10^{-6}*	>0.1cc

* Pressurization conditions determined by the equation:

$$R_1 = \frac{LP_E}{P_o}\left(\frac{M_A}{M}\right)^{1/2}\left\{1-e^{-\left[\frac{Lt_1}{VP_o}\left(\frac{M_A}{M}\right)^{1/2}\right]}\right\} e^{-\left[\frac{Lt_2}{VP_o}\left(\frac{M_A}{M}\right)^{1/2}\right]}$$

TABLE I-B - RADIOISOTOPE

MIL-STD	Pressure Time (hours)	Pressure PSIA	Reject Point	Package Volume
202	Per equip. mfg's manual		1×10^{-8}	All
750	0.1	73.5*	1×10^{-8}	All
883	0.2	29.4*	5×10^{-8}	All

* Minimums - Pressurization conditions must satisfy the equation:

$$Q = \frac{R}{SKt\left(P_e^{\,2}-P_i^{\,2}\right)}$$

Examination of the exposure conditions, reject points and the formulas suggests that significantly different results could be obtained on a population of devices, depending on the specification selected for use. Figure 1 shows that this is true. The population used was made up of "rejects." It was tested using MIL-STD-750 helium conditions, vacuum baked for 24 hours, tested for residual helium, then tested to MIL-STD-883 helium conditions. After another 24 hour vacuum bake period the devices were tested to 750 radioisotope conditions, baked, checked for residual krypton, then tested to 883 radioisotope conditions.

The data resulting from the two radioisotope tests are essentially the same. There are more "acceptable" devices on the 883 condition plot only because the reject point is one half decade larger than the 750 limit.

The results of the helium testing show the differences that were suggested by Table I. There is more scattering of the population using the longer pressurization time of MIL-STD-750. The 750 data indicates that more of the devices have leaks near the gross leak part of the range and also shows devices with finer leaks than indicated by the 883 data. Examination of Figure 2 will show the reasons for this situation. In Figure 2c note that a device with an actual leak rate of 10^{-7} atm cc/sec would read out at 5×10^{-9} atm cc/sec when bombed for one hour and at 1×10^{-8} atm cc/sec when bombed for four hours if both pressurizations were at 30 PSIG. If the actual leak rate is 10^{-6} atm cc/sec the indicated values are 5×10^{-7} and 1×10^{-6} at one and four hours respectively.

Examination of Figure 2b shows that this problem is corrected to some extent by the differences in

specified pressures. The 10^{-7} leaker indicates about 10^{-8} when pressured at 60 PSIG and $2x10^{-8}$ at 90 PSIG which does not compensate for the half decade difference created by the bomb time.

Therefore, if one helium tested devices of the volume being discussed to the MIL-STD-750 conditions, all of those which passed would have leak rates of less than $1x10^{-7}$. If this same group were tested to MIL-STD-883 conditions, all of those passing would have leak rates of less than $2x10^{-7}$.

Another factor which has to be considered is the internal free volume of the package under test. Figure 2a shows that under the same bomb conditions a leak of 10^{-7} could read in the 10^{-10}, 10^{-9} or 10^{-8} range depending on the volume. The remaining factor is the time from removal of pressure to readout. Figure 2d shows that this affects primarily the gross end of the range. Volume and time from pressure off to read are not factors in the case under discussion but are just as important as those affecting it.

It has now been said that the radioisotope test of MIL-STD-750 correlated with the radioisotope test of MIL-STD-883, and that although the helium tests did not correlate, the reasons why are understood. The other correlation to be considered is that of helium to radioisotope. Figure 1 shows a lack of correlation except over short spans within the range being tested. These are located at about 10^{-7} to nearly 10^{-6} in the 883 plot and if Curve A in Figure 3 is examined one can see why. This is the range in which the mass spectrometer readout is approximately equal to the actual leak rate. Curve B in Figure 3 indicates that this should occur at a lower actual leak rate value when MIL-STD-750 conditions are used. The 750 plot in Figure 1 indicates this is true although only a short span at about 10^{-7} can actually be called good correlation.

This all adds up to the fact that if variables data is to be used for establishing correlation between helium and radioisotope test, then the pressure/time relationship must be calculated in advance. Also that the mass spectrometer readings must be converted to actual leak rates. If attribute type correlation is required, then only the spectrometer value at the desired actual leak rate has to be known.

Another point about correlation present in Figure 1 is that as values approach the gross range the larger the difference between helium and radioisotope readings. This may be partially attributed to molecular flow being assumed in the helium formula and viscous flow in the radioisotope formula. The flow in the 10^{-6} and 10^{-5} range is considered to be transitional by most, so neither formula will result in describing the actual leak value concisely. For practical purposes, however, this is not important as long as the test defines these devices as leakers.

One can readily conclude from the above that it is essential that pressures and times be properly computed and adhered to if devices are to have the required hermeticity leak rates. The selection of arbitrary times and pressures coupled with acceptance of uncorrected readouts can result in devices which have leak rates a decade too large being installed in a system. This cannot be overemphasized in the case of frequency control devices which typically have small internal free volumes. Re-examination of the c curve in Figure 2a will show that the fine leak test conditions must be carefully chosen to ensure that it will overlap or even meet the lower limit of the gross leak test.

Each of the specifications cited at the beginning contains conditions for fluorocarbon bubble gross leak testing. Only MIL-STD-883 contains the weight gain condition. The non back pressured bubble test should not be considered for use unless the device being tested has an internal free volume of greater than 1cc. The fine leak test on devices smaller than this will not extend to meet lower limit of it.

The back pressure bubble condition will detect leakers into the upper part of the 10^{-6} range and the weight gain condition as low as $2x10^{-6}$. These limits are the result of cessation of fluid flow through holes smaller than this at pressure differentials usable for such testing. This can be seen in Figure 4, which shows the flow rate through various leak sizes. The leak size to leak rate relationship is shown in Figure 5. Devices with leak rates larger than the cited capabilities can escape detection, however, if the leak is made up of multiple small paths equivalent to one hole of 10^{-6} mid range size.

There is not a test or series of tests which will assure with complete confidence that all leakers have been removed from a population when the testing is complete. However, if one determines and uses the proper test conditions, and uses calibrated test equipment and qualified personnel, the escape rate can be minimal in spite of the size holes being searched for.

The formulas cited and limits of the test conditions, both fine and gross, are discussed more fully in technical report RADC-TR-75-89 issued in April 1975 by Rome Air Development Center.

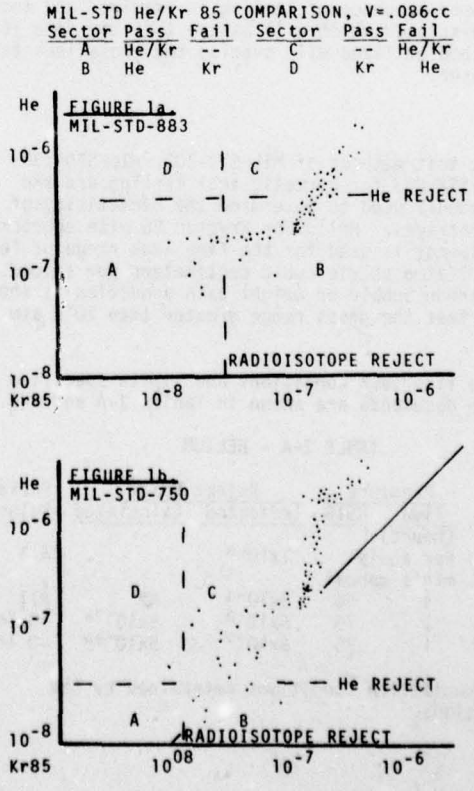

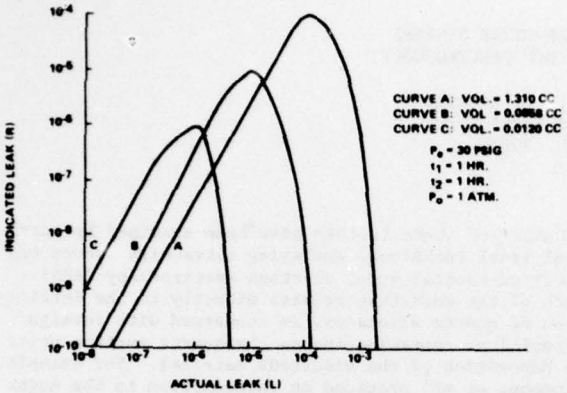

FIGURE 2a. COMPARISON OF VOLUME CHANGES

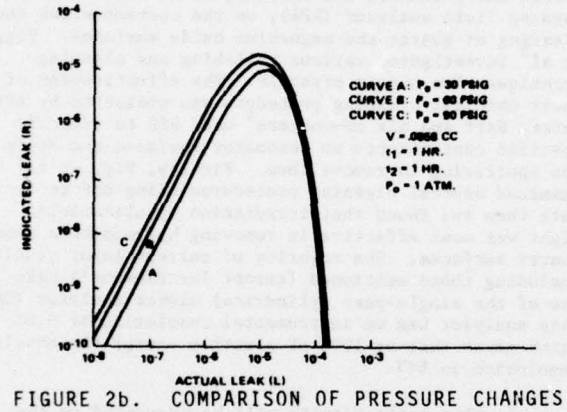

FIGURE 2b. COMPARISON OF PRESSURE CHANGES

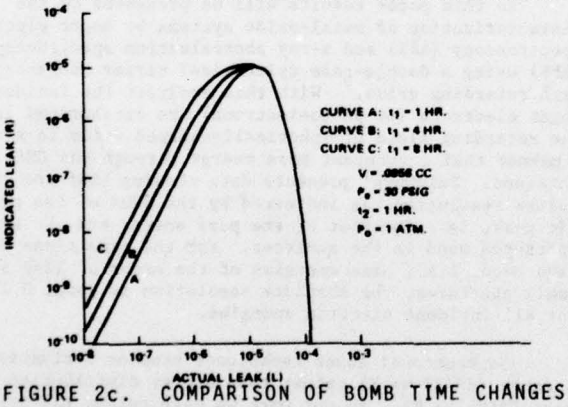

FIGURE 2c. COMPARISON OF BOMB TIME CHANGES

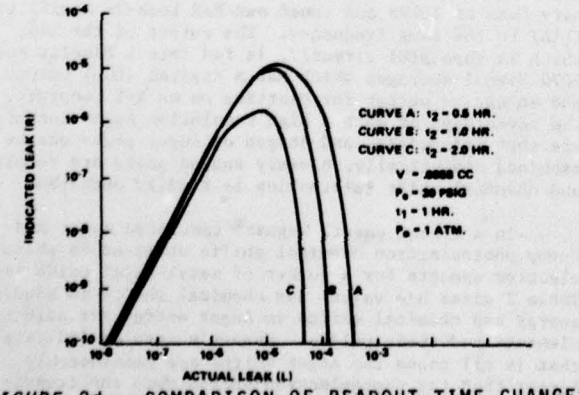

FIGURE 2d. COMPARISON OF READOUT TIME CHANGES OF THE HELIUM LEAK RATE FORMULA

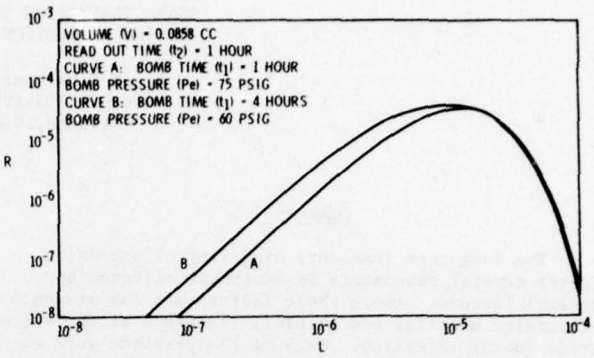

FIGURE 3. TO-100 TIME/PRESSURE SEQUENCE

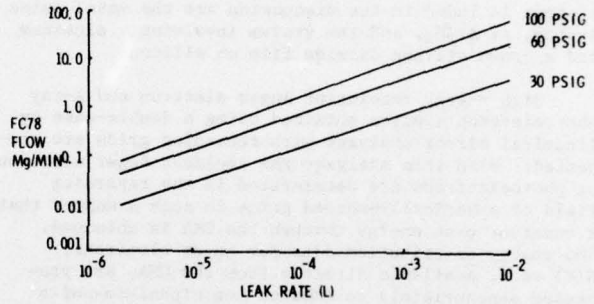

FIGURE 4. FLOW RATE OF FLUID INTO LEAKERS

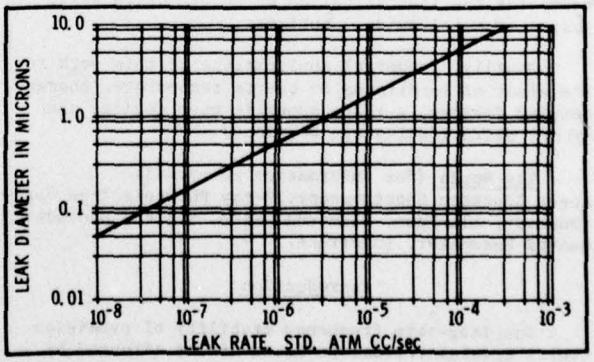

FIGURE 5. LEAK RATE VERSUS LEAK DIAMETER

CHARACTERIZATION OF METAL-OXIDE SYSTEMS BY HIGH RESOLUTION ELECTRON SPECTROSCOPY

E. J. Scheibner and W. H. Hicklin
Georgia Institute of Technology
Atlanta, Georgia 30332

Summary

The long-term frequency stability of precision quartz crystal resonators is adversely affected by several factors. Among these factors are the presence of foreign material and chemical reactions at the electrode-quartz interface. Much of the previous work employing electron spectroscopy is related directly to the fabrication of quartz resonators and is concerned with the identification of foreign material or contamination on the quartz surface prior to the deposition of the electrode material. The research described in this paper is directed towards a knowledge of the chemical reactions that take place between a reactive metal electrode and the quartz crystal. Metal-oxide systems included in the discussion are the metal-oxide system, Al-Al_2O_3, and the system involving aluminum and a grown silicon dioxide film on silicon.

High energy resolution Auger electron and X-ray photoelectron spectra obtained using a double-pass cylindrical mirror analyzer with retarding grids are presented. With this analyzer the incident Auger electrons or photoelectrons are decelerated in the retarding field of spherically-shaped grids in such a manner that a constant pass energy through the CMA is obtained. The energy distribution data for Auger electrons, N(E) vs E, available directly from the CMA, are processed appropriately to enhance the signal-to-noise ratio. This technique is to be compared with conventional Auger techniques which present derivative data, dN(E)/dE vs E.

The intensities and shapes of Auger and photoelectron peaks for the metal and its oxide are examined analytically in terms of lifetime broadening and electron-phonon scattering and attenuation lengths in the oxide are derived from integrated intensity data as a function of oxide thickness. Chemical shift information for the different metal-oxide systems provides a means for the identification of intermediate solid-phases at metal-oxide interfaces.

Finally, potential applications of this work to the study of interfaces in quartz resonators, charge coupled devices, surface acoustic wave devices and hybrid microcircuits are mentioned.

Key Words (for information retrieval)
Auger Electron Spectroscopy, X-ray Photoelectron Spectroscopy, Aluminum, Aluminum Oxide, Silicon Dioxide, Quartz Resonator, Interface.

Introduction

The long-term frequency stability of precision quartz crystal resonators is adversely affected by several factors. Among these are time-dependent changes in the mass of the resonator, the composition and partial pressures of gases in the resonator package, changing stresses in the resonator due to thermal mismatch between the electrode material and quartz and relaxation of the electrode material, stresses caused by the mounting structure and contacts, foreign material and chemical reactions at the electrode-quartz interface, and changes in the quartz crystal structure.[1] A number of these factors have been examined by surface analytical techniques employing ultra-high vacuum and electron-excited Auger electron spectroscopy (AES). Much of the work that relates directly to the fabrication of quartz resonators is concerned with foreign material or contamination on the quartz surface prior to deposition of the electrode material. For example, Simmons, et al[2] provided an introduction to the Auger effect and presented AES results, obtained with a retarding field analyzer (RFA), on the contamination and cleaning of quartz and magnesium oxide surfaces. Vig, et al[3] investigated various polishing and cleaning techniques for quartz crystals. The effectiveness of their chemical cleaning procedure was evaluated by AES. Later, Hart and his co-workers[4] used AES to identify specific contaminants on resonator surfaces and argon ion sputtering to remove them. Finally, Vig, et al[5,6] examined several cleaning procedures using AES to evaluate them and found that irradiation by ultraviolet light was most effective in removing hydrocarbons from quartz surfaces. The majority of current Auger studies including those mentioned (except for Simmons[2]) make use of the single-pass cylindrical mirror analyzer (CMA). This analyzer has an instrumental resolution of 0.6% which means that at 1000 eV electron energy the absolute resolution is 6eV.

In this paper results will be presented on the characterization of metal-oxide systems by Auger electron spectroscopy (AES) and x-ray photoelectron spectroscopy (XPS) using a double-pass cylindrical mirror analyzer with retarding grids.[7] With this analyzer the incident Auger electrons (or photoelectrons) are decelerated in the retarding field of spherically-shaped grids in such a manner that a constant pass energy through the CMA is obtained. Palmberg[7] presents data showing that the absolute resolution, as indicated by the FWHM of the elastic peak, is a function of the pass energy and the size apertures used in the analyzer. For the conditions we have used, i.e., pass energies of the order of 50eV and small apertures, the absolute resolution is about 0.7eV for all incident electron energies.

Conventional Auger techniques present derivative spectra (dN/dE vs E) rather than energy distribution data (N(E) vs E). In our work we have pulsed the primary beam at 12KHz and tuned our PAR Lock-In Amplifier (LIA) to the same frequency. The output of the LIA, which is then N(E) directly, is fed into a Nicolet Model 1072 Signal Averager which has a digital (BCD) output and an analog output for plotting on an X-Y recorder. The advantages of such a high resolution Auger technique are that intensities and shapes of Auger peaks can be examined analytically, closely spaced peaks are resolved, and chemical shift information is readily obtained.

In a recent paper, Wagner[8] tabulated Auger and X-ray photoelectron chemical shifts observed in photoelectron spectra for a number of metal-metal oxide pairs. Table I gives his values for chemical shifts in binding energy and chemical shifts in Auger energy for selected elements and their oxides. Wagner's results indicate that in all cases the Auger shifts are considerably larger than the photoelectron shifts when the transitions involve only core-level electrons. The large

Auger shifts have been investigated theoretically by Shirley and co-workers[9] who relate them directly to the much larger extra-atomic electron relaxation in the doubly-charged final state of the Auger process as compared to the singly-charged final state of the photoelectron process. As a practical consequence of these results it is now feasible to examine by high resolution Auger techniques interface reactions such as might occur at the interface between a reactive metal electrode and a quartz resonator. Other systems that might be studied in detail are metal-metal oxide systems, such as Aℓ-$Aℓ_2O_3$ and reactions at the interface between a metal electrode and a grown silicon dioxide film. In the later case, for an aluminum electrode, bulk thermodynamic free energy considerations predict that the aluminum will reduce the SiO_2 forming an $Aℓ_2O_3$ phase at the Aℓ-SiO_2 interface.

Experimental Results

Specimens used in this initial investigation were obtained from (111) n-type silicon wafers which were thermally oxidized to a thickness of 1000Å, then coated with a 400Å thick aluminum film. After cleaning, the wafers were oxidized in dry oxygen at 1150°C and then given a heat treatment in dry nitrogen at 1150°C for 10 minutes. Prior to the metal deposition the oxidized wafers were dipped in an aqueous HF solution, rinsed in de-ionized water and blown dry in nitrogen. Aluminum was sputtered onto the wafers in a Sloan DC Sputtergun system at an argon pressure of 5-6μm. The advantages of this type system are that the substrate is maintained at a low temperature and that high sputtering rates can be obtained. For the above specimens the substrate temperature was about 70°C and the deposition rate for aluminum was 500Å/min. Subsequent annealing in nitrogen at successively higher temperatures enables a study of the solid phase growth of aluminum oxide at the Aℓ-SiO_2 interface. Some of the above specimens were annealed in dry nitrogen at 470°C for about 20 minutes while others were not annealed.

Figure 1 shows an Auger concentration profile obtained by argon ion sputtering through one annealed specimen at a rate of 50Å per minute. The peak-to-peak amplitudes of the Aℓ(1393eV), O(510eV), and Si(1616eV) peaks were recorded simultaneously with the sputter removal of material. In this mode of display the energy peaks due to Aℓ and $Aℓ_2O_3$ and those due to Si and SiO_2 are not separable. A continuous recording can provide however additional information on the Auger signals within each multiplex channel. The schematic diagram indicates an expected natural oxide on the aluminum film and an intermediate $Aℓ_2O_3$ between the aluminum and the silicon dioxide. At successive points in the profiling, the argon ion sputtering was stopped, the system was pumped to approximately 10^{-9} Torr and high resolution XPS or AES scans were obtained. The first results were for the natural oxide on the aluminum film.

Aℓ-$Aℓ_2O_3$ System

Figure 2 shows a broad XPS scan over a 1000eV range of binding energies taken from the oxidized aluminum surface before the initiation of argon ion sputtering and using MgKα radiation. The oxygen Auger peaks and the O-1s photoelectron peak are due to the oxide, carbon and nitrogen are indicated as contaminants and the Aℓ2s peaks are a combination of photoelectrons from the aluminum in the oxide and the aluminum metal. Auger peaks occur in XPS spectra at an apparent binding energy equal to the difference between the x-ray photon energy and the Auger electron energy. Thus, an oxygen Auger peak occurs at 744eV which is equal to 1254eV - 510eV.

High resolution (E_p = 50eV) photoelectron spectra of the Aℓ~2p photoelectron peak are shown in Figure 3 for the specimen before sputtering (trace A), after 30Å removal (trace B) and for the aluminum (trace C). The total thickness of the oxide film was of the order of 35-40Å. The chemical shift between the Aℓ-2p aluminum peak at 71.7eV and the Aℓ-2p oxide peak at 74.2eV of 2.5eV is in agreement with Wagner's data.[8] Qualitatively, the intensity of the aluminum peak decreases with an increase in oxide thickness while the oxide peak increases with oxide thickness.

Figure 4 shows the broad Auger spectrum, dN(E)/dE vs E, from the oxide surface. The presence of oxygen is indicated by the strong peak at 510eV and Cℓ and C are present as contaminants. The high energy KLL Aℓ peak includes contributions from both the oxide and the metal.

Figure 5 shows a portion of the high resolution KLL spectrum including the strong KL_2L_3 transition, a weaker KL_2L_2 transition, the bulk plasmon peak (E_p) and two surface plasmon peaks (E_{sp}). Characteristic energy losses, ΔE, due to the excitation of bulk plasma oscillations in aluminum are usually about 15eV, as observed, and the energy losses due to surface plasma oscillations are a factor of $1/\sqrt{2}$ or $1/\sqrt{3}$ lower depending upon whether the interface is planar or spherical, respectively.

Figure 6 shows high resolution (E = 100eV) Auger spectra, N(E) vs E, for the KL_2L_3 transitions before sputtering (trace A), after 15Å removal (trace B), after 30Å removal (trace C) and for the aluminum (trace D). The total thickness of the oxide film was of the order of 35-40Å. As mentioned previously these high resolution data were obtained by pulsing the primary electron beam, tuning the Lock-In Amplifier to the pulse rate, and performing signal averaging for the indicated number of scans. The different shifts between the Aℓ-KL_2L_3 peak at 1388eV and the oxide peaks at 1380.7eV and 1380.3eV indicate slight variations in oxide composition. The aluminum curve (trace D) shows weak peaks at 1378.9eV and 1382eV. The 1382eV peak is due to KL_2L_2 Auger transitions. The peak at 1378.9eV is associated with the excitation of surface plasmons by Auger electrons from the KL_2L_3 peak. It's value suggests that the vacuum-metal interface after sputtering is roughened rather than planar. The increasing intensity at the left of each trace results from the bulk plasmon peak. Trace C includes contributions from the KL_2L_2 Auger peak and from the surface plasmon peak although the plasmon peak appears shifted to a lower ΔE value. The reduced ΔE would be plausible since the appropriate factor relating the surface and bulk plasmon energies is $1/\sqrt{1+\varepsilon}$ for a thick oxide on aluminum and perhaps a higher value is in order for the very thin oxide in C.

Aℓ-SiO_2 System

Figure 7 shows preliminary results of sputtering through an annealed specimen in order to obtain information about the formation of an intermediate oxide phase at the Aℓ-SiO_2 interface. The high resolution photoelectron traces A and B are for 200Å and 250Å removed respectively and show only the Aℓ-2p peak at 71.7eV since the positions are well removed from the interface. As the interface is approached the additional peak developing at approximately 74.4eV is attributed to the Aℓ-2p electrons from the Aℓ in $Aℓ_2O_3$ although further studies may indicate the presence of aluminum hydroxide. For trace C, 300Å had been removed and for D, 380Å. A decrease in the Aℓ peak amplitude is also observed in correspondence with the profile data shown in Figure 1.

Further studies of the Aℓ-SiO_2 system using both high resolution XPS and AES techniques are continuing.

Al-Quartz System

Studies of the aluminum electrode-quartz resonator system following the methods used for the $Al-Al_2O_3$ and $Al-SiO_2$ system should have considerable significance for understanding the frequency stability of quartz crystal resonators with aluminum (or other reactive metal) electrodes. It is therefore strongly suggested that such studies be pursued.

Data Analysis

Analysis of the Auger spectra for the $Al-Al_2O_3$ system is presented in detail in this section in order to illustrate the general treatment which can be applied to either Auger or x-ray photoelectron high resolution data.

The data analysis involves consideration of the background, the instrument resolution and the line shape. Usually one would deconvolute the known instrument function and inelastic loss peaks (obtained from the elastic peak spectrum) from the Auger spectra. Such a technique often leaves residual inelastic peaks and requires data of excellent statistical quality to be fully successful. An alternative procedure that is advantageous with data of high resolution is to least-squares fit the convolution of line shape and instrument function to the experimental peaks. This procedure retains all the information contained in the experimental spectrum.

The experimental shape of a single peak is assumed to be a Voigt function, a convolution of a Lorentzian (L) and a Gaussian (G). Fitting this function to the experimental data requires repeated convolutions and a knowledge of the functional form of the experimental line shape. Moreover the computations are quite time-consuming. We have approximated the Voigt function by a linear combination of L and G components in the form

$$f(\Gamma,\zeta,E) = h\left[\zeta\Big/\left[1+\left(\frac{E-E_0}{.5\Gamma}\right)^2\right] + (1-\zeta)\exp\left[-\left(\frac{E-E_0}{b\Gamma}\right)^2\right]\right] \qquad (1)$$

where $b = 1/2\sqrt{\ln 2}$ and h, E_0, and Γ are the height, position and FWHM of the peak; ζ is the L-G mixing coefficient determined from the best fit of $f(\Gamma,\zeta,E)$ to the experimental peak. Wertheim, et al[10] have shown that $f(\Gamma,\zeta,E)$ provides an excellent representation of the Voigt line shape if the entire line is used in determining ζ. Then one can find Γ_G and Γ_L from graphs relating these quantities to Γ and ζ.[10] In practice we use a non-linear least squares fitting program to find not only ζ but h, E_0 and Γ also. Typically, we obtain E_0 and Γ to a precision that is over an order of magnitude better than the instrument resolution.

As seen previously in Figure 6 each Auger spectrum comprises a metal peak, an oxide peak and an inelastic loss background. Two small peaks under the oxide peak are associated with the KL_2L_2 transition and the first surface plasmon from the metal peak. We fit all these peaks, one at a time, with Voigt functions using the non-linear least squares fitting procedure discussed above. We assume the background is linear over the energy range of the spectra, and we find its slope and intercept after subtracting the fitted peak shape from the experimental spectrum. This procedure is then repeated with the new values for peaks and background until there is little change in peak and background values from one iteration to the next. The computer program that we have developed does this fitting automatically and it works quite well for reasonable starting guesses for the peak and background values.

Figures 8-11 show results of the fitting procedures for the four spectra of the $Al-Al_2O_3$ experimental data. The solid lines are the experimental curves and the crosses are the computer generated points. Figure 10 exhibits a slight discrepancy since the KL_2L_2 and surface plasmon peaks were fixed in the position of Figure 11. Subsequent refinement of the data analysis[11] which allows these peak positions to relax to the best fit, shows a much closer agreement with the experimental curves.

The metal and oxide peak positions and widths and the widths of the Lorentzian (lifetime) and Gaussian components are listed in Table II. One striking effect to be noted is the significant broadening of the oxide peak vs its metal peak. This recently discovered chemical effect has also been seen in the XPS spectra of several polar compounds.[12,13] The conclusion that this is mainly a non-lifetime effect seems to be born out in our analysis by the greater increase of the Gaussian component over the Lorentzian component in going from the metal to the oxide peak. Citrin et al[13] postulate that this change in linewidth is due mainly to phonon broadening. The effect must be localized however since the width of the metal peak remains relatively constant even with an oxide overlayer. The widths of the Gaussian and Lorentzian components vary among the metal peaks. This variation may be due in part to inexact knowledge of the background slope. To determine the background more precisely we would need to obtain more of the spectrum on the high energy side of the metal peak.

Integrated intensities for each metal and oxide peak are obtained after removal of the background and the neighboring peaks by first integrating the experimental curve over the finite energy range chosen in the fitting program. Usually this energy range is about 8eV centered on the peak position. The area on the tail region of the peak is taken from the fitted curve. The total area or integrated intensity for the metal peaks is normalized with respect to the metal peak from pure aluminum. The normalization of oxide peak areas is obtained, less accurately, by scaling the oxide peak areas according to the oxide thicknesses. In Figure 12 the normalized integrated intensities for the Auger metal and oxide peaks are plotted as a function of t/λ where λ is the attenuation length ($\sim$30Å). Also shown for comparison are the normalized integrated intensities for the x-ray photoelectron metal and oxide peaks obtained from the experimental curves of Figure 3. The solid lines are derived theoretically, following Shelton,[14] by considering the geometry of the sample and the CMA (the angle between the CMA axis and the sample normal is 30°) and the aperture angle and width of the CMA (42.3° and 6° respectively). Two emission functions are used, a cosine distribution and an isotropic distribution. The cosine distribution is used for the metal peaks since it is the expected distribution if the substrate is uniform and isotropically absorbing. The isotropic distribution is used for the oxide since it is a first approximation to emission from single atoms.

Table III gives a comparison of the attenuation lengths for Al_2O_3 obtained in our work with other values obtained experimentally or theoretically. Our value for λ is at variance with the free-electron-like attenuation length calculated by Penn[15] and with the experimental value of 16.7 $\pm$ .6Å at 1400eV obtained by Battye et al.[16] Penn treats the valence electrons as an interacting electron gas. He then can write the inelastic collision cross-section and thus the attenuation length in terms of the valence electron's quasiparticle self-energy and lifetime. The contribution from the core electrons to

the attenuation length, which is small, is treated in a tight-binding approximation. Penn's model, which includes exchange and correlation among the valence electrons, yields a value of λ = 18.4Å at 1400eV. We have at present no good explanation for the differences between our data and that of others. However, we have used high resolution data and the values for the attenuation length are consistent for both the oxide and the metal peaks. Lotz[16,17] applied the tight-binding method to both the valence electrons and the core electrons and obtained a value of λ = 28Å for Al_2O_3 in agreement with our value of $\lambda = 30 \pm 3$Å.

Applications

Potential applications of the methods described to the study of interfaces in quartz crystal resonators include the reaction of aluminum electrodes with residual gases in the resonator package, solid phase reactions at the aluminum-quartz interface and chemical characterization of quartz crystal surfaces after cleaning. Other devices in which an aluminum-silicon dioxide or quartz interface occurs are the CCD transversal filters[18] and surface acoustic wave devices.[19] The thin film metallization of oxides in hybrid microcircuits has been discussed in detail by Mattox.[20] An important problem area for study by high resolution electron spectroscopy would be the adhesion between thin metal films and oxide substrates.

Conclusions

The frequency stability of quartz crystal resonators is influenced by physical and chemical properties of interfaces. While conventional Auger techniques can provide elemental identification of contaminants on quartz crystal surfaces we have shown that high resolution Auger and x-ray photoelectron spectroscopic techniques can provide chemical information about interfaces in quartz resonators and other metal-oxide systems. The significant chemical shifts between Auger and photoelectron peaks for the metal and the oxide enable the identification of separate solid state phases, the positions of oxide peaks may be related to compositional changes in the oxide and the peak widths are indicative of electron-phonon scattering and lifetime effects. An electron attenuation length in Al_2O_3 is derived from the integrated intensities of Auger and photoelectron peaks.

Acknowledgements

We gratefully acknowledge the support of the Office of Naval Research, Contract No. N00014-75-C-0909, monitored by Dr. Larry Cooper. We also appreciate the assistance of Dr. Larry Davis of Physical Electronics Industries in devising the instrumental method and the development of the computer program by Dr. M.W.Ribarsky of our staff.

References

1. J. R. Vig and E. Hafner, "Packaging Precision Quartz Crystal Resonators," Technical Report ECOM-4134, U. S. Army Electronics Command, Fort Monmouth, NJ, July 1973. Copies available from NTIS, accession number AD 763215.

2. G. W. Simmons, W. H. Hicklin and R. K. Hart, Proceedings, 24th Annual Symposium on Frequency Control, U. S. Army Electronics Command, Fort Monmouth, NJ, p. 111 (1970). Copies available from Electronics Industries Association, 2001 Eye Street, NW, Washington, DC 20006.

3. J. R. Vig, H. Wasshausen, C. Cook, M. Katz and E. Hafner, Proceedings, 27th Annual Symposium on Frequency Control, U.S. Army Electronics Command, Fort Monmouth, NJ, p. 98 (1973). Copies available from NTIS, accession number AD 771042.

4. R. K. Hart, W. H. Hicklin and L. A. Phillips, Proceedings, 28th Annual Symposium on Frequency Control, U.S. Army Electronics Command, Fort Monmouth, NJ, p. 89 (1974). Copies available from Electronics Industries Association, 2001 Eye Street, NW, Washington, DC 20006.

5. J. R. Vig, C. F. Cook, Jr., K. Schwidtal, J. W. LeBus and E. Hafner, Proceedings, 28th Annual Symposium on Frequency Control, U. S. Army Electronics Command, Fort Monmouth, NJ, p. 96 (1974). Copies available from Electronics Industries Association, 2001 Eye Street, NW, Washington, DC 20006.

6. J. R. Vig, J. W. LeBus and R. L. Filler, Proceedings, 29th Annual Symposium on Frequency Control, U. S. Army Electronics Command, Fort Monmouth, NJ, p. 220, (1975). Copies available from Electronics Industries Association, 2001 Eye Street, NW, Washington, DC 20006.

7. P. W. Palmberg, J. Vac. Sci. Technol., 12, No. 1, 379, Jan/Feb 1975.

8. C. D. Wagner, presented at the Discussions of the Faraday Society, Vancouver, Canada, July 1975.

9. S. P. Kowalczyk, L. Ley, F. R. McFeely, R. A. Pollak, and D. A. Shirley, Phys. Rev. B, 9, 381 (1974).

10. G. K. Wertheim, M. A. Butler, K. W. West and D.N.E. Buchanan, Rev. Sci. Inst. 45, 1369 (1974).

11. E. J. Scheibner and M. W. Ribarsky, to be published.

12. P. H. Citrin, P. M. Eisenberger, W. C. Marra, T. Aberg, J. Ultriainen and E. Kallne, Phys. Rev.B. 10, 1762 (1974).

13. P. H. Citrin, P. Eisenberger and D. R. Hamann, Phys. Rev. Lett. 33,965 (1974).

14. J. C. Shelton, J. Elect. Spect. and Rel. Phenom, 3, 417 (1974).

15. D. R. Penn, Phys. Rev. B, to be published.

16. F. L. Battye, J. G. Jenkin, J. Liesegang and R.C.G. Leckey, Phys. Rev. B 9, 2887 (1974).

17. W. Lotz, Z. Phys. 206, 205 (1967).

18. C. R. Hewes, R. W. Brodersen and D.D. Buss, Proceedings, 29th Annual Symposium on Frequency Control, U.S. Army Electronics Command, Fort Monmouth, NJ, p. 77 (1975). Copies availabe from Electronics Industries Association, 2001 Eye Street, NW, Washington, DC 20006.

19. J. S. Schoenwald, W. R. Shreve and R. C. Rosenfeld, Proceedings, 29th Annual Symposium on Frequency Control, U.S. Army Electronics Command, Fort Monmouth, NJ, p. 150 (1975). Copies available from Electronics Industries Association, 2001 Eye Street, NW, Washington, DC 20006.

20. D. M. Mattox, Thin Solid Films 18, 173 (1973).

TABLE I.

CORE-ELECTRON BINDING ENERGIES AND TRANSITIONS
FOR CHEMICAL SHIFTS BETWEEN ELEMENT AND ITS OXIDE

(MgKα - 1253.6 eV)

Element Or Oxide	Atomic Number Of Element	Binding Energy E_B (PE)	Kinetic Energy E(PE) (MgKα)	Auger Energy E(A)	Chemical Shift E_B(PE)	Chemical Shift -ΔE(A)
		$2p_{3/2}$		$KL_{23}L_{23}$		
Mg	12	49.8	1203.8	1185.8		
Mg(ox)		51.2	1202.4	1179.5	1.4	6.3
Al	13	72.8	1180.8	1393.1		
Al(ox)		75.4	1178.2	1386.4	2.6	6.7
Si	14	99.4	1154.2	1615.7		
Si(ox)		103.3	1150.3	1608.7	3.9	7.0
		$2p_{3/2}$		$LM_{45}M_{45}$		
Cu	29	932.4	321.2	918.8		
Cu_2O		932.2	321.4	916.9	-0.2	1.9

TABLE II

Auger KL_2L_3 ANALYSIS

Thickness	Peak	FWHM	Lifetime	Gaussian*
--	1388.05eV	1.76eV	.858eV	.905eV
-15Å	1388.03	1.81	1.03	.877
-30Å	1388.03	1.83	1.50	.270
-75Å	1388.05	1.84	1.38	.508
--	1380.68	2.99	1.41	1.89
-15Å	1380.41	3.35	1.55	2.27
-30Å	1381.29	4.00	1.78	2.88

*Instrument function removed
(Instrument function FWHM = 0.7eV)

TABLE III

COMPARISON OF ATTENUATION LENGTHS FOR Al_2O_3

PRESENT WORK

28.49 Å Al

31.42 Å Oxide

Ave. = 30.0 ± 3 Å
(±1.3 Å RMS DEV.)

OTHER WORK

EXPT
16.7 Å (Battye et al)

THEORY*
18.4 Å (Penn, 1976)
28 Å (Lotz, 1967)

*Penn is free-electron-like
Lotz is tight-binding

Fig. 1 Auger Composition Profile

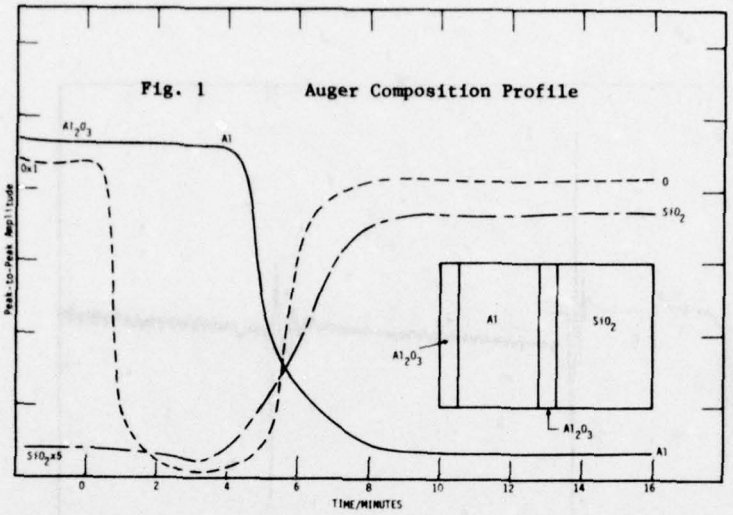

Fig. 2 Broad X-ray Photoelectron Scan of Binding Energies for Oxidized Aluminum

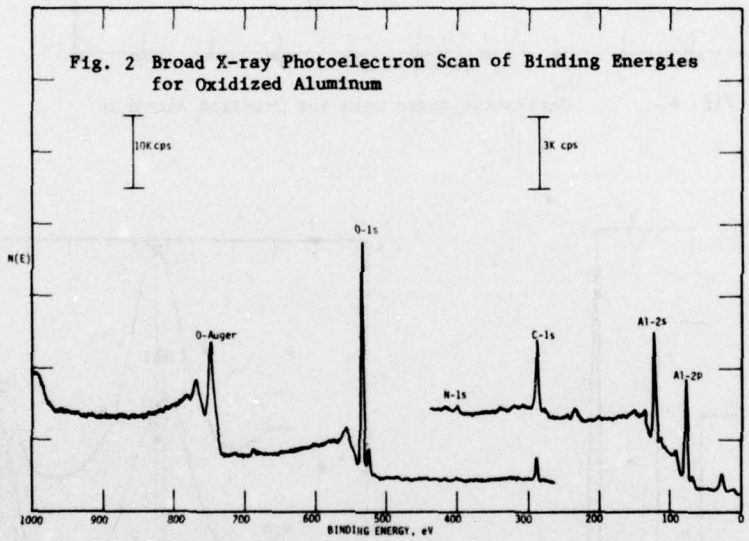

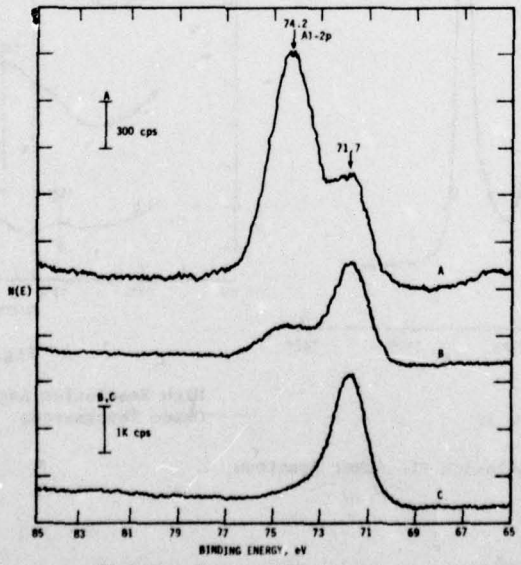

Fig. 3 High Resolution XPS Spectra for Different Oxide Thicknesses

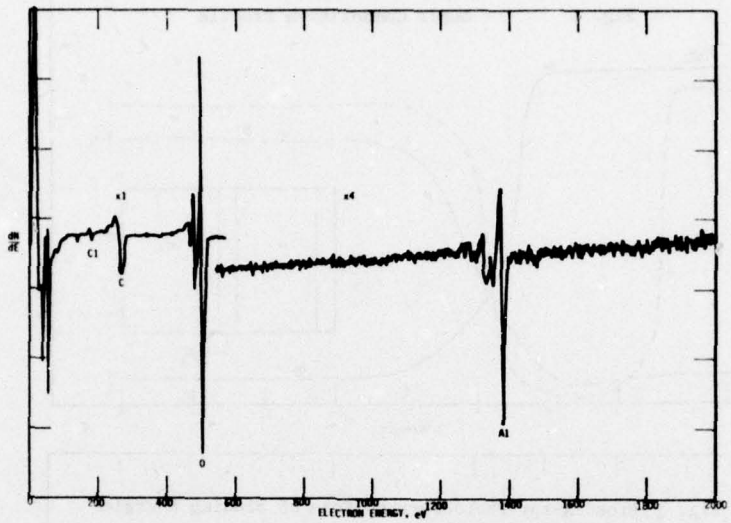

Fig. 4 Derivative Auger Data for Oxidized Aluminum

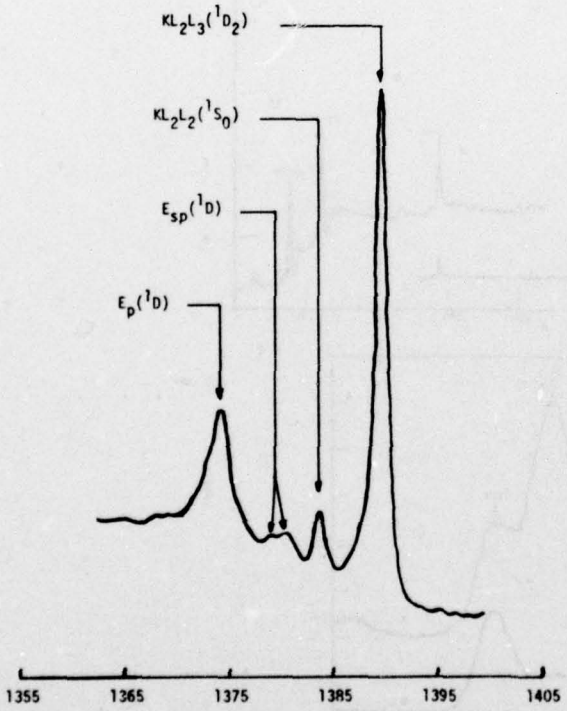

Fig. 5 Portion of High Resolution KLL Auger Spectrum

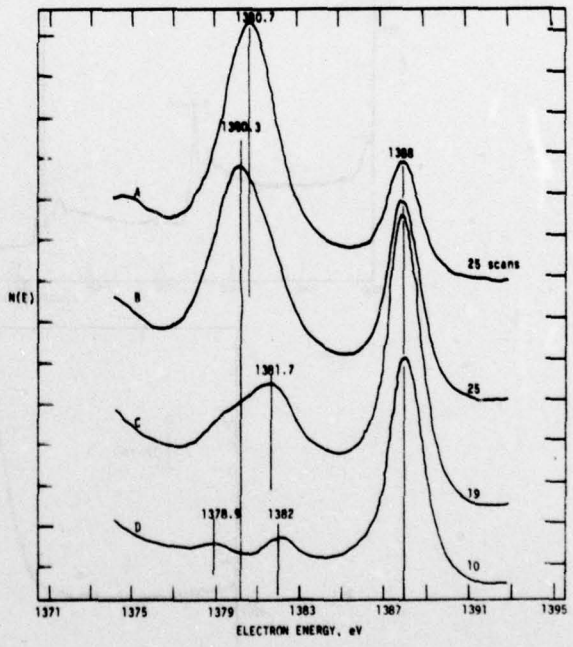

Fig. 6

High Resolution Auger Spectra for Different Oxide Thicknesses

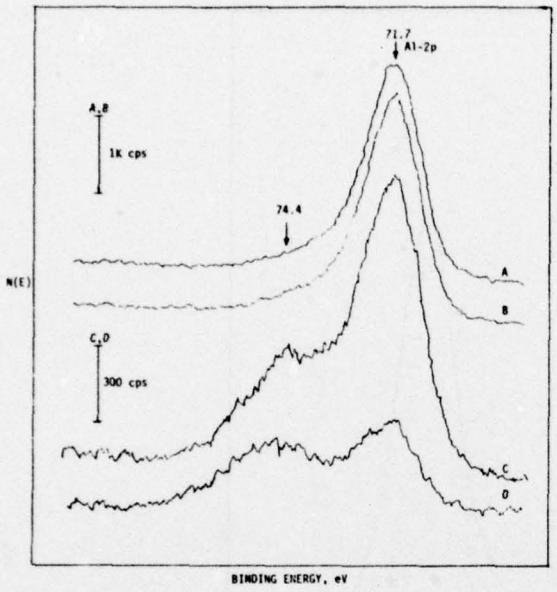

Fig. 7

High Resolution XPS Spectra for Different Thicknesses Approaching the Aluminum - SiO_2 Interface

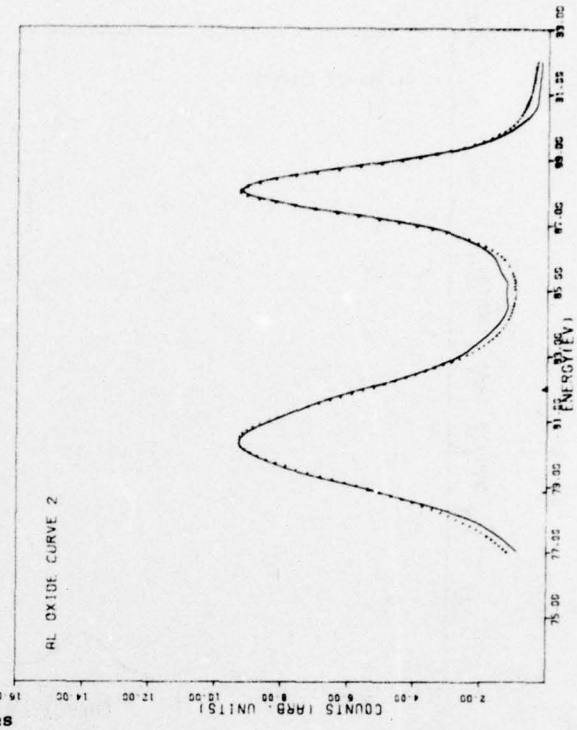

Fig. 9 Computer Results for Oxide Curve 2

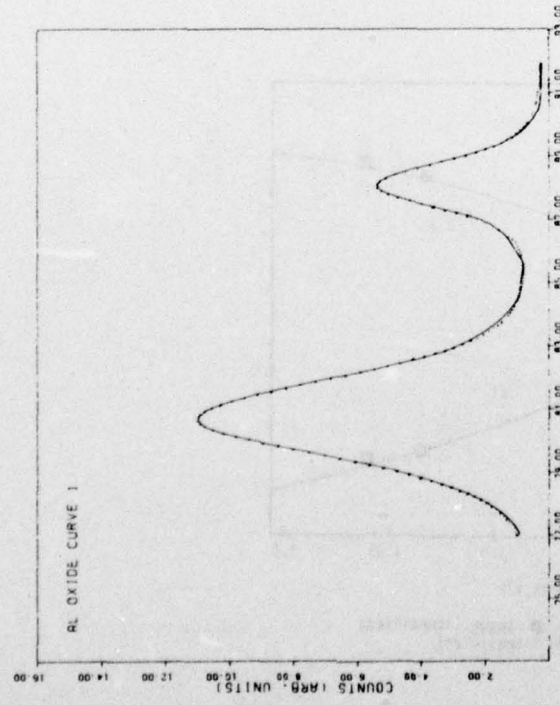

Fig. 8 Computer Results for Oxide Curve 1

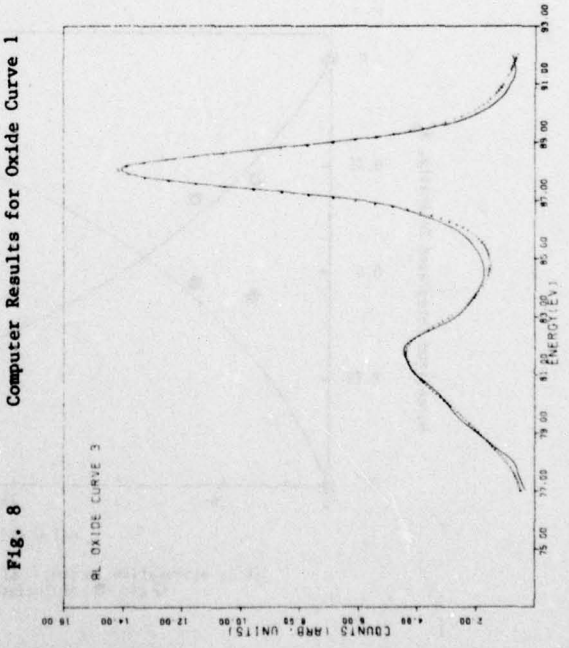

Fig. 10 Computer Results for Oxide Curve 3

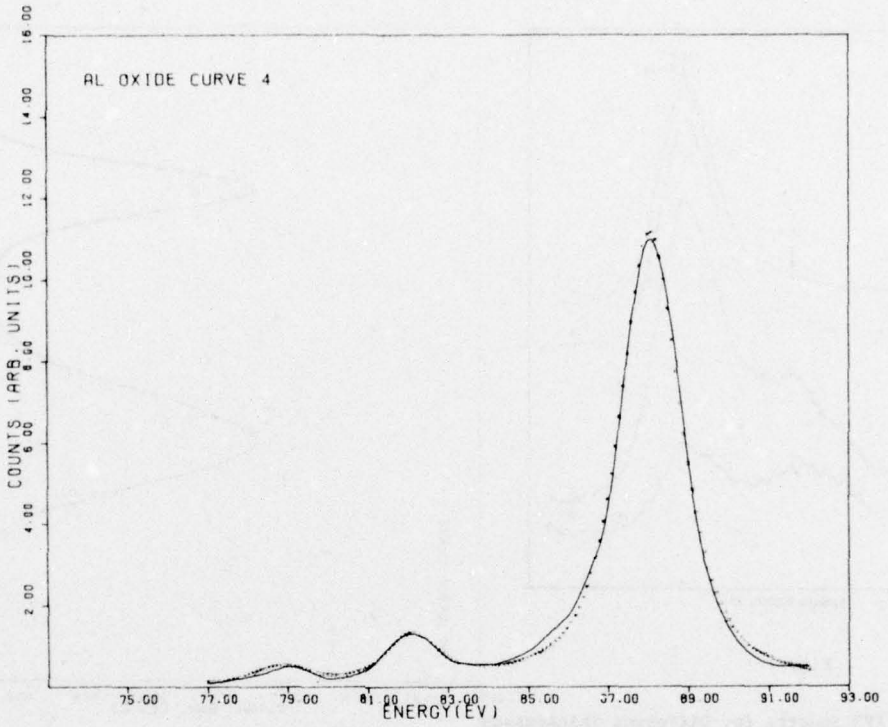

Fig. 11 Computer Results for Oxide Curve 4

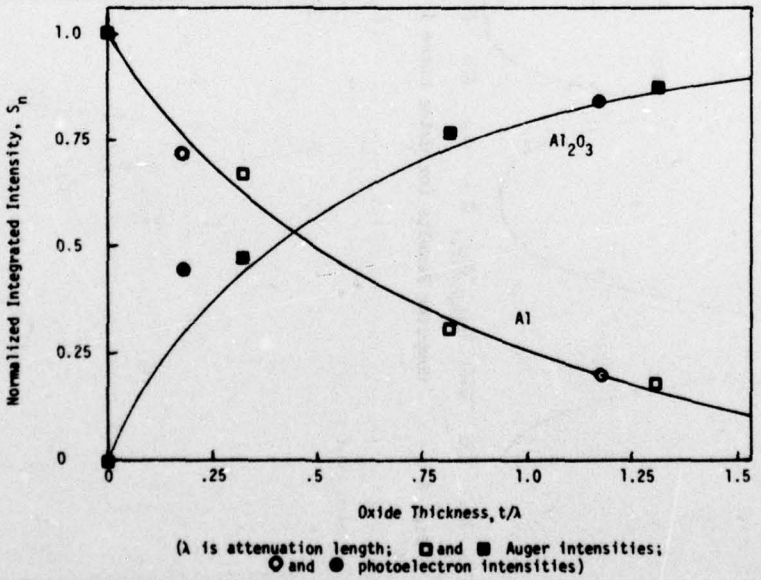

Fig. 12 Attenuation Plots of Normalized Integrated Intensities as a Function of Oxide Thickness

A NOVEL METHOD OF ADJUSTING THE FREQUENCY OF ALUMINUM PLATED QUARTZ CRYSTAL RESONATORS*

Virgil E. Bottom

Tyco Crystal Products, Inc.

Summary

Aluminum is preferred as an electrode material for VHF quartz crystal units because it is inexpensive, adheres well to polished quartz surfaces, has good electrical conductivity and, better than any other metal, matches the acoustic impedance of quartz. Another important advantage of aluminum is that the metal film is protected by the oxide layer which forms on its surface. However the development of the oxide layer results in frequency changes called "aging". Units may be heat treated to pre-age the aluminum electrodes but the frequencies must subsequently be adjusted in some manner and this usually initiates a new cycle of aging. The present paper describes a method of adjusting the frequencies of aluminum plated quartz resonators in which the thickness of the aluminum oxide is used to make the frequency adjustment. Units fabricated in this way show less aging than do units fabricated by conventional methods.

Key words (for information retrieval). Anodic Oxidation, Quartz Crystal Unit, Aging.

The Oxidation of Aluminum

When a freshly prepared aluminum surface is first exposed to air an oxide film begins to form on the surface. Within an hour, under typical room conditions, the thickness of the oxide grows to about 10 Å (1.0 nm). The thickness continues to increase; reaching about 20 Å in a day and about 45 Å in a month. Very little growth occurs after the film reaches a thickness of about 50 Å[1].

The rate of oxidation is only slightly dependent upon the temperature below about 300°C. Above 300°C the rate of growth increases with the temperature and at 450°C the rate is about twice the room temperature rate. The rate of growth at any temperature is increased by an increase in the humidity. Fairly rapid oxidation can be produced at a temperature of 350°C by introducting steam into the oxidation chamber[1].

The growth of the oxide on the aluminum electrodes of a quartz resonator causes mass loading with an accompanying frequency decrease. We may calculate the expected frequency change in the following way. Consider, for example, a 20 MHz AT-cut quartz blank operated on its fundamental frequency mode. Using the relationship frequency x thickness = constant, it may readily be shown that a change of 100 Å in the thickness of the blank (50 Å from each side) causes a frequency change of 2,368 kHz. The mass per unit area of a layer of quartz having a thickness of 50 Å is 1.32 $\mu g/cm^2$. For very small frequency changes we may consider the frequency changes to be linearly proportional to the mass changes. It is permissible to do this since the mass is added at a point of zero stress and therefore the elastic effects are not important.

*Patent Pending

Therefore the addition of 1.32 $\mu g/cm^2$ to both surfaces of the 20 MHz plate causes a decrease of about 2.4 kHz in the frequency.

In forming the oxide of aluminum, 1.32 $\mu g/cm^2$ of oxygen combine chemically with 1.48 $\mu g/cm^2$ of aluminum to form 2.80 $\mu g/cm^2$ of Al_2O_3. Taking the density of aluminum oxide to be 3.20 g/cm^3 the thickness of the resulting oxide layer is about 88 Å. A film of aluminum having a mass of 1.48 $\mu g/cm^2$ has a thickness of about 55 Å. Hence we may say that the conversion of 55 Å of aluminum into 88 Å of Al_2O_3 (on both electrodes) results in a frequency decrease of about 2.4 kHz on a 20 MHz plate. The thickness of the oxide is about 1.6 times the thickness of the aluminum used in its production.

Since the growth of the oxide causes the frequency to decrease about 27 Hz/Å, the growth of the natural oxide layer which reaches a maximum thickness of about 50 Å should cause a decrease of about 1.3 kHz or about 65 ppm. Frequency changes of this magnitude are commonly observed.

During the period of growth of the oxide layer the aluminum is separated from the atmospheric oxygen by the oxide layer already formed. For growth to continue either oxygen atoms must penetrate the oxide to reach the metal beneath or aluminum atoms must diffuse through the oxide to reach the oxygen outside. A number of studies have shown [3,5] that it is the aluminum ions which diffuse through the oxide. Mott [2,3] has proposed two theories to explain why the oxide ceases to grow when it reaches a thickness of about 50 Å. In his first theory (1940) he postulated that the growth ceases because the electrons required for charge equilibrium can pass through the oxide by "tunnelling" only if the thickness is less than about 50 Å. *In his later theory* (1947) *he suggested* that the work function might be small enough to permit thermionic emission from the aluminum to the oxide and that the thickness is limited by temperature. Further experimental work is required to determine which theory provides the best explanation.

Anodic Oxidation

It is well known that the thickness of the oxide layer on an aluminum surface can be increased by anodic oxidation[4]. The aluminum to be anodized is made the anode in an electolytic cell containing a suitable electrolyte. If the electrolyte provides oxygen bearing cations and is one which does not react chemically with the oxide, an oxide layer is formed, the thickness of which is directly proportional to the applied voltage. The oxide film thus formed is anhydrous, non-porous and of uniform thickness.

Many investigations have been made of the relationship between the thickness of the oxide and the anodizing voltage. A review of these studies has been given by Young[5]. The results are in rather poor agreement as may be seen from Table I. The disagreement may be due to uncertainties concerning:

a. The density of the oxide which is known to vary with thickness.
b. The solubility of the oxide in the electrolyte,
c. The roughness of the surface of the substrate.
d. Filament material incorporated in the oxide.
e. Cleanliness of the substrate.

TABLE I

(6)	Walkenhorst (1947)	13.7 Angstroms/volt
(7)	Deryagin and Friedland (1948)	11.7
(8)	Hass (1949)	13.0
(9)	Bahn and Böttger (1953)	12 to 18.5
(10)	Hennig (1956)	16.5
(11)	Van Geel and Schelen (1957)	12.7

The frequency change of a high frequency quartz resonator affords an especially sensitive method for determining the thickness of the oxide layer. The method is, however, subject to the same uncertainties as those listed above; particularly the density of the oxide. Our results indicate that the thickness of the oxide increases 12.3 ± 0.1 Å/V if the density of the oxide is taken to be 3.20 $\mu g/cm^3$ (see references 1,5).

Figure 1 shows the changes of frequency vs. the voltages used in adjusting the frequencies of several 20 MHz AT-cut plates. The slope of each curve is 350 Hz/V. When the curves are extrapolated to $\Delta f = 0$, a threshold voltage ranging from a few tenths of a volt to 2 or 3 volts is obtained. This threshold voltage is a measure of the thickness of the natural oxide layer which depends upon the history of the surface. A freshly prepared aluminum surface has a threshold voltage of less than one volt corresponding to an oxide thickness of less than about 10 Å. A threshold voltage of 1 to 3 volts is found with films which have been aged for several days or which have been heat treated. Naturally the threshold voltage for a film which has been anodized is equal to the voltage used in the anodization. It is convenient to speak of the thickness of the oxide layer in terms of the threshold voltage or the voltage used to prepare it. A one-volt layer has a thickness of about 12 Å and thus a thirty-volt film has a thickness of about 360 Å. The fully developed natural oxide film is therefore a four-volt film.

At any given voltage the rate of growth of the oxide and therefore the rate of decrease of the resonator frequency decreases with time. Figure 2 shows the frequency change with time for several different anodizing voltages. In each case about 75% of the total change occurs in the first two or three seconds with about 90% occurring in the first ten seconds. The upper limit of the anodizing voltage is determined by the practical limitations of the amount of aluminum available and by the time required. Thirty volts is about the limit for a typical production process although higher voltages can be used under special conditions. The frequency of a 20 MHz AT-cut plate can be reduced over 10 kHz by the use of an anodizing voltage of 30 volts.

After base plating the frequency of a 20 MHz plate should be ideally between 2 and 10 kHz above the nominal frequency. Given blanks in this frequency range after base plating and reasonable setting tolerances, the units can be set on frequency in one, or at most two, anodizing steps. If the frequency of the unit after base plating is below the range just specified, the frequency may be increased by immersing the plated blank in a dilute alkali solution. In this connection it is remarkable that the thickness of the oxide is not reduced in the process. Starting with an oxide layer of given thickness, say 100 Å, the frequency of the unit may be increased by an amount corresponding to the removal of more than 100 Å of oxide, yet the thickness of the oxide remains 100 Å.

Anodic oxidation provides a nearly ideal method for adjusting the frequency of an aluminum plated quartz resonator since the thickness of the oxide layer can be made much thicker than the natural thickness of 50 Å while it is being used to adjust the frequency. The term ANOX* has been defined as a noun to replace the term "anodic oxidation" as it is applied to quartz crystal units. It may also be used as a verb to mean "to adjust the frequency of a piezoid by the process of anodic oxidation".

Procedure

The thickness of the aluminum film used to provide the electrodes of a VHF quartz resonator depends upon a number of factors including the harmonic overtone and energy trapping considerations. Typically films having thickness between 500 and 1500 Å are used. The film must be thick enough to provide the required electrical conductance and to supply enough metal for the frequency adjusting process. It must be remembered that in the ANOX process, aluminum is consumed when the frequency is either increased or decreased. As we have seen, a 30-volt oxide layer has a thickness of about 360 Å and a layer of aluminum 230 Å thick is consumed in its formation. The remaining aluminum must be thick enough to provide the necessary electrical conductance.

As previously stated the frequency of a 20 MHz plate should be between 2 and 10 kHz above the nominal frequency. It is not necessary for the base plate tolerance to be this close, however. In practice the base plate window may lie between the upper limit of 10 kHz above the nominal frequency and some lower limit determined by the amount of aluminum deposited. For example, if an electrode thickness of 1250 Å is used, corresponding to a plate-back of 60 kHz (or 0.15 f^2), the frequency of the resonator can safely be raised 20 kHz by removing some of the aluminum chemically. Thus the plate-back window is from -20 + 10 kHz from the nominal frequency. If thicker electrodes can be tolerated, or if lower film conductance is acceptable, an even wider window may be provided.

A solution of 10 g of NaOH per liter of deionized water is a suitable medium for increasing the frequency of the base-plated unit to the frequency required for anodic oxidation. In addition to making the base-plate window wider, chemically raising the frequency insures a clean surface from which to start the anodization. The rate of frequency change is very strongly temperature dependent so that it is desirable to control the temperature of the solution a few degrees above room temperature.

*ANOX is a trade mark of Tyco Crystal Products, Inc.

The change of frequency is a linear function of time (except for the first few seconds) and the operator quickly learns to determine the time required to produce a desired frequency change.

If the frequency of the resonator is n Hz above the required frequency, the anodizing voltage is given by

$$V = V_o + (n/A) \qquad (1)$$

where A is a constant called the "ANOX constant". A depends upon the frequency and the harmonic order of the resonator and to a slight degree on the electrode size. V_o is the threshold voltage. The value of the ANOX constant can be determined from the following formula which can readily be derived from the relationship between the frequency change and the oxide thickness assuming that the thickness changes at the rate of 12.3 Å/V and the oxide density is 3.2 g/cm^3. It is thus found that *

$$A = 0.87\ h\ f_1^2 \qquad (2)$$

where h is the harmonic order 1, 3, 5, 7, ... and f_1 is the fundamental frequency expressed in megahertz. A is given in hertz per volt.

In order to insure that the oxide layer developed on the electrodes is substantially thicker than the natural 4-volt layer, an anodizing voltage of at least 5 volts should be used. This means that the frequency of the unit should be reduced by at least 5A where A is given by Eq. 2. Thus the frequency of a 60 MHz, 3rd overtone unit must be reduced by at least 5.2 kHz.

Figure 3 shows the apparatus required. A Heathkit Regulated Power Supply (Model 1P-28) is a convenient power source. Several suitable electrolytes are known. Among those listed in the literature are: ammonium citrate, ammonium pentaborate, ammonium phosphate, boric acid, oxalic acid and tartaric acid. Each of these has been used with satisfactory results. The pH of the electrolyte must be adjusted with an appropriate acid or base so that the electrolyte does not react chemically with the oxide. Pure chemicals must be used and care must be taken to avoid contamination of the ANOX solution. The cathode is a sheet of pure aluminum.

The process of adjusting the frequency by anodic oxidation is simple and under good conditions an experienced operator can finish units to frequency at the rate of one per minute. The equipment required is also relatively simple and inexpensive. In addition to the power supply, a suitable oscillator and counter and an ultrasonic washer are needed.

It is necessary that the quartz surface on which the aluminum electrodes are deposited in base-plating be very clean. Otherwise the aluminum films will loosen during chemical etching or anodic oxidation. The process thus provides an excellent check for the adherence of the aluminum. "Sleeping sickness" characterized by abnormal behavior at low drive levels is virtually non-existent in units which are made by the ANOX process.

*Here and elsewhere in this paper it is understood that the blanks are polished.

Naturally care must be exercised to insure that the unit is thoroughly rinsed after each operation and that the solutions and the rinse waters are not contaminated. Ultrasonic rinsing in at least three stages of deionized water followed by one rinse in electronic grade methanol is recommended. Drying should be done with a jet of nitrogen since compressed air is seldom free of oil.

Advantages of the ANOX Process

The ANOX process offers a number of advantages over conventional methods of adjusting the frequency of a VHF crystal unit. The more important of these advantages are the following.

1. The thickness of the oxide is proportional to the voltage so that the frequency of a unit can be changed by a predictable amount by the use of a predetermined voltage. This feature makes the process adaptable to microprocessing techniques.
2. No material other than aluminum and its oxide is added to the quartz thereby eliminating all problems of diffusion of one metal into another, incompatibility of different metals, aherence of a second metal to the aluminum oxide and discontinuity of acoustic impedance.
3. The geometry and symmetry of the resonator are not disturbed since both electrodes receive the same treatment. In overplating, metal is commonly deposited on one side only and not always uniformly over the electrode. Any disturbance of the symmetry of the plating is conducive to the excitation of the inharmonic overtone modes, commonly called "spurs".
4. Blanks are cleaned as a part of the frequency adjustment process and may be cleaned ultrasonically again before encapsulation if required.
5. The equipment required is relatively simple and inexpensive and operator training is minimal. Simple graphs provide the operators with the necessary frequency/voltage data.
6. The problem of abnormal behavior at low drive level or "sleeping sickness" scarcely exists in crystal units made by the ANOX process because no loose particles of plating or particles of dust or other materials remain on the surface of the quartz.

The over-all yield of units meeting specifications is generally much higher from an ANOX line than from a line making comparable units by over-plating to frequency.

Aging

The most important advantage of the ANOX process is the freedom from aging due to oxidation of the plating. Figure 4 shows the aging of two groups of 47.050 MHz third overtone AT-cut units. The units of the two groups received identical treatment except that the ANOX process was used with one group and over-plating with silver was used with the other. The units are enclosed in standard HC-18 holders and solder sealed in an entirely conventional manner.

After 308 days at 120°C the average frequency change of the units made by the ANOX process is -10 ppm with a standard deviation of ± 6 ppm. By comparison the average change of frequency of the units made by over-plating with silver is -72 ppm with a

standard deviation of ± 30 ppm. None of the units received any kind of pre-aging treatment; the first measurements having been made within an hour after the units were set on frequency. The graphs indicate that the aging of the units made by the ANOX process is substantially complete whereas the frequencies of the other units are continuing to decrease. If the behavior over a period of ten months is extrapolated to a period of ten years the units made by the ANOX process will have changed about 12 ppm while the units made by over-plating will have changed about 100 ppm. Since the units in both groups received identical treatment in all respects except for the method of adjusting the frequency, it appears that the difference between their aging rates must be ascribed to changes occurring in the electrodes and not to contamination, stress relaxation or any effect associated with the quartz. Some residual aging, common to both groups, may be due to the method of encapsulation and more work is required to determine whether or not this and stress relaxation are significant factors. There can be no doubt that the oxidation of the plating was the most important factor in the aging of aluminum plated units and that this can be greatly reduced if not eliminated by anodic oxidation.

Conclusions

The frequencies of aluminum plated quartz resonators may be adjusted by the use of anodic oxidation. The process is simple and easily controlled and the equipment is inexpensive. The yield of a production line using the ANOX process is high compared with that of a line using conventional methods.

The aging of aluminum plated VHF quartz resonators is largely due to the growth of the oxide layer on the electrodes. The oxide layer created by anodic oxidation is made thicker than the terminal thickness of the natural oxide layer so that no further oxidation occurs and aging is hereby minimized.

The ANOX process is especially useful in adjusting the frequencies or VHF dual and monolithic coupled resonators where the required frequency adjustments can be made by anodizing the electrodes independently. It may also be used to adjust the band width of coupled resonators by selectively mass loading a separate plated area.

REFERENCES

1. Georg Hass, J. Opt. Soc. Am. 39, 532-540 (1949)
2. N. F. Mott, Trans. Faraday Soc. 35, 1175-1177 (1939) and 36, 472-482 (1940)
3. N. F. Mott, Trans. Faraday Soc. 43, 429-434 (1947)
4. Conrad J. Dell'Oca, Thin Solid Films 26, 371-380 (1975)
5. L. Young "Anodic Oxide Films" Academic Press (1961) Chapter 17.
6. W.Walkenhorst, Naturwiss. 34, 373 (1947)
7. B. V. Deryagin and R. M. Friedland, Z. tech Phys. U.S.S.R. 18, 1443 (1948)
8. Ref. 1 loc. cit. page 535
9. R. Bahn und O. Böttger, Z. fur Physik 135, 376-379 (1953)
10. M. Hennig, Z. fur Physik 141, 296-310 (1956)
11. W. Ch. van Geel and B. J. J. Schelen, Philips Res. Rep. 12, 240-245 (1957)

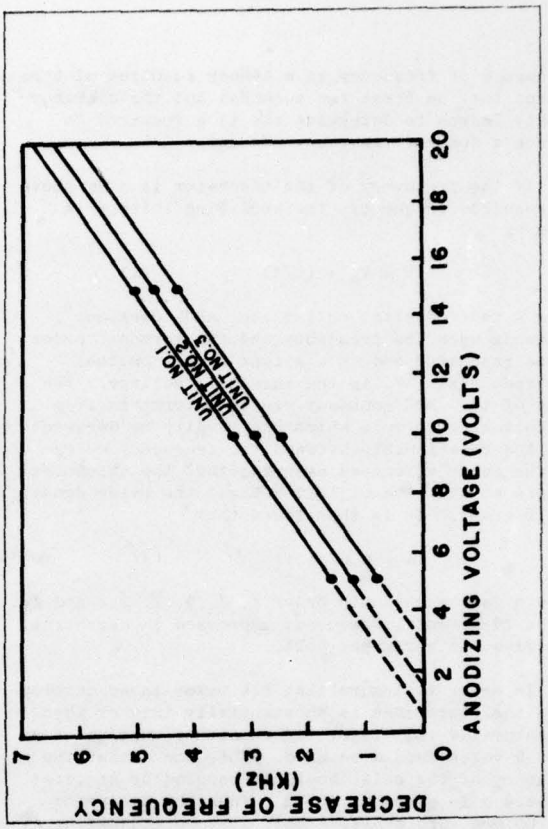

Figure 1 : Anodizing voltage vs. frequency change (20 Mhz AT-cut)

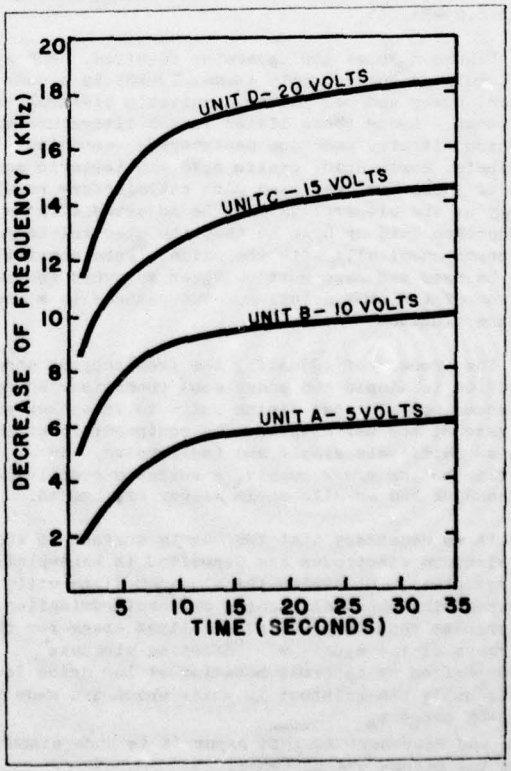

Figure 2 :Decrease of frequency vs. time for various anodizing voltages(56.9 Mhz AT-cut)

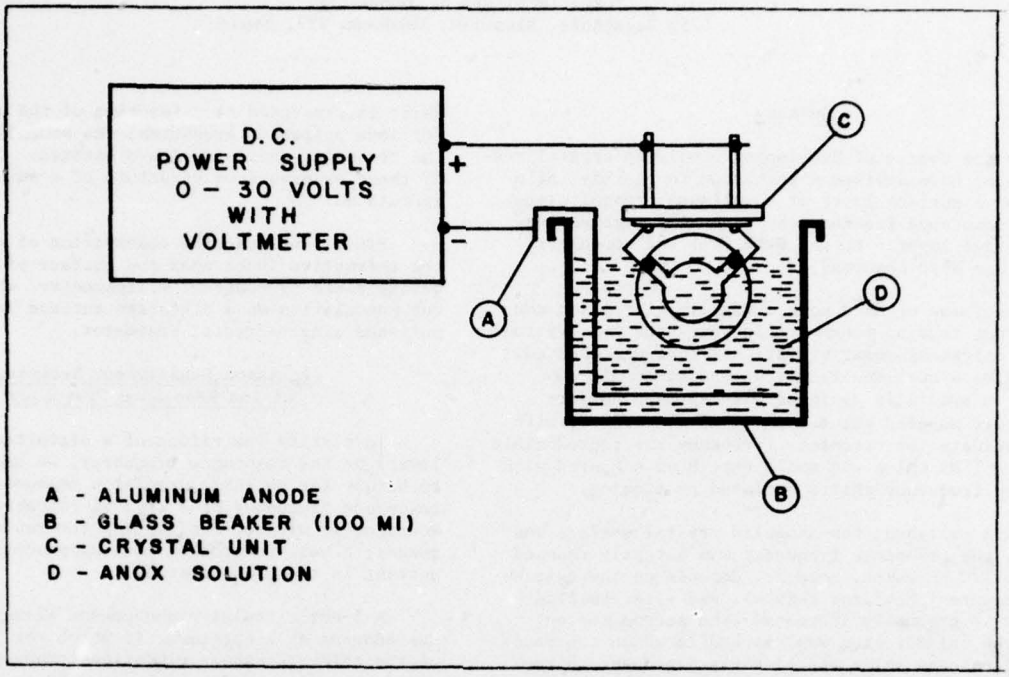

Figure 3 : Apparatus for adjusting resonator frequency by anodic oxidation

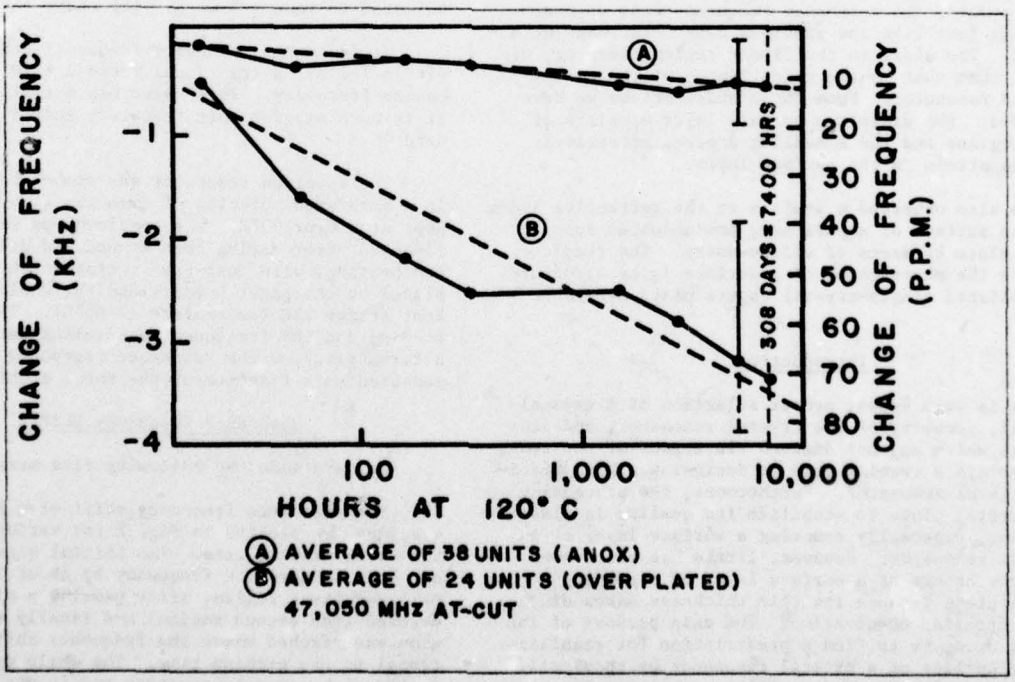

Figure 4 : Change of frequency vs. hours at 120° C

SURFACE LAYER OF A POLISHED CRYSTAL PLATE

Hitohiro Fukuyo and Nobunori Oura
Tokyo Institute of Technology
4259 Nagatsuta, Midoriku, Yokohama 227, Japan

Summary

In the course of developing precision crystal resonators we have devised a technique to clarify influences of a surface layer of a polished crystal plate on its resonance frequency by gradually etching away the surface layer. At the same time the annealing effect was also observed.

Specimens we used were 5-MHz circular plano-convex AT-cut crystal resonators in which the 5th overtone of the thickness-shear vibrational mode was excited. Every time a specimen resonator was etched it was placed on specially designed air-gap type holders which were mounted between parallel electrodes; with these holders the resonance frequency was reproducible within ± 1 Hz which was small enough as compared with observed frequency shifts produced by etching.

As a polished, non-annealed crystal surface was etched, the resonance frequency was abruptly reduced by about 20 Hz which, however, depends on the polishing pressure (the first region), and after passing a minimum it gradually increased (the second region) until the third region was reached in which the resonance frequency shift was linearly dependent on the etching time. An abrupt frequency decrease in the first region is a new finding. When a polished resonator of the same geometry was annealed at 520°C before having been etched, on the other hand, the resonance frequency was reduced by almost the same amount as a frequency shift observed in the first region; as it was etched, the resonance frequency went up monotonically just like the previous case after passing a minimum. The slope in the linear region, however, was sharper than that in the third region of the non-annealed resonator. From these observations we have concluded: the distorted surface layer consists of three regions and the annealing process effectively releases strain in the surface layer.

We also observed a profile of the refractive index near the surface of a polished, non-annealed fused quartz plate by means of ellipsometry. The result supports the observation of a surface layer structure of a polished single-crystal quartz plate mentioned above.

Introduction

As is well known, proper selection of a crystal material, geometry of the crystal resonator, and its supports which may not disturb vibrations of the resonator plays a crucial role in designing a high precision crystal resonator. Furthermore, the processing of a crystal plate to stabilize its quality is also important, especially removing a surface layer of a polished resonator. However, little has been known about the nature of a surface layer of a polished crystal plate because its thin thickness makes difficult a detailed observation. The main purpose of the current study is to find a prescription for stabilizing the quality of a crystal resonator by chemically etching a distorted surface layer or by annealing it.

We first show a technique for making precision measurement of the resonance frequency and chemical etching processes. The observed resonance frequency shift is presented as a function of the etching time for some polishing pressures; the annealing effect on the frequency shift is also presented. On the basis of these observations structure of a surface layer is speculated.

Finally we describe observation of a profile of the refractive index near the surface of a fused quartz plate by means of ellipsometry, which supports our speculation on a distorted surface layer of a polished single-crystal resonator.

Precision Measurement Technique of the Resonance Frequency

To clarify the effect of a distorted surface layer[1] on the resonance frequency, we had to develop a technique for reliable precision measurement of the resonance frequency of a crystal resonator which allows mounting it without influencing the resonance frequency; a well-controlled etching process is also important in the present study.

A 5-MHz circular plano-convex AT-cut resonator was adopted as a specimen, in which the 5th overtone of the thickness-shear vibrational mode was excited to reduce the effect of holders as much as possible. The planar face of a resonator was supported by three thin paper pillows arranged in a triangle and an air gap 50 μm wide was maintained between the resonator and the lower electrode as shown in Fig. 1; the paper holders served as very nice cushions. The upper electrode was adjusted to make a 3-mm air gap above the resonator.

We found the resonance frequency was reproducible within ± 1 Hz, a fractional ratio 2×10^{-7} to the resonance frequency. This value was satisfactory because it is much smaller than frequency shifts to be measured.

The specimen resonator was etched for a given time in a saturated solution of ammonium fluoride which was kept at 0°C or 25°C. The specimen was carefully cleansed after having been etched and dried by infrared heating; with dust-free surfaces the specimen was placed on the paper holders and the whole thing was kept at the ZTC temperature (~60°C). The chemical etching and the frequency measurement were repeated alternately, and the resonance frequency shift was measured as a function of the total etching time.

Resonance Frequency Shifts

We have made the following five measurements.

(A) The resonance frequency shift of a non-annealed specimen is plotted in Fig. 2 for various values of the total etching time. The initial slight etching abruptly reduced the frequency by about 20 Hz, which we call the first region; after passing a minimum it increased (the second region) and finally the third region was reached where the frequency shift is proportional to the etching time. The whole cycle was repeated with several specimens and it was found that the amount of the first abrupt frequency shift was dependent on the polishing pressure.

(B) When an etched specimen reached the third region

a convex face of the resonator was polished again and measurement was continued. The initial dip was observed again but its depth was almost halved probably because the planar face was kept free from repolishing; the second region following the dip was also small (see Fig. 3).

(C) A polished crystal was initially annealed at 520°C. The resonance frequency was reduced by about 20 Hz before being etched and the first abrupt shift of the resonance frequency was no longer observed as it was etched, as shown in Fig. 4. It follows that the first region was released by annealing.

(D) In the third region the specimen was annealed at 520°C. The resonance frequency was reduced, by annealing, down to almost the original value and then it increased linearly in the etching time with a larger slope as shown in Fig. 5.

(E) An annealed specimen was repolished in its third region, and then the frequency shift was measured as it was etched, the result being plotted in Fig. 6. We obtained a similar result to case A. This fact shows that the third region will be followed by the fourth region in which the resonator is almost free from strain or distortion.

Optical Observation of the Surface Layer

A profile of the refractive index near the surface of a crystal was observed by means of an optical method called ellipsometry. Since a single-crystal quartz is birefringent, a fused quartz was used as a specimen. With this technique,[2] an equivalent refractive index of a surface layer and its equivalent thickness can be measured. The measurement was repeated by repeating the chemical etching. From these quantities for various etching times, we determined a model profile of the refractive index which best fit the observation; the result is shown in Fig. 7.

Discussion

From the observation we have described above, we make the following speculations.

(A) and (B): An abrupt shift down of the resonance frequency denoted as the first region and a relatively rapid frequency rise in the second region are generated by polishing.

(A) and (C): The polishing process raises the resonance frequency as denoted by the first region and it is removed by annealing. The second region is, however, stable against annealing and does not contribute to raising the resonance frequency.

(A) and (D): The third region is also generated by the polishing process and contributes to raising the resonance frequency; this region vanishes after annealing.

(D) and (E): The frequency shift created by the third region is tantamount to a change in the thickness of the crystal plate as large as 70 Å or more than this.

The profile of the refractive index reflects the above-mentioned structure of a distorted surface layer of a polished single-crystal resonator.

The above discussion is summarized as: the surface layer of a polished crystal plate consists of three different layers. The first layer which works to raise the resonance frequency is very thin and it is removed by a slight etching or annealing. The second layer is thicker than this and cannot be removed by annealing. The third layer is very thick and works to raise the resonance frequency; it is removed by annealing.

Conclusion

We have found the effect of a surface layer of a polished crystal plate on its resonance frequency and obtained a prescription for stabilizing the resonance frequency by chemical etching and annealing. We desire to clarify crystallographical structure of a distorted surface layer of a polished crystal plate in a further study.

Acknowledgments

The authors would like to thank Prof.Dr. T. Musha for the interesting discussion on this study. Thanks are also due to Mr. S. Kamihoriuchi, Mr. F. Shishido, Mr. N. Kitajima, Mr. S. Kanazawa and Mr. H. Kohno for their cooperation throughout this work.

References

1. S. Nonaka, "The Fundamental Studies on the Lapped and Polished Layers of Crystal Plate and the Evaporated Metal Electrode," Doctor Thesis at Tokyo Institute of Technology, March 1969.

2. H. Yokota, "Ellipsometry in the Measurement of Surfaces and Films," Junkatsu, Vol.19, No.3, 1974, pp.229-235.

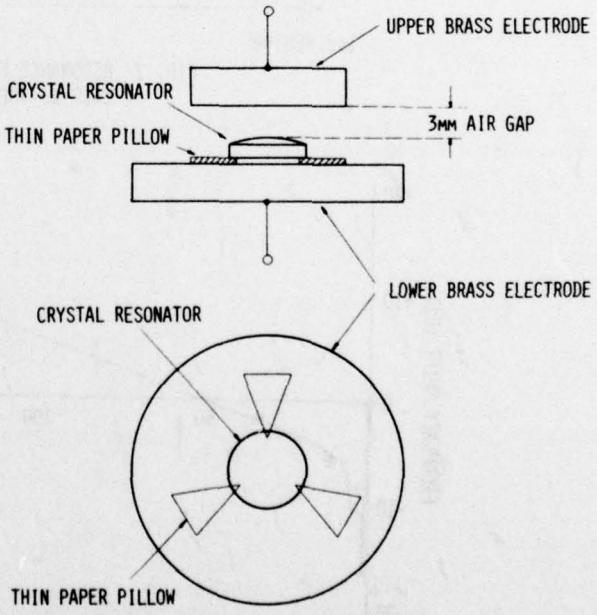

FIG. 1 CRYSTAL RESONATOR MOUNTING

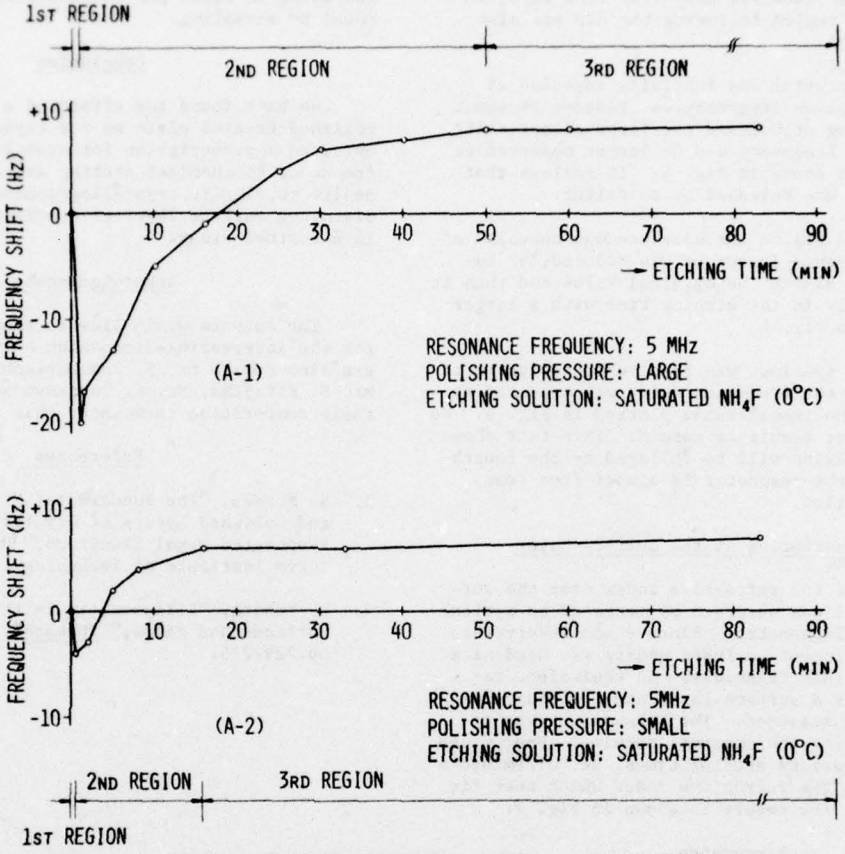

FIG. 2 RESONANCE FREQUENCY SHIFT vs. ETCHING TIME
CASE A: THE RESONATOR WAS NOT ANNEALED

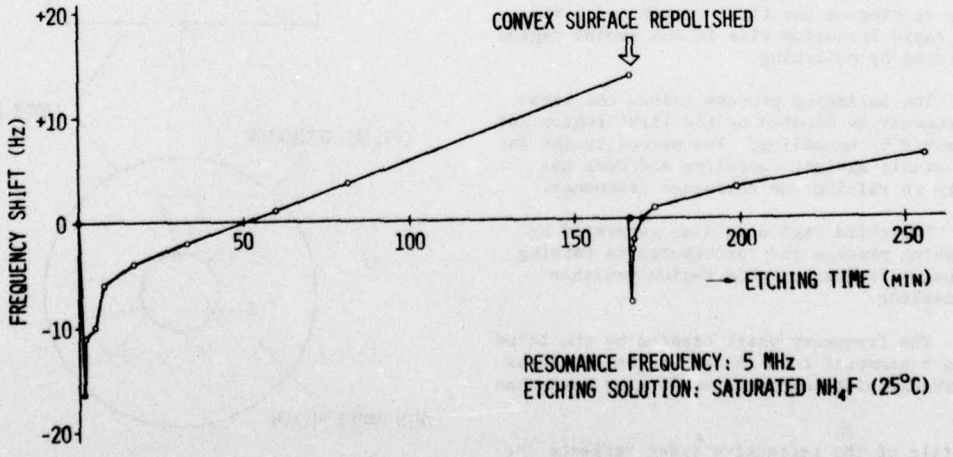

FIG. 3 RESONANCE FREQUENCY SHIFT vs. ETCHING TIME
CASE B: A CONVEX SURFACE WAS REPOLISHED
IN THE 3RD REGION

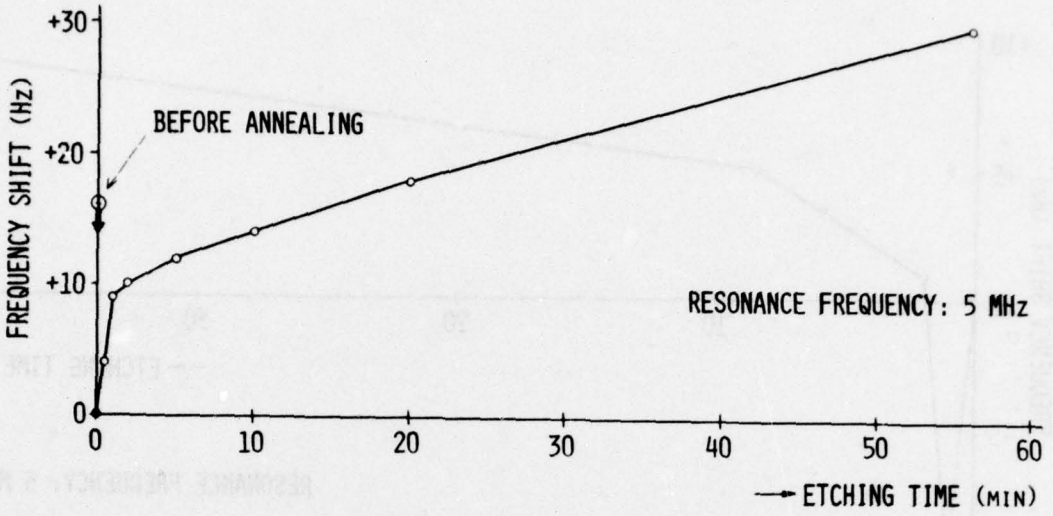

FIG. 4 RESONANCE FREQUENCY SHIFT vs. ETCHING TIME
CASE C: THE RESONATOR WAS ANNEALED AT 520°C
AFTER POLISHED

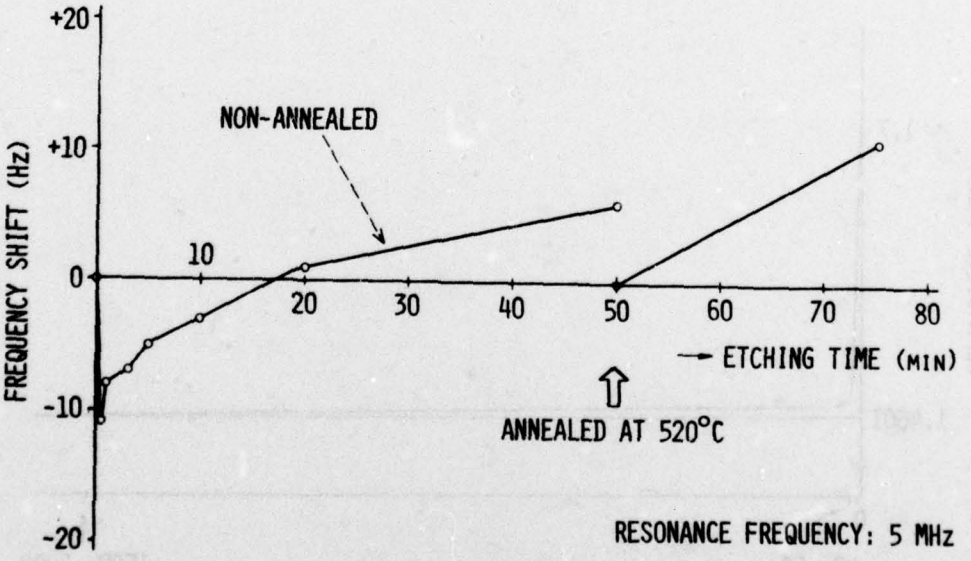

FIG. 5 RESONANCE FREQUENCY SHIFT vs. ETCHING TIME
CASE D: THE RESONATOR WAS ANNEALED
IN THE 3RD REGION

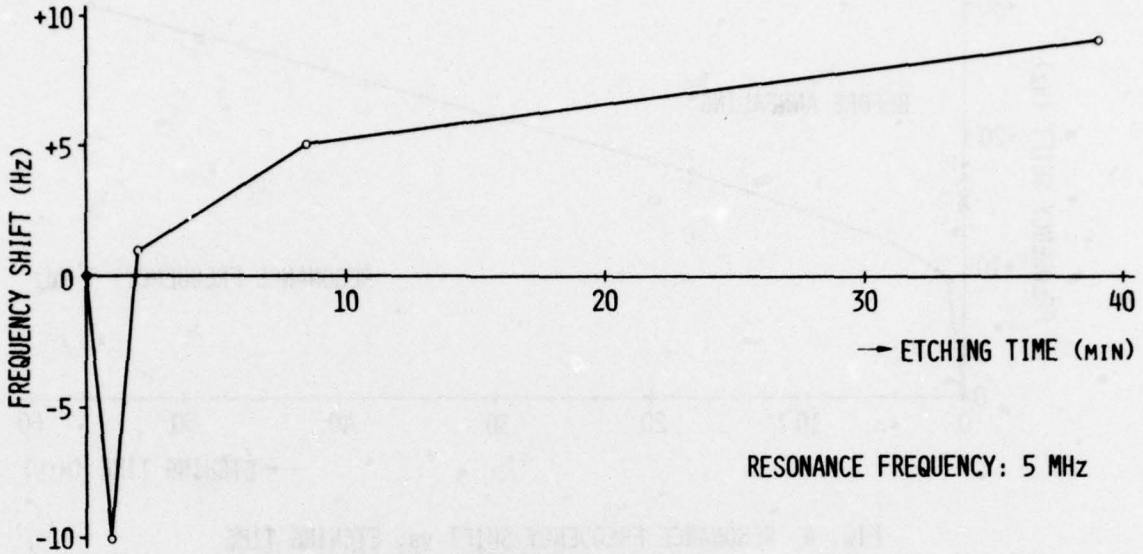

FIG. 6 RESONANCE FREQUENCY SHIFT vs. ETCHING TIME
CASE E: THE RESONATOR WAS REPOLISHED
AFTER ANNEALED

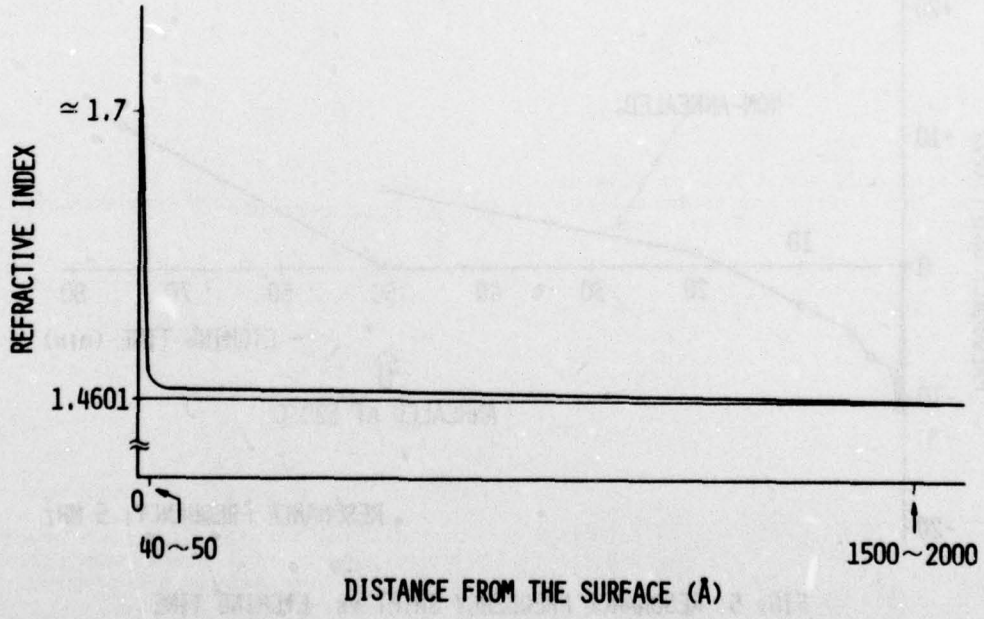

FIG. 7 PROFILE OF THE REFRACTIVE INDEX IN A SURFACE
LAYER OF A POLISHED FUSED QUARTZ PLATE

A METHOD OF ANGLE CORRECTION

Dieter Husgen
Claud C. Calmes, Jr.
Savoy Electronics, Inc.
Ft. Lauderdale, Florida

Summary

Angle correction has become necessary because of the tighter angle requirements needed for today's crystals and the inability of the cutting operation to stay within the required angle of cut. This report shows an easy method of correcting the quartz crystal orientation angle by covering half the crystal blank with an etch resistant material and placing it in an etch solution. The minimum thickness disadvantage of mechanical angle correction can be overcome by using the etch method, but the amount of correction is limited to ±4'.

Introduction

In the manufacture of AT cut crystals, the trend is to tighter temperature coefficients, (TC tolerance). An example is ±5 ppm from -10 to + 70°C specified for land mobile crystals. Another example is ±2.5 ppm from -10 to + 60°C specified for crystals used in base stations. This requires blanks with an angle tolerance of plus or minus half a minute of arc.

The accuracy of the saws under normal manufacturing conditions is still not much better than ±1'. The diamond blade saws at Savoy Electronics generally hold within ±4' providing the saw blade is in good condition. A slurry saw user reported ±2' angular spread for both the sawing and transfering error. Therefore, only about 50% or less of the blanks cut are usable for tight tolerance temperature coefficient crystals.

In order to use the crystal blanks when there is no requirement for those with larger tolerances, the orientation angle has to be changed. The technique of angle correction is to shift the two surfaces of the plane parallel blank by a certain angle, so that the angle between the crystal structure and the surface is correct.

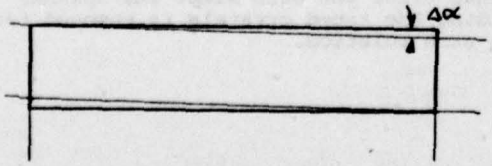

Fig. 1

Mechanical Method

Angle correction is usually accomplished mechanically. The mechanical method is to lap or grind the blanks at an angle to the surface. A blankholder, usually a vacuum type, holds the blank at an angle to the grinder or lap plate and grinds or laps the angle correction away. The other side of the blank has to be corrected also to get a fully corrected blank. If only one side is corrected, the results after lapping will be half corrected. The disadvantages of the mechanical method are only one to six blanks can be corrected at a time, it requires skilled personnel, and the minimum thickness is about 0.015 inches. The ability to make rather large angle corrections is the chief advantage.

Etch Method

Angle correction using an etch solution is accomplished by etching away specific areas of the blank, so that in the following lapping process, the angle shifts. This method has four steps. First approximately half of the surface area on both sides of the blank has to be covered with an etch resistant material.

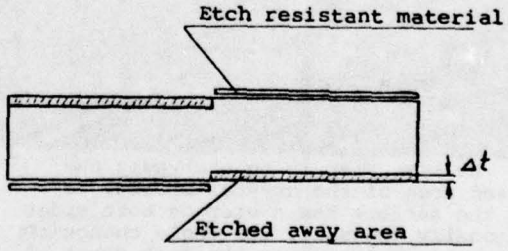

Fig. 2

Circuit plating tape (3M #1280) was found to be a good etch resistant material. The tape is held by a special fixture. The crystal blanks are placed on the edge of the fixture and pressed against the tape.

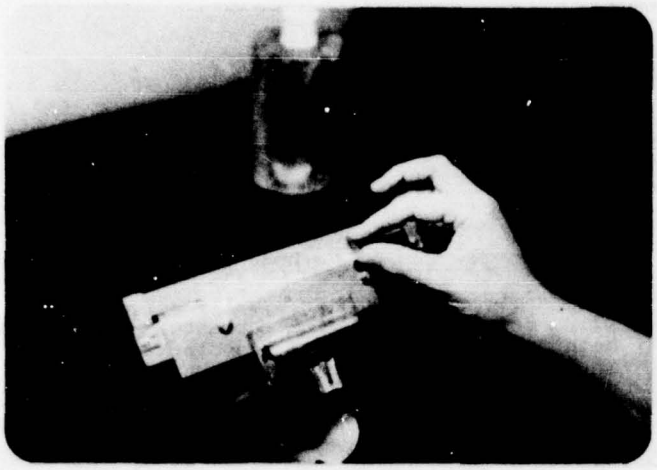

Then a piece of tape is placed on the front side of the crystals, and the tape with the crystals attached in removed from the special fixture. These strips of tape and crystals are placed in a plexiglass spinner. These spinners hold 80 blanks each.

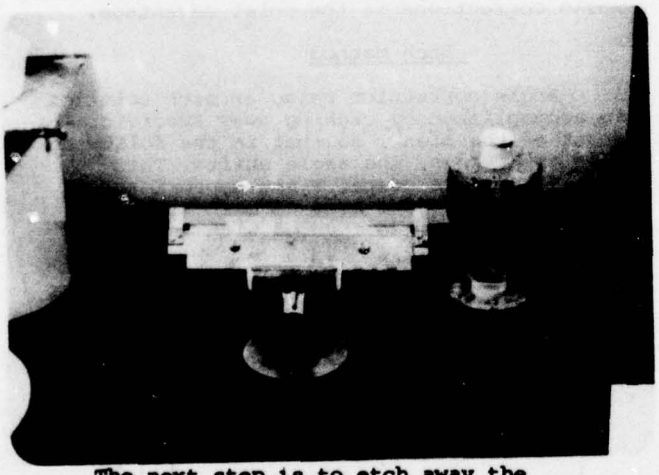

The next step is to etch away the exposed area of the crystal blanks, so that the surface has a step on both sides (diagonally opposed). The angle change $\Delta\alpha$ is approximate equal to the etch depth Δt divided by half the length of the blank ($\ell/2$).

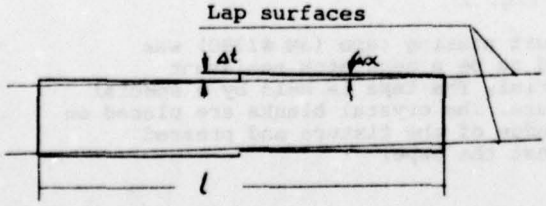

Fig. 3

$$\tan\alpha = \frac{\Delta t}{\ell/2} = \Delta\alpha \qquad \text{(in radian)}$$

The etch depth is a function of etch activity and time. The etch activity is held as constant as practical by controlling the temperature (80°C) and by keeping undissolved etch crystals (annonium bifluoride) in the solution (saturated solution). The activity is also checked to the following steps:

CHECK THE ACTIVITY
OF THE ETCH SOLUTION

	EXAMPLE
1) Make a frequency measurement on an unplated blank	5.800 MHz
2) Etch the blank a standard time	20 seconds
3) Make a frequency measurement	5.820 MHz
4) Calculate the Δ f	= 20 KHz

FIG. 4

If the Δf varies, the etch time for a particular angle correction has to be changed in such a way that the amount of etch (Δt) remains constant. The amount of correction can be determined empirically and a correction table made for different activities as follows:

AMOUNT OF CORRECTION	ETCH TIME IN MINUTES STANDARD ETCH OF		
	18 KHz	20 KHz	22 KHz
1'	5.0	4.5	4.0
2'	10.0	9.0	8.0
3'	15.0	13.5	12.0
4'	20.0	18.0	16.0

FIG. 5

The maxium angle change is about 4', because the tape does not hold up much over 20 minutes at 80°C.

The tape is removed from the crystal blanks after the etch step. The spinner holding the taped crystals is removed from the etch solution.

and placed in a large beaker of cool water. Some of the crystals fall off the tape when it shrinks due to the cool water, but others have to be pulled off. No problems occur from adhesive sticking to the crystals since most of it stays on the tape.

The final step is to lap the half etched crystal blanks plane parallel. This is done in a planetary lapping machine. The crystals must be lapped enough to remove the step resulting from the etching.

The advantage of this method is that much thinner blanks can be corrected and the disadvantage is the maximum correction of 4'.

Experiment

Paint and tape were tried as an etch resistant covering.

The following paints were tried:

- Acrylic Krylon
- Lacquer
- Aerosol Undercoat
- Parafin, dissolved in alcohol

Acrylic Krylon was the best paint, but the longevity in the etch solution was not good. Parafin did not stand up to the temperature.

The following tapes were tried:

- Scotch Magic Transparent #810
- Scotch Magic Transparent #600
- 3M Circuit Plating Tape #1280

The 3M tape held up very good and it is now used in production.

Two etch solutions were tried. The first was a concentrated solution of ammonium bi-fluoride at 80°C, which is also used in production for other purposes. The second was a mixture of hydrofluoric acid and ammonium bi-fluoride at room temperature. Room temperature was chosen because it would be desirable to have an active acid that is not heated to avoid the problems with the temperature resistance of the covering material. However, the activity of this acid only ¼ of ammonium bi-fluoride at 80°C, therefore, ammonium bi-fluoride is now in use.

Results

The following results were obtained using the 3M #1280 tape and ammonium bi-fluoride at 80°C:

RESULTS ANGLE CORRECTION

Blanks .450 sq. Frequency 6450 KHz.

Angle 35°13'±.5' Correct to 35°14' $\triangle\ominus$ =1'

Angle double checked before corrected

X-Ray measurement after etch correction and lapping to 7800 KHz.

Quantity	Angle
24	35°13'±.5'
239	35°14'±/5'
48	35°15'±.5'
311	= 76% within ±.5'

FIG. 6 The blanks were X-Ray measured twice; therfore, the initial accuracy was approximately 95% within ±.5'
Result: 76% of the blanks came up to the desired angle within ±.5'

RESULTS ANGLE CORRECTION

Blanks .407 sq. Frequency 6450 KHz.

Angle 35°21'±.5' Correct to 35°23'

$\Delta\Theta$ = 2'

X-Ray measurement after etch correction and lapping to 7800 KHz.

#1 Quantity	Angle
71	35°21'±.5'
233	35°22'±.5'
395	35°23'±.5'
47	35°24'±.5'
9	35°25'±.5'
755	= 52% within ±.5' = 89% within ± 1.5'

#2 Quantity	Angle
41	35°21'±.5'
66	35°22'±.5'
352	35°23'±.5'
226	35°24'±.5'
120	35°25'±.5'
805	= 44% within ±.5' = 80% within ± 1.5'

FIG. 7 The amount of correction is plus 2'. for both groups.
Group #1 is slightly under corrected
Group #2 is slightly over corrected
The blanks were only measured once on the X-Ray machine before correction.
The initial accuracy was only approximately 80% within ±0.5'; therfore, the end result does not show an exact picture.

RESULTS ANGLE CORRECTION

Blanks .407 sq. Frequency 6450 KHz

Angle 35°08'±.5' Correct to 35°10' $\Delta\Theta$=2'

Angle couble checked before corrected

X-Ray measurement after etch correction and lapping to 7800 KHz.

Quantity	Angle
4	35°09'±.5'
30	35°10'±.5'
6	35°11'±.5'
40	=75% within ±.5'

FIG. 8 The correction angle is plus 2'.
The blanks were double X-ray measured.
The end result shows 75% of the blanks after correction are within ±.5'

RESULTS ANGLE CORRECTION

Blanks .407 sq. Frequency 4400 KHz.

Angle 35°20'±.5' Correct to 35°23' $\Delta\Theta$=3'

X-Ray measurement after etch correction and lapping to 6450 KHz.

Quantity	Angle
47	35°21'±.5'
93	35°22'±.5'
420	35°23'±.5'
137	35°24'±.5'
49	35°25'±.5'
746	= 56% within ±.5' = 87% within ± 1.5' or 72% within ± 1'

FIG. 9 The correction plus 3'.
These blanks were only X-Ray measured once, and they are thicker than the others.
The end result shows that 56% are within ±.5'

Conclusion

The investment in tooling and equipment necessary to implement this method is quite small. Very little training is needed to put this method into practice. However, some engineering will have to be done, because the etch charts used to determine the etch time are empirical and may vary from one manufacturer to another. The variation would be due to the finish on the test blank and the activity fo the etch. Furthermore, each blank size should have an appropriate etch chart.

Over 50,000 crystal blanks have been angle corrected using the etch method; thus rendering what would otherwise be excess inventory into usable blanks.

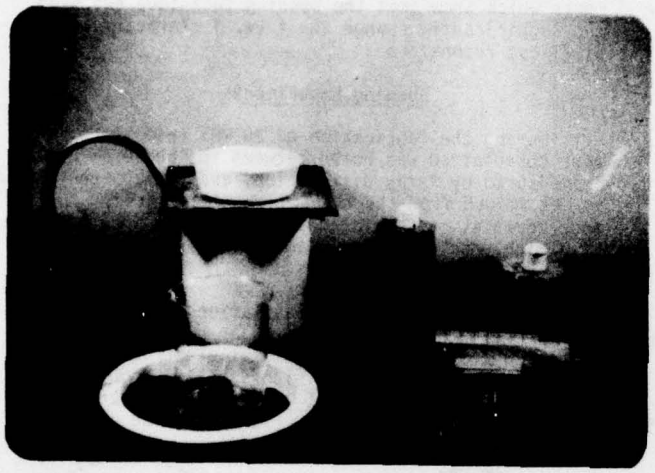

THE EFFECT OF BONDING ON THE FREQUENCY VS. TEMPERATURE CHARACTERISTICS OF AT-CUT RESONATORS

Raymond L. Filler and John R. Vig
US Army Electronics Technology and Devices Laboratory (ECOM)
Fort Monmouth, NJ 07703

Summary

Although the frequency vs. temperature (f vs. T) characteristics of quartz resonators depend primarily on the angle of cut of the quartz plate with respect to the natural crystallographic axes, processing variables such as the stresses due to the mounting clips, bonding agents, and electrodes can also have important effects. For thin resonator plates, in particular, it has been found that the bonding technique employed can produce large rotations in the f vs. T characteristics. Changes in the f vs. T characteristics which correspond to shifts in apparent angle of several minutes have been observed. This paper discusses experiments which have defined the effect of bonding on the apparent angle.

Nickel electrobonding was used throughout these experiments because this technique permits precise control of the bonded area, the thickness of the bonding film, and the intrinsic stress in the film. The experiments were performed on 6.4 mm (0.250") diameter, 20 MHz AT-cut plates. The bonding areas were small (1 mm^2) ovals placed along a blank diameter. The shift in apparent angle was measured as a function of the orientation of this diameter with respect to XX'. Downward shifts in apparent angles were observed when the bonding areas were oriented along the ZZ' direction; upward shifts were observed along the XX' direction. For a 50 μm (2 mils) thick bonding film, a change in bonding orientation from ZZ' to XX' produces an apparent angle shift of over 6 minutes.

The shifts in apparent angle were found to be a function of the shape, area, and thickness of the bonding agent, and of the orientation of the bonding area with respect to the crystallographic axes of the plate. By carefully controlling the geometry and orientation of the bonding spots, the effect of bonding on resonator frequency can be minized, or alternately, predictable shifts in apparent angle can be produced. Thus the bonding method can possibly serve as a convenient means of "angle correcting".

Key words. Quartz-Resonators, Quartz, Bonding, Frequency vs. Temperature-Characteristic, Resonator, Piezoelectric-Crystals, Frequency-Control, Frequency-Standards, Stresses, Aging (Materials).

Introduction

The frequency versus temperature (f vs. T) characteristic of a quartz resonator depends primarily on the angle of cut of the resonator blank. There are, however, secondary factors introduced during the processing which can also influence this characteristic. Among these are the stresses due to mounting, bonding and the electrodes.

Young, et al., have demonstrated by an X-ray source image distortion technique the existence of process-induced strains, including "cement-strains" due to the bonding agent[1]. The effects of such "cement strains" on resonator performance have not, however, been measured previously. This paper discusses experiments which show that the bonding technique employed can significantly change the f vs. T characteristics of AT-cut resonators.

Bonding Experiments

During the fabrication of 20 MHz resonators, a poor correlation was noted between the angle of cut, as measured by X-ray diffraction, and the apparent angle, as determined from the f vs. T characteristic. This poor correlation persisted even after the incorporation of a highly accurate laser assisted X-ray goniometer[2] into the fabrication process.

At the time of these observations, two different 20 MHz resonator designs were under development. For both resonator designs, the nickel electrobonding technique was used to bond the blanks to the mounting clips. The bonded areas of the two designs are shown as the blackened portions in Figure 1. One design was

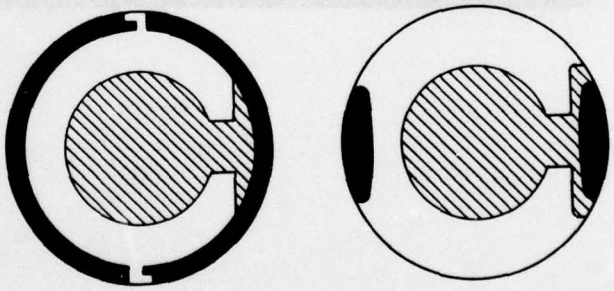

Figure 1. Bonding Areas on Low Shock and High Shock Resistant Crystals

for a high shock resistant Temperature Compensated Crystal Oscillator (TCXO) application in which the edges of the blank were strengthened by extending the nickel plating around nearly the whole circumference of the blank. Two small diametrically opposed gaps in the plating serve to prevent electrical shorts between the two semicircular halves of the edge plating. The second design, with the small bonded areas, was for a low shock TCXO application. The centers of the bonded areas in both designs were oriented along the ZZ' crystallographic direction of the blanks.

Resonators of the high shock design were found to have a f vs. T characteristic which one would normally associate with blanks whose angles of cut are higher than the measured X-ray angles. Resonators of the low

shock design, however, had apparent angles which were consistently lower than the X-ray angles. Moreover, the discrepancies between apparent angles and X-ray angles increased as the thickness of the the nickel film used for bonding was increased.

These observations suggested that the poor correlations between the apparent angles and X-ray angles were related to the bonding films. The tight tolerances on the f vs. T characteristics of these TCXO crystals made a better understanding of these observations essential.

A group of resonators were fabricated as shown in Figure 2. The resonator blanks were 20 MHz fundamental, plano-plano, AT cut, natural quartz, with a diameter of 6.35 mm (0.250 inch), final lapped with 5 μm aluminum oxide abrasive, beveled, then etched 800 kHz. After measuring the angles of cut carefully, chromium-gold tabs were vacuum evaporated onto the blanks near the edges. The tabs, which consisted of 200 Å of Cr + 120 Å of Cr-Au mixture + 600 Å of Au, define the areas on the blanks to be plated during nickel electrobonding. These areas, indicated as the "bonded areas" in Figure 2, are 0.5 mm wide and 2 mm long (0.020" X

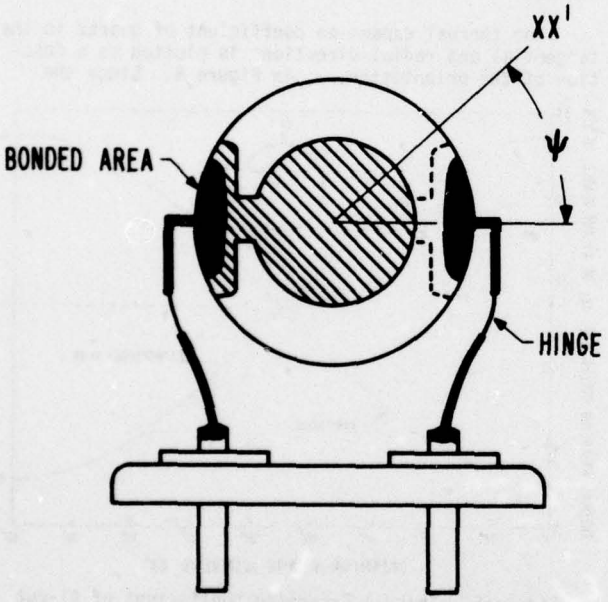

Figure 2. Resonator with Bonding Area Orientation, ψ, Shown.

0.080"). The bonding orientation angle, ψ, between the diameter defined by the centers of the tabs and the XX' crystallographic orientation of the blanks was measured by conoscopic observation in a polarizing microscope[4].

The mounting clips were 0.76 mm wide, 5.1 mm long, 51 μm thick (0.030" X 0.200" X 0.002") steel. The clips were positioned on the base (HC-25) in such a manner that when the resonators were mounted, the radial force exerted by the clips was near the minimum required to hold the crystals in place. An area on each clip was masked to assure that the clips were not stiffened by the nickel during electrobonding. One of these areas is labeled as the "hinge" in Figure 2.

The crystals were bonded into the bases using the nickel electrobonding process described previously[3]. The nickel plating took place in a temperature controlled plating bath at 48 C. The thickness of nickel deposited during bonding was a constant 50 μm (2 mils) throughout this experiment. The thickness was controlled by using a constant plating current density and a constant plating time, and was checked by measuring the thickness on a control sample. The circular electrodes had a 3.2 mm diameter, and consisted of vacuum evaporated gold, with a plateback of 350 kHz. The resonators were sealed with a dry nitrogen atmosphere inside the enclosures.

The f vs. T characteristic was measured, and the apparent angle was determined from the curve relating the normalized difference between turning point frequencies, δF, to the angle of cut, as shown in Figure 3.

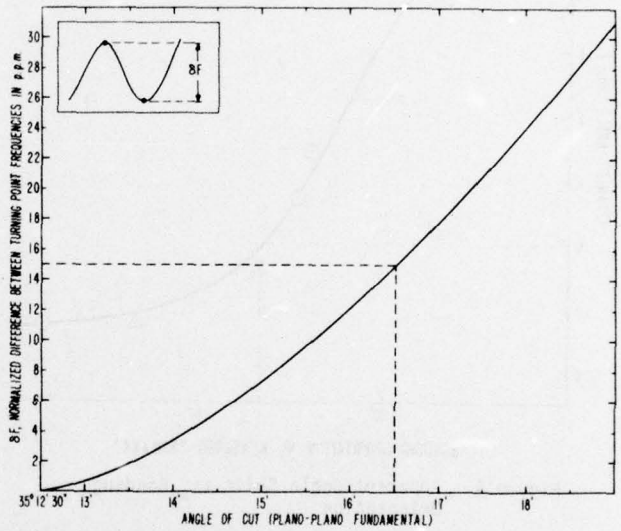

Figure 3. Difference Between Turning Point Frequencies vs. Angle of Cut

The curve is a plot of the relationship[5]

$$\delta F = \frac{4(b^2 - 3ac)^{3/2}}{27c^3} \qquad (1)$$

where a, b and c are the usual temperature coefficients of the first, second and third order, respectively. For example, as shown by the dashed line in Figure 3, when δF = 15 ppm, the apparent angle is 35° 16' 30". After so determining the apparent angles of a group of resonators, the resonator blanks were stripped of all metal and reprocessed using the identical fabrication proceedure, except that for each crystal, the bonding orientation, ψ, was changed. The f vs. T characteristics were remeasured and the apparent angles were determined as before. It was found that all the apparent angles had changed. The changes were a function of bonding orientation. Those whose bonding orientations were changed towards XX' shifted upward in apparent angle; those whose bonding orientations were changed toward ZZ' shifted downward in apparent angle.

To insure that the observed shifts were due to the bonding only, and not due to the stresses exerted by the mounting clips, one clip on each of several resonators was cut and rejoined with 76 μm (3 mil) diameter gold wire. The changes in apparent angles due to this modification were found to be negligible. That the

changes were due to the bonding films only was also confirmed by the fact that when the thickness of the nickel bonding films were increased without changing any of the other processing parameters, the magnitude of the apparent angle shifts also increased.

The reprocessing of resonators was repeated until a curve of apparent angle shift vs. bonding orientation was obtained, as shown in Figure 4. The vertical

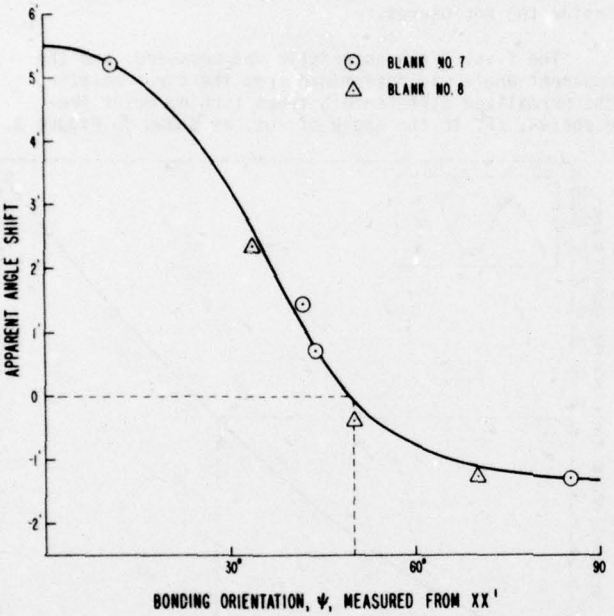

Figure 4. Apparent Angle Shift vs. Bonding Orientation

axis is the apparent angle shift, in minutes, measured from the angle of cut of the blank (as determined by X-ray diffraction). The curve shown is the best fit through numerous data points. The actual data points for two of the blanks are shown by the triangles and circles. The orientation which produces zero shift in apparent angle is about $50^\circ \pm 5^\circ$.

For example, the angle of cut of blank No. 7 was measured to be 35° 16' 41". With 35° 12' 30" as the reference angle, the standard value of the normalized difference between turning point frequencies, δF, as calculated from equation (1) above, is 15.9 ppm. When the bonding orientation, ψ, was 11°, the measured δF was 54.09 ppm, which corresponds to an apparent angle of 35° 21' 53"; i.e., the apparent angle shift was +5' 12". When this same blank was refabricated with $\psi = 85^\circ$, δF = 8.25 ppm was measured. This corresponds to an apparent angle of 35° 15' 12"; i.e., the apparent angle shift was -1' 29". Therefore, for the same blank reprocessed from $\psi = 11^\circ$ to $\psi = 85^\circ$, the total shift in apparent angle was 6' 41", and the total shift in δF was 45.8 ppm.

Several blanks were also processed with a silver conductive cement as the bonding agent. After these blanks were reprocessed so as to shift the bonding orientation from near XX' to near ZZ', shifts in apparent angles as high as 4 minutes were measured, however, a systematic study of angle shift vs. bonding orientation was not attempted due to the difficulty of controlling the area and thickness of the cement applied.

Discussion of Results

The curve in Figure 4 explains the seemingly anomalous behavior of the two TCXO crystal designs mentioned earlier. For both designs, the blanks were mounted along ZZ'. The low shock design produced a downward shift in apparent angle, as would be expected from Figure 4. The upward shift in angle produced by the high shock design is also explained by Figure 4, because when the angle shifts are summed over all bonding orientations encompassed by the edge plating on the high shock design, the net angle shift is clearly upward.

The angle shifts are believed to be due to the temperature dependent stresses produced by the bonding agent. As the temperature of the resonator is changed, the stresses due to the difference in thermal expansion coefficients between the bonding agent and the quartz also change. For a given bonding procedure, the shifts in δF due to these thermal stresses are expected to be proportional to the difference in thermal expansion coefficients, the difference in elastic constants, and to the stress sensitivity coefficient of quartz.

The thermal expansion coefficient of quartz in the tangential and radial directions is plotted as a function of the orientation, ψ, in Figure 5. Since the

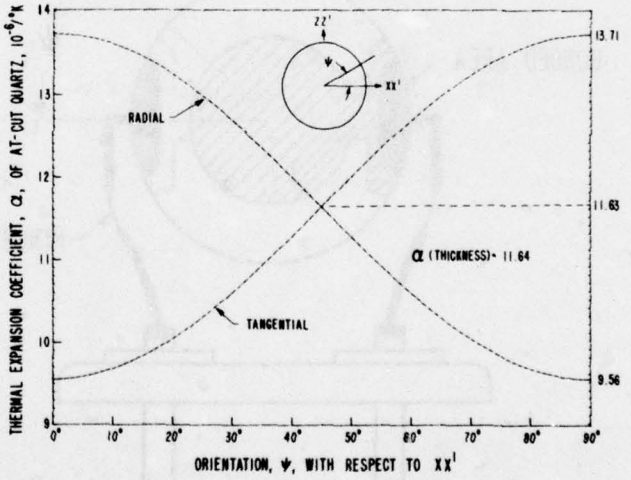

Figure 5. Thermal Expansion Coefficient of AT-cut Quartz vs. Orientation

bonding agents are generally isotropic, it is not possible to achieve an exact match to the thermal expansion coefficient of quartz.

The stress sensitivity coefficient of quartz for an isotropic stress in the active area of the resonator has been calculated by EerNisse[6] for the rotated Y-cut family. To explain the angle shift data of Figure 4, however, the stress sensitivity coefficient for an anisotropic stress applied in the plane of the blank near the edges would be needed as a function of orientation, ψ. Such information is not currently available.

Applications

1. Aging and Thermal Hysteresis

We have seen that the bonding agent can produce significant shifts in f vs. T characteristics. For

example, as was discussed previously, when blank No. 7 of Figure 4 was bonded near the XX' orientation, the measured δF differed from the value one would normally expect from the angle of cut by nearly 40 ppm. At the upper turning point, for example, a relaxation of the thermal stresses could produce a frequency change, i.e., aging, of over 10 ppm. Similarly, if the frequency of this resonator is measured at a given temperature, then remeasured at the same temperature after having experienced a temperature excursion, the frequency will be different if during the temperature excursion the stresses at the quartz-bonding agent interface change. Therefore, the stresses due to the bonding agent may lead to significant aging and thermal hysteresis effects.

To minimize the contribution of the bonding agent to aging and thermal hysteresis, resonators should be bonded along the orientation which produces zero shift in apparent angle. Interestingly, and perhaps not coincidentally, the optimum orientation for minimizing the effects of bonding, about 50° from XX', is near the optimum orientation for minimizing the effects of mounting stresses. Ballato[7] has shown that for a radial force applied to the edge of an AT-cut plate, the force-frequency coefficient is zero when the force is applied at about 60° from XX'.

2. Angle Correction

The effect of bonding on the f vs. T characteristic can be utilized to intentionally change the apparent angles of blanks whose angles of cut would normally place them outside the usable range. For example, for the bonding configuration described above, according to the results presented in Figure 4, the range of "angle correction" is from 5.5 minutes up to 1.5 minutes down. Of course, this range can be varied by varying the bonding configuration, i.e., the area, shape and thickness of the bonding agent applied. To minimize the effect of angle correction on resonator stability, the bonding agent used should be one which shows minimum stress relief at the normal operating temperatures of the resonator.

3. High Shock Resistant Resonators

Among the requirements on a shock resistant TCXO crystal under development is a f vs. T characteristic in which the frequency excursion between turning points is 18 ±5 ppm, and that the resonator survive a 15,000g shock of 6 msec duration, with minimal change in frequency. These two requirements seemed for a long time to be incompatible. The high shock bonding configuration shown in Figure 1 strengthened the resonator sufficiently to allow it to survive the 15,000g shock. The bonding, however, also shifted the apparent angle to such an extent, that the yield on high shock crystals with acceptable f vs. T characteristics was extremely low.

The results presented in Figure 4 allowed us to redesign the high shock crystals in a manner which now permits a much higher yield on the f vs. T characteristics. In Figure 4, the upward angle shift at the XX' bonding orientation is about four times as large as the downward shift at the ZZ' orientation. The bonded area was therefore made wider in the vicinity of the ZZ' orientation so as to compensate for the greater shift produced by the bonding near XX'. The new bonding configuration is shown in block in Figure 6. The shift in apparent angle due to this bonding configuration is near zero.

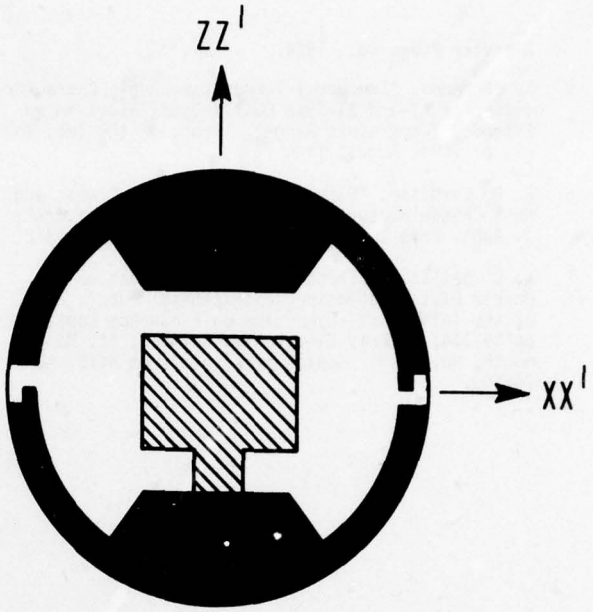

Figure 6. Angle Shift Compensated Bonding Area on High Shock Resistant Resonator

Conclusions

The bonding has been shown to be capable of producing significant changes in the f vs. T characteristics of AT-cut resonators. The effect of bonding on resonator frequency can be minimized by a careful choice of bonding configuration. The effect can also be used to produce predictable changes in f vs. T characteristics.

Acknowledgements

The authors would like to thank Dr. E. Hafner for his helpful comments, Dr. A. Ballato for providing Figures 3 and 5, and Mr. L. Nelson for making the f vs. T measurements.

References

1. R. A. Young, R. B. Belser, A. L. Bennett, W. H. Hicklin, J. C. Meaders, and C. E. Wagner, "Special X-ray Studies of Quartz Frequency Control Units", Proc. 19th Annual Symposium on Frequency Control, pp 23-41, 1965, copies available from NTIS AD 471229.

2. J. R. Vig, "A High Precision Laser Assisted X-ray Goniometer for Circular Plates", Proc. 29th Annual Symposium on Frequency Control, pp 240-247, 1975, copies available from the Electronics Industries Assoc., 2001 Eye Street, NW, Washington, DC 20006. Article also available as ECOM R&D Tech. Rept. 4376, Dec. 1975, NTIS Accession No. AD A018520.

3. J. R. Vig, J. W. LeBus and R. L. Filler, "Further Results on UV Cleaning and Ni Electrobonding", Proc. 29th Annual Symposium on Frequency Control, pp 220-229, 1975, copies available from EIA - see Ref No. 2.

4. See e.g., N. H. Hartshorne and A. Stuart, Practical Optical Crystallography, Chapter 5, American

Elsevier Publ. Co., 1964.

5. R. Bechmann, "Frequency-Temperature-Angle Characteristics of AT-and BT-Type Quartz Oscillators in an Extended Temperature Range". Proc. of the IRE, Vol. 48, p. 1494, August 1960.

6. E. P. EerNisse, "Simultaneous Thin-Film Stress and Mass Change Measurements Using Quartz Resonators", J. Appl. Phys., Vol. 43, pp 1330-1337, April 1972

7. A. D. Ballato, "Effects of Initial Stress on Quartz Plates Vibrating in Thickness Modes", Proc. of the 14th Annual Symposium on Frequency Control, pp 89-114, US Army Electronics Command, Ft. Monmouth, NJ, 1960. Copies available from NTIS, AD 246500.

DESIGN CONSIDERATIONS IN STATE-OF-THE-ART SIGNAL PROCESSING AND PHASE NOISE MEASUREMENT SYSTEMS

by

F. L. Walls, S. R. Stein, James E. Gray
and David J. Glaze
Frequency and Time Standards Section
National Bureau of Standards
Boulder, Colorado 80302

Introduction

The recent rapid improvement of oscillator phase noise has resulted in significantly more stringent requirements for signal handling equipment. However, information concerning the phase noise performance of the two most important types of circuits - amplifiers and mixers - is often difficult to find. Some general principles are presented which allow one to estimate the phase noise performance of an amplifier. Also, techniques are described which permit one to obtain the best possible results from the traditional double balanced mixer. A measurement set-up which has 15 to 25 dB improvement in its noise floor is shown in detail to illustrate proper mixer drive and termination. Although traditional circuits can with extreme care achieve S_ϕ = -175 dB or slightly better, this is not sufficient for all present requirements. One technique to obtain an additional improvement of 10 to 40 dB in measurement system noise is to reduce the mixer and amplifier contributions to the noise floor by the use of correlation techniques. A circuit to accomplish this is discussed along with some preliminary results.

One of the most frequently needed systems in the study and use of oscillators is the phase-lock loop. However, since the performance of this system is often incidental to the ultimate goal of the experimenter, e.g. the measurement of phase noise, the design of such a system is sometimes given too little consideration, resulting in unanticipated difficulties and wasted time. The design of an extremely simple phase-lock loop which is suitable for almost all high stability oscillator applications is discussed with particular attention to the advantages over more traditional circuits.

I. PHILOSOPHY OF LOW NOISE AMPLIFIER DESIGN

If an amplifier were driven from a noiseless oscillator, then the output phase spectrum would typically have a flicker noise region at low frequencies and a white noise region at higher frequencies. The break between the two is usually between one and one hundred Hz and the white noise extends out to the bandwidth of the amplifier. The source of the white noise modulation can be identified and the magnitude estimated, but similar generalizations can not be made for the flicker noise. Nevertheless, empirical guidelines can be established which should ensure against unnecessarily poor flicker noise performance.

Provided that the integrated noise of the amplifier over its entire bandwidth is small compared to the signal power, half the thermal noise power contributes to the phase modulation of the signal. Thus the spectral density of phase fluctuations due to noise of the amplifier is

$$S_\phi(f) = S_0/2P_s \qquad (1)$$

where S_0 is the spectral density of the noise power and P_s is the power available to a matched load. For Johnson noise, the most common situation,

$$S_0 = kT = 4 \times 10^{-21} \text{ J}$$

and the achievable phase noise performance is -184 dB below a 1 rad^2/Hz for a 1 V_{rms} signal from a 50Ω source.

In contrast to the white phase noise which is added to the carrier by the amplifier, the flicker phase noise is produced by direct phase modulation in the active element. It has been found empirically that a transistor stage which does not use emitter degeneration typically has phase noise given by $S_\phi(f) \simeq 10^{-11}$ rad^2/f. However the use of local RF negative feedback can reduce this noise power by as much as a factor of 10^4.[1] Passive elements can also contribute to the flicker phase noise. Electrolytic, ceramic, and silver mica capacitors and carbon composition resistors can give excessive flicker noise and should only be used in non-critical locations.

Three design requirements for low phase noise amplifier design follow from the above discussion. Firstly, each stage of an amplifier must incorporate emitter degeneration to minimize the flicker phase modulation. Secondly, critical passive components should be examined for excessive phase noise. Finally, the signal level must be always maintained at a high enough level to achieve the desired white phase noise level.

In order to illustrate the influence of this philosophy on the design of an amplifier, a new isolation amplifier is described. This amplifier was developed to provide a high degree of isolation between very low phase noise RF signals which are used to compare atomic and other frequency standards.

II. WIDE-BAND LOW-NOISE ISOLATION AMPLIFIER

The amplifier shown in Figure 1 is designed to operate from one to several hundred megahertz. In order to minimize current drain a method of achieving high isolation which used a small number of stages was needed. This requirement was satisfied by a cascaded pair of common base transistor stages, Q_1 and Q_2. A signal applied to the output port propagates towards the input through the collector-base capacitance of Q_1. The 2N3904 was selected because of its small output capacitance, 4 pF. Since the base of Q_1 is grounded through a capacitor and the emitter looks into the high output impedance of the preceding stage, the signal is low pass filtered. A second stage of filtering is performed by the transistor Q_2 in the same way. It is also possible for a signal to propagate from the output to input through the bias chain. Transmission through this path is reduced to the same level as transmission through the transistor chain by the cascaded low

pass filters. Typical isolation which is achieved is greater than 120 dB at 5 MHz degrading to 100 dB at 50 MHz.

The common emitter input stage determines the collector current of the transistors. The 27Ω dc emitter resistance produces an average collector current of 40 mA. Noise performance is generally best when the amplifier operates well within the class A region. With a 50Ω load this amplifier can produce an output of nearly 1 V_{rms} (13 dBm) with minimum distortion. The gain of the amplifier is determined by the load resistance and the unbypassed portion, 27Ω, of the emitter resistance. With the values shown, the full output swing occurs for an input of approximately 1.5 V_{ptp}.

The white noise floor which one would estimate for this amplifier is S_ϕ = -184 dB. The measured noise floor is shown as curve A of Figure 2. The noise floor appears to be only -174 dB, but since this level corresponds to the measurement system noise it can only be said that the amplifier is not worse than this. The measured flicker phase noise of the amplifier is $S_\phi = 10^{-14}$ rad^2/f. This performance level is reached because each transistor has a reasonable amount of local RF negative feedback. The emitters of Q_1 and Q_2 both look into the high dynamic impedance of the preceding stage while the emitter of Q_3 has the unbypassed 27Ω resistor. For a given application, this unbypassed resistor should be made as large as possible, limited only by the necessity of having full output voltage swing.

In addition to achieving low noise levels it is necessary to minimize microphonics and pickup of power-line frequencies and other signals. For this reason, no use has been made of filter inductors or coupling transformers. It is also possible that temperature changes could cause sufficient collector current variation to degrade the flicker performance. As a result, the diode has been included in the bias chain to further stabilize the collector current. It should be placed in physical contact with transistor Q_3. The amplifier has been constructed on a double sided printed circuit board measuring 3.25 cm x 9 cm. The art work for this circuit board is available from the authors.

III. DOUBLE BALANCED MIXERS AND PHASE NOISE MEASUREMENT SYSTEMS

The most common and also most sensitive method of measuring phase noise is to use a double balanced mixer. If the input ports are driven by quadrature signals, then the output voltage is proportional to the phase deviation of the input signals from the quadrature condition. The spectral density of the phase noise can be calculated from the very simple expression

$$S_\phi(f) = \left[\frac{V_n(f)}{V_s}\right]^2 \qquad (2)$$

where $V_n^2(f)$ is the noise density in units V^2/Hz at the output of the mixer and V_s is the sensitivity of the mixer in V/rad.

A variety of circuits for the measurement of phase noise have been discussed extensively in the literature. Here we will look closely at specific problem areas common to all circuits using double balanced mixers: components, input drive levels and output termination. Data are presented which show that proper treatment of these details results in a 15 to 25 dB improvement in the performance of phase noise measurement systems.

Figure 3 shows a typical double balanced mixer. The best performance has been obtained with units which use hot carrier diodes in the ring. Some differences may also result from the type of transformers in the coupling circuits. The noise observed at the output of the mixer, consisting of mixer and amplifier contributions, is nearly constant over a range of input power level. However, the output signal, proportional to the phase fluctuations, increases with the drive power. The best signal-to-noise ratio for Fourier frequencies in the white noise region is obtained at very high drive levels. For one type of mixer, using a single diode in each arm, the best noise floor was obtained with approximately 30 mA rms current at each input. This drive level exceeded the manufacturer's maximum drive current specification. The optimum drive is not necessarily the same for all Fourier frequencies. The same mixer performed best below 40 Hz at lower drive level. Since such a double balanced mixer is a dynamic impedance the average drive current does not sufficiently describe the operating conditions. The optimum method of coupling to the mixer also depends upon the output impedance of the signal source. Although the use of 50Ω pads to attenuate the drive level is traditional, a series resistor whose value is chosen to set the desired current often gives superior performance. The improvements which are observed may be due to reduced ringing of the drive currents.

The signal-to-noise ratio at the mixer output is also affected by the type of termination used. Since the mixer has a low output impedance, near 50Ω, the dc termination must be high impedance compared to 50Ω. Failure to observe this may result in 6 dB or more loss in signal level. However, it has been determined empirically that the mixer must be terminated differently at RF. In the circuit shown in Figure 4 the impedance to ground at the output of the mixer is 1 kΩ at dc and approximately 50Ω at 10 MHz. The net result of the high drive level and the output termination is illustrated in Figure 5, which shows the beat frequency between the two oscillators in Figure 4 at low drive level (sinewave) and high drive level (clipped waveform). The slope of the clipped waveform at the zero crossings is more than twice the slope of the sinewave. It follows from Eq. (2) that the noise floor is improved more than 6 dB by this technique. The increase in slope is not realized without appropriate termination, but the optimum circuit has not been determined. The noise floor achieved with the circuit of Figure 4 is shown in curve C of Figure 2. The spectral density of phase is -150 dB at 1 Hz and drops to a floor of -176 dB.

Several other special circumstances may occur. One may wish to measure the signal from a device which has insufficient output power to drive a double balanced mixer. Figure 6 shows a simple buffer amplifier which may be used under the circumstances. In keeping with the stated philosophy of amplifier design, this circuit can drive a mixer with a nominal 50Ω input impedance with a 1 V_{rms} signal in class A operation. The mixer input impedance appears as an unbypassed 200Ω in the emitter circuit which results in excellent flicker noise performance. As shown in curve B of Figure 2, the spectral density of phase is -149 dB at 1 Hz and falls off to the noise floor of the measurement system. The 10 dB improvement in flicker noise over the previously described isolation amplifier is probably due to the greater emitter degeneration or lower intrinsic flicker noise in the 2N5943 transistor compared to the 2N3904 or both. The 2N5943 was suggested for use in this circuit by Charles Stone of Austron Inc.

If the device being tested is capable of more output power than a standard double balanced mixer can accept, then it is possible to achieve even lower noise floors. Provided the driving voltage exceeds about 1 V_{rms}, it is possible to use a high level mixer. Such a device has more than one diode in each leg of the ring and is therefore able to achieve higher output voltage without a

corresponding increase in the noise. The circuit diagram of the mixer in Figure 3 shows two diodes in each leg. Using a mixer with three diodes per leg a noise floor of -184 dB was achieved with a drive level of 1.6 V_{rms}. If the oscillator's output impedance is low but the voltage is insufficient to drive a high level mixer a step-up transformer can be used to obtain the appropriate drive voltage. Since the signal and noise power increase by the same ratio, the spectral density of phase of the device under test is unchanged but the noise floor of the measurement system is reduced.

IV. CORRELATION TECHNIQUE

With all of the improvements described the traditional double balanced mixer phase noise measurement system is unable to resolve the noise floor of the best oscillators and amplifiers.

If times 20 or more frequency multiplier chains with noise levels 20 dB below that of the measurement system shown in Figure 2 were available, then that would solve the present problem. So far we are unaware of such multiplier chains, although some prototype multiplier chains show white noise floors 5 to 10 dB below Figure 2. It would also be convenient if the measurement system were broadband so as to accept carrier frequencies from approximately 1 to 100 MHz. Figure 7 shows the block diagram of a phase noise measurement system which is inherently very broadband and also has the capability of improving the measurement system noise by at least 20 dB. It consists primarily of two equivalent traditional phase noise measurement systems.

At the output of each double balanced mixer there is a signal which is proportional to the phase difference, $\Delta\phi$, between the two oscillators and a noise term, V_N, due to contributions from the mixer and amplifier. The voltages at the input of each bandpass filter are

$$\begin{aligned} V_1(\text{BP filter input}) &= A_1\,\Delta\phi(t) + C_1 V_{N1}(t) \\ V_2(\text{BP filter input}) &= A_2\,\Delta\phi(t) + C_2 V_{N2}(t) \end{aligned} \tag{3}$$

where $V_{N1}(t)$ and $V_{N2}(t)$ are substantially uncorrelated. Each bandpass filter produces a narrow band noise function around its center frequency f:

$$\begin{aligned} V_1(\text{BP filter output}) &= A_1[S_\phi(f)]^{1/2} B_1^{1/2} \cos\,[2\pi ft + \Psi(t)] \\ &+ C_1[S_{VN1}(f)]^{1/2}\ B_1^{1/2} \cos\,[2\pi ft + \eta_1(t)] \\ V_2(\text{BP filter output}) &= A_2[S_\phi(f)]^{1/2} B_2^{1/2} \cos\,[2\pi ft + \Psi(t)] \\ &+ C_2[S_{VN2}(f)]^{1/2}\ B_2^{1/2} \cos\,[2\pi ft + \eta_1(t)] \end{aligned} \tag{4}$$

where B_1 and B_2 are the equivalent noise bandwidths of filters 1 and 2 respectfully. Both channels are bandpass filtered in order to help eliminate aliasing and dynamic range problems. The phases $\Psi(t)$, $\eta_1(t)$ and $\eta_2(t)$ take on all values between 0 and 2π with equal likelihood. They vary slowly compared to 1/f and are substantially uncorrelated. When these two voltages are multiplied together and low pass filtered only one term has finite average value. The output voltage is

$$\begin{aligned} V_{out}^2 &= 1/2\ A_1A_2\ S_\phi(f)\ B_1^{1/2}B_2^{1/2} + D_1\langle\cos[\Psi(t) - \eta_1(t)]\rangle \\ &+ D_2\langle\cos[\Psi(t) - \eta_2(t)]\rangle + D_3\langle\cos[\eta_1(t) - \eta_2(t)]\rangle. \end{aligned} \tag{5}$$

For times long compared to $B_1^{-1/2}B_2^{-1/2}$ the noise terms D_1, D_2 and D_3 tend towards zero as $\sqrt{t}$. Limits in the reduction of these terms are usually associated with harmonics of 60 Hz pickup, dc offset drifts, and nonlinearities in the multiplier. Also if the isolation amplifiers have input current noise then they will pump current through the source resistance. The resulting noise voltage will appear coherently on both channels and can't be distinguished from real phase noise between the two oscillators. One half of the noise power appears in amplitude and one half in phase modulation.

Curve A of Figure 8 shows $S_\phi(f)$ for the mixer and dc amplifiers in Channel 1 and 2 when used separately. The mixers in this case have three diodes in each leg instead of the two shown in Figure 3 and are driven with approximately 5 V_{ptp} at 5 MHz from 10Ω source impedance using 33Ω series resistors. Curve B Figure 8 indicates the correlated component of this noise between the two channels. In order to predict performance in a specific measurement using this scheme, the noise level of the isolation amplifiers used would have to be added to Curve A and proportionately to Curve B.

The above data clearly indicate that significant improvements over any presently existing phase noise measurement system can be obtained using correlation techniques. Such improvements are vitally necessary in order to measure present state-of-the-art signal processing equipment and to test future components and circuits. The simple single frequency correlator used in this experiment could be replaced by a fast digital system which would simultaneously compute the correlated phase noise for a large band of Fourier frequencies. Ultimate noise floors could probably be reduced 40 dB below the noise level of a single channel.

V. PHASE-LOCK TECHNIQUES

One of the most ubiquitous elements of phase noise measurement systems is the phase-lock loop.[2,3] When the phase noise of a pair of oscillators is measured a phase-lock loop is normally used to maintain a condition of approximate phase quadrature. For accurate measurements it is necessary to keep the phase error less than about 1/6 rad despite any initial frequency offset between the two oscillators or any frequency drift during the course of the measurement. The phase-lock loop is usually the most neglected element of the measurement system because its purpose is only tangential to the measurement requirements. As a consequence it often performs marginally. In this section the requirements for a phase-lock system are discussed and an extremely simple yet elegant circuit is presented which more than meets these requirements.

A specific example illustrates the problem: Design a feedback loop to lock a 5 MHz VCO to a reference oscillator with a unity gain frequency of .16 Hz and calculate the open loop frequency difference for phase error of 1/6 rad. The VCO has a tuning rate of 5×10^{-3} Hz/V and the phase deviation from quadrature. One solution, the first order phase-lock loop, is shown in Figure 9. The 50Ω resistor and 0.1 μF capacitor are for proper termination of the mixer and do not contribute appreciably to the frequency response of the phase-lock loop. The open loop gain of this servo is

$$\begin{aligned} G_{servo}(\omega) &= \frac{2\ (5\times10^{-3}\ \text{Hz/V})\ (0.17\ \text{V/rad})\ G_{amp}(\omega)}{j\omega} \\ &= \frac{5.3\times10^{-3}\ G_{amp}(\omega)}{j\omega} \end{aligned} \tag{6}$$

where $G_{amp}(\omega)$ is the frequency response function of the amplifier. For the first order loop the amplifier has constant gain and the open loop gain of the servo system falls off at 6 dB/octave at all frequencies as shown in the dashed curve of Figure 10. This type of response results from the fact that a phase error measured at the mixer is corrected by changing the frequency of the VCO, i.e., the feedback loop contains one inherent integration.

To produce a unity gain frequency of 0.16 Hz, or an attack time of one second, requires amplifier gain of 185. The loop produces negligible correction for Fourier frequencies greater than 1 Hz and may therefore be used to make phase noise measurements in this frequency range. The open-loop frequency offset which corresponds to a 1/6 rad phase error is

$$\Delta\nu = (1/6 \text{ rad})\ (0.17 \text{ V/rad})(5 \times 10^{-3}\text{Hz/V})(185)$$
$$= 2.5 \times 10^{-2} \text{ Hz} \qquad (7)$$

or only 5 parts in 10^9 at 5 MHz. It is often difficult to achieve and maintain such a small frequency offset. However, the following circuit increases the dc gain of the feedback loop by 10^5 and decreases the phase error proportionally, The improved performance is achieved by adding a stage of quasi-integration which makes a second order loop as shown in Figure 11. The first stage of amplification is the same as in the first order loop. The second stage has gain equal to R_1/R_2 for Fourier frequencies larger than $1/(2\pi R_1 C_1)$. If R_1C_1 exceeds the attack time of the first order loop the new phase-lock loop is stable. It is critically damped when R_1C_1 is approximately four times the attack time and has good step response for R_1C_1 between 1 and one and five times the attack time. The solid curve in Figure 10 is the magnitude of the open loop gain of the second order loop assuming $R_1 = R_2$. Figure 12 compares the step response of a first order loop to that of a second order loop with R_1C_1 equal to the attack time.

The second order loop increases the long-term gain by the open loop gain of the second operational amplifier provided that the leakage resistance, R_l, of the capacitor is sufficiently large. The open loop frequency offset between the two oscillators which can be tolerated is therefore increased to a limit determined either by the maximum voltage swing of the second amplifier or the maximum tuning available in the VCO. The second order loop can be implemented with a single operational amplifier rather than the two which were shown for clarity. In this case the attack time is adjusted by varying the input resistor, R_2, of the operational amplifier, A_2 and omitting amplifier A_1 in Figure 11.

ACKNOWLEDGMENTS

The authors would like to thank Charles Stone of Austron Inc. for many helpful conversations and in particular for his advice concerning low noise transistors and other components.

REFERENCES

[1] Donald Halford, A.E. Wainwright, and James A. Barnes, in Proc. 22nd Annual Symposium on Frequency Control (NTIS Accession No. AD 844911), 1968, p. 340.

[2] F. M. Gardner, Phaselock Techniques (John Wiley, New York, 1966).

[3] Don Kesner, EDN 5 Jan 1973, p. 54.

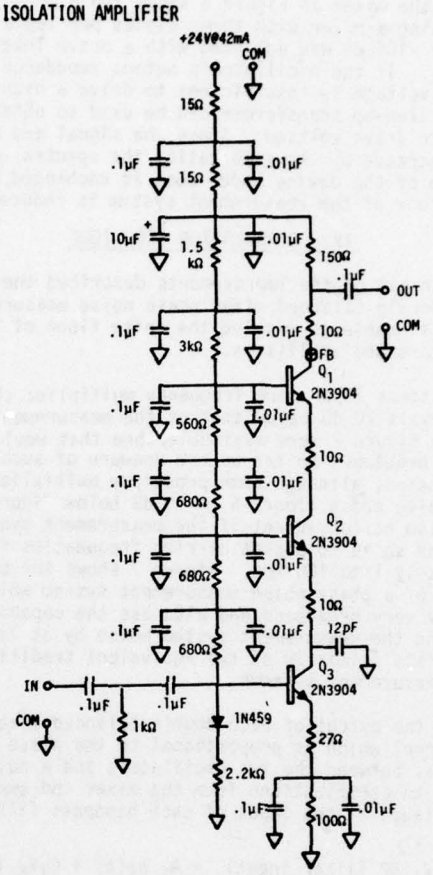

Fig. 1 Schematic of 1 MHz to 200 MHz isolation amplifier. The isolation is -120 dB at 5 MHz. Art work for this amplifier is available from the authors.

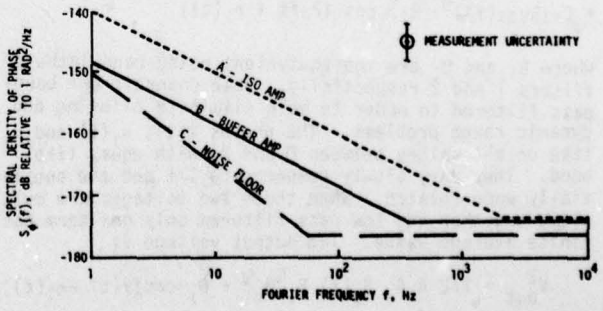

Fig. 2 Spectral density of phase, $S_\phi(f)$, for A) the isolation amplifier of Figure 1 at 5 MHz, B) the buffer amplifier of Figure 6 at 5 MHz, C) noise floor of the measurement systems of Figure 4 with a single diode mixer.

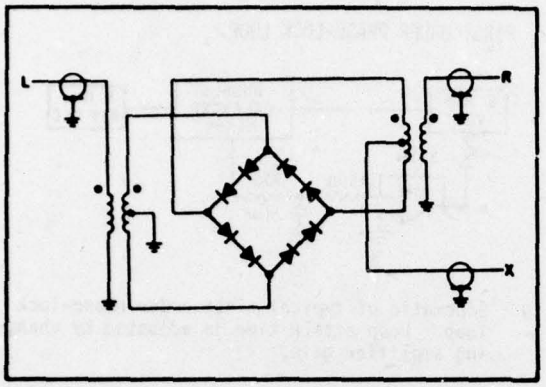

Fig. 3 Schematic of a double balanced mixer. This particular mixer is shown with two diodes in each leg.

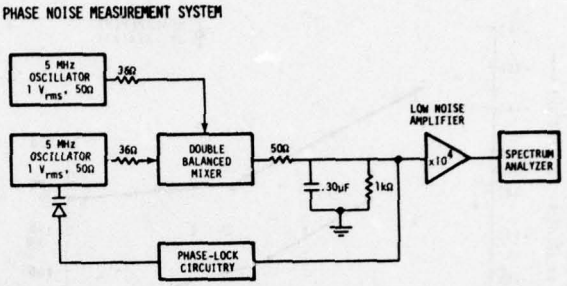

Fig. 4 Typical system for measuring $S_\phi(f)$ of a pair of equal frequency oscillators. Noise floor for this system is shown in Figure 2, curve C.

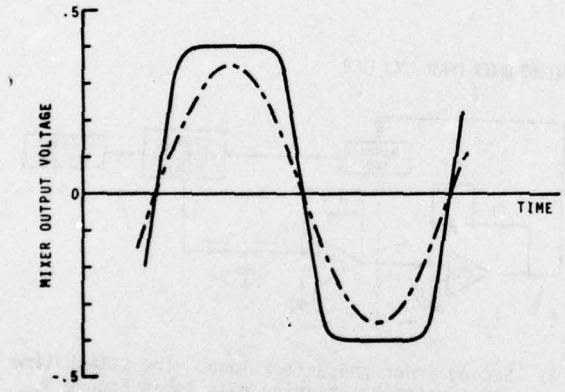

Fig. 5 Filtered waveform at the output (x port) of double balanced mixer due to frequency difference between signals at R and L ports. The solid curve is obtained at high drive levels while the dashed curve is obtained at low drive levels.

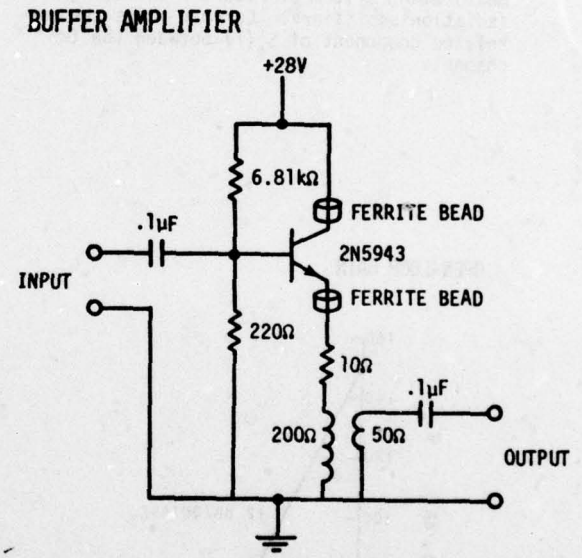

Fig. 6 Very low noise buffer amplifier which can be used to drive mixers. The noise performance is shown in Figure 2 curve B.

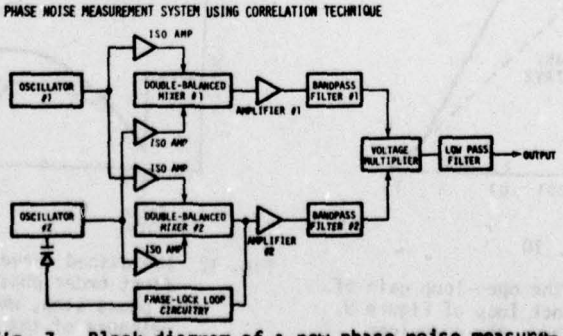

Fig. 7 Block diagram of a new phase noise measurement system which is broadband and features low noise.

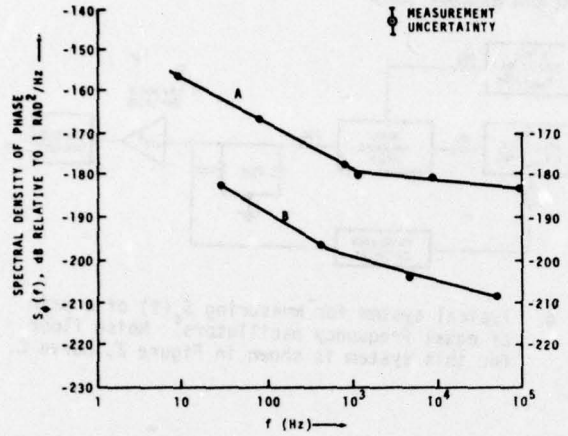

Fig. 8 Curve A shows $S_\phi(f)$ for each channel of the measurement system of Figure 7 excluding the isolation amplifiers. Curve B shows the correlated component of $S_\phi(f)$ between the two channels.

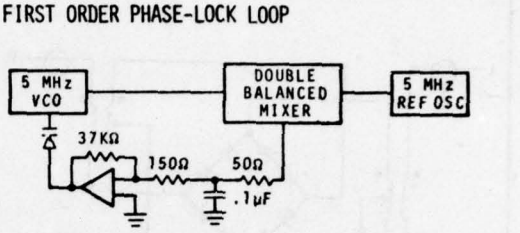

Fig. 9 Schematic of typical first order phase-lock loop. Loop attack time is adjusted by changing amplifier gain.

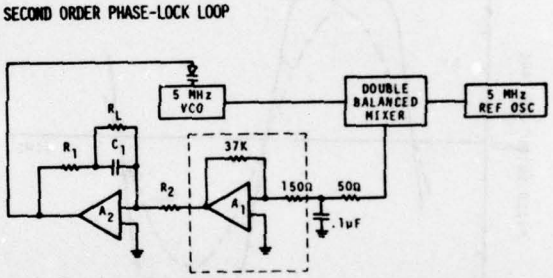

Fig. 11 Second order phase-lock loop. The attack time is adjusted by changing gain as in Figure 9. The time constant R_1C_1 is adjusted to be 1 to 5 times longer than the attack time.

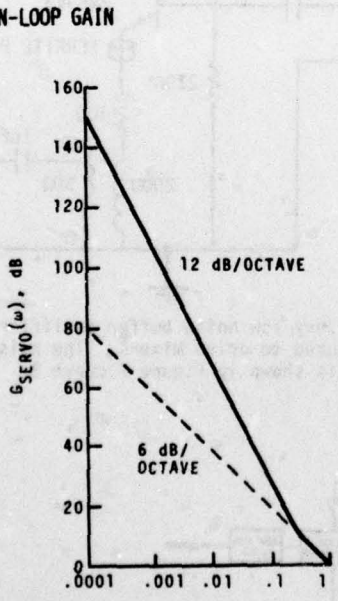

Fig. 10

The dashed curve shows the open-loop gain of the first order phase-lock loop of Figure 9, while the solid curve shows the open-loop gain of the second order phase-lock loop of Figure 11.

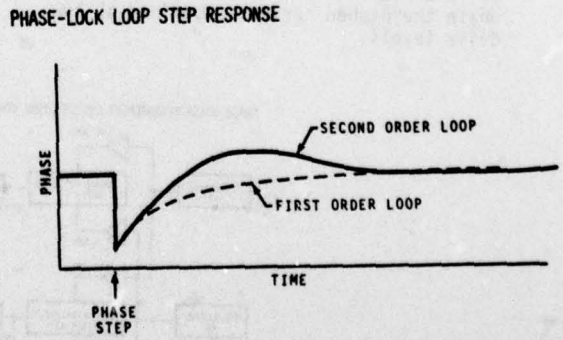

Fig. 12 The dashed curve shows the response of the first order phase-lock loop of Figure 9 to a phase step, while the solid curve shows the response of the second order phase-lock loop of Figure 11, with R_1C_1 = the attack time.

AN ULTRASTABLE LOW POWER 5 MHz QUARTZ OSCILLATOR QUALIFIED FOR SPACE USAGE

Jerry R. Norton
Applied Physics Laboratory
The Johns Hopkins University
Laurel, Maryland

Summary

An Ultrastable Quartz Oscillator has been developed and qualified for use in earth orbiting spacecraft. Units of this design have achieved a frequency stability of 3×10^{-13}. By using hybrid circuit fabrication techniques and a very effective "Super Insulation" system, the redundant oscillator package occupies a volume of 57.6 cubic inches, weighs 2.2 pounds, and requires only 0.6 watt of DC power at an ambient temperature of 25° C.

Introduction

A series of space qualified oscillators was developed at the Applied Physics Laboratory beginning in the late 1950s for use in the Navy Navigation Satellites (formerly called Transit satellites). Each successive design has resulted in improved oscillator performance and an increasingly accurate satellite navigation fix capability.

The primary objective of the new oscillator design was to develop a very high performance unit that required little power and minimal weight and volume. The oscillator must survive a vigorous vibration environment during a Scout rocket launch and retain its high performance during a minimum 5 year mission in an earth orbit environment of 600 nmi. A uniformly predictable aging rate without frequency perturbation is also desirable.

Design Details

Figure 1 shows the assembled oscillator package (top removed) with the two independent oscillators. Mounted along the upper side of the package are two conventional PC (printed circuit) boards, one for each oscillator. Located on each board is a 5 MHz output amplifier, a voltage regulator, and an oven heater power amplifier. A cylindrical Vacuum Flask Assembly below each PC board contains an Oscillator/Temperature Control Assembly which, together with the PC board, comprise a complete oscillator.

The Vacuum Flask Assembly is suspended within the oscillator package by a series of nylon cords. Four groups of cords, two of which are visible in the photograph and two identical groups below each flask, form a dynamic suspension system which isolates the flask from vibration. By varying the stress in the cord system, the dynamic characteristics may be adjusted to achieve the desired vibration isolation. Due to the very low thermal conductivity of nylon cord, the suspension system also contributes to thermal isolation of the Oscillator/Temperature Control Assembly located within the vacuum flask.

A description of the Vacuum Flask Assembly beginning on the inside and working toward the outside follows. Circuits within the Vacuum Flask are physically miniaturized by using hybrid circuit fabrication techniques. Shown in Figure 2, circuitry for the oscillator is fabricated on a miniature PC board which is 1.2 inches in diameter. Chip component resistors, capacitors, and transistors with typical dimensions of 80 x 50 x 10 mils are simultaneously attached to the PC board by a solder reflow technique. A modified Pierce oscillator circuit is used with negative feedback applied to reduce flicker noise and stabilize circuit gain.

Figure 3 shows the oscillator circuit board attached to the left end of the Oscillator/Temperature Control Assembly. A protective cap is placed over the board to prevent damage to the small chip components. On the opposite end of the assembly is the oven control circuitry, also fabricated by hybrid circuit techniques. A single proportional oven controller is employed to maintain the quartz crystal and critical portions of the electronic circuits at the turning point temperature of the crystal. Considerable effort was expended to not only maintain the crystal at its turning point temperature, but to minimize thermal gradients within the Oscillator/Temperature Control Assembly.

A 5 MHz 5th overtone quartz crystal manufactured by Bliley Electric (BG61AH-5S) is enclosed in the crystal housing between the oscillator and the oven control boards. An oven heater is wound on the outside of the crystal housing.

The effort to minimize thermal gradients was continued in the thermal insulation system with the use of a form of insulation called "Super Insulation". This insulation consists of alternate layers of radiation reflective aluminized Mylar and a porous low thermal conductivity Tissuglas paper. A cutaway drawing (Figure 4) shows the layers of insulation wrapped around the Oscillator/Temperature Control Assembly. Layers of insulation are also placed at each end of the assembly. The joints between the rolled horizontal and the stacked vertical insulation layers represent the major thermal leakage paths in the insulation system. Therefore, in an effort to redistribute and equalize the thermal paths, a metal shell with a high thermal conductivity was placed between inner and outer groupings of the insulating blanket. "Super Insulation" has a thermal conductivity three orders of magnitude less than Urethane Foam.

In order to realize the insulating qualities of "Super Insulation" the system

must be evacuated to a pressure of 10^{-4} torr. This is accomplished very simply by venting the enclosure to the vacuum of outer space once orbit is achieved.

Performance Data

The goals for oscillator performance were realized in the present design. Figure 5 shows typical 24 hour drift rates for two oscillators. Data for oscillator A covers a 14 day period and has an average daily drift rate of 1.58×10^{-11}/24 hours. Oscillator B has an average daily drift rate of 1.94×10^{-11}/24 hours for a 17 day period. A plot of fractional frequency stability (Allan Variance) for averaging times (τ) from 0.1 sec to 1000 sec is presented in Figure 6 (measurement system noise bandwidth is 60 kHz). This graph is a composite of data from several oscillators, the bar at each (τ) indicates the maximum and minimum data from the group of oscillators. The line connecting the various averaging times is the average Allan Variance for the group of oscillators. Oscillator performance as a function of temperature varying from -23° C to +55° C is shown in Figure 7. Frequency shift $\Delta f/f$ is relative to an ambient temperature of 25° C. The maximum frequency shift is 1×10^{-12}/° C. Total power consumption for the oscillator, electronics, and oven heater as a function of temperature is also presented.

Other operating parameters are:

Frequency shift resulting from a change in oscillator load resistance of ±10% is 7.4×10^{-12}.

Frequency shift resulting from a change in input power supply voltage of ±5% is 6.42×10^{-12}/volt.

Spurious response
Harmonic: 55 dB below 5 MHz carrier
Non-harmonic: 65 dB below 5 MHz carrier in a 100 Hz/BW

Figure 8 is a typical strip chart recording of $\Delta f/f$ as a function of time between two oscillators.

Both natural and synthetic quartz material has been used to fabricate resonators. The synthetic quartz was manufactured by Sawyer Research Products, Inc. and was Swept Electronic Grade material. Comparable performance is achieved from either type of quartz resonator when used in oscillators. Synthetic quartz resonators are used for flight hardware because of less sensitivity to radiation effects from the orbital environment.

Quality Assurance and Test Program

In order to achieve a 5 year life, component types are selected with great care. Components are purchased to carefully written specifications, and each is screened to eliminate visual and electrical defects during incoming inspection at APL. All components used in the construction of flight qualified hardware are operated at 70% or less than the manufacturer's maximum rated parameters. Components which might be susceptible to the radiation levels found at 600 nmi altitudes receive additional screening in order to eliminate those which are sensitive to radiation. Throughout the fabrication of an oscillator, numerous visual and electrical inspections are made by both quality assurance personnel and the Design Engineer to ensure that assembly is not only in accordance with applicable drawings and good workmanship practics, but also the high performance intent of the design.

Once fabricated, each oscillator package undergoes a very extensive test program. During thermal vacuum testing to simulate the space environment, all pertinent electrical parameters are tested. The oscillator package has been qualified to withstand levels of up to ± 25 g of sinusoidal vibration between 90 and 150 Hz.

In addition to the above, the oscillator package contains two completely independent 5 MHz quartz oscillators to provide redundancy if the operating unit should develop erratic performance or fail during the 5 year period. Only one oscillator is operated at any given time. The redundant oscillator package has a volume of 57.6 cubic inches and weighs 2.2 pounds. A photograph of the assembled 5 MHz Ultrastable Oscillator package is shown in Figure 9.

Conclusion

The design goals for a new generation quartz oscillator have been fulfilled. Compared to the last generation oscillator design, several operating parameters were improved by a factor of ten and weight, volume, and power consumption have been reduced. As described herein, a redundant oscillator package has been fabricated and fully qualified for use in an earth orbiting satellite.

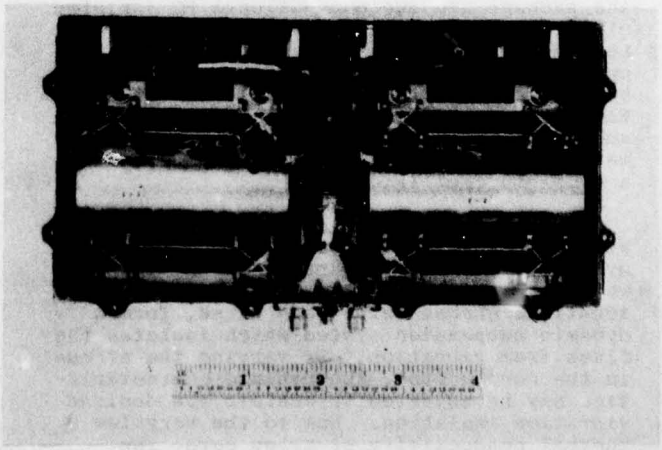

Figure 1

Ultrastable 5 MHz Quartz Oscillator Package

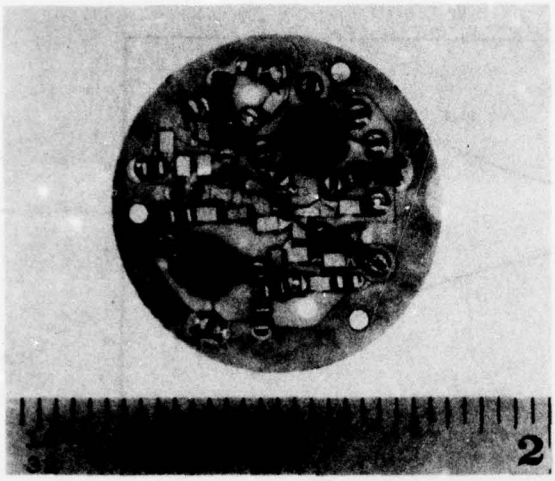

Figure 2 - Oscillator Hybrid Circuit

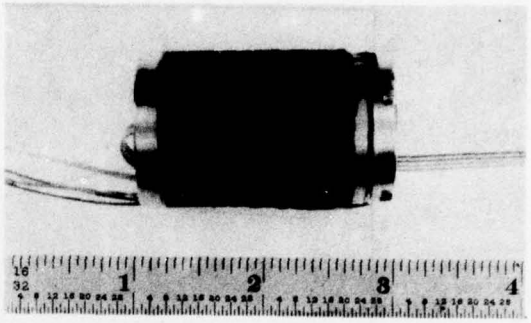

Figure 3

Oscillator/Temperature Control Assembly

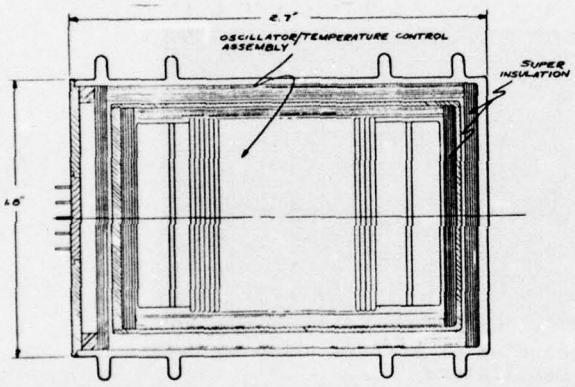

Figure 4 - Vacuum Flask Assembly

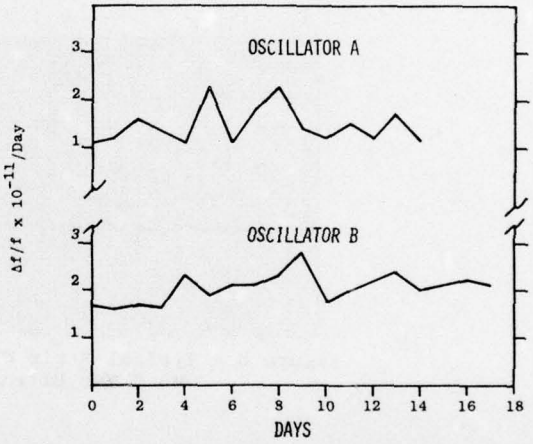

FIGURE 5 24 HR. DRIFT RATE (TYPICAL)

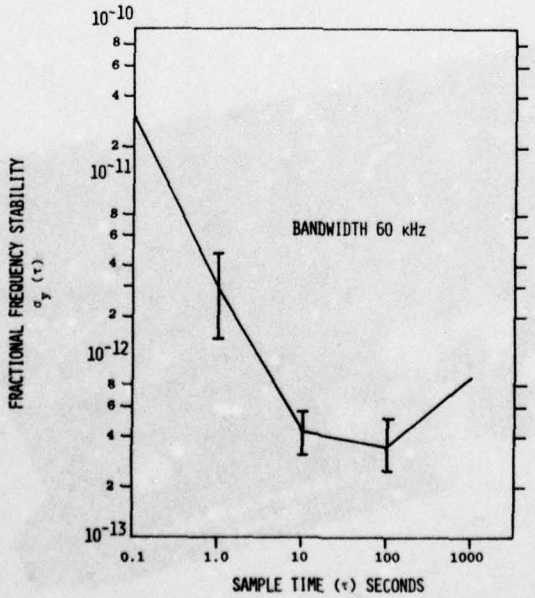

FIGURE 6 ALLAN VARIANCE VS. SAMPLE TIME

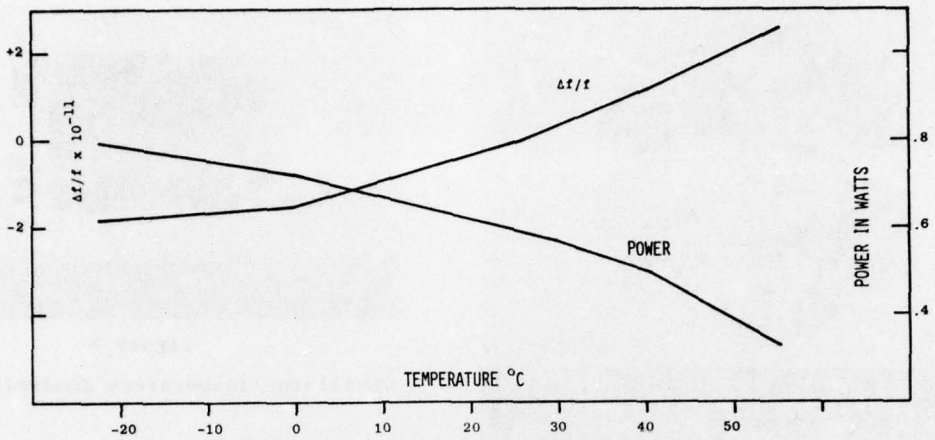

FIGURE 7 OSCILLATOR PERFORMANCE AS A FUNCTION OF TEMPERATURE

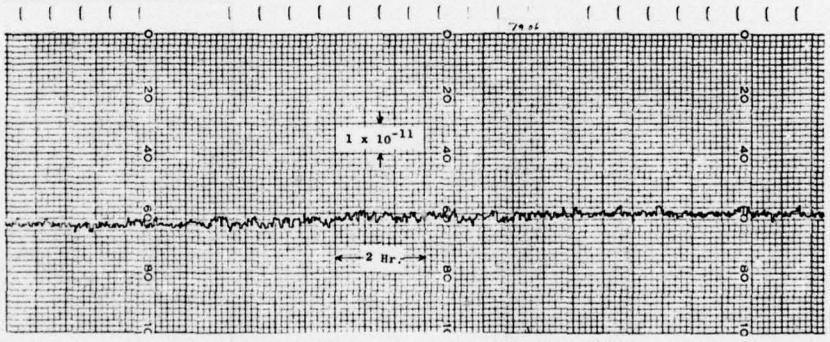

Figure 8 - Typical Strip Chart Recording of $\Delta f/f$ Vs. Time Between Two 5 MHz Ultrastable Oscillators

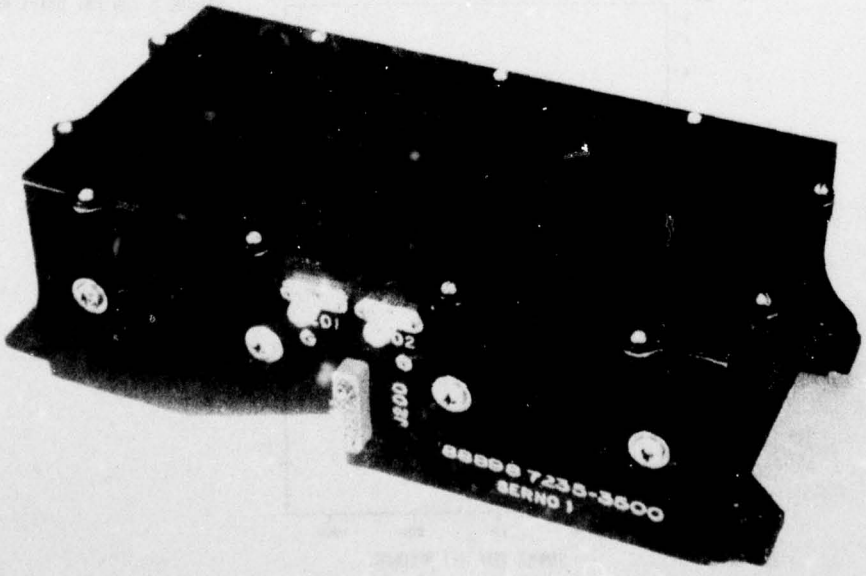

Figure 9 - Assembled 5 MHz Ultrastable Oscillator Package

STABLE OSCILLATOR FOR PIONEER VENUS PROGRAM

Martin B. Bloch, Marvin P. Meirs and Ted M. Robinson
Frequency Electronics, Inc.
New Hyde Park, New York

Summary

Frequency Electronics, Inc. has developed a stable quartz crystal oscillator for the Pioneer Venus Program. This oscillator maintains a total accuracy of lppl0^{9} during the approach to Venus; during the severe deceleration that occurs in entering the Venusian atmosphere, which is approximately 100 times as thick as the Earth's atmosphere, and the descent to the surface of Venus, where it experiences a severe heat rise to 340^{0} F.

The techniques of the design are discussed with regard to meeting the requirements of small size, low weight, low power, and good frequency stability. A stainless-steel Dewar flask was used to survive the 700 G deceleration pulse, and also provide the required insulation to meet the other requirements.

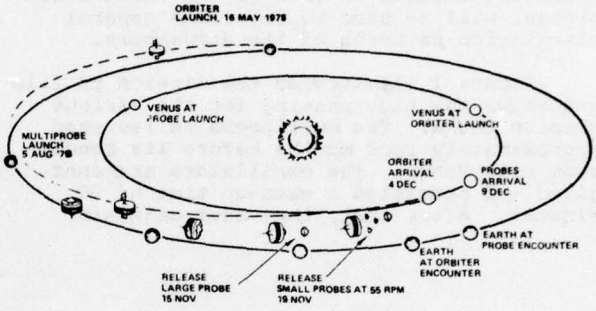

PIONEER VENUS MISSION PROFILE

FIGURE 1

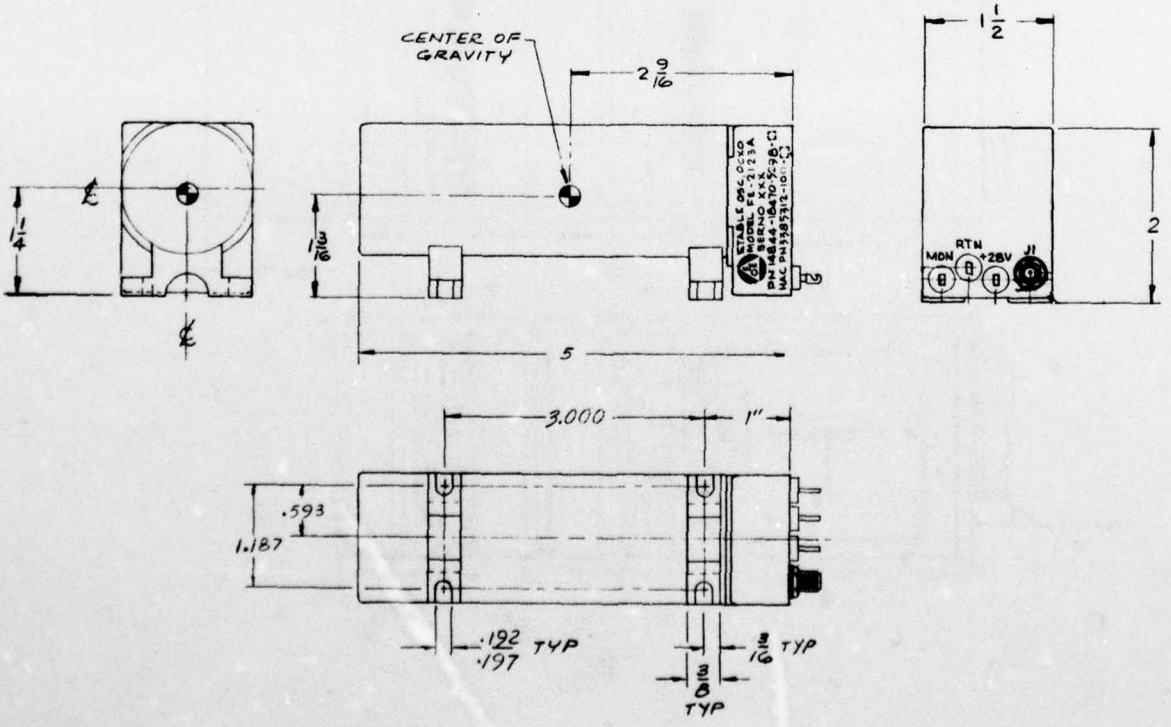

STABLE OSCILLATOR, OCXO
PIONEER VENUS
MODEL FE-2123A, OUTLINE DRAWING
FIGURE 2

Introduction

The Pioneer Venus Program is a scientific mission designed to learn more about that planet. The mission consists of two spacecraft; an orbiter, which will orbit the planet Venus, and a multiprobe spacecraft, which will release and deploy one large probe and three small probes into the Venusian atmosphere for eventual landing on the surface of Venus. The stable oscillators, which are located in each of the three small probes, will be used to determine general circulation patterns of the atmosphere.

Figure 1 illustrates the mission profile and shows the time phasing for the various mission tasks. The multiprobe is launched approximately four months before its rendezvous with Venus. The oscillators are energized and permitted a warm-up time of 90 minutes. After that, they must maintain frequency accuracy through a 22 minute pre-entry phase, entry, and a 60 minute descent phase.

The stable oscillator is located on th upper shelf of the small probe. The probe pressurized with one atmosphere of nitrogen

Design

The physical measurement of these osci lators was limited to 1.5" x 2" x 5". The actual outline configuration is shown in Figure 2. Most of the circuitry is housed the 1.5" diameter tube portion. A detailed view of this A1 assembly is shown in Figure

A1A1 is the oscillator printed-circuit board, which is located in the sealed inner oven enclosure, Item 17. Printed-circuit board, A1A2, is the inner-oven control and

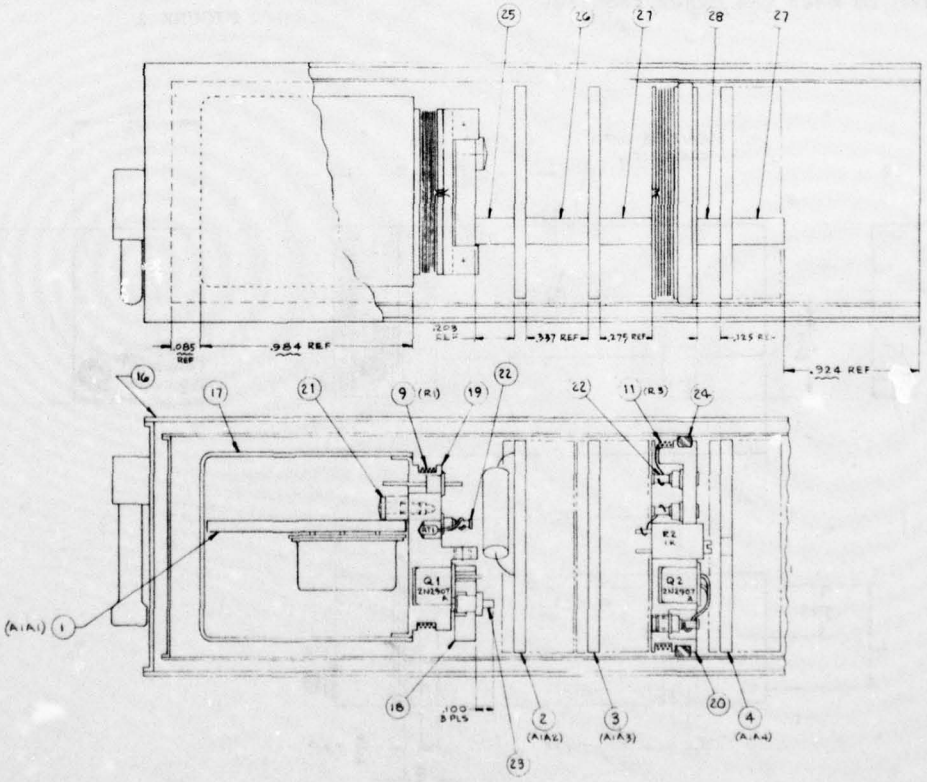

A1, OSCILLATOR SUBASSY
STABLE OSCILLATOR, OCXO
PIONEER VENUS
FIGURE 3

AD-A046 089 ARMY ELECTRONICS COMMAND FORT MONMOUTH N J F/G 9/5
PROCEEDINGS OF THE ANNUAL SYMPOSIUM ON FREQUENCY CONTROL (30TH)--ETC(U)
1976 H K ZIEGLER

UNCLASSIFIED NL

4 OF 6
AD A046089

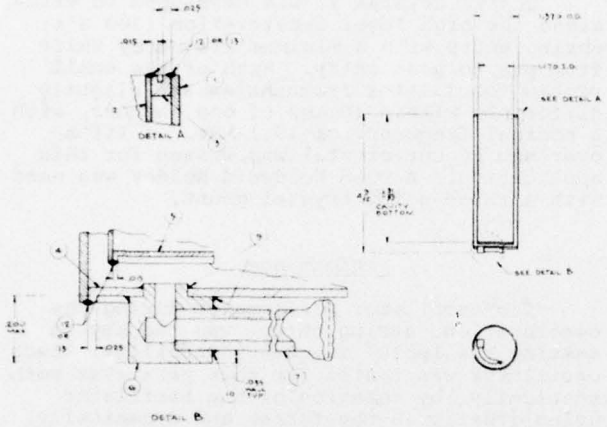

FLASK, VACUUM
STABLE OSCILLATOR, OCXO
PIONEER VENUS
FIGURE 4

sets the temperature on heater R1, Item 9, using sensor RT1. A1A3 is the output amplifier printed-circuit board, and A1A4 is the outer-oven control printed-circuit board, which controls heater R3, Item 11. The double oven was used to precisely control the crystal temperature during the severe temperature excursion during the descent to Venus.

All of this circuitry is located inside the stainless-steel Dewar flask, Item 16. A detailed drawing of the flask is shown in Figure 4. Electron Beam welding techniques were used to manufacture this flask. An inner wall thickness of 0.015 inch was used to minimize conduction losses through the walls of the Dewar. The stainless-steel Dewar was used in lieu of a glass Dewar to meet the high G acceleration requirements.

Figure 5 shows a detailed photograph of the stable oscillator. The voltage regulator printed-circuit board was mounted outside the Dewar flask, on the cover assembly. This

FREQUENCY ELECTRONICS MODEL FE-2123A
PIONEER VENUS PROBE
OCXO, DISASSEMBLED VIEW
FIGURE 5

cover was then solder sealed to the housing, to insure that the oscillator would be maintained in a constant pressure atmosphere.

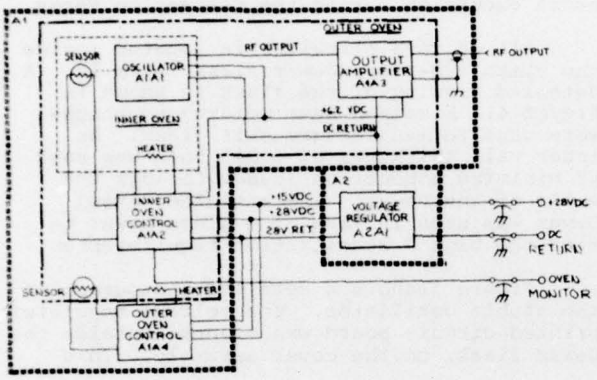

BLOCK DIAGRAM
STABLE OSCILLATOR, OCXO
PIONEER VENUS
FIGURE 6

A block diagram of the stable oscillator circuitry is shown in Figure 6. The oscillator circuitry used was a Butler configuration. This configuration used a minimum number of parts, which kept the size to a minimum, and also was capable of achieving the $1ppl0^9$ stability over the 82 minute mission environment. The schematic of the oscillator circuit is shown in Figure 7.

Quartz crystal Y1 was developed to withstand the high level deceleration (700 G's) during entry with a minimum frequency shift from pre to post-entry. Each of the small probes' oscillator frequencies are slightly different, within 10 kHz of one another, with a nominal frequency of 19.1 MHz. A fifth overtone FC Cut crystal was chosen for this application. A TO-8 Koldweld holder was used with a three-point crystal mount.

Performance

The oscillator performance during the deceleration, during entry, was the key to meeting the $1ppl0^9$ frequency stability. Each oscillator was tested for this parameter both statically, by rotation of the oscillator using gravity as the force, and dynamically, by accelerating up to 700 G's (qualification level) and 565 G's (acceptance level) by use of a hydraulic centrifuge and recording data, both immediately before and immediately after the acceleration. Figure 8 shows the frequency change due to the static rotation of the oscillator. Figure 9 is the summary data from the dynamic acceleration testing of the same oscillator. After each oscillator was tested, it was then rotated to the optimum axis to obtain minimum frequency change.

Figure 10 shows the acceptance level thermal profile for the total 82 minute mission. The mounting surface temperature goes from -4° F to $+122^{\circ}$ F, while the convected heat flux inside the probe varies from -4° F to $+325^{\circ}$ F. The upper curve shows the frequency variation as a function of time when exposed to this environment.

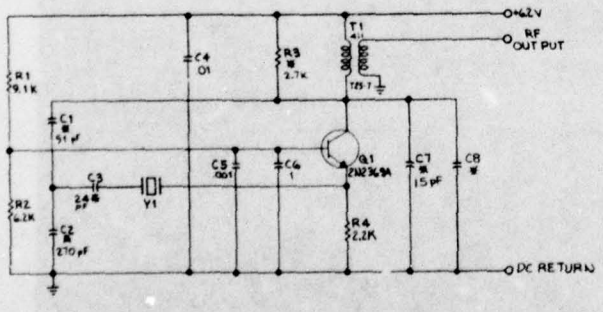

A1A1, OSCILLATOR
STABLE OSCILLATOR, OCXO
PIONEER VENUS
FIGURE 7

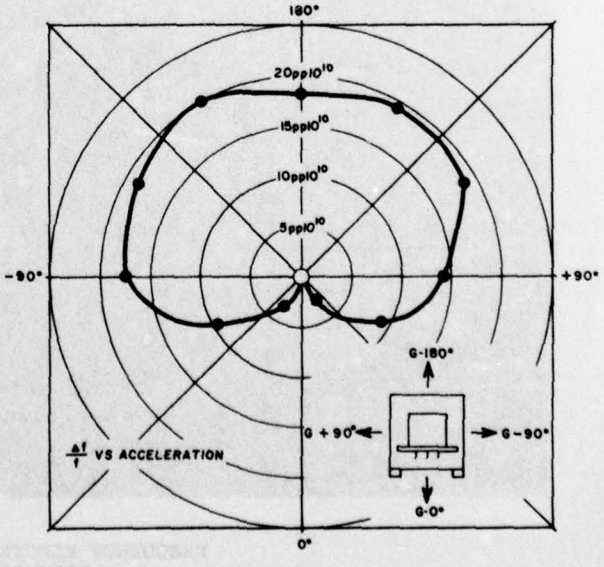

FREQUENCY VS STATIC 'G' ACCELERATION
FIGURE 8

The table of Figure 11 is a summary of the pertinent stable oscillator requirements and the results actually received. The oscillators used slightly more energy than originally anticipated. This was due primarily to the stainless-steel Dewar flask, which has a thermal loss factor approximately 50 % greater than a glass Dewar flask. Experimentation has been performed on a titanium Dewar flask, whose thermal loss is equivalent to the glass Dewar. All other design objectives were met or exceeded.

ANGLE	$\frac{\Delta f}{f_o}$ pp10^{10}	
	565 G's	700 G's
0°	-4.7	-4.8
- 90°	-0.9	+1.4
+ 90°	+2.4	+4.7
-165°	-1.0	+1.4

FREQUENCY VS DYNAMIC HIGH 'G' ACCELERATION
FIGURE 9

Conclusions

Oscillators can be designed to meet deceleration forces up to 700 G's, through the use of unconventional stainless-steel Dewar flasks, as opposed to glass Dewar flasks. With careful design of crystals and attention to temperature characteristics, frequency stabilities of ± 1pp10^9 are achievable within operating temperatures of - 4° F to + 122° F, as exhibited on hostile environments, such as found on Venus and other extra-terrestial planets in outer space.

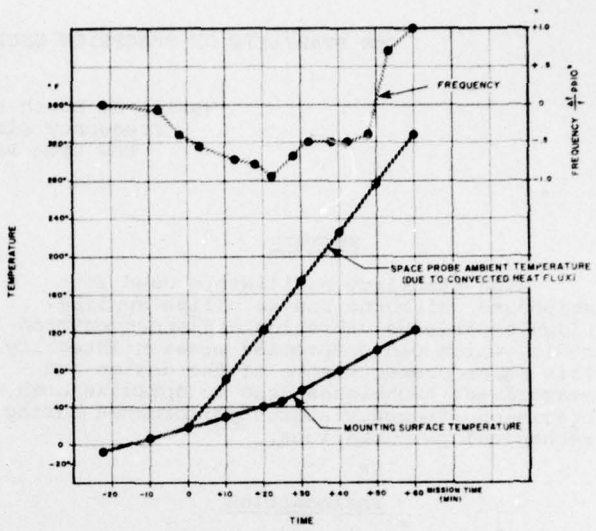

MISSION THERMAL PROFILE
PIONEER VENUS
FIGURE 10

PARAMETER	OF[illegible]	ACTUAL
Size	5x1	5x1.5 (Dia.)
Weight	14 oz.	8.5 oz.
Input Power (25.2 to 33 Vdc)	7 W peak	6 W peak
Warm-Up Time	90 min.	90 min.
Warm-Up Energy	175 W-min.	210 W-min.
Accuracy After 90 min.	1 pp10^6	5 pp10^8
Frequency Stability (82 min. mission)	±1 pp10^9	±1 pp10^9
Phase Noise (6 Hz BW)	.017 degrees Rms	.002 degrees Rms

PIONEER VENUS
19.1 MHz STABLE OSCILLATOR
TABLE OF CHARACTERISTICS
FIGURE 11

THE STABILITY OF PRECISION OSCILLATORS IN VIBRATORY ENVIRONMENTS

Martin B. Bloch and Alfred I. Vulcan
Frequency Electronics, Inc.
New Hyde Park, New York

Summary

High stability oscillators used for shipboard, airborne and satellite applications experience vibration and shock environments, which can compromise mission integrity. This paper presents some of the design and measurement techniques used to optimize high precision frequency source performance during mechanical perturbations.

Introduction

In assuring mission integrity, both the survivability aspects of oscillator design as well as the minimization of phase noise induced by vibration are studied. In the following paragraphs data is presented for ship and aircraft frequency standards operating at 5 MHz, as well as higher frequency, satellite VCXO's, TCXO's, and ovenized units. Although many factors contribute to phase noise degradation, those which have the major impact and are emphasized in this paper are:

1. Crystal Characteristics
2. Circuit Configuration
3. Vibration Isolation and Package Design

The design guidelines discussed below have proven to be useful in minimizing induced noise.

Designing For A Mission

It is imperative that for a given mission, the complete shock and vibration spectra be defined, including magnitude, direction, frequency profile, and mechanical resonance characteristics in mounting structures. Once these factors are determined, the optimum oscillator location in the vehicle, axis orientations, and electrical characteristics are chosen to minimize induced frequency instabilities.

Several programs for which hardware was developed and tested with these parameters as design drivers are itemized in Table 1.

Survivability Aspects

It is important to differentiate between engineering practices, which are directed at increasing the probability of an oscillator "Living-Thru" a relatively short term high "G" period, and those which minimize phase noise during lower level events lasting for a

TABLE 1

SUMMARY OF OSCILLATOR STABILITY AND SHOCK/VIBRATION REQUIREMENTS

PROGRAM	STABILITY	SHOCK OR VIBRATION
GPS Master Oscillator	5×10^{-12}/second -100 dBc at 100 Hz	$0.5G^2$/Hz survivability
Space Shuttle Master Oscillator	-130 dBc at 100 Hz	$0.12G^2$/Hz operating
Space Shuttle 4 Channel VCXO	45 millidegrees in 300 Hz bandwidth	$0.1G^2$/Hz operating
Mariner-Jupiter-Saturn Probe	4×10^{-12}/second	$0.1G^2$/Hz survivability
Pioneer-Venus Probe	$\pm 1 \times 10^{-9}$	705 G deceleration operating
WSQ-2 shipborne Oscillator	1.8 millidegrees	0.1 inch double amplitude operating
Airborne Command Post Master Oscillator	1.8 millidegrees	$0.0028G^2$/Hz operating

longer period of time. Quite often a design tailored for a specific application necessarily results in compromising other performance aspects. For example, utilization of a steel or titanium Dewar flask for high shock and vibration environments results in a slightly heavier and less thermally efficient source. Thus, a complete trade-off study must be made to define the best overall design for a given situation.

An oscillator which must survive a severe shock, and/or vibration event, uses ruggedized construction techniques, including ribs, braces, etc., necessary to ensure mechanical integrity. The development of the metal Dewar flask has enabled us to design physically smaller units than those utilizing glass flasks, which require a large volume of internal vibration and shock isolating material. The thermal efficiency of a steel flask is typically 35 % worse than glass, but with titanium, the efficiency is comparable to glass. The use of metal flasks has proven feasible for both the GPS and Pioneer-Venus Missions. Another important aspect of survivability-directed design practices is the encapsulation of components and subassemblies within an oscillator to prevent lead breakage or catastrophic component failure during high-level shock and vibration. Manufacturing techniques, which minimize the probability of this type of failure, also help to reduce phase noise levels during lower level vibrations. Component bonding to surfaces, which are mechanically resonant, at an induced vibration frequency, or to structures whose movement is not attenuated by internal mechanical isolating materials, should, of course, be avoided. A preliminary mechanical analysis of the internal subassemblies is made, taking into account resonant points and G loading factors. Quite often, a low level sine-vibration scan is made of these parts to get the required data. After this is accomplished, the design of internal resilient mounts is undertaken, using pre-stressing factors and material elastic constants, to optimize the low-frequency roll-off characteristics of the complete mounting system. A mechanical mock-up can then be fabricated and tested to verify the design. When the mechanical constraints of a given package do not allow sufficient isolation at low frequencies, external vibration isolators must be considered.

Of prime importance in attaining the required goals is the design of the crystal resonator. All of the techniques used to minimize G effects at the crystal are useless unless the crystal is properly designed and located in the assembly. The following describes some of the design criteria and experimental results obtained on crystal oscillators manufactured for various high-vibration environments.

Factors Affecting Oscillator Stability During Vibration

Theoretically, any frequency or phase determining element in an oscillator is a potential noise inducer. Fortunately, the major contributors can be isolated by the use of a computerized worst-case analysis, which relates output frequency to component value variations. All paper analysis, as well as data taken on operating devices, indicate

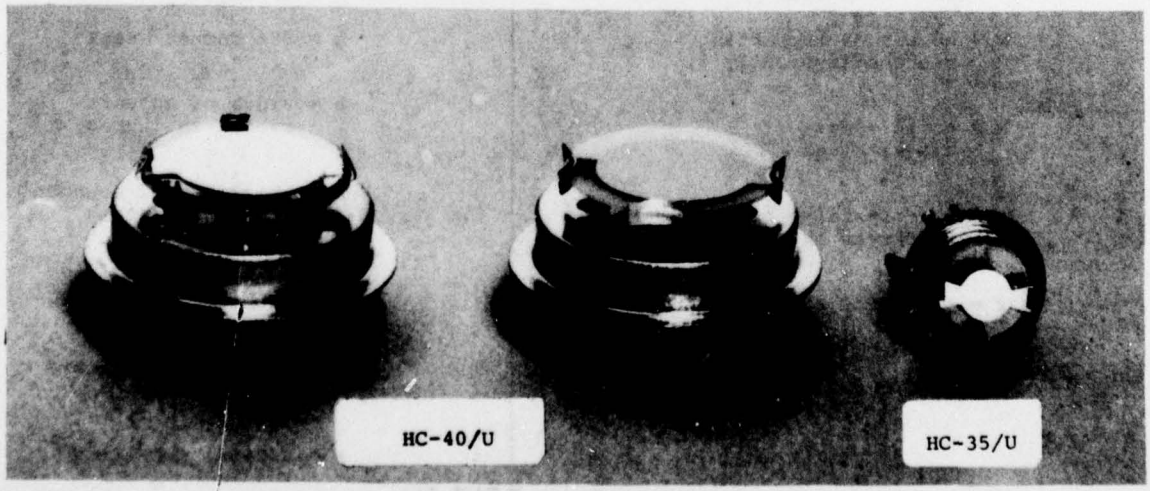

FIGURE 1

3 CRYSTAL UNITS

that the quartz resonator is the major contributor of vibration induced phase and frequency noise.

For a given oscillator circuit design in a specified environment, the three (3) major factors contributing to vibration induced phase noise are the crystal parameters, the circuit configuration, and the effect of vibration isolation.

Crystal Effects. The crystals utilized in the oscillators described in the following paragraphs are manufactured under stringent quality controls, which ensure their suitability to high reliability applications. Figure 1 shows typical resonators fabricated for these applications. Third and Fifth Overtone 5 MHz units in HC-40/u(C) holders, as well as Fundamental, Third and Fifth Overtone HC-35/u(TO-5) resonators operating in the 15 MHz to 22 MHz range were used in the described units.

The crystals are fabricated using high vacuum technology, hydrogen firing and cold sealing. Thermal compression or epoxy bonding are used for electrode adherence.

Of fundamental importance is ensuring that the mechanical self resonance of the crystal lies well outside of the vibration input spectra. Figure 2 is the basic equation which determines the crystal structure resonance. For all of the crystals used, these resonances range from 3000 to 4500 Hz. Data taken with 2, 3, 4, and 6 point mounts, indicates that the 3 point mount is the most suitable from the standpoint of high survivability and induced phase noise. In addition, stresses set up in the crystal blank with 4 and 6 point mounts cause unpredictable temperature performance with these resonators. This is important in applications requiring a high degree of frequency repeatability after temperature and power cycling.

All of the crystals to be used in hard environments are screened with a slow-scan sinusoidal vibration at levels of 2 to 10 G's, from 10 to 2000 Hz, in 3 axes. A transmission jig is used for this testing with the

CALCULATION FOR CRYSTAL STRUCTURAL RESONANCE

$$f_r = \frac{\sqrt{N}}{2\pi}\sqrt{\frac{EIg}{Wl^3}} = \frac{\sqrt{N}}{2\pi} \times \sqrt{\frac{E\ (bh^3/12)\ g}{Wl^3}}$$

Where: $I = \frac{bh^3}{12}$ = 2nd moment of area of ribbon

N = number of supporting ribbons (typically 3)

$W = \pi r^2 tp$ = mass of cystal blank

t = k/f crystal = resonator thickness in inches

r = radius of resonator in inches

$k = 65.4 \times 10^3$ inch hertz

$f_{crystal}$ = fundamental frequency of crystal in hertz

g = 386 inches/(sec)^2

b = width of support ribbon in inches

h = thickness of support ribbon in inches

l = length of support ribbon in inches

$E = 30 \times 10^6$ lbs/square inch

P = 0.09563 lbs/(inch)^3

f_r = 3517 Hz

FIGURE 2

CALCULATION FOR CRYSTAL STRUCTURAL RESONANCE

minimum loss frequency and series resistance being monitored. Crystals with even momentary anomalies in either parameter are rejected. This sine scan tests the integrity of the mounting structure and bond quality, and provides a valuable indication of wafer mounting stresses.

Given an electrical specification for an oscillator, the choice of resonator, i.e., AT or FC Cut, as well as the angle of the cut, is generally governed by thermal considerations. The overtone of the resonator is a function of the required stability and pull range. Fortunately, the decisions made regarding these parameters have little effect on the phase noise susceptibility of the resonator, but rather the actual physical design of the device, including lead and bond integrity, as well as surface contouring, is of prime importance. It has been shown repeatedly that the bi-convex crystal has lower phase noise susceptibility than a plano-convex design. Typically, a 6 to 15 dB improvement is attained with the latter, and it is employed for the most stringent applications.

Crystal orientation, relative to the external vibration vectors, is an important consideration when a crystal is mounted in a given assembly. Many missions have a worst axis for vibration, and it is along this axis, that the crystals least susceptible axis should lie, for lowest induced noise. Experimental data indicates that the axis perpendicular to the surface of the crystal is the least sensitive one. Several researchers have published similar results, and from a theoretical standpoint, it appears reasonable since there is minimum energy coupling into the thickness-shear-mode, from normally directed vibration stresses.

Circuit Contributions To Phase Noise. Figure 3 shows a typical high-stability oscillator designed for severe environmental conditions. Although of lesser affect than crystal susceptibility, mechanical stresses set up in active and passive circuit elements, by external perturbations, can seriously degrade oscillator stability, if not considered. Simple flexure of a printed-circuit board, with resulting modulations of stray circuit capacitances at a critical point, is almost impossible to experimentally isolate, and must be eliminated in the early development stages.

Manually variable elements, such as trimmer capacitors and potentiometers, can become noisy with time. This can compromise stability and induce fixed-frequency offsets, of parts in 10^{-9}. It should be a goal of

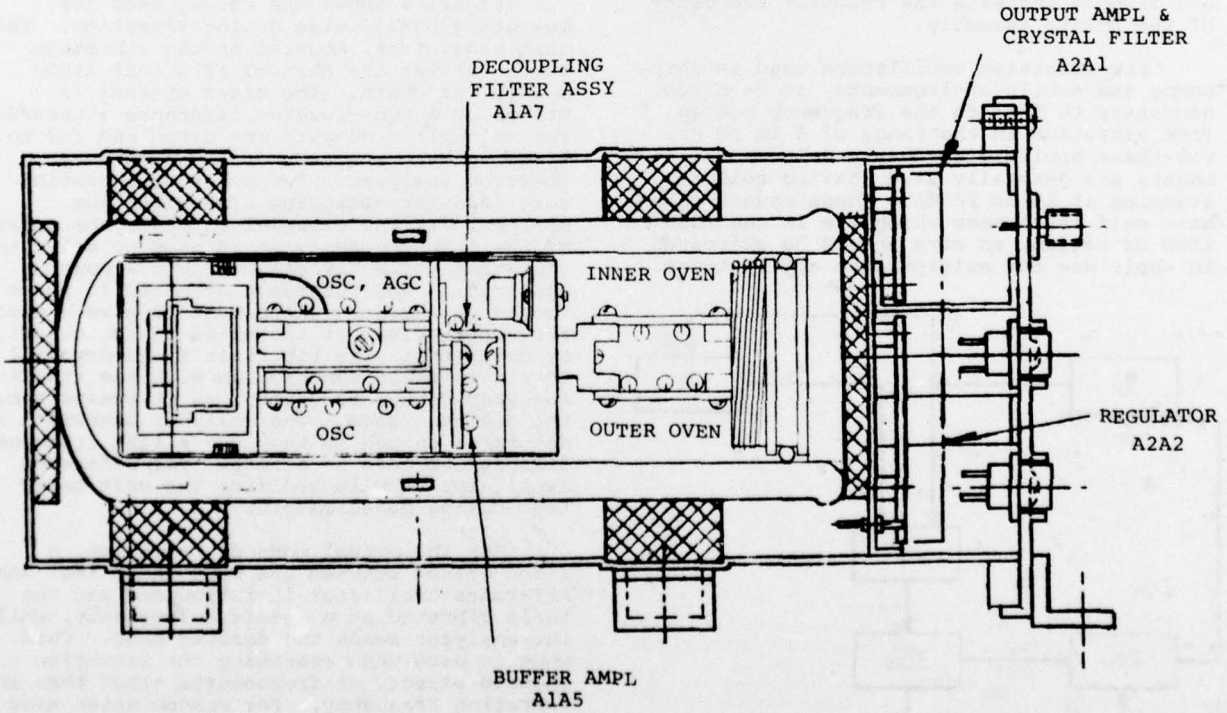

FIGURE 3
CROSS SECTION OCXO
FLTSATCOM OSCILLATOR

every good design to eliminate these elements by replacing them with fixed-value components after the circuit is aligned. Not only will unpredictable sources of future noise be eliminated, but the reliability of the whole assembly increased.

One of the worst offenders in the generation of noise, during shock and vibration, is LC and crystal filters used for spurious signal supression or noise shaping. All of the considerations that go into the selection of the oscillator crystal, should be applied to filter crystals as well; since induced phase modulations in a filter, even though it may be isolated by 100 dB from the oscillator circuit, can degrade phase noise.

Vibration Isolation. The same factors discussed in Survivability Aspects above regarding survivability, are applicable to the reduction of phase noise under vibration. The Dewar flask is mounted on pre-stressed rubber shock mounts, whose low frequency rolloff starts at 120 Hz. The entire assembly within the flask is potted with a lightweight foam material. The density of the foam is carefully controlled during curing to minimize the generation of internal stresses, and provide the proper density for efficient vibration damping. Resilient pads located between subassembly printed-circuit boards are used to increase the resonant frequency of the entire assembly.

For precision oscillators used in shipborne and mobile environments, it is often necessary to isolate the frequency source from vibration in the range of 5 to 30 Hz. For these applications heavy duty shock mounts are generally used, having rolloffs starting at 15 to 20 Hz. These mounts often have self resonances which lie in the 1000 to 1500 Hz region, so care should be exercised in their use for multipurpose applications.

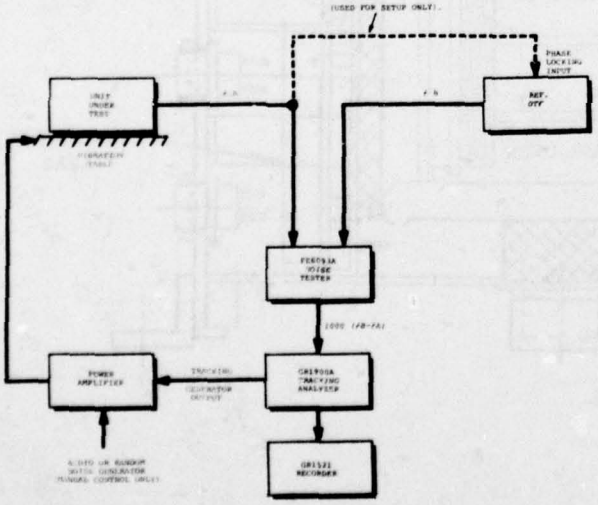

FIG 4
VIBRATION TEST SETUP

NOISE TEST USING INTERPOLATION OSCILLATOR

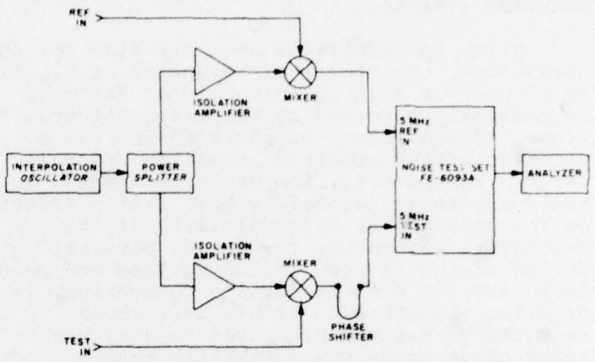

FIGURE 5

Measurement Techniques

Figure 4 shows the set-up used for measuring phase noise during vibration. The unit under test, mounted on the vibration table, drives one channel of a dual X1000 multiplier chain. The other channel is driven by a non-vibrated reference standard. The multiplier outputs are mixed and fed to a tracking wave analyzer or low-frequency spectrum analyzer. Two modes of operation were used for measuring sine-vibration spectra. In the closed-loop mode, the output of the tracking analyzer is used to drive the vibration table directly through a power amplifier. The reference standard is phase locked to the unit under test to give a zero frequency offset at the noise tester output. By doing this, the vibration frequency will remain in exact synchronism with the tracking analyzer center frequency, as it sweeps over the desired range. The analyzer bandwidth is set large enough so that any slight frequency differences have no affect. The reference oscillator is unlocked from the unit under test during measurements.

For the manual mode of operation, a fixed offset between the unit under test and reference oscillator is introduced and the table vibrated at a specific frequency, while the analyzer scans the desired band. This mode is used when searching for vibration induced effects at frequencies other than the vibration frequency. For random noise measurements, the manual mode must, of course, be used.

Although the noise tester operates with 5 MHz input signals, oscillators at other frequencies can be measured by mixing them to

5 MHz with a high stability local oscillator. Figure 5 shows how two identical oscillators can be used in conjunction with an interpolation oscillator to provide data at frequencies other than 5 MHz. By proper phasing, noise contributions of the interpolation oscillator will not affect the data.

When making noise calculations, using the techniques used above, the following criteria is observed:

A. A bandwidth normalization factor is not applied to discrete noise spectra.

B. A 3 dB factor for identical oscillators cannot be subtracted from the noise measurements when the unit under test is vibrated.

C. Measuring equipment must be located as far as possible from the vibration equipment, due to mechanical and acoustical pickup.

D. Interconnecting cables should be secured to non-vibrating structures to reduce extraneous phase perturbations.

Computer analysis of phase L(f) into radians, and Hz deviations, are possible.

Also the affect of phase locked loops in operational situations should be included in data reduction.

Measurement Results

Static Measurements

The most fundamental test of an oscillator, subjected to high environment stresses, is the static orientation test. This consists of rotating the unit through 360° in each of its three orthogonal axes. Figure 6 is a chart showing typical results for a properly designed crystal oscillator. This test rejects poor crystal wafer mounts, improper crystal mounting within the oscillator, and gross component problems. Figure 7 is the radial coordinate plot for the Pioneer-Venus Oscillator showing a maximum offset of 0.9×10^{9}.

FREQUENCY CHANGE DUE TO ORIENTATION DATA SHEET

Degrees	X Axis Orientation	Y Axis Orientation
	Output Frequency	Output Frequency
0°	0 Ref	+ $1pp10^9$
30°	+ $.3pp10^9$	+ $.6pp10^9$
60°	+ $.6pp10^9$	+ $.3pp10^9$
90°	+ $.9pp10^9$	0
120°	+ $1.1pp10^9$	+ $.1pp10^9$
150°	+ $1.3pp10^9$	+ $.2pp10^9$
180°	+ $1.4pp10^9$	+ $.3pp10^9$
210°	+ $.9pp10^9$	+ $.2pp10^9$
240°	+ $.6pp10^9$	+ $.1pp10^9$
270°	+ $.3pp10^9$	0
300°	+ $.3pp10^9$	+ $.3pp10^9$
330°	+ $.1pp10^9$	+ $.6pp10^9$
360°	0	+ $1pp10^9$

CRYSTAL TYPE: AT CUT BI-CONVEX 5MHz
5TH OVERTONE CRYSTAL
THERMO COMPRESSION BONDED

FIGURE 6

FIGURE 7

STATIC 'G' SENSITIVITY

19MHz 5th OVERTONE PLANO CONVEX CRYSTAL

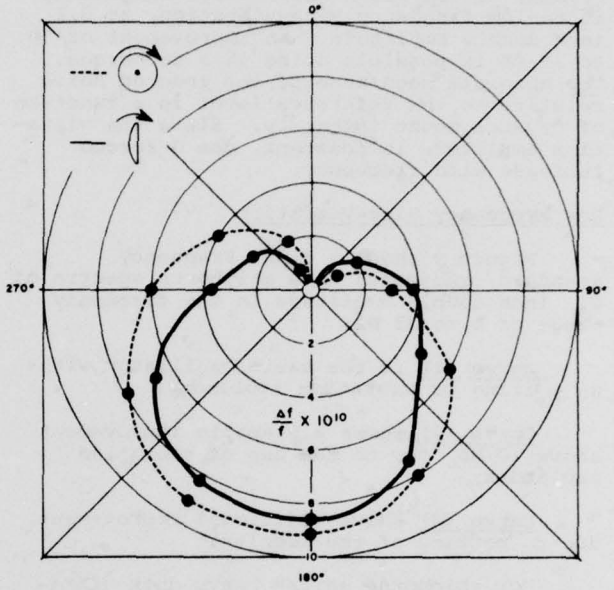

DYNAMIC ORIENTATION EFFECT

Θ AXIS

5 MHz FIFTH OVERTONE CRYSTAL

3 POINT MOUNT

FIGURE 8

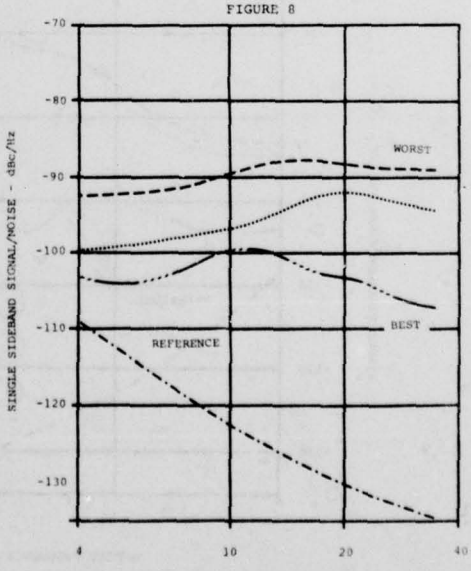

Dynamic Orientation

Figure 8 shows the effect of rotating a crystal around its Z axis, while subjecting it to low frequency sine-vibration, at 0.1 inch double amplitude. An improvement of 10 to 15 dB is possible using this technique. The absolute magnitude of the induced noise relative to the reference level is a function of crystal mount integrity. Since the vibration amplitude is constant, the G forces increase with frequency.

Low Frequency Sine-Vibration

Figure 9 shows a 5 MHz Frequency Standard, subjected to a shipborne spectra of 0.1 inch double amplitude in the frequency range of 4 to 33 Hz:

Curve (1) is the basic oscillator with no potting or vibration isolators;

Curve (2) shows a dramatic improvement above 10 Hz, due to the use of vibration isolators;

Curve (3) shows additional improvement, due to potting of the modules.

For shipborne units, heavy duty vibration mounts are necessary if the best integrated phase noise is required.

LOW FREQUENCY SINE VIBRATION
5 MHz FIFTH OVERTONE CRYSTAL
3 POINT MOUNT
SIDE-SIDE AXIS
VIBRATION LEVEL: 0.1 INCH DA
FIGURE 9

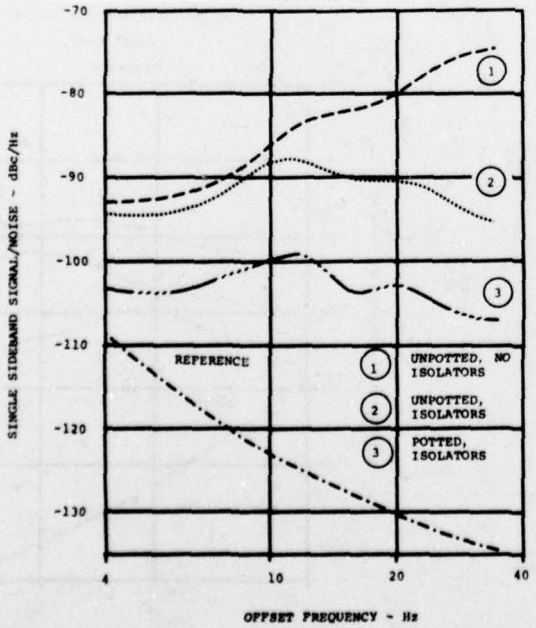

WIDEBAND SINE VIBRATION
5 MHz FIFTH OVERTONE
CRYSTAL
DTF STANDARD, AN/URQ-23(XB-1)
FIGURE 10

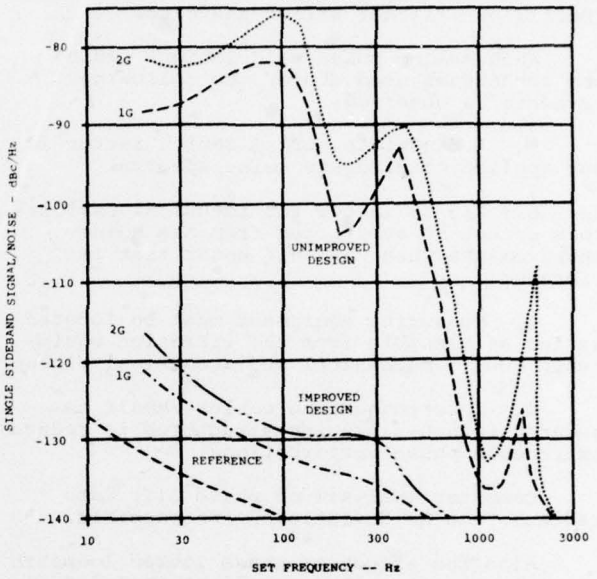

Wide-Band Sine-Vibration

Figure 10 shows the results of subjecting a 5 MHz Frequency Standard to wideband Sine-Vibration.

The upper curves are for an off-the-shelf laboratory type standard. The improvement shown in the lower curves is due to the affect of potting, especially of the output crystal filter. Additional improvements, due to orientation and vibration isolators are apparent. The cancellation of orientation effects is feasible for shipborne applications, where a fixed oscillator location is used. A bi-convex crystal was used in the oscillator shown in the lower curves. It should be noted that the final data at 2 G's is only 10 to 15 dB above non-vibration reference level.

Random Vibration

Figure 11 illustrates the effect of subjecting a 5 MHz oscillator to an airborne environment of 0.03 G^2/Hz.

The lower curves show the improvement due to utilization of all of the techniques described in this paper. No low frequency isolators are employed, but a bi-convex crystal was used. In the front-back plane, the improved oscillator is only 2 to 3 db worse than the reference.

Conclusions

This paper presented some design techniques, which have proven useful in the design of Frequency Standards subjected to vibratory environments. These techniques included:

A. Careful circuit design, using computerized worst case analysis.

B. Complete definition of mission environmental conditions.

C. Proper crystal selection and design.

D. Use of internal resilient shock mounts.

E. Use of external, low frequency shock mounts.

F. Implementation of component bonding and assembly potting.

G. Testing of mechanical mock-ups to define G levels within the structure.

RANDOM VIBRATION
$0.03G^2/Hz$ 5-500 Hz
-6 dB/OCTAVE 500-2000 Hz
5 MHz OSCILLATOR
FIGURE 11

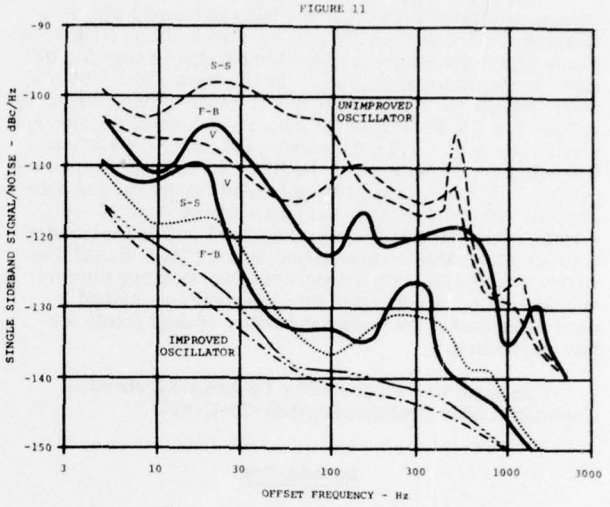

A MINIATURE HIGH STABILITY TCXO USING DIGITAL COMPENSATION

Alan B. Mroch and Glenn R. Hykes
Collins Radio Group, Rockwell International

Abstract

A miniature high-stability temperature-compensated crystal oscillator (HSTCXO) has been developed with new features for eventual use in SSB communications equipment. These new features are a wider temperature range for the same temperature stability (±5 pp 10^8 from -46 to +85 °C), single supply (10 ±0.5 V), low power consumption (less than 100 mW), a CMOS compatible output (10-V square wave) and small size (2.75 x 1.5 x 0.5 inches, 6.98 x 3.81 x 1.27 cm). Other important features of the HSTCXO are a 50-ohm output (0.125 V rms), insensitivity to load variations and voltage variations (±5 pp 109) and fast warmup (1 pp 10^8 in 1 minute). The TCXO uses a conventional analog thermistor network for coarse compensation, and a CMOS digital fine correction system with a programmable memory for fine compensation. A computer data interpolation method is used to minimize the required number of data points for fine correction.

This work was supported by US Army Electronics Command under Contract DAAB07-73-C-0137.

Introduction

Temperature compensated crystal oscillators have been in commercial production for about 15 years and are being reproduced at a reasonable cost for stabilities of ±5 pp 10^7 from -40 to +70 °C. Stabilities of ±5 pp 10^8 have been achieved over a narrow temperature range in quite small quantities. To attempt to use a thermistor resistor network to compensate a crystal oscillator over a wide temperature range to stabilities of pp 10^8, has been too time consuming and expensive to be practical. Some of the limitations have been and still are the electrical hysteresis of the crystals due to thermal cycling, interaction of network adjustments, and component retraceability with temperature.

In recent years, the use of digital computers both large and small have been used by industry to calculate real values of thermistors and resistors to generate the 3rd order voltage curve required to compensate the crystal oscillator. This approach along with the "segmented" approach works reasonably well until stabilities of 5 pp 10^8 are attempted over an extended temperature range.

The temperature compensation described in this paper had its origin in the laboratories at the Collins Radio Company in 1970 and early 1971. An HSTCXO Study, Contract DAAB07-71-C-0136 was granted by the Solid-State and Frequency Control Division, Electronics Component Laboratory, United States Army Electronics Command (USAEC). This contract called for 10 feasibility models operating at 5 MHz. These required 3 power supplies and a 6.5-cubic-inch volume.

An additional contract, High Stability Temperature Compensated Crystal Oscillator Study, Contract DAAB07-73-C-0137, was granted to improve the performance and reduce package size from 6.5 to 2.0 cubic inches. This work was completed on five exploratory models during 1974 and 1975. An extension of the above contract was granted to change the frequency from 5 MHz to 4.5 MHz, provide a CMOS output, and reduce the input power to less than 100 milliwatts. Also included, was the request to extend the ambient operating range from -46 to +85 °C and maintain the ±5 pp 10^8 frequency stability.

Digital Compensation

It is possible to replace the compensation network with some kind of a temperature sensor, a memory, and means of converting the stored information into useful form for the modulator. In this method the memory stores the required correction at each chosen temperature increment and is addressed by the temperature sensor. The memory output can use a D/A converter to develop the output to the modulator. To accomplish this for a TCXO by strictly digital means would require a very large memory. However, the crystal can be considered to have a good frequency vs temperature memory, if the effects of hysteresis, which are time and temperature dependent, are excluded. Since the AT cut crystals used for this application have a slope of 0.5 to 1.0 ppm per °C around room temperature, use of coarse compensation to reduce the storage memory can be very helpful. Used in this HSTCXO is a coarse compensation network to reduce the overall frequency vs temperature to less than 1 ppm over the ambient temperature range. Therefore, the digital portion has only to reduce this by a factor of 10 to achieve the design specification goal of ±5 pp 10^8.

CMOS circuitry lends itself well to this application for its inherently low power consumption and the low counter frequencies that can be used for satisfactory operation. Total power required to operate the digital compensation circuitry described, excluding the PROM, was in the order of 15 milliwatts.

HSTCXO Description

The purpose of this program was the development and construction of five high-stability temperature-compensated crystal oscillators (HSTCXO) for use as a reference oscillator in an advanced SSB communications system.

A block diagram of the HSTCXO is shown in figure 1. Temperature compensation is achieved by using both analog and digital techniques.

The rf circuit consists of a modified Pierce oscillator followed by a cascode amplifier. A common emitter amplifier drives a linear amplifier IC for the 50-ohm sine wave output. The other CMOS output is derived from a complementary pair operating as a high speed switch. Both of the stages are stacked in pairs to save power. Power consumption of the oscillator and amplifiers is about 40 milliwatts from the single 10-V supply. Included in this portion is the voltage regulator, which provides a stable dc source for the complete HSTCXO. Necessary load isolation was obtained by paying careful attention to rf circuit grounds and by providing sufficient active stages between the crystal and load.

Coarse compensation was accomplished by conventional means, using three thermistors and six resistors to generate the required 3rd order voltage curve. A stability of ±5 parts in 10^7 was obtained from -46 to +85 °C using only the coarse compensation network. By using a crystal with a Δf between turning points of 50 ppm, the upper turning point temperature was near +80 °C. This saved the use of additional thermistor/resistor network parts usually required when operating much above the crystal upper turning point.

Separate varactors are used for the coarse and digital compensation because the frequency sensitivity is very different. For example, the frequency pullability for the coarse varactor is about 10 ppm per volt, whereas the digital varactor pullability is adjusted to about 1 pp 10^8 per volt.

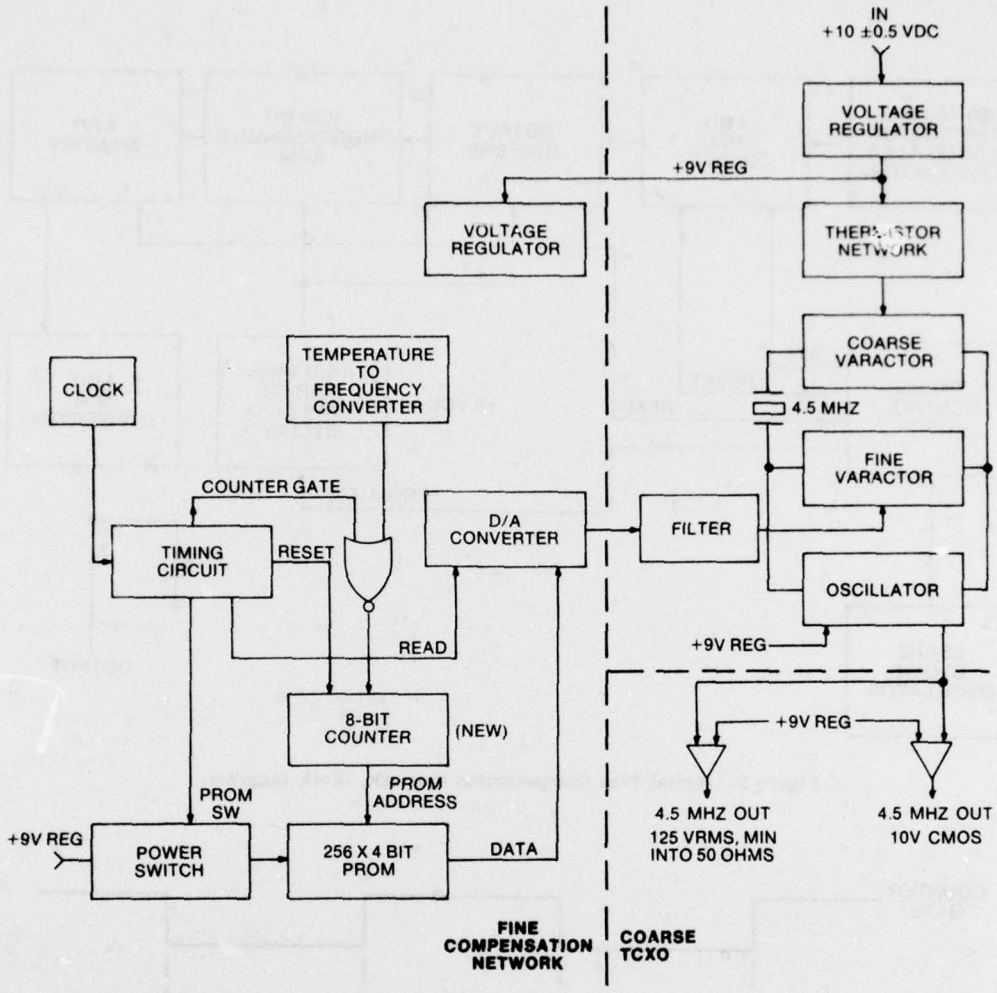

Figure 1. 4.5 MHz HSTCXO, Block Diagram.

CMOS Digital Circuitry

The block diagram of the CMOS digital circuitry is shown in figure 2. Its purpose is to correct the 4.5-MHz frequency to within ±5 parts in 10^8. The coarse network has corrected the frequency to within ±5 parts in 10^7 so a frequency error reduction of 10 is involved. This is accomplished with a programmable memory (PROM) that stores the proper correction, word, and a D/A converter to convert the word to the fine Varicap voltage at regular intervals over the -46 to +85 °C temperature range.

Two RC oscillators are used to provide the input signals for the digital compensation circuit. The first operates as a clock at a frequency of 25 kHz to provide the timing pulses for the gate, reset, and read functions. The other oscillator operates as a temperature sensor as its frequency varies from 50 to 100 kHz by use of a sensistor in the feedback network. The PROM is addressed by the digital dividers which count the frequency of the temperature-sensitive oscillator. Output buffers are used to provide the necessary interface between CMOS circuitry used and the TTL PROM inputs.

To meet the overall power requirement of 100 mW max, the PROM must be switched on for a short duty cycle (figure 3 of the timing diagram). The power switching circuit, shown in detail in figure 4, accomplishes this. To prevent the oscillator from losing fine compensation during the off cycle of the PROM, a 4-bit shift register memory is used; this retains the last PROM word until the next update. A 4-bit D/A converter is used to convert the register output into 16 equally spaced voltages. This consists of an R/2R resistive ladder where R is equal to 25 kilohms. An RC filter follows the D/A converter to attenuate the frequency modulation of the carrier at 25 kHz and to produce a smooth function of the compensation voltage without discrete voltage steps. If the temperature is such that the decimal PROM address is between example 100 and 101, the resultant output will be summation of the two output voltages. The signal-to-noise measurements made on the HSTCXO's show that all sidebands are greater than -115 dB below the carrier.

The PROM has been commercially available since 1970 when Harris Semiconductor introduced their first reliable programmable memory, the PROM-0512. In this HSTCXO, a 1024-bit PROM is used with the 256 x 4-bit format, giving 256 addressable memory slots, each having a choice of 16 words. Since the temperature range of -46 to +85 °C is equal to a ΔT of 131 °C and 256 addresses are available, it is possible to provide almost a word correction for every 0.5 °C.

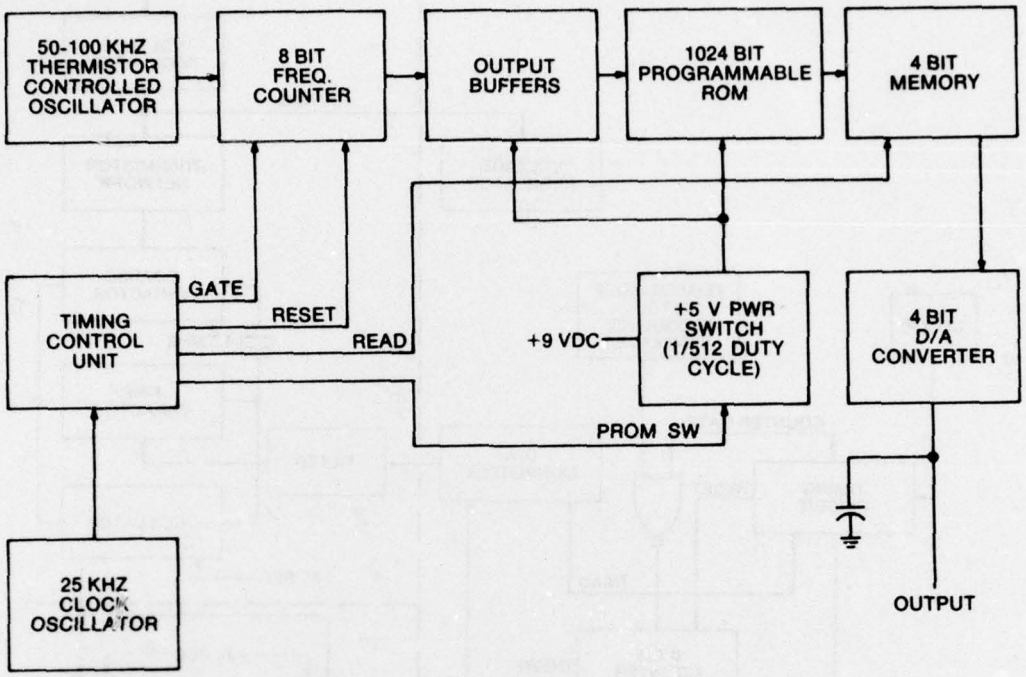

Figure 2. Digital Fine Compensation Network, Block Diagram.

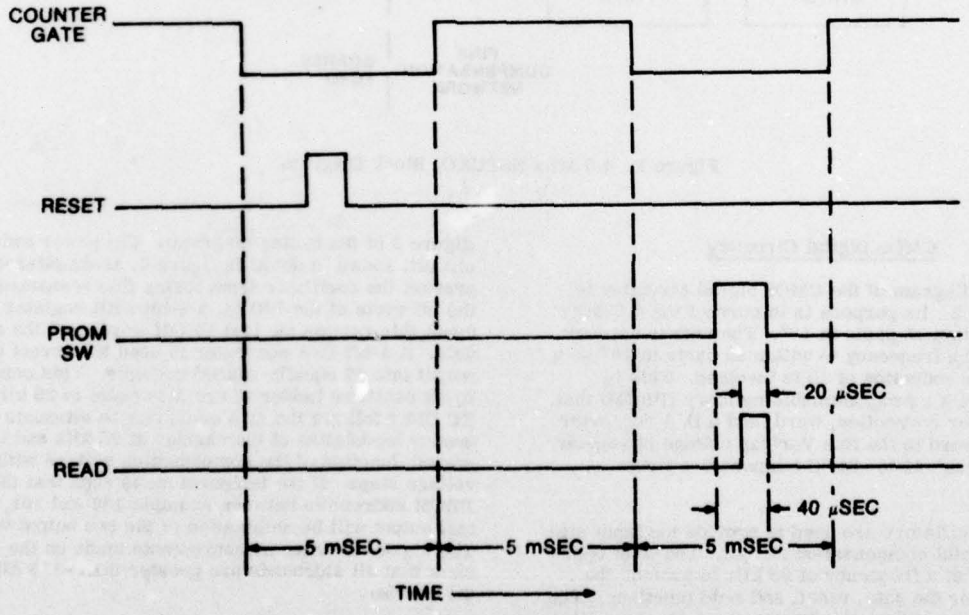

Figure 3. Timing Diagram.

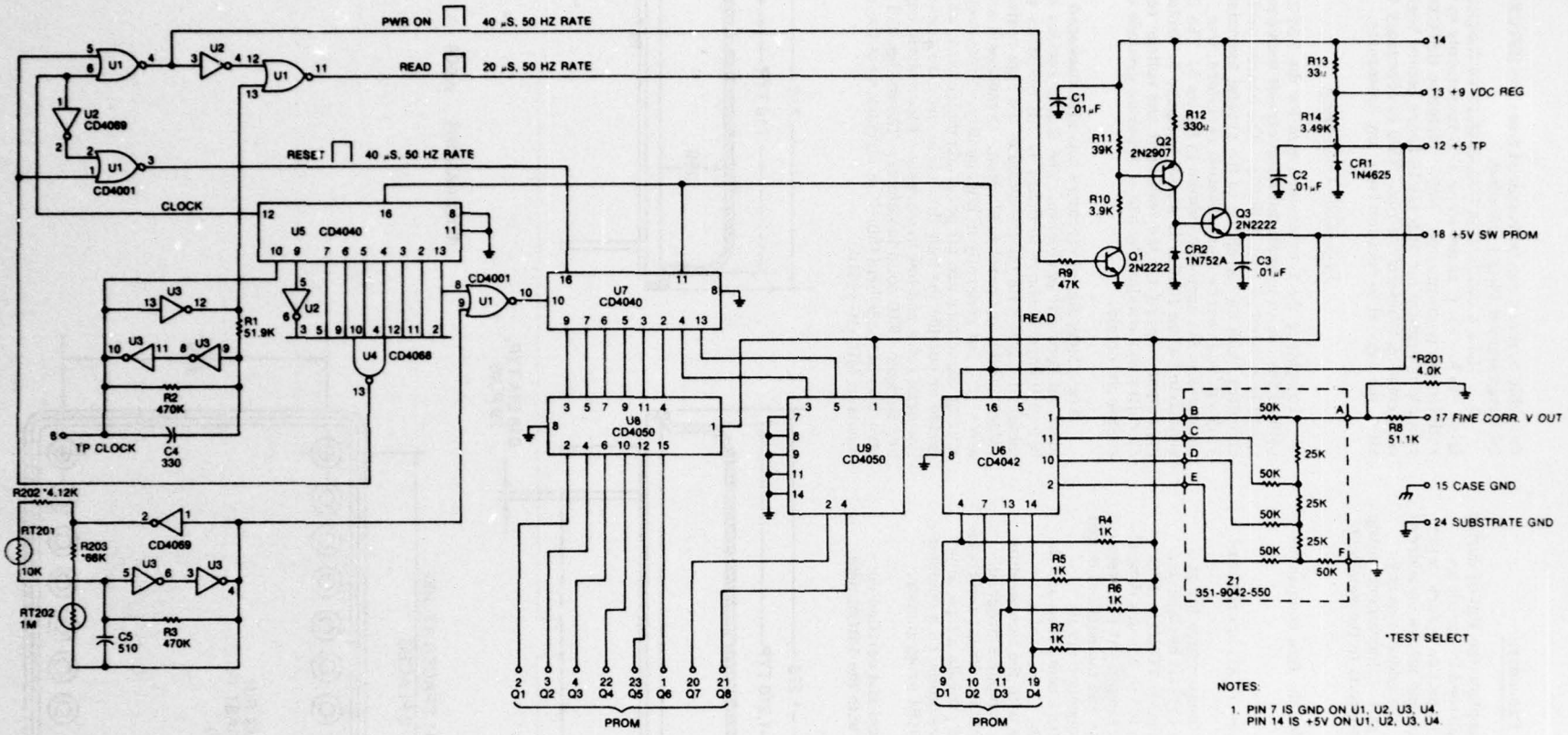

Figure 4. Digital Compensation, Schematic Diagram.

Fine Compensation Procedure

A means must be provided to replace the PROM during fine compensation. This is accomplished by use of an interface adapter consisting of a 16-position rotary switch with binary to 7-segment conversion and allows an address readout at any temperature. Thus, the address at any temperature is read and recorded at 4 °C increments along with the required word which corresponds to the smallest frequency error at 4.5 MHz.

The important steps involved for the fine compensations are as follows:

1. Seal the cover on the coarse TCXO in preparation for fine compensation.
2. Stabilize the unit at room temperature for at least 10 hours to recover from any crystal hysteresis. Beginning at -46 °C, stabilize the sealed TCXO in 4 °C increments (this may require from 0.5 to 2 hours depending upon the ambient temperature change). At each temperature, record the PROM address and the decimal output word that produces the smallest frequency error.
3. Tabularize and record PROM addresses and the desired corresponding output words.
4. Key punch computer cards with the temperature, address, and word input data. The computer program developed for this project will perform a linear interpolation between the 4 °C input data and provide a tape output suitable for automatic PROM programming on a commercial programmer such as the I/O ROM programmer, model 101-24430.
5. After PROM is programmed and verified correctly by comparing the input data with the PROM data, the cable harness can be removed from the HSTCXO and the programmed PROM installed.
6. Make a confirming temperature vs frequency run from -46 to +85 °C at the same 4 °C increments to verify satisfactory performance. Note: Stabilize HSTCXO at room temperature for at least 10 hours before beginning confirmation temperature run. This is necessary to allow the crystal to recover from any hysteresis.

Packaging Techniques

To achieve the 2-cubic-inch size for the HSTCXO without the use of hybrid, thin-film circuit techniques would have been an impossibility. The coarse oscillator circuitry, with the exception of the crystal thermistors, Varicap, and coarse compensation resistors, was packaged in the enclosure shown in figure 5. The finished substrate before lidding is shown in figure 6. Isolation of the output stages from the oscillator and voltage regulator circuitry was obtained by use of separate grounds on the coarse substrate.

The CMOS digital circuitry was also packaged in an identical hermetic enclosure. The digital section substrate before lidding is shown in figure 7. All resistors are metal film type with the exception of the high resistance values, which are purchased chips. Components selected are small, but generally of high quality. Frequency determining capacitors are all porcelain dielectrics, whether inside or outside the thin-film enclosures, to achieve very low drift rates and low hysteresis. Electrolytic capacitors are Sprague 193D solid tantalums. The design and construction of the hybrid thin-film circuits meet the requirements of MIL-M-38510.

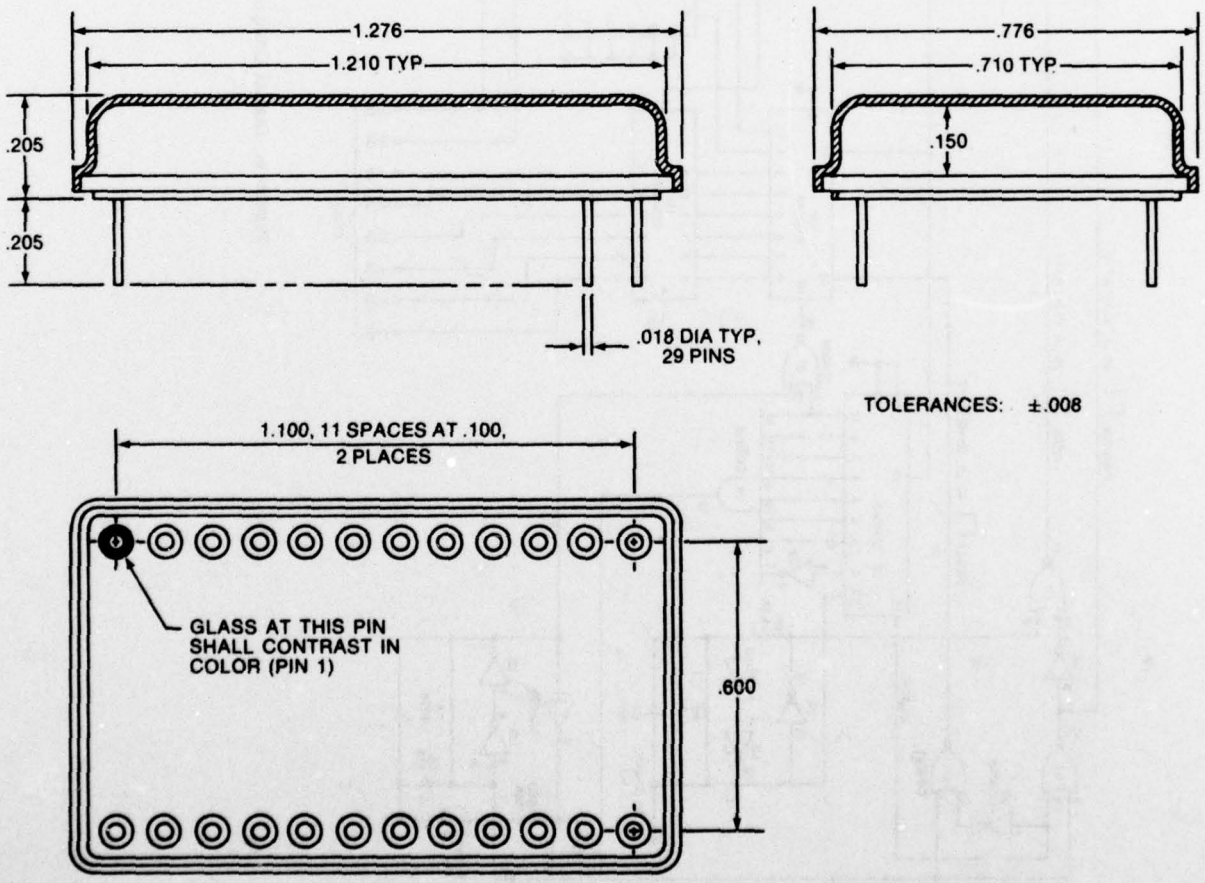

Figure 5. Coarse and Digital Enclosures.

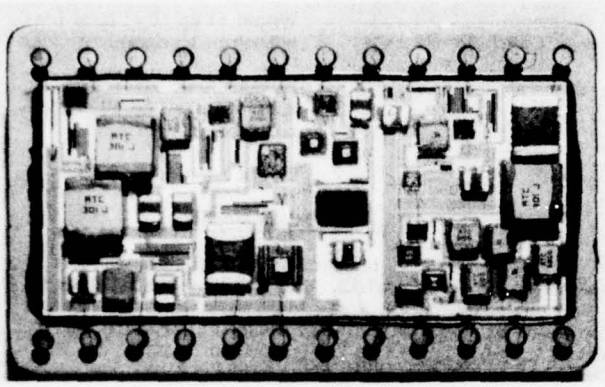

Figure 6. Coarse Oscillator.

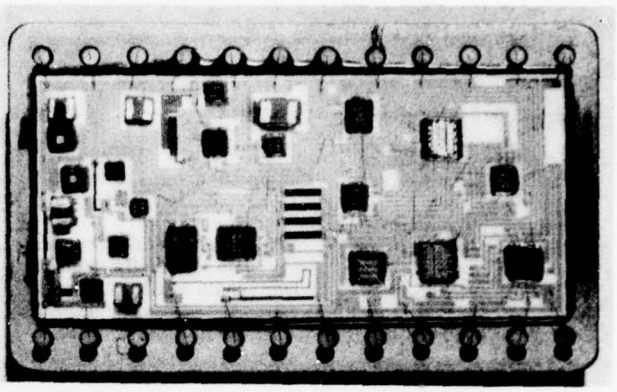

Figure 7. Digital Circuitry.

The illustration in figure 8 shows the packaging concept. The package is a hermetically sealed, copper enclosure with a volume of 2 cubic inches. Exterior dimensions are 0.492 x 1.492 x 2.742 inches, maximum, as shown. The input/output terminals also serve as the mounting pins as shown in bottom view of HSTCXO, figure 9.

Inside the package are two compartments: The coarse TCXO side and the digital (fine) compensation side. This is shown in photo in figure 10. Two small printed circuit boards are used to interconnect the various parts and the thin-film packs. The crystal is wrapped with copper foil to minimize temperature gradients. Glass cased crystals were used because they gave the best frequency retrace characteristic.

Two leads go from the coarse oscillator into the digital side; one carries the regulated +9 V dc and the other the dc voltage to the fine Varicap. The thin-film packages are heat sinked to the exterior copper enclosure, again reducing the thermal gradient to a minimum.

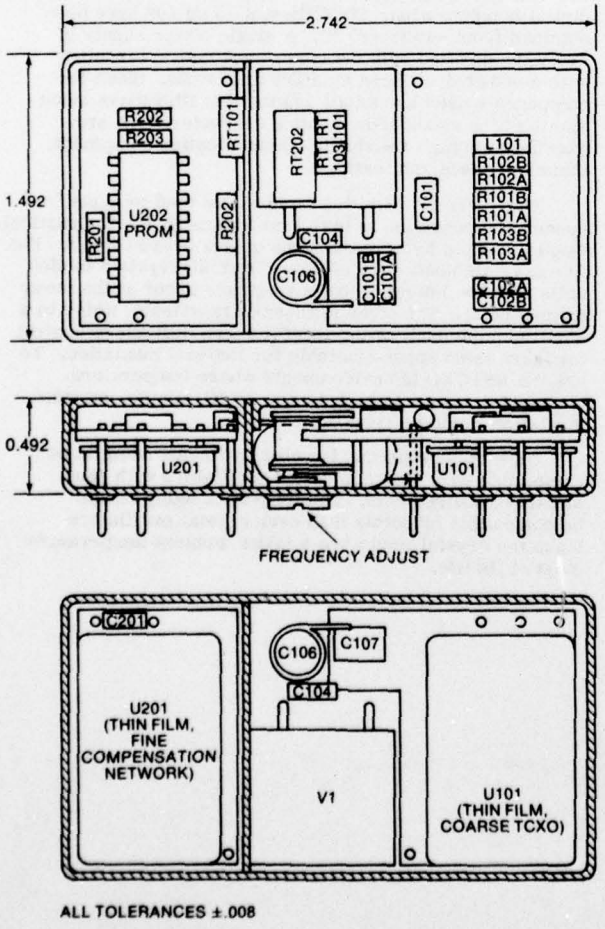

Figure 8. Two-Cubic-Inch TCXO Packaging Concept.

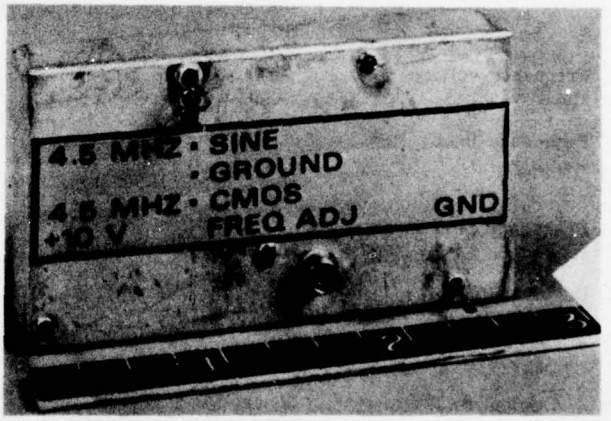

Figure 9. HSTCXO, Bottom View.

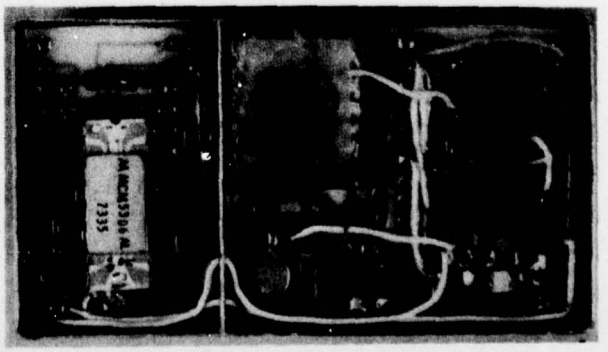

Figure 10. HSTCXO, Top View With Covers Removed.

Design Goals

Listed below are the objectives of this HSTCXO study:

Nominal output frequency:	4.5 MHz
Frequency-temperature stability: (steady-state)	±5 pp 10^8 from -46 to +85 °C
Frequency-temperature stability: (retrace)	The frequency change resulting from thermally induced hysteresis shall not exceed ±3 x 10^{-8} at temperatures of -46, +30 and +85 °C when subjected to the following temperature cycle: -57 to -46 to +30 to 85 to -46 to 85 to +30 °C. The HSTCXO shall be maintained at a storage temperature of -57 °C for a minimum of 16 hours preceding the test and frequency shall be recorded following a 1-1/2-hour stabilization period at each temperature. The maximum time permitted for any one temperature change shall be one hour.
Frequency-temperature stability: (transient)	±5 pp 10^8 for a ramp 10 °C change, 1 °C/minute ramp starting at -40, -5, +30 and +65 °C stabilized temperatures respectively.
Frequency-voltage stability:	±5 pp 10^9 (+10 ±0.5 V dc).
Frequency-load stability:	±5 pp 10^9 (output A 50 ±5 ohms, output B 30 ±5 pf).
Frequency adjustment range:	±1 ppm, minimum.
Output Voltage:	
Output A:	0.125 V rms, minimum, in 50 ohms.
Output B:	Square wave, 10-volt CMOS compatible, 30-pF load.
Input power:	10 V ±0.5 V, 10 mA max (output A, 50 ohms, output B, 30 pF)
Warmup:	Within ±1 pp 10 of final frequency in 1 minute.
Spectral purity:	Nonharmonic discrete, spurious shall be 100 dB or more below carrier.
Size:	2.75 x 1.5 x 0.5 inches.

Data on HSTCXO Models

The frequency vs temperature data for four models is shown in figures 11 and 12. Note the overall similarity to each other. In theory, it should be possible to compensate to less than 1 pp 10^8, but when reduced to practice, an overall stability of ±5 pp 10^8 is difficult to obtain due to crystal hysteresis and other anomalies.

The voltage coefficients for the oscillators were less than 5 parts 10^{10} for the specified supply change of 10 V dc ±0.5 V. The maximum frequency change due to a load change of 50 ohms was less than 2 parts 10^9. Maximum power input on four models was 84 milliwatts with a +10.5 V dc supply. The unwanted spurious outputs were found to be greater than -100 dB down 2 kHz away from the carrier. The frequency-temperature stability (retrace) was not as good as desired due to the limiting criteria of the crystals themselves, plus component retrace over temperature.

Conclusions

Successful design, construction, and operation of the two cubic inch HSTCXO's have been demonstrated using digital compensation. Stabilities of ±5 pp 10^8 have been obtained from -46 to +85 °C. A single power supply of +10 V dc supplied both the coarse and digital circuitry with a power drain less than 100 milliwatts. Since the components used are small and the thin film parts much smaller, the shock and vibration characteristics are excellent for high reliability communication equipment, including space applications.

There are two limiting factors that tend to make frequency compensation to less than 5 parts in 10^8 impractical. One is thermal hysteresis in the quartz crystal itself. The five crystals used were selected from 20 crystals to pick units with the lowest frequency retrace error at the lower turning point. The other is thermal transients, which in a small volume such as the HSTCXO, are difficult to control for there is no space available for thermal insulation. To use the HSTCXO in environments where temperature transients may be as high as 5 to 10 °C/minute, external insulation would be required.

High-volume production cost estimates seem to be compatible with oven controlled oscillators with equal stability requirements. The long-term aging should be compatible or better than oven crystal oscillators since the crystal would see a lower ambient temperature most of its life.

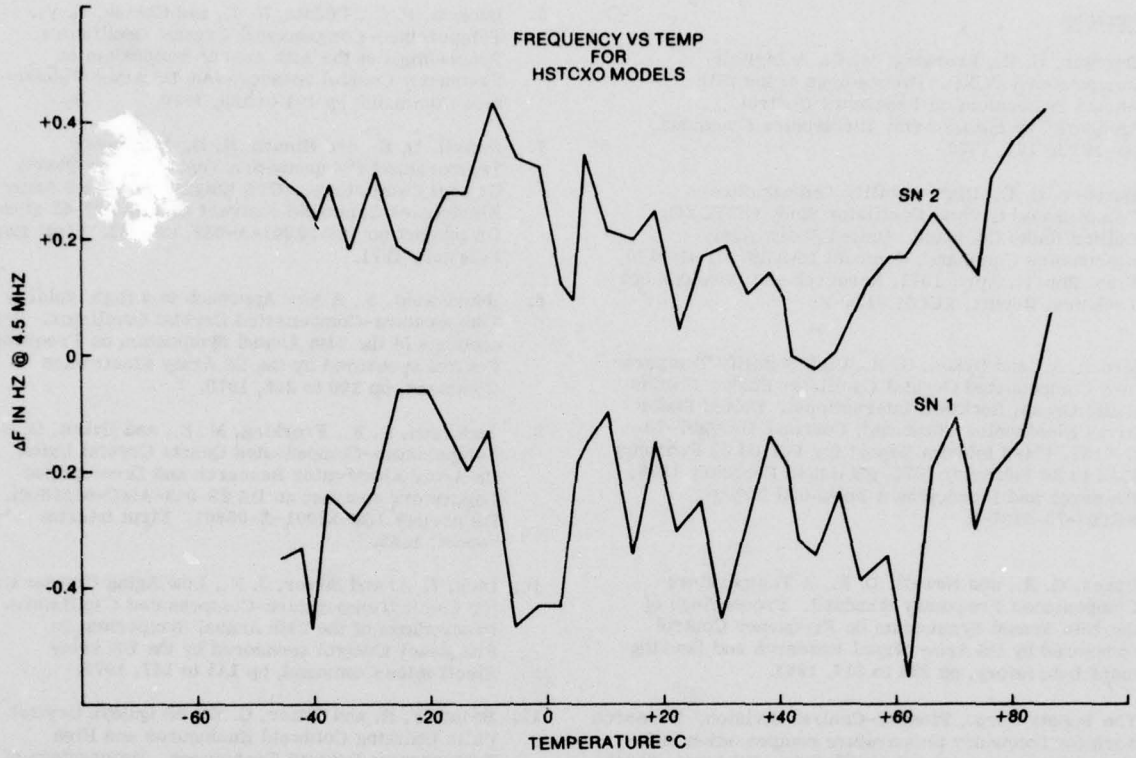

Figure 11. Frequency Vs Temperature for HSTCXO Models SN 1 and SN 2.

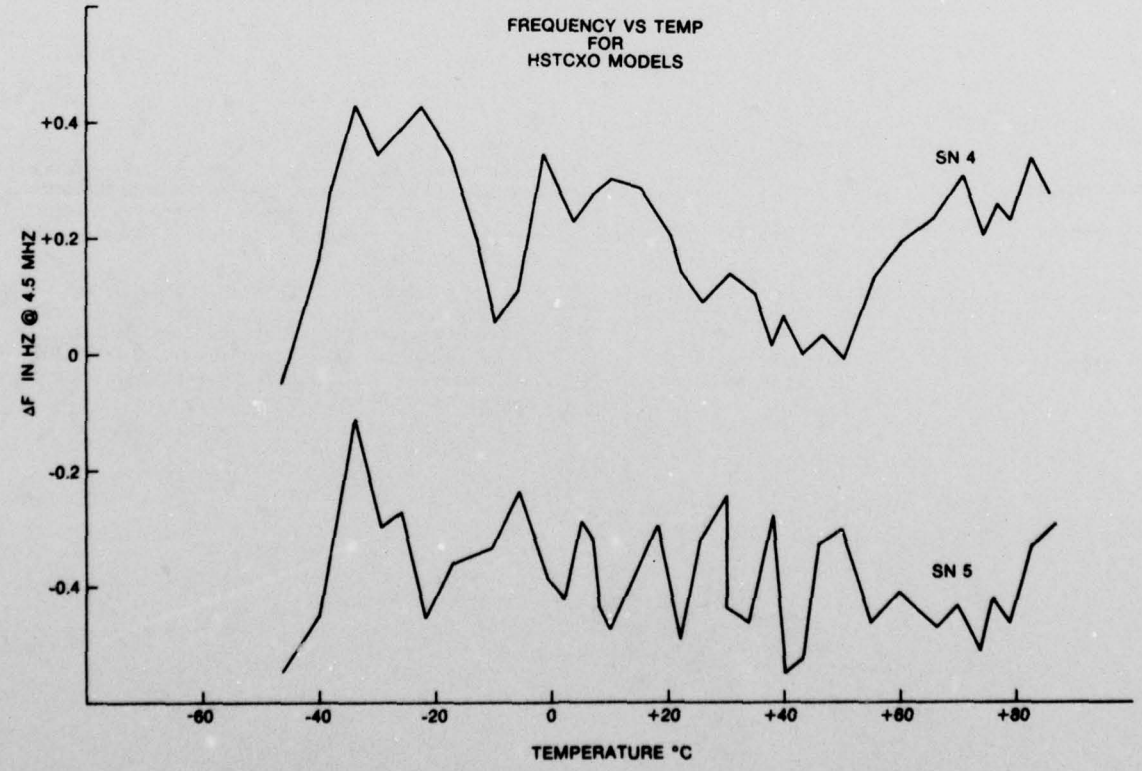

Figure 12. Frequency Vs Temperature for HSTCXO Models SN 4 and SN 5.

Bibliography

1. Buroker, G. E., Frerking, M. E., A Digitally Compensated TCXO. Proceedings of the 27th Annual Symposium on Frequency Control Sponsored by the US Army Electronics Command, pp 191 to 198, 1973.

2. Buroker, G. E., High-Stability Temperature-Compensated Crystal Oscillator Study (HSTCXO) Collins Radio Company. United States Army Electronics Command, Contract DAAB07-71-C-0136, Final Report, April 1971, Research and Development Technical Report, ECOM 0136-F.

3. Mroch, A., and Hykes, G. R., High Stability Temperature Compensated Crystal Oscillator Study. Collins Radio Group, Rockwell International. United States Army Electronics Command, Contract DAAB07-73-C-0137, Third Interim Report for Period 28 February 1974 to 28 February 1975, published February 1976, Research and Development Technical Report, ECOM-73-0137-3.

4. Hykes, G. R., and Newell, D. E., A Temperature-Compensated Frequency Standard. Proceedings of the 15th Annual Symposium on Frequency Control sponsored by US Army Signal Research and Development Laboratory, pp 298 to 317, 1961.

5. The Bendix Corp., Pioneer-Central Division. Research work for frequency temperature compensation techniques for quartz crystal oscillators. US Army Signal Research and Development Laboratory contract no. DA 36-039.SC-90782. Final report, October 1963, ASTIA no AD437825.

6. Duckett, P. D., Peduto, R. J., and Chizak, G. V., Temperature-Compensated Crystal Oscillators. Proceedings of the 24th Annual Symposium on Frequency Control sponsored by US Army Electronics Command, pp 191 to 199, 1970.

7. Newell, D. E., and Hinnah, H. D., Frequency Temperature-Compensation Technique for Quartz Crystal Oscillators. (CTS Knights, Inc.) US Army Electronics Command contract no DAAB07-67-C-0433, DA project no 146-22001-A-058, task 02. Final Report, February 1971.

8. Schodowski, S., A New Approach to a High Stability Temperature-Compensated Crystal Oscillator. Proceedings of the 24th Annual Symposium on Frequency Control sponsored by the US Army Electronics Command, pp 200 to 208, 1970.

9. Anderson, E. E., Frerking, M. E., and Hykes, G. R., Temperature-Compensated Quartz Crystal Units. US Army Electronics Research and Development Laboratory contract no DA 28-043-AMC-00210(E), DA project 1G6-22001-A-05801. First interim report, 1965.

10. Dick, L. A. and Silver, J. F., Low Aging Crystal Units for Use in Temperature-Compensated Oscillators. Proceedings of the 24th Annual Symposium on Frequency Control sponsored by the US Army Electronics Command, pp 141 to 147, 1970.

11. Brand, F. R. and Ritter, G. E., SB Quartz Crystal Units Utilizing Coldweld Enclosures and High Temperature Bakeout Techniques. Proceedings of the 21st Annual Symposium on Frequency Control sponsored by the US Army Electronics Command, pp 224 to 243, April 1967.

DESIGN OF VOLTAGE CONTROLLED CRYSTAL OSCILLATORS

Stuart J. Lipoff
Arthur D. Little, Inc.
Cambridge, Massachusetts

Summary

Voltage Controlled Crystal Oscillator (VCXO) frequency modulators have found increasing use in recent years in portable Frequency Modulation (FM) equipment as an alternative to a standard crystal oscillator followed by a phase modulator. This paper will consider the advantages of using a direct FM VCXO over an indirect FM phase modulator. A model for the crystal and frequency control element will be developed and basic circuit design considerations will be presented. Conditions necessary to minimize audio distortion generated by the VCXO modulator will be dealt with in detail.

Key words (for information retrieval)
Crystal, FM, Frequency Modulation, Land Mobile, Linearization, Oscillator, Quartz, Quartz Crystal, Radio, VCXO, Voltage Controlled.

Introduction

Present audio frequency response requirements of FM modulators in the land mobile radio services span the range of 67 to 3000 Hz.[1] The low end limit of 67 Hz is determined by the need to transmit Continuous Tone Controlled Squelch System (CTCSS)[2] in the range of 67 to 270 Hz at 1 KHz deviation. The upper limit of 3000 Hz is set by Federal Communications Commission regulations and the need to transmit speech in the range of 300 to 3000 Hz at 5 KHz deviation. This need to transmit the low audio frequencies imposes the most severe requirement on the phase modulator.[3]

Let D = Frequency deviation in Hz
Fa = Audio modulating frequency in Hz
ϕ = Maximum phase modulation capability of the phase modulator in radians
M = Minimum number of times phase modulator output must be multiplied to produce 5 KHz deviation

$$D = Fa\,\phi \tag{1}$$

For CTCSS modulation of 67 Hz at 1 KHz deviation and $\phi = \pi/2$

$$D_{ctcss} = 105 \text{ Hz} \tag{2}$$

$$M_{ctcss} = 9.5 \tag{3}$$

For speech of 300 Hz at 5 KHz deviation and $\phi = \pi/2$

$$D_{speech} = 471 \text{ Hz} \tag{4}$$

$$M_{speech} = 10.6 \tag{5}$$

Assuming that frequency multipliers are implemented with a combination of doubler (x2) and tripler (x3) stages.

Let N = Minimum number of required multiplier stages
i = Positive integer 0,1,2,...
j = Positive integer 0,1,2,...
K = Smallest positive integer such that K> M and

$$K = 2^i x 3^j \tag{6}$$

$$N = i+j \tag{7}$$

From (3) and (5) above the smallest value of K that satisfies (6) is K=12 for i=2 and j=1. Assuming that it is possible to build a perfectly linear phase modulator with $\pi/2$ phase deviation, the best circuit reduction possible would be an oscillator-tripler stage followed by two doubler stages. However, practical implementations of phase modulators have required x 18 multiplication to achieve reasonable levels of audio distortion. It will be shown that the minimum frequency deviation required for a VCXO modulator is limited by quartz crystal economies, and that this minimum deviation is lower than that required by the phase modulator.

Use of a VCXO modulator will then provide the following benefits:

1. Less multiplier stages reduce cost, size, and battery drain.
2. For the common used AT cut crystals in HC-18/U holders it is possible to realize economies in crystal selection by using a fundamental crystal frequency between 5 and 10 MHz.

Use of a phase modulator would require a 2.5 MHz crystal in the limit case of the Low VHF Band (30-50 MHz) and K=12, however, 2.5 MHz crystals are not readily available in HC-18/U holders.[4,5]

Crystal Model

Figure 1 is the model to be used for the crystal in the vicinity of fundamental resonance.[6,7,8,9,10]

For $\omega_s < \omega < \omega_a$
Let ω_s = Series resonance
ω_a = antiresonance due to C_o
C_L = load capacitance for design center frequency
ω_{c_L} = design center frequency due to $C_o + C_L$ antiresonance

$$\Delta_{c_o} \triangleq \frac{\omega_a - \omega_s}{\omega_s} \tag{8}$$

$$\Delta \triangleq \frac{\omega - \omega_s}{\omega_s} \tag{9}$$

$$\Delta_{c_L} \triangleq \frac{\omega_{c_L} - \omega_s}{\omega_s} \tag{10}$$

A typical crystal would have the following worst case specification:

$$\omega_s = 2\pi\ 20x10^6,\ C_o = 5x10^{-12},\ \Delta_{c_L} = 330x10^{-6},\ R_1 = 25$$

The above specification is sufficient to determine each element in Figure 1. The following calculations assume that $X_{L_1} >> R_1$

$$\omega_s = \frac{1}{\sqrt{L_1 C_1}} \tag{11}$$

In Figure 2, L_{eq} is the equivalent inductance for $\omega_s < \omega_{c_L}$

$$\omega_{c_L} = \frac{1}{\sqrt{L_{eq}\,(C_o + C_L)}} \tag{12}$$

$$L_{eq} = \frac{1}{\omega_{c_L}^2\,(C_o + C_L)} \tag{13}$$

$$\omega_{c_L} L_{eq} = \omega_{c_L} L_1 - \left(\frac{1}{\omega_{c_L} C_1}\right) = \frac{\omega_{c_L}^2 L_1 C_1 - 1}{\omega_{c_L} C_1} \quad (14)$$

$$\frac{C_1}{C_o + C_L} = \left(\frac{\omega_{c_L}}{\omega_s}\right)^2 - 1 \cong 2\Delta_{c_L} \text{ for } (\omega_{c_L} - \omega_s) << \omega_s \quad (15)$$

$$C_1 = 2(C_o + C_L)\Delta_{c_L} \cong 2\,(5\text{x}10^{-12} + 32\text{x}10^{-12})\,330\text{x}10^{-6} = .0244 \text{ pF} \quad (16)$$

$$L_1 = \frac{1}{\omega_s^2 C_1} = \frac{1}{(2\pi\ 20\text{x}10^6)^2\ .0244\text{x}10^{-12}} = 2593\ \mu\text{H} \quad (17)$$

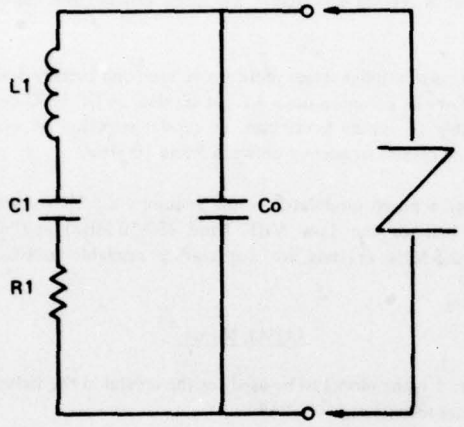

FIG 1

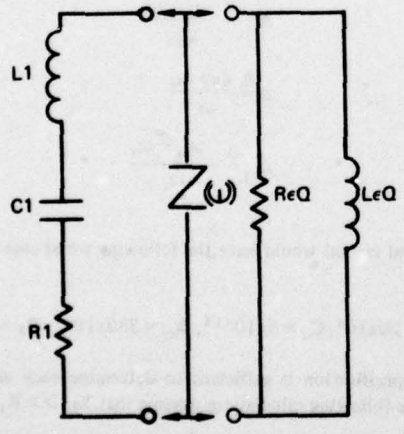

FIG 2

The model of Figure 1 with the values calculated in (16) and (17) above was entered into the Ac-Coded Circuit Analysis Program.[12] The computer model is shown in Figure 3. Using this model a circuit analysis was performed with the results shown in Figure 4. The frequency for analysis was varied from 10 KHz below the 20 MHz series resonant frequency to 60 KHz above series resonance. Data presented in Figure 4 is defined as follows:

Freq – Frequency of analysis
Z – Magnitude of crystal impedance
PH – Phase angle of crystal impedance
Z_r – Real part of crystal impedance
Z_j – Imaginary part of crystal impedance
L – Equivalent inductance in μH
C – Equivalent capacitance in pF
DF – KHz offset from series resonance of 20 MHz

XTAL FOR FS = 20 MHZ AND CO = 5 PF AND DF = 330 PPM (32 PF LOAD) AND RS = 25 OHMS

Parameter No.	Name	Nodes From	To	Nominal Value
1	I1	0	1	1.0000E 0
2	CO	0	1	5.0000E-12
3	C1	1	2	2.4410E-14
4	L1	2	3	2.5932E- 3
5	R1	3	0	2.5000E 1

FIGURE 3

The model exhibits the proper behavior of a series resonance at 20 MHz with a net equivalent real impedance of 25 ohms, and net equivalent capacitance of -32 pF at 330 PPM offset from series resonance. With a 32 pF load on the crystal model, an antiresonance will occur at the 330 PPM offset with a net equivalent real impedance of 33.6 ohms. Since the analysis shows good agreement with the predictions of (16) and (17), the simplifying assumptions made in deriving the equations are justified.

Crystal Impedance Variation vs Frequency

For the previously considered phase modulator, the worst case crystal limitations occurred when building a transmitter on 30 MHz. Assuming that the crystal fundamental frequency may be selected on a cost-size basis only, a multiplier ratio of x 3 will require a crystal fundamental range of 10 to 17 MHz to cover the 30 to 50 MHz Low VHF Band. To provide a 5 KHz deviation with a x 3 multiplication ratio, the VCXO must be capable of ± 1.7 KHz deviation at the fundamental. Figure 5 is an expanded analysis of the data of Figure 4 about the 32 pF antiresonance of the crystal. The range of the analysis spans the ± 1.7 KHz range of interest. Using the above model, the functional relationship of the crystal impedance vs. DF will be studied.

$$Z_j \cong \frac{-1}{\frac{1}{\omega L_{eq}} - \omega C_o} \quad (18)$$

using 13

$$Z_j = \frac{-1}{\left(\frac{\omega C_1}{\omega^2 L_1 C_1 - 1}\right) - \omega C_o} = -\frac{(\omega/\omega_s)^2 - 1}{2\Delta_{c_o} C_o \omega - C_o \omega\,(\omega/\omega_s)^2 - 1} \quad (19)$$

$$Z_j \cong \frac{-2\Delta}{\omega C_o\,(2\Delta_{c_o} - 2\Delta)} = \frac{1}{\omega C_o\left(\frac{\Delta_{c_o}}{\Delta} - 1\right)} \text{ for } (\omega - \omega_s) << \omega_s \quad (20)$$

for $\omega < \omega_a$

$$Z_i = \frac{1}{\omega C_o}\left[(\Delta/\Delta_{c_o}) + (\Delta/\Delta_{c_o})^2 + (\Delta/\Delta_{c_o})^3 + \ldots\right] \quad (21)$$

XTAL Z ABOUT FS=20MHZ FOR CO=5PF, DF=330PPM(32PF LOAD), AND RS=25 OHMS

FREQ IN MHZ
L IN UH
C IN PF
DF (RELATIVE TO FS=20MHZ) IN KHZ

	FREQ	Z	PH	ZR	ZI	L	C	DF
1#	19.990	271.3	-86	17.43	- 270.78	- 2.2	29.0	-10
2#	19.991	248.6	-86	18.01	- 247.94	- 2.0	32.0	- 9
3#	19.992	225.1	-85	18.61	- 224.30	- 1.8	36.0	- 8
4#	19.993	200.7	-85	19.28	- 199.80	- 1.6	40.0	- 7
5#	19.994	175.6	-84	19.94	- 174.43	- 1.4	46.0	- 6
6#	19.995	149.5	-82	20.69	- 148.10	- 1.2	54.0	- 5
7#	19.996	122.7	-80	21.43	- 120.79	- 1.0	66.0	- 4
8#	19.997	96.1	-77	22.26	- 92.43	- .7	86.0	- 3
9#	19.998	67.1	-70	23.11	- 62.96	- .5	130.0	- 2
10#	19.999	40.2	-53	24.02	- 32.30	- .3	250.0	- 1
11#	20.000	25.0	- 1	24.99	- 40	0	20,000.0	0
12#	20.001	41.9	52	26.07	32.83	.3	- 240.0	1
13#	20.002	72.8	68	27.22	67.49	.5	- 120.0	2
14#	20.003	107.5	75	28.45	103.65	.8	- 77.0	3
15#	20.004	144.5	78	29.75	141.43	1.1	- 56.0	4
16#	20.005	183.6	80	31.16	130.93	1.4	- 44.0	5
17#	20.006	224.7	82	32.63	222.27	1.8	- 36.0	6
18#	20.007	267.8	83	34.27	265.58	2.1	- 30.0	7
19#	20.008	313.1	83	36.00	311.01	2.5	- 26.0	8
20#	20.009	360.7	84	37.85	358.71	2.9	- 22.0	9
21#	20.010	410.8	84	39.82	408.88	3.3	- 19.0	10
22#	20.011	463.6	85	41.96	461.69	3.7	- 17.0	11
23#	20.012	519.3	85	44.29	517.36	4.1	- 15.0	12
24#	20.013	578.0	85	46.89	576.13	4.6	- 14.0	13
25#	20.014	640.2	86	49.80	638.28	5.1	- 12.0	14
26#	20.015	706.1	86	52.61	704.09	5.6	- 11.0	15
27#	20.016	775.9	86	55.93	773.91	6.2	- 10.0	16
28#	20.017	850.2	86	59.51	848.11	6.7	- 9.4	17
29#	20.018	929.3	86	63.43	927.12	7.4	- 8.6	18
30#	20.019	1,013.7	86	67.79	1,011.42	8.0	- 7.9	19
31#	20.020	1,104.0	86	72.47	1,010.57	8.8	- 7.2	20
32#	20.021	1,200.7	86	77.77	1,198.18	9.5	- 6.6	21
33#	20.022	1,304.7	86	83.82	1,301.96	10.0	- 6.1	22
34#	20.023	1,416.7	86	90.28	1,413.80	11.0	- 5.6	23
35#	20.024	1,537.7	86	97.73	1,534.62	12.0	- 5.2	24
36#	20.025	1,668.9	86	106.36	1,665.55	13.0	- 4.8	25
37#	20.026	1,811.7	86	115.77	1,807.96	14.0	- 4.4	26
38#	20.027	1,967.4	86	126.41	1,963.37	16.0	- 4.0	27
39#	20.028	2,138.2	86	138.87	2,133.69	17.0	- 3.7	28
40#	20.029	2,326.2	86	153.51	2,321.11	18.0	- 3.4	29
41#	20.030	2,534.1	86	169.88	2,528.43	20.0	- 3.1	30
42#	20.031	2,765.4	86	189.71	2,758.90	22.0	- 2.9	31
43#	20.032	3,024.2	86	212.73	3,016.69	24.0	- 2.6	32
44#	20.033	3,315.6	86	240.73	3,306.89	26.0	- 2.4	33
45#	20.034	3,646.4	86	273.62	3,636.12	29.0	- 2.2	34
46#	20.035	4,025.0	86	314.63	4,012.64	32.0	- 2.0	35
47#	20.036	4,462.5	85	365.90	4,447.45	35.0	- 1.8	36
48#	20.037	4,973.9	85	429.45	4,955.30	39.0	- 1.6	37
49#	20.038	5,579.5	85	512.76	5,565.90	44.0	- 1.4	38
50#	20.039	6,308.0	84	621.34	6,277.34	50.0	- 1.3	39
51#	20.040	7,200.9	84	780.26	7,159.65	57.0	- 1.1	40
52#	20.041	8,320.4	83	976.84	8,262.86	66.0	- 1.0	41
53#	20.042	9,764.9	83	1,281.64	9,680.43	77.0	- .8	42
54#	20.043	11,698.4	81	1,753.62	11,566.22	92.0	- .7	43
55#	20.044	14,416.1	80	2,543.09	14,180.02	110.0	- .6	44
56#	20.045	18,503.8	78	4,001.59	18,065.83	140.0	- .4	45
57#	20.046	25,295.0	74	7,148.16	24,263.69	190.0	- .3	46
58#	20.047	38,448.2	68	15,805.68	35,049.17	280.0	- .2	47
59#	20.048	69,554.4	45	49,560.84	43,801.00	380.0	- .2	48
60#	20.049	97,380.5	-17	93,213.43	-28,216.41	-220.0	.3	49
61#	20.050	56,039.8	-59	28,818.65	-47,014.39	-370.0	.2	50
62#	20.051	34,440.2	-72	10,733.37	-32,708.51	-260.0	.2	51
63#	20.052	24,914.4	-77	5,434.59	-24,314.45	-180.0	.3	52
64#	20.053	19,586.4	-81	3,241.20	-19,325.48	-150.0	.4	53
65#	20.054	16,229.2	-82	2,144.11	-16,088.94	-130.0	.5	54
66#	20.055	13,914.8	-84	1,520.28	-13,831.50	-110.0	.6	55
67#	20.056	12,228.4	-85	1,134.42	-12,175.67	- 97.0	.7	56
68#	20.057	10,946.8	-85	878.47	-10,910.49	- 87.0	.7	57
69#	20.058	9,938.0	-86	700.78	- 9,913.28	- 79.0	.8	58
70#	20.059	9,125.5	-86	572.01	- 9,107.84	- 72.0	.9	59
71#	20.060	8,456.6	-87	475.60	- 8,443.21	- 67.0	.9	60

FIGURE 4

Since crystal specifications are more often given in terms of Δ_{c_L} instead of Δ_{c_o}, it is desirable to express (21) in terms of Δ_{c_L}.

From (15)

$$\frac{C_1}{C_o} = 2\,\Delta_{c_o} \quad (22)$$

$$\frac{\Delta_{c_o}}{\Delta_{c_L}} = \frac{C_o + C_L}{C_o} \quad (23)$$

Substituting (23) in (21)

$$Z_i = \frac{1}{\omega C_o}\left[\frac{\Delta C_o}{\Delta_{c_L}(C_o + C_L)}\right] + \left[\frac{\Delta C_o}{\Delta_{c_L}(C_o + C_L)}\right]^2 + \ldots \quad (24)$$

$$Z_i = K_1\left[K_2\Delta + (K_2\Delta)^2 + \ldots\right] \quad (25)$$

XTAL Z ABOUT FS=20MHZ FOR CO=5PF, DF=330PPM(32PF LOAD), AND RS=25 OHMS

FREQ IN MHZ
L IN UH
C IN PF
DF (RELATIVE TO FS=20MHZ) IN KHZ

	FREQ	Z	PH	ZR	ZI	L	C	DF
1#	20.0050	183.6	80	31.2	180.9	1.4	-44.0	5.0
2#	20.0051	187.6	80	31.3	185.0	1.5	-43.0	5.1
3#	20.0052	191.6	81	31.4	189.0	1.5	-42.1	5.2
4#	20.0053	195.7	81	31.6	193.1	1.5	-41.2	5.3
5#	20.0054	199.8	81	31.7	197.2	1.6	-40.4	5.4
6#	20.0055	203.9	81	31.9	201.4	1.6	-39.5	5.5
7#	20.0056	208.0	81	32.0	205.5	1.6	-38.7	5.6
8#	20.0057	212.1	81	32.2	209.7	1.7	-38.0	5.7
9#	20.0058	216.3	81	32.3	213.8	1.7	-37.2	5.8
10#	20.0059	220.5	82	32.5	218.0	1.7	-36.5	5.9
11#	20.0060	224.7	82	32.6	222.3	1.8	-35.8	6.0
12#	20.0061	228.9	82	32.8	226.5	1.8	-35.1	6.1
13#	20.0062	233.1	82	33.0	230.8	1.8	-34.5	6.2
14#	20.0063	237.4	82	33.1	235.0	1.9	-33.9	6.3
15#	20.0064	241.8	82	33.3	239.3	1.9	-33.3	6.4
16#	20.0065	246.0	82	33.4	243.7	1.9	-32.7	6.5
17#	20.0066	250.3	82	33.6	248.0	2.0	-32.1	6.6
18#	20.0067	254.6	82	33.8	252.4	2.0	-31.5	6.7
19#	20.0068	259.0	83	33.9	256.8	2.0	-31.0	6.8
20#	20.0069	263.4	83	34.1	261.2	2.1	-30.5	6.9
21#	20.0070	267.8	83	34.3	265.6	2.1	-30.0	7.0
22#	20.0071	272.2	83	34.4	270.0	2.1	-29.5	7.1
23#	20.0072	276.7	83	34.6	274.5	2.2	-29.0	7.2
24#	20.0073	281.1	83	34.8	279.0	2.2	-28.5	7.3
25#	20.0074	285.6	83	34.9	283.5	2.3	-28.1	7.4
26#	20.0075	290.1	83	35.1	288.0	2.3	-27.6	7.5
27#	20.0076	294.7	83	35.3	292.6	2.3	-27.2	7.6
28#	20.0077	299.3	83	35.4	297.1	2.4	-26.8	7.7
29#	20.0078	303.8	83	35.6	301.7	2.4	-26.4	7.8
30#	20.0079	308.4	83	35.8	306.4	2.4	-26.0	7.9
31#	20.0080	313.1	83	36.0	311.0	2.5	-25.6	8.0
32#	20.0081	317.7	84	36.1	315.7	2.5	-25.2	8.1
33#	20.0082	322.4	84	36.3	320.4	2.5	-24.8	8.2
34#	20.0083	327.1	84	36.5	325.1	2.6	-24.5	8.3
35#	20.0084	331.8	84	36.7	329.8	2.6	-24.1	8.4
36#	20.0085	336.6	84	36.9	334.6	2.7	-23.8	8.5
37#	20.0086	341.4	84	37.1	339.3	2.7	-23.5	8.6
38#	20.0087	346.2	84	37.3	344.2	2.7	-23.1	8.7
39#	20.0088	351.0	84	37.4	349.0	2.8	-22.8	8.8
40#	20.0089	355.8	84	37.6	353.8	2.8	-22.5	8.9
41#	20.0090	360.7	84	37.8	358.7	2.9	-22.2	9.0

FIGURE 5

From (25) above it is hypothesized that Z will be a nearly linear function of DF over the 1.7 KHz range interest about the 32 pF antiresonance. Figure 6 is a linear regression analysis of the data of Figure 5 to test the hypothesis. The regression shows excellent correlation with a maximum error of 1.5% and a standard error of 1.4%. Figure 7 is a plot of the regression line and the data of Figure 5 with the crystal impedance as a function of DF. For the purpose of further analysis the regression result will be used.

$$Z_i = 44.41307\ DF - 43.82805 \quad (26)$$

Oscillator Design Considerations

Figure 8 is the schematic diagram of a colpitts oscillator circuit with a varactor diode added in series with the crystal to permit VCXO operation.[13,14] Good design practice dictates chosing C4 and C5 large compared to 32 pF so that the load seen by the crystal is almost totally determined by D2. Doing so insures that the operating frequency is nearly independent of transistor variations. In Figure 8 then the crystal sees only D2 and C3 as a load. It is necessary to select the varactor and the proper bias to provide a 32 pF load for the crystal. Since the oscillator frequency is a direct function of the varactor bias, the bias supply must be regulated, nominal bias voltage is limited on the low side by the combination of RF peak voltage plus the audio peak voltage. The bias voltage must be large enough to insure the varactor diode remains reverse biased. On the high side, bias voltage must be low enough to permit regulation over the battery life voltage variations without excessive current drain or

circuitry. A voltage of about 7 volts will satisfy both conditions above for a nominal 12.5 volt nickel-cadmium battery supply. R2 is selected to reduce variations in bias voltage due to Irev of the varactor diode, and yet not reduce the varactor Q. Finally C3 will be made small enough compared to D2 so as to provide enough range to adjust the oscillator over the calibration tolerance of the crystal and still provide resolution to set the oscillator on frequency. The tank circuit in the collector is tuned to x 3 the fundamental crystal frequency, which is then amplified without further multiplication straight through to the antenna. Other oscillator considerations not related to the VCXO are well covered in the literature.[15,16]

LINEAR REGRESSION ANALYSIS

Ind. Variable: DF
Dep. Variable: ZI

Intercept	=	-43.82805
Regression Coefficient	=	44.41307
Std. Error of Reg. Coef.	=	.179
Computed T Value	=	248.405
Correlation Coefficient	=	1.000
Std. Error of Estimate	=	1.355

ANALYSIS OF VARIANCE FOR THE REGRESSION

Source of Variation	D.F.	Sum of Sq.	Mean Sq.	F. Value
Attributable to Regression	1	.113E+06	.113E+06	.617E+05
Deviation from Regression	39	71.561	1.835	
Total	40	.113E+06	2832.356	

Y Observed	Y Estimated	Residual	Std. Residual
180.900	178.237	2.662	1.966
185.000	182.679	2.321	1.714
189.000	187.120	1.880	1.388
193.100	191.561	1.539	1.136
197.200	196.003	1.197	.884
201.400	200.444	.956	.706
205.500	204.885	.615	.454
209.700	209.326	.374	.276
213.800	213.768	.323E-01	.238E-01
218.000	218.209	-.209	-.154
222.300	222.650	-.350	-.259
226.500	227.092	-.592	-.437
230.800	231.533	-.733	-.541
235.000	235.974	-.974	-.719
239.300	240.416	-1.116	-.824
243.700	244.857	-1.157	-.854
248.000	249.298	-1.293	-.958
252.400	253.739	-1.339	-.989
256.800	258.181	-1.381	-1.019
261.200	262.622	-1.422	-1.050
265.600	267.063	-1.463	-1.080
270.000	271.505	-1.505	-1.111
274.500	275.946	-1.446	-1.068
279.000	280.387	-1.387	-1.024
283.500	284.829	-1.329	-.981
288.000	289.270	-1.270	-.938
292.600	293.711	-1.111	-.820
297.100	298.153	-1.053	-.777
301.700	302.594	-.894	-.660
306.400	307.035	-.635	-.469
311.000	311.476	-.476	-.352
315.700	315.918	-.218	-.161
320.400	320.359	.409E-01	.302E-01
325.100	324.800	.300	.221
329.800	329.242	.558	.412
334.600	333.683	.917	.677
339.300	338.124	1.176	.868
344.200	342.566	1.634	1.207
349.000	347.007	1.993	1.471
353.800	351.448	2.352	1.738
358.700	356.890	2.810	2.075

FIGURE 6

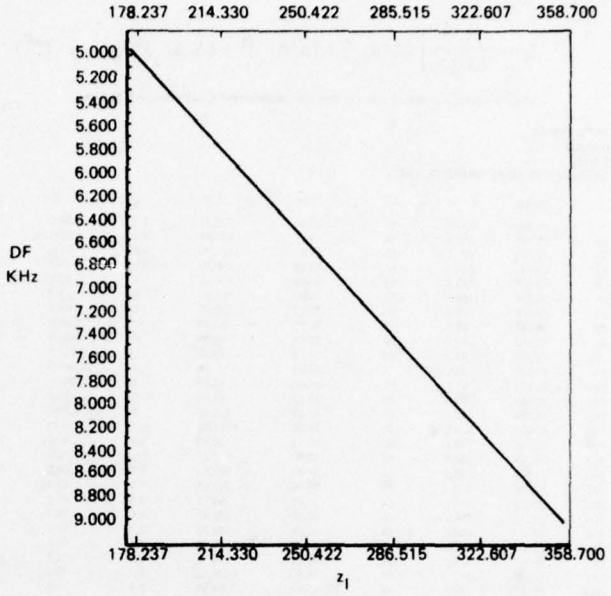

FIG 7

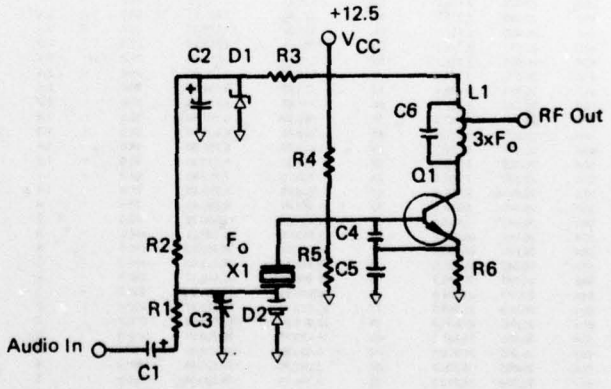

FIG 8

VCXO Design

From (26) it is apparent that the functional relation between the varactor voltage and the oscillator frequency deviation will be the same as the functional relation between the varactor voltage and the varactor impedance. The general relation between the varactor capacity, C_t, and the reverse bias voltage, V, is given by[17]

$$C_t = C_c + \frac{C_j}{\left(1 + \frac{V}{V_f}\right)^{\gamma}} \tag{27}$$

γ varies with the junction diffusion profile of the diode. V_f is the contact potential of the diode, and C_c is the fixed capacity of the package and device. For a typical abrupt junction varactor, the formula becomes.

$$C_t = .18\ \text{pF} + \frac{C_j}{\left(1 + \frac{V}{.6}\right)^{.44}} \tag{28}$$

Since C_c is small compared with the other term, and V_f is small compared to V; then C_t may be approximated by

$$C_t = \frac{C_j}{\sqrt{1+V}} \tag{29}$$

This approximation is accurate to 1.5% over the range of V from 4 to 10 volts for C_t=32 pF at 7 volts. Using a nominal value of V=7 volts and C_t=32 pF C_j is given by

$$C_j = \sqrt{1+7}\ \ 32\ \text{pF} \tag{30}$$

Varactor diodes are usually specified with V=4 volts, using (29) and (30) C_t=40 pF. Commercially available varactor diodes have C_t's from 6.8 to 100 pF at V=4 volts. Using (26), (29) and (30) the oscillator deviation vs varactor voltage is

$$DF = \frac{Z_j + 43.82805}{44.41307} \tag{31}$$

$$DF = \frac{\frac{1}{\omega C_j} + 43.8280805}{44.41307} \cong \frac{\frac{\sqrt{1+V}}{2\pi\ 20 \times 10^6 \times 9.05 \times 10^{-11}} + 43.8}{44.4} \tag{32}$$

(32) is plotted in Figure 9 showing DF vs V. Since a deviation of 1.7 KHz is necessary at the crystal fundamental to produce 5 KHz deviation at the operating frequency (x 3), the linearity of this curve over that range is of interest. From Figure 9 notice it is necessary to go about V=4 volts for -1.7 KHz deviation to about V=10 volts for +1.7 KHz deviation. This approximately ±3 volts swing sets the lower limit on the audio driving voltage of 6 volts peak to peak. Since the curve of Figure 9 does not appear to be very linear, the audio distortion should be expected to suffer.

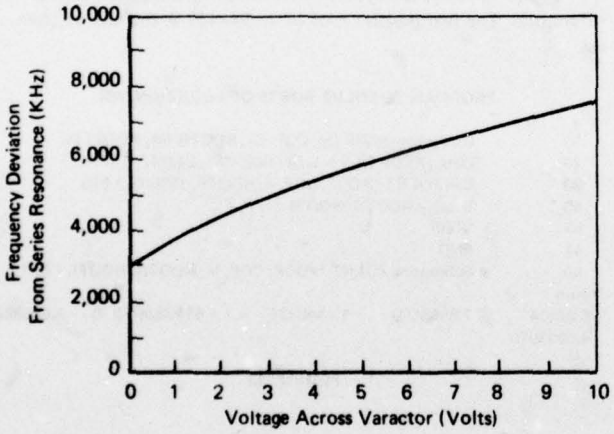

FIG 9

A maximum of 10% distortion is permitted, but good design practice dictates keeping the nominal distortion due to the varactor under 1% to allow for tolerance variations and the distortion in the audio amplifier driving the modulator. Figure 10 is a Fourier analysis[18] of the expected recovered audio for a sine wave input to the modulator described by (32). The audio voltage input level was adjusted to permit a maximum of ±5 KHz deviation at the operating frequency. From Figure 10 the total harmonic distortion is 6%; clearly this is too high.

VCXO Linearization

Figure 11 shows the circuit of Figure 8 with the frequency adjust capacitor C3 replaced by a parallel inductor L1. If the reactance of L1 is larger than that of D2, the parallel combination will

Non Linearized VCXO Deviation
Deviation Set to be ± 5KHZ Max at Operating Freq=3 x Crystal Freq
2/23 17:12

Fourier Analysis
The technique used here is the Cooley-Tukey algorithm

Do you want to read data from a file? Yes

Type the input file -- Name: Data

Do you want the results written on a file? No

Input data echo check --
Type 0 for none, 1 for data only, or 2 for labeled data: 1

-.000	.311	.556	.711	.764
.711	.556	.311	-.000	-.343
-.668	-.909	-1.000	-.909	-.668
-.343				

Do you want to correct any array values? No

The Average Value is .058 The RMS Value is .622

The Harmonic	Peak Value	% of Fundamental	Degrees of Displacement
Fundamental	.87	100	90
2	.06	6	360
3	.01	0	*
4	.00	0	*
5	.00	0	*
6	.00	0	*
7	.00	0	*

*Component too small for displacement to have any meaning.

Non Linearized VCXO Deviation vs. Sine Wave Input to Varactor
Deviation Set to be ± 5KHZ Max at Operating Freq=3 x Crystal Freq

Title -- NLVCXO KHZ 5KHZ = 1 Normalized

	V	DEL	DEL V
1#	7.000000000	6686.050824	-1.7881393408E-11
2#	8.561303756	7104.893010	3.1130531097E-01
3#	9.866435577	7512.516135	5.5587918569E-01
4#	10.745178566	7771.245608	7.1111686936E-01
5#	11.053752068	7859.789134	7.1424298501E-01
6#	10.745178565	7771.245608	7.1111686916E-01
7#	9.866435575	7512.516134	5.5587918530E-01
8#	8.561303753	7104.893009	3.1130531042E-01
9#	6.999999997	6686.050823	-7.1525573631E-10
10#	5.448696241	6013.941786	-3.4326542237E-01
11#	4.133564421	5472.135895	-6.6824895625E-01
12#	3.254821433	5070.242055	-9.0948526010E-01
13#	2.946247932	4919.384155	-1.0000000003E+00
14#	3.254821436	5070.242057	-9.0948525905E-01
15#	4.133564427	5472.135898	-6.6834895447E-01
16#	5.448696250	6013.941789	-3.4326542033E-01

FIGURE 10

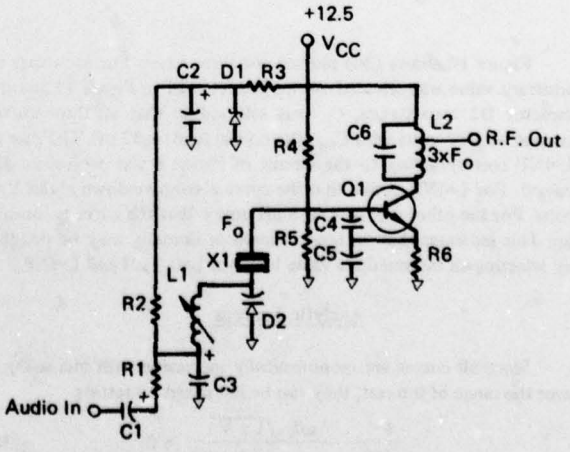

FIG 11

look net capacitive. By chosing L1 and D2 properly, this net capacitance can be made equal to 32 pF; and L1 can serve the same function as the vernier adjust capacitor in Figure 8. In Figure 1, C3 is chosen to look like a RF short to the inductor but still have relatively high reactance over the audio range. All other components are chosen with the same considerations analogous to Figure 8. By proper choice of L1 and D2 in Figure 11 the undesirable nonlinearity of the circuit of Figure 8 can be considerably reduced.

In Figure 12

$$\frac{1}{\omega C_{eq}} = \frac{1}{\omega C_t - \frac{1}{\omega L}} = \frac{\omega L}{\omega^2 L C_t - 1} \tag{33}$$

$$C_{eq} \approx C_t - \frac{1}{\omega^2 L} \tag{34}$$

using (29)

$$C_{eq} = \frac{C_i}{\sqrt{1+V}} - \frac{1}{\omega^2 L} = \frac{\omega^2 L C_i - \sqrt{1+V}}{\omega^2 L \sqrt{1+V}} \tag{35}$$

using (31)

$$DF = \frac{\frac{\omega L \sqrt{1+V}}{\omega^2 L C_i - \sqrt{1+V}} + 43.82805}{44.41307} \tag{36}$$

$$DF \sim \frac{\omega L \sqrt{1+V}}{\omega^2 L C_i - \sqrt{1+V}} \tag{37}$$

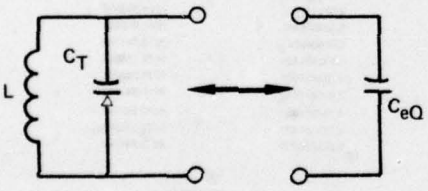

FIG 12

Figure 14 shows (36) plotted for three cases. For each case an arbitrary value was selected for the inductor L1 in Figure 11 and the varactor D2 capacitance, C_i, was selected so that all three curves crossed at V=7 volts with C_{eq} (the crystal load) = 32 pF. The case of *L=INF corresponding to the circuit of Figure 8 was previously discussed.* For L=INF notice that the curve is concave down about V=7 volts. For the other case of L=0.5 μH notice that the curve is concave up. This indicates that an improvement in linearity may be possible by selecting an intermediate value between L=0.5 μH and L=INF.

Analytic Analysis

Since all curves are monotonically increasing with increasing V over the range of interest, they can be linearized by setting

$$\frac{\delta^2}{\delta V} \frac{\omega L \sqrt{1+V}}{\omega^2 L C_i - \sqrt{1+V}} = 0 \tag{38}$$

Expanding (37) in a power series

$$\omega L \left[\frac{\sqrt{1+V}}{\omega^2 L C_i - \sqrt{1+V}} \right] \tag{39}$$

$$K \approx \omega^2 L C_i \tag{40}$$

$$\frac{\sqrt{1+V}}{K - \sqrt{1+V}} = \frac{(1+V)^{1/2}}{K} + \frac{1+V}{K^2} + \frac{(1+V)^{3/2}}{K^3} + \ldots \tag{41}$$

$$\frac{\delta}{\delta V} \frac{\sqrt{1+V}}{K - \sqrt{1+V}} = \frac{(1+V)^{-1/2}}{2K} + \frac{1}{K^2} + \frac{3(1+V)^{1/2}}{2K^3} + \frac{2(1+V)}{K^4} + \ldots \tag{42}$$

$$\frac{\delta^2}{\delta V^2} \frac{\sqrt{1+V}}{K - \sqrt{1+V}} = -\frac{(1+V)^{-3/2}}{4K} + \frac{3(1+V)^{-1/2}}{4K^3} + \ldots = 0 \tag{43}$$

$$K^4 - 3(1+V)K^2 - 8(1+V)^{3/2}K - 15(1+V)^2 \cong 0 \tag{44}$$

set V=7 volts

$$K^4 - 24K^2 - 181K - 960 = 0 \tag{45}$$

Figure 13 shows the roots of (45) solved by using the POLRT[19] subroutine. The real positive root of 7.8948459 is the one of interest.

PROGRAM TO SOLVE ROOTS OF EQUATION (45)

```
 10        Dimension XCOF (5), COF (5), ROOTR (4), ROOTI (4)
 20        Data [XCOF (I), I = 1, 5] /-960, -181, -24.0, 1/
 30        Call POLRT (XCOF, COF, 4, ROOTR, ROOTI, I ER)
 40        Display ROOTR, ROOTI
 50        STOP
 51        END
 60        Subroutine POLRT (XCOF, COF, M, ROOTR, ROOTI, I ER)
> Run
-5.066741   7.8948458   -1.4140524   -1.4140524   0  0   -4.6903915
 4.6903915
```

FIGURE 13

$$K \cong 7.9 = \omega^2 L C_i \tag{46}$$

By choosing L and C_i subject to the constraint of (46) the second derivative of (36), with respect to V, will be zero about V=7. In addition L and C_i in parallel must provide a net equivalent 32 pF load to the crystal for V=7 or stated analytically

$$C_i = \sqrt{8}\left(32\text{ pF} + \frac{1}{\omega^2 L}\right) \tag{47}$$

Solving (46) and (47) simultaneously for ω=2π 20 MHz yields L=3.54836242 μH and C_i=140.987105 pF. Or expressing the varactor capacity at the conventional V=4 volts, C_i=63.05 pF. For the above example both L1 and D2 (Figure 11) have values within the ranges normally available at 20 MHz, and therefore the circuit is practically realizable.

In Figure 14 notice that for L=3.5 μH the concave nature of the curves does in fact disappear.

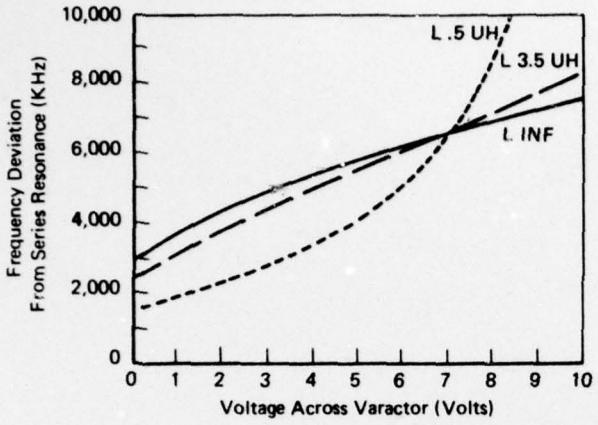

FIG 14

Figure 15 is the Fourier analysis for a sine wave input to the modulator described by (36) for the linearized values given by (46) and (47). This analysis is analogous to that of Figure 10. Distortion is reduced from the 6% of the circuit of Figure 8 to below the resolution of the analysis program for Figure 11.

Linearized VCXO
Deviation Set to be ± 5KHZ Max at Operating Freq=3 x Crystal Freq
2/23 18:20

Fourier Analysis
The technique used here is the Cooley-Tukey algorithm

Do you want to read data from a file? Yes

Type the input file -- Name: *Data*

Do you want the results written on a file? No

Input data echo check --
Type 0 for none, 1 for data only, or 2 for labeled data: 1

.000	.378	.702	.972	1.000
.922	.702	.378	-.000	-.375
-.892	-.906	-.982	-.906	-.692
-.375				

Do you want to correct any array values? No

The Average Value is .005 The RMS Value is .699

The Harmonic	Peak Value	% of Fundamental	Degrees of Displacement
Fundamental	.99	100	90
2	.00	0	*
3	.00	0	*
4	.00	0	*
5	.00	0	*
6	.00	0	*
7	.00	0	*

*Component too small for displacement to have any meaning.

Linearized VCXO Deviation vs. Sine Wave Input to Varactor
Deviation Set to be ± 5KHZ Max at Operating Freq=3 x Crystal Freq

Title -- LVCXO		KHZ	5KHZ = 1 Normalized
	V	DEL	DELN
1#	7.000000000	6585.913563	1.07297056936-10
2#	6.148622034	7215.400323	3.77707353326-01
3#	9.122376776	7756.355547	7.02293633126-01
4#	9.773018892	8122.764634	9.32147988606-01
5#	10.001494020	8252.512730	1.00000000026+00
6#	9.773018891	8122.764634	9.22147988146-01
7#	9.122376774	7756.355546	7.02293632646-01
8#	8.148622032	7215.400322	3.77707352686-01
9#	6.999999998	6585.913562	-6.61638363236-10
10#	5.851377964	5961.510438	-3.74857048446-01
11#	4.877623223	5431.937108	-6.92413914986-01
12#	4.226881107	5075.562819	-9.06253146486-01
13#	3.998505660	4949.526337	-9.81870800856-01
14#	4.226881109	5075.562821	-9.06253148586-01
15#	4.877623228	5431.937112	-6.92413913366-01
16#	5.851377970	5961.510442	-3.74857046316-01

FIGURE 15

Conclusion

By employing a circuit like Figure 11 with proper choice of components, it is possible to compensate for the normally present nonlinearities of a VCXO FM modulator. Component values necessary to achieve this linearization have practical values and therefore the technique is realizable for practical cases.

References

1. "EIA Standard-Land Mobile Communications FM or PM Transmitters 25-470 MHz," RS-152A, New York: Electronic Industries Association.

2. "EIA Standard-Continuous Tone Controlled Squelch System (CTCSS)," RS-220, New York: Electronic Industries Association.

3. D.H. Hamsher, Communications System Engineering Handbook, New York: Mc-Graw Hill, 1967, pp. 17-1 to 17-48.

4. Motorola Communications and Electronics, Inc., "Data Sheet Miniature Crystals HC 18/U or HC 25/U," TIC-3448, Chicago, Ill.

5. U.S. Government "MIL Specification MIL-C-3098D," CR-64/U.

6. "IRE Standards on Piezoelectric Crystals–The Piezo Electric Vibrator: Definitions and Methods of Measurement, 1957," Proc. IRE pp. 353-358, March 1957.

7. F.K. Priebe, and A.D. Ballato, "Comparison of Various Methods Used for Determination of Quartz Crystal Parameters in the Frequency Range 1 to 30 MHz," Proc. 18th Annual Symposium on Frequency Control, pp. 458-486.

8. E. Hafner, "The Piezoelectric Crystal Unit–Definitions and Methods of Measurement," Proc. of IEEE, Vol. 57, No. 2, pp. 179-201, Feb. 1969.

9. E.A. Gerber, "State of the Art–Quartz Crystal Units and Oscillators," Proc. IEEE, Vol. 54, No. 2, pp. 103-116, Feb. 1966.

10. D. Kemper, and L. Rosine, "Quartz Crystals for Frequency Control," Electro-Technology, pp. 43-49, June 1969.

11. J. McDermott, "Focus on Piezoelectric Crystals and Devices," Electronic Design 17, pp. 44-54, August 16, 1973.

12. "AC-Coded," Cupertino California: Tymshare Inc., 1970.

13. Microwave Devices Group, Motorola Semiconductor Products Inc., "FM Modulation Capabilities of Epicap VVC's," Application Note AN-210, Phoenix, Arizona.

14. R.L. Kent, "The Voltage Controlled Oscillator (VCXO) and its Capabilities and Limitations," Proc. 19th Annual Symposium on Frequency Control, pp. 642-654, 1965.

15. Clarke and Hess, Communications Circuits, Reading, Mass: Addison-Wesley, pp. 245-255, 1971.

16. F. Palenschat, "Design RF Oscillators from Transistor Data Sheets," Electronic Design 20, pp. 70-74, September 27, 1974.

17. R.D. Pollard, M.J. Howes, and D.V. Morgan, "Considerations of Accuracy in the Determination of the Capacitance-Voltage Law Parameters of Microwave Diodes," Proc. IEEE, pp. 323-325, Feb. 1975.

18. "#Fourier," Cupertino, California: Tymshare Inc.

19. "Batch Fortran," Cupertino, California: Tymshare Inc., p. 251, 1972.

PHASE NOISE MEASUREMENT USING A HIGH RESOLUTION COUNTER WITH ON-LINE DATA PROCESSING

Luiz Peregrino
David W. Ricci
Hewlett-Packard Company
Santa Clara, California

Summary

The measurement of close-in phase noise using time domain techniques will be discussed. A review of the theoretical basis for the measurements and some extensions will be presented. A system for making the measurements using a high resolution reciprocal counter and a desk top calculator will be described. The capabilities of the system will be reviewed.

Introduction

The measurement of phase noise can be made by a variety of methods which are described in the current literature. However, if one desires to measure the spectral characteristics close into the carrier, the task becomes difficult and time consuming. Measurements down to the 10 to 100 Hz range can be accomplished with spectrum or wave analyzers depending on the noise level. Measurements much below these offset frequencies are virtually impossible with these techniques.

The techniques to make measurements closer to the carrier usually resort to time domain analysis which is also described in the current literature. The primary impediment to the utilization of these techniques has been the lack of equipment to make it easy to use. Recent equipment advances such as programmable instruments and versatile calculators, for example, have provided the means to implement these techniques.

Before describing the measurement system, a review of the theoretical basis for the measurement will be presented. Most of this review will follow the standard literature with some exceptions that will tend to put more emphasis on the calculator utilization.

A general transfer function will be derived for the counter-calculator system which should cover a standard frequency measurement or comparison of the phase between two oscillators or the phase of an oscillator compared to itself through a delay line.

For a constant gate time (or constant delay), the transfer function can be written as the product of two functions, one controlled by the counter (or delay line) and the other by the calculator.

We prove that a linear combination of frequency measurements is equivalent to a filter which can be adjusted by proper choice of the linear combination coefficients. A particular choice of coefficients is assumed for which we derive closed formulas for the continuous and the delta function (bright line) spectral densities. The minimum spectral level due to counter quantization is derived.

Derivation of Time Domain Relationships to Phase Spectra Characteristics

Definitions and Notation

Let us begin with a brief review of random variables, linear systems, notations and definitions.

Let $x(t)$ be a real random variable. The auto correlation function of $x(t)$ is defined as:

$$R_x(t,\tau) = \langle x(t) \cdot x(t+\tau) \rangle \tag{1}$$

where $\langle\ \rangle$ means statistical or ensemble average.

If $x(t)$ is stationary in the wide sense, then the auto correlation does not depend on t and we can write:

$$R_x(\tau) = \langle x(t) \cdot x(t+\tau) \rangle \tag{2}$$

If $x(t)$ is ergodic, then the statistical average can be replaced by time average.

We will assume without any loss of generality that the mean value of $x(t)$ is zero. In this case we have:

$$R_x(0) = \langle x^2(t) \rangle = \sigma_x^2 \tag{3}$$

The spectral density of $x(t)$ is defined as the Fourier transform of its auto correlation function:

$$S_x(\omega) = \int_{-\infty}^{\infty} R_x(\tau)\, e^{-j\omega\tau} dt \tag{4}$$

The inversion formula gives:

$$R_x(\tau) = \frac{1}{2\pi} \int_{-\infty}^{\infty} S_x(\omega)\, e^{+j\omega\tau} d\omega \tag{5}$$

Let a linear time invariant system with transfer function $H(\omega)$ be driven by the random variable $x(t)$. The output of the system represented by $m(t)$ will be also a random variable as in Fig. 1.

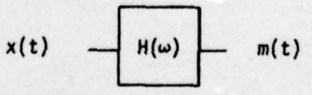

Figure 1

It can be shown that:

$$S_m(\omega) = \left| H(\omega) \right|^2 S_x(\omega) \tag{6}$$

Equation 6 will be used to determine $S_x(\omega)$ in the next section. For more details see references 1,2 and 3.

Measuring Spectral Density

Normally a narrow band filter represented by $H(\omega)$ is used to determine the spectra of the random variable $x(t)$ as explained below. Two special cases are considered.

A. Continuous Spectra - The spectral density can be considered approximately constant over the filter bandwidth and we can write:

$$\sigma_m^2 = R_m(0) \tilde{=} S_x(\omega_o) \frac{1}{\pi} \int_{\omega_1}^{\omega_2} |H(\omega)|^2 d\omega$$

$$\tilde{=} \frac{1}{\pi} |H(\omega_o)|^2 \cdot (\omega_2 - \omega_1) \cdot S_x(\omega_o) \qquad (7)$$

where ω_o is the filter center frequency and ω_1, ω_2 define the filter band. (We have used the fact that $|H(\omega)|$ and $S_x(\omega)$ are even functions of ω.)

Solving for the spectral density we get:

$$S_x(\omega_o) \tilde{=} \frac{\sigma_m^2}{\frac{1}{\pi} \int_{\omega_1}^{\omega_2} |H(\omega)|^2 d\omega} \tilde{=} \frac{\sigma_m^2}{\frac{1}{\pi} |H(\omega_o)|^2 (\omega_2 - \omega_1)} \qquad (8)$$

Where σ_m^2 can be determined with an average power meter or using samples of K measurements of m as:[1,4,5]

$$\sigma_m^2 = \left\langle \frac{1}{K-1} \sum_{i=1}^{K} (m_i - \frac{1}{K} \sum_{j=1}^{K} m_j)^2 \right\rangle$$

$$= \left\langle \frac{1}{K-1} \left[(\sum_{i=1}^{K} m_i^2) - \frac{1}{K} (\sum_{j=1}^{K} m_j)^2 \right] \right\rangle^* \qquad (9)$$

If we use only one sample of K measurements of m(t), we get an estimation of σ_m^2 which is satisfactory for most cases.

B. The Spectra Contains Delta Functions. This is the case when x(t) contains periodic terms, then the result of the integration is no longer dependent on the filter bandwidth.

For example let x(t) be given by:

$$x(t) = x_p \cdot \cos \omega_o t = \frac{1}{2} x_p [e^{j\omega_o t} + e^{-j\omega_o t}] \qquad (10)$$

We have:

$$S_x(\omega) = 2\pi \left(\frac{x_p}{2}\right)^2 [\delta(\omega - \omega_o) + \delta(\omega + \omega_o)] \qquad (11)$$

Which gives:

$$\sigma_m^2 = |H(\omega_o)|^2 \frac{1}{2} x_p^2 \qquad (12)$$

Note that $\frac{1}{2} x_p^2$ is the average power of x(t).

It should be pointed out that during all the derivations we will use the "two-sided" spectral density, that is the integrations will be from $-\infty$ to $+\infty$. This will keep our Fourier transform pairs in the standard notation used by most EE's. Fourier frequency will be in radians per seconds.

Frequency Counter as a Linear System

Consider the signal

$$V(t) = V_o \cdot \cos(2\pi\gamma_o t + \theta_o + \theta(t)) \qquad (13)$$

where V_o and γ_o are the nominal amplitude and frequency and $\theta(t)$ represents a random phase variation. θ_o is chosen such that $\langle\theta(t)\rangle = 0$.

Any amplitude variation is assumed to be eliminated by limiters or some other method and for this reason is disregarded.

The signal phase is defined as:

$$\phi(t) = 2\pi\gamma_o t + \theta_o + \theta(t) \qquad (14)$$

The signal frequency $\nu(t)$ and the angular frequency $\Omega(t)$ are related by:

$$2\pi\nu(t) = \Omega(t) = \frac{d\phi}{dt} \qquad (15)$$

and are assumed to be positive for all t, which is equivalent to $\phi(t)$ be a monotonic increasing function of time, that is, $2\pi\nu_o - \theta(t) > 0$.

Counter Model

An ideal counter can be modeled as a system that measures phase variation over an interval of time τ, called gate time, and divides the result by $2\pi\tau$.

Let $\nu(t)$ represent the result of a counter measurement, then have:

$$\nu(t) = \frac{1}{2\pi\tau} \cdot [\phi(t) - \phi(t-\tau)] \qquad (16)$$

Taking the Fourier transform from both sides and using the shifting theorem, we have:

$$\Gamma(\omega) = \frac{1}{2\pi\tau} [\Phi(\omega) - \Phi(\omega) e^{-j\omega\tau}] \qquad (17)$$

Here the upper case letters are used to represent the Fourier transform.

---

*For complex m(t), σ_m^2 is given by:

$$\sigma_m^2 = \left\langle \frac{1}{K-1} \sum_{i=1}^{K} |m_i - \frac{1}{K} \sum_{j=1}^{K} m_j|^2 \right\rangle$$

$$= \left\langle \frac{1}{K-1} \left[(\sum_{i=1}^{K} |m_i|^2) - \frac{1}{K} |\sum_{j=1}^{K} m_j|^2 \right] \right\rangle$$

Which can be reduced to:

$$\Gamma(\omega) = \frac{\omega}{2\pi} \cdot \frac{\sin \omega\tau/2}{\omega\tau/2} \cdot e^{-j\omega\tau/2} \cdot \Phi(\omega) \qquad (18)$$

We may conclude that the counter is a linear system with transfer function (or gain) given by:

$$H_\phi(\omega) = \frac{\omega}{2\pi} \frac{\sin \omega\tau/2}{\omega\tau/2} \cdot e^{-j\omega\tau/2} \qquad (19)$$

Where the index ϕ in transfer function means that it applies for the phase as input.

The transfer function when the angular frequency $\Omega(t)$ is considered as input is given by:

$$H_\Omega(\omega) = \frac{1}{j\omega} H_\phi(\omega) = \frac{1}{2\pi j} \cdot \frac{\sin \omega\tau/2}{\omega\tau/2} e^{-j\omega\tau/2} \qquad (20)$$

Practical Counters

Below are some problems that we might incur due to practical considerations.

In reality a counter detects and counts zero crossings of the signal being measured. If the phase of the input signal is a monotonic increasing function of time, as it was assumed, then the model is quite satisfactory.

On the other hand if the phase of the input signal can decrease, which is equivalent to a negative frequency, then we may get extra counts, for example in the vector diagram representation of the signal, Fig. 2. Every time that the resultant vector crosses the Y axis from right to left, we get a count; if the vector goes back we will get an extra count.

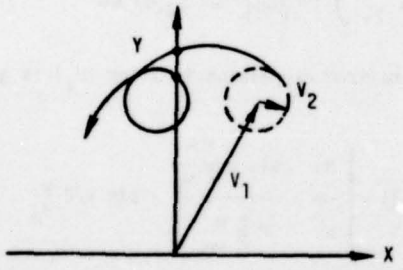

Figure 2

In Fig. 2, V_1 represents a sine wave and V_2 a interference that causes phase modulation.

Practical counters also have quantization problems, that is the number of counts is an integer and any fraction of 2π in the phase variation is disregarded. This problem is reduced by reciprocal counters with a high frequency clock. In a reciprocal counter, the actual gate time is a multiple of the signal period and if the phase fluctuation is not too large ($\dot{\theta}(t) << 2\pi\nu_o$), then the gate time can be assumed constant as far as the counter transfer function is concerned.

The last problem in a real counter is the sampling, that is the counter output is not a continuous variable but a sequence of numbers obtained at the end of each gate time. A special case solution is presented in reference 5, Appendix 1.

Modifying the Counter Transfer Function

In order to measure spectral density, we want the counter to look like a very narrow band filter, ideally we want a delta function.

A weighted combination of a sequence of measurements taken at different times will give:

$$m(t) = \sum_{i=0}^{M} \alpha_i \cdot \nu_i \qquad (21)$$

where $\nu_i = \nu(t_i)$

Let Fig. 3 represent the phase as a function of time, τ_i the gate time and t_i the time at the end of the i reading. The last reading is taken at the time which is considered to be the current time, that is $t_o = t$.

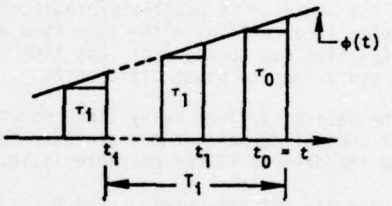

Figure 3

Replacing Y(t) as function of $\phi(t)$ and defining $T_i = t_o - t_i$ we have:

$$m(t) = \frac{\alpha_o}{2\pi\tau_o}\left[\phi(t) - \phi(t-\tau_o)\right] +$$

$$\ldots + \frac{\alpha_M}{2\pi\tau_M}\left[\phi(t-T_M) - \phi(t-T_M-\tau_M)\right] \qquad (22)$$

Taking the Fourier transform we get the transfer function:

$$H_\phi(\omega) = \left[\frac{\alpha_o}{2\pi\tau_o}(1-e^{-j\omega\tau_o}) +\right.$$

$$\left. \ldots + \frac{\alpha_M}{2\pi\tau_M} e^{-j\omega T_M}(1-e^{-j\omega\tau_M})\right] \qquad (23)$$

The counter calculator equivalent transfer function can be adjusted to approximate the desired filter transfer function by proper choice of α_i, τ_i and T_i. The weights α_i can be complex and their phase is equivalent to a change in the time the measurements are made, which can be used to simulate a variable time between measurements.

If we make the gate time τ_i a constant τ and the time between consecutive measurements, defined as dead time, a constant τ_d we have:

$$H_\phi(\omega) = \left[\alpha_0+\alpha_1 e^{-j\omega(\tau+\tau_d)} +\ldots+ \alpha_M e^{-jM\omega(\tau+\tau_d)}\right] \cdot$$

$$\left[\frac{\omega}{2\pi} \cdot \frac{\sin \omega\tau/2}{\omega\tau/2} \cdot e^{-j\omega\tau/2}\right] \qquad (24)$$

The first bracket, which is mainly determined by the calculator via the α_S, can be interpreted as a truncated complex Fourier series and its terms can be adjusted as a series representation of the desired filter function[6,7]. The second bracket can be considered as a fixed filter and for large M the first bracket completely determines H_ϕ.

Other types of measurement such as comparing the phase of two oscillators of same frequency or comparing the phase of an oscillator to itself, using a delay line, will have the same type of transfer function due to the fact that time differences are equivalent to phase differences.

In the case of a fixed delay line, we use the calculator controlled part of the transfer function to achieve the desired filter characteristic.

A particular but very useful choice[7] is $\alpha_i = (-1)^i$ which reduces m(t) to:

$$m(t) = (y_0 - y_1) + (y_2 - y_3) + \ldots + (y_{M-1} - y_M) \qquad (25)$$

Let N = (M+1)/2 be the number of pairs of measurements represented by the terms in parenthesis, then we can reduce H_ϕ to:

$$H_\phi(\omega) = \left[1+e^{-j2\omega(\tau+\tau_d)} + \ldots e^{-j(N-1)2\omega(\tau+\tau_d)}\right]$$

$$\cdot\ 2\sin\left(\omega\frac{\tau+\tau_d}{2}\right)\cdot\frac{\omega}{2\pi}\frac{\sin \omega\tau/2}{\omega\tau/2} e^{-j\omega(\tau+\tau_{d/2})} \qquad (26)$$

The bracket can be recognized as a geometric series which gives:

$$H_\phi(\omega) = \frac{\omega}{\pi} \cdot \frac{\sin \omega\tau/2}{\omega\tau/2} \cdot \sin\left(\omega\frac{\tau+\tau_d}{2}\right) \cdot$$

$$\frac{\sin N\omega(\tau+\tau_d)}{\sin \omega(\tau+\tau_d)} \cdot e^{-j\omega[N(\tau+\tau_d)-\tau_{d/2}]} \qquad (27)$$

A very important point to be kept in mind is that in general this corresponds to a filter with many pass bands.

For most practical cases, the phase noise is a fast decreasing function of ω and only the first pass band of H_ϕ has to be considered, as in references 6 and 7, which have plots of $|H_\Omega(\omega)|$ which is equal to $|H_\phi(\omega)/\omega|$. Error will occur depending on how fast the phase noise decreases as a function of ω such as ω^{-3}, ω^{-2}, ω^0 = constant, and we may have to consider more than one pass band.[6,7]

Calculation of Spectra Density

So far we have proven that the linear combination of the frequency measurements m(t) can be considered as the output of a filter whose input is $\phi(t)$ and transfer function H_ϕ or input $\Omega(t)$ and transfer function $H_\Omega(\omega)$. This is represented in the block diagram, Fig. 4.

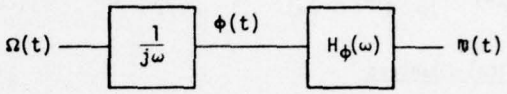

Figure 4

As in the linear system we have two cases.

A. Continuous Spectra - The spectra can be considered as constant over the filter bandwidth. Using the fact that $\alpha_m^2 = R_m(0)$ and eq. 5, we have:

$$\sigma_m^2 = \frac{1}{2\pi}\int_{-\infty}^{+\infty} \left|H_\phi(\omega)\right|^2 S_\phi(\omega)d\omega \qquad (28)$$

If we use $H_\Omega(\omega)$ instead of $H_\phi(\omega)$, we have:

$$\sigma_m^2 = \frac{1}{2\pi}\int_{-\infty}^{+\infty} \left|H_\Omega(\omega)\right|^2 \omega^2\, S_\phi(\omega)\, d\omega \qquad (29)$$

A normalized expression in ω for $|H_\phi|$ is given as:

$$|H_\phi(\omega)| = \left| \frac{N\omega}{\pi} \cdot \frac{\sin r\frac{\pi}{2}\frac{\omega}{\omega_0}}{r\frac{\pi}{2}\frac{\omega}{\omega_0}} \cdot \sin \pi/2\,\frac{\omega}{\omega_o} \right.$$

$$\left. \cdot \frac{\sin N\pi\frac{\omega\pm\omega_0}{\omega_0}}{N\sin\pi\frac{\omega\pm\omega_0}{\omega_0}} \right| \qquad (30)$$

Where r and ω_0 are:

$$r = \frac{\tau}{\tau+\tau_d} \qquad (31)$$

$$\omega_0 = \frac{\pi}{\tau+\tau_d} \qquad (32)$$

We have used the fact that sin(x) only changes the sign when we add or subtract π to x to obtain the term $(\omega \pm \omega_o)/\omega_o$. For large N and $|\omega \pm \omega_o| << \omega_o$ we can approximate $|H_\phi|$ as:

$$|H_\phi| \tilde{=} \left| \frac{N\omega_o}{\pi} \cdot \frac{\sin r\pi/2}{r\pi/2} \cdot \frac{\sin N\pi \frac{\omega \pm \omega_o}{\omega_o}}{N\pi \frac{\omega \pm \omega_o}{\omega_o}} \right| \qquad (33)$$

Note that $|H_\phi|$ is equal to a constant times $|\sin(x)/x|$ centered at $+\omega_o$ and $-\omega_o$. Solving the integral (28), we have:

$$S_\phi(\omega_o) \cong \frac{\sigma_m^2}{\frac{1}{\pi}\left|H_\phi(\omega_o)\right|^2 \frac{\omega_o}{N}} = \frac{1}{8}\left(\frac{r\frac{\pi}{2}}{\sin r\frac{\pi}{2}}\right)^2 \frac{\sigma_m^2}{N f_o^3} \qquad (34)$$

Where ω_o/N can be interpreted as the equivalent bandwidth in radians per second (see Fig. 5) and $f_o = \omega_o/2\pi$.

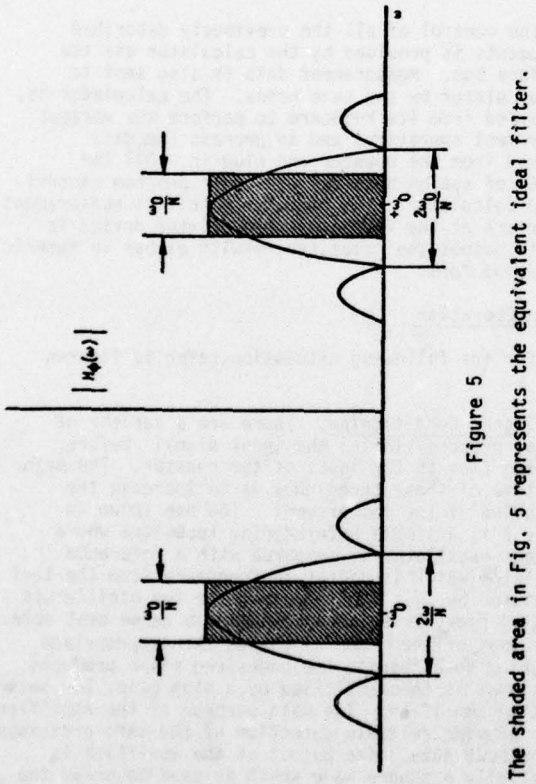

Figure 5 The shaded area in Fig. 5 represents the equivalent ideal filter.

If we select $\tau_d = \frac{1}{3\tau}$, then the multiple responses of $H_\phi(\omega)$ do not begin until $5\omega_o$ is reached. See figure 6.

$$S_\phi(\omega_o) \tilde{=} \frac{1}{8}\left(\frac{\pi/3}{\sin\pi/3}\right)^2 \frac{\sigma_m^2}{N f_o^3} \qquad (35)$$

$$S_\phi(\omega_o) \tilde{=} .183 \frac{\sigma_m^2}{N f_o^3} \qquad (36)$$

The phase spectral density due to the pass band centered at ω_o can be determined by equation (36) where σ_m^2 can be determined by numerical methods.

B. Power Spectra Contains Delta Function (Bright Line). Let us consider the special case of a phase modulated signal such as

$$V = V_o \cos(\Omega_o t + \theta_p \cos \omega_o t) \qquad (37)$$

The phase spectra for the modulation is:

$$S_\theta(\omega) = 2\pi (\tfrac{1}{2}\theta_p)^2 [\delta(\omega-\omega_o) + \delta(\omega+\omega_o)]$$

$$= (\tfrac{1}{2}\theta_p)^2 [\delta(f-f_o) + \delta(f+f_o)] \qquad (38)$$

The signal can be expanded in the usual form using Bessel functions and for small θ_p we have:

$$J_o(\theta_p) \tilde{=} 1$$

$$J_1(\theta_p) \tilde{=} 1/2\ \theta_p$$

$$\mathcal{L}(f) \tilde{=} (\tfrac{1}{2}\theta_p)^2 \delta(f-f_o) \qquad (39)$$

Where $\mathcal{L}(f)$ is defined as the energy at $\Omega_o + \omega_o$ per Hz divided by the total energy.

From the previous equations (37, 38), we conclude that $\mathcal{L}(f)$ and the "two-sided" phase noise S_ϕ are approximately equal for small θ_p.

The relation between σ_m^2 and θ_p is obtained by solving the integral (28) giving:

$$(\tfrac{1}{2}\theta_p)^2 = \frac{\sigma_m^2}{2\left|H_\phi(\omega_o)\right|^2} = \left[\frac{\sigma_m^2}{\frac{1}{\pi}\left|H_\phi(\omega_o)\right|^2 \frac{\omega_o}{N}}\right]\left(\frac{f_o}{N}\right) \qquad (40)$$

From the previous equation, we conclude that we can determine the phase spectrum as for the continuous case and multiply the result by f_o/N, to obtain $(\frac{1}{2}\theta_p)^2$.

The presence of delta functions (bright lines) can easily be detected due to the fact that σ_m^2 is not dependent on N, as is indicated by the equation relating σ_m^2 and $(\frac{1}{2}\theta_p)^2$.

So far we have relations to determine the phase spectral density $S_\phi(\omega)$ and the bright lines intensity $(\frac{1}{2}\theta_p)^2$. In the next section, we will derive the system resolution using a statistical approach to the quantization problem.

Estimation of the System Resolution

The system resolution is determined by the minimum time variation that the reciprocal counter can resolve, which is the clock period.

Let τ_c be the clock period, τ the gate time and ν_i the frequency of the input signal.

We will assume that the noise of the input signal will cause a maximum time variation of $\zeta \tau_c$ during the gate time. Let $\delta\nu$ represent the resultant frequency variation then we have:

$$\delta\nu = \frac{\tau_c}{\tau} \nu_i \tag{41}$$

If we assume that ζ is uniformly distributed from -1 to +1 and that the resultant $\delta\nu$ in each frequency measurement is independent of all previous ones, than m(t) is the sum of independent uniformly distributed random variables.

Using the central limit theorem, we concluded that for large N the random variable m(t) is approximately Gaussian with variance equal to the sum of the variances for each frequency measurement resulting in:

$$\sigma_m^2 = 2N\left[\frac{1}{3}\left(\frac{\tau_c}{\tau}\nu_i\right)^2\right] \tag{42}$$

where 2N is the number of frequency measurements and the term in brackets is the variance of $\delta\nu$.

This implies in a resolution given by:

$$S_\phi(\omega_0) \cong \left(\frac{r\pi/2}{\sin r\pi/2}\right)^2 \frac{\tau_c}{3r^2} \frac{\nu_i^2}{f_0} \tag{43}$$

The Measurement System

System Description

The system consists of five major components: a high resolution reciprocal counter (HP 5345A) with external gating capabilities, a measurement storage plug-on unit (HP 5358A), a mixer/amplifier unit (HP 10830A), a desk top calculator (HP 9825A) and printer/plotter output device (HP 9871A) as shown in figure 7. Communication and control between the various instruments is provided by a digital interface system (HP-Interface Bus). In addition, a test tone generator (HP 10831A) and time of day clock are included to enhance the system's capabilities. A functional block diagram is shown in figure 8.

The counter provides the system with the ability to make high resolution (2 nsec) period or time interval measurement or frequency (by the reciprocal technique). This determines the system's sensitivity floor limit as will be shown later. In addition, the counter has the ability to be gated from an external sample time signal. This is necessary in order to utilize various sampling functions and thus determine the offset frequency at which a spectra measurement is made.

The counter by itself does not have sufficient control or data output capacity, so a measurement storage plug in unit is included. It extends several capabilities of the counter. The front panel gate times are (as in most counters) in decade steps. This does not allow enough flexibility for spectra characterization so a gate generator is incorporated in the plug-in which generates a measurement time (τ) signal in the range of 1 to 999 x 10^6 μsec. The dead time between measurements (τ_d) is also controllable via the plug-in. The plug-in also stores the measurement data in a buffer memory for output over the interface bus to the calculator.

The measurement cycle of the counter is also controlled by the plug in by-passing such things as the display cycle to minimize the dead time between measurements. Dead time as low as 15 μs can be achieved.

The mixer/amplifier unit provides a means to further increase the system's resolution by heterodyning the test signal down to a low frequency signal by mixing it with an offset reference oscillator. It includes the necessary filtering, bandwidth control amd amplifiers to properly condition the input signals for application to the counter.

The control of all the previously described instruments is provided by the calculator via the interface bus. Measurement data is also sent to the calculator by the same means. The calculator is programmed from its keyboard to perform the various measurement operations and to process the data received from the counter and plug-in. All the aspects of system behavior are under program control of the calculator. The operator specifies measurement parameters at the keyboard. The printer device is used to output the processed results either in numeric or plotted form.

System Operation

For the following discussion,refer to figures 7 and 8.

Signal Conditioning. There are a variety of ways of preconditioning the input signal before applying them to the input of the counter. The major objective of these techniques is to increase the resolution of the measurement. The one shown in Figure 8 is a simple heterodyning technique where the test oscillator is compared with a reference oscillator which is offset in frequency from the test oscillator by ν_i. The output of the two oscillators is mixed together to produce an audio range beat note. The output of the mixer is passed thru appropriate filtering to eliminate the undesired mixer products. The signal is then amplified by a high gain, low noise, limiting amplifier. The main purpose of the amplifier is to provide reliable detection of the zero crossings of the beat note. The output of the amplifier is essentially a square wave which is used to drive the input of the counter. This approach is necessitated by the wide bandwidth (500 MHz) of the counter input and the resulting input noise which makes it impossible to detect a low frequency zero crossing with a 2 nsec resolution. As such the amplifier is provided with bandwidth control so that the input noise bandwidth can be adjusted to be compatible with the signal being measured.

The technique of comparing two oscillators, while it has some disadvantages, is still the best overall method of performing this measurement. It is not possible to measure the carrier directly, especially at microwave frequencies, with sufficient resolution, thus some down conversion technique is required. The problem is the noise contributed by the local (reference) oscillator. In order for it to be negligible its spectra must be 10 to 20 dB below the test oscillator in which case the error is small (.4 to .2 dB respectively). When it is not possible to obtain a reference oscillator which is better than the test oscillator, then two oscillators of assumed identical spectral characteristics can be used and the measurement result taken as the average of the two. This approach will always measure the worst of the two with a maximum error of less than 3 dB. The uncertainty of which oscillator is the poorest of the pair can be resolved by taking 3 or more and comparing them in all combinations (A vs B, A vs C, B vs C, etc.). This approach will identify both the best and the worst of the group.

The remaining problem with the heterodyning technique is the requirement that the reference oscillator be offset from the test oscillator. In certain cases (cesium, rubidium or crystal oscillators for example), it is difficult or impractical to offset them, and as such, a different signal conditioning approach is required. These have been discussed in the literature[8]. The main requirement in terms of the current approach is to present the counter with a signal which is representative of the phase of the test oscillator and whose period is measurable by the counter with sufficient resolution to be meaningful.

Counter Operation. The counter counts the number of cycles of the input signal that occurs within the gate time and the number of cycles of the 500 MHz time base that occurred from the first zero crossing after the opening of the counter's main gate to the last zero crossing after the closing of the gate. Thus, the measurement consists of two numbers: 1) the number of cycles of the input and, 2) the elapsed time in 2 nsec steps that it took the n cycles to occur.

The operation of the counter and plug-in unit are directed by commands received over the interface bus from the calculator. These are determined by the stored program in the calculator. Each series of measurement is made by programming the counter to the desired function (period, frequency, time interval), setting up the desired gating function (measurement and dead time) and the number of measurements to be made. The resulting data is stored in the plug-in in order to reduce the dead time between measurements and subsequently transferred to the calculator via the interface bus for processing.

Sampling Functions.

The frequency selective characteristics of the counter is determined by the way the measurement data is acquired by the counter (i.e. the measurement and dead time) and the processing algorithm used in the calculator (i.e. the choice of α's) as given by eq. 24. A variety of resulting transfer functions have been discussed in the literature[6,7]. The most attractive of these from the point of view of an on line process is the so called modified Hadamard variance or 50% dead time sampling function proposed by Baugh (see Reference 7, p 225, Figure 6). The reason for this choice is the sampling function has two α coefficients which are zero and the counter can be allowed to reset and transfer data during these intervals. Hence the counter is essentially free from dead time constraints when using this sampling function. Secondly, the sampling function is a short sequence suitable to on line processing & allows measurements to be made out to a reasonable distance away from the carrier.

Software.

The software (the stored program in the calculator) determines a significant portion of the system's behavior and performance characteristics. The set-up of the operating modes of the instrument and the method of data reaction is determined by the program written for the calculator. As such the system has a great deal of flexibility in executing various sampling and processing methods as a function of writing the appropriate program.

System Performance

Sensitivity: The system's sensitivity using the simple heterodyning method and the 50% dead time sampling function is given by eq. 43. Evaluating this gives a family of curves as shown in figure 9. Eq. 43 assumes no other sources of noise in the system. This is valid as long as the mixer and amplifier noise are designed to be below this limit. As can be seen, the sensitivity increases with a decrease in the beat frequency (ν_i) and as the offset frequency is increased.

In the primary region of interest (10 Hz and below), the sensitivity is quite good compared to most oscillators available today. In the region above 10 Hz, which is primarily for comparison with other techniques, the sensitivity can be inadequate. In these cases other resolution enhancement techniques, such as multiplying the input signals to microwave frequencies, can be used.

Maximum Offset Frequency: The maximum offset frequency is limited by the counter's dead time and number of measurements required per cycle of the sampling function. In the case of the 50% dead time sampling, the upper offset frequency is given by:

$$f_{max} = \frac{1}{6\tau_d}$$

Since the counter is only able to measure an integral number of cycles of the input, one of these is equal to the dead time, this can also be related to the beat note frequency, thus

$$f_{max} = \frac{\nu_i}{6}$$

Filter Bandwidth: The approximate equivalent filter bandwidth as given in figure 5 is

$$B = \frac{f_o}{N}$$

It is important to note two characteristics: 1) As the filter fundamental response f_o is moved closer to the carrier, the bandwidth of the filter becomes proportionally smaller, and 2) By increasing N, the bandwidth can be made arbitrarily small. Both of these facts are what allows this method to measure phase noise arbitrarily (in theory) close to the carrier, whereas traditional analog methods are

limited by the skirts of analog filters.

Digital Filter Harmonic Responses

As shown in figure 6, the harmonics of the digital filter have the same response as the fundamental response. The usual assumption is that the spectra in the region of interest is declining at a rate of f^{-2} or greater, and that the number of harmonic responses is limited to a finite number by the selectable IF filter and thus the error is negligible. However, this assumption must be verified each time a different class of oscillator is measured as white phase noise can contribute significantly. Further, so called bright lines occurring at any of the harmonic responses will produce erroneous results. The problem of white phase noise is discussed by Lesage and Audoin[6]. The problem of bright lines (usually 60 and 120 Hz and harmonics thereof) can be coped with by judicious choice of the offset frequencies and/or bandwidths.

Performance Verification

Several methods were used to verify the results obtained by this measurement technique.

FM Modulation: By applying a FM modulated signal of a known index of modulation and using the relationship given by eq. 40, the measured value of the sidebands can be compared with those values predicted by the modulation index.

The index of modulation is given by

$$\beta = \frac{\Delta f}{f_m} \approx \theta_p$$

where f_m is the modulation frequency. If the modulation index is small, $\beta << \frac{\pi}{2}$, then the value of the sideband at $f_c + f_m = \beta/2$.

Sensitivity Floor Verification: The system's resolution limit as given by eq. 43 was verified experimentally. A test tone was generated by dividing a good crystal oscillator's output frequency down to a variety of frequencies suitable as a beat note input to the system. The frequency dividers were digital circuits (74LS161's) operated in a manner so as to introduce a minimum of phase noise. The resultant signals could be calculated to be much below the sensitivity limit of the system. If the square wave outputs of the dividers were applied to the amplifier, the results were much better than the model predicted. This is explained by the fact that the square wave eliminated trigger errors and both the counter's time base and the test tone were derived from very stable crystal oscillators and a degree of synchronization occurred. If the outputs of the dividers were filtered to create sine waves, a $\pm$ one count error due to trigger noise could be observed and good correlation to the resolution floor model occurred.

Correlation with Other Techniques: In the region of offset frequencies where other techniques can be used, measurements were made on various oscillators and the results compared. Results correlated within 3 to 6 dB. One difficulty with correlating these results is estimating the mean value of the spectra using spectrum or wave analyzers. This tends to be subject to operator judgment.

Sample Results

A typical printout of the system is shown in figure 10. A series of measurements are made at the specified frequencies and digital filter bandwidths. The measurements are repeated at each frequency for specified numbers of "sweeps" to provide some statistical information about the measurements since the measured value represents an estimation of the mean value of the spectra. The results can also be presented in graphical form as shown in figure 11. Here the "X" represents the average of the values measured and the "-", the one sigma value of the variations.

Conclusions

The use of time domain techniques for close-in phase noise measurements can now be performed in a practical manner. Use of a high resolution reciprocal counter gives good sensitivity for offset frequencies below 100 Hz. By combining a programmable calculator with the programmable instrumentation, results can be obtained in the time it takes to collect the data.

Acknowledgement

The authors wish to thank Mohamed Sayed, David Chu and Holly Cole for their comments and proof reading and Sharon Gantman for her diligency in preparing the manuscript.

References

1. Athanasios Papoulis, Probability, Random Variables, and Stochastic Process, McGraw Hill.
2. Laning and Batlin, Control Systems Engineering, McGraw Hill.
3. W.B. Davenport and W.L. Post, Random Signals and Noise, McGraw Hill.
4. N.B.S. Technical Note 632, U.S. Department of Commerce, National Bureau of Standards.
5. "Characterization of Frequency Stability," IEEE Transactions on Instrumentation and Measurement, pp 105-120, May 1971.
6. P. Lesage and C. Audoin, "A Time Domain Method for Measurement of Spectral Density of Frequency Fluctuations at Low Fourier Frequencies," Laboratorie do L'Horloge Atomique, Bat. 221, Universite' Paris, Sud 91405, Orsay, France.
7. Richard A. Baugh, "Frequency Modulation Analysis with Hadamard Variance," Proc. Freq. Ctl. Sump., pp 222-225, April 1971.
8. David W. Allen, "The Measurement of Frequency and Frequency Stability of Precision Oscillators", NBS Technical Note 669, May 1975.

FIGURE 6

Equivalent Digital Filter

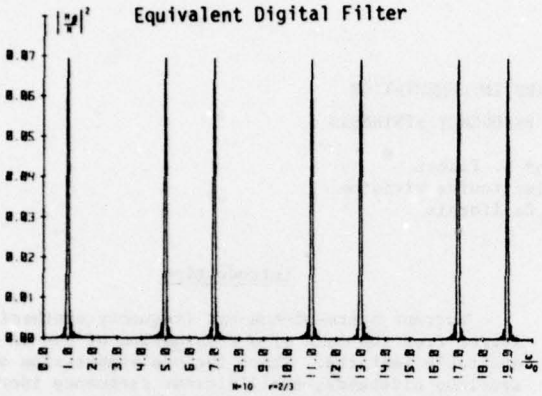

Figure 7 HP 5390A Frequency Stability Analyzer System Configuration

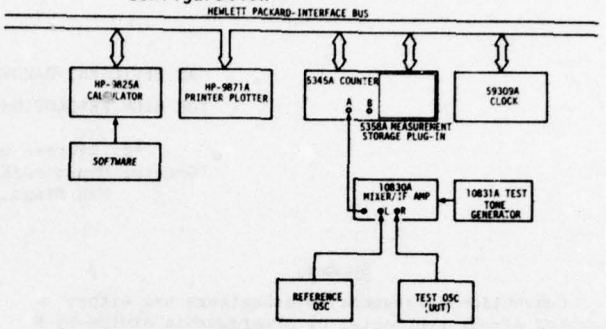

FIGURE 8

Phase Noise Measuring System Functional Block Diagram

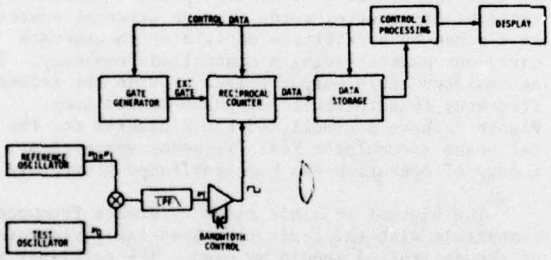

FIGURE 9

Phase Noise Sensitivity Limit

(- 73 + 20 log ν_1 -10 log τ)

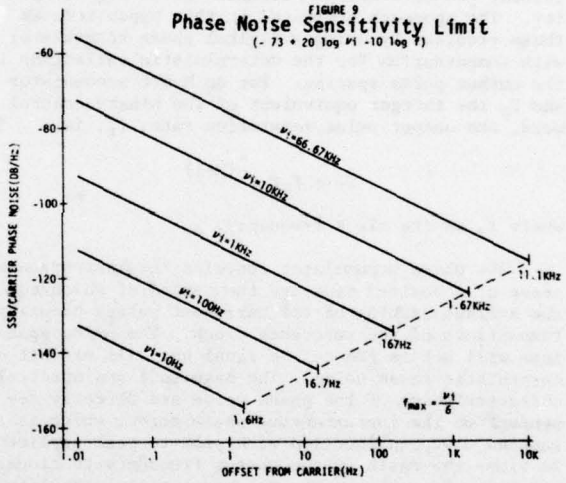

FIGURE 10

Sample Printout

*** PHASE NOISE ANALYSIS ***

PHASE NOISE PACKAGE (9825) rev 05-26-76-2310

MEASUREMENT DESCRIPTION:

10544A-h36 VS 10544A-h36
DATE 05/26/76 TIME 23:23:00

MEASUREMENT PARAMETERS:

N= 10
f0 FREQUENCY 1000 MS

	SSB/CARRIER PHASE NOISE (DB/HZ)					
FREQ=	10.0	2.5	1.0	0.5	0.2	MS
TA =	0.92	0.32	0.05	0.03	0.01	MS
FLOOR	-123.2	-117.0	-113.0	-110.6	-106.8	DB
SAMP						
1	-125.1	-116.3	-103.5	-91.8	-79.9	
2	-126.0	-118.4	-104.6	-95.2	-80.6	
3	-125.0	-112.7	-103.7	-93.6	-79.7	
4	-126.0	-117.7	-104.7	-91.5	-77.1	
5	-122.3	-110.9	-103.0	-92.3	-77.2	
AVG=	-124.4	-115.4	-103.9	-92.7	-78.8	
SIG=	1.5	2.5	0.6	1.5	1.4	
MAX=	-126.0	-118.9	-104.7	-95.2	-80.6	
MIN=	-122.3	-112.7	-103.0	-91.5	-77.2	

END TIME:01:52:03

FIGURE 11

Sample Plot

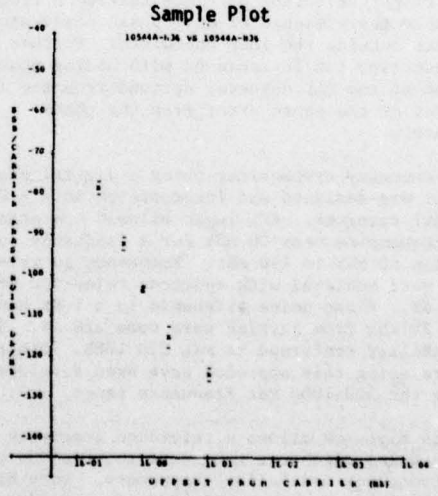

AN EFFICIENT HARDWARE IMPLEMENTATION FOR HIGH RESOLUTION FREQUENCY SYNTHESIS

B. Bjerede and G. Fisher
General Dynamics/Electronics Division
San Diego, California

Summary

Conventional frequency synthesizers use either iterated direct synthesis, or programmable divide-by-N phase lock, or digital sinusoidal table look-up techniques. These approaches suffer from one or more of the disadvantages of poor spurious suppression or close-in phase noise performance, poor frequency resolution, output bandwidth limitations or high complexity. The approach presented in this paper reduces these problems by using a digital phase accumulator with compensation for the deterministic variations in the output pulse spacing. For an M-bit accumulator and F_n the integer equivalent of the binary control word, the output pulse repetition rate, f_r, is

$$f_r = F_n f_c 2^{-(M-1)}$$

where f_r is the clock frequency.

The phase accumulator contains the instantaneous phase of a desired sinewave the period of which equals the average spacing of the carry-out pulses occuring at transitions of the reference clock. The pulse spacings will not in general be equal but will exhibit deterministic phase noise. The magnitude and spectral characteristics of the phase noise are directly dependent on the instantaneous phase error, which is a sampled sawtooth function with peak-to-peak amplitude 2π times the ratio of the output frequency to clock reference frequency. The carry-out signal provides the input to a phase-locked loop (PLL) which filters the phase noise except low frequency spectral components. Proper selection of clock reference frequencies will insure the presence of only phase noise spectral components outside the loop bandwidth. Further phase noise reduction can be achieved with analog phase compensation at the PLL detector derived from the digital complement of the phase error from the phase accumulator.

A frequency synthesizer using a digital phase accumulator was designed and incorporated into a HF (2-30 MHz) receiver. ECL logic allowed operation at clock frequencies near 30 MHz for a frequency output range from 80 MHz to 110 MHz. Frequency increments of 0.05 Hz were achieved with spurious rejection greater than 80 dB. Phase noise sidebands in a 1 Hz bandwidth removed 25 kHz from carrier were down 120 dB. Short term stability conformed to MIL STD 188B. Other synthesizers using this approach have been developed, one covering the 500-1000 MHz frequency range.

This approach allows a reference frequency to the PLL of several megahertz to insure suppression of reference frequency modulation components. Very high frequency resolution can be achieved with considerable reduction in hardware requirements over state-of-the-art indirect synthesis techniques.

Introduction

Current state-of-the-art frequency synthesizers suffer from the lack of a combination of one or more desirable features. These include suppression of spurious sidebands, small minimum frequency increments, low phase noise sidebands, and simple hardware implementation (3). Tierney, Rader and Gold (4) have pioneered recent efforts in the area of digital frequency synthesizers in an effort to develop digital implementations for high performance with minimum hardware.

Design and implementation of a new approach to frequency synthesis using a digital phase accumulator will be described. The digital phase accumulator accepts binary control words from an external source and is clocked by a reference oscillator to generate carry-out pulses having a controlled frequency. The accumulator carry output pulses provide the reference frequency to a conventional phase-locked loop. Figure 1 shows a simplified block diagram for the digital phase accumulator (ϕA) frequency synthesizer. The theory of operation has been published previously (1).

The highest possible clock reference frequency compatible with the logic type used for implementation of the digital ϕA should be used. The carry-out repetition pulses are normally generated at sufficiently high rates to guarantee high rejection of reference harmonics which are far outside the PLL loop bandwidth. A real improvement in spurious harmonic rejection can therefore be realized over conventional indirect frequency synthesizers.

Analog phase compensation within the loop can substantially reduce the predictable phase error generated in the reference frequency by the digital ϕA. Good short-term frequency stability can be achieved over a wide range of frequencies with major reduction in hardware requirements.

Performance criteria for the total frequency synthesizer are dependent upon specified design goals for the digital ϕA and the PLL. Factors relating to the ϕA include accumulator word length, the frequency and stability of the clock reference signal and the particular logic family chosen. Loop operation is based upon the sensitivity of the voltage controlled oscillator, loop bandwidth and transient response, and accuracy and timing of the compensating analog phase signal derived through digital-to-analog (D/A) conversion. Suppression of phase noise sidebands are determined by the resonator Q-value, the power level and the inherent and injected noise of the VCO.

The theory of the digital phase accumulator and requirements of PLL operation are presented in the following paragraphs. A detailed discussion of the origin

and nature of the phase jitter in the ϕA carry-out pulse train is given with a solution for its undesirable effects on the sinusoidal output frequency generated by the PLL. A hardware realization is described with experimental verification of performance.

Digital Phase Accumulator

The main function of the digital ϕA is its ability to generate pulses of linearly controlled frequency. Operation is based on periodic binary addition of a selected binary control word, F_n, to the last previous resulting addition from the accumulator. Given an M-bit binary latched accumulator programmed for the binary ADD mode, the accumulator output word is represented by the binary modulo 2^M addition,

$$S_n = F_n + S_{n-1} \text{ (modulo } 2^M) \qquad (1)$$

where S_n is the current accumulator output, and n any discrete instant in time. The discrete time intervals correspond to the reference clock period, $T_c = 1/f_c$, so that S_n is updated synchronously every T_c seconds. A carry-out pulse is generated during a clock pulse at each overflow of the accumulator by the most significant bit (MSB) of the accumulator word. The remainder from the addition following the previous clock pulse is latched and becomes the new addend during the current clock period.

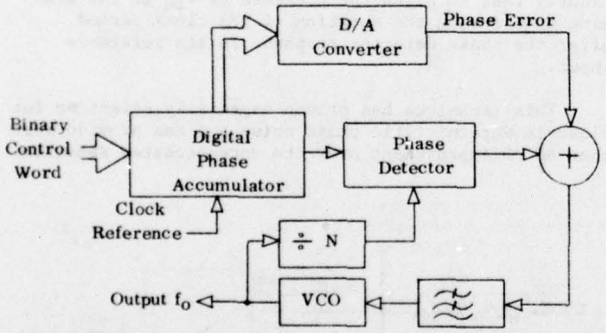

Figure 1. Simplified Block Diagram of Digital Phase Accumulator Frequency Synthesizer

Figure 2 gives the simplified block diagram of a 32-bit digital phase accumulator showing generation of the phase compensation signal. Look-ahead carry is employed within the architecture to maximize allowed throughput rates and minimize add time. Sixteen word segments are processed by each ALU as shown by the system signal flow in Figure 2. The numbers shown in parentheses with the discrete variables indicate the bit range associated with that segment of the word.

For the M = 32 bits accumulator of Figure 2 the average repetition rate of the carry-out pulses is expressed as,

$$f_r = f_c K 2^{-(M-1)} = f_c/[2^{(M-1)}/K] \qquad (2)$$

where K is the decimal integer equivalent of the binary control word F_n and the least significant bit corresponds to 2^0.

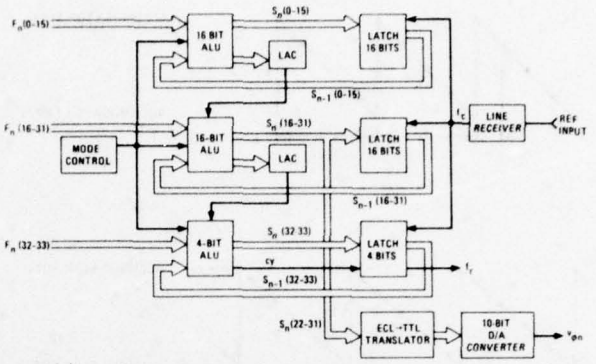

Figure 2. Digital Phase Accumulator, 32-Bits With D/A Phase Error Translation

Since the accumulator output pulses are synchronized to the reference clock they are not in general evenly spaced. For a given accumulator word length and fixed control word and reference frequency the output pulse repetition pattern will consist of a periodic sequence of two pulse rates, the long term average of which is given by Equation 2.

For the case where the ratio of the binary magnitudes $2^{M-1}/K$ of Equation 2 is an integer number, then f_r is an exact subharmonic of f_c. With this type of operation the accumulator is filled uniformly during each period, $T_r = 1/f_r$, with the carry-out pulse generated with no remainder to carry over to the subsequent addition. With all zeros entering the accumulator as the new addend the decimal integer equivalent of F_n is summed synchronously into the accumulator until it is again filled accompanied by the generation of a carry-out pulse, and the process continues.

For other selected control words whose binary equivalent is not an exact divisor of 2^{M-1} (i.e. the ratio $2^{M-1}/K$ contains a fractional component) the accumulator will not fill uniformly during each successive T_r period. Then the remainder after carry-out generation is not zero but will exhibit periodic variation over a specified number of T_r periods. A variation in the number of clock pulses required to produce a carry-out results, however this number repeats periodically and is entirely predictable given f_c, F_n, and and M. This predictable variation is responsible for phase jitter in the ϕA output signal and directly produces deterministic phase noise in the desired PLL carrier waveform.

Figure 3 demonstrates the two cases just described, determined by the ratio $2^{M-1}/K$. Figure 3(A) shows the case in which $2^{M-1}/K$ is an exact integer and the accumulator latched binary content is plotted as a function of time. After every 4 clock pulses the accumulator is filled and generates a carry output pulse with no remainder, that is, $f_r = f_c/4$. The resulting sawtooth pattern is periodic with period $T_r = d_1 = 1/f_r$. Figure 3(B) represents accumulator content as a function of time for $2^{M-1}/K$ a fraction equal to 4.5, that is, $f_r = f_c/4.5$. Since the fractional portion is 0.5 the sawtooth pattern has an average period $T_r = (d_1 + d_2)/2 = 1/f_r$, so that the pattern repeats every two carry-out pulses. Dual frequency components $1/d_1$ and $1/d_2$ in the carry-out pulses are therefore generated alternately. Remainders of zero and $F_n/2$ in the accumulator therefore alternate to produce phase jitter with period $d_1 + d_2$ and peak-to-peak variation in amplitude of $2\pi f_r/f_c$ radians.

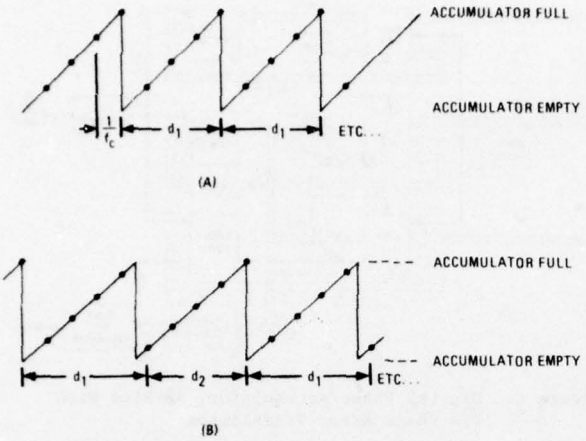

(A) $2^M/F_n$ AN EXACT INTERGER

(B) $2^M/F_n$ A FRACTION RESULTING IN DUAL FREQUENCY COMPONENTS $1/d_1$ AND $1/d_2$

Figure 3. Sawtooth Representation of Accumulator Content at Each Clock Pulse

The binary representation of the phase jitter in the PA output can be derived directly from a digital output segment of the PA as shown in Figure 2. Sufficient bits are required for precision to produce an accurate analog signal using D/A conversion. The MSB used in F_n becomes the MSB in the designation of the phase noise with 8 or 10 bits adequate for a practical representation of the generated phase noise.

The precision and repetition rate of the PA output pulses are controlled by the accumulator size, clock frequency, and bit length of the binary control word, F_n. Given a fixed accumulator word length a higher maximum output repetition rate can be achieved only by an increase in the clock reference frequency. The logic family and layout used in the PA implementation in turn impose limitations on the maximum clock rate through finite propagation delays. Higher resolution in the output pulses for incremental frequency changes can be achieved with longer ϕA word lengths. However, this will tend to lower the maximum attainable reference frequency to the PLL, aside from somewhat increased hardware requirements.

Phase Noise Considerations

Since the reference frequency to the PLL is typically several megahertz suppression of reference sidebands is achieved through proper loop filter design (2). However, the phase jitter created by the digital ϕA, described in the previous section and depicted in Figure 3, can manifest itself in phase noise which may span a very wide frequency range (from dc to hundreds of kilohertz). Periodic phase noise can therefore be generated on the desired output signal and prove quite troublesome, particularly the frequencies within the PLL loop bandwidth. Techniques to minimize the effects of and eliminate the source of deterministic phase noise are here delineated, including pertinent hardware considerations.

Reduction by Loop Bandwidth

Deterministic phase noise can be suppressed in the PLL by a sufficiently narrow loop bandwidth to attenuate all higher frequency components. Phase noise reduction is achieved in proportion to the ratio between loop bandwidth and repetition frequency of the phase noise, i.e. ω_n/f_c. Higher order components resulting from possible incidental FM will also be suppressed by the loop.

Reduction by Analog Phase Compensation

Lower frequency components of deterministic phase noise can be greatly reduced by direct compensation within the loop. Analog representation of the phase noise can be derived from the analog equivalent of a word segment from the ALU output of the digital ϕA. The MSB of the digital word at the ALU output should correspond to the most significant nonzero bit of the binary input control word. For high accuracy the word segment should consist of a sufficient number of bits (usually 8 or more). Digital-to-analog (D/A) conversion using the offset binary mode with current output will produce the bipolar complement of the analog phase error $v_{\phi n}$.

Figure 4 shows the schematic representation of the PLL with the summing node for analog phase compensation. The current input compensation signal $v_{\phi n}$ is summed with an output signal from the phase detector to effectively cancel the effect of reference phase jitter and prevent it from entering the loop. The compensation error is periodic and corresponds to a ramp consisting of discrete steps of duration T_c with period equal to the phase noise repetition frequency. The peak-to-peak level of the ramp entering the PLL is adjusted to provide the correct compensation signal. The settling time of the D/A converter must be sufficiently fast to allow the presence of $v_{\phi n}$ at the summing node during the duration of the clock period after the phase detector responds to its reference input.

This technique has proven especially effective for close-in deterministic phase noise and can provide more than 40 dB improvement over the uncompensated spectrum.

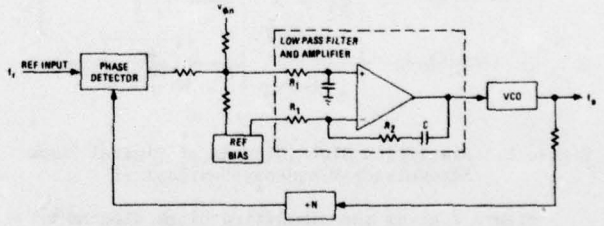

Figure 4. Phase Locked Loop Showing Summing Node for Analog Phase Compensation

Reduction by Multiple Clock Frequencies

To further insure elimination of all phase noise components from the output spectrum the phase noise frequency components must be maximized with respect to their frequency. A very effective means to guarantee that all components are far removed from the loop bandwidth is to employ multiple clock reference frequencies. For a clock signal which generates low frequency phase noise components for a given input binary control word, a different clock frequency is chosen. The new clock frequency will, of course, require a different binary control word to generate the same reference

frequency, f_r, to satisfy Equation 2. However, the period of the lowest frequency component of phase jitter will be sufficiently small to be easily suppressed by the loop. As a minimum requirement, therefore, two clock frequencies must be selected.

Low frequency phase noise components will be strongest very near, but not exactly at, phase accumulator output frequencies corresponding to integer subharmonics of the clock reference frequency. In addition, some fractional subharmonics ($2^{M-1}/K$ a fraction) can produce significant, although much weaker, phase noise components in the PLL output for a given loop bandwidth. Those fractional subharmonics with small fractional components (multiples of 1/2, 1/3, 1/4) generate by far the greatest noise in the output spectrum and require additional suppression. To accomplish this a search is made for two practical clock frequencies which maximizes the separation between all integer and fractional subharmonics over the output frequency range of interest.

A pattern of the interleaving critical frequencies is selected as optimal and the two corresponding clock frequencies chosen for synthesizer operation. For a specified VCO output frequency, therefore, the clock frequency is selected which produces a ϕA output frequency farthest from the critical subharmonics of that clock frequency. Three clock frequencies may provide greater separation and may be beneficial for very large percentage output bandwidths.

A digital frequency synthesizer based on a digital ϕA and employing correct loop bandwidth characteristics and techniques of analog phase compensation and multiple clock reference frequencies to the ϕA will guarantee near 100% elimination of all phase noise components. Care must also be taken in design of the PLL filter and VCO and noise-free power sources to insure absence of any degradation of the output signal.

Hardware Implementation

A ϕA-type digital frequency synthesizer was built to serve as the local oscillator (LO) in a HF (2-30 MHz) receiver. A frequency range from 82-110 MHz was a requirement of the LO due to the 80 MHz IF frequency of the receiver. The frequency resolution was required to be 1 Hz.

The digital ϕA was designed for 32-bit operation as shown in Figure 2 and was implemented using emitter-coupled logic for maximum throughput rates. Digital translation and a 10-bit D/A converter was used to provide the analog phase compensation signal to the PLL. For 32-bit operation minimum frequency steps of 0.2 Hz are attained with a maximum allowable throughput rate of 31 MHz. To achieve the desired output frequency range a fixed loop multiplication of 32 was required.

Analysis showed two clock frequencies to be sufficient to provide high separation between all critical output frequencies. A system limitation of 100 kHz clock frequency spacing multiples indicated 27.9 MHz and 29.1 MHz achieved best separation while maximizing the absolute clock frequencies. The clock reference frequency was selected manually by gating the desired clock to the accumulator. The PLL loop bandwidth and transient response were designed for high spurious rejection and phase noise suppression with the aid of analog phase compensation. A highly sensitive VCO was designed using a high-Q varactor tuned tank circuit.

Total hardware requirements consisted of two single-layer circuit boards, each 10 in. by 4.25 in. in size. A 29-bit binary control word was used with the remainder of the input bits fixed at zero. Ribbon cables provided direct interface to the external manual controller.

Spectrum analysis of the VCO output sinusoid showed spurious noise and phase noise suppression of more than 80 dB across the frequency band. Noncoherent phase noise sidebands were 120 dB below the carrier removed 25 kHz in a 1 Hz bandwidth. Excellent short term stability was achieved, within standards set forth by MIL-STD 188B.

Reference frequencies to the PLL in the range from 2.56 MHz to 3.44 MHz insured ample suppression of reference frequency modulation components, a problem in many conventional synthesizers. The high reference frequencies also allow for switching times orders of magnitude faster than conventional indirect synthesizers.

A similar synthesizer has been successfully implemented in a microwave measurement unit for an automated test system. Frequency requirements were 500-1000 MHz with 10 Hz steps achieved using a 28-bit phase accumulator. Loop multiplication was fixed at 400. Spurious rejection of greater than 60 dB was achieved across the frequency band using a commercially available VCO.

References

1. B.E. Bjerede, G.D. Fisher, "A New Phase Accumulator Approach to Frequency Synthesis," Proceedings, IEEE NAECON 76, pp 928-932, May 1976.

2. F.M. Gardener, Phaselock Techniques, John Wiley & Sons, New York, 1966.

3. J. Gorski-Popiel, Frequency Synthesis: Techniques and Applications, IEEE Press, New York, 1975.

4. J. Tierney, C.M. Rader, B. Gold, "A Digital Frequency Synthesizer," IEEE Trans. Audio and Electroacoustics, AU-19, 48 (1971).

SAW RESONATORS AND COUPLED RESONATOR FILTERS

E. J. Staples and R. C. Smythe
Piezo Technology Inc., Orlando, Florida

Abstract

The behavior of SAW resonators and coupled resonator filters on ST-Quartz is examined. SAW resonance phenomena are explained in terms of two-dimensional symmetric and antisymmetric modes. The effects of energy trapping are considered and the results of transducer apodization shown. Because of the two-dimensional symmetry, SAW resonators may be coupled using transverse or inline modes. Typical SAW coupled-resonator filter responses for each type of coupling are discussed. Using two SAW two-pole devices a four-pole filter response is demonstrated.

I. Introduction

The acoustic surface wave crystal resonator, which has recently generated considerable interest in the field of frequency control[1] and ultrasonics[2], will be discussed in this paper. The SAW resonator makes use of two grating reflectors to form a surface wave cavity. By means of an interdigital transducer (IDT), electrical signals are converted to acoustic waves and conversely. The operating characteristics of the cavity depend upon the reflection coefficients of each reflector, the substrate material, and the electro-acoustic field of the IDT itself.

In this paper experimental and theoretical behavior of SAW resonators and coupled-resonator filters will be examined. These devices are of potential interest for narrow band filtering applications in the 50-1000 MHz ranges because of their high Q's and low frequency temperature coefficients. Further advantages of SAW resonators for filter applications are: 1) fundamental mode operation to at least 1000 MHz; 2) small size; 3) ruggedness and ease of mounting; and 4) low natural impedances. Most important of all, inter-resonator coupling may be achieved, leading to some valuable monolithic filter structures.

II. SAW Resonance

A number of experimental resonators have been fabricated. The basic resonator structure shown in Figure 1-a was photo-etched in aluminum films on ST-quartz blanks, 1 mm thick and 14 mm in diameter. Using silver epoxy, the blanks were then mounted in standard HC-6 crystal cans and sealed in dry nitrogen/helium gas at atmospheric pressure. Multi-level photolithographic processing steps involving thin-film deposition and etching were used throughout the resonator fabrication. The distributed reflectors contained 200 reflecting aluminum stripes, approximately 1 micron in thickness as shown in Figure 1-b. The length of each stripe was $100\lambda_R$ (λ_R = 42 microns) where λ_R is twice the grating periodicity. A thin (100 Å) film of chrome was placed under the reflecting stripes to insure adhesion and eliminate periodic electrical loading of the quartz surface. The reflectors were separated by $41.5\lambda_{IDT}$ edge-to-edge and a 40.5 finger-pair IDT was placed symmetrically between the reflectors. The transducer periodicity, λ_{IDT}, was 84.5 microns, center frequency approximately 75 MHz, and the aluminum 1000 Å in thickness.

Resonator characteristics were measured using a Wayne-Kerr admittance bridge, model B801, with an HP spectrum analyzer and tracking generator for bridge detector and source. The resonator lumped parameter equivalent circuit shown in Figure 1-c was assumed in the analysis and interpretation of the experimental results shown in Table I.

TABLE I

NOMINAL EQUIVALENT CIRCUIT PARAMETERS

F_o	- - - - -	74.6 - 74.8 MHz
Q	- - - - -	16,000 MHz
R_a	- - - - -	6000 Ohms
R_1	- - - - -	50-100 Ohms
C_o	- - - - -	10 pF (typ)
C_1	- - - - -	.004 - .007 pF
L_1	- - - - -	500-1000 μH
C_o/C_1	- - - - -	1300-1700

Using the bridge, the resonator swept-frequency response could be examined in detail as well as characterized quantitatively in terms of equivalent circuit admittances measured directly on the bridge.

Figure 2 is a typical response obtained with the admittance bridge adjusted to balance out the effect of resonator static capacitance, C_o, and transducer radiation resistance, R_a. Spurious modes (S_1-S_6) at frequencies other than the principal resonance frequency (S_o) are clearly seen on the high frequency side of the response. These spurious modes are transverse modes produced by the leaky impedance discontinuity along the transverse edges of the resonator.

SAW resonance phenomena may be explained in terms of standing surface acoustic waves symmetric or antisymmetric about a two dimensional coordinate system as shown in Figure 3. In the direction of propagation (inline) the distributed reflectors create symmetric and antisymmetric inline modes or standing waves. Normally the resulting inline mode spectrum is reduced to a single inline mode by selecting the proper reflector separation and bandwidth.

Associated with each inline mode is a finite spectrum of transversely trapped (guided) modes[3]. Trapped energy modes in bulk-wave resonators are well known[4]. For the bulk-wave case, the resonator consists

essentially of a plate having a region whose cut-off frequency, due to a combination of piezoelectric and mass loading, is lower than that of the surrounding region. The loading is usually modeled by an appropriate difference in the densities of the two regions. Although structural analogies between the bulk wave and surface wave devices are incomplete it may be noted in the bulk-wave case that this difference in densities is equivalent to a velocity difference.

The analogy between a trapped-energy, bulk-wave resonator and the SAW resonator of Figure 1 is not exact because the region of fast surface wave velocity, outside of the reflectors, contains no reflecting stripes which are analogous to the reflecting walls of a bulk-wave crystal resonator. Since a transverse discontinuity does exist, even though a somewhat leaky one, the trapped modes occur only weakly as in the response of Figure 2. The analogy is stronger for the case shown in Figure 4. Here a region of slow wave velocity is formed using a thin film over the transducer and reflectors, however, the reflectors have been extended beyond the film into the region of relatively fast wave velocity to demonstrate the trapping phenomenon. The results shown are for a slow region width of $40\lambda_R$ and a reflector width of $100\lambda_R$. The trapped modes are now enhanced because the energy outside the guided region as well as within the guide is reflected.

Trapped-energy, transverse modes would represent a serious problem were it not for the ability to apodize the IDT and hence alter the transverse amplitude distribution of the transducer. Apodization of the IDT has a large effect upon the resonator spurious mode spectrum. Illustrating this, Figure 5 shows the response of a resonator similar to the one of Figure 4, except for an apodized IDT. In this case no trapped unwanted modes are observed. The ability to weight the excitation function of the resonator is not shared in practice by bulk-wave trapped-energy resonators and is unique to SAW technology itself. Because the SAW resonator may be apodized and selected transverse modes preferentially excited, very wide, and hence very low impedance, resonators may be fabricated without transverse modal interference.

III. Coupled Resonators and Filters

Since the acoustic surface-wave resonator possesses two-dimensional symmetry, a coupled-resonator filter may be implemented by either inline or transverse coupling of individual resonators. Representative structures for both inline and transverse coupling are shown in Figure 6-a and 6-b respectively.

For inline coupling the desired modes are the first symmetric and antisymmetric inline modes. For small coupling, the structure of Figure 6-a will have a two-pole filter response for which the center reflector controls the degree of coupling between the two resonators or, equivalently, the modal frequency separation and hence the filter bandwidth.

For the transversely coupled resonator[5] filter of Figure 6-b the desired modes are the first symmetric and antisymmetric transverse modes. Coupling in this case is controlled by the width and separation of the trapped regions and the amount of trapping applied in these regions.

To study transverse coupling, resonators were constructed on ST-quartz as previously described; however, in this case two unapodized IDT's were placed between the reflecting arrays as in Figure 6-b. The trapped regions were $10\lambda_R$ wide and separated by $5\lambda_R$. Transverse coupling between the IDT's is shown in Figure 7. Low-Q dielectric films accounted for the high insertion loss in this early prototype. The spurious activity on the high frequency side of the response is due to coupling between higher order transverse modes. Apodization of the IDT's might be used to alter or reduce the relative amplitude of these modes.

Inline coupling produces a filter response quite different from transverse coupling due to acoustic transmission outside of the reflector stopband. An example of inline coupling between SAW resonators can be seen in Figure 8; the filter response is shown for unmatched 50 ohm terminations. In this example 300 reflecting stripes were used in the outer reflectors and 150 for the middle reflector. The transverse dimension of the structure was $100\lambda_R$ and the IDT's were apodized to suppress higher order transverse modes. The inline-coupled resonator modes can clearly be seen; the deep null between them indicative of the mismatched (low) terminating impedance. Far from resonance the reflectors appear transparent and the background spurious level is caused by direct IDT-to-IDT acoustic transmission. The ultimate spurious level can be quite high, typically greater than -90 dB $\pm$ 5 MHz from the center frequency.

Near resonance the inline coupled resonator response becomes maximally flat when the filter is terminated in its midband characteristic impedance. Passband response is illustrated in Figure 9 for various values of terminating impedance. A simple series C, paralle L matching network as shown in Figure 10 was used to transform the 50 ohm source and load to the desired impedance level. The small spurious resonances appearing within the passband and on the high frequency side of the filter response of Figure 9 are due to higher order transverse modes not completely eliminated by the transducer apodization.

Filters of the above type have been built with insertion losses typically 1 dB and percentage bandwidths from 0.01-0.1%. For the filter shown the bandwidth is 70 kHz at 75 MHz. In Figure 11 the modal frequency separation, which can be related to the filter bandwidth, is plotted as a function of the number of center reflector stripes, N_c, for the inline coupled structure. In the limit of no center reflector the coupled modes degenerate into the symmetric and anti-

symmetric inline modes of the single remaining resonator.

A four-pole filter response may be obtained by cascading two of the above 2-pole monolithic structures as shown in Figure 12. For the prototype response shown the insertion loss was typically 3 db. The ultilization of SAW resonators in filters with more than four-poles is limited at present due to the relatively low Q-fractional bandwidth product.

IV. Discussion and Conclusions

SAW resonators have been shown to possess both inline and transverse modes. Inline modes may be analyzed using transmission line models. The transversely bound modes associated with each inline mode may be predicted with reasonable accuracy using energy waveguiding concepts. Apodization of the exciting IDT has been shown to provide preferential excitation of these transverse modes.

Although SAW resonators represent an improvement over presently available bulk resonators in the upper VHF range, they nevertheless have at present certain practical limitations, some of which are: relatively low Q, typically less than 20,000 at 100 MHz (this is not an inherent limitation, the intrinsic Q being approximately 100,000 for ST-cut quartz[6]); C_o/C_1 slightly better than a 3rd overtone AT-cut bulk resonator; and temperature stability inferior to an AT-cut bulk resonator. In many applications temperature stability is an over-riding consideration. For comparison, the stability of ST-quartz SAW resonators is shown in Figure 13, together with that of an AT-cut bulk resonator. Two-pole filter characteristics have been experimentally demonstrated for both inline and transversely coupled resonators. In both cases, the coupling is the result of symmetric and antisymmetric mode excitation about an appropriate center line. One method of extending these techniques to multi-pole filter responses using tandem-connected or cascaded two-pole SAW monolithics has been shown. These new surface wave filters are expected to find applications as narrow band low-loss filters in the 50-1000 MHz range.

1. 29th Annual Symposium on Frequency Control, U.S.Army Electronics Command, Ft. Monmouth, New Jersey, (1975).

2. 1975 Ultrasonics Symposium Proceedings, Los Angeles, Calif., Sept. 1975, IEEE Cat. No. 75 CHO 994-4SU.

3. E.J. Staples and R.C. Smythe, "Surface Acoustic Wave Resonators on ST-Quartz", Proc. 1975 Ultrasonics Symposium; p. 307.

4. N. Shockley, D.R. Curran, and D.J. Koneval, "Energy Trapping and Related Studies of Multiple Electrode Filter Crystals", 17th Annual Symposium on Frequency Control, 1963, p. 88.

5. H.F. Tiersten and R.C. Smythe, "Guided Surface Wave Filter", Proc. 1975 Ultrasonics Symposium; p. 293.

6. R.C.M. Li, J.A.Aluson, and R.C. Williamson, "Surface-Wave Resonators Using Grooved Reflectors," Proc. 29th Annual Frequency Control Symposium, p. 167; 1975.

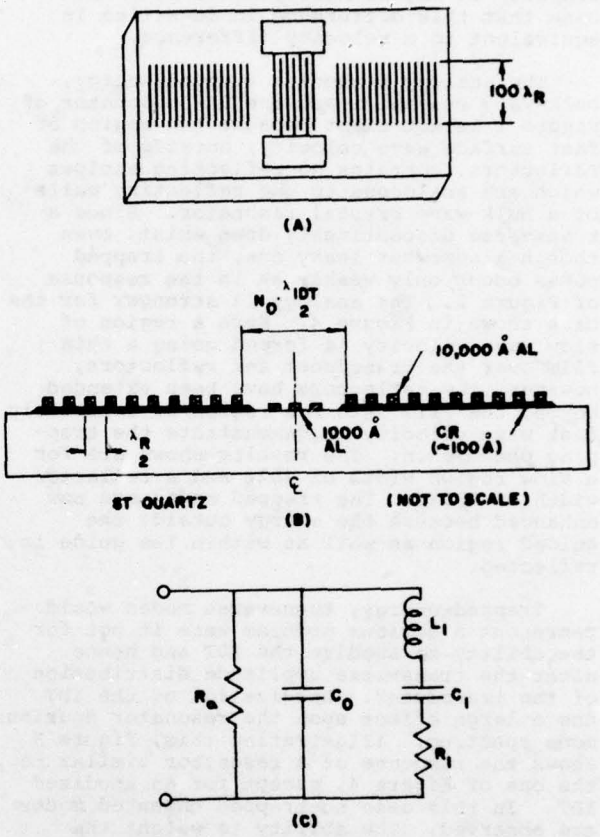

Figure 1

(a) Surface acoustic wave (SAW) resonator structure, (b) Side view (not to scale) showing fabrication details and (c) SAW resonator equivalent circuit.

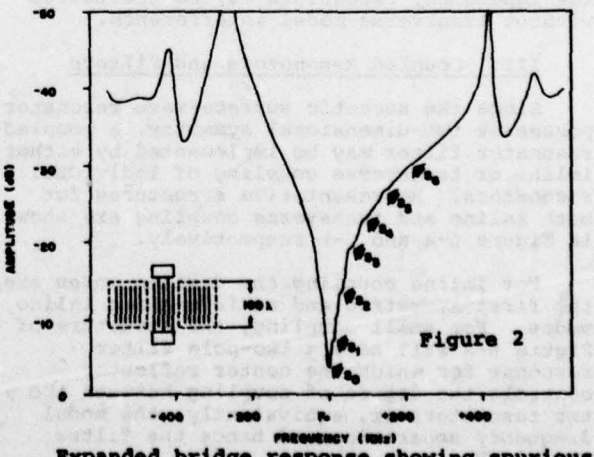

Figure 2

Expanded bridge response showing spurious resonator modes.

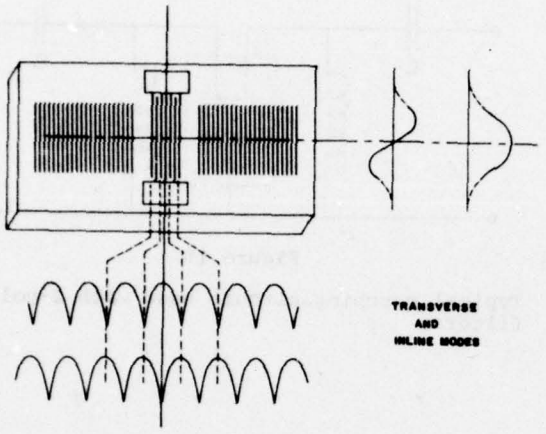

Figure 3

SAW resonator modes symmetric and antisymmetric about a two-dimensional coordinate system.

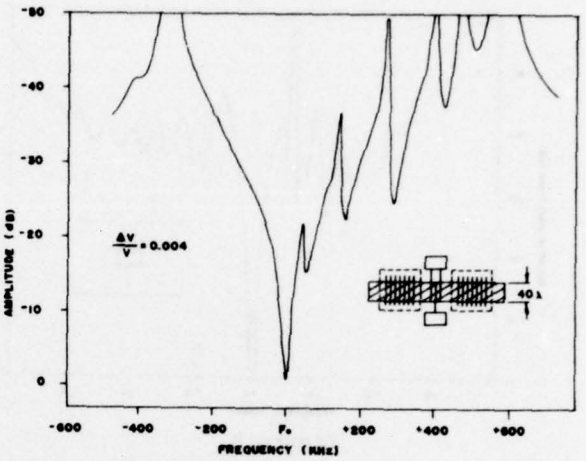

Figure 4

Unapodized, trapped energy SAW resonator bridge response.

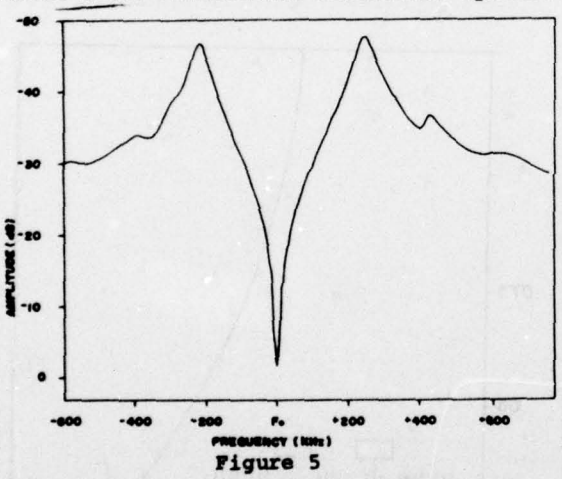

Figure 5

Apodized, trapped energy SAW resonator bridge response.

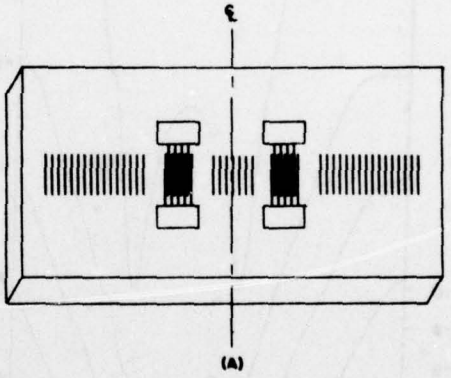

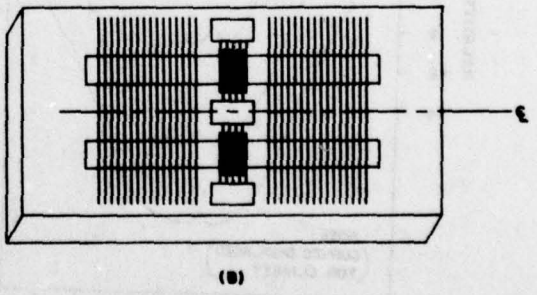

Figure 6

Representative structures for (a) Inline and (b) Transverse coupling of SAW resonators.

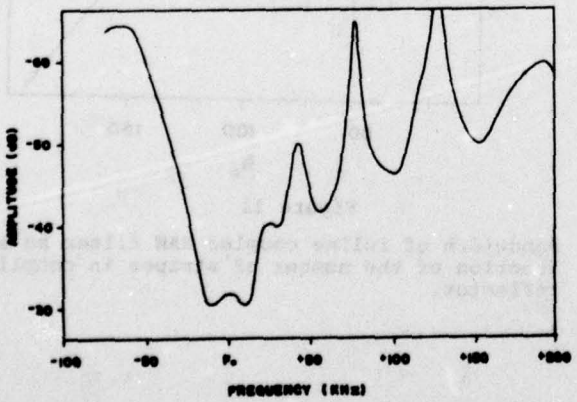

Figure 7

Unmatched (50Ω), 2-pole filter response using transversely coupled SAW resonators.

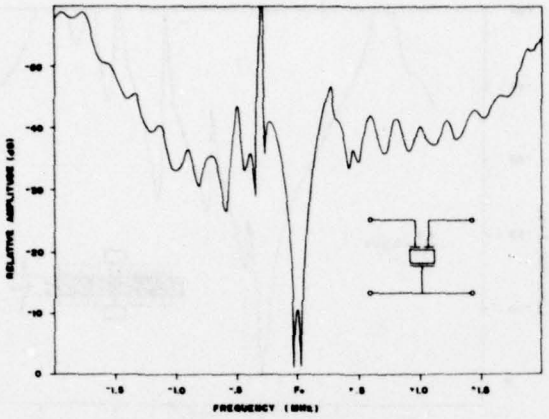

Figure 8

Unmatched (50Ω), 2-pole filter response using inline coupled SAW resonators.

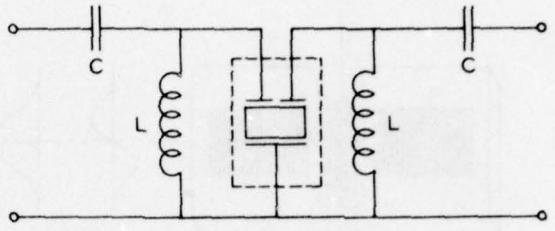

Figure 10

Typical matching circuit used with 2-pole SAW filters.

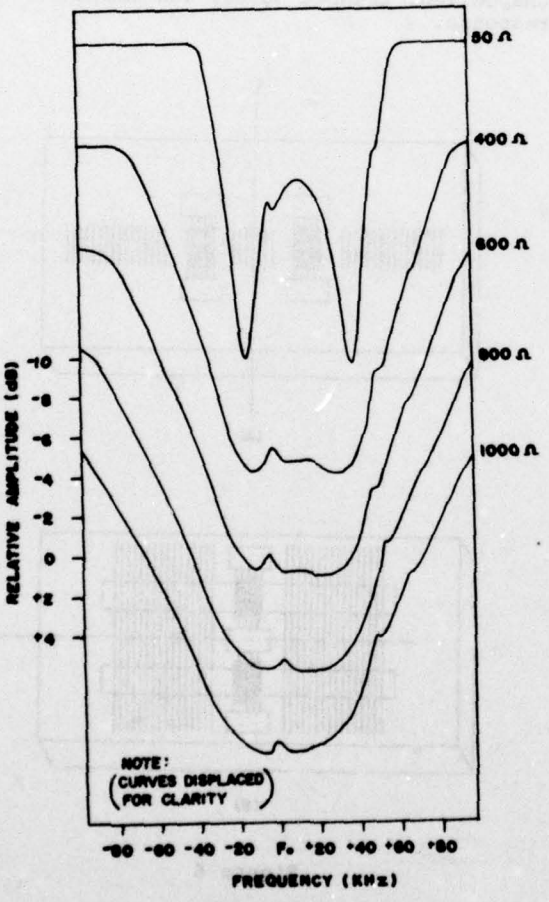

Figure 9

Two-pole filter response as a function of matching impedance for inline coupled resonators.

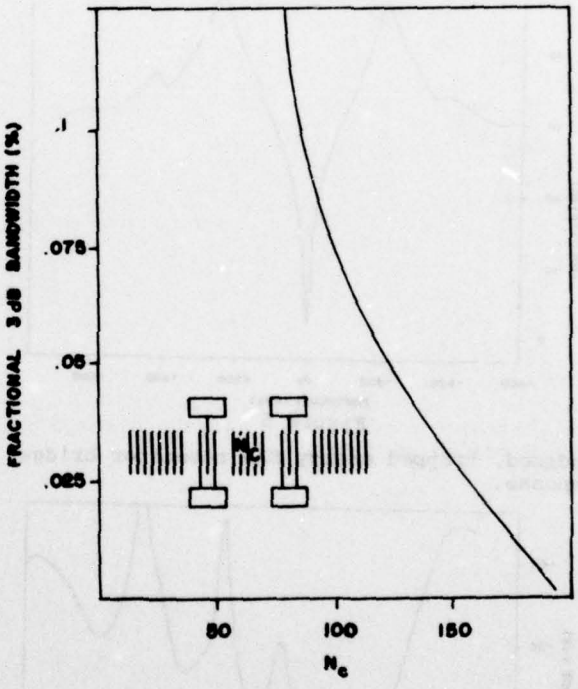

Figure 11

Bandwidth of inline coupled SAW filter as a function of the number of stripes in coupling reflector.

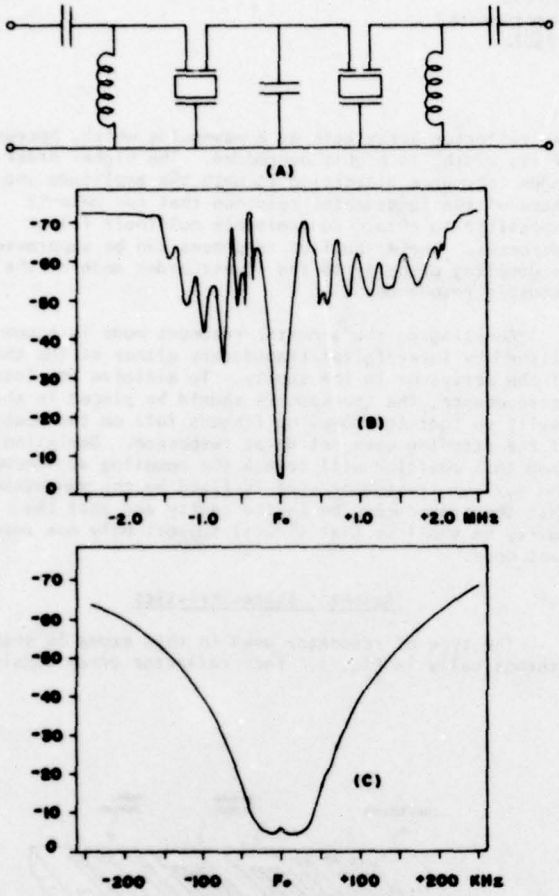

Figure 12

Four-pole, Tandem connected SAW filter,
(a) Matching circuit, (b) Wide-band response,
(c) Expanded response.

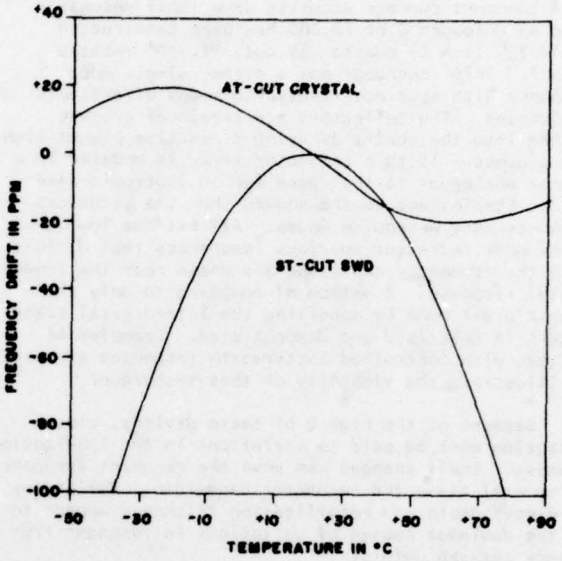

Figure 13

Temperature stability of ST-cut SAW resonator compared to that of an AT-cut bulk resonator.

TWO-PORT QUARTZ SAW RESONATORS

William R. Shreve
Texas Instruments Incorporated
Dallas, Texas 75222

Summary

A two-port surface acoustic wave (SAW) resonator with an unloaded Q of 20,000 has been constructed on 47.25° (z x ℓ) quartz (ST cut, 42.750° rotated y cut). This resonator has a clean, single mode response with spurious transverse modes effectively suppressed. The reflectors are arrays of grooves etched into the quartz by using a reactive plasma etching process. If this reflector array is modeled in a manner analogous to that used for an isotropic waveguide, Staples and Smythe showed that the structure supports many waveguide modes. All but the lowest order mode represent spurious resonances that distort both the resonator amplitude and phase near the fundamental response. A method of coupling to only the lowest order mode by apodizing the interdigital transducers is described and demonstrated. Examples of filters with controlled Butterworth responses are used to illustrate the viability of this technique.

Because of the high Q of these devices, close attention must be paid to variations in the fabrication process. Small changes can move the resonant frequency by several times the resonator bandwidth. Variations in groove depth and metallization thickness appear to be the dominant causes of variations in resonant frequency between wafers.

Deviations from the design frequency caused by fabrication necessitate post-fabrication frequency tuning in many oscillator and narrowband filter applications. Preliminary results of tuning with a thin dielectric overlay of ZnO are presented.

Introduction

Surface acoustic wave (SAW) resonators have been built with sufficiently high Q and predictable performance to demonstrate their potential for UHF oscillator and narrow band filter applications. A SAW resonator consists of two distributed reflectors, each consisting of an array of surface perturbations on half wavelength centers. The arrays define a cavity which will resonate when the effective cavity length is an integral number of half-wavelengths. Distributed reflector arrays of this type are highly reflecting only over a narrow band of frequencies (the stop band of the array). At other frequencies, most of the energy incident on the reflectors is transmitted. The cavity and reflector can be designed so that only one resonance occurs within the stop band. Such a design results in a fundamental mode resonator with no spurious cavity resonances to generate interference. Reflectors of this type do have stop bands at harmonics of this fundamental,[1] but spurious responses at these frequencies are effectively suppressed by coupling and electrically matching to the fundamental. The individual reflectors within an array can consist of any of a number of surface perturbations including grooves,[2,3] deposited metal,[4] dielectric layers,[5] or implanted ions.[6]

The reflector array is typically on the order of 100 wavelengths wide. The net effect of the individual perturbations is to introduce a perturbation over the entire area covered by the array. If this perturbation results in a reduced velocity under the array (as it does for grooves, aluminum, gold, or ZnO reflectors), the reflector array acts as a waveguide which, because of its width, is highly overmoded. The higher order modes introduce distortion in both the amplitude and phase of the fundamental response that can make it impossible to obtain controllable multipole filter responses. These spurious responses can be suppressed by coupling properly to the lowest order mode of the acoustic resonance.

Coupling to the acoustic resonant mode is accomplished by interdigital transducers either at the ends of the arrays or in the cavity. To minimize the loss at resonance, the transducers should be placed in the cavity so that the coupling fingers fall on the peaks of the standing wave set up at resonance. Deviation from this position will reduce the coupling at resonance. The maximum transducer size is fixed by the requirements that the transducers be in the cavity and that the cavity be small so that it will support only one resonant mode.

Resonant Characteristics

The type of resonator used in this study is shown schematically in Fig. 1. Each reflector array consists

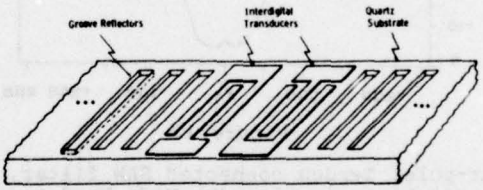

Figure 1. Schematic of two-port SAW resonator using groove reflectors on ST quartz.

of 400 grooves. The grooves are 100 wavelengths long, approximately 0.25 wavelengths wide, and on the order of 0.013 wavelengths deep. Two aluminum transducers each consisting of 29 pairs of electrodes are placed in the unetched cavity to couple energy in and out. These transducers must be positioned in precisely the right position within the cavity to obtain the optimum response, but small errors will only lead to a decrease in coupling to the resonant mode. Transducer position can be used as a means for controlling the strength of coupling into and out of a resonator. The design of the transducer also controls the impedance of the completed resonator and the transducer capacity can be used to simplify matching to an external impedance.

Typical performance for a two-port resonator is shown in Fig. 2. The picture of a device shows two

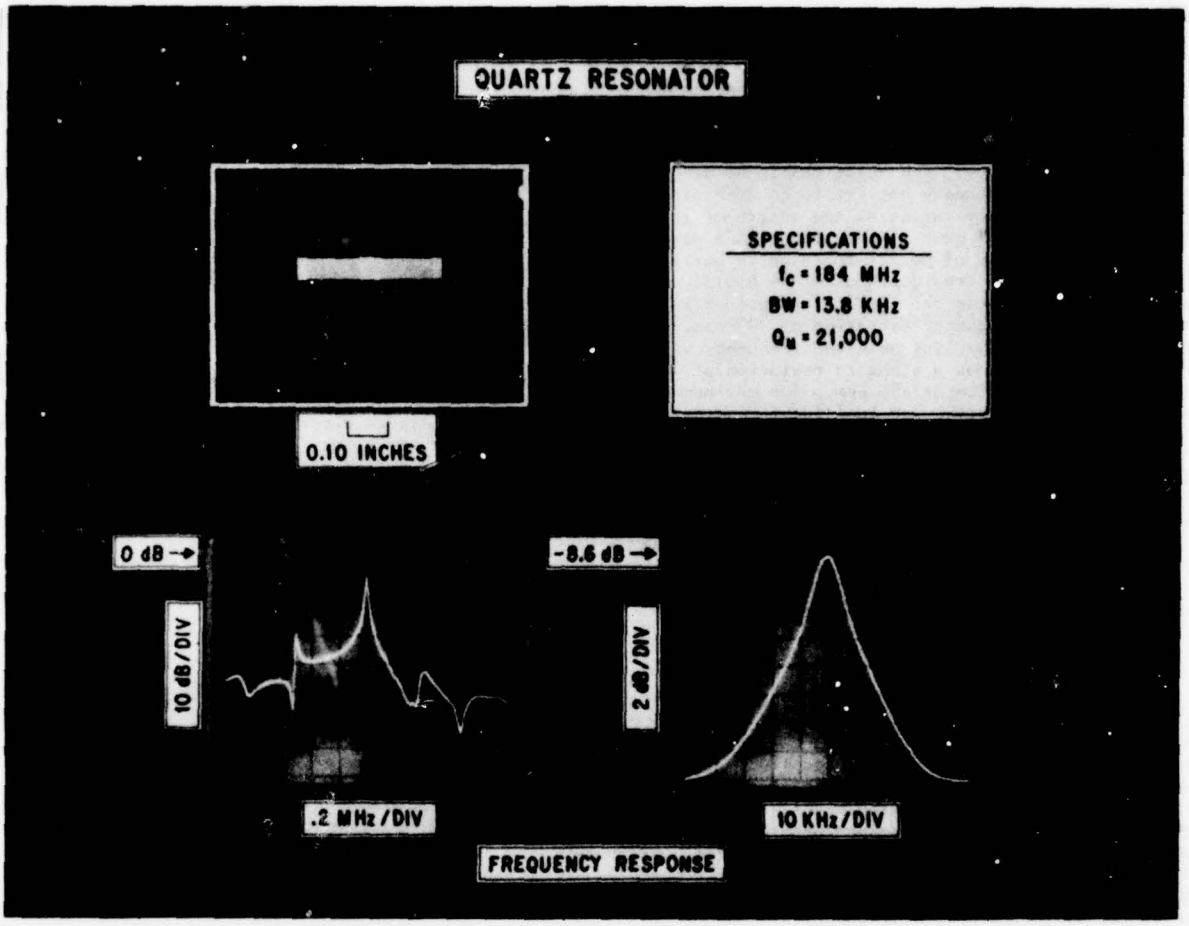

Figure 2. Two-port quartz SAW resonator. Top left: picture of resonator. Top right: measured characteristics. Bottom: frequency response.

transducers in the cavity (distinguishable by the dark bonding pads), diffraction from the two grooved arrays, and extra transducers at the ends of the arrays. The frequency response of the device shows the resonance peak and a background level generated by direct acoustic transmission between the transducers. This background is a characteristic of two-port surface wave resonators and shows up in filters made from these resonators. In terms of modeling, this level shows up as a resistance shunting the series resonant arm as opposed to the shunt capacity characteristic of one-port resonators. The device shown in Fig. 2 has an unloaded Q (Q_u) of 21,000. The unloaded Q is the ratio of the energy stored to the energy dissipated per cycle in the cavity. It is an upper limit for the loaded Q (f_o/BW). An extensive discussion of resonator Q can be found in Reference 7.

One of the major sources of loss in the groove reflector quartz resonator is air loading. The unloaded Q of a 194 MHz resonator can be increased from 18500 in air to 25500 in vacuum. The reciprocal of Q_u is a measure of the loss in the resonator. Thus, the change in $1/Q_u$ is a measure of the attenuation introduced by air loading. In this case the change is 14.7×10^{-6}. This result is equivalent to an attenuation of 0.40 dB/μsec when normalized to 1 GHz. (Air loading loss is proportional to frequency.) The corresponding experimental value published by T. L. Szabo and A. J. Slobodnik, Jr., is 0.47 dB/μsec.[8]

Fabrication

Fabrication of plasma etched quartz SAW resonators is a multistep process. At each step, uncertainties are introduced which affect the frequency of the final device. For devices like that shown in Fig. 2, the center frequency can vary by more than the device bandwidth. There are several possible sources of this error. The effect of small orientation errors in the velocity of ST-cut wafers has been considered by Bell.[9] A misorientation of the plate normal by ±0.25 degrees leads to a maximum frequency shift of ±92 parts per million (ppm). Alignment of the resonator pattern with the X axis of the crystal is less critical; an error of ±0.5 degrees causes a shift of ±15 ppm.

The thickness of the aluminum fingers appears to be extremely critical. In theory[10] variation of the thickness of an ideal solid aluminum film on ST quartz from 1225 Å to 1300 Å (3%) should cause a velocity shift of ±17 ppm at 200 MHz. In practice shifts

corresponding to ±180 ppm for this change in metal thickness have been observed in resonators on different quartz slices. The large discrepancy between theory and experiment is currently under investigation.

Fabrication of the reflectors also affects the resonator frequency. The reflector width has a large effect on the reflection amplitude per stripe. The width also affects the phase of reflection and therefore the resonant frequency. The relationship between the groove width and frequency has yet to be determined. The resonant frequency varies as the square of the groove depth. For ST quartz, this leads to a maximum frequency uncertainty of 90 ppm for a depth variation of 2.5% about the desired depth of $h/\lambda = 0.013$. The net result of all these fabrication variations is an expected maximum frequency variation of 377 ppm. In experiments at 185 MHz, the observed frequency variation across a slice has a standard deviation of ±40 ppm and a maximum deviation of ±75 ppm. The maximum observed variation from slice to slice for slices from the same stone is 140 ppm with a standard deviation of ±60 ppm. These variations are well below the expected maximum because not all variations are necessarily in the same direction (some may cancel) and orientation differences are reduced by comparing devices from the same slice and slices from the same stone. The numbers show that standard processes for surface wave resonators lead to a requirement for post fabrication frequency tuning of about 300 ppm.

Post Fabrication Tuning

Surface wave resonator tuning can be accomplished by using dielectric overlays, laser trimming (applicable to resonators using metal films), electrical trimming (applicable to resonators on high coupling materials), and reflector thinning (applicable to overlay reflectors). For resonators with groove reflectors, a zinc oxide layer over the entire resonator provides the tuning range required to make up for fabrication variations. The excess loss introduced by tuning can be measured by the change in the reciprocal of unloaded Q. For tuning up to 300 ppm in frequency at 195 MHz this change is as large as 3.0×10^{-6}. This value corresponds to about one-fifth the loss introduced by air loading at this frequency. As the tuning range is increased to three parts per thousand, the loss becomes equal to that for air loading. For devices operated in air, tuning of up to 300 ppm introduces only a slight performance degradation. Further tuning causes an unacceptable Q degradation; the phase slope for oscillator applications is significantly degraded and for filter applications the loss for a specified bandwidth is increased.

Waveguide Modes

Surface wave reflectors perturb the surface of the crystal and in many cases (including groove reflectors) result in a reduced surface wave velocity. This reduced velocity turns the 100 wavelength wide array into a waveguide that is highly overmoded. E. J. Staples and R. C. Smythe have analyzed this effect in a manner analogous to that used for trapped energy modes in bulk wave resonators.[11] An example of the effects of this multimoding is shown in Fig. 3. When resonators of this type are used in narrow band filters, the effects of the unwanted modes can become even more severe as illustrated by the two-pole filter response shown in Fig. 4. One technique which can be used to suppress these modes is to use narrow arrays which support only one waveguide mode. This solution is not always practical due to impedance considerations at the input transducer. The technique used in this work involves coupling to only the lowest order mode in the waveguide by matching the potential generated by the

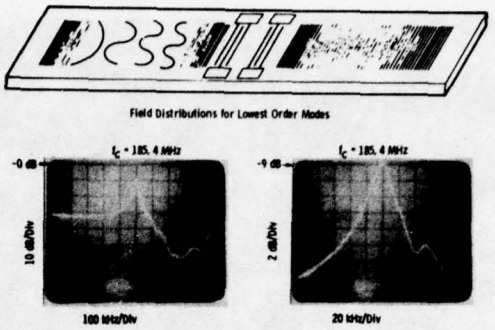

Figure 3. Waveguide modes in a two-port resonator. Top: resonator schematic illustrating the field amplitude distribution across the waveguide for the lowest order modes. Bottom: frequency response of resonator showing the distortion introduced by waveguide modes.

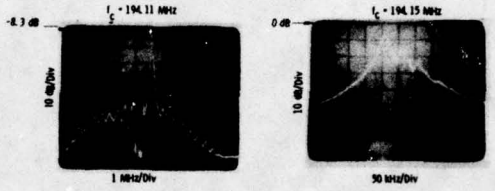

Figure 4. Frequency response of a "two-pole" filter constructed with two resonators with spurious waveguide modes.

coupling transducer to the potential variation across the waveguide. Determination of the field distribution across the waveguide array on an anisotropic substrate cannot be solved in closed form and variational techniques must be used. In this case, the problem is further complicated by the complex nature of the boundary condition at the edge of the array. Some feeling for the nature of the field distribution can be obtained from the analogy to bulk wave resonances pointed out by Staples and Smythe.[11] Solutions of problems involving bounded resonant systems vary in a sinusoidal manner, so a cosine weighting function across the guide was chosen for this work. This weighting is accomplished by apodization of the coupling transducer as shown in Fig. 5. Typical responses for devices with this design are shown in Fig. 2 and Fig. 5. In both cases the responses are free from amplitude distortion caused by waveguide modes. It should be noted that any perturbation on the surface of the resonator that causes unwanted modes to couple strongly to the desired mode will reintroduce distortion in the resonator response. The unloaded Q of the 388 MHz resonator shown in Fig. 5 is 10,000. This is the first demonstration of SAW resonator operation above 200 MHz with a Q this high.

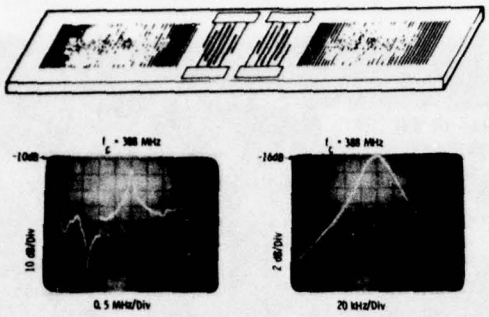

Figure 5. Apodization of coupling transducers to suppress waveguide mode interference. Top: schematic of resonator with apodization, active transducer region shaded. Bottom: frequency response of 388 MHz resonator with apodized transducers.

Modeling

With the transducers apodized to suppress waveguide mode distortion, the two-port resonator can be modeled by a simple equivalent circuit. The arrays are modeled as lossless transmission lines with periodic discontinuities. These lines are combined with a simple model for the interdigital coupling transducers to model the entire resonator. Near resonance, this circuit model for a symmetric resonator can be reduced to the form shown in Fig. 6.[12]

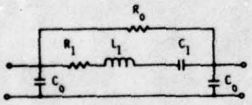

184 MHz Resonator

	Experiment	Theory
R_1 (Ω)	200	200*
L_1 (mH)	3.4	3.8
C_1 (pF)	0.00022	0.00020
R_o (Ω)	16000	18000
C_o (pF)	1.9	1.9

* Value obtained by fitting to experimental data for a 400 reflector array of grooves (d/λ = 0.023).

Figure 6. Equivalent circuit for two-port resonator. The table compares experimental and theoretical results for a 184 MHz resonator on ST quartz.

The circuit elements with cosine apodization of the coupling transducers are related to the substrate characteristics and design parameters as follows:

$$R_1 = \frac{1 - |\Gamma|}{2|\Gamma|} R_o$$

$$L_1 = \frac{L R_o}{4|\Gamma| f_o}$$

$$C_1 = \frac{1}{(2\pi f_o)^2 L_1}$$

$$C_o = \frac{2}{\pi} N (\varepsilon_p + \varepsilon_o) w + C_p$$

$$R_o = [4k^2 (\varepsilon_p + \varepsilon_o) w f_o N^2]^{-1}$$

where N = the number of pairs of electrodes in the transducer

ε_p = the effective substrate dielectric constant

w = the maximum aperture of the transducer

k^2 = the substrate electromechanical coupling constant

f_c = the transducer center frequency

f_o = the resonant frequency

Γ = the array reflection coefficient

L = the effective cavity length.

C_p is the stray capacity from bonding pads. The model relates design parameters and material constants to a simple circuit similar to that used for bulk resonators. For filter design, this model is essentially the same as one used for bulk wave resonators in ladder networks.[13] Because the model for the array is based on lossless transmission line segments, the magnitude of the reflection coefficient must be determined from experimental data. Until the loss mechanisms are identified, this fit must be repeated at each frequency of operation. The fit can be made to the loss at resonance alone. The theory then allows one to predict the resonator Q_u ($Q_u = W_o L_1 / R_1$) and therefore the measured bandwidth. This procedure has been followed for a 184 MHz resonator, and the results are shown in Fig. 6. The experimental values for R_o and C_o are determined from resonator out-of-band rejection and input capacity at low frequency respectively. The agreement between experiment and theory is good.

Filter Design

The model for the two-port resonator permits the synthesis of resonators that are optimized to particular filter designs. Given the maximum Q available in a resonator, the desired filter bandwidth, and number of poles in the filter, one can determine all the circuit element values for filters of the type shown in Fig. 7.[14,15] This circuit illustrates the use of two-port resonators in a two-pole filter. In many cases the resonator can be designed to reduce the number of external circuit elements required to match the resonator to the external circuit. Proper design of the coupling transducer capacity C_o at the ends of the filter combined with the proper choice of the inductor L_T allow one to match the filter over a narrow band near resonance.

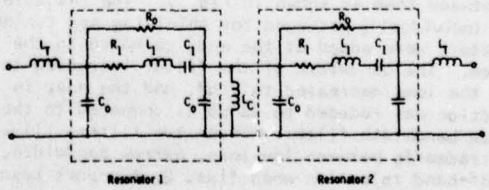

Figure 7. Equivalent circuit of two-pole filter mode using two-port resonators.

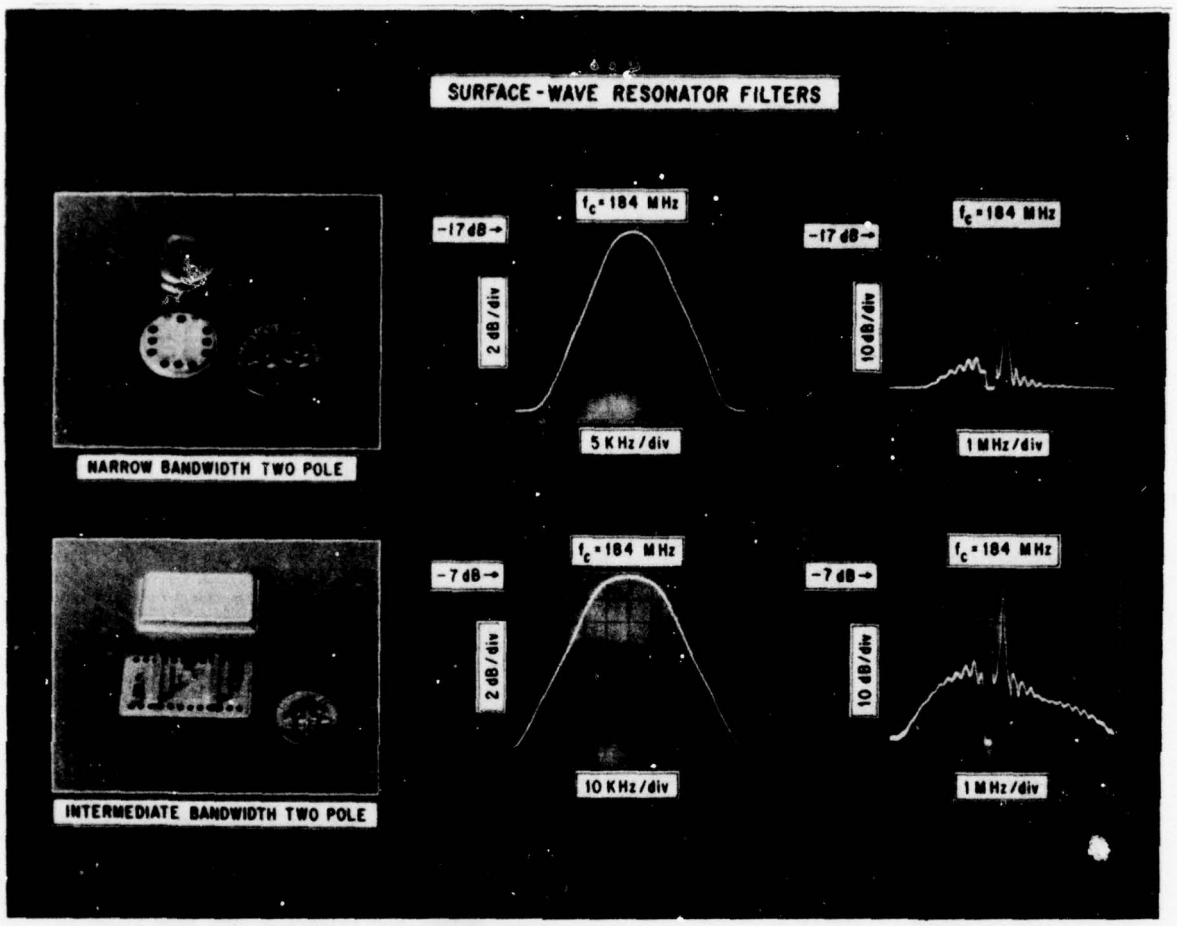

Figure 8. Examples of two-pole filters made with two-port resonators coupled electrically. Top: narrow bandwidth filter. Bottom: intermediate bandwidth filter.

Two examples of filters built with two-port resonators are shown in Fig. 8. The narrow bandwidth filter is made by directly cascading two resonators in a TO-8 header as shown in the photograph. No external matching to a 50 ohm system is required. The resulting filter had a 17 dB loss, 17 kHz bandwidth, and 48 dB near in rejection. To increase the bandwidth, the coupling between resonators was increased by adding an inductor L_c between them as shown in Fig. 7. The resonators were individually packaged for shielding and tuning inductors were added at the ends to match to the 50 ohm system. The bandwidth of the filter increased to 40 kHz, the loss decreased to 7 dB, and the near in rejection was reduced to 32 dB as compared to the narrow bandwidth filter. These two filters illustrate the tradeoffs between low loss, narrow bandwidth, and out-of-band rejection when fixed Q_u two-port resonators are used in multipole filters.

Conclusion

Two-port SAW resonators consisting of plasma etched groove reflectors in ST quartz and aluminum coupling transducers have been made with Q 's over 20,000 and with accurate control (±150 ppm) of resonant frequency. Spurious waveguide mode distortion of the frequency response can be eliminated by apodization of the coupling transducers. Variations in resonant frequency caused by fabrication uncertainties can be compensated for by tuning with a dielectric overlay of ZnO. The resultant resonator can be modeled on an ad hoc basis by a simple equivalent circuit that is applicable to the design of multipole filters.

Acknowledgements

The author wishes to acknowledge those who helped with this manuscript: Dennis Saunders for resonator testing, resonator tuning, filter construction, and figure preparation; Steven Miller and Bob Vess for resonator fabrication; Robert Wagers and Delamar Bell, Jr., for helpful discussions, Billy Davis and David Carroll for drafting the figures used here, and Irene P. Robbins for typing this manuscript.

References

1. R. C. M. Li and J. Melngailis, "The influence of stored energy at step discontinuities on the behavior of surface-wave gratings," IEEE Trans. Sonics Ultrasonics, SU-22:3, pp. 189-198, May 1975.

2. R. C. M. Li, J. A. Alusow and R. C. Williamson, "Experimental exploration of the limits of achievable Q of the grooved surface-wave resonator," 1975 Ultrasonics Symp. Proc., IEEE Pub. No. 75 CHO 994-4SU, pp. 279-283, September 1975.

3. S. P. Miller, R. E. Stigall and W. R. Shreve, "Plasma etched quartz SAW resonators," 1975 Ultrasonics Symp. Proc., IEEE Pub. No. 75 CHO 994-4SU, pp. 474-477, September 1975.

4. E. J. Staples, "UHF surface acoustic wave resonators," Proc. 28th Annual Frequency Control Symp., U. S. Army Electronics Command, Ft. Monmouth, N. J., pp. 280-285, May 1974.

5. E. J. Staples, J. S. Schoenwald, R. C. Rosenfeld and C. S. Hartmann, "UHF surface acoustic wave resonators," 1974 Ultrasonics Symp. Proc., IEEE Pub. No. 74 CHO 896-1SU, pp. 245-252, November 1974.

6. P. Hartemann, "Acoustic surface wave resonator using ion-implanted gratings," 1975 Ultrasonics Symp. Proc., IEEE Pub. No. 75 CHO 994-4SU, pp. 303-306, September 1975.

7. D. T. Bell, Jr., and R. C. M. Li, "Surface-acoustic-wave resonators," Proc. IEEE, 64:5, pp. 711-721, May 1976.

8. T. L. Szabo and A. J. Slobodnik, Jr., "The effect of diffraction on the design of acoustic surface wave devices," IEEE Trans. Sonics Ultrasonics, SU-20:3, pp. 240-251, July 1973.

9. D. T. Bell, Jr., "Phase errors in long surface wave devices," 1972 Ultrasonics Symp. Proc., IEEE Pub. No. 72 CHO 708-8SU, pp. 420-423, October 1972.

10. R. S. Wagers, private communication.

11. E. J. Staples and R. C. Smythe, "Surface acoustic wave resonators on ST quartz," 1975 Ultrasonics Symp. Proc., IEEE Pub. No. 75 CHO 994-4SU, pp. 307-310, September 1975.

12. W. R. Shreve, "Surface-wave two-port resonator equivalent circuit," 1975 Ultrasonics Symp. Proc., IEEE Pub. No. 75 CHO 994-4SU, pp. 295-298, September 1975.

13. *Reference Data for Radio Engineers*, 5th Edition, Indianapolis, Ind.: H. W. Sams and Company, Inc., 1968.

14. D. T. Bell, Jr., and L. H. Ragan, "Filter networks using SAW resonators," 1975 Ultrasonics Symp. Proc., IEEE Pub. No. 75 CHO 994-4SU, pp. 395-99, September 1975.

15. L. H. Ragan, "Surface acoustic wave resonator filters," 1976 Microwave Symp. Proc., IEEE Pub. No. CH 1087-6MTT, pp. 286-288, June 1976.

SURFACE ACOUSTIC WAVE RING FILTER*

Frank Sandy and Thomas E. Parker
Raytheon Research Division
Waltham, Massachusetts 02154

Abstract

A new geometry for surface acoustic wave filters has been developed which provides bandwidths of up to 2 percent with an insertion loss under 3 dB and out-of-band rejection of over 60 dB. This ring filter geometry consists of four 90° reflecting gratings at the corners of a rectangular propagation path. Interdigital transducers are placed between opposite pairs of gratings. The gratings are nearly perfect reflectors over a narrow frequency band and reflect energy from one transducer to the other. Since the energy launched in both directions by the input transducer gets reflected to the output transducer, the 6 dB of bidirectional loss normally associated with SAW delay lines is not present. Thus, if the transducers are well matched, very low loss is attainable. Furthermore, since the gratings become transparent to acoustic waves at frequencies outside of the device passband, the two transducers are not acoustically coupled at those frequencies. This provides the high out-of-band rejection which is not obtainable from a conventional SAW resonator whose transducers are still acoustically coupled far from resonance.

The bandpass of the device is determined primarily by the reflectivity response of the grating. The reflectivity per line as a function of position in the grating must be varied gradually to avoid reflectivity sidelobes. The shape factor of the filter response can be increased further by choosing the number of fingers of the transducers such that the first frequency null of the transducer response occurs at a desirable point on the grating reflectivity response curve.

The transducers must be well matched not only to reduce insertion loss but to insure that all of the acoustic energy makes only a single transit halfway around the ring. Acoustic energy not coupled out on this first pass makes multiple resonant transits around the ring causing pass band ripple with a frequency determined by the ring transit time.

Results are presented showing filter responses of devices built on lithium niobate with gratings consisting of aluminum lines, aluminum lines between ion-etched grooves and depth-weighted ion-etched grooves, and devices built on ST-cut quartz with gratings consisting of gold lines recessed in ion-etched grooves.

Introduction

The ring filter is a new surface acoustic wave device configuration that evolved from work on SAW resonators aimed at increasing their bandwidth and their out-of-band rejection. It retains the advantages of low insertion loss which resonators achieve by confining virtually all of the acoustic energy between reflective gratings. However, many resonator filter geometries do not provide good ultimate rejection. The reason for this can be seen from the simple two-port resonator geometry shown in Fig. 1. At frequencies far from resonance, the gratings become transparent to surface acoustic waves and the device then closely resembles an ordinary SAW delay line with non-negligible insertion loss. The ring filter geometry, as will be seen, is such that out of the desired passband there is no direct acoustic transmission between the input and output transducer and hence there is very high out-of-band rejection. There are coupling schemes for SAW resonators that increase the out-of-band rejection, but they do it at the expense of bandwidth. The ring filter has been capable of achieving bandwidths up to 2 percent or more with at least 60 dB of out-of-band rejection.

The ring filter geometry is capable of resonating and its use of reflective gratings makes it physically resemble a resonator. However, in normal operation it is not resonant and it should be considered a transversal filter.

Ring Filter Geometry

The surface acoustic wave ring filter geometry is shown in Fig. 2. Acoustic energy is launched by the input transducer in two directions. The acoustic energy propagating in each of these directions is reflected towards the output transducer by the two 90° reflecting gratings on each side as in a reflective array compressor (RAC).[1] The gratings can consist of ion-etched grooves, metal stripes providing piezoelectric shorting, metal or dielectric stripes providing mass loading, raised ridges, or any other form of periodic discontinuity. If the input transducer is properly matched, all of the input energy is coupled into the two useful acoustic paths without the bidirectionality loss normally associated with SAW transducers. By symmetry if the output transducer is properly matched and the acoustic waves from the two paths arrive uniformly with equal phase and amplitude, all of the acoustic energy will be coupled out to the electric output port. Furthermore, if the gratings are highly reflecting, virtually all of the power launched into the acoustic waves will reach the output. Thus the insertion loss is inherently very low and there can be negligible triple-transit signal.

The primary frequency-selective elements of this filter are the gratings, although the transducer response can also contribute to the out-of-band attenuation. The frequency response of the grating can be tailored either by amplitude weighting the reflectivity per stripe along the grating or by frequency modulating the spacing of the stripes as in a chirped pulse expander. Although very broad pulse expander RAC's are readily constructed with low reflectivity gratings, we have found from computer modeling that high reflectivity chirped gratings giving nearly total reflection over their band are difficult if not impossible to design. This is due to the incoherent scattering of acoustic energy by the discontinuities in the grating prededing those with which the incident acoustic beam is resonant.[2] We have therefore tailored our grating reflectivity spectra only by amplitude weighting. The most readily achieved method of amplitude weighting is to use grooves with varying depths as the reflecting discontinuities. Mass loading stripes or ridges can also be varied in thickness. However, the reflectivity of metal stripes due to piezoelectric shorting is not

*Work supported by U. S. Army Electronics Command under Contract No. DAAB07-75-C-1348.

sensitive to thickness. To some extent, reflection amplitude can be modulated by varying the lengths of the stripes. However, this can generally only be done on the trailing end of the grating with the stripes getting monotonically shorter since the stripes may also perturb the acoustic velocity and the wave front would be distorted beyond the shortened stripes.

The angle of the grating stripes is determined by the ratio of velocities of the surface waves in the two orthogonal directions of propagation. The SAW velocities unperturbed by the grating stripes are the correct velocities to use for the first grating line and nearly exactly correct for all of the leading lines from which most of the reflection takes place. If the reflecting stripes significantly perturb the SAW velocities, this grating angle will not lead to a perfect 90° reflection from lines deep within the grating. However, energy will only reach those lines at out-of-band frequencies where loss of power is acceptable. If the first few grating lines are truncated so that the grating pattern edge facing the transducers is parallel to the transducer fingers, then the velocities of the surface wave as perturbed by the grating should be used to compute the grating angle throughout the grating. However, if the leading edge is squared off, the reflected acoustic beam profile becomes much less uniform and cannot be completely absorbed by the output transducer.

If all of the acoustic energy incident on the output transducer is not coupled out, the remainder will make another transit around the ring. The device will then be a resonator. This is not desirable since it creates a comb structure of resonant modes in the transmission pass band. Proper matching of the transducers can be viewed as completely overcoupling these resonances to blur them together and produce a smooth pass band.

Spurious responses are also inherently low in this ring geometry. Bulk waves generated by the input transducer are not reflected at the same angle as surface waves due to differing anisotropies in their velocities. Thus, they do not reach the output transducer.

Lithium Niobate Ring Filters

Our first ring filters on YZ $LiNbO_3$ substrates used aluminum stripes as the grating structure. The transducers had 21 fingers, making them very broadband compared to the reflection band of the gratings. Their acoustic aperture was 100 wavelengths so that when inductively tuned they would be well matched with 50 ohms radiation resistance. This also provided the transverse beam with 100 reflecting stripes. The gratings originally had an excessive length of 300 stripes so virtually no acoustic energy reached the far end at the band center.

Results from such a ring filter are shown in Fig. 3. This filter had 3.5 dB insertion loss and a 1 percent 3 dB bandwidth at 65 MHz. However, because the gratings have a uniform reflectivity per stripe, the total reflection of the gratings has pronounced sidelobes which show up in the filter response. If the total reflection were low, these sidelobes would have the familiar sin x/x frequency dependence. For the high reflection case considered here, the exact shape differs. The spacing of the sidelobes is determined by the reciprocal of the length of the whole gratings. The 3 dB width of the filter response, however, is determined by the reciprocal of the effective length of that part of the grating which contributes to the in-band reflection. Since nearly all of the power is reflected in much less than the full grating length, the 3 dB bandwidth is much greater than the sidelobe spacing.

A trivial means of amplitude weighting the reflectivity per stripe is to truncate or square off the ends of the gratings furthest from the transducers. The lengths and hence the reflection coefficient amplitude of these truncated end lines then varies linearly with position. This amplitude modulation smears out the sidelobe structure as can be seen in Fig. 4. However, this amplitude weighting of the trailing end of the grating has very little effect on the in-band response.

The 3 dB width of the filter response can be broadened by increasing the reflectivity per stripe and hence decreasing the effective length of the grating at band center. This we have done by combining two reflection mechanisms. A device similar to the one previously described was made with 9300 Å ion-etched grooves using the aluminum grating as an etch mask. Since the reflections from the piezoelectric shorting of the aluminum add in phase with the reflections from grooves between the aluminum stripes, the aluminum grating was then left in place. The filter response from the combined grating is shown in Fig. 5. The bandwidth is nearly doubled by the increased reflectivity. The insertion loss of this device has also been reduced to 2.5 dB. This is the lowest loss we have achieved so far.

A much more sophisticated amplitude weighting function can be obtained if only grooves are used. In particular, if the groove depth as a function of position is the square root of a Hamming function, the reflection spectra of a pair of gratings will be similar to that of a Hamming filter which has 42 dB sidelobes. It will deviate from the Hamming response at the center of the band because the gratings are strongly reflecting there and each line of the reflector does not see the same incident energy. However, in the out-of-band region, the grating is weakly reflecting and since the purpose of this amplitude weighting is to control the out-of-band filter shape, it is sufficient that the response approach that of a Hamming filter in that region.

The response of two ring filters using grooves alone is shown in Fig. 6. In one device the grooves are a uniform 9400Å in depth, but are truncated as previously at the trailing end of the grating. Because of the reduced reflectivity per stripe of the grooves alone, the 3 dB band width is reduced to 0.5 percent. However, the insertion loss of this unit remained low at 2.5 dB. In the second device the groove depths are modulated by the square root of a Hamming function with a maximum depth of 8000 Å. The 3 dB bandwidth is reduced further by a small amount, but the skirts are steepened substantially. The 40 dB shape factor is reduced from 10 to 4.6. Out-of-band sidelobes start about 40 dB down near that expected from a Hamming filter. This is the desired effect of amplitude weighting the reflectivity. Greater bandwidth can be achieved by using deeper (more reflecting) grooves. However, if the grooves are deepened too much the near-in sidelobes start to distort and increase in height. To prevent this, the number of stripes over which the Hamming profile is applied should be decreased appropriately.

If the gratings on the two sides of the ring are not exactly identical, the wave on one side may traverse a slightly longer path and arrive at the output transducer out of phase with the wave from the other side. The acoustic energy will then not all be coupled out by the output transducer and the remainder will make another transit around the ring. This device will then be a multimode resonator with low insertion loss only at those frequencies where the multi-transit signals arrive back at the output transducer in phase with the

first transit signal. This behavior is shown by the large in-band ripple in Fig. 7. This ripple can be removed by separately measuring the phase of each half of the ring and adding an aluminum phase correction pad.

Far from the pass band, the insertion loss keeps increasing with frequency deviation. Minor pass bands occur at some harmonics and subharmonics of the pass band. The worst of these are the fifth harmonic at about 330 MHz and the third subharmonic at about 22 MHz. Responses at both of these frequencies are about 65 dB below the main pass band. The weak fifth harmonic response is expected, but the subharmonic response was not and is not yet understood. However, it is small enough not to be a problem.

The input impedance of the $LiNbO_3$ ring filter is shown in Fig. 8a on a Smith chart plot, without a load, and in Fig. 8b with a 50-ohm load. The dominant loop in both figures is due to the transducer and its series matching inductor. The numerous subsidiary loops centered near 50 ohms are the multiple resonant modes of the ring. These occur only when energy is not being coupled out by the output transducer on the first transit. When a 50-ohm load is put on the output transducer, the resonances nearly disappear indicating good output coupling efficiency.

The minimum input resistance shown in the Smith charts of Fig. 8 is 12 ohms far from the pass band. This resistance is due primarily to the transducer fingers and is a series resistance that is also present in the pass band. It contributes 1 dB loss per transducer in this particular device. By increasing the thickness of the aluminum fingers, this has been cut in half in later devices including the ones whose insertion loss is shown in Figs. 5 and 6.

Other sources of loss in these devices include residual SAW leakage past the gratings, scattering of surface waves into bulk waves by the grating, and incomplete coupling of the acoustic beam to the output transducer due to loss in uniformity of its profile. The magnitude of each of these terms remains to be understood.

As would be expected, the ring filters on lithium niobate are somewhat temperature dependent. The +91 ppm/°C temperature coefficient of delay of YZ lithium niobate causes a shift in the center of the passband of 0.1 percent for a temperature change of only 11°C. However, the low anisotropy of the temperature coefficient on Y-cut lithium niobate results in virtually no change in the correct grating angle with temperature and hence the minimum insertion loss is temperature insensitive.

ST-Quartz Ring Filters

Because of the temperature dependence of lithium niobate, ring filters were also constructed on ST-cut quartz. The transducer and grating patterns initially used on quartz were similar to those used on $LiNbO_3$. The transducer aperture was again 100 wavelengths but the number of fingers was 51 instead of 21.

Since the piezoelectric shorting effect is negligible on quartz, a different reflection mechanism had to be used. It was desired to have as large a bandwidth as possible. As seen with the $LiNbO_3$ ring filters, unless the grooves are extremely deep, the bandwidths are only moderate. Therefore, a mass loading technique using gold stripes was used. Gold stripes alone however give less reflection than would be expected from their mass loading. The reason is that in addition to the mass loading reflection there is a topographic reflection from the raised strip. Unlike the reflections from grooves and piezoelectric shorting on $LiNbO_3$ which conveniently added in phase, the mass loading and topographic reflections of gold stripes are 180 degrees out of phase and tend to cancel each other. This problem was avoided by first ion-etching grooves in the substrate and then recessing the gold stripes in the grooves. This eliminated (or reduced) the topographic reflection, leaving the larger mass loading reflection alone.

Figure 9 shows the insertion loss of a quartz ring filter with 2000 Å thick gold stripes in 3500 Å grooves. The 3 dB bandwidth is 1.4 percent, but there is a 3 dB ripple in the pass band. Part of the ripple is caused by a phase mismatch between the two acoustic paths, but part is also due to the incomplete coupling of acoustical energy into electrical energy. Electrical matching of quartz ring filters has proven to be very difficult. This is due to the low capacitance of quartz transducers making the effect of parasitic capacitances more pronounced, the low radiation resistance of 100 wavelength apertures, 12 ohms, making the effect of parasitic resistances more pronounced and the necessity for large inductors usually with lower Q's. The device shown in Fig. 9 used 4:1 impedance transformers in addition to inductors for matching. This brought the sum of radiation resistance and parasitic resistance to well over 50 ohms.

Figures 10a and 10b show the insertion loss as a function of frequency for another quartz ring filter. This figure clearly shows the high out-of-band rejection of the ring geometry. This device had recessed gold stripes of only 1100 Å thickness and consequently had a relatively narrow bandwidth. It also shows lower in-band ripple. The electrical matching of this device was performed by T. Lukaszek[3] who supplied these figures.

The 40 dB shape factor in Fig. 9 is 3.6, although a weighted grating was not used. The transducers on the quartz ring filters have 51 fingers and therefore the transfer function of the transducers whose first nulls occur at ± 4 percent of center frequency contributes substantially to steepening the skirts. A combination of transducer design and grating amplitude weighting should prove very effective at reducing the shape factor even further.

A third device with 2200 Å gold stripes in 2600 Å grooves was fabricated and the insertion loss for this device is shown in Fig. 11. This device was different from the first two in that two series transducers of 50 λ aperture each, as shown in Fig. 12, were used for input and output. A 3 dB bandwidth of 2.3 percent, and a 40 dB shape factor of 2.4 were obtained, but some ripple was still present in the pass band. The radiation resistance for this device should have been 50 ohms, but with series inductors a value of only 35 ohms was observed. This was due to parasitic capacitances which become even more pronounced in this geometry. With 2 to 1 transformers a minimum insertion loss of 4 dB and a ripple of 1.5 dB was obtained.

For the ring geometry, the temperature dependence of the pass band frequency is determined by the temperature coefficient of delay for the launching and receiving directions only. The temperature coefficient of the transverse direction has no direct effect on the passband frequency. Therefore, ring filters built on ST-cut quartz show essentially no change in pass band frequency with temperature. However, the anisotropy of the temperature coefficient for the two directions is large and therefore the correct grating angle varies with temperature. An increase in

insertion loss is expected as the temperature varies from room temperature. An increase of 3 dB for $\Delta T = 45°C$ was measured on the quartz ring filters. Reduction of the acoustic beam aperture would reduce the sensitivity of the device to grating angle errors and hence reduce its temperature dependence. However, the amount the aperture can be reduced is limited by the necessity of the acoustic beam to cross enough reflecting stripes in the transverse direction to give good reflection.

Conclusions

A novel SAW device employing an acoustic ring geometry has been demonstrated. It provides several potential advantages for VHF and UHF band pass filter applications. It offers insertion loss less than 3 dB with bandwidth over 2 percent. Probably its most remarkable feature is extremely clean out-of-band rejection of well over 60 dB, rarely achieved with SAW devices. Shape factor is controlled by proper weighting of the reflectivity per stripe and appropriate choice of length of transducers.

Devices have been demonstrated using both lithium niobate and quartz substrates along with a variety of acoustic reflection techniques. Some of these techniques involve novel properly phased combinations of reflection mechanisms. One problem area, which is yet to be solved, deals with the temperature dependence of the devices. That is, with devices using lithium niobate substrates, the center frequency or pass band shifts with temperature. With ST-cut quartz devices, although the frequency is temperature-stable, there is a slight insertion loss dependence on temperature.

References

1. R. C. Williamson and H. I. Smith, IEEE Trans. SU-20, 113 (1973).
2. F. Sandy, 1975 Ultrasonics Symp. Proc., IEEE Pub. No. 75-CHO-994-4SU, p. 385, (Sept. 1975).
3. T. Lukaszek, private communication.

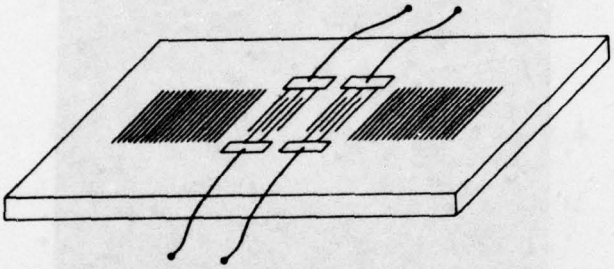

Figure 1. Two-Port SAW Resonator.

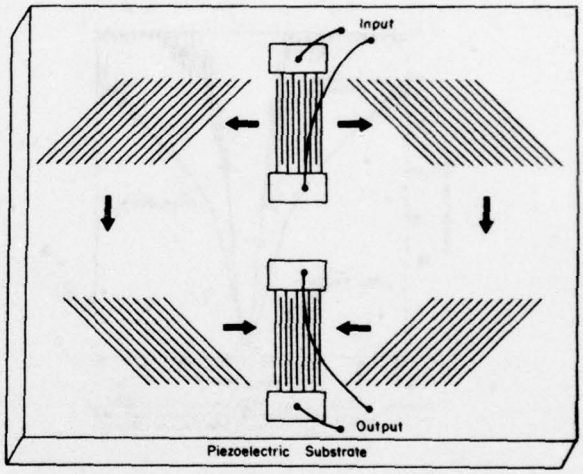

Figure 2. Basic SAW Ring Filter Geometry.

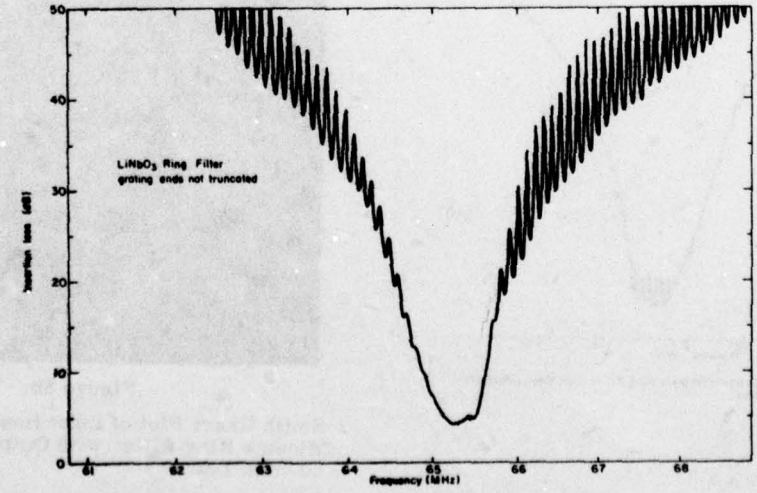

Figure 3. Insertion Loss of a Lithium Niobate Ring Filter with Aluminum Stripe Gratings not Truncated On Trailing End.

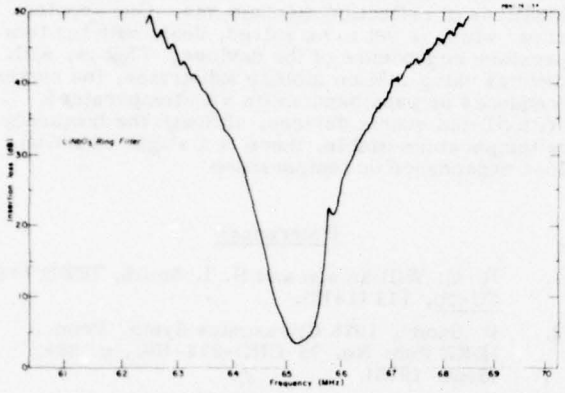

Figure 4. Insertion Loss of a Lithium Niobate Ring Filter with Aluminum Stripe Gratings Truncated on Trailing End.

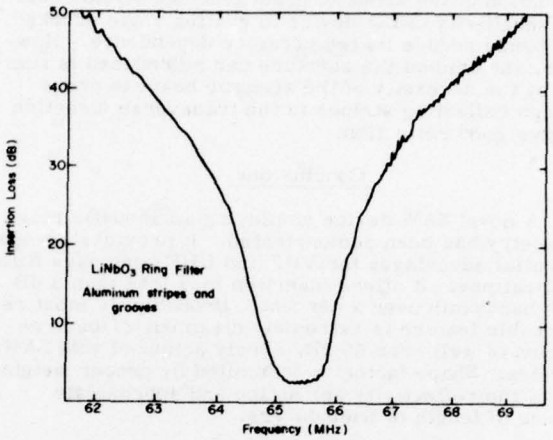

Figure 5. Insertion Loss of a Lithium Niobate Ring Filter with Ion-Etched Grooves *Between Aluminum Stripes*.

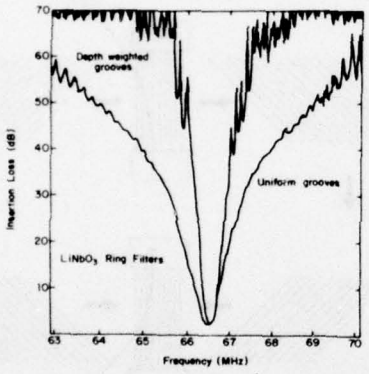

Figure 6. Insertion Loss of a Lithium Niobate Ring Filter Using Uniform 9400Å Deep Ion-Etched Grooves and Grooves Weighted with a Hamming Profile Having a Maximum Depth of 8000Å.

Figure 8a.

Smith Chart Plot of Input Impedance of a Lithium Niobate Ring Filter with Output Open.

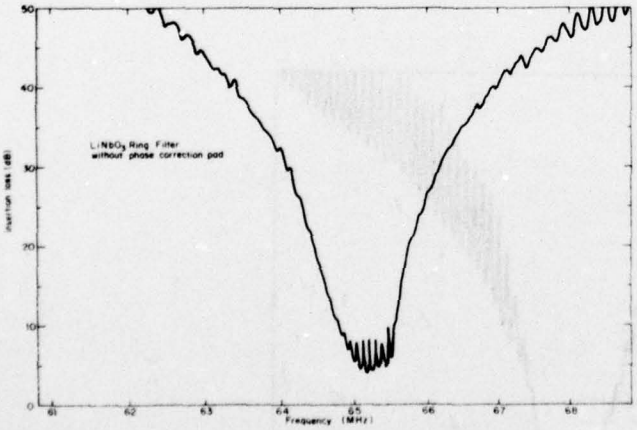

Figure 7. Insertion Loss of a Lithium Niobate Ring Filter with Phase Mismatch Between the Two Paths.

Figure 8b.

Smith Chart Plot of Input Impedance of a Lithium Niobate Ring Filter with Output Terminated in 50 Ohm Load.

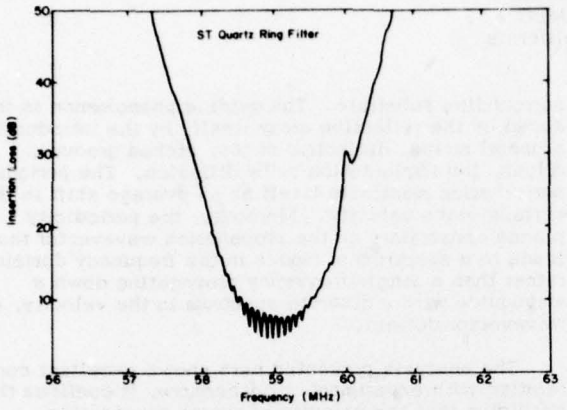

Figure 9. Insertion Loss of an ST-Quartz Ring Filter with 2000Å Gold Stripes Recessed in 3500 Å Grooves.

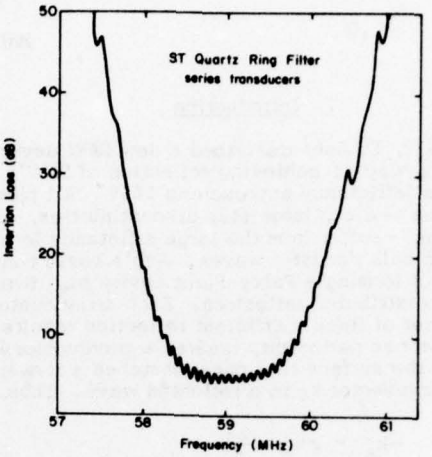

Figure 11. *Insertion Loss of an ST-Quartz Ring Filter* Using 2200Å Recessed Gold Stripes and Two Series Transducers.

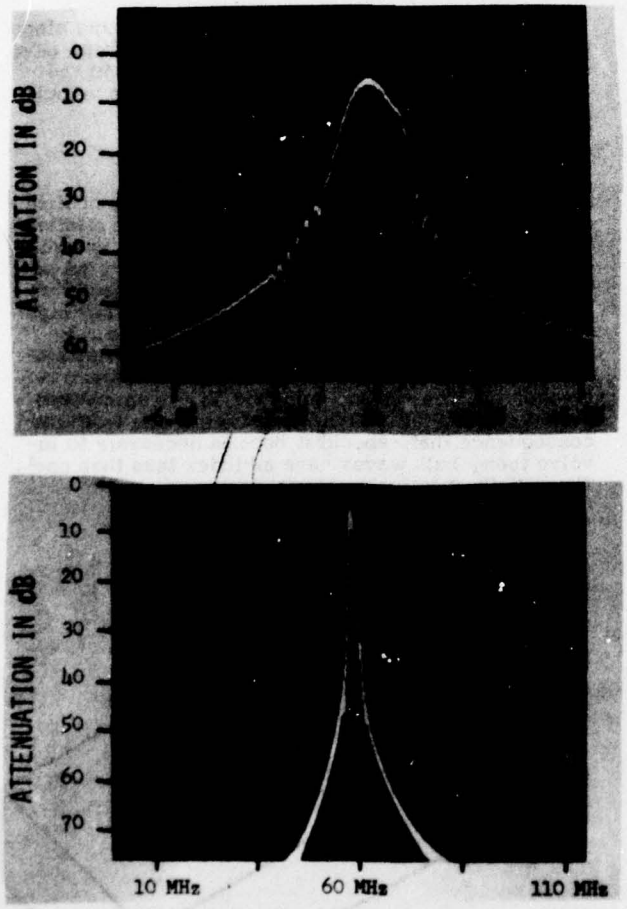

Figure 10.

Insertion Loss of an ST-Quartz Ring Filter Using 1100Å Recessed Gold Stripes.[3]

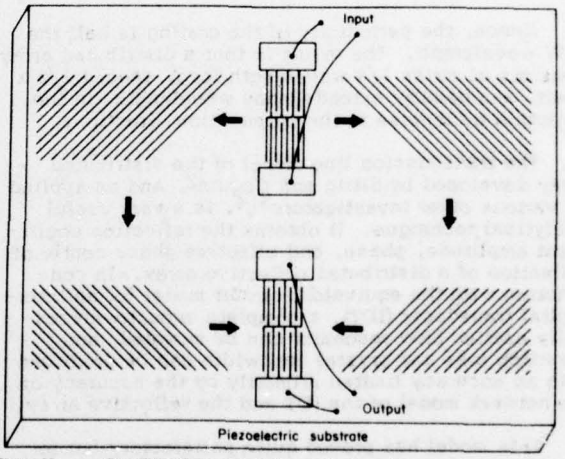

Figure 12. Ring Filter Geometry with Two Series Transducers and Truncated Gratings.

OPTICAL WAVEGUIDE MODEL FOR SAW RESONATORS

Jeff Schoenwald
Teledyne MEC
Palo Alto, California

Introduction

In 1972, E. Ash[1] described a new SAW device that outlined a way of achieving reflection of SAW's with a potential efficiency approaching 100%. All previous approaches -- e.g., large step discontinuities, edge reflections -- suffer from the large efficiency for conversion to bulk acoustic waves. Ash's basic concept consists of forming a Fabry-Perot cavity from two arrays of distributed reflectors. Each array contains a periodic set of lines. Efficient reflection results from an array whose periodicity creates a wavevector $k_g = \pm 2\pi/d$ in the surface that phase-matches a forward SAW of wavevector k_s to a reflected wave. Thus,

$$-k_s = +k_s - \frac{2\pi}{d} \tag{1}$$

or

$$2k_s = \frac{2\pi}{d} = k_g \tag{2}$$

If $K_s = 2\pi/\lambda$, then:

$$\frac{2}{\lambda} = \frac{1}{d}, \text{ or} \tag{3a}$$

$$d = \frac{\lambda}{2}. \tag{3b}$$

Hence, the periodicity of the grating is half the SAW wavelength. The result is that a distributed array consists of strips 1/4 wavelength long, spaced 1/2 λ apart, and usually extends many wavelengths in the direction transverse to the propagation direction.

The transmission line model of the distributed array developed by Sittig and Coquin[2], and as applied by various other investigators[3,4], is a very useful analytical technique. It obtains the reflection coefficient amplitude, phase, and effective phase center of reflection of a distributed reflective array. In conjunction with the equivalent circuit model for an interdigital transducer (IDT), a complete acousto-electrically excited SAW resonator can be modeled, and insertion loss and crystal bandwidth can be predicted with an accuracy limited primarily by the accuracy of the network model of the IDT and the reflective array.

This model has proved quite satisfactory but for one phenomenon: The transmission line model is inherently one-dimensional and cannot represent the transverse standing-wave structure that exists in a slow-wave, closed resonant structure[5]. It is convenient to obtain a simple model that easily facilitates a calculation of the transverse modes that are common to the resonator structure. Although it would be elegant to derive a first-principle calculation based solely on the material constants and boundary conditions on the stress and electrical potential, such a technique is neither straightforward nor transparently accessible for easy application[6].

The waveguiding nature of reflective arrays is treated by analogue with optical slab waveguides[7]. The imposed boundary conditions lead to discrete modes of propagation. All that is required to calculate these modes is the aperture of the guide and the velocity difference between the waveguiding structures and the surrounding substrate. The guiding phenomenon is induced by the reflective array itself, by the introduction of metal strips, dielectric strips, etched grooves, ridges, ion implantation or by diffusion. The periodic perturbation manifests itself as an average shift in the surface-wave velocity. Moreover, the periodicity places constraints on the propagation wavevector that leads to a spectrum of modes in the frequency domain rather than a single frequency propagating down a waveguide with a discrete spectrum in the velocity, or wavevector domain.

The analysis presented here shows excellent correlation with experiment. Furthermore, it confirms the suspicion that the velocity of waves propagating through a reflective array of metal strips a quarter-wavelength long is not the arithmetic mean $[(V_0 + V_\infty)/2]$ but is in fact somewhat closer to the metalized velocity.

The optical model is applied to a propagating plane wave in an infinite periodic array. The stopband associated with Bragg reflections is a function of the Fourier component of the "optical" index (the velocity ratio) at the reflective grating wavevector.

The Surface Waveguide

In optics, the ratio between the velocity of light in vacuum and in another medium defines the relative refractive index of that interface. Similarly, we shall define a refractive index, N_2, for a SAW wave propagating with a Rayleigh velocity V_2, on a surface that has been slowed relative to the free surface Rayleigh velocity (V_1) by alteration of the surface: i.e., by metalization, mass loading deposition, ion implantation, etc. (Figure 1). For convenience and future reference, the free surface velocity, V_1, is normalized to unity, and N_1 is defined as equal to one (with the consequence that, should it become necessary to involve them, bulk waves have an index less than one). Thus, $N_2V_2 = 1$.

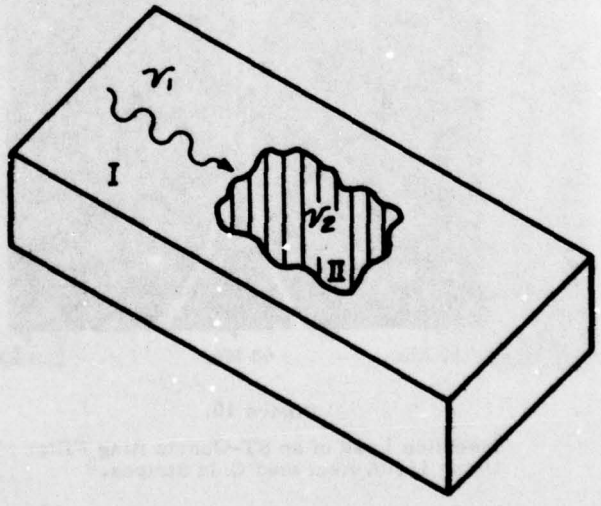

Figure 1.

On the assumption that we are regarding SAW waves as plane waves and thus neglecting the excitation of bulk waves necessary to satisfy the boundary condition at the interface between the two surface regions, Snell's law for the refraction of a SAW across the boundary is identical to the optical analogue (Figure 2):

$$N_2 \sin\theta_2 = \sin\theta_1 . \tag{4}$$

The obvious consequence is that when $N_2 > 1$, a wave incident on the boundary from Region 2 can undergo total internal reflection (TIR) for an angle of incidence greater than θ_{2c}, the critical angle:

$$\theta_{2c} = \sin^{-1}\left(\frac{1}{N2}\right) . \tag{5}$$

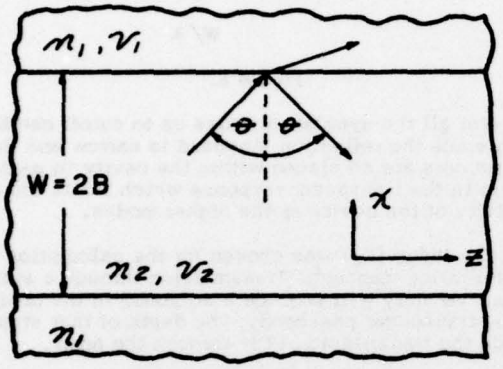

Figure 2.

As an example, a thinly metalized surface of $LiNbO_3$ ($\Delta V/V_\infty \approx -.025$, depending on cut and propagation direction) has an effective index of

$$N_2 = \frac{1}{1 + \Delta V/V} \cong 1.0256. \tag{6}$$

Thus, TIR takes place for angles of incidence greater than 77°, and such a wave can be trapped in the slower region.

Since we wish to consider waves that propagate along a slow corridor of the substrate, we must find the normal modes that satisfy the appropriate boundary conditions. A rigorous statement of the correct boundary conditions is beyond the scope of this paper[8], and it is to the optical model we look for a simplification in finding the normal modes. In that case, the conditions simply require the wave amplitude and its first derivative to be continuous across the boundary between the two regions[7]. Referring to Figure 3, the wave propagates parallel to the interfaces (the Z direction) and is a sinusoidal function in the X-direction within the waveguide (Aperture 2B) and exponentially decaying with X in Region 1.

Because the transducer has symmetric structure, only symmetric modes will be examined although the antisymmetric modes are found just as directly.

In Region 2, let the wave amplitude be

$$\psi_2(X,t) = A_2 \cos k_x\psi \, e^{i(kz-\omega t)}, \tag{7a}$$

and in Region 1,

$$\psi_1(X,t) = A_1 e^{-\varkappa(|x|-b)} e^{i(kz-\omega t)}, \tag{7b}$$

where ω is the circular frequency.

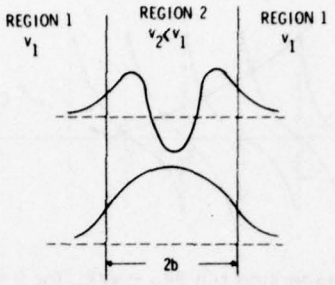

Figure 3.

Requiring $\psi_1(X=B) = \psi_2(X=B)$ and $d\psi_1/dX|_B = d\psi_2/dX|_B$ yields the transcendental relation

$$\tan k_x B = \frac{\varkappa}{k_x} \tag{8}$$

where

$$k_x^2 = \omega^2 N_2^2 - k_z^2 \tag{9a}$$

$$\varkappa^2 = k_z^2 - \omega^2 = \omega^2(N_2^2 - 1) - k_x^2 . \tag{9b}$$

It must be pointed out at this time that the waveguide structure consists of a periodic array of strips and the average velocity in the array, from which we obtain N_2, is some weighted value between that of a free surface and that of a smooth, fully loaded region. Nevertheless, the periodicity gives rise to a frequency band of efficient reflection.

Since it is waves within this frequency band that concern us, we will use the fact--to be shown later--that all waves in the frequency stopband have the same real component of wavevector; i.e., $k_s = k_g/2$. In other words, their wavelengths are identical. The imaginary component represents spatial decay of the wave amplitude with penetration into the reflective array. It is the imaginary component of k_z which contains the frequency dependence of the wavevector. We will normalize this constant wavelength to unity. Thus, $\mathrm{Re}(k_z) = 2\pi/1 = 2\pi$. We will neglect the imaginary part of k_z for now since it will be shown later that it is quite small. Then, we have

$$k_x^2 = \omega^2 N_2^2 - (L\pi)^2 \tag{10a}$$

$$\varkappa^2 = (2\pi^2 - \omega^2). \tag{10b}$$

The dispersion relation (8) may be rewritten

$$\tan B\sqrt{\omega^2 N_2^2 - 1} = \frac{\sqrt{(2\pi)^2 - \omega^2}}{\sqrt{\omega^2 N_2^2 - (2\pi)^2}} . \tag{11}$$

We may now solve for the normal mode frequencies in the stopband which are constrained to have a constant real k_z. Examination of the right side of (11) indicates that ω is constrained to the range

$$\frac{2\pi}{N_2} < \omega < 2\pi \tag{12}$$

so that (11) yields real solutions. The dispersion (8) is plotted in Figure 4.

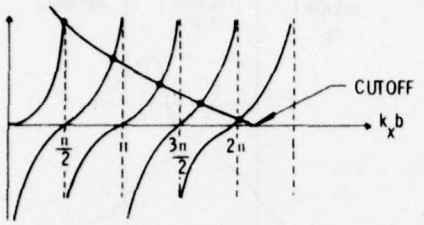

Figure 4. Dispersion tan $Bk_x = \varkappa/k_x$ for B = 25, N_2 = 1.006.

The high frequency cutoff at $\omega = 2\pi$ can be expressed another way. From Equations (8) and (9b), it is evident that cutoff occurs when k = 0, or

$$\omega_c^2(N_2^2 - 1) = k_{x_c}^2 \qquad (\omega_c = 2\pi). \tag{13}$$

If, for example, N_2 = 1.0256 (see Equation 6) $k_{x_c}' = 1.4308$, and the angle of incidence formed by k_{x_c}' and k_z (= 2π) is 77°, → the critical angle. Thus, any wave with a larger k_{x_c} will have a smaller attack angle and will not be trapped in the waveguide.

As will be seen in the next section, the waveguide normal mode dispersion may be utilized to obtain information about the index (or relative velocity) of the trapping region; i.e., the distributed reflective array.

Experimental Verification of the Waveguide Model

Consider the resonance response of an ST-quartz resonator two-port. The reflective array was formed by etching the substrate, leaving the aluminized pattern in bas relief. The etched depth was 750 Å, and the pattern was designed for operation at 140 MHz. A series of modes are evident as small humps or the high frequency side of the main resonance, as shown in Figure 5. The device aperture $2B = 100\lambda_o$ where λ_o is the wavelength in the grating at 140 MHz.

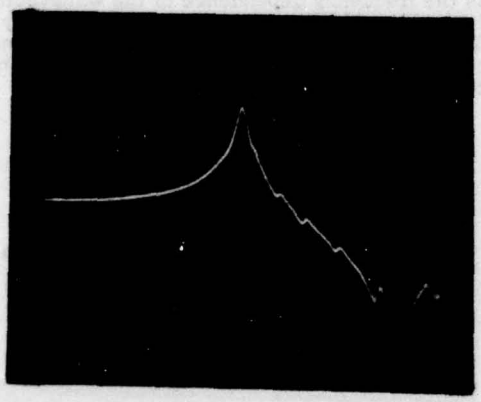

Figure 5. Frequency response of a two-port ST-quartz etched groove resonator at 140 MHz. Vertical: 10 dB/div; horizontal: 100 kHz/div.

As stated earlier, the constant wave number is a result of the periodicity in the reflective array. The main resonance is a consequence of the Fabry-Perot cavity; its length being exactly that required to excite the fundamental mode. The higher frequency, weaker resonances are the result of a finite cavity aperture, 2B. Figure 6 shows the agreement between the waveguide calculation, Equation 11, and the experimentally measured, normalized frequencies of the test device.

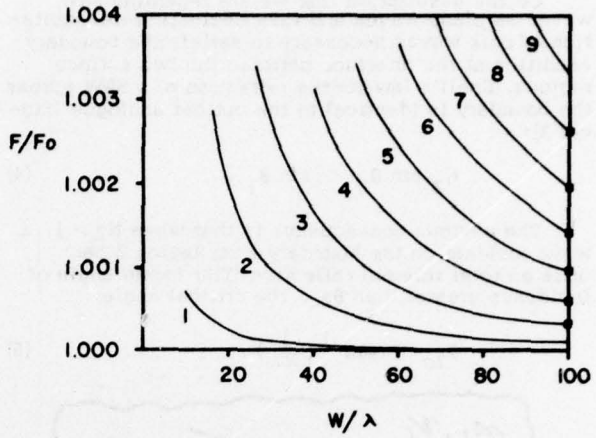

Figure 6.

Not all the symmetric modes up to cutoff can be seen since the reflection stopband is narrow and the transducers are so placed within the cavity to produce a zero in the transducer response which limits the detectivity of the device at the higher modes.

The index (N_2) was chosen for the calculation in the following manner[4]: Transmission through a single reflective array will produce a stopband in the center of the transducer passband. The depth of that stopband yields the transmission $|T|^2$ through the array,

$$\text{Stopband depth (dB)} = 10 \log |T|^2 . \tag{14}$$

The reflection coefficient R is related by $|R|^2 = 1 - |T|^2$ (neglect losses) and N_2 can be computed from

$$|R| = \frac{N_2^{2m} - 1}{N_2^{2m} + 1} \tag{15}$$

where m is the total number of periods in the distributed reflector.

As in the optical model, the velocity ratio N_2 is used, not the impedance ratio. From (15), we may compute N_2, the velocity ratio of adjacent elements of the index. Experience with reflective arrays and long transducers has indicated that the velocity of a wave on a 50% periodicity metalized substrate of quartz or $LiNbO_3$ is not the mean of the free and fully metalized substrate when the period is half the wavelength, but is weighted toward the metalized velocity, being only 20% to 30% of the velocity difference above the metalized velocity. This defines an effective velocity ratio for the distributed reflector as a waveguide which we call N'. It is this number we use for N_2 in (5), (6), (10), (11), (12), (13) and (15). In the case of etched grooves or ridges, an effective index N_2 is obtained by using (14) and (15) plus a measurement of the transmission stopband to calculate the relative strip-to-gap index. This index is interpolated to arrive at a value for the effective waveguide index. The ridge to valley index, n, is computed to be 1.0096 from which is obtained an approximate waveguide velocity index of 1.007. Figure 6 shows the computed (solid lines) and experimental mode frequencies (squares) versus aperture. As stated before, the mode number must be judiciously chosen when the bandwidth of two adjacent modes could overlap and mask their separate existence.

If trapping index is a variable, as in the case when the thickness of a trapping film can be varied, it is desirable to compute the index that will limit the mode

spectrum for a given aperture. Figure 7 shows the dependence of the differential index (N' -1) on aperture to limit the symmetric mode density. One must remain below a certain differential index for a given aperture, or below a certain aperture for a given differential index, to limit the mode spectrum. The curves shown are the limiting loci for one, two and three symmetric modes.

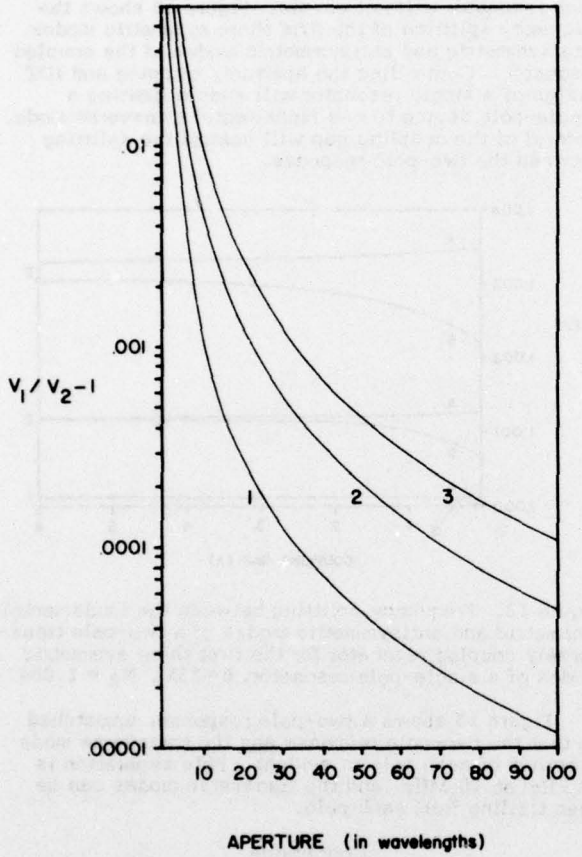

Figure 7.

Another way of representing the mode population versus aperture for a given trapping index is shown in Figure 8. For example: given a reasonable aperture of, say, 40 λ, maintaining only the first symmetric mode requires a trapping film of differential index of .05% or less. The technical problem is reduced to one of calibrating a film's index versus thickness for a given frequency.

Wave Propagation in a Periodic Array

To substantiate the claim that the observed transverse modes propagate with the same wavevector, we refer to a simple analysis familiar in X-ray crystal scattering[9]. A similar observation was made by Emtage[10] and Ingebrigtsen[11]. A plane wave propagating through a periodic structure undergoes reflection when the Bragg condition--Equation 2--is satisfied. At this point, the wavevector becomes complex--the real part is independent of frequency and the imaginary part, which to a first approximation is quadratic in frequency, specifies the attenuation of the forward wave (Figure 9). Several simplifying assumptions have been made: Only the fundamental Fourier component of the periodic perturbation is included in the coupling equations. Higher order terms contribute with

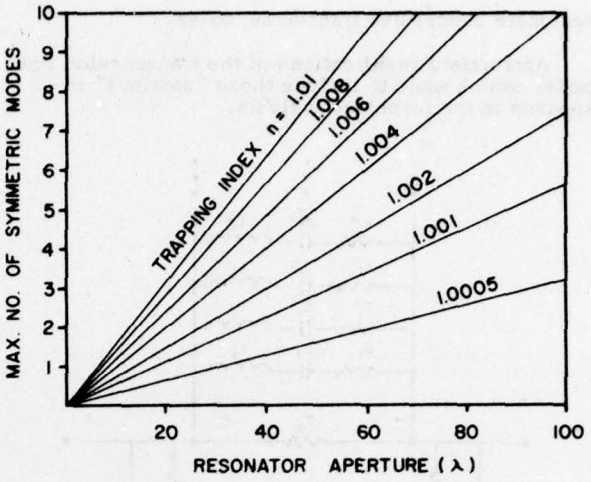

Figure 8.

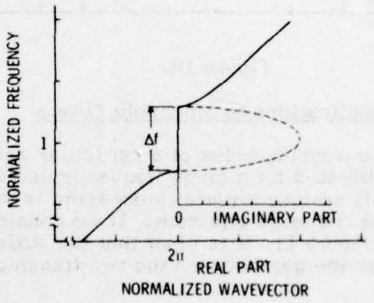

Figure 9.

decreasing amplitude. The array is assumed to be of infinite extent--both transversely and longitudinally. For the moment, we are not concerned with waveguiding, but only with periodicity-induced dispersion. Further, the interaction is assumed weak so that, once reflected, a wave in the reverse direction undergoes no further reflection. If all components of the grating were considered, if the array were finite in extent and multiple reflections included, the wavevector dispersion would be somewhat more complicated, having the nonquadratic shape that is typical of the "inverted sin x/x" behavior observed in transmission through an array[4,12]. The significant result of this exercise is that, within the stopband of the reflector, the wavevector (real part) is not sensitive to frequency.

It can be shown that the relative index, N, can then be either calculated or measured as shown earlier, yielding a completely consistent prediction of Δ f, the stopband width, despite the assumption of an infinite array.

Effect of Waveguiding on the Equivalent Circuit Model

Now that the physical basis of the transverse modes is clear and a simple representation is available, it is easy to make a first guess at necessary modifications to the equivalent circuit as described by various authors. Figure 10 is a suggested but by no means definitive model for a two-port, one-pole SAW resonator. C_o and R_o are the static capacitance and the radiation resistance of the input/output transducers near resonance. All terms subscripted with a 1 are the motional lumped elements that describe the resonance frequency, Q, and loss of a resonance: the superscripted primes

designate successive transverse modes.

Appropriate modifications of the transmission line model can be made to include these "spurious" responses in the resonator analysis.

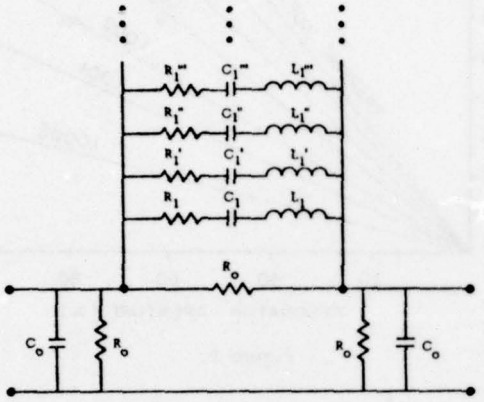

Figure 10.

Applications to Multipole Filters

Once the trapping index of a particular material has been calibrated for a given frequency versus thickness, we will assume material processing is capable of controlling the mode structure. If we consider the structure in Figure 11, it is clear that the modes can couple across the gap between the two trapping regions.

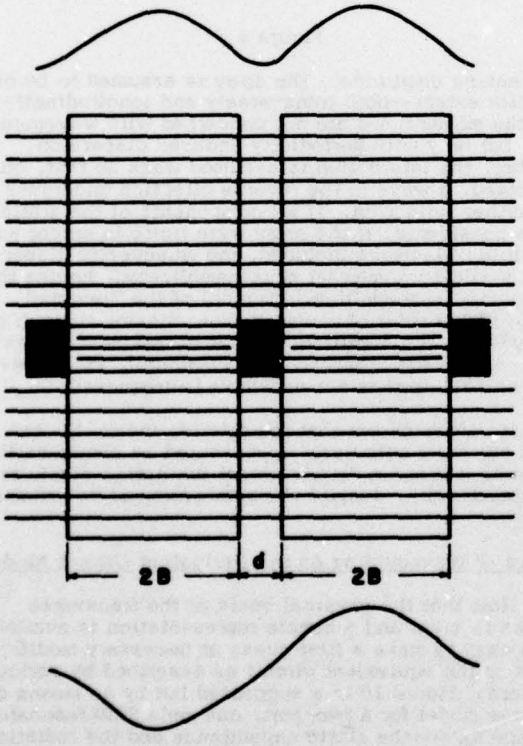

Figure 11. Transversely coupled resonators. Upper curve: First symmetric mode. Lower curve: First antisymmetric mode.

Here we have separated the roles of waveguide and reflector--the reflector now constitutes a region of reflectivity alone and the trapping index is defined between the region under the trapping film and the reflector region not under the film. The lowest mode in each resonator can couple in a symmetric and antisymmetric way to give two coupled modes. Because of different phase velocities, modes of differing order in each resonator will not couple. Figure 12 shows the frequency splitting of the first three symmetric modes into symmetric and antisymmetric modes of the coupled resonator. Controlling the aperture, trapping and IDT design of a single resonator will enable limiting a single-pole device to one fundamental transverse mode. Control of the coupling gap will control the splitting between the two-pole response.

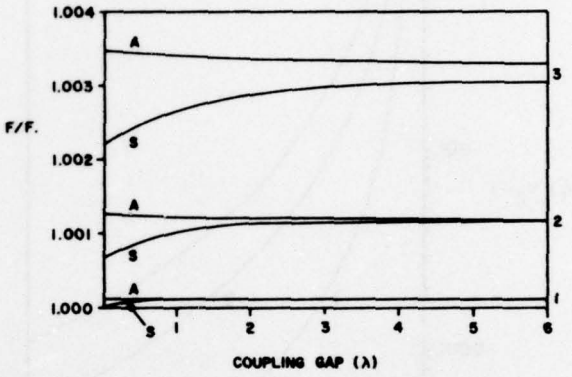

Figure 12. Frequency splitting between the fundamental symmetric and antisymmetric modes of a two-pole transversely coupled resonator for the first three symmetric modes of a single-pole resonator. $B=25\lambda_o$, $N_2 = 1.004$.

Figure 13 shows a two-pole response, unmatched so that the two-pole response and the transverse mode spectrum of each pole is evident. Pole separation is 73 kHz at 70 MHz and the transverse modes can be seen trailing from each pole.

Conclusion

We have at hand a simple model that is tractable for resonator design. Limitation of spurious response for frequencies above 70 MHz has a significant advantage over bulk crystal filters. Multipole coupling is simply described and should be easily controlled.

The author wishes to thank Texas Instruments, where a portion of this research was done.

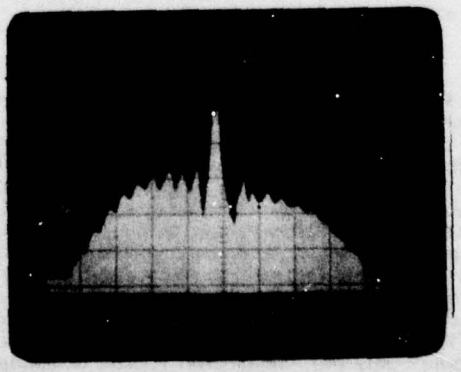

Figure 13a. Log ref = +7 dB. IL = -9 dB. Vertical: 10 dB/ div. Horizontal: 0.5 MHz/div.

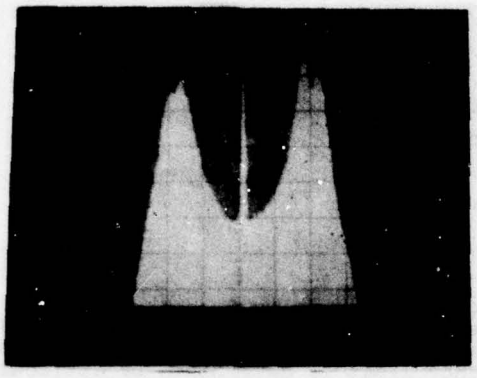

Figure 13b. 2 dB/div vertical, 20 kHz/div horizontal. Central spike is marker at 70.0000 MHz. Note mode structure in upper and lower peaks.

References

1. E.A. Ash, IEEE Symposium on Microwave Theory and Techniques held in Newport Beach, CA, May 11-14, 1970.

2. E.K. Sittig and G.A. Coquin, "Filters and Dispersive Delay Lines Using Repetitively Mismatched Ultrasonic Transmission Lines," IEEE Trans. Sonics and Ultrasonics, SU-15 (1968), pp. 111-119.

3. See, for example, Proc. Ultrasonics Symp., 1974 and 1975, for many papers on surface-wave resonators.

4. E.J. Staples, "UHF Surface Acoustic Wave Resonators", 28th Annual Frequency Control Symposium Proceedings, pp. 280-285; May 1974.

5. I.M. Mason, J. Chambers, and P.E. Lagasse, "Laser-probe analysis of field distributions within acoustic-surface-wave planar resonators," Electron Lett., vol. 11, pp. 288-290, July 10, 1975.

6. B.K. Sinha and H.F. Tiersten, "An Analysis of the Reflection of Surface Waves by an Array of Reflecting strips using Derived Approximate Equations," Proc. Ultrasonics Symposium (IEEE Pub. 75 CHO 994-4SU), pp. 447-451, Sept. 1975.

7. P.K. Tien, R. Ulrich, and R.J. Martin, "Modes of propagating light waves in thin deposited semiconductor films," Appl. Phys. Lett., vol. 14, 1969, p. 291.

8. B.A. Auld, "Acoustic Fields and Waves in Solids: Vols. I and II," Wiley, New York, 1973.

9. C. Kittel, "Quantum Theory of Solids", J. Wiley, N.Y., 1963.

10. P.R. Emtage, "Self-Consistent Theory of Interdigital Transducers," Proc. IEEE Ultrasonics Symp. (IEEE Pub. 72 CHO 708-SU) pp. 397-402, Oct. 1972.

11. K.A. Ingebrigtsen, "Analysis of Interdigital Transducers," Proc. IEEE Ultrasonics Symp. (IEEE Pub. 72 CHO 708-SU) pp. 403-407.

12. R.C. M. Li, A. Alusow, and R.C. Williamson, "Surface-wave resonators using grooved reflectors," in Proc. 29th Annual Frequency Control Symp. (U.S. Army Electronics Command, Ft. Monmouth, N.J.), pp. 167-176, May 1975.

DESIGN OF QUARTZ AND LITHIUM NIOBATE SAW RESONATORS USING ALUMINUM METALLIZATION

W.H.Haydl, P.Hiesinger, R.S.Smith, B.Dischler and K.Heber
Institut für Angewandte Festkörperphysik
der Fraunhofer Gesellschaft
D-7800 Freiburg, Eckerstr. 4, W.Germany

Summary

This paper deals primarily with the placement of transducers within the cavity of surface acoustic wave (SAW) resonators, and their effect on the overall resonator frequency characteristic.

SAW resonators are very frequency sensitive devices. At the resonance frequency, the phase per roundtrip of a wave must be a multiple of 2π radians. The inclusion of coupling transducers in the space between reflectors will in most cases introduce additional reflection. Transducers, if they reflect, must therefore be considered to be part of the reflector. Exceptions are the so called double- or split-finger transducers which exhibit low reflection when properly terminated. Depending on the transducer to reflector spacing, the resultant combined reflection may cause severe distortions in the resonator frequency characteristic.

If the transducers are placed at a maximum of the standing wave pattern, the reflection from the transducers will be 90 degrees out of phase with the component reflected by the reflectors. This will always lead to a distortion of the frequency response. The use of non-reflecting double-electrode transducers will eliminate this unsymmetry and the associated frequency shift. The maximum operating frequency at which a distortion-free response is possible will however then be limited to less than 400 MHz, using photolithography ($\sim 1\mu$m line width).

Transducers may however also be placed in such a manner, that they are "part of the reflector", in which case the two reflected components are either in phase or out of phase. The transducers are then $\lambda/8$ off a standing wave maximum with the coupling not being optimum but still sufficient. Such a transducer-reflector arrangement will lead to an undistorted symmetrical frequency response. Since it is not necessary to use double-electrode transducers, the maximum frequency is about 800 MHz, using photolithography. A symmetrical and undistorted frequency response is thus possible at higher frequencies at the expense of a somewhat weaker coupling to the cavity.

Introduction

A new type of surface acoustic wave device, the SAW resonator, has emerged within the past few years.[1-8] This new SAW concept has lead to considerable activity in the development of narrowband filters and oscillators in the frequency range from 10 to several thousand MHz. Although the typical range of application will be that which cannot be covered by volume wave resonators: the range from about 50 to perhaps 2000 MHz. The upper frequency limit is determined by difficulties which arise in the technology, because electrode dimensions are less than 1 μm at frequencies above about 1000 MHz. The lower limit is set by the size of the resonator structure and the cost of the substrate.

In contrast to conventional SAW devices which utilize traveling waves, where great efforts are taken to eliminate surface wave reflections and to design electrodes such that reflection stop bands fall outside the device pass band, for SAW resonators reflections are wanted and operation is at the stop band frequency. The obtainable Q's of SAW resonators lie an order of magnitude below those of conventional volume wave resonators. The factor which limits the Q of SAW resonators appears to be the partial conversion and scattering of surface waves into bulk waves.[9]

Volume waves may efficiently be reflected from polished surfaces which represent broadband reflectors. Volume wave resonators consisting of quartz plates $\lambda/2$ thick, where λ is the acoustic wavelength, operating at the fundamental frequency of 50 MHz are however as thin as 50 μm, and hence quite fragile and difficult to mount.

In contrast to bulk waves, surface waves cannot efficiently be reflected from a single surface,[10] such that periodically distributed reflectors must be used.

Figure 1 illustrates the operating frequency range and Q of both volume and surface wave reflectors for comparison.

Planar SAW resonators with distributed reflectors have much similarity with optical resonators of the Fabry-Perot type. Actively investigated within the last two years by several research groups both in the US and in Europe, they are extremely promising devices for a great number of communications applications. We shall attempt to describe simple resonators on YZ lithium niobate and on ST quartz with emphasis on the effect of some of the design parameters on the resonator and filter performance. We have concentrated on devices which are fabricated in a simple one-step process using a single Al evaporation with subsequent etching.

Although the principle of the SAW resonator is relatively simple, the proper design is difficult, and we are still far from fully understanding these devices. Many second order effects need still to be investigated. SAW propagation properties as a function of metallization parameters need to be determined.

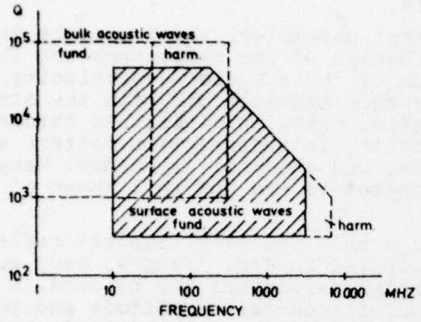

Fig. 1 Application range of bulk and SAW resonators. The upper limit for SAW resonators is about 1000 MHz using photolithography and about 3000 MHz using electron-beam lithography. Harmonic operation of SAW resonators is not feasable at this time.

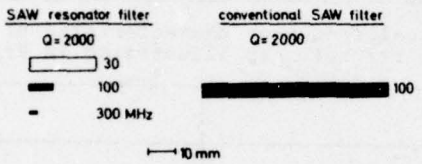

Fig. 2 Comparison of the size of conventional SAW- and SAW resonator-filters. The size of a conventional SAW filter is proportional to the desired Q, whereas that of a SAW resonator is independent of Q. The size of both classes of devices varies inversely with frequency.

Even if all these properties are known with great accuracy, the surface wave propagation velocity throughout a crystal varies considerably such that it is not possible to design a SAW resonator to operate at a given frequency. Therefore, one of the most important problems is to find means for adjusting the final operating frequency of the devices.[11,12] Clearly, such fine tuning methods must be simple , inexpensive and not time consuming. Similar problems however occur with bulk wave resonators and they have been overcome. We believe that the same applies to SAW resonators.

To summarize, the properties of SAW resonators are shown in Table 1.

The basic resonator

The basic structure of a SAW resonator is illustrated in Fig.3, where separate interdigital transducers are used for input and output. Additional structures may be placed in the space between the reflectors to provide increased rf shielding between input and output, coupling to other resonators, or frequency tuning. One port resonators usually employ a transducer placed in the center of the resonator. The device illustrated in Fig.3 may also be operated in a one port mode by properly terminating the second transducer, preferably reactively in order not to draw energy from the cavity and thus reducing the Q of the device.[13]

The transducers are very broadband components with a 3 dB bandwidth of 1-50 %, where-

TABLE 1

Properties of SAW resonators

ADVANTAGES:

1. High fundamental operating frequency and large range (30-1000/3000 MHz) as illustrated in Fig.1
2. Because of planar technology compatible with standard IC technology
3. Rugged
4. Potentially inexpensive
5. Small in size, with size decreasing with frequency as is illustrated by Fig.2
6. Low impedance levels are possible (100-1000 ohms)
7. The planar character permits variation of phase within resonator structure to achieve tuning and pass band shaping[13,11]
8. Suppression of spurious responses possible over a large frequency range[8]

DISADVANTAGES:

1. Excitation of bulk waves, and conversion of surface waves into bulk waves limits the Q to about 2000-20000
2. Until now only a weak third harmonic response has been observed (with double-electrode transducers). Thus, harmonic operation to reach GHz frequencies seems not possible
3. Expensive electron beam lithography necessary at higher frequencies (> 1000 MHz)

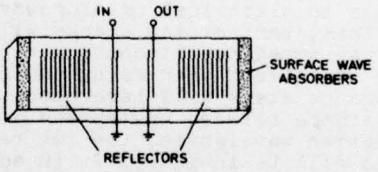

Fig. 3 Schematic representation of a 2-port SAW resonator. Tunable one-port operation is also possible by properly terminating the second port.[13]

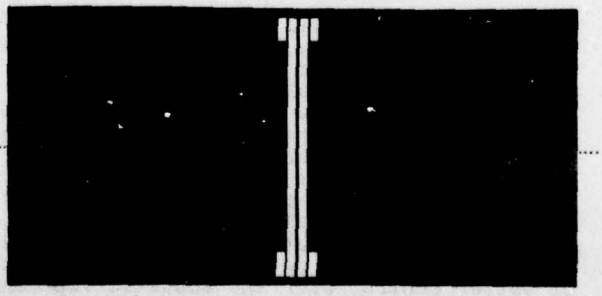

Fig. 4 Actual layout of 2-port SAW resonator with double electrode transducers having 2.5 finger pairs and two rf shields. The transducer to reflector spacing is for optimal coupling. Only a small portion of the 500 reflecting strips of this experimental device are shown.

as the reflector bandwidth lies an order of magnitude below this, typically 0.1-1 %.

The reflectors are of a distributed nature. They consist of periodically spaced reflecting elements such as strips or grooves. Several possible techniques for realizing reflectors are illustrated in Fig.5.

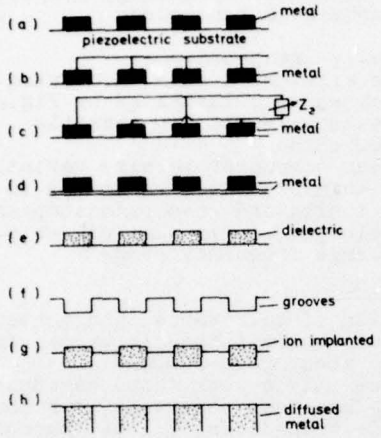

Fig.5 Eight different ways to construct reflecting arrays for surface acoustic waves. The reflective properties of metal strips on high-coupling materials, such as lithium niobate, are highly dependent on external impedance and interconnection patterns.[14]

Analogous to electrical or microwave transmission lines, part of the energy will be reflected at impedance discontinuities. The reflected waves from increasing and decreasing impedance steps will have opposite phase. If the distance between upstep and downstep is one quarter wavelength, the two reflected components will be in phase. If in addition, the distance between upsteps or downsteps is half a wavelength, the contributions from the individual reflecting elements will also be in phase.

Several possibilities exist to achieve a change in acoustic impedance

$$Z_{ac} = (\rho v)^{1/2} \qquad (1)$$

where ρ is the material density and v the surface wave velocity. Unfortunately a change of only ρ or only v is , except for some special cases, generally not possible. The change in Z_{ac} for the various reflector technologies is therefore difficult to predict. In Fig. 5(a) through (d) we illustrate several reflector configurations where reflection and propagation properties are effected by the electrical connection of the individual reflector strips. In (d) and (e) mass loading is used. It has the advantage of better control over the acoustic impedance discontinuity step ΔZ since it is quite easy to control the thickness of deposited films. Etched (ion, plasma, sputter and chemical)[15] grooves may be employed as reflectors as illustrated in (f). Ion implanted[16] and diffused metal[17] reflectors have also been used succsessfully in the past.
Which type of reflectors to be used, depends on the required resonator properties, and to some extend on the technologies which are available.

Important parameters which must be known for the design of the reflectors are the variation of the surface wave velocity and the impedance mismatch ΔZ with the strip to space ratio, metal or dielectric thickness, groove depth, interconnection pattern and impedance, and external impedance. Many of these parameters are not well known at this time.

Although only the very simplest reflector is illustrated in Fig. 3 and 4, very much more complex reflectors may be used. A reflector with certain amplitude and phase characteristics may be synthesized, similarly to transducers for surface wave bandpass filters. As we shall show later, the transducer is actually part of the reflector and must be treated as such by adding amplitude and phase.

Frequency characteristic of resonator

A typical frequency characteristic of a two-port resonator is illustrated in Fig.6.

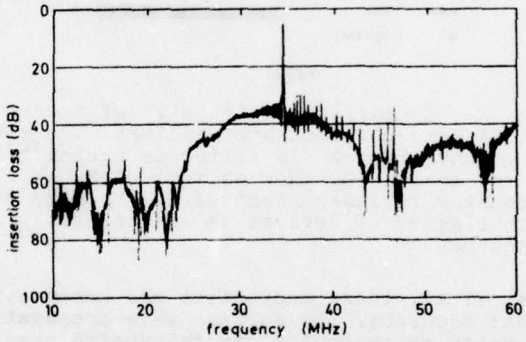

Fig. 6 Typical frequency characteristic of a two-port SAW resonator filter. Load impedance=50 ohms, N_r=500, N_t=2.5 double electrodes, W=100 $^r d_r$, YZ ^{t}lithium niobate, aluminum metallization. Pattern as shown in Fig. 4. The sharp peaks throughout spectrum are plate modes.

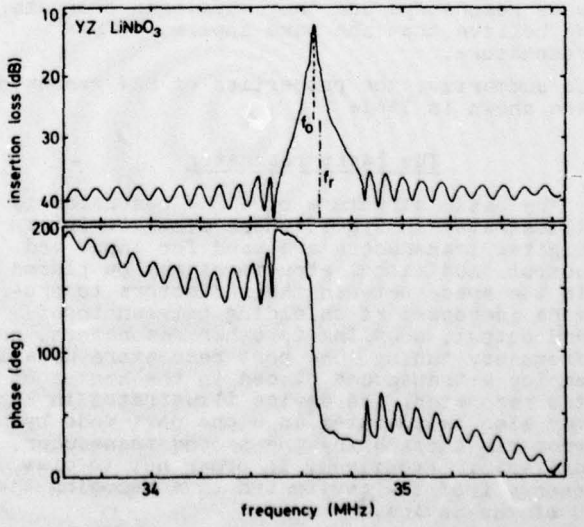

Fig. 7 Detailed frequency and phase response of device illustrated in Fig.6 and 4.

The broad sin X/X type response at the -40dB level is due to direct transmission between transducers. How this response can be minimized or totally eliminated will be discussed in more detail below, in the section on sin X/X suppression. The resonance peak is shown in detail in Fig 7. This response was obtained with a device as illustrated in Fig. 4. It may be noticed that the resonance frequency f_o does not quite coincide with the center frequency of the reflectors f_r. This is one of the major problems encountered in the design of single-mode resonators. The reasons for it are an uncorrect spacing between reflectors, or reflections inside the cavity, as will be discussed in detail in following sections.

Design parameters

The relevant dimensions for the design of a typical 2-port resonator are shown in Fig. 8. The reflector may be any one of the various types illustrated in Fig. 5. N_r is the number of reflector elements (strips), and N_t is the number of transducer finger pairs. For the electrodes, which may be single or double electrodes, the center line of the electrode is relevant. The distance l_{rt} is generally kept a minimum because of uncertainties in the various surface wave velocities under reflectors, transducers, metal pads, etc, and in order to obtain less sensitive conditions for the correct placement of the transducers. The cavity length l_c depends on the number of resonance peaks which are desired within the passband of the reflectors. This is generally only one, hence if the penetration depth l_p is known, the reflector-reflector spacing l_{rr} can be determined. The penetration depth l_p is, as will be shown below, proportional to the slope of the reflector phase, and increases away from the reflector center frequency f_r.

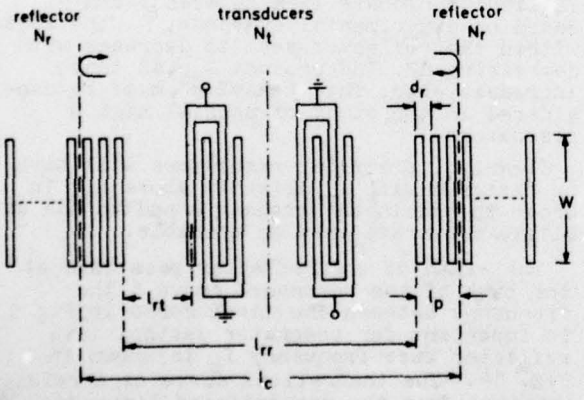

Fig. 8 Two-port resonator parameters

Reflective properties of simple reflector

Perhaps the most important structure of the SAW resonator are the main reflectors, which reflect close to 100% of the incident energy. In its most simple form, a reflector consists of an array of perturbations for surface waves spaced one half wavelength (center to center) apart. Exactly which wavelength to be used will be discussed in detail below. Examples of several techniques, as illustrated in Fig. 5, for realizing surface wave reflectors have been discussed and demonstrated by several authors. For special resonator applications only certain technologies may be applicable. But if surface wave resonators are to be inexpensive , temperature stable devices, they must be realizable with materials such as quartz, and must require only simple technology, such as a single metallization and photoresist step. Because of this reason we will concentrate on discussing the design of devices requireing only one metallization step: aluminum on ST quartz and lithium niobate. Shorted aluminum strips and grooves are believed to be the methods which lend themselves for inexpensive mass production of resonators since they require few processing steps.

Metal strips cause an impedance mismatch ΔZ due to:

1. mass loading due to the metal
2. electric field shorting under the strip
3. electric field shorting between strips.

The reflective properties are effected by the strip interconnection scheme and any external impedance connected between strips or groups of strips.

There exists no simple relationship between the acoustic impedance step ΔZ and the average velocity v_r under the grating, and little data is available to date.

Several theoretical discussions of periodic reflectors for surface waves exist so far.[18,19] The most useful model has been a transmission line equivalent which is capable of calculating phase and amplitude for a periodic grating reflector, specifying the number of reflector elements N_r and the impedance mismatch ΔZ. Typical amplitude and phase responses are illustrated in Fig.9 and 10. The calculated reflector pass band has a

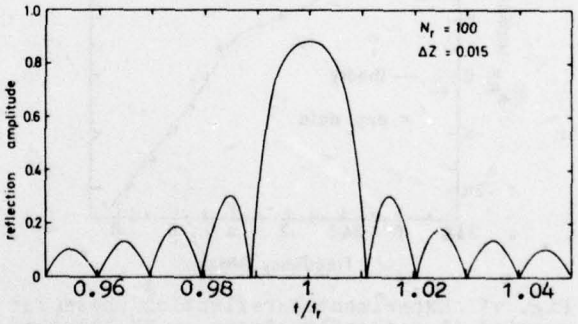

Fig. 9 Calculated amplitude of the reflection using the transmission line model.[18]

sin X/X form, and becomes increasingly flat at its maximum with increasing ΔZ or N_r. As we shall demonstrate below, the shape of the reflector characteristic can be observed experimentally with a multimode cavity where many resonances occur within the reflector pass band (see Fig.33).

The reflector phase characteristic as determined by experiment is for comparison illustrated in Fig. 11.

Losses are always present in a reflector, and must therefore also be considered in the

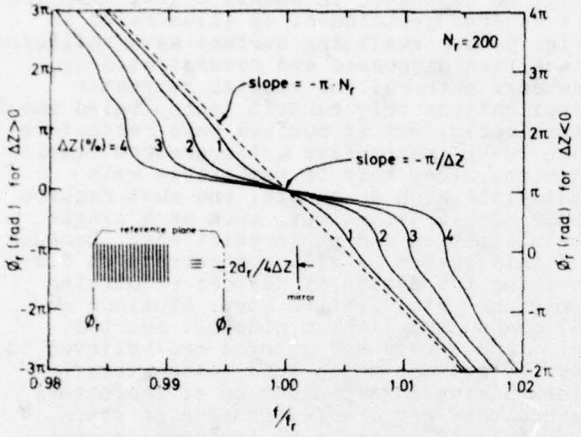

Fig. 10 Calculated phase of the reflection using the transmission line model.[14]

design of SAW resonators. Unfortunately they cannot be determined theoretically, and it is necessary to determine their effect on the resonator performance by experiment. Reflector losses limit the reflection and thus the total required number of reflector elements. This means that the 3 dB bandwidth or Q and the insertion loss of a resonator do not vary above a critical number N_{rc} of reflector elements. This behavior has been investigated by us with simple two-port resonators on YZ lithium niobate and on ST quartz. Our results are illustrated in Fig. 12 and 13.

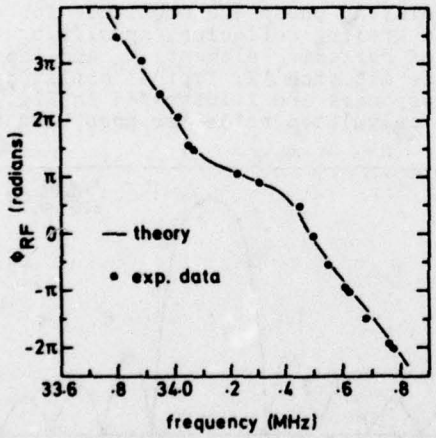

Fig. 11 Experimental reflection phase for shorted Al reflector strips on YZ lithium niobate.[14]

The point at which the Q of the devices drops sharply is well defined, especially when ΔZ is large. The value of Q is a very sensitive function of the reflection coefficient, as is well known from the fields of optics and microwaves. An attempt has been made to fit the experimental data using the transmission line model. This is shown by the solid lines in Fig. 12 and 13. Because we have only used unapodized structures in our experiments, transverse modes appear close to the resonance frequency and effect the 3 dB bandwidth which is used in our definition of the Q here. The effect can be seen in Fig. 13.

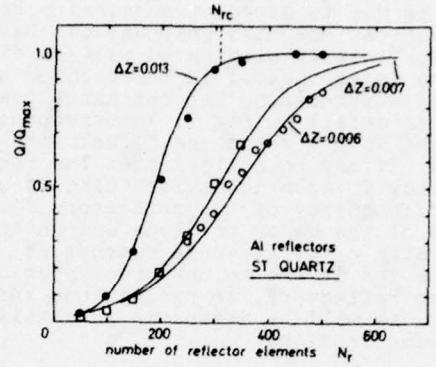

Fig. 12 Measured (dots) and calculated (lines) variation of Q with lossy reflector.

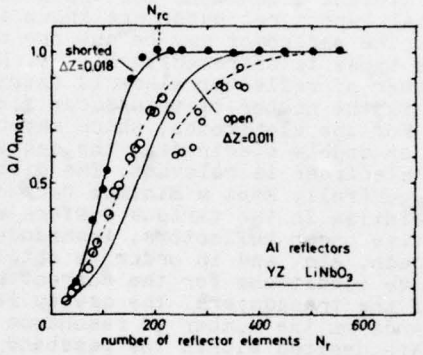

Fig. 13 Measured(dots) and calculated (lines) variation of Q with lossy reflector. The jump at N_r=200 is due to the presence of a transverse mode near the resonance frequency.

Experimentally we find a critical $N_{rc} \cdot \Delta Z$ product which for both ST quartz and YZ lithium niobate lies between 3 and 4. Based on experimental evidence, the losses within the reflector seem to decrease with decreasing ΔZ. The product $N_{rc} \cdot \Delta Z$ thus increases also. This behavior must be considered in the study of special high Q resonators.

Clearly , practical resonators will have to be designed with N_r slightly above N_{rc} in order to obtain the highest Q and to use as little substrate area as possible.

The width of the reflector pass band at the base of the resonance curve (the frequency between the first zeros in Fig.9) is important for resonator design. This reflector base frequency f_b is shown in Fig. 14. The theoretical curve is a relation obtained from the transmission line model.[18]

Although only the simplest reflectors have so far been investigated, more complicated structures may be used to realize specific amplitude and phase characteristics. The ideal reflector for many applications should not have the sin X/X type amplitude characteristic of Fig.9, but rather a flat pass band and no sidelobes. Such a characteristic may be obtained by weighting the reflection along the reflector structure. Several

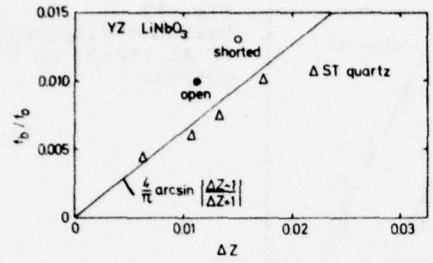

Fig. 14 Experimental and theoretical values for the reflector base frequency f_b .

weighting schemes are applicable, similar to those used for conventional SAW filters. One major difference however exists. The weighting for reflectors should be such that no energy is lost from the cavity. By weighting the length of the reflectors, varying away from the center in a cos X fashion, efficient reflection occurs only at the center of the structure. Experimental results, showing a 2-port resonator response free of ripples and transverse modes,[20] are illustrated in Fig. 15. Both the insertion loss (5-7 dB for unweighted reflectors) and the 3 dB bandwidth have increased because of the losses introduced with length weighting of the reflector strips. It is therefor desireable to use constant aperture weighting such as strip withdrawal, strip position or strip width weighting. Some of these weighting methods are currently being investigated by us.

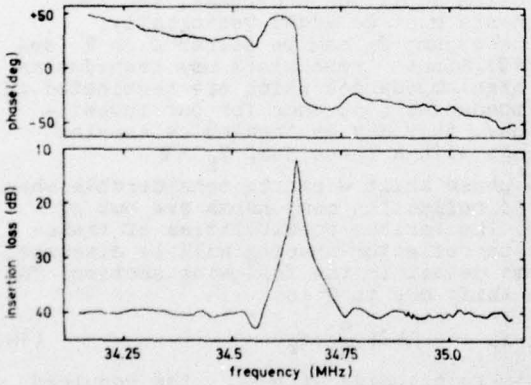

Fig. 15 Amplitude and phase characteristics of a resonator with length weighted reflector strips (cos X type weighting function) and unweighted transducers.

Sin X/X suppression

Because of direct surface wave transmission between input and output transducers of a two-port resonator, the sin X/X type response is present. Because of the limited Q, this value cannot be much more than~30 dB below the resonance peak. The sin X/X response can be reduced or eliminated by

-- using a narrowband reflective grating to change the direction of wave propagation to an L or Z path
-- electrically cascading two-port resonators via transducers or multistrip couplers
-- by using unidirectional transducers which radiate toward the reflectors

The reflector penetration depth

This distance is defined by the slope of the reflector phase characteristic, as shown in Fig. 10, and is given by the expression

$$l_p = \frac{v_r}{4\pi} \left|\frac{d\phi_r}{df}\right| \qquad (2)$$

where v_r is the average reflector velocity. The penetration depth l_p is the distance from the edge of the reflector at which an acoustic single plane mirror is located, as shown in Fig.16. At or near the reflector center frequency f_r , the penetration depth takes on the simple form of $2d_r/4\Delta Z$, with reference to Fig. 10. If the resonance frequency frequency f_o differs from f_r , the mirror is located at a greater distance from the edge of the reflector. This implies an increase in the cavity length, and as we shall see later a decrease in the cavity mode spacing.

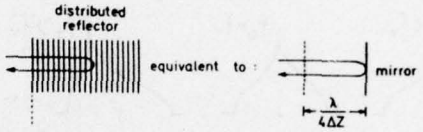

Fig. 16 Around the center frequency of the reflectors , the model of an acoustic mirror located at the distance shown may be used.

Velocity correction

In this section we shall discuss the spacing between reflectors for simple resonators. Reflections from transducers are neglected.

The requirement for resonance is that the phaseshift across the cavity (one transit) must be

$$\phi_T = n_T \pi \qquad \text{radians,} \qquad (3)$$

where n_T is an integer. Resonance occurs at frequency f_o.

The space inside the cavity may consist of a number of sections with slightly different surface wave propagation velocities. The phase shift of a wave per transit may be expressed by

$$\phi_T = 2\pi \sum_i \frac{l_i}{\lambda_i} + \phi_r \qquad (4)$$

where l_i are the physical lengths of the various sections between reflectors, and ϕ_r is as shown in Fig. 10. Defining

$$v_i = v_f + \Delta v_i \qquad (5)$$

$$v_i = v_i/v_f = 1 + \Delta v_i \qquad (6)$$

$$\Delta v_i = \Delta v_i/v_f \qquad (7)$$

and $$\lambda_i = 2\, d_r + \lambda_f(\Delta v_i - \Delta v_r) \quad , \qquad (8)$$

where v_i and λ_i are the velocity and wavelength of section i respectively, v_f and v_r are the free surface and reflector velocities. In the above expressions we have used the reflector periodicity d_r and the reflector surface wave velocity v_r as reference.

If the sum term of equ.4 is not a multiple of π , the operating frequency f_o will not

coincide with the reflector center frequency f_r. The value of ϕ_r from equ. 4 will then determine the operating frequency. Around f_r, the frequency shift is given by

$$f_o - f_r = \Delta f = -|\Delta Z| \frac{\phi_r}{\pi} f_r \quad \ldots\ldots \Delta Z > 0 \qquad (9)$$

$$= -|\Delta Z| \frac{\phi_r - \pi}{\pi} f_r \quad \ldots\ldots \Delta Z < 0 \qquad (10)$$

In order to obtain a symmetrical frequency response curve, ϕ_r must be zero or π, with reference to Fig. 10. Thus a cavity length or reflector-reflector spacing correction of

$$\Delta l_{rr} = 2 d_r \Delta \phi_T \qquad (11)$$

$$= d_r (n_T - \phi_T / \pi) \qquad (12)$$

where $\Delta \phi_T = \phi_T - n_T$. (13)

The effect of $\Delta \phi_T$ on the resonator frequency characteristic is illustrated in Fig. 17.

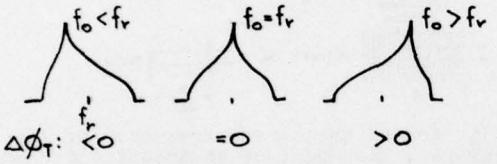

Fig. 17 Resonator frequency response if the cavity is (a) too short, (b) correct, (c) too long.

In order to be able to make the proper cavity length correction Δl_{rr}, one must know all velocities within the resonator cavity, as well as the velocity variations with external impedance for transducers, with metallization thickness and metallization ratio. Unfortunately, very little data is available at the present time. We have used with some success values of

=-0.024 for fully metallized surfaces,
=-0.018 for shorted aluminum strips,[21]
=-0.007 for open aluminum strips,[21]
=-0.018 for transducers, single electrodes, terminated in a low impedance,

for YZ lithium niobate.

The effect of mass loading, i.e. a change in metallization thickness for a particular resonator configuration is illustrated in Fig. 18. We wish to point out the fact that the rate of frequency variation depends on the particular design.

For ST quartz, the electric field shorting effect is small. The effect of mass loading on velocity (frequency) is shown for an Al metal grating.

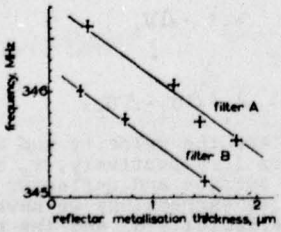

Fig. 18 Frequency dispersion of two YZ lithium niobate resonator filters with Al metallization thickness. Slope=-70KHz/µm.[4]

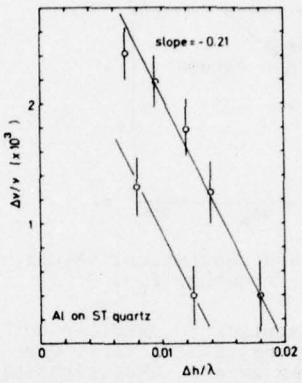

Fig. 19 Measured dispersion of Al strips on ST quartz.

Reflection correction

If single-electrode transducers are used, considerable reflection may already occur at the transducers. This can give rise to a phase shift which causes a distortion in the frequency response and a frequency shift as was illustrated in Fig.17 for the case of velocity correction. In Fig. 20 we illustrate a very simplified model . Two components of reflection one from the transducer, the other from the reflector, are considered. Multiple reflections are neglected. The difference in phase of the two components is $2\phi_{rt} + \phi_r - \phi_t$.

In order to obtain the total reflection amplitude and phase, the two components must be added vectorially. The phase jump ϕ_r may be either 0 or π (see Fig. 10). Since resonators use transducers with high impedances which are terminated in low impedances (50 ohms for our investigations), they may be treated as shorted gratings with a phase jump $\phi_t = \pi$.

The phase shift Θ can be considerable when the two reflection components are out of phase. The various possibilities of transducer to reflector spacing will be discussed in some detail in the following section. The phase shift due to Θ is

$$f_o - f_r = -|\Delta Z| \frac{\Theta}{\pi} f_r \qquad (14)$$

If f_o is to coincide with f_r, the required cavity length correction is

$$\Delta l_{rr} = d_r (n_T - \Theta/\pi) \qquad (15)$$

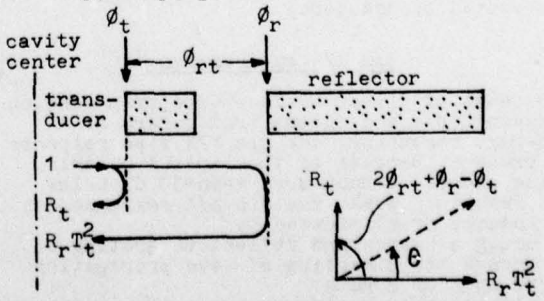

Fig. 20 Addition of reflection component from transducer. The addition of the two components results in a phase shift Θ.

Figure 21 shows the reflection and transmission, as calculated using the transmission line model, for a single electrode transducer. Note for example that the amplitude reflection R for a 30 finger pair transducer is about 0.5 for a ΔZ of 0.01.

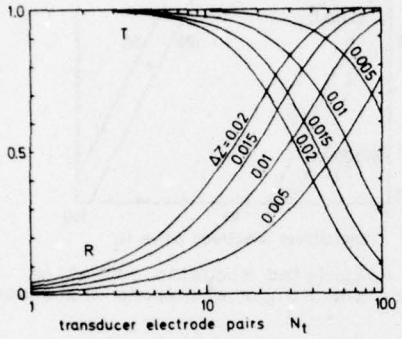

Fig. 21 Calculated amplitude reflection and transmission coefficients for single electrode transducers.

Reflector-transducer spacing

The placement of the transducers from the reflectors is a very critical parameter. For some cases the standing wave pattern inside the cavity has been determined experimentally either by placing a number of transducers spaced by varying amounts from the reflector on the substrate[14], measuring the phase of the reflected signal, or by optical probing.[6] Depending on the sign of the impedance discontinuity ΔZ, the standing wave pattern of the surface waves will be as is illustrated in Fig. 22.

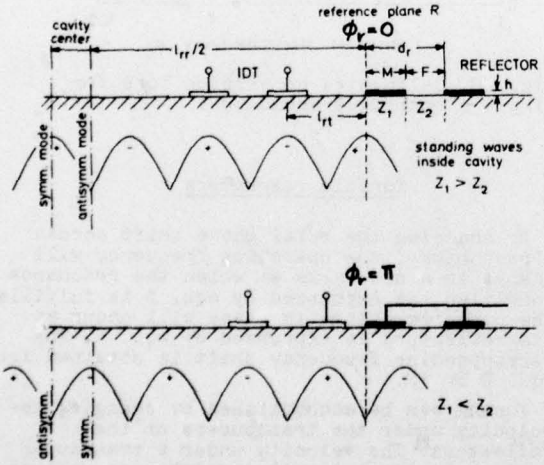

Fig. 22 Standing wave pattern and transducer-reflector spacing l_{rt} for optimum coupling for
(a) positive ΔZ
(b) negative ΔZ.
For optimum coupling, the transducer electrodes are positioned at the peaks of the standing waves.

Optimum coupling is achieved by placing the transducers on the peaks of the standing waves. It may be noted from Fig 22, that this will however lead to a disturbance of the periodicity between reflector and transducer. This may cause undesired effects such as additional phase shifts, as was discussed in the previous section and illustrated in Fig. 20. Indeed, we have observed large distortions in the resonator frequency characteristics of two-port devices on ST quartz and YZ lithium niobate, when the reflector-transducer spacing was optimum for coupling to the standing wave pattern. These devices had a large reflection component from transducers or additional strips inside the cavity. Our experimental observations are illustrated in Fig.23 through 26. Both, the distortion and the frequency shift of the main resonance, are now theoretically predictable. It is also quite apparent that, if this type of transducer placement is wanted, only nonreflecting double electrode transducers will result in an undistorted response. This will however limit the operating frequency to about 400 MHz, if conventional photolithography is used.

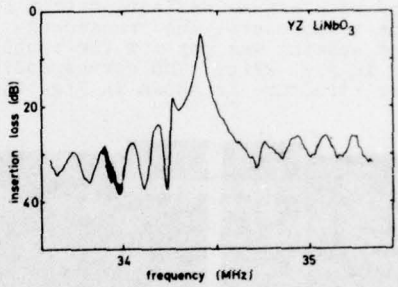

Fig. 23 Frequency response of a two-port resonator with strong reflection from transducers and additional strips in cavity. The transducer-reflector spacing was optimum for coupling, as shown in Fig.22(b). The corresponding resonator structure is shown in Fig.24

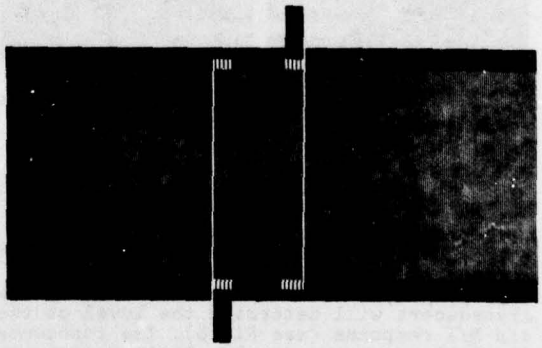

Fig. 24 Metallization pattern for two-port resonator . The response is illustrated in Fig. 23

In order to obtain a distortion free response, single electrode transducers must be placed such that the two reflected components are in phase. The transducer may then be considered to be part of the reflector.

For the design of resonators we have listed the reflector properties for ST quartz and YZ lithium niobate in Table 2, as well as the transducer placement in Table 3. For both cases, $\Delta Z < 0$ and $\Delta Z > 0$, there is a transducer-reflector spacing l_{rt} for which the two reflection components are in phase. The coupling to the standing wave pattern will be reduced, since the transducers are $\lambda/8$ off the standing wave peaks.

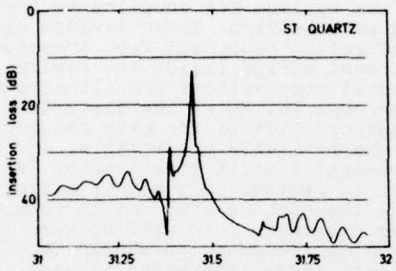

Fig. 25 Frequency response of a two-port resonator with strong reflection from single electrode transducers. The transducer-reflector spacing was optimum for coupling, as shown in Fig. 22(b). The corresponding resonator structure is shown in Fig. 26.

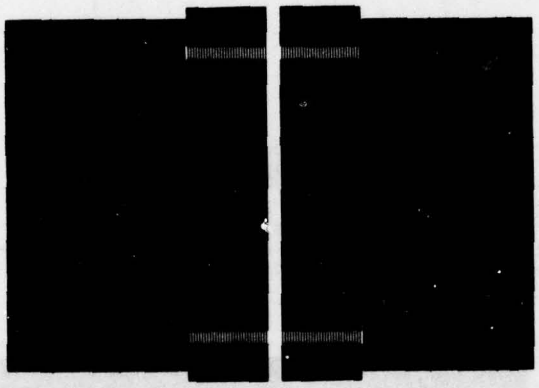

Fig. 26 Metallization pattern for two-port resonator. The response is illustrated in Fig. 25

Impedance levels

In order to calculate the transducer impedance in the frequency range outside the resonance, we have provided design data in Fig. 27 and 28. The conversion loss for two transducers will determine the level of the sin X/X response (see Fig.6). The impedance level at resonance may be obtained from an equivalent series RLC circuit description. A coarse approximation is

$$R_{res} = R_a (l_e/\lambda)/Q \qquad (16)$$

R_a must be chosen such as to maximize the sinX/X suppression and minimize insertion loss.

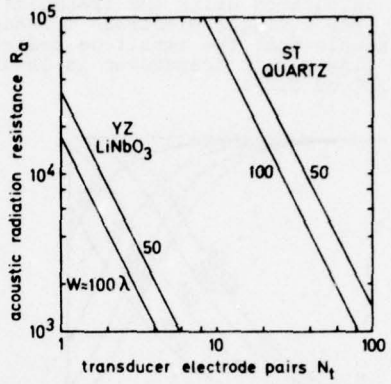

Fig. 27 Calculated acoustic radiation resistance for single electrode transducers.

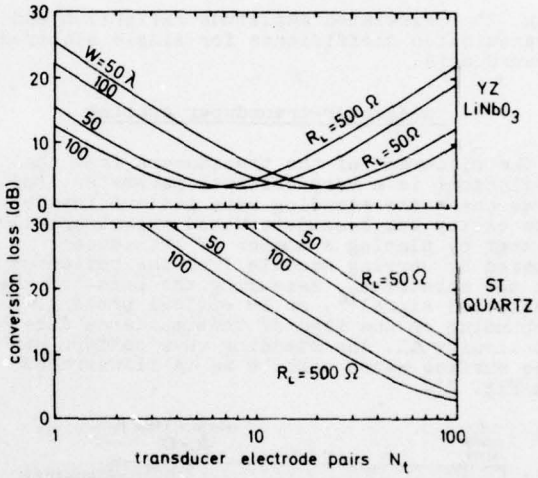

Fig. 28 Calculated conversion loss for single electrode transducers.

Tunable resonators

By changing the total phase shift across a resonator , the operating frequency will change to a new value at which the resonance condition, as expressed by equ. 3 is fulfilled. The opposite change in phase will occur at the reflectors as expressed by equ. 4. The corresponding frequency shift is obtained from equ. 9 or 10.

Tuning can be accomplished by changing the velocity under the transducers or the reflectors[13]. The velocity under a transducer depends on its internal impedance as well as its terminating impedance. The effect is also proportional to the electromechanical coupling coefficient k^2 . For lithium niobate, tuning is is illustrated in Fig. 29 and 30. The resonator with tuning transducer is illustrated in Fig. 31. Both resistive and capacitive impedances were used for tuning. Maximum tuning rate occurs when the transducer impedance equals

the external impedance. Resistive tuning is undesireable since it removes energy from the cavity and thus lowers the Q and increases the insertion loss. Because of the small coupling of ST quartz, electronic tuning is only possible over a very small range (0.01%).

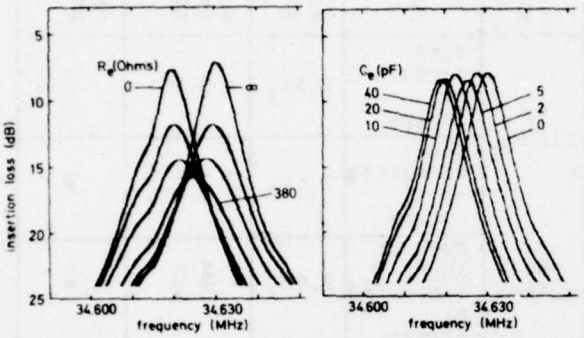

Fig. 29 Tuning characteristics with external resistance R_e and capacitance C_e for a three port resonator on YZ lithium niobate.

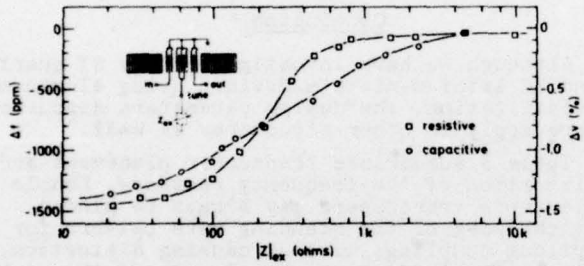

Fig. 30 Electrical tuning of the resonance frequency of a SAW resonator on YZ lithium niobate.

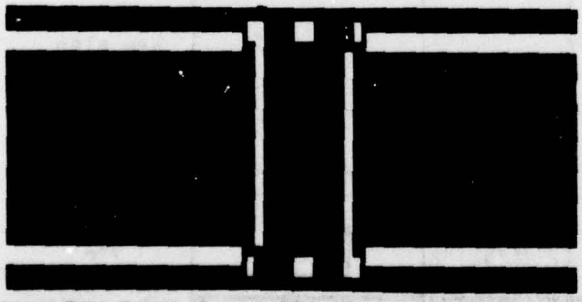

Fig. 31 Typical metallization pattern of a two-port resonator with tuning transducer in center of cavity.

Cascaded resonators

SAW resonators may be coupled in many different ways. We can distinguish between electrical and acoustic coupling methods.

Electrical coupling is possible by electrical connections between individual cavities, which may be accomplished by interconnecting transducers, or by coupling strips. Some of th the reflector metal strips may extend from o one resonator to another. One simple example of electrically cascading several devices is illustrated in Fig 32. Direct transmission between transducers of individual resonators must be avoided in order to obtain high sin X/X response suppression. About 110 dB suppression has been obtained to date by cascading four devices. Improvements in the insertion loss are possible by matching all input and output transducers.

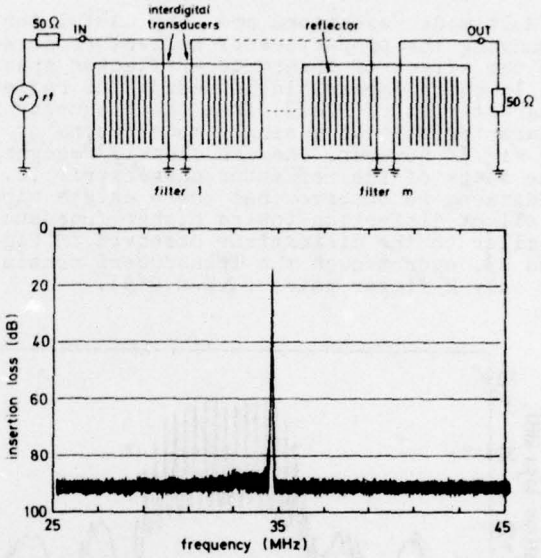

Fig. 32 Electrically cascaded SAW resonators. Three devices were cascaded to obtain 80 dB sin X/X suppression.

Multimode resonators

As the cavity length l_c increases, more modes appear within the pass band of the reflectors. Fig. 33 illustrates the response of a multimode resonator on YZ lithium niobate , using 250 open circuited aluminum strips , an aperture W of 100 d_r , single electrode 2 finger pair transducers, and a reflector-reflector spacing of 36 mm. The high insertion loss is due to tne low number of reflecting strips (N_{rc} = 400) and the large cavity length. The observed 3 dB bandwidth gave a loaded Q of 10 000.

The mode spacing of a multimode resonator is given by

$$f = \frac{v}{2\,l_c} = \frac{v}{2(l_{rr}+2l_p)} \qquad (17)$$

where v is some average velocity throughout the resonator, for simplicity. The penetration depth l_p varies with frequency about f_r as the slope of the reflector phase, given by equ. 2. The mode spacing is thus maximum at the reflector center frequency f_r and decreases away from f_r . From the mode spacing it is thus possible to determine the penetration depth l_p, as well as the impedance mismatch ΔZ.

We have constructed oscillators using two-port multimode resonators. Frequency hopping between modes was possible by varying the phase around the loop. It is believed that such multimode oscillators and filters are useful in communications systems. The unequal

mode or channel spacing is of less consequence if an identical device with equal channel spacing is used at the other terminal.

We have also cascaded electrically identical multimode devices and obtained increased suppression between modes. Devices having different mode spacing have also been cascaded to obtain only one or several specific modes selectively.

Multimode resonators are very useful for studying the properties of reflectors as well as the effect of transducer-reflector spacing. It is quite impossible to deduce the reflector characteristic (Fig.9) from the frequency characteristic of a single mode resonator. In Fig.33 however, one can clearly recognize the shape of the reflector characteristic. In addition, we observe that there exists already a slight distortion toward higher frequencies, similar to the distortions observed in Fig.23 and 25, even though the transducers consist of only 2 finger pairs ($\Delta Z=0.015$).

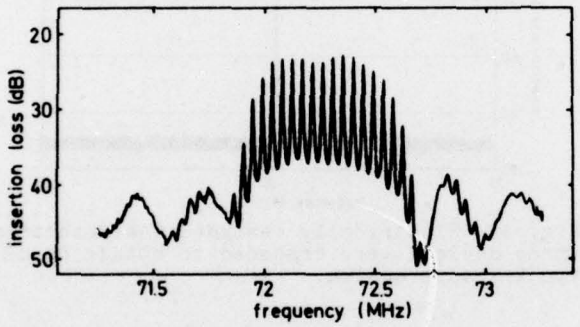

Fig. 33 SAW multimode resonator.

TABLE 2

substrate	reflector	acoustic impedance	acoustic impedance mismatch ΔZ	reflector phase ϕ_r (rad)
YZ $LiNbO_3$	open circuited Al strips	$Z_1>Z_2$	+ 0.011	0
	short circuited Al strips	$Z_1<Z_2$	- 0.015 - 0.018	π
ST quartz	open or short circuited Al strips	$Z_1<Z_2$	$-\frac{2}{3}\frac{h}{\lambda}$	π

$\lambda \cong 2\, d_r$

h = metallization thickness

$\Delta Z=\frac{Z_1-Z_2}{Z_2}$

Conclusion

Although we have investigated only ST quartz and YZ lithium niobate devices using aluminum metallization, the design parameters discussed here apply to other structures as well.

Table 3 summarizes transducer placement and distortion of the frequency response. Double electrode transducers may always be placed at the peak of the standing wave pattern for optimum coupling, without causing distortion. Single electrodes must be placed off the peak for a distortion free response.

TABLE 3

transducer – refl.	transducer coupling	ΔZ	ϕ_t	ϕ_r	ϕ_{rt}	l_{rt}	reflection components
	red.	>0	π	0	$n\pi$	$(n-\frac{1}{4})\frac{\lambda}{2}$	red. reflection 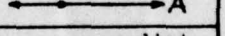
	opt.	>0	π	0	$(n+\frac{1}{4})\pi$	$n\frac{\lambda}{2}$	dist. 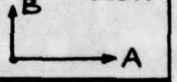
	red.	>0	π	0	$(n+\frac{1}{2})\pi$	$(n+\frac{1}{4})\frac{\lambda}{2}$	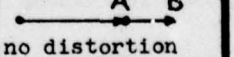 no distortion
	opt.	<0	π	π	$(n-\frac{1}{4})\pi$	$(n-\frac{1}{2})\frac{\lambda}{2}$	dist. 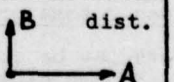
	red.	<0	π	π	$n\pi$	$(n-\frac{1}{4})\frac{\lambda}{2}$	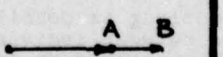 no distortion
	red.	<0	π	π	$(n+\frac{1}{2})\pi$	$(n+\frac{1}{4})\frac{\lambda}{2}$	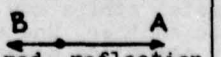 red. reflection

see also Fig.20 for symbols

$A= R_r T_t^2$

$B= R_t$

$\lambda \cong 2d_r$

red.=reduced
opt.=optimum
dist.=distorted

References

1. E.J. Staples, "UHF surface acoustic wave resonators", in Proc. 28th Annual Frequency Control Symp. (U.S. Army Electronics Command, Ft. Monmouth,NJ), pp. 280-285, May 1974.
2. R.C.M. Li, J.A. Alusow, and R.C. Williamson, "Surface-wave resonators using grooved reflectors", in Proc. 29th Annu. Frequency Control Symp. (U.S. Army Electronics Command, Ft. Monmouth, NJ), pp. 167-176, May 1975.
3. G.L. Matthaei, B.P. O'Shaughnessy, and F. Barman, "Relations for analysis and design of surface-wave resonators", IEEE Trans. Sonics Ultrasonics, vol. SU-23, Mar. 1976.
4. J.S. Schoenwald, W. R. Shreve, and R.C. Rosenfeld, "Surface acoustic wave resonator development", in Proc. 29th Annual Frequency Control Symp. (U.S. Army Electronics Command, Ft. Monmouth, NJ), pp. 150-157, May 1975.
5. D.T. Bell, Jr., and R.C.M. Li, "Surface-acoustic-wave resonators", Proc. IEEE, vol. 64, no. 5, pp. 711-721, May 1976.
6. J.S. Schoenwald, R.C. Rosenfeld, and E.J. Staples, "Surface wave cavity and resonator characteristics-VHF to L-band", in 1974 Ultrasonics Symp. Proc. (IEEE Pub. 74 CHO 896-1SU), pp. 253-256, Nov. 1974.
7. P.S. Cross, W.H. Haydl, and R.S. Smith, "Design and applications of two-port SAW resonators on YZ-lithium niobate", Proc. IEEE, vol. 64, no. 5, pp. 682-685, May 1976.
8. P.S. Cross, R.S. Smith, and W.H. Haydl, "Electrically cascaded surface-acoustic-wave resonator filters", Electron. Lett., vol. 11, no. 11, pp. 244-245, May 29, 1975.
9. R.C.M. Li, J.A. Alusow, and R.C. Williamson, "Experimental exploration of the limits of achievable Q of the grooved surface-wave resonator", in 1975 Ultrasonics Symp. Proc. (IEEE Pub. 75 CHO 994-4SU), pp. 279-283, Sept. 1975.
10. W.H. Haydl, "Surface wave reflection from right angle corners in gallium arsenide", Proc. 1973 IEEE Ultrasonics Symp. (IEEE Pub. 73 CHO 807-8SU), pp. 363-368.
11. W.H. Haydl and P.S. Cross, "Fine tuning of surface-acoustic-wave resonator filters with metallization thickness", Electron. Lett., vol. 11, no. 12, pp. 252-253, June 12, 1975.
12. W.H. Haydl, "Precision narrowband surface wave band pass filters", in 1974 Ultrasonics Symp. Proc. (IEEE Pub. 74 CHO 896-1SU), pp. 429-432.
13. P.S. Cross, W.H. Haydl, and R.S. Smith, "Electronically variable surface-acoustic-wave velocity and tunable SAW resonators", Appl.Phys.Lett., vol. 28, pp. 1-3, Jan. 1976.
14. P.S. Cross, "Reflective arrays for SAW resonators", in 1975 Ultrasonics Symp. Proc. (IEEE Pub. 75 CHO 994-4SU), pp. 241-244, Sept. 1975.
15. S.P. Miller, R.E. Stigall, and W.R. Shreve, "Plasma etched quartz SAW resonators", in 1975 Ultrasonics Symp. Proc. (IEEE Pub. 75 CHO 994-4SU), pp. 474-477, Sept. 1975.
16. P. Hartemann, "Acoustic surface wave resonator using ion-implanted gratings", in 1975 Ultrasonics Symp. Proc. (IEEE Pub. 75 CHO 994-4SU), pp. 303-306, Sept. 1975.
17. R.V. Schmidt, "Acoustic surface wave velocity perturbations in $LiNbO_3$ by diffusion of metals", Appl.Phys.Lett., vol. 27, no. 1, pp. 8-10, July 1, 1975.
18. E. K. Sittig and G.A. Coquin, "Filters and dispersive delay lines using repetitively mismatched ultrasonic transmission lines", IEEE Trans. Sonics Ultrasonics, vol. SU-15, pp.111-119, Apr. 1968.
19. B.K. Sinha and H.F. Tiersten, "An analysis of the reflection of surface waves by an array of reflecting strips using derived approximate equations", 1975 Ultrasonics Symp. Proc. (IEEE Pub. 75 CHO 994-4SU), pp. 447-452, Sept. 1975.
20. E.J. Staples and R.C. Smythe, "Surface acoustic wave resonators on ST quartz", in 1975 Ultrasonics Symp. Proc. (IEEE Pub. 75 CHO 994-4SU), pp. 307-310, Sept. 1975.
21. C. Maerfeld and P. Tournois, "Perturbation theory for the surface-wave multistrip coupler", Electron. Lett., vol. 9, no. 5, pp. 115-116,Jan. 1, 1973.

Acknowledgement

The authors would like to thank Miss A. Kilius, Mrs. A. Helde, and Mr. J. Rüdiger for their assistance in fabricating the devices. We also acknowledge the contributions Dr. P. Cross made during his stay at our facilities.

AGING EFFECTS IN PLASMA ETCHED SAW RESONATORS*

D. T. Bell, Jr. and S. P. Miller

Texas Instruments Incorporated
P. O. Box 5936, M/S 134
Dallas, Texas 75222

Summary

The development of plasma etched surface acoustic wave (SAW) resonators makes possible narrowband filters and stable oscillators in the VHF and UHF ranges. To be effective in these applications, the devices must have lower aging rates than currently estimated for SAW delay line oscillators.

Low aging rates are obtained for buik mode resonators when particular care is paid to the mechanical and chemical environment of the surfaces. The processing required for plasma etched SAW resonators is substantially different from the standard techniques used for crystal resonators, being based on photolithographic techniques used for SAW devices and semiconductor circuitry.

Key fabrication and packaging processes are being evaluated for their effect on aging rates. In the work reported here, accelerated rates at 250°C have been measured for 48 days to minimize the time required to determine the most important processes and their effect on room temperature aging. Surface preparation, cleaning and lithography processes, storage, and packaging were the variables chosen based on crystal resonator experience.

Substantial aging was seen in devices made on substrates polished with conventional (cerium oxide) optical polishing procedures. After an initial stabilization period of 45 minutes, all the "clean" variables were very similar with rates less than 10 ppm per doubling of the aging time up to 8 days. Rates for longer times as well as all vacuum sealed devices were substantially degraded by contamination from the mounting material. The best results were obtained with unsealed packages which allowed outgassing products to escape. Rates of less than 5 ppm per doubling were obtained over the entire range of times to 48 days at 250°C, with rates better than 2 ppm per doubling over an intermediate two week period. The correct acceleration factor for the 250°C aging temperature used is not known and is the subject on continuing investigation.

Key words: SAW Resonators, Aging, Frequency Stability, Accelerated Aging.

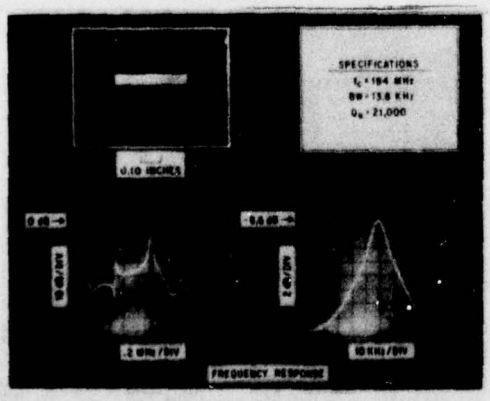

1. Plasma Etched Quartz SAW Resonator.

Introduction

This paper covers the first stage of a program to improve the long term stability of surface acoustic wave (SAW) resonators by identifying and eliminating the major factors responsible for their aging. Previous work on aging of SAW devices has been motivated by the requirements of delay line oscillators and filters.[1-3] Sufficiently low aging was found in these cases, near room temperature and over a relatively short period of time, to justify the use of the devices in their intended application. The advent of the SAW resonator with its much higher Q makes necessary a more thorough investigation. An example of a plasma etched resonator and its response are shown in Figure 1.[4] An unloaded Q greater than 20,000 at 200 MHz is typical of the performance possible with SAW resonators and justifies their use in oscillators and narrowband filters. To obtain maximum benefit from the high Q, it is necessary that the devices maintain a long term stability of a few parts per million (ppm). Thus the primary objective of the program is to develop SAW resonators with long term stability compatible with their high Q. A secondary objective is to characterize the aging processes in sufficient detail that the useful life and reliability of the device in field service may be estimated with reasonable confidence.

The scope of this paper is to present the results obtained through May 1976. A brief review of some basic principles of aging processes will be given, followed by a more extensive discussion of the experimental program and measurement procedures. The results are summarized for 12 separate combinations of eight process variables. These results form the basis of the next phase of the program.

Basic Principles

An extensive literature has been developed to explain and predict the failure of components as a function of time and stress level. Much of the theory is developed in the context of failure rates for semiconductor components (see for example the reviews of Reynolds[5] and Peck and Zierdt[6]), but it has also been applied to the aging rates of quartz resonators.[7,8]

The ideal case is illustrated in Figure 2. The property of interest (frequency change in our case) is monitored as a function of time at some temperature T_1. The resultant data ploted on a log t scale produces a straight line described by the equation $DF = A + B \log t$. The same data taken at a higher temperature results in a new straight line with a steeper slope. The assumption is that the lines will continue to be straight as they are extrapolated to longer times. The more rapid change at higher temperatures is desirable as it shortens the time required to obtain a significant change in the property of interest. Room temperature results are determined by means of the graph at the right of Figure 2. Some property characteristic of the aging process is chosen, such as the frequency shift DF at time t_1. Then to the extent that a single thermally activated process dominates the aging, a plot of log DF vs inverse temperature 1/T, will be a straight line with slope equal to the activation energy. The higher temperature results are simply extrapolated to the lower service temperature of interest, T_0.

* This work was sponsored by the Naval Research Laboratory, Contract N00014-75-C-0824

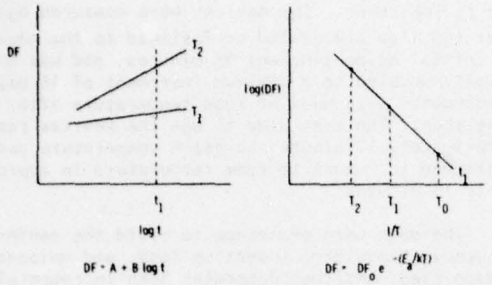

2. Ideal Isothermal Aging - Time and Temperature Dependence.

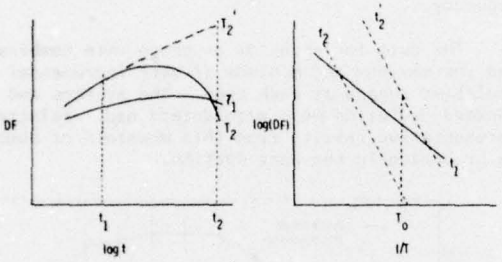

3. Practical Isothermal Aging - Time and Temperature Dependence.

The experimental procedure is straightforward.[8] Data is taken at several high temperatures. The frequency shifts are extrapolated to the time of interest, then plotted vs 1/T to determine the frequency shifts to be expected at lower temperatures.

In practice, the procedure is not so obvious due to the effects shown in Figure 3. Most aging processes are complex, resulting in isothermal lines which are not straight. Moreover, the activation energies of the separate processes may not be even approximately the same. Mechanical application of the ideal procedure will result in different low temperature results depending upon the time chosen for the determination and the relative magnitudes of the activation energies. Sufficient data must be taken, therefore, to assure that the extrapolations are based on the part of the data which represents the processes which are active at the service temperature.

The aging of an early plasma etched resonator at 150°C shown in Figure 4. The two curves represent two separate resonances of the same device. This curve shows that the aging process, at least on this sample of one, is a complex process and care is required in analysing the data. The magnitude of the aging is large enough to matter, since the shift is larger than the device bandwidth. In addition, the time required to characterize the aging at 150°C is excessive for the initial stages of the investigation where many possible causes must be eliminated as rapidly as possible. On the basis of these results, the aging temperature was raised to 250°C.

Experimental Program

Processing steps in the fabrication, mounting, and packaging of the SAW resonator were examined for possible contributions to aging of the device. Several of these were thought to be contributing to the aging, based on similarities to results reported for crystal resonators. Alternate processes were designed for these steps and a separate lot of devices was run for each. The devices were aged at 250°C for increasing periods of time. All measurements were made at room temperature.

Fabrication and Packaging Variations

In an attempt to identify critical processes resulting in device aging, a series of fabrication and packaging variations was implemented for comparison to a "standard" process. Each standard operation and its variation are summarized in Table I, along with the lot designation. The first five lines are fabrication variables and the rest concern packaging variables. The results shown in the table will be discussed in Section IV.

Typically, a chemical-mechanical polish process using Syton is used for all quartz SAW applications, but the more conventional optical polishing process with cerium-oxide was thought to be of interest for this study (Lot A). The quartz substrates of Lot B were chemically etched with concentrated hydrofloric acid 1 minute at room temperature after the standard chem-mechanical polish. The post polish etch was performed to investigate the potential aging effects of the amorphous quartz resulting from the polishing action as well as provide some stress relief to microcracks in the surface. The variation in Lot D was to deposit the aluminum transducer metallization with no elevated substrate temperature, the argument being that the small difference in film adhesion and/or grain size might affect the aging. Lots E and F were directed at controlling the organics present from normal SAW processing. In the normal process, devices were ashed in a conventional plasma system to remove resist residues. In Lot E, ashing was omitted after the last resist removal. In Lot F, devices were stored under a UV light at all times prior to header seal.[9] These five variations completed the resonator fabrication portion of this study.

The assembly operation for each device lot was bassically performed by mounting two SAW resonators in a TO-8 header as shown in Figure 5. The device was mounted with an adhesive at only one end in an attempt to minimize header-device temperature coefficient effects. The devices were shimed during the thermal compression ball-bonding operation so as not to deform the "diving-board" type mount. The actual devices can be seen in Figure 6, where the TO-8 header assembly is shown on top of the test fixture.

The assembly variations used in this study are also summarized in Table I. The devices in Lot G were mounted with Ablfilm 517 epoxy and sealed in a vacuum atmosphere. The vacuum seal was obtained by soldering

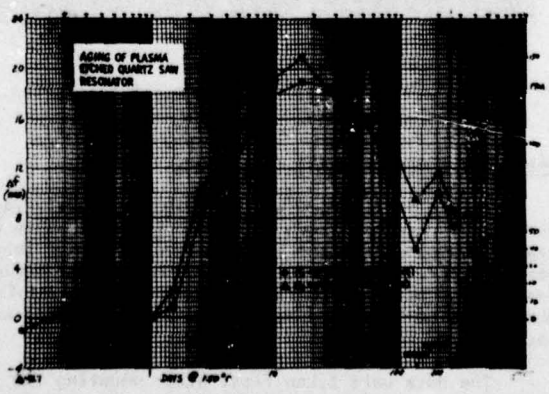

4. Aging of an Early Resonator at 150°C.

copper tubes into the TO-8 lids, drawing a vacuum after a conventional lid seal operation, and crimping the copper tubing. This package is also shown in Figure 6. Lot H devices were mounted with the same Ablfilm epoxy but sealed in a nitrogen atmosphere with a conventional lid seal operation. During the preseal bake step, the lids are normally placed onto the header, but in Lot J, the headers were uncovered during the bake-out. The next assembly variations were also associated with the sealing operation and mounting material. The vacuum sealing process was used again with a change in the mounting material (normally Dow Corning RTV-3145). A space qualified Dow RTV (6-1104) was used in Lot K because of its low percentage of condensable volatiles. Lot L used the standard 3145 RTV, with the vacuum seal operation. In the last test lot, the devices were not hermetically sealed. The lids were merely crimped on in an air atmosphere. Finally, two lots of control samples were processed with the standard SAW fabrication procedures.

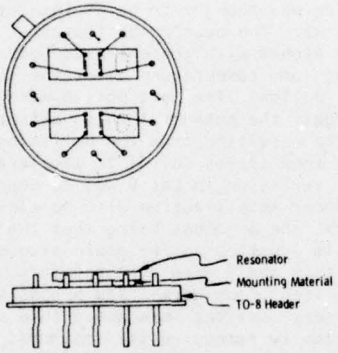

5. SAW Resonator Mounting for Aging Studies.

6. Example Packages Sitting on the Electrical Test Fixture.

Measurement and Analysis Procedures

Device performance was evaluated by displaying the narrowband response shown in Figure 1 with a sweep generator and measuring the key frequencies with a laboratory counter. In particular, the frequency of maximum response, upper and lower 3 dB frequencies and minimum insertion loss were determined on each device at each step of the aging.

The data were taken first after mounting the device on the TO-8 header. The short times and low temperatures used in the processing to that point make it unlikely that the exact time to the first measurement is important. The devices were measured again after the lids are sealed or fastened to the headers. The initial aging time was 45 minutes, and was continually doubled to a maximum increment of 16 days. Measurements were made at room temperature after each aging step. The oven used to age the devices required approximately 10 minutes to reach temperature and was programmed to return to room temperature in approximately 15 minutes.

The data were processed to yield the center frequency, bandwidth, insertion loss, and unloaded Q at each step, and then determine both incremental and cumulative changes in the parameter. The frequency of maximum response was used only to check the data for consistancy and as a measure of the skewness of the response. The 3 dB frequencies may be determined much more accurately and were used to calculate the center frequency.

The data for each lot or group were combined to find the maximum and minimum of each incremental and cumulative change at each step. The average and standard deviation were also determined. Selected representative results from this mountain of numbers are presented in the next section.

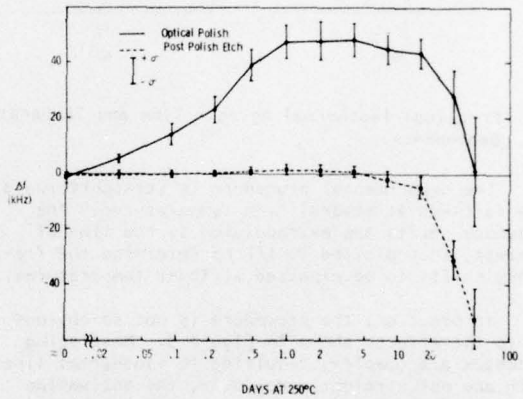

7. Isothermal Aging of 184 MHz SAW Resonators - Lots A and B (Optical Polish and Post Polish Etch).

Results

Processing Variations

Frequency shifts for lots A (conventional optical polish) and B (chemical post polish etch) are shown in Figure 7. In each case, the curve is drawn through the average of the 10 devices used and the error bars correspond to one standard deviation. The reference frequency is the value measured immediately after mounting and the first data point at t = 0 is the change resulting from sealing the lid to the header.

To facilitate comparison between lots in Table I, these curves are broken into four characteristic regions. First, the initial aging is lumped into a single number, the total change through the first step of 0.031 days. Then most of the lots have a fairly straight region of uniform slope from 0.031 to approximately 1.0 day. There is usually another region of constant slope, not always as clear as for Lot A, from 1.0 to 16 days. Then most lots take a nosedive beyond 16 days, as shown for both lots in Figure 7.

The first conclusion to be drawn from Figure 7 is that conventional optical polishing leaves a surface susceptible to aging. This is not surprising, as it is

generally known to be the case for crystal resonators and the polished surface has also been shown to be inferior for surface wave propagation.[10] The second point is that the performance deteriorates rapidly after 16 days.

The fabrication variations (Lots A through F) show essentially the same results for all variations except optical polishing and are not significantly different from the controls. Their effects are either not detectible at the accuracy of these measurements or are being masked by some uncontrolled variable.

Packaging Variations

Three mounting materials and three internal atmospheres were examined as packaging variations. The most notable effect shown in Table I is the substantial aging of all devices which were evacuated prior to sealing (Lots G, K, and L). A post-mortem on selected devices showed significant damage of the surface. A photograph of the space between transducers of a device from Lot L is shown in Figure 8. It is clear that the normal cure cycle on the RTV is not adequate to prevent outgassing or perhaps decomposition at 250°C.

One lot was aged in unsealed packages. The lids were crimped to assure that they would stay on the package and prevent gross contamination of the surface, but the leak rate was high enough to permit free exchange of gas between the package and room atmosphere. The frequency changes for this lot are compared to Lot B on a 5X expanded frequency scale in Figure 9. Unlike all the other lots, the frequency remained constant to ±20 ppm (4 kHz) over the entire period. This is additional evidence that the outgassing of the mounting material is responsible for the accelerating degradation of all other lots for times beyond one day. A second conclusion is that the aging to be expected of aluminum electrodes is not as significant for SAW resonators as for bulk resonators. This is at least partly true because of the smaller fractional coverage of the active area by the electrodes. After an initial pre-aging period, the unsealed devices aged at approximately 2 ppm per doubling of the aging time at 250°C.

Acceleration Factor

The data collected to date are insufficient to determine the acceleration factor with any degree of certainty. Both more accurate frequency measurements and a series of experiments at several lower temperatures will be required to determine the acceleration resulting from the high temperature aging. Crystal resonators have been evaluated extensively. The activation energy determined in one recent study[8] was 0.7 eV, yielding an acceleration of 2000 from 25 to 150°C and another factor of 30 from 150 to 250°C. The apparent activation energies of a

TABLE I
RESONATOR AGING TESTS
(days at 250°C)

PROCESS STEP	STANDARD	VARIATION	LOT	Δf (ppm) per doubling 0 to .031	.031 to 1.0	1.0 to 16	16 to 48
Polish	Chem-Mech.	Standard Optical	A	30	60	-5	-150
Post Polish Etch	None	Chemical	B	- .2	2.2	-9	-170
Aluminum Dep.	Hot	Cold Shot	D	-5	0	-22	-360
Ash after last resist removal	Yes	No	E	-4	-1.3	-17	-260
Store under UV light	No	Yes	F	-5	.3	-17	-250
Mount to Header	RTV 3145	Vacuum, Epoxy	G	-140	-110	-27	-2000
		Epoxy, N_2	H	-12	-10	-13	-1000
Pre-seal Bake	Lids on	Lids off	J	5	.6	-7.5	-450
Seal	N_2	Vacuum, 1104	K	18	-135	-400	-
		Vacuum, RTV	L	-12	-150	-240	-
		Air, crimped lids	M	-2.4	5	-1.6	-5.4
Controls	Standard	None	C1	7.3	-3.6	-10	-200
			C3	-1.1	1.3	-10	-130

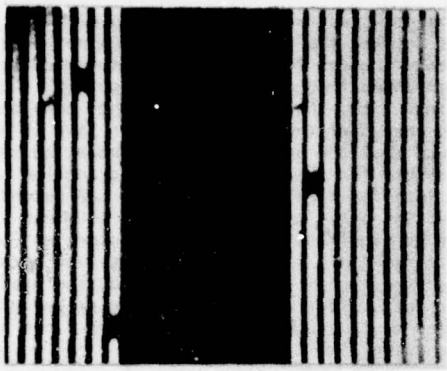

8. Surface Damage of Vacuum Sealed Resonator After 16 Days at 250°C, Showing Region Between the Transducers.

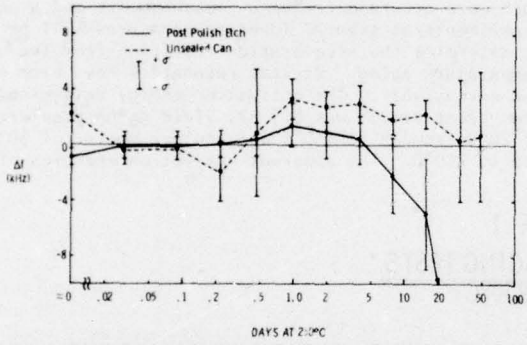

9. Isothermal Aging of 184 MHz SAW Resonators - Lots B and M (Post Polish Etch and Unsealed Can).

wide range of quite dissimilar devices tend to cluster around 0.7 eV. Assuming the same is true for the SAW resonator, then the two weeks of stable operation after one day of pre-aging at 250°C corresponds to a period of 2 x 60,000/52 = 2000 years. This would be adequate for most purposes but is awkward to verify by direct measurement. The above calculation can be at best an educated guess until more data is acquired at intermediate temperatures to isolate the properties of the process responsible for aging at lower temperatures.

Summary and Conclusions

A set of fabrication and packaging variables were tested to determine their effect on the aging rate at 250°C of plasma etched two-port quartz SAW resonators. Substantial aging was seen in devices made on substrates polished with conventional (cerium oxide) optical polishing procedures. After an initial stabilization period of 45 minutes, all the "clean" variables were very similar with rates less than 10 ppm per doubling of the aging time up to 8 days. Rates for longer times as well as all vacuum sealed devices were substantially degraded by contamination from the mounting material. The best results were obtained with unsealed packages which allowed outgassing products to escape. Rates of less than 5 ppm per doubling were obtained over the entire range of times to 48 days at 250°C, with rates better than 2 ppm per doubling over an intermediate two-week period. The effect of the aluminum electrodes must have been small to allow this low a rate. The correct acceleration factor is not known and is the subject of continuing investigation.

Acknowledgements

The assistance of Bob Vess and Larry Simonson in designing and executing the fabrication and packaging procedures is gratefully acknowledged. The results would not have been possible without the patient and painstaking work of Jim Hilton and Dennis Saunders.

References

1. M. Lewis, "The surface acoustic wave oscillator - a natural and timely development of the quartz crystal oscillator," Proc. 28th Annual Frequency Control Symp., U. S. Army Electronics Command, Ft. Monmouth, N. J., pp. 304-314, May 1974.

2. T. E. Parker and M. B. Schulz, "Stability of SAW controlled oscillators," 1975 Ultrasonics Symp. Proc., IEEE Pub. No. 75 CHO 994-4SU, pp. 261-263, September 1975.

3. J. R. Moulic, "Observation of long term velocity drift in $LiNbO_3$," 1975 Ultrasonics Symp. Proc., IEEE Pub. No. 75 CHO 994-4SU, pp. 511-513, September 1975.

4. W. R. Shreve, "Two-port quartz SAW resonators," Proc. 30th Annual Frequency Control Symp., U. S. Army Electronics Command, Ft. Monmouth, N. J., June 1976.

5. F. H. Reynolds, "Thermally accelerated aging of semiconductor components," Proc. IEEE, 62:2, pp. 212-22, February 1974.

6. D. S. Peck and C. H. Zierdt, Jr., "The reliability of semiconductor devices in the Bell System," Proc. IEEE, 62:2, pp. 185-211, February 1974.

7. A. W. Warner, D. B. Fraser, C. D. Stockbridge, "Fundamental studies of aging in quartz resonators," IEEE Trans. Sonics Ultrasonics, 12, pp. 52-59, June 1965.

8. S. H. Olster, et al., "A6 Monolithic crystal filter design for manufacture and device quality," Proc. 29th Annual Frequency Control Symp., U. S. Army Electronics Command, Ft. Monmouth, N. J., pp. 105-112, May 1975.

9. J. R. Vig, J. W. LeBus, R. L. Filler, "Further results on UV cleaning and Ni electrobonding," Proc. 29th Annual Frequency Control Symposium, U. S. Army Electronics Command, Ft. Monmouth, N. J., pp. 96-108, May 1975.

10. D. T. Bell, Jr., "Growth, orientation, and surface preparation of quartz," 1972 Ultrasonics Symp. Proc., IEEE Pub. No. 72 CHO 708-8SU, pp. 206-10, October 1972.

11. V. E. Bottom, "A novel method of adjusting the frequency of aluminum plated quartz crystal resonators," Proc. 30th Annual Frequency Control Symp., U. S. Army Electronics Command, Ft. Monmouth, N. J., June 1976.

THE PERIODIC GRATING OSCILLATOR (PGO)

R. D. Weglein and O. W. Otto
Hughes Research Laboratories
Malibu, California 90265

Summary

The principal aspects of the PGO are reviewed and some new performance data is reported. The distinctive element of this device is a pair of ion-etched gratings that determines the oscillation frequency as well as the noise characteristic in the vicinity of the carrier. The PGO has some unique features of advantage at high microwave frequencies and in applications where excessive long-term drift is intolerable.

We report on the adjustment of the turn-around temperature by variation of the x- and z-path length ratio of the device on y-cut quartz. We also report on the measured noise performance of two versions of the PGO as compared against a well-developed bulk crystal oscillator, all at 97 MHz. The noise spectra are measured under quiescent conditions and under random vibration, with the PGO having much higher immunity to vibration than the crystal oscillator.

Introduction

A new type of surface acoustic wave (SAW) delay line oscillator which makes use of a pair of ion-etched reflective gratings as frequency-determining elements has been described.[1] The gratings are arranged in a Z- or U-path configuration (Fig. 1) so as to couple two mutually orthogonal propagation directions having linear temperature coefficients of delay (TCD) of opposite sign (e.g., x- and z-propagating y-cut quartz). By suitably adjusting the pathlength ratio of the two propagation directions, temperature stability comparable to ST-quartz is achieved. The small area, relatively broadband thin-film interdigital transducers in the periodic grating oscillator (PGO) serve only the transduction function while the ion-etched gratings provide the required filtering function.

In this paper we present new data on the adjustability of the temperature characteristics of the PGO. In addition, noise characteristics of two varieties of laboratory PGO's (so-called Z- and U-path) are compared against a thoroughly engineered crystal oscillator (all at 97 MHz multiplied to X band) under quiescent and under vibration conditions. The PGO shows a clear advantage over the crystal oscillator in a vibration environment.

Adjustable Temperature Stable Operation

The basic principle for the temperature-stable operation of the PGO is that of selecting the ratio of pathlengths for the two orthogonal propagation directions that results in a cancelling of the linear delay-temperature coefficients at the desired operating temperature. A derivation of the temperature stability condition was reported earlier.[1] It turns out that if the reflections are right angle and all propagation directions are pure mode, the temperature stability condition reduces to (for both Z- and U-path devices)

$$\gamma_x n_x + \gamma_z n_z = \gamma_{ext} \qquad (1)$$

where n_x and n_z are the x- and z-directed pathlengths in wavelengths, γ_x and γ_z are the linear TCD's along the x and z directions and γ_{ext} is the combined TCD of all the external feedback circuitry. By adjusting n_x and n_z, opposite signs for γ_x and γ_z can result in complete mutual cancellation except for the small contribution required by γ_{ext}.

The frequency variation with temperature in conventional SAW oscillators using ST-quartz exhibits an approximately parabolic characteristic about the turn-around temperature T_o, of the form

$$\frac{\Delta f}{f_o} \simeq B\,(T-T_o)^2 \qquad (2)$$

where $B \simeq -32 \times 10^{-9}/°C^2$.[5] To achieve temperature-stable operation, it is desirable to locate T_o near the ambient temperature prevailing in the particular application. This may be performed by simultaneous rotation of the crystal cut[5] and adjustment of the film thickness of the aluminum transducer metallization.[6] In the PGO, however, where y-cut quartz is the temperature-stable substrate,[1] the location of T_o is independent of any metal film thickness considerations. T_o may be positioned over a wide temperature range, simply by varying the delay ratio between the x- and z-directed acoustic path lengths, n_x and n_z. This change in delay ratio may be implemented by providing for several transducers along the x-direction of the photomask. By simply connecting the input to alternate transducer positions, the n_x/n_z ratio is readily and predictably varied. In our device three transducers were used at each port with different intertransducer delays so that nine different delay ratios could be effected with one mask and one lithography step. We present here experimental verification of the technique and some comparison with the predicted shift of T_o with a change in x-directed delay.

The two experimental curves shown in Fig. 2 were measured on the same PGO device, with different transducer connections. For the two cases, the change in delay corresponds to a Δn_x of approximaately 30 wavelengths, or about 0.30 microseconds. The corresponding change in turn-around temperature is seen to be 17°C. Predictions of the shift of T_o with n_x may be made if the value of B and the total path length are known.[1] Table I summarizes the predicted and experimentally measured T_o-shift with n_x based on the data in Fig. 2.

TABLE I
TURNAROUND TEMPERATURE (T_o) ADJUSTMENT IN PGO-Z

T_o	21°	38°
n_z	155.23	155.23
n_x	445.03	474.98
n_T	591.81	630.21
$B^*(10\text{-}9/°C)^2$	-38.2	-69.05
$\partial T_o/n_z$ (calc.)	.39°C/λ_x	
$\partial T_o/n_x$ (meas.)	.57°C/λ_x	

*$B = \Gamma''/2$ of Ref. 1

It is seen that the measured T_0 sensitivity to n_x is 0.57°C/wavelength, somewhat larger than anticipated. Although this discrepancy is not fully understood, it is a consequence of the somewhat different second-order coefficients of the two measured curves (different B's). These coefficients as well as the turnaround temperature T_0 are influenced by the temperature dependence of the external circuit elements and, in particular, the tuning inductance.[5] These factors were not accounted for in the present experiment. Experiments are in progress to separate the intrinsic y-cut quartz behavior from the external temperature-dependent effects and will be reported on at a later time.

Noise Performance

In this section we compare the noise power spectra of two periodic grating oscillator devices against that of a conventional oscillator, all oscillating within 1.0 MHz of 97 MHz. The two PGO devices are constructed on y-cut quartz with x- and z-propagation directions, one in a Z-path configuration (100 reflectors/grating) and one in a U-path configuration (400 reflectors/grating). Both devices nominally satisfy Eqn. (1) with $\gamma_{ext} = 0$.

The power spectra of the oscillators were measured at X band using a conventional varactor multiplier chain (96x). A standard noise measurement test set was employed that detects amplitude (AM) or phase (FM) noise on microwave signals in the 9-10 GHz frequency range. The technique allows for the determination of the noise power density to within an offset frequency of 1 kHz of the X-band carrier. The single-sideband noise power spectral density of the 97 MHz oscillators in dB/Hz is readily calculable using the known measurement bandwidth (0.1 kHz or 1 kHz) and the multiplication ratio. In our calculations it was assumed that the oscillator was driven by white noise at the amplifier output and that no additional phase noise was introduced by the multiplier chain.[7]

In Fig. 3 the noise power spectrum of the Z-path PGO at 97 MHz is compared against that of a well-developed 5th-overtone quartz bulk crystal oscillator operating at the same frequency. Both oscillators are under quiescent conditions. The lower noise of the crystal oscillator compared to the PGO is readily apparent, decreasing from 20 dB lower at 1 kHz offset to only 5 dB lower at 20 kHz offset. The poorer noise characteristic of the PGO is due in part to its modest equivalent filter Q.

The same two oscillators are compared again in Fig. 4 under random vibration levels of 8G RMS between 20 and 2000 Hz ($.032G^2/Hz$). While the PGO noise level is raised uniformly by about 10 dB, the noise of the crystal oscillator is raised 20 to 30 dB and exhibits several resonant spikes which rise an additional 20 to 30 dB. At these resonances the crystal oscillator spectrum is poorer than that of the PGO by 40 dB. The resonant spikes in the crystal oscillator are characteristic modes of vibration in the bulk crystal plate and depend on its support structure and its general sensitivity to acceleration.[8]

No serious attempt has been made to date to design the PGO circuitry with minimum vibration sensitivity in mind, whereas the crystal oscillator represents the current state of development in engineering practice. One would, therefore, expect improvement of PGO noise power spectrum under vibration in a mechanically well-engineered SAW oscillator package. The sharp increase in the noise spectra within 2kHz of the carrier of both oscillators is somewhat suspect of arising not in the oscillators themselves but in the electrical circuit and connecting cable associated with the vibration table platform.

The relative immunity to vibration of the SAW oscillator in general and the periodic grating oscillator in particular, is a direct consequence of the fact that the piezoelectric crystal substrate supporting the surface wave topography does not undergo distortion (bending or twisting), since the substrate is thick compared to the wavelength and firmly supported on a rigid base.[9]

In Fig. 5, the noise power spectra in the quiescent state of the PGO-Z and crystal oscillator are replotted and summarized. Also shown is preliminary data of a PGO-U oscillator taken in the same manner as for the other oscillators. We have also included the intercepts of the noise power spectra prediction[10] and RMS frequency (f_D) calculated from the assumption of simple FM theory ($S/N = 20 \log f_m/\sqrt{2}f_D$). The ordinate shows noise power in dB/Hz versus offset frequency out to 1 MHz. In all cases the curves are normalized to 97 MHz as previously outlined. For the Z-path configuration of the PGO, the expected noise peaks for the other modes at 160 kHz intervals are clearly evident. These modes are absent in the U-path configuration since the grating filter bandwidth is identical to the reciprocal delay of the device. Both the noise floor and intercept regions, corresponding to the reciprocal delay frequencies are in reasonable agreement with predictions. The lower noise floor of the PGO-U is a direct consequence of the higher Q of the grating filter in this design. It is interesting to observe that the transition from the noise floor regime to the region where phase noise dominates (20 dB/decade) is somewhat slow, resulting in a narrower than expected oscillator linewidth. Finally it can be seen that the crystal oscillator noise spectrum exhibits a minimum at a level 7 dB lower than the PGO-U at an offset frequency of about 3 kHz, but looses this distinction quickly to the PGO-U at offset frequencies beyond 18 kHz.

Conclusions

The PGO has a number of distinct fabrication and environmental advantages. For high frequency devices lithography resolution requirements are relaxed about 40% over standard transducer electrodes or resonator elements at the same frequency. Yield is increased not only by the coarser pattern but also because ion-etched reflective elements are highly defect tolerant, as has been amply substantiated by reflective arrays in dispersive filters. Additional benefits accrue at high frequencies from the fact that the large coherent reflections characteristic of the multi-element periodic impedance discontinuities of transducer structures are virtually absent, as are the associated metallic layer-induced propagation losses.

The absence of metal film-substrate interfaces in the frequency determining element of the ion-etched filters is expected to significantly increase the long-term frequency stability of the oscillators, and particularly the long-term drift and variation associated with such interfaces.

Because of the parabolic frequency dependence on temperature that the PGO exhibits it is important that the turnaround temperature can be positioned over a wide range. The periodic grating oscillator, as described previously,[1] lends itself uniquely to this adjustment without resorting to changes in crystal cuts, and without dependence on metal film thickness. Finally, the turnaround temperature may be suitably changed using a single mask design and in essentially a single lithograph step on the y-cut quartz substrate.

SAW oscillators have been predicted to be relatively rugged devices, free from constant acceleration, shock and vibration, characteristic of bulk crystal oscillators.[3] The insensitivity of SAW devices in general arises from the fact that essentially no surface strain is produced in a typical thick, well-anchored surface-wave substrate that is subjected to large stress forces. These predictions are well borne out in experimental results presented here.

Acknowledgements

The authors gratefully acknowledge the work of H. L. Garvin and his staff, for the ion-etch of the devices used in these experiments. R. Dimon performed the lithography and device fabrication. Special acknowledgement goes to B. R. Blanchard for his continued interest in this program, as well as for the measurement of the oscillator noise performance.

References

1. O. W. Otto and R. D. Weglein, "Surface Acoustic Wave Oscillator Using Reflective Gratings," 1975 Ultrasonic Symposium Proceedings, IEEE Cat. No. 75-CHO-45U, p. 994.

2. H. M. Gerard, O. W. Otto, R. D. Weglein, "Development of a Broadband Reflective Array 10,000:1 Pulse Compression Filter," 1974 Ultrasonic Symposium Proceedings, IEEE Cat. No. 74-CHO 896-1SU.

3. G. F Johnson, "Vibration Characteristics of Crystal Oscillators," Proc. 21st Annual Frequency Control Symposium, p. 287-293, 1967.

4. M. F. Lewis, J. Crabb and J. D. Maines, "Surface Acoustic Wave Oscillators: Mode Selection and Frequency Modulation," Electronic Letters 9, No. 10, p. 197-197 (17 May 1973).

5. J. F. Dias, et al., "The Temperature Coefficient of Delay-Time For x-Propagating Acoustic Surface-Waves on Rotated y-Cuts of Alpha Quartz," IEEE Trans. on Sonics and Ultrasonics SU-22, No. 1, p.46-50, (Jan. 1975).

6. S. J. Kerbel, "Design of Harmonic SAW Oscillators Without External Filtering and New Data on the Temperature Coefficient of Quartz," 1974 Ultrasonic Symposium Proceedings, IEEE Cat. No. 74 CHO 896-1SU, p. 276-281.

7. Fred L. Walls and Adreas DeMarchi, "RF Spectrum of a Signal After Frequency Multiplication; Measurement and Comparison with a Simple Calculation," IEEE Trans. on Instrumentation and Measurements IM-24, p. 210-217 (Sept. 1975).

8. P. C. Y. Lee, et al., "Effects of Initial Bending on the Resonance Frequency of Crystal Plates," Proc. 28th Annual Frequency Control Symposium, p. 14-18, 1974.

9. D. E. Cullen and T. M. Reeder, "Measurement of SAW Velocity vs. Strain for yx and ST Quartz," 1975 Ultrasonic Symposium Proceedings, IEEE Cat. No. 75 CHO 994-4SU, p.519-522.

10. M. F. Lewis, "Some Aspects of SAW Oscillators," 1973 Ultrasonic Symposium Proceedings, IEEE Cat. No. 73 CHO 8G7-8 SU, p. 344-347.

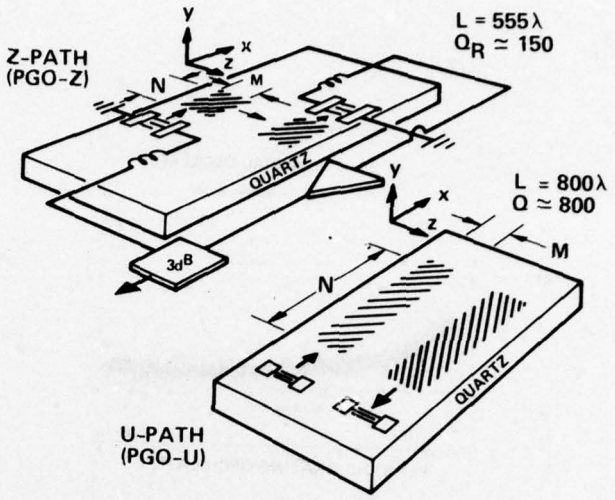

Figure 1. Periodic Grating SAW Oscillator Configurations.

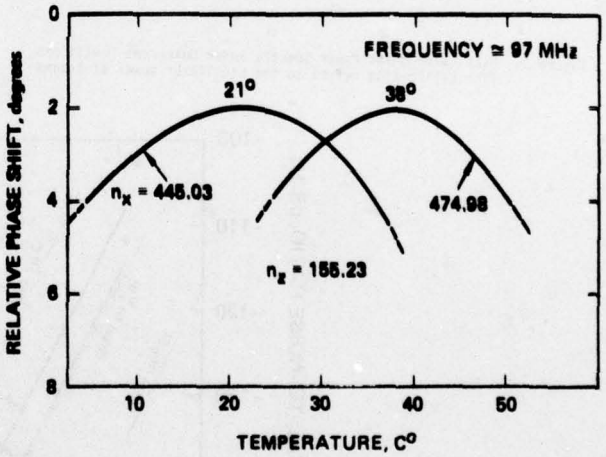

Figure 2. Variation of Turn-Around Temperature T_0 with Delay.

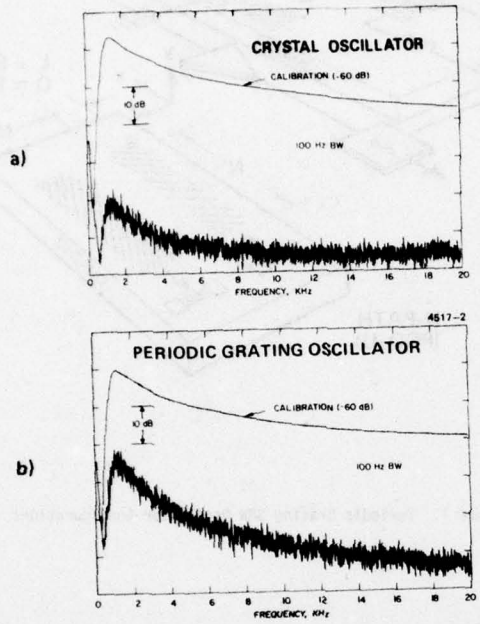

Figure 3. Oscillator Noise Power Spectra Under Quiescent Conditions. (The calibration refers to the oscillator power at X-band)

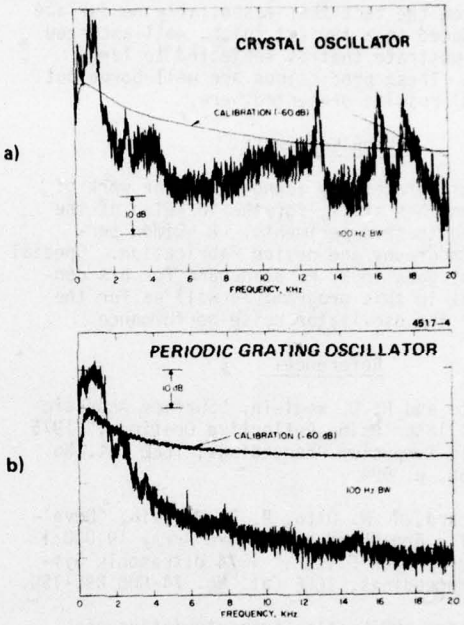

Figure 4. Oscillator Noise Power Spectra Under Random Vibration (.08 g^2RMS, 20-2000 Hz). (The calibration refers to the oscillator power at X-band.)

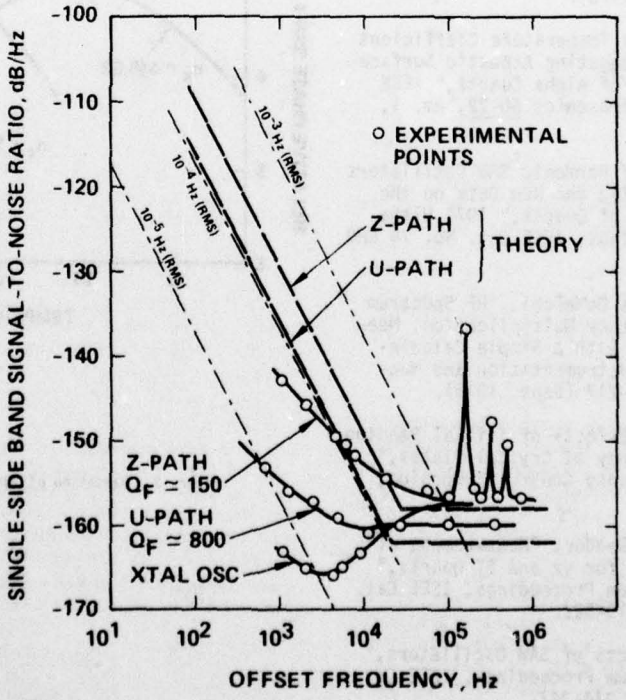

5. Noise Characteristic of 97 MHz PGO SAW Oscillators.

For optimum coupling, the transducer electrodes are positioned at the peaks of the standing waves.

be placed such that the two reflected components are in phase. The transducer may then be considered to be part of the reflector.

FAST FREQUENCY HOPPING WITH SURFACE ACOUSTIC WAVE (SAW) FREQUENCY SYNTHESIZERS

L. R. Adkins
Rockwell International, Electronics Research Division
Anaheim, California

Abstract

The SAW frequency synthesizer reported here derives from the basic single mode SAW oscillator. As in the SAW oscillator configuration, input and output transducers are connected together through an amplifier, but for the synthesizer the IDTs in the feedback loop are designed so that the entire comb of frequencies which can be sustained in oscillation is retained. This comb of frequencies will propagate down the delay line as a surface acoustic wave and the individual frequencies may be selected by means of a series of receiving IDTs deposited on the substrate. Each of the receiving IDTs will have a center frequency corresponding to one of the comb frequencies and its frequency response will be such that all of the comb frequencies except the one desired will occur at the response nulls. Thus, each receiving IDT will have an output consisting of a single frequency of high spectral purity. The advantages this approach for frequency hopping application is that a single delay line and feedback loop generates a number of frequencies which are available at all times. Thus, the speed at which desired frequencies can be selected will be determined solely by the speed of the external switches. High performance MOS/CMOS IC switches are now available with switching times on the order of 2 nsec. In this paper the results of theoretical and experimental investigations of this synthesizer approach will be presented.

Introduction

The basic Surface Acoustic Wave (SAW), oscillator consists of a simple delay line with input and output interdigital transducers (IDTs) connected through an amplifier to form a positive feedback loop. This device is capable of supporting a comb of frequencies with frequency separation proportional to the length of the delay path. Most of the SAW oscillator configurations discussed in the literature[1,2] have been designed so that all of the comb frequencies but one fall in the nulls of the transducer frequency response. Thus, a single mode of high spectral purity is obtained. It is the purpose of this paper to show how the complete comb can be utilized in the design of a multimode frequency synthesizer and how individual components of this comb can be selected at ultrafast rates. The basic idea of this device is outlined in the following section and experimental results are presented in Section III.

Basic Principles

The SAW synthesizer scheme is shown schematically in Figure 1. Transducers T_1 and T_2 are connected through an amplifier to form a feedback loop; frequency components which experience a phase shift equal to an integral multiple of 2π radians and for which the amplifier gain is sufficient to overcome the total losses in the loop can be sustained in oscillation. If suitable phase locking techniques are employed all of the allowed modes within the bandpass of the system can be stabilized to obtain a uniform frequency comb. The resulting signal travels down the delay line as a surface acoustic wave and individual components of the comb are selected by means of interdigital transducers. These IDTs are designed so that only the frequency of interest lies within the passband of the frequency response while others fall in the frequency response nulls. The particular transducer output (and, hence, the particular frequency), may be selected by means of high speed PIN diode switches. The great advantage of this SAW multimode synthesizer approach is that once stable oscillation is established the frequency spectrum will be present in the line at all times. Thus, the rate at which a particular frequency component can be selected will be limited solely by the speed of the switches. There will be no need for lengthy delays while a frequency mode is locked into oscillation.

To clarify the operation of this system, consider the basic SAW oscillator shown in Figure 2. The condition that a signal of frequency ω experience a phase shift equal to an integral multiple of 2π radians is given by

$$\frac{\omega L}{v} + \phi = 2n\pi \qquad (1)$$

where L is the transducer separation, ϕ is the phase shift in the network external to the SAW delay line and v is the SAW velocity. If $L = M\lambda_o$, where M is a large integer and λ_o is the center frequency wavelength, then, neglecting ϕ, the allowed frequencies of oscillation are

$$f_n = f_o\left(1 \pm \frac{n}{M}\right) \qquad (2)$$

It can be shown[3] that the network Q and, hence, the stability is proportional to M. Thus, to maintain high spectral purity and to minimize the effect of the external phase shift it is necessary that M be very large, at least 1,000. This implies a comb of closely spaced frequencies since from equation (2)

$$\Delta f = f_o/M \qquad (3)$$

where Δf is the spacing between the spectral components of the comb. At typical IDT center frequencies of 100 MHz Δf will be on the order of 100 KHz, and to select out individual frequencies from such a comb with transducers having standard Sin X/X responses would require IDTs quite large in physical extent, ~3 cm. This would greatly restrict the number of outputs allowable on a substrate of reasonable size. Therefore the frequency response of the transducer system must be tailored so that only frequency components separated by at least one (and preferably more) MHz fall within the passband.

If the SAW oscillator is activated simply by turning on the amplifier a stable comb of frequencies will not normally be obtained. This is so because when this activation procedure is followed the signal is built up from thermal noise. Following Lewis[1] the output of the feedback loop $V_o(\omega)$ is given by

$$V_o(\omega) = GV_i(\omega)\left[e^{j\omega t} + A(\omega)e^{j\omega(t-\tau)} + A^2(\omega)e^{j\omega(t-2\tau)} + \cdots\right] \qquad (4)$$

where G is the amplifier gain, $A(\omega)$ is the product of the amplifier gain and the delay line insertion loss, τ is the delay in the acoustic path and $V_i(\omega)$ is the initial signal input into the amplifier. If $A(\omega)$ is near unity then $V_o(\omega)$ will continue to grow until the saturation level of the amplifier is reached. If $\Delta\omega$ is the overall bandwidth of the system and P_o is the saturation power of the amplifier then

$$\int_{-\frac{\Delta\omega}{2}}^{\frac{\Delta\omega}{2}} P(\omega)\,d\omega = P_o$$

defines the output spectrum where $P(\omega) = \dfrac{V_o(\omega) \times V_o^*(\omega)}{R}$.

R_a must be chosen such as to maximize the sinX/X suppression and minimize insertion loss.

with tuning transducer is illustrated in Fig. 31. Both resistive and capacitive impedances were used for tuning. Maximum tuning rate occurs when the transducer impedance equals

Since the initial signal into the amplifier $V_i(\omega)$ arises from the noise in the system it is a random function of frequency and will in general be different each time the system is activated. Thus, the output power spectrum can not be predicted. Computer simulations of two frequency combs supported by a SAW oscillator are shown in Figure 3. These two combs were obtained by turning on the amplifier at different times. The uneveness and unpredictability exhibited by these two simulations is confirmed by experiment.

To obtain a stable, uniform comb of frequencies from the SAW oscillator phase locking techniques must be used. One approach (shown schematically in Figure 4a) would be to initiate the oscillations with a pulse from an external generator clocked at a rate to produce the desired comb spacing in the frequency domain. Provided proper phase relationships are maintained, the comb in the oscillator loop will build up from the injected signal resulting in a uniform spectrum. Figure 4b shows an active phase locking technique similar to that described by Gilden, et al[4]. Here the signal circulating in the feedback loop is mixed with a local oscillator (which could be a SAW oscillator) of frequency Δf defined in equation 3. This mixing process will develop side bands corresponding in phase and spacing to the feedback supported frequencies defined by the SAW line. This will assure the maintenance of a stable, uniform comb of phase coherent frequencies within the bandpass of the system. An advantage of this approach is that it can be automated by tapping some of the RF signal out of the loop, detecting (with r-F detector) and amplifying this signal. Tne video output from the amplifier is then employed as the modulation reference into the mixer. This system is described in Ref. 4. Thus there are several techniques for obtaining a stable comb of frequencies from the SAW oscillator. The particular phase locking techniques employed in an actual device will depend on such factors as convenience, power consumption and cost.

The basic design of the receiving transducers is straightforward. The frequency response of a standard transducer with uniform finger overlap is of the form $\text{Sin } \omega t/\omega t$ where ω is one radial frequency and t is the width (in time) across the transducer. Clearly nulls will occur whenever $\omega t = n\pi$. Thus, if nulls separated by a frequency of Δf are desired then the time delay across the transducer must be

$$t = \frac{1}{\Delta f}$$

and the physical extent x of the IDT in the direction of SAW propagation must be $x = vt = v/\Delta f$. This simple criterion will be modified by such factors as diffraction and dispersion, but it is sufficient for a first order estimation of transducer size.

Experiments

To demonstrate the validity of the concepts summarized above, experiments were performed with operating SAW oscillator devices. The multimode oscillator was fabricated by modifying an existing delay line structure which was designed to operate at a center frequency of 140 MHz. The time domain separation of the IDTs in the feedback loop was approximately 8 μsec or 1120 wavelengths at center frequency, and the frequency response of the IDT system was such that the comb periodicity was 10 MHz. Two mode selection transducers were deposited on the substrate. One of these had a center frequency of 140 MHz while the other had a center frequency of 130 MHz. The dimensions of these transducers satisfied the mode selective requirements described in Section II.

PIN diode switches fabricated using silicon-on-sapphire technology were employed at the selection transducer outputs. The basic circuit for these switches is shown in Figure 5. As will be seen in the diagram the switch consists of a tee configuration of three vertical junction diodes. The polarity of the current flowing into the bias part defines the switching function. If the current is positive diodes d_1 and d_2 are forward biased and appear as small resistances to the RF input. Under these conditions d_3 is reversed biased and appears as small shunt capacitance. Thus, with a positive bias current flowing the switch is "on". With a negative current input to the bias port the diode conditions are reversed. Diodes d_1 and d_2 appear as capacitances while d_3 appears as a shunt resistance. Very little RF input signal gets through to the output and thus the switch is "off". With the PIN diode switches recently developed at Rockwell on/off ratios greater than 60dB are obtained when operating at frequencies near 200 MHz. Switching rates are extremely rapid for these switches, approximately 2 nsec.

The frequency comb produced by the oscillator is shown in Figure 6. This photograph was obtained by feeding the oscillator output into a spectrum analyzer. The comb was stabilized using the active phase locking technique described in Section II. The horizontal scale in the photograph is 5 MHz/div and it will be seen that a frequency spacing of 10 MHz has been established. Once the comb was locked in place the spectrum was very stable over a time span of several hours (the longest period observed). No phase noise measurements were made on this particular device although the phase noise has been established for a similar single mode SAW oscillator fabricated at Rockwell. For that device the noise was 55dB down at 100 KHz with 1 KHz bandwidth. Similar results would be expected with this device.

The 140 MHz and 130 MHz outputs from the selection transducers are shown in Figure 7. The outputs were obtained by operating the diode switches manually. Examining the outputs individually it was found that the Q and stability of the selected modes were the same as for the corresponding frequency component in the comb. The most obvious characteristic of the outputs shown in the photographs is that the isolation of the main signal from all other modes is only about 20dB. The main reason for the relatively high spurious response with this prototype model was determined to be a combination of high SAW insertion loss and electromagnetic feedthrough. As pointed out above, the on/off isolation of the switches is at least 60dB at these frequencies, and therefore any leakage through the switches makes only a minor contribution to the observed spurious. Also, any degrading effect arising from an imperfect transducer response function was determined to be small. This was most readily seen by placing an absorber of rubber cement on the crystal surface and noting that virtually all of the spurious spectrum remained. On the other hand the insertion loss was approximately 45dB and the RF pickup signal was only 20dB below this. Therefore it is clear that the signal isolation can be substantially increased by adjusting the transducer Ra to reduce the SAW insertion loss (and thus increase the signal to spurious ratio) and by improved package design. From previous measurements of the transducer response function and from previous experience with SAW lines for which electromagnetic pickup is a problem, it is estimated that a signal isolation of 60dB can readily be achieved and even higher isolations, up to the limit imposed by the switches are possible.

Conclusion

One approach to utilizing the frequency comb defined by a multimode SAW oscillator in a rapidly selectable frequency synthesizer has been presented in this paper. The validity of the approach has been demonstrated experimentally with a prototype model. The manner in which a device such as this would be employed in a particular system will depend to a large extent on the

application, required frequency spacing, etc. For example, it is easy to visualize how a very small number of SAW components described above could be used to synthesize a large number of frequency components if judicious use is made of a few mixers at the transducer outputs. From the criteria given above it can be shown that about ten output IDT's with 10 MHz bandwidth can be comfortably contained on a reasonable size (~3 in.) quartz crystal. If the output bandwidth (and hence, the comb frequency spacing) is 2 MHz only five transducers can be deposited on the same crystal. However, it can be shown that by properly combining (through a mixer) the ten outputs of two SAW synthesizers with 10 MHz frequency spacing and the five outputs of two synthesizers with 2 MHz spacing, 1,000 frequency components separated by one MHz can be obtained. It is clear that these four SAW elements coupled with a microprocessor to control the PIN diode switches can provide a very compact, low cost fast lapping frequency synthesizer system. Other applications and frequency combinations can be readily derived from the basic approach.

References

1. M. F. Lewis, Ultrasonics, May 1974, pp. 115-123.
2. T. E. Parker and M. B. Schulz, 1975 Ultrasonics Symposium Proceedings, 75 CHO 994-4SU, pp. 261-263.
3. Merrion Lewis, Component Performance and Systems Applications of Surface Acoustic Wave Devices, IEEE Conference Publication No. 109 (Sept. 1973), pp. 63-72.
4. M. Gilden, T. M. Reeder and A. J. DeMaria, 1975 Ultrasonics Symposium Proceedings, 75 CHO 994-4SU, pp. 251-254.

Figures

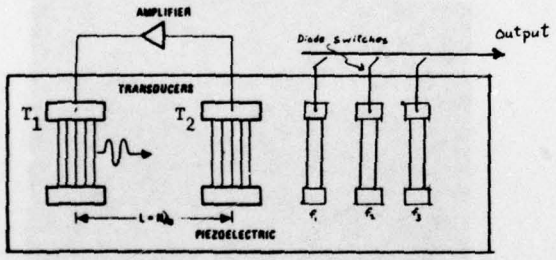

Figure 1 Saw Synthesizer

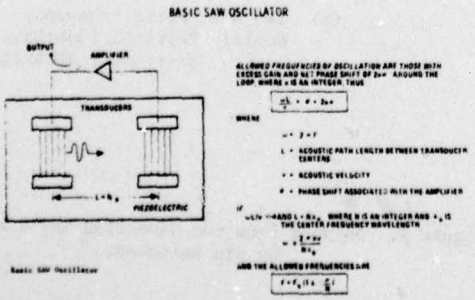

Figure 2. Basic SAW Oscillator

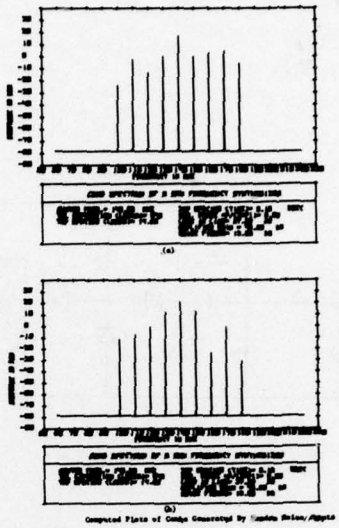

Figure 3. Computer plots of frequency combs generated by random noise inputs.

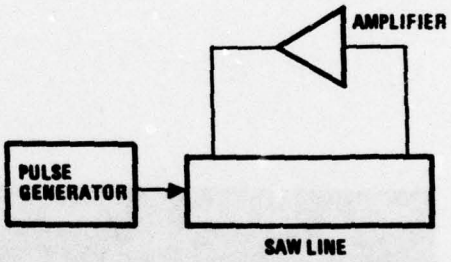

Figure 4. Frequency combination techniques.
(a) Pulse injection

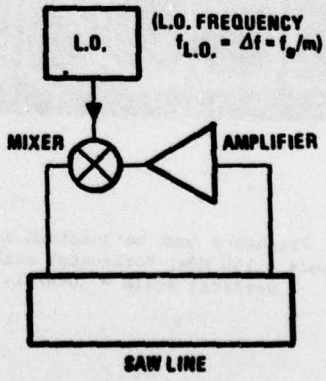

(b) Active phase locking

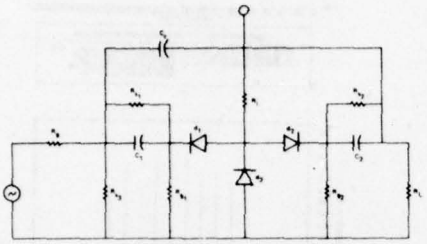

Figure 5. Schematic of single PIN diode switch.

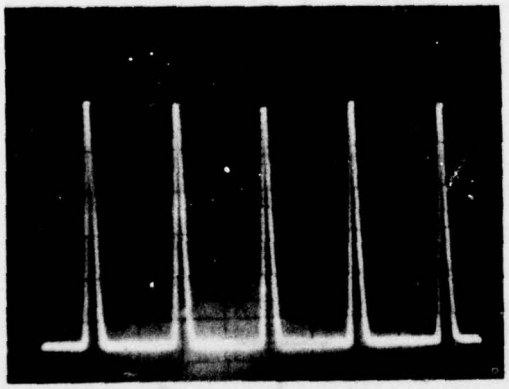

Figure 6. Frequency comb on spectrum analyser. Center frequency = 140 MHz; Horizontal scale = 5 MHz/div; vertical scale = 10dB/div.

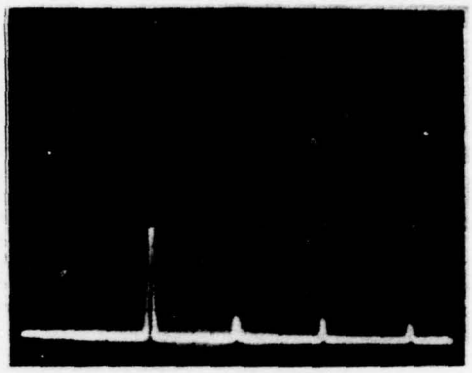

(a) 130 MHz Center Frequency
Scale: Vertical 10dB/Div.
Horizontal 5MHz/Div.

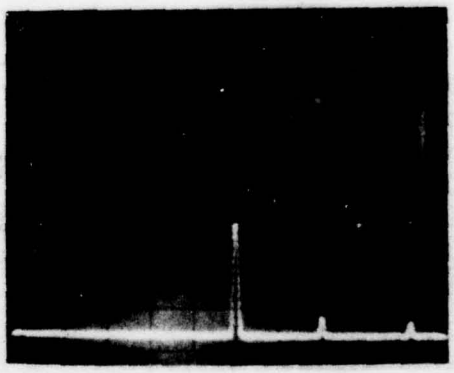

(b) 140 MHz Center Frequency
Scale: Vertical 10dB/Div.
Horizontal 5MHz/Div.

Figure 7. Outputs from two detection IDT's selected by pin switches.

FREQUENCY CONTROL AND TIME INFORMATION IN THE NAVSTAR/GLOBAL POSITIONING SYSTEM

F. E. Butterfield
Aerospace Corporation
El Segundo, California

Abstract

NAVSTAR/Global Positioning System (GPS) is a tri-service program for worldwide radio navigation using synchronized transmissions from a satellite constellation. All satellite clocks are referenced to a single ground based clock through periodic observations at fixed known locations, followed by a linearized real-time least squares estimation computation which establishes orbits and satellite time simultaneously. Time corrections are made as necessary through messages imposed upon the continuous satellite transmissions.

Satellite clocks are pseudo-random code generators driven by atomic standards from which the two carriers are also derived. Digital data are imposed modulo 2 on the PN code with data and code transitions coincident. The message content includes time of day, clock state (including effects of relativity), ephemeris, and almanac.

In the first phase of the program, six satellites will be placed in inclined 12-hr orbits such that they appear together over the U.S. daily. At completion, the second phase is expected to have at least nine satellites in orbit with two always in view around the world. The final phase plan calls for twenty-four satellites.

For a user at an unknown location, time is a normal output of the navigation fix obtained from observations on four satellites and an iterative location solution. The error budget for this case includes allowance for receiver noise, the atmosphere effect on propagation, uncertainties in the satellite clocks and orbits, and the effect of the geometrical situation (multipath transmission and geometric dilution of precision).

For greatest precision, the long code component of the transmission will be used. It will provide spatial resolution better than 100 feet and time resolution better than 100 nsec. A short code component is also available on one carrier which is modulated at 1/10 the rate of the long code and transmitted at 3 dB higher power level.

Key Words (for information retrieval) NAVSTAR/Global Positioning System, Geometric Dilution of Precision, satellites, navigation.

Introduction

In December of 1973, the Department of Defense began implementation of the Concept Validation Phase (Phase I) of the NAVSTAR/Global Positioning System. The initial apparatus for this new radio navigation program, now nearing completion, consists of six satellites with launch vehicles, a ground operations or control network, and six types of user equipment. This equipment will be emplaced and operated during the next year and three quarters in preparation for consideration by the Defense System Acquisition Review Council for continuation into Phase II, the System Validation Phase. In this phase, a limited operational capability will be established by 1981, consisting of nine orbiting satellites uniformly distributed in three orbit planes. Carried on into Phase III, the Production Phase, the system will contain in 1983 or 1984 eight satellites in each of these three planes for a total of 24.

Orbits

The orbit descriptions for the three phases are given in Table 1. For Phase I, the initial tolerances on these orbits are:

Period	±2 sec
Eccentricity	0.01
All Angular quantities	±2°

Since the program is in an early stage, these and other specifications may change as experience is gained with the actual hardware.

Ephemeris Determination

The satellites are equipped with coherent transmitters operating at 1575.42 and1227.6 MHz, and driven by atomic clocks with frequency stability specifications as shown in Figure 1. These transmissions will be monitored in Guam, Alaska, Hawaii, and Vandenberg Air Force Base (VAFB), California. The monitor station clocks are cesium standards. The time of arrival of transmission epochs will be observed at these monitor sites and passed to the Naval Surface Weapons Center (NSWC) at Dahlgren, Virginia where ephemerides will be estimated.

The NSWC computation will be carried out periodically and the results combined with daily monitor station observations in a second computation conducted at VAFB. These daily estimates will be used to describe the current ephemerides and clock states to users (navigators). The specified precision of these estimates in Phase I is indicated in Table 2. It is expected these values can be obtained with the rubidium standards on the Phase I satellites and the clock values may be considerably better.

The time reference for these estimates will be one of the monitor station standards. Thus, GPS system time is atomically derived and can be compared to UTC. In Phase I, differences will be a matter of record but not compensated by resetting satellite clocks. If individual satellites deviate from system time by more than 1 msec, they will be reset. In all cases the satellite clock state will be determined in GPS time.

Satellite transmissions are phase modulated carriers. At 1575 MHz, two modulations are used simultaneously. The first is one long pseudo-random binary sequence with shortest interval of 98 nsec deviating carrier phase ±90°. The second is a periodic pseudo-random binary sequence with shortest interval of 980 nsec and repetition rate of 1000 complete sequences per sec. The second binary sequence deviates the carrier 0° and 180°. The first sequence is called the P sequence, the second the C/A sequence. Their transitions are simultaneous and their epochs are common. The daily ephemeris and clock

state data derived at VAFB are added in binary form (modulo 2) to both the P and C/A sequences at 50 bps.

Conceptually, the process is illustrated in Figure 2. Only the P sequence and data are ordinarily applied to the 1227 MHz carrier in the Phase I satellites.

Transmitted Data

The content of the 50 bps data stream is not limited to information about ephemeris and clock. The full message for a selected satellite is diagrammed in Figure 3. It is organized in 6 sec, 300 bit segments transmitted in succession without interruption.

Except for the sections designated TLM and HOW, segment Ia is repeated in segments IIa, IIIa, IVa... until 120 repetitions have occurred. Then the content of the segment is changed to more closely represent the expected ionosphere correction and clock performance. Segments designated with a, b, and c are treated this way. Segment IId is not necessarily a repetition of Id. Segment IIe is not a repetition of Ie. These last segments carry almanac information about the other satellites in the constellation. Since this information is 190 bits per satellite, and since it is required much less urgently than the data of segments designated a, b, and c, it is transmitted approximately once every 15 min. It is not expected to be changed frequently; its primary use is in the process of signal acquisition. The clock state given in the almanac is expected to be represented there within ± 10 μsec of the actual satellite clock state.

The sections designated TLM contain a preamble and telemetry information connected with satellite operations. The preamble sets the reference for all successive bits.

The sections designated HOW are "hand over words" that describe the state of the P sequence at the beginning of the next 6 sec data interval. This information, read off the detected C/A signal, is used to set the P sequence generators in preparation for a transfer to P signal at the start of the next data interval.

All of the data in the data message, except for HOW, TLM are provided to the satellites by the upload station of the control or network. Nominally, this operation is conducted once a day.

The satellites generate the HOW and TLM words and the necessary parity connected with them. The satellites also respond to initializing and control commands from the upload station and the Air Force Satellite Control Facility. Clock frequency and code phase are both adjustable from the ground. There is an additional variety of commands that can cause the satellite to deviate temporarily from its predicted status. If the satellite is in this condition, appropriate warnings appear in the data message.

There are two relativistic influences to be accounted for: the satellite velocity and the gravity field. They introduce a constant frequency change and variations proportional to orbit eccentricity. The constant term is accommodated by a frequency offset in the atomic standard. The variations are incorporated in coefficients in the data message.

Performance

Navigation accuracy (and time recovery accuracy) is dependent upon the geometric disposition of the satellites and the signal conditions. The satellite output requirements are given in Table 3 in terms of the power developed in specific antennas on the earth. Since the signals penetrate both the ionosphere and the troposphere, the delay properties of these regions are important. The troposphere effects are expected to be modeled on the basis of local conditions. The ionosphere effects can be modeled or isolated by use of both the 1227 and 1575 MHz signals, which are simultaneously modulated in the satellite. Another effect of importance in navigation is that of multiple path propagation. This effect is rapidly varying in aircraft mounted terminals due to instability in attitude. For ground installations, the effect may vary more slowly and require additional integration for greatest precision. In time transfer applications where locations are known, the multipath effects can be reduced by use of moderate directivity in the terminal antenna.

The specified apportionment of navigation measurement errors is given in Table 4. These figures are the portions of measurement error that are uncorrelated over the satellites being used for navigation. The geometric effects are illustrated quantitatively in Figure 4 that shows the Phase III statistics on Geometric Dilution of Precision and its components. Navigation error, then, is the product of the measurement error and the appropriate dilution of precision factor.

One or more of the six Phase I satellites will be visible from any point on the earth almost all of the time, but they appear in groups suitable for navigation periodically. Because of the orbit period chosen, ground tracks repeat and the groupings persist at the geographical locations shown in Figure 5. The groupings occur at earlier local times on successive days. The time difference is 4 min per day. With the limited number of satellites in Phase I the dilution of precision factors exceed those of the full Phase III constellation.

Table 1. GPS Orbits

Period	- 43, 073.26 sec			
Eccentricity	- 0			
Inclination	- 63°			
Argument of Perigee	- 0°			
Phase I	Right Ascension of Ascending Node(1)	Mean Anomaly(2)		
Orbit Plane		A	B	
A	240°	-23.2° 16.8 56.8	16.8° 56.8 96.8	
B	120			
Phase II		A	B	C
A	240	0	0	0
B	120	120	120	120
C	0	240	240	240
Phase III		A	B	C
A	240	0 45 90	15 60 105	-15 30 75
B	120	135 180 225	150 195 240	120 165 210
C	0	270 315	285 330	255 300

(1) Referenced 21 March 1971

(2) Reference Midnight GMT 21 March 1971 (Right Ascension of Prime Meridian is 178.4°)

Table 2. Accuracy of Transmitted Ephemerides - Phase I

Component	Error (1σ) after 24 hr.
Radial	0.7m
Intrack	3.5m
Crosstrack	0.7m
Clock Bias	100 nsec
Clock Drift	1×10^{-12}
Clock Drift Rate	4×10^{-13}/day

Table 3. Signal Levels from Linearly Polarized Antenna with 3 dB Gain

Channel \ Signal	P	C/A
1575 MHz	-163 dBW and -160 dBW	
1227 MHz	-166 dBW or -166 dBW	
All transmissions are RHCP		

Table 4. GPS Error Budget (Phase III)

Space Vehicle Ephemeris	5 ft
Atmosphere	8 to 17
Space Vehicle Group Delay	3
Receiver Noise and Resolution	5
Multipath	4 to 9
Total RSS	12 to 21 ft

Satellite Clock Stability

PHASE I

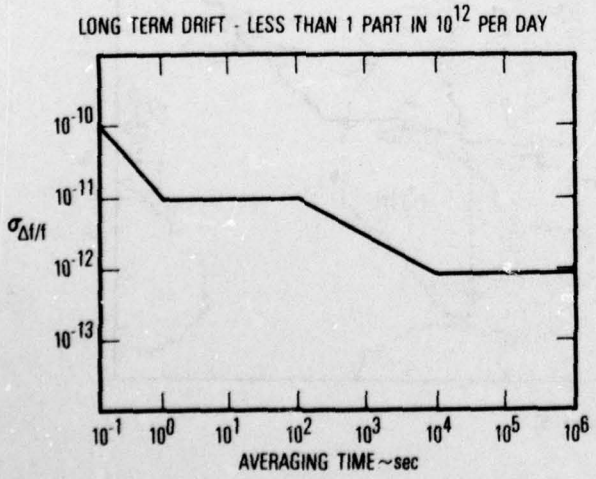

Figure 1.

Signal Assembly and Modulation for 1575 MHz Carrier

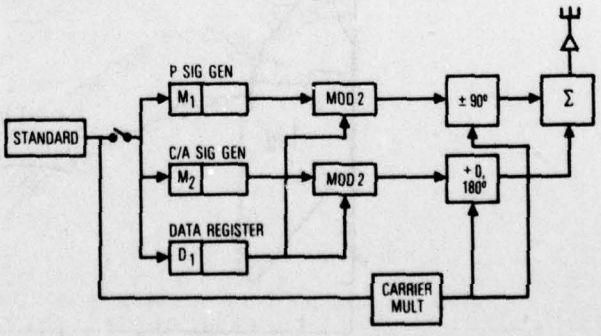

Figure 2.

Message Structure

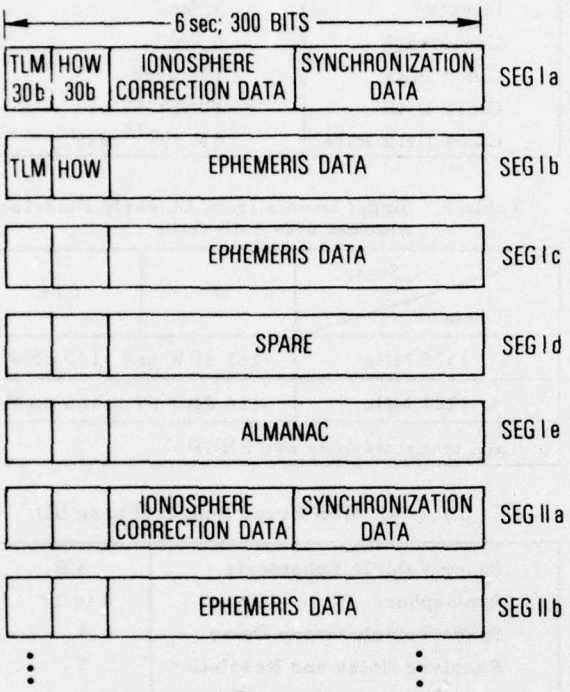

Figure 3.

GPS Phase III - Global Geometric Performance

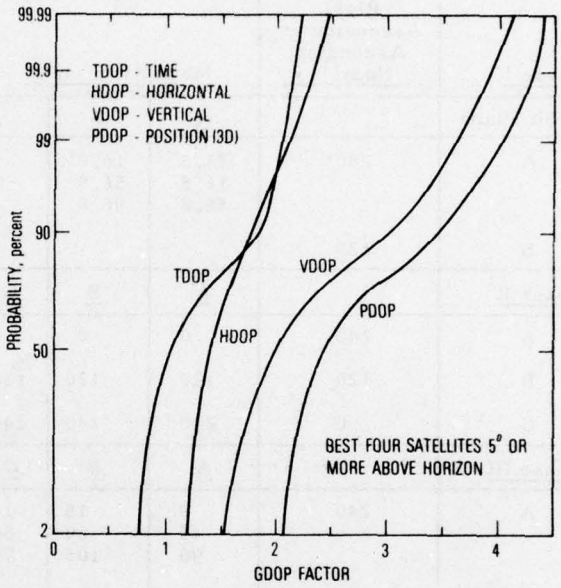

Figure 4.

Areas in Which Phase I Satellites Provide PDOP Less Than 4 as a Function of Time (hours)

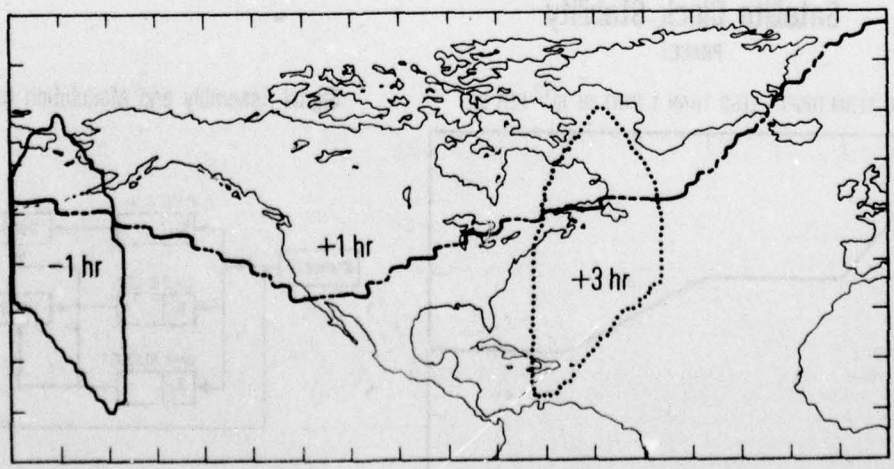

Figure 5.

TIME REQUIREMENTS IN THE NAVSTAR GLOBAL POSITIONING SYSTEM (GPS)

A. J. Van Dierendonck
General Dynamics Electronics Division
San Diego, California

M. Birnbaum
Space and Missile Systems Organization (SAMSO)
Los Angeles, California

Summary

GPS navigation is accomplished by one-way time measurements. One nanosecond time error equals 0.984 feet range error. Thus, time control and distribution are essential to GPS. The GPS Control Segment (CS) controls GPS time. The GPS Space Vehicles (SVs) distribute GPS time. Thus, requirements related to time are specified to the CS and the SVs.

There are three basic requirements (specified jointly to the CS and SVs) on GPS time derived from the system concept which provide: 1) compatibility with other timing and navigation systems; 2) "fast" User acquisition of GPS "P" signals, 3) continuous User navigation accuracy.

The requirement of GPS time to be compatible with other timing and navigation systems is a requirement for the CS to initialize and maintain GPS time to within 100 microseconds of Coordinated Universal Time (UTC). GPS will use external data that are time-tagged with UTC, and other systems will use GPS for time transfer.

For "fast" acquisition of the GPS "P" signal, the User must have the capability of acquiring that signal *directly*. To do so he is dependent on the a priori knowledge of the SV's times (to within about 10 microseconds) and positions (to within about 10,000 feet). Thus, the CS is required to initialize and control the SV clocks to within this tolerance, and the SVs clocks must be capable of being initialized and controlled to this tolerance. Precise a priori knowledge of time is not required for *normal* User acquisition of the GPS "C/A" signal

User navigation accuracy is directly related to his current knowledge of SV clock time. Thus, SV clocks are required to maintain a running time that is predictable to within GPS performance requirements. The CS is then required to predict their times, to generate SV clock update parameters, and to upload these parameters into the SVs.

To provide continuous user navigation, the SVs are required to continuously radiate signals with superimposed navigation parameters to the users. The CS is required to format these parameters and SV processor control parameters compatible with the SV processor design.

These basic requirements flow down to more specific derived requirements.

Introduction

GPS measurements are corrected transit times of SV generated signals radiated to a receiving User. Since the system is passive, the measurements are meaningful only if the times at which they are transmitted and received are precisely known. The fact is they are not, and the User must correct the apparent transit time with information supplied to him or solved for by him.

In Figure 1, four SVs are shown as required for a three-dimensional navigation solution. This is because the User does not normally know his time - User Time (UT). The offset of this time with respect to GPS time at the time of simultaneous receptions is denoted Δt_u and is common to all four measurements. The GPS reception time is:

$$t_R = UT - \Delta t_u \qquad (1)$$

and the GPS transmission time for SV i is:

$$t_{T_i} = t_{Ts_i} - \Delta t_{s_i}, \quad i=1,\ldots,4 \qquad (2)$$

where t_{Ts_i} is the SV time at time of transmission and Δt_{s_i} is the offset of this time with respect to GPS time. The atmospheric delays from the SV i are Δt_{A_i}. Random variations in the atmosphere, multipath and general transmitter and receiver noises are ignored; c is the speed of light.

The transit time is truly the difference between the GPS transmit time and the GPS receive time. It represents the true slant range except for the propagation delays (the Δt_{A_i}). The User's apparent transit time defines the pseudo-range measurement. The true slant ranges are:

$$R_i = c(t_R - t_{T_i}) - c\Delta t_{A_i}, \quad i=1,\ldots,4 \qquad (3)$$

while the corresponding pseudo-range measurements are

$$\tilde{R}_i = R_i + c\Delta t_{A_i} + c(\Delta t_u - \Delta t_{s_i}) = c(UT - t_{Ts_i}) \qquad (4)$$

Obviously, there are the three basic corrections that the User must account for to derive true slant range. The first is the SV clock offset which must be supplied to him; the second is the atmospheric delay, which only he can estimate as it depends on his geometry; the third is his clock offset which only he can determine - the reason for the fourth SV.

Supplying the User with a precise SV clock offset is the joint responsibility of the GPS Control Segment and the GPS Space Vehicle Segment (SVS). This objective and responsioility define the time requirements in GPS, which is, of course, the topic of this paper. A brief overview of the GPS segments and their relationship is given in Appendix I. These time requirements in GPS fall in one of three categories:

1) GPS time synchronization with UTC
2) SV time and data control for User acquisition
3) SV time and data control for precise continuous User navigation

The requirements of these categories will be discussed followed by considerations for the Phase III

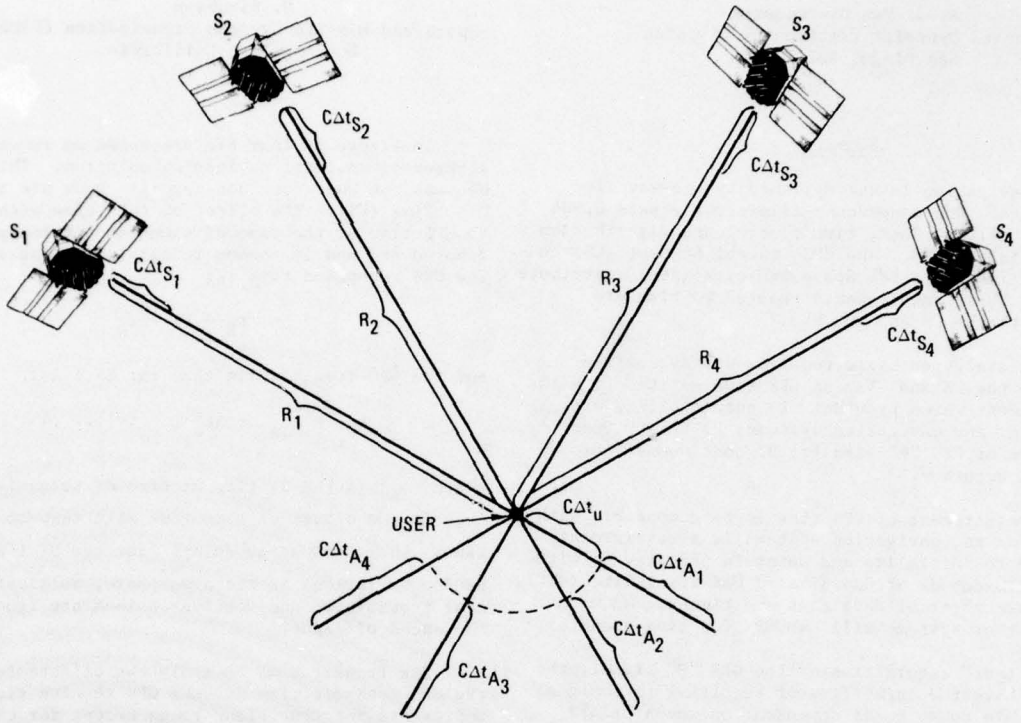

Figure 1. Relationship of Times Between SVs and User and Their Respective Ranges

operational GPS. The requirements discussed are for the Phase I concept validation of GPS, however, most of them extend to Phase III requirements.

GPS Time Synchronization with UTC

CS Specified Requirement

There is a requirement that the CS reference time shall not deviate from Coordinated Universal Time (UTC) by more than 100 microseconds.(1) The intent of this requirement is to synchronize GPS time with UTC. The purposes of this requirement are both internal to GPS as well as for external systems. Internally, the CS has components which are agencies that have no physical access to GPS time. These agencies - the Air Force Satellite Control Facility (AFSCF) has access to UTC, and the Naval Surface Weapons Center (NSWC) works with data referenced to UTC.

The AFSCF controls the Air Force SVs and provides a backup upload capability for the CS. It also performs the initial tracking of those SVs and provides the initial ephemeris epoch state to the CS for each of those SVs. None of these functions require time synchronization any more accurate than a second or two, but they do indeed require time synchronization.

NSWC periodically provides the CS with a reference ephemeris for each SV. These references are determined using data measured and time-tagged by the CS. Therefore, they should be, and will be, referenced to GPS time. NSWC does, however, as does the CS, use UTC time-tagged Sun and Moon locations in their respective ephemeris determination processes. Again, this does not require an accurate time synchronization, but does require "a" synchronization.

GPS Users, also internal to GPS, benefit by knowing GPS time prior to navigating with GPS. The extent of the benefit depends on how accurate their knowledge is. The maximum benefit is to know it to within 10 to 20 microseconds so as to perform direct "P" code acquisition. This requires that they have a stable frequency standard in order to stay synchronized to GPS time once they have ascertained it. Although synchronizing GPS time to within 100 microseconds to UTC may provide a marginal direct "P" code acquisition, the intent of the requirement is not, at least during the concept validation phase, to provide the capability to initialize Users with UTC.

Certainly a very important use of GPS is for time transfer for initializing or interfacing with external systems. This is probably where the real requirement for synchronizing GPS time to UTC really lies. However, to the authors' knowledge, there is no specific requirement to do it within 100 microseconds.

Although there doesn't appear to be a concrete reason for the 100-microsecond requirement during the initial phase of GPS, there is a requirement for "a" synchronization to UTC. Since a 100-microsecond synchronization is not an unreasonable requirement to

AD-A046 089 ARMY ELECTRONICS COMMAND FORT MONMOUTH N J F/G 9/5
PROCEEDINGS OF THE ANNUAL SYMPOSIUM ON FREQUENCY CONTROL (30TH)--ETC(U)
1976 H K ZIEGLER

UNCLASSIFIED NL

5 OF 6
AD
A046089

achieve with the use of a "flying" clock, it has been generally accepted as the requirement.

Related Requirements

There are four related requirements on the CS that serve to reduce the nuisance factor of maintaining synchronization of GPS time to UTC. These requirements specify the stability, the estimation accuracy and the control of the CS Monitor Station (MS) clocks, which provide the GPS time reference. These requirements are much more stringent than necessary for synchronization to UTC, as they are meant to maintain internal GPS system accuracy. They will be discussed in detail as requirements for SV time and data control for precise continuous User navigation. They do, however, eliminate the need for frequent monitoring and/or reinitializing GPS time with respect to UTC.

Derived Requirements

Although they are not specifically stated in any GPS system level or segment level specifications, there *are* requirements imposed on the CS that were derived during the design process. These are the requirements to: 1) initialize an MS clock with an external time source; 2) initialize the Upload Station (ULS) clock; 3) periodically verify the time difference between an MS time and UTC; and 4) publish the time difference between GPS time and UTC.

The reason for the first of these requirements is obvious. It is only necessary to do so at one MS as all other MSs are initialized via signals received from an SV. All MSs are capable of receiving a one second pulse from a "flying" clock (calibrated to UTC) to initilialize a time counter at a time entered into the MS computer. An operator-induced signal within the second prior to the correct pulse enables the counter. This initialized MS is the first "Master" MS as its time is considered perfect (within a known bias). The precise times at the other MSs are estimated through SV tracking and estimation.

The requirement to initialize the ULS (computer) clock is necessary regardless of the difference between GPS time and UTC because it is shut down whenever it is not in use. Time is necessary in the ULS for antenna pointing and for upload verification (within a second or two). The ULS computer or operators never have access to GPS time, but the operator does have access to UTC (via his calibrated watch). As will be discussed later, there can be a significant difference between GPS time and UTC (although known). Since the ULS receives parameters from the Master Control Station (MCS) used in functions of GPS time, either the operator or the computer must correct for the difference.

Of course, GPS time as defined by the "Master" MS and UTC are going to drift apart mostly because frequency standards cannot be perfectly calibrated. Since, the frequency difference won't be known initially, it will be necessary to verify the time difference between GPS time and UTC at later dates. Changes in the time difference may be predicted based on these verifications. To accommodate these verifications the MS clocks provide an output pulse every six seconds. Measuring time between one of these pulses and a one second pulse from a calibrated "flying" clock accommodates the verification.

To reset GPS time is disruptive to the continuous operation of the GPS system. Because UTC is not a continuous time reference (it has occasional one second jumps to be consistent with the earth's rotation rate), and because GPS time will drift away from UTC, maintaining GPS time to within 100 microseconds of UTC would be disruptive to the GPS system. To have discontinuities in GPS time would cause Users to lose lock from the GPS signals, and would cause extreme difficulties within the CS to coordinate the discontinuity. Thus, the requirement to merely publish the time difference between GPS time and UTC was derived. This publication is interpreted to meet the intent of the original 100-microsecond requirement.

SV Time and Data Control for User Acquisition

It is essential that the GPS SVs timing be under strict control to enable the Users to acquire their signals. The CS and the SVS are jointly required to maintain that control.

GPS Specified Requirements

This joint requirement is reflected in part in the overall GPS System Specification[2] that is referred to by the CS and SVS Segment Specifications.[1,3] The requirement is in the form of a definition of the Navigation Signal Structure. The specification states that the waveform shall be specifically designed to allow system time to be conveniently and directly extracted in terms of standard units of days, hours, minutes and integer multiples and submultiples of the second. It specifies the SVs "P" (precision) signal timing. The Pseudo-Noise (PN) code chipping rate is defined to be 10.23 megabits per second. The code epoch shall be made to occur exactly 7 days of elapsed system time after its last epoch by resetting itself routinely at seven day intervals. The measure of this elapsed time shall be the number of X1 (the first of two PN codes Modulo 2 summed together) epochs, termed the "Z" count, which have been counted since the PN code epoch. The time between X1 epochs shall be exactly 1.5 seconds of SV time. Thus, a Z count is worth approximately 1.5 seconds of GPS time.

The Z count shall be transmitted every six seconds, and shall be contained in the Handover Word (HOW) of the also Modulo 2 summed synchronous data bit stream D, and represents the system time at the start of the next data subframe (a subframe is six seconds long). The Z count value and the time of the PN code epoch shall be adjustable. Furthermore, all SVs shall transmit the same Z count within an accuracy dictated by derived requirements.

The C/A (clear/acquisition) signal code shall have a chipping rate of 1.023 megabits per second. Its XG code epoch shall occur every millisecond. There shall be a navigation data bit transition every 20 milliseconds, providing data at a rate of 50 bits per second. These bit transitions, the PN code epochs, the XG code epochs, the X1 code epochs and the D data bit stream epochs shall all occur in synchronization at their respective integral multiple rate. All rates shall be coherently derived from the frequency standard, and at the same rate on both the L_1 and L_2 frequency carriers, whose frequencies shall also be derived from that same standard.

The GPS System Specification also specifies the content of the signal data stream D. For the User the signal data has two functions. One is to allow the User to navigate continuously, which is discussed later, and the other is to aid the User to acquire the transmitted signals. Certain timing information in the data is essential for User acquisition:

1) System time
2) A preamble for synchronization

3) Subframe identification
4) SV clock information for all SVs

The system time shall be in the form of the Z count in the Handover word as described earlier. The preamble shall be a fixed 8-bit word that appears at the start of each subframe (every six seconds) which also shall coincide with an X1 code epoch and shall occur at the Z count transmitted in the previous HOW word. There shall also be a subframe identification in the HOW word, however, since the data stream epochs occur in synchronization with the PN code epochs, this information is redundant with the Z count.

For normal acquisition on "C/A", this is all the timing information that is required by the User, since once he has obtained synchronization with the data stream and received the Z-count, he is able to transfer to "P" signal tracking and collect data required for navigation. For direct acquisition on "P", however, the User requires a priori information on the SV whose signal he is trying to acquire. This information may have been prestored by the User, which is only useful if he knows GPS time and his position to within a few thousand meters. To normally know this information, he would normally have been tracking another SV signal. Thus, so that he may obtain the necessary information to directly acquire a new SV's signal, all SV data streams shall contain information on all SV positions and clocks (almanacs). This information shall appear in subframe 5 of the data stream, providing almanacs on the SVs on a rotating basis. The information on a given SV shall appear at least every 25th frame (made up of 5 subframes), or every 750 seconds. The clock information required in the almanac is the SV's time offset and drift, which provides the offset to within an accuracy dictated by derived requirements.

These system level timing requirements are all on the SVS, except for the requirements to synchronize the Z counts on all SVs and to provide the almanac contents. These two requirements are assigned to the CS.

SVS Specified Requirements

In addition to the GPS specified requirements, the SVS also has requirements from the SVS Specifications that control the SVs timing to enable User acquisition. These are three requirements on the Clock (oscillator) Assembly accuracy and control. The first is a frequency accuracy. The frequency error of the SV emission shall be less than one part in 10^8 during the life of the SV. An error of this magnitude represents a time drift of 864 microseconds a day and dictates derived requirements on the almanac word sizes jointly with the requirements on the frequency of Z count/code phase adjustments.

The second requirement is a requirement for digital tuning. That is, a capability shall be provided to reset the frequency in steps no larger than one part in 10^{10} over a range of ±4 parts in 10^9 around the nominal frequency via the TT&C (telemetry) subsystem. The purpose of this requiremnt is to minimize the SV clock time drift, and thus, minimize the derived requirements stated in the previous paragraph.

The third requirement is the requirement on the code reset. That is, the code phase and Z counter shall be capable of being reset to the nearest chip (98 nanoseconds) using the CS control link (upload). The necessity for this requirement is to maintain synchronization of timing between SVs and to minimize navigation data word sizes.

CS Specified Requirements

In addition to the GPS specified requirements, the CS also has two requirements from the CS Specifications that control the SVs timing to enable User acquisition. The first requirement is that the Master Control Station (MCS) shall be capable of generation of clock control commands (e.g., digital tuning) when required to maintain system accuracy, and to format these commands for upload to the SV. The formatted Z-count adjustment commands are included in normal CS uploads to the SV. The frequency adjustment commands will be commanded by the AFSCF via the TT&C command subsystem.

The second requirement is that the MCS shall be capable of generating an almanac for up to 24 SVs. The accuracy of the almanac shall be sufficient to allow each user to acquire the GPS navigation signals and get a position fix in a specified time. The almanac data shall be formatted for upload to each SV and are included in normal CS uploads to the SVs. The almanac clock data is obtained from a prediction of SV clock parameters, which are products of a related requirement on the CS. That requirement is for the generation of clock update parameters, whose accuracy must be much greater than required for the almanac. They are generated for User navigation purposes, and will be discussed in detail as requirements for SV time and data control for precise continuous User navigation.

Derived Requirements

Certain requirements not specified at the GPS system level or segment level were derived for the control of SV time and data to enable User acquisition. These are the requirements on the synchronization of time between the SVs, and thus, a requirement on the size of SV clock correction words in the navigation and almanac data. The derived requirement on synchronizing all SV's time to within one millisecond of GPS time is based on a derived requirement that all SVs transmit the same bit of the navigation data at the same time. Thus, the Users know what data they are collecting based on what time it is, or, for the sequential User (time-sharing one channel among 4 SVs), making it possible to collect data from all visible SVs on a reasonable time-sharing basis.

The time of the PN code epoch is not specified in either of the system level or segment level specifications. It has been defined to be approximately midnight Saturday Night/Sunday Morning.

SV Time and Data Control for Precise Continuous User Navigation

Given that the User is able to acquire and track an SVs signal and demodulate the system data, his next task is to navigate to an accuracy dictated by his mission. To do this he needs precise continuous knowledge of the position, velocity and time of up to four SVs in a desirable geometry. The CS and the SVS are required to provide this information to the User. The requirements for providing that SV time information is discussed here.

GPS Specified Requirements

The specification on User navigation accuracy in the GPS system is expressed indirectly in terms of User Equivalent Range Error (UERE). The navigation accuracy (one sigma) is normally estimated as the UERE times GDOP, where GDOP is the Geometric Dilution of Precision. GDOP is defined as the square root of the trace of the navigation and time error covariance

matrix (4 by 4) for the case where the pseudo-range measurement errors have unit variance and are uncorrelated. GDOP depends only on the relative geometry of the User and the SVs. At the same time, UERE is defined to be that uncorrelated portion of the observed range error.

The SV time error is directly a User Equivalent Range Error since it is always along the line-of-sight. It is also separated from the total UERE specification and is specified in the budget for the SV group delay. For Phase I, the specified budget is a UERE of nine feet (≈9.146 nanoseconds) (one sigma) that shall be applicable for two hours after all SVs are updated. For Phase III, the specified budget is a UERE of three feet (≈3.049 nanoseconds) (one sigma) that shall be applicable for twenty-four hours after all SVs are updated. This SV group delay is defined as the summation of delay uncertainty due to effects in the SV such as unmodeled clock drift and uncalibrated delay in signal equipment.

This UERE specification is a requirement on the CS and SVS jointly. It is a requirement on the SVS to provide predictable clock time offsets to within the SV group delay specification, allowing for reasonable CS prediction errors. Likewise, there is a requirement on the CS to predict the SV clock time offsets to within the SV group delay specification, allowing for unpredictable random SV clock errors. There is no clear division of the SV group delay error budget between the SVS and the CS, primarily because the stability of the SV group delay affects the CS's ability to predict it.

The GPS System Specification also specifies the content of Subframe 1 of the SV signal data stream, which the CS is required to provide. Subframe 1 shall consist of TLM and HOW words (provided by the SVS) and Data Block 1 (provided by the CS). Data Block 1 shall be generated by the CS and shall contain the frequency standard corrections. Corrections for relativistic phenomena shall be included within this data.

The purpose of Data Block 1 is to provide the User with SV clock correction information to correct for SV clock offsets to within the specified UERE (one sigma). In addition, because the SV clocks are at a different gravitational potential and are traveling faster than clocks on the earth, their times must be corrected for general relativistic effects. Although these effects wouldn't be classified as SV group delay, they are included in the clock correction information.

SVS Specified Requirements

In addition to the GPS specified requirements, the SVS also has requirements from the SVS Specifications that control the SVs timing for precise User Navigation. These are requirements on equipment group delay and on timing stability and clock drift. The specification states that the group delay from clock to radiated output shall be calibrated prior to launch. The effective group delay uncertainty of the PRN signal shall be less than 1.5 nanoseconds(one sigma) during normal operations, and less than 2.5 nanoseconds (one sigma) during SV eclipse operations. Equipment group delays are equivalent to time offsets. Therefore uncertainties which are biases, or very long time-constant variations, are of no consequence because they appear to be a clock time offset or drift. However, random or short time-constant equipment group delays affect the CS's ability to predict the SV clock drift. The purpose of this requirement is to minimize that effect.

Regarding timing stability, the specification states that, for all on-orbit conditions, the frequency stability shall be within the requirements specified in Figure 2. This figure represents the square root of Allan 2-sample variance[4] specification on clock stability. This translates to a clock time uncertainty versus time that is presented in Figure 3. In this figure, time drift representing the specified stability of Figure 2 is compared to that obtained in testing various frequency standards, two of which are engineering models of standards to be launched with GPS SVs. The 2.5 hour point represents the 2 hours after all SVs are updated, since the update time is estimated to be 0.5 hours.

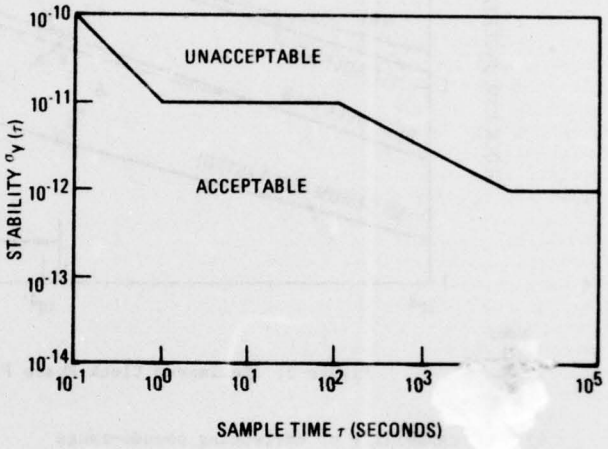

Figure 2. Clock Frequency Stability

CS Specified Requirements

The CS is required to provide the content of Data Block 1 which the User applies to correct for the SV time offset. The CS Specification states that the MCS shall be capable of processing retrieved data to generate a clock update (i.e., clock bias, clock frequency offset, and relativity effect) for each SV (up to 24) accurate to the level specified in the GPS Error Budget. The MCS shall generate these clock update parameters relative to the clock that is designated by the operator to be the master clock. The MCS shall be capable of formatting all SV update data consistent with the GPS signal structure, generating the SV data files and transmitting them to the ULS. The ULS shall be the primary means for uploading the GPS navigation subsystem with valid navigation data.

Related Requirements

In order for the CS to predict and generate SV clock update parameters to the accuracy level specified in the GPS Error Budget, it has these related requirements on its internal timing:

1) The requirement on stability and accuracy of the MS clocks
2) The backup power requirement to provide continuity of time
3) The capability to choose which clock is the master clock without destroying the continuity of time

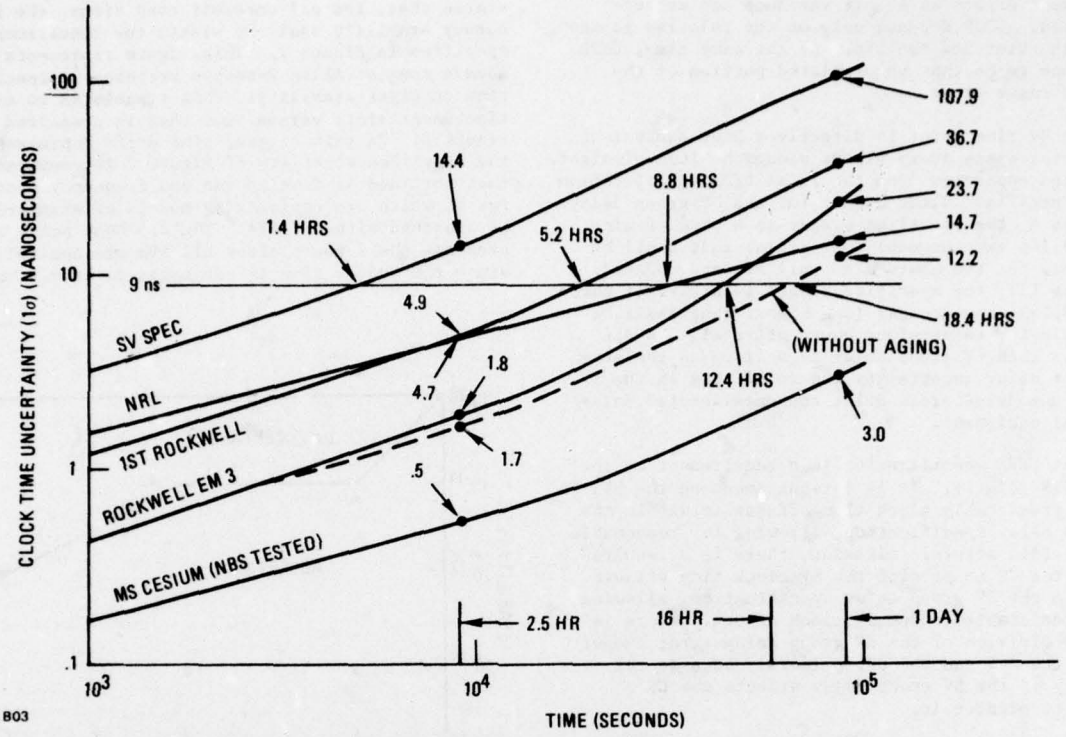

Figure 3. Estimated Clock Phase Prediction Error for Tested Standards

4) The capability of correcting pseudo-range measurements for SV clock relativistic effects

5) The capability to perform an optimal estimate of all CS clocks

6) To provide a system performance evaluation function to monitor the characteristics of all GPS clocks

The CS Specification states that each MS shall utilize a frequency standard for deriving its reference timing functions. The standard shall have a stability (the square root of Allan variance) of 1 part in 10^{11} for one second averaging and 1 part in 10^{13} for 10^4 seconds averaging. The standard shall not deviate from its assigned frequency (using averaging periods of 100 seconds or longer) by more than 5 parts in 10^{12} for up to one year after calibration. This requirement essentially specifics that high performance Cesium beam frequency standards be used in the MSs. The purpose of this high performance stability requirement is to enable an estimation of SV clock parameters without influence from the characteristics of the MS clocks.

With respect to power outage, the CS Specification requires that the MS components, e.g., time, timing, and frequency references, which require continuous power shall have backup power supplies that will provide 2 hours of operation in event of power outage. Besides reducing the nuisance factor, this requirement provides for a continuity of time in the MSs so that re-initialization and estimation of MS time will only be required after long-term power failures. Re-initialization and estimation puts the SVs in the role of providing the GPS time reference instead of the MSs, thus degrading the capability to estimate and predict SV time.

Because power outages and/or other equipment failures are bound to occur, there is a requirement that the MCS shall be capable of providing the operator with the means to select which CS clock shall be used as the Master Clock. If the "Master" MS loses its time reference, or if its time reference is in a degraded condition, another MS shall be designated the Master MS with a negligible shift in GPS time (expected to be no worse than 2 to 3 nanoseconds with a step change in frequency of no worse than 1 part in 10^{12}). This requirement ensures that there will always be a CS time reference of a quality required to estimate and predict SV time.

Secular relativistic effects on SV clocks, although significant, are not important to the estimation of SV clock parameters or SV ephemerides because they are not distinguishable from deterministic SV clock frequency offsets. These apparent offsets are common to both the CS and the User. Thus, they can be absorbed in the predicted SV clock parameters. However, there are also periodic relativistic effects on the SV clocks that are impossible to absorb in reasonable clock estimation models. Therefore, it is important that these periodic effects be accounted for in CS measurement processing as well as for SV clock parameter updates. Thus, the MCS shall be capable of correction of ranging data for relativistic effects.

The next CS requirement related to predicting and generating SV clock parameters is that the MCS shall be capable of performing an optimal estimation of all CS clock update parameters. Since the MSs are providing the time references for estimating the SV clock parameters, it is obvious that the relative difference between each non-Master MS clock and the Master MS clock must also be estimated.

A system performance evaluation function is also a requirement on the CS. This requirement, although not critical to the estimation of SV clock parameters, provides for a real time evaluation of the estimation and prediction process as well as the health and performance of the various system clocks. Specifically, the MCS shall provide performance evaluation of: 1) residuals between the latest observed SV clock state and the state predicted by clock parameters in the navigation data frame (an evaluation of the difference between what the User is receiving and what the CS is currently estimating); 2) residuals between the estimate of the SV clock state at the latest epoch and the state which was predicted for that epoch 1, 4, 12, and 24 hours before (an evaluation of the stability of the SV clock); and 3) the uncorrected, synchronization error between the GPS time standard and all MS and SV clocks (an at a glance evaluation of all the system clocks as compared to GPS time to monitor the performance of the MS clocks and to ensure the required synchronization between all clocks and GPS time).

Derived Requirements

Many of the requirements specified by the GPS system level and segment level specifications regarding SV time and data control for precise continuous User navigation are not specific. The reason for this is that the requirements affect the designs in three segments - the CS, the SVS, and the User Segment (US). Many of these requirements could not be defined at the time the system and segment level specifications were generated, because they had to be derived jointly by the three segments. The vehicle for deriving these requirements is an Interface Control Working Group made up of members of the three segments. The resulting document is an *Interface Control Document* (ICD)(5) referenced in the GPS system and all segment level specifications. This document imposes derived requirements on all three segments. The requirements regarding SV time and data control for precise continuous User navigation are:

1) Differential SV group delay between L_1 and L_2 "P" signals
2) L_1-L_2 correction for single frequency Users
3) The exact contents of Data Block 1
4) The format of Data Block 1
5) The User algorithms for SV clock corrections

The first of these requirements was not addressed in the SVS Segment Specification. It is only important to the two-frequency User if the differential group delay is random or time varying with a short time constant, for the same reasons discussed earlier for the SVS Specification on equipment group delay. The ICD states that the differential group delay between the radiated L_1 and L_2 "P" signals shall be specified as consisting of random plus bias components. The mean differential delay shall be defined as the bias offset in the (L_1-L_2) P differential delay. For a given Navigation Subsystem redundency configuration, the mean delay shall not exceed 15.0 nanosec. The random variations about the mean shall not exceed 1.5 nanosec (one sigma). Since both the CS and the two-frequency User use the L_1-L_2 difference for ionospheric corrections, any differential delay is mutiplied by a factor of 1.5625. Thus the 15 nanoseconds results in a 23.44 nanosecond SV clock offset. Because this would be normally absorbed in the SV clock offset estimate and prediction, it will have no effect on the two-frequency User. It will have an effect on the single-frequency User, since the observed clock offset to him does not include this delay.

As a safeguard against an appreciable differential group delay between the SV L_1 and L_2 "P" signals, a requirement was derived to provide for an L_1-L_2 correction for the single frequency User. The ICD states that the L_1-L_2 correction term, T_{GD}, is an estimated correction term to account for SV differential group delay between L_1 and L_2. This correction is only for the benefit of L_1 Users because SV clock corrections are based on two frequency corrections. The L_1 User shall correct SV PRN code phase time, t_{Ts_i}, with the equation

$$t_{Ts_i} = t_{Ts_i} + T_{GD} \tag{5}$$

The CS will be required to estimate T_{GD} during periods when the ionospheric delay is at a minimum.

The CS is required to provide the content of Data Block 1 as described in the ICD. In addition to T_{GD} and eight ionospheric model coefficients, Data Block 1 shall contain the SV clock correction parameters. These parameters shall be the three polynomial coefficients a_o, a_1 and a_2, a reference GPS time since weekly epoch, t_{oc}, and an age of data (clock), AODC. The polynomial shall describe the SV PRN code phase (clock) offset, Δt_{s_i}, with respect to GPS time, t_{T_i}, at the time of data transmission. These coefficients described the offset for the interval of time (one hour as a minimum) in which the parameters are transmitted. The polynomial shall also describe the offset for an additional one-half hour (i.e., one-half hour subsequent to the beginning of transmission of the next set of coefficients) to allow time for the User to receive the message for the new interval of time. The age of data word (AODC) shall provide the User with a confidence level in the SV clock correction. AODC represents the time difference (age) between the Data Block 1 reference time (t_{oc}) and the time of the last measurement update (t_L) used to estimate the correction parameters. That is,

$$\text{AODC} = t_{oc} - t_L \tag{6}$$

Describing the SV clock correction as a polynomial satisfies the requirement to provide the User with data for continuous navigation.

The CS also has a requirement to format the Data Block 1. Of importance in these discussions is the range and scale factor of the SV clock correction parameters and the L_1-L_2 correction. Table 1 specifies the format of these parameters as given in the ICD. The scale factors determine the accuracy. They were selected to provide correction accuracy on the order of a nanosecond. The ranges were dictated primarily by the worst case SV clock drift characteristics, the desire to minimize the number of SV clock control commands, and the requirement to synchronize the PN code epochs of the various SVs. The range of a_o (976.6 microseconds) indicates the accuracy of that synchronization.

For continuous SV clock correction the User shall correct the time received from the SV with the equation (in seconds)

$$t_{T_i} = t_{Ts_i} - \Delta t_{s_i} \tag{7}$$

where

$$\Delta t_{s_i} = a_o + a_1 (t_{T_i} - t_{oc}) + a_2 (t_{T_i} - t_{oc})^2 \tag{8}$$

Note that equations (7) and (8) as written are coupled. While these coefficients a_o, a_1, and a_2 are generated by using GPS time as indicated in equation (8), the sensitivity of Δt_{s_i} to t_{T_i} is negligible.

Table 1. Data Block 1 Parameters

Parameter	No. of Bits	Scale Factor (LSB)	Range*	Units
T_{GD}	8	$2^{-31} \approx 4.66 \times 10^{-10}$	$\pm 2^{-24} \approx \pm 5.96 \times 10^{-8}$	Sec
AODC	8	$2^{11} = 2048$	$2^{19} = 524288$	Sec
t_{oc}	16	$2^{4} = 16$	604,784	Sec
a_2	8	$2^{-55} \approx 2.78 \times 10^{-17}$	$\pm 2^{-48} \approx \pm 3.553 \times 10^{-15}$	Sec/sec^2
a_1	16	$2^{-43} \approx 1.14 \times 10^{-13}$	$\pm 2^{-28} \approx \pm 3.725 \times 10^{-9}$	Sec/sec
a_o	24	$2^{-33} \approx 1.164 \times 10^{-10}$	$\pm 2^{-10} \approx \pm 9.766 \times 10^{-4}$	Sec

*(±) indicates that sign bit shall occupy the most significant bit (MSB)

NOTE: All binary numbers shall be two's complement.

This negligible sensitivity will allow the User to approximate t_{T_i} by t_{Ts_i} in equation (8). The parameters a_o, a_1 and a_2 shall include all general relativistic effects on the SV clock.

Summary of GPS Time Synchronization

The time synchronization between GPS time and UTC, the MS clocks, the SV clocks, and the User clocks is summarized in Figure 4. This diagram illustrates the maximum clock offsets between the various clocks and GPS time and an expected or required Phase I tolerance on the estimate of those offsets. The MS and some User maximum offsets (3.1 sec) are dictated by the size of the pseudo-range register in their respective receivers. Normally, this offset will never be more than a few millisec. The User tolerance was obtained by multiplying a GPS specification specified UERE of 18 to 24 ft times an expected TDOP of 2.5. (TDOP is the Time Dilution of Precision.)

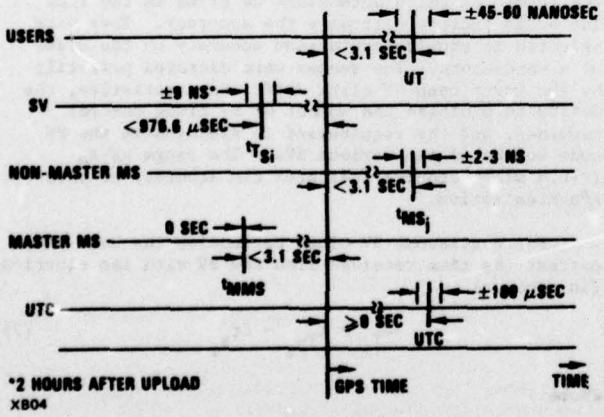

Figure 4. GPS Time Synchronization for Phase I

Consideration for Phase III

Relative to GPS time, there are surely numerous improvements that can be made over the Phase I system. Certainly the most important will be the evolution of better frequency standards, especially those qualified for space vehicles. Another very important improvement could be in the ability to estimate and predict their behavior in the space vehicle environment. The concept validation will provide increased knowledge in both of these areas.

Another important consideration for time in the operational GPS is its relationship to the Universal Coordinated Time (UTC). Without very much difficulty, GPS time could be synchronized to UTC to within a few nanoseconds - at least to a known difference. This could be easily realized by placing a GPS User Set in coincidence with a UTC time reference and continually monitoring the time difference between GPS time and UTC. In fact, the GPS User Set could be slaved to a UTC standard. A normal User set will solve for the difference in time.

The fact that there will be a difference between GPS time and UTC does not pose a problem to the time transfer Users, for in Phase III, that time difference can be transmitted via the navigation data stream as part of Data Block 1.

APPENDIX I

The relationship between the Control Segment (CS), the Space Vehicle Segment (SVS) and the User Segment (US) of the Global Positioning System is illustrated in Figure 5.

To the User GPS appears to be a passive system, since all he observes are the L_1 and L_2 navigation signals from the SVS. The CS, however, not only observes the L_1 and L_2 navigation signals, but also communicates with the SVS via an S-band uplink. The received signals provide ranging data and upload verification through the Monitor Stations (MS) to the Master Control Station (MCS) via dedicated communication lines. The MCS is a data processing facility that uses this ranging data to estimate and predict the SVS ephemerides and clock characteristics. Periodically, it formats the predictions along with other Space Vehicle (SV) processor control data, passes this data to the Upload Station (ULS), which in turn uploads the data into the SVs via the S-band link. At a time dictated by control data upload into the SVs, the SVS will commence to transmit the new upload data, providing the Users with fresh, accurate navigation information.

The Air Force Satellite Control Facility (AFSCF) is not part of either of these segments, except that it provides a backup upload capability. The AFSCF does, however, control the SV except for the normal day-to-day primary SV uploading.

The Naval Surface Weapons Center (NSWC) acts as part of the CS. Their role is to provide reference ephemeris data and force model parameters to the MCS, which are based on measurement data provided to them by the MCS.

The Inverted Range Control Center (IRCC) is a test facility for GPS during the Phase I operations, but does not interface with the segments except as a receiver of signals. During non-testing periods, however, the IRCC has the capability of being a backup MS, and could serve as one, if needed.

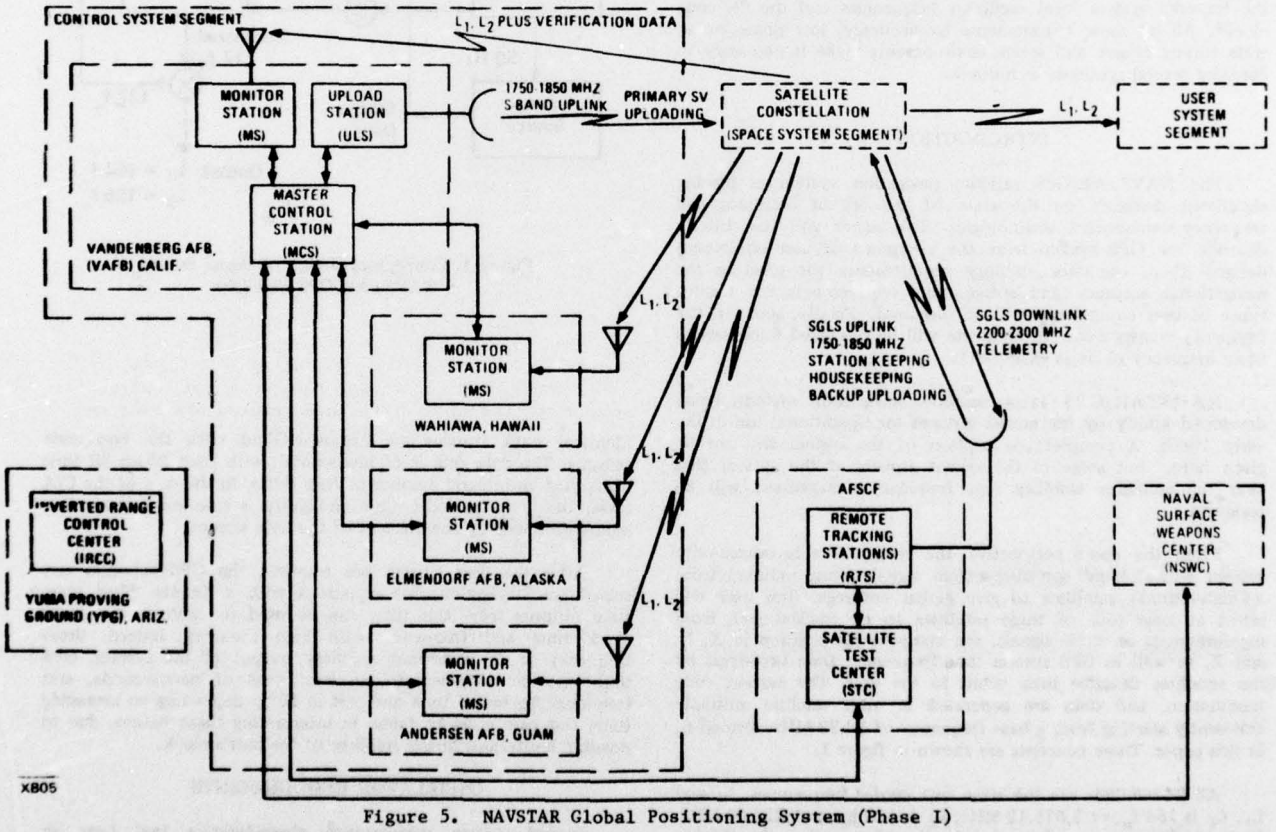

Figure 5. NAVSTAR Global Positioning System (Phase I)

References

1. System Segment Specification for the Control Segment of the NAVSTAR Global Positioning System, Phase I, SS-CS-101B, 30 Sep 74.

2. System Specification for the NAVSTAR Global Positioning System, Phase I, SS-GPS-101B, 15 Apr 74.

3. System Segment Specification for the Space Vehicle System Segment of the NAVSTAR Global Positioning System, Phase I, SS-SVS-101A, 20 Jun 74.

4. Time and Frequency: Theory and Fundamentals; Byron E. Blair, Editor, National Bureau of Standards Monograph 140, May 1974.

5. Space Vehicle Nav System and NTS PRN Navigation Assembly/User System Segment and Monitor Station, Interface Control Document MH08-00002-400, Revision E, 19 Sep 75.

OSCILLATOR AND FREQUENCY MANAGEMENT REQUIREMENTS FOR GPS USER EQUIPMENTS

Robert A. Maher
Texas Instruments Incorporated
Dallas, Texas

SUMMARY

The NAVSTAR/GPS (Global Positioning System) is a spread-spectrum precision satellite navigation system scheduled for operational use starting in the early eighties. Significant demands will be placed on oscillator stability and frequency management technologies to achieve the full navigational accuracy and antijam potentials intended for the system. This paper discusses these requirements for a variety of types of GPS User Equipments. Also discussed are various related frequency/time management requirements for the user equipments. The frequency management requirements involve calibration of the reference oscillator against the GPS system time/frequency as well as phase-stable synthesis of the required system local oscillator frequencies and the PN code clocks. All of these requirements on accuracy, low phase noise, wide tuning ranges, and severe environments make it necessary to consider several synthesis techniques.

INTRODUCTION

The NAVSTAR/GPS satellite navigation system is placing significant demands on the state of the art of oscillator and frequency-management technologies. This paper will first briefly describe the GPS system from the viewpoint of user equipment design. Then, oscillator stability requirements for meeting the navigational accuracy and antijamming requirements for various types of user equipments will be discussed. Finally, some of the frequency-management requirements will be discussed using several basic frequency plans as examples.

NAVSTAR/GPS is a satellite navigation system being developed jointly by the armed services for operational use in the early 1980s. A complete description of the system will not be given here,[1] but some of the salient aspects of the system that bear on oscillator stability and frequency-management will be reviewed.

From the user's perspective, the system is a broadcast-only system with L-band spread-spectrum signals being radiated from 24 high-altitude satellites to give global coverage. The user will select at least four of these satellites to be tracked and, from measurements on these signals, can compute his position in X, Y, and Z, as well as GPS system time/frequency. Data broadcast by the satellites describe their orbits to the user. The carrier, code modulation, and data are generated in each satellite mutually coherently starting from a base frequency of 10.23 MHz, termed f_o in this paper. These concepts are shown in figure 1.

All 24 satellites use the same two carrier frequencies, L_1 and L_2. L_1 is 154 f_o, or 1,575.42 MHz; L_2 is 120 f_o, or 1,227.60 MHz. Each satellite uses a distinct set of codes, and code division multiplex is used to separate the satellite signals from each other. The use of two different frequencies from each satellite allows measurements to be made by the user for ionospheric delay correction. Two codes are used. One, termed C/A, is a Gold code and is periodic in 1 ms and has a chip rate of $f_o/10$ chips per second; the other, termed the P-code, has a period of one week, and a chip rate of f_o chips per second. Both codes can be simultaneously present on quadrature components of the carrier.

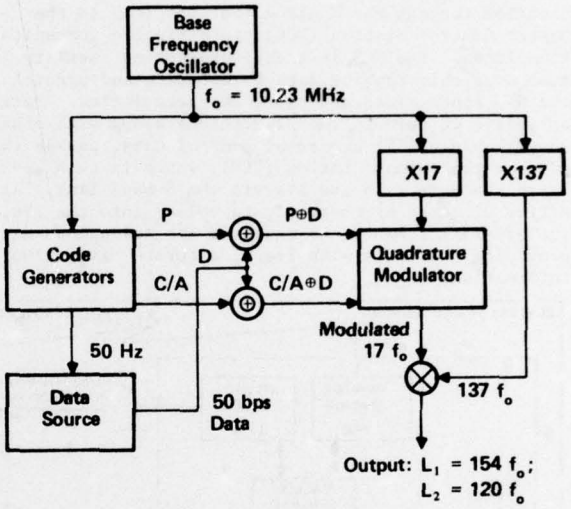

Figure 1. Conceptual Design of Signal Source in NAVSTAR/GPS Satellites

Identical data streams are exclusive-ORed with the two code streams. The data rate is 50 bits/second, with each 20 ms bit time occupying an integral number of chip times. In the case of the C/A code, the 1 ms periodic time ambiguity is resolved by the data modulation and by the content of the data stream.

After the user system has acquired the GPS satellites and solved the navigation/time equations with a Kalman filter, then state outputs from this filter can be used to calibrate the user's clock time and frequency with high accuracy; indeed, time/frequency is an important ancillary output of the system. GPS time can be obtained to at least tens of nanoseconds, and frequency to better than one part in 10^{10}, depending on averaging time. But care must be taken in interpreting these figures, due to possible limitations in the stability of the user's clock.

OSCILLATOR REQUIREMENTS

Several system performance characteristics that bear on oscillator stability requirements will be discussed in this section. Parameters chosen as examples are intended to be representative of the range of user equipment types that are being considered. These range from inexpensive, low-accuracy, single-channel systems to multiple-channel, high-dynamic, high-antijam missile equipments. The various oscillator stability requirements are summarized in Table I. The basic measure of oscillator stability used is the well known Allan Variance[2] for various specified gate times.

TABLE I. SUMMARY OF OSCILLATOR STABILITY REQUIREMENTS

Reason	Measurement Gate Time, τ (seconds)	Square Root of Allan Variance, σ	Assumptions	
Doppler Search	$>10^3$	10^{-7}	±150 Hz cell; one cell due to oscillator uncertainty; L_1 operating frequency	
Dead Reckoning	100 10	10^{-10} 10^{-9}	≈ 10-foot drift	
Sequential Pseudorange Measurement	5 0.5	6.7×10^{-10} 6.7×10^{-9}	5-foot error; GDOP = 3	
Noise in PLL Due to Oscillator	1	2.5×10^{-11}	BL = 1 Hz	0.1 radians, rms; L_1 operating frequency (includes any degradation due to multiplication)
	0.063	4×10^{-10}	BL = 15 Hz	
	10^{-2}	2.5×10^{-9}	BL = 100 Hz	
Pseudorange Noise (Incremental Range)	0.1	6.7×10^{-10}	Error due to oscillator: 0.02 m/0.1 second	

Carrier Tracking Bandwidth and Antijam Margin

The term "carrier tracking bandwidth" in this paper refers to the bandwidth, B_L, of whatever servo loop is being used to track the carrier's phase (or frequency) after carrier acquisition has been accomplished. Generally speaking, the narrower this bandwidth, the greater will be the antijam (A/J) margin for maintaining carrier lock. For the user to initially obtain the 50 bps navigation (satellite ephemeris) data the C/N_o must be at least +25 dBHz or so, which implys a maximum P-code A/J margin of 45 dB to obtain data.

But once the ephemeris data for a given satellite is obtained, it will be valid to reasonable navigation accuracy for about an hour. During this time, one can utilize narrower carrier-tracking bandwidths to track the satellite signal in the presence of a higher level of jamming, even though the data is not currently obtainable. In this circumstance, data modulation becomes a frustration to narrowing the bandwidth since there is no pure carrier component broadcast and a costas-type phase detector must be used, with its attendant squaring loss and higher threshold accepted.[3]

Oscillator stability becomes of increasing concern as the carrier-tracking bandwidth is lowered. An expression that gives the required Allan Variance for a given carrier loop bandwidth and desired rms phase error due to oscillator instability is given by Equation 1.

$$\sigma = K \frac{\Delta\theta}{\omega_o \tau}$$

where

σ = square root of Allan variance

$\Delta\theta$ = allowable phase error, radians rms, due to oscillator short-term stability

ω_o = carrier frequency, radians/second

τ = gate time, chosen to be the reciprocal of the equivalent noise bandwidth of the carrier tracking phase-lock loop

K = 2.5 for 2nd order δ = 0.707 loop

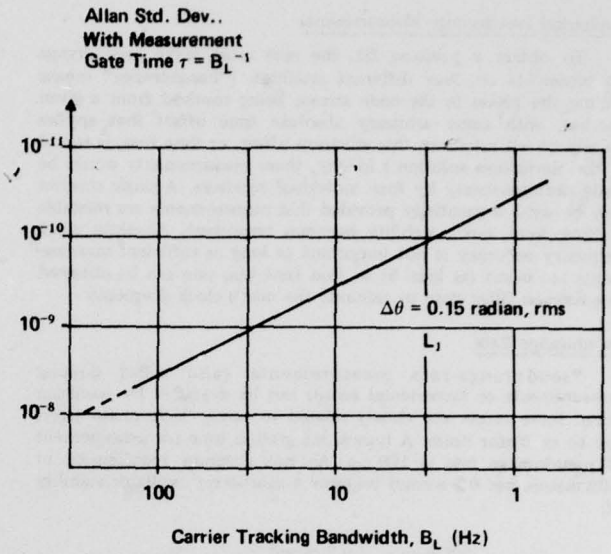

Figure 2. Oscillator Stability Requirements for PLL Noise

This expression holds true with good accuracy for a wide range of spectral dependencies of oscillator noise.[4] Assuming a phase jitter of 0.15 radian rms and the L_1 carrier frequency, application of Equation 1 gives the results shown in figure 2. It should also be noted that for carrier-tracking bandwidths much less than 10 to 15 Hz, allowable user dynamics become restricted unless estimation by an inertial system is used to aid the carrier loops.

A plot of achievable antijam margin can be generated using the above results, and assuming the squaring loss considerations discussed earlier. These results are shown in figure 3 as tolerable J/S level versus carrier-tracking loop bandwidth. For the higher jamming a hold-on mode of operation is assumed wherein the data is not currently obtainable; only tracking and navigation with previously obtained ephemeris data are being done. The curve assumes a constant 0.15 radian rms phase error due to local oscillator instability, as given by Equation 1. Also assumed is a constant 11 dB SNR in the loop bandwidth.

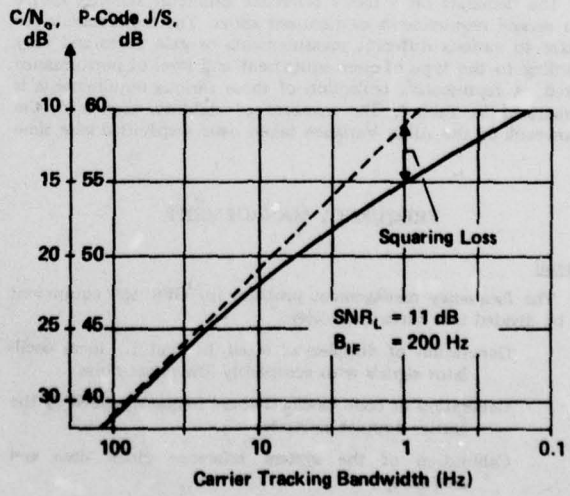

Figure 3. Jamming Level Versus Carrier-Tracking Bandwidth

Sequential Pseudorange Measurements

To obtain a position fix, the user must make pseudorange measurements on four different satellites. ("Pseudorange" means finding the phase in the code stream being received from a given satellite, with some arbitrary absolute time offset that applies equally on all satellites; this arbitrary offset, or time bias, is solved in the navigation solution.) Ideally, these measurements would be made simultaneously by four individual receivers. A single receiver may be used sequentially provided that measurements are relatable in time; here, clock stability becomes important. Absolute clock frequency accuracy is not important as long as sufficient measurements are taken (at least 5) so that time bias rate can be obtained as a Kalman filter state to calibrate the user's clock frequency.

Pseudorange Rate

Pseudorange-rate measurements (also called doppler measurements or incremental range) can be degraded by oscillator noise; these errors are closely related to carrier loop phase errors due to oscillator noise. A typical integration time for measurement of pseudorange rate is 100 ms. An rms accuracy requirement of 0.02 meters per 0.1 second requires a short-term oscillator stability of:

$$\sigma = \frac{0.2 \text{ m/sec}}{c} = \frac{0.2 \text{ m/sec}}{3.10^8 \text{ m/sec}} = 6.7 \times 10^{-9}$$

Dead Reckoning

The dead-reckoning problem is one of clock extrapolation and is closely akin to the sequential pseudorange problem, which is one of clock interpolation. The dead-reckoning problem can occur if one (or more) of the navigation satellite signals is unavailable, due, for example, to a spate of excessive jamming or an occlusion of the line-of-sight path. Then, it may be desirable to carry on navigation, or at least to minimize the amount of clock drift to minimize direct (P-code) reacquisition time. Table I shows the clock stability required for an assumed 10-foot rms position drift.

Long-Term Frequency Accuracy

The requirements for long-term frequency accuracy are determined primarily by the doppler search requirement. A typical doppler search cell size is ±150 Hz. To have one additional cell to search because of oscillator inaccuracy dictates an absolute frequency accuracy of $\pm 10^{-7}$ for 1.5-GHz (L_1) operation.

Summary of Oscillator Requirements

The demands on a user's reference oscillator stability derive from several requirements as discussed above. The requirements are relative to various different measurements or gate times and vary according to the type of user equipment and level of performance desired. A representive collection of these various requirements is summarized in Table I. The measure of stability used is σ, the square-root of the Allan Variance taken over a specified gate time τ.

FREQUENCY MANAGEMENT

General

The frequency management problem for GPS user equipment can be divided into three categories:

- Generation of doppler-corrected L_1 and L_2 local oscillator signals with acceptably low phase noise
- Generation of code clocks that are frequency-aided by the carrier doppler estimates
- Calibration of the system reference clock time and frequency.

Frequency Plans

A short discussion of possible frequency plans will be given here. The set of alternatives discussed is by no means exhaustive; indeed, an extremely wide range of frequency plans is possible. Rather, it is hoped that the examples chosen will illustrate some of the salient considerations. Representative doppler magnitudes are shown in Table 2 for three types of user equipment.

TABLE II. REPRESENTATIVE DOPPLER MAGNITUDES

User Equipment	Relative Velocity, V (meters/sec)	V/C	Hz at L_1 (kHz)	Hz at f_o (Hz)
Manpack	±1,100	$\pm 3.7 \times 10^{-6}$	±5.8	±38
HDUE	±2,200	$\pm 7.3 \times 10^{-6}$	±11.6	±75
Missile	±10,000	$\pm 3.3 \times 10^{-5}$	±52.5	±341

Three possible plans are shown in basic form in figure 4. These are the long-loop, short-loop, and (1 + v/c) approach. Doppler at the base frequency is designated as $f_o' = f_o + \Delta f$. In all instances double conversion is somewhat arbitrarily assumed, with nominal intermediate frequencies of 18 f_o and f_o. Code Injection precedes the first conversion. In the long-loop approach, all doppler is removed at the first conversion. All of the circuitry following the first conversion can then have minimum bandwidth; with all of the code and doppler removed the minimum IF bandwidth is determined solely by the 50 bps data modulation.

With the short-loop approach the dopper is removed on conversion to baseband Fixed first and second local oscillator frequencies are then possible, but then the IFs must handle the full doppler range. An obvious intermediate approach would be to remove all the doppler at the second conversion.

The (1 + v/c) approach has all signals and local oscillator frequencies scaled by the fractional doppler shift (1 + v/c), where v is the user/satellite relative velocity, and c is the speed of light. An advantage of the (1 + v/c) approach is that a doppler-corrected clock (e.g., 17 f_o') is directly available for the code generator.

The choice of 18 f_o as the first IF in these examples has the advantage of allowing the use of a simple 3/4 multiple in choosing between the L_1 and L_2 receive frequencies. IFs at f_o, or multiples thereof, run the risk of self-jamming due to the local code clock at f_o. Choice of other IFs is of course possible, but will require slightly more complex synthesis of the local oscillators.

The long-loop and (1 + v/c) approaches are shown in more detail in figures 5 and 6, respectively. The L_2 case is shown with parentheses. A digital carrier loop filter is indicated in figure 5. Here the digitized costas loop phase error is operated on digitally in closed-loop fashion to produce a doppler frequency-control word to drive an incremental phase modulator (IPM), which will modify the multiplied reference frequency (136 f_o or 102 f_o) by an amount necessary to remove the doppler. If (1 + v/c) is the correct proportional doppler shift, then (1 + Kv/c) is the proper multiplier for the first local oscillator in the long-loop approach shown. For L_1, K = 154/136; for L_2, K = 120/102. If a digitally-controlled advance-retard clock generator modifies the reference frequency, 17 f_o according to K = 1, then a properly corrected doppler code clock results.

Note that in the long-loop approach shown in figure 5 synthesis of all frequencies starts with a fixed reference frequency at f_o = 10.23 MHz.

A 1023/1000 shift of the f_o reference frequency provides a convenient 10 MHz signal for the various system clocks and for the range counter.

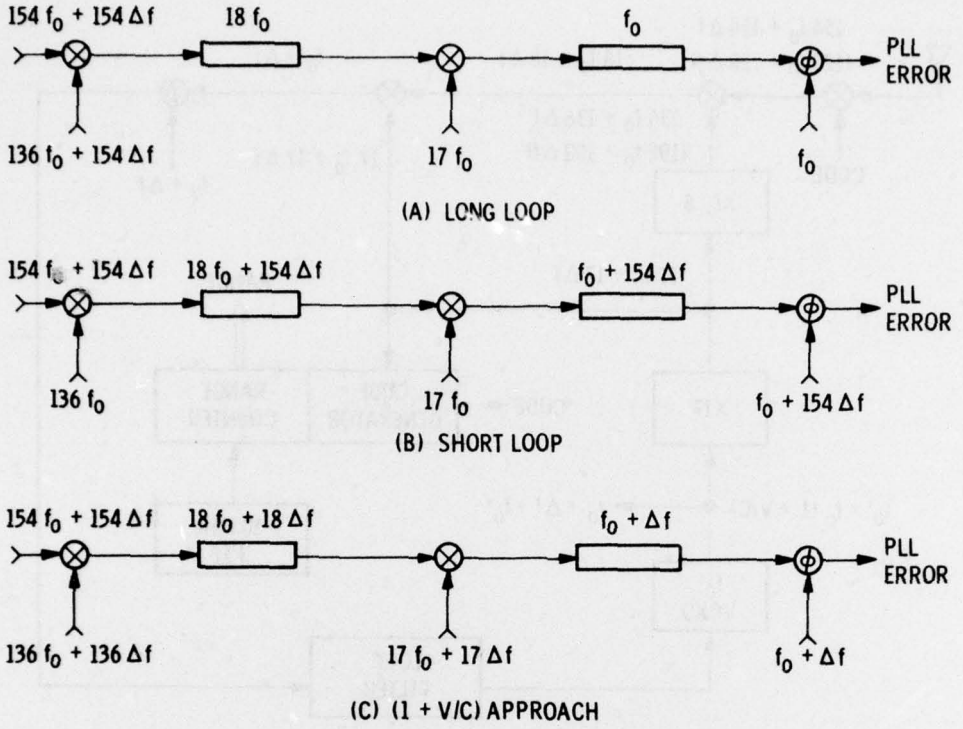

Figure 4. Three Basic Frequency Plans

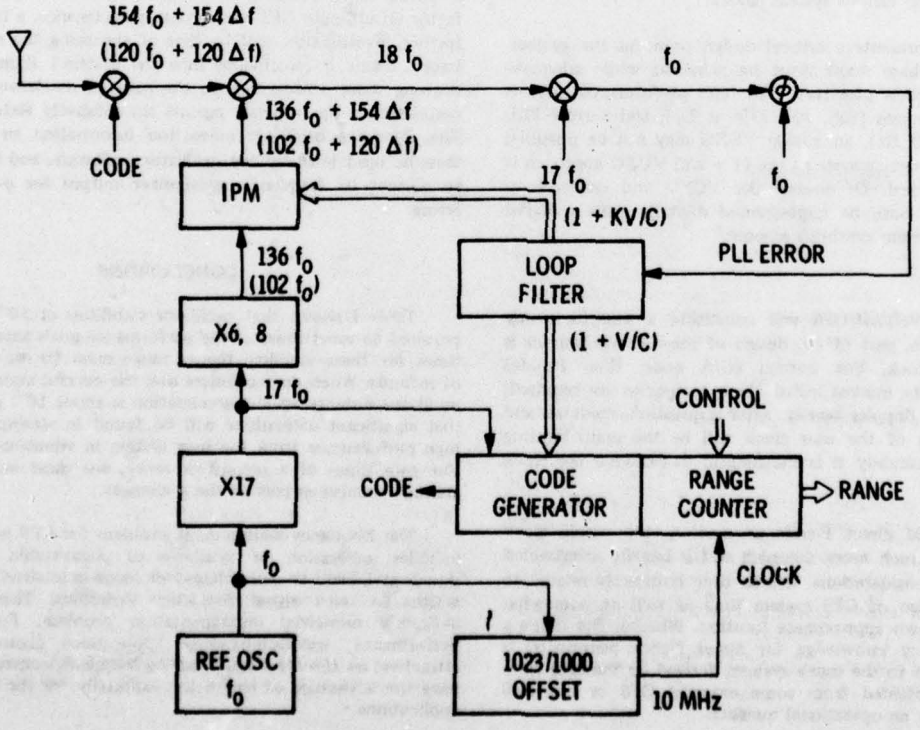

Figure 5. Detail of Long Loop

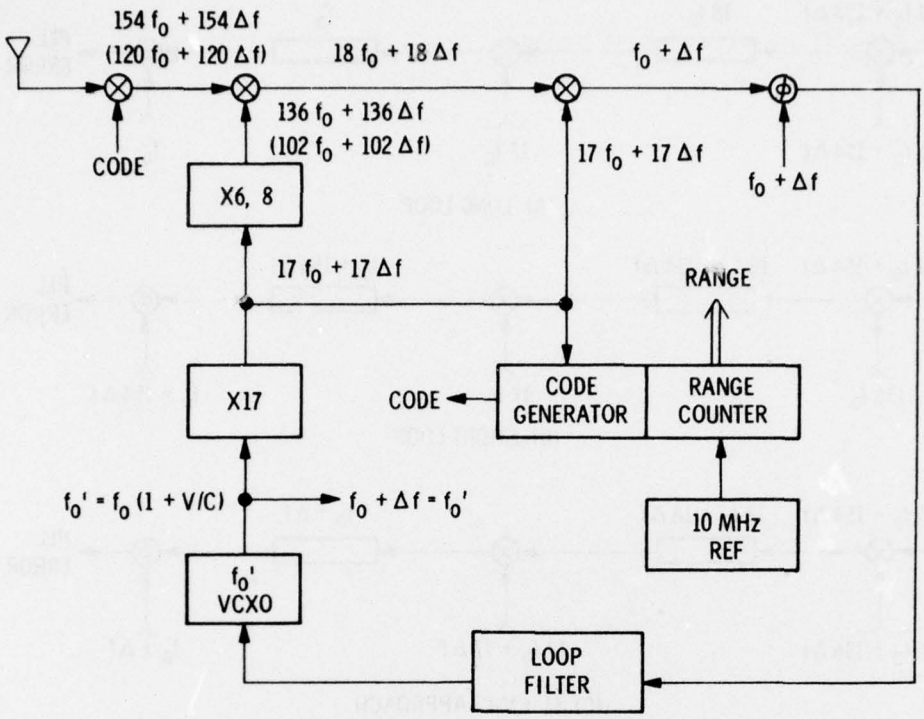

Figure 6. Detail of (1 + v/c) Approach

In the (1 + v/c) approach shown in figure 6 all local oscillators and code clocks are multiples of a variable frequency source at $f_o' = f_o + \Delta f$. The 17 f_o' second local oscillator signal can be used directly as a doppler-corrected code clock. A 10 MHz reference oscillator provides the various system clocks.

The VCXO represents a critical design point in the system, inasmuch as low phase noise must be achieved while adequate doppler tuning range is preserved. For high performance systems with wide tuning ranges (e.g., ±50 kHz at L_1), and narrow PLL bandwidths (e.g., 10 Hz), an analog VCXO may not be possible; but for lower-performance systems the (1 + v/c) VCXO approach is simple and economical. Of course, the VCXO and carrier loop filter functions can both be implemented digitally with a digital filter and an appropriate synthesis scheme.[5]

Clock Calibration

Since the NAVSTAR/GPS will constitute a time/frequency dissemination system, part of the design of the user equipments is to calibrate its clock. For normal (C/A code, then P-code) acquisition, only very modest initial clock accuracies are required, mainly to facilitate doppler search. After acquisition, medium- and long-term stabilities of the user clock will be the main limiting factors on how accurately it is meaningful to calibrate the clock time/frequency.

In the case of direct P-code acquisition, the whole clock problem becomes much more complex and is heavily intertwined with operational considerations. Search time is directly related to the user's knowledge of GPS system time as well as, somewhat paradoxically, his own approximate location. Whether the user's *a priori* time/frequency knowledge for direct P-code acquisition is regarded as intrinsic to the user's system, derived by the user from GPS earlier, or obtained from some external GPS or non-GPS source, is essentially an operational question.

The means of calibrating the user's clock time/frequency from the GPS signals is mainly a problem in the navigation software. More sophisticated high performance (high-antijam) system designs can consider inertial aiding to the GPS receiver and navigation software. Since oscillator *g* sensitivity will be a significant limiting factor on ultimate GPS user system performance, a fruitful area for further investigation will be that of absorbing the reference oscillator's 3-axis *g* sensitivities into the system's Kalman filter, and learning these sensitivities on the basis of accelerometer inputs as correlated in the software against the relatively stable GPS signals. The reference oscillator correction information so obtained can then be used both by the navigation software, and by the receiver to correct its frequency synthesizer output for *g*-induced phase errors.

CONCLUSIONS

Table I shows that oscillator stabilities of 10^{-9} to 10^{-10} are required to meet most of the performance goals assumed. The gate times for these stability figures range from 10 ms to several tens of seconds. When one considers that the current state of the art for oscillator stability against acceleration is about 10^{-9} per *g*, it is seen that significant difficulties will be found in attempting to obtain high performance from the user system in vibration environments. For gate times of a second or more, one must include oscillator attitude changes as part of the *g* changes.

The frequency-management problem for GPS user equipments includes generation or synthesis of phase-stable local-oscillator signals at L-band to close phase-lock loops in relatively narrow bandwidths to track signal frequency variations. This constitutes a definitely nontrivial implementation problem. For the higher-performance, wide-tuning-range applications digital synthesis is attractive; on the other hand, analog frequency-controlled oscillators have the advantage of simplicity, especially for the less demanding applications.

The frequency-management picture is completed by recognizing that the user's clock must be calibrated by including appropriate states in the navigation filter, which itself may be aided by an inertial measurement unit in certain GPS applications.

ACKNOWLEDGEMENTS

The author would like to express his gratitude to Drs. Troy Fucsher, Jerry Holmes, and Allen Jones for many very helpful discussions on the topics discussed in this paper.

REFERENCES

1. "Frequency Control and Time Information in the NAVSTAR/ Global Positioning System" by F.E. Butterfield, Aerospace Corporation 30th Annual Frequency-Control Symposium, Atlantic City, N.J., June, 1976.

2. See, for example, "Characterization of Frequency Stability" by James Barnes, et al., *IEEE Transactions on Instrument and Measurement*, May 1971.

3. As the satellite data content is highly redundant in nature, there have been proposals to eliminate the Costa's operation by multiplying out the data using almost-perfect *a priori* knowledge of the data for short periods of time.

4. This useful relationship is due to work by Dr. Troy Fucsher of Texas Instruments. It is relatively invariant to exact loop characteristics after normalization to the loop noise bandwidth.

5. See, for example, "A Dynamic NAVSTAR GPS Frequency Synthesizer" by Paul Van Broekhoven of the Charles Stark Draper Laboratory, Inc. Presented at NAECON-76.

NAVSTAR GLOBAL POSITIONING SYSTEM OSCILLATOR REQUIREMENTS FOR THE GPS MANPACK

Jack Moses
Magnavox Government and Industrial Electronics Company
Advanced Products Division
Torrance, California

Summary

The selection of an oscillator for the NAVSTAR GPS Phase I Manpack is constrained by many factors. The paper examines the oscillator requirements by first postulating the operational scenario of the potential manpack user and reconciles these requirements against the system performance capability. In addition, the paper examines and analyzes the following major areas in order to succinctly define and coherently summarize the multitude of factors affecting the oscillators requirements.

1. Oscillator warm-up characteristics as it affects frequency accuracy required to meet initial signal acquisition.
2. Required short-term stability and aging rate (long term stability) necessary to meet direct P subsequent fix performance accuracy and PN correlation code tracking accuracy.
3. Fractional frequency stability degradation due to environmental factors and its effects on signal acquisition.
4. Oscillator spectral purity as it affects phase errors in the receiver tracking loops and its associated degradation in system C/N_0.
5. Mechanical vibration induced frequency modulation of the crystal oscillator and the resultant system performance degradation.
6. Oscillator phase noise effects on phase slips in the carrier loop.

The paper concludes by summarizing the present oscillator technology available to manpack development by examining many parameters such as warm-up time, fractional frequency stability, power, size and weight.

Introduction

Global Positioning System Description

The Global Positioning System (GPS) is a satellite-based radio navigation system which is presently planned for evolution to an operational system in three phases. Phase I is primarily a Development Test and Evaluation (DT&E) program where the objective is to validate the system concept with six satellites. This will provide a continuous position and velocity fix capability at selected ground locations for periods of two hours per day. Phase II will involve expanding the satellite configuration to nine satellites (three satellites in each of three orbit planes). This will provide a limited global operational capability. Phase III will be the operational development of the final GPS satellite configuration.

The Phase III GPS satellite orbit configuration is a 3 x 8 (three planes, eight satellites per plane) constellation. Each satellite is in a 12-hour (altitude ≈3.16 earth radii) orbit inclined at 63 degrees.

The overall GPS system will be composed of the following basic segments

- Master Control and Tracking Stations
- Uploading Stations
- Satellites
- User Navigator

The basic GPS operational concept is described as follows: A ground tracking network periodically measures and updates the ephemeris of each satellite in addition to the satellite oscillator (i.e., clock) phase and frequency. The tracking stations must be located relative to the space vehicles such that sufficient data can be measured to maintain high precision ephemeris and inter-satellite clock synchronization. The stations will be located in the CONUS or U.S. territory. The uploading stations provide the terminal for communicating this data to the satellites for subsequent broadcast to the user. Each satellite will continuously transmit this information together with binary coded ranging signals to the users. Each satellite CW navigation signal will be transmitted on two L-band channels; L_1 which is nominally centered at 1575.42 MHz and L_2 which is nominally centered at 1227.6 MHz. The signal waveform is a composite of two pseudo-random noise (PN) phase-shift-keyed (PSK) signals transmitted in phase quadrature. These two signals are referred to as the P-signal and the C/A-signal. The P-signal provides the capability for high precision navigation, is resistant to ECM and multipath, and can also be denied to unauthorized users by means of transmission security (TRANSEC) devices.

The C/A-signal provides a clear (i.e., unprotected) ranging signal for users whose navigation requirements are less precise. In addition, this signal serves as an acquisition aid for authorized users to gain access to the P-signal. The C/A-designation indicates the "clear" and "acquisition" functions of this waveform.

Orthogonal binary coded sequences from the satellites provide a capability for identifying each individual satellite. This is a common technique known as Code Division Multiple Access (CDMA). By means of a correlation detector, the time shift between transmission of the signal and arrival of the signal as determined by the user's receiver clock is measured. This time shift is composed of two parts: the signal propagation delay from the satellite transmitter to the user and the unknown offset of the user clock. The effects of satellite ephemeris errors and satellite clock errors are assumed to be small (or amenable to accurate compensation) by the user. Using the known velocity of propagation, this time measurement can be converted to an equivalent range. This is often referred to as a pseudo-range measurement, denoting the measured range offset due to the user's clock time error. If the user knows the satellite position (i.e., transmitted ephemeris) and has a "sufficient set" of pseudorange measurments, it is possible for him to uniquely establish his geographic position and clock time offset. A "sufficient set" basically means a minimum of four independent range measurements.

In principal, if a user had an accurate clock synchronized to system time he could measure the precise time a signal from a satellite was received; thus, only three independent range measurements would be required for a position fix. Unfortunately, equipping each user with a sufficiently accurate clock and synchronizing it to the satellites' time would be prohibitively expensive and cumbersome. To circumvent this difficulty the GPS user is equipped with a fairly inexpensive crystal clock.

This paper describes requirements on the crystal clock needed to meet the system performance of the Phase I Manpack.

Mission Scenario

The selection of the oscillator for the GPS Phase I Manpack development is dependent upon the user's operational scenario, but, in addition is driven by the constraints imposed by the Manpacks' size, weight, power and performance goals.

A GPS army user can be either a foot soldier or a vehicular unit. It is required that a user be able to position fix from a cold start (normal acquisition) and from a hot start (direct acquisition). The user is allowed 5 minutes from a cold start for oscillator warmup after which time he must be able to position fix within 100 seconds. Subsequent fixes are at 15 minute intervals for the duration of the mission of 48 hours. These requirements are for Phase III when the GPS is fully operational. The Phase I Manpack has relaxed requirements in that the user is allowed 15 minutes to position fix from a cold start and the first fix time is 225 seconds. Furthermore, the system design will be based on a 24 hour mission duration. All system requirements for the Magnavox Phase I Manpack are dictated by CID-US-113, the system specification. [1]

Oscillator Requirements for Signal Acquisition

The GPS Manpack user must first acquire the navigation ranging signals from at least four satellites before a navigation fix can be obtained. The Manpack has two modes of acquisition. The normal acquisition mode is defined as acquisition of the L_1 C/A signal followed by the acquisition of its associated P signal. The direct acquisition mode is defined as acquisition of the P signal without the aid of the C/A signal. In the Manpack there are two cases where direct P signal acquisition is required:

1. Under unfavorable jamming conditions, the Manpack user will directly acquire the P signal. To do so, however, requires highly accurate knowledge of system time. The time transfer capability is facilitated by having another user or station transmit system time and almanac data via a radio link, using a radio unit such as an AN/PRC-25 or 77. In this mode of acquisition the radio link errors are important and the search time ambiguity region predominates with the stability of the user's oscillator being not the critical factor.
2. The Manpack user has the requirement for initiation of subsequent fixes fifteen minutes after a previous fix. Since these intervals are small, the stability of the oscillator is important since it is the predominate factor in bounding the uncertainty region.

Normal Acquisition

Precision ranging measurement cannot be made until the end of the receiver's equipment stabilization period (ESP). For the Manpack, ESP is the elapsed time from equipment turn-on until the start of the acquisition mode which is not to exceed 15 minutes over all ambient temperatures from -20°C to 55°C. Final oscillator stability is not required until the end of ESP. Theoretically no measurements should be made prior to equipment stabilization due to the random warm-up characteristics of the crystal oscillator. Before the process of signal acquisition can begin which is at the start of the time to first fix (TTFF) period, the frequency offset must not be too large so as to significantly add to user velocity uncertainty thus increasing the search aperture and TTFF.

The synchronization problem in either normal or direct P acquisition is one of searching a region of ambiguity for the proper cell containing the signal. Figure 1 illustrates the factors which define the constraining limits of the ambiguity region. The limits of time ambiguity are dictated by: (1) clock instabilities or long term instability important for direct P-acquisition over long intervals of time outage, (2) propagational delay between satellite and user. The limits of

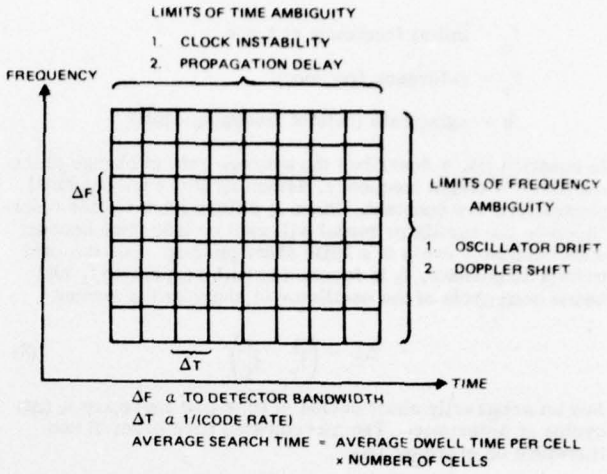

Figure 1. Ambiguity Region for Synchronization

frequency ambiguity are (1) oscillator drift resulting in a frequency offset due to oscillator warm-up characteristics, and (2) doppler shift which includes user and satellite velocity uncertainties. By using a priori knowledge of user/satellite position and velocity, time and frequency uncertainties are reduced to meet TTFF requirements. Nevertheless, time and frequency uncertainties still exist. To meet the Manpack's specified TTFF, the user clock uncertainty, assumed to be in the order of one minute, specifies the time domain search for the first signal to be conducted uniformly over the full 1023 chip period of C/A code. The bounded frequency uncertainty taking into account user velocity uncertainty and user's estimate of satellite doppler induced by the user's position uncertainty results in bounding the maximum oscillator offset to ±100 Hz (1σ) which results in a frequency accuracy at the L band frequency of 1.575 GHz to be not less than

$$\frac{\Delta F}{F} = \frac{\pm 100 \text{ Hz}}{1.575 \times 10^9} = \pm 6 \times 10^{-8}$$

This would be the frequency accuracy requirement at the end of ESP (15 min) to begin the C/A signal acquisition process and meet the Manpack's TTFF requirement under ideal conditions. However, environmental factors acting randomly degrade the stability in a root sum square manner. The fractional frequency stability degradation, described later, under extreme worst case conditions is $\pm 5 \times 10^{-8}$. To overcome this effect, the frequency accuracy should be $\pm 3 \times 10^{-8}$ at the end of the equipment stabilization period over the temperature range of -20°C to 55°C to meet the Manpack's TTFF requirement.

Direct Acquisition

As previously indicated, the Manpack set has a P-signal direct acquisition requirement wherein a subsequent fix is required 15 minutes after a previous fix. The current Manpack specification indicates that the time to subsequent fix (TTSF) be no greater than 20 seconds for a user position uncertainty of 1 km. Searching out the time ambiguity region is the predominant factor in meeting the subsequent fix requirement. Oscillator stability is important in bounding this uncertainty to acceptable limits. To determine the frequency stability requirement for the direct P acquisition, it is first necessary to examine the oscillator's clock model.

Clock Model. The oscillator's frequency at any time t can be expressed as

$$f_t = f_o + (a)(f_r)(t) \qquad (1)$$

where f_t = frequency at time t

f_o = initial frequency at t = o

f_r = reference frequency

a = aging rate (rate of frequency shift)

In equation (1), a describes the average rate of change of the oscillator's output frequency, assuming that environmental parameters are constant. Since f_t differs from f_r, the clock based on the oscillator model will gain or lose time because each oscillator cycle is a little short or long. For the case when a is positive, f_t is increasing with respect to f_r and hence each cycle of the oscillator is short by the amount

$$\Delta L = \left(\frac{1}{f_r} - \frac{1}{f_t}\right) \tag{2}$$

For an arbitrarily short period of time (Δt) there are f_t (Δt) cycles of difference. The incremented time error E can therefore be expressed as

$$E = \left(\frac{1}{f_r} - \frac{1}{f_t}\right) f_t \, (\Delta t) \tag{3}$$

In the limit

$$dE = \left(\frac{f_t}{f_r} - 1\right) dt \tag{4}$$

To obtain the accumulated error, dE can be integrated which results in

$$E = E_o + \left(\frac{f_o - f_r}{f_r}\right) t + \frac{a}{2} t^2 \tag{5}$$

where E_o = initial time error

$\Delta f = (f_o - f_r)$ = initial frequency error

a = oscillator aging rate

t = elapsed time

Equation (5) can also be expressed as

$$E = E_o + \left(\frac{\Delta F}{F}\right) t + \frac{a}{2} t^2 \tag{6}$$

where $\frac{\Delta F}{F}$ = fractional frequency stability.

Of the 20 seconds required for the TTSF, 2.5 seconds are required to search and acquire each satellite using direct acquisition. One p chip code = 100 nsec. The search rate is 50 PN chips/sec; thus, the time uncertainty is

$$E = 2.5 \text{ sec} \left[\frac{50 \text{ chips}}{\text{sec}}\right] \left[\frac{100 \text{ nsec}}{\text{chip}}\right] = 12.5 \, \mu\text{sec}$$

To this uncertainty must be added the user position time uncertainty. This then specifies the total time ambiguity region. For the Manpack, the position uncertainty is 1 km which translates into 33 p chips or 3.3 μsec. Thus the total time uncertainty is 15.8 μsec. From equation (6), the required fractional frequency stability can be calculated assuming the following:

E_o = 0.2 sec

t = time interval between fixes = 15 min.

Therefore,

$$E = 0.2 + \frac{\Delta F}{F} (900 \text{ sec}) + \frac{a}{2} (900 \text{ sec})^2$$

For typical aging rates of crystal oscillators ranging from 1×10^{-8}/day to 1×10^{-10}/day for the short durations in the time interval the last term is negligible; therefore,

$$\frac{\Delta F}{F} = \frac{(15.8 - 0.2) \times 10^{-6}}{900} = \pm 2 \times 10^{-8}$$

When subsequent fixes are made, the oscillator has reached its ultimate stability which is on the order of $\pm 1 \times 10^{-9}$. With the induced random environmental degradation of $\pm 5 \times 10^{-8}$, the required fractional frequency stability is reduced to $\pm 7 \times 10^{-8}$ which is still well within the $\pm 2 \times 10^{-8}$ required to meet the subsequent fix requirement.

Environmental Degradation Frequency Stability

Environmental effects on the Manpack such as temperature variations, vibration, g-force loading, shock, load changes and voltage changes can all contribute to the fluctuations in the crystal oscillator's output frequency. These perturbations are independent, normally distributed, random variables (actually, the perturbations are independently caused but are not normally distributed). The combined RMS perturbation is the square root of the sum of the variances of the individual perturbation. The effects of the environmental factors tend to degrade the fractional frequency stability in a root sum square (RSS) manner. The resultant 1σ deviation of all factors is given by

$$\sigma_{\Delta F} = \sqrt{\sum_{i=1}^{N} \left(\sigma_{\Delta F_i}\right)^2} \tag{7}$$

where

$\sigma_{\Delta F}$ = standard deviation of the induced change

$\sigma_{\Delta F}$ can be evaluated for a good crystal oscillator considering the environmental factors. Table I lists 1σ values of these factors at the L-Band frequency of 1.575 GHz.

Table I. Environmental Effects on the Oscillator

Parameter	Stability	Induced Changed	$1\sigma_{\Delta F}$ at L-Band (Hz)
Temperature Fluctuations	1×10^{-9}	-20°C to 55°C	1.6
Vibration	2×10^{-9}/G	2.5	5.0
Shock	2×10^{-9}/G	11 g	22.
G-Force Loading	1×10^{-9}/G	2.5 g	2.5
Voltage Change	1×10^{-9}	5%	1.6
Load Change	1×10^{-9}	10%	1.6

The resultant $1\sigma_{\Delta F}$ deviation for the above factors given by equation (7) is

$$\sigma_{\Delta F} = \sqrt{3(1.6)^2 + (5)^2 + (22)^2 + (2.5)^2} = 24 \text{ Hz}$$

or a $3\sigma_{\Delta F}$ worst case of 72 Hz.

Thus, the environment will cause the crystal oscillator's output frequency to randomly change by 72 Hz (3σ) worst case. This results in an effective fractional frequency degradation of

$$\frac{\Delta F}{F} = \frac{72\ \text{Hz}}{1.6 \times 10^{9}} = \pm 5 \times 10^{-8}$$

Carrier Incidental FM

In specifying the receiver performance of the GPS Manpack, practical implementation losses must be considered since they tend to degrade the theoretically achievable performance. There are five areas of receiver implementation losses that are of concern. They are: (1) receiver noise factor loss; (2) filtering and waveform distortion; (3) correlator loss; (4) oscillator phase jitter (incidental FM); (5) quantization and sampling. Receiver implementation losses have been specified not to exceed 2 dB to meet the required receiver performance. We will now examine in detail oscillator phase jitter and its effects on receiver performance. Other losses are analyzed elsewhere.[2]

Incidental frequency or phase modulation of the transmitted carrier or of the receiver local oscillator degrades receiver performance by introducing an additional tracking error, over and above the noise-induced tracking error in the Costas carrier tracking loop. This causes a reduction in the loop signal-to-noise, but more important, results in stressing the linear range limits (±0.5 radians) of the loop phase detector, and as a result causes the loop to be more susceptible to losing lock. This analysis treats incidental modulation from two sources: (1) the RF front end local oscillator multiplication induced phase noise; (2) the mechanical vibration induced frequency modulation of the reference oscillator crystal.

Multiplication Induced Phase Noise

For the specified user dynamics defined in Table II, the GPS Manpack employs a second order Costas loop (or its squaring loop equivalent) for deriving a "coherent" reference for demodulation.

Table II. User Dynamics

Dynamics	User	
	Manpack	Vehicle
Velocity (m/sec)	0 - 10	0 - 30
Acceleration (m/sec^2)	2.5	6.0
Acceleration duration (sec)	4	4

A block diagram of the Costas loop with additive white Gaussian noise and phase noise is shown in Figure 2. The Costas loop parameters are specified in Table III.

The total mean squared phase error in the Costas loop is made up of oscillator phase jitter and receiver noise. Assuming the phase jitter is a stationary random process, the two contributions to the mean squared loop phase error may be identified as the following:

Noise jitter contribution

$$\sigma_m^2 = \int_0^\infty S_\phi(f) / 1 - H(jw) /^2 df \qquad (8)$$

Receiver noise

$$\sigma_n^2 = \frac{N_O}{C} \int_0^\infty /H(jw)/^2\, df = \frac{N_O B_L}{C} \qquad (9)$$

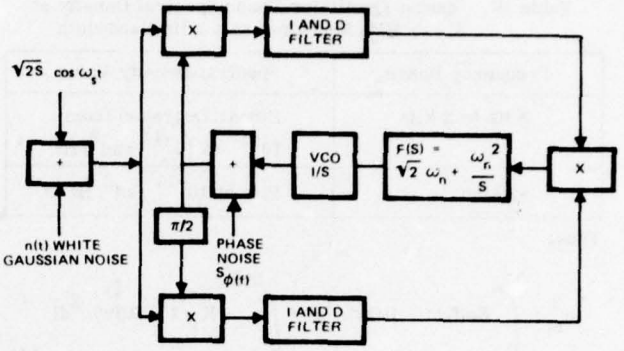

Figure 2. Second Order Costas Loop Block Diagram

Table III. Costas Loop Parameters

Parameter	
Loop Order	2nd
Threshold C/No (dB-Hz)	26
Loop Noise Bandwidth B_L (Hz)	20
Sampling Rate (samples/sec)	250
Data Rate (bits/sec)	50

where, H(s) - Closed loop transfer function

B_L - One sided loop noise bandwidth

S(f) - Spectral density of the phase jitter

Thus, the total mean squared phase error for the Costas loop is given by

$$\sigma_T^2 = \sigma_m^2 + \sigma_n^2 \qquad (10)$$

$$\sigma_T^2 = \int_0^\infty S\phi(f) / 1 - H(jw) /^2 df + \frac{N_O B_L}{C} \qquad (11)$$

The receiver's master crystal oscillator is at a frequency of 5.115 MHz. Its phase noise spectral density measured in a 1 Hz bandwidth is given in Table IV.

Since the GPS operating frequency at L_1 is 1575 MHz, there is a multiplication factor of approximately 308 which increases the oscillator phase noise spectral density by approximately 50 dB. A well designed multiplier circuit does not contribute additional noise beyond this theoretical factor. This results in an expression for the spectral density:

$$S\phi(f) = \frac{29.2 \times 10^{-5}}{\omega^{4/3}}\ \text{rad}^2/\text{Hz} \qquad (12)$$

For a second order loop

$$/1 - H(jw)/^2 = \frac{\omega^4}{\omega^4 + \omega_n^4}; \quad \omega_n = 1.89\, B_L \qquad (13)$$

Table IV. Master Oscillator Phase Spectral Density at 5.115 MHz Measured in a 1 Hz Bandwidth

Frequency Range	Spectral Density Value
2 Hz to 2 kHz	Linear Decrease from 10^{-10} to 10^{-14} rad^2/Hz
>2 kHz	Flat at 10^{-14} rad^2/Hz

Thus,

$$\sigma_m^2 = \int_o^\infty S\phi(f)/1 - H(jw)/^2 df + \int_o^{2\pi fc} K_1/1 - H(jw)/^2 df \qquad (14)$$

where,

fc = synthesizer low pass filter cutoff frequency = 100 kHz

$K_1 = 10^{-9}$ rad^2/Hz

$$\sigma_m^2 = \int_o \frac{29.2 \times 10^{-5}}{\omega^{4/3}} \left[\frac{\omega^4}{\omega^4 + \omega_n^4}\right] df + \int_o^{2x10^5} 10^{-9} \left[\frac{\omega^4}{\omega^4 + \omega_n^4}\right] df \qquad (15)$$

$$\sigma_m^2 = 4.65 \times 10^{-5} \int_o^\infty \frac{\omega^{8/3}}{\omega^4 + \omega_n^4} dw + \frac{10^{-9}}{2\pi} \int_o^{2x10^5} \frac{\omega^4}{\omega^4 + \omega_n^4} dw \qquad (16)$$

First evaluating

$$4.65 \times 10^{-5} \int_o^\infty \frac{\omega^{8/3}}{\omega_n^4 + \omega^4} dw$$

let $u = \omega/\omega_n$

$$\sigma_m^2 = 4.65 \times 10^{-5} \int_o^\infty \frac{\left(\frac{\omega}{\omega_n}\right)^{8/3} w_n^{-4/3}}{1 + \left(\frac{\omega}{\omega_n}\right)^4} w_n \, du$$

$$\sigma_m^2 = \frac{4.65 \times 10^{-5}}{(\omega_n)^{1/3}} \int_o^\infty \frac{u^{8/3}}{1 + u^4} du$$

$$\int_o^\infty \frac{X^{n-1}}{1 + X^m} dx = \frac{\pi}{m \sin \frac{n\pi}{m}}$$

for noninteger n

$$\sigma_m^2 = \frac{4.65 \times 10^{-5}}{3\sqrt{38}} \left[\frac{\pi}{4 \sin \frac{11\pi/3}{4}}\right] = 4.2 \times 10^{-5} \text{ rad}^2$$

The second contribution to $\sigma^2 m$ is

$$\frac{10^{-9}}{2\pi} \int_o^{2\pi x10^5} \frac{\omega^4}{\omega^4 + \omega_n^4} dw$$

For $w \gg \omega_n$ the integral approximates to

$$\frac{10^{-9}}{2\pi} \int_o^{2x10^5} \left[\frac{\omega^4}{\omega^4}\right] dw = \frac{10^{-9} \times 2\pi \times 10^{+5}}{2\pi} = 10^{-4} \text{ rad}^2$$

$$\sigma_m^2 = 0.42 \times 10^{-4} + 1 \times 10^{-4} = 1.42 \times 10^{-4} \text{ rad}^2$$

$$\sigma_m = 0.012 \text{ rad}$$

$$\sigma_T^2 = \sigma_m^2 + \sigma_n^2$$

$$\sigma_n^2 = \frac{N_o B_L}{C}$$

For C/N_o = 26 dB-Hz and B_L = 20 Hz

$$\sigma_n^2 = 0.052 \text{ rad}^2$$

$$\sigma_T^2 = 0.00142 + 0.052 = 0.05342 \text{ rad}^2$$

The new C/N_o for this mean squared error is

$$\sigma_T^2 = B_L / C/N_o$$

$$C/N_o = B_L/\sigma_T^2 = 20/0.05342 = 374 \text{ or } 25.7 \text{ dB-Hz}$$

Degradation due to oscillator noise jitter in the Costas loop is then 26 dB-Hz - 25.7 dB-Hz = 0.3 dB-Hz.

Phase Noise and Jitter Due to Vibration. We now examine in detail the mechanical vibration induced frequency modulation of the reference oscillator crystal. Of specific concern is the error signal in the second order Costas loop which tracks the carrier. The magnitude of the error signal which is induced by incidental frequency modulation can be related to the signal-to-noise degradation and loss-of-lock degradation.

Acceleration of the crystal oscillator in the receiver causes its output frequency to change slightly, and we model this behavior as a linear relation: i.e.,

$$\frac{\Delta f}{f_o} = K \, (a/g) \qquad (17)$$

Where a/g is the acceleration relative to 32 ft/sec^2, K is the constant of proportionality, and $\Delta f/f_o$ is the fractional deviation of frequency. Typical values for K on any of the three axis, X, Y and Z of a good crystal oscillator range from 1 x 10-9/g to 3 x 10-9/g. Taking the maximum value of K, we have at the GPS L_1 frequency, f_o = 1.6 GHz.

$$\Delta f = 5 \text{ Hz/g} \qquad (18)$$

Vibration applied to the receiver for purposes of testing may be sinusoidal, random or shock. If the oscillator is rigidly mounted, the vibration is applied to the crystal. A soft mount designed to isolate the crystal from vibration can reduce the transmitted vibration at higher frequencies at the cost of a resonance increasing the vibration of lower frequencies. The vibration requirements of the Manpack are such that the set shall operate with vibration isolators during vehicle use and withstand without vibration isolators in a non-operating condition the following vibration requirements.

1. Sinusoidal Vibration

Jitter Frequency (fm)	Displacement (D. A.)	Acceleration
5 Hz	1.2 inches	1.5 g
20 Hz	0.075 inches	1.5 g
38 Hz	0.021 inches	1.5 g
40 Hz	0.020 inches	1.6 g
50 Hz	0.020 inches	2.5 g
60 Hz	0.014 inches	2.5 g
100 Hz	0.005 inches	2.5 g
200 Hz	0.0013 inches	2.5 g
500 Hz	0.0005 inches	5.0 g

Where acceleration is given by:

$$\frac{4\pi^2 f_m^2 (D/2)}{386} \qquad (19)$$

where,

f_m = Jitter Frequency

D = Double amplitude displacement

2. Random Vibration. No requirement.
3. Shock, 15 g for 11 millisecond, half sinusoid.

Vibration Effects on Hard Mounted Oscillator. Let us now assume that the vibration is fully applied to the oscillator which is hard mounted in the receiver. For the specified vibration using (18), we find the phase deviation for the different jitter frequencies is specified in Table V.

Table V. Phase Deviation Caused by Sinusoidal Vibration

Jitter Frequency (f_m)	Frequency Deviation Δf	Phase Deviation $\Delta f/f$
5 Hz	7.5 Hz	1.5 rad
20	7.5	0.37
38	7.5	0.20
40	8.0	0.20
50	12.5	0.17
60	12.5	0.21
100	12.5	0.125
200	12.5	0.0625
500	25.0	0.050

The rms loop phase tracking error is given by[3]

$$\epsilon_{rms} = \sqrt{\frac{1}{2}\left(\frac{\Delta f}{f_m}\right)^2 \left[\frac{1}{1 + \frac{f_n}{f_m}^6}\right]} \qquad (20)$$

where,

Δf = frequency deviation

f_m = jitter frequency

f_n = loop natural frequency = 6 Hz

Equation (20) is plotted in Figure 3.

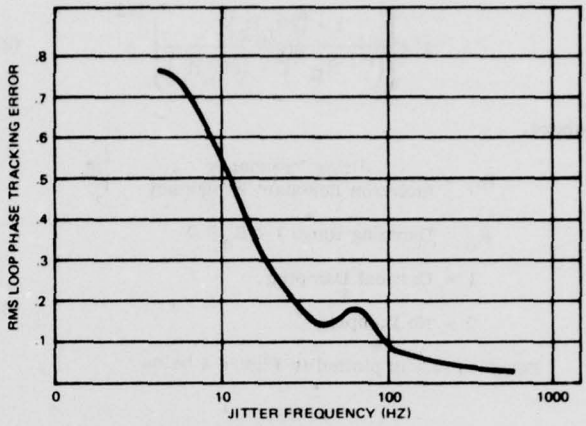

Figure 3. Loop Phase Tracking Error for Sinusoidal Jitter

Examination of Figure 3 indicates the sinusoidal jitter environment primarily causes a severe problem in the vicinity of the loop natural frequency f_n = 6 Hz due to the phase deviation peak at that frequency. System performance specifications and good engineering design practice dictate that the peak crystal oscillator vibrationally induced tracking error not exceed 0.1 rad. Figure 3 indicates that at the loop natural frequency the rms loop phase tracking error is 0.75 rad. This causes an effective signal power loss in the loop of[4]

$$\frac{Seff}{S} = \left[J_o\left(2\,\epsilon_{max}\right)\right]^2 \qquad (21)$$

or at 6 Hz

$$J_o^2\,(2.05) = 0.05 \text{ or } 13 \text{ dB}$$

This is far too excessive and vibration isolation is required to reduce tracking error and the resultant effective power loss to acceptable limits.

The shock environment of 15g (peak for a half sinusoid) for 11 msec corresponds to an average frequency of

$$\frac{2}{\Pi}\left(\frac{5 \text{ Hz}}{g}\right)(15g) = 48 \text{ Hz}$$

or a sudden phase change of

$$\Delta\phi = 2\Pi f \Delta t = 6.28 \times 48 \times 0.011 = 3.3 \text{ radians}$$

This cannot be tracked by the narrow Costas loop. However, the phase discontinuity is like a momentary phase slip and the Costas loop does not actually lose lock. The recovery time to pull into a small phase error is inversely proportional to the loop bandwidth; and the error rate for data is high during this transient.

Vibration Effect on Soft Mounted Oscillator. In view of the peak in the phase error for a sinusoidal vibration at the loop natural frequency of 6 Hz, the possibility of isolating the oscillator by a soft mount is examined. The problems occur when the Manpack is mounted in the jeep and is subjected to severe vibration. A vibration isolation system is required which has a natural resonant frequency at <6 Hz. The amplitude transfer function of the mount is the transmissibility and is given by[5]

$$T = \left[\frac{1 + \left(2R_\Omega R_e\right)^2}{\left(1 + R_\Omega{}^2\right)^2 + \left(2R_{f_c} R_c\right)}\right]^{1/2} \qquad (22)$$

where,

$$R_\Omega = \frac{\text{Jitter Frequency}}{\text{Isolation Resonant Frequency}} = \frac{f_m}{f_r}$$

R_c = Damping Ratio $1 \geq R_c \geq 0$

1 = Critical Damping

0 = No Damping

Equation (22) is plotted in Figure 4 below.

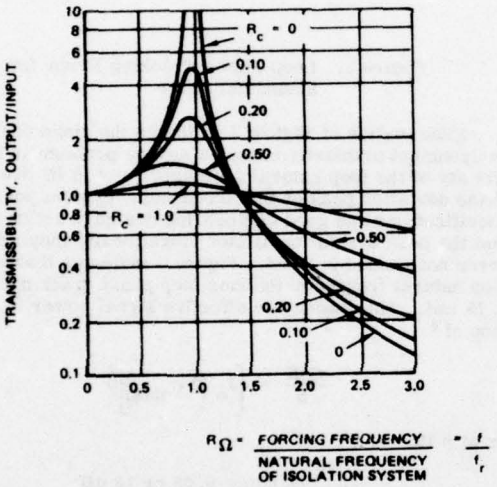

Figure 4. Theoretical Performance of Isolation System

The large peak in the transfer function is obviously a problem if it coincides with or exceeds the Natural Frequency of the loop, and if the vibration is applied at or near the resonance. Choosing the natural frequency of the isolation system at 1.5 Hz and damping of 0.1, the peak loop phase error φ_m in the second order loop with natural frequency f_n for an applied sinusoidal jitter is given by[4]

$$\varphi_m = \theta_i\, T \left[\frac{f^2}{\left(f^4 + f_n{}^4\right)^{0.5}}\right] \qquad (23)$$

where,

T is the transmissibility

θ_i - phase deviation which could be produced on the crystal in a hard mount.

f_n = 6 Hz

At the frequency of 5 Hz

$$\varphi_m = (1.5)\,(0.1)\left[\frac{(5)^2}{\left(5^4 + 6^4\right)^{0.5}}\right]$$

$$\varphi_m = 0.085 \text{ rad}$$

This is within the peak crystal oscillator vibrationally induced tracking error of 0.1 rad. The effective signal power loss with vibration isolation is then

$$\frac{\text{Seff}}{S} = \left[J_o\,(2\varphi_m)\right]^2 \qquad (24)$$

or at 6 Hz

$$J_o{}^2\,(0.170) = 0.985 \text{ or } 0.1 \text{ dB}$$

Considering the shock with the vibration isolating system proposed, we observe that the shock has the effect of causing the oscillator to vibrate at the resonance of the mount. Since the mount is very underdamped and the shock vibration is short, we can solve the transient problem as an impulse of acceleration applied to an undamped resonance. The acceleration transmitted to the oscillator is sinusoidal at the resonance f_r = 1.5 Hz of the mount and is the peak phase deviation of the sinusoid which is 3.3 radians. Taking into account the capability of the second order loop with natural frequency f_n = 6 Hz to track sinusoidal phase jitter, we find the peak phase error is[4]

$$\varphi_m = \theta_i \left[\frac{f_r{}^2}{\left(f_r{}^4 + f_n{}^4\right)^{0.5}}\right] \qquad (25)$$

$$\varphi_m = 3.3\left[\frac{(1.5)^3}{(1.5)^4 + (6)^4\,0.5}\right]$$

$$\varphi_m = 0.255 \text{ rad}$$

This is considerably less than the shock produced from a hard mounted oscillator, and well within limits of tracking capability of the loop. This results from the resonance of the mount being considerably below the natural frequency of the loop.

Oscillator Short Stability Requirements as They Affect Code Loop Performance

Just as oscillator phase noise is important in the Costas carrier tracking loop which extracts pseudorange rate, so it is important in the code tracking loop which determines pseudorange. The Manpack employs an early late (E/L) non-coherent code tracking loop which is implemented as a first order loop. This is permissible since the code loop is aided by the carrier loop whose bandwidth is sufficiently wide to follow all specified signal dynamics. In fact, since the code frequency is derived from the carrier, nearly all signal dynamics are absent as far as code tracking is concerned.

The primary requirement upon the oscillator stability for ranging is not in terms of absolute accuracy but in terms of its short term stability to ensure that it doesn't move about during measurements.

Short-Term Stability

The short-term stability of an oscillator characterizes the statistical fluctuations about the average output frequency. The short-term phase fluctuations observed in the output of a quartz crystal oscillator are attributed to three major effects. One type of fluctuation results from thermal and shot noise generated in the crystal and associated oscillator circuitry. A flat power spectral density is associated with this type of noise. A second type of fluctuation attributed to the crystal unit and circuit fluctuation changes, is flicker noise. The resultant power spectral density appears to have a 1/F characteristic. The third type of fluctuation is produced by additive noise. These dominant effects on short-term stabilities, as a function of averaging time, are shown in Figure 5. The short-term fractional frequency stability is then given by

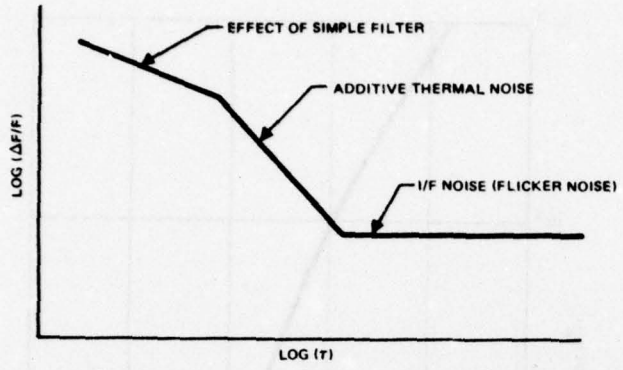

Figure 5. Dominent Effects Upon Short-Term Stabilities

$$\frac{\Delta F}{F} = \sqrt{\sigma^2 (N, \tau)} \tag{26}$$

Where,

$\sigma^2 (N, \tau)$ is the variance of N adjacent samples of the average frequency

τ = averaging time

The fractional frequency stability of a good crystal oscillator as a function of averaging time is shown in Figure 6. For the Manpack the requirement for short-term stability is to bound the oscillator drift with respect to the chosen point of PN correlation during the 20 msec averaging time. Design criteria dictates that this should be on the order of ±4 nsec. Thus, the rms fractional frequency deviation is

$$\sigma_\tau = \left(\frac{\Delta F}{F}\right) \tau \tag{27}$$

$$\frac{\Delta F}{F} = \frac{\pm 4 \times 10^{-9}}{20 \times 10^{-3}} = \pm 2 \times 10^{-7}$$

Figure 6 indicates that for an averaging time (τ = 20 msec) the fractional frequency stability is $\pm 1 \times 10^{-9}$. Thus the spectral purity of a good crystal oscillator in the time domain is well within limits of meeting performance.

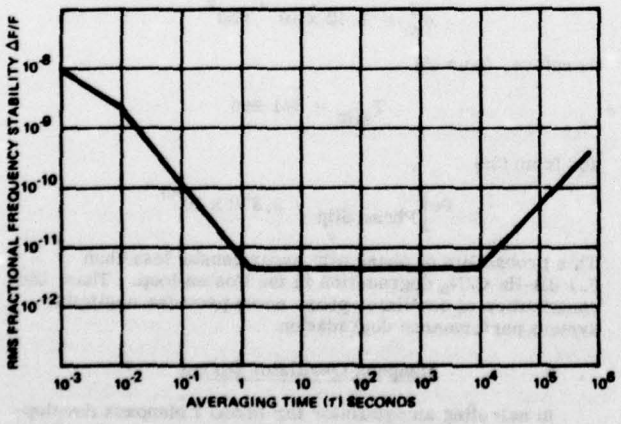

Figure 6. Short Term Stability Characteristics of Quartz Crystal Oscillator

Let us now examine the degradation in ranging accuracy in the code loop caused by oscillator phase noise. Table IV previously specified the oscillator phase spectral density. The relationship between spectral density in the frequency domain and time stability is given by Reference 6. This relationship is shown in Table VI.

Table VI. Relationship Between Spectrum and Time Stability

$S_\phi(f)$	$\sigma^2(2,\tau)$
$K_2 f^{-2}$	$K_2 (2\pi)^2 \tau/6$
$K_1 f^{-1}$	$K_1 2\ln 2$
K_o	$K_o/2\tau$

The resultant oscillator phase noise density transferred to the code frequency of 10.23 MHz is

$$S_\phi(f) = \frac{3 \times 10^{-8}}{\omega^{4/3}} \text{ rad}^2/\text{Hz} \tag{28}$$

The mean squared jitter in the code loop is then

$$\sigma_m^2 = \int_o^\infty S_\phi(f) /1 - H(j\omega)/^2 \, df \tag{29}$$

For the first order code loop

$$/1 - H(j\omega)/^2 = \frac{\omega^2}{\omega^2 + \omega_n^2} ; \quad \omega_n = 4B_L \tag{30}$$

The code loop bandwidth is 0.6 Hz, therefore ω_n = 2.4 Hz.

Evaluation of (4) results in a mean squared jitter of

$$\sigma_m = 1.45 \times 10^{-4} \text{ rad}$$

The oscillator jitter in the code loop translates into a ranging error of

$$\Delta R = \frac{\sigma_m/2\pi}{\Delta} \tag{31}$$

Where Δ = 1 p chip = 100 ft. Therefore,

$$\Delta R = 2.3 \times 10^{-3} \text{ ft}$$

The present Manpack system has a code phase resolution quantized to 1/64 of a code chip which for the p signal is

$$\Delta \frac{\text{range}}{\text{code}} = \frac{100 \text{ ft}}{2^6} = 1.570 \text{ ft}$$

The degradation due to oscillator noise jitter in code tracking performance is given by

$$10 \log \left[\frac{\Delta}{\Delta - \Delta R}\right] \tag{32}$$

This evaluates to

$$10 \log \left[\frac{1.570}{1.570 - 0.0023}\right] = 0.006 \text{ dB}$$

This is negligible in comparison to the jitter causing 0.3 dB degradation in the carrier tracking loop. This results primarily from the spectral density being decreased by 50 dB in the carrier loop as opposed to only 4 dB in the code loop.

Effects of Oscillator Phase Noise on Phase Slips in the Costas Loop

The GPS Manpack receiver must regenerate the reference carrier from the sidebands of the NAVSTAR double-sideband suppressed carrier signal. In doing so there is a phase ambiguity in decoding the navigation data. One way of resolving the O, π phase ambiguity is by employing differential data encoding where, for instance, a one is transmitted as a phase change and a zero conveyed by the absence of phase change. The performance of such a scheme for perfect carrier regeneration is termed differential phase shift keying (ΔPSK).

The classical method of differential data encoding however is not implemented in the GPS navigational data encoding structure. Rather the last bit of the previous word is employed for supplying the polarity reference for data demodulation. However, under the thermal noise conditions the performance of these two differential encoding schemes is about the same.

With differential encoding of data to resolve the ambiguity of tracking, phase slips of the tracking loop contribute to the error rate in the output data. Let us now examine the degradation in probability of error for phase slips for a ΔPSK system with thermal noise against the Manpack system which takes into consideration the existence of oscillator phase noise and the usual additive receiver noise.

The probability of phase slips caused errors for a Costas loop for just thermal noise is given by[7]

$$P_e\Big]_{\substack{\text{Phase}\\ \text{Slip}}} = \frac{4}{\pi} B_L T_b \exp\left[\frac{-E_b/N_o}{2 B_L T_b}\right] \tag{33}$$

where,

$$B_L = 20 \text{ Hz}$$

$$T_b = \frac{1}{\text{Data Rate}} = \frac{1}{50 \text{ bps}} = 0.02 \tag{34}$$

$$E_b/N_o = C/N_o - 10 \log \text{data rate} \tag{35}$$

Equation (33) is plotted in Figure 7. For the required C/N_o of 26 dB - Hz we see that the possibility of error for a phase slip is

$$Pe\Big]_{\text{Phase Slip}} = 2.312 \times 10^{-5}$$

We now examine the probability of error for phase slips taking into account the oscillator phase noise and receiver additive noise.

The probability of phase slips with oscillator phase noise is given by

$$Pe\Big]_{\text{Phase Slip}} = \frac{1}{R_b T_{slip}} \tag{36}$$

where R_b = data rate = 50 bps and

$$T_{slip} = \frac{\frac{\pi}{4} \exp\left[\frac{0.5}{\sigma_n^2 + \sigma_m^2}\right]}{B_L} \tag{37}$$

where

B_L = 20 Hz

σ_n^2 = mean squared phase error due to noise

σ_m^2 = mean squared phase error due to oscillator noise jitter.

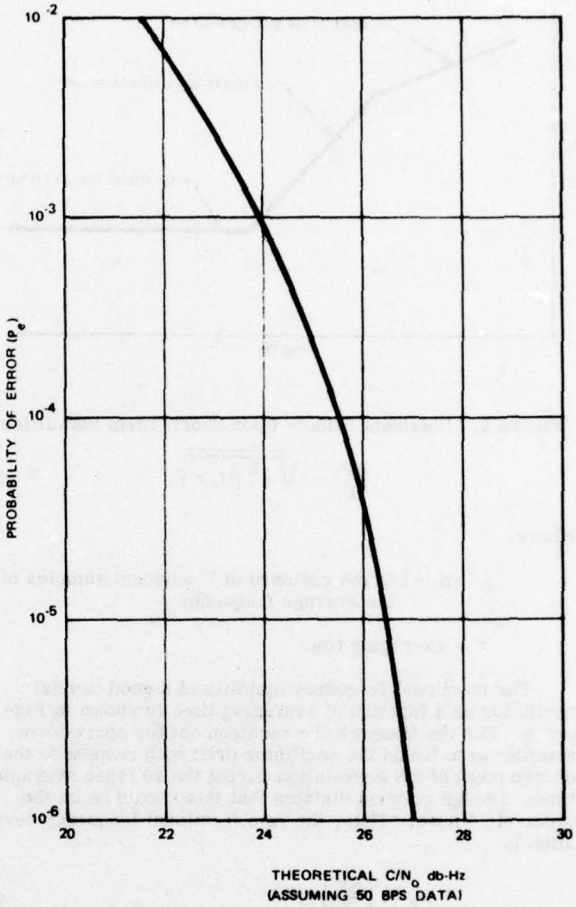

Figure 7. Probability of Phase Slip Caused Errors for Costas Loop Vs Theoretical C/N_o

previous analysis indicated that

$$\sigma_n^2 = 0.05 \text{ rad}^2$$

$$\sigma_m^2 = 1.42 \times 10^{-4} \text{ rad}^2$$

therefore, from (5)

$$T_{slip} = 841 \text{ sec}$$

and from (36)

$$Pe\Big]_{\text{Phase Slip}} = 2.378 \times 10^{-5}$$

This probability of phase slip error causes less than 0.1 dB-Hz C/N_o degradation in the Costas loop. Thus, the contribution of oscillator phase noise provides negligible system performance degradation.

Manpack Oscillator Survey

In selecting an oscillator for Phase I Manpack development, careful consideration must be given to one that meets the following requirements:

a. Required stability (short term and long term) necessary to meet system performance.
b. Fast warm-up.

c. Good phase noise and environmental stability characteristics to minimize system performance degradation.
d. Low power consumption.
e. Small size.
f. Low cost
g. Availability.

Five manufacturers have been identified that can potentially meet the requirements for Manpack oscillator. They are:

1. Bendix Corporation's development for Ecom; Fast warm-up tactical miniature crystal oscillator (TMXO).
2. Hewlett-Packard Model 10543A.
3. Frequency Electronics Corporation model FE-22-D0313 modified.
4. Austron, Texas; Sulzer Model 1120.
5. Collins Radio Group, Cedar Rapids, Iowa; Development for ECOM of the high stability temperature compensated crystal oscillator (HSTCXO).

Table VII presents the specifications from the manufacturer listed for the oscillators in columns 2 and 4 and the goals established in columns 1, 3 and 5.

Table VII. Oscillator Specifications

	Manufacturer				
Description	(1) Bendix	(2) Hewlett-Packard	(3) Frequency Electronics	(4) Austron	(5) Collins Radio
Frequency	5 or 5.115 MHz	5.0 MHz	5.0 or 5.115 MHz	5.115 MHz	5.0 MHz
Stabilization Time (at 25°C)	$\pm 3.3 \times 10^{-8}$ of abs frequency after 1 minute	$\pm 2 \times 10^{-9}$ of abs frequency after 30 minutes	$\pm 2 \times 10^{-8}$ of abs frequency after 6 minutes	$\pm 2 \times 10^{-8}$ of abs frequency after 5 minutes	$\pm 1 \times 10^{-8}$ of abs frequency after 1 minute
Short Term Stability	$\pm 1 \times 10^{-11}$ for averaging time of 1 sec to 20 min	$\pm 1 \times 10^{-11}$ for averaging times 1 sec to 100 sec	$\pm 1 \times 10^{-10}$ for averaging times of 1 sec	$\pm 3 \times 10^{-11}$ for averaging time of 1 sec	$\pm 1 \times 10^{-11}$ for averaging times of 1 sec
Aging Rate	$\pm 2 \times 10^{-10}$/week after 30 day stabilization	$\pm 5 \times 10^{-10}$/day $\pm 1.5 \times 10^{-7}$/ year	$\pm 5 \times 10^{-10}$/day after 1 hr	$\pm 1 \times 10^{-9}$/day after 72 hours stabilization	$\pm 2 \times 10^{-10}$/day after 30 days stabilization
Warm-Up Power	10 watt max for 0.1 min over -40°C to 75°C	8 watts max at 25°C	5 watts peak at 25°C (2 min)	5 watts peak at 25°C	10 watts max for 0.5 min over -40°C to 80°C
Continuous Operating Power	250 mw over -40°C to 75°C	3.5 watts at 25°C	0.4 watts at 25°C	3 watts at 25°C	150 mw over -40°C to 80°C
Temperature Stability	$\pm 1 \times 10^{-8}$ over -40°C to 75°C	$\pm 5 \times 10^{-9}$ over -55°C to 71°C	$\pm 1 \times 10^{-9}$ over -20°C to 40°C	$\pm 2 \times 10^{-8}$ over -20°C to +55°C	$\pm 5 \times 10^{-8}$ over -40°C to 80°C
Load Stability	$\pm 1 \times 10^{-9}$ for 5% load change at 50 ohms	$\pm 2 \times 10^{-10}$ for 10% load change at 50 ohms	$\pm 2 \times 10^{-10}$ for 5% load change at 50 ohms	$\pm 5 \times 10^{-9}$ for 5% load change at 50 ohms	$\pm 5 \times 10^{-9}$ for 5% load change at 50 ohms
Voltage Stability	$\pm 1 \times 10^{-9}$ for 5% voltage change at 12 VDC	$\pm 1 \times 10^{-10}$ for 10% voltage change at 20 VDC	$\pm 2 \times 10^{-10}$ for 10% voltage change at 12 VDC	$\pm 5 \times 10^{-9}$ for 10% voltage change at 28 VDC	$\pm 5 \times 10^{-9}$ for 10% voltage change at 12 VDC
Acceleration Sensitivity	$\pm 5 \times 10^{-9}$/g along any axis	$\pm 1 \times 10^{-9}$/g along any axis	$\pm 1 \times 10^{-9}$/g along any axis	$\pm 5 \times 10^{-9}$/g along any axis	$\pm 5 \times 10^{-9}$/g along any axis
Vibration Sensitivity	$\pm 5 \times 10^{-9}$/g during vibration without vibration isolators	$\pm 1 \times 10^{-9}$/g during vibration without vibration isolators	$\pm 1 \times 10^{-9}$/g during vibration without vibration isolators	$\pm 5 \times 10^{-9}$/g during vibration without vibration isolators	$\pm 5 \times 10^{-9}$/g during vibration without vibration isolators
Frequency Shock Stability	$\pm 5 \times 10^{-9}$/g after 50g, 11 msec	$\pm 1 \times 10^{-9}$ after 50g, 11 msec	$\pm 1 \times 10^{-9}$ after 50g, 11 msec	$\pm 1 \times 10^{-9}$ after 50g, 11 msec	$\pm 5 \times 10^{-9}$/g after 50g, 11 msec
Spurious Output	Down 90 dB from rated output	Down 100 dB from rated output	Down 100 dB from rated output	Down 80 dB from rated output	Down 100 dB from rated output
Harmonic Output	Down 30 dB from rated output	Down 30 dB from rated output	Down 40 dB from rated output	Down 30 dB from rated output	Down 30 dB from rated output

Table VII. (Continued)

Description	Manufacturer				
	(1) Bendix	(2) Hewlett-Packard	(3) Frequency Electronics	(4) Austron	(5) Collins Radio
Phase Noise (measured in a 1 Hz Bandwidth at an offset from 5 MHz)	10 Hz, - 110 dB 100 Hz, -130 dB 10 kHz, -140 dB	10 Hz, -120 dB 100 Hz, -135 dB 1 kHz, -145 dB 10 kHz, -145 dB	2 Hz, -108 dB 20 kHz, -160 dB	10 Hz, -110 dB 20 kHz, -145 dB	10 Hz, -110 dB 20 kHz, -140 dB
Volume (in^3)	1.0	30	6.5	19.5	2
Weight (oz)	8	20	5	9	10

Acknowledgements

Information for this paper was derived in part from a funded contract study titled "DESIGN DEVELOPMENT STUDY FOR PHASE I NAVSTAR GLOBAL POSITIONING SYSTEM MANPACK/VEHICULAR SET" accomplished in May 1975 for the Joint Program Office, Deputy of Space Navigation Systems, Headquarters, Space and Missile Systems Organization, Air Force Systems Command.

References

1. "Prime Item Development Specification for the Manpack/Vehicular Navigation Set of the Navstar GPS User Equipment Set Phase I" Specification Number CID-US-113, 26 February 1976.

2. "Navstar GPS X-Set Receiver Performance Flow Down Specifications" by G. Haefner, J. Moses et al. Magnavox Reference Number R-5227, 18 December 1975.

3. "A Proposal to SAMSO/JPO for the Navstar Global Positioning System, Volume 2 User System Segment" June 1974.

4. "Down Converter Phase Noise, Action Item Control No. 5" by C. R. Cahn, Interoffice Communication, 14 March 1975.

5. "Vibration Analysis for Electronic Equipment" by Dave S. Steinberg, A Wiley Interscience Publication.

6. "Characterization of Frequency Stability" by James A. Barnes, et al, IEEE Transactions in Instrumentation and Measurement, Vol. IM-20, No. 2, May 1971.

7. "Magnavox Communication and Navigation, Spread Spectrum Applications and State of the Art Equipments" by C. R. Cahn, Magnavox Report MX-TM-3134-32, dated 22 November 1972.

MINIMUM VARIANCE METHODS FOR SYNCHRONIZATION OF AIRBORNE CLOCKS

Richard J. Kulpinski
MITRE CORPORATION
Bedford, Massachusetts

Summary

This paper considers the application of minimum variance methods to the process of synchronizing geographically separated clocks using known configurations in which time-of-arrival measurements are made on radiated signals. Configurations are those that involve interrogation and reply between a user and a single doner, and one-way propagation between a user and the multiple sites of a reference system. Focus is on moving clocks using the latter category which is shown also to be a means of fixing location.

The relationship of variables to time-of-arrival measurements is described for stationary and moving users, for atomic and crystal clock and for ground wave and line-of-sight propagated signals.

Minimum variance concepts for solution of clock's variables are described in detail. Measurements over a period of time are applied to the solution of the clock's variables; additional sites of the reference are accepted as time-of-arrival related to them occur in time. Methods are presented for recursive processing which result in short histories of prior measurements being applied for estimating variables of the clock's location and much longer histories for clock related variables of time and frequency offset. Resulting reductions in the uncertainty of time offset causes the solution of clock's position to have diminished uncertainty. Fading memory techniques are described which cause measurements to be discounted as a function of their age.

Parametric expressions are given for accuracy as a function of the number and distribution of sites of the time reference, the location of the offset clock relative to the reference sites, types of observations, frequency of measurements and the rate of discounting/fading. Differences in accuracy between users with atomic clocks where frequency offset is assumed zero and crystal clocks where frequency offset is a variable are provided.

The Synchronization Problem

Time is divided into a sequence of intervals. Events are scheduled, executed and recorded as happening in terms of a specified reference for the intervals of time. The interval sequence may be peculiar to specific systems and their application or a universally recognized standard. Like intervals of time marked by separated clocks are likely to be offset in time. An interval of time is determined by the elapse of a specified number of cycles of oscillation. Because the frequency of clocks' oscillations are likely to be different than that of the reference particularly if crystal devices are used, the offset in time will not remain constant. The frequency of an oscillator may also change with time. Time offset, frequency offset, and frequency offset rate are variables that relate the behavior of one clock to another. Knowledge of their value at one instant of time enables their value to be predicted for other instances of time. Using radiated signals the value of these variables can be estimated.

The beginning of intervals and radiated signals either coincide or they are displaced by a known amount. Methods presented enable the solution of when received signals were emitted and therefore the solution of the offset in time between local and reference intervals. When variables which define how time offset changes are also estimated, synchronism between solution times is maintained.

Signals are likely to be received with some uncertainty because of receiver noise and other random effects. Random error in the measurements will cause the solution of variables to have error. The uncertainty that results when a solution is obtained with no more than a sufficient number of measurements for a solution may be acceptable. The uncertainty can be diminished with additional data taken over a longer span of time. The concept of averaging, curve fitting or smoothing is applied. Prior data is processed with recent measurements to obtain a less variable estimated of the behavior of the local clock relative to a reference.

Signaling for the Transfer of Reference Time

To determine the amount of offset in time and frequency it is necessary to determine the propagation delay in the transfer of timing signals from one location to another. Two signaling approaches are examined.

Propagation delay can be computed directly as a result of a cooperative exchange of signals between two terminals. Two way signaling methods are discussed briefly.

Other methods provide for signal transmission in only one direction. With one way signal systems any number of participants can synchronize with the reference system unincumbered by cues and signaling protocol usually necessary with two way signaling methods.

To maintain synchronism by receiving one way propagated signals while moving, units must be able to fix their location relative to the source of timing signals. The means for fixing location may be independent of the timing signal. Alternatively intervals of time may be related to intervals between periodic transmissions of systems configured for location fixing; signals used for ranging can be used to transfer time. Receivers are able to determine their location and therefore when received ranging signals were transmitted and can predict when future ordered signals will be emitted. Periodic transmissions of location fixing systems such as Loran, Omega and proposed satellite systems can provide a reference for the division of time. These are specific examples of a general form which will be discussed and which we will call a reference system: a configuration of spatially separated, mutually timed

and located units by which users' timing and location can be determined from one way propagated signals. Most common are reference systems in which signals are broadcast cyclically from units of the reference. In an alternative configuration, units of the reference system receive signals periodically triggered by the user's clock. Remotely then the user's location, time offset, and frequency offset relative to the reference system can be determined.

When signals necessary for a solution of time offset are transmitted simultaneously, or nearly so, the solution may be made without consideration of vehicle motion and unknown frequency offset. The estimate is of a single fix nature; the computed value of time offset applies for the instant the signals were transmitted.

In general, the occurrence of signal transmissions for time dissemination need not be constrained to occur grouped so that vehicle motion and frequency offset are absent as variables in the solution of time offset. Such grouping may not be an alternative; signals sufficient for a solution may be emitted disjointly over a span of time. The functional relationship between variables of position and time offset applicable for one instant of time and their value at other instances is assumed known. Because of this, measurements taken at various instances over the span can be expressed in terms of variables for a specified instance and their solution obtained.

Clocks and Their Behavior

Whenever measurements over a span of time are processed in the solution of variables, a functional description of the way variables change with time is necessary. Suitable models are described based on characteristics of available crystal and atomic devices. There are fundamental differences between the two classes. In contrast to atomic sources, the frequency of crystal devices is uncertain enough to require attention, and is sometimes considered a source of error. Yet because frequency offset is very stable and its behavior reliably predictable, it can be estimated accurately in real time along with time offset.

A generally accepted expression for the trajectory of time offset is given by the following equation, and is illustrated in Fig. 1:

$$\Delta T(t) = \Delta T(t_o) + \alpha(t_o)(t-t_o) + \frac{\beta}{2}(t-t_o)^2 + \varepsilon(t) \qquad (1)$$

where

fo	Frequency of local oscillator.
fr	Frequency of reference oscillator.
$\Delta T(t)$	Time offset at time t.
$\Delta T(t_o)$	Initial setting error.
$\alpha(t_o)$	Frequency offset $(f_o - fr)/fr$; a dimensionless quantity expressed as parts in 10^{10}.
β	Rate of change of frequency offset or long term drift $(\dot{f}_o - \dot{fr})/fr$; usually given the dimension of parts in 10^{10}/day.
$\varepsilon(t)$	Other factors, particularly random perturbations. The effect called short-term stability is represented by this term.

Depending on the interval during which data are taken, and depending on whether a crystal or atomic device is used for the clock's oscillator, either frequency offset or frequency offset rate, or both, may be assumed to be zero and dropped from the model without a decline in acceptable accuracy.

As a practical matter for many field applications, the frequency offset rate may be considered to be zero in modeling the behavior of crystal devices. Frequency offset, denoted ΔT, is thus assumed constant, and the following model can be used:

$$\Delta T_t = \Delta T_{t_o} + (t-t_o)\,\dot{\Delta T}$$

$$\dot{\Delta T} = \text{constant.} \qquad (2)$$

Conceptually, the model is a straight-line representation of a process with a slightly quadratic behavior. The consequences of the approximation are illustrated in Fig. 2. A filter based on (2) would make a straight-line fit to a slightly quadratic data history. Because of the modeling approximation, the period of time over which observation may be used to influence the solution is limited. Fig. 2 shows some typical values. A bias error of less than 30 ns in the solution of time offset will result if the frequency change rate β is less than 1 part in 10^7/day after power has been applied for a short time. It appears that after warmup, the trajectory may be modeled with constant frequency offset, and long integration intervals may be applied. During warmup, the integration interval is shortened to a few data points. By applying such a model, some economy in the amount of processing is obtained.

For purposes of estimating time offset, the frequency offset of atomic devices can be assumed to be zero. For frequency offset of 1 part in 10^{11}, time offset will change at the rate of 1 ns every 100 s. For estimating time offset with data taken over a 600-s interval, for example, a model of constant time offset will cause a 3-ns lag between the estimated and actual value-insignificant compared with other sources of uncertainty.

Acceleration and temperature change will cause the frequency of a crystal device to change from its previous constant value. The ability of a filter to respond to change depends on its time constant. Long time constants are applied to obtain large reduction in the random variation of the filter's output, but cause the filter to respond sluggishly to change at its input. For such a situation, the resulting transient discrepancy is only as small as the sensitivity of the crystal device to effects of the environment.

Acceleration induced stresses cause a step shift in the frequency of the crystal's oscillations. Consider application of precision oscillator having an acceleration-induced frequency shift of 1 part in 10^9/g. Fig. 3 illustrates consequences of an aircraft making a 1-g turn, one more g than when flying level, at a velocity of 1000 ft/s; time in the turn is approximately 30 s, and during the turn, the oscillator's frequency shifts 1 part in 10^9 as a result of the 1-g acceleration. Because of the long integration time of the filter for this example, 200 s, the estimate of time offset lags the actual value by 25 ns at the end of a 30-s maneuver. Following the acceleration, the oscillator's frequency returns to the value it had prior to the maneuver.

The resonant frequency of quartz crystal oscillators depends on the temperature of the crystal and other components. The first consideration is to assure that the frequency offset remains within acceptable limits over the expected operating temperature so that the norminal frequency can be used to convert elapsed cycles of oscillation to time of propagation. For example, the measured propagation time

over a 300 nm path will be within 10 nanoseconds of the true time of propagation if the frequency of the local oscillator is within 5 parts in 10^6 of the nominal frequency. Oscillators are readily available for which offset in frequency is within this limit. For longer propagation distances such as to synchronous orbits, offset on the order of 1 part in 10^7 would limit error in the measured propagation time to be less than 10 nanoseconds. Although frequency offset between reference and local clock is a solution variable, the reference itself may be offset from its nominal value and therefore a residual error in the measurement of propagation time will remain.

The actual behavior of time offset may depart from the modeled behavior because of change in frequency offset due to change in temperature. It is necessary to assure that the rate of change of frequency offset due to temperature change is slow enough for the time offset filter to respond to the change. How the frequency of any particular oscillator unit will change in an actual situation cannot be ascertained from the commonly presented frequency offset vs temperature curves. Fig. 4 is an example of the way frequency offset changes as a function of temperature change for an AT cut crystal.[1] The temperature at which the maximum and minimum points of the curve appear depends on the cut of the crystal. This particular crystal has a temperature coefficient of about 1 part in 10^8/°C at a temperature 2°C away from the zero point. Other crystal types have completely parabolic frequency versus temperature curves.

Because it takes time for energy to dissipate, a somewhat constant rate of change of frequency is likely with change in ambient temperature. As an example, a discrepancy of about 50 ns between the actual and estimated time offset will result with a 200-ns filter when frequency offset changes from a constant value at a rate of 1 part in 10^9/10 min for a duration of 10 min, after which frequency becomes constant. For operation within the region of Fig. 4 in wh which the temperature coefficient is 5 parts in 10^8/°C, the change in temperature must not exceed 0.22°C during a 10-min period. To assure this, a thermostatically controlled oven is necessary. If an oven is used, it will probably be designed to operate at a zero coefficient point, which will be at a temperature slightly higher than the system operating temperature.

The notion conveyed by the phrase "short-term stability" is quite different from the similar sounding "long-term stability:" long-term stability-systematic change of frequency, short term stability-random variation of frequency. Fig. 5 is representative of data on short-term stability and indicates that for intervals of time less than 10 s, the variation in indicated elapsed time will be less than 0.1 ns. As a practical matter, for applications of this paper, short-term stabiltiy may be ignored as a source of uncertainty in the behavior and modeling of clocks.

Measured Elapsed Time, Propagation Time and Time Offset

The relationship between measured elapsed time, propagation time between reference and local clock and time offset is defined.

Fig. 6 shows intervals of time as marked by the reference system and intervals of time as marked by the local clock for which time offset and values of other variables is to be determined. The intervals shown in Fig. 6 are merely for illustration; any sequence known to the local clock is applicable.

With each transmission a measurement of elapsed time is made. The measurement denoted θ_{n-j} is the difference between the receiver's timing of the beginning of an interval and the receipt of the signal emitted when the transmitter times the beginning of the interval to have occurred. Measurements by both the reference and local clock are illustrated. Measurements are expressed as a function of quantities of unknown value: the time for propagation of the signal from transmitter to receiver and the offset in timing between like intervals as marked by the transmitter and receiver.

For an interval numbered n-j

$$\theta_{n-j} = PT_{n-j} \mp \Delta T_{n-j} \tag{3}$$

where

θ_{n-j} Observation on a signal transmitted during the interval denoted n-j.

PT_{n-j} Propagation time.

ΔT_{n-j} Time offset.

In the expression, the combination $\mp$ appears, the minus sign applies when observations are made by the user, and the plus sign applies when observations are made by the reference configuration.

A sufficient number of observations are made and these processed to determine the properties of the user at a common time t_n. Variables of propagation time and time offset defined for various intervals during which measurements were made must be expressed in terms of variables applicable for the time of the solution t_n.

For time offset

$$\Delta T_n = \Delta T_{n-j} + \tau_j \dot{\Delta T} \tag{4}$$

$$\dot{\Delta T} = \text{constant}$$

where

τ_j Elapsed time between n and n-j.

ΔT_n Time offset between n and n-j.

$\dot{\Delta T}$ Time offset rate, in general constant, but zero for atomic clocks.

Configurations for the Transfer of Time

The way PT_{n-j} is expressed in terms of variables for a specific time depends on how many terminals of the reference are involved.

Two-Way Signaling and a Single Doner

With no more than a single reference terminal a two-way exchange of signals between the local clock and the reference terminal is necessary. Each makes a measurement of elapsed time on the other's transmission. If the propagation time between terminals is changing, the rate of change is assumed to be constant over the interval of time necessary for the transmission of signals. Constant rate of change of propagation time is an approximation and applicable for only short intervals of time. The potential for flight path changes does not warrant the use of exact descriptions applicable for extended lengths of time.

Four variables appear in the solution equations: time offset, frequency offset, propagation time and rate of change of propagation time. The assumed behavior of propagation time is given by (8). For the situation with dynamics, four independent measurements are necessary: for an initial solution normally two measurements are made by the user on two signals of the reference separated in time and two measurements are made by the reference on transmissions by the user. Measurement values are communicated to a single location for solution of variables. Note that propagation time is an explicit variable; neither the velocity or mode of propagation appear as factors in the solution equations. Reciprocity is assumed but signals transmitted by the reference may experience effects different than those emitted from the local clock.

Multiple Reference Terminals

Consider a reference configuration consisting of a number of mutually timed and spatially separated units. Solution of clock's properties can be made with either the reference or user transmitting. When observations are made at the user's receiver on transmissions of a sufficient number of units of the reference, onboard solution follows. No transmission is required by the user. On the other hand, observations taken at a sufficient number of units of the reference when communicated to a common location allow solution of the user's properties by the reference system.

The way in which signals propagate must be defined functionally. Propagation time is expressed in terms of the known location of the reference and unknown location of the user and an assumed velocity of signal propagation. Specific expressions are given in appendix I for line-of-sight and ground wave propagated signals. If the user is moving, its location at various times when signals are emitted must be expressed in terms of its location at a specific time for which the clocks properties are to be updated; constant velocity motion is assumed and is reliably applicable for no more than short intervals of time.

There are normally six variables: horizontal position and velocity, and time and frequency offset. Altitude is assumed known from an onboard altimeter. To provide for a usefully accurate solution when observations are one way, three graphically separated sites of the reference are necessary. Normally each site transmits in turn and the group repeats cyclically. For an initial solution there must be as many independent measurements as variables. When there are insufficient measurements in a single group, then more than one group must be observed to obtain a solution. With two or more groups, there may be more than sufficient observations and a least squares solution criterion is appropriate.

Minimum Variance Solution Methods

First considered are expressions for the minimum variance solution of the properties of the clock using measurements of time-of-arrival of signals received in short interval of time. The solution of variables as well as the variances and correlation of their probable error is determined. Following each solution additional time-of-arrival measurements are made and with these alone a solution is also possible. Applicable expressions are given. Recusive minimum variance method is discussed next. The prior solution predicted to the time of the current estimate represents information on the current state of the clock and is applicable as data in the minimum variance solution. Estimates of time and frequency offset with a smaller standard deviation can be obtained by taking into account prior solution predicted to the time of the current solution. Recursive minimum variance concepts have received considerable attention in the past decade.[2,5,7] Their application to the process of synchronism of clocks is discussed.

Solution Based Solely on Time of Arrival Measurements

Consider the following statement of the problem and its solution. Suppose that a number of measurement quantities are available at discrete instances of time (t_{n-i}, t_{n-j}, $\cdots$, t_{n-k}) with the observation at time t_{n-j} denoted θ_{n-j}. Suppose that θ_{n-j} is related to the state S(n) at time t_n by

$$\theta_{n-j} = J_{n-j}S(n) + \upsilon_{n-j} \tag{5}$$

where υ_{n-j} represents the measurement error that occurs at n - j. Denote the set of such relationships of a group of observations by

$$\theta = J\,S(n) + V \tag{6}$$

where

$$E\left|V\right| = 0,\quad E\left|VV^T\right| = R.$$

Then the minimum variance estimate of S(n) is obtained by computing

$$S(n) = (J^TR^{-1}J)^{-1}J^TR^{-1}\theta. \tag{7}$$

The matrix $(J^TR^{-1}J)^{-1}$ is the convariance of the solution error, with the diagonal elements representing the variance of the solution error.

It is assumed for details of the following that equal uncertainty exists for all observations, and that the error in the observations are uncorrelated; $R_{k\delta k1} = \delta^2_m I$. When the dominant source of random uncertainty is caused by quantization of arrival time, such an assumption is reasonable. When receivers are implemented to provide a relative measure of signal-to-noise ratio, observations can be weighted proportional to signal-to-noise ratio with consideration for the presence of quantization error. Note that with the assumption $R = \sigma^2_m I$,

$$(J^TR^{-1}J)^{-1} = \sigma^2_m(J^TJ)^{-1},\ \text{and}\ J^TR^{-1}D\theta = \frac{1}{\sigma^2_m}(J^TD\theta).$$

With equal weighting of observations, calculations can be made without considering the specific value of σ^2_m, but the computed covariance is normalized to the value of σ^2_m.

The way vehicle velocity and frequency offset enter into the problem and the way they can be treated as solution variables is discussed.

Two Way Signaling With a Single Doner

A reasonable approximation, at least for short intervals, by which propagation time at various instances can be related to propagation time at a specific time is to assume constant rate of change:

$$PT_n = PT_{n-j} + \tau_j\dot{PT} \tag{8}$$

$$\dot{PT} = \text{Constant}.$$

If the vehicle's state at time n is defined as

$$S(n) = [PT_n \Delta T_n \dot{P}T \Delta\dot{T}]^T, \tag{9}$$

then, in general, the observation at time n-j is related to the state at time n by

$$\theta_{n-j} = [1 \pm 1 - \tau_j \mp \tau_j]\, S(n) + \upsilon_{n-j}. \tag{10}$$

Given the sequency of four transmissions shown in Fig. 7 for example, the following set of simultaneous equations exists:

$$\begin{bmatrix}\theta_1\\ \theta_2\\ \theta_3\\ \theta_4\end{bmatrix} = \begin{bmatrix}1+1 & -\tau_1 & -\tau_1\\ 1-1 & -\tau_2 & +\tau_2\\ 1+1 & -\tau_3 & -\tau_3\\ 1-1 & -\tau_4 & +\tau_4\end{bmatrix} S(n) + \begin{bmatrix}V_1\\ V_2\\ V_3\\ V_4\end{bmatrix} \tag{11}$$

which define the ingredients for a minimum-variance solution. If, for example, each of the four transmissions indicated in Fig. 7 is equally spaced T s apart, and the solution is for T s from the time of the last reply, then by applying (7) and (11), time and frequency offset can be computed as follows:

Solution	Variance
$\Delta T = \frac{1}{4}(-2\theta_1 + \theta_2 + 4\theta_3 - 3\theta_4)$	$\frac{15}{8}\sigma_m^2$
$\Delta\dot{T} = \frac{1}{4T}(-\theta_1 + \theta_2 + \theta_3 - \theta_4)$	$\frac{\sigma_m^2}{4T^2}$

(12)

where σ_m^2 is the variance in uncertainty of θ_i and is assumed equal and uncorrelated among observations. The variance in the solution due to random uncertainty in the observation is as indicated. If, for example, σ_m were equal to ± 30 ns, then the uncertainty in ΔT would be about 45 ns. The uncertainty in frequency offset for T = 1 s would equal 1.5 parts in 10^8. The indications are that as the time between replies is increased, then accuracy in frequency offset is increased. However, the equations are appropriate for as long as the vehicle's motion generates constant rate of change of propagation time and frequency offset is constant. For aircraft, maneuvers are likely, and therefore T must be kept short.

One-Way Propagation With Multiple Sites

A reasonable assumption is that the user is moving at constant velocity for at least a short interval of time:

$$\begin{aligned}\phi_n &= \phi_{n-j} + \tau_j\dot{\phi}\\ \dot{\phi} &= \text{constant}\\ \lambda_n &= \lambda_{n-j} + \tau_j\dot{\lambda}\\ \dot{\lambda} &= \text{constant}.\end{aligned} \tag{13}$$

The state of the user is defined by six variables:

$$S(n) = [\lambda_n \phi_n \Delta T_n \dot{\lambda}\ \dot{\phi}\ \Delta\dot{T}]^T. \tag{14}$$

The observation θ_{n-j} at time n - j is related to the state at time n by the following general expression:

$$\theta_{n-j} = f[(\phi_n - \tau_j\dot{\phi}), (\lambda_n - \tau_j\dot{\lambda})] \mp \Delta T_n \pm \tau_j\Delta\dot{T} + \upsilon_{n-j}. \tag{15}$$

The term f[] relates the propagation time at time n - j to state variables at time n. The specific details of f[] depend on whether the signals are propagated line-of-sight or on the surface of the ellipsoidal earth, and are discussed in Appendix I. Equation (15) is nonlinear. Gauss's method of differential corrections is used to obtain a solution of the state, given a number of observations. The linear terms of a Taylor expansion of (15) about an assumed value of the state at time n denoted $S_a(n)$ are retained. Given a number of observations, a set of linear equations can be formed. Taylor expansion of (15) has the form

$$[\theta_{n-j}(m) - \theta_{n-j}(a)] = [\beta_{j\lambda}\ \beta_{j\phi}\ \mp 1\ \ -\tau_j\beta_{j\lambda}\ \ -\tau_j\beta_{j\phi}\ \ \pm\tau_j][S(n) - S_a(n)] \tag{16}$$

or

$$D\theta_{n-j} = J_{n-j}DS_n + \upsilon_{n-j}.$$

The term $\theta_{n-j}(a)$ is a computed value of the observation obtained by substituting the assumed state $S_a(n)$ for the variables of (15). The term $\beta_{j\phi}$ is computed as

$$\beta_{j\phi} = \left.\frac{\partial PT_{n-j}}{\partial\phi_n}\right|_{S=S_a(n)}. \tag{17}$$

Explicit expressions for PT_{n-j} and $\beta_{j\phi}$ and $\beta_{j\lambda}$ are given in Appendix I for both line-of-sight and ground-wave-propagated signals.[6]

There are normally six variables, although, depending on whether the vehicle is stationary and frequency offset is known to be negligible, various combinations of three to six variables may need to be considered to obtain an unbiased estimate of time and frequency offset. There must be at least as many independent observations as variables. To provide for a usefully accurate solution when observations are one way, three graphically separated sites of the reference are necessary. Normally, each site transmits in turn and the group repeats cyclically. When there are insufficient observations in a single group, then more than one group must be observed to obtain a solution. With one group, there may be insufficient observations. With two or more groups, there may be more than sufficient observations, and a least squares solution criterion is appropriate. Given p observations, the following relationships exist:

$$\begin{bmatrix}D\theta_1\\ \vdots\\ D\theta_p\end{bmatrix} = \begin{bmatrix}\beta_{1\lambda} & \beta_{1\phi} & \mp 1 & -\tau_1\beta_{1\lambda} & -\tau_1\beta_{1\phi} & \pm\tau_1\\ \vdots & & & & & \\ \beta_{p\lambda} & \beta_{p\phi} & \mp 1 & -\tau_p\beta_{p\lambda} & -\tau_p\beta_{p\phi} & \pm\tau_p\end{bmatrix} DS(n) + \begin{bmatrix}\upsilon_1\\ \vdots\\ \upsilon_p\end{bmatrix} \tag{18}$$

or

$$D\theta = J\,DS(n) + V.$$

The minimum-variance solution of the differential coorection $DS(n) = S(n) - S_a(n)$ is obtained by

$$DS(n) = (J^T R^{-1} J)^{-1} J^T R^{-1} D\theta. \qquad (19)$$

The assumed state is corrected by the amount of the computed differential. The assumed state may not be sufficiently close to the actual state, so that the second-order terms dropped in the Taylor expansion are actually negligible. It is usually true that the solution will be closer to the actual state than the prior assumed value. Because of this, the usual procedure is to reiterate the solution using the solution of the first iteration as the assumed value for the second, and so on, until DS is smaller than a specified threshold.

The variance to which the solution of time and frequency offset and other variables will be determined is given by the diagonal elements of the matrix $(J^T R^{-1} J)^{-1}$. The accuracy depends on the geometry of the reference sites and the user. Consider a situation using Fig. 8 to illustrate performance. For the situation, one transmission from each site represents a group, and two groups are observed with τ denoting the group repetition interval. The standard deviation of time offset for a solution time just following the completion of the second group and when the six variables of (14) are estimated is as given in Fig. 8. The standard deviation of frequency offset is $(2/\tau^2)^{1/2}$ multiplied by the value of the contours of these figures. Contours of Fig. 8 are normalized to the measurement uncertainty. Between updates, synchronization uncertainty will increase because of the uncertainty in estimated frequency offset. At a time just before the completion of the reception of signals of the following group, the standard deviation in synchronization will be $\sqrt{5}$ times the values given for contours of Fig. 8. Performance for various other situations is given in Table I.

Recursive Minimum Variance Methods

Estimates of time and frequency offset with a smaller standard deviation can be obtained by using as data the predicted solution of the state for the time of the current solution along with the time-of-arrival measurements since the prior solution. Measurements of time-of-arrival and the predicted estimate influence the current update inversely proportional to values assigned the variance of their probable error. The variance of the probable error of the solution relative to that for time-of-arrival measurements is obtained with each computation of a solution. Variance of the probable error of the predicted solution can be computed. A pitfall in the application of recursive methods is to use the predicted variance of probable error without modification. With each succeeding update the computed variance of the solution error decreases, asymptotically approaching zero. The consequence is that the most recent time-of-arrival measurement will have negligible influence on the current solution. An assumption implicit in the mechanics of commonly presented formulations is that the mean value of the behavior of the system whose properties are to be estimated can be modeled accurately over an indefinite length of time and this leads to an asymtotically zero variance computed for the solution error. Usually, models of process behavior fit reality only in a piecemeal fashion. Finite computer precision is also a factor overlooked. The amount of reduction in variance is limited because of finite precision and this implies that only a limited amount of past data can be used to influence the current update. Unless precautions are taken, incomplete descriptions of process dynamics can cause divergence between the actual and computed behavior of the process.

As a practical matter, vehicle velocity is modeled as constant velocity. Because maneuvers and deviations from the assumed flight path are possible, the predicted location and velocity for the time of the next solution may not have a mean value consistent with the clock's actual location. The solution of time and frequency offset will therefore be influenced by erroneous data if predicted position and velocity are used as data in the solution. To prevent uncertainty in the modeled flight path of the vehicle from affecting the accuracy of the estimate of time offset, the variables of the vehicle's path are discounted completely and not allowed to influence the current update. Complete discounting is achieved by assigning very large value to the variance of their probable error.

Because oscillators used in clocks behave uniformly and predictably, the modeled dynamics of time offset conforms to reality for as much as a few hundred seconds or longer. The predicted estimate of time and frequency offset have a mean value consistent with the actual value and thus is used as data to influence the current update. With each update, the uncertainty in time and frequency offset diminishes. Fading memory techniques are applied and cause the variances of the predicted estimate of the variables of the clock to approach a non zero steady state value. This assures that recent observations of time-of-arrival influence to a degree the current solution and therefore the solution is able to respond to unmodeled slow changes in the behavior of the clock. Fading memory techniques cause the influence of prior data on the current update to diminish as a function of data age.

The following sequence of computations enable recursive minimum variance solutions and allow complete discounting of position and motion variables to be effected each update:[5]

$$\begin{aligned} S(n/n) &= S(n/n-q) + C(n/n)J^T R^{-1}\,D\theta \\ S(n/n-q) &= \Phi\, S(n-q/n-q) \\ C^{-1}(n/n) &= C^{-1}(n/n-q) + J^T R^{-1} J \\ C^{-1}(n/n-q) &= \frac{1}{Z}\,(\Phi^T)^{-1} C^{-1}(n-q/n-q)\,\Phi^{-1}. \end{aligned} \qquad (20)$$

The way the state changes between solutions is assumed known and is defined by Φ

$$\Phi = \begin{bmatrix} I_1 & \tau_q I_2 \\ 0 & I_2 \end{bmatrix} \qquad (21)$$

where the dimensions of each identity I_1 depend on which elements make up the state. For stationary vehicles, the velocity terms may be elmininated, and for atomic clocks, the variable for frequency offset may be eliminated.

Equation (20) may appear incomplete in that the term often denoted Q, which represents process uncertainty, is absent:

$$C(n/n - q) = \Phi\, C(n - q/n - q)\, \Phi^T + Q. \qquad (22)$$

Both modeling uncertainty and limited computer precision are handled practically using a technique called fading memory. The constant Z in (20) where (1<Z<2) causes the covariance to approach a finite nonzero steady state. Its application is discussed in detail below.

In (20), the term S(n/n) is the solution for the current update, and S(n - q/n - q) is the solution for the prior update with τ_q s between updates. The term S(n/n - q) represents the prior solution predicted to time n. The terms C(n/n) and C(n/n - q) represent the covariance of the error of the current solution and predicted state, respectively.

In the mechanization of an algorithm having a state of r variables, the term $J^TR^{-1}J$ is an r x r matrix and $J^TR^{-1}D\theta$ is an r x 1 column vector. Storage is assigned for these two matrices. Following an update, the term $C^{-1}(n/n - q)$ is computed and placed in storage assigned for $J^TR^{-1}J$. Storage $J^TR^{-1}D\theta$ is set equal to zero. Both $D\theta_i$ and J_i are computed following each measurement or when time permits. The products $J_i^TR_i^{-1}J_i$ and $J_i^TR_i^{-1}D\theta_i$ are also formed and added to the contents of storage for $C^{-1}(n/n - q)$ and $J^TR^{-1}D\theta$ as appropriate.

Obtaining the Initial Solution

An initial solution and its covariance can be computed using equations (20) with appropriate initial conditions as discussed in the following. Initial solution for the case of two way signaling with a single doner and for the case of signaling with multiple reference sites is discussed separately.

For the configuration in which a local unit exchange timing signals with a single reference an initial solution can be computed using equations (20) with J_{n-j} defined as in equation (10) and S(n/n-q), $C^{-1}(n/n-q)$ and θ_{n-j} (a) set equal to zero for the first three lines of equation (20).

For the case of multiple reference sites, the matrix J is the result of linearization about an assumed solution. The term S(n/n-q) is set equal to the assumed solution. For the initial solution, S(n/n-q) is the receiver's best guess of its state and it is used to compute J_i and $D\theta_i$. For the initial solution $C^{-1}(n/n-q)$ is set equal to zero, indicating no confidence in the initial guess. If iterations are necessary to converge to an initial solution $C^{-1}(n/n-q)$ is set equal to zero for each iteration. If in updates following initialization $C^{-1}(n/n-q)$ is set equal to zero, then only time-of-arrival measurements between updates influence the current update; past estimates of the state have no effect.

Complete Discounting of Flight Variables

In updates following the initial, the predicted variables associated with the position and velocity of the state are discounted completely because of uncertainty in the modeled flight path of the vehicle. Complete discounting is implemented as follows: All elements of $C^{-1}(n/n-q)$ related to variables of the vehicle's position and motion are assigned zero value. The elements associated with the variables of the clock are assigned the inverse covariance of the predicted state of the clock for the time of the current update. Therefore the last expression in (20) is not used as indicated. Define $C_{\Delta T,\dot{\Delta T}}(n-q/n-q)$ as the covariance of the solution error of the clock's state for the previous update, then

$$C_{\Delta T,\dot{\Delta T}}(n/n-q) = \Phi\, C_{\Delta T,\dot{\Delta T}}(n-q/n-q)\, \Phi^T \qquad (23)$$

and therefore $C^{-1}(n/n-q)$ has the form

$$C^{-1}(n/n-q) = \begin{bmatrix} 0 & & & \\ & 0 & & \\ & & 0 & \\ & & & [C^{-1}_{\Delta T,\dot{\Delta T}}(n/n-q)] \end{bmatrix} \qquad (24)$$

With each update, the uncertainty in time offset diminishes. Even though position and velocity are discounted completely, uncertainty in the estimate of these variables also diminishes. Accuracy of position and velocity asymptotically approaches that obtained with an a priori perfectly synchronized clock. The proportion of uncertainty in the estimate of position that is diminished because of an accurate estimate of time offset is appreciably greater than that obtained from using the flight dynamics for the allowable short period of time. Thus little is lost because of complete discounting, while there is considerable gain through preventing uncertainty in vehicle motion from biasing the estimate of time offset.

Implementation of Fading Memory on Clock's Variables [3,4]

Beginning with the initial update, a steady state covariance can be approached with successive updates by multiplying the term C (n/n-q) by the value $Z = k^{\tau_q}$ prior to computing a new update, where τ_q is the time between the last and current update and k is a constant (1<k<2). Such a mechanism causes only a limited number of past observations to affect the current solution. The solution will respond to unmodeled slow changes in process behavior. This approach is sometimes called fading memory, as the influence of past data and measurements is diminished as a function of age.

The amount of fade, or the steady-state value of the covariance, is controlled by the value of k (1<k<2). When k = 1, all prior observations are given equal weight. With this, the covariance of the solution error would approach zero with time. With k such that Z has a value in the vicinity of Z = 2, only the most recent observations influence the solution's outcome. With k = 1.1, data from an interval 24 seconds old will have weight 0.1 relative to the current data. With k = 1.004, data from an interval 572 seconds old have weight 0.1 relative to the current interval.

Expected Performance Random Uncertainty

Parametric relationships for the expected accuracy following initialization and during steady state are given in Table I for a number of cases. For the multiple-site situation, one or more observations related to each site form a group of p observations. Like observations are repeated at an interval of τ s. Expressions of Table I are specifically for the case in which p observations are on simultaneously transmitted signals. Fig. 9 illustrates the situation. In reality, signals may be transmitted at various times within a group interval. The assumption of simultaneous signals has less cluttered expressions, which in the outcome

convey quite well general conclusions about accuracy. For initialization, two groups are used. Expressions for accuracy are given when the state is determined immediately following the second group, denoted TA, and for a time immediately preceding the reception of the third group, denoted TB. Comparison indicates how the accuracy of predicted time offset degrades because of uncertainty in the estimate of offset rate. Because in the steady state many past observations affect the current update, the steady-state accuracy is quite insensitive to the specific transmission format and the time for which the solution applies. In Table I, accuracy for the steady state is for the predicted estimate at a time just before the next group.

The upper left 3 x 3 partition of the inverse covariance for various situations contains the following matrix denoted A_s:

$$A_s = \frac{1}{\sigma_m^2} \begin{bmatrix} \sum_{i=1}^{P} \beta_{i\lambda}^2 & \Sigma\beta_{i\phi}\beta_{i\lambda} & \Sigma^{\mp}\beta_{i\lambda} \\ & \Sigma\beta_{i\phi}^2 & \Sigma^{\mp}\beta_{j\phi} \\ \text{symmetrical} & & P \end{bmatrix}. \qquad (25)$$

The third diagonal element of A_s^{-1} provides the solution to $\sigma^2_{\Delta Ts}$. Fig. 8 shows contours for $\sigma_{\Delta Ts}/\sigma_m$ for the site geometry shown in the figure.

Note from Table I that steady-state variance for time offset is essentially equal for all situations except one. For the case of a moving user with a crystal clock, the standard deviation of time offset is about $\sqrt{2}$ larger than for other situations.

Expected Performance Systematic Error

In addition to random uncertainty, various systematic sources of error also exist. For example, even after careful calibration, there will still remain uncertainty in the propagation path and in the time assumed for the signal to move from transmitter to antenna and from antenna to the detection logic. Although small by themselves, these factors may be manifested as much larger errors in the solution, in much the same way that random errors in the observations affect the solution. Filtering processors act to diminish the random variation in the solutions, but the systematic error of the solution remains virtually unchanged.

In general, between updates, the same combination of observations is collected. Although the observation errors differ among links of the group, it is generally true that for each link, certain observation errors will remain constant for succesive groups.

Denote $\varepsilon\theta$ as a vector of systematic error of an observation group. Because the systematic error is considered constant over an integration time, the solution of variables of frequency offset and vehicle velocity do not incur error as a result. Denote $[\varepsilon\lambda \ \varepsilon\phi \ \varepsilon\Delta T]^T$ as the error of the solution due to systematic error then

$$[\varepsilon\lambda \ \varepsilon\phi \ \varepsilon\Delta T]^T = (H^T H)^{-1} H^T \varepsilon\theta$$

where the ith row of H is the left partition of the observation vector; for a multiple-site situation, for example:

$$J_i = [\beta_{i\lambda} \ \beta_{i\phi} \ \overline{+} \ 1 \ \vdots \ -\tau_i\beta_{i\lambda} - \tau_i\beta_{i\phi} \pm \tau_i].$$

Note that $(H^T H)^{-1} = A_s^{-1}$ of the observation group.

Consequences of various systematic error can therefore be evaluated.

An Illustration of Performance

Fig. 10 summarizes conditions and expected performance for the results shown in Figs. 11 and 12 of an actual flight. The aircraft transmits once per second. Observations of a group are made at the three reference sites on a single transmission of the aircraft. Because of this, solutions of position and time offset can be made independent of the vehicle's velocity and the frequency offset of its clock. These single-fix solutions are indicated by the symbol □ in Figs. 11 and 12. In addition, the sequence of observations is filtered using (20) with complete discounting of variables of the vehicle's path at each update. The distribution of probable error expected for both situations is illustrated in Fig. 10. Clocks with 10-MHz oscillators were used, causing ±50-ns quantization of signal arrival time. The solution of position and time offset during steady-state operation with k = 1.005 is plotted in Figs. 11 and 12, respectively, with the symbol Δ. The spread in the single-fix solution of time offset is about ±750 ns, while that after filtering is about ±100 ns. The rate of change of time offset evident in Fig. 12 is about 1 μs/s, indicating that the frequency offset of the user's clock is about 1 part in 10^6.

Summary and Conclusion

Minimum variance methods have been described for time dissemination methods using both one way and two-way signal propagation. Other variables besides time offset appear in the solution equations. When propagation delay is not known before hand, it must be estimated, either directly as a variable with the two way methods, or indirectly as a result of position estimation using one-way methods. Frequency offset and vehicle velocity may appear as variables. With a sufficient number of observations spaced over time, these also can be estimated from the timing signal.

Precautions necessary in implementation of recursive minimum variance methods have been presented. Complete discounting of predicted estimate of variables of position and velocity has been introduced to prevent uncertainty in vehicle motion from biasing the estimate of time offset. Fading memory has been applied to variables of clock's behavior to allow the recursive process to respond to slow changes and unmodeled factors related to clock's behavior.

APPENDIX I

EQUATIONS FOR PROPAGATION DISTANCE[6]

Equations are given for $\theta_{n-1}(a)$, $\beta_{i\lambda}$ of (16) and (17) for both line-of-sight and surface-wave propagation. Consider first some preliminary remarks concerning the parametric description of the earth's shape.

A reference ellipsoid, generated by rotating an ellipse about its minor axis with the major axis generating the equatorial plane, is the analytical basis of geodetic datum. Two variables are sufficient to define a datum: the distance along the major axis from the axis of rotation to the surface is called the semi-major axis, denoted A, and flattening, denoted F. Eccentricity, denoted e, is used:

$$e^2 = 2F - F^2.$$

The distance from the surface of the ellipsoid to the axis of rotation of the ellipsoid along a line normal to the surface and through the local point is called the normal length and is denoted N where

$$N = \frac{A}{(1 - e^2 \sin^2 \phi)^{1/2}}$$

and ϕ is the angle made by the normal with the equatorial plane and is called the geodetic latitude. The angle made by the local meridian with the prime meridian is the geodetic longitude, denoted λ, and geodetic height, denoted Z, is the distance along the normal from the local point to the surface of the geodetic datum. For the following, denote ϕ_i, λ_i, Z_i as the coordinates of the ith unit of the reference system related to the signal emitted at time n - j and ϕ_j, λ_j, Z_j as the assumed or predicted coordinates of the participant at time n - j.

Line of Sight Propagation

The predicted propagation distance between points i and j for a signal transmitted at time n - j is denoted $C\,PT_{n-j}(a)$ and is computed by

$$C\,PT_{n-j}(a) = \sqrt{[R_i \cos \phi_i]^2 + [R_j \cos \phi_j]^2 - 2R_iR_j \cos \phi_i \cos \phi_j \cos \Delta\lambda + [(N_i(1-e^2) + Z_i) \sin \phi_i - (N_j(1-e^2) + Z_j) \sin \phi_j]^2}$$

where

$$R_i = N_i + Z_i \text{ and } R_j = N_j + Z_j.$$

Following (17)

$$\beta_{j\phi} = R_iR_j (\cos \phi_i \sin \phi_j \cos \Delta\lambda - \sin \phi_i \cos \phi_j)/C\,PT_{n-j}(a)$$

$$\beta_{j\lambda} = R_iR_j (\cos \phi_i \cos \phi_j \sin (\lambda_j - \lambda_i))/C\,PT_{n-j}(a).$$

Ground-Wave Propagation

Using the Andoyer-Lambert methods were σ is the great circle distance in radians between points i and j, the true propagation distance is

$$C\,PT_{n-j}(a) = A\sigma + \delta s$$

$$\cos \sigma = \sin \phi_i \sin \phi_j + \cos \phi_i \cos \phi_j \cos (\Delta\lambda)$$

$$\delta s = p (\sin \phi_i + \sin \phi_j)^2 + q (\sin \phi_i - \sin \phi_j)^2$$

$$p = A (1 - (1 - e^2)^{1/2})(3 \sin \sigma - \sigma)/8 \cos^2 \tfrac{1}{2} \sigma$$

$$q = A (1 - (1 - e^2)^{1/2})(3 \sin \sigma + \sigma)/8 \cos^2 \tfrac{1}{2} \sigma.$$

Following (17)

$$\beta_{j\phi} = A (\cos \phi_i \sin \phi_j \cos \Delta\lambda - \sin \phi_i \cos \phi_j)/\sin \sigma$$

$$\beta_{j\lambda} = A (\cos \phi_i \cos \phi_j \sin (\lambda_j - \lambda_i))/\sin \sigma.$$

References

1. W. L. Smith, "Quartz crystal controlled oscillators," Bell Telephone Lab., Rep. 25335-H, March 15, 1963.
2. R. B. Blackman, "Methods of orbital refinement," Bell Syst. Tech. J., vol 43, pp. 885-909, May 1964.
3. J. Zaborszky, "A practical non-diverging filter," AIAA J., vol. 8, pp. 1127-1133, June 1970.
4. H. W. Sorenson and J. E. Sacks, "Recursive fading memory filtering," Inform. Sce., vol. 3, pp. 101-119, 1971.
5. H. W. Sorenson, "Kalman filtering techniques," in Advances in Control Systems, vol. 3, C.T. Leondes Ed. New York: Academic, 1966, p. 219.
6. C. W. Ewing and M. M. Mitchell, Introduction to Geodesy. New York: American Elsevier, 1970.
7. H. W. Sorenson, "Least-squares estimation: From Gauss to Kalman," IEEE Spectrum, vol. 58, pp. 63-68, July 1970.
8. C. E. Ellingson and R. J. Kulpinski, "Dissemination of system time," IEEE Trans. Comm., vol. COM-21, pp. 605-624, May 1973.

Acknowledgement

This work was sponsored by the Electronics System Division, Air Force Systems Command, under Contract ESD F19628-76-C-0001.

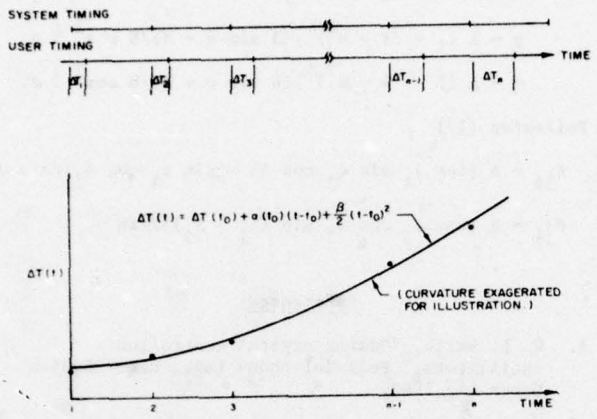

Fig. 1. Data history and trajectory of time offset.

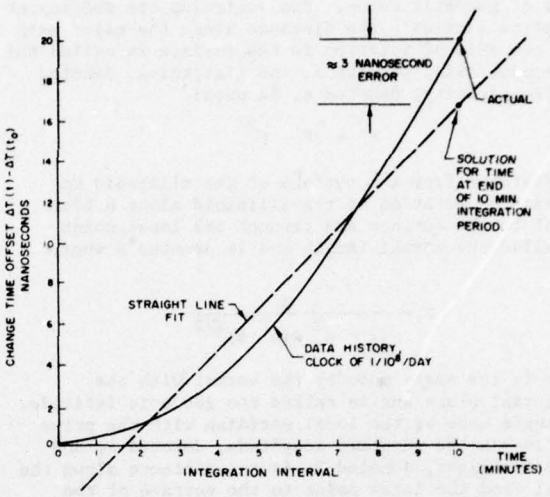

INTEGRATION PERIOD (MINUTES)	LONG TERM STABILITY PARTS/DAY			BIAS ERROR (NANOSECONDS)
	1×10^{-9}	1×10^{-8}	1×10^{-7}	
2	012	.12	1.2	
6	.11	1.1	11.0	
10	.3	3.0	30.0	

Fig. 2. Difference between actual and estimated time offset when frequency offset is assumed constant but is changing at a constant rate.

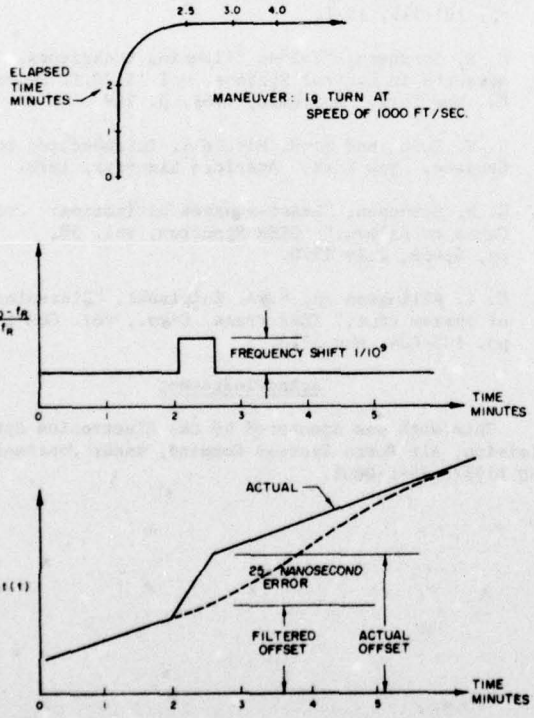

Fig. 3. Transient discrepancy between actual and estimated time offset caused by acceleration-induced step shift in the clock's oscillator frequency and by long time constant estimator.

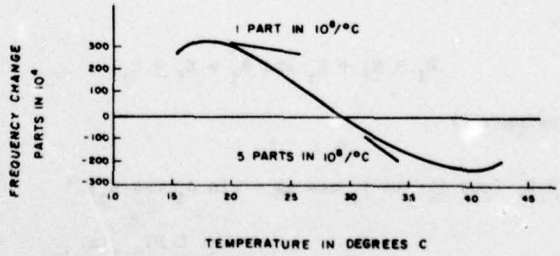

Fig. 4. Frequency change versus temperature, AT cut crystal.

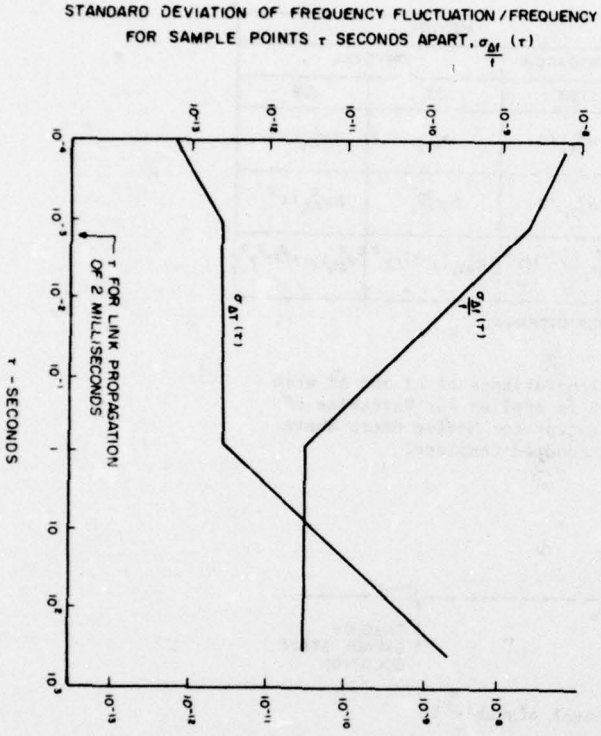

Fig. 5. Short-term stability versus elapsed time τ.

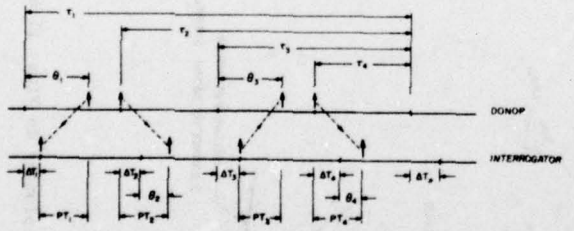

Fig. 7. Parameters of a two-way signaling sequence with flexible time of signal transmission. Sequence is sufficient to estimate time offset, frequency offset, propagation delay, and rate of change of propagation delay.

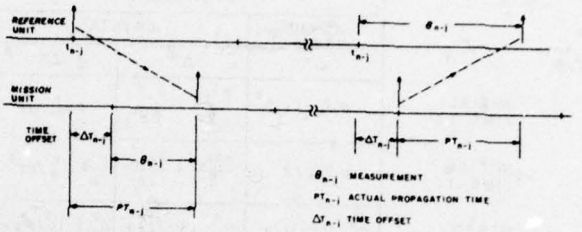

Fig. 6. Relationship between measured elapsed time, actual propagation time, and time offset.

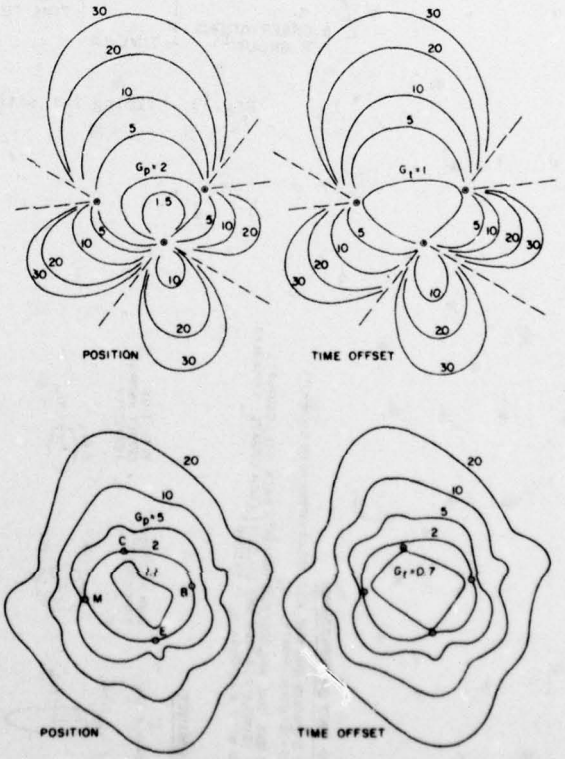

Fig. 8. Constant uncertainty isograms. These contours show how much larger the standard deviation of the solution error will be than the standard deviation of the measurement error for equal uncertainty in each measurement with the solution determined with measurements associated with each site. $G_t = \sigma_{\Delta T}/\sigma_m$ $G_p = (\sigma_\phi^2 + \sigma_\lambda^2)^{1/2}/\sigma_m$.

	STATIONARY			MOVING		
	ATOMIC	CRYSTAL		ATOMIC	CRYSTAL	
	ΔT	ΔT	$\dot{\Delta T}$	ΔT	ΔT	$\dot{\Delta T}$
INITIAL TIME TA	$\sigma^2_{\Delta T_s}/2$	$\frac{\sigma^2_{\Delta T_s}}{2} + \frac{\sigma_m^2}{2p}$	$2\sigma_m^2/p\tau^2$	$\sigma^2_{\Delta T_s}/2$	$\sigma^2_{\Delta T_s}$	$2\sigma^2_{\Delta T_s}/\tau^2$
INITIAL TIME TB	$\sigma^2_{\Delta T_s}/2$	$\frac{\sigma^2_{\Delta T_s}}{2} + \frac{9\sigma_m^2}{2p}$	$2\sigma_m^2/p\tau^2$	$\sigma^2_{\Delta T_s}/2$	$5\sigma^2_{\Delta T_s}$	$2\sigma^2_{\Delta T_s}/\tau^2$
STEADY STATE	$\sigma^2_{\Delta T_s}(\gamma-1)/\gamma$	$\sigma^2_{\Delta T_s}(\gamma-1)/\gamma$	$\sigma_m^2(\gamma-1)^3/\tau^2 p\gamma^2$	$\sigma^2_{\Delta T_s}(\gamma-1)/\gamma^2$	$2\sigma^2_{\Delta T_s}(\gamma-1)/\gamma^2$	$\sigma^2_{\Delta T_s}(\gamma-1)^3/\tau^2\gamma^2$

$\gamma = k^\tau$, k = DISCOUNT CONSTANT, AND τ = GROUP INTERVAL

TABLE I

Parametric Relationships for the Solution Variance of ΔT and $\dot{\Delta T}$ when in Every Second Group, Each Update $\gamma^2 = Z$ is Applied for Variables of the Vehicle's and Clock's Trajectory, Except for Moving Users Where Variables of the Vehicle's Path Are Discounted Completely

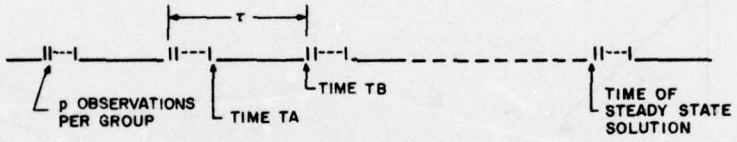

Fig. 9. *Timing for situations of Table I.*

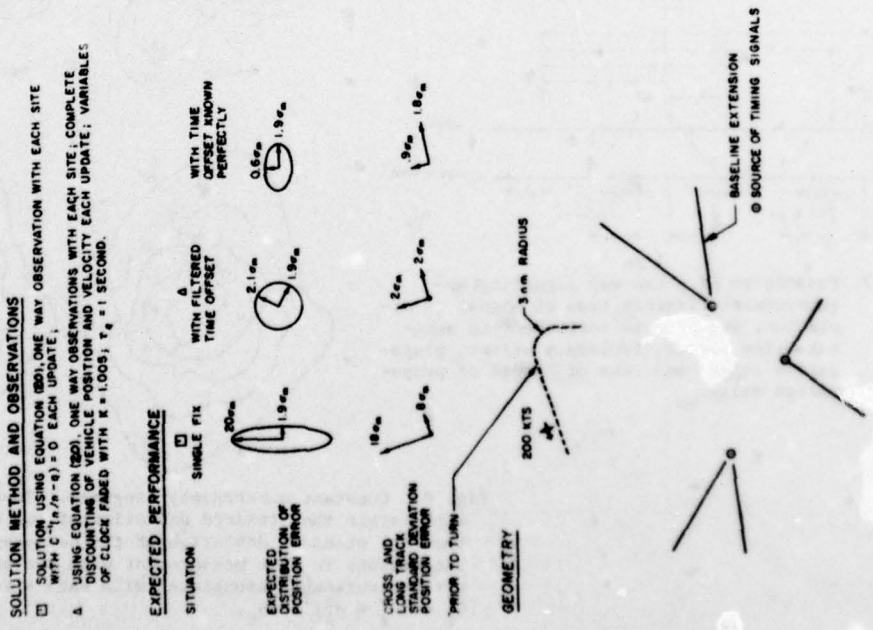

Fig. 10. Description of situations plotted in Figs. 11 and 12.

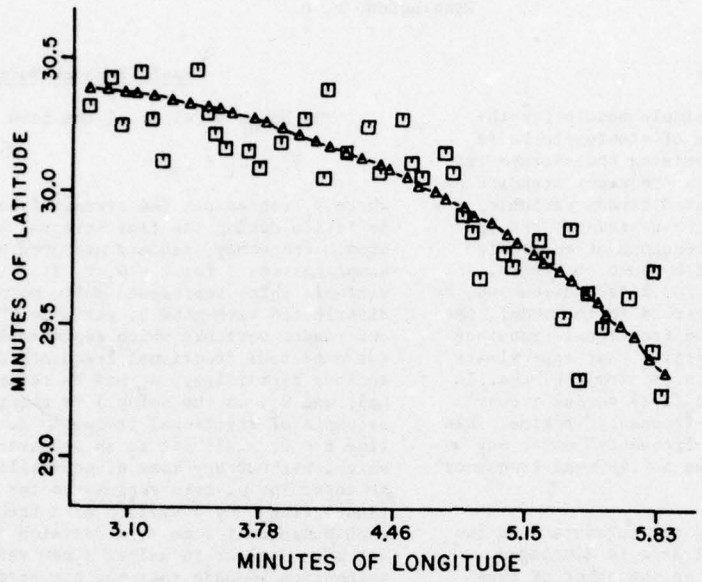

Fig. 11. Plot of single-fix and clock-aided solutions of position.

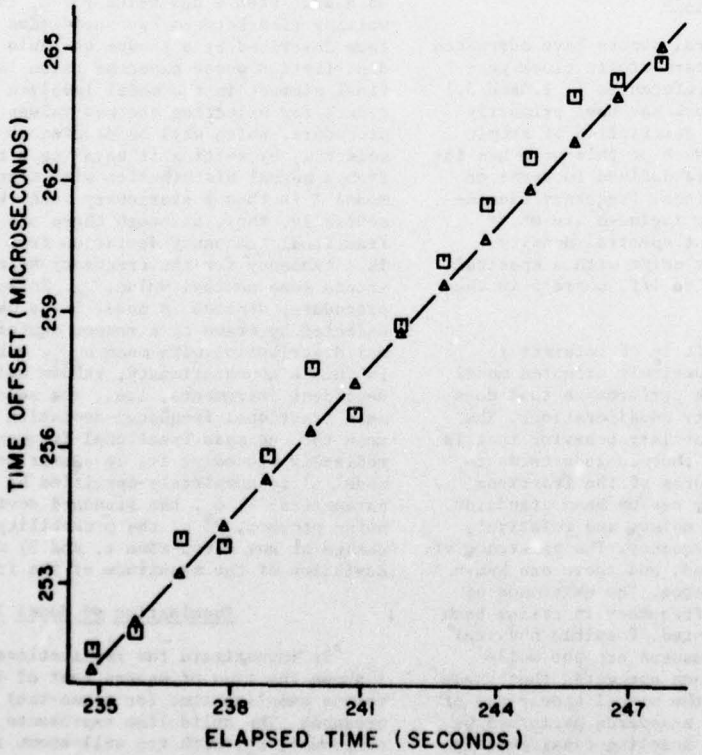

Fig. 12. Solution of time offset during the turn of Fig. 10. Conceptual description contained in Fig. 1.

A HEURISTIC MODEL OF LONG-TERM ATOMIC CLOCK BEHAVIOR

D. B. Percival
U. S. Naval Observatory
Washington, D. C.

Summary

A class of conceptually simple models for the long-term frequency variations of atomic clocks is presented. The basic model simulates the average fractional frequency deviation of a frequency standard as the sum of a normally distributed random variable, ε_t, and a random variable, μ_t, which represents the spontaneous changes in the mean frequency of an atomic clock which have been reported by some observors. Various statistical processes for μ_t are discussed. By a suitable choice of the parameters in the model, the resulting sequence of simulated fractional frequency deviates has statistical properties that approximate the statistical characteristics of atomic clocks. In particular, the shape of the $\sigma_{\bar{y}}(2,\tau)$ versus τ curve shows a well-defined "flicker-frequency" region. This result suggests that "flicker-frequency" noise may be a result of spontaneous changes in the mean frequency of an atomic clock.

The problem of estimating the parameters in two forms of the model from actual data is discussed. Under the hypothesis that one or the other of these two forms of the model is true, cumulative sum control chart theory is considered as a solution to the problem of determining when frequency changes in atomic clocks occur.

Introduction

In the last decade, several papers have addressed the problem of modeling long-term atomic clock performance. (See, for example, references 1, 2, and 3.) The purpose of this body of work has been primarily to provide a good statistical description of atomic clock frequency instability. Much of this work has included noise elements which are defined in terms of the spectral density of fractional frequency fluctuations. Two elements generally included are white frequency noise with a constant spectral density function and flicker-frequency noise with a spectral density function proportional to $1/f$, where f is the Fourier frequency variable.

For heuristic purposes, it is of interest to consider a fairly simple, intuitively oriented model of long-term cesium beam clock performance that does not start with spectral density considerations. The model should reflect the instability behavior that is empirically observed. It will thus include terms to model two of the salient features of the fractional frequency deviates produced by cesium beam standards: uncorrelated Gaussian (white) noise, and relatively abrupt changes in the mean frequency. The existence of white noise is well-established, and there are known physical reasons for its presence. The existence of abrupt changes, or steps, in frequency in cesium beam standards is less well-documented. Possible physical causes for abrupt frequency changes are not well-understood. In fact, it has been suggested that these steps are merely a result of the visual appearance of phase recordings of frequency standards perturbed by flicker-frequency noise.[1] The modeling considered in this paper will explore the relationship between flicker-frequency noise and abrupt changes in frequency and the extent to which they are interchangeable mathematical descriptions of a type of cesium beam frequency instability.

Basic Form of Model

The basic model is of the form

$$\bar{y}_t = \mu_t + \varepsilon_t,$$

where $\bar{y}_t$ represents the average fractional frequency deviation during the time interval t to $t + \tau$ of an atomic frequency standard measured over some arbitrary sampling time τ for $t = 0, \tau, 2\tau, \ldots$; ε_t is a random variable which represents white noise and is normally distributed with mean 0, variance σ_e^2; and μ_t is a second random variable which represents the current mean (or expected) fractional frequency deviation. (In another terminology, μ_t may be referred to as the signal, and ε_t, as the noise.) To generate a simulated sequence of fractional frequency deviates beginning at time $t = 0$, μ_0 is set to an arbitrary initial value, which, without any loss of generality, may be regarded as zero. The μ_0 term represents the initial mean fractional frequency deviation of a frequency standard. At each subsequent time t, a decision is made either to let $\mu_t = \mu_{t-1}$ or to select a new value for μ_t. If the assumption is made that the occurrence of changes in μ_t may be described by a Poisson process, the decision rule governing changes in μ_t is quite simple. At each time t, a coin is flipped which has a probability of p of coming up heads and of $1 - p$ of coming up tails. If the coin comes up tails, then $\mu_t = \mu_{t-1}$. If it comes up heads, then a new value for μ_t is selected. The waiting time between two successive changes in μ_t is thus described by a random variable with a geometric distribution whose expected value is equal to $1/p$. The final element in the model involves specifying the procedure for selecting the new values of μ_t. One possible procedure, which will be denoted as model I, is to select μ_t by setting it equal to a random number drawn from a normal distribution with mean μ_0, variance σ_f^2. Model I is thus a stationary model which states, essentially, that, although there are changes in the mean fractional frequency deviation from time to time, there is a tendency for the frequency standard to remain around some nominal value, μ_0. In a second possible procedure, denoted as model II, a new value of μ_t is selected by means of a random number drawn from a normal distribution with mean μ_{t-1}, variance σ_f^2.* Model II is thus a non-stationary, random walk model with independent increments, i.e., the selection of the new mean fractional frequency deviation is dependent only upon the one mean fractional frequency deviation immediately preceding it. To summarize, either model I or model II is completely specified by three essential parameters: 1) σ_e, the standard deviation of the white noise process, 2) p, the probability of a frequency change at any given time t, and 3) σ_f, the standard deviation of the magnitude of the frequency changes.

Examination of Model I

To investigate the implications of model I, figure 1 shows the type of square root of the Allan variance versus sampling time (or sigma-tau) curve that model I produces. The solid line represents the white noise component, ε_t, with its well-known $\tau^{-\frac{1}{2}}$ behavior. The

*A model similar to model II has been examined in detail by G. A. Barnard.[4] He also briefly discusses a model similar to model I, which he attributes to A. J. Duncan.

position of this line on the graph is determined completely by the σ_e parameter. The dashed hill-shaped curve represents the μ_t component caused by frequency changes, μ_t. Setting p and σ_f positions this curve uniquely on the graph, but varying these two parameters does not alter the basic shape of the curve. The height of the curve is determined by σ_f. Increasing σ_f moves the curve vertically up on the graph. The horizontal position of the curve is determined by p. The peak of the curve occurs at approximately the sampling time given by 2/p, so that decreasing p moves the curve horizontally to the right. The upper curve with dashes and dots represents the summation of the ϵ_t and μ_t curves, which will be the sigma-tau curve of the average fractional frequency deviations. By judiciously positioning the ϵ_t and μ_t curves, a transition region on the sigma-tau curve of $\bar{y}_t$ is produced which will look superficially like a flicker-frequency noise region, i.e., a region that has a slope of zero. This effect is enhanced when uncertainty is introduced into the sigma-tau curve due to a finite data length, as is shown in figure 2. Here, a sequence of 1200 variates was drawn from a model I process, each variate representing the average fractional frequency deviation for one day. This figure shows that a model I process can produce a sigma-tau curve that closely approximates that given by commercial cesium beam standards.

Since all of the parameters needed to specify model I are observable, the validity of model I may be examined further. σ_e may be estimated by the square root of the Allan variance. With a frequency step detection algorithm suitable for the types of steps hypothesized by model I, σ_f and p may be estimated. With these estimates of σ_e, σ_f, and p from real data, a theoretical sigma-tau curve may be derived under model I and compared to the actual sigma-tau curve calculated from the data. This comparison will give some indication of the validity of model I.

To find a suitable frequency step detector for the model I process, some methods from cumulative sum control chart theory may be applied.[5] This body of statistical theory is concerned with detecting subtle changes in a process mean. In the models considered here, the process is the fractional frequency deviates produced by an atomic frequency standard. The cumulative sum technique involves forming a sequence of numbers, S_t, defined at each time t in the present case by

$$S_t = \sum_{i=0}^{t} \bar{y}_i .$$

With the exception of a multiplicative constant, S_t is equivalent to a relative phase value at time t. By plotting S_t versus time, changes in the mean fractional frequency deviation appear readily as changes in the slope of the S_t curve. Woodward and Goldsmith have described a useful technique for detecting the point in time at which a process mean changed, based upon an examination of the S_t time series.[6] This detection algorithm is illustrated in figure 3. Here, a S_t time series is plotted which was derived from a sequence of 50 random numbers representing fractional frequency deviates, $\bar{y}_i$, for i = 1 to 50. The first 25 random numbers were drawn from a normal distribution with mean 0, variance 1, and the last 25, from a normal distribution with mean ½, variance 1. To apply the detection algorithm to determine whether there has been a change in the mean fractional frequency deviation between time t = 1 and t = 50, a line, denoted as k on figure 3, is drawn from the point at t = 1 to the point at t = 50 on the cumulative sum (or phase) plot. The slope of this line k is directly proportional to $\bar{y}$, the average fractional frequency deviation from time t = 1 to t = 50. Next, all the points on the phase plot between time t = 1 and t = 50 are examined, and the point is determined which is furthest away perpendicularly from the initial line. In this example, the point at t = 31 is furthest away. Two more lines are now drawn, one from t = 1 to t = 31, and a second from t = 31 to t = 50. These are indicated by the lines on figure 3 labeled, respectively, k' and k". The slopes of these two lines are directly proportional to $\bar{y}'$ and $\bar{y}''$, the average fractional frequency deviations from, respectively, time t = 1 to t = 31 and time t = 31 to t = 50. A test for a significant difference between $\bar{y}'$ and $\bar{y}''$ is made using a t-test, where the square root of the residual variance is estimated by the square root of the Allan variance. If the difference between $\bar{y}'$ and $\bar{y}''$ is significant, then the algorithm has identified a frequency change at time t = 31.

This detection algorithm is easily extended to search for frequency changes sequentially. In the above example, the end time t = 50 was arbitrarily chosen for illustrative purposes. Suppose that the above testing procedure were performed sequentially for end times t = 3, 4,..., 49 with no frequency changes detected. If, at end time t = 50, the t-test were to indicate that $\bar{y}'$ and $\bar{y}''$ are not significantly different, the testing procedure would be repeated anew at time t = 51. If, however, the t-test were to indicate that $\bar{y}'$ and $\bar{y}''$ are significantly different, then subsequent analysis at time t = 51 would use the point at t = 31 as the new first point on the phase plot, i.e., all points before time t = 31 are ignored. Since a large number of dependent t-tests are made, the size of the critical region must be very small in order to minimize the number of false detections. In the work done here, the size of the critical region was selected as .001.

The application of this detection algorithm to simulated model I data indicates that it can detect frequency changes quite well. This simulation work indicates, however, that quite long data samples are needed to estimate the parameters p and σ_f in model I with good confidence. This is due to the fact that, in order to produce a sigma-tau curve resembling that given by a cesium beam frequency standard, the probability of a frequency change on any given day must be small, being typically less than .02. Thus, for a data sample of length three years, 22 or fewer frequency changes would be expected. The corresponding estimate of σ_f from this length of data sample may be a factor of two off. Thus, even with simulated model I data, there is only reasonable agreement between a sigma-tau curve derived via estimates of the parameters p and σ_f and the true theoretical sigma-tau curve. In using real data, there is an additional source of variation, since the true sigma-tau curve is not known and can only be estimated by the usual methods.

Figure 4 shows a comparison of the two ways of estimating the sigma-tau curve using real data. Cs 591/1 is a conventional cesium beam standard, for which there are 1137 days of comparison data against A.1(USNO,MEAN), the internal time scale produced at the Naval Observatory. After a linear frequency drift of 4.1 parts in 10^{-13} per year was removed, the frequency change detection algorithm detected 9 frequency steps in this 1137 day time interval, yielding an estimate of p of .01 and of σ_f of 1.2 parts in 10^{-13}. Values for the square root of the Allan variance derived from these estimated parameter values using model I are represented by the triangles. The standard estimates for the square root of the Allan variance are given by the circles. The agreement between the two estimates is fairly good. By this criterion, Cs 591/1 seems to be well-described by a model including only white frequency noise and abrupt frequency changes. There is no need to include flicker-frequency

noise to account for the observed sigma-tau curve.

Examination of Model II

Model II may be examined in a manner analogous to model I. Figure 5 shows the theoretical sigma-tau curve for a model II process and its two components. Again, the position of the ε_t line on the graph is completely determined by the σ_e parameter, and the position of the μ_t line, by the σ_f and p parameters. The same frequency change detection algorithm previously described may be used to estimate the σ_f and p parameters. Figure 6 shows a comparison between two different estimates of the sigma-tau curve for Cs 346/1, one estimate, represented by the triangles, via the estimated model II parameters, and the other estimate, represented by the circles, via the usual direct computation. Cs 346/1 is a conventional cesium beam standard for which there are 1200 days of comparison against A.1(USNO,MEAN). After a linear frequency drift of 3.5 parts in 10^{-13} per year was removed, the frequency detection algorithm detected 32 frequency steps in this 1200 day interval, yielding an estimate for p of .03 and for σ_f of 1.1 parts in 10^{-13}. Figure 6 indicates that Cs 346/1 is well-modeled by a model II process, at least as far as the sigma-tau curve is concerned.

Conclusions

In general, either model I or model II was able to adequately characterize the long term behavior of conventional commercial cesium beam standards, with a few notable failures. However, for high performance commercial cesium beam standards, neither model fit well, in the sense that the sigma-tau curves estimated via the model parameters did not match those estimated via direct computation. In most cases, the lack of fit was due to estimates of p and σ_f which were too large. (The estimates of p and σ_f may have been inflated in a few cases due to some non-linear drifts in frequency that were present.) This lack of fit may indicate that the statistical characteristics of high performance standards cannot be adequately modeled by model I or model II.

Thus, for some conventional commercial cesium beam standards, a combination of white noise and abrupt frequency shifts can explain much of the observed frequency instabilities. In the models described here, the flicker-frequency noise contribution to spectral density oriented models has been absorbed by the frequency step element. To this extent, flicker-frequency noise and abrupt frequency changes are equivalent approximate mathematical descriptions of a type of cesium beam frequency instability. These two mathematical descriptions are not identical, since, among other reasons, it has been pointed out that flicker-frequency noise is self-similar, i.e., a uniform expansion or contraction of a phase plot would not visually change the statistical characteristics of the plot[1]. A model I process, however, would not be self similar.

Acknowledgements

I would like to acknowledge Dr. G. M. R. Winkler of the Naval Observatory, with whom I have had many helpful discussions concerning the material in this paper. I would also like to thank Dr. James A. Barnes, Dr. Stephen Jarvis, and Mr. David W. Allan of the National Bureau of Standards for allowing me to see some of their unpublished work on models for oscillator frequency instability.

References

1. Allan, D. W., et al., "Performance, Modeling, and Simulation of Some Cesium Beam Clocks," Proceedings of 27th Annual Symposium on Frequency Control, pp. 334 - 346 (1973).

2. Ganter, W. A., "Modeling of Atomic Clock Performance and Detection of Abnormal Clock Behaviour," NBS Technical Note 636 (March 1973).

3. Mealy, G. L., "Sensor Data Bank Development: Time Standard Error Models and Data File," Technical Report AFAL-TR-75-65, Air Force Avionics Laboratory (June 1975).

4. Barnard, G.A., "Control Charts and Stochastic Processes," J. Roy. Stat. Soc., Series B, 21, pp. 239 - 271 (1959).

5. Van Dobben de Bruyn, C. S., Cumulative Sum Tests: Theory and Practice, Griffin's Statistical Monographs and Courses No. 24, Charles Griffin and Co. Ltd., London (1968).

6. Woodward, R. H., and Goldsmith, P. L., Cumulative Sum Techniques, Imperial Chemical Industries Monograph No. 3, Oliver and Boyd Ltd., London (1964).

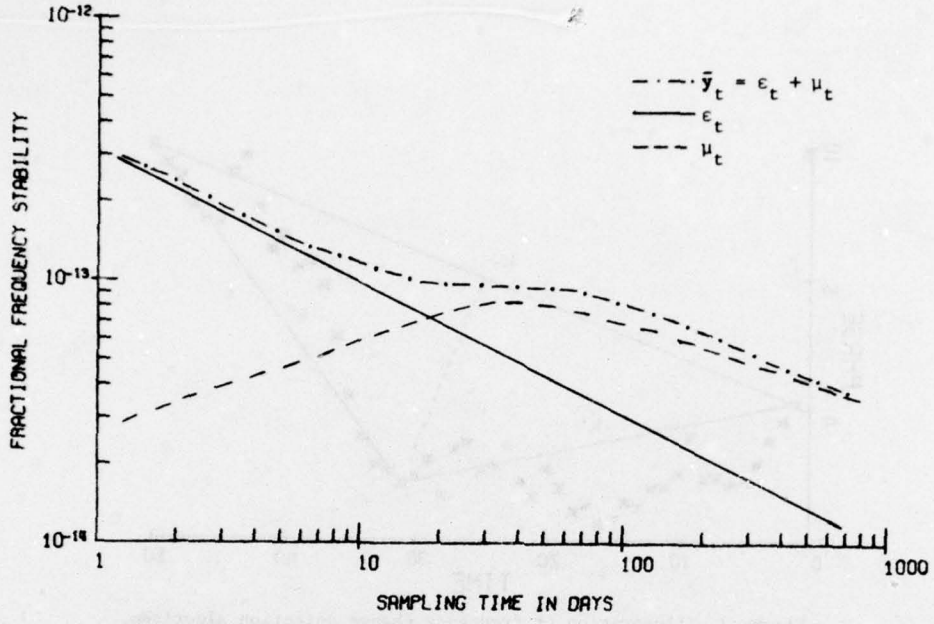

Figure 1. Theoretical $\sigma_{\bar{y}}(2,\tau)$ versus τ curve for $\bar{y}_t$ representing a model I process.

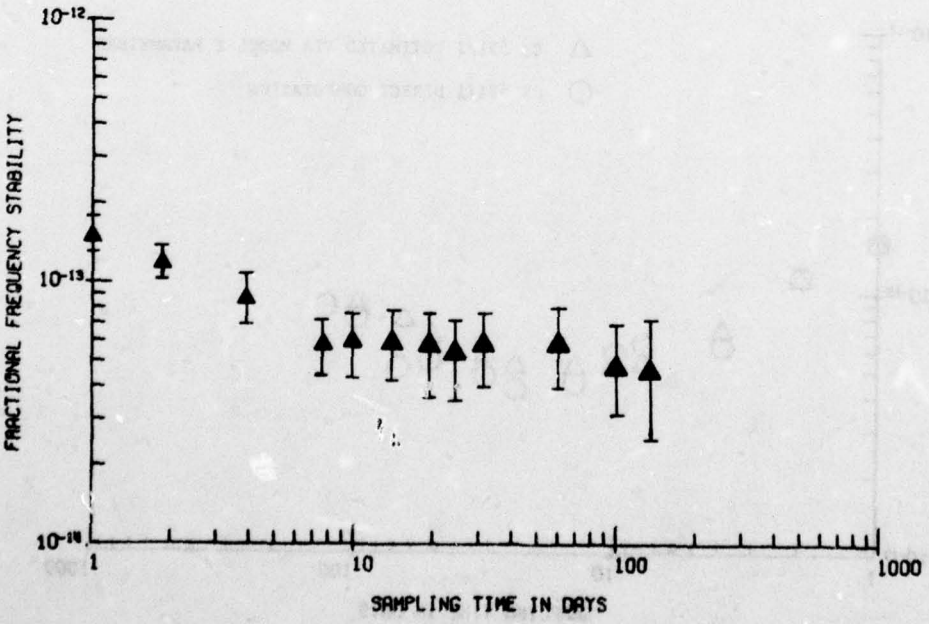

Figure 2. $\sigma_{\bar{y}}(2,\tau)$ versus τ curve for a simulated model I process representing a 1200 day data sample.

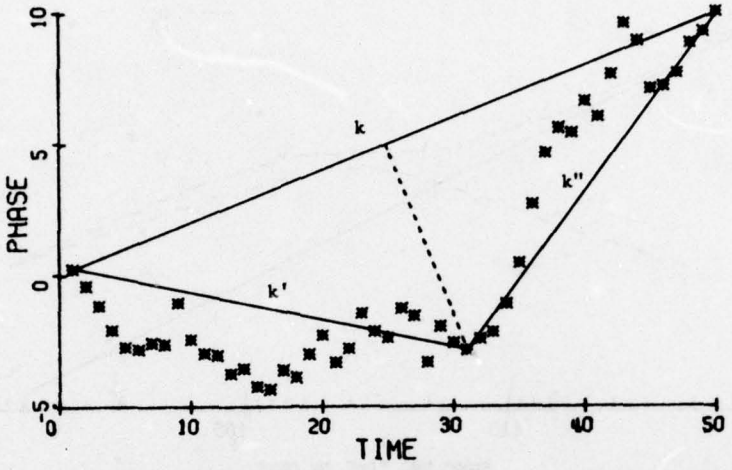

Figure 3. Illustration of frequency change detection algorithm. The slopes of the lines k, k', and k" are referred to in the text as, respectively, $\bar{y}$, $\bar{y}'$, and $\bar{y}''$. The units for the x and y axes are arbitrary.

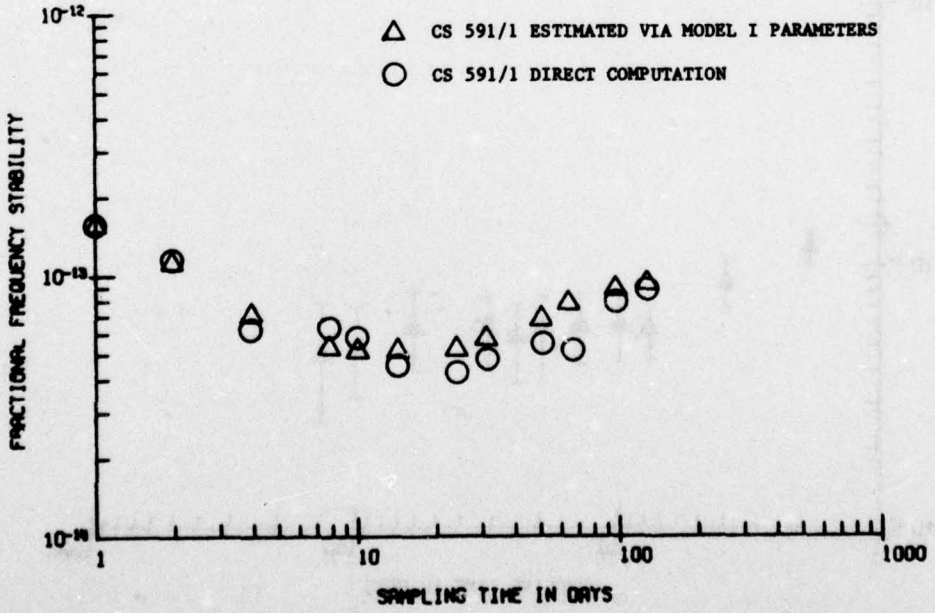

Figure 4. Comparison of $\sigma_y(2,\tau)$ versus τ values calculated directly and via estimated model I parameters for Cs 591/1.

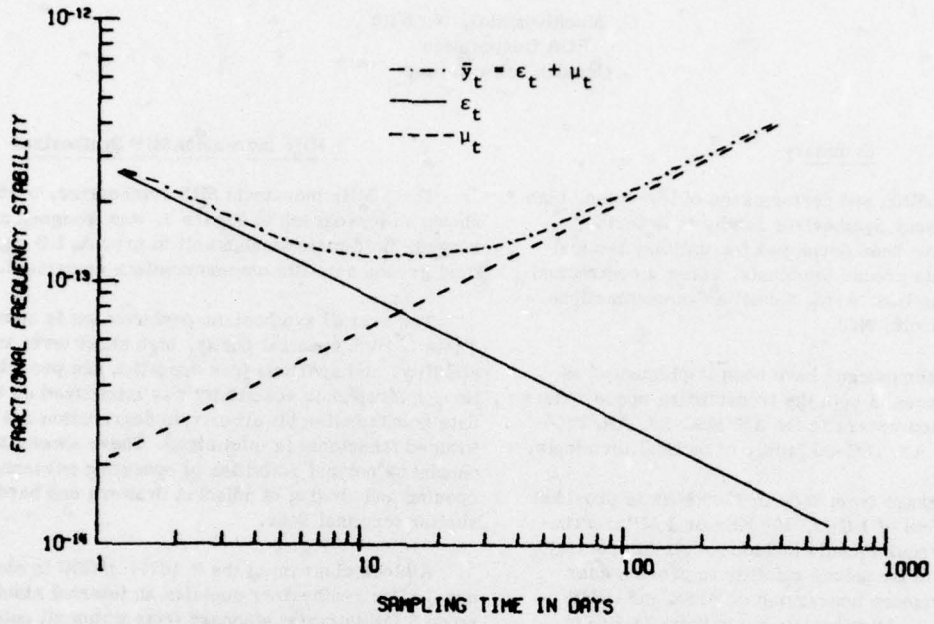

Figure 5. Theoretical $\sigma_{\bar{y}}(2,\tau)$ versus τ curve for $\bar{y}_t$ representing a model II process.

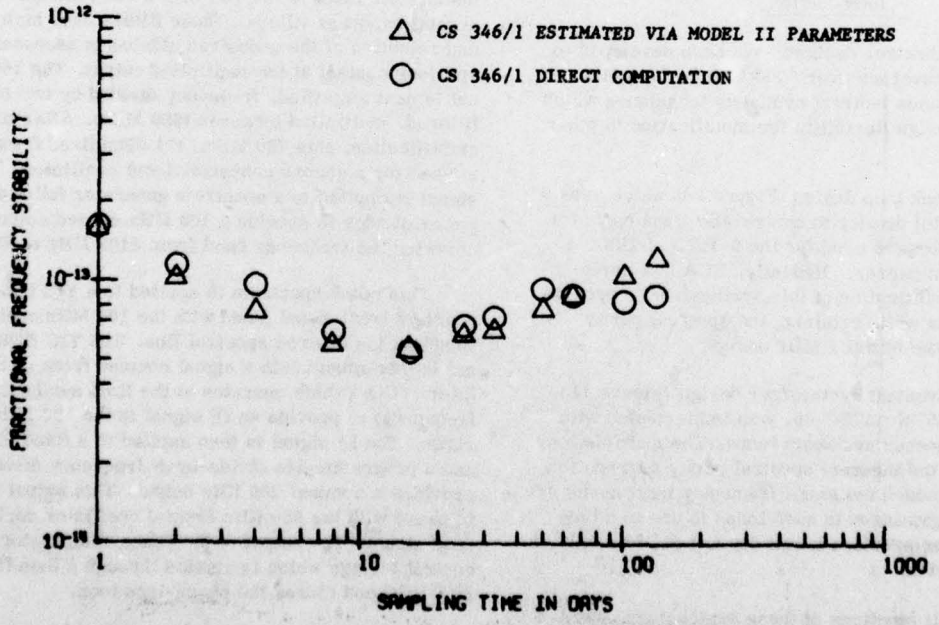

Figure 6. Comparison of $\sigma_{\bar{y}}(2,\tau)$ versus τ values calculated directly and via estimated model II parameters for Cs 346/1.

MICROWAVE FREQUENCY SYNTHESIS FOR SATELLITE COMMUNICATIONS GROUND TERMINALS

G. Mackiw and G. W. Wild
RCA Corporation
Camden, New Jersey

Summary

Design, construction and performance of low noise, high stability SHF Frequency Synthesizer family is described. The synthesizers have been developed for military tactical and strategic satellite ground terminals, under a contractual effort directed by the U.S. Army Satellite Communications Agency, Fort Monmouth, N.J.

These synthesizer designs have been implemented as local oscillator sources in both the transmitting upconverters and receiving downconverters in the AN/MSC-59, AN/TSC-85 (V1/V2), and the AN/TSC-86 family of tactical terminals.

Frequency coverage from 6500 to 7700 MHz is provided with tuning increments of 1 KHz, 100 KHz or 1 MHz. Principal performance requirements include excellent spectral purity and short term frequency stability to provide near transparency in frequency conversion of BPSK and QPSK carriers containing modulation data rates from 75 B/S to 20 MB/S.

These equipments exhibit phase noise of -28 dBc on both sides of the carrier with offsets of 10 Hz to 300 KHz and 300 KHz to 20 MHz, spurious outputs of -80 dBc 1 MHz beyond carrier, and frequency stability of $1 \times 10^{-10}/0.1$ second and $\pm 5 \times 10^{-9}/24$ hours.

Introduction

Two basic synthesizer designs have been developed to provide frequency coverage over 6500 MHz to 7700 MHz band. Each design uses indirect synthesis techniques which provide inherent design flexibility for modification to other microwave bands.

A single feedback loop design (Figure 1A) which uses a programmable digital divider to control the frequency of a microwave oscillator was used for the 0-1677( )/GSC, 1 MHz increment synthesizer. Recently, RCA has implemented a design modification of this synthesizer to provide 100 KHz increments while retaining the spectral purity characteristics of the initial 1 MHz design.

The 1 KHz increment synthesizer design (Figure 1B), nomenclatured 0-1678( )/TSC-86, was implemented with three indirect frequency synthesis loops. The multiple loop design overcomes the inherent spectral purity degradation of a single loop in which too small frequency increments are attempted. The degradation in such loops is due to a long countdown, a low comparison frequency and consequently, a narrow loop bandwidth.

Various circuit functions of these synthesizers were implemented with both microwave integrated circuit (MIC) and fired-film hybrid construction. These techniques reduced equipment size, provided desirable maintenance modularization features, and reduced connector and cable interfaces which impact reliability and cost.

1 MHz Increment SHF Synthesizer

The 1 MHz increment SHF synthesizer, 0-1677( )/GSC, shown on photograph in Figure 2, was designed as a small, rugged, field maintainable unit to provide LO signals in tactical ground satellite communications equipment.

The overall synthesizer performance is summarized in Table I. High spectral purity, high short term and long term stability, and spurious free operation are provided. In addition, microphonic sensitivity was minimized so that QPSK data transmission bit error rate degradation due to shock induced transients is minimized. These shocks may be caused by normal activities of operating personnel including opening and closing of adjacent drawers and hard closing of shelter terminal door.

A block diagram of the 0-1677( )/GSC is shown in Figure 3. The synthesizer contains an internal stable, low noise 5 MHz crystal standard from which all output frequencies are referenced. The 5 MHz signal interfaces a divide by R network, a X4 frequency multiplier, and a 5 MHz buffer output. The divide by R circuit ($\div 20$) provides 250 KHz square wave output used as a reference signal in the phase comparator. The 20 MHz output from the X4 multiplier is filtered with a 20 MHz crystal bandpass filter and applied to a 20 MHz harmonic generator. Output of the harmonic generator containing both the fifth and the ninth harmonics of the 20 MHz input is filtered with a 100 MHz and 180 MHz crystal bandpass filters. These filters have high selectivity and rejection of the undesired sidebands necessary for low spurious content at the multiplied output. The 180 MHz signal is next amplified, frequency divided by two (90 MHz), filtered, multiplied by seven (630 MHz). After filtering and amplification, this 630 MHz, +11 dBm fixed frequency output is used for a second converter local oscillator. The 100 MHz signal is applied to a spectrum generator followed by a power divider to provide a 100 MHz spaced comb spectrum covering the frequency band from 6400 MHz to 7500 MHz.

This comb spectrum is applied to a YIG bandpass filter which is front-panel tuned with the 100 MHz control switch to select the desired spectral line. The YIG filter output signal is then mixed with a signal coupled from an SHF Oscillator (VCO) (which operates at the final synthesizer output frequency) to provide an IF signal in the 100 MHz to 200 MHz range. The IF signal is then applied to a fixed divide-by-K and a programmable divide-by-N frequency divider which provides a nominal 250 KHz output. This output is compared in phase with the 250 KHz crystal oscillator derived reference signal. The output of the phase comparator provides a control voltage which is applied through a loop filter to the SHF VCO and closes the phase-lock loop.

The two 250 KHz signals are also applied to a lock detector circuit which monitors frequency coherence between the two input signals. Loss of frequency coherence, which results when the loop falls out of phase lock, triggers an "Out of Lock" front panel indicator light.

The SHF VCO is a Gunn Oscillator containing both electrical and mechanical tuning. When in-lock, the electrical tuning range is sufficient to maintain hold-in lock over all required environmental conditions. When the frequency is changed by more than a few MHz, the front panel oscillator mechanical tuning is used to return the oscillator frequency within the loop acquisition range. With the out-of-lock lamp and meter monitoring of the loop phase error, fast and accurate tuning of the synthesizer can be accomplished.

Frequency Selection

A steady state frequency diagram of the 1 MHz increment synthesizer scheme is shown in Figure 4. When the loop is locked, the frequencies of the input signals into the phase detector are equal. From the diagram it may be seen that under this condition the output frequency F_o is related to the reference crystal oscillator frequency f_r as follows:

$$F_o = (\alpha + \frac{NK}{R}) f_r \quad (1)$$

where the parameters are:

f_r = 5×10^6 Hz (Crystal standard frequency)

α = 20 (64 + M); M = 0, 1, 2...11 (100 MHz steps) (Total frequency multiplication)

R = 20 (Fixed divider frequency division)

N = 100 + L; L = 0, 1, 2...99 (10 MHz, 1 MHz steps) (Programmable frequency division)

K = 4 (Prescaler frequency division)

Substituting these parameter values into the expression of the output frequency yields:

$$F = 6.5 \times 10^9 + M \times 10^8 + L \times 10^6 \text{ Hz} \quad (2)$$

100 KHz Increment Synthesizer

The 100 KHz increment synthesizer design was developed by modification of the 1 MHz increment design. To achieve the 100 KHz increments, the parameters shown in the static diagram in Figure 4 were changed to the following: K = 1, R = 50, N = 1000 + L; L = 0, 1, 2...999 (10 MHz, 1 MHz, and 100 KHz steps). With these parameters the phase comparison is performed at 100 KHz, and the programmable divider must operate with 100 to 200 MHz input without a prescaler.

In addition, the phase comparator and loop filter designs were also changed to provide a higher loop gain.

The natural frequency of the loop was maintained at approximately 10 KHz resulting in operating characteristics of the 100 KHz increment synthesizer essentially identical to the original 1 MHz increment design.

1 KHz Increment Synthesizer

The 1 KHz increment SHF synthesizer, 0-1678( )/TSC-86, shown on photograph in Figure 5, was designed for use in strategic ground satellite communication equipment where fine frequency increment selection is required. To achieve the level of performance, summarized in Table 2, a triple loop design was used as illustrated on the block diagram, Figure 6. As shown on the diagram, the synthesizer consists of a frequency standard, fixed frequency generator module, spectrum filter (YIG), 1 MHz step control module, 1 KHz step control module, main loop module and an SHF VCO.

The frequency standard is a stable low noise 5 MHz crystal oscillator which is also capable of being locked to an external atomic clock for improved long term stability. The fixed frequency generator module is identical to that used on the 0-1677( )/GSC. It accepts the 5 MHz input and by direct multiplication, division and filtering provides 100 MHz, 180 MHz and 630 MHz outputs.

The SHF reference frequency for main loop mixing with the SHF/VCO is obtained with a comb generator and YIG Filter as previously described. The YIG filter is tuned in 100 MHz increments with the front panel frequency selection switch.

1 MHz Step Module

The 1 MHz step module provides an output to the main loop in the frequency range from 180 MHz to 279 MHz in 1 MHz increments. The UHF VCO (1) drives a divide by eight circuit within its frequency control loop. The output of the fixed divider is next applied to a ÷ N circuit, which is switch programmable to provide integral frequency division from 180 to 279. The divider output, nominally 125 KHz, is compared in phase with the 125 KHz reference signal which is derived by frequency division (÷40) of the 5 MHz reference. The output of the phase comparator is then passed through a loop filter and provides an error signal to control the VCO. When in phase lock, the VCO provides an output frequency referenced to the Frequency standard and is adjustable in 1 MHz steps. A lock detector is used to drive a front panel out-of-lock lamp.

1 KHz Step Module

The 1 KHz Step Module similarly contains a UHF VCO (2) locked through a programmable divider to a 10 KHz reference signal. The output of this VCO, which operates over 200 MHz to 209.99 MHz frequency range, is mixed with 180 MHz signal from Fixed Frequency Generator to develop an intermediate frequency in the 20 MHz to 30 MHz band. This IF drives a programmable ÷ M circuit which under locked condition provides a 10 KHz output. This ÷ M output is compared in phase with a 10 KHz reference signal obtained by frequency division (÷ 500) of the 5 MHz reference. The phase comparator output controls the UHF VCO via a loop filter.

The ÷ M circuit is programmable over the division range from 2000 to 2999 with a three digit decade switch. The 1 KHz step module output is obtained by dividing the VCO frequency (÷ 200) to yield a 1 MHz to 1.049950 MHz signal, adjustable to 50 Hz steps. A lock detector monitors loop phase lock and drives a front panel out-of-lock lamp.

Main Loop Module

The Main Loop module mixes the signal coupled from the SHF VCO (which operates at the desired output frequency) with the output from the YIG filter to produce a 200 MHz to

299.999 MHz IF. This IF is amplified and mixed with the 180 MHz to 279 MHz output from the 1 MHz Step module to produce 20 MHz to 20.999 MHz second IF. After amplification and filtering, this signal is divided by a factor of 20 to the 1 MHz to 1.049950 MHz range and phase compared with the output from the 1 KHz Step module. This Main Loop phase comparator output, after loop filtering controls the SHF VCO to close the main phase lock loop. The SHF VCO design is identical to that used for the 1 MHz increment synthesizer.

Frequency Selection

A steady state frequency diagram of the 1 KHz increshown in Figure 7. When phase locked, input frequencies to the respective phase comparators are equal. Referring to the diagram, it may be seen that the output frequency F_o is related to the loop parameters as follows:

$$F_o = F_1 + F_2 + 20F_3 \tag{3}$$

where:

$$F_1 = \alpha\, fr \tag{3a}$$

$$F_2 = \frac{N}{5} fr \tag{3b}$$

$$F_3 = \frac{1}{200}\left(\frac{M}{500} + 36\right) fr \tag{3c}$$

Substituting for F_1, F_2 and F_3 yields:

$$F_o = \left[\frac{1}{10}\left(\frac{M}{500} + 36\right) + \frac{N}{5} + \alpha\right] fr \tag{4}$$

where:

fr = 5 MHz (Frequency of Standard)

α = 20 (63 + ℓ) (Frequency Multiplication)
ℓ = 0, 1, 2 -- 11

N = 180 + n (Frequency division in 1 MHz loop)
n = 0, 1, 2 -- 99

M = 2000 + m (Frequency division in 1 KHz loop)
m = 0, 1, 2 -- 999

Substituting for the above provides:

$$F_o = 6500 + 100\ell + n + \frac{m}{1000}\ \text{MHz} \tag{5}$$

Equation (5) shows that the above system is capable of the frequency coverage extending from 6.5 GHz to 7.699999 GHz with 1 KHz increments. Frequency selection is made through control of the YIG filter (100 MHz increments) and the 1 MHz (+N) and 1 KHz (+M) dividers without interaction. Selection is performed via a seven digit decade front panel switch.

Phase Noise Analysis

The effect of the synthesizer parameters upon output phase noise resulting from contributions of the reference crystal oscillator and SHF Voltage Controlled Oscillator, may be determined with the use of Figure 8.

No(s) is the phase noise at the synthesizer output and N1(s) and N2(s) are the equivalent noise generators representing the SHF VCO and the crystal oscillator. Since the NI(s) and N2(s) are random independent noise sources, the total phase noise output may be obtained by superposition as follows:

$$No(s) = \frac{No}{N1}(s)\Big|_{N2(s)=0} \times N1(s) + \frac{No}{N2}(s)\Big|_{N1(s)=0} \times N2(s) \tag{6}$$

Contribution of each source is calculated with the other source equal to zero. From Figure 8 the following expressions are obtained:

$$\frac{No}{N1}(s) = \frac{1}{A}\,\frac{S}{S/A + F(s)} \tag{7}$$

$$\frac{No}{N2}(s) = \left(\alpha + \frac{KN}{R}\right)\frac{F(s)}{S/A + F(s)} \tag{8}$$

where:

$$A = \frac{\delta\mu}{KN}\ \text{loop gain} \tag{8a}$$

With a lead-lag loop filter used:

$$F(s) = \frac{(S/\omega_1 + 1)}{(S/\omega_2 + 1)} \tag{9}$$

which substituted into (7) and (8) yields:

$$\frac{No}{N1}(s) = \frac{1}{A}\,\frac{S(S\omega_2 + 1)}{S^2/A\omega_2 + S(1/A + 1/\omega_1) + 1} \tag{10}$$

$$\frac{No}{N1}(s) = \left(\alpha + \frac{KN}{R}\right)\frac{(S/\omega_1 + 1)}{S^2/A\omega_2 + S(1/A + 1/\omega_1) + 1} \tag{11}$$

These are second order responses where the natural frequency ω_o and the damping ratio ζ are:

$$\omega_o = \sqrt{A\omega_2} \tag{12}$$

$$\zeta = \frac{1}{2}\left(\frac{\omega_2}{\omega_o} + \frac{\omega_o}{\omega_1}\right) \tag{13}$$

Normalizing equations 10 and 11 with respect to ωo and using substitutions of equations 12 and 13 yields:

$$\frac{No}{N1}(s) = \frac{S(S + \omega_o/A)}{S^2 + 2\zeta S + 1} \tag{14}$$

$$\frac{No}{N2}(s) = \left(\alpha + \frac{KN}{R}\right)\frac{(2\zeta - \omega_o/A)S + 1}{S^2 + 2\zeta S + 1} \tag{15}$$

The equations 14 and 15 indicate that the loop acts as a complimentary set of low pass and high pass filters. The noise generated in the SHF VCO is attenuated below the natural frequency of the loop while the noise from the crystal oscillator, multiplied to SHF, is attenuated above the natural frequency.

For the 1 MHz increment synthesizer, the equations 14 and 15 and their asymptotes are shown in Figure 9. In general, the exact shape of the response, i.e., the deviation from the asymptotes and the response 6-12 dB/octave break points depend upon the damping and the natural frequency to loop gain ratios.

The phase noise of the 1 MHz increment synthesizer output $N_O(s)$ and the phase noise of the two contributary oscillators $N_1(s)$ and $N_2(s)$ are shown in Figure 10. The measured output phase noise was comparated with calculated $N_O(s)$ using measured data for $N_1(s)$ and $N_2(s)$, and equations 6, 10 and 11. The close agreement between measured and calculated $N_O(s)$ indicates minimum synthesizer circuit degradation and the principle noise contribution to the output is caused by the SHF VCO and the crystal oscillators.

In the case of the 100 KHz increment design, the phase detector and the loop filter have been changed. Here a digital type phase detector was used which provided an output current proportional to the phase difference between the input signals. With a simple RC loop filter, the control voltage developed across the filter output as a function of the input phase difference is:

$$\frac{V_o(s)}{\phi e} = \beta \frac{RC\,S + 1}{CS} \tag{14}$$

where:

β - phase detector sensitivity - amps/rad

R, C - loop filter values

From the above it may be seen that the block diagram of Figure 8 supplies, with β replacing δ, K = 1, and

$$F(s) = \frac{RC\,S + 1}{CS}$$

Substituting these into equations (7) and (8) yields:

$$\frac{No}{N1}(s) = \frac{C}{A} \quad \frac{S^2}{S^2 \frac{C}{A} + S\,RC + 1} \tag{15}$$

$$\frac{No}{N2}(s) = \left(\alpha + \frac{N}{R}\right) \frac{S\,RC + 1}{S^2 \frac{C}{A} + S\,RC + 1} \tag{16}$$

The expressions are also of second order and the natural frequency and the damping ratio are:

$$\omega_o = \sqrt{A/C} \tag{17}$$

$$\zeta = \frac{R}{2}\sqrt{AC} \tag{18}$$

Normalizing equations 15 and 16 with respect to ω_o they become:

$$\frac{N_O}{N_1}(s) = \frac{S^2}{S^2 + 2\zeta\,S + 1} \tag{19}$$

$$\frac{N_O}{N_2}(s) = \frac{2\zeta\,S + 1}{S^2 + 2\zeta\,S + 1} \tag{20}$$

The equations (19) and (20) are shown in Figure 11 (for $\zeta = 0.5$). It should be noted that below natural frequency N_O/N_1 has a continuous slope of 40 dB/decade. This is equivalent of having an infinite loop gain, and the loop operates with a zero steady state phase error. In addition, phase noise advantage is obtained at low Fourier frequencies, where the dominating SHF VCO phase noise is more deeply suppressed.

Similar analysis has been performed on the 1 KHz increment synthesizer. Though the analysis for the multiloop design is somewhat more involved, the basic technique remains the same. In this case, the total noise output is obtained by superposition of four terms, namely that due to the SHF VCO, the UHF FCO in the 1 MHz loop, the UHF VCO in the 1 KHz loop, and the crystal oscillator multiplied to the SHF output frequency.

The measured output phase noise of the 100 KHz and 1 KHz increment synthesizers differs little from the 1 MHz design (Figure 10). Some advantage in the frequency offset region of 1 KHz to 20 KHz is obtained with the multiloop 1 KHz increment design, due to the wider bandwidth in its main loop.

Figure 12 illustrates short term stability measurements taken on a 1 KHz increment synthesizer which provides a measure of the phase noise performance in the time domain.

Spurious and Loop Stability Considerations

Since phase comparator circuits provide outputs which contain leakage of the input comparison frequencies and their harmonics; additional filtering between the phase comparator and the VCO is required. This low pass filter serves to attenuate these comparison frequency components, which in turn controls undesirable modulation of the SHF VCO to acceptable spurious output levels.

Without filtering and delay within the phase lock loop, the loop is unconditionally stable. With this filter, however, instability due to the added phase shift can occur if too wide a loop bandwidth is attempted. During the design of these synthesizers it was determined that when such a filter is used the phase shift of the filter at the natural frequency should be less than 20 degrees. The loop then remains stable and the filter effect upon the loop response is minimal. The filter designs for the synthesizers described here suppressed the spurious sidebands to -80 dBc, with the loop bandwidth (natural frequencies) not exceeding one tenth of the comparison frequencies.

Equipment Construction

Each synthesizer has been constructed as a complete assembly which is front panel removable from the satellite terminal upconverter and down-converter drawer. Regulated dc power is supplied by the converter drawer power supply.

The 0-1677( )/GSC uses five plug-in modules: 5 MHz Crystal Oscillator, Fixed Frequency Generator, Yig Filter, Control Module and SHF VCO. The 0-1678( )/TSC-86 uses

seven modules: 5 MHz Crystal Oscillator, Fixed Frequency Generator, Yig Filter, 1 MHz Step Module, 1 KHz Step Module, Main Loop, and SHF VCO.

Special RCA design fired film hybrid and thin film MIC circuits are used in these modules. Three MIC designs are used in each synthesizer type; and seven fired film hybrid circuits are used in the 0-1677 and fourteen hybrid circuits are used in the 0-1678.

Rapid synthesizer operating status and fault isolation to the module level is accomplished with the use of front panel status lamps and a converter drawer monitor meter. Monitor outputs from each module are made available to a front panel meter selector switch for this purpose. The primary synthesizer status indicator is the main loop "Out-of-Lock" lamp which requires proper operation of the entire synthesizer to be extinguished.

Conclusion

Design and performance characteristics of two basic military SHF synthesizers were described. Each uses indirect synthesis techniques in which an SHF oscillator is phase locked with digitally controlled feedback loops to a crystal derived reference. Analytical methods of relating the phase noise of the locked oscillator and the reference crystal oscillator to the synthesizer output phase noise was presented. These designs demonstrated that with care in circuit design, these two oscillators provide the only significant contribution to the phase noise at the synthesizer SHF output.

Acknowledgements

The authors wish to acknowledge the contributions and guidance provided by many personnel of the U.S. Army Satellite Communications Agency, Fort Monmouth, N.J. who sponsored this development effort as part of the Small SHF Satellite Ground Terminal Program. Additionally, we acknowledge the many RCA Government Communications Systems Division contributors to the design, development, construction and testing of these frequency synthesizers.

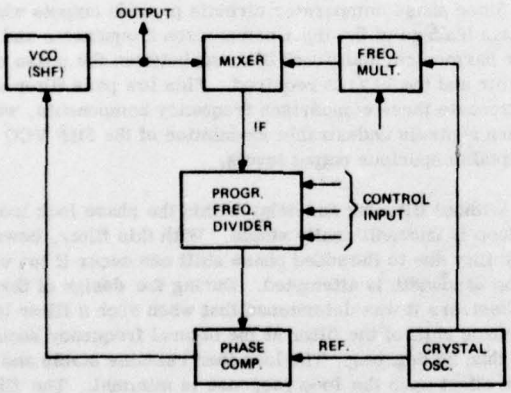

FIGURE 1a. SINGLE FEEDBACK LOOP SYNTHESIZER

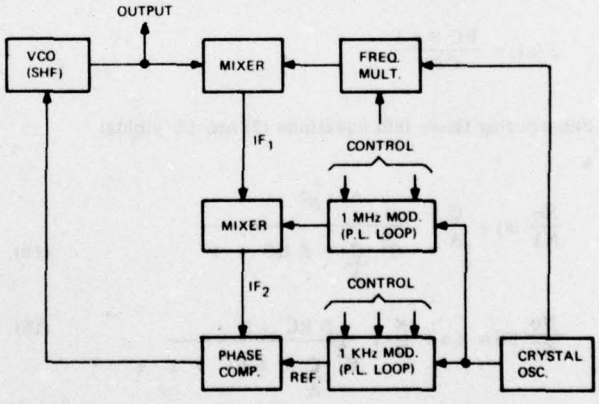

FIGURE 1b. MULTIPLE LOOP SYNTHESIZER

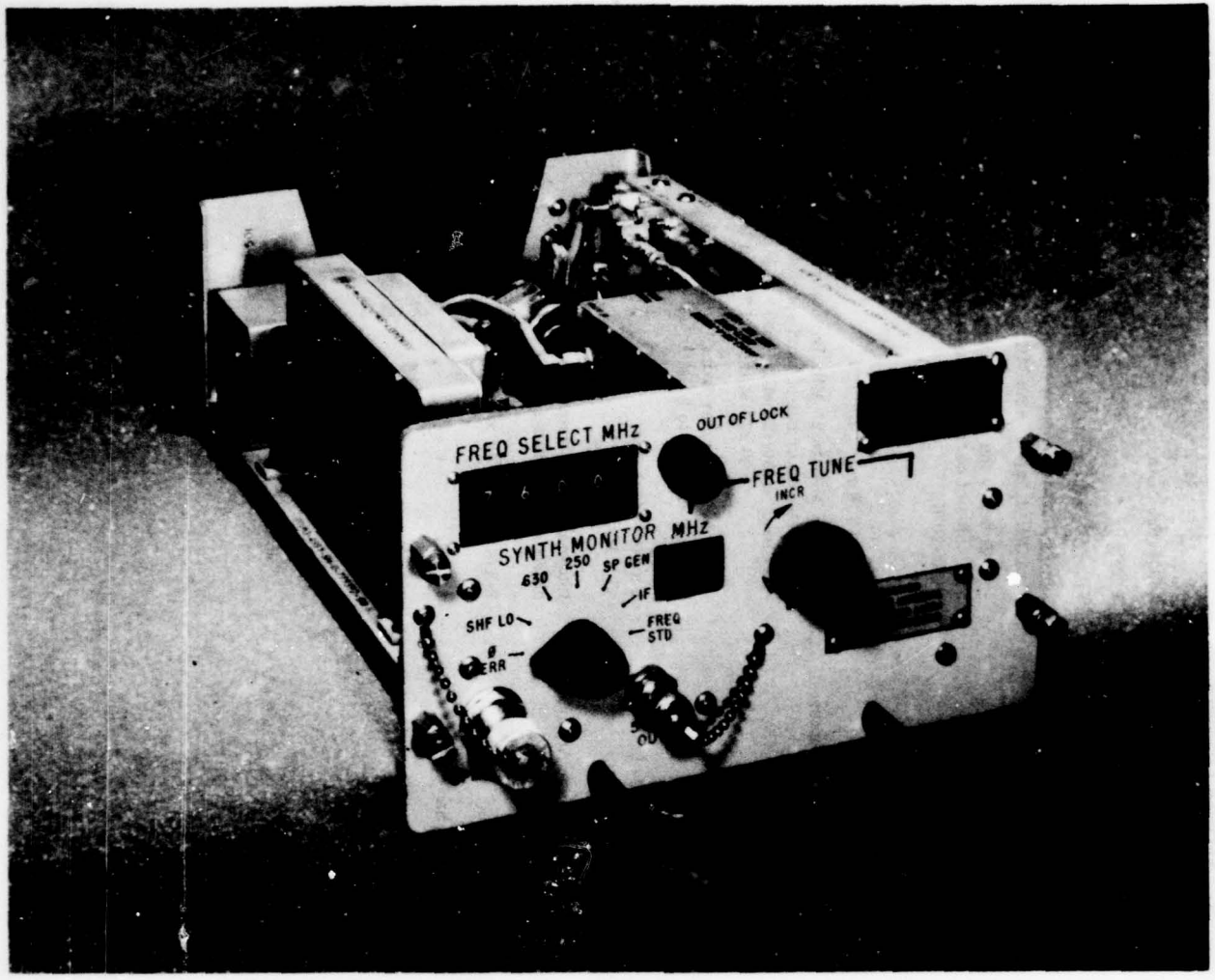

FIGURE 2. 0-1677( )/GSC, SHF FREQUENCY SYNTHESIZER (1 MHz INCREMENT)

TABLE 1

PERFORMANCE SUMMARY (1 MHz INCREMENT)

∩-1677 FREQUENCY SYNTHESIZER

1.	Variable Frequency Output (SHF)	
	Frequency Range:	6500-7699 MHz
	Frequency Increments:	1 MHz
	Output Level:	+10 dBm minimum, +16 dBm maximum
	Spurious Outputs:	-80 dB: all spurious 1 MHz beyond carrier -125 dB: $f_o \pm (680 \pm 20)$ MHz
	Phase Noise:	-35 dB below the carrier when measured on both sides of carrier in bandwidth from 130 Hz to 20 Hz
2.	630 MHz Output	
	Level:	+9 to +13 dBm
	Spurious Outputs:	-80 dB: 1 MHz to 20 MHz from carrier -70 dB: All other out of band spurious -90 dB: $f_o \pm$(630 ±20 MHz, 700 ±20 MHz, 560 ±20 MHz, and 70 ±20 MHz)
	Phase Noise:	-46 dB below carrier from 10 Hz to 300 KHz and 300 KHz to 20 MHz
3.	Frequency Stability:	1×10^{-10}/0.1 sec. $\pm 3 \times 10^{-7}$/year
4.	Frequency Accuracy:	Internal 5 MHz frequency standard adjustable to better than 1×10^{-8}.
5.	Size:	9-1/4" x 5-1/4" x 12"
6.	Weight:	11 lbs.

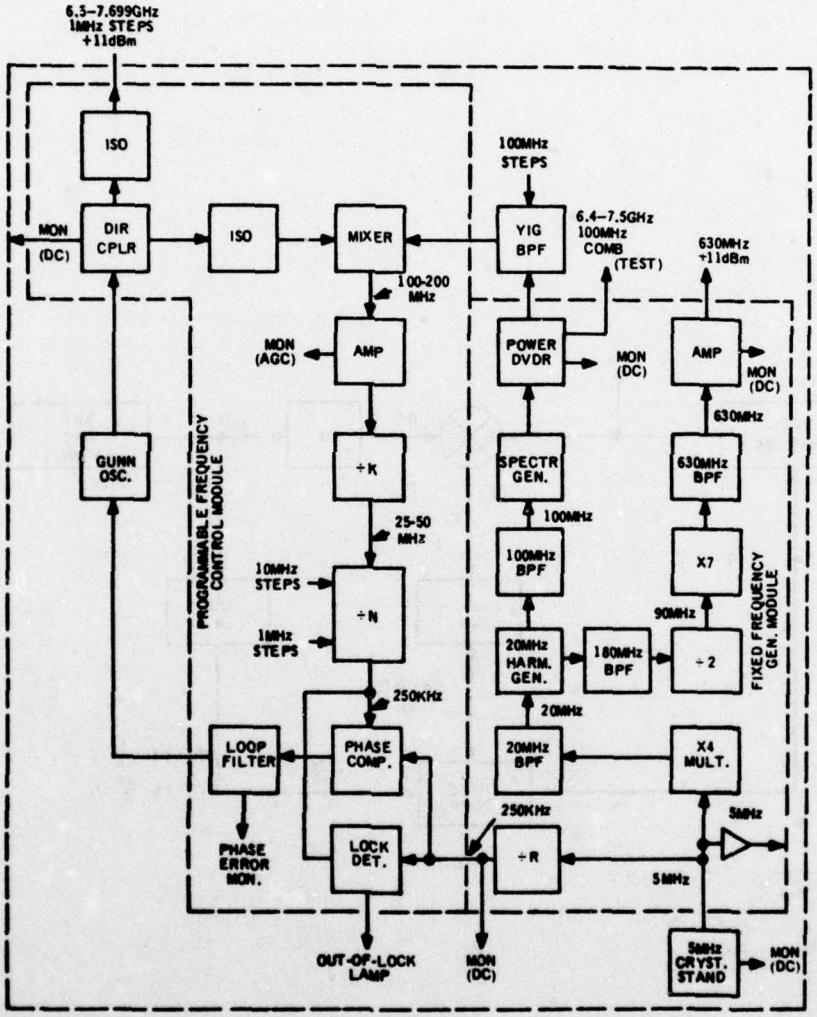

FIGURE 3
BLOCK DIAGRAM
1 MHz FREQUENCY SYNTHESIZER

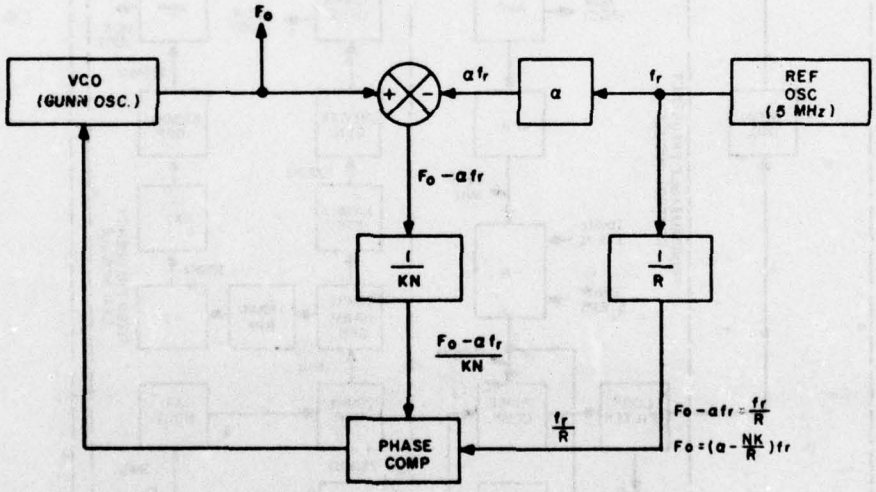

FIGURE 4
SIMPLIFIED STATIC BLOCK DIAGRAM
(1 MHz INCREMENT SYNTHESIZER)

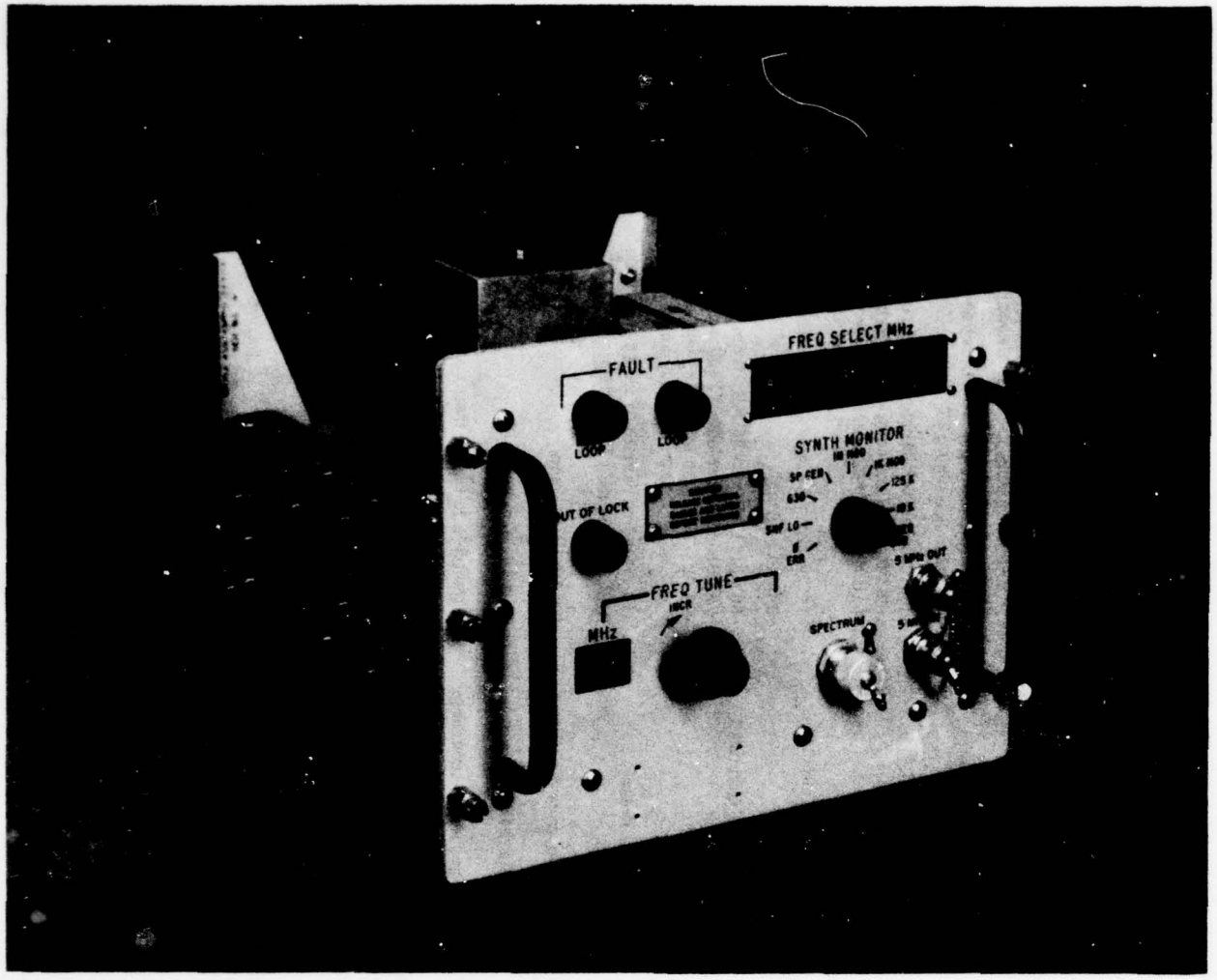

FIGURE 5. 0-1678( )/TSC-86, SHF FREQUENCY SYNTHESIZER (1 KHz INCREMENT)

TABLE 2

0-1678 FREQUENCY SYNTHESIZER PERFORMANCE SUMMARY

1.	Variable Frequency Output (SHF)	
	Frequency Range:	6500-7699.999 MHz
	Frequency Increments:	1 KHz
	Output Level:	+10 dBm minimum, +16 dBm maximum
	Spurious Outputs:	-80 dB: all spurious 1 MHz beyond carrier -125 dB: $f_o \pm (680 \pm 20)$ MHz
	Phase Noise:	-28 dB below the carrier measured on both sides of carrier bandwidth covering offsets of 10 Hz to 300 KHz and 300 KHz to 20 MHz.
2.	630 MHz Output	
	Level:	+9 to +13 dBm
	Spurious Outputs:	-80 dB: 1 MHz to 20 MHz from carrier -70 dB: All other out of band spurious -90 dB: $F_o \pm$(630 ±20 MHz, 700 ±20 MHz, 560 ±20 MHz, and 70 ±20 MHz)
	Phase Noise:	-46 dB below carrier from 10 Hz to 300 KHz and 300 KHz to 20 MHz
3.	Frequency Stability:	1×10^{-10}/0.1 sec.
	(Internal)	$\pm 5 \times 10^{-9}$/24 hrs.
4.	Frequency Accuracy:	Adjustable to better than 1×10^{-8} (Internal Crystal Oscillator) External 5 MHz synchronization available.
5.	Size:	9-3/4" x 7-1/4" x 12"
6.	Weight:	17 lbs.

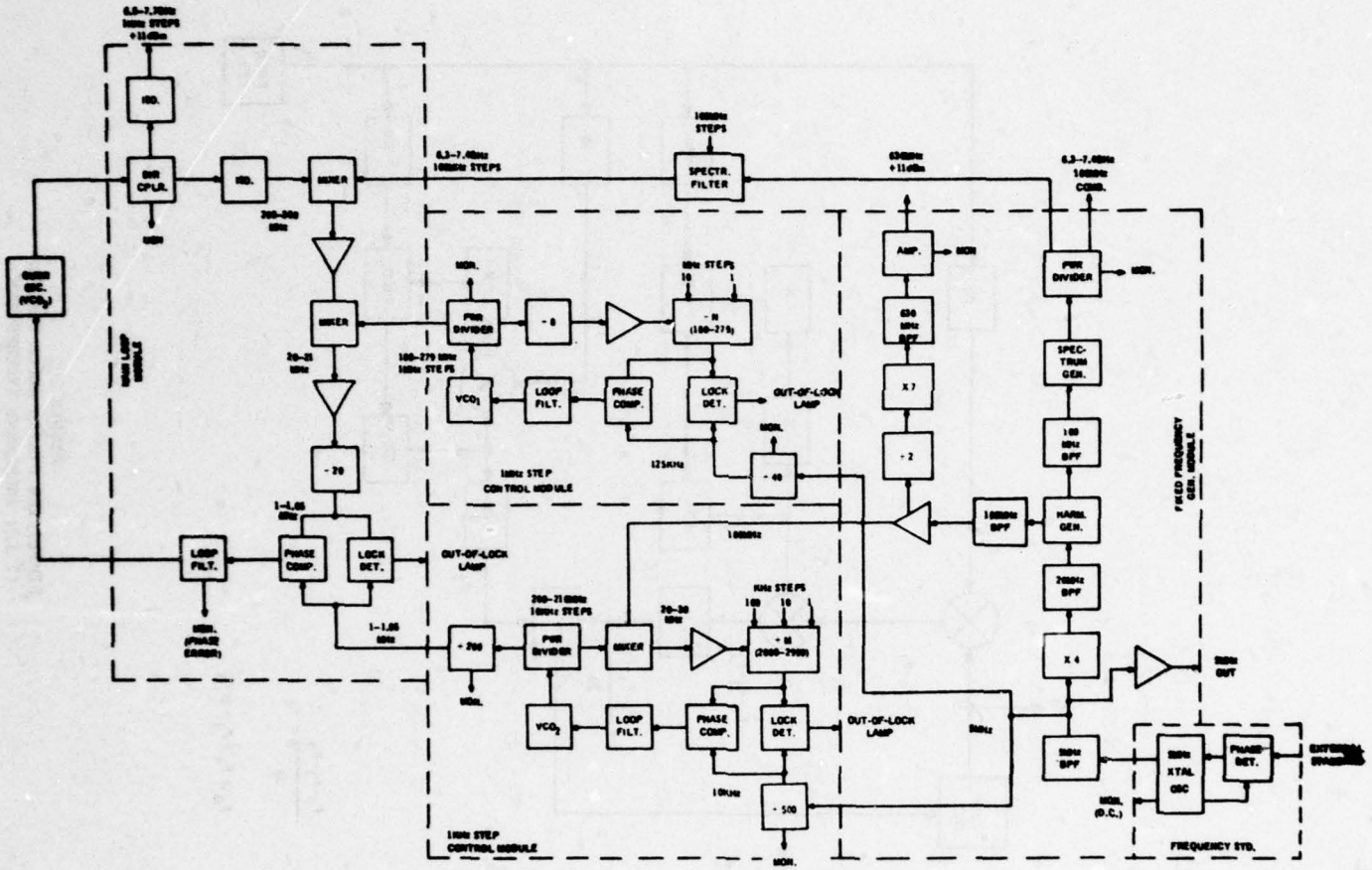

FIGURE 6. 1 KHz STEP SHF FREQUENCY SYNTHESIZER BLOCK DIAGRAM

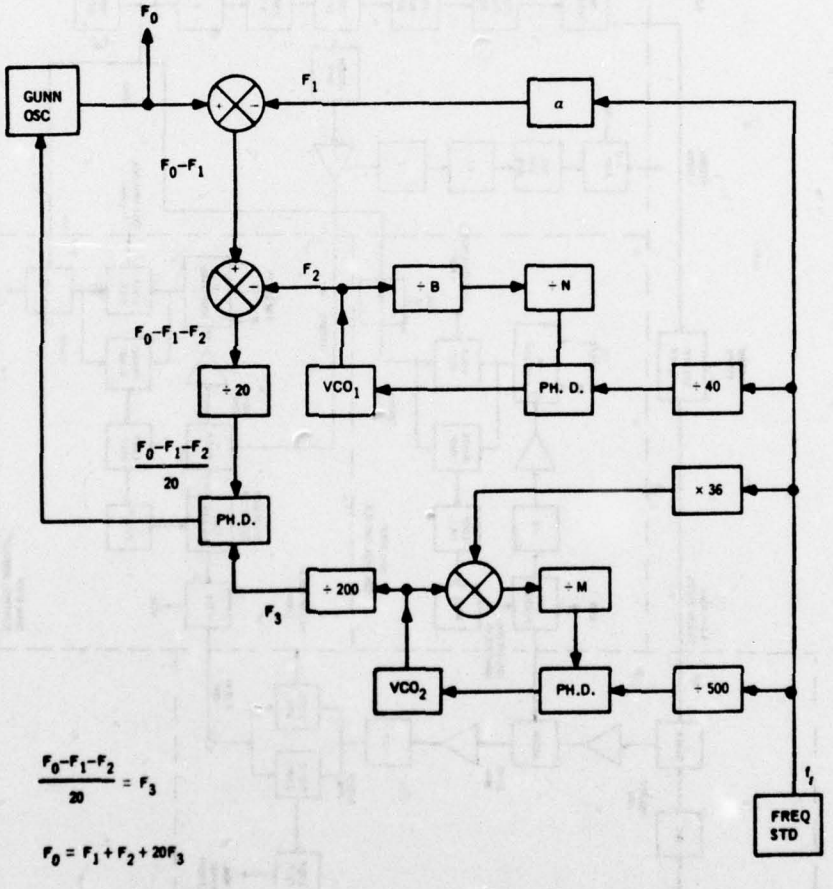

FIGURE 7
SIMPLIFIED STATIC BLOCK DIAGRAM
(1 KHz INCREMENT SYNTHESIZER)

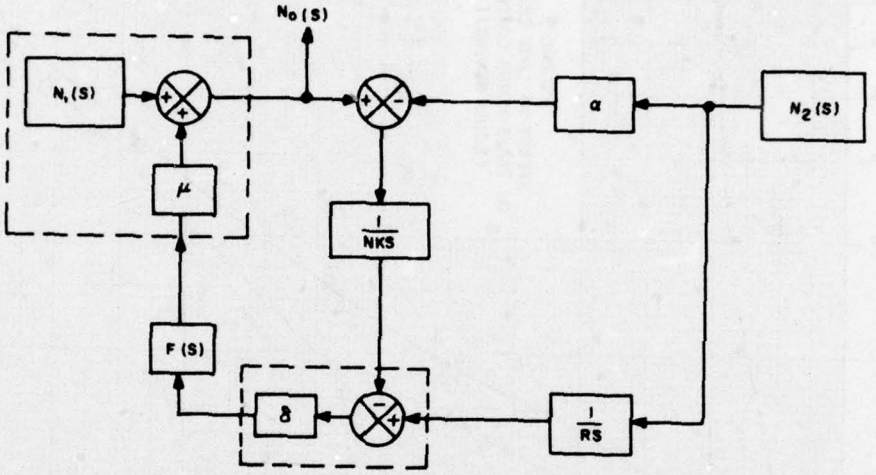

FIGURE 8. SIMPLIFIED DYNAMIC BLOCK DIAGRAM WITH EQUIVALENT NOISE GENERATORS

Where:

$N_o(s)$	-	Phase noise spectral density at output
F(s)	-	Loop filter transfer function
δ	-	Phase detector sensitivity (volts/radian)
μ	-	SHF VCO sensitivity (radian/volt second)
α	-	total frequency multiplication
N, K, R	-	Frequency divisions
$N_1(s)$	-	Phase noise spectral density of SHF VCO
$N_2(s)$	-	Phase noise spectral density of crystal standard
S	-	Complex frequency ($S = \sigma + jw$)

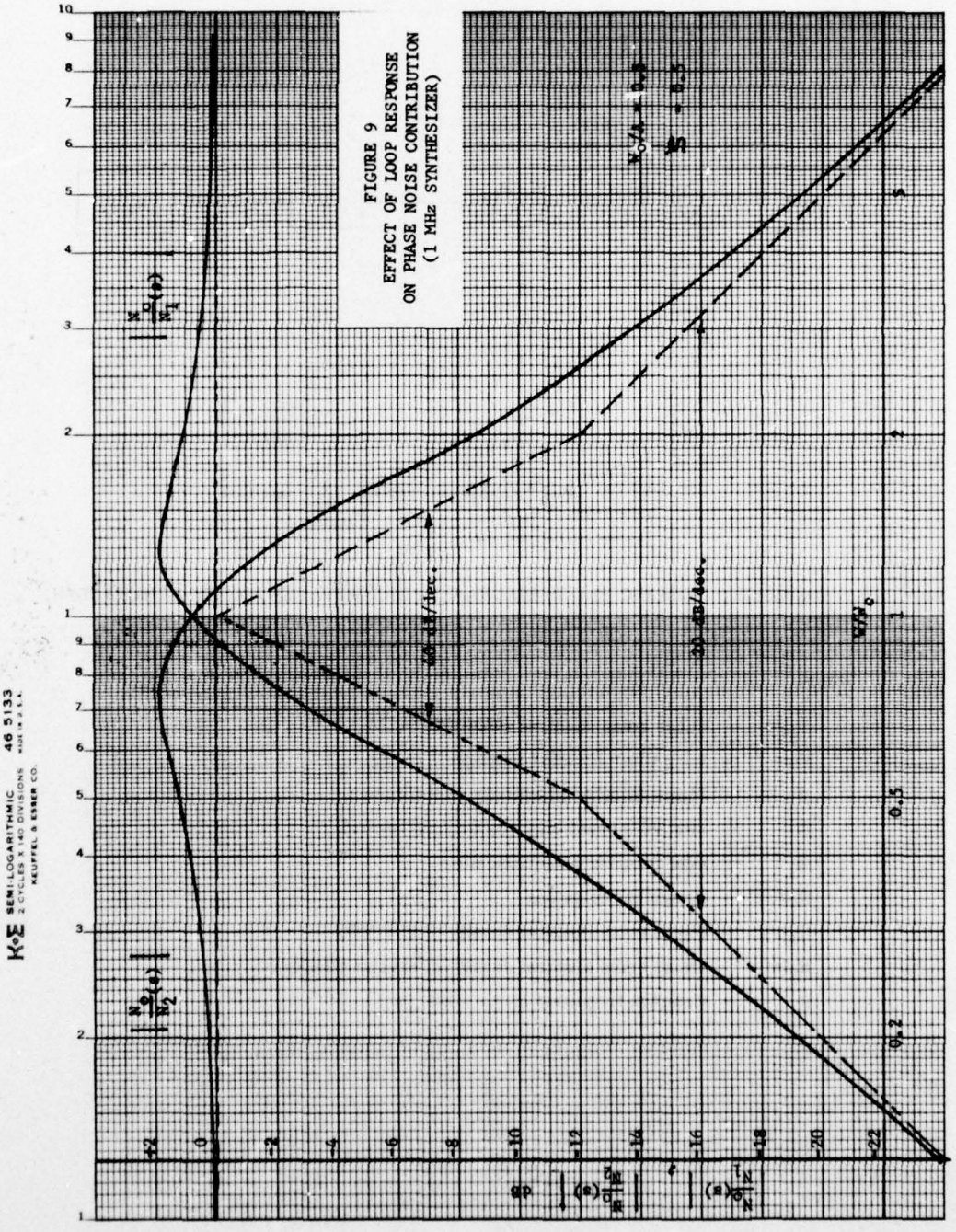
FIGURE 9
EFFECT OF LOOP RESPONSE
ON PHASE NOISE CONTRIBUTION
(1 MHz SYNTHESIZER)
K∘E SEMI-LOGARITHMIC 46 5133
2 CYCLES X 140 DIVISIONS
KEUFFEL & ESSER CO.
40 dB/dec.
20 dB/dec.
0.5
0.2

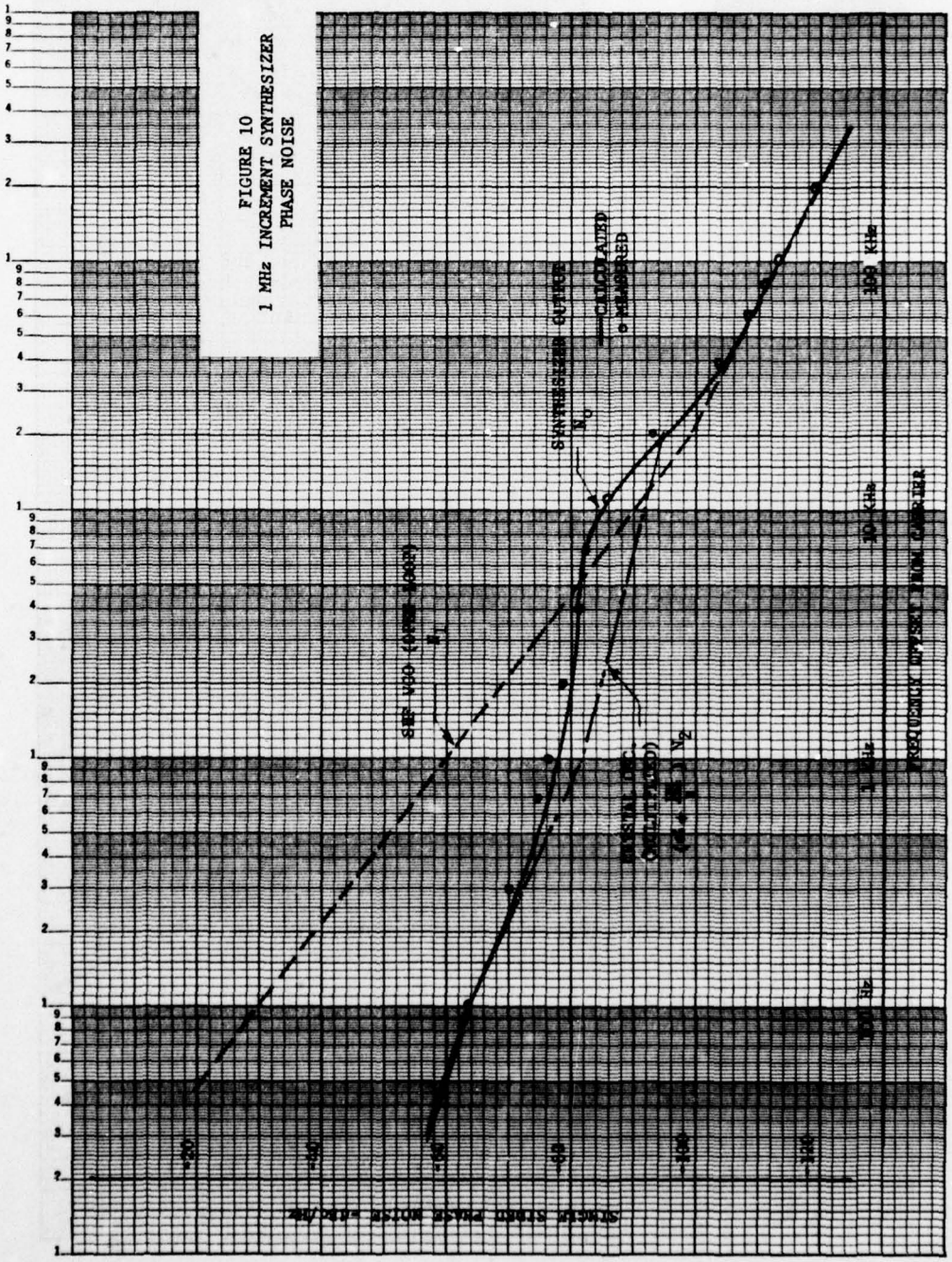
FIGURE 10
1 MHz INCREMENT SYNTHESIZER
PHASE NOISE
SYNTHESIZER OUTPUT
CALCULATED
MEASURED
REFERENCE (CRYSTAL OSCILLATOR)
SSB VCO (FREE RUNNING)
FREQUENCY OFFSET FROM CARRIER
SINGLE SIDED PHASE NOISE dBc/Hz

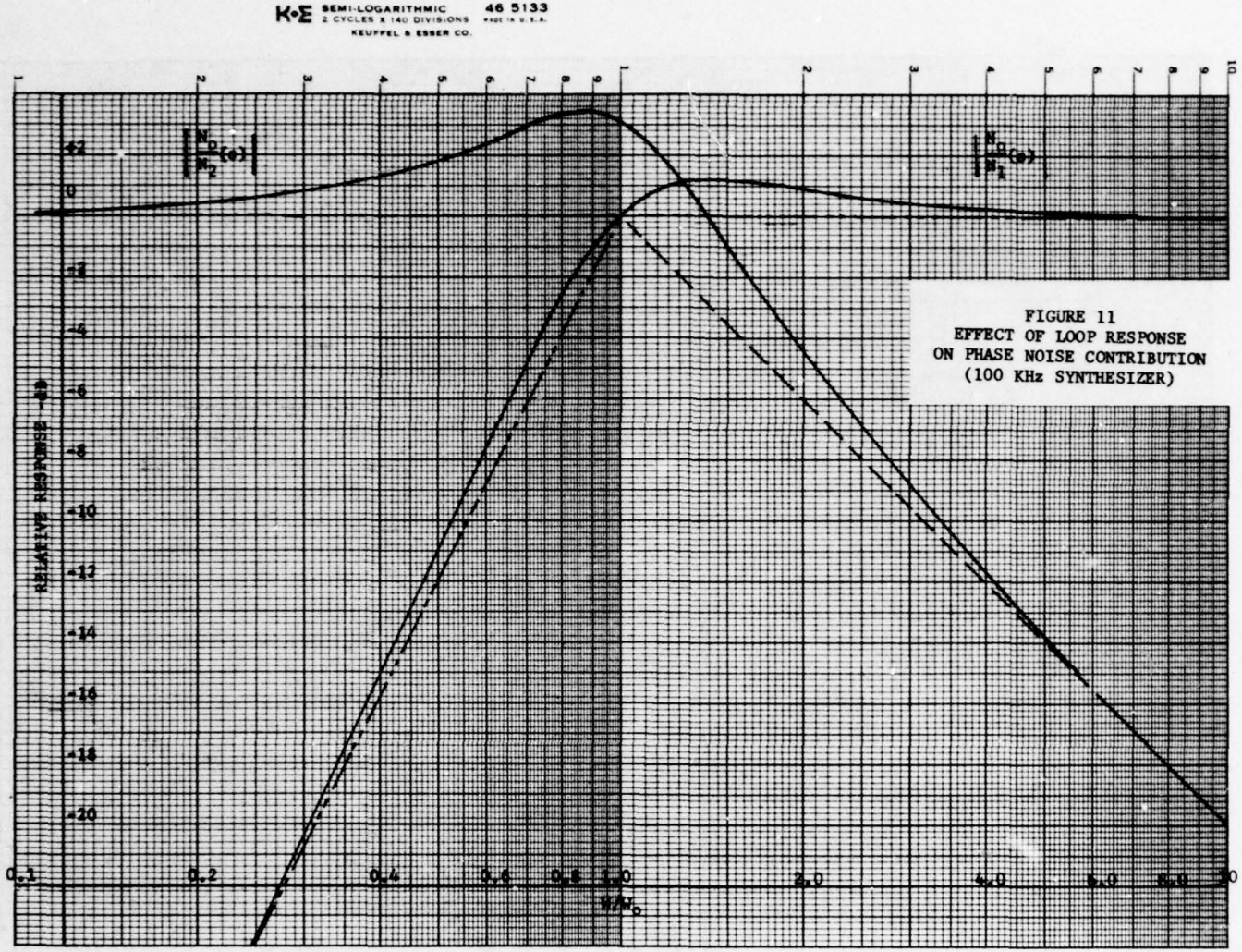

FIGURE 11
EFFECT OF LOOP RESPONSE
ON PHASE NOISE CONTRIBUTION
(100 KHz SYNTHESIZER)

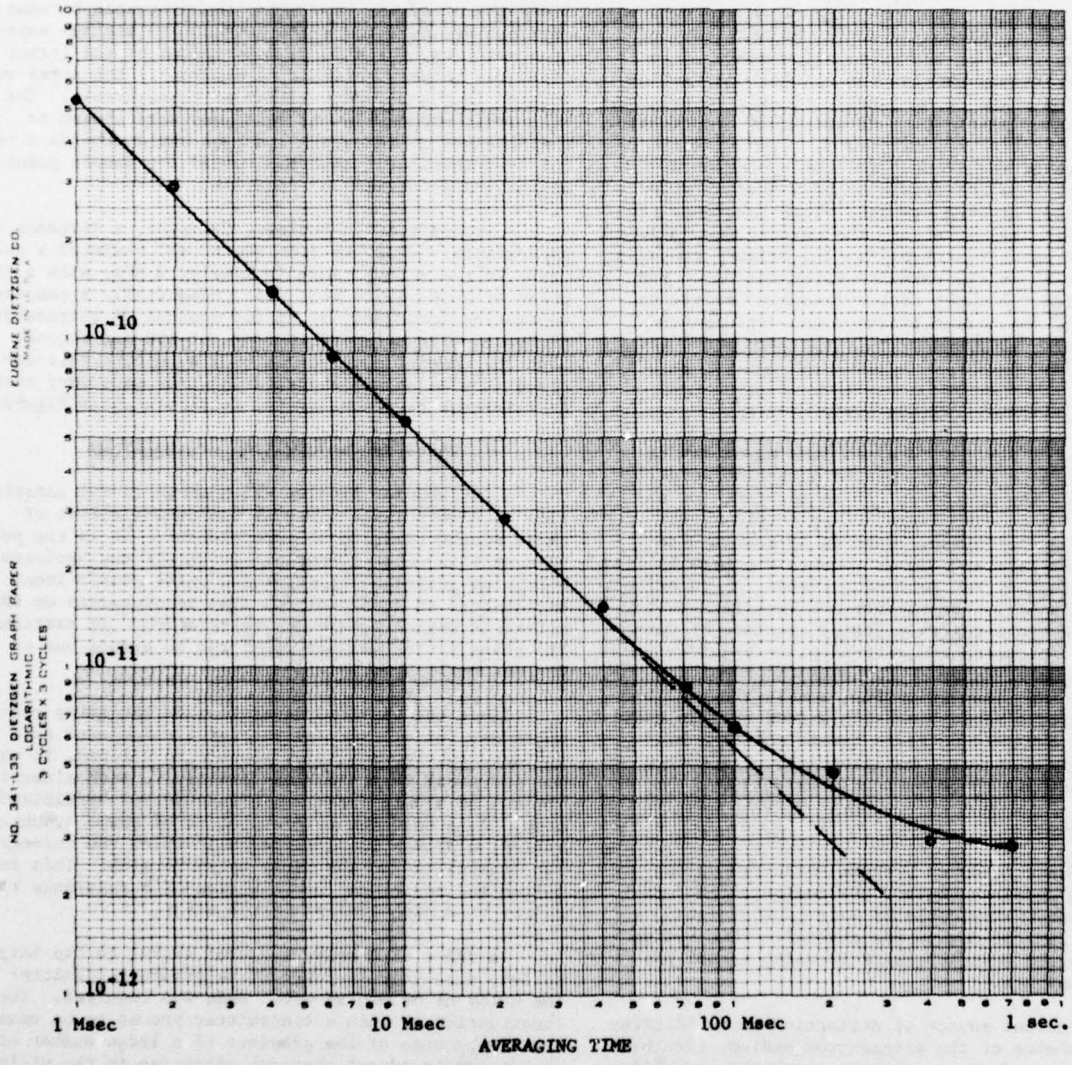

FIGURE 12. MEASURED SHORT TERM STABILITY
(1 KHz INCREMENT FREQUENCY SYNTHESIZER)

PHASE SYNCHRONIZATION OF A LARGE HF ARRAY BY A LOCAL BROADCAST STATION

S. Hassan Taheri
Bernard D. Steinberg
Donald L. Carlson
Valley Forge Research Center
University of Pennsylvania

Summary

In recent years research has been conducted at the Valley Forge Research Center in the field of very large antenna arrays with high angular resolution, called radio cameras. When the size of an aperture becomes very great, problems arise in the stability of the refractive index of the propagation medium. In order to quantitatively examine the spatial correlation function of the phase of an ionospherically refracted signal, an experimental 40 km HF array was constructed.

An important requirement for the operation of this huge array was the provision of a phase stable local oscillator at each station. This reference signal was obtained by extracting the carrier from a local broadcast band transmission. The primary emphasis of this paper is on the hardware subsystem which was used to provide the phase stable frequency reference. In particular, the characteristics and performance of the receiver designed for this task are presented in detail. [1]

Introduction (The Radio Camera)

The angular resolution of an imaging device is the order of the reciprocal of the number of wavelengths across the aperture. If an aperture (or antenna) can be made very large, in principle a very narrow beam can be formed. When an RF aperture becomes sufficiently large so as to obtain unusually fine angular resolution, the resulting system is, in effect, a radio camera [2]. Two significant requirements for such a device are a sparsely filled aperture of randomly located elements and self-adaptive beamforming [3]. For example, in order to equal the resolving power of a 2-inch lens at optical wavelengths, an L-band radio camera would nominally extend over 20 miles. Although the emphasis in radio camera research has been placed on microwave operation, the HF spectrum has also proven to be of much interest. [4]

Large HF Arrays

In a recent research program conducted at the Valley Forge Research Center, the design of the maximum HF aperture which could be made to function as a diffraction limited device was studied. This system concept involved adaptive, self-focusing signal processing techniques.

The principal source of distortion in an HF array is the turbulence of the propagation medium, for the characteristics of the ionosphere are both temporally and spatially varying. Nonhomogeneities in the ionospheric refractive index are responsible for inducing spatial variations in the phase of a signal passing through the ionosphere. In the case of both point to point communications and over-the-horizon radar, this phase correlation distance approximates the nominal, maximum useful aperture for an HF antenna.

HF Array Experimental Program

In order to quantitatively evaluate the spatial correlation function of the phase of a signal passing through the ionosphere, a complex experimental program was designed. Eight receivers, specially constructed for this experiment, were installed at array element stations over a region approximately 40 km in extent. Since the array was very thin, the distances between adjacent elements was quite large. The minimum separation was 2 km, while 20 km was typical of the larger distances between neighboring elements. The array was located in the Delaware Valley of Pennsylvania. The relatively random element locations were chosen so that the set of interpair spacings would provide a useful distribution of abscissa values for sample points on the phase correlation function.

A transmitter in Boulder, Colorado, a distance of approximately 2,400 km from the array, radiated a pulse train in the mid-HF range (nominally 9 MHz) with a peak power of 20 kw [5]. This unit, essentially a computer controlled ionosonde, generated nominal 64 microsecond HF bursts with a repetition rate of 100 per second. Both the carrier and repetition frequencies were derived from an atomic standard and thus were very stable. An illustration of the system is presented in Figure 1.

Phase Synchronization of the Array

A fundamental problem encountered in the construction of a very large array is the establishment of phase synchronization at each element. It is the purpose of this paper to explain in detail the hardware subsystem dedicated to providing phase stable local oscillators at each station. The requirements on the reference signal were quite restrictive. In particular the phase jitter was not permitted to exceed one or two degrees rms.

Since the physical separation of the array elements was quite large and the terrain included such surface features as hills, roads, and streams, it was not practical to run cables directly to each element. The use of atomic frequency standards was prohibited by cost. As a solution to the problem of phase synchronization, a design was considered in which the reference was transmitted to the array by an RF link. This required the additional construction of a reference receiver from each station in the array.

In order to provide a useful signal to the large system, a relatively powerful reference transmitter in the noisy HF or medium wave bands was required. The construction of such a transmitter proved to be unnecessary because of the presence of a large number of high power broadcast stations operating in the vicinity of the test area. This method seemed quite attractive after consideration was given to the high stability and closely controlled accuracy of the broadcast station carrier frequencies as required by the FCC. One of the 50 kW broadcast stations in the Delaware Valley, KYW, was chosen as the reference. The signal from this station provided the array with a very high signal level at a frequency of 1060 kHz.

Broadcast Signal Properties

Several different designs were considered for the extraction of the carrier from the broadcast transmission. The original plan called for the use of phase-lock techniques for the recovery of the carrier from the amplitude modulated signal. The time constant of the PLL was made approximately one second to ensure that the output phase corresponded to the average AM carrier phase. Some difficulty was encountered when it was noted that phase modulation was resulting from the unbalanced amplitude modulation sidebands of the carrier. This method, nevertheless, showed considerable promise for a stable and accurate frequency reference. Any future design work should include a thorough analysis of the use of PLL techniques in this application. [6,7]

There were several possible causes for the unbalance in the sidebands. One obvious possibility was a slight misadjustment at the transmitting station. A more likely cause was unbalance from the receiver circuitry itself. It was also possible that propagation conditions could favor one sideband of the broadcast transmission. In any case, the effects of phase modulation were of great concern. Figure 2 presents a vector illustration of the phase jitter resulting from a significant unbalance in the sidebands of a 100% tone modulated signal.

The method chosen to reduce this effect called for the insertion of a high Q crystal filter tuned to 1060 kHz in each receiver. The nominal bandwidth of each circuit was 10 Hz, sufficient to reduce the residual phase modulation to approximately 1^{o} rms. These results were extremely encouraging and permitted the successful extraction of the carrier for use as a phase stable frequency reference.

Reference Receiver

The block diagram of the entire reference receiver is shown in Figure 3. The crystal filter was placed after a RF amplifier tuned to 1060 kHz. A MOSFET stage with very high input impedance was inserted at the output of the filter to provide isolation by minimizing the loading of the crystal. A cascode bipolar transistor stage was included for further signal amplification. Finally, a comparator integrated circuit was used to provide hard limiting and to produce a square wave output compatible with TTL circuits.

The number of components used in the construction of the reference receiver was quite limited. The circuit diagram, presented in Figure 4, reveals the simplicity of the unit.

Frequency Synthesizer

A frequency synthesizer, constructed with a TTL phaselock loop, was used to provide phase stable local oscillator signals throughout the HF spectrum at multiples and fractional multiples of the reference frequency of 1060 kHz. The synthesizer was a versatile device with a large inherent flexibility of operation. The circuit itself was straightforward, consisting of a PLL with programmable output frequency. A simple block diagram of the frequency synthesizer is shown in Figure 5.

The counter M may be set to any integer from 10 to 19, thus establishing the oscillation frequency of the VCO by varying the divisor in the feedback path. Further control over the output frequency was accomplished by adjusting the value of P for either 1, 2, or 4. The output frequency was then $(M/P)f_x$, where the reference frequency f_x was 1060 kHz.

In order to have a small phase error in the output of the synthesizer, the reference signal was required to be highly stable. Any phase jitter in the reference would be multiplied in the frequency synthesis process. For example, a $\pm 10^{o}$ peak jitter in the reference phase would result in a peak phase jitter of $\pm 100^{o}$ after frequency multiplication by a factor of 10, provided that the synthesizer did not introduce any additional phase jitter of its own. This would result in a relative peak phase fluctuation of $\pm 200^{o}$ between two receivers. Subh large phase errors would tend to mask any true fluctuations due to changes in the ionosphere and thereby diminish the usefulness of the measured data.

It may be noted that there were 30 different local oscillator frequencies. It is also of interest that these square wave signals had high third and fifth harmonic content. Thus many more possible frequencies were available had they been needed. Harmonic operation, however, should be avoided if possible because of degradation in receiver performance. [8]

The frequency multiplication process performed in the synthesizer was necessary due to the low frequency of the reference signal. As a consequence the phase jitter also was multiplied. In view of this important consideration, it is interesting to consider the use of a VHF broadcast signal as the reference. If a suitable station could be found, division rather than multiplication could be employed which would diminish the resultant phase jitter from that inherent in the original signal. This method is quite attractive if a compatible VHF broadcast signal is available. Most commercial VHF signals, however, have unsymmetrical sidebands, e.g., FM, TV, which make the problem of jitter-free carrier extraction inherently more difficult.

Remaining Receiver Circuitry

To facilitate measurement of phase fluctuations at several frequencies within the HF spectrum a wideband superheterodyne unit was included in the design of the HF pulse receiver. A variable frequency RF amplifier allowed for the selection of the HF frequency in use. A two-stage IF amplifier with 60 dB gain was also developed in addition to a double balanced mixer with 12 dB of conversion gain. The local oscillator was obtained from the frequency synthesizer. A hard limiter was provided to produce an output signal compatible with TTL logic requirements.

The remainder of the system consisted of fairly complex logic stages. These circuits, however, did not affect the operation of the basic receiver already discussed. Their function was to perform tracking of the pulse train as the time of arrival of the HF bursts varied and also to carry out the actual phase measurement operation. In addition, a complex data recording system was necessary to interface the output of the receiver with the magnetic tape data storage unit. [9,10]

Phase Error

With proper tuning of the crystal filter, the relative phase jitter between two receivers was observed to be on the order of 1^{o} rms. This value was measured by comparing the reference signals from two receivers on alternate traces of an oscilloscope. By using the delayed sweep capability, a magnification of one cycle after a substantial time interval revealed the phase modulation inherent between the two signals. This process is illustrated in Figure 6.

Thus, in a typical frequency synthesizer multiplication by a factor of 10, the relative phase error was approximately 10^{o} rms. This amount of phase jitter, which set the resolution limit of the entire system [11] was satisfactory for the intended purpose.

Phase jitter tolerance in phased arrays relates directly to the loss in array gain. Specifically the factor by which the gain decreases is $\exp(-\sigma_\phi^2)$ where σ_ϕ is the standard deviation of phase error. For example, a 1 dB gain loss will occur for a phase uncertainty of approximately 0.5 radians rms. This value was used to specify that the tolerance of the reference signal before frequency multiplication must not be greater than several degrees rms. It may also be noted that the loss in gain is quite rapid with increasing phase error, since for a one radian rms error there will be nearly a 5 dB loss in gain. [12]

Summary

Described in this paper is a simple and attractive method for establishing a phase stable reference whenever a high power broadcast station is available, provided only that the frequency tolerance and stability required in the system do not exceed those employed at the broadcast station.

References

1. Bernard D. Steinberg, "Measurement of the Spatial Correlation Function of an HF Wave After Passage through the Ionosphere," Valley Forge Research Center Quarterly Progress Report No. 15, November 1975.

2. Bernard D. Steinberg, "Design Approach for a High Resolution Microwave Imaging Radio Camera," Journal of the Franklin Institute, Volume 296, No. 6, pp. 415-432, December 1973.

3. Bernard D. Steinberg, "Microwave Imaging - the Radio Camera," Principles of Aperture and Array System Design, section 11.3, John Wiley and Sons, New York, 1976.

4. Raymond S. Berkowitz, "Large HF Array," VFRC QPR No. 8, March 1974.

5. The Dynasonde transmitter is operated by the Environmental Research Laboratory National Oceanic and Atmospheric Administration, U.S. Department of Commerce, Boulder, Colorado We are indebted to Dr. W. N. Hess, Director, for placing the facility at our disposal, and to Mr. John Wright for his technical assistance in operating this equipment.

6. Floyd M. Gardner, Phaselock Techniques, John Wiley and Sons, New York, 1966.

7. Earl N. Powers, "Coherent Array Module, PLL Design", VFRC QPR No. 5, May 1973.

8. S. Hassan Taheri, "Large HF Array," VFRC QPR No. 12, February 1975.

9. S. Hassan Taheri, "Large HF Array," VFRC QPR No. 13, May 1975.

10. S. Hassan Taheri, "Large HF Array," VFRC QPR No. 14, August 1975.

11. S. Hassan Taheri, "Receiver System Design for HF Spatial Correlation Experiments," VFRC QPR No. 11, November 1974.

12. Bernard D. Steinberg, "Tolerance Theory," Principles of Aperture and Array System Design, Chapter 13, John Wiley and Sons, New York, 1976.

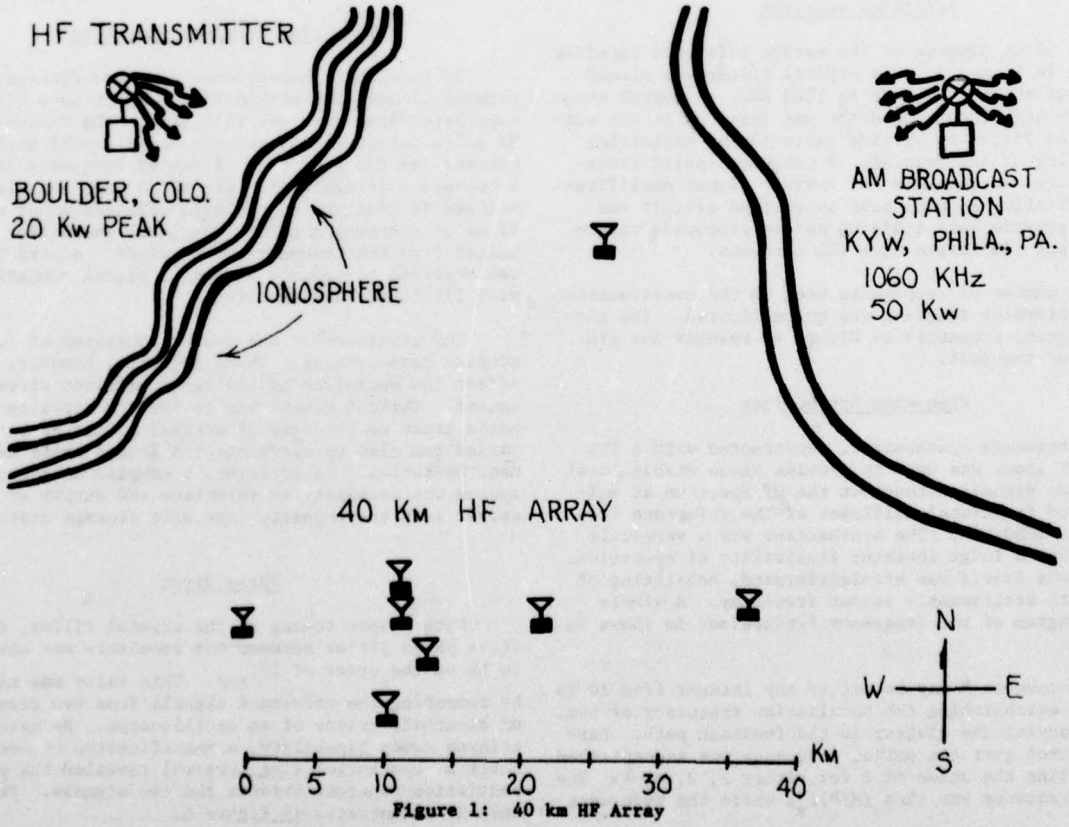

Figure 1: 40 km HF Array

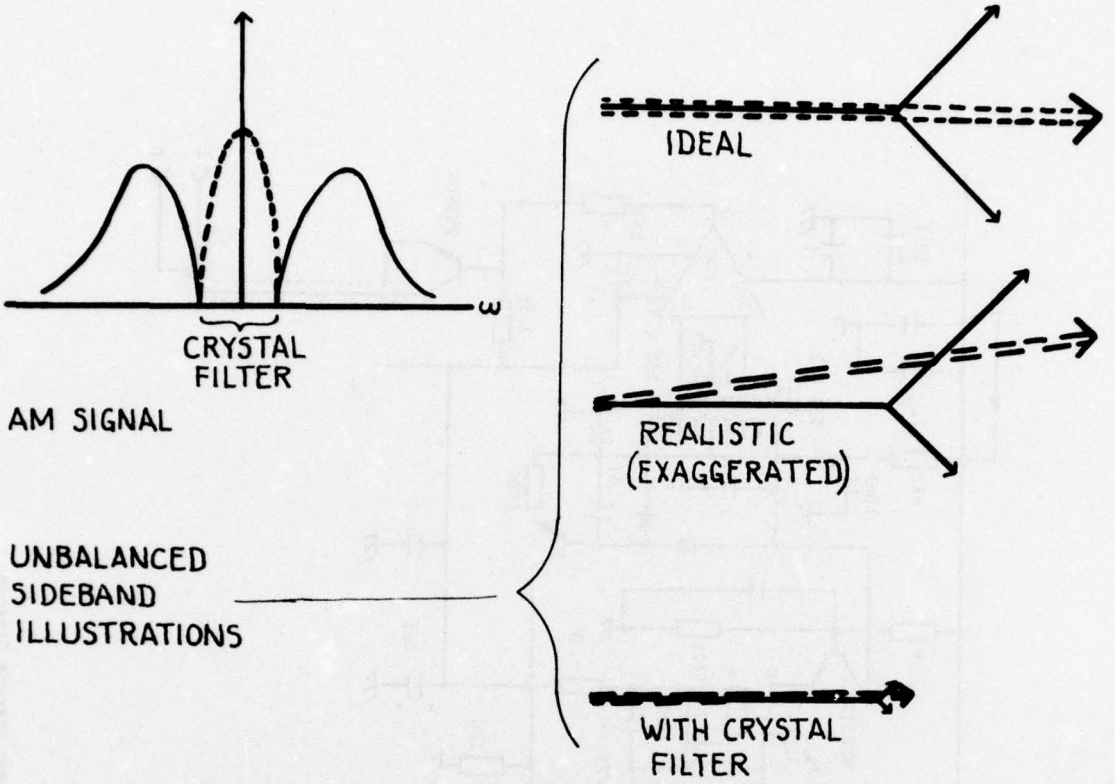

Figure 2: AM Broadcast Signal

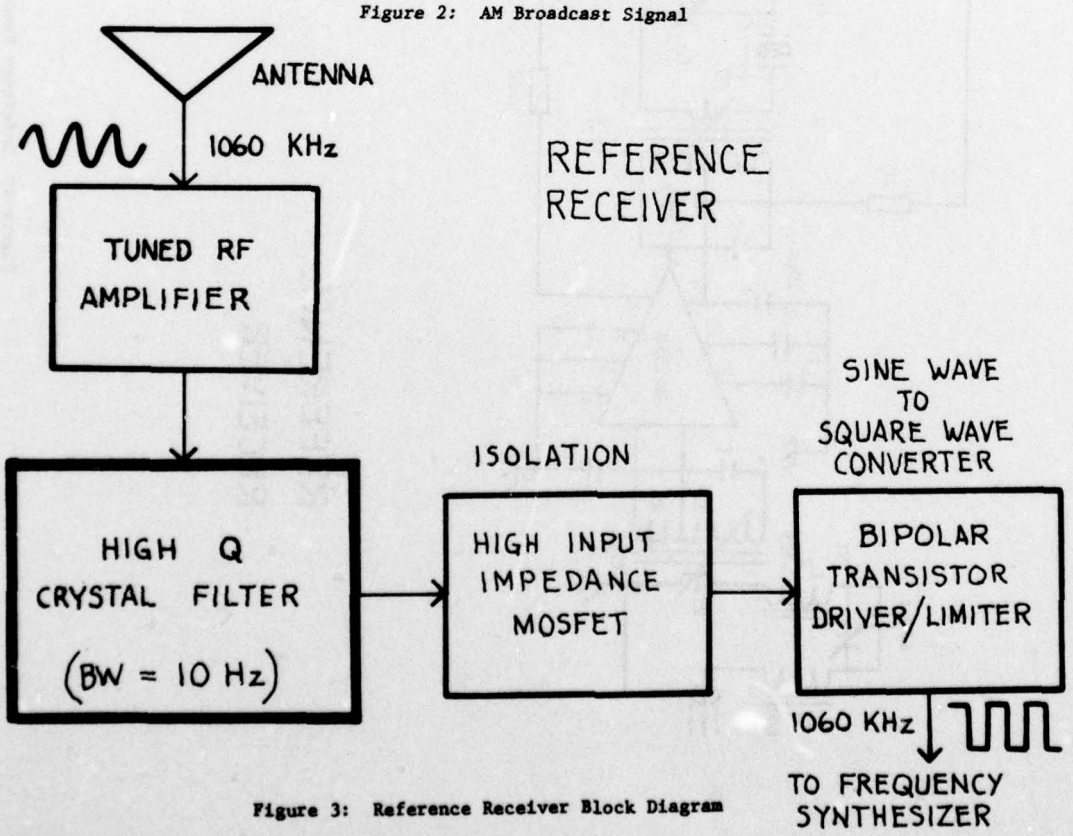

Figure 3: Reference Receiver Block Diagram

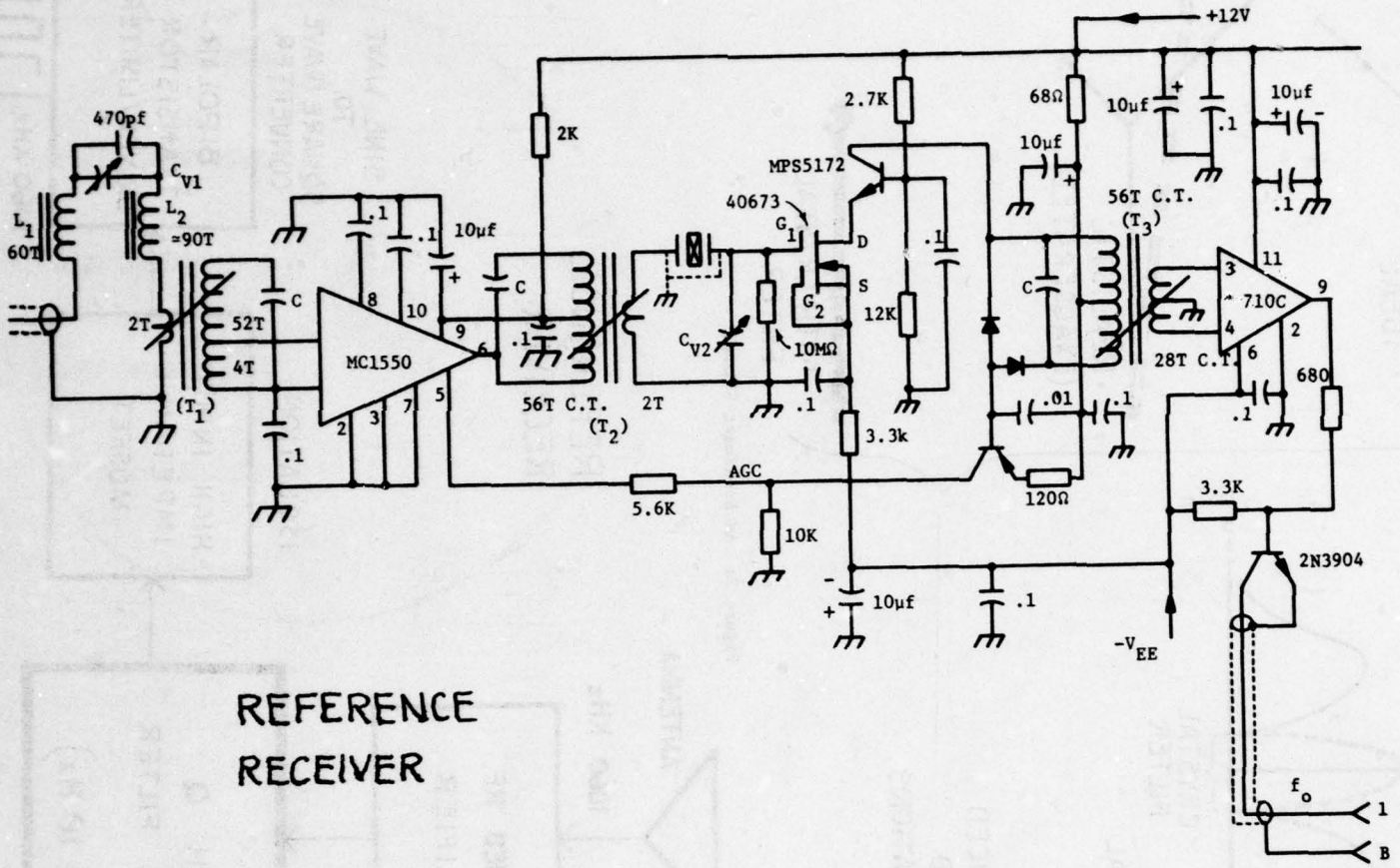

REFERENCE
RECEIVER

Figure 4: Reference Receiver Circuit Diagram

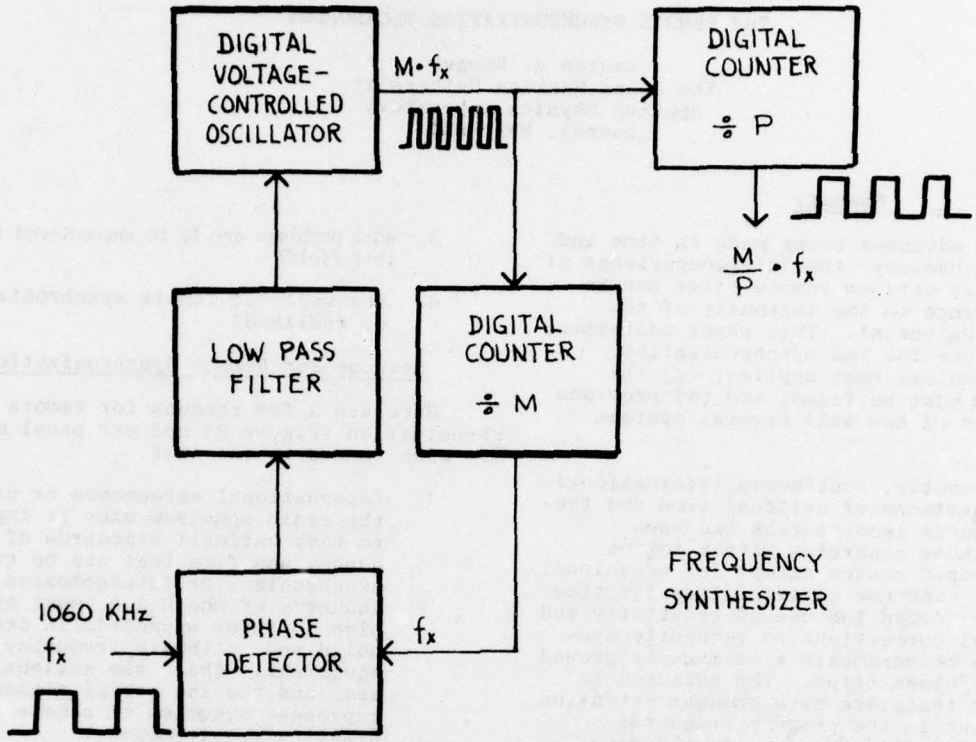

Figure 5: Frequency Synthesizer Block Diagram

MEASUREMENT OF PHASE ERROR IN REFERENCE SIGNAL

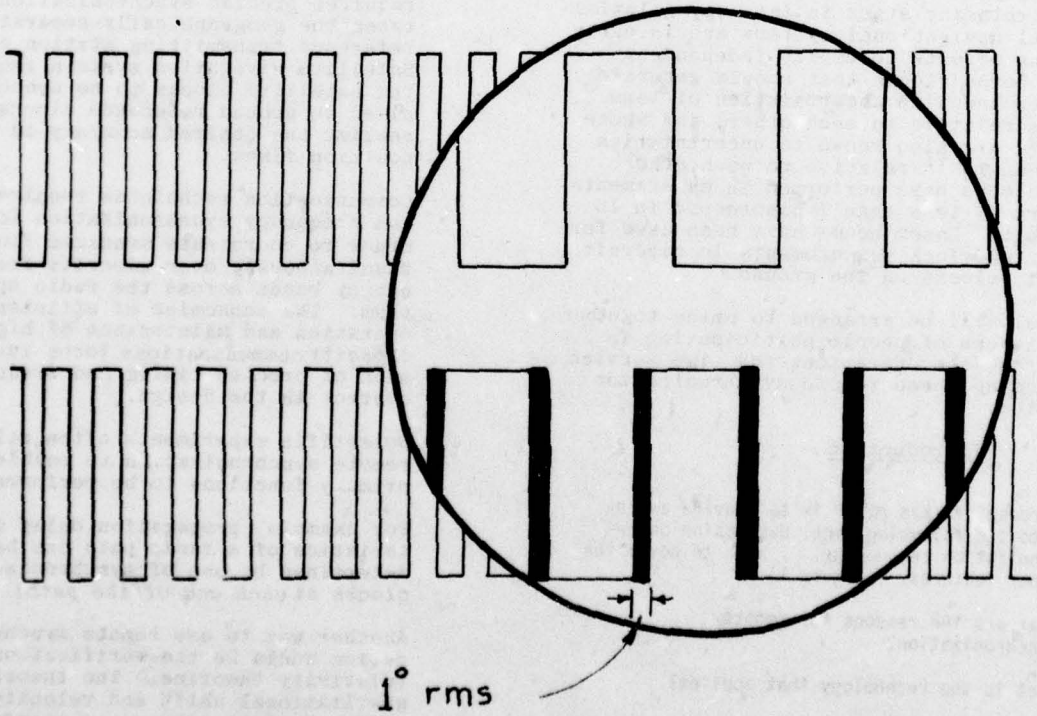

Figure 6: Measurement of Phase Error in the Reference Signal

THE REMOTE SYNCHRONIZATION TECHNOLOGY

Lauren J. Rueger
The Johns Hopkins University
Applied Physics Laboratory
Laurel, Maryland

Summary

With the advances being made in time and frequency technology, the intercomparisons of time scales at various remote sites has become a challenge to the ingenuity of the Modern Time Scientist. This paper addresses; (a) the reasons for the synchronization; (b) the technology that applies; (c) the problems that must be faced; and (d) provides some examples of how well several systems have worked.

Until recently, continuous international precise comparisons of national time and frequency standards laboratories had been limited to those countries within common range of Loran-C chains except for occasional clock trips. The use of satellites for time transfer has forced the use of relativity and gravitational corrections to reconcile synchronization measurements also made by ground and aircraft clock trips. The advances in precise time transfers have brought attention to limitations in the primary standards ability to independently provide the same frequency in different laboratories.

Frontiers in precision time synchronization now include centimeter surveying capabilities over thousands of kilometers by radio telescopes referencing to noise modulations of exploding stars in far away galaxies. Operational navigational systems are in early engineering efforts to employ independent satellite borne clocks that should generate time scales known to uncertainties of less than 10^{-7}s relative to each other, and whose frequencies are also known to uncertainties of less than 10^{-12} relative to each other. Airborne clocks have performed in experiments with errors of less than 1 nanosecond in 15 hour flights. Laser beams have been used for synchronizing clock measurements in aircraft with atomic clocks on the ground.

A panel will be arranged to bring together the experiences of people participating in the research, the operations and time service fields needing these remote synchronization capabilities.

Introduction

The purpose of this paper is to provide an introduction to the following panel discussion on remote synchronization technology. I wish to cover the following four features. (Figure 1)

1. What are the reasons for remote synchronization?
2. What is the technology that applies?
3. What problems are to be encountered in this field?
4. How well can remote synchronization be realized?

Reasons For Remote Synchronization

Here are a few reasons for remote synchronization (Figure 2) and our panel members may wish to add to the list.

1. International agreements on use of the radio spectrum make it important to have national standards of Frequency and Time that can be remotely synchronized or intercompared. The industry of the U.S.A. must synchronize to these standards in order to build and calibrate frequency related equipment. Thus, the national standards and the industrial standards represent examples of remote synchronization requirements.

2. Navigation techniques make use of synchronization in several ways. Navigation by stars requires clocks set to the time scales of the star tables. Loran-C and Omega navigation requires precise synchronization between the geographically-separated reference transmitting station clocks. Satellite navigation systems require the satellite clocks to be synchronized to ground reference clocks to realize the desired accuracy in position fixes.

3. Communication techniques require time and frequency synchronization in order to coordinate messages flowing simultaneously over discrete frequency bands across the radio spectrum. The economics of efficient operation and maintenance of high-capacity communications force inclusion of precise timing and frequency control in the design.

4. Scientific experiments often rely on remote synchronization to enable primary functions to be performed.

   For example, propagation delay characteristics of a radio path can be determined by use of synchronized clocks at each end of the path.

   Another way to use remote synchronization would be the verification of relativity theories. The theories of gravitational shift and velocity shift of atomic frequency standards

have been confirmed in an experiment with atomic standards carried in a high velocity airplane traveling at different altitudes. Another experiment of a similar nature is soon to be carried out to greater precision with an atomic standard in a high altitude rocket probe.

The tectonic plates in the earth's crust are believed to move a few centimeters per year; experiments are planned to measure this effect by making precise determinations of the distance between stations located on separate tectonic plates at times spaced a year or more apart. The experiment requires the stations to observe randomly modulated microwave signals from distant galaxies to synchronize the clocks at the two stations and to provide data to determine the separation distance.

Remote Synchronization Technology

In order to understand each other, a few basic definitions (Figure 3) relating to remote synchronization need to be established. First, let us consider what is meant by a Time Scale. A Time Scale is made up of two elements, a starting place (or date) and a rate of progression of events (or frequency). Frequency is the number of events per unit of time. A clock is a physical device for measuring a time scale. It must have a source of frequency, a means of accumulating the count of events, a means to be set to a specific date and usually has a display or output code indicating the accumulated time.

Next, we should consider how the time scales of two clocks can be compared to each other. In Figure 4, several situations are indicated for the frequency and time errors that accrue as a function of time when a clock is driven by a frequency that is equal to the reference clock frequency; if the frequency is higher than the reference clock frequency; if the frequency is lower than the reference clock frequency; if the frequency is changing from lower to higher; and finally, if the frequency is changing from higher to lower than the reference clock frequency. As you may have guessed, two independent clocks do not advance at the same rates when examined in detail at high resolution.

The equation of frequency for a working clock (Figure 5) as a function of time is: $f_t = f_o + af_R t$. where f_t is the frequency at time, t; f_o is the initial frequency; f_R is the reference frequency; and a is the rate of drift per unit time, $\frac{\Delta f}{f_R \Delta t}$.

The time error equation as a function of time is: $E_t = E_o + \frac{f_o - f_R}{f_R} t + \frac{at^2}{2}$ where E_t is the time error at time, t; E_o is the initial time error; $\frac{f_o - f_R}{f_R}$ is the initial offset in frequency; and a is as defined above.

These equations are assuming a rather simple model for the clock behavior - a linear drift in frequency with time. For precision standards this turns out to be actually very good because the higher order terms seem to be influenced by random effects that do not fit a simple model. It has been observed with quality crystal oscillators, that the linear term dominates the frequency equation and the quadratic coefficient of frequency has a magnitude about equal to its uncertainty. I introduced these equations only to show how a clock's time or accumulated time quickly becomes a complicated function.

When two clocks are compared, it is convenient to express the errors in one relative to the other in terms of either $\frac{\Delta t}{t}$ or $\frac{\Delta f}{f}$. Figure 6 shows how an offset error accumulates time errors over a range of .001 microsecond to 1000 microseconds for offsets ranging from 10^{-9} to 10^{-14} over periods of 1 hour to 100 days. This table helps one to determine how frequent recalibration is required given a frequency offset and an allowable time error.

A test setup suitable for making laboratory measurements of $\frac{\Delta f}{f}$ directly on a strip chart is shown in Figure 7. The example indicates a beat note of 1 Hz whose period is measured to 1 microsecond resolution to provide 10^{-12} resolution in frequency. Full scale on the strip chart will depend on which digits of the counter are selected for display on the chart; ranging from 10^{-5} to 10^{-12} full scale.

Remote synchronization implies the direct comparison of two time scales in instruments at some point or points in the system (Figure 8). The comparisons can be made either by carrying clocks from one site to the other, or by sending one time scale signal to the other site, or by measuring at each site a time signal that is propagated from a third source.

1. In the portable clock transfer method, the portable clock is set at the reference site. It is taken to the remote site where the remote clock is set to the portable unit. The portable clock is then returned to the original site and the portable clock closure error is determined; the closure error is the net time lost or gained relative to the reference clock during the round trip. The error is distributed to the date of the setting of the remote clock and the remote clock so corrected either physically or by bookkeeping on the corrections.

2. The remote clock can sometimes be set to signals derived directly from the reference clock received over some propagation medium. If the propagation medium is known and its delays determinable, these delays can be corrected in the remote clock. If the delays are not known, the reference clock can be slaved to the received signal, but then it suffers the consequences of propagation variations.

3. A third party signal is a covisible signal against which both the reference clock and remote clock can be measured. The reference and remote clocks are synchronized when the difference in the propagation paths between the third party signal and the separate clocks is corrected.

Problems in Remote Synchronization

Problems in synchronization start with the clocks. There are two major errors to be considered in clocks. (Figure 9) They are the accuracy of the frequency source and the accuracy of setting the reference date.

There are at least six synchronization problem areas to be considered. (Figure 10)

1. Maintenance of accurate frequency in the remote clock
2. Provision of accurate time transfer to the remote clock
3. Determination of propagation path delays between the reference clock and the remote clock
4. Maximization of the frequency calibration interval
5. Determination of the effects of noise
6. Determination of effects of environmental changes

The first depends on the kind of frequency standard that can be provided and its susceptibility to changes due to the aging or environmental effects. The time transfer accuracy is instrumentation sensitive. The propagation path delays are in many cases subject to variations which are not easily corrected. The interval between calibrations is longer for more stable standards, is longer when wide tolerance in time error is permitted, is longer when resets are more accurate. The economics of remote site synchronization is strongly driven by the recalibration interval. The frequency standard at the remote site must be good enough to hold acceptably low clock errors between recalibrations. Remote site instrumentation can be quite simple if portable clock transfers are made, however, these trips may be so expensive that more complex receiver instrumentation may be justified. As the accuracy to be maintained at the remote site becomes more critical, recalibrations can become so frequent that they become continuous - this is the case in the Very Long Baseline Interferometry work.

The effects of noise on the remote site synchronization must be considered. In highly industrialized areas, the Radio Frequency Interference precludes the use of many convenient propagation links for synchronization. Likewise, there are regions on the earth where noise domination of the radio spectrum limits the methods of synchronization available.

The effects of environment changes on remote site standards can be severe. Frequency standards are usually susceptible to everything you can imagine; to vibration, magnetic fields, temperature extremes, voltage variations, and various forms of nuclear radiation.

Examples of Performance Realized

Presented herein, are some examples of what is being done presently in remote synchronization. These are not intended to be comprehensive, but are intended to give the impression that there are many applications.

International Standards are compared at about 10^{-13} in frequency; 100 nanoseconds in time.

Navigation by Loran-C has stations synchronized to better than 2μ sec. of UTC; slave stations hold to substantially better than 1 microsecond.

Greenwich time ball is dropped within 0.1 second of noon for the ships in the TAMES river to set their chronometers on their way out to sea.

The Transit navigation satellites maintain time to within ±50 Microsec. of UTC and ground control stations are synchronized to each other to offsets known to 1.5 microsec. The satellite frequencies are determined to $2X10^{-11}$. Experimental time transfers have been made over short local ranges using ground to satellite links to resolutions of 10 nanoseconds. Time transfers spanning one orbital period have been made to 45 nanosecond resolutions.

The Timation III satellite has been used for international time transfers as low as 100 nanoseconds; USA to Australia, Japan and England.

Experiments with ATS-1 have provided ±11 nanosecond time transfers across the USA.

Portable clock transfers over 20 mile distances have provided less than 1 nanosecond errors; over 800 miles distances, they have provided ±27 nanosecond errors; around the world, they have provided about 50 nanosecond errors.

VLBI experiments have realized time transfer resolutions of about 0.15 nanoseconds in selected cases.

Laser beam time transfers have been made over 10 to 20 mile links to about 0.1 nanosecond.

Introduction of Panel Members

1. Mr. L. J. Rueger, The Johns Hopkins University, Applied Physics Laboratory. Chairman, Project Scientist for Navy Navigation Satellite System

2. Mr. David Allan, National Bureau of Standards, Time/Frequency Section National Standards of Frequency

3. Dr. Carroll Alley, University of Maryland
Relativity Experiments

4. Dr. Thomas Clark, Goddard Space Flight Center/NASA
VLBI Experiments

5. CDR William Huston, U.S. Navy, SAMSO Space and Missile System Organization
Global Positioning System - System Timing

6. LCDR William Jones, U.S. Coast Guard
Loran-C Systems

7. Dr. Burton R. Saltzberg, Bell Laboratories
Digital Communications

8. Dr. A. J. Van Dierendonck, General Dynamics Corporation
Global Positioning System - Ground Station Designer

9. Dr. G. M. R. Winkler, U.S. Naval Observatory, Time Service Division
DoD Time Services

Acknowledgements

The material for this report was obtained from published literature and from papers presented at open meetings. Published material included proceedings of the Frequency Control Symposiums, proceedings of the Precision Time and Time Interval Conferences, bulletins from the U.S. Naval Observatory, bulletins and monographs from the U.S. National Bureau of Standards, application technical notes from the Hewlett Packard Company, and reports prepared for and by NASA on timekeeping investigations.

Bibliography

1. H. Hellwig,"Atomic Frequency Standards, A Survey" p. 315 Proc. 28th Annual Symposium on Frequency Control, (1974)

2. Time and Frequency: Theory and Fundamentals; NBS Monograph 140 (1974) Chapters 1, 4, 5, 10 & 11.

3. Volume VII Standard Frequencies and Time Signals (Study Group 7), International Radio Consultive Committee (CCIR), XIIIth Plenary Assembly, Geneva, 1974.

4. R. J. Taylor, "Satellite to Ground Experiments", p. 384, Proc. 28th Annual Symposium on Frequency Control (1974)

5. Series 17 Bulletins, U. S. Naval Observatory

6. H. M. Smith, et.al., "International Time Transfer Between USNO and RGO via NTS-1 Satellite", p. 341, Proc. of 7th Annual Precision Time and Time Interval (PTTI) Applications and Planning Meeting, Dec. 2-4, 1975

7. A. R. Chi and E. Byron, "A Two-Way Time Transfer Experiment Using A Synchronous Satellite", p. 357, Proc. of 7th PTTI (1975)

8. K. Putkovich, "High Precision Time Transfer Methods", p. 323 Proc. of 7th PTTI (1975)

9. W. J. Klepczynski, "High Precision Time Transfers in the Field", p. 285, Proc. of 7th PTTI (1975)

10. I. I. Shapiro, "VLBI: Past, Present and Future" paper given at 7th PTTI (1975)

11. P. F. MacDoran, et.al., "Radio Interferometric Geodesy Using A Rubidium Frequency System", p. 439, Proc. of 7th PTTI (1975)

12. C. Alley, "Subnanosec - Laser - Pulse Time Transfer to an Aircraft to Measure the General Relativity Altitude Effects on Atomic Clock Rates", paper given at, 7th PTTI (1975)

13. Application Note 52-2, Nov. 1975, Hewlett-Packard Company

14. E. F. Osborne, "Global Timing Systems of Nanosecond Accuracy Using Satellite References", TG-1086, Oct. 1969, Technical Report of The Johns Hopkins University, Applied Physics Laboratory.

POINTS TO BE COVERED

1. **REASONS FOR REMOTE SYNCHRONIZATION**
2. **TECHNOLOGY THAT APPLIES**
3. **PROBLEMS IN REMOTE SYNCHRONIZATION**
4. **EXAMPLES OF PERFORMANCE REALIZED**

FIGURE 1

REASONS FOR REMOTE SYNCHRONIZATION

1. NATIONAL STANDARDS OF TIME/FREQUENCY COMPARED/ DISSEMINATION
2. NAVIGATION
   - USER CLOCKS
   - TRANSMITTER SYNCHRONIZATION; LORAN-C, OMEGA
   - SATELLITES IN FREQ. OR TIME SYNCH.
3. COMMUNICATIONS
   - RADIO SPECTRUM ALLOCATIONS
   - HIGH DATA RATE SYSTEMS
4. SCIENTIFIC EXPERIMENTS
   - MEASURE MEDIA PROPAGATION CHARACTERISTICS
   - CONFIRM THEORY OF GRAVITATIONAL AND VELOCITY SHIFT OF ATOMIC FREQ. STDS.
   - SYNCH ON RANDOM MODULATION FROM PULSARS

FIGURE 2

BASIC DEFINITIONS

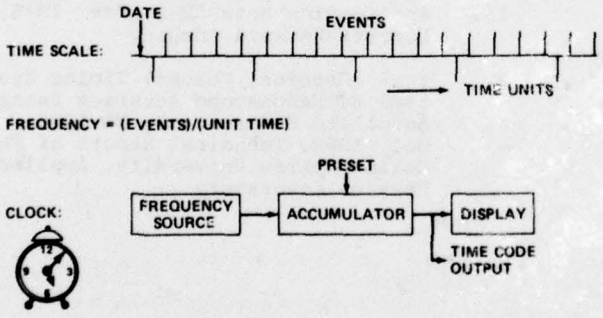

FIGURE 3

TIME-FREQUENCY RELATIONS OF 2 CLOCKS

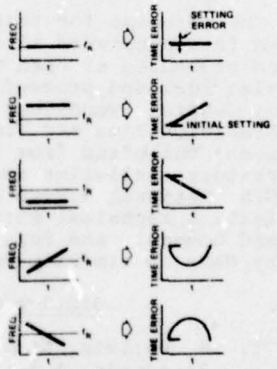

FIGURE 4

FREQUENCY AND TIME ERROR EQUATIONS

FREQUENCY EQUATION: $f_t = f_o + a\, f_R\, t$

f_t = frequency at time t

f_o = initial frequency

f_R = Reference frequency

a = rate of drift, $\left(\frac{\Delta f}{f_R \Delta t}\right)$

TIME ERROR EQUATION: $E_t = E_o + \left[\frac{f_o - f_R}{f_R}\right] t + \frac{a\, t^2}{2}$

E_t = time error at time t

E_o = initial error

$\left[\frac{f_o - f_R}{f_R}\right]$ = initial offset freq.

FIGURE 5

CLOCK TIME ERROR VERSUS FREQUENCY OFFSET

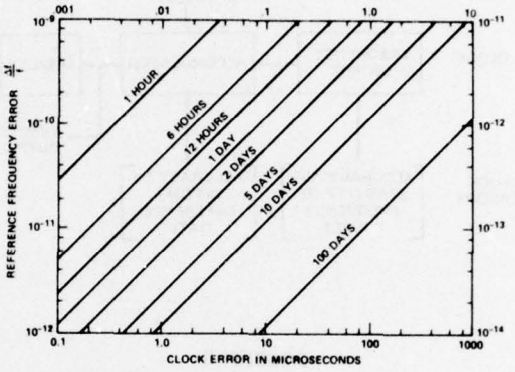

FIGURE 6

SET UP TO MEASURE $\frac{f}{f}$ DIRECTLY

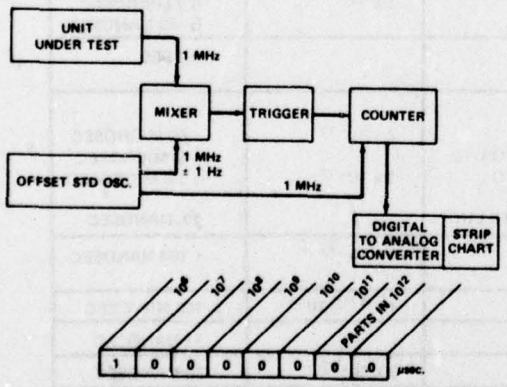

FIGURE 7

REMOTE SYNCHRONIZATION TECHNIQUES

1. PORTABLE CLOCK
   - SET TO REFERENCE CLOCK
   - TRAVELS TO REMOTE SITE
   - REMOTE SITE SET TO PORTABLE CLOCK
   - TRAVELS TO REFERENCE SITE
   - MEASURE PORTABLE CLOCK ERROR
   - PROPORTION MEASURED CLOCK ERROR TO DATE OF REMOTE SITE SETTING AND CORRECT REMOTE SITE CLOCK
2. DIRECT RECEPTION AT REMOTE SITE OF SIGNAL FROM REFERENCE CLOCK
   - CORRECT FOR PROPAGATION DELAYS ALONG PATH
   - SLAVE TO RECEIVED SIGNAL
3. COMMON RECEPTION OF 3rd PARTY SIGNAL
   - CORRECT FOR DIFFERENCE IN PROPAGATION PATHS (3rd PARTY-TO-REFERENCE) AND (3rd PARTY TO REMOTE SITE)

FIGURE 8

MAJOR CLOCK ERRORS

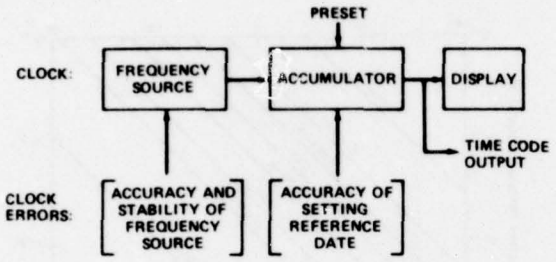

FIGURE 9

SYNCHRONIZATION PROBLEM AREAS

- MAINTENANCE OF ACCURATE FREQUENCY
- PROVISION OF ACCURATE TIME TRANSFER
- DETERMINATION OF PROPAGATION PATH DELAYS
- MAXIMIZATION OF FREQUENCY CALIBRATION INVERVAL
- DETERMINATION OF EFFECTS OF NOISE
- DETERMINATION OF EFFECTS OF ENVIRONMENTAL CHANGES

FIGURE 10

PERFORMANCE OBTAINED FOR REMOTE SYNCHRONIZATION

	MEASURED FREQUENCY	TIME
INTERNATIONAL STANDARDS	$10^{-13} - 10^{-14}$	100 NANOSEC
LORAN-C TRANSMITTERS		
– RELATIVE TO UTC	10^{-12}	2.0 MICROSEC
– INTERNAL TO CHAIN		0.2 MICROSEC
– SHORT TERM STABILITY		5–40 NANOSEC
GREENWICH ROYAL OBSERVATORY TIME BALL DROP TO UTC		0.1 SEC
TRANSIT NAVIGATION SYSTEM		
– OPERATIONAL SATELLITES RELATIVE TO UTC	2×10^{-11}	± 50 MICROSEC
– OPERATIONAL GROUND STATIONS RELATIVE TO UTC		± 5. MICROSEC
– OPERATIONAL GROUND STATIONS RELATIVE TO EACH OTHER	5×10^{-12}	± 1.5 MICROSEC
– EXPERIMENTAL TIME TRANSFERS BY SATELLITE LINK		10. NANOSEC
TIMATION – III INTERNATIONAL TIME TRANSFERS BY SATELLITE LINK	5×10^{-12}	± 100 NANOSEC
TWO-WAY TIME TRANSFERS BY DCA SATELLITES	$10^{-12} - 10^{-14}$	100 NANOSEC
NASA ATS-1 TIME TRANSFER ACROSS USA		11 NANOSEC
TV-LINE 10 TIME TRANSFER UP TO 20 MILES	3×10^{-13}	30 NANOSEC
PORTABLE ATOMIC CLOCK TIME TRANSFERS		
– 20 MILE TRIPS	10^{-13}	1 NANOSEC
– 800 MILE TRIPS	10^{-12}	± 27 NANOSEC
– AROUND THE WORLD	2×10^{-13}	50 NANOSEC
VERY LONG BASELINE INTERFEROMETER TIME TRANSFERS	5×10^{-14}	0.15 NANOSEC
LASER BEAM TIME TRANSFERS OVER 10 TO 20 MILES	5×10^{-14}	0.1 NANOSEC

FIGURE 11

VELOCITY DISTRIBUTION MEASUREMENTS OF CESIUM BEAM TUBES

David A. Howe

Frequency & Time Standards Section
National Bureau of Standards
Boulder, Colorado 80302

Abstract

This paper presents the current collection of Cs beam tube velocity distributions using an automated measurement system. The pulse technique of atomic velocity selection is the method incorporated in the system. Measurements were made on tubes used at the U.S. Naval Observatory and at the NBS Boulder Laboratories. The data reveal that analysis of beam optics is directly possible to a high degree. Frequency stability $\sigma_y(\tau)$ is shown for some of the standards with tubes involved in the tests, and correlations between beam distribution features and $\sigma_y(\tau)$ are discussed. Paricular attention is put on the differences in characteristics among tubes at nominal and high temperatures, old versus new tubes, and single beam compared to multi-beam tubes.

Introduction

About five years ago, a method was realized of directly measuring a Cs beam tube atomic velocity distribution by taking advantage of the dual-interaction cavity arrangement which is commonly used [1]. The method calls for the R.F. excitation signal to enter the tube's microwave cavity in precisely timed bursts. The tube will yield a Ramsey spectrum only for those atoms traveling at a velocity such that it is properly excited by both interaction windows. An analogy can be drawn between this method and a mechanical chopper method as shown in Fig. 1. A properly excited atom will have velocity

$$V_k = \frac{L}{nT_k}$$

where L = length between interaction regions,
T_k = kth period of R.F. bursts
and n = integer (1, 2, 3...)

In the commonly encountered case where tube optics limit the high and low velocities, one can assume n = 1 or 2. Furthermore one can unambiguously select velocities with proper synchronous detection of the Ramsey pattern and proper choice of burst width and power [2]. This measurement technique is known as the pulsed method of velocity measurement.

Knowledge of the atomic velocity distribution yields information about the design of the optics in a beam tube. One can accurately judge the effects of mechanical adjustments or environmental influences by noting changes in the distribution or uncommon characteristics. Moreover, one can calculate the frequency offset of the device due to the second-order Doppler effect.

This paper presents velocity distribution measurements which have been made to date. Except for NBS-4 and NBS-6 (laboratory standards at the National Bureau of Standards), all of the distributions were from commercial Cs tubes.

Procedure

A computer-assisted system was built for acquiring velocity distributions virtually automatically. The system provides an R.F. microwave signal to the Cs tube's cavity in programmed burst lengths and over a range of repetition rates. The R.F. power level is also programmed into the system. Besides the cavity connection, the signal from the tube's detector is connected to the system. With the tube operating in the mono-velocity mode, the intensity of the Ramsey spectrum is determined by square-wave modulation between the Ramsey center peak and the first adjacent valley frequencies. A synchronous (or lock-in) demodulator is used to establish the amplitude and the result is recorded on a reel-to-reel tape storage peripheral.

After the system has gathered data over a prescribed range of mono-velocities, each value at V_k is multiplied by T_k (the corresponding k^{th} pulse period) in order to get $\rho(v)$. This multiplication equalizes the data points since long pulse periods make the tube operate with a smaller duty cycle than short pulse periods; therefore, the Ramsey amplitude will necessarily be smaller. After this, $\rho(v)$ is normalized to unity, and one obtains a plot similar to that shown in Fig. 2.

Fig. 3 has plots comparing a typical beam tube distribution as measured at the detector with the kind of distribution one might see out of the oven. In most beam tubes, the oven operates at approximately 90° C. The corresponding most probable velocity is about 2.4×10^4 cm/s. The fact that many tubes show contours in their respective $\rho(v)$ which are substantially different indicates that the resultant velocity distribution is determined at essentially all points by the optics configuration [3].

Data

To date, 17 commercial Cs tubes have been measured using the velocity acquisition system. It takes about one hour to prepare the tube and system for a measurement and about another hour to collect a 40-point plot of the distribution. Most of the tubes were from standards used by the U.S. Naval Observatory, Time Services Division. Many others were from the NBS Boulder Laboratory. In each plot, the R.F. microwave pulse width (τ) and power (P) above optimum power in C.W. mode (P_o) are listed.

The distributions of the NBS primary Cs standards, NBS-4 and NBS-6, were measured and the results are shown in Fig. 4. The plots denoted by "measured $\rho_x(v)$" were those taken using the pulse technique. Also shown on these graphs are velocity distributions which were computed from the Ramsey spectra at different R.F. microwave power settings [4]. Agreement between the measurement of $\rho(v)$ using the pulse technique and the computed distribution based on Ramsey spectra is within 5%.

NBS-4 (Fig. 4) has a length between cavity interaction regions of about 0.5 m and uses off-axis geometry. One notes considerable attenuation of velocities around 2.0×10^4 cm/s. This is principally due to a vane centered in each cavity window, hence the center of the beam cross-section. The addition of the vanes tends to make the tube act like a two-beam configuration.

NBS-6 (Fig. 5) is a long device having a length between interaction regions of 3.74 m. On-axis geometry is used and the positions of detector and oven can be changed along the length and laterally to the beam. Also, beam stops can be positioned along the beam. Fig. 5

shows a velocity distribution taken from NBS-6 for a particular optics configuration. A plot of the distribution based on Ramsey spectra is again included.

The next set of eight figures are distributions from commercial tubes. Figures 6, 9, 10, and 12 are from single-beam tubes. The others in this set employ multiple-beam configurations, and one sees a trend toward more than one peak feature in these plots. This is especially noticeable in Fig. 8. With the tube represented in Fig. 8, two distributions were measured; one is the tube after one hour of warm-up and the other one day warm-up. All of these tubes were in standards showing a history of good stability performance, and the tubes were measured under factory-specified conditions, i.e., normal oven temperature, normal C-field, etc.

Fig. 14 is the velocity distribution of a malfunctioning single-beam tube. The standard was being repaired at the time of the measurement and had been subject to an excessive mechanical blow of some sort. The shock caused the standard to fail to lock properly. The velocity distribution result shows a noticeable departure from the distributions which one commonly sees with this particular tube. One notes considerable broadening around the peak as well as less high-velocity attenuation.

The next set of four figures are distributions from properly operating commercial tubes. All of these tubes are multiple-beam devices except for the one plotted in Fig. 17, a single-beam device. The tube of Fig. 15 shows a pronounced double-peak characteristic again as a result of the superposition of distributions. The slight scattering of points indicated in Fig. 17 was due somewhat to the lower-than-normal signal out of the tube's detector. It was necessary to average the synchronous detector output at each point over a longer time in order to get a reasonably continuous curve.

The next two tubes (Figs. 19 and 20) were older commercial devices having a continuously operating lifetime of about 5 years. They had shown good service records, and long-term stability approached 2×10^{-13} $[\sigma_y(\tau)]$. No obvious abnormalties are evident in the distributions.

One powerful use of the velocity measurement system is in characterizing the ageing process in tubes. With measurements taken at regular intervals over the life of a tube, one can observe changes in the beam as a diagnostic aid. The system will be used again to remeasure many of the tubes measured to see what ageing effects take place.

The last two tubes (Figs. 21 and 22) were operated at an oven temperature which was 12° higher than normally specified. This was done in order to obtain greater signal-to-noise ratio out of the detector so that short-term stability of the standards could be improved. Both were multiple-beam tubes and no radical departures from a normal distribution exist. With the tube of Fig. 22, a velocity distribution was measured with the oven at its normal operating temperature. The fact that one sees a slight increase in the high and low velocity components at a higher oven temperature indicates that the total beam cross-section has increased.

It is instructive to compare the velocity distribution measurements to stability measurements for a given tube operating as a frequency standard. Generally speaking, one can site types of undesirable effects in the beam trajectory as a function of time. The detected signal is dependent upon the mechanical stability of the oven, state-selector magnets, mass-spectrometer and electron multiplier (if any), and ionizer. Furthermore, there is sensitivity to fluctuations in the Cs emission characteristics of the oven. We shall catagorize these types of effects as "beam noise" and will ignore the detected signal sensitivity to R.F. microwave power and power supply fluctuations although they do affect the detected signal.

Velocity distribution measurements using the pulse technique enable direct monitoring of beam noise in a Cs tube to some degree. Beam noise would give rise to fluctuations in the distribution as a function of time. The measurement system computes an average distribution over about a 100 second period per data point. Assuming gaussian noise, the measurement estimate per point should improve with averaging time. Thus, the plots of distributions do not disclose information about beam noise as the plots are presented in this manuscript. However, if one were to make successive measurements over a given averaging time and noted the extent of fluctuations in the distribution from measurement to measurement, it would be possible to substantiate whether a possible lack of stability of the standard at that averaging time was traceable to beam noise.

Fig. 23 shows four plots of $\sigma_y(\tau)$ using the Allan variance of the standards containing the tubes shown in Figs. 9, 11, 16, and 17. The standards were measured against the U.S. Naval Observatory time scale (A.1, mean). Correlation exists between the approximate flicker-floor value and the width around the peak of the velocity distribution for the corresponding tube; wider peaks have higher flicker levels. The width generally increases as the beam cross-section increases. One can make the argument that tubes having optics designed for narrow beam widths (relative to the length between interaction regions) tend to make the center frequency less sensitive to beam noise since all non-uniformities across the width are lowered as the cross-section decreases[5]. Fig. 24 is a plot of $\sigma_y(\tau)$ between NBS-4 and the tube of Fig. 7 which was in a commercial standard showing particularly good stability. The tube was a multiple-beam device.

It should be noted that the width of the distribution around the peak may be an indicator of frequency sensitivity to beam noise. If, however, the beam noise itself is very low, then the beam cross-section may be made large without a sacrifice in stability.

Conclusions

The large number of Cs beam tubes that exists today makes it desirable to look at methods of testing and evaluation. Direct measurement of the velocity distribution is possible for all tubes with Ramsey cavities - and is a helpful diagnostic in characterizing the tube independent of other things. Velocity distributions have been shown of 17 commercial Cs tubes, NBS-4 and NBS-6. The plots are entirely governed by beam optics, and correlation did exist between the width of the distribution around the peak and long-term stability of the frequency standards containing the tube. Subsequent measurements will be made of some of the tubes again to look at ageing effects and other possible correlations.

Acknowledgment

Special thanks to Dr. Gernot Winkler and his staff of the U.S. Naval Observatory for their assistance in many aspects of this work.

References

[1] H. Hellwig, S. Jarvis, Jr., D.J. Glaze, D. Halford, and H.E. Bell, Proc. 27th Annual Symposium on Frequency Control, Fort Monmouth, NJ, 1973.

[2] D.A. Howe, H.E. Bell, and H. Hellwig, Proc. 28th Annual Symposium on Frequency Control, Fort Monmouth, NJ, 1974.

[3] N.F. Ramsey, Molecular Beams, Oxford University Press, 1956.

[4] S. Jarvis, Jr., Metrologia, Vol. 10, pp. 87-98, 1974.

[5] S. Jarvis, Jr., NBS Technical Note 660, 1975.

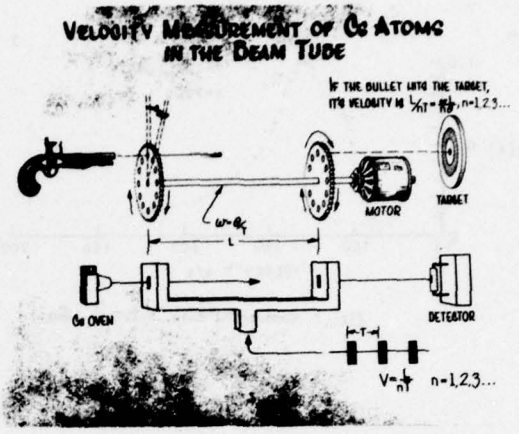

Fig. 1 A mono-velocity mode of operation can be established for a Cs beam tube by making the R.F. excitation signal appear in bursts of prescribed period and width.

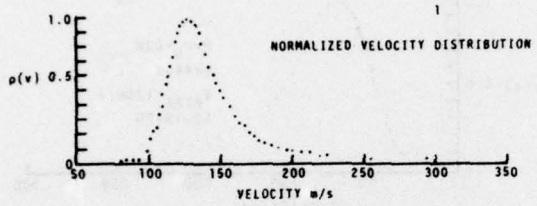

Fig. 2 The Ramsey intensity is measured for a series of selected atomic velocities. The results are normalized to unity.

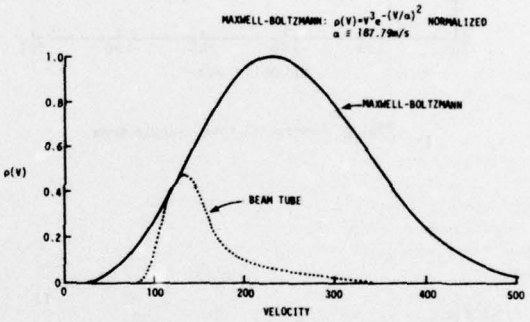

Fig. 3 By comparing a typical beam tube distribution as measured at the detector with the kind of distribution one might see out of the oven, it is evident the beam optics play a major role in determining the contour of the tube's distribution.

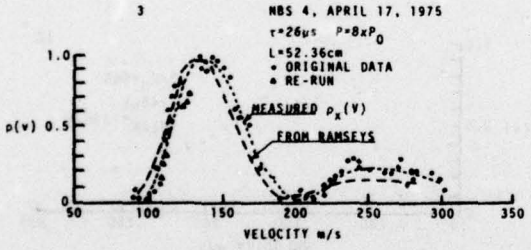

Fig. 4 NBS-4 primary cesium standard with off-axis geometry has a distinct attenuation of atoms at 2 x 10^5 cm/s because of a vane in each R.F. interaction region.

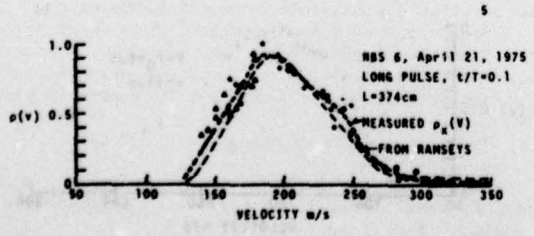

Fig. 5 NBS-6 primary cesium standard incorporates on-axis geometry. A variety of distributions are possible with NBS-6 due to the movable oven and detector.

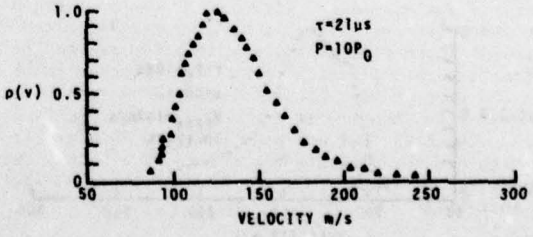

Fig. 6 Commercial tube, single-beam.

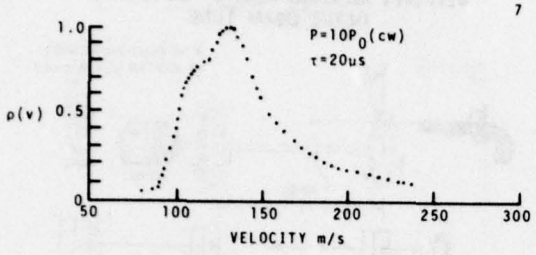

Fig. 7 Commercial tube, multiple-beam.

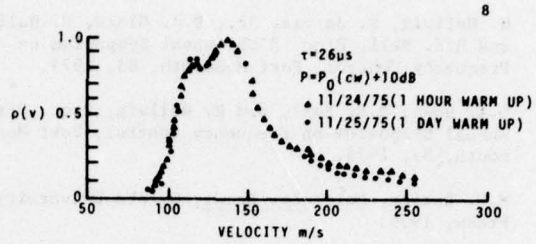

Fig. 8 Commercial tube, multiple-beam.

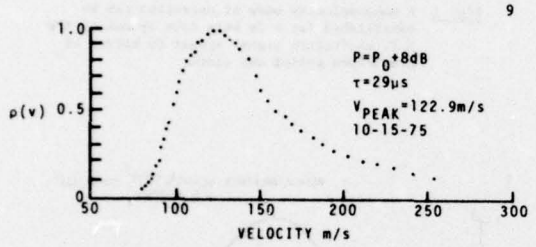

Fig. 9 Commercial tube, single-beam.

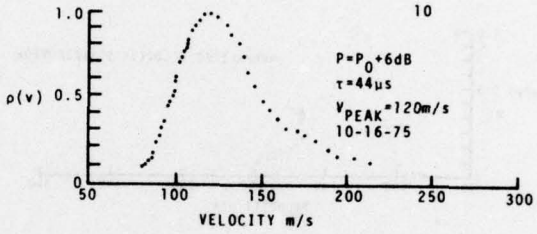

Fig. 10 Commercial tube, single-beam.

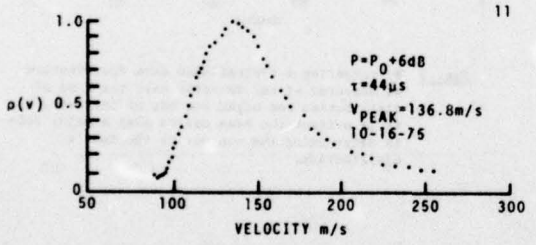

Fig. 11 Commercial tube, multiple-beam.

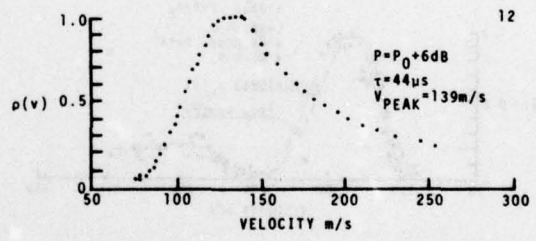

Fig. 12 Commercial tube, single-beam.

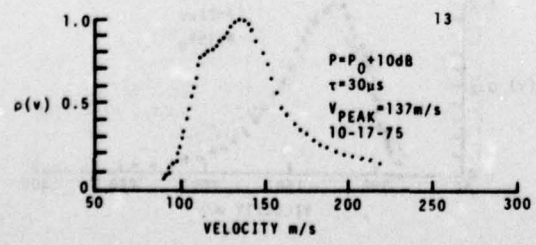

Fig. 13 Commercial tube, multiple-beam.

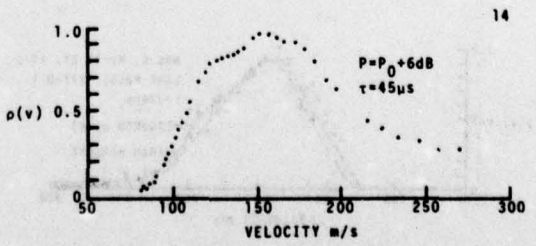

Fig. 14 Malfunctioning commercial tube, single-beam.

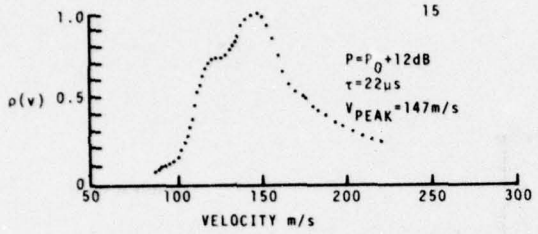

Fig. 15 Commercial tube, multiple-beam.

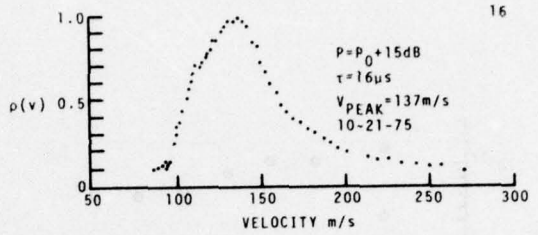

Fig. 16 Commercial tube, multiple-beam.

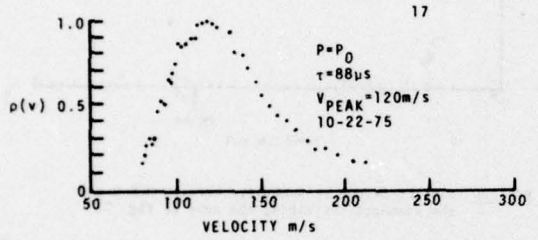

Fig. 17 Commercial tube, single-beam.

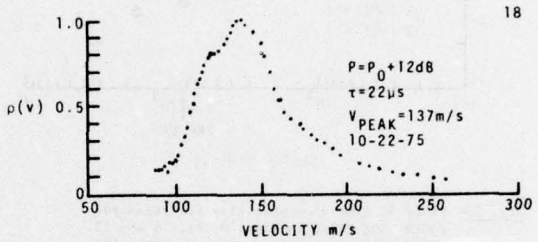

Fig. 18 Commercial tube, multiple-beam.

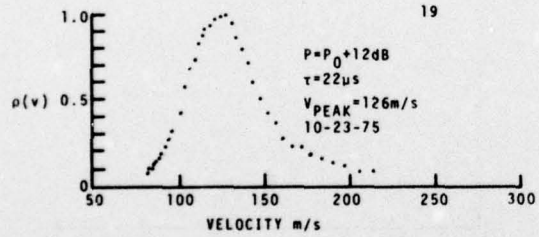

Fig. 19 Commercial tube, single-beam, five year life.

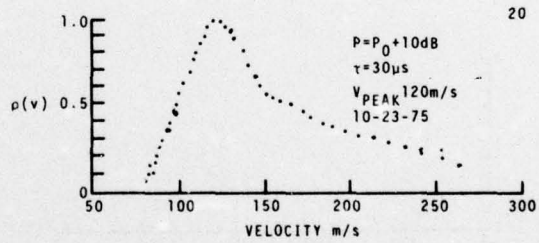

Fig. 20 Commercial tube, single-beam, five year life.

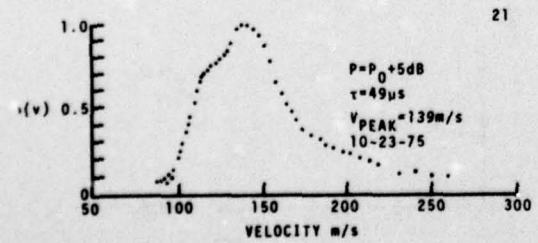

Fig. 21 Commercial tube, multiple-tube, high oven temperature.

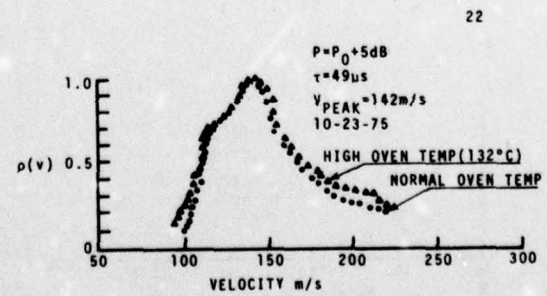

Fig. 22 Commercial tube, multiple-beam, high oven temperature and normal oven temperature.

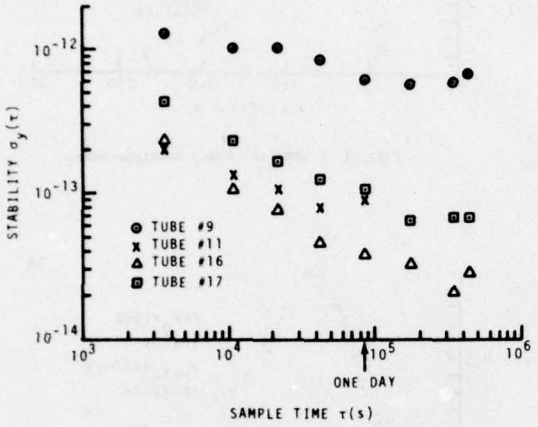

Fig. 23 Plots of frequency stability for standards containing tubes in Figs. 9, 11, 16 and 17. Higher flicker levels seem to go with wider peak feature in velocity distributions for this set of measurements.

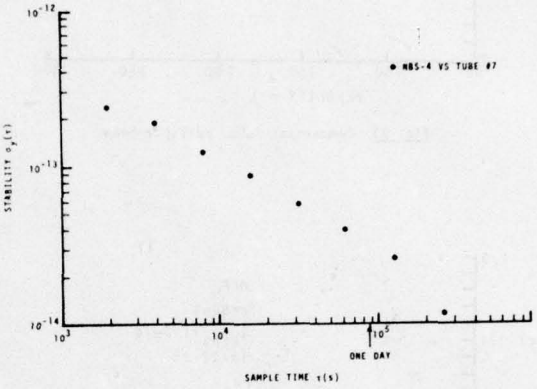

Fig. 24 Plot of frequency stability between NBS-4 and the standard containing the tube of Fig. 7.

PERFORMANCE OF A DUAL BEAM HIGH PERFORMANCE CESIUM BEAM TUBE

Gary A. Seavey Louis F. Mueller
Hewlett-Packard Company
Santa Clara, California

Summary

The dual beam high performance cesium beam tube general design and operation is discussed. Computer generated theoretical performance predictions are compared to typical performance measurements on a large sample of tubes. Improvement in cesium beam tube performance (figure of merit) as a result of a new cesium oven design and a configuration change of the tube's cesium detector is presented. A few tubes were subjected to adverse environments and the beam tube performance after these tests is discussed. Also a slightly modified dual beam high performance cesium beam tube was subjected to high level random vibrations and it's performance before and after the vibration is presented. The possibility of achieving greater than typical performance for relatively short periods of time, for special applications, is discussed. Measurements of accuracy, stability for various time periods and stability in dc magnetic fields carried out on HP 5061A primary frequency standards equipped with dual beam high performance cesium beam tubes is presented.

Introduction

The dual beam high performance cesium beam tube was developed by Hewlett-Packard Company in 1971. During the past three years Hewlett-Packard has been producing the tube to be sold as an option (designated option 004) with the HP 5061A primary frequency standard.[1] Figure 1 shows the high performance tube and an HP 5061A. Utilization of the option with the HP 5061A allows one to realize improved short-term stability, reproducibility, settability, and decreased sensitivity to dc magnetic fields.

General Design and Operation

The dual beam high performance cesium beam tube is a passive atomic resonator whose internal components are shown in Figure 2 and are: a cesium oven, which forms and aims the two cesium beams; the state selector magnets, which by means of a magnetic field gradient, spatially separate the atoms of each beam into two energy groups; the microwave cavity, in which an energy state change of the atoms is induced; the hot-wire ionizer, which ionizes the atoms that have undergone an energy state change; the mass spectrometer, which separates the cesium ions from unwanted noise contributing ions; the electron multiplier, which convert the ions to electrons and amplifies the electron current to a level compatible with subsequent electronics; the ion pump, which maintains a high vacuum within the tube; magnetic shielding, which minimizes effects of external magnetic fields; solenoid type windings, which produce the homogeneous magnetic field (C field) over the region of the microwave cavity and for degaussing the beam tube magnetic shields. Also the tube contains gettering material which collects and traps the unwanted expended cesium atoms.

The primary life limiting elements in cesium beam tubes are the cesium supply and the gettering system. The cesium supply and gettering system in the dual beam high performance cesium beam tube have been designed for a five year operating life, as has the standard tube.

The cesium oven or cesium source forms and aims the two cesium beams by means of a multi-tube collimator. We use dual beams primarily to double the output signal to the ionizer which gives a $\sqrt{2}$ increase in the Signal-to Noise ratio at the input to the electronics. A second advantage of the dual beam, which has been designed in, is relative immunity to acceleration effects. The cesium beam intensity is controlled by the temperature to which the cesium is heated by the oven. Additionally there are intentional conductance limitations in the oven and collimator which reduce the beam intensity. These conductances within the oven are designed to prevent liquid cesium from escaping the oven.

The state selection magnets produce an inhomogeneous, 10^4 gauss peak, magnetic flux density. The beam comprised of cesium atoms in two energy level groups, as depicted in Figure 3, passes through this large magnetic field gradient. Since:

1. an atom's energy is dependent on magnetic field intensity;

2. the magnetic field intensity is dependent on position in the state selector magnet gap;

3. physical systems tend to the lowest potential energy possible;

then the atoms experience a force in the direction of the magnetic field gradient. The atoms in the levels of F=3 and F=4, m_F=-4 group are deflected towards stronger magnetic fields. The atoms in the remaining F=4 levels are deflected towards weaker magnetic fields. Hence the atoms of each of the two beams are spatially separated into two energy level groups.

The first state selector magnet separates the atoms into two energy level groups such that the F=3 levels and F=4, m_F=-4 level are directed through the microwave cavity while the remaining group of the F=4 levels is prevented from passing through the microwave cavity.

The second state selector magnet separates the cesium beam which has traveled through the microwave cavity into two groups, the atoms that have not undergone a transition to the F=4 group are directed away from the hot-wire ionizer and the atoms that have undergone a transition to the F=4 group are deflected onto a path toward the hot-wire ionizer. Thus the majority of atoms that are ionized by the hot-wire ionizer are atoms that have experienced an energy transition while traveling through the microwave cavity.

The microwave structure first proposed by Professor Ramsey is a center feed, U-shaped microwave cavity which is machined to close tolerances from oxygen-free copper. The outside configuration of the microwave cavity is fabricated in such a way that it positions the C-field windings and the C-field magnetic shield.

The hot-wire ionizer is a flat tantalum ribbon running at approximately 1000° Celsius. The cesium atoms which have undergone an energy transition in the microwave cavity are directed toward the ionizer by the second state selector magnet. The atoms intercepted by the ionizer first stick, then are ionized, and finally evaporated and accelerated into the mass spectrometer.

The mass spectrometer spatially separates the cesium ions from any other unwanted noise producing ions, such as potassium, and focuses the cesium ions into the electron multiplier.

The electron multiplier, which is of the box and grid design, converts the 1×10^{-11} ampere ion current to an electron current and then amplifies the electron current to approximately 10^{-7} amperes which becomes the input for the signal processing electronics of the HP 5061A.

Figure 2 depicts the paths of the cesium atoms through the beam tube. The solid lines indicate the path of the atoms that contribute to the signal and the dashed line indicates the path of the atoms that do not contribute to the signal.

Comparison Theoretical Vs. Actual Performance

A computer program was developed to model the dual beam high performance cesium beam tube and the theoretical performance was calculated based on this model.[2] The pertinent parameters obtained from the computations are as follows:

1. Total beam intensity arriving at the hot-wire ionizer, 7.2×10^{7} atoms/sec. (1.15×10^{-11}a)

2. Linewidth of the field independent transition (F=3, m_F=0 to F=4, m_F=0) is 327 Hz.

3. Figure of merit, 31

An initial production group of approximately 30 tubes was produced that exhibited performance somewhat less than predicted. An investigation was carried out to determine the cause of this disagreement. A cesium source problem was discovered as was an improvement in the detector configuration.

The cesium source or "oven problem" which caused erratic beam intensity performance and some very early failures, due to decreased signal level, required a redesign of the cesium oven. This has long since been completed, and since we have seen no recurrences we feel confident that the problem is cured.

In Figure 4 the shaded area depicts the figure of merit of the initial group, and the outlined area, the figure of merit of the most recent 150 units. The figure of merit increased 44% to a mean value of 24.

Typical performance after the modifications as measured on over 150 tubes:

1. Total beam intensity, 1×10^{-11}a

2. Linewidth, 358 Hz

3. Figure of merit, 24.

The most important of these parameters in characterizing overall tube performance is the figure of merit. The figure of merit is defined to be the beam tube output signal to noise ratio as measured in a 1/4 Hz bandwidth, divided by the linewidth of the field independent transition. This ratio is weighted by a factor obtained from the curveshape of the field independent transition. Figure 5 depicts the pertinent measurements and their relation to the figure of merit.[3]

Typical Performance in an HP 5061A

Figure 6 is a frequency offset histogram of HP 5061A option 004 based on final test data for over 100 instruments.

The frequency stability specification for the 5061A option 004 is based on a realized figure of merit of 10. The high performance tube figure of merit mean of 24, if realized in the environmental and instrument conditions prevailing, would give a 100 second stability of 3.5×10^{-13}. Published data of NBS shows a realized stability of 5×10^{-13} at 100 seconds. The specification sheet calls for less than 8.5×10^{-13}. These NBS data also indicate that the $\tau^{-1/2}$ relation holds past 10^4 seconds, giving 5×10^{-14} at 10^4 seconds.[4]

The specification limit for sensitivity to magnetic fields is $\pm 2 \times 10^{-13}$ for a 2 gauss field in any direction. A typical measurement yields:

side to side	$\pm 1 \times 10^{-13}$
top to bottom	$\pm 5 \times 10^{-14}$
front to rear	$\pm 5 \times 10^{-15}$

The reproducibility specification of 3×10^{-12} is obtainable when the HP 10638A Degausser is used with the HP 5061A Option 004. This reproducibility is shown by the accuracy histogram Figure 6. The function of the degausser is to relax the magnetic domaines of the inner shield to an equilibrium magnetization after a change in the "C-field" current. The degausser accomplishes in 20 minutes the relaxation that might otherwise proceed for weeks causing a shift in frequency as the "C field" changes. A high level degaussing is recommended at turn on, and can be performed as the oven is heating. Low level degaussing can be performed without causing the instrument to unlock, and is recommended after changes in "C field", or magnetic environment changes are made. Reproducibility is defined as the independently set up instrument frequency comparison to the NBS frequency standard.

The settability specification of $\pm 1 \times 10^{-13}$ requires the use of the degausser. Settability or calibration refers to the ability to make relatively small, predictable changes to the output frequency of the standard. One minor division on the "C field" control corresponds to a nominal change of 5×10^{-14} in output frequency and 2 in the logging numbers on the "C field" dial which reads from 0 to 1000.

Typical performance with regard to settability is 1×10^{-14} which includes control linearity,

operator, beam tube and degausser effects.

Operating life data are still scarce, but recently two early tubes were returned at end of life after more than 4 years in service. These tubes were of the old oven design.

High Level Vibration

A dual beam high performance cesium beam tube was modified for the Global Positioning System evaluation program.[5] The modifications were to strengthen it structurally and change the internal wiring so that the tube could be subjected to high level random vibration and not experience mechanical or electrical failure.

The random vibration characteristics were: acceleration spectral density of 0.35 G^2/Hz from 125 Hz to 1200 Hz, below 125 Hz and above 1200 Hz the vibration spectral density decreases by 6 dB/octave until a total frequency band of 20 Hz to 2000 Hz is reached. Figure 7 is the plot of acceleration spectral density vs. frequency for the above mentioned vibration. This vibration characteristic integrates to approximately 25 g rms.

The tube was measured in an HP 5061A frequency standard prior to the vibration, then subjected to the vibration while non-operating and then remeasured in the same HP 5061A frequency standard. A comparison of this electrical performance before and after the vibration is tabulated below:

	Accuracy	Short Term Stability (10 second averaging)
before vibration	4.5×10^{-14}	1.33×10^{-12}
after vibration	11.1×10^{-14}	1.68×10^{-12}
specification	$300. \times 10^{-14}$	2.70×10^{-12}

Modified Performance for Special Applications

The figure of merit (stability) of a cesium beam tube is determined, as mentioned previously, by the signal-to-noise ratio, the linewidth and curve shape factor. In any given beam tube the linewidth and curve shape are relatively constant, but the signal-to-noise ratio can be changed within limits by changing the beam intensity, i.e. oven temperature. Since the vapor pressure of cesium doubles for approximately a 10° Celsius increase in oven temperature, one expects such a change to give a doubling of cesium beam intensity, a $\sqrt{2}$ improvement in figure of merit and a doubling of consumption of cesium, or halving of operating life.

Cesium beam tubes have been operated with oven temperatures increased 12° Celsius from nominal for periods of hundreds of hours. If the cesium vapor pressure is made too great scattering occurs in the beam which adversely affects the curve shape and linewidth which would shorten the operating life and yield no benefits.

Similarly a reduction in cesium oven temperature will give reduced beam intensity, cesium consumption, and figure of merit, with expected longer life. The practical limitation here would be the need for a detectable signal level which would set a low temperature limit.

Adverse Environments

Randomly chosen tubes have been subjected to adverse environments. One such test was to subject a tube to high level shock. The test called the "hammer blow" is carried out by mounting the tube to a large steel carrier and then striking the carrier with a 400 lb. hammer. The hammer swings through 1, 3, and 5 foot drops in each of three axes for a total of nine blows. The 5 foot drop generates shocks on the order of 1500 g at the table. The tube successfully passed this shock test without mechanical or electrical damage, or measurable change.

Acknowledgements

The authors wish to express their appreciation to R. C. Hyatt, R. F. Lacey, D. W. Allan for discussions invaluable in the preperation of this paper and to Sal Blas and Liz Cypert for their efforts in preparing the illustrations and manuscript.

References

1. R. C. Hyatt, L. F. Mueller, T. N. Osterdock "A High Performance Beam Tube for Cesium Beam Freuency Standards," Hewlett Packard Journal, September 1973, p.14.

2. Unpublished work, L. S. Cutler, R. F. Lacey

3. R. F. Lacey, A. L. Helgesson, J. H. Holloway "Short-Term Stability of Passive Atomic Frequency Standards," Proc. IEEE, 54, 2, p. 170, February 1966.

4. H. Hellwig, P. W. Allan, F. L. Walls "Time and Frequency," Proc. Fifth International Conference on Atomic Masses and Fundamental Constants (AMCO-5) June 1975.

5. Contract No. N00173-75-C-0471 (NRL).

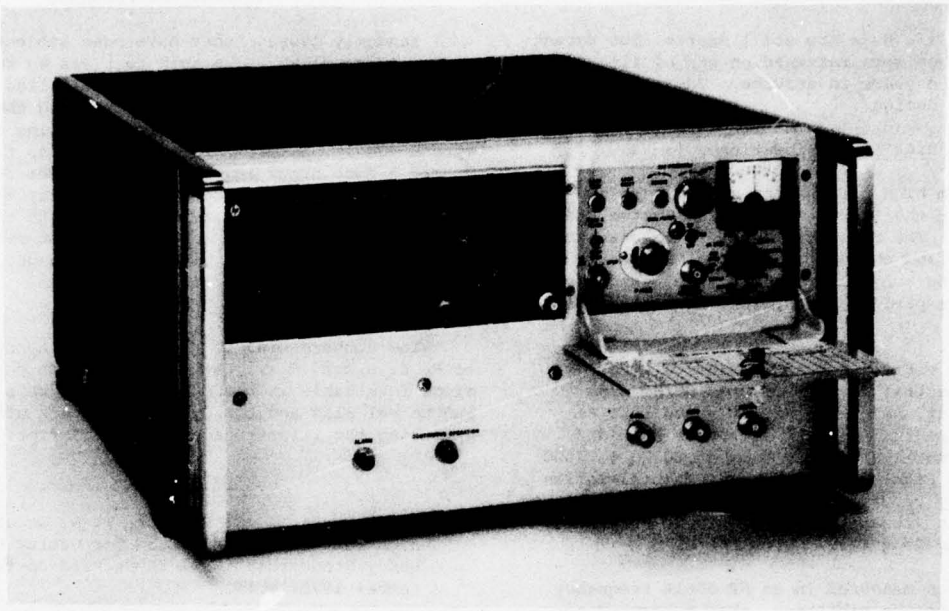

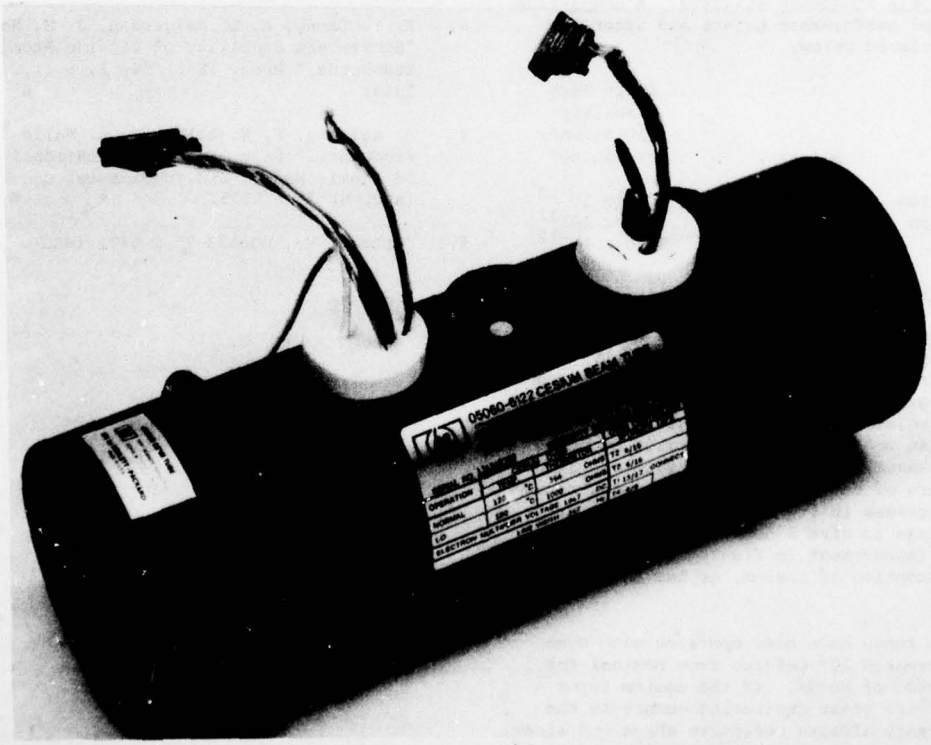

Figure 1. a)HP 5061A, b)Dual Beam High Performance Cesium Beam Tube

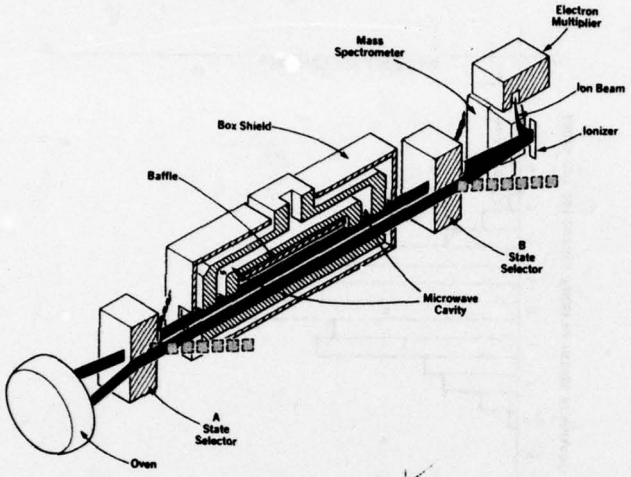

Figure 2.

Pictorial Representation of Dual Beam High Performance Cesium Beam Tube

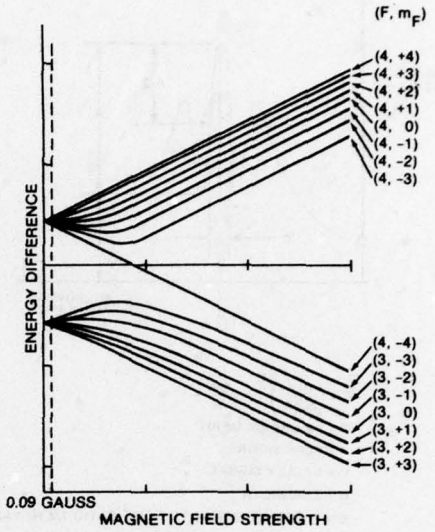

Figure 3. Energy Level Diagram of Cesium[133].

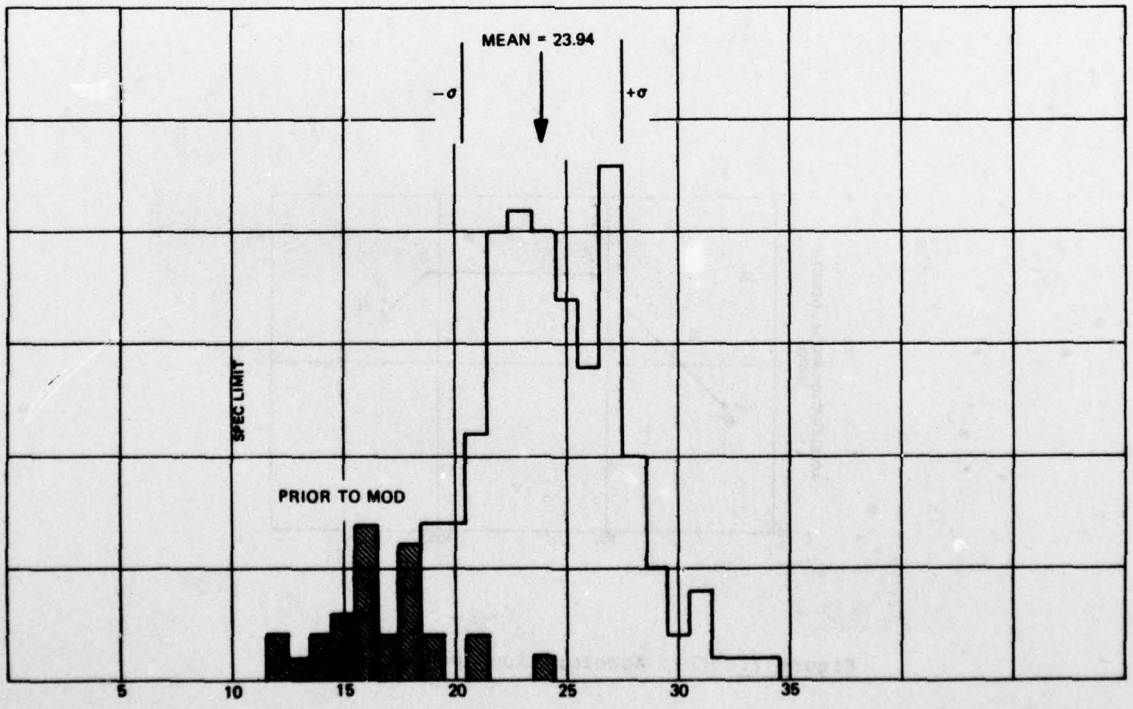

Figure 4. Figure of Merit Histogram

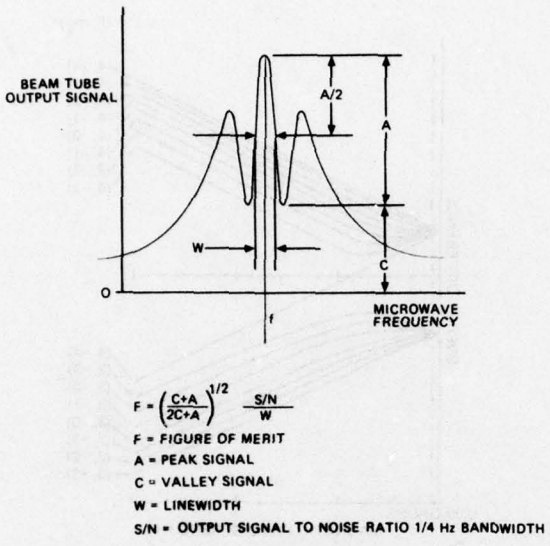

$$F = \left(\frac{C+A}{2C+A}\right)^{1/2} \frac{S/N}{W}$$

F = FIGURE OF MERIT
A = PEAK SIGNAL
C = VALLEY SIGNAL
W = LINEWIDTH
S/N = OUTPUT SIGNAL TO NOISE RATIO 1/4 Hz BANDWIDTH

Figure 5. Figure of Merit

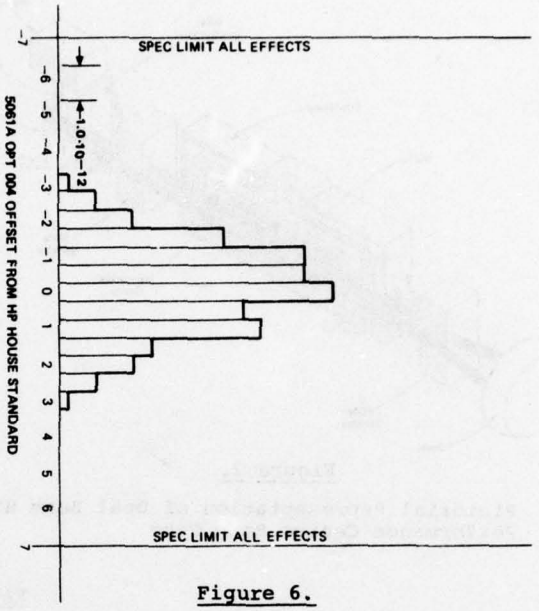

Figure 6.

HP 5061A Opt 004 Frequency Accuracy Histogram

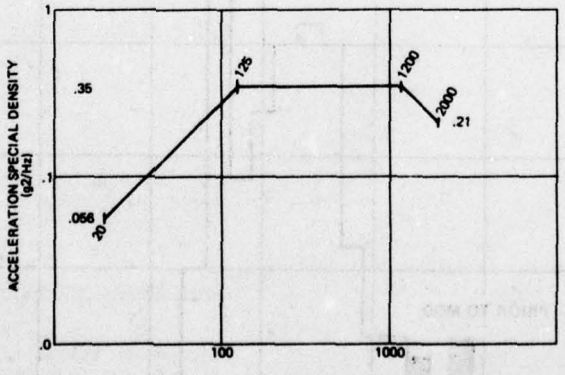

Figure 7. Acceleration Spectral Density

MEASURED PERFORMANCE AND ENVIRONMENTAL SENSITIVITIES OF A RUGGED CESIUM BEAM FREQUENCY STANDARD

Michael C. Fischer Charles E. Heger
Hewlett-Packard Company
Santa Clara, California

Summary

Several units of Hewlett-Packard's Model 5062C Cesium Beam Frequency Reference have been subjected to test conditions covering a more severe range of environments than any similar instrument previously. Measurements of changes in output frequency, or in many tests phase, resulting from the changes in environment are analyzed and reported with hypotheses as to the physical processes responsible for the effects.

The variables studied are: temperature; humidity; acceleration: shock, vibration; susceptibility to electromagnetic interference: radiated, conducted, power variations; simultaneous cycling of temperature, vibration and power; and opportunities for operator error.

Introduction

The subject of this paper is a particular type of cesium beam frequency standard, the Hewlett-Packard Model 5062C, Fig. 1, and its performance under environmental stress. This instrument, while being designed to perform well in very rough environments has performance in benign environments very similar to its predecessor instruments. The five subjects to be discussed are:

1. Temperature & humidity
2. Electromagnetic susceptibilities
3. Acceleration, shock, and vibration
4. Reliability under simultaneous multiple stress
5. The instrument's susceptibility to human beings

Background

The original format of this instrument was conceived in response to the needs of some of the earlier commercial aircraft collision avoidance systems. A significant component of that format was an extremely compact cesium beam tube, only 16 centimeters long, Fig. 2. The details of this tube are well covered in an article in the H-P Journal of March 1976. From the viewpoint of environmental sensitivity, this small tube has a basically similar layout to the high performance tube, also known as option 4 of the 5061A instrument.

Thermal Environment

Ambient Temperature

The effect of ambient temperature on the 5062C is shown in Fig. 3. Note that the data end points were taken at temperatures outside the specified operating temperature limits. This is data taken on the production line from a random sample of six recent production units. Clearly no single effect dominates these results. The most probable sources for the shifts seen here are power shift, C field shift, and quartz oscillator shift, all versus temperature.

Considering each of these, starting with power shift, the cesium beam tubes have some small remaining frequency versus RF power sensitivity. Along with this, the circuitry supplying RF to the beam tube will have a small output power variation with temperature.

The C field current can vary slightly with temperature depending on the accuracy of thermal compensation of the circuitry which controls this current.

The quartz oscillator has a temperature coefficient which can be in the neighborhood of 5×10^{-9} at temperature extremes, versus the 25°C value. The servo loop, in reducing this shift to 5×10^{-12} must exhibit an overall dc gain of 10^3. Since the open loop gain of the entire servo loop excluding the integrator operational amplifier is 1/2, this amplifier and its associated circuitry must have a dc voltage gain of 2×10^3 or 66 dB and very good offset versus temperature performance. The integrator input resistor is 10^5 ohms which requires that the feedback leakage resistance of the integrating capacitor, its shorting relay and the integrator bounding diodes all combined in parallel must remain above 200 megohms.

Another aspect of temperature effect is in the one pulse per second and one pulse per minute outputs of the clock options; the variation in propagation delay of their divider chains relative to the phase of the 5 MHz output signal which drives them. These shifts have been measured and are found to be of little consequence. The peak changes from the 25°C reference value measure from zero to +7 nanoseconds at -28°C and -3 to +3 nanoseconds at +65°C.

Temperature, Non-operating

The frequency change caused by a non operating test of -40°C for 72 hours followed by an increase to +65°C for 4 hours was measured to be 2×10^{-13} during four hour frequency measurement intervals. The only significance of this is that it equals the typical four hour stability, that is $\sigma y(\tau) = 2 \times 10^{-13}$ for τ=14400 seconds. This can also be considered the one-sigma measurement uncertainty, therefore there was no measurable degradation.

Temperature & Humidity

The 5062C was preconditioned before humidity testing by baking it in a dry test chamber at between 40 and 50°C for two hours before returning to 25°C and 50% relative humidity to measure its pre-test frequency. The unit was subjected to five days of 95% humidity with the temperature cycled for 16 hours each day at 50°C. The remainder of the 24 hour cycles consisted of a 1 1/2 hour transition to 30°C for five hours and a 1 1/2 hour transition back to 50°C. The phase of the 5.0 MHz output signal from the unit under test was monitored, relative to the house standard, continuously during the five day humidity test and the peak fractional frequency change from the 25°C pre-test measurement was 1.2×10^{-12}. The frequency

measurements taken at 50°C, 95% R.H. showed no change from the pre-test value.

Electromagnetic Susceptibility

A rather thorough series of electromagnetic susceptibility tests have been conducted on the 5062C. In addition to all applicable portions of MIL-STD-461A, two special magnetic field tests and a pulse output spike test were included. The MIL-STD-461A tests are summarized below:

Radiated Susceptibility

RS01	magnetic fields	30 Hz to 30 kHz
RS02	magnetic fields from 2 turns of wire around instrument	20 amps of 60 Hz, and 100 volt spike
RS03	electric field 1.0 volt per meter	14 kHz to 10 GHz

Conducted Susceptibility

CS01	applied to power leads while in operation	30 Hz to 400 MHz
CS02	same	
CS03	same	100 volt spike

The results of the MIL-STD-461A tests were that none of the tests caused any measurable perturbation to the output frequency or phase or to the time-keeping of the clock option.

The clock option pulse output, one pulse per second, and in option 10, one pulse per minute, have been subjected to an injected noise immunity test which they passed without measurable effect. The test was the injection into the pulse output connector of a 200 volt pulse, at least one microsecond wide, from a source impedance of 50 ohms.

We would expect to find some perturbation from certain frequencies of strong ac magnetic fields as well as from powering the instrument as frequencies within a few hertz of the 137 Hz servo loop carrier and its second harmonic.

The field strengths required to cause measurable effects would have to approach one gauss or more. Smaller field strengths are covered by the RS01 test. The servo carrier frequency was carefully chosen to avoid the 50 to 60 Hz region as well as 400 Hz. For these reasons, extensive testing with magnetic fields and power near 137 and 274 Hz have not been undertaken. Further discussion related to this area is under the subject of vibration.

AC Magnetic Fields

The 5062C was subjected to ac magnetic field tests of 0.2 millitesla (2 gauss) peak-to-peak at 50 and 400 Hz while frequency shift was being monitored for eight hour measurement intervals. While most of the six different combinations of field orientation and frequency resulted in changes of only a few parts in ten to the 13th, the two worst combinations caused frequency changes of 8 and 11 x 10^{-13}.

DC Magnetic Fields

In the tests with a 0.2 millitesla dc field, only one orientation caused any measurable frequency change, that being the one parallel to the C field direction in the beam tube. This worst case change was 4 x 10^{-13}. The influence of an external dc magnetic field is seen in two areas; the beam tube and the RF chain, with the beam tube being the more important. Since the observed sensitivity of the 5062C in its most sensitive axis, vertical lines of flux, is typically a frequency change of 1 x 10^{-13} per 1 x 10^{-4} tesla (1 gauss), the magnetic shielding effectiveness can be calculated. The sensitivity of the cesium atom itself is proportional to the operating C field which is 10μT (100mG) in the 5062C, resulting in $\Delta f/f$ of 9 x 10^{-5} per tesla. The shielding effectiveness, expressed as a ratio of magnetic flux densities is 90,000:1.

The influence of a dc magnetic field on the RF chain is less important. To examine the mechanism, the signal from the phase modulator is 5 MHz which has been sine wave phase modulated, with 137 Hz. Viewing this signal as frequency modulated, a non linear FM to AM conversion can occur when it passes through a de-tuned resonant circuit. Such de-tuning could be caused by an external dc magnetic field affecting the nonlinear permeability of a ferrite core inductor. FM to AM conversion is not a problem unless a following stage exhibits AM to PM conversion, a near certainty. By this meams then, some small amount of incidental phase modulation can occur at the second harmonic of the modulation frequency due dc magnetic fields.

This second harmonic PM, considered as FM, will have a phase relationship to the desired fundamental FM, due to the way it was generated, which will not affect the symmetry of the modulation waveform seen by the cesium atoms, however.

Large Magnetic Field, Non Operating

The cesium standard was subjected to a 25 oersted (2000 A/m) field (as used for ship degaussing) of first dc, then one hertz ac for a five minute duration each, in each of the three mutually perpendicular major axes of the instrument. The frequency measurements before and after this showed a shift of 3 x 10^{-13} which is not significant, being very near the resolution of the measurement time interval used.

Power Failure Tests

When forcing the instrument to automatically switch power sources among external ac, external dc, and internal battery, the phase of the 5 MHz output was monitored with a resolution of one nanosecond. No phase steps were observed.

Acceleration

The significantly sensitive components in a cesium standard to acceleration are the beam tube and the quartz oscillator.

Considering the beam tube first, the 5062C tube has twelve beams passing through it to two groups of six, see Fig. 4. The acceleration sensitive deflections applied to the two beams are arranged so that one is the mirror image of the other, to achieve cancellation. Further details on this were reported to this symposium in 1971 in a paper by Ron Hyatt and others.

Due to this low sensitivity design of the beam tube, the larger contributor to errors induced by accelerations is the quartz oscillator. Its sensitivity is typically 1×10^{-9} per g of acceleration, for the quartz oscillator alone.

Vibration

For vibration frequencies above the control loop corner frequency in a cesium standard, the quartz oscillator is essentially on its own, Fig. 5. Accordingly, FM sidebands or perturbation of the short term stability is to be expected. In the 5062C the loop time constant is typically 1/3 second for a corner frequency of 3 radians per second or 1/2 hertz. Any mechanical resonances will scale up the effect by a factor equal to the Q of the resonance.

Some recent sine wave vibration tests on an early prototype 5062C at 2 g peak from 14 Hz to 2000 Hz showed no damage to the instrument and generally good agreement with the FM sidebands that would be predicted by 1×10^{-9} per g, except for mechanical resonances. The worst of these resonances accentuated the FM by about 30 dB near 750 Hz, indicating a mechanical Q of 30, a reasonable expectation for typical chassis structures, Fig. 6. The relationship used to predict the FM sideband is

$$\mathcal{L}_a (f_v) = 20 \log \frac{f_o S_{osc} a}{2 f_v}$$

where

$\mathcal{L}_a \equiv$ single sideband to carrier ratio, dB

$f_v \equiv$ vibration frequency, Hz

$f_o \equiv$ carrier frequency, Hz

$S_{osc} \equiv$ oscillator acceleration sensitivity coefficient, $\Delta f/f$ per g

$a \equiv$ peak acceleration, g

These sine wave vibration tests also extended below 14 Hz, down to 5 Hz at 0.2 inch, double amplitude and the frequency was swept logarithmically versus time from 5 Hz to 2 kHz. In this method of testing the only two frequencies which caused a measurable time keeping error to accumulate were 750 Hz and 137 Hz. To explore the 750 Hz resonance, a one minute dwell at that frequency was found to cause a 60 nanosecond time error to accumulate. The corresponding frequency error would indicate that the crystal was not being controlled by the cesium loop. This was confirmed by an out of lock indication. The probable mechanism is the extreme FM depressing the RF power level applied to the beam tube. This could occur with a modulation index approaching 1 at the 9.2 GHz frequency, or 10^{-3} at 5 MHz. This calculates to a 5 MHz sideband amplitude of -71 dB relative to the carrier, while a measurement showed -73 dB during the dwell.

The disturbance caused as the vibration frequency passed through 137 Hz amounted to 10 nanoseconds. The vibration frequency sweep rate in that region is 1.4 Hz per second which is slow enough relative to the control loop bandwidths in the instrument to resemble a few seconds of dwell. The instrument is vulnerable at this frequency because it is the modulation frequency, or in other words, the carrier frequency of the instrument's servo loop.

Some sensitivity was expected at a third vibration frequency, 274 Hz, the second harmonic of the modulation. However no measurable phase or time errors were found in several sweeps through 274 Hz. The built-in monitoring circuitry detected the disturbance to normal operation at 274 Hz as well as 137 Hz and 750 Hz and the alarm lamp triggered in each case. Actual data plots are not shown here because the test project is continuing and further analysis will be required.

Shock

Two shock tests were done on the instrument. The first was a 30 g, 1/2 sine, 11 ms, non-operational test which verified ruggedness for shipment and portable use handling.

The second is often called the "hammer blow test" and although is usually a non-operational, survival-type test; it was done with the unit fully operational and being phase compared against a standard.

The test consists of allowing a 400 pound steel weight, the hammer, to fall thru 1, 3 and 5 ft arcs, in each of three axes for a total of 9 blows, striking a steel carrier to which the instrument is attached. The carrier floats on a very compliant suspension so that it responds freely to the impact. The mounting structure used to mount and contain the 5062C was attached only at normally available mounting points on the instrument and the mount stiffness simulated a heavy rack mounted situation. At impact the 5 MHz phase took small jumps of 20 nS and then only during the larger 3' and 5' drops. The alarm light of the unit was also tripped when a phase jump occured. The mechanism for the phase jump and alarm light is the rapid acceleration of the quartz crystal in the precision 5 MHz oscillator. This acceleration has most of its energy at frequencies above the bandwidth of the instrument's control loop. The acceleration causes a short duration lurch of frequency offset (which integrates to a phase ramp or step) resulting in a pulse of error signal in the control loop. This causes the alarm lamp to trip via the excess error signal channel in the self-check logic section.

Immediately after the effect of each blow was registered, the continous operation lamp was reset manually. After all blows were completed no change in the instrument's basic frequency or any other parameters were noted.

Reliability, Multiple Stress Testing

In order to measure the reliability of the 5062C option 10 under conditions of maximum environmental stress, a severe test was undertaken which involved simultaneous cycling of extremes of temperature, input power and vibration all simultaneously on four units. Temperature was cycled between the limits of -28°C and +65°C four complete cycles per day. The dwell time at the two temperature extremes was 2.4 hours with the transitions taking 2.4 hours (0.65°C/minute). A vibration level of 1.0 g peak at about 25 Hz was applied for 10 minutes out of each hour during the normal eight hour work day. In addition, the input power was varied every 24 hours between hi, nominal, & low line ac, and hi, nominal, & low external dc, and internal batteries for a total of seven input power situations.

Since the units were operated from internal batteries each day for 30 minutes, the energy drained from the batteries during discharge had to be recharged

in the 23 1/2 hours before the next discharge period. If the batteries were not receiving sufficient charge, the effect would be cumulative, and at some point would not stand up to a 1/2 hour discharge. To further strain the system, the temperature was constantly being cycled during recharge. If the temperature compensation of the charger did not closely match the battery, the undercharge situation (or overcharge which could be as disastrous due to excessive sulfation, etc.) would be aggravated. The result was that after a total of 1375 instrument test hours, no degradation in battery performance was noted.

More importantly, no relevant failure occured during the entire test sequence, and all measured parameters such as 5 MHz phase vs. time, output levels and clock timekeeping, operated flawlessly.

This test demonstrated a 2500 hour MTBF under extreme conditions, which indicates an expected MTBF almost 10 times that, in more normal use.

Personnel

Finally, it has been found that operating and service personnel can represent an environmental hazard to the instrument. In response to this, every opportunity was taken to make the instrument simple to operate and maintain.

For example, the turn on procedure is four steps:

1. Connect power
2. Wait 15 minutes
3. Set mode and modulation switches on
4. Press logic reset button to get a green light

Also to aid in service, the top and bottom covers have board locations, adjustments and major test points silk screened on the inside. All boards are keyed to prevent accidental insertion in the wrong socket. All regulated power supplies are current limited to protect against accidental shorts. The high voltage power supplies have dividing resistors built-in so that a low voltage meter is used to test their output.

Acknowledgements

The authors appreciate the assistance and data supplied by Rob Burgoon, Liz Cypert, Chuck Little, Lou Mueller, Gary Seavey, and Joe White.

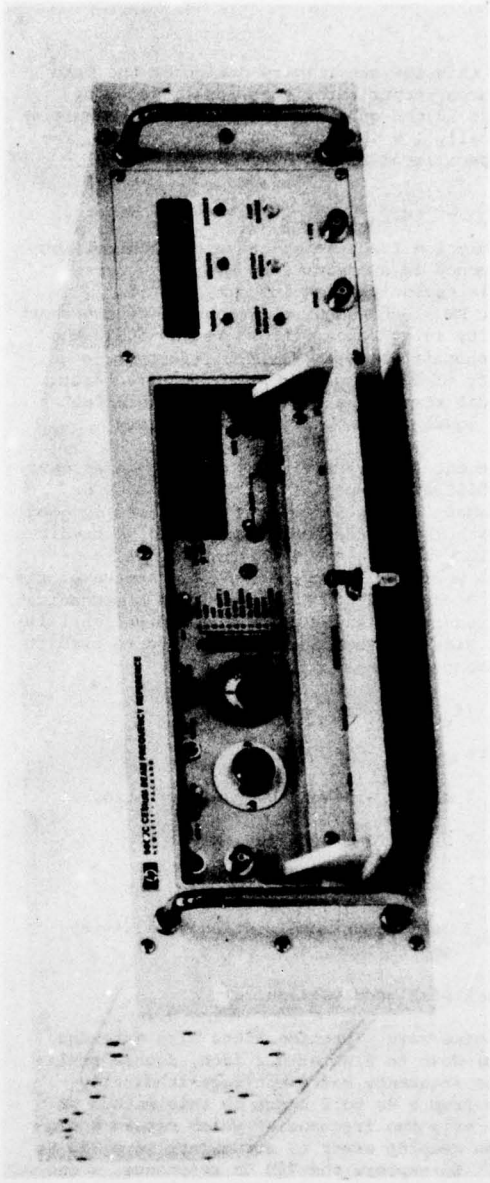

Figure 1

Hewlett-Packard Model 5062C

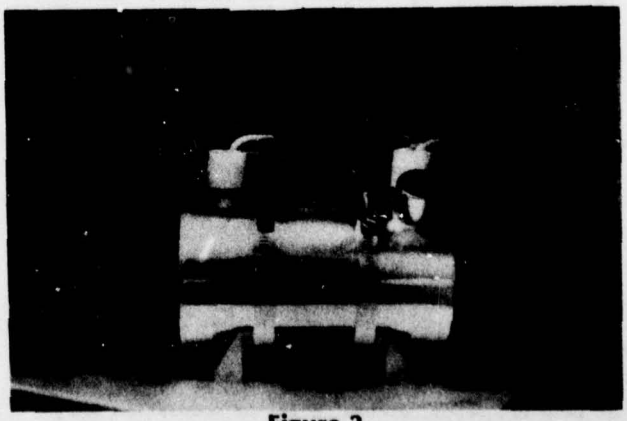

Figure 2

Cesium beam tube used in Model 5062C

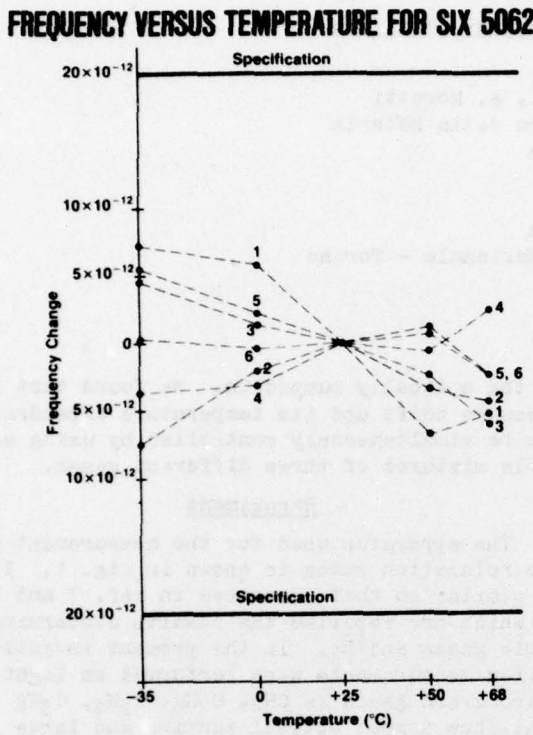

Figure 3

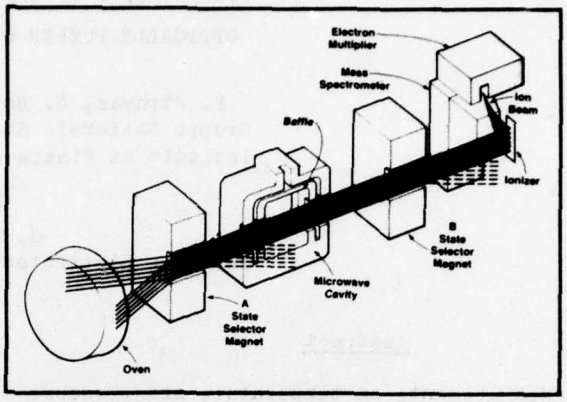

Schematic diagram of internal structure of cesium beam tube used in Model 5062C

Figure 4

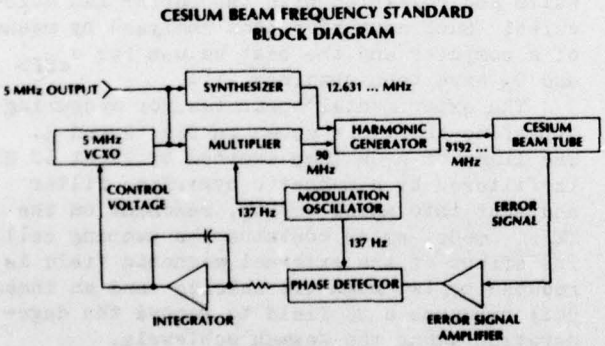

Figure 5

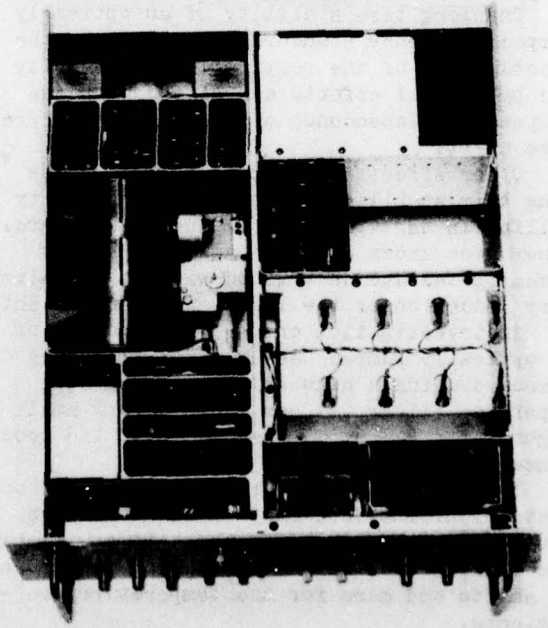

Model 5062C, top view, cover removed.

Figure 6

OPTIMIZATION OF THE BUFFER GAS MIXTURE FOR OPTICALLY PUMPED Cs FREQUENCY STANDARDS

F. Strumia, N. Beverini, A. Moretti
Gruppo Nazionale Struttura della Materia
Istituto di Fisica - Pisa

and

G. Rovera
Istituto Elettrotecnico Nazionale - Torino

Abstract

Measurements on temperature and pressure shifts of the hyperfine transition (F=4, m_F= = 0 ⟶ F=3, m_F=0) of Cesium have been performed for various buffer gases. The hyperfine relaxation cross section $\sigma_{<SI>}$ and the diffusion coefficient D_o of Cesium in the same gases were also measured.
The results are useful in order to select buffer gas mixtures to be used in a Cs vapor frequency standard, with an appropriate frequency shift, a near-zero temperature coefficient, and a high optical pumping efficiency.

Introduction

The long term stability of an optically pumped frequency standard is limited by the fluctuations of the pumping light intensity and by thermal effects associated with the temperature dependence of the buffer gas pressure shift.

Other effects contribute to reduce the long term stability. Among this the cavity pulling is negligible in a passive standard. Other less known effects cannot be easily investigated and understood without a preliminary reduction of the light and pressure shift.

An investigation on the performances of an optically pumped Cesium vapor frequency standard using a high efficiency magnetic hyperfine filter (1) has shown a very small light shift (2) as a consequence of the good symmetry of the filtered line.

The effects of buffer gases on the ground state hyperfine frequency of Cs atoms were investigated by several authors (3,4,5,6) but the results show discrepancies for the pressure shifts and more for the temperature coefficients.

We have performed measurements on those gases which are also promising for an efficient optical pumping. Two independent experimental apparatuses were used, one for the measurement of the shift of the o⟷o Cs line, and the other one for the measurement of the relaxation rates, the diffusion coefficient and the hyperfine relaxation cross section of the optically pumped Cs. We found that the pressure shift and its temperature dependence can be simultaneously controlled by using suitable mixtures of three different gases.

Experiment

The apparatus used for the measurement of the relaxation rates is shown in fig. 1. It is similar to that described in ref. 7 and 8 in which are reported the results concerning noble gases and N_2. In the present investigation measurements were performed on light hydrocarbon gases as CH_4, C_2H_6, C_2H_4, C_3H_8 that show a good optical pumping and large negative shifts.

The hyperfine ralaxation times have been measured as a function of the Cesium vapor density. The experimental values extrapolated to zero Cs density give the relaxation rate as a combined effect of diffusion to the cell walls and collision with the buffer gas molecules. Such data have been analyzed by means of a computer and the best values for $\sigma_{<SI>}$ and D_o have been obtained (7).

The experimental apparatus for measuring hyperfine shifts is shown in fig. 2 and 3. The light of a Cs lamp excited by RF at 60 MHz is filtered by a magnetic hyperfine filter and sent into an Al cavity, resonant on the TE_{011} mode, which contains the pumping cell. The effect of the external magnetic field is reduced by two magnetic shields and an inner coil produces a DC field to remove the degeneration among the Zeeman sublevels.
The strength of the DC field is keept around 0.08 Oersted producing an increase of the o — o line frequency of about 0.3 Hz.
The temperatures of the magnetic filter and of the pumping cell are controlled and monitored by means of thermocouples. The temperature of the cell can be varied from room temperature (≃ 20 °C) up to 60 °C.
A thermostat is used to maintain the temperature constant during a single measurement with an accuracy better than ± 0.2 °C. The RF excitation at about 9.192 GHz is obtained by

direct multiplication (x 1458) from a low--noise synthetizer with a resolution of 5×10^{-4}Hz, driven by a commercial Cesium--beam frequency standard. A low frequency modulation at 37 Hz is applied to the microwave by phase modulation of the 6.304 MHz at the imput of the multiplication chain. The effect of the RF excitation on the transmitted intensity light is detected at the photocell, and the signal is sent to a phase sensitive detector, lock-in amplifier type, used as a null detector. The measuring apparatus, shown in fig. 3, gives an accuracy for the frequency measurements of the order of 2×10^{-10} for signal amplitudes, at the photocell, ranging from 200 μV to 3 μV. The most important error source in the measurement of the pressure shifts comes from the uncertainty in the buffer gas density in the cells. This difficulty follow either from the low precision of the manometer in the pressure range of a few torr or from the impossibility to maintain the cell temperature constant during the sealing off from the vacuum station. This second error source is probably the most responsible for the large scattering between previous measurements. In ref. 9 and 10 a two step sealing off practice was used in order to avoid large errors. In the present investigation we adopted another procedure. A few minutes before sealing them off, the cells were immersed in a water bath whose temperature was measured with a precision better than ± 0.5°C. The glass tube used to connect the cells to the vacuum station was very thin so that its volume was negligible as compared to that of the cells. In this way we can estimate that the sealing-off error does not exceed $\pm$ 1%.

The cells were prepared on a vacuum system using a molecular sieve and an ion pump, in order to avoid contamination by oil and were filled following the procedure described in ref. 7. The pressure was monitored by an absolute metallinc gauge with a resolution of 0.1 Torr. The gauge was calibrated by means of a primary mercury standard. In this way we reach on accuracy of $\pm$ 0.1 Torr. All the pressure values were referred at 0°C.

Results

The measurements were carried out on buffer gases added to pure Cs metal. In fig.4 the behaviour of the hyperfine relaxation as a function of the buffer gas density is shown. The results shown concern CH_4, $C2H_6$, C_2H_4, C_3H_8 C_4H_{10}. Analogous results for noble gases and N_2 are resported in ref. 7 and 8. Also H_2 was tested as a buffer gas. Good signals were observed immediately after the preparation of the cells but we observed that a chemical reaction takes place between H_2 and Cs with a speed much higher as compared to the other alkali metals. In few days the cells stopped to absorb Cs resonance light. The measured data are not reported since the H_2 density in the cells varies with time. The continuous lines in fig. 4 are the best fit of the experimental data obtained by fitting with the help of a computer, the diffusion equation:

$$1) \qquad \frac{\partial}{\partial t}\langle S\cdot 1\rangle = D\nabla^2\langle S\cdot 1\rangle - K\langle S\cdot 1\rangle$$

where $D = D_0 \frac{P_0}{P}$, $K = N\bar{v}_r \sigma_{\langle S\cdot 1\rangle}$

A detailed solution can be found in ref. 7.

The pressure and temperature coefficients of the shifts were evaluated at 0°C, with reference to the Cs nominal hyperfine transition frequency $\nu_0 = 9192\ 631\ 770$ Hz, using the following relation

$$2) \qquad \nu - \nu_0 = P_0\left[\beta + \delta(T - T_0)\right]$$

where P_0 is the gas pressure in the cell referred to the temperature $T_0 = 273.16$ °K, β is the pressure shift coefficient expressed in Hz/Torr at 0°C, δ is the temperature coefficient in Hz/Torr · K.

In the evaluation of the results the light shift effect has not been taken into account it 4.6×10^{-12}/1% of change of light intensity and it is negligeable as compared to the indetermination of the pressure measurement. A typical experimental result in the shift determination is shown in fig. 5. The values of the coefficients D_0, $\sigma_{\langle S1\rangle}$, β, δ obtained by solving the eq. 1 and 2 are given in Table I. From the values given in Table I we see that N_2, He, CH_4, C_2H_6, and C_3H_8 are the buffer gases giving the largest signals. In order to compensate both the pressure and temperature shift the value of the ratio β/δ should be the same for two different gases. This does not happen even though the couple N_2, C_3H_8 is very close to this requirement. An easy compensation can be obtained by using a mixture of three different buffer gases. In this case we can obtain a full compensation of the temperature dependent part of the shift and select a prefixed value β_M for the mixture. The composition of the mixture can be calculated by solving the following algebraic system:

$$3) \qquad \begin{cases} a + b + c = 1 \\ a\cdot\delta_a + b\cdot\delta_b + c\cdot\delta_c = 0 \\ a\cdot\beta_a + b\cdot\beta_b + c\cdot\beta_c = \beta_M \end{cases}$$

Where a, b and c are the fractions of each gas in the mixture density. For each mixture there is a pressure range giving the better signal according to the values of σ and D of the mixture. By a proper choice of β_M we can obtain a predetermined line shift and the strongest signal. The shift is eliminate for any pressure if $\beta_M = 0$. As an example for a mixture $He+N_2+C_3H_8$ with a = 0.013, b = 0.748, C = 0.239 or a mixture $H_e+N_2+C_2H_6$ with a = 0.327, b = 0.309, C = 0.364 we have $\delta_M = \beta_M = 0$. In this case the cesium frequency in a cell is equal to that of umperturbed cesium. However we can also use a value $\beta_M \neq 0$ in order to simplify the synthesis of the radiofrequency at 9.192 GHz.

Conclusion

We have shown that a satisfactory control of the buffer gas pressure shift and its temperature dependence in a Cesium frequency standard can be obtained by suitable mixtures of three gases such as $N_2+H_2+C_2$ or $N_2+H_2+C_3H_8$. Since we have found also a very small light shift we should expect that the long term stability of an optically pumped Cs frequency standard will be significantly improved.

References

1. N. Beverini, F. Strumia: Opt. Comm. 2, 189 and 356 (1970) USA Patent n.
2. E. Bava, A. De Marchi, G. Rovera, N. Beverini, F. Strumia: Alta Frequenza 44, 574-284 E (1975).
3. E.C. Beaty, P.L. Bender, A.R. Chi: Phys. Rev. 112, 450 (1958).
4. M. Arditi, T.R. Carver: Phys. Rev. Lett., 1, 800 (1961).
5. C. Beer Jr.: "The Pressure Shift of the Cs Ground State Hyperfine Frequency", Thesis, Pennsylvania State Univ. 1970.
6. R.A. Bernheim, L.M. Kohuth: J. Chem. Phys. 50, 899 (1969).
7. N. Beverini, P. Minguzzi, F. Strumia: Phys. Rev. 4A, 550 (1971) and Phys. Rev. 5A, 993 (1972).
8. N. Beverini, F. Strumia, P. Violino: Zeit. Physik 265, 189 (1973).
9. G. Missout, J. Vanier: IEEE Trans. Instr. and Meas. 24, 180 (1975).
10. G. Rovera, A. Demarchi, J. Vanier: Trans. on Instr. and Meas.(Sept. 1976).

TABLE I

Experimental results for the hyperfine relaxation and for the pressure shift of Cesium.

Gas	$\sigma_{<SI>}$ x 10^{-22} cm^2	D_0 $cm^2/s.$	β Hz/Torr	δ Hz/Torr ^oK	β/δ ^oK	RF signal arb-units
He	0.28±0.03[a]	0.20±0.04[a]	1185±46	1.49±0.15	795	1
Ne	0.93±0.09[a]	0.153±0.014[a]	---	---		1
Ar	10.4±1.0 [a]	0.134±0.02 [a]	-191.4±3[c]	-1.05±0.05[c]	182	0.5
Kr	255±36 [b]	0.138±0.03 [b]	-1450±50[c]	-1.9±0.5 [c]	763	0.15
N_2	6.0±0.4 [a]	0.087±0.015[a]	924.7±7	0.623±0.05	1484	1
CH_4	4.1±0.6	0.28±0.05	-1050±30	-1.47±0.09	714	1
C_2H_6	8.5±1.0	0.21±0.03	-1852±30	-1.87±0.02	990	1
C_3H_8	14.9±2.0	0.143±0.025	-2959±37	-2.03±0.08	1457	1
C_2H_4	59.5±6.0	0.174±0.034	---	---	---	---
C_4H_{10}	---	---	-3995	-2.0	1997	1

a - from ref. 7; b - from ref. 8; c - from ref. 10

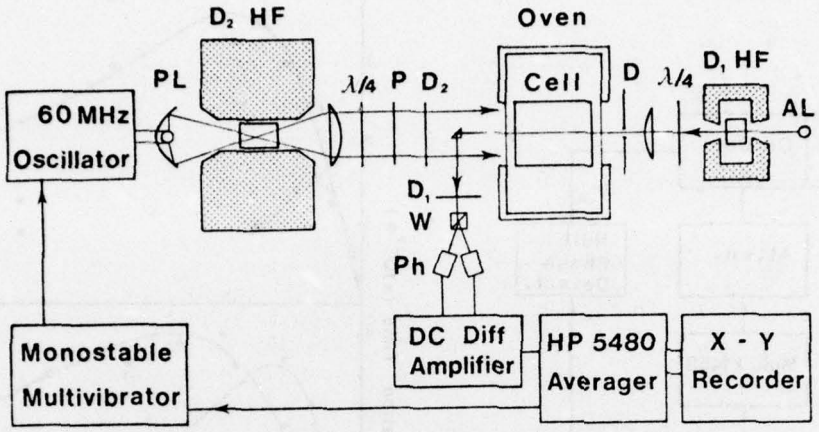

Fig. 1 - Experimental apparatus for measuring the relaxation rates.

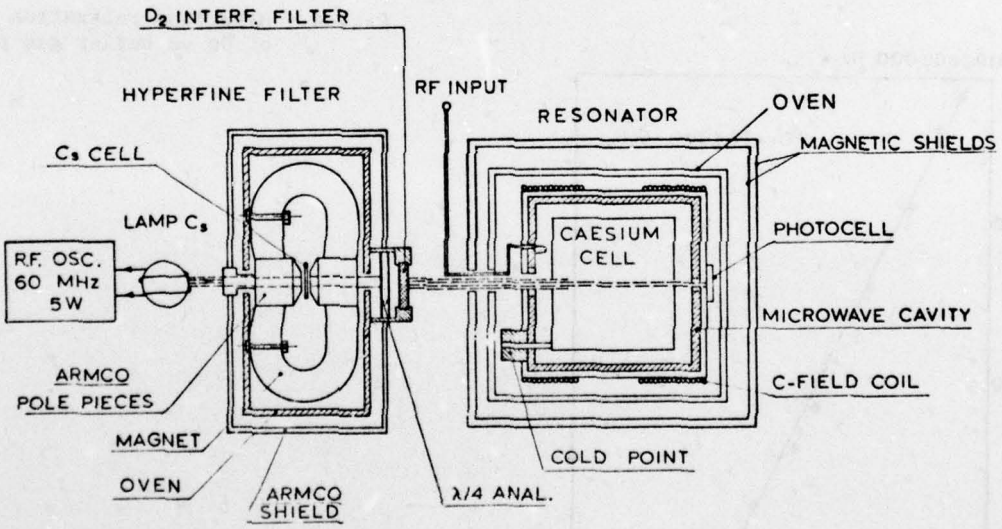

Fig. 2 - Experimental apparatus for measuring the hyperfine shift.

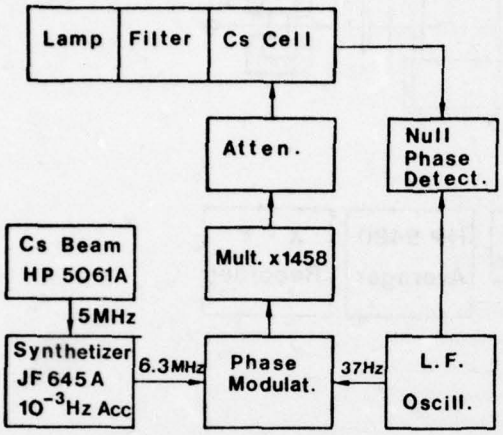

Fig.3 - Block diagram of the electronic measuring system

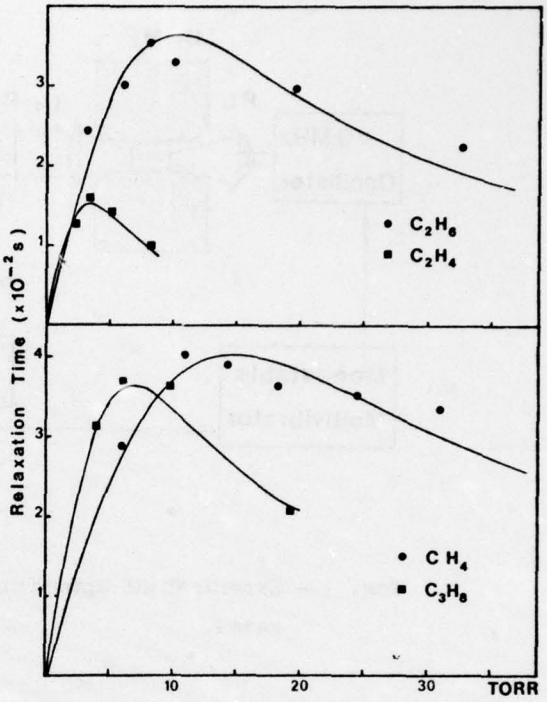

Fig. 4 - Hyperfine relaxation time of Cs vs buffer gas pressure

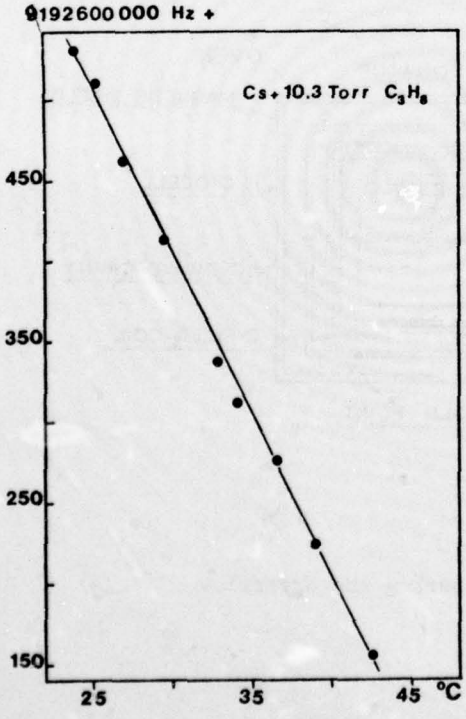

Fig. 5 - Hyperfine shift of Cs line as a function of temperature for a cell felled with C_3H_8

AD-A046 089 ARMY ELECTRONICS COMMAND FORT MONMOUTH N J F/G 9/5
PROCEEDINGS OF THE ANNUAL SYMPOSIUM ON FREQUENCY CONTROL (30TH)--ETC(U)
1976 H K ZIEGLER

UNCLASSIFIED NL

6 OF 6
AD
AD46089

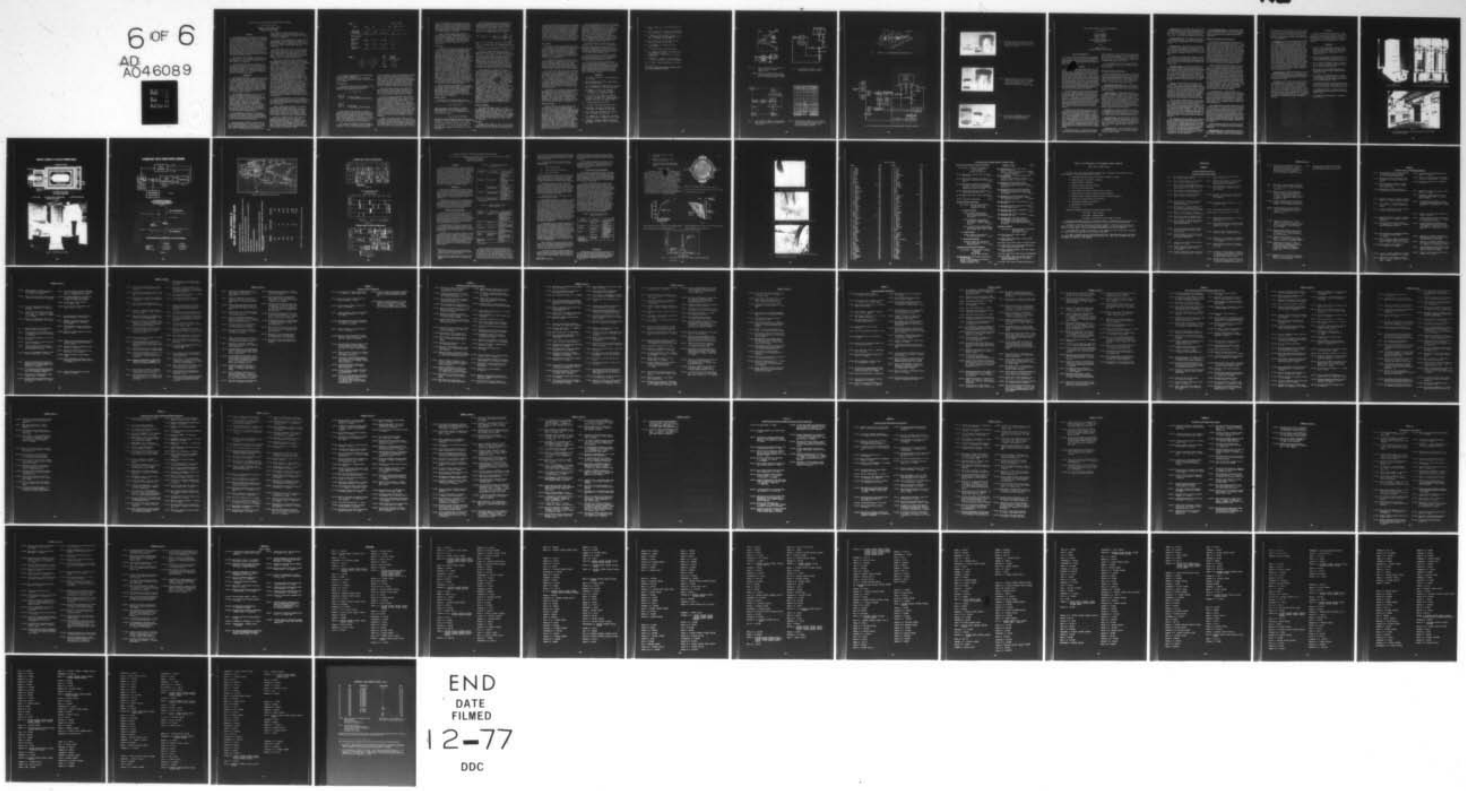

END
DATE
FILMED
12-77
DDC

A NEW KIND OF PASSIVELY OPERATING HYDROGEN FREQUENCY STANDARD*

F. L. Walls and H. Hellwig

Frequency & Time Standards Section
National Bureau of Standards
Boulder, Colorado 80302

ABSTRACT

The philosophy behind a new design of a passively operating hydrogen frequency standard will be described. Basically the hydrogen atoms are stored in a conventional, coated quartz bulb, which is contained in a TE_{011} cavity. The H-atoms are interrogated by driving the traditional 1,0 to 0,0 transition with an external frequency source and comparing the amplitude and/or phase of the output signal from the cavity with the input signal. The goal of this design is to achieve long term frequency stability of better than 1 part in 10^{14} for measurement times from 1 day to 1 year. This is done by increasing the cavity linewidth and decreasing the hydrogen resonance linewidth as compared to typical values for an oscillating maser.

The possibility of significant size reductions based on the use of small dielectric cavities and lower beam intensities, at little or no sacrifice in long term stability, is pointed out.

A new cavity control servo is described which allows the rapid stabilization of the cavity resonance frequency to better than 10^{-14} in its effect of pulling the hydrogen resonance. The reduction of other systematic effects to below 10^{-14} fractional frequency uncertainty and instability is discussed, including spin exchange and magnetic interactions.

INTRODUCTION

The purpose of this paper is to describe the design and report some preliminary measurements on a new kind of passive hydrogen frequency standard which shows great promise of achieving stabilities of better than 1×10^{-14} for averaging times from one day to perhaps a year. In addition, we hope to prove that the design concepts brought forth in this passive H-maser approach allow one much greater flexibility in trading various parameters off against one another in order to satisfy other criteria, such as the reduction of size or of selected systematic effects.

For timekeeping applications the goal is to minimize the time dispersion over many days or even years [1]. Presently, the best that can be done with any frequency standard, including hydrogen and cesium standards, is several parts in 10^{-14} per year [2] -- the only probable exceptions being the primary cesium standards. Requirements in navigation (Global Positioning System) are roughly equivalent to a frequency stability of 1×10^{-14} for 1 to 10 days [3]. It has been the requirement for very good long term stability, rather than the quest for absolute accuracy, which motivated us to look at the possibilities offered by passive hydrogen devices.

Before embarking on the analysis of systematic effects--the elimination of which is the real essence of good long term stability--we want to briefly decribe a typical active or self-oscillating hydrogen maser and several passive hydrogen standard options.

Hydrogen frequency standards, whether active or passive, are based on the F = 1, m_F = 0 to F = 0, and m_F = 0 hyperfine transition at 1420 MHz in the ground state of atomic hydrogen, which is illustrated in Fig. 1 [4,5]. Production and state selection of the atomic hydrogen is typically accomplished via the scheme shown in the lower portion of this figure. The state selection magnet shown is a hexapole but could be a different configuration.

Figure 2 shows a block diagram of a typical active hydrogen maser. By adjusting various parameters such as hydrogen beam intensity, storage time, cavity Q, etc., the energy radiated by the hydrogen atoms can be made to exceed cavity losses, and the system breaks into oscillation.

The weak signal of 10^{-12} to 10^{-13} W is then phase compared with a local oscillator, using multiplication and heterodyne techniques in order to preserve signal-to-noise. The output of the phase comparator is then used to phase-lock the local oscillator to the hydrogen signal. Note that in an active hydrogen maser no microwave signal is injected into the cavity.

Several passive hydrogen frequency standards have been proposed in the past. The first passive frequency standard was proposed and a prototype built by H. Hellwig in 1970 [6,7]. A simplified block diagram is shown in Fig. 3, which is similar to Fig. 2 except for the addition of a signal that is injected into the cavity region. Phase comparison of the output signal with the input signal allows one to frequency lock the local oscillator to the hydrogen phase dispersion signal. Fig. 4 shows such a hydrogen dispersion signal. The hydrogen signal was separated from other dispersive effects by squarewave modulating the H signal at $\simeq$ 1 Hz via hydrogen beam modulation or Zeeman quenching and detecting the resulting phase modulation with a $\simeq$ 1 Hz synchronous detector. Stabilities of $\simeq 2 \times 10^{-12}\,\tau^{-1/2}$ in a 30 Hz bandwidth were observed with this system [7]. Our present design is an outgrowth of this work. Figure 5 shows a hydrogen beam tube built and tested in 1971 [8]. This beam tube featured a linewidth similar to the active maser and detection of the hydrogen atoms, which had undergone the appropriate transition. As we will see later, this approach virtually eliminates cavity pulling. However, the then available detectors for thermal hydrogen atoms in arrangements which had sufficiently narrow linewidths had poor signal-to-noise, which prevented the attainment of good stabilities in a reasonable time.

H. Peters proposed and built in 1971 a beam tube with cooled hydrogen atoms not using any storage bulbs [9]. This reduced cavity pulling and eliminated wall shifts while featuring good signal-to-noise. However, the linewidth was much wider.

Figure 6 shows the block diagram of our presently operating passive hydrogen maser design. It uses a conventional beam system to produce the state selected atomic hydrogen. The cavity is of standard size and presently has a loaded Q of almost 40000. The design and the reasons behind it will be discussed in detail in the context of reviewing various systematic effects.

Basically, a 5 MHz oscillator is multiplied and mixed with a synthesizer output to produce the hydrogen resonance frequency. This microwave signal is then injected into the cavity and allowed to interact with the cavity and the hydrogen atoms. The output signal is then processed in order to frequency lock the local oscillator to the hydrogen resonance and the TE_{011} cavity resonance to the local oscillator.

TABLE 1

DEVICE	Q_{CAV}	Q_H	K	$\nu_{CAV} - \nu_H$ (Hz) FOR $\frac{\nu - \nu_H}{\nu_H} = 10^{-14}$
CONVENTIONAL ACTIVE MASER	35,000	1×10^9	3.5×10^{-5}	0.4
PASSIVE MASERS:				
PRESENT NBS MASER	40,000	5×10^8	8×10^{-5}	0.2
DIELECTRIC CAVITY	5,000	2×10^9	2.5×10^{-6}	5.7
HIGH-Q CAVITY HIGH-H-Q	40,000	1×10^{10}	4×10^{-6}	3.5

TABLE 2

$\overline{H}$	$\Delta\nu_z$	$\left[\frac{\Delta H}{H}\right]$	SHIELDING FACTOR 10^{-4} T Ext Field
1×10^{-8} T	2.7×10^{-5} Hz	25%	4×10^4
1×10^{-7} T	2.7×10^{-3} Hz	0.25%	4×10^5
2×10^{-6} T	1.1 Hz	.0006%	1.6×10^7

The significant systematic effects which trouble hydrogen frequency standards are:
1) Cavity pulling, 2) Magnetic field, 3) Crampton effect [10], 4) Second-order Doppler, 5) Wallshift, and 6) Spin exchange.

Cavity Pulling

In our opinion the most serious limitation to long term stability is cavity pulling. Approximate equations [11] governing this effect are:

$$\frac{\nu - \nu_H}{\nu_H} \quad K(\nu_{CAV} - \nu_H)$$

$$K \simeq \left(\frac{Q_{CAV}}{Q_H}\right)^2$$ DETECTION OF ATOMS (FAR BELOW OSCILLATION THRESHOLD)

$$K \simeq \left(\frac{Q_{CAV}}{Q_H}\right)$$ DETECTION OF rf (ALL MASERS, ACTIVE & PASSIVE)

After looking at the equations it is easy to understand the early enthusiasm for the passive hydrogen beam frequency standards, which detected atoms, as they virtually eliminated cavity pulling. All of the present devices sample the field intensity, i.e., all masers - active and passive - suffer from cavity pulling which varies linearly with the ratio of the cavity Q to the line Q, multiplied by the cavity offset.

For a typical active maser the cavity pulling is indicated in Table 1: assuming a cavity Q of 35000 and a line Q of 1×10^9 it is not surprising that many effects are capable of shifting the frequency many parts in 10^{14}. Note that in order to achieve one part in 10^{14} long term stability the cavity must be stabilized to 3 parts in 10^{10}. Obvious sources capable of moving the cavity this amount are cavity temperature, bulb temperature, mechanical strain, electrical changes in the cavity walls, changes in the coupling to the cavity, leakage of radiation from the cavity to the outside, etc., all of which are likely to be functions of time.

One of the primary reasons we have chosen this passive approach is that it allows considerable flexibility to choose design parameters such as cavity Q and line Q in order to reduce cavity pulling because no oscillation threshold conditions have to be met.

In our full-sized cavity design we have chosen to increase line Q to approximately 10^{10}. This will be accomplished by decreasing the hydrogen density in the bulb and increasing the storage time a factor of 10. So far, we have achieved a Q_H of 5×10^9. The physical limit to this approach is ultimately wall relaxation. [12] This reduces the basic sensitivity to cavity pulling as well as the frequency shift and broadening due to spin-exchange collisions by a factor of 10 and reduces by the same factor the amount that the servo has to split resonance line in order to achieve a desired stability. In addition it reduces the required beam intensity by a factor of 100 which has major implications in terms of future size and weight of passive hydrogen frequency standards.

Figures 7 and 8 show a model of the full sized cavity which we are presently using. The cavity length is adjusted by rotating the quartz barrel using a design of R. Vessot [13]. Note that 120 degree rotation changes the length by about 1 cm. The top has a choke flange which is designed to help suppress TM modes in the cavity

and eliminate radiation losses from the top of the cavity. The TM modes are troublesome in that they are degenerate with some coaxial transmission modes and hence couple through the gaps around the cavity endplates to the outside. Any change in the outside environment thus affects the TM modes which can then pull the desired TE_{011} cavity mode.

Figure 7 shows a dielectrically loaded TE_{011} cavity with a Q of approximately 6000 along side the standard cavity. The interior of the dielectric shell is the storage bulb. This provides a cavity which is exceptionally rugged and very much smaller than a standard cavity. The cavity pulling sensitivity is also small because of its low Q (see Table 1).

Cavity Servo

In addition to decreasing the inherent sensitivity to cavity pulling, the resonance frequency of the cavity can be easily locked to the H resonance frequency in our passive design. As depicted in Fig. 6, the signal from the 5 MHz local oscillator is phase modulated, multiplied, and mixed to produce a phase modulated 1420 MHz carrier. After transmission through the cavity, the 1420 MHz signal contains amplitude modulation at the fundamental of the phase modulation with intensity and sign determined by the cavity offset. After heterodyning to 20 MHz, the signal (now pure amplitude) is processed by a synchronous detector to correct the cavity frequency via tuning elements connected to the cavity output. Using 12.5 KHz phase modulation we have demonstrated that one can easily reduce the cavity offset to less than 5 Hz in only 20 seconds. Using the large bulb with a hydrogen line Q of 5×10^9 to 10^{10} in the full sized cavity, we can reduce the effect of cavity pulling to below 10^{-14} in about 10 minutes. Therefore changes in the output frequency, due to cavity pulling, should easily be stable to parts in 10^{15} in long term even in the presence of environmental perturbations, due to the low sensitivity to cavity pulling and the high signal to noise which permits a correction of the cavity frequency in a time rapid compared to most environmental changes.

The 12.5 KHz modulation sidebands are 10 dB below the 1420 MHz carrier; the modulation is fast compared to the hydrogen linewidth and the Zeeman separation of approximately 140 Hz. The 12.5 KHz sidebands were measured to remain equal in amplitude to about 10^{-4} after several months of operation. No significant perturbation to the resonance itself occurs using this cavity stabilization technique.

Magnetic Fields

The shift of the resonance frequency due to a magnetic field is ($\Delta\nu_H$ in Hz, H in Tesla, 1T = 10^4 G)

$$\Delta\nu_H = 2.750 \times 10^{11} \overline{H^2}$$

where the average is over the entire storage bulb. The average magnetic field is measured via the Zeeman effect $\nu_z = 1.4 \times 10^{10} \bar{H}$. Therefore the shift term should be written as

$$\Delta\nu_H = 2.75 \times 10^{11}[\bar{H}^2 + \overline{\Delta H^2}]$$

where $\overline{\Delta H^2}$ is the mean squared field deviation from the average over the bulb as measured via ν_z. In order to keep the offset due to $\overline{\Delta H^2}$ less than 10^{-14}, this term must be kept below $(7 \times 10^{-9}\ T)^2$ or $(70\ \mu G)^2$, which is relatively easy at magnetic fields below 10^{-7}T (1 mG) (see Table 2).

Another systematic effect is a perturbation discussed by Crampton (Crampton effect) [10] which is caused by the presence of radial rf and dc magnetic field components in the storage region coupled to a difference in the populations $\rho_{1,1}$ and $\rho_{1,-1}$ of the 1,1 and 1,-1 states due to the state selection process. This frequency shift $\Delta\nu_{CE}$ is given by

$$\Delta\nu_{CE} = K\gamma_H \left(\rho_{1,+1} - \rho_{1,-1}\right)\left(\frac{\tau_c}{1+(\omega_z \tau_c/2)^4}\right)\left[\frac{H_r^{rf}}{H_z^{rf}} \frac{\vec{r}}{\vec{r}} H^{dc}\right]_{BULB}$$

where γ_H is the relaxation rate due to spin exchange and τ_c is the average time for a hydrogen atom to cross the bulb. K is $\simeq 2 \times 10^{11}$ Hz /T, subscripts r and z designate radial and axial components of the magnetic fields.

One way to substantially reduce this effect is to operate at fields of 2×10^{-6} Tesla(20 milligauss) where the $\omega_z \tau_c$ term reduces the effect by more than 100. Table 2 shows the relationship between magnetic field and required magnetic field stability and shielding factor in order to achieve a fractional frequency stability of 1×10^{-14}, we see that this solution is unacceptable for achieving long term stability, as it requires a stability of residual magnetic fields of 1×10^{-11} T (0.1 μG) which is very difficult and may even exceed the long term stability of residual magnetization of presently available magnetic shielding

Our solution to this problem is to operate at a very low spin exchange relaxation rate, which is necessary anyway to achieve the desired line Q of 10^{10}. This greatly reduces the Crampton shift. If necessary, further reduction will be accomplished by equalizing the 1,1 and the 1,-1 populations using a dc neck coil; this we have already demonstrated for our present device. The use of population mixing reduces the Crampton effect reduces the signal by 50%. A more elegant scheme is to use double state selection, which removes both the 1,1 and 1,-1 states [ ]. Double state selection would increase the signal a factor of 3, for the same spin exchange rate, over the state mixing method and, in principle, totally eliminate the Crampton effect. This is more feasible with the passive system than in an active maser because of the reduced requirements on beam intensity. Another approach to reduce this effect is via careful centering of the storage bulb. This is difficult in a standard design because the storage bulbs are usually not perfectly symmetric. In our small dielectric cavity design the storage bulb is the inside of the dielectic shell and can be easily machined to be symmetric to better than 1%. This alone should be enough to greatly reduce the effect.

Second Order Doppler

The second order Doppler shift is 1.3×10^{-13} per degree Kelvin for atomic hydrogen. This means that the temperature needs to be stable to only 0.07 K in order to maintain an uncertainty of less than 1×10^{-14}. In our present design the temperature is stable to about 0.01 K per day, using only the outside oven. Eventually both the inner and outer oven will be used. It appears relatively easy to obtain temperature stabilities of 0.01 K per year.

Wall Shift

The wall shift is about 3×10^{-11} for a 15 cm bulb. H. Peters [15] has shown that the wall shift is at least stable to parts in 10^{13} per year. Only further work

using better time scales which should include hydrogen standards will reveal the time stability of this shift. The measurements of Crampton [16] on spin exchange indicate that shifts due to paramagnetic gasses in the bulb region could be very important. As a consequence the stability of the wall shift may be influenced by cleanliness and by the stability of the background pressure. Preparation of the storage bulb prior to coating, coating material, method of coating, and even bulb operating temperature may also be important at the 1×10^{-14} level. Much work remains to be done in this area for all types of hydrogen storage devices.

Spin Exchange

The presence of appreciable hydrogen density in the storage bulb, which is desirable for strong signals, causes a frequency broadening and shift because the hyperfine frequency is perturbed during collisions. The spin exchange contribution to the linewidth is typically a fraction of a Hz [17] and uncompensated frequency pulling is of the order of percents of the broadening, i.e., fractionally, parts in 10^{12} for typical active maser operation.

In virtually all active maser designs, spin exchange broadening is compensated for by cavity pulling [18]. The residual frequency offset can then be substantially reduced. This spin exchange tuning requires beam intensity modulations and an auxiliary frequency standard (another H-maser had to be used to achieve excellent stability over many days [19,20]).

In our full size cavity design the spin-exchange frequency shift will be reduced to about 3×10^{-13} by a tenfold reduction in hydrogen density in the bulb. This permits a tenfold improvement in line Q which reduces cavity pulling and relaxes requirements on the servo. In order to maintain 1×10^{-14} frequency stability the hydrogen density must be stabilized to about 3%. This is presently being done by stabilizing the rf discharge power and hydrogen pressure in the discharge bulb. Additionally, we plan to monitor the amplitude of the second harmonic of the 0.1 Hz hydrogen modulation signal using it as a diagnostic tool (see next Section).

The passive maser could be spin exchange tuned via beam modulation as in a conventional maser; however, amplitude modulation of the microwave signal will accomplish virtually the same result without any beam modulation. This utilizes the dependence of hydrogen line Q on the transition probability which depends on the microwave power. Of course, this technique will require a careful elimination of amplitude to frequency conversion in the electronics.

Hydrogen Line Servo

Figure 6 shows that the signal from the 5 MHz local oscillator is not only phase modulated at 12.5 KHz but also at a low frequency of about 0.1 Hz. This causes the 1420 MHz carrier to be phase modulated at 0.1 Hz. After interacting with the hydrogen atoms in the cavity, the 1420 MHz signal contains amplitude modulation at 0.1 Hz with the intensity and sign determined by the frequency difference between the injected signal and the resonance frequency of the hydrogen atoms. The amplitude modulation is detected after heterodyning the 1420 MHz signal to 20 MHz and passing it through a narrow band filter in order to preserve signal-to-noise. A synchronous detector converts this signal into a dc voltage for correcting the frequency of the local oscillator. Dispersion effects in the rest of the electronics are negligibly small over a band of 0.1 Hz.

Preliminary measurements with a 15 cm bulb with a linewidth of approximately 3 Hz and a cavity of 40,000 yield a one second stability of 8×10^{-12} which improves as the square root of time at least out to 1800 seconds. These measurements are very important because with a linewidth of 3 Hz, the standard is 10 to 20 times more sensitive to most systematic effects than our new system presently under construction. It will feature a cylindrical bulb of 18 cm diameter and 20 cm height. Tests of this bulb in a different maser yield an increase in line Q of nearly 10 and a signal-to-noise about 10 times larger than presently achieved (see Fig. 9).

We therefore expect to achieve a short term stability of $\sigma_y(\tau) \leq 1 \times 10^{-12}\ \tau^{-1/2}$. These results coupled with measurements reported above on the reduction of cavity pulling, indicate that the full size passive hydrogen maser just described is capable of achieving a frequency stability of better than 1×10^{-14} from 1 day to perhaps a year.

We also believe that it is possible to achieve stabilities very close to this level in a passive maser measuring approximately 16" in diameter and 30" long using the small dielectric cavity.

Also it should be noted that the ability to reduce cavity pulling independently to 1×10^{-14}, to be spin exchanged tuned via microwave amplitude modulation as well as beam intensity modulation, and the ability to operate over more than an order of magnitude change in hydrogen density makes the passive masser a powerful tool for investigating systematic effects and physical processes.

REFERENCES

1. D. W. Allan, H. Hellwig, D. J. Glaze, Metrologia 11, 133 (1975).
2. Bureau International de l'Heure, Annual Report, Paris, published annually.
3. F. E. Butterfield, Proc. 30th Annual Freq. Control Symp., Ft. Monmouth, NJ (1976) to be published.
4. K. Kleppner, H. C. Berg, S. B. Crampton, N. F. Ramsey, R. F. C. Vessot, H. E. Peters, J. Vanier, Phys. Rev., 138, A972 (1965).
5. R. F. C. Vessot, M. W. Levine, P.W. Zizewitz, P. Debely, N. F. Ramsey, Proc. Int. Conf. on Prec. Meas. and Fund. Const., National Bureau of Standards Special Publ. No. 343, 27 (1970).
6. H. Hellwig, Metrologia 6, 56 (1970).
7. H. Hellwig, H. Bell, Metrologia 8, 96 (1972).
8. H. Hellwig, H. Bell, Proc. 26th Annual Freq. Control Symp., Ft. Monmouth, NJ, 242 (1972).
9. H. E. Peters, Proc. 26th Annual Freq. Control Symp., Ft. Monmouth, NJ, 230 (1972).
10. S. B. Crampton, H. T. M. Wang, Proc. 28th Annual Freq. Control Symp., Ft. Monmouth, NJ, 355 (1974).
11. J. Viennet, C. Audoin, M. Desaintfuscien, Proc. 25th Annual Freq. Control Symp., Ft. Monmouth, NJ, 337 (1971).

12. R. F. C. Vessot, M. W. Levine, Metrologia 6, 116 (1970).

13. R. F. C. Vessot, M. W. Levine, Proc. 28th Annual Freq. Control Symp., Ft. Monmouth, NJ, 408 (1974).

14. C. Audoin, M. Desaintfuscien, P. Piejus, J. P. Schermann, Proc. 23rd Annual Freq. Control Symp., Ft. Monmouth, NJ, 288 (1969).

15. H. E. Peters, D. B. Percival, Proc. 4th PTTI Meeting, Washington, DC., 55 (1972).

16. S. B. Crampton, H.T. M. Wang, Phys. Rev. A 12, 1305 (1975).

17. P. L. Bender, Phys. Rev. 132, 2154 (1963).

18. S. B. Crampton, Ph.D. Thesis, Harvard University, 1964, unpublished. See also J. Vanier, R. F. C. Vessot, Appl. Phys. Letters 4, 122 (1964).

19. O. Gheorghiu, J. Viennet, P. Petit, C. Audoin: C. R. Acad. Sc. Paris 278, Series B, 1059 (1974).

20. D. Morris, K. Nakagiri, Metrologia 12, 1 (1976).

---

*This work was supported by the Naval Research Laboratory, Contract #N00173-75-F-D-046.

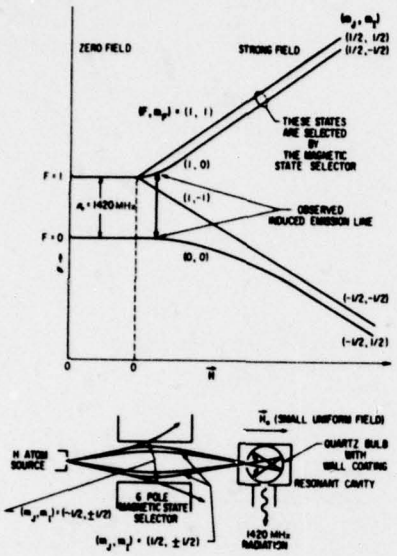

Fig. 1 Top Atomic hydrogen hyperfine ground state energy levels in an applied magnetic field.

Bottom Schematic of system typically used to create and state select atomic hydrogen for use in hydrogen frequency standards.

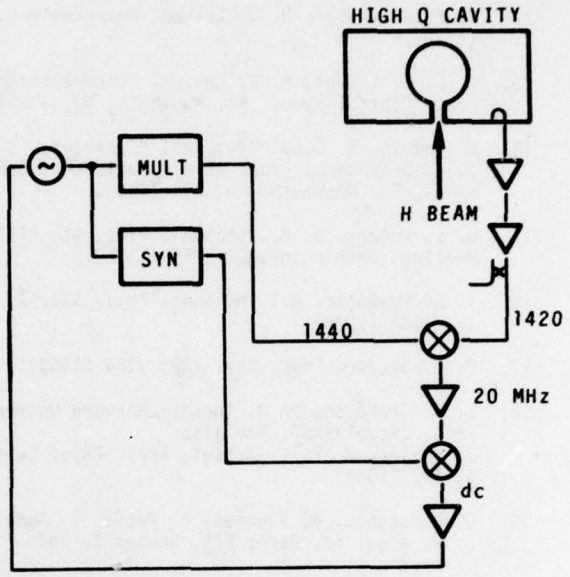

Fig. 2 Simplified block diagram of an active hydrogen maser frequency standard.

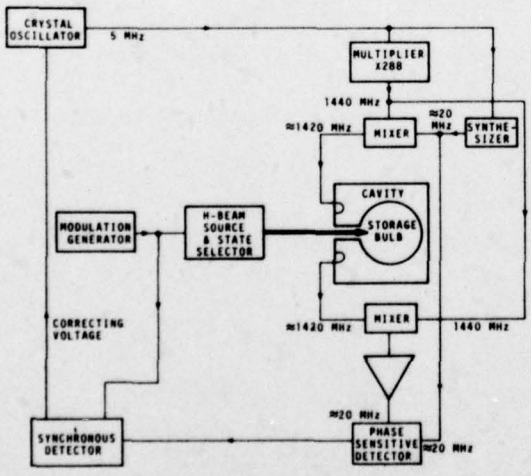

Fig. 3 Simplified block diagram of passive hydrogen maser frequency standard using dispersion locking [6,7].

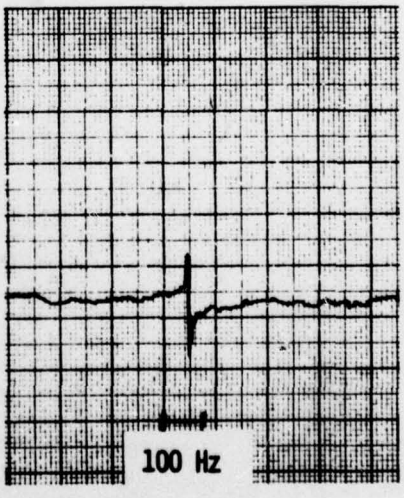

Fig. 4 Dispersion signal appearing at the output of the 20 MHz phase sensitive detector of Fig. 3 as the interrogation frequency is swept through the hydrogen resonance.

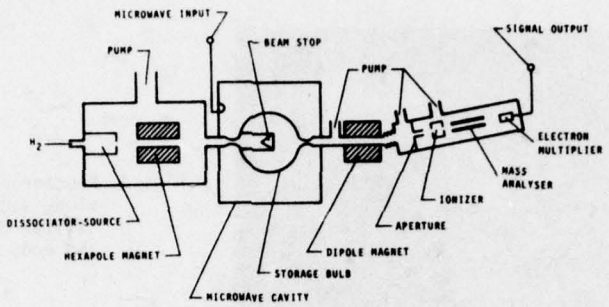

Fig. 5 Schematic of the hydrogen beam storage device [8].

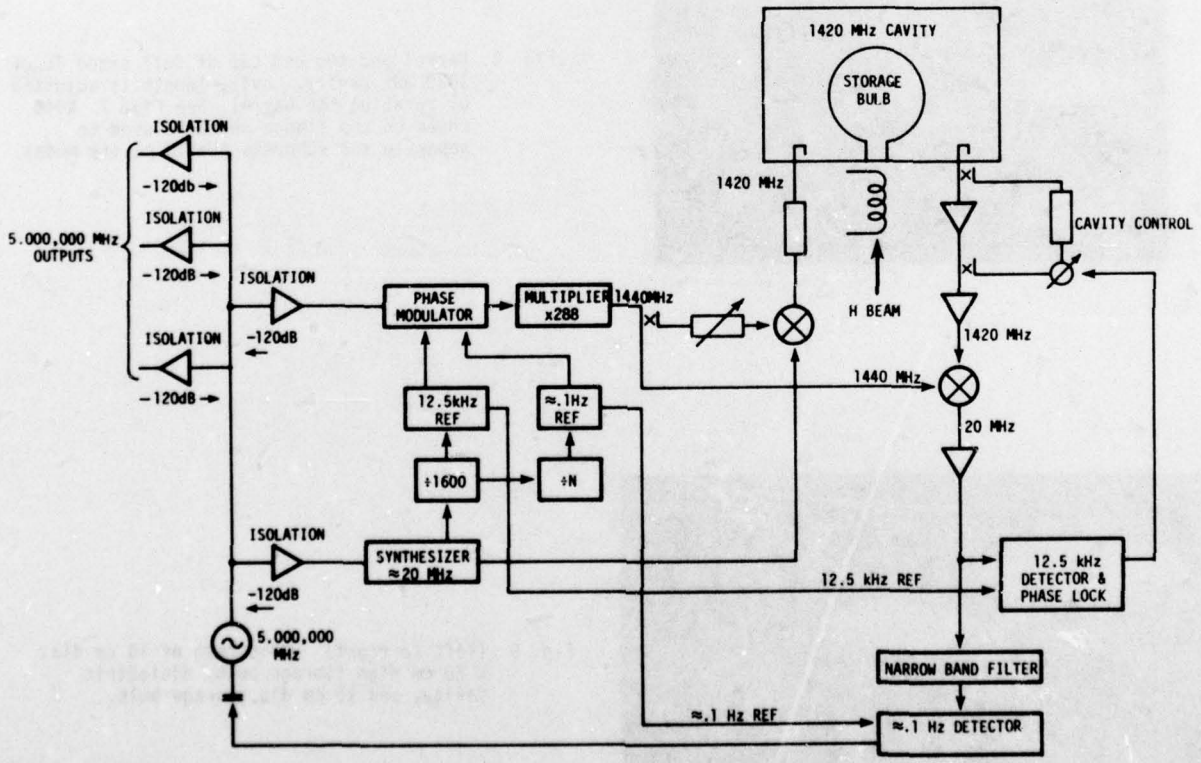

Fig. 6 Block diagram of our present passive hydrogen maser frequency standard.

Fig. 7 Photograph of small TE_{011} dielectric cavity along side a model full sized TE_{011} 1420 MHz cavity. Barrel of actual cavity is quartz and ends are aluminum.

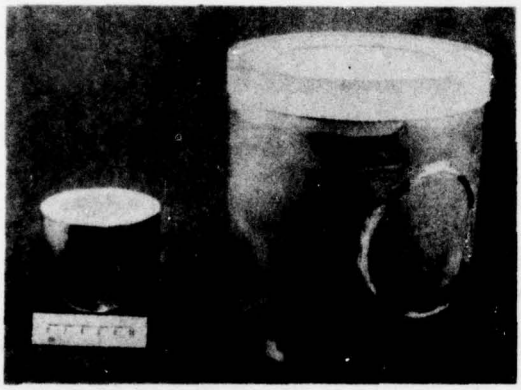

Fig. 8 Barrel and top end cap of full sized TE_{011} 1420 MHz cavity. Cavity length is adjusted by rotating the barrel. See Fig. 7. Note choke on top flange which is used to separate and suppress the TM cavity modes.

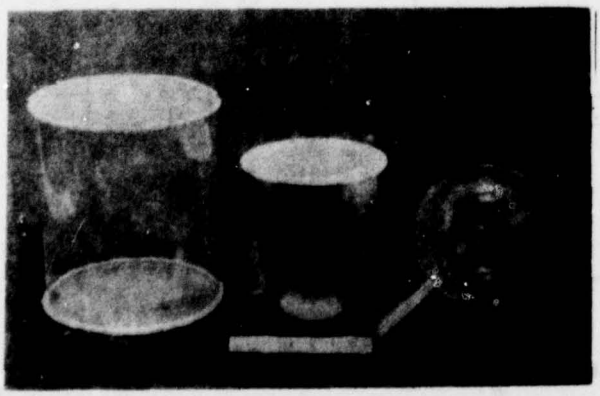

Fig. 9 (left to right) Photograph of 18 cm dia. x 20 cm high storage bulb, dielectric cavity, and 15 cm dia. storage bulb.

NASA ATOMIC HYDROGEN STANDARDS PROGRAM

— AN UPDATE —

Victor S. Reinhardt
Donald C. Kaufmann
William A. Adams
John J. DeLuca
NASA/Goddard Space Flight Center
Greenbelt, Maryland

and

Joseph L. Soucy
Bendix Field Engineering Corporation

Special Acknowledgement

The authors would like to make a special acknowledgement to Harry E. Peters. Harry Peters designed all of the frequency standards discussed in this paper, and until his recent retirement was the principal force behind NASA's hydrogen standards program.

Introduction

[illegible] Goddard Space Flight Center, NASA has had [illegible] whose principal task has been to develop and test field operable hydrogen masers. After successful results with an experimental maser (NX-1), the NP series of prototype masers was developed. Figure 1 shows a picture of an NP maser. These masers have been extensively tested in many years of field use around the world. This extensive field use, amounting to over 25 years of accumulated experience with the NP masers, allows us to draw some valuable conclusions as to the reliability and lifetime of the component parts of hydrogen masers under actual field conditions. The latter part of this paper will present reliability data on the NP masers and draw conclusions from this data.

The NASA program did not stop with the development of the NP series. Based on experience with the NP masers, two new experimental masers (NX-2 and NX-3) were built. Figure 2 shows NX-2 as well as the first experimental maser, NX-1. In this paper we will also compare the performance of the NP masers and the new NX masers. Presently, in a joint program with the Applied Physics Laboratory (APL) of Johns Hopkins University a new series of field operable hydrogen masers (NR series) is being developed. Some of the novel features of the NR masers will also be discussed.

Another task of the NASA program has been to develop atomic hydrogen primary frequency standards in order to calibrate our field operable hydrogen masers. Our goal is to develop a primary standard with a fractional accuracy of 10^{-14}. We are developing two such standards: a hydrogen beam frequency standard[2,3] and a Concertina Hydrogen Maser.[4] The hydrogen beam frequency standard is shown in Figure 2. Presently all effort on the beam standard is being directed towards developing a hydrogen detector with high signal to noise ratio. A palladium-silicon MOSFET detector being developed by our microelectronics division is showing promise.

The Concertina Maser is a variable volume hydrogen maser which uses an FEP teflon bellows as the variable volume storage bulb. Figure 3 shows the Concertina storage bulb in various states of elongation. We have achieved oscillation with the Concertina Maser, but haven't obtained a very good tuning factor as yet. Presently we are redesigning the Concertina Maser to remedy this situation.

We have included mention of the two calibrations standards for completeness. There will be no further mention of them in this paper.

NASA Maser Design and Performance

Before discussing NP maser reliability, we would like to discuss some of the noteworthy features of NASA masers and compare the performance of the NP and NX masers. Figure 4 shows the principal elements of a NASA hydrogen maser. Figure 5 shows a picture of some of these elements from an NP maser. The noteworthy features are as follows:

Large Hydrogen Source Bulb. The R.F. dissociator is a cylindrical bulb two inches in diameter by two inches high. The large size of the bulb enables it to run reliably with just convection cooling.

Palladium Purifier. To supply hydrogen to the R.F. Dissociator, a palladium purifier is used. In the NP masers, the purifier consists of a palladium-silver pellet brazed to stainless steel tubing. In order to wet the stainless steel tubing it is necessary to use a high temperature silver solder which sometimes alloys with the palladium pellet. In the NX and NR masers, the stainless steel tubing is nickel plated before brazing. This allows the use of lower temperature eutectic silver solder for the braze, eliminating the alloying problem and producing a more reliable bond.

State Selector. In the NX and NR masers, there is an electromagnetic quadrupole state selector. This state selector configuration has a high focussing efficiency allowing the use of smaller pumps and contributing to long pump life.

Replaceable Pumps. Both the NX and NR masers allow the ion pumps to be replaced without letting the masers up to air. The masers each use two 60 l/sec Varian Associates Noble Vac Ion pumps. Reduced hydrogen consumption should allow 15 to 20 years of pump life before replacement is required.[1]

Small Entrance Stem. The one inch diameter entrance stem reduces the size of holes in the magnetic shielding reducing inhomogeneity effects.

Magnetic Shields. The NP masers use a quadruple layer of Molypermalloy shielding which has a shielding factor of 800. In the NX and NR masers, a fifth shield has been added which consists of a rectangular box that forms part of the maser frame. This increases the shielding factor to 15,000.

Elongated Storage Bulb. The elongated cavity and the large cylindrical storage bulb yield a high filling factor[5], and a reduced magnetic inhomogeneity shift[6,7] as well as high line Q.[5]

Aluminum Cavity. The microwave cavity in NASA masers is aluminum whose high thermal expansion is put to use to tune the cavity by changing the cavity temperature. With use of aged thermistors in the temperature control loop, frequency stability is better than one part in 10^{14} over a one day period.[1]

Presently we are working on a new design for the cavity using a combination of low temperature coefficient materials and aluminum which will greatly reduce the temperature sensitivity of the cavity, but will still allow the cavity to be temperature tuned.

Electronics Package. All of the critical electronics is in a temperature controlled package between the inner and outer magnetic shields to minimize thermal instability effects from either the receiver system or the thermal control system. In the NP and NX masers, the receiver front end is a low noise amplifier to ensure good short term stability. In the NR maser, APL is adding an isolator to reduce coupling between the cavity and the low noise amplifier, and is adding an image reject filter to improve the receiver noise figure by 3 db.

Autotuner. Another feature of NASA masers is automatic flux tuning. Figure 6 shows a block diagram of the autotuner. The autotuner is described in detail in reference 5. In the NP masers, the flux tuning information is converted into a sign bit which is averaged and used to control the cavity frequency. In the NX maser, the autotuner also supplies magnitude information to the averager to take advantage of the improved crystal reference oscillators now available. In the NR masers, the autotuner will use a microprocessor which will also control all other key functions in the maser.

When the autotuner changes the maser flux during operation, a phase shift occurs due to amplitude to phase conversion. This phase shift, 10 to 20 ps in the NP masers, is large enough to severely degrade short term stability. In the NX maser we have reduced this phase shift to less than 1 ps with an amplitude to phase compensator. Figure 7 shows the phase shift with and without compensation. Notice that with compensation there is still a transient phase disturbance even though the net effect is zero. We are presently trying to reduce this disturbance by developing a system to change the flux slowly.

Since changing the maser flux disturbs maser operations, there is a possibility that the phase shift from high to low flux and from low to high flux will not be equal. This means that there may be a cumulative phase shift which would effect the accuracy of an autotuned hydrogen maser used as a primary standard. We performed an experiment to check this possibility, and found that the phase shifts cancelled to: 0.19 ps ±0.4 ps. For our autotuning system, this would produce a fractional frequency error of less than 1.7×10^{-15}, a negligible error for most applications.

Environmental Performance. Figure 8 summarizes the effects of environmental changes on the fractional frequency stability of NP and NX masers. The NP data was measured at Haystack Observatory[8], the NX data at Goddard Space Flight Center.

Reliability and Operating Life of NASA Masers

Since 1969, NP hydrogen masers have seen extensive field use around the world supporting many programs. Figure 9 shows the locations where NP masers have been in use, and Figure 10 lists some of the programs which were supported. In many instances, NP masers made multiple trips to the locations indicated in the map. Figure 11 lists the total number of trips and the mileage for each NP maser. During the past six years, the average NP maser has made 14 trips and has traveled 28 thousand miles. The point of all these statistics is that the field use of the NP masers in the past six years has been far flung and extensive, so that from the history of the NP masers during this period, we can draw conclusions as to the reliability of the component parts of hydrogen masers of the NASA design under fairly rugged conditions.

Figure 12 indicates the operational history of NASA masers. NX-I is included because of its long operation (since September, 1967) and as a comparison example of a NASA maser operating under laboratory conditions. Before going on to discuss failures, we would like to describe some of our relevant operating procedures and how we define a failure. NP masers were transported by air cargo or truck and experienced personnel were always sent with the masers to help set them up at remote sites. If travel was less than 8 hours, the masers were sent fully operating on storage battery power. For longer trips (up to 21 days), NP masers were sent with only its pumps under power. On the one trip NX-1 made, it was totally dismantled. After masers were shipped, it was sometimes necessary to replace burnt out display bulbs or tighten loose cables. This will be considered part of normal maintenance required due to handling.

In discussing failures, we shall divide them into two classes: electronic and non-electronic failures. Since standard commercial electrical components are used in NASA masers, and in many cases breadboard electronics, we do not consider our electronics failures relevant to any considerations for future masers. We will therefore not consider electronics failures. For completeness, however, Figure 13 indicates these failures.

Non-electronic failures and major modifications in NX-1 are shown in Figure 14. The length of down time in this chart is not necessarily an indication of the severity of the failure; many times personnel who could repair the masers were not available or were only available on a limited basis. Notice that the failure rate of NP-4 was high compared with the other masers; NP-4 had continual vacuum problems, either from a slow leak or a contaminated system which could not be found. This caused the maser output to decay slowly, indicating that good vacuum conditions are indeed essential to long term maser operation.

Using our operational history we can draw the following conclusions as to the reliability and lifetime of NASA maser components:

Hydrogen Source Bulb. The large diameter pyrex bulb runs reliably for many years if the vacuum and hydrogen supply are clean. In both NP-1 and NP-2, the source bulb has

lasted greater than 7 years, and in NP-3, 4-1/2 years until its bulb cracked. In NP-3 after the purifier was repaired, due to some contamination in the hydrogen line and a bad source oscillator, the source ceased to produce atomic hydrogen. The source cleaned itself up, however, after running several days on clean hydrogen.

Storage Bulb. As a matter of procedure, storage bulbs were recoated whenever masers were taken apart, so some of the recoatings shown are not because of lifetime limitations. NP-4 indicates that vacuum leaks degrade storage bulb lifetime. When the storage bulbs of NP-3 and NP-4 were replaced, it was noted that the teflon coating failed the water drop test in a spot opposite the entrance stem. Since the NP masers have a single vacuum system and contamination products from outside the bulb can be exposed to the storage bulb only from near the source region, this bad spot does not necessarily mean that contamination products are coming from the source bulb itself. The NX masers have a double vacuum system, so future results may isolate the cause of this bad spot. In NP-3, when the bulb was replaced there was no indication of a drop in maser power, so this recoating cannot be counted as an indication of the bulb lifetime in a properly operating maser. Even counting this, for NP-1, NP-2, and NP-3, we have an average storage bulb lifetime of greater than 6 years.

Palladium Purifier. Both purifier failures were caused by leaks opening up in the purifiers. As mentioned previously, our new fabrication method should solve this problem. Even with this, the existing design lasted, on the average, for greater than 6.8 years.

Ion Pumps. The ion pumps worked reliably in NP-1 and NP-3 for greater than 6 or 7 years. In NP-2, the failure was a vacuum leak which had nothing to do with the pump itself. Pump pressure in the NP masers is typically 3.6 to 4.8×10^{-7} torr, so at these pressures many years of reliable operation can be expected. In NX-2 and NX-3, operating pressure is 1 to 2×10^{-7} torr. When NX-2 and NX-3 were run at approximately 5 times normal pressure, in six months NX-2 developed a shorted pump element. This indicates that one should run at low pressures to ensure reliable pump operation.

Conclusions

Experience with NASA field operable masers indicates that one can obtain many years of reliable operation with hydrogen masers, even in rugged conditions. Projecting to possible spacecraft use, our data indicate that the technology for reliable space qualified hydrogen masers is already available.

References

1. Harry E. Peters, "Characteristics of Advanced Hydrogen Maser Frequency Standards," Proceedings of the Fifth NASA/DOD Precise Time and Time Interval Planning Meeting, NASA Doc. X-814-74-225, pg. 283 (Greenbelt, 1973).

2. Harry E. Peters, "Topics in Atomic Hydrogen Standard Research and Applications," Proceedings of the Frequency Standards and Metrology Seminar (Quebec, 1971).

3. Harry E. Peters, "Hydrogen as an Atomic Beam Standard," Proceedings of the 26th Frequency Control Symposium, USAEC (Ft. Monmouth, 1972).

4. Harry E. Peters, "The Concertina Hydrogen Maser," Proceedings of the 29th Frequency Control Symposium (Atlantic City, 1975).

5. H. E. Peters, T. E. McGunigal, and E. H. Johnson, "Hydrogen Standards Work at Goddard Space Flight Center," Proceedings of the 22nd Frequency Control Symposium, USAEC (Atlantic City, 1968).

6. S. Crampton and H. Wang, "Density-Dependent Shifts of Hydrogen Maser Standards," Proceedings of the 29th Frequency Control Symposium, USAEC (Atlantic City, 1975).

7. V. Reinhardt and H. Peters, "An Improved Method for Measuring the Magnetic Inhomogeneity Shift in Hydrogen Masers," Ibid.

8. A. E. Rogers, Private Communication. (Haystack Observatory, 1976).

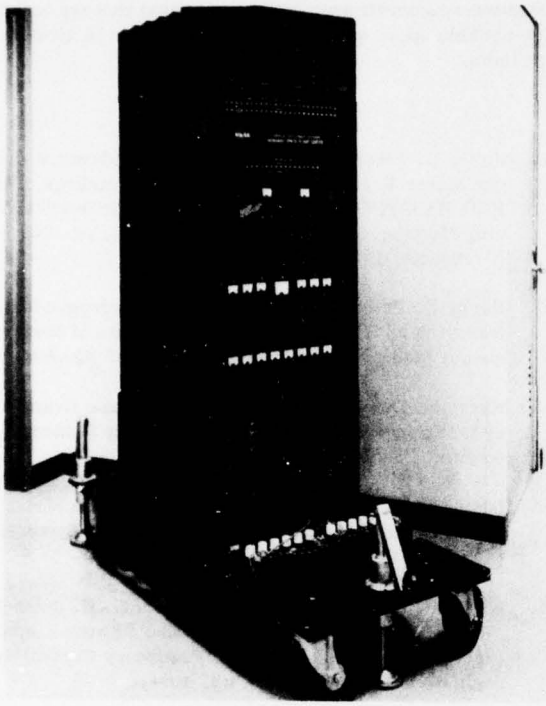

Figure 1.
An NP Hydrogen Maser

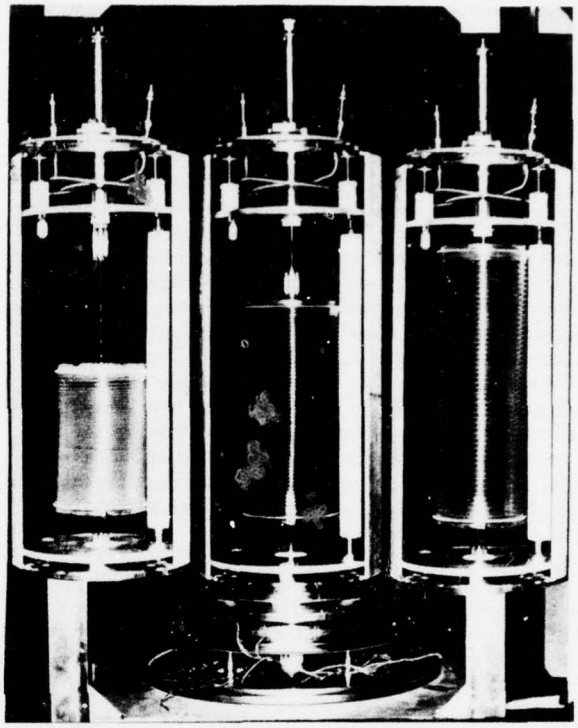

Figure 3.
The Concertina Storage Bulb in Various Stages of Elongation

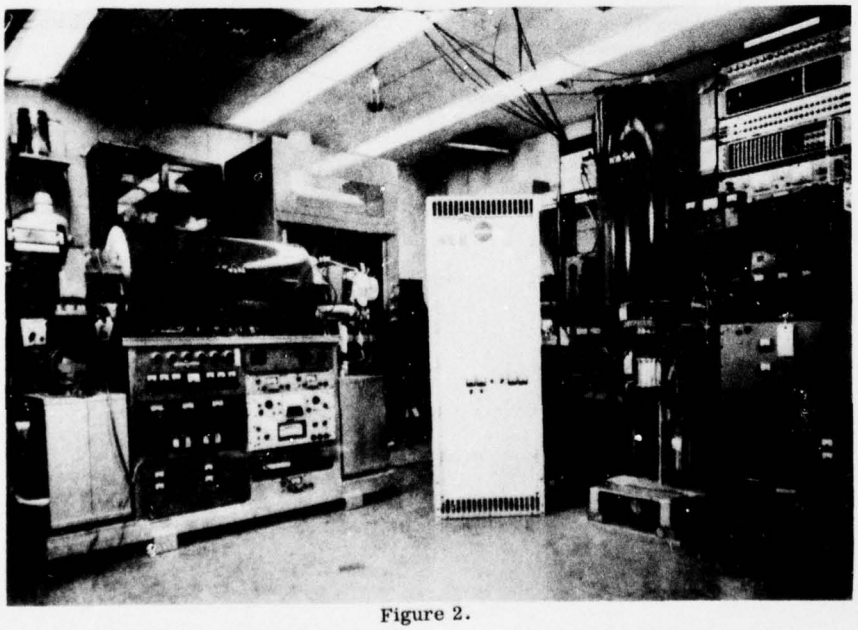

Figure 2.

NASA Hydrogen Standards: (from right to left) NX-1, NX-2, and the Hydrogen Beam Standard

PRINCIPAL ELEMENTS OF THE NASA HYDROGEN MASER

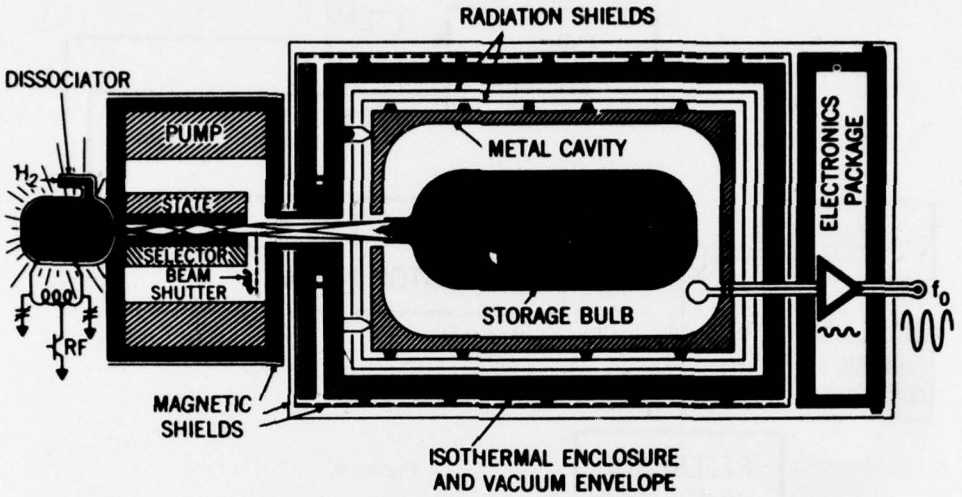

Figure 4.

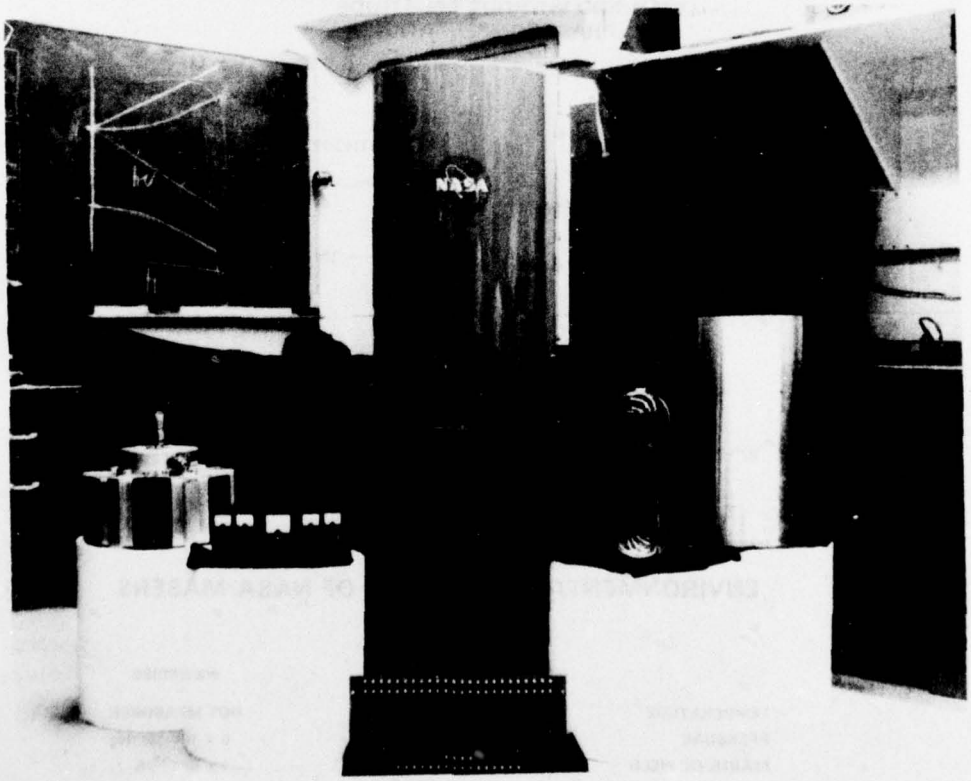

Figure 5. The Parts of an NP Maser

ELEMENTARY AUTO TUNER BLOCK DIAGRAM

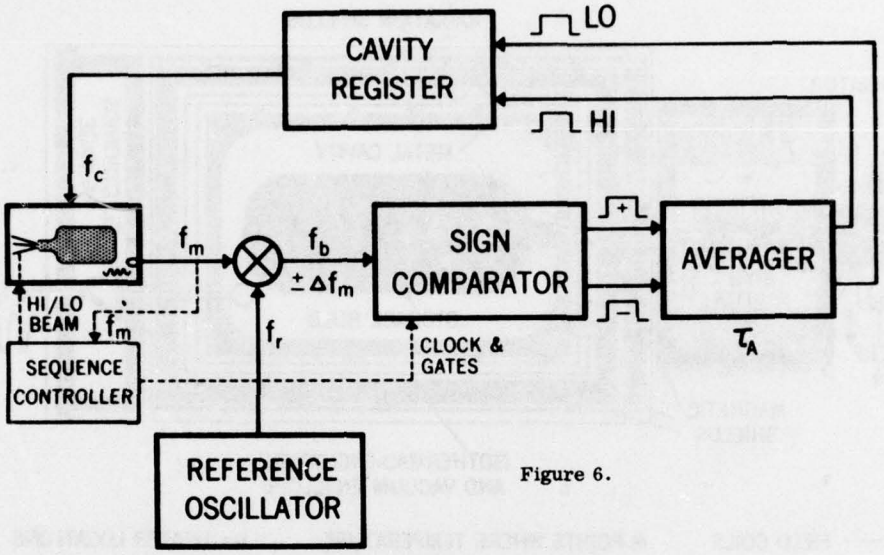

Figure 6.

AUTOTUNING PHASE SHIFT WITH AND WITHOUT AMPLITUDE TO PHASE COMPENSATION

Figure 7.

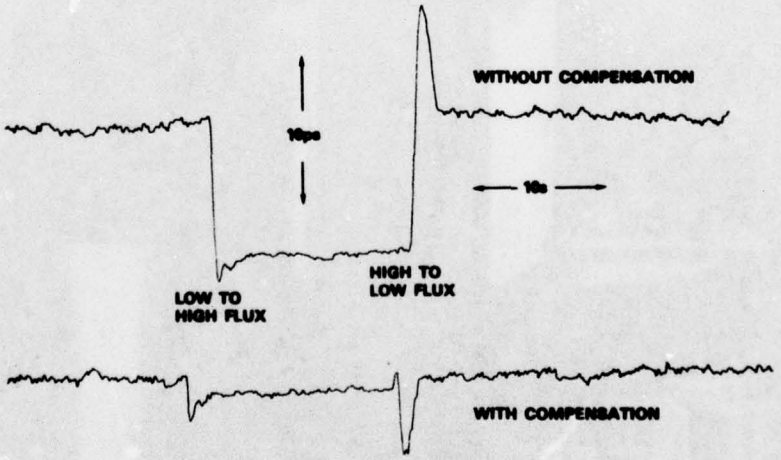

ENVIRONMENTAL SENSITIVITY OF NASA MASERS

	NP SERIES	NX SERIES
TEMPERATURE	2×10^{-14}/°C	NOT MEASURED
PRESSURE	$< 4 \times 10^{-14}$/"Hg	5×10^{-15}/"Hg
MAGNETIC FIELD	5×10^{-12}/G	1×10^{-13}/G

Figure 8.

PROGRAMS SUPPORTED BY NASA BUILT NP TYPE HYDROGEN MASERS

- STUDY OF CELESTIAL WATER SOURCES
- DOUBLE DIFFERENTIAL VERY LONG BASE LINE INTERFEROMETRY (DDVLBI)
- MM-71 TRACKING AND CALIBRATION EXPERIMENT
- ATOMIC CLOCK RELATIVITY EXPERIMENT IN HIGH FLYING AIRCRAFT
- QUASAR PATROL
- POLAR MOTION MEASUREMENTS
- STAR MAPPING
- DETERMINATION OF EARTH'S ROTATIONAL VARIATIONS
- SENSITIVITY OF H-MASERS TO PRESSURE' TEMPERATURE AND MAGNETIC FIELD VARIATIONS.

Figure 10.

H-MASER	NO. OF TRIPS	MILEAGE
NX	1	400
NP-1	14	27,400
NP-2	16	50,700
NP-3	16	20,200
NP-4	10	12,600
	57	111,300

Figure 11. Number of Trips and Miles Traveled by NASA Masers

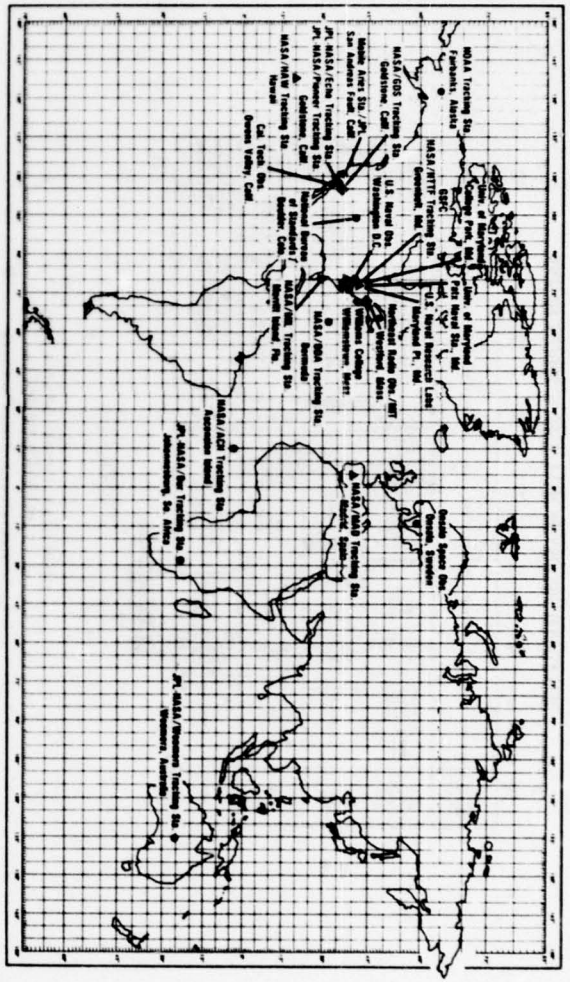

Figure 9. Locations of NP Maser Field Use

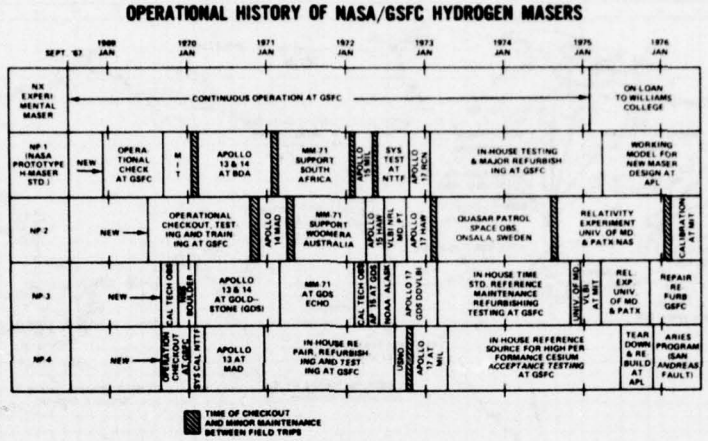

Figure 12.

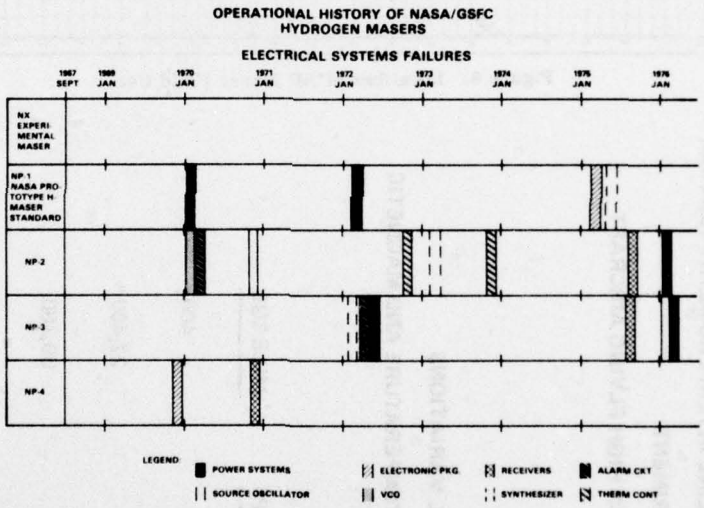

Figure 13.

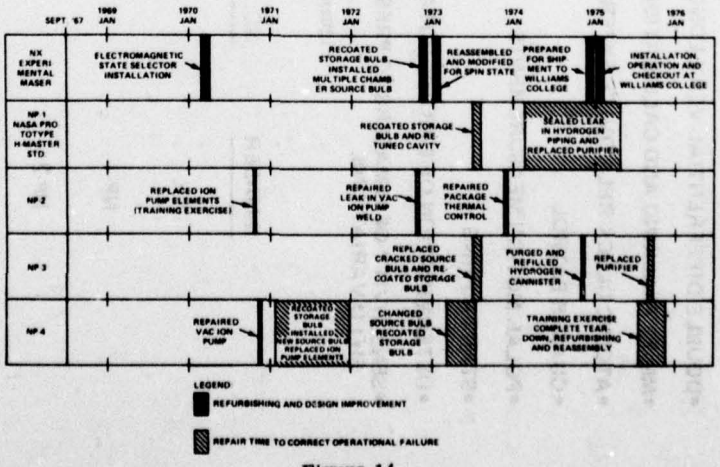

Figure 14.

A STUDY TO IDENTIFY HYDROGEN MASER FAILURE MODES*

A. E. Popa, H. T. M. Wang, W. B. Bridges, A. N. Chester, J. E. Etter, and B. L. Walsh**
Hughes Research Laboratories
Malibu Canyon Road
Malibu, California 90265

Summary

Technical problem areas are presented that may adversely affect the reliability of extended spaceborne operation of a hydrogen maser frequency standard in the Navstar Global Positioning System. Included are failures that have occurred in past maser designs even though such failures are now understood and could be circumvented in future designs. It is concluded that all the failure mechanisms are amenable to space qualification engineering. The greatest potential problem areas are dissociator stability and atom production, storage bulb lifetime in a space radiation environment, and radiation damage to the electronics subsystem, particularly sensors.

Introduction

This study was undertaken to identify technical problem areas that may adversely affect the reliability of spaceborne operation of a hydrogen maser frequency standard in the Navstar Global Positioning System (GPS). From this analysis of existing maser designs, areas for design improvement can be identified.

In this paper we attempt to list all possible failure mechanisms that may occur in both spaceborne and ground-based hydrogen masers. Included are failures that have occurred in past maser designs, even though such failures are now understood and could be circumvented in future designs.

Physics Unit Failure Modes

Tables 1 and 2 list the various components that comprise the physics unit of a hydrogen maser. Associated with each component or element are one or more modes of failure that have been observed in past maser designs or that we project as possibilities for a spaceborne maser design. For each failure mode several possible causes are listed; the asterisks indicate known chronic cases.

Hydrogen supply and regulation components are low risk items because of the past experience with similar space-qualified gas supply systems. Careful engineering of the final hardware design is all that is required here.

Difficulties with the rf discharge plasma hydrogen dissociator have been common in the past, but recent experience has improved typical operating life to three or more years. Figure 1 is a schematic representation of a typical spherical glass bulk dissociator plasma with capacitively coupled electrodes. The power is fed into the bulb by displacement current through the glass walls to the conducting hydrogen plasma within.

Table 1. Principal Failure Modes – Physics Unit (1)

4416-19

COMPONENT	FAILURE MODE	POSSIBLE MECHANISM
H_2 SUPPLY	LOSS OF H_2 FLOW CONTROL	VALVE HEATER BURN-OUT PRESSURE SENSOR MALFUNCTION CONTROL SYSTEM FAULT GAS LEAK POWER LOSS
DISSOCIATOR	DISCHARGE CEASES	*IMPEDANCE CHANGE THRU CONTAMINATION *WALL EROSION RF DRIVER FAILS CONTROL CIRCUIT FAILS POWER LOSS
	H ATOM PRODUCTION DECLINES ("WHITES OUT")	*WALL RECOMBINATION GAS CONTAMINATION *WALL SPUTTERING SERVO CONTROL FAILURE
COLLIMATOR	DECREASED THROUGHPUT OF COLLIMATED ATOMS	MECHANICAL CRACKING WALL EROSION WALL CONTAMINATION CAUSING RECOMBINATION *MISALIGNMENT
STATE SELECTOR	DECREASED THROUGHPUT OF FOCUSSED ATOMS	LOSS OF POLE STRENGTH MISALIGNMENT

*HIGHEST RISK ITEMS

Table 2. Principal Failure Modes – Physics Unit (2)

4416-20

COMPONENT	FAILURE MODE	POSSIBLE MECHANISM
STORAGE BULB	LOSS OF SIGNAL AND/OR STABILITY	*DECREASED STORAGE TIME BY TEFLON IRRADIATION DAMAGE *CHANGE IN WALL SHIFT BY RADIATION DAMAGE *MECHANICAL FRACTURE MISALIGNMENT DURING LAUNCH MICROWAVE LOSSES DUE TO BULB IRRADIATION
MICROWAVE CAVITY	LOSS OF SIGNAL AND/OR STABILITY	LOSS OF CAVITY Q THRU COATING SEPARATION STRESSES ON CAVITY
ION PUMP	LOSS OF VACUUM	*MECHANICAL STRESS (Ti HYDRIDE) *HIGH VOLTAGE SHORTS (ZERO G)
VACUUM SYSTEM	LOSS OF VACUUM	OUTGASSING VIRTUAL LEAKS DISCHARGE SPUTTERING
MAGNETIC SHIELDING	LOSS OF STABILITY	EXCESSIVE EXTERNAL MAGNETIC INTERFERENCE
THERMAL SUBSYSTEM	LOSS OF TEMPERATURE UNIFORMITY OR STABILITY*	POWER LOSS *AGING OF THERMAL SENSORS CONTROL CIRCUIT FAILURE STRESS-INDUCED MECHANICAL FRACTURE
MAGNETIC FIELD AND DEGAUSSING COILS	LOSS OF STABILITY	COIL BURN-OUT CONTROL CIRCUIT FAILURE POWER LOSS

*HIGHEST RISK ITEMS

Figure 2 illustrates the potential distribution near the glass walls, showing the potential fall or "wall sheath" necessary to satisfy boundary conditions on wall current. The wall sheath has the effect of increasing the energy with which positive ions strike the wall; this, in turn, greatly increases the yield of wall material sputtered by the incident ions. Figure 3 shows the typical steep dependence of sputtering yield

*This work was supported by the Naval Research Laboratories under Contract N00014-75-C-1149, Robert B. Moore, Scientific Officer.

**Hughes Aircraft Company, Space and Communications Group, P.O. Box 92919, Los Angeles, CA 90009.

on ion energy for the low energies typical of the wall sheath. Only a one or two volt change in wall sheath can cause an order of magnitude change in the sputtered material yield.

The improvements in dissociator bulb life observed empirically in recent years can probably be attributed to

- Increase in bulb size
- Better coupling into the plasma
- Lower drive power.

These three factors serve to decrease the displacement current density through the walls and decrease the energies of the ions incident on the bulb walls. Further improvement may be possible by further changes in configuration and choice of wall materials.

While the multitube glass collimators themselves have exhibited little difficulty, mechanical strains in the region adjacent to the collimator often produce problems in conventional designs. Careful attention to mechanical design and vacuum interlocks that prevent large transient pressure differentials across the collimator bundle during startup should eliminate this potential failure point.

No areas of high risk are associated with the maser state selector magnet.

The principal potential cause of failure resulting from the hydrogen storage bulb is degradation of the Teflon© coatings from the space radiation environment. Increased recombination rates will occur if the fluorine bonds are broken to produce more chemically active sites. Microcracks in the coating which expose the underlying SiO_2 will also increase the probability of recombination. Changes in the wall shift may be produced by radiation, although this has not been documented experimentally. We have performed dose calculations on a typical maser design in the Navstar GPS orbit and have obtained values of 7000 rads (Tf) for seven years in the natural background and 18,000 rads (Tf) if a nuclear event is added. These values are known experimentally not to cause any gross degradation of Teflon. ©

A spaceborne maser development program will require accelerated radiation testing to determine if any wall shift and linewidth changes occur for the radiation dose encountered in the Navstar orbit. We have found x-ray diffraction measurements can detect slight changes in Teflon © below the threshold of gross radiation damage. For example, thin Teflon © solar cell covers exposed to doses several times greater than that encountered by Navstar show a development of crystallinity as illustrated in Fig. 4. Whether changes observed by x-ray diffraction will correlate with degradation in maser performance remains to be determined.

The microwave cavity structure offers small failure risk. Substantial weight savings through the use of advanced composite materials technology will indirectly contribute to the reliability of the entire maser by reducing structural stresses.

The ion vacuum pump is a well-developed component. However, a zero-g environment offers the potential hazard of free-floating particles which can short the high voltage elements. Special attention to mechanical design will be required to keep stresses caused by conversion of titanium to titanium hydride from creating distortions that would short out internal electrodes.

Of the remaining components in Table 1, only the thermal sensors are likely to be a problem in the spaceborne maser design. Calibration drift with radiation dose or thermal cycling will have to be investigated carefully.

Electronics Unit Failure Modes

All electronic subsystems are subject to failure mechanisms that are generally well known. Thermal fatigue, chemical diffusion, and electromigration are particular hazards for devices dissipating high power, while contamination and corrosion, shorts (from loose metallic particles) and bond failures are encountered by all electronic components.

In Table 3 the principal failure modes for the hydrogen maser electronics unit are listed. The highest risk is associated with space-radiation damage and inadequate thermal sinking of the higher power solid state devices. In the past, point contact devices, such as Schottky mixers, have been subject to contact failure in vibration; however, recent work at Hughes and other laboratories has produced techniques to greatly reduce the occurrence of this potentially serious problem. Many electronic problems can be eliminated by careful inspection as shown in the Scanning Electron Microscope (SEM) pictures, Figs. 5, 6, and 7. Figure 5 is a mechanically stable Schottky diode whisker contacting a gold electrode imbedded in the semiconductor surface. Figure 6 shows a blunted whisker that has mechanically moved off the gold electrode causing a failure. The SEM picture shown in Fig. 7 graphically illustrates the result of electromigration. In this case potassium contamination left from wafer processing has migrated to the whisker causing diode failure.

Table 3. Principal Failure Modes — Electronics Unit (3)

4416-7

COMPONENT	FAILURE MODE	POSSIBLE MECHANISM
CRYSTAL OSCILLATOR	EXCESSIVE FREQUENCY AGING LOSS OF SIGNAL	*RADIATION DAMAGE TO QUARTZ VIBRATION INDUCED FRACTURES
SYNTHESIZER	DEGRADED STABILITY	RADIATION DAMAGE TO JUNCTIONS
VARACTOR	DEGRADED OUTPUT SIGNAL LEVEL	RADIATION DAMAGE INCREASES REVERSE LEAKAGE CURRENT
MIXERS	DEGRADED NOISE FIGURE LOSS OF SIGNAL	*RADIATION DAMAGE INCREASES SERIES RESISTANCE POINT CONTACT FAILURE IN VIBRATION
DISSOCIATOR DRIVER AND POWER OSCILLATORS	OUTPUT POWER DEGRADATION	*THERMAL AGING

*HIGHEST RISK ITEMS

Conclusions

Although there are many difficult problem areas that may adversely affect the reliability of a long lived spaceborne hydrogen maser frequency standard, all are amenable to space qualification engineering. We feel the greatest potential problem areas at present are

© is DuPont trademark.

- Dissociator stability and atom production
- Storage bulb lifetime in a space radiation environment
- Radiation damage to the electronics subsystem components, particularly sensors.

Acknowledgments

We began our hydrogen maser studies by visiting a number of organizations active in the maser field and related activities. Specifically, we would like to acknowledge contributions from the following groups: H. E. Peters (NASA, retired) and V. S. Reinhardt at the NASA Goddard Space Flight Center; N. F. Ramsey and D. Larson at Harvard University; our own divisions at Hughes Aircraft Company working in related areas of technology; R. Sydnor and P. Dachel at the Jet Propulsion Laboratory of California Institute of Technology; R. L. Easton, V. Folen, and R. B. Moore at the Naval Research Laboratories; H. Hellwig and F. Walls of the Boulder Laboratories of NBS; R. F. C. Vessot and M. W. Levine at Smithsonian Astrophysical Observatory; and S. B. Crampton and H. T. M. Wang (now with Hughes Research Laboratories) at Williams College.

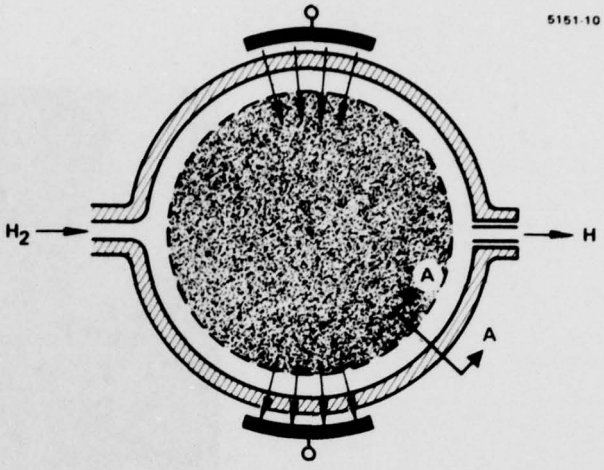

Fig. 1.
Schematic representation of the plasma within an rf excited dissociator showing displacement current through the walls under the electrodes.

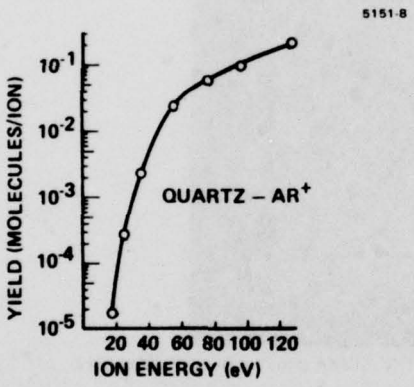

Fig. 3.
Sputtering yield of SiO_2 molecules from a SiO_2 surface under bombardment of low energy argon ions.

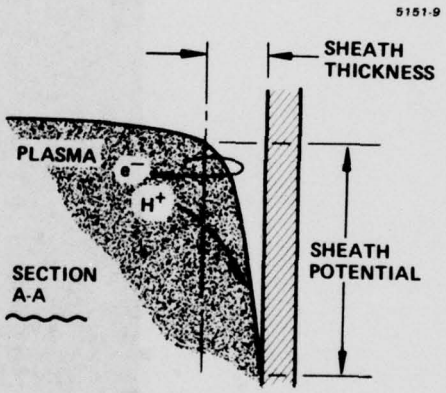

Fig. 2.
Plot of potential versus radius in a section through the plasma sheath near the glass wall.

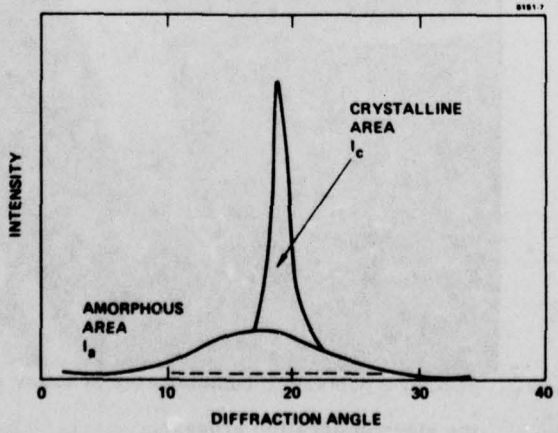

Fig. 4. X-ray diffraction pattern of radiation-damage Teflon solar cell covers.

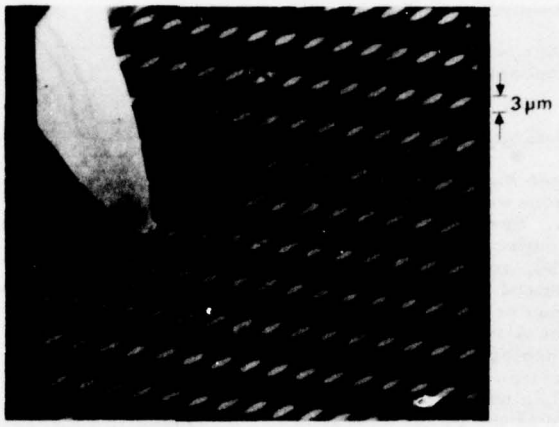

Fig. 5. SEM of a mechanically stable Schottky point contact.

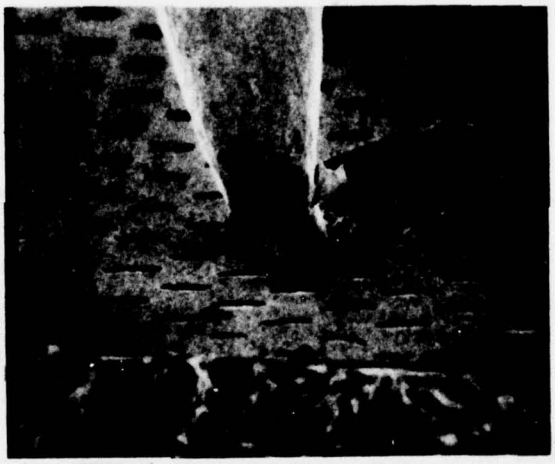

Fig. 6. SEM of a blunted Schottky diode point contact that has mechanically failed.

Fig. 7. SCM of a potassium contaminated Schottky diode illustrating the electromigration process.

INDEX OF AUTHORS

SPECIFICATIONS AND STANDARDS GERMANE TO FREQUENCY CONTROL

Institute of Electrical and Electronic Engineers

Order through: Institute of Electrical and Electronic Engineers
345 E. 47th Street
New York, New York 10017

176-1949 Piezoelectric Crystals (ANSI C83.3-1972) (Reaff 1971) $ 4.00

177-1966 Piezoelectric Vibrators, Definitions and Methods of Measurement for (ANSI C83.17-1970) $ 4.00

178-1958 Piezoelectric Crystals, Determination of the Elastic, Piezoelectric, and Dielectric Constants of, also, the Electromechanical Coupling Factor (ANSI C83.23-1960) $ 3.50

179-1961 Piezoelectric Ceramics, Measurements of (ANSI C83.24-1962) (Reaff 1971) $ 3.50

180-1962 Ferroelectric Crystal Terms, Definitions of $ 3.00

319-1971 Piezomagnetic Nomenclature $ 4.00

Electronic Industries Association

Order through: Electronic Industries Assn.
2001 Eye Street, N.W.
Washington, D.C. 20006

(a) Holders and Sockets

RS-192-A, Holder Outlines and Pin Connections for Quartz Crystal Units. (Standard Dimensions for older types.) $ 5.00

RS-367, Dimensional and Electrical Characteristics Defining Receiver Type Sockets. (Includes crystal sockets.) $15.00

RS-417, Crystal Outlines (Standard dimensions and pin connections for current quarts crystal units - 1974) $ 5.80

(b) Production Tests

RS-186-D, Standard Test Methods for Electronic Component Parts $ 5.20

(c) Application Information

Components Bulletin #6, Guide for the Use of Quartz Crystal Units for Frequency Control $ 3.60

International Electrotechnical Commission

Order through: American National Standards Institute
1430 Broadway
New York, New York 10018

IEC Publication 122-1 (1962) Quartz Crystal Units for Oscillators
Section 1, Standard Values and Conditions.
Section 2, Test Conditions
including Amendments 1 and 2 $12.10
Amendment 1 (1967) $ 1.05
Amendment 2 (1969) $ 1.00

IEC Publication 122-2 (1962) Quartz Crystal Units for Oscillators,
Section 3, Guide in the Use of Quartz Oscillator Crystals, including Amendment 1 $13.30
Amendment 1 (1969) $ 1.05

IEC Publication 122-3 (1962) Quartz Crystal Units for Oscillators,
Section 4, Standard Outlines, including Supplements 122-3A, 122-3B and 122-3C $20.70

IEC Publication 283 (1968) Methods for the Measurement of Frequency and Equivalent Resistance of Unwanted Resonances of Filter Crystal Units $ 5.25

IEC Publication 302 (1969) Standard Definitions and Methods of Measurement for Piezoelectric Vibrators Operating Over the Frequency Range up to 30 MHz. $ 9.45

IEC Publication 314 (1970) Temperature Control Devices for Quartz Crystal Units, including 1st. Supplement 314A (1971) $22.55

IEC Publication 314A (1971) 1st Supplement to 314 (1970) $11.00

IEC Publication 368 (1971) Piezoelectric Filters, including Supplement 368A $24.70

IEC Publication 368A (1973) 1st Supplement to Publication 368 (1971) $15.25

IEC Publication 368B (1975) 2nd Supplement to Publication 368 (1971) $16.00

IEC Publication 444 (1973) Basic Method for the Measurement of Resonance Frequency and Equivalent Series Resistance of Quartz Crystal Units by Zero Phase Technique in a π - Network $12.10

Department of Defense

Order through: Naval Publication and Form Center
5801 Tabor Avenue
Philadelphia, PA 19120

MIL-C-3098 Crystal Unit, Quartz, General Specification For

MIL-H-10056 Holders (Enclosures), Crystal, General Specification For

MIL-STD-683 Crystal Units, Quartz; And Holders, Crystal

MIL-C-39020 Crystal Units, Quartz Established Reliability, General Specification For

MIL-F-28734 Frequency Standards, Cesium Beam, General Specifications For

MIL-O-55310 Oscillators, Crystal, General Specification For

MIL-F-18327 Filters, High Pass, Low Pass, Band Pass, Band Pass Suppression and Dual Functioning, General Specification For

MIL-O-39021 Oven, Crystal, General Specification For

INDEX TO THE PROCEEDINGS OF THE FREQUENCY CONTROL SYMPOSIUM

1956 (10TH) TO 1976 (30TH)

This index consists of a subject index and an author index. Each paper has been assigned to one of twelve categories. The subject categories are as follows:

1. Fundamental Properties of Natural and Synthetic Piezoelectric Crystals
2. Theory and Design of Piezoelectric Resonators
3. Radiation Effects on Resonators
4. Resonator Processing Techniques and Aging
5. Filters and Surface Wave Devices
6. Quartz Crystal Oscillators and Frequency Control Circuitry
7. Quantum Electronic Frequency Standards (Microwave Frequencies)
8. Quantum Electronic Frequency Standards (Visible and Infrared Frequencies)
9. Frequency and Time Coordination and Distribution
10. Applications of Frequency Control Devices
11. Measurements and Specifications
12. Other Topics

The papers are numbered according to the following numbering system:

first number = subject category

second number = symposium number

third number = page number of the first page of the paper

For example, paper number 11-24-301 is listed under category 11 - Measurements and Specifications, it is in the Proceedings of the 24th Symposium, and the paper starts on page 301 of this Proceedings volume.

The papers are listed first according to the subject categories. Within each subject category, the papers are listed in the the order of the Proceedings volume numbers, then under each Proceedings volume, according to the page numbers. (There were no Proceedings published prior to the 10th Symposium.)

In the author index the names of the authors are listed alphabetically; and for each author, the papers are listed chronologically according to the Proceedings volume number.

This index is intended to be revised and updated periodically. Please send comments and corrections to: John Vig, US Army Electronics Technology and Devices Laboratory, ATTN: DRSEL-TL-MF, Ft. Monmouth, NJ, 07703 or telephone (201) 544-4275 or (201) 544-4805.

SUBJECT INDEX

CATEGORY 1:

Fundamental Properties of Natural and Synthetic Piezoelectric Crystals

CATEGORY 1 (Cont'd):

1-26-106 Observations on the Mechanical Strain in Quartz Crystals under Electric Field using Strain-Gauge Instrumentation and Their Application for Determining the Goodness of Raw Quartz Crystals - R. Parshad and V. R. Singh, National Physics Lab., India

1-28-8 Measurement of Nonlinear Elastic, Piezoelectric, Dielectric Coefficients of Quartz Crystal. Applications - R. Besson, University of Besançon

1-28-117 Defects in Synthetic Quartz Crystal and Their Influences on the Electrical Characteristics of Quartz Crystal Resonator - J. Asahara, K. Takazawa, H. Yazaki, J. Okuda, N. Asanuma, K. Nagai, Toyo Communications Equipment Co., Ltd.

1-28-125 Analysis of Synthetic Quartz for Stringent Frequency Versus Temperature Applications - L. Conlee, D. Reifel, Motorola, Incorporated

1-28-129 Characterization of Cultured Quartz for Use in Medium Precision AT-Cut Quartz Resonators - J. H. Sherman, Jr., General Electric Company.

1-29-98 Production and Perfection of "r-Face" Quartz - R. L. Barnes, E. D. Kolb, P.L. Key and R. A. Laudise, Bell Laboratories and E. E. Simpson and K. M. Kroupa, Western Electric Company

1-29-139 New Piezoelectric Materials which Exhibit Temperature Stability for Surface Waves - R. W. Weinert, T. J. Isaacs, Westinghouse Research Laboratories

1-29-143 Temperature Stable Materials for SAW Devices - T. E. Parker, M. B. Schulz, Raytheon Research Division and H. Wichansky, ECOM

1-29-211 Influence of the Inclusions in Synthetic Quartz Crystal on the Electrical Characteristics of Quartz Crystal Resonator - J. Asahara, E. Yazaki, K. Takazawa and K. Kita, Toyo Communication Equipment Company, Ltd.

1-30-71 Secondary Ferroics and Domain-Divided Piezoelectrics - L. E. Cross and R. E. Newnham, Pennsylvania State University

1-30- New Temperature Compensated Materials with High Piezoelectric Coupling - P. H. Carr, Air Force Cambridge Research Laboratories

CATEGORY 2:

Theory and Design of Piezoelectric Resonators

2-10-1 The Piezoelectric Survey of Strain Patterns in Thickness Shear Quartz Resonators - K. S. Van Dyke, Wesleyan University

2-10-10 Mathematical Theory of Vibrations of Elastic Plates - R. D. Mindlin, Columbia University

2-10-46 Frequency Temperature Behavior of AT-Cut Quartz Resonators - A. R. Chi, Frequency Control Branch, SCEL

2-10-182 Some Phenomena in VHF Crystal Units - E. Hafner, Frequency Control Branch SCEL

2-11-1 Mathematical Theory of Vibrations of Elastic Plates - R. D. Mindlin, Columbia University

2-11-41 Strain Patterns in Thickness-Shear Quartz Resonators - K. S. Van Dyke, Wesleyan University

2-11-78 *A Study of VHF Crystal Units* - Erich Hafner, Frequency Control Branch, USASEL

2-12-2 Mathematical Theory of Vibrations of Elastic Plates and Bars - R. D. Mindlin, Columbia University.

2-12-9 Frequency Spectra in Quartz Resonators - C. R. Mingins, R. W. Perry and D. W. Macleod, Lowell Technological Institute

2-13-53 Some New Results in the Mathematical Theory of Vibrations of Crystal Plates - R. D. Mindlin

2-13-54 Modes of Vibration of Quartz Crystal Resonators Investigated by Means of the Probe Method - I.Koga, H. Fukuyo and J. E. Rhodes

2-13-207 Quartz Crystals at Low Temperatures - P. A. Simpson and A. H. Morgan

2-14-35 Influence of Lattice Parameters on the Properties of Crystal Resonators - W. P. Mason

2-14-53 Measurements of the Vibrations of Quartz Plates - I. Koga, Y. Tsuzaki, S. N. Witt, Jr., and A. L. Bennett

2-14-67 Coupled Contour and Thickness Shear Vibrations - R. D. Mindlin

2-14-89 Effects of Initial Stress on Quartz Plates Vibrating in Thickness Modes - A.D. Ballato

2-14-179 Design of Low Frequency AT-cut Resonators - L. A. Tyler

2-15-1 Mathematical Theory of Vibrations of Crystal Plates - R. D. Mindlin

2-15-2 Performance of Quartz Resonators near the Alpha-Beta Inversion Point - J. C. King, and D. B. Fraser

2-15-22 Frequency-Temperature Behavior of Thickness Modes of Double-Rotated Quartz Plates, R. Bechmann, A. D. Ballato and T. J. Lukaszek

2-16-33 Causes of Internal Friction in Crystal Resonators - E. Hafner

2-16-46 Effects of External Forces on the Frequency of Vibrating Crystal Plates - C. R. Mingins, L. C. Barcus and R. W. Perry

2-16-77 Frequency Temperature Characteristics of Quartz Resonators Derived from the Temperature Behavior of the Elastic Constants - R. Bechmann, A. D. Ballato and T. J. Lukaszek.

2-17-28 Measurement of Amplitude Distributions of Vibrating AT-Cut Crystals by Means of Optical Observations - G. Sauerbrey

2-17-51 Reactions of a Vibrating Piezoelectric Crystal Plate to Externally Applied Forces - C. R. Mingins, L. C. Barcus and R. W. Perry

2-17-88 Energy Trapping and Related Studies of Multiple Electrode Filter Crystals - W. Shockley, D. R. Curran, D. J. Koneval

2-17-190 Status of Quartz Crystal Research and Development - G. K. Guttwein

CATEGORY 2 (Cont'd):

2-18-93 Energy Trapping and the Design of Single and Multi-Electrode Filter Crystals - D. R. Curran, D. J. Koneval

2-18-120 Effect of Electrode Size on Thickness Shear Vibrations of Quartz Plates - R.D. Mindlin

2-19-22 The Study of Quartz Resonators by X-Ray Diffraction Topography - W. J. Spencer, K. Haruta

2-19-23 Special X-Ray Studies of Quartz Frequency Control Units - R. A. Young, R. B. Belser, A. L. Bennett, W. R. Hicklin, J. C. Meaders and C. E. Wagner

2-19-212 Studies in the Mathematical Theory of Vibrations of Crystal Plates - R. D. Mindlin

2-20-1 X-ray Diffraction Study of Vibrational Modes - K. Haruta, W. J. Spencer

2-20-14 Characteristics of the Electrostrictor as a Lumped Electrostrictive Active Resonator, A. A. Gundjian

2-20-32 An Active Crystal Resonator - D. L. White, W.-C. Wang

2-20-33 The Force Sensitivity of AT-cut Quartz Crystals - J. M. Ratajski

2-20-50 Transient Reactions to Stress Changes in Vibrating Crystal Plates - C. R. Mingins, R. W. Perry and L. C. Barcus

2-20-252 Studies in the Mathematical Theory of Vibrations of Crystal Plates - R.D. Mindlin

2-21-3 Anharmonic, Thickness-Twist Overtones of Thickness-Shear and Flexural Vibrations of Rectangular, AT-cut, Quartz Plates - R. D. Mindlin and W. J. Spencer

2-21-28 On the Sinusoidal Steady-State Characteristics of Multi-electroded Piezoelectric Devices - E. P. EerNisse, R. Holland

2-21-63 Investigation of Resonant Modes of Planoconvex AT-Plates - G. Sauerbrey

2-21-72 Amplitude Distribution Determination by an X-Ray Diffraction Technique - C. E. Wagner, R. A. Young

2-21-115 Practical Consequences of Modal Parameter Control in Crystal Resonators - G. K. Guttwein, T. J. Lukaszek and A. D. Ballato

2-21-402 The Unwanted Responses of the Crystal Oscillator Controlled by AT-Cut Plate - H. Fukuyo, H. Yoshie and M. Nakazawa

2-21-420 Activity Dips in AT-Cut Crystals - A. F. B. Wood, A. Seed

2-21-436 On Activity Dips of AT Crystals at High Level of Drive - C. Franx

2-22-1 Electro-mechanical Vibrations in Centrosymmetric Crystals - R. D. Mindlin

2-22-2 Parametric and Other Nonlinear Elastic Effects in Piezoelectric Resonators - E. P. EerNisse

2-22-55 Hysteresis Effects in Quartz Resonators - D. L. Hammond, C. A. Adams and A. Benjaminson

2-22-269 The Role of Crystal Parameters in Circuit Design - E. Hafner

2-23-26 Analysis of Contoured Piezoelectric Resonators Vibrating in Thickness-Twist Modes - M. Onoe, K. Okada

2-23-39 Resonance Frequencies of Monolithic Quartz Structures - A. Glowinski

2-23-56 Electric Field Effects in Monolithic Crystal Filters - H. F. Tiersten

2-23-128 Anomalous Vibrations in AT-Cut Plates - I. Koga

2-23-143 A Novel Algorithm for the Design of the Electrodes of Single-Mode AT-Cut Resonators, J. H. Sherman, Jr.

2-24-17 Thickness-Twist Vibrations of a Quartz Strip - R. D. Mindlin

2-24-33 Frequency-Temperature Dependence of Thickness Vibrations of Piezoelectric Plates - K. Hruska

2-24-46 The Effect of Static Electric Fields on the Elastic Constants of α - Quartz - J. A. Kusters

2-24-55 Selected Topics in Quartz Crystal Research - C. A. Adams, G. M. Enslow, J. A. Kusters and R. W. Ward

2-24-64 Defects and Frequency Mode Patterns in Quartz Plates - E. W. Hearn, G. H. Schwuttke

2-25-58 Acoustical and Optical Activity in Alpha Quartz - R. D. Mindlin, Columbia University, R. A. Toupin, IBM

2-25-63 Extensional, Flexural and Width-Shear Vibrations of Thin Rectangular Crystal Plates, P. C. Y. Lee, Princeton University

2-25-109 Evaluation of Quartz for High Precision Resonators - B. R. Capone, A. Kahan, Air Force Cambridge Research Laboratory, and Baldwin Sawyer, Sawyer Research Products

2-25-139 The Current Dependency of Crystal Unit Resistance at Low Drive Level - S. Nonaka, T. Yuuki and K. Hara, Nippon Electric Company, Ltd., Japan

2-26-84 Theory of Vibrations of Plates - R. D. Mindlin, Columbia University

2-26-85 An Approximate Theory for High-Frequency Vibrations of Elastic Plates - P. C. Y. Lee, Princeton University and Z. Nikodem. Foster-Wheeler Corp.

2-26-86 Transmission-Line Analogs for Stacked Piezoelectric Crystal Devices - A. Ballato, ECOM

2-26-108 The Temperature Dependence of the Force Sensitivity of AT-Cut Quartz Crystals - C. R. Dauwalter, Massachusetts Institute of Technology

2-26-148 Research and Development of a New Type of Crystal - The FC Cut - G. Lagasse, J. Ho and M. Bloch, Frequency Electronics, Inc.

2-27-1 Elastic Waves and Vibrations in Deformed Crystal Plates, P. C. Y. Lee, Y. Wang and X. Markenscoff, Princeton University

2-27-7 Finite Element Calculations Relevant to AT-Cut Quartz Resonators - D. R. Cowdrey, Cambridge University, and J. R. Willis, University of Bath

2-27-11 Design Equations for Bi-and Plano-Convex AT-Cut Resonators - W. D. Beaver, Comtec Economation

2-27-20 Mass Effects on Crystal Resonators with Arbitrary Piezo-coupling - A. Ballato and T. Lukaszek, US Army Electronics Technology and Devices Laboratory

2-27-30 Rectangular AT-Cut Resonators - J. J. Royer, Bell Telephone Laboratories

2-27-35 X-Ray Topography of Quartz Resonators - C. J. Wilson, University of Cambridge

2-28-1 Analysis of Intermodulation in Rotated Y-Cut Quartz Thickness-Shear Resonators - H. F. Tiersten, Rensselaer Polytechnic Institute

2-28-5 Intermodulation in Thickness-Shear Resonators - R. C. Smythe, Piezo Technology Inc.

2-28-14 Effects of Initial Bending on the Resonance Frequencies of Crystal Plates - P.C.Y. Lee, Y. S. Wang and X. Markenscoff, Princeton University

2-28-19 Influence of Environment Conditions on a Quartz Resonator - M. Valdois, J. Gagnepain and J. Besson, ONERA

2-28-44 Analysis of Trapped Energy Resonators Operating in Overtones of Thickness-Shear - H. F. Tiersten, Rensselaer Polytechnic Institute

2-28-67 High-Q BT-Cut Resonators in Flat Configuration - P. K. Schmitt, AEG - Telefunken

2-28-73 Further Development on Precision Quartz Resonators - M. Bloch J. Denman, Frequency Electronics

2-28-270 Bulk and Surface Acoustic Wave Excitation and Network Representation - A. Ballato, ECOM

2-29-1 Quartz Resonator Frequency Shifts Arising from Electrode Stress - E. P. EerNisse, Sandia Laboratories

2-29-26 Determination of the Electromechanical Coupling Factor of Quartz Bars Vibrating in Flexure or Length-Extension - J. Hermann Centre Electronique Horloger S. A.

2-29-35 Simple Exact Solutions for Thickness Shear Mode of Vibration of a Crystal Strip - Y. Mochizuki, Shizuoka University

2-29-42 Miniature AT-Cut Strip Resonators with Tilted Edges - M. Onoe and M. Okazaki, University of Tokyo

2-29-49 Analysis of Nonlinear Resonance in Rotated Y-Cut Quartz Thickness-Shear Resonators - H. F. Tiersten, Rensselaer Polytechnic Institute

CATEGORY 2 (Cont'd):

2-29-5 Relationship of Resonant Frequency of Quartz Crystal to Mass Loading - O. Lewis, Xerox Corporation, Chih-shun Lu, Inficon, Inc.

2-29-10 Higher-Order Temperature Coefficients of Frequency of Mass-Loaded Piezoelectric Crystal Plates - A. Ballato and T. Lukaszek, ECOM

2-29-54 Plate Constants and Dispersion Relations for Width-Length Effects in Rotated Y-Cut Quartz Plates - T. R. Meeker, Bell Laboratories

2-29-65 Waves and Vibrations in an Infinite Piezoelectric Plate - P. C. Y. Lee, S. Syngellakis, Princeton University

2-29-71 Analysis of Trapped Energy Resonators Operating in Overtones of Coupled Thickness-Shear and Thickness-Twist - H. F. Tiersten, Rensselaer Polytechnic Institute

2-29-76 Vibrational Response of a Sonar Transducer Using Piezoelectric Finite Elements - J. T. Hunt, University of California

2-29-195 A Length-Thickness Flexure Mode Quartz Resonator - R. W. Allington, Instrumentation Specialties Company

2-30-1 Effects of Acceleration on the Resonance Frequencies ofCrystal Plates - P. C. Y. Lee and Kuang-Ming Wu, Princeton University

2-30-8 Calculation on the Stress Compensated (SC-Cut) Quartz Resonator - E. P. EerNisse, Sandia Laboratories

2-30-32 Frequency/Temperature, Activity/Temperature Anomalies in High Frequency Quartz Crystal Units - J. Birch and D. A. Weston, General Electric Company Limited

2-30-40 The Relationship Between Plateback, Mass Loading and Electrode Dimensions for AT-Cut Quartz Crystal Having Rectangular Resonators Operating at Fundamental and Overtone Modes - J. F. Werner and A. J. Dyer, General Electric Company Limited

2-30-54 Dimensioning Rectangular Electrodes and Arrays of Electrodes on AT-Cut Quartz Bodies - J. H. Sherman, General Electric Company

2-30-65 Laser Interferometric Measurement of the Vibration Displacements of a Circular Plano-Convex AT-Cut Quartz Crystal Resonator - K. Iijima, Y. Tsuzuki, Y. Hirose and M. Akiyama, Yokohama National University

2-30-84 Fundamental Noise Studies of Quartz Resonators - J. J. Gagnepain, E.N.S.C.M.B.

2-30-132 Temperature Characteristics of High Frequency Lithium Tantalate Plates - J. Detaint and R. Lancon, C.N.E.T.

2-30-141 The Angular Dependence of Piezoelectric Plate Frequencies and Their Temperature Coefficients - A. Ballato and G. J. Iafrate, US Army Electronics Command

2-30-167 Analysis of Tuning Fork Type Crystal Unit and Application into Electronic Wrist Watch - S. Kanbayashi, S. Okano, K. Hirama and T. Kudama, Toyo Communication Equipment Co., Ltd., and M. Konno and Y. Tomikawa, Yamagata University

2-30-175 Analytical and Experimental Investigations of 32 KHz Quartz Tuning Forks - J. A. Kusters, C. A. Adams and H. E. Karrer, Hewlett-Packard, and R. W. Ward, Litronix Corp.

2-30-184 An Approximate Theory for the High-Frequency Vibrations of Piezoelectric Crystal Plates - S. Syngellakis and P. C. Y. Lee, Princeton University

2-30-191 The Vibration of a Biconvex Circular AT-Cut Plate - N. Oura and H. Fukuyo, Tokyo Institute of Technology and A. Yokoyama, Kumamoto University

2-30-196 Properties of a Flat Rectangular Quartz Resonator Vibrating in a Coupled Mode - A. E. Zumsteg and P. Suda, SSIH-QUARTZ

2-30-202 Miniaturized Circular Disk AT-Cut Crystal Vibrator - Y. Oomura, Tokyo Metropolitan University

CATEGORY 3:

Radiation Effects on Resonators

3-12-101 Pile Irradiation of Quartz Crystal Units - F. E. Graham, A. F. Donovan, Admiral Corp.

3-13-37 Defects of the Quartz System Produced by Neutron Irradiation - R. Weeks

3-14-138 Nuclear Radiation Effects in Quartz Crystals - J. M. Stanley

3-16-7 Effects of Reactor Irradiation on Thickness Shear Crystal Resonators - J. C. King, D. B. Fraser

3-17-127 Aging Characteristics of Quartz Resonators with Comments on the Effects of Radiation - R. B. Belser, W. H. Hicklin

3-20-32 Radiation Effects in Frequency Control Devices - J. M. Stanley

3-23-178 Effects of Gamma Irradiation on Frequency Stability of 5th Overtone Crystal Oscillators - C. A. Berg, J. R. Erickson

3-27-113 Rapid Annealing of Frequency Change in High Frequency Crystal Resonators Following Pulsed X-Irradiation at Room Temperature - J. C. King, H. H. Sander, Sandia Laboratories.

3-27-120 Crystal Controlled Oscillators for Radiation Environments - R. E. Paradysz, W. L. Smith, Bell Telephone Laboratories

3-27-124 Calculation of Transient Thermal Imbalance within Crystal Units Following Exposure to Pulse Irradiation - E. F. Hartman, J.C.King, Sandia Laboratories

3-27-128 Transient X-Ray Induced Conductivity in Single Crystal Quartz - R. C. Hughes, Sandia Laboratories

3-27-136 Hydrogen Diffusion in Quartz: The Kinetics of a One-Dimensional Process - A. Sosin, University of Utah

3-27-139 Effects of a Co-60 Gamma-Ray Irradiation on the Optical Properties of Natural and Synthetic Quartz from 85 to 300 K. - P. L. Mattern, Sandia Laboratories and K. Lengweiller and P. W. Levy, Brookhaven National Laboratory

3-27-153 A Review of Impurity Atom Defects in α-Quartz as Observed by Electron Paramagnetic Resonance - J. A. Weill, University of Saskatchewan

3-28-143 The Effect of Gamma Irradiation on the Temperature-Frequency Characteristic of AT-Cut Quartz - H. J. Benedikter, J. H. Sherman, General Electric Company, and R. D. Gillespie, III, Applied Radiant Energy Corporation

CATEGORY 4:

Resonator Processing Techniques and Aging

4-10-122 Aging Study of Quartz Crystal Resonators - R. B. Belser and Walter H. Hicklin - Georgia Institute of Technology

4-10-190 Crystal Unit Design for Use in a Ground Station Frequency Standard - A. W. Warner, Bell Telephone Laboratories, Inc.

4-10-513 Tests on Hermetic Enclosures of Piezoelectric Quartz Crystals - B. W. Schumacher, Ontario Research Foundation

4-10-524 Production Procedures for VHF Crystals - R. D. Cortwright, Union Thermoelectric Corp.

4-10-540 Manufacturing Problems Connected with High Precision Crystals - J. M. Wolfskill - Bliley Electric Company

4-10-569 Manufacturing Problems Connected with Miniaturized Crystals - George K. Bistline, Jr., McCoy Electronics Company

4-10-573 Automatic X-Ray Sorter for Crystal Blanks - Lester V. Wise, Bulova Research and Development Laboratories, Inc.

4-11-157 Aging Study of Quartz Resonators - Richard B. Belser, Walter H. Hicklin, Georgia Institute of Technology

4-11-189 High Temperature AT-Cut Crystal Units - Charles W. Mann, Reeves-Hoffman Division

4-11-214 High Temperature, Low Frequency Crystal Units - J. M. Wolfskill, Bliley Electric Company

4-11-240 High Precision Crystal Units - L. Dick, The James Knights Company

4-11-256 Stability of Quartz Resonators at Very Low Temperatures - F. P. Phelps, National Bureau of Standards

4-11-277 Fundamental Studies on an Improved Crystal-Controlled Frequency Standard - M. D. Fagen, W. L. Smith, Bell Telephone Laboratories

4-12-37 Effects of Plating to Frequency on the Stability of Quartz Resonators - Richard B. Belser and Walter H. Hicklin, Georgia Institue of Technology

4-12-162 Research at NBS Boulder Laboratories on Quartz Crystal Resonators and Oscillators at Low Temperatures - F. P. Phelps and A. H. Morgan, National Bureau of Standards

4-12-211 Ruggedization of Low Frequency Crystal Units - J. M. Wolfskill, Bliley Electric Company

4-12-241 Phase Stable Quartz Crystal Units - Louis A. Dick, The James Knights Company

4-12-260 Moderate Precision Crystal Units - Donald L. Hammond, Scientific Radio Products, Inc.

4-12-281 Low Frequency XY'Flexure Crystal Units - A. S. Matistic, Bulova Watch Co., Electronics Division

4-12-296 Design Data for HF AT Crystal Units - L. Tyler and C. Rutkowski, Union Thermoelectric Corporation

4-12-316 Design Parameters for VHF Crystal Units - D. McKeown, Frequency Control Division USASEL

4-13-71 Aging Studies on Crystal Units - R. B. Belser and W. H. Hicklin

4-13-109 Aging Characteristics of Quartz Crystal Units P. Mulvihill

4-13-406 Phase Stable Crystal Units - L. Dick

4-13-423 Glass Inclosed Moderate Precision Crystal Units - E. M. Shideler and D. L. Hammond

4-13-430 Glass Inclosed Miniaturized Crystal Units - H. Long

4-13-445 High Temperature Crystal Units Employing Thermocompression Techniques - J. Griffin

4-13-498 Development and Production of Glass Inclosed Quartz Crystals - R. S. Sennett, D. Eisen and L. R. Clark

4-13-512 Fabrication of High Precision 5 Mc Crystal Units - J. M. Wolfskill, R. T. Schlaudecker

4-13-529 Results of Pilot Runs in a Mechanized Crystal Plant - A. Mann

4-13-535 Production of VHF Crystal Units - G. F. Fisher

4-14-68 Parallel Field Excitation of Thickness Modes of Quartz Plates - R. Bechmann

4-14-115 The Aging of Aluminum Plated 16.5 Mc. AT-cut Quartz Resonators - R.B. Belser & W. Hicklin

4-14-154 Development of Precision Crystal Units for Satellite Use - J. M. Wolfskill and R. T. Schlaudecker

4-14-397 Tuning Forks as Circuit Elements - M. Pleasure

4-15-49 Temperature Compensation of Piezoelectric Resonators by Mechanical Stress - E. A. Gerber and M. H. Miles

4-15-66 Stability Studies of Quartz Crystals for Satellites - R. B. Belser and W. H. Hicklin

CATEGORY 4 (Cont'd):

4-15-109 Micro-Module and Ultra-Miniaturized Crystal Units - R. R. Bigler

4-15-113 Precision Glass Enclosed Crystal Units - E. M. Shideler and P. E. Bryan

4-15-125 Precision Quartz Resonators - D. L. Hammond

4-16-110 Aging of Quartz Resonators at Fundamental and Overtone Modes with Comments on Radiation Effects - R. B. Belser and W. H. Hicklin

4-16-146 Recent Developments in Miniaturized Glass Enclosed Crystal Holders - G. K. Bistline, Jr.

4-16-156 Improved Ceramic Envelopes for Micromodule Crystal Units - J. H. Sherman, Jr.

4-16-169 Temperature Compensated Quartz Crystal Units - R. J. Munn

4-17-4 Studies on High Precision Resonators - R. A. Sykes, W. L. Smith and W. J. Spencer

4-17-215 Precision Crystal Units - D. L. Hammond, C. Adams and L. Cutler

4-17-233 High Q Crystal Units - W. Ianouchevsky

4-17-248 Use of Parallel-Field Excitation in the Design of Quartz Crystal Units - A. W. Warner

4-17-267 Crystal Units for Single Sideband Application - P. Bryan and E. M. Shideler

4-17-272 Design Equations for Plano-Convex AT-Filter Crystals - W. G. Stoddard

4-17-283 Development Status of Quartz Micromodule Crystal Units - P. J. Staelens

4-17-302 Improvements in Technique for Thermo-Compressing Mounting Wires to Quartz Crystal Plates - J. P. Griffin

4-17-325 Problems Associated with Precision Quartz Resonators - W. J. Spencer

4-18-129 Aging Analysis of AT-Cut Quartz Resonators of Natural, Cultured and Swept Varieties - R. B. Belser, W. H. Hicklin

4-18-166 Design and Performance of a New Series of Cold Welded Crystal Unit Enclosures - R. J. Byrne and R. L. Reynolds

4-18-181 A New Design for Microminiature Crystals - W. G. Stoddard

4-18-193 Glass Enclosed Crystal Units for Temperature Compensated Oscillators - G. Bistline, Jr., and D. B. Jacoby

4-18-204 New Developments in Glass Enclosed Crystal Units - D. M. Eisen

4-18-217 Reliability of Quartz Crystal Units - J. M. Stanley and P. E. Mulvihill

4-18-426 On the Control of the Temperature Coefficient of Frequency of AT-Crystals - C. Franx

4-18-597 High-Q, BT-Cut, Quartz Resonator Units - A. Seed

4-19-78 Miniature Single Sideband Crystal Units - J. M. Wolfskill and R. A. Spurlin

4-19-105 Passive Temperature Compensation of Quartz Crystals for Oscillator Applications - S. B. Boor, W. H. Horton and R. B. Angove

4-19-125 Seal Test Methods and Evaluation of Enclosures for Crystal Units - R. L. Reynolds and R. J. Byrne

4-19-137 Application of Leak Theory to Crystal Testing - J. W. Marr and J. H. Sherman, Jr.

4-20-161 Comments on Unwanted Responses in VHF Crystals - E. A. Gerber

4-20-167 Discussion of 3.0 and 5.0 MHz, SSB Crystals Precise and Uniform - R. F. Woolley and G. Lagasse

4-20-180 Aging of Aluminum Plated 3-MC Semi-Precision Resonators - R. B. Belser and W. H. Hicklin

4-20-192 Aging Characteristics of Quartz Crystal Resonators - J. H. Armstrong, P. R. Blomster and J. L. Hokanson

4-20-208 Quartz Crystal Life Test Data - F. Wolf and G. Bistline

4-20-219 Five Megacycle Fifth Overtone Resonators Operating Near the Inflection Temperature - J. G. Leach

4-20-234 Microminiature Cold Weld Crystal Units - A. Seed

4-20-530 Low Power Crystal Ovens - M. Bloch, J. Ho and I. Math

4-21-200 The Transient Thermal Characteristics of Quartz Resonators and their Relation to Temperature-Frequency Curve Distortion - L. E. Schnurr

4-21-211 AT-cut Resonators with Annular Electrodes - R. B. Belser and W. H. Hicklin

4-21-224 SSB Quartz Crystal Units Utilizing Coldweld Enclosures and High Temperature Bakeout Techniques - F. R. Brandt and G. E. Ritter

CATEGORY 4 (Cont'd):

4-21-244 Increased Crystal Unit Resistance at Oscillator Noise Levels - M. Bernstein

4-22-67 Design Considerations for Oscillator Crystals - G. K. Guttwein, A. D. Ballato and T. J. Lukaszek

4-22-89 Advancements in Production of 5-MHz Fifth Overtone High Precision Crystal Units - J. M. Wolfskill

4-22-118 Kold-Seal Thermal Compression Bonded Crystals - J. Denman, G. Lagasse, M. Bloch and J. Ho

4-22-136 Quartz Crystal Aging - E. Hafner and R. S. Blewer

4-22-155 Improvements in Sealing HC-26/U and HC-27/U Glass Holders - G. Gibert

4-22-226 Micro Resonators in Integrated Electronics - J. H. Staudte

4-23-132 Comparison of Aging Performance of 5-MHz Resonators plated with Various Electrode Metals - R. B. Belser and W. H. Hicklin

4-23-163 Laser Machining Thin Film Electrode Arrays on Quartz Crystal Substrates - J. L. Hokanson

4-24-111 Auger Spectroscopy in Studies of the Aging Factors of Quartz Crystal Resonators - G. W. Simmons, W. H. Hicklin and R. K. Hart

4-24-117 5 MHz BT Cut Resonators - J. G. Leach

4-24-126 Mode Control and Related Studies of VHF Quartz Filter Crystals - T. J. Lukaszek

4-24-141 Low Aging Crystal Units for Use in Temperature Compensated Oscillators - J. F. Silver and L. A. Dick

4-24-148 Dynamic Temperature Behavior of Quartz Crystal Units - W. H. Hicklin

4-24-157 The Direct Temperature Control of Quartz Crystals in Evacuated Enclosures - F. G. Tinta, A. S. Matistic and G. A. Lagasse

4-26-71 Thermocompression Bonding to Quartz Crystals - R. J. Byrne, Bell Telephone Laboratories.

4-26-78 Modern Technologies - F. Ura, Hewlett-Packard Laboratories

4-26-120 Frequency Control Devices for High Stability Remote Sensor Transmitters - J. M. Stanley, H. Wasshausen and S. Schodowski, ECOM

4-26-152 Precision and SSB Crystal Units for Temperature Compensated Crystal Oscillators - R. K. Hart and W. H. Hicklin, Georgia Institute of Technology

4-27-42 Low Frequency Resonators of Lithium Tantalate - M. Onoe, University of Tokyo, T. Shinada, K. Itch and S. Miyazaki, Kinsekisha Laboratory, Ltd.

4-27-50 Subminiature Quartz Tuning Fork Resonators - J. Staudte, Statek Corporation

4-27-73 The Molecular Nature of Adsorption on Silica Surfaces - M. L. Hair, Xerox Corporation

4-27-79 Clean Surface Technology - M. L. White, Bell Telephone Laboratories

4-27-89 Thin Film Metallization of Oxides - D. M. Mattox, Sandia Laboratories

4-27-98 Surface Preparation and Characterization Techniques for Quartz Resonators - J. Vig, H. Wasshausen, C. Cook, M. Katz and E. Hafner, U. S. Army Electronics Technology and Devices Laboratory (ECOM)

4-28-85 The Structure and Properties of Thin Metal Films - D. M. Hoffman, RCA

4-28-89 Methods of Cleaning Contaminants from Quartz Surfaces During Resonator Fabrication - R. K. Hart, W. H. Hicklin, L. A. Phillips, Georgia Institute of Technology

4-28-96 Surface Studies for Quartz Resonators - J. Vig, C. F. Cook, Jr., K. Schwidtal, J. W. LeBus and E. Hafner, ECOM

4-28-109 Stabilization of Resonance Frequencies in Piezoelectric Ceramic Resonators Against Sudden Temperature Change - M. Takahashi, F. Yamauchi and S. Takahashi, Nippon Electric Company

4-29-128 A Survey of Ion Beam Milling Techniques for Piezoelectric Device Fabrication - R. N. Castellano and J. L. Hokanson, Bell Telephone Laboratories

4-29-187 32 kHz Quartz Crystal Unit for High Precision Wrist Watch - J. Engdahl and H. Matthey, OMEGA, SSH-Quartz Division

4-29-202 A New Ceramic Flat Pack for Quartz Resonators - P. D. Wilcox and G. S. Snow, Sandia Laboratories, E. Hafner and J. R. Vig, ECOM

CATEGORY 4 (Cont'd):

4-29-220 Further Results on UV Cleaning and RF Electrobonding - J. R. Vig, J. W. LeBus and R. L. Filler, ECOM

4-29-230 On the Origin of the 'Second Level of Drive' Effect in Quartz Oscillators - J. E. Knowles, Mullard Research Laboratories

4-29-240 A High Precision Laser Assisted X-Ray Goniometer for Circular Plates - J. R. Vig, ECOM

4-30-23 Fracture Resistance of Synthetic α-Quartz Seed Plates - D. L. Brownlow, Bell Laboratories

4-30-78 A New Piezoelectric Resonator Design - R. Besson, E.N.S.C.M.B.

4-30-209 Direct Plating to Frequency - a Powerful Method for Crystals with Closely Controlled Parameters - R. Fischer, Kristall Verarbeitung

4-30-232 Design of a Nozzle Beam Type Metal Vapor Source - R. P. Andres, Princeton University

4-30-237 An Evaluation of Leak Test Methods for Hermetically Sealed Devices - R. E. McCullough, Texas Instruments

4-30-240 Characterization of Metal-Oxide System by High Resolution Electron Spectroscopy - E. J. Scheibner and W. H. Hicklin, Georgia Institute of Technology

4-30-249 A Novel Method of Adjusting the Frequency of Aluminum Plated Quartz Crystal Resonators - V. E. Bottom, TYCO Crystal Products

4-30-254 Polishing Layer of Crystal Plates - H. Fukuyo and N. Ohura, Tokyo Institute of Technology

4-30-259 A Method of Angle Correction - D. Husgen and C. C. Calmes, Savoy Electronics

4-30-264 The Effect of Bonding on the f vs. T Characteristics of AT-Cut Resonators - R. L. Filler and J. R. Vig, US Army Electronics Command

4-30-224 Ceramic Flat Pack Enclosures for Precision Quartz Crystal Units - R. Donald Peters, General Electric Company

CATEGORY 5:

Filters and Surface Wave Devices

5-10-339 High-Frequency Crystal Filters - D. I. Kosowsky, Hycon Eastern, Inc.

5-11-535 Latest Developments in Mechanical Filters - J. C. Hathaway, Collins Radio Company

5-11-556 High-Frequency Crystal Filters - Leo Storch, Hughes Aircraft Company

5-12-437 Filter Crystals - R. Bechmann, Frequency Control Division, USASEL

5-12-475 High Frequency Crystal Filters - R. A. Sykes Bell Telephone Laboratories

5-12-501 Type NB Bandpass Crystal Filters - Leo Storch, Hughes Products

5-13-404 Single-Side-Band Crystal Filters - M. Dishal

5-13-405 Quartz Crystal Mechanical Filters - H. Yoda

5-14-361 VHF Crystal Filters - F. K. Priebe and D. Schwab

5-15-318 Transfer Function Synthesis of Quartz Crystal Filters - E. C. Ho

5-16-347 HF and VHF Crystal Filters - S. Malinowski and D. Schennberg

5-16-373 High Frequency Crystal Electromechanical Filters - Y. Nakazawa

5-17-566 Recent Developments in Crystal Filters - D. I. Kosowsky and C. Hurtig

5-18-536 The Synthesis of Crystal-Capacitor Tandem Lattice All-Pole Bandpass Filters on the Insertion-Loss Basis - R. C. Smythe

5-18-558 Crystal Filter Techniques - S. Malinowski

5-19-42 Ultrasonic Tapped Delay Lines for Filter Applications - G. A. Coquin

5-19-213 Factors in the Design of VHF Filter Crystals - D. R. Curran and D. J. Koneval

5-19-269 Improvements of Quartz Filter Crystals - T. J. Lukaszek

5-19-509 Design of SSB and VHF Crystal Filters - E. C. Ho and R. H. Tuznik

5-19-534 Trapped Energy Modes, Network Synthesis, and the Design of Quartz Filters - A. D. Waren, W. J. Gerber and D. R. Curran

5-20-103 Improved VHF Filter Crystals using Insulating Film Techniques - D. J. Koneval, W. J. Gerber and D. R. Curran

5-20-131 Design and Fabrication of Modern Filter Crystals - A. Ballato, T. Lukaszek, H. Wasshausen and E. Chabak

5-20-266 High Frequency Crystal Filters Employing Multiple Mode Resonators Vibrating in Trapped Energy Modes - M. Onoe, H. Jumonji and N. Kobori

5-20-288 High Frequency Monolithic Crystal Filters with Possible Application to Single Frequency and Single Side Band Use - R. A. Sykes and W. D. Beaver

5-20-309 Incorporation of Multi-Resonator Crystals into Filters for Quantity Production - H. Mailer and D. R. Beuerle

5-20-343 Tolerance Considerations in Crystal Filter Design - R. C. Smythe

5-20-352 A Temperature Compensation Technique for Crystal Filters - E. C. Ho and K. Lichtenfeld

5-21-83 Alternate Approaches to High Frequency Filter Crystals - D. A. Roberts, D. J. Koneval and T. R. Sliker

5-21-138 Physical Realization of Miniature Bandpass Filters with Single Frequency or Single Sideband Characteristics - D. I. McLean

5-21-160 Theory of Thickness-Shear Vibrators, with Extensions and Applications to VHF Acoustically-Coupled-Resonator Filters - W. H. Horton and R. C. Smythe

5-21-179 Theory and Design of the Monolithic Crystal Filter - W. D. Beaver

5-22-188 High Frequency Crystal Mechanical Filters - H. Yoda, Y. Nakazawa and N. Kobori

5-23-65 The Development of High Performance Filters Using Acoustically Coupled Resonators on AT-Cut Quartz Crystals - J. F. Werner, A. J. Dyer and J. Birch

5-23-76 High Frequency Crystal Monolithic (HCM) Filters - H. Yoda, Y. Nakazawa and N. Kobori

5-24-16 Surface Waves and Devices - H. J. Shaw

5-24-74 Review of Digital Filtering - J. D. Heightley

5-24-78 Active Filter Capabilities - P. Geffe

5-24-83 Generalized Filters Using Surface Ultrasonic Waves - M. G. Holland

5-24-84 Monolithic Crystal Filters - R. J. Byrne

5-24-93 Preparation of Quartz Crystal Plates for Monolithic Crystal Filters - A. J. Miller

5-24-104 A Technique for Automatic Monolithic Crystal Filter Frequency Adjustment - R. P. Grenier

5-24-21 Zero Temperature Coefficient Ultrasonic Delay Lines Utilizing Synthetic Quartz Crystals as Delay Media - M. Onoe, Y. Mochizuki

5-25-246 Energy Trapping in a Lithium Tantalate X-Cu Resonator - K. Sawamoto, Elec. Comm. Lab., Nippon Tel. & Tel., Japan

5-25-251 CdS-Quartz Monolithic Filters for Use in the 100-500 MHz Frequency Range - D. A. Roberts, Gould Inc.

5-25-262 Consideration About Channel Filters for a New Carrier Frequency System with Mechanical Filters - H. Schussler, AEG-Telefunken, Germany

5-25-271 Semi-Monolithic Quartz Crystal Filters and Monolithic Quartz Filters - L. Bidart, C.E.P.E., France

5-25-280 Monolithic Crystal Filters for Frequency Division Multiplex - P. Lloyd, Bell Telephone Laboratories, Inc.

5-25-287 Composite Filter Structures Incorporating Monolithic Crystal Filters and L-C Networks H. A. Simpson, E. D. Finch, Jr., R. K. Weeman and A. N. Georgiades, Bell Telephone Laboratories, Inc.

5-26-164 VHF/UHF Bandpass Filters Using Piezoelectric Surface Wave Devices - C. S. Hartman, T. F. Cheek and H. G. Vollers, Texas Instruments, Inc.

5-26-171 Charge Transfer Devices in Frequency Filtering - D. D. Buss, C. R. Reeves, W. H. Bailey and D. R. Collins, Texas Instruments Incorporated

5-26-180 Intermodulation in Crystal Filters - S. Malinowski and C. Smith, Motorola, Inc.

5-26-187 The Design of Compact Monolithic Crystal Filters for Portable Telecommunications Equipment - G. R. Kohlbacher, AEG-Telefunken West Germany

5-26-193 A Superconductive Tunable Filter With Broad Tuning Range - J. R. Vig and E. Gikow, ECOM

5-27-227 Monolithic Crystal Filter with Attenuation Poles Utilizing 2-Dimensional Arrangement of Electrode - Y. Masuda, I. Kawakami and M. Kobayashi, OKI Electric Industry Co.,Ltd.

5-27-233 Effects of Asymmetry in Trapped Energy Piezoelectric Resonators - A. Glowinski, R. Langon and R. Lefevre, Centre National d'Etudes des Telecommunications

5-27-243 Experimental Investigations of Intermodulation in Monolithic Crystal Filters - W. H. Horton and R. C. Smythe, Piezo Technology Inc.

5-27-246 Single Mode Resonance in Lithium Niobate/Lithium Tantalate for Monolithic Crystal Filters - J. W. Burgess, The Plessey Company Limited

5-27-253 Some Practical Design Considerations of Dispersive Surface Wave Filters - W. J. Skudera USA Electronics Technology and Devices Laboratory (ECOM) and H. M. Gerard, Hughes Aircraft Company

5-27-262 A Novel Frequency Selective Device: The Stacked Crystal Filter - A. Ballato and T. Lukaszek, Frequency Control & Signal Processing Devices Technical Area, USA Electronics Technology & Devices Laboratory, (ECOM)

5-28-33 Filter Applications in Communications and Electronics Industry - C. F. Kurth, Bell Telephone Laboratories

5-28-43 Energy Trapped Vibrations in Lithium Tantalate and Lithium Niobate Resonators - M. C. Hales, J. W. Burgess and R. J. Porter, The Plessey Company

5-28-256 RF Oscillator Control Utilizing Surface Wave Delay Lines - H. G. Vollers and L. T. Claiborne, Texas Instruments

5-28-260 Surface Acoustic Wave Oscillator Experiments - A. K. Nandi, S. T. Costanza and C. E. Wheatley III, Rockwell International

5-28-266 Surface Acoustic Wave Oscillators - H. E. Karrer and J. F. Dias, Hewlett-Packard

5-28-280 UHF Surface Acoustic Wave Crystal Resonators - E. J. Staples, Texas Instruments

5-28-286 On the Design of Elastic Surface Wave Filters with no Tuning Coil - H. Sato, K. Yamanouchi and K. Shibayama, Tohoku University and S. Nishiyama, Nihon Dempa Kogyo Company Limited

CATEGORY 5 (Cont'd):

5-28-299 Low-Loss Unidirectional Acoustic Surface Wave Filters - R. C. Rosenfeld, C. S. Hartman and R. B. Brown, Texas Instruments

5-28-304 The Surface Acoustic Wave Oscillator - A Natural and Timely Development of the Quartz Crystal Oscillator - M. F. Lewis, Royal Radar Establishment

5-29-77 Frequency Filtering Using Charge Coupled Devices - C. R. Hewes, D. D. Buss and R. W. Brodersen, Texas Instruments Inc.

5-29-88 Practical Application of CCD-Transversal Filters in Communication Systems - R. D. Baertsch, W. J. Butler, W. E. Engeler, H. S. Goldberg, O. Mueller, C. M. Puckette, J. J. Tiemann and J. J. VandeGraaf, General Electric Company

5-29-105 A6 Monolithic Crystal Filter Design for Manufacture and Device Quality - S. H. Olster, I. R. Oak, Western Electric Company, and G. T. Pearman, R. C. Rennick and T. R. Meeker, Bell Laboratories

5-29-113 Manufacture of Monolithic Crystal Filters for the A-6 Channel Bank - H. F. Cawley, J. D. Jennings, J. I. Pelc, P. R. Perri and F. E. Snell, Western Electric Company, and A. J. Miller, Bell Laboratories

5-29-120 Polylithic Crystal Filters - D. F. Sheahan, GTE Lenkurt

5-29-135 A Survey of Current SAW Device Capabilities - L. T. Claiborne, Texas Instruments, Inc.

5-29-150 Surface Acoustic Wave Resonator Development - J. S. Schoenwald and W. R. Shreve, Texas Instruments Inc., R. C. Rosenfeld, Motorola, Inc.

5-29-158 Equivalent Circuit and Properties of Surface Wave Planar Resonators - K. M. Lakin and T. R. Joseph, University of Southern California

5-29-167 Surface-Wave Resonators Using Grooved Reflectors - R. C. M. Li, J. A. Alusov and R. C. Williamson, Massachusetts Institute of Technology

5-29-177 Oversampled SAW Filter Transducers - B. J. Hunsinger, University of Illinois, R. J. Kansy, Magnavox

5-29-181 Experimental Investigation of Mass-Producible Acoustic Surface Wave Filter - G. Coussot, G. Menager, Thomson-CSF Labs.

5-30-12 Static Strain Effects on Surface Acoustic Wave Delay - R. B. Stokes and K. M. Lakin, University of Southern California

5-30-103 An Analysis of Overtone Modes in Monolithic Crystal Filters - H. F. Tiersten, Rensselaer Polytechnic Institute

5-30-109 A Hybrid Integrated Monolithic Crystal Filter - T. Watanabe and K. Okuno, Nippon Electric Company

5-30-119 Surface Acoustic Wave VIF Filters for TV Using ZnO-Sputtered Film - S. Fujishima, H. Ishiyama, A. Inoue and H. Ieki, Murata Mfg. Co.

5-30-123 Filtering with Analog CCD and SAW Devices - D. Buss, L. Claiborne, C. Hartmann and C. Hewes, Texas Instruments

5-30- SAW Resonators and Coupled Resonator Filters - F. J. Staples and R. C. Smythe, Piezo Technology Inc.

5-30-322 Two-Port Quartz SAW Resonators - W. R. Shreve, Texas Instruments

5-30-334 Surface Acoustic Wave Ring Filter - T.E. Parker, F. Sandy, Raytheon Research Division

5-30-340 Optical Waveguide Model for SAW Resonators - J. Schoenwald, Teledyne MEC

5-30-346 Design of Quartz and Lithium Niobate SAW Resonators Using Aluminum Metallization - W. H. Haydl, P. Hiesinger, B. Dischler and R. Smith, Institute for Applied Solid State Physics

5-30-358 Aging Effects in Plasma Etched SAW Resonators - D. T. Bell, S. P. Miller and L. A. Simonson, Texas Instruments

5-30-363 The Periodic Grating Oscillator (PGO) - R. D. Weglein and O. W. Otto, Hughes Research Laboratories

5-30-367 Fast Frequency Hopping with Surface Acoustic Wave (SAW) Frequency Synthesizers - L. R. Adkins, Rockwell International

5-30-157 Progress Report on Surface Acoustic Wave Device MMT - A. R. Janus, Hughes Aircraft

CATEGORY 6:

Quartz Crystal Oscillators and Frequency Control Circuitry

6-10-197 A Frequency Standard at Low Temperature - W. D. George, National Bureau of Standards

6-10-268 The Evaluation of Phase-Stable Oscillators for Coherent Communication System - Walter K. Victor, Jet Propulsion Laboratory

6-10-354 Design Data for Crystal Oscillators - H. E. Gruen, Armour Research Foundation

6-10-390 Long and Short Term Frequency Stability of UHF Cavity-Controlled Oscillators - R. E. Meek, Georgia Institute of Technology

6-10-422 A Precision Crystal Oven - M. D. McFarlane and Ramey B. Metz, Robertshaw-Fulton Controls Co.

6-10-470 The Magnetron Beam Switching Tube as a High Speed Frequency Divider - Hilary Moss, Burroughs Research Center

6-10-506 Change of State Crystal Ovens - E. Snitzer and R. Strong, Brown Instrument Co., Division Minneapolis-Honeywell Regulator Co.

6-11-426 Crystal Oven Developments - Maynard D. McFarlane, Robertshaw-Fulton Controls Co.

6-11-502 Design Criteria for Vacuum Tube Crystal Oscillators - H. E. Gruen, Armour Research Foundation

6-11-518 Studies on Transistor Crystal Oscillators - Everett Eberhard and William R. McSpadden, Motorola, Inc.

6-11-586 A Portable Frequency Standard - Robert L. Craiglow, Collins Radio Company

6-11-614 Frequency Translator for MASER - S. Schneider, Polarad Electronics Corp.

6-12-131 Fundamental Studies on an Improved Crystal-Controlled Standard - W. L. Smith and A. W. Warner, Bell Telephone Laboratories.

6-12-406 A Precision Delayed Pulse Generator as a Variable Time Interval Standard - Dexter Hartke, Marvin Willrodt and Donald Broderick, Hewlett-Packard Company

6-12-420 Frequency Multiplication with Phase-Locked Oscillators - Harold T. McAleer, General Radio Company

6-13-165 Tuning Fork Precision Oscillators - H. E. Gruen and O. Colpen

6-13-182 Designing Transistor Oscillator for Crystals - J. Sherman, Jr.

6-13-191 Highly Stable Crystal Oscillators for Missile Application - A. W. Warner and W. L. Smith

6-13-232 Missile-borne Frequency Standard - H. P. Brower

6-13-350 Parametric Frequency Multiplication for Atomic Frequency Standards - R. Rafuse

6-13-371 Automatic Phase Lock Frequency Control for Mobile Equipment - Lt. Col. J. A. Loutit and R. Story

6-13-566 A Compact Frequency Translator for Use with the Ammonia MASER - W. K. Saunders

6-14-192 Stability of Crystal Oscillators - E. Hafner

6-14-200 Quartz Crystal Units and Precision Oscillators for Operation in Severe Mechanical Environments - A. W. Warner and W. L. Smith

6-14-242 Effects of Thermal Noise on the Frequency of a Regenerative Oscillator - M. J. E. Golay

6-14-381 Development of Quartz Crystal Synthesizers - J. M. Shapiro and W. A. Schultz

6-14-421 Frequency and Phase Control of Local Oscillators by Transmitters of Standard Frequency - L. Mooser

6-15-139 Precision Crystal Frequency Standards - W. J. Spencer and W. L. Smith

6-15-251 Frequency Control by Means of a Phase Tracking VLF Receiver - O. J. Baltzer

6-15-278 APC with Pulse Reference - T. J. Rey

6-15-282 Design of Low Power Crystal Oven - I. A. Black, A. Everest and T. P. Heuchling

6-15-297 A Temperature-Compensated Frequency Standard - G. R. Hykes and D. E. Newell

6-16-328 Multiple-Stage Varactor Harmonic Generators - M. E. Hines, A. Blaisdell, F. Collins, W. Priest, L. Baldwin and S. Johnson

6-16-391 Stability of Tunnel Diode Oscillators - F. Sterzer

6-16-405 Precision Quartz Crystal Controlled Oscillator for Severe Environmental Conditions - W. J. Spencer and W. L. Smith

6-16-422 Thermoelectric Temperature Control - T. D. Merritts and J. C. Taylor

6-16-438 The Effects of Noise on Oscillator Frequency Stability - L. Saporta and G. Weiss

6-16-448 Measurements on Oscillator Stability Improvement by Means of High Purity Nickel Cathode Tubes - C. J. G. Abom

CATEGORY 6 (Cont'd):

6-17-464 Progress and Problems in Quartz Crystal Circuitry and Measurements - O. P. Layden

6-17-482 Problems of Frequency Multiplication in Atomic Standards - H. D. Guy

6-17-491 Temperature Compensation of Quartz Crystal Oscillators - D. E. Newell, R. H. Bangert

6-17-508 Theory of Oscillator Design - E. Hafner

6-17-587 Frequency Synthesizing Techniques Permitting Direct Control and Rapid Switching - R. R. Stone and H. F. Hastings

6-18-487 Advances in Crystal Oscillator and Resonator Compensation - D. E. Newell, H. Hinnah and R. Bangert

6-18-535 Short Term Stability of High Precision Crystal Oscillators - M. B. Bloch and K. Toerper

6-18-584 A Frequency Synthesis Technique Using Digital Controlled Division - R. H. Bancroft, Jr., and M. W. Burt

6-19-43 Progress and Problems in Short Term Stability - W. A. Edson

6-19-565 A High Frequency Synthesizer Using Digital Techniques for Economy of Power and Space - J. D. Hill and T. C. Thomas

6-19-580 Cubic Inch Frequency Synthesizers - E. Ulicki

6-19-617 Recent Developments in Crystal Oscillator Temperature-Compensation - D. E. Newell, H. D. Hinnah and R. H. Bangert

6-19-642 The Voltage-Controlled Crystal Oscillator (VCXO), Its Capabilities and Limitations - R. L. Kent

6-19-658 Warm-Up Characteristics of Oscillators Employing 3 M.C. Fundamental Crystals in HC-27/U Enclosures - R. J. Munn

6-20-464 Microminiaturization of Time and Frequency Control Equipments - F. Van Steen and R. Troell

6-20-500 Military Synthesizer Design, Analog and Digital - R. Aughey and A. Seipel

6-20-501 Spurious Oscillation in Crystal Oscillators - M. E. Frerking

6-20-517 Generation of Selectable Precise Fractional Frequency Offsets - B. Parzen

6-20-544 Programmed Oscillators for Doppler Radar Systems - G. D. Thompson, Jr., R. L. Sydnor

6-20-624 Sidereal Time Standard at the National Radio Astronomy Observatory - C. C. Bare and D. L. Thacker

6-20-629 An Analysis of a Low Information Rate Time Control Unit - L. Fey, J. A. Barnes and D. W. Allan

6-21-259 Present Status in Short Term Frequency Stability - L. S. Cutler

6-21-264 Study of Short Term Stability of Crystal Oscillator - B. Boychuk, M. Bloch, G.Weiss and A. Thumin

6-21-287 Vibration Characteristics of Crystal Oscillators - G. F. Johnson

6-21-294 Frequency Synthesizers - R. R. Stone, Jr.

6-21-308 RADA Frequency Synthesizer - R. J. Breiding and C. Vammen

6-21-331 A Low Power - Remotely Controlled Satellite Frequency Standard - M. Bloch, J. Ho, I. Math and J. Teitelbaum

6-21-345 Microminiature Crystal Oscillator - H. P. Thomas, J. H. Sherman, Jr., and R. C. Early

6-21-370 Automated Crystal Oscillator Design - R. L. Craiglow

6-21-377 Variable Frequency Voltage Controlled Oscillators Incorporating Quartz Crystal Units - D. J. Healey, III

6-22-298 Automatic Compensation Equipment for TCXO's - H. Hinnah and D. E. Newell

6-22-311 Recent Improvements to TCXO - P. G. Vovelle

6-22-325 Temperature Compensation of AT Cut Crystals by Thermally Controlled Non-Linear Reactances - E. A. Roberts

6-22-340 Flicker Noise of Phase in RF Amplifiers and Frequency Multipliers: Characterization, Cause and Cure - D. Halford, A. E. Wainwright and J. A. Barnes

6-22-354 The LOH Frequency Synthesizer - R. J. Hughes and R. J. Sacha

6-23-187 A Report on Segmented Compensation and Special TCXO's - D. E. Newell and H. Hinnah

6-23-192 Temperature-Compensated Crystal-Controlled Oscillators Operating from 800 kHz to 1500 kHz - H. A. Batdorf

6-23-198 Frequency Standards for Communications - E. N. LeFevre

6-23-201 Digiphase Frequency Synthesizer - G. C. Gillette

6-23-211 A Miniature Precision Digital Frequency Synthesizer - R. J. Hughes and R. J. Sacha

6-24-191 Temperature Compensated Crystal Oscillators - P. Duckett, R. Peduto and G. Chizak

6-24-200 New Approach to a High Stability Temperature Compensated Crystal Oscillator - S. Schodowski

6-24-209 An Ultra Low Noise Direct Frequency Synthesizer - D. G. Meyer

6-25-231 The Design and Performance of an Ultra-Pure, VHF Frequency Synthesizer for Use in HF Receivers - M. E. Peterson, Collins Radio Co.

6-25-240 The Spectral Frequency Synthesizer - D. R. Lohrmann and A. R. Sills, USAECOM

6-26-43 Two Stage Self Limiting Series Mode Type Quartz Crystal Oscillator Exhibiting Improved Short-Term Frequency Stability - M. M. Driscoll, Westinghouse Electric Corp.

6-26-50 Low Noise Frequency Multiplication - R. A. Baugh, Hewlett Packard Co.

6-26-55 The Design and Performance of an Ultra Low-Noise Digital Frequency Synthesizer for Use in VLF Receivers - M. Peterson, Collins Radio Co.

6-26-132 A Temperature Compensated Crystal Oscillator Utilizing Three Crystals - K. Hirama, Toyo Communication Equipment Co., and M. Onoe, University of Tokyo, Japan

6-26-140 Low Power Crystal Oscillator for Electronic Wrist Watch - H. Yoda, H, Ikeda and Y. Yamabe, Nihon Kogyo Co., Ltd., Japan

6-26-264 The Disciplined Time/Frequency Standard: A New Multi-Function Crystal Oscillator - D. Babitch, J. Ho, and M. Bloch, Frequency Electronics, Inc.

6-26-279 Quasiperiodic Frequency Synthesis - Prof. Dr. G. Becker, Physikalisch-Technische Bundesanstalt, West Germany

6-27-157 Q-Multiplied Quartz Crystal Resonator for Improved HF and VHF Source Stabilization - M. M. Driscoll, Westinghouse Electric Corp.

6-27-170 Low Noise UHF Crystal Controlled Source - D. J. Healey, Westinghouse Electric Corp.

6-27-180 A 500 MHz Low Noise General Purpose Frequency Synthesizer - W. F. Byers, K. W. Craft and G. H. Lohrer, General Radio Co.

6-27-191 Digitally Compensated TCXO - G. E. Buroker and M. E. Frerking, Collins Radio Co.

6-27-199 A Fast Warmup Quartz Crystal Oscillator - H. M. Greenhouse, R. L. McGill and D. P. Clark, The Bendix Corp.

6-27-218 High Stability Integrator-Controlled Oven for Crystal Oscillators - T. Hamatsuki, H. Uchida, U. Goto, Nippon Electric Co.Ltd.

6-28-150 Phase Noise of Various Oscillators at very Low Fourier Frequencies - D. Babitch and H. Fallek, Hewlett Packard

6-28-160 Relations Between Spectral Purity and Frequency Stability - J. Rutman, ADRET

6-28-166 On 1/f-Noise in Diodes and Transistors - O. Mueller, General Electric Co.

6-28-181 The Design and Performance of a Crystal Oscillator Exhibiting Improved Short Term Frequency Stability - J. Groslambert, G. Marianneau, M. Olivier and J. Uebersfeld, C. N. R. S., Besançon

6-28-203 Abnormal Crystal Oscillator Frequency Change with Load Capacitance and its Elimination - S. Nonaka, Nippon Electric Co.

6-28-211 Compensated Wide Band Voltage Controlled Oscillator for the Viking Program - M. Bloch, M. Meirs and M. Rosenfeld, Frequency Electronics

6-28-214 Microcircuit Temperature Compensated Crystal Oscillator (MCTCXO) - D. L. Thomann, CTS Knights, Inc.

6-28-221 New Approach to the Design of Crystal Oscillators - Y. Ohata, Defense Academy, Japan

6-28-232 Explicit Expressions for TCXO Design - S. K. Sarkar, Croven Limited

6-28-237 Computer Design and Analysis for High Precision Oscillators - J. Ho, R. Nardin, Frequency Electronics Inc.

6-28-243 A Method for Estimating the Frequency Stability of an Individual Oscillator - J. E. Gray and D. W. Allan, National Bureau of Standards

6-29-248 Low Noise Microwave Oscillator Design - G. Jerinic, N. Gregory and W. Murphy, Raytheon Co.

6-29-264 Aerospace Radar Stalo-Synthesizers - R. C. Kley, Jr., RCA

6-29-285 Data Collection Platforms - K. L. Farber, American Electronics Laboratories, Inc.

CATEGORY 6 (Cont'd):

6-29-294 An Analysis of Frequency Stability for TCXO - S. Fujii and H.Uchida, Nippon Electric Company, Ltd.

6-29-300 VCXO: Theory and Practice - J. Helle, Campagnie d'Electronique et de Piezo-electricite

6-29-308 1/f Resonant Frequency Fluctuation of a Quartz Crystal - T. Musha, Tokyo Institute of Technology

6-29-311 Internal Noise of a Quartz Crystal Oscillator, Influence of the Parallel Capacitance - R. Brendel, J. Groslambert, G. Marianneau, M. Oliver and J. Uebersfeld, C. N. R. S. Besançon

6-30-420 Microwave Frequency Synthesis for Satellite Communications Ground Terminals - G. Mackiw and G. Wild, RCA

6-30-275 An Ultra-Stable Low Power 5 MHz Quartz Oscillator Qualified for Space Usage - J. R. Norton, Johns Hopkins University

6-30-279 *Stable Oscillator for Pioneer Venus Program* - M. P. Meirs, T. Robinson and M. B. Bloch, Frequency Electronics

6-30-284 The Stability of Precision Oscillators in Vibratory Environments - A. Vulcan and M. Bloch, Frequency Electronics

6-30-292 A Miniature High Stability TCXO Using Digital Compensation - A. Mroch and G. Hykes, Collins Radio Group

6-30-301 Linearization of Direct FM Voltage Controlled Crystal Oscillators - S. J. Lipoff, Bell & Howell

6-30-309 System for Automatic Phase Noise Measurement - L. Peregrino and D. Ricci, Hewlett-Packard

6-30-318 An Efficient Hardware Implementation for High Resolution Frequency Synthesis - B. Bjerde and G. Fisher, General Dynamics

CATEGORY 7:

Quantum Electronic Frequency Standards (Microwave Frequencies)

7-10-259 Atomic and Molecular Frequency Standards - R. Dicke, Princeton University

7-11-307 Rubidium Oscillator Experiments - T. R. Carver, Princeton University

7-11-318 Optical Pumping, Buffer Gases and Walls - W. B. Hawkins, Yale University

7-11-324 Hot Sources for MASER - M. W. P. Strandberg Massachusetts Institute of Technology

7-11-335 MASER Progress and Phase Lock Techniques - F. O. Vonbun and G. M. R. Winkler, Frequency Control Branch, USASEL

7-11-352 MASER Engineering at Jet Propulsion Laboratory - W. Higa, Jet Propulsion Lab.

7-11-373 Precision Atomic Beam Techniques - P. Kusch, Columbia University

7-11-385 Performance of Cesium Beam Standards and Future R&D Plans - F. H. Reder and S. H. Roth, Frequency Control Branch, USASEL

7-12-517 Progress in MASER Work at USASEL - F. H. Reder, Frequency Control Division, USASEL

7-12-534 Measurement of MASER Frequency in Terms of Cesium Standard - G. M. R. Winkler, Frequency Control Division USASEL

7-12-538 MASER Research at Neuchâtel University, Switzerland - J. Bonanomi, Neuchâtel University

7-12-551 Beam MASER Techniques - Walter H. Higa, Jet Propulsion Laboratory

7-12-569 A Sealed-Off MASER - S. Johnson, Polytechnic Research and Development Co., Inc.

7-12-577 Realization and Measurement of Long Free Atom Spin State Life Times- H. Dehmelt, University of Washington

7-12-593 Optical Detecting of Cesium Hyperfine Transition - Peter L. Bender and Earl C. Beaty, Nat'l Bureau of Standards and Andrew R. Chi, U. S. Naval Research Laboratory

7-12-606 Gas Cell "Atomic Clocks" Using Buffer Gases and Optical Orientation - M. Arditi, Federal Telecommunication Labs.

7-12-625 Discussion of Some Limits of Atomic Frequency Control - T. R. Carver, Princeton University

7-12-632 Design Considerations of Atomic Beam Frequency Standards for Missile Environment - R. T. Daly, TRG Incorporated

7-13-266 Atomic Beam Work at the National Physical Laboratory during 1958-1959 - L. Essen

7-13-276 National's Militarized Cesium Beam Frequency Standards - A. McCoubrey

7-13-297 TRG Missile-borne Cesium Beam Standard - R. Daly

7-13-309 Broken Beam Experiment at Harvard University - D. Kleppner

7-13-546 Missile-borne MASER - F. H. Reder and C. Bickart

7-13-575 Gas MASER for Frequency Control - J. F. Lotspeich and M. L. Stitch

7-13-583 MASER Frequency Stability - J. A. Barnes and R. Mockler

7-13-596 Ammonia MASER Work at Bell Telephone Laboratories - L. D. White

7-13-603 MASERs with Slow Molecules - J. G. King

7-13-604 Suitable Molecules for Utilizing MM-Wave Transitions for Frequency Control - J. Gallagher

7-13-618 MASER Laboratory Frequency Standard - F. Vonbun

7-13-632 Triple Resonance Method to Achieve Narrow and Strong Spectral Lines - C. Alley

7-13-648 Gas Cell Frequency Standards Using Buffer Gases and Buffer Walls - R. Whitehorn

7-13-655 Evaluation of ITT Breadboard Gas Cell Frequency Standard - M. Arditi

7-13-668 Hyperfine Transitions in Rubidium 87 Vapor E. C. Beaty, P. Bender and A. Chi

7-13-676 Gas Cell Work at the Space Technology Laboratories - D. J. Farmer, J. M. Andres and G. I. Inouye

7-13-683 Study of the Spin Relaxation of Optically Aligned Rubidium Vapor - W. Franzen

7-14-250 Work on Atomic Frequency Standards at the Nat'l Physical Laboratory during 1959-1960 - L. Essen

7-14-261 A Superior Atomic Clock for Continuous Long Time Operation - G. Winkler

7-14-298 NBS Atomic Frequency Standards - R. Mockler and R. E. Beehler

7-14-310 Molecular Beam Devices with Storage Boxes - N. F. Ramsey, D. Kleppner and H. M. Goldenberg.

7-14-315 Missile-borne Atomicron Frequency Standard - A. O. McCoubrey

CATEGORY 7 (Cont'd):

7-14-328 Effect of Molecular Frequency Spread on Emission in Cavities - I. R. Senitzky

7-14-329 Frequency Shifts of Microwave Resonance in a Gas Cell Using Optical Pumping - M. Arditi and T. R. Carver

7-14-330 Design Considerations for a Self-Contained Ammonia Maser Oscillator - S. Hopfer

7-14-354 Description of a Long Cesium Beam Frequency Standard - P. Kartaschoff, J. Bonanomi and J. DeParins

7-15-156 The Atomic Clock as a Phase-Stable Oscillator for Deep Space Communication - L. Malling

7-15-168 Frequency Control of NBA on an International System (II) - W. Markowitz and R. G. Hall

7-15-180 The Atomic Hydrogen Maser - N. F. Ramsey

7-15-181 Frequency Control by Gas Cell Standards - Fundamental Problems in the Light of Recent Experimental Results - M. Arditi

7-15-203 The Ultimate Signal to Noise Possibilities of a Maser - I. R. Senitzky

7-15-204 Choice of a Molecular Transition for Frequency Control in the Millimeter Wave Region - F. Barnes, D. Burkhard and M. Mizushima

7-15-210 Deuterated Ammonia Submillimeter Maser - A Progress Report - V. E. Derr, J. J. Gallagher and M. Lichtenstein

7-16-256 Advances in CW Solid State Optical Masers - C. G. B. Garrett

7-16-257 Frequency Characteristics of an Optical Maser - A. Javan and T. S. Jaseja

7-16-258 Spectral Distribution of Induced and Spontaneous Emission by a Molecular Beam in a Cavity- I. R. Senitzky

7-16-259 Comparison of Performance Criteria of Frequency Standards - C. L. Searle and D. A. Brown

7-16-267 Theory of Resonance Frequency Shift Due to the Radiation Field - M. Mizushima

7-16-287 The Atomic Hydrogen Maser - N. F. Ramsey

7-16-305 Generation of Phase-Locked Millimeter Waves for Frequency Control - R. G. Strauch, R. E. Cupp, J. W. Dees and J. J. Gallagher

7-17-176 Application of Superconductivity to Frequency Control - W. Hartwig

7-17-329 Achievements and Problem Areas of Atomic Frequency Control - F. H. Reder

7-17-372 Frequency Beat Experiments with Hydrogen Masers - R. F. C. Vessot and H. E. Peters

7-17-392 Experimental Evaluation of a Thallium Beam Frequency Standard - R. E. Beehler and D. J. Glaze

7-17-408 Recent Developments in the Field of Atomic Frequency and Time Standards in Switzerland - J. Bonanomi

7-17-409 Excitation of Millimeter Wave Transitions for Frequency Control - R. G. Strauch, R. E. Cupp and J. J. Gallagher

7-17-438 Development and Performance of a Miniaturized Cesium Beam Tube - J. George

7-17-449 Performance and Application of Gas Cell Frequency Standards - D. J. Farmer

7-17-462 Report on the Frequency of Hydrogen - W. Markowitz

7-18-265 A Discussion of the Properties of Four Molecular Beam Detectors - F. Barnes, S. Andresen, C. Shipley and D. Foiani

7-18-283 Hydrogen Maser Work at USAEL - H. G. Andresen, C. J. Bickart

7-18-299 Recent Developments in Hydrogen Masers - R. F. C. Vessot, H. E. Peters and J. Vanier

7-18-308 The NPL Frequency Standard - L. Essen, J. McA. Steele and D. Sutcliffe

7-18-322 Recent Progress in Cesium Beams at National - J. George, E. Wunderer and T. Athanis

7-18-344 A Modern Solid State Portable Cesium Beam Frequency Standard - A. S. Bagley and L. S. Cutler

7-18-366 Progress in the Development of a Cesium Beam Oscillator for Aerospace Guidance - J. H. Holloway and R. H. Woodward

7-18-384 A Militarized Solid State Cesium Beam Frequency Standard - A. Orenberg

7-19-298 A Militarized Solid State Cesium Beam Frequency Standard - S. Fast, J. George, G. Simpson and C. Lydiard

7-19-332 Long Time Constant Servo System for Cesium Beam Frequency Standard - H. Daams and A. G. Mungall

7-19-344 Characteristics of a High Performance Cesium Beam Frequency Standard - J. Holloway and R. Sanborn

7-19-369 Line Width Investigation of Millimeter Electric Resonance Molecular Beam Transitions - R. G. Strauch, R. E. Cupp, V. E. Derr and J. J. Gallagher

CATEGORY 7 (Cont'd):

7-19-385 Methods and Results for Reducing Cavity Pulling Effects of the Hydrogen Maser Frequency - H. Andresen

7-19-402 A Comparison of Performance Characteristics of Hydrogen, Rubidium and Ammonia Masers - R. Vessot, J. Vanier, H. E. Peters and L. Mueller

7-19-416 Large Storage Bulb for Hydrogen Frequency Standard - N. F. Ramsey

7-19-417 The Effects of Optical Pumping on the Rb^{87} Maser Oscillator - P. Davidovits and W. A. Stern

7-20-364 On the Power Output of the Optically Pumped Rb^{87} Maser - J. Vanier

7-20-365 High-Power Maser Atomic Frequency Standards - R. Novick, W. Happer and W. A. Stern

7-20-370 Stark-Filtered Intensity-Pumped Maser Atomic Frequency Standards - W. A. Stern, W. Happer and R. Novick

7-20-377 Millimeter and Submillimeter Wave Molecular Beam Investigations - J. J. Gallagher, R. E. Cupp and R. A. Kempf

7-20-387 Recent Developments in Hydrogen Masers - N. F. Ramsey

7-20-389 Studies of Field Effect Transistors for Use in Atomic Beam Tube Detectors - J. H. Holloway and P. Penfield, Jr.

7-20-402 Servo-Controlled Hydrogen Maser Cavity Tuning - H. G. Andresen and E. Pannaci

7-20-416 A Thallium Atomic Beam Tube for Frequency Control - R. F. Lacey

7-20-424 Some Accuracy Limiting Effects in an Atomic Beam Frequency Standard - R. J. Harrach

7-20-436 The Canadian Cesium Beam Frequency Standard - A. G. Mungall, H. Daams and R. Bailey

7-20-448 Performance Characteristics of a Portable Cesium Beam Standard - L. N. Bodily

7-21-467 Molecular and Atomic Beam Geometry Optimization - J. DePrins, P. J. Wauters and S. G. Andresen

7-21-483 A New Cesium Beam Resonator - J. George

7-21-484 A Proposed Barium Oxide Molecular Beam Frequency Standard - H. Hellwig

7-21-491 Determination of the Ta^{205} Ground State hfs Transition Frequency - R. F. Lacey

7-21-500 Recent Developments in Atomic Hydrogen Masers - N. F. Ramsey

7-21-543 Atomic Hydrogen Maser Work at L.S.R.H. Neuchâtel, Switzerland - Ch. Menoud, J. Racine and P. Kartaschoff

7-21-568 Recent Development on the Rubidium 87 Maser - J. Vanier

7-22-452 Large Storage Box Hydrogen Maser - E. E. Uzgiris and N. F. Ramsey

7-22-464 Hydrogen Standard Work at Goddard Space Flight Center - H. E. Peters, T. E. McGunigal and E. H. Johnson

7-22-493 Application of the Transient Behavior to the Study of the Hydrogen Maser - C. Audoin, M. Desaintfuscien and J. P. Schermann

7-22-517 Some Experimental Results of BaO Applicable to a Molecular Beam Frequency Standard - S. G. Andresen, H. O. Mortelmans, P. J. Wauters and J. DePrins

7-22-529 Barium Oxide Beam Tube Frequency Standard - H. Hellwig, R. McKnight, E. Pannaci and G. Wilson

7-22-545 Phase Shift in Microwave Ramsey Structures - R. F. Lacey

7-22-559 Study of Phenomena Affecting the Composition of Rubidium Vapor Cells - M. P. R. Thomsen, L. J. Stief and R. J. Fallon

7-22-573 Extension of Frequency Control Techniques to the Submillimeter Wavelength Region - R. A. Kempf, R. E. Cupp, W. T. Smith and J. J. Gallagher

7-22-605 Progress in the Development of Hydrogen Masers - M. Baker, M. Levine, L. Mueller and R. Vessot

7-23-263 Light Modulation at the Rb^{87} Hyperfine Frequency - H. Tank and W. Happer

7-23-271 An Optically Pumped Rb^{85} Maser Frequency Standard - W. A. Stern and R. Novick

7-23-274 A Report on the Performance Characteristics of a New Rubidium Vapor Frequency Standard - D. H. Throne

7-23-279 Improved State Selection for Hydrogen Masers - R. F. Lacey and R. F. C. Vessot

7-23-284 Recent Results Concerning the Hydrogen Maser Wall Shift Problem - E. E. Uzgiris and P. W. Zitzewitz

CATEGORY 7 (Cont'd):

7-23-288 A New Method for Measurement of the Population Difference of Hyperfine-Levels of Stored Atoms - C. Audoin, M. Desaintfuscien, P. Piejus and J. P. Schermann

7-23-297 Atomic Hydrogen Standards for NASA Tracking Stations - H. E. Peters, T. E. McGunigal and E. H. Johnson

7-24-246 Areas of Promise for the Development of Future Primary Frequency Standards - H. Hellwig

7-24-259 Hydrogen Maser with Deformable Storage Bulb - P. Debely

7-24-263 Surface Collision Frequency Shifts in the Atomic Hydrogen Maser - P. W. Zitzewitz

7-24-270 Studies of Hydrogen Maser Wall Shift for High Molecular Weight Polytetrafluorethylene - R. F. C. Vessot and M. W. Levine

7-24-279 New Information on the Physics of Rubidium Gas Cells - P. Bender and V. W. Cohen

7-24-280 Progress Report on the Rubidium 85 Maser - J. Vanier, R. Vaillancourt, G. Missout and M. Tetu

7-24-285 An Optically Pumped Parametric Frequency Converter - H. Tang and W. Happer

7-24-294 Cesium Beam Servo System Using Square Wave Frequency Modulation - H. Daams

7-24-308 New Primary Cesium Beam Frequency Standard, F. Kupersmith, C. Thornburg and J. Ho

7-24-361 The NBS Atomic Time Scale System: AT(NBS), SAT(NBS), and UTC(NBS) - D. W. Allan, J. E. Gray and H. E. Machlan

7-25-46 History of Atomic and Molecular Control of Frequency and Time - N. Ramsey, Harvard University

7-25-297 Cesium Atomic Beam Frequency Standards - R. Beehler, NBS Boulder Laboratory

7-25-309 Frequency Biases in a Beam Tube Caused by Ramsey Cavity Phase Differences - H. Hellwig, J. A. Barnes, D. J. Glaze, National Bureau of Standards

7-25-313 Performance of Newly Developed Cesium Beam Tubes and Standards - R. Hyatt, D. Throne, L. S. Cutler, J. H. Holloway and L. F. Mueller, Hewlett-Packard Company

7-25-325 A Field Independent Optically Pumped ^{85}Rb Maser Frequency Standard - W. A. Stern, General Time Corp., and R. Novick, Columbia University

7-25-331 Miniaturized, Rapid Warm Up Rubidium Frequency Source - M. M. Zepler, Plessey Com., Ltd., England

7-25-337 Discussion of Cavity Pulling in Passive Frequency Standards - J. Viennet, C. Audoin, and M. Desaintfuscien, Lab. de L'Horloge Atomique, France

7-25-343 Hydrogen Maser Wall Shift Experiments at the Nat'l Research Council of Canada - D. Morris, Nat'l Research Council, Canada.

7-25-348 Hydrogen Maser Frequency Standard - C. Finnie, R. Sydnor and A. Sward, Jet Propulsion Laboratory

7-26-202 Joseph H. Holloway (1929-1971) - Twenty Years of Progress in Atomic Frequency Standards - A. McCoubry, Varian Associates and L. Cutler, Hewlett-Packard Co.

7-26-211 Automatic Frequency Controlled Rubidium Frequency Standard - Y. Sato, H. Kumamoto, H. Oyamada and H. Uchida, Nippon Electric Company, Ltd., Japan

7-26-216 Rubidium Frequency and Time Standard for Military Environment - M. E. Frerking and D. E. Johnson, Collins Radio Company

7-26-223 Further Results on the Rubidium-87 Maser Frequency Standard - W. A. Stern, General Time Research Center, and R. Novick, Columbia Astrophysical Laboratory, Columbia University

7-26-225 Short Term Stability of Rb^{87} Maser - M. Tetu and Jacques Vanier, Laval University, Canada

7-26-230 Hydrogen as an Atomic Standard - H. Peters, NASA, Goddard Space Flight Center

7-26-242 Experimental Results with Atomic Hydrogen Storage Beam Systems - H. Hellwig and H. E. Bell, NBS

7-26-248 Precision Absolute Frequency and Wavelength Measurements in the Infrared: A Review of Activities at MIT - J. G. Small, J. P. Monchalin, M. J. Kelly, F. Keilmann, A. Sanchez, S. K. Singh, N. A. Kurnit and A. Javan, Massachusetts Institute of Technology

7-26-257 A Superconducting Cavity Stabilized Oscillator - S. R. Stein and J. P. Turneaure, Stanford University

7-26-319 Absolute Frequency of an Atomic Hydrogen Maser Clock - E. E. Peters, NASA, and R. G. Hall and D. B. Percival, US Naval Observatory

7-27-317 A Preliminary Report on Cs V, New NRC Long-Beam Primary Frequency and Time Standard - A. G. Mungall, R. Bailey, H. Daams, D. Morris and C. C. Costain, National Research Council of Canada

CATEGORY 7 (Cont'd):

7-27-334 Some Performance Data for the Standards in the National Bureau of Standards Atomic Time Scale System - D. W. Allan, D. J. Glaze, H. E. Machlan, A. E. Wainwright, H. Hellwig, James A. Barnes and J. E. Gray, NBS

7-27-347 Recent Progress on the NBS Frequency Standards - D. J. Glaze, H. Hellwig, S. Jarvis and A. E. Wainwright, NBS

7-27-357 Time Domain Velocity Modulation as a Tool to Evaluate Cesium Beam Tubes - H. Hellwig, S. Jarvis, D. J. Glaze, D. Halford and H. E. Bell, NBS

7-27-367 Developments of Hydrogen Masers as Frequency Standards at Orsay - P. Petit, J. Viennet, R. Bartillet, M. Desaintfuscien and C. Audoin, University of Paris

7-27-387 A New Miniature Rubidium Gas Cell Frequency Standard - E. Jechart, EFRATOM

7-27-390 Evaluation of a Rubidium Standard for Satellite Application - R. B. Moore, S. A. Nichols and J. D. White, Naval Research Laboratory

7-27-400 Cavity Tuning & Light Shift in the RB^{87} Maser - G. Busca, M. Tetu and J. Vanier, Laval University

7-27-404 Status of the Development of the Rubidium-87 Maser Frequency Standard - W. A. Stern and E. Aulich, General Time Research Center, and R. Novich, Columbia University

7-27-406 S and X-Band Superconducting Cavity Stabilized Oscillators - J. J. Jimenez and A. Septier, University of Paris

7-27-414 The Development of Superconducting Cavity Stabilized Oscillators - S. R. Stein and J. P. Turneaure, Stanford University

7-28-247 Atomic Frequency Standard Relativistic Doppler Shift Experiment - Harry Peters and Victor Reinhardt, NASA, Goddard Space Flight Center

7-28-315 Atomic Frequency Standards, A Survey - H. Hellwig, National Bureau of Standards

7-28-340 A Consideration of Rubidium Lamp Stability for Rubidium Frequency Standard - H. Oyamada, K. Takahashi, Y. Sato and H. Uchida, Nippon Electric Co.

7-28-344 A Compact Rb^{87} Maser(1) - G. Busca, J. Racine and J. Vanier, Laval University

7-28-350 Mg Frequency Standard: Optimization of the Metastable Atomic Beam - F. Strumia, P. Minguzzi, M. Francesconi and R. Benedetti, University of Pisa

7-28-355 Density-Dependent Shifts of Hydrogen Maser Standards - S. B. Crampton, H.T.M. Wang, Williams College

7-28-362 Preliminary Research and Development of the Cesium Tube Accuracy Evaluation System - D. A. Howe, H. E. Bell and H. Hellwig, National Bureau of Standards

7-28-401 Satellite Application of a Rubidium Frequency Standard - S. Nichols, J. White, Naval Research Laboratory

7-29-321 Application of Superconductivity to Precision Oscillators - S. R. Stein, National Bureau of Standards

7-29-352 A New Compact Cesium Beam Frequency Standard - E. Graf and Leland F. Johnson, Oscilloquartz SA, and R. A. Kern, Frequency and Time Systems, Inc.

7-29-357 An Improved Method for Measuring the Magnetic Inhomogeneity Shift in Hydrogen Masers - V. S. Reinhardt and H. E. Peters, NASA/Goddard Space Flight Center

7-29-362 The Concertina Hydrogen Maser - H. E. Peters NASA/Goddard Space Flight Center

7-29-371 The Hydrogen Maser Wall Shift Problem - J. Vanier, R. Larouche, Universite Laval, and C. Audoin, Universite de Paris Sud

7-29-383 Theoretical and Experimental Studies of Some Problems Related to the Passive Rubidium Gas Cell Frequency Standard - G. Missout and J. Vanier, Université Laval

7-29-387 A Digital 5.00688 MHz Synthesizer and Squarewave FM Servo System for Cesium Standards - D. A. Howe and H. F. Salazar, National Bureau of Standards

7-30-414 A Heuristic Model of Long-Term Atomic Clock Behaviour - D. B. Percival, US Naval Observatory

7-30-451 Velocity Distribution Measurements of Cs Beam Tubes - D. A. Howe, National Bureau of Standards

7-30-457 Performance of a Dual Beam High Performance Cesium Beam Tube - G. Seavey, Hewlett Packard

7-30-463 Measured Performance and Environmental Sensitivities of a Rugged Cesium Beam Frequency Standard - M. C. Fisher and C. E. Heger, Hewlett Packard

7-30-468 Optimization of the Buffer Gas Mixture for Optically Pumped Cs Frequency Standards - F. Strumia, N. Beverini, A. Moretti, Gruppo Nazionale Strutture della Materia, Piza, Italy, and G. Rovera, Istituto Elettrotecnico Nazionale, Torino, Italy

7-30-473 A New Kind of Passively Operating H-Frequency Standard - F. L. Walls and H. Hellwig, National Bureau of Standards

CATEGORY 7 (Cont'd):

7-30-481 Nasa Atomic Hydrogen Frequency Standards Program - An Update - V. S. Reinhardt, D. C. Kaufman, W. A. Adams and J. J. DeLuca NASA/Goddard Space Flight Center and J. L. Soucy, Bendix Field Engineering Corp.

7-30-489 A Study to Identify Hydrogen Maser Failure Modes - W. B. Bridges, A. N. Chester, J. E. Etter, A. E. Popa, B. L. Walsh and T. M. Wang, Hughes Research Laboratories

CATEGORY 8:

Quantum Electronic Frequency Standards (Infrared and Visible Frequencies)

8-15-225 The Optical Maser - W. Kaiser

8-17-425 Frequency Standards in the Optical Range - G. Gould

8-21-455 Techniques for Generating, Detecting and Phase Stabilizing Submillimeter Coherent Radiation - G. W. Bechtold, V. E. Derr and W. T. Smith

8-23-305 Frequency Mixing and Multiplication in the Far Infrared and Infrared - A. Javan

8-23-306 Pressure Shift and Broadening of Methane Line at 3.39 Micron Studied by Laser-Saturated Molecular Absorption - R. L. Barger and J. L. Hall

8-23-307 Stability Investigations of HCN Laser - V. J. Corcoran, R. E. Cupp and J. J. Gallagher

8-23-312 Laser Frequency Stabilization Using a Primary Frequency Reference - S. Ezekiel

8-24-233 Laser Frequency Stabilization Techniques and its Applications - H. S. Boyne

8-24-240 Automatic Frequency Control and Phase-locking of Lasers - V. J. Corcoran, R. E. Cupp and J. J. Gallagher

8-24-275 Frequency Stabilization of Co_2 Lasers with Respect to Passive SF_6 and CO_2 Line Centers - P. Rabinowitz, R. Keller and J. T. LaTourrette

8-26-250 A Stabilized HCN Laser for Infrared Frequency Synthesis - J. S. Wells, NBS

8-27-376 Characteristics of the 644 nm He-Ne Laser Stabilized by Saturated Absorption in Iodine-Vapour - A. J. Wallard, National Physical Laboratory

8-27-382 Molecular Beam Stabilized Laser - L. A. Hackel, D. C. Youmans and S. Ezekiel, Massachusetts Institute of Technology

8-27-386 Influence of Hyperfine Structure of Methane Stabilized He-Ne Laser - C. Borde and J. Hall, National Bureau of Standards

8-28-348 Infrared Rectification and Frequency Mixing in a Thin Film Metal, Metaloxide, Metal Diode Structure - A. Javan and J. G. Small, Massachusetts Institute of Technology

8-29-316 Frequency Stabilization of a CW Dye Laser and Lasr Saturation of Atomic Beams - R. L. Barger, T. C. English and J. B. West, National Bureau of Standards

8-29-328 High Speed Rectifying Junctions in the Infrared Regions: Recent MIT Developments - A. Sanchez, Massachusetts Institute of Technology

8-29-330 Frequency Stabilization of CO_2 Lasers - C. Freed, Massachusetts Institute of Technology

8-29-338 Potential Frequency Accuracy of the CO_2 Fluorescence Saturation Dip - M. J. Kelley, J. E. Thomas, J. P. Monchalin, N. A. Kurnit, and A. Javan, Massachusetts Institute of Technology

8-29-344 Limitations on Miniature Molecular Frequency Sources - J. J. Gallagher, Georgia Institute of Technology

CATEGORY 9:

Frequency and Time Coordination and Distribution

9-10-216 Comparison Measurements on Frequency Standards - J. A. Pierce, Harvard University

9-11-574 Low Frequency Standard Transmissions - W. D. George, National Bureau of Standards

9-12-648 Comparison of Atomichrons with British Cesium Beam Frequency Standard - A. O. McCoubrey, National Company, Inc.

9-12-665 Comparison of Atomic and Astronomical Time - William Markowitz, U. S. Naval Observatory

9-13-316 The System of Atomic Time, A.1 - W. M. Markowitz

9-13-318 Atomic Frequency Standards for Propagation Studies - J. Pierce

9-13-342 Synchronized Clock Experiment - R. Bridgham, G. Winkler and F. H. Reder

9-14-254 Preliminary Results on Project WOSAC - G. Winkler and F. Reder

9-14-267 Results of GBR Experiment - J. Pierce

9-14-275 Stabilization of VLF Transmissions at NBA - H. Hastings and W. Markowitz

9-14-276 Timing Potential of Loran-C - G. Hefley, R. F. Linfield and R. H. Doherty

9-15-226 Final Results of a World-Wide Clock Synchronization Experiment (Project WOSAC) - F. Reder, P. Brown, G. Winkler and C. Bickart

9-16-227 Synchronization of Local Frequency Standards with VLF Transmissions - R. R. Stone, Jr.

9-16-249 Time Keeping Satellites - R. H. Dicke

9-16-250 Theory of Time Keeping in Space - R. K. Sachs

9-18-251 High Precision Frequency and Clock Synchronization Techniques on an International Basis - W. Markowitz

9-18-395 VLF Frequency Synchronization Provided with FSK Capability - R. R. Stone and T. H. Gee

9-19-195 A Report on the Hewlett-Packard Flying Clock Experiment Number Two - L. N. Bodily

9-19-297 Clock Synchronization Via Relay II, Preliminary Report - W. Markowitz and C. A. Lidback

9-20-577 A Digital Servo for Frequency and Time Scale Conversion - P. Kartaschoff and H. Brandenberger

9-20-588 Time Synchronization of Remote Clocks Using Dual VLF Transmissions - A. R. Chi and S. N. Witt

9-20-612 VLF Envelope Timing Experiment - D. Himes

9-20-613 Use of Loran-C for Timing and Frequency Comparison - L. D. Shapiro

9-21-509 Frequency Comparison System for Spacecraft Relativity Experiment - D. Kleppner

9-22-383 Recent Improvements in the U. S. Naval Observatory Timekeeping and Time Distribution Operations - G. M. R. Winkler

9-22-384 Clock Error Statistics as a Renewal Process - G. E. Hudson and J. A. Barnes

9-22-419 Results of Differential Omega Test and Evaluation Program - J. R. Wright

9-22-441 Precise Frequency Comparison using a Frequency Tracking Technique - W. V. Burhop and L. G. Wilson

9-23-18 International Coordination of Radio Time Signal Emissions - H. Smith

9-23-236 Use of the Loran-C System for Time and Frequency Dissemination - LCDR P. E. Pakos

9-23-248 An Application of Statistical Smoothing Techniques on VLF Signals for Comparison of Time Between USNO and NBS - A. Guetrot, D. W. Allan, L. S. Higbie and J. Lavanceau

9-23-249 A Coordinate Frequency and Time System - G. E. Hudson, D. W. Allan, J. A. Barnes, J. Lavenceau, R. G. Hall and G. M. R. Winkler.

CATEGORY 9 (Cont'd):

9-24-315 Time/Frequency Technology in System Development - R. E. Perkinson

9-24-322 A Survey of Time and Frequency Dissemination Techniques - J. Jesperson

9-24-325 Time and Frequency Transfer Via Microwave Link - D. Phillips, R. Phillips and J. O'Neill

9-24-332 Diurnal Phase of VLF Signals Near Antipode of a Transmitter - A. R. Chi

9-24-339 A Second Satellite Oscillator Experiment - R. Easton, C. Bartholomew and J. Bowman

9-24-345 The Omega Navigation System as a Source of Frequency and Time - W. Palmer

9-25-152 Time Control of Frequency Shift Keyed Transmissions at VLF - R. R. Stone and T. H. Gattis, Naval Research Laboratory, and T. N. Lieberman, NELEX

9-25-159 Omega VLF Timing - E. R. Swanson, Naval Electronics Laboratory Center

9-25-167 Time Dissemination Capabilities Using the Omega System - L. Fey, National Bureau of Standards

9-25-171 Use of Loran C Over Land - B. Wieder, Institute for Telecommunication Services

9-25-179 One Way Time Dissemination from Low Altitude Satellites - L. Reuger, Applied Physics Laboratory, Johns Hopkins University

9-25-186 Time Transfer by Defense Communications Satellite - J. A. Murray, D. L. Pritt, L. W. Blocker, W. E. Leavitt and P. M. Hooton, Naval Research Laboratory, and W. D. Goring, Naval Electronics Systems Command

9-25-194 Long Term Accuracy of Time Comparisons Via TV Radio Relay Links - S. Leschiutta, Instituto Elet. Nazionale, Italy

9-25-195 Precision and Accuracy of Remote Synchronization Via Portable Clocks, Loran C, and Network Television Broadcasts - D. W. Allan, D. D. Davis, B. E. Blair and H. E. Machlan, National Bureau of Standards

9-25-209 Methods of Local Time and Frequency Transfer - D. H. Phillips, R. E. Phillips, J. A. Bowman and J. J. O'Neill, Naval Research Laboratory

9-25-217 International Coordinated Clock Time and the Coming Improvements in System "UTC" - G. M. R. Winkler, U. S. Naval Observatory

9-26-269 The Standards of Time and Frequency in the U. S. A. - J. A. Barnes, NBS and G. M. R. Winkler, USNO

9-26-292 Nationwide Precise Time and Frequency Distribution Utilizing an Active Code Within Network Television Broadcasts - D.A. Howe, NBS

9-26-309 Time Transfer Using Nearly Simultaneous Reception Times from a Common Transmitter - D. W. Allan and H. E. Machlan, NBS and J. Marshall, Hewlett-Packard Co.

9-26-317 Standard Frequency and Time Service Using Radio Broadcasting Facilities - L. H. Montgomery, Vanderbilt University and Station WSM

9-27-270 Time Synchronization of NASA Tracking Stations via LORAN-C - W. E. Mazur, NASA Goddard Space Flight Center

9-27-277 International Time Transfer Using the Timation II Satellite - J. A. Buisson, Naval Research Laboratory

9-27-286 Diurnal and Seasonal Variations in Atmospheric Time Delay - D. M. LeVine, University of Maryland

9-27-290 Application of Phase Stable VLF Signals in Small Aircraft - J. J. Tymczysyn, Federal Aviation Administration

9-27-296 Active and Passive Relative Synchronization of Remote Clocks in a Time Ordered System - P. Coralnick and R. C. Stow, Singer General Precision

9-27-304 Accuracy of Overland Radio Location System at Fort Hood Using 1.5 to 2.0 MHz Frequency Region - J. R. Wright, Tracor

9-27-312 UHF Frequency Translator Based on Regenerative Division - J. O'Neill, D. Phillips and R. Stone, Naval Research Laboratory

9-28-373 Reference Frequency Transmission over Bell System Radio and Coaxial Facilities - R. F. Powers, Bell Telephone Laboratories

9-28-379 A Comparison of the Cesium and Hydrogen Hyperfine Frequencies by Means of Loran C and Portable Clocks - V. Reinhardt, Harvard University and J. Lavanceau, U. S. Naval Observatory

9-28-384 Satellite to Ground Timing Experiments - R. J. Taylor, Johns Hopkins University

9-28-389 Collecting and Processing PITI Data - L. C. Fisher, U. S. Naval Observatory

CATEGORY 9 (Cont'd):

9-28-395 Frequency Synthesizer for Normalizing the Frequency and Time Scales of Crystal Clocks on Orbiting Satellites - L. J. Rueger and A. G. Bates, Johns Hopkins University

9-28-406 Digital Clock Synchronization via Switch Long Distance Telephone Lines - C. C. Costain and L. G. Miller, National Research Council of Canada; A. Nishimura, Edmunde Newhall Associates

9-28-408 Performance Data of Space and Ground Hydrogen-Masers and Ionospheric Studies for High Accuracy Frequency Comparison Between Space and Ground Clocks - R. F. C. Vessot and M. W. Levine, Smithsonian Astrophysical Observatory

9-29-384 Sub-Microsecond Time Transport with a Rubidium Portable Clock - H. Hellwig and A. E. Wainwright, National Bureau of Standards

9-30-401 Minimum Variance Numerical Methods for Synchronizing Airborne Clocks - R. J. Kulpinski, MITRE Corporation

9-30-438 Phase Synchronization of a large HF Array by a Local Broadcast Station - S. H. Taheri, B. D. Steinberg and D. L. Carlson, University of Pennsylvania

9-30-444 The Remote Synchronization Technology - L. J. Rueger, Johns Hopkins University

CATEGORY 10:

Applications of Frequency Control Devices

10-10-439 Crystal Requirements for Future Military Equipment - J. M. Havel, Frequency Control Branch, SCEL

10-12-193 A Frequency Standard for Use in Missiles - H. Paul Brower, Collins Radio Company

10-13-248 A Communications Requirement of the Space Age - W. Victor

10-13-261 Frequency Control Devices and the Micro Module Program - M. Bernstein

10-14-404 Frequency Standards for Military Applications - D. E. Johnson and J. P. Fredericks

10-21-512 The Design of an Atomic Hydrogen Maser System for Satellite Experiments - R. Vessot, M. Levine, L. Mueller and M. Baker

10-22-206 The Application of Piezoelectric Coupled-Resonator Devices to Communication Systems - W. L. Smith

10-22-342 Crystal Oscillator Satellite Experiment - R. Easton, A. Bartholomew, D. Phillips and M. Bloch

10-23-1 Frequency Control Requirements for the Mallard Communication System - J. DelVecchio and J. Dressner

10-23-8 Application of Precise Time-Frequency Technology in Multi-Function Systems - T. C. Viars

10-23-14 Frequency Control for Tactical Net SSB Equipment - O. P. Layden

10-23-157 A Flexure-Mode Quartz for an Electronic Wrist Watch - M. P. Forrer

10-25-70 Quartz Crystal Applications in Digital Transmission - R. B. Robrock II, Bell Telephone Laboratories, Inc.

10-25-74 Frequency Control Devices for Mobile Communications - R. J. Munamaker, Motorola, Inc.

10-25-75 The Crystal Controlled Electronic Wrist Watch System: A Si-gate and CMOS-MSI Approach - R. G. Daniels and F. H. Musa, Motorola, Inc.

10-25-82 Frequency and Time in Airtraffic Control and Collision Avoidance Application - V. I. Weihe, Consultant

10-25-88 Application of Crystal Clocks for Navigation and Time-Ordered Communication - R. J. Kulpinski, MITRE Corporation

10-25-94 Time Synchronized Ranging System - R. M. Aughey, Singer-General Precision, Inc., Kearfott Div.

10-25-102 Piezoelectric Sensors for Use as Pollution Detectors, Meteorology Monitors and Research Instruments - J. Kertzman, Consultant

10-25-104 The Present State of the Art in Piezoelectric Sensors - W. King, Esso Research and Engineering Company

10-25-125 Quartz Crystal Units for High G Environment - M. Bernstein, USAECOM

10-26-4 Precise Time and Frequency in a Communication System - H. Folts, Defense Communications Engineering Office

10-26-8 Synchronization in High Capacity Broadband Carrier Systems - J. F. Barry and S. Narayanan, Bell Telephone Laboratories

10-26-15 Frequency Control Aspects in Army Communications and Surveillance - E. Hafner, ECOM

10-26-21 Short Term Frequency Stability in Coherent Radar Applications - W. K. Saunders, Harry Diamond Laboratories

10-26-113 Frequency Control Requirements for Remote Sensor Systems - W. D. Lawrence, Defense Special Projects Group

10-27-39 Quartz Crystal Units for Space Applications - C. Gilbert, S. Broussou and J. Morel, Compagnie d' Electronique et de Piézo-Electricité-C.E.P.E.

10-29-417 Time Standard Error Modeling with Applications to Satellite Navigation - G. L. Mealy and D. R. Vander Stoep, The Analytic Sciences Corporation

CATEGORY 10 (Cont'd):

10-30-371 Frequency Control and Time Information in the NAVSTAR/Global Positioning System - F. E. Butterfield, Aerospace Corporation

10-30-375 Time Requirements in the NAVSTAR Global Positioning System (GPS) Control Segment - A. J. Van Dierendonck, General Dynamics

10-30-384 Oscillator and Frequency Management Requirements for GPS User Equipments - R. A. Maher, Texas Instruments

10-30-390 NAVSTAR Global Positioning System - Oscillator Requirements for the GPS Manpack - J. Moses, Magnavox

CATEGORY 11:

Measurements and Specifications

11-10-305 VHF Crystal Measurements - G. K. Guttwein and D. Pochmerski, Frequency Control Branch, SCEL

11-10-323 A New Method for Measuring the Equivalent Parameters of VHF Quartz Crystals - Douglas W. Robertson, Georgia Institute of Technology

11-10-496 A Counter Transfer Oscillator System for Microwave Frequency Measurements - Alan Bagley and Dexter Hartke, Hewlett-Packard Company

11-11-402 Frequency Control Standardization Trends Within the International Electrotechnical Commission - W. J. Young, Standard Telephones and Cables (England)

11-11-441 Equipment for Detecting Unwanted Modes in Oscillator Crystals - Joseph Loos, Motorola, Inc.

11-11-457 Low Frequency C. I. Meter AN/TSM-14 - E. A. Gilbert, Radio Frequency Laboratories, Inc.

11-11-463 VHF C.I. Meter AN/TSM-15 - D. Pochmerski, Frequency Control Branch, USASEL

11-11-479 Crystal Measuring Techniques Above 200 mc/sec - Samuel N. Witt, Jr., Georgia Institute of Technology

11-11-597 Precision Measurement of Short Time Intervals - F. K. Priebe, D. Schwab and H. D. Tanzman, Frequency Control Br., USASEL

11-12-334 Measuring the Resonance Frequency of Quartz Crystals with Improved Accuracy - A. O. Platt, H. G. Tobinski and H.E.Gruen, Armour Research Foundation

11-12-359 An Instrument for Detecting Unwanted Modes in Oscillator Crystals - Joseph Loos, Motorola

11-12-383 VHF Crystal Parameter Measurements - Samuel N. Witt, Jr., Georgia Institute of Technology

11-13-123 Measurement of HF Crystal Units with Increased Accuracy - D. Pochmerski and C. L. Shibla

11-13-137 Methods of Measuring Quartz Crystal Units at VHF - S. Witt

11-13-354 Measuring Instruments for Determination of Electrical Characteristics of Quartz Over the Range from 0 to 300 mc - H. Flicker

11-13-384 Short-term Frequency Stability Measurements - H. D. Tanzman

11-15-98 Higher Precision Crystal Measurements 1 - 15 Mc - M. Bernstein

11-15-261 The Effects of Frequency Multipliers on the Uncertainty of a Frequency Measurement - J. Rarity, L. Saporta and G. Weiss

11-16-187 The Measurement of the Parameters of High Frequency Filter Crystals - F. K. Priebe

11-17-289 Reliability of Military Quartz Crystal Units - W. Ingling and C. E. Jones

11-17-312 Spurious Modes in AT-Cut Quartz Crystals - A. E. Anderson

11-17-314 Temperature Testing Tight Tolerance Crystal Units - G. Bistline, Jr.

11-17-316 The Hybrid-Coil Bridge Method of Measuring Unwanted Modes of Vibration in Quartz Crystals - W. H. Horton and R. C. Smythe

11-17-537 Accuracy of VHF Filter Crystal Measurements - A. D. Ballato and F. K. Priebe

11-17-602 Measurement of the Instantaneous Frequency and Phase Stability of Frequency Standards by Means of Frequency Comparators - B. Perzen

11-18-243 Frequency and Timing Control Requirements for Future Military Communication Equipment - M. M. Baltas

11-18-407 Quantity Testing of Moderate-Precision Crystal Units - G. E. Buroker

11-18-441 Design Considerations for Crystal Impedance Meters - C. L. Shibla

11-18-458 Comparison of Various Methods Used for Determination of Quartz Crystal Parameters in the Frequency Range 1 to 30 MC - F. K. Priebe and A. D. Ballato

11-19-49 Aerospace Crystal Environmental Requirements - D. B. Leeson

11-19-436 Comparison of Crystal Measurement Equipment - W. H. Horton and S. B. Boor

11-19-469 Automatic Crystal Aging Assembly - M. Bernstein

CATEGORY 11 (Cont'd):

11-19-487 Attenuation and Resistance Measurements of Unwanted Modes of Quartz Crystals - F. K. Priebe

11-19-655 Modification of Crystal Impedance Meter TS-710/TSM - C. L. Shibla

11-20-465 Measurement of Mode Parameters by Sweep Frequency Methods in the Frequency Range from 20 to 250 MHz - F. K. Priebe and A. D. Ballato

11-20-636 Precision Frequency Measurement of Satellite Emitted Beacon Signals - P. R. Arendt

11-20-648 Experimental Frequency-Measuring Receiver System - F. D. Lewis

11-20-661 Digital and Automatic Printing Frequency Counter System - U. E. Adelsberger

11-20-672 A New Instrument for Automatic Measurement of Microwave Frequencies - R. L. Allen

11-21-273 Short Term Frequency Stability Measurements - M. E. Frerking

11-22-46 Writing Crystal Specifications - J. Holmbeck

11-22-163 Temperature Testing Quartz Crystals, Equipment and Methods - G. Bistline and R. Pompeo

11-22-164 Reliable and Repeatable Measurements of Frequency and Resistance Changes of Quartz Crystals due to Wide Temperature Variations - R. Schade

11-22-232 Precision Measurement of the Frequency Aging of Quartz Crystal Units - M. Bernstein

11-22-248 Measurement Techniques for Quartz Crystals - C. A. Adams

11-22-259 Technique for Crystal Resonance Measurements Based on Phase Detection in a Transmission Type Measurement System - R. P. Grenier

11-22-282 Newly Developed Crystal Measurement Instruments - O. P. Layden, A. D. Ballato and C. L. Shibla

11-22-592 Long-Term Frequency Stability Measurement of Rubidium Gas Cell Frequency Standards - A. R. Chi, J. H. Roeder, S. C. Wardrip and B. Kruger

11-23-93 Vector Voltmeter Crystal Measurement System - M. E. Frerking

11-23-102 On Precision Measurements of Frequency and Resistance of Quartz Crystal Units - C. Franx

11-23-111 Another Look at Specifying a Crystal - D. W. Nelson

11-23-122 Temperature Run, MIL-C-3098, Amendment I - R. Pompeo and F. Wolf

11-23-223 A Carrier Suppression Technique for Measuring S/N and Carrier/Sideband Ratios Greater than 120 dB - C. H. Horn

11-24-168 Precision Measurement of Crystal Frequency by Means of "Center Line Method" - I. Koga

11-24-177 Quartz Crystal Measurements - E. Hafner, A. Ballato and P. Blomster

11-24-301 Frequency Comparison of Five Commercial Standards with a NASA Experimental Hydrogen Maser - A. R. Chi, F. G. Major and J. E. Lavery

11-25-113 Measurement of Vibration Modes of Piezoelectric Resonators by Means of Holography - Y. Tsuzuki, Y. Hirose and K. Ijiama, Yokahama National University of Japan

11-25-118 Study of Frequency Control Devices in the Scanning Electron Microscope - R. J. Gerdes and C. E. Wagner, Georgia Institute of Technology

11-25-134 Using a Pendulum Diffractometer to Improve Precision of X-Raying Quartz Crystals - G. E. Nemetz, General Electric Company

11-25-148 Standards and the Frequency Control Industry - J. D. Holmbeck, Northern Engineering Laboratories

11-25-222 Frequency Modulation Analysis with the Hadamard Variance - R. A. Baugh, Hewlett-Packard Company

11-25-226 High Quality Quartz Crystal Oscillators: Frequency Domain and Time Domain Stability - H. Brandenberger and F. Hadorn, Ebauches, S. A. Switzerland and D. Halford and J. H. Shoaf, National Bureau of Standards

11-26-20 Problems in the Definition and Measurement of Frequency Stability - J. A. Barnes, NBS

11-26-29 Flicker and Frequency Phase, and White Frequency and Phase Fluctuations in Frequency Sources - D. J. Healey, III, Westinghouse Electric Corporation

CATEGORY 11 (Cont'd):

11-26-79 Calculator Controlled Testing of Crystals and Crystal Filters - G. E. Nelson, Hewlett-Packard Laboratories

11-26-159 The Practical Aspects of International Standardization in the Frequency Control Field - E. Kentley, C. R. Snelgrove Company, Canada

11-26-258 US Army Calibration Program - J. M. Rivamonte, Redstone Arsenal, Alabama

11-26-260 USAF Time and Frequency Calibration Program - J. F. Barnaba, Newark Air Force Station, Ohio

11-27-55 Practical Crystal Measurements and Standardization - W. S. Metcalf, Cathodeon Crystals Limited

11-27-63 An Automatic Crystal Measurement System - H. S. Pustarfi and W. L. Smith, Bell Telephone Laboratories

11-27-421 Spectral Density Analysis: Frequency Domain Measurements of Frequency Stability - D. Halford, J. H. Shoaf and A. S. Risley National Bureau of Standards

11-27-432 A New Development in the Field of Spectrum Analyzers - K. Zirwick, Rohde and Schwarz

11-27-440 Short and Long Term Stability Measurements Using Automatic Data Recording System - J. Bowman, Naval Research Laboratory

11-28-49 Precision Determination of Parameters of VHF Crystals - L Koga, Kokusai Denshin Denwa Company

11-28-177 Direct Measurements of The Inherent Frequency Stability of Quartz Crystal Resonators - A. E. Wainwright, F. L. Walls and W. D. McCaa, National Bureau of Standards

11-28-184 Low Noise Measuring Techniques - M. Bloch, A. Vulcan, Frequency Electronics, Inc.

11-28-190 L(f) Measurements on UHF Sources Comprising VHF Crystal Controlled Oscillator Followed by a Frequency Multiplier - D. J. Healey III, Westinghouse

11-29-237 A Rapid and Simple In-Process Test Method Designed to Improve Quality of Quartz Resonators in Current Demand Today - P. Bryan, Colorado Crystal Corporation

11-29-270 Test Set for the Measurement of Transmitter Stability Parameters - J. M. Milan, ITT Gilfillan

11-29-394 A Time Domain Method for Measurement of the Spectral Density of Frequency Fluctuations at Low Fourier Frequencies - P. Lesage and C. Audoin, Université Paris-Sud

11-29-404 Picosecond Time Difference Measurement System - D. W. Allan, National Bureau of Standards and H. Daams, National Research Council

11-29-412 Timekeeping and the Reliability Problem - D. B. Percival and G. M. R. Winkler, U. S. Naval Observatory

11-29-425 NTS-1 (Timation III) Quartz and Rubidium Oscillator Frequency Stability Results - T. B. McCaskill and J. A. Buisson, Naval Research Laboratory

11-30-92 Implementation of Bridge Measurement Techniques for Quartz Crystal Parameters - E. Hafner, US Army Electronics Command and W. Riley, GenRad

11-30-269 Design Considerations in State-of-the-Art Signal Processing and Noise Measurement Systems - F. L. Walls, S. R. Stein, J. E. Gray, D. J. Glaze and D. W. Allan, National Bureau of Standards

CATEGORY 12:

Other Topics

12-10-455 A Transistorized 1 Mc/Sec Frequency Counter - Nisson Sher and Ralph Goodwin, Philco Corporation

12-12-623 The Velocity of Light - J. R. Zacharias, Massachusetts Institute of Technology

12-12-624 Experimental Tests of Special and General Relativity by Accurate Timing Devices - C. H. Townes, Columbia University

12-13-477 Analysis and Presentation of Data for a Manufacturers' Handbook - R. Bennett, C. Rutkowski and L. A. Tyler

12-13-542 Induced and Spontaneous Emissions in a Coherent Field - I. R. Senitzky

12-13-543 A Relativity Experiment with MASERs - J. Cedarholm

12-13-629 Time Scales in the Structure of the Universe - R. H. Dicke

12-13-697 Frequency Control Research and Development in Western Europe - J. C. B. Missel

12-14-217 The Micro-Module Program - V. Kublin

12-14-248 Is the Fine Structure Constant Invariant - R. H. Dicke

12-16-211 The Coming Era of Microelectronics - J. D. Meindl and M. Tobman

12-16-241 Frequency Control Research and Development in Western Europe - U. Adelsberger

12-18-5 Professor Cady's Work in Crystal Physics - H. Jaffe

12-18-12 Developments in Ultrasonics - W. P. Mason

12-18-43 Piezoelectricity - Frequency Control - R. Bechmann

12-19-59 The Increasing Applications of Tuning Forks and Other Vibrating Metal Resonators in Frequency Control Systems - F. Dostal

12-20-70 Crystals and Filters - The State-of-the-Art in Europe - W. J. Young

12-22-35 Frequency Management and Spectrum Development within the Executive Branch of the Government - W. E. Plummer

12-22-42 Piezoelectric Training Program at McMurry College - V. E. Bottom

12-22-168 Report and Analysis of 1967 Quartz Crystal Industry Survey - J. H. Sherman, Jr.

12-23-313 Precision Time Measurements of Optical Pulsars - P. Boynton, R. B. Partridge and D. T. Wilkinson

12-24-1 Introductory Session Honoring Roger Sykes on His Retirement - E. A. Gerber

12-24-8 Introductory Session Honoring Roger Sykes on His Retirement - W. P. Mason

12-24-13 Introductory Session Honoring Roger Sykes on His Retirement - J. M. Wolfskill

12-24-172 A Report on IEC Technical Committee TC-49 - C. Franx

12-25-1 A Quarter Century of Progress in the Theory and Development of Crystals for Frequency Control and Selection - E. A. Gerber, USAECOM and R. A. Sykes, Bell Telephone Laboratories

12-26-1 An Overview of Electronic Equipment Reliability - A. W. Rogers, ECOM

12-28-57 Technical Aspects of Crystal Wrist Watches - H. Yoda and N. Horie, Nihon Dempa Kogyo Company, Ltd.

AUTHOR INDEX

PROCEEDINGS - ANNUAL FREQUENCY CONTROL SYMPOSIA

No.	YEAR	DOCUMENT NO.	OBTAIN FROM*	COST
10	1956	AD 298322	NTIS	$13.75
11	1957	AD 298323	"	16.25
12	1958	AD 298324	"	16.25
13	1959	AD 298325	"	18.75
14	1960	AD 246500	"	11.75
15	1961	AD 265455	"	10.50
16	1962	AD 285086	"	12.00
17	1963	AD 423381	"	16.25
18	1964	AD 450341	"	16.25
19	1965	AD 471229	"	16.25
20	1966	AD 800523	"	16.25
21	1967	AD 659792	"	13.75
22	1968	AD 844911	"	16.25
23	1969	AD 746209	"	9.75
24	1970		EIA	6.50
25	1971	AD 746211	NTIS	10.50
26	1972	AD 771043	"	10.00
27	1973	AD 771042	"	12.00
28	1974		EIA	7.50
29	1975		EIA	8.00
30	1976		EIA	8.00

*NTIS - National Technical Information Service
Sills Building
5285 Port Royal Road
Springfield, Virginia 22161

NTIS prices are as of October 1976 and are subject to change without notice.

*EIA - Publications Committee
Annual Frequency Control Symposium
c/o Electronic Industries Association
2001 Eye Street, N.W.
Washington, D.C. 20006

Remittance must be enclosed with all orders. For orders placed with NTIS from outside the United States, add $2.50 per copy for handling and mailing (surface mail).

When referencing these Proceedings, please use the format shown in the following examples:

(1) W.D. Beaver, "Theory and Design of the Monolithic Crystal Filters" Proceedings, 21st Annual Symposium on Frequency Control, US Army Electronics Command, Fort Monmouth, N.J. pp 179-199, (1967). National Technical Information Service Accession Nr. AD 659792.

(2) H. M. Greenhouse, R.L. McGill, D.P. Clark, "A Fast Warmup Quartz Crystal Oscillator". Proceedings 27th Annual Symposium on Frequency Control, US Army Electronics Command, Fort Monmouth, N.J. pp 199-218, (1973). Copies available from Electronic Industries Association, 2001 Eye Street, NW, Washington, D.C. 20006.